申报	系列：教师系列
	专业：农业机械化工程
	职称：教授

业绩成果材料

（申报人的业绩成果材料包括论文、科研项目、获奖以及其他成果等）

单　位（二级单位）：　　工程学院　　

姓　名　　张亚莉　　

材料核对人：　　单位盖章：

核对时间：

华南农业大学制

目　录

一、教学研究业绩

1.教学研究项目：广东省教育厅关于公布2025年广东省研究生教育创新计划项目的立项通知（主持）.....1
2.教学研究项目：广东省教育厅关于2024 年度广东省本科高校教学质量与教学改革工程建设项目的立项名单的通知（主持）.....5
3.教学研究项目：关于公布华南农业大学2025年校级本科教学质量与教学改革工程项目立项名单的通知（主持）.....11
4.教学研究项目：关于华南农业大学 2023年校级教改项目和质量工程项目的立项通知及有关佐证材料（参加）.....15
5.教学成果奖立项通知：2025年广东省人力资源和社会保障厅、广东省教育厅关于表彰全省学校（高等教育）优秀教学成果奖的决定（参加）.....24
6.教学成果奖证书：2025年校级本科教学成果一等奖（参加）.....29
7.教学成果奖证书：2021年校级本科教学成果二等奖（参加）.....30
8.编写教材：《试验设计与数据统计分析》（副主编）.....31

二、科研项目

1.主持：关于国家重点研发计划“工厂化农业关键技术与智能农机装备”重点专项2023年度项目的立项通知及课题二主持有关佐证材料.....36
2.主持：广东省重点领域研发计划项目“水稻生产地面-航空高效施药智能装备研究与示范”子课题佐证材料.....45
3.主持：广东省省级科技计划项目“精准农业航空遥感技术及平台在巴基斯坦的示范应用”佐证材料.....58

4.主参：广东省自然科学基金面上项目“多旋翼农用无人机能源载荷动态匹配机制”项目佐证材料.....61
5.主参：广州市科技计划项目“基于 GNSS-RTK 的精准农业航空遥感技术与应用”项目佐证材料.....65

三、论文、著作等

1.检索证明.....71
2.以第一作者发表本专业论文情况
2.1.CURI-YOLOv7: A Lightweight YOLOv7tiny Target Detector for Citrus Trees from UAV Remote Sensing Imagery Based on Embedded Device. Remote Sensing, 2023, 15, 4647.....79
2.2.Advances and Developments in Monitoring and Inversion of the Biochemical Information of Crop Nutrients Based on Hyperspectral Technology. Agronomy, 2023, 13, 2163 96
2.3.Detection of Power Poles in Orchards Based on Improved Yolov5s Model. Agronomy, 2023, 13, 1705 .105 121
2.4.Research hotspots and frontiers in agricultural multispectral technology: Bibliometrics and scientometrics analysis of the Web of Science. Frontiers in Plant Science, 2022, 13, 955340 135
2.5.Detection of Rice Spikelet Flowering for Hybrid Rice Seed Production Using Hyperspectral Technique and Machine Learning. Agriculture, 2022, 12, 755 152
2.6.Research Progress and Prospects of Agricultural Aero-Bionic Technology in China. Applied Science,

2021,11, 10435.....169
2.7. Development and Prospect of UAV-Based Aerial Electrostatic Spray Technology in China. Applied Science, 2021, 11, 4071 187
2.8.国外农业航空静电喷雾技术研究进展与借鉴. 农业工程学报，2021，37(6)：50-59. 202
2.9.基于可见光图像的水稻颖花开花状态检测方法. 农业工程学报，2021，37(9)：253-262 212
2.10.M45 型多旋翼植保无人机减量施药对稻飞虱防治效果的影响. 华南农业大学学报, 2022, 41(6): 36-42 222
2.11.基于改进 APF-FMT*的农业机器人路径规划算法. 华南农业大学学报，2024,45（3）：408-415 229
3.以通讯作者发表本专业论文情况
3.1.Non-destructive prediction of soluble solids content and firmness and maturity determination of guava fruit using color and fluorescence imaging. Postharvest Biology and Technology 227 (2025) 113620 237
3.2.Multiple light sources excited fluorescence image-based non-destructive method for citrus Huanglongbing disease detection. Computers and Electronics in Agriculture 237 (2025) 110549.....246
3.3.Droplet distribution in cotton harvest aid application vary with the interactions among the unmanned aerial vehicle spraying parameters. Industrial Crops &Products. 2021, 163, 113324.....262
3.4.Citrus huanglongbing detection: A hyperspectral

data-driven model integrating feature band selection with machine learning algorithms. Crop Protection 188 (2025) 107008.....272
3.5.Design of Chili Field Navigation System Based on Multi-Sensor and Optimized TEB Algorithm. Agronomy, 2024, 14, 2872 283
3.6.Fluorescence spectroscopy detection of carbendazim residue in cucumber juice based on BC. Journal of Food Composition and Analysis , 2024, 130(2024): 106157 300
3.7.Deep-Learning Based Rice Disease and Insect Pest Detection on a Mobile Phone. Agronomy, 2023, 13, 2139 311
3.8.Inversion of Leaf Area Index in Citrus Trees Based on Multi-Modal Data Fusion from UAV Platform. Remote Sensing, 2023, 15, 3523.....331
3.9.Design and validation of a multi-objective waypoint planning algorithm for UAV spraying in orchards based on improved ant colony algorithm. Frontiers in Plant Science, 2023, 14: 1101828.....353
3.10.Extraction of Citrus Trees from UAV Remote Sensing Imagery Using YOLOv5s and Coordinate Transformation. Remote Sensing, 2022, 14, 4208.....367
3.11.Canopy Volume Extraction of Citrus reticulate Blanco cv. Shatangju Trees by UAV Image-Based Point Cloud Deep Learning. Remote Sensing. 2021, 13, 3437 388

3.12.Identification of Male and Female Parents for Hybrid Rice Seed Production Using UAV-Based Multispectral Imagery. Agriculture，2022，12，1005.....408
3.13.Lightweight Semantic Segmentation Network for Realtime Weed Mapping Using Unmanned Aerial Vehicles. Applied Sciences，2020，10，7132.....424
3.14.WSN-Assisted UAV Trajectory Adjustment for Pesticide Drift Control. Sensors，2020，20，5473...435
3.15.基于深度强化学习的农田节点数据无人机采集方法. 农业工程学报，2022，38(22)：41-51.....461
3.16.P20 型植保无人机防治稻纵卷叶螟的减量施药研究. 农业工程学报，2021，37(15)：53-59.....473
3.17.基于无人机遥感影像的沙糖橘果树提取方法研究. 华南农业大学学报，2020，41(6)：126-133.....480

四、科研成果

1.科技奖励证书
1.1.广东省农业技术推广一等奖“智能植保无人机装备及施药技术的研发与示范推广”.....488
1.2.大北农科技奖“植保无人飞机精准喷施关键技术创新与应用”.....489
2.知识产权
2.1.专利授权证书：发明专利-一种用于检测植物表皮荧光特性的图像获取装置.....490
2.2 专利授权证书：发明专利-一种用于 DS18B20 温度传感器的总线信号隔离电路.....491
2.3.专利授权证书：发明专利-一种专用于农田信息检测小

车的电路系统.....492
2.4.专利授权证书：发明专利-基于手持式分光辐射谱仪的水稻颖花开花状态检测方法.....493
2.5.专利授权证书：发明专利-一种搭载于植保无人机的静电喷雾装置.....494
2.6.专利授权证书：发明专利-一种基于无人机遥感影像的杂交水稻父母本识别提取方法.....495
2.7.专利授权证书：发明专利-一种植保无人机液位测量装置.....496
2.8.专利授权证书：发明专利-太阳能农用无人机及农情遥感监测方法.....497
2.9.专利授权证书：发明专利-一种航空静电喷雾设备中的喷头调节装置.....498
2.10.专利授权证书：实用新型专利-一种存储式采摘机器人.....499
2.11.专利授权证书：实用新型专利-一种陆空两用单驱动的多旋翼无人机.....500
2.12.专利授权证书：实用新型专利-一种航空静电喷雾设备中的挂载安装机构.....501
2.13.专利授权证书：实用新型专利-一种可收集式小功率马铃薯收获机.....502
2.14.专利授权证书：实用新型专利-一种便携式光谱仪检测装置.....503
2.15.专利授权证书：实用新型专利-一种水体参数检测装置.....504
2.16.专利授权证书：实用新型专利-一种可防潮除湿的电气箱.....505

2.17.专利授权证书：实用新型专利-一种水流速度检测装置.....506
2.18.专利授权证书：实用新型专利-一种植保无人机的药液余量检测装置.....507
2.19.专利授权证书：实用新型专利-一种农田水层高度在线监测装置.....508
3.标准
3.1 行业标准：NY/T3893-2021 遥控飞行喷雾机棉花脱叶催熟作业规程，农业农村部.....509
3.2 行业标准：NY/T4260-2022 植保无人飞机防治小麦病虫害作业规程，农业农村部.....515
4.科研平台
4.1 国家精准农业航空施药技术国际联合研究中心.....522

五、其他业绩

1.指导学生学科竞赛
1.1.第二十七届中国机器人及人工智能大赛全国总决赛二等奖“机器人应用赛（授粉机器人）”.....523
1.2.2025 年睿抗机器人开发者大赛（RAICOM）全国总决赛三等奖“银龄守护适老化服务机器人创新竞赛”.....524
1.3.第 21 届全国大学生信息安全与对抗技术竞赛智能安全赛全国总决赛二等奖“植保机器人”.....525
1.4.第二十五届中国机器人及人工智能大赛全国总决赛二等奖“机器人应用赛（智慧农业）”.....526
1.5.2025 中国智能机器人格斗及竞技大赛（学生赛）一等奖“智能机器人创新设计”.....527
1.6.中国国际飞行器设计挑战赛暨科研类全国航空航天模型锦标赛二等奖“模拟搜救”.....528

1.7.广东省“菱朗杯”第十届广东省汽车与农机电子环保大赛优秀指导老师.....529
2.个人荣誉
2.1.校级“十佳本科生班主任”证书.....530
2.2.校级“优秀共产党员”证书.....531
3.社会服务
3.1.国家航空植保科技创新联盟副秘书长.....532
4.国际交流
4.1.主持：2025 年国家留学基金委“精准农业航空应用技术国际化创新型人才培养项目”.....533

广 东 省 教 育 厅

粤教研函〔2025〕1号

广东省教育厅关于公布2025年广东省研究生教育创新计划项目的通知

各研究生培养单位:

为加强创新人才培养体系建设，进一步改革培养机制和创新人才培养模式，加强研究生创新能力培养的平台建设，形成有利于高层次、高质量、创造性人才培养的研究生培养体系，进一步提高研究生的培养质量，今年我厅继续实施广东省研究生教育创新计划项目。经学校推荐并组织专家评审，现认定“第十二届全国中文学科博士生学术论坛”等90个项目立项为2025年广东省研究生学术论坛，“2025年中国哲学暑期讲习班”等36个项目立项为2025年广东省研究生暑期学校，“香港高水平大学研究生教育对比研究”等182个项目立项为2025年广东省学位与研究生教育改革研究项目，“磁共振成像数据分析专题”等99项课程立项为2025年广东省研究生课程建设项目，“MBA《创新创业管理》教学案例库”等97个项目立项为2025年广东省专业学位研究生教学案例库建设项目，“中山大学-深圳市捷佳伟创新能源装备股份有限公司专业学位研究

生教育创新基地”等89个基地为2025年广东省联合培养研究生创新基地。具体名单附后。

请各有关高校根据相关的规定要求，切实履行管理职责，进一步完善管理制度，规范项目管理，为项目实施提供支持保障，确保实施进度，达到预期目标。

附件：2025年广东省研究生教育创新计划项目一览表（分发）

广东省教育厅

2025年6月27日

公开方式：依申请公开

校对人：杨立群

2025年广东省研究生教育创新计划项目一览表（华南农业大学）

序号	学校名称	项目类别	项目（基地）名称	学科领域	负责人姓名	项目批准号
1	华南农业大学	学位与研究生教育改革研究项目	“双一流”学科建设与拔尖创新型研究生人才的“双向融合”培养模式探索	种子科学与技术	何永奇	2025JGXM_020
2	华南农业大学	学位与研究生教育改革研究项目	“双一流”背景下农林类高校研究生导学思政育人模式探析——基于华南农业大学的实证研究	思想政治教育	陈建平	2025JGXM_021
3	华南农业大学	学位与研究生教育改革研究项目	“专业学位研究生专项制改革项目”研究生培养模式的机制和推广研究	畜牧	谢青梅	2025JGXM_022
4	华南农业大学	学位与研究生教育改革研究项目	基于“百千万工程”的环境学科研究生培养模式创新研究	环境科学与工程	林云琴	2025JGXM_023
5	华南农业大学	学位与研究生教育改革研究项目	人工智能产教融合协同育人模式与机制研究	计算机应用技术	王美华	2025JGXM_024
6	华南农业大学	学位与研究生教育改革研究项目	基于“科教+产教”双融合驱动的专业学位研究生校企协同育人机制改革与探索	工学	王建华	2025JGXM_025
7	华南农业大学	学位与研究生教育改革研究项目	MTI农业科技翻译人才产学研用一体化培养模式研究	翻译学	杜　娇	2025JGXM_026
8	华南农业大学	学位与研究生教育改革研究项目	数字技术赋能研究生思想政治教育精准化研究	马克思主义理论	唐土红	2025JGXM_027
9	华南农业大学	联合培养研究生创新基地	广东长隆集团有限公司	兽医学	孙　坚	/
10	华南农业大学	联合培养研究生创新基地	广州市威控机器人有限公司	机械（机器人工程）	莫嘉嗣	/
11	华南农业大学	联合培养研究生创新基地	广东非遗梦文化产业有限公司	设计学	曾智林	/
12	华南农业大学	研究生课程建设项目	农产品安全生产技术与应用	资源利用与植物保护	钟国华	2025KCJS_017
13	华南农业大学	研究生课程建设项目	茶叶生物化学研究法	茶学	张凌云	2025KCJS_018
14	华南农业大学	研究生课程建设项目	高级植物学	农学	白　玫	2025KCJS_019
15	华南农业大学	研究生课程建设项目	有限元与ANSYS	农业工程	胡圣荣	2025KCJS_020

序号	学校名称	项目类别	项目（基地）名称	学科领域	负责人姓名	项目批准号
16	华南农业大学	研究生课程建设项目	新能源材料与器件	化学工程与技术	梁业如	2025KCJS_021
17	华南农业大学	研究生学术论坛	广东省研究生“青发”学术论坛	作物学	赫圣博	2025XSLT_012
18	华南农业大学	研究生学术论坛	广东省研究生学术论坛-预防兽医学分论坛	兽医学	郭亚琼	2025XSLT_013
19	华南农业大学	研究生学术论坛	广东省研究生学术论坛-新一代电子信息技术分论坛	电子信息技术	李　震	2025XSLT_014
20	华南农业大学	专业学位研究生教学案例库建设项目	植物病原真菌学教学案例库建设	资源利用与植物保护	孔广辉	2025ANLK_008
21	华南农业大学	专业学位研究生教学案例库建设项目	动物微生态与肠道免疫教学案例库	畜牧	张新珩	2025ANLK_009
22	华南农业大学	专业学位研究生教学案例库建设项目	工程伦理教学案例库建设	机械	张亚莉	2025ANLK_010
23	华南农业大学	专业学位研究生教学案例库建设项目	数智时代《财务管理》教学案例库	会计	周小春	2025ANLK_011
24	华南农业大学	专业学位研究生教学案例库建设项目	城乡治理中的政府实践与公共政策创新	公共管理	张　玉	2025ANLK_012
25	华南农业大学	专业学位研究生教学案例库建设项目	法学研究生教学案例库建设	法律	邢长策	2025ANLK_013

广 东 省 教 育 厅

粤教高函〔2024〕30号

广东省教育厅关于公布2024年度广东省本科高校教学质量与教学改革工程建设项目立项名单的通知

各本科高校:

按照《广东省教育厅关于开展2024年度广东省本科高校教学质量与教学改革工程项目申报推荐工作的通知》等文件安排，经学校遴选推荐、省教育厅审核、公示、复审等环节，现将2024年省本科高校质量工程建设项目立项名单予以公布，并就有关事项通知如下:

一、立项情况

确定立项建设省级实验教学示范中心35个、教学研究中心1个、校企联合实验室31个、科产教融合实践教学基地66个、大学生社会实践教学基地47个、教师教学发展中心3个、课程教研室147个、现代产业学院32个、专项人才培养计划54项、高等教育教学改革项目850项。具体立项名单见附件。

二、项目管理

（一）本次公布项目均为省质量工程建设项目，建设项目经学校组织建设、校内结题并通过省教育厅统一组织项目验收后，正式认定为省级项目。

（二）项目正式实施前，请确保已对项目建设目标、建设举措、预期成果、建设进度安排等进行科学论证，论证专家应不少于5人，且至少有三分之一来自外校。论证后的目标、任务等将作为项目结题验收时的重要依据。

（三）项目日常管理由学校主管部门负责，学校应统筹做好项目中期检查、校内结题验收等工作。校内结题时，邀请校外评审专家人数不得少于专家总人数的三分之二。满足以下条件的项目，经学校正式申请，可以参与省教育厅统一组织的项目验收:

1.项目已完成立项时设定的主要建设任务和目标;

2.项目已取得标志性建设成果，且该成果已在教学实践中得到检验和有效应用;

3.已按照要求完成项目校内结题;

4.符合当年度省统一验收规定的其他条件。

各校质量工程建设项目管理情况，将作为学校下一年度项目立项限额的参考依据。

（四）项目实施过程中，其名称、建设内容（任务）、建设目标、建设周期、主要负责人、预期成果等发生重大变更的，需由时任项目负责人在发生变更后及时提出，经学校项目主管

部门审核后由学校正式来函说明原因；擅自变更上述内容的，验收评定时列为不通过。

三、其他事项

（一）2024 年度各校向省教育厅推荐并获得立项的项目，学校须将项目校内评审、推荐及论证相关材料妥善保存，留底备查。

（二）各校要统筹本校“冲补强”提升计划资金及自有资金对立项项目予以资助，项目获得学校资助情况将作为项目结题验收时重要考察因素之一。如项目建设中取得具有推广价值的优秀成果，请及时形成书面材料报省教育厅高教处。

联系人：李成军，联系电话：020-37626882。

附件：2024 年度广东省本科高校教学质量与教学改革工程建设项目立项名单

广东省教育厅

2024 年 12 月 19 日

公开方式：依申请公开

校对人：李成军

附件：

2024年度广东省本科高校教学质量与教学改革工程立项项目名单

序号	项目类型	单位名称	项目名称	负责人
1	实验教学示范中心	中山大学	医学院基础医学实验教学中心	田国宝
2	实验教学示范中心	中山大学	微电子科学与工程实验教学中心	虞志益
3	实验教学示范中心	华南理工大学	生物医学创研创新实验中心	付晓玲
4	实验教学示范中心	华南理工大学	集成电路教学与创新实验中心	李斌
5	实验教学示范中心	华南理工大学	电工电子实验教学示范中心	汪娟娟
6	实验教学示范中心	暨南大学	密码科学与技术实验教学示范中心	赖俊祚
7	实验教学示范中心	南方医科大学	法医病理学实验教学示范中心	乔东访
8	实验教学示范中心	南方医科大学	医学人才临床综合能力培养数字化实验教学示范中心	沈洁
9	实验教学示范中心	广州中医药大学	中医养生学实验教学示范中心	黎晖
10	实验教学示范中心	广州中医药大学	临床技能培训实验教学示范中心	邬素珍
11	实验教学示范中心	华南师范大学	教育学实验教学示范中心	李盛兵
12	实验教学示范中心	广东工业大学	人因环境实验教学示范中心	周祥
13	实验教学示范中心	广东海洋大学	数字经济与产业发展综合实验教学示范中心	周昌仕
14	实验教学示范中心	仲恺农业工程学院	大数据技术实验教学示范中心	刘双印
15	实验教学示范中心	广东药科大学	中医临床技能教学示范中心	肖炜
16	实验教学示范中心	岭南师范学院	地理学实验教学示范中心	牛东风
17	实验教学示范中心	广州大学	心理学实验教学示范中心	聂衍刚
18	实验教学示范中心	广州医科大学	医学模拟教育中心	刘翔
19	实验教学示范中心	深圳大学	前沿交叉学科教学实验中心	李猛
20	实验教学示范中心	南方科技大学	人工智能实验教学示范中心	郝祁

序号	项目类型	单位名称	项目名称	负责人
484	高等教育教学改革项目	暨南大学	基于科产教融合理念的《金融工程》课程改革创新与实践	唐弢
485	高等教育教学改革项目	暨南大学	AI 赋能“组织学与胚胎学”智慧课程精准施教的探索与实践	王广
486	高等教育教学改革项目	暨南大学	基于 5E 教学模式的“材料分析与表征实验”教学改革研究与实践	文伟
487	高等教育教学改革项目	暨南大学	基于 OBE 理念的“Python 数据挖掘与可视化”课程“四维融合”创新教学改革研究与实践	谢贤芬
488	高等教育教学改革项目	暨南大学	基于知识图谱的“微机原理与应用”AI 课程建设与实践	谢勇君
489	高等教育教学改革项目	暨南大学	AI 驱动的“师-生-机”三元融合智慧课程体系的构建及其在混合式教学中的创新实践	杨帅
490	高等教育教学改革项目	暨南大学	文明互鉴视域下外国文学课程群课程思政建设与实践	曾诣
491	高等教育教学改革项目	暨南大学	人工智能视域下培养应用型新闻人才 社会调查能力的改革与实践	张岚
492	高等教育教学改革项目	暨南大学	AI 赋能的光电专业港澳台侨学生教育个体性与适应性改革与实践	郑华丹
493	高等教育教学改革项目	暨南大学	人工智能赋能新媒体艺术人才培养的创新与实践	郑晓君
494	高等教育教学改革项目	暨南大学	基于人工智能+药物分析的复合型人才培养模式改革与实践	周海波
495	高等教育教学改革项目	暨南大学	港澳台侨生（外招生）精神护理人才培养的智能化混合教学模式探索	朱晓雯
496	高等教育教学改革项目	华南农业大学	基于新质生产力的水产养殖学专业实践教学体系构建与实践	孙际佳
497	高等教育教学改革项目	华南农业大学	基于 OBE 理念的工程伦理教学实施体系研究与实践	张亚莉
498	高等教育教学改革项目	华南农业大学	“长基计划”下新文科历史学课程体系的改革与实践	衷海燕
499	高等教育教学改革项目	华南农业大学	整体性比较视角下高校“四史”教育之党史课程内容体系构建研究	王景奇
500	高等教育教学改革项目	华南农业大学	电类基础课程群融合协同《数字电子技术》课程思政建设模式探索与实践	赵文锋

华南农业大学文件

华南农教〔2025〕57号

关于公布华南农业大学2025年度校级本科教学质量与教学改革工程项目立项名单的通知

各学院、部处、各单位:

根据《关于开展2025年度校级本科教学质量与教学改革工程项目申报工作的通知》精神,经项目负责人申请、所在单位推荐、本科生院审核、学校组织专家评审和公示(无异议)等程序,决定立项“善境伦理学与风景园林专业实践教学深度融合的探索与实践”等127个项目为2025年度校级本科教学改革项目,立项“筑基·焕新·赋能:食品质量与安全专业‘新工科’建设暨工程教育认证提质创新工程”等52个项目为2025年度校级本科质量工程项目。具体名单见附件。

请各项目负责人按照项目建设任务及要求,及时开展各项改

革工作；各单位要切实履行项目建设主体责任，加强对项目建设的督促、指导，以确保项目建设任务高质量完成。

特此通知。

附件：1. 2025年度校级本科教学改革项目立项名单

2. 2025年度校级本科质量工程项目立项名单

华南农业大学

2025年10月14日

（联系人：孙齐胜；电　话：85288020）

公开方式：主动公开

华南农业大学党政办公室　　2025年10月15日印发

2025年度质量工程项目立项名单

序号	项目类别	项目名称	所属单位	项目负责人	职称	项目组成员
1	专业认证	筑基·焕新·赋能：食品质量与安全专业 “新工科”建设暨工程教育认证提质创新工程	食品学院	徐振林	教授	雷红涛、赵雷、温棚、宋明月、刘晓娟、周爱梅
2	专项人才培养计划	农林院校“智能建造”人才特色班	水利与土木工程学院	李俞谕	教授	张巍、邓建良、李高扬、唐贵和、吕艳梅、黄欢、黄俐、黄继志、杨雨冰
3	校企联合实验室	汽车氛围灯交互设计校企联合实验室	工程学院	曾志雄	高级实验师	高锐涛，苑绍波，江晓聪，李莎莎，杨慧珠，唐孟军，郭晓燕 康志锋，汪隽，赵腾远，郭涵，曾志雄，金鸿，张焕林，王珏
4	现代产业学院	现代演艺产业学院	艺术学院	郝丽	副教授	米平平、郑琳喆、郑丽娜、冯逸章、何唱、王芳、杨翠钰
5	现代产业学院	粤派新式焙烤现代产业学院	食品学院	赵雷	教授	徐振林、杜冰、雷红涛、方祥、范小平
6	课程教研室	土壤生物学课程教研室	资源环境学院	张池	副研究员	刘承帅、宋孟珂、赵兰凤、冯宏、童辉、孙少龙、彭桂香、龚贝妮、徐会娟、蔡燕飞
7	课程教研室	人居环境科学美育教研室	水利与土木工程学院	郭焕宇	教授	李春阳、李晓雪、戚芳妮、舒畅
8	课程教研室	土木工程专业智能建造模块课程教研室	水利与土木工程学院	张敏	副教授	杨雨冰，陈幸斌，王海洋，黄继志，陈穗茵
9	课程教研室	概率论与数理统计课程教研室	数学与信息学院、软件学院	李朗	副教授	张娜、朱玲湘、朱艳科、徐小红、夏英俊、利小玲
10	课程教研室	数据科学与大数据技术教研室	数学与信息学院、软件学院	黄沛杰	副教授	肖磊、刘汉兴、王金凤、林毅申、徐禹洪、古万荣、陈霓、蓝连涛
11	课程教研室	民商民诉法教研室	人文与法学学院	刘万洪	副教授	杨波、张艳琼、顾方愉、钟晓雯、陈莉、刘雪梅、陈维君
12	课程教研室	世界史课程教研室	人文与法学学院	殷小平	副教授	邵兆颖、王跻崭、朱亮、宋跃华、刘玲娣、衷海燕、袁建新
13	课程教研室	森林培育教研室	林学与风景园林学院	何茜	教授	邱权、陈祖静、潘澜、刘效东
14	课程教研室	《水生生物学》课程教研室	海洋学院	杨慧荣	教授	陈世俊 张娅 唐汇娟 何玉慧 李雪竹 杨敏 杨子拓

40	全英教学课程	用户研究与产品定义/User Research and Product Definition	艺术学院	王珺	讲师	陈哲、薛拥军、盘湘龙
41	全英教学课程	全英课程建设项目 《Creative Jewelry Design》设计课	艺术学院	周兮	讲师	梁卉莹、杨翠钰、潘子广
42	全英教学课程	全英课程《计算机图形学》	数学与信息学院、软件学院	廖彬	讲师	蔡贤资，张连宽，梁茹冰，聂笃宪
43	全英教学课程	软件工程全英课程教学	数学与信息学院、软件学院	聂笃宪	副教授	张连宽，梁茹冰，毛卫华，廖彬，刘鹏飞
44	全英教学课程	兽医药理学/Veterinary Pharmacology	兽医学院	于洋	副教授	孙坚、任昊
45	全英教学课程	食品仪器分析（Food Instrumental Analysis）全英课程建设项目	食品学院	宋明月	副教授	陈运娇、肖苏尧
46	全英教学课程	“发酵工程工艺原理”全英课程建设	食品学院	刘韵乐	副教授	徐学锋、魏韬
47	全英教学课程	国际商事仲裁案例研习	人文与法学学院	官隆清	讲师	徐芳、孙梦
48	全英教学课程	法律英语	人文与法学学院	徐冬晓	讲师	王琳、刘凯先
49	全英教学课程	金融计量学全英课程	经济管理学院	王雄志	副教授	谭莹、蔡键，周丽云
50	全英教学课程	公司战略管理全英课程	经济管理学院	左伟	副教授	汪凤桂、蔡文鋆
51	全英教学课程	公共心理学 Public Administration psychology	公共管理学院	张雯闻	副教授	贾海薇 邓永超 贾昕珊 刘辉
52	全英教学课程	《试验设计与数据处理》全英课程建设	工程学院	张亚莉	副教授	杨丹彤、贾瑞昌、黄世醒

华南农业大学文件

华南农教〔2023〕68 号

关于公布华南农业大学 2023 年度校级教改项目和质量工程项目立项的通知

各学院、部处、各单位:

根据《广东省教育厅关于开展 2023 年度广东省本科高校教学质量与教学改革工程项目申报推荐工作的通知》和学校《关于开展 2023 年度本科教学质量与教学改革工程项目申报工作的通知》要求，为进一步推进学校教学改革，建设一流本科教育，提升人才培养质量，学校组织开展了 2023 年度校级本科教学质量与教学改革工程项目遴选工作。

经项目负责人申请、所在单位遴选推荐、学校组织专家评审和公示无异议等程序，确定“高阶思维视域下《种子生物学》‘四维融合’混合式教学模式改革与实践”等122个项目立项为2023年度校级教学改革项目，具体名单见附件1；确定“绿

色与智能精准纳米农药实验室”等47个项目立项为2023年度校级质量工程项目，具体名单见附件2。

请各项目负责人按照项目建设任务及要求，及时开展各项工作，加快推进学校人才培养改革，并力争取得高水平的教学成果。各单位要切实履行项目建设主体责任，加强对项目建设的督促、指导，以确保项目能如期高质量完成建设任务。

特此通知。

附件：1. 华南农业大学2023年校级教改项目立项名单

2. 华南农业大学2023年校级质量工程项目立项名单

华南农业大学

2023年12月13日

（联系人：孙齐胜、孙　航，电　话：85288020、85280052）

公开方式：主动公开

华南农业大学党政办公室　　2023 年 12 月 25 日印发

附件2

华南农业大学2023年校级质量工程项目立项名单

序号	项目编号	项目类别	项目名称	负责人	项目负责人单位
1	ZLGC202301	校企联合实验室	绿色与智能精准纳米农药实验室	张志祥	植物保护学院
2	ZLGC202302	科产教融合实践教学基地	应用化学科产教融合实践教学基地	汤日元	材料与能源学院
3	ZLGC202303	科产教融合实践教学基地	华南农大-梅州广顺海肉牛全产业链科产教融合实践教学基地	李耀坤	动物科学学院
4	ZLGC202304	科产教融合实践教学基地	华南农业大学-广东中芯种业养猪学科产教融合实践教学基地	洪林君	动物科学学院
5	ZLGC202305	科产教融合实践教学基地	大数据分析与应用校企双创实践教学基地	余平祥	数学与信息学院、软件学院
6	ZLGC202306	大学生社会实践教学基地	华南农业大学—广东东图规划科技有限公司	袁中友	公共管理学院
7	ZLGC202307	现代产业学院	陈皮产业学院	梁社坚	生命科学学院
8	ZLGC202308	专项人才培养计划	“大数据+市场营销”实验班人才培养实践探索	林家宝	经济管理学院
9	ZLGC202309	课程教研室	包装印刷技术课程教研室	范小平	食品学院
10	ZLGC202310	课程教研室	岭南建筑课程教研室	周彝馨	水利与土木工程学院
11	ZLGC202311	课程教研室	无机及分析化学实验教研室	倪春林	材料与能源学院

38	ZLGC202338	“大国三农”课程	深挖教学资源、助力乡村振兴—《领导力与高效管理》课程建设探索	郭萍	经济管理
39	ZLGC202339	“大国三农”课程	《公共政策学》“大国三农”课程建设	姜国兵	公共管理学院
40	ZLGC202340	全英课程	《材料工艺与设备》全英课程建设	董汉武	材料与能源学院
41	ZLGC202341	全英课程	全英课程《射频电路理论与设计》建设项目申报书	王建	电子工程学院(人工智能学院)
42	ZLGC202342	全英课程	模式识别与机器学习	骆威	数学与信息学院、软件学院
43	ZLGC202343	全英课程	《用户界面设计》全英课程建设	欧阳文昱	艺术学院
44	ZLGC202344	全英课程	生物专业英语	黄晓	生命科学学院
45	ZLGC202345	全英课程	美国简史	王跻崭	人文与法学学院
46	ZLGC202346	全英课程	国际知识产权保护法	杜菁	人文与法学学院
47	ZLGC202347	全英课程	“农业机械学”全英授课研究与实践	贾瑞昌	工程学院

华南农业大学

全英课程建设项目申报书

申报单位：工程学院

申 报 人：贾瑞昌

课程名称：农业机械学（中文）

Agriculture Mechanics （外文）

课程代码：622114

联系电话：----------

E—MAIL：rcjia@scau.edu.cn

申报日期：2023 年 11 月 30 日

二 〇 二 三 年 十 月

一、课程及主讲教师基本情况

<table>
<tr><td rowspan="2">课程名称</td><td>中文</td><td colspan="4">农业机械学</td></tr>
<tr><td>外文</td><td colspan="4">Agriculture Mechanics</td></tr>
<tr><td colspan="2">课程代码</td><td colspan="2">622144</td><td>学分</td><td>4</td></tr>
<tr><td colspan="2">原版教材名称</td><td colspan="2">Agricultural Machinery for rice production</td><td>原版教材主编</td><td>Shao Yaojian</td></tr>
<tr><td colspan="2">原版教材出版社</td><td colspan="2">Guangdong Science and Technology Press</td><td>出版时间</td><td>1995.12</td></tr>
<tr><td colspan="2">主要参考书</td><td colspan="5">李宝筏.农业机械学.中国农业出版社.2019</td></tr>
<tr><td rowspan="6">课程主讲人</td><td>姓　　名</td><td colspan="2">贾瑞昌</td><td>性别</td><td colspan="2">男</td></tr>
<tr><td>出生年月</td><td colspan="2"></td><td>民　族</td><td colspan="2">汉族</td></tr>
<tr><td>最终学位/授予国家</td><td colspan="2">硕士/中国</td><td>职称/职务</td><td colspan="2">讲师</td></tr>
<tr><td>国外学习/工作研究经历</td><td colspan="5">2014.5-2015.5 美国堪萨斯州立大学 访问学者</td></tr>
<tr><td>近两年承担的本科教学工作（含课程名称、学时等）及教学研究情况（含时间、项目名称、获奖情况等）</td><td colspan="5">农业机械学（双语）　　144 学时
农业生产机械化　　128 学时
机器人概论　　192 学时

2020（JG20174）教学改革项目“　新工科背景下农机丁颖班创新能力培养的研究”2022 已结题

2014 年“以产业发展为导向的农业工程类专业建设研究与实践”项目获得国家教学成果二等奖</td></tr>
<tr><td colspan="6"></td></tr>
<tr><td rowspan="5">课程组其他人员简况</td><td>姓名</td><td>性别</td><td>出生年月</td><td>学历</td><td>职称</td><td>承担的工作</td></tr>
<tr><td>张亚莉</td><td>女</td><td></td><td>博士</td><td>副教授</td><td>经济作物部分</td></tr>
<tr><td>齐龙</td><td>男</td><td></td><td>博士</td><td>研究员</td><td>绪论，全局</td></tr>
<tr><td>杨文武</td><td>男</td><td></td><td>博士</td><td>副教授</td><td>试验</td></tr>
<tr><td></td><td></td><td></td><td></td><td></td><td></td></tr>
</table>

四、经费预算

经费总额		（万元）		备注
序号	支出科目	预算	支出用途	
1	出版/文献/信息传播/知识产权事务费	0.1	发表论文	其中资料费、文印费不得超过经费总额的10%
2	数据采集费			
3	设备费及材料费			原则上设备费不得超过项目总经费的30%，材料费不得超过项目的10%
4	差旅费	0.3	参与教学研讨会	差旅费不得超过经费总额的30%，报账时需附相关会议通知、调研函等相关材料
5	咨询费			咨询费不得超过经费总额的10%。
6	其他支出	0.6	网站改版升级	在项目实施过程中发生的除上述费用之外的其他必要支出，如课程建设录制费、教学网站建设与维护费和培训费等，按照国家及学校有关规定执行。
合　计		1		

五、承诺与责任

1. 本课程团队保证课程资源及申报材料不存在政治性、思想性、科学性和规范性问题，知识产权清晰，不涉及国家安全和保密的相关规定。

2. 本团队承诺将严格按照申报表要求完成项目的研究工作，接受学校的阶段检查，并配合做好结题验收或鉴定工作。

3. 本项目立项后每年开课次数不少于1次，且建设期内至少开设3-4次全校性的示范课。

课程负责人签字：

日期：2023-12-2

六、单位意见

所在单位意见	同意推荐。 单位负责人签字：李平 单位公章 2023 年 12 月 4 日

七、学校主管部门意见

负责人签字：　　（公章） 年　　月　　日

广东省人力资源和社会保障厅
广东省教育厅文件

粤人社发〔2025〕47号

广东省人力资源和社会保障厅 广东省教育厅
关于表彰全省学校（高等教育）
优秀教学成果奖的决定

各地级以上市教育局、人力资源和社会保障局，各高等学校，省直有关单位：

近年来，全省高校深入学习贯彻习近平新时代中国特色社会主义思想，全面落实立德树人根本任务，牢记为党育人、为国育才初心使命，在推进教育强省、科技创新强省、人才强省建设中，

凝练出一批提高人才培养质量的优秀成果。

在各高校推荐基础上，经有关程序，决定授予819项优秀教学成果为2025年全省学校（高等教育）优秀教学成果奖。其中：本科类优秀教学成果奖640项（含特等奖40项、一等奖200项、二等奖400项），研究生类优秀教学成果奖179项（含特等奖10项、一等奖49项、二等奖120项）。

希望各高校和教育工作者深入贯彻党的二十大和二十届历次全会精神，深入贯彻习近平总书记对广东系列重要讲话和重要指示精神，再接再厉，开拓创新，进一步加强高等教育教学研究和改革工作，大力弘扬教育家精神，提升教书育人本领，为加快建设教育强省、推动广东在推进中国式现代化建设中走在前列作出新的贡献。

附件：2025年全省学校（高等教育）优秀教学成果奖获奖成果名单

广东省人力资源和社会保障厅　　广东省教育厅

2025年12月25日

公开方式：主动公开

序号	成果名称	完成人	牵头完成单位
396	身心互哺 分类分层 数字赋能：大学“体心融合”课程改革与实践	陈赛红、蒋街良、蔡煜浩、陈佳、梁艳、刘亮、谭智斌、赵可意、唐伊美、胡敏蕊	广州理工学院
397	民办高校“一体两翼三协同”外语专业人才培养模式创新与实践	章美芳、冯军霞、邓博文、刘香萍、马郁、廖益清、郭遂红、蔡俊、冉海涛、吕丽红、周杨、申丹、徐付娟、李欣	广州理工学院
398	面向中小型企业的“四融双驱式”智能制造类应用型人才培养探索与实践	朱亚峰、李玉忠、张德福、王如意、袁洁贞、陈婵媛、贾林锋、文龙振、庞姗	广州理工学院
399	诗词弦歌：工科大学四场域、五融合、六举措一体化美育新模式	张强、张海鸥、张明军、谢丽娜、黄牧乾	广州软件学院
400	数智物流“π型”人才培养模式的创新与实践	刘保庵、胥爱霞、刘瀛寰、许晓君、钱可欣、徐辉、李文娟、林育焜、卢逸璨、赵沅君	广州软件学院

二、2025年全省学校（高等教育）优秀教学成果奖（研究生类）获奖成果名单

特等奖（10项）

序号	成果名称	完成人	牵头完成单位
1	“从阿者科出发”：深入中国田野的研究性教学与实践	保继刚、杨兵、刘逸、翁时秀、左冰、梁增贤、黄琢玮、张骁鸣、何莽、陈钢华	中山大学
2	有机光电材料研究生“四统一”创新人才培养模式探索与实践	马於光、曹镛、黄飞、刘琳琳、苏仕健、彭俊彪、王丹、陈军武、兰林锋、孟勋	华南理工大学
3	研究生思政共同体“一·九·零·六”育人模式的构建与实践	孙彧、李朋军、程京武、吴昱、韩刚、戴玉洁、邓双全、周楠楠	暨南大学
4	“情怀引领、创新赋能、实践强基”现代农机类研究生培养模式构建与应用	罗锡文、胡炼、汪沛、林佩云、何杰、钱立雄、臧英、邱亚龙、李君、王红军	华南农业大学
5	“十大十制”基础医学拔尖人才培养创新模式的构建与实践	高天明、黎孟枫、马骊、刘叔文、吴砂、白晓春、钟世镇、赵小阳、姚开泰、黄文华、罗深秋、赵克森、丁彦青、黄巧冰、曹雄、徐湘民、夏来新、张琳、赵亮、董为人、梁莉、邱钰晖	南方医科大学
6	“理论-方法-应用”三元融合：面向人工智能时代的“法商融合”研究生课程体系改革与实践	鲁晓明、姚志伟、张肇廷、耿颖、刘薇、王海洋、黄伟文	广东财经大学
7	基于乡村振兴视野下的工艺美术研究生人才培养模式构建	林蓝、齐喆、余潮松、韦潞、罗保权、庞国华、谭红宇、金生花、杜沁芬、苏若山	广州美术学院
8	双核定向、双擎驱动、双重赋能：职业技术教育硕士研究生培养模式创新与实践	邓文新、陈泳竹、陈伟、刘海兰、杨蕾、郭腾飞、兰金林、蒋凡、杨勇、王敏、单纯、徐伟、邓兰、巫兴宏、尧勇	广东技术师范大学
9	网络强国战略下实战创新型网安人才“三段三融合”培养模式的“方班”实践	方滨兴、田志宏、王乐、鲁辉、许嘉、唐可可、张帆、张怡凯、齐佳音、徐国爱、蒋琳、陈艳利、廖清	广州大学
10	面向国家战略定制化培养卓越工程人才—南方科技大学产教融合培养实践与探索	薛其坤、方红卫、汪宏、叶飞、程鑫、张建明、唐瑜、潘权、余浩、孙大陟、万玉喜、张程程、梁佳惠、叶田田	南方科技大学

一等奖（49项）

序号	成果名称	完成人	牵头完成单位
1	面向健康中国战略的医学研究生“胜任力导向型”分类培养体系创新与实践	匡铭、肖莉华、李辉雁、戴国琳、胡文杰、陈崴、王骥、谭进富、刘晨、尹军强	中山大学
2	"并行计算•AI+”创新型计算机研究生培养体系建设与实践	肖侬、吴维刚、陈志广、杨跃东、江颖、张献伟、李冠彬、谭宁、黄凯、颜晓辉	中山大学

序号	成果名称	完成人	牵头完成单位
49	价值引领、多元驱动、产教融合的信息类研究生培养模式创新与实践	翟懿奎、王天雷、曾庆光、麦超云、郑学强、周德华、柯峰、曾虹程、谢皓、徐颖、文益民、洪智勇、黄一桂、李骁、张桂荣	五邑大学
二等奖（120项）			
1	“双轮驱动，三链融合”的公共卫生医防管复合型人才培养体系构建及实践	王庆、夏敏、林华亮、杜志成、陈雯、王燕芳、卢次勇、柳雁、董光辉、胡汝为、吴昊、吴可盈、张周斌、袁俊、侯建荣	中山大学
2	校企平台、渐进实践、全链协同的强化专业型研究生工程实践创新能力培养模式	刘强、刘济科、蔡铭、黄林冲、刘鹏图、刘巨江、周少锐、蒋格格、付杰、饶军、李军、李熙莹	中山大学
3	医学研究生思政教育“四维四协同”育人模式创新与实践	匡铭、肖莉华、李辉雁、胡文杰、王晓桃、张航、贺鑫、郭玥、戴国琳、周怡	中山大学
4	五位一体，三重联动——研究生教育融入粤疆医学人才联合培养的“中大模式”	林天歆、胡晓丹、吴庆、赵亮宇、许可慰、汤育新、郑俊炯、钟淑萍、肖非、邹小广、张琪、吴小剑、杨清华、刘济科	中山大学
5	“生态协同、长效赋能”的研究生产教育人模式创新与实践	高平奇、林豪、韩灿、郁建灿、侯仰龙、操志伟	中山大学
6	面向国家战略的极地复合型人才培养体系创新与实践	程晓、赵羲、陈卓奇、惠凤鸣、叶玉芳、王雪、梁琦、李腾、何连、郑雷	中山大学
7	基础外科学院——推动高质量外科研究生人才培养新模式建设	谭进富、匡铭、张昆松、莫承强、李辉雁、谢文轩、陈泽斌、黄应雄、梁玲、李雯雯	中山大学
8	“力·度”育人理念引领的环境生态领域研究生“GLOBAL”能力培养创新实践	王诗忠、张妙月、林庆祺、刘文深、秦俊豪、金　超、汤叶涛、倪卓彪、晁元卿、曹　越、彭灵灵、孟凡刚、杨　欣、赵春梅	中山大学
9	自主知识体系进课堂：中观经济学的教研融合式教学改革创新与实践	徐现祥、李善民、林建浩、张莉、刘贯春、毕青苗、贾微晓、王方方、肖奎喜、徐雷、张小茜、任泽宇、江嘉骏、钟一彪	中山大学
10	科产教深度融合的“三链五维”育人体系驱动研究生创新能力培养探索	胡文浩、欧田苗、胡海燕、邓鸿、熊小峰、陈杰	中山大学
11	“临床导向，基础创新，学科交叉”干细胞与再生医学复合人才培养的探索与实践	项鹏、王涛、陈小沥、柯琼、黄玮俊、丁英、曹楠、向秋玲、张宏波、张小然	中山大学
12	顶尖学者引领机制创新赋能：构建“中大特色”国际化研究生联合培养新范式	苏成勇、江继军、陈洪燕、王静思、潘梅、陈小明、王大为、李忠曙、张利、张杰鹏	中山大学
13	卓越工程师的“五融合”培养	王为、梅俊、Jean-Marie BOURGEOIS-DEMERSAY、徐瑶、袁岑溪、马显锋、刘李云、潘大为、马江山、王岩、郭勇强、马宇、刘洋、倪木一、王志斌	中山大学
14	两融三创多元驱动：面向城乡高质量发展的建筑类卓越创新人才培养改革与实践	彭长歆、王世福、肖毅强、林广思、罗建河、陶金、赵渺希、叶红、魏宗财、赖文波	华南理工大学
15	一核双驱三融通：面向新型能源体系的复合型人才培养探索与实践	李立涅、唐文虎、朱建全、荆朝霞、武志刚、董美蓉、季天瑶、雪映、刘刚、涂颖文	华南理工大学
16	降碳减污创新拔尖人才培养模式研究与实践	胡芸、朱能武、严克友、叶代启、万金泉、石振清、邱光磊、陈燕、卢桂宁、冯春华	华南理工大学
17	面向全球治理需求的理工科高校研究生拔尖创新人才培养改革与实践	朱献珑、陈艳艳、巫喜丽、雷霄、战双鹏、苏娉、贾海龙、陈宏俊、王立松、李京廉、朱善华、周爽、吴赟、甄玉宝、莫启扬	华南理工大学
18	“理念引领、战略驱动、交叉融合”——化学学科研究生培养模式创新探索与实践	伍婉卿、江焕峰、邓远富、祝诗发、张玳、曾伟、尹标林、林东恩、黄良斌、李建晓	华南理工大学
19	“一体三元四驱”食品类专业卓越研究生人才培养体系探索与实践	李晓玺、娄文勇、赵谋明、王永华、杨晓泉、韩　忠、林恋竹、朱　良、苏健裕、蒲洪彬	华南理工大学
20	服务国家战略的湾区风景园林产教创融合实践教学模式探索	林广思、高伟、李敏稚、赖文波、陈崇贤、Jason Zhisen Ho（何志森）、萧蕾、冯娴慧、王南希、孙卫国、夏宇、叶劲枫、胡峰	华南理工大学
21	“1+2+4”体系：面向大湾区的一流商科研究生人才培养创新路径探索与实践	黄嫚丽、李炜文、许治、张俊生、 张卫国、黎文靖、蒋峦、乐琦、曾萍、 周骐、谢礼珊、叶飞	华南理工大学

序号	成果名称	完成人	牵头完成单位
22	体教融合 知行互促：体育研究生 “双轨互哺”培养创新与实践	高晓波、樊莲香、万发达、霍德利、陈丹、边宇、佘曦、黄炜皓、徐雷、杨管	华南理工大学
23	面向新一代移动通信的“三元协同”产业创新人才培养探索与实践	薛泉、车文荃、温淼文、冯文杰、秦培、朱浩慎、唐锟、吴亮、廖绍伟、曹云飞、朱剑锋、刘寻、Ioannis Vardaxoglou	华南理工大学
24	构建校企协同育人矩阵，打造“三通三融三链”湾区智造人才培养模式	瞿金平、雷育胜、李巍华、魏争、冯彦洪、冷金岩、王迪、宋长辉、李宗涛、谢正超	华南理工大学
25	光铸卓越：“思政引领 五维驱动”——光学工程研究生培养模式探索与实践	关柏鸥、黄睿、狄红卫、薛枫、王思聪、曾庆慧、孙玉环、卢惠辉、郭团、辛洪宝	暨南大学
26	GLOBE型国际商务人才培养模式创新与实践	吴菁、姜丽群、王玉、刘新荣、柳向东、苏晓艳、佘林蔚、吕映含、徐焱军、唐庆峰	暨南大学
27	内改外驱、产教融合、协同创新：电子信息专业学位研究生培养模式构建与实践	狄红卫、卢惠辉、陈振强、方俊彬、关贺元、曾庆慧、朱思祁、郑华丹、陈耀飞、张子邦	暨南大学
28	数据驱动、AI赋能：经管数据科学 “五位一体”教学体系的构建与实践	王斌会、谷世乾、柳向东、李爱梅、欧锦文、侯雅文、王术、刘潇	暨南大学
29	农业生物学研究生“思政引领-学科驱动-价值塑造”三阶育人模式创新与实践	陈乐天、周海、王应祥、吕剑红、安娜、梁春江、白玫、曹茜茜、文继开、庄楚雄	华南农业大学
30	服务乡村振兴的低空技术与工程紧缺人才培养模式的创新与实践	李震、兰玉彬、熊万杰、陈海波、邓小玲、陈盛德、张波、李继宇、张亚莉、陆健强	华南农业大学
31	价值引领 纵横贯通 致远致用：风景园林研究生育人体系构建与实践	李晖、刘小蓓、陈燕明、叶昌东、林敏慧、翁殊斐、刘京一、李自若、李晓雪、冼丽铧	华南农业大学
32	畜牧专业学位硕士研究生培养产科教融通的华农-温氏“科创中心”模式	张永亮、孙宝丽、张祥斌、吴珍芳、廖新俤、孙京臣、邓铭、陈婷、罗君谊、习欠云、孙加节、聂庆华、陈丽、陈峰	华南农业大学
33	铸心·强术·重行：服务乡村振兴的风景园林研究生“政校企社”人才培养实践	汤辉、赵建华、李晖、林敏慧、程晓山、卢丹梅、佘美萱、陈思颖、孟威、黄柏石	华南农业大学
34	薪火相传，融合创新：“思政-专业-产业”三圈联动的新兽医人才培养新范式构建与实践	孙坚、陈晓梅、张建民、戴雪飞、冯耀宇、于洋、黄竣聪	华南农业大学
35	“双碳”目标下林业工程“三铸魂四融通五驱动”人才培养模式的创新与实践	孙理超、王清文、欧荣贤、田立、胡传双、易欣、郭垂根、梁雅晶、樊奇、郝笑龙	华南农业大学
36	面向大湾区功能食品产业的"重教-强研-推产"研究生三链融创培养模式与实践	肖杰、陈运娇、宋明月、曹庸、赵力超、苗建银、刘晓娟、周爱梅、兰雅淇、吕慕雯	华南农业大学
37	真场景，实应用：面向农业数智化转型的信息管理类硕士培养模式创新与实践	熊俊涛、张建桃、韦婷婷、宋歌、佘平祥、张勇威、黄丽清、黄文玲、邓金、古万荣	华南农业大学
38	五力协同、铸魂强能：医学研究生 “大思政课”育人创新实践	任映红、张原英、曾楠、黄文华、 陈瑜、陈化、蒋伟、纪超凡、吴玲、汤慧杰、苑琳琳、谭晓雪	南方医科大学
39	“交叉创新·实战赋能·国际协同”公共卫生高层次急需人才培养体系的构建与实践	吴娴波、毛琛、凌志海、邹飞、彭鸿娟、张持晨、胡光丽、杜娟、赵卫、万成松、王亚惠、陈江涛、杨杏芬、何剑峰、李旭东	南方医科大学
40	临床需求与学科交叉双轮驱动的检验医学拔尖创新人才培养模式构建与实践	郑磊、王前、司徒博、周宏伟、李博、王海芳、唐本忠、左大明、张清宇、张静	南方医科大学
41	“四维精研·双环协同”的中外合作公共卫生政策与管理研究生培养实践	王冬、钱怡、胡光丽、彭鸿娟、欧玮艳、王思涵、江泳仪、吴洁莹、洪亦卿、苑琳琳	南方医科大学
42	破界·聚力·赋能：高层次医工交叉复合型超声人才培养模式创新与实践	李颖嘉、刘再毅、张煜、张妍琰、李胜利、涂盈锋、吴芃、秦耿耿、赵冰夏、黄晓媚、韩楚、马焕容、梁瑜	南方医科大学
43	面向国家战略需求的高层次护理人才分类培养模式的创新与实践	张立力、史蕾、赵阳、蔡文智、黄文华、周春兰、李漓、张持晨、陈仲清、杨智慧	南方医科大学
44	分层递进，需求引领——临床医学专业型硕士研究生临床胜任力培养的创新与实践	田京、凌志海、胡光丽、杨文娇、钱丹丹、石佳靓、方碧妹、张颖	南方医科大学


華南農業大學
本科教学成果奖
获奖证书
获奖成果：面向国家需求的一流精准农业航空人才培养体系创新与实践
获 奖 者：兰玉彬、陈海波、邓小玲、陈盛德、熊万杰、张 波、李继宇、张亚莉
获奖等级：一等奖
证书编号：JXCG24009
2025年9月9日


華南農業大學
SOUTH CHINA AGRICULTURAL UNIVERSITY
1909
華南農業大學
教学成果奖
获奖证书


获奖成果：以国家级一流混合课程应用为抓手 培养农业航空方向新农科创新人才
获奖者：兰玉彬、张 波、李继宇、李玉玲、邓小玲、陈盛德、韩宇星、张亚莉、文 晟、漆海霞
获奖等级：二等奖
证书编号：JXCG21035
华南农业大学
二〇二一年六月

试验设计与数据统计分析

Experimental Design and Statistical Analysis

武　涛　齐　龙◎主编

区颖刚　刘庆庭　张亚莉◎副主编

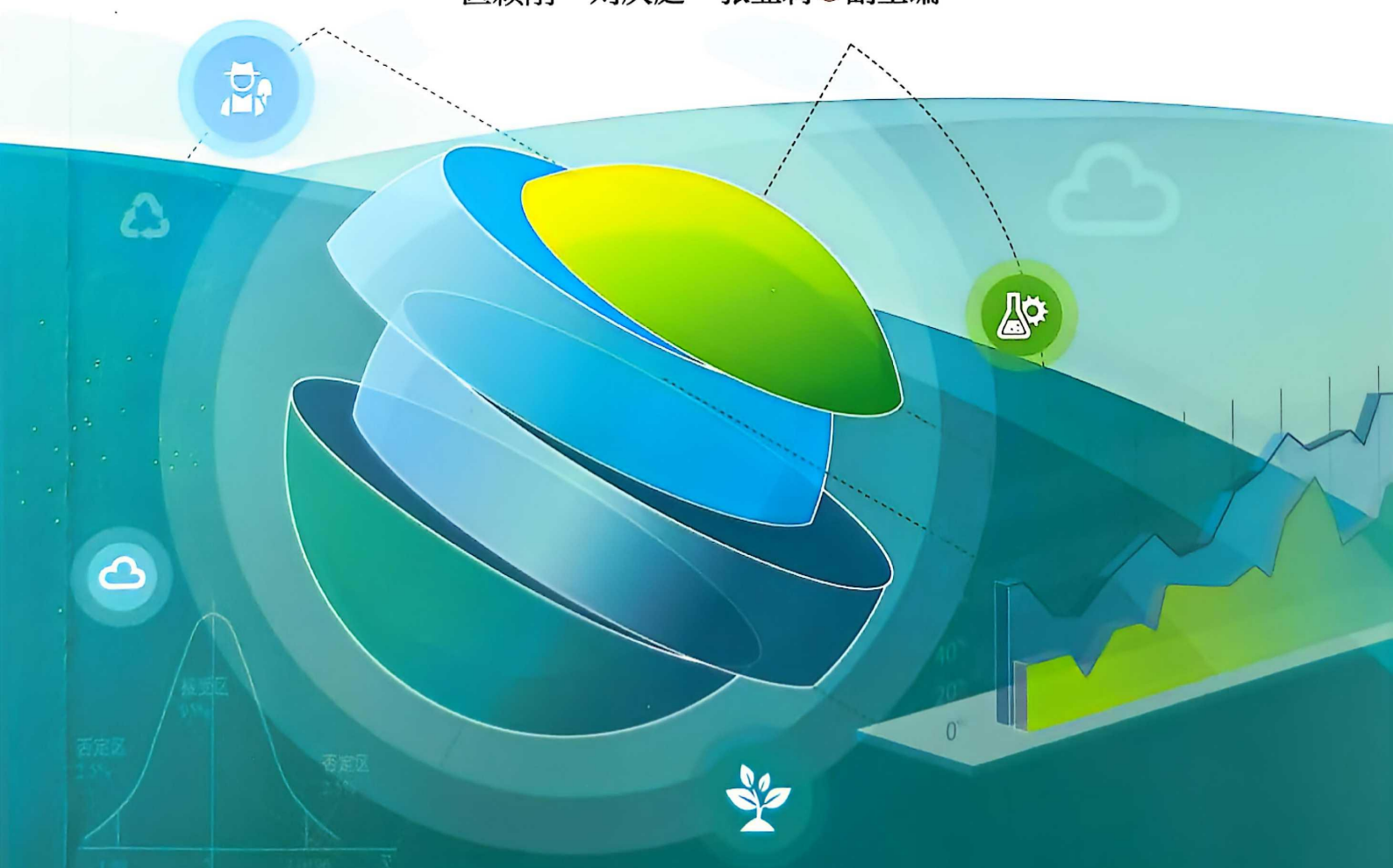

暨南大學出版社
JINAN UNIVERSITY PRESS

图书在版编目（CIP）数据

试验设计与数据统计分析/武涛，齐龙主编；区颖刚，刘庆庭，张亚莉副主编．—广州：暨南大学出版社，2023.10
ISBN 978-7-5668-3766-0

Ⅰ.①试… Ⅱ.①武…②齐…③区…④刘…⑤张… Ⅲ.①试验设计②统计分析 Ⅳ.①O212.6②O212.1

中国国家版本馆 CIP 数据核字（2023）第 170973 号

试验设计与数据统计分析

SHIYAN SHEJI YU SHUJU TONGJI FENXI

主　编：武　涛　齐　龙

副主编：区颖刚　刘庆庭　张亚莉

……

出 版 人：张晋升
责任编辑：黄　球
责任校对：刘舜怡　许碧雅
责任印制：周一丹　郑玉婷

出版发行：暨南大学出版社（511443）
电　　话：总编室（8620）37332601
　　营销部（8620）37332680　37332681　37332682　37332683
传　　真：（8620）37332660（办公室）　37332684（营销部）
网　　址：http://www.jnupress.com
排　　版：广州良弓广告有限公司
印　　刷：佛山市浩文彩色印刷有限公司
开　　本：787mm×1092mm　1/16
印　　张：13.25
字　　数：280 千
版　　次：2023 年 10 月第 1 版
印　　次：2023 年 10 月第 1 次
定　　价：52.80 元

（暨大版图书如有印装质量问题，请与出版社总编室联系调换）

目 录

CONTENTS

前 言 …… 001

第 1 章 绪论

1.1 试验设计与统计处理方法在实验研究工作中的地位 …… 001
1.2 试验统计学的逻辑 …… 002
1.3 试验设计及统计分析应考虑的问题 …… 004
1.4 试验指标、因素与水平 …… 005
1.5 总体、参数、样本、统计量 …… 007
1.6 总体或样本的数学特征数 …… 009

第 2 章 统计假设的检验

2.1 统计假设检验的基本原理 …… 013
2.2 两尾检验与一尾检验 …… 016
2.3 t 检验 …… 017
2.4 两样本平均数“差异”的检验 …… 018
2.5 方差比较的统计检验 …… 024

第 3 章 方差分析

3.1 方差分析的基本方法 …… 027
3.2 完全随机设计 …… 031
3.3 F 检验 …… 033
3.4 多重平均数的比较 …… 035
3.5 方差分析的数学模型 …… 038
3.6 二因素试验的方差分析 …… 044

3.7 贡献率 …… 049
3.8 随机区组设计的方差分析 …… 050
3.9 随机区组的线性模型及期望方差 …… 053
3.10 二因素随机区组试验设计的方差分析 …… 058
3.11 方差分析的基本假设 …… 062

第4章 正交试验设计及其方差分析

4.1 正交试验设计及正交表概述 …… 063
4.2 正交试验设计的几何图形 …… 066
4.3 选用正交表设计试验 …… 067
4.4 正交试验的方差分析 …… 072
4.5 正交试验方差分析的特点 …… 075
4.6 有交互作用的试验 …… 076
4.7 水平数不同的正交试验 …… 081
4.8 多指标分析 …… 088
4.9 正交试验设计小结与讨论 …… 094

第5章 直线回归及相关

5.1 回归和相关的概念 …… 095
5.2 直线回归方程 …… 096
5.3 直线回归方程的计算格式 …… 098
5.4 一元线性回归的数学模型 …… 101
5.5 回归参数及误差项的估计值的统计性质 …… 102
5.6 直线回归假设的检验 …… 103
5.7 相关检验 …… 111
5.8 回归方程的稳定性及 y 值的预测和控制 …… 114
5.9 两条回归直线的比较 …… 118
5.10 一元非线性回归（可化为线性回归的问题） …… 121
5.11 加权回归 …… 127
5.12 通过原点的回归 …… 128
5.13 注意事项 …… 130

第6章 多元线性回归

6.1 引言 …… 131
6.2 用矩阵法解多元线性回归方程 …… 133
6.3 多元线性模型的另一形式 …… 138
6.4 回归方程的显著性检验 …… 142
6.5 回归系数的显著性检验 …… 146
6.6 相关检验 …… 151
6.7 过原点的二元回归 …… 153
6.8 多项式回归 …… 156

第7章 回归正交设计

7.1 引言 …… 163
7.2 相关矩阵 …… 163
7.3 一次回归的正交设计 …… 165
7.4 一次回归正交设计的应用 …… 173
7.5 快速登高法 …… 178

附录1 常用正交表 …… 185
附录2 相关系数临界值表 …… 201

参考文献 …… 203

中国农村技术开发中心文件

国科农技字〔2023〕25号

关于国家重点研发计划“工厂化农业关键技术与智能农机装备”重点专项2023年度项目立项的通知

各项目牵头单位:

国家重点研发计划“工厂化农业关键技术与智能农机装备”重点专项2023年度项目立项工作已经完成，具体立项情况详见附件。

请你们会同各项目承担单位，根据《国务院办公厅关于改革完善中央财政科研经费管理的若干意见》（国办发〔2021〕32号）、《国家重点研发计划资金管理办法》（财教〔2021〕178号）、《国家重点研发计划管理暂行办法》（国科发资〔2017〕152号）等文件要求，依照项目（课题）

任务书，认真落实项目承担单位法人责任，合理配置单位人力、物力、财力资源，为项目（课题）实施提供必要条件保障；大力弘扬科学家精神，加强作风和学风建设，营造良好创新环境；加强项目（课题）之间的衔接与交流，促进项目（课题）间资源与信息的开放共享，提高项目实施绩效；做好知识产权和档案管理，加强项目成果凝练。严格按照中央财政科研经费管理的有关规定，资金专款专用，纳入单位财务统一管理；加强经费管理，强化预算执行，提高资金使用效益。落实科技报告管理有关规定，项目（课题）实施期间实行重要事项报告制度；自觉接受专项统一的协同联动与相关监督，确保项目（课题）的研发目标和任务按期完成。

附件：1.国家重点研发计划“工厂化农业关键技术与智能农机装备”重点专项2023年度项目立项表

2.项目立项批复

中国农村技术开发中心

2023年12月27日

附件 1

国家重点研发计划“工厂化农业关键技术与智能农机装备”重点专项 2023 年度项目立项表

序号	项目编号	项目名称	项目牵头单位
1	2023YFD2000100	粮食生产大数据平台研发与应用	北京市农林科学院信息技术研究中心
2	2023YFD2000200	大载荷植保智能无人机创制与应用	广州极飞科技股份有限公司
3	2023YFD2000300	新能源园艺作业动力机械创制开发	潍柴雷沃智慧农业科技股份有限公司
4	2023YFD2000400	粮食作物规模化制繁种智能化技术与装备研发	海南大学
5	2023YFD2000500	玉米大豆复合种植智能装备创制与应用	农业农村部南京农业机械化研究所
6	2023YFD2000600	日光温室数字化管理及小型成套作业装备创制与应用	中国农业机械化科学研究院集团有限公司
7	2023YFD2000700	肉牛规模化智能养殖技术与装备研发	东北农业大学
8	2023YFD2000800	绿色智能高效养鸡工厂创制与应用	中国农业大学
9	2023YFD2000900	马铃薯规模化生产全程智能作业装备创制与应用	中机美诺科技股份有限公司
10	2023YFD2001000	油菜/花生全程智能作业装备创制与应用	农业农村部南京农业机械化研究所
11	2023YFD2001100	标准化果园智能化生产技术装备创制与应用	第一拖拉机股份有限公司
12	2023YFD2001200	露地蔬菜全程无人化生产技术装备创制与应用	中国农业机械化科学研究院集团有限公司
13	2023YFD2001300	蔬菜产地智能化高效处理技术与装备研发	中国农业机械化科学研究院集团有限公司
14	2023YFD2001400	盐碱地智慧生态农业关键技术研发与集成应用	山东省农业科学院

附件 2-2

“大载荷植保智能无人机创制与应用”项目立项批复

一、项目名称（编号）：大载荷植保智能无人机创制与应用（2023YFD2000200）。

二、项目牵头单位：广州极飞科技股份有限公司，项目负责人：薛新宇。

三、项目执行年限：4。

四、项目总经费：4000 万元，其中中央财政经费 2000 万元。

五、项目目标和主要考核指标

项目目标：针对丘陵、水田及高秆作物、果树、特色经济作物的大载荷、长航时、高效率精准植保作业需求，重点突破旋翼类无人机减阻提效气动布局、电动载荷动力总成、飞行姿态智能控制等关键技术及零部件，创制长续航大载荷电动旋翼类植保无人机；突破油动大载荷无人机高效动力系统、大扭矩动力输出、飞行姿态智能控制等关键技术及零部件，创制长续航大载荷油动无人植保作业机；突破作业信息精准获取、固/液态药物精准喷施等关键技术及零部件，研制大载荷无人机搭载集成装置；研究作业路径规划、动态避障、多机协同作业等关键技术，研发端—边—云协同的无人机—地面站—云平台系统。在典型地区开展示范应用。

主要考核指标：本项目预期突破大载荷长航时植保无人机作业关键核心技术6项；创制整体智能化程度≥90%的系列高效植保无人机6种以上；制定起草行业/企业技术或产品标准5项，培养研究生32名，培训农技人员或农民1000名以上，开展示范应用总面积16万亩以上。详细考核指标以项目任务书为准。

六、项目课题安排

序号	课题编号	课题名称	课题负责人	课题承担单位	中央财政经费（万元）
1	2023YFD2000201	长续航大载荷电动旋翼植保无人机创制	薛新宇	广州极飞科技股份有限公司	400
2	2023YFD2000202	长续航大载荷油动旋翼植保无人机创制	张亚莉	华南农业大学	400
3	2023YFD2000203	农情信息无人机遥感精准获取技术与集成装置研发	刘飞	浙江大学	400
4	2023YFD2000204	大载荷植保无人机固/液态药物精准喷施关键技术及部件研发	张瑞瑞	北京市农林科学院智能装备技术研究中心	400
5	2023YFD2000205	大载荷植保无人机集成应用及绿色安全协同管控技术与系统	徐阳	农业农村部南京农业机械化研究所	400

（此件依申请公开）

抄送：科学技术部科技资源统筹司、监督评估与科研诚信司，农业农村部科学技术司，教育部科学技术与信息化司、北京市科学技术委员会、黑龙江省科学技术厅、山东省科学技术厅、河南省科学技术厅、广东省科学技术厅、海南省科学技术厅、农业装备产业技术创新战略联盟。

中国农村技术开发中心　　2023年12月27日印发

课题编号：2023YFD2000202　　密　级：公开

国家重点研发计划
课题任务书

课题名称：长续航大载荷油动旋翼植保无人机创制

所属项目：大载荷植保智能无人机创制与应用

所属专项：工厂化农业关键技术与智能农机装备

项目牵头承担单位：广州极飞科技股份有限公司

课题承担单位：华南农业大学

课题负责人：张亚莉

执行期限：2023 年 12 月 至 2027 年 11 月

中华人民共和国科学技术部制

2023 年 12 月 09 日

0003YF 2023YFD2000202 2023-12-09 18:18:44

课题基本信息表

<table>
<tr><td>课题名称</td><td colspan="5">长续航大载荷油动旋翼植保无人机创制</td></tr>
<tr><td>课题编号</td><td colspan="5">2023YFD2000202</td></tr>
<tr><td>所属项目</td><td colspan="5">大载荷植保智能无人机创制与应用</td></tr>
<tr><td>所属专项</td><td colspan="5">工厂化农业关键技术与智能农机装备</td></tr>
<tr><td>密级</td><td colspan="2">■公开 □秘密 □机密</td><td>单位总数</td><td colspan="2">4</td></tr>
<tr><td>课题类型</td><td colspan="5">□基础前沿■重大共性关键技术□应用示范研究□其他</td></tr>
<tr><td>课题活动类型</td><td colspan="5">□基础前沿■应用研究□试验发展</td></tr>
<tr><td>课题研究
所属学科</td><td colspan="5">自然科学相关工程与技术
农业工程</td></tr>
<tr><td>课题成果应
用的主要国
民经济行业</td><td colspan="5">农、林、牧、渔业
农业
谷物种植
稻谷种植</td></tr>
<tr><td>课题的社会
经济目标</td><td colspan="5">农林牧渔业发展
农林牧渔业体系支撑</td></tr>
<tr><td>经费预算</td><td colspan="5">总需求 800.00 万元，其中中央财政专项资金需求 400.00 万元</td></tr>
<tr><td rowspan="2">课题周期节点</td><td>起始时间</td><td>2023 年 12 月</td><td>结束时间</td><td colspan="2">2027 年 11 月</td></tr>
<tr><td>实施周期</td><td>共 48 个月</td><td>预计中期时间点</td><td colspan="2">2025 年 11 月</td></tr>
<tr><td rowspan="8">课题
承担
单位</td><td>单位名称</td><td colspan="2">华南农业大学</td><td>单位法定
代表人姓名</td><td>薛红卫</td></tr>
<tr><td>单位性质</td><td colspan="2">大专院校</td><td>组织机构代码</td><td>124400004554165634</td></tr>
<tr><td>单位主管部门</td><td colspan="2"></td><td>隶属关系</td><td>地方</td></tr>
<tr><td>单位所属地区</td><td colspan="2">广东省</td><td>地市（市、自
治州、盟）</td><td>广州市　天河区</td></tr>
<tr><td>通信地址</td><td colspan="2">广州市天河区五山路 483 号</td><td>邮政编码</td><td>510642</td></tr>
<tr><td>单位开户名称</td><td colspan="4">华南农业大学</td></tr>
<tr><td>开户银行
（全称）</td><td colspan="2">中国工商银行股份有限公司
广州五山支行</td><td>汇入地点</td><td>广东省　广州
市</td></tr>
</table>

项目牵头承担单位（甲方）：

法定代表人签字（签章）：

（公章）

2023年12月12日

项目负责人签字（签章）：

2023 年12月12 日

课题承担单位（乙方）：

法定代表人签字（签章）：

（公章）

2023 年12月 12日

课题负责人签字（签章）：

2023 年 12月12日

受理编号：c195371900005　　项目编号：2019B020221001

项目下达文号：

广东省重点领域研发计划项目

任务书

项目名称：水稻生产地面-航空高效施药智能装备研究与示范

专项名称：智能农机装备

项目起止时间：2019年 01月 01日　至　2021年 12月 30日

管理单位(甲方)：广东省科学技术厅

牵头承担单位一（乙方）：广州极飞科技有限公司

项目推荐（主管）单位（丙方）：广州市科技创新委员会

通讯地址：广东省-广州市-天河区高普路115号极飞科技

邮政编码：510663　　单位电话：020-85207212

项目负责人：薛新宇　　联系电话：020-85207212

项目联系人：黄丹　　联系电话：15915880264

广东省科学技术厅
二〇一九年制

（广东科技微信公众号）

（受理纸质材料二维码）

六、参与人员信息

项目负责人：

姓名	性别	年龄	职务	职称	学位	在项目中承担的任务	所在单位	签名
薛新宇	女		农业部岗位体系专家	研究员	博士	项目总体设计	广州极飞科技有限公司	薛新宇

主要研究开发人员：

姓名	性别	年龄	职务	职称	学位	在项目中承担的任务	所在单位	签名
张亚莉	女		副主任	副教授	博士	植保无人机智能传感器	华南农业大学	张亚莉
邓继忠	男		副主任	教授	博士	低空遥感与农情分析	华南农业大学	邓继忠
孔伟	男		无	助理研究员	硕士	喷杆平衡技术	农业农村部南京农业机械化研究所	孔伟
丁素明	男		无	研究员	学士	整机设计	农业农村部南京农业机械化研究所	丁素明
黄丹	女		总经理助理兼部门经理	未取得	硕士	自主避障技术研究	广州极飞科技有限公司	黄丹
张建瓴	男		无	副教授	博士	农业航空作业规程	华南农业大学	张建瓴
陈盛德	男		无	助理研究员	博士	农业航空施药技术	华南农业大学	陈盛德
欧阳帆	男		无	助理研究员	博士	精准施药系统	华南农业大学	欧阳帆
曾文	男		无	讲师	博士	精准施药技术	华南农业大学	曾文

九、签约各方

管理单位（甲方）： 广东省科学技术厅 （盖章）

单位地址： 广东省广州市连新路171号

法定代表人（或授权代表）： 王瑞军 （签章）

联系人（经办人）姓名： 叶毓峰 （签章）

Email： yeyf@gdstc.gov.cn QQ：

电话： 020-83163906 微信：

2019年 7 月 11 日

牵头承担单位一（乙方）： 广州极飞科技有限公司 （盖章，单位法人章或单位法人授权章）

单位地址： 广东省广州市天河区高普路115号极飞科技

法定代表人（或法人代理）： 彭斌 （签章）

联系人（项目主管）姓名： 黄丹 （签章）

Email： huangdan@xa.com QQ：

电话： 020-85207212 微信：

2019 年 5 月 6 日

项目推荐（主管）单位（丙方）： 广州市科技创新委员会 （盖章，单位法人章或单位法人授权章）

单位地址： 广东省广州市越秀区广州市越秀区府前路1号市政府大院

法定代表人（或法人代理）： 王桂林 （签章）

联系人（项目主管）姓名： 社基处 （签章）

Email： lijh@gz.gov.cn QQ：

电话： 020-83124045 微信：

2019 -05- 07

年 月 日

2019B020221001

广东省重点领域研发计划项目

二级合同书

项目名称：水稻生产地面-航空高效施药智能装备研究与示范

专项名称：智能农机装备

项目起止时间：2019 年 01 月 01 日至 2021 年 12 月 30 日

项目负责人：薛新宇

项目承担单位（甲方）：广州极飞科技有限公司

课题负责人： 张亚莉

课题承担单位（乙方）：华南农业大学

一、项目主要研究内容

1. 植保无人机施药关键技术研究：

针对农田复杂环境下雾滴穿透性差、附着率低及航空施药过程中，因水稻长势、病虫害特征及飞行状态变化而导致施药效果不理想的问题，开展植保无人飞机变量施药、静电施药等精准航空施药关键技术研究；

2. 植保无人机施药作业效果检测；

3. 开展航空农药药剂筛选和环境影响评估；

4. 协助开展植保无人机精准施药技术示范推广；

5. 参与研究南方水田作业的地面-航空智能施药技术体系建设。

二、项目验收指标

序号	指标	中期指标值	完成时指标值	评测方式/方法
1	申请专利 7 件，其中发明专利 5，实用新型专利 2 件	申请发明专利 2 件，实用新型专利 1 件	获得两件发明专利授权，3 件发明专利受理，2 件实用新型专利授权	专利受理通知书/专利授权证书
2	高水平学术论文	发表论文 2 篇，其中 SCI/EI 论文 1 篇	发表论文 4 篇，其中 SCI/EI 论文 2 篇	论文发表证明/论文收录证明
3	人才培养	2 人	5 人	/

三、进度计划

起止时间	主要工作内容
2019.01.01-2019.12.31	完成植保无人机变量施药技术、超低空静电施药技术等关键施药技术研究；申请发明专利 2 件，实用新型专利 1 件；发表 SCI/EI 论文 1 篇。
2020.01.01-2020.12.31	完成植保无人机施药作业效果检测；开展航空药剂筛选和环境影响评估；申请发明专利 2 件，实用新型专利 1 件，发表 SCI/EI 论文 2 篇。
2021.01.01-2020.12.31	协助申报单位开展植保无人机精准施药技术示范推广；完成课题技术总结；申请发明专利 1 件；发表 SCI/EI 论文 1 篇。

四、参与人员

项目负责人

序号	姓名	年龄	职务/职称	学位	在项目中承担的任务	所在单位	签名
1	张亚莉		副教授	博士	全面负责/无人机智能传感器技术	华南农业大学	

主要研究开发人员

序号	姓名	年龄	职务/职称	学位	在项目中承担的任务	所在单位	签名
1	邓继忠		副主任/教授	博士	低空遥感与农情分析	华南农业大学	
2	张建瓴		副教授	博士	农业航空作业规程	华南农业大学	
3	陈盛德		助理研究员	博士	精准施药技术	华南农业大学	
4	欧阳帆		助理研究员	博士	精准施药系统	华南农业大学	
5	曾文		讲师	博士	精准施药技术	华南农业大学	
6	张波		高级工程师	博士	农业航空大数据应用平台	华南农业大学	
7	何效平		讲师	硕士	农业航空知识产权	华南农业大学	
8	陈鹏超		博士研究生	硕士	农业航空药效研究	华南农业大学	
9	王林琳		博士研究生	学士	农业航空智能传感器技术	华南农业大学	

10	白禄超	25	未取得	本科	精准施药技术	华南农业大学	白禄超
11	祁媛	23	未取得	本科	精准施药系统研发	华南农业大学	祁媛
12	黄华盛	31	未取得	硕士研究生	精准航空施药系统研发	华南农业大学	黄华盛
13	刘轶伦	23	未取得	本科	精准施药技术研究	华南农业大学	刘轶伦
14	刘峰	23	未取得	本科	智能化飞行控制技术研究	华南农业大学	刘峰

五、项目经费

（一）省财政科技资金拟投入总额（大写）壹佰叁拾万元整；（小写）130.00 万元；

（二）省财政科技资金分期下达计划；（此为正常情况下预计拨付计划，中期评估或验收结题不通过的，甲方有权停止或核减拨付后续资金）：

分期	经费（万元）
第 1 期	19.5
第 2 期	84.5
第 3 期	26

（三）总经费及省财政科技资金投入情况（单位：万元）

项目总经费投入	省财政科技资金	自筹经费			合计
		自有经费	地方政府投入	其它	
130	130	0	0	0	130
自筹资金投入情况说明					
无					

	省财政科技资金	
支出经费	经费额（万元）	用途说明
1、直接费用	109.55	直接费用
（1）设备费	26	用于变量喷洒等技术研究设备购买、研发试制等费用支出
（2）材料费	32.8	与项目相关的材料费用
（3）测试化验加工外协费	0	产品测试、外协加工等费用
（4）燃料动力费	0	生产车间或实验室发生的水电等费用
（5）差旅费/会议费/国际合作与交流费	14.35	项目学术交流等活动发生的差旅费、住宿费、交通等费用
（6）出版/文献/信息传播/知识产权事务费	10.8	知识产权申请、资料等费用
（7）劳务费	22.8	参与项目研究的研究生、博士后、访问学者以及项目聘用的研究人员、科研辅助人员等费用
（8）人员费	0	用于项目主要成员费用的开支
（9）专家咨询费	2.8	项目实施过程中专家咨询等费用
（10）直接费用其他支出	0	与项目研发相关的直接费用其他支出
2、间接费用	20.45	项目管理、绩效奖励等费用
（1）间接成本	0	项目承担单位提供现有仪器设备及房屋、水费、电费等
（2）管理成本	6.5	项目管理费
（3）绩效支出	13.95	项目参与人员绩效奖励
3、其他支出费用	0	/
合计	130.0	/

	担保条款，作为本合同正式内容一部分。当乙方不履行或不完全履行本合同，以及没有或没有完全承担违约责任时，乙方的保证单位承担连带保证责任。
第十三条	本合同一式三份，各份具有同等效力。甲保存两份，乙方存一份，本合同自签字之日起生效，有效期至项目结题后一年内。各方均应负合同的法律责任，不应受机构、人事变动的影响。

八、签约各方

项目承担单位：广州极飞科技有限公司（盖章）

项目联系人：

年　月　日

课题承担单位：华南农业大学（盖章）

课题负责人：

课题联系人：

年　月　日

项目编号：2019B020221001



广东省重点领域研发计划项目验收书

项目名称：	水稻生产地面-航空高效施药智能装备研究与示范
下达文件编号：	粤科资字〔2019〕128号
专 项 名 称：	智能农机装备
牵头承担单位一（盖章）：	广州极飞科技有限公司
牵头承担单位二（盖章）：	
验收形式：	现场验收
组织验收单位（专业机构）：	广东省科技厅
验收日期：	2023-01-12

2019B020221001076

广东省科学技术厅
二〇二一年制

一、项目基本信息

项目名称	水稻生产地面-航空高效施药智能装备研究与示范		
专项名称	智能农机装备		
牵头承担单位一（盖章）	广州极飞科技有限公司		
牵头承担单位二（盖章）			
参与单位1	华南农业大学		
参与单位2	农业农村部南京农业机械化研究所		
其他参与单位	广东省农业科学院植物保护研究所、现代农装科技股份有限公司		
项目支持金额	500万元		
项目执行期	2019-01-01 至 2022-06-30		
项目负责人一	薛新宇	联系电话	13923094784
项目负责人二		联系电话	
项目联系人	陈世印	手机	13751841056
通信地址	广东省广州市天河区高普路115号C座		
邮政编码	510663		
验收日期	2023-01-12		

20193020221001076

附件一：录入专家意见

广东省科技计划项目财务验收意见表			
项目编号	2019B020221001	负责人	薛新宇
项目名称	水稻生产地面-航空高效施药智能装备研究与示范		

经广州市诚谨会计师事务所有限责任公司进行项目专项审计，项目经费的来源和使用符合有关专项经费管理办法的规定，项目经费单独核算、专款专用。项目执行期内，累计新增销售收入 10195万元，累计新增利税 2358 万元。

财务验收结论：（■）通过 （□）不通过 （□）结题

财务验收专家签字：

日 期：

2019B020221001076

附件二

广东省重点领域研发计划项目验收意见表			
项目名称	水稻生产地面-航空高效施药智能装备研究与示范		
项目编号	2019B020221001	负责人	薛新宇
承担单位	广州极飞科技股份有限公司		

验收专家成员			
姓　名	单　位	职务职称	签　名
马志光	广东省现代农业装备研究所	正高级工程师	
黄海坤	广东产品质量监督检验研究院	正高级工程师	
王毅	仲恺农业工程学院	教授	
陈黎明	广东机电职业技术学院	正高级工程师	
毛钟红	广州大学	副研究员	

2023 年 1月12日，广东省科技厅在广州极飞科技股份有限公司组织召开了由广州极飞科技股份有限公司牵头，农业农村部南京农业机械化研究所、华南农业大学、广东省农业科学院植物保护研究所、现代农装科技股份有限公司参与的“水稻生产地面-航空高效施药智能装备研究与示范”(编号:2019B020221001)项目验收会。验收专家组审阅了项目验收相关材料、听取了项目组汇报，并对项目进行了现场考察，经质询形成如下验收意见:

1.项目验收资料齐全、规范，符合验收要求。

2.项目开展对地面-航空高效施药技术和能装备研究，解决高地隙底盘防滑减阻、底盘减振、变量施药、航线自主规划、自主避障和仿地飞行等技术问题，研制出智能化植保无人机和水田自走式精量施药喷杆喷雾机，试验的核心示范面积和辐射示范面积均达到任务书指标要求。项目申请发明专利18件，其中授权6件，实用新型授权 15件;发表高水平论文 13 篇，制定作业规程2 项，培养人才19人;制定团体准1项，企业准1项。

3.项目技术就绪度经工业和信息化部电子第五研究所评审达到TRL8 级。

4.经广州市诚谨会计师事务所有限责任公司进行项目专项审计，项目经费的来源和使用符合有关专项经费管理办法的规定，项目经费单独核算、专款专用。项目执行期内，累计新增销售收入 10195万元，累计新增利税 2358 万元。

专家组认为，该项目完成了任务书的各项指标，同意通过验收。

验收结论：（■）通过　(□)不通过　(□)结题

验收专家组组长签字：

日　期：

2019B020221001076

受理编号：c1831550100092　　项目编号：2018A050506073

文件编号：粤科规财字〔2018〕252号（国际合作）

广东省省级科技计划项目

合同书

项目名称：精准农业航空遥感技术及平台在巴基斯坦的示范应用

专项资金类别：协同创新与平台环境建设

计划类别：国际科技合作领域

项目起止时间：2018-12-01　至　2021-12-31

管理单位（甲方）：广东省科学技术厅

承担单位（乙方）：华南农业大学

乙方主管部门（丙方）：华南农业大学

通讯地址：广东省广州市天河区五山路483号

邮政编码：510642　　单位电话：020-38632819

项目负责人：张亚莉　　联系电话：020-85285036

项目联系人：张亚莉　　联系电话：13316055930

2018A050506073

广东省科学技术厅
二〇一七年制

（广东科技微信公众号）　　（受理纸质材料二维码）

四、承担、参与单位工作分工及经费分配情况

承担/参与单位名称（盖章）	工作分工	总经费分摊（万元）	省科技厅经费分配（万元）
华南农业大学	（1）小型农用无人机低空遥感信息获取与农情信息精准管理决策支持系统 （2）遥感信息解析技术研究	30.00	30.00
PMAS-Arid Agriculture University Rawalpindi	（1）遥感信息解析技术研究与农情信息精准管理 （2）巴基斯坦Rawalpindi应用示范基地建设	0	0.00
University of Sargodha	（1）巴基斯坦Sargodha应用示范基地建设	0	0.00
广州极飞科技有限公司	（1）电动多旋翼植保无人机技术 （2）精准农业航空遥感信息获取作业平台研发	70.00	20.00
	合计	100.00	50.00

2018A050506073

九、本合同签约各方

管理单位（甲方）：　广东省科学技术厅 （盖章）

单位地址：　连新路171号

法定代表人（或授权代表）：　王瑞军　（签章）

立项责任人：　万卉芊　（签章）

年　月　日

承担单位（乙方）：　华南农业大学　（盖章）

二级部门：　华南农业大学工程学院

单位地址：　五山路483号

法定代表人（或法人代理）：　陈晓阳　（签章）

联系人（项目主管）姓名：　郑鹏　（签章）

Email：　kjcgxk@scau.edu.cn

电话：　020-85283435　/　13560344902

开户单位名称：　华南农业大学

开户银行及帐号：　广东广州工行五山支行　3602002609000310520

年　月　日

乙方主管部门（丙方）：　华南农业大学　（盖章）

单位地址：　五山路483号

法定代表人（或法人代理）：　陈晓阳　（签章）

年　月　日

2018A050506073

受理编号：c21140500002325

项目编号：2021A1515010736

文件编号：粤基金字〔2021〕4号

广东省基础与应用基础研究基金项目

合同书

项目名称：多旋翼农用无人机能源载荷动态匹配机制

项目类别：广东省自然科学基金-面上项目

项目起止时间：2021-01-01 至 2023-12-31

管理单位（甲方）：广东省基础与应用基础研究基金委员会

依托单位（乙方）：华南农业大学

通讯地址：广东省广州市天河区五山路483号

邮政编码：510642 单位电话：020-85283435

项目负责人：李继宇 联系电话：020-85281443

（广东科技微信公众号） （查看合同书信息） （受理纸质材料二维码）

广东省基础与应用基础研究
基金委员会
二〇二〇年制

2021A1515010736

五、人员信息

项目负责人

姓名	证件号码	年龄	性别	职称	学历	在项目中承担的任务	所在单位	签名
李继宇	422127197912090019	42	男	教授	博士研究生	项目负责人	华南农业大学	

项目组主要成员

姓名	证件号码	年龄	性别	职称	学历	在项目中承担的任务	所在单位	签名
张亚莉	370682197507250061	46	女	副教授	博士研究生	静态模型解算	华南农业大学	
金济	420803198010204515	41	男	讲师	硕士研究生	动态负载分解	华南农业大学	
巫瀚	445102199706061418	24	男	未取得	本科	动态负载分类与计算	华南农业大学	
龙波	362430199610220030	25	男	未取得	本科	电池能量密度匹配	华南农业大学	
张植勋	44050819980906393X	23	男	未取得	本科	匹配模型计算	华南农业大学	

2021A1515010756

六、工作分工及经费分配

承担/参与单位名称 (盖章)	工作分工	总经费分摊 (万元)	省基金委经费分配 (万元)
华南农业大学	独立承担	10.00	10.00
	合计	10.00	10.00

2021A1515010736

八、本合同签约各方

管理单位（甲方）：　　广东省基础与应用基础研究基金委员会 （盖章）

法定代表人（或法人代理）：曾路 （签章）

2021 年 03 月 25 日

依托单位（乙方）：华南农业大学 （盖章）

法定代表人（或法人代理）：刘雅红 （签章）

联系人（项目主管）姓名：安沛 （签章）

Email：414484016@qq.com

电话：020-85283435 / 13535577893

开户单位名称：华南农业大学

开户银行名称：广东广州工行五山支行

开户银行帐号：3602002609000310520

2021 年 4 月 9 日

联系人（项目负责人）姓名：李继宇 （签名）

Email：26260378@qq.com

电话：020-85281443

2021 年 4 月 8 日

项目编号：201807010039

广州市科技计划项目

合同书

项目名称：基于GNSS-RTK的精准农业航空遥感技术与应用

计划类别：对外科技合作计划

专题名称：对外研发合作专题

起止时间：2018年04月01日 至 2021年03月31日

承担单位：华南农业大学

组织单位：华南农业大学

责任处室：科技交流合作处

填表日期：2018年01月18日

广州市科技创新委员会

（2017年版）

一、项目基本信息

<table>
<tr><td>项目名称</td><td colspan="5">基于GNSS-RTK的精准农业航空遥感技术与应用</td></tr>
<tr><td>研究类别/
所属技术领域</td><td colspan="5">农业与食品-农业环境保护与生态农业-农业环境监测与控制技术</td></tr>
<tr><td rowspan="7">承担单位</td><td>名　　称</td><td colspan="4">华南农业大学</td></tr>
<tr><td>通信地址</td><td colspan="4">广州市天河区五山路483号</td></tr>
<tr><td>邮政编码</td><td>510642</td><td>传　　真</td><td colspan="2">85281885</td></tr>
<tr><td>单位特性</td><td></td><td>单位类型</td><td colspan="2">高等院校</td></tr>
<tr><td>统一社会信用代码
或组织机构代码</td><td colspan="4">455416563</td></tr>
<tr><td>法定代表人</td><td>陈晓阳</td><td>电子邮箱</td><td colspan="2">xychen@scau.edu.cn</td></tr>
<tr><td>联系人</td><td>侯建国</td><td>联系电话</td><td colspan="2">02038632413</td></tr>
<tr><td rowspan="2">合作单位</td><td>序号</td><td>名称</td><td>单位类型</td><td>联系人</td><td>联系电话</td><td>所属国别
或地区</td></tr>
<tr><td>1</td><td>广州市中海达测绘仪器有限公司</td><td>股份有限公司</td><td>林钦坚</td><td>020-28688287</td><td>中国</td></tr>
</table>

20180701003

二、项目组人员信息

项目负责人	姓名	兰玉彬	证件类型	护照	证件号码	545731967	性别	男
	出生年月	1961年07月11日	民族	汉族	国籍	美国	学历	博士研究生
	学位	博士	学位授予国家（或地区）	美国	职务	主任	职称	教授
	所学专业	农业工程	手机号码	13922707507	办公电话	02085281421	电子邮箱	ylan@scau.edu.cn

项目组成员（含项目负责人）

序号	姓名	证件类型	证件号码	年龄	性别	职务	职称	学历	现从事专业	分工	所在单位	签名
1	兰玉彬	护照	545731967	55	男	主任	教授	博士研究生	农业航空	项目负责人	华南农业大学	
2	张亚莉	身份证	370682197507250061	42	女	无	副教授	博士研究生	农业航空	光谱信息分析与处理	华南农业大学	
3	李继宇	身份证	422127197912090019	38	男	无	副教授	博士研究生	农业航空	遥感无人机精准导航技术	华南农业大学	
4	邓继忠	身份证	650103196312 10323X	54	男	无	教授	博士研究生	农业航空	农情解析技术及精准管理决策支持系统	华南农业大学	
5	邓小玲	身份证	445122197807180420	39	女	无	副教授	博士研究生	农业航空遥感	遥感信息提取和处理	华南农业大学	
6	漆海霞	身份证	610103196903213708	48	女	无	副教授	博士研究生	农业航空	遥感信息地面验证	华南农业大学	

四、项目主要验收指标

（一）主要技术指标
突破基于GNSS-RTK的小型无人机控制和精准导航技术、小型无人机遥感信息获取技术和解析技术各1项。研制小型化超轻型高动态性集成厘米级无人机差分定位与定姿模块（GNSS-RTK）1套，研制农用无人机遥感平台1个，研发农情解析及管理系统1套，在巴基斯坦共建示范基地或者国际研究分中心1个。项目结题发表EI/SCI论文2篇，申请发明专利3项，培养博士研究生1人，硕士生2人。

20180701039

八、项目承担单位（乙方）与合作单位合作内容

承担单位名称：华南农业大学

任务分工：小型农用无人机低空遥感信息获取与农情信息精准管理决策支持系统研究

知识产权分配：1

市科创委经费分配额度（万元）：85.00

自筹经费出资额度（万元）：0

（单位公章）

2018 年 3 月 22 日

合作单位（1）名称：广州市中海达测绘仪器有限公司

任务分工：厘米级农用无人机GNSS-RTK差分定位与定姿模块研制

知识产权分配：2

市科创委经费分配额度（万元）：15.00

自筹经费出资额度（万元）：100.00

（单位公章）

2018 年 3 月 20 日

20180701039

九、合同书各方签章

签订地点：广州市越秀区

广州市科技创新委员会（甲方）：广州市科技创新委员会

项目经办人（签章）：黄运纬　　联系电话：

责任处室负责人（签章）：

（公　章）

2018年 5月 3日

项目承担单位（乙方）：华南农业大学

二级部门：华南农业大学工程学院

项目负责人（签章）：

财务负责人（签章）：

财务负责人联系电话：02085287402

帐户名：华南农业大学　　帐号：3602002609000310520

开户银行：广东广州工行五山支行

法定代表人 （签章）：

（公　章）

2018年 5月 2日

组织单位（丙方）：华南农业大学

项目经办人（签章）：

（公　章）

2018年 5月 2日

20180701039

SCAULIB202625962

检索证明

根据委托人提供的论文材料，委托人华南农业大学工程学院 张亚莉(学科类型:自然科学) 7 篇论文收录情况如下表。

序号	论文名称	发表刊物及发表的年月卷期/页码等	作者排名	论文等级	作者文中单位	收录情况	影响因子	中科院大类分区
1	CURI-YOLOv7: A Lightweight YOLOv7tiny Target Detector for Citrus Trees from UAV Remote Sensing Imagery Based on Embedded Device	REMOTE SENSING 出版年：2023 出版日期：OCT 卷期：15 19 页码：- 文献号：4647 文献类型：Article	第一作者	A 类	华南农业大学工程学院	SCI	IF2-year=4.2 IF5-year=4.9 （2023）	地球科学 2 区 Top 期刊：否 OA 期刊：是 （2023）
2	Advances and Developments in Monitoring and Inversion of the Biochemical Information of Crop Nutrients Based on Hyperspectral Technology	AGRONOMY-BASEL 出版年：2023 出版日期：AUG 卷期：13 8 页码：- 文献号：2163 文献类型：Review	第一作者	A 类	华南农业大学工程学院	SCI	IF2-year=3.3 IF5-year=3.7 （2023）	农林科学 2 区 Top 期刊：否 OA 期刊：是 （2023）
3	Detection of Power Poles in Orchards Based on Improved Yolov5s Model	AGRONOMY-BASEL 出版年：2023 出版日期：JUL 卷期：13 7 页码：- 文献号：1705 文献类型：Article	第一作者	A 类	华南农业大学工程学院	SCI	IF2-year=3.3 IF5-year=3.7 （2023）	农林科学 2 区 Top 期刊：否 OA 期刊：是 （2023）

4	Research hotspots and frontiers in agricultural multispectral technology: Bibliometrics and scientometrics analysis of the Web of Science	FRONTIERS IN PLANT SCIENCE 出版年：2022 出版日期：AUG 11 卷期：13 页码：- 文献号：955340 文献类型：Article	第一作者	A 类	华南农业大学 工程学院	SCI	IF2-year=5.6 IF5-year=6.8 （2022）	生物学 2 区 Top 期刊：是 OA 期刊：是 （2022）
5	Detection of Rice Spikelet Flowering for Hybrid Rice Seed Production Using Hyperspectral Technique and Machine Learning	AGRICULTURE-BASEL 出版年：2022 出版日期：JUN 卷期：12 6 页码：- 文献号：755 文献类型：Article	第一作者	B 类	华南农业大学 工程学院	SCI	IF2-year=3.6 IF5-year=3.6 （2022）	农林科学 3 区 Top 期刊：否 OA 期刊：是 （2022）
6	Research Progress and Prospects of Agricultural Aero-Bionic Technology in China	APPLIED SCIENCES-BASEL 出版年：2021 出版日期：NOV 卷期：11 21 页码：- 文献号：10435 文献类型：Review	第一作者	B 类	华南农业大学 工程学院	SCI	IF2-year=2.838 IF5-year=2.921 （2021）	工程技术 4 区 Top 期刊：否 OA 期刊：是 （2021）
7	Development and Prospect of UAV-Based Aerial Electrostatic Spray Technology in China	APPLIED SCIENCES-BASEL 出版年：2021 出版日期：MAY 卷期：11 9 页码：-	第一作者	B 类	华南农业大学 工程学院	SCI	IF2-year=2.838 IF5-year=2.921 （2021）	工程技术 4 区 Top 期刊：否 OA 期刊：是 （2021）

		文献号：4071 文献类型：Review						

说明：论文等级和中科院大类分区按《华南农业大学学术论文评价方案（试行）》划分。

报告免责声明:如未盖章,报告无效

检索员：刘汉忠

华南农业大学图书馆

2026-03-12

SCAULIB202625967

检索证明

根据委托人提供的论文材料，委托人华南农业大学工程学院 张亚莉(学科类型:自然科学) 14 篇论文收录情况如下表。

序号	论文名称	发表刊物及发表的年月卷期/页码等	作者排名	论文等级	作者文中单位	收录情况	影响因子	中科院大类分区
1	Non-destructive prediction of soluble solids content and firmness and maturity determination of guava fruit using color and fluorescence imaging	POSTHARVEST BIOLOGY AND TECHNOLOGY 出版年：2025 出版日期：SEP 卷期：227 页码：- 文献号：113620 文献类型：Article	共同通讯作者（倒数第一）	T2 类	华南农业大学工程学院	SCI	IF2-year=6.8 IF5-year=7.5 （2024）	农林科学 1 区 Top 期刊：是 OA 期刊：否 （2025）
2	Multiple light sources excited fluorescence image-based non-destructive method for citrus Huanglongbing disease detection	COMPUTERS AND ELECTRONICS IN AGRICULTURE 出版年：2025 出版日期：OCT 卷期：237 页码：- 文献号：110549 文献类型：Article	共同通讯作者	T2 类	华南农业大学工程学院	SCI	IF2-year=8.9 IF5-year=9.3 （2024）	农林科学 1 区 Top 期刊：是 OA 期刊：否 （2025）
3	Droplet distributions in cotton harvest aid applications vary with the interactions among the unmanned	INDUSTRIAL CROPS AND PRODUCTS 出版年：2021	共同通讯作者	T2 类	华南农业大学工程学院	SCI	IF2-year=6.449 IF5-year=6.508 （2021）	农林科学 1 区 Top 期刊：是 OA 期刊：否

华南农业大学图书馆 信息检索专用章

	aerial vehicle spraying parameters	出版日期：MAY 卷期：163 页码：- 文献号：113324 文献类型：Article						（2021）
4	Citrus huanglongbing detection: A hyperspectral data-driven model integrating feature band selection with machine learning algorithms	CROP PROTECTION 出版年：2025 出版日期：FEB 卷期：188 页码：- 文献号：107008 文献类型：Article	共同通讯作者（倒数第一）	A 类	华南农业大学工程学院	SCI	IF2-year=2.5 IF5-year=3.0 （2024）	农林科学 2 区 Top 期刊：否 OA 期刊：否 （2025）
5	Design of Chili Field Navigation System Based on Multi-Sensor and Optimized TEB Algorithm	AGRONOMY-BASEL 出版年：2024 出版日期：DEC 卷期：14 12 页码：- 文献号：2872 文献类型：Article	通讯作者	A 类	华南农业大学工程学院	SCI	IF2-year=3.4 IF5-year=3.8 （2024）	农林科学 2 区 Top 期刊：否 OA 期刊：是 标注：Mega-Journal （2025）
6	Fluorescence spectroscopy detection of carbendazim residue in cucumber juice based on BC	JOURNAL OF FOOD COMPOSITION AND ANALYSIS 出版年：2024 出版日期：JUN 卷期：130 页码：- 文献号：106157 文献类型：Article	通讯作者	A 类	华南农业大学工程学院	SCI	IF2-year=4.6 IF5-year=4.6 （2024）	农林科学 2 区 Top 期刊：是 OA 期刊：否 （2025）

华南农业大学图书馆 信息检索专用章

7	Deep-Learning-Based Rice Disease and Insect Pest Detection on a Mobile Phone	AGRONOMY-BASEL 出版年：2023 出版日期：AUG 卷期：13 8 页码：- 文献号：2139 文献类型：Article	通讯作者	A 类	华南农业大学工程学院	SCI	IF2-year=3.3 IF5-year=3.7 （2023）	农林科学 2 区 Top 期刊：否 OA 期刊：是 （2023）
8	Inversion of Leaf Area Index in Citrus Trees Based on Multi-Modal Data Fusion from UAV Platform	REMOTE SENSING 出版年：2023 出版日期：JUL 卷期：15 14 页码：- 文献号：3523 文献类型：Article	通讯作者	A 类	华南农业大学工程学院	SCI	IF2-year=4.2 IF5-year=4.9 （2023）	地球科学 2 区 Top 期刊：否 OA 期刊：是 （2023）
9	Design and validation of a multi-objective waypoint planning algorithm for UAV spraying in orchards based on improved ant colony algorithm	FRONTIERS IN PLANT SCIENCE 出版年：2023 出版日期：FEB 2 卷期：14 页码：- 文献号：1101828 文献类型：Article	共同通讯作者（倒数第一）	A 类	华南农业大学工程学院	SCI	IF2-year=4.1 IF5-year=5.3 （2023）	生物学 2 区 Top 期刊：是 OA 期刊：是 （2023）
10	Extraction of Citrus Trees from UAV Remote Sensing Imagery Using YOLOv5s and Coordinate Transformation	REMOTE SENSING 出版年：2022 出版日期：SEP 卷期：14 17 页码：-	通讯作者	A 类	华南农业大学工程学院	SCI	IF2-year=5.0 IF5-year=5.6 （2022）	工程技术 2 区 Top 期刊：是 OA 期刊：是 （2022）

华南农业大学图书馆 学术信息检索专用章

		文献号：4208 文献类型：Article						
11	Canopy Volume Extraction of Citrus reticulate Blanco cv. Shatangju Trees Using UAV Image-Based Point Cloud Deep Learning	REMOTE SENSING 出版年：2021 出版日期：SEP 卷期：13 17 页码：- 文献号：3437 文献类型：Article	通讯作者	A 类	华南农业大学工程学院	SCI	IF2-year=5.349 IF5-year=5.786 （2021）	工程技术 2 区 Top 期刊：是 OA 期刊：是 （2021）
12	Identification of Male and Female Parents for Hybrid Rice Seed Production Using UAV-Based Multispectral Imagery	AGRICULTURE-BASEL 出版年：2022 出版日期：JUL 卷期：12 7 页码：- 文献号：1005 文献类型：Article	通讯作者	B 类	华南农业大学工程学院	SCI	IF2-year=3.6 IF5-year=3.6 （2022）	农林科学 3 区 Top 期刊：否 OA 期刊：是 （2022）
13	Lightweight Semantic Segmentation Network for Real-Time Weed Mapping Using Unmanned Aerial Vehicles	APPLIED SCIENCES-BASEL 出版年：2020 出版日期：OCT 卷期：10 20 页码：- 文献号：7132 文献类型：Article	共同通讯作者（倒数第一）	B 类	华南农业大学工程学院	SCI	IF2-year=2.679 IF5-year=2.736 （2020）	工程技术 3 区 Top 期刊：否 OA 期刊：是 （2020）

华南农业大学图书馆 信息检索专用章

14	WSN-Assisted UAV Trajectory Adjustment for Pesticide Drift Control	SENSORS 出版年：2020 出版日期：OCT 卷期：20 19 页码：- 文献号：5473 文献类型：Article	通讯作者	B 类	华南农业大学 工程学院	SCI	IF2-year=3.576 IF5-year=3.735 （2020）	工程技术 3 区 Top 期刊：否 OA 期刊：是 （2020）

说明：论文等级和中科院大类分区按《华南农业大学学术论文评价方案（试行）》划分。

报告免责声明:如未盖章,报告无效

检索员：田成

华南农业大学图书馆

2026-03-13

华南农业大学图书馆SCAU LIBRARY

remote sensing

MDPI

Article

CURI-YOLOv7: A Lightweight YOLOv7tiny Target Detector for Citrus Trees from UAV Remote Sensing Imagery Based on Embedded Device

Yali Zhang [1,2,3], Xipeng Fang [1,3], Jun Guo [1,3], Linlin Wang [4], Haoxin Tian [5], Kangting Yan [3,6] and Yubin Lan [2,3,6,*]

1 College of Engineering, South China Agricultural University, Wushan Road, Guangzhou 510642, China; ylzhang@scau.edu.cn (Y.Z.); xpfang@stu.scau.edu.cn (X.F.); junguo@stu.scau.edu.cn (J.G.)
2 Guangdong Laboratory for Lingnan Modern Agriculture, Guangzhou 510642, China
3 National Center for International Collaboration Research on Precision Agricultural Aviation Pesticide Spraying Technology, Guangzhou 510642, China; ktyan@stu.scau.edu.cn
4 School of Artificial Intelligence, Shenzhen Polytechnic University, Shenzhen 518055, China; wanglinlin@szpt.edu.cn
5 College of Automation Engineering, Nanjing University of Aeronautics and Astronautics, Nanjing 211106, China; hxtian@stu.scau.edu.cn
6 College of Electronic Engineering and College of Artificial Intelligence, South China Agricultural University, Wushan Road, Guangzhou 510642, China
* Correspondence: ylan@scau.edu.cn

Abstract: Data processing of low-altitude remote sensing visible images from UAVs is one of the hot research topics in precision agriculture aviation. In order to solve the problems of large model size with slow detection speed that lead to the inability to process images in real time, this paper proposes a lightweight target detector CURI-YOLOv7 based on YOLOv7tiny which is suitable for individual citrus tree detection from UAV remote sensing imagery. This paper augmented the dataset with morphological changes and Mosica with Mixup. A backbone based on depthwise separable convolution and the MobileOne-block module was designed to replace the backbone of YOLOv7tiny. SPPF (spatial pyramid pooling fast) was used to replace the original spatial pyramid pooling structure. Additionally, we redesigned the neck by adding GSConv and depth-separable convolution and deleted its input layer from the backbone with a size of (80, 80) and its output layer from the head with a size of (80, 80). A new ELAN structure was designed, and the redundant convolutional layers were deleted. The experimental results show that the GFLOPs = 1.976, the parameters = 1.018 M, the weights = 3.98 MB, and the mAP = 90.34% for CURI-YOLOv7 in the UAV remote sensing imagery of the citrus trees dataset. The detection speed of a single image is 128.83 on computer and 27.01 on embedded devices. Therefore, the CURI-YOLOv7 model can basically achieve the function of individual tree detection in UAV remote sensing imagery on embedded devices. This forms a foundation for the subsequent UAV real-time identification of the citrus tree with its geographic coordinates positioning, which is conducive to the study of precise agricultural management of citrus orchards.

Keywords: citrus trees; remote sensing; YOLOv7; lightweight; target detector

check for updates

Citation: Zhang, Y.; Fang, X.; Guo, J.; Wang, L.; Tian, H.; Yan, K.; Lan, Y. CURI-YOLOv7: A Lightweight YOLOv7tiny Target Detector for Citrus Trees from UAV Remote Sensing Imagery Based on Embedded Device. *Remote Sens.* **2023**, *15*, 4647. https://doi.org/10.3390/rs15194647

Academic Editor: Pedro Melo-Pinto

Received: 17 July 2023
Revised: 25 August 2023
Accepted: 18 September 2023
Published: 22 September 2023

Copyright: © 2023 by the authors. Licensee MDPI, Basel, Switzerland. This article is an open access article distributed under the terms and conditions of the Creative Commons Attribution (CC BY) license (https://creativecommons.org/licenses/by/4.0/).

1. Introduction

Agricultural aviation constitutes a pivotal component of modern agriculture [1]. In recent years, there has been a notable surge in the development of agricultural aircrafts in China [2]. In tandem with the inception and advancement of precision agricultural aviation [3], the utilization of UAV remote sensing has the potential to harness fine-scale and dynamically continuous monitoring across farmlands [4]. This technology harbors extensive prospective applications in monitoring crop growth trends [5]. Notably, China stands as one of the foremost citrus-producing nations [6]. Leveraging UAV imagery

presents inherent advantages in fruit tree management, encompassing tasks such as quantification [7], surveillance [8], pest and disease monitoring [9], prescription mapping [10], and identification as well as localization [11]. In the realm of research, endeavors have been undertaken to amalgamate deep learning with UAV imagery [12], facilitating information extraction [13] and segmentation [14]. This amalgamation furnishes a potent instrument for the evolution of precision agriculture, aimed at enhancing productivity and optimizing resource allocation.

An increasing number of scholars are refining existing deep learning algorithms to meet the demands of UAV image detection. Wang et al. [15] synergized YOLOX with migration learning to enhance the accuracy of male cob detection within UAV images, thereby furnishing a high-precision detection methodology tailored for UAV imagery of male corn cobs. Bao et al. [16] introduced a wheat count detection model using TPH-YOLO (YOLO with transformer prediction heads). They employed transformer prediction heads with transfer learning and other strategies to elevate wheat counting accuracy in UAV images. Zhang et al. [17] adopted data augmentation through Mixup and replaced the C3 module with the GhostBottleneck module. Coupled with the Shuffle Attention (SA) module, this approach heightened the focus on small targets. Their creation, YOLOv5s Pole, is geared towards the deployment of agricultural UAV airborne equipment. Luo et al. [18] put forth a YOLO-DRONE that employs distinct activation functions in shallow and deep networks. This algorithm simplifies the recognition of UAV remote sensing images. Zhu et al. [19] introduced the YOLOv4 -Mobilenetv3—CBAM—ASFF—P algorithm, which significantly reduces the model's size compared to the original YOLOv4 while achieving a 98.21% mAP. This adaptation enhances the accuracy of detecting canopy layers in UAV photographs of fruit trees.

The algorithms advanced by scholars in the aforementioned study indeed exhibited enhanced detection accuracy in comparison to the original algorithms. However, these algorithms suffer from challenges such as high GFLOPs and parameter counts, as well as weighty files, resulting in sluggish performance on embedded devices. Consequently, they are unsuitable for processing UAV aerial images targeting citrus trees. Thus, it is of great significance to develop a target detector that can be carried on an embedded device and achieve the imagery processing of citrus orchards. Due to the limited arithmetic power of the embedded devices carried by agricultural UAVs [20,21], this study concentrates on a specific application scenario involving UAV aerial images of citrus trees. The primary emphasis is on strategies to curtail the GFLOPs requirements of the airborne model, optimize the balance between the number of parameters and the model size, and enhance the model's detection speed when operating on embedded devices.

This study introduces a lightweight YOLOv7tiny target detector named CURI-YOLOv7, specifically designed for detecting citrus trees using UAV remote sensing imagery on embedded devices. To achieve this, several key designs choices have been made. First, the CURI-YOLOv7 utilizes a MobileOne-block based backbone structure, leading to a substantial reduction in the model's parameter count. Second, an SPPF structure is employed in place of the original structure, significantly enhancing the model's inference speed. Third, a lightweight ELAN (L-E) structure is adopted as a replacement for ELAN, thereby mitigating the impact of non-critical information on the model. Finally, the neck structure is revamped using GSConv and depth-separable convolution techniques, effectively eliminating the cumbersome target detection layer and thereby resolving the issue of sluggish inference speed on embedded devices. In comparison to alternative target detection algorithms, CURI-YOLOv7 boasts a more lightweight overall network structure. Simultaneously, there are reductions in both GFLOPs and parameter counts, accompanied by a notable improvement in frames per second (FPS). This combination of enhancements renders CURI-YOLOv7 particularly well-suited for deployment on agricultural UAVs and associated image processing tasks. Furthermore, it aligns seamlessly with the application scenario of UAV aerial citrus tree detection, making it an appropriate choice for precision management of citrus orchards.

2. Materials and Methods

2.1. Collection and Production of Datasets

The citrus tree images were collected at citrus orchards in Sihui City, Guangdong Province, China (23°36′N, 112°68′E), as shown in Figure 1. The temperature at the time of the experiment was 35.2 °C, and the humidity was 61.7%. A DJI Phantom 4 RTK quadrotor UAV was selected to collect data. The flight altitude of the aircraft was set to 50 m, the heading overlap rate was 80%, the side overlap rate was 80%, the camera angle was 90°, the ground sample distance (GSD) was 1.3699 cm/pixel, and the pixel size was 4864 × 3648 (pixels). After data augmentation, 1640 images were obtained for this experiment. The topography of the citrus groves is close to the plain, with an average slope of less than 5°. The citrus trees inside the zones were 1.5–2 m tall with an average crown diameter of 2 m. The trees were all spaced about 3 m apart. Due to the presence of water tanks and irrigation pipes throughout the rows of fruit trees, it was not possible for ground equipment to pass between the rows of citrus trees. Therefore, the dataset could only be collected using aerial photography from UAVs and could not be collected by ground trolleys or other ground equipment.

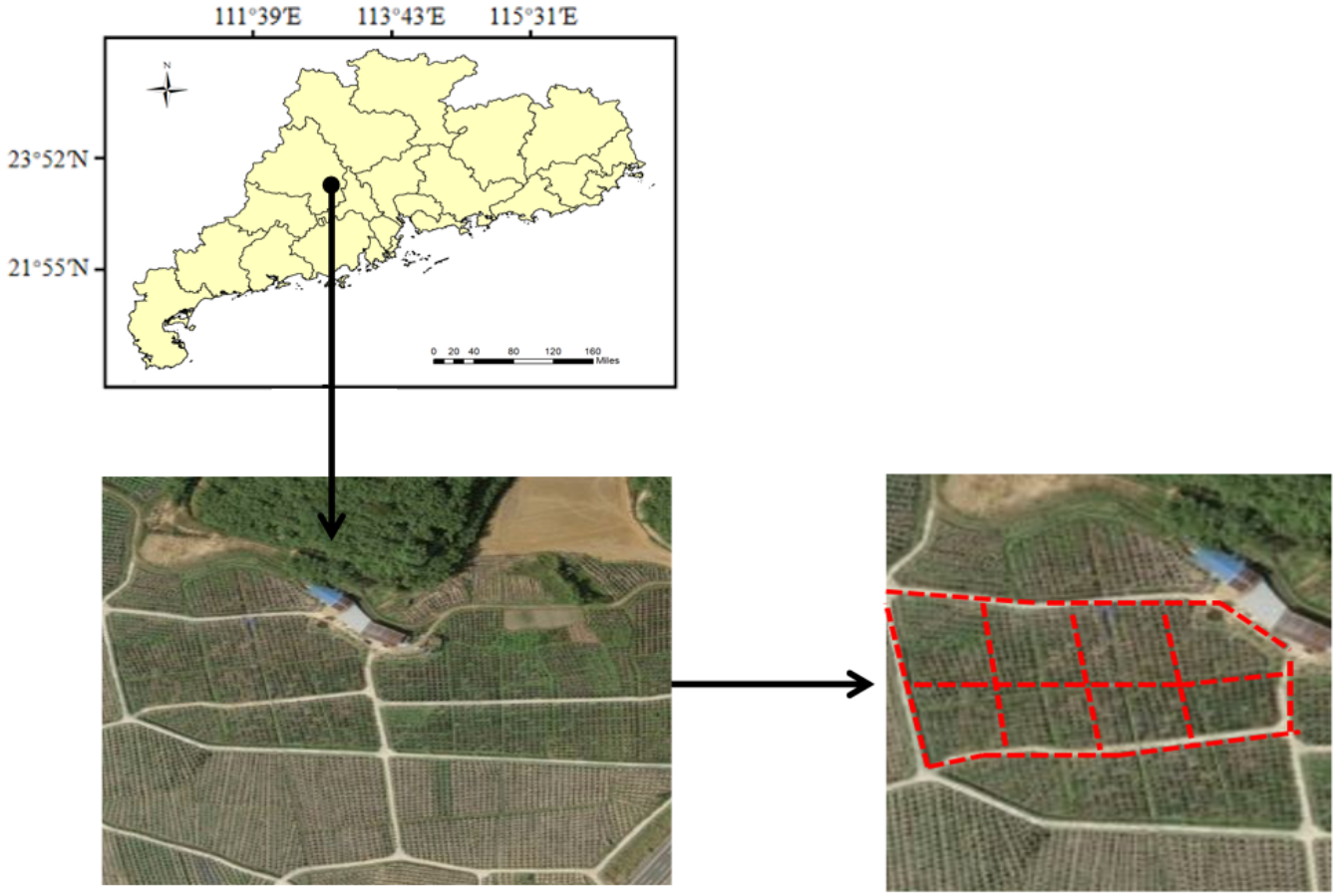

Figure 1. Location of data collection sites (23°36′N, 112°68′E): (**a**) shows the experiment area located in Guangdong; (**b**) the dashed box shows part of the collection area.

CNNs often face the risk of overfitting caused by limited data [22]. To address this problem, this study used various data augmentation methods, including morphological processing data augmentation, Mosica data augmentation, and Mixup data augmentation. Morphological processing includes rotation and overturn. It can improve the robustness of the model and improve models' performance. Mosica and Mixup data augmentation are the original data augmentation methods included in the YOLOv7 target detector. Mosica data

augmentation can effectively improve the model's ability to learn the correlation between objects in the dataset. Mixup data augmentation can effectively reduce the overfitting phenomenon and improve the generalization ability of the model. Figure 2 shows a demonstration of morphological processing data augmentation.

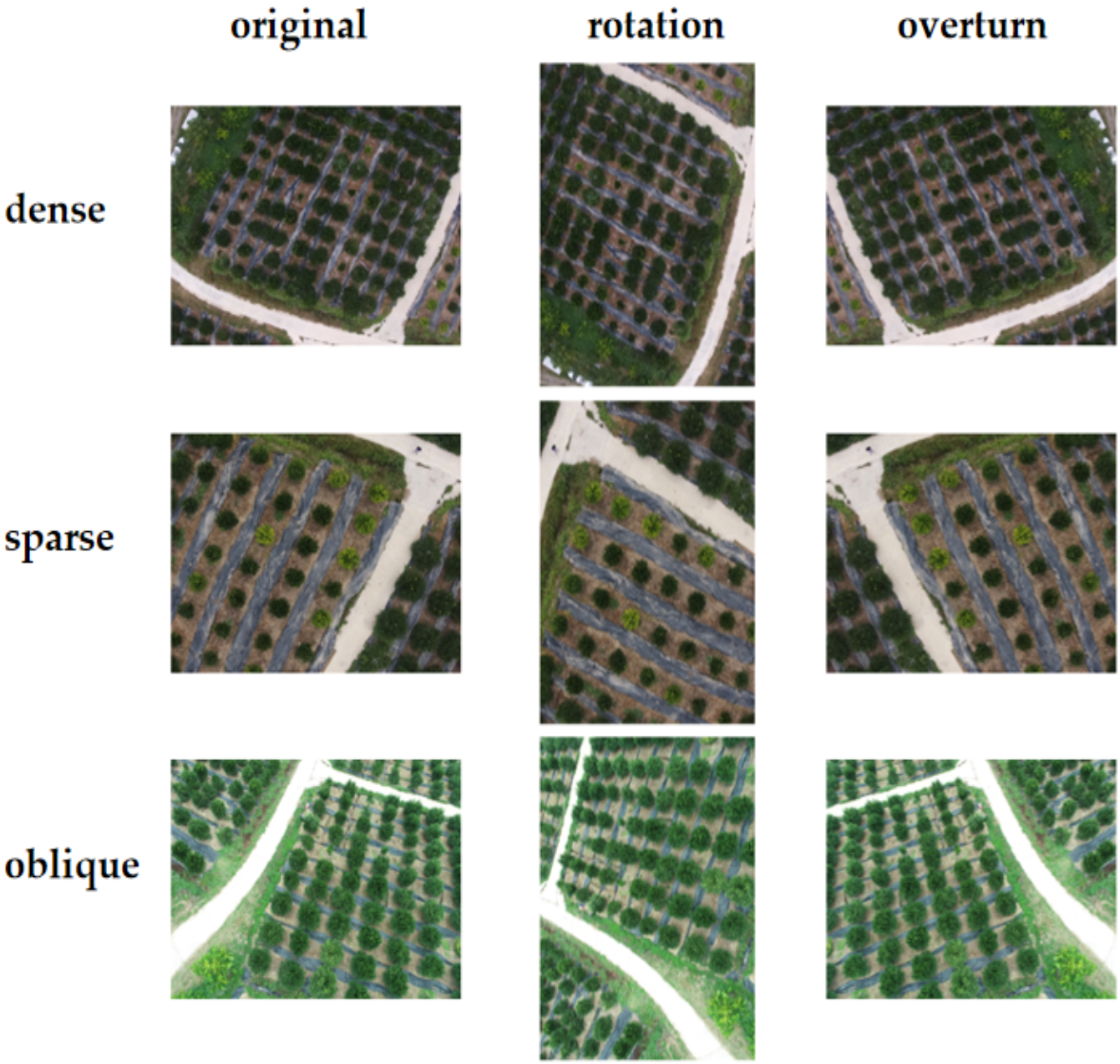

Figure 2. Example of morphological data augmentation.

Manual annotation of images is also required in order to obtain accurate data parameters [23]. In this study, labelimg [24] was used as the dataset labelling tool. Rectangular labels were used for labelling and saved as XML files in Pascal VOC format. A total of 1640 images were divided into (training set:validation set):test set = (9:1):1. At the time of labelling, citrus trees were not labelled if they were obscured by more than two-thirds in the corners of the image. Similarly, citrus trees in the seedling stage or smaller-sized citrus trees were not labeled.

2.2. CURI-YOLOv7 Structure Detail

CURI-YOLOv7 is a weight-improved target detector based on YOLOv7tiny. It focuses on enhancing the detection speed on both computer and embedded devices while minimizing any potential degradation in target detection precision and recall. Additionally, CURI-YOLOv7 effectively reduces the number of parameters and GFLOPs required by the model. The network structure diagram is shown in Figure 3, and the main improvements reducing its weight are as follows:

(1) Redesigned backbone based on MobileOne-block structure
(2) Replaced the original structure with a faster structure named SPPF
(3) Removed the big target detection layer and redesigned the input structure and output structure of PANet
(4) Replaced the ELAN structure in YOLOv7tiny with Lightweight-ELAN (L-E).
(5) Replaced the convolutional layer in the neck network using GSConv and depthwise separable convolution.

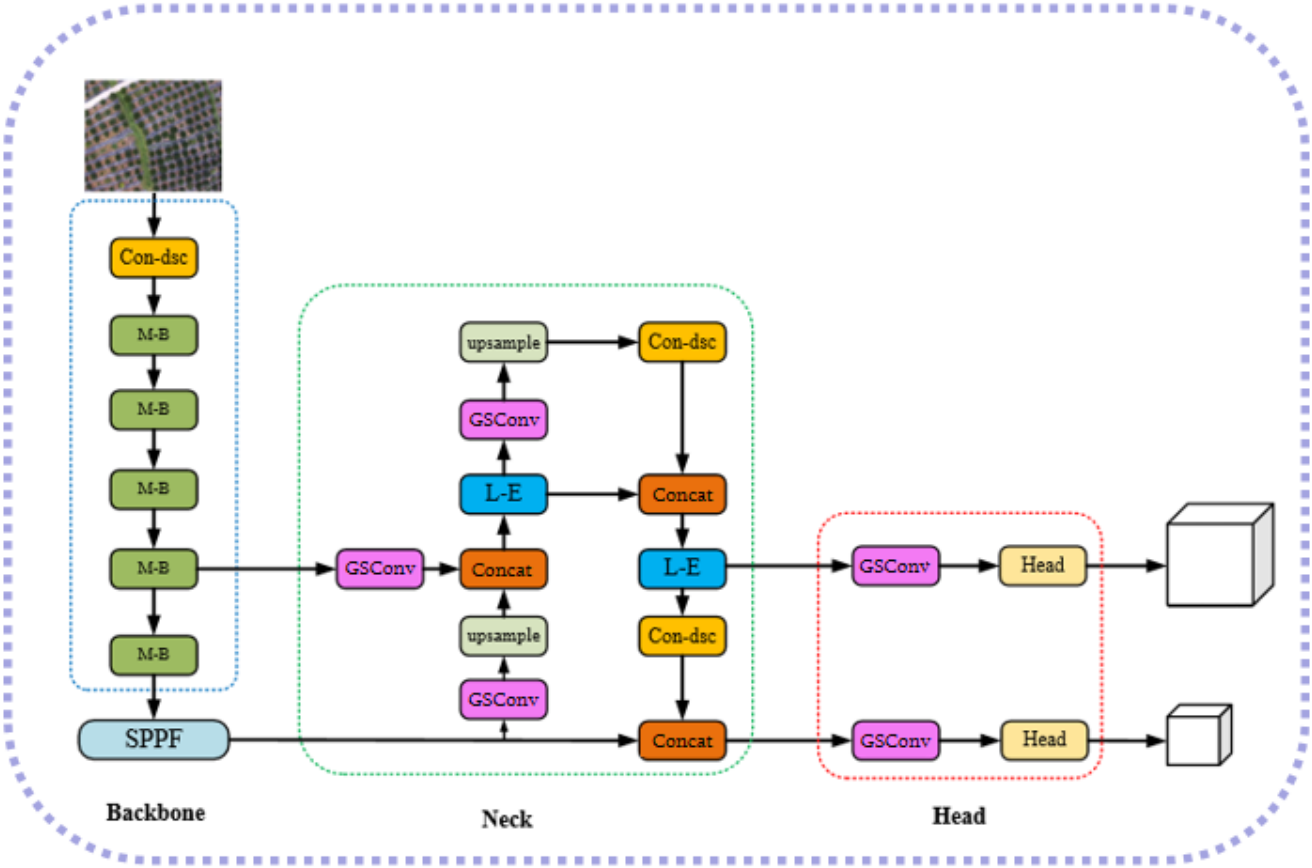

Figure 3. Structure of CURI-YOLOv7.

2.2.1. Construction of Backbone

MobileOne [25] is a lightweight backbone developed by Vasu. et al. in 2022 that features a simple and lightweight architecture. The structure of MobileOne is displayed in Figure 4. In terms of the concept of reparameterization, MobileOne incorporates a multi-branch structure that significantly reduces parameters and enhances the computational speed of the model.

The CURI-YOLOv7 target detector refers to MobileOne, utilizing the MobileOne-block as the base module of the backbone. Its structure and the number of input and output channels are shown in Table 1. This paper exclusively employs the training structure of MobileOne-block. Con_des in the table represents the depthwise separable convolution,

and the input shape of CURI-YOLOv7 is (640, 640, 3). To adjust the input channels of the backbone, a depthwise separable convolution is added. The utilization of the designed CURI-YOLOv7′s backbone instead of YOLOv7′s CSPDARKNET indeed leads to an improvement in the inference speed of the model. This enables the deployment of inference models in embedded devices and the real-time target detection of individual trees in citrus orchards in our study.

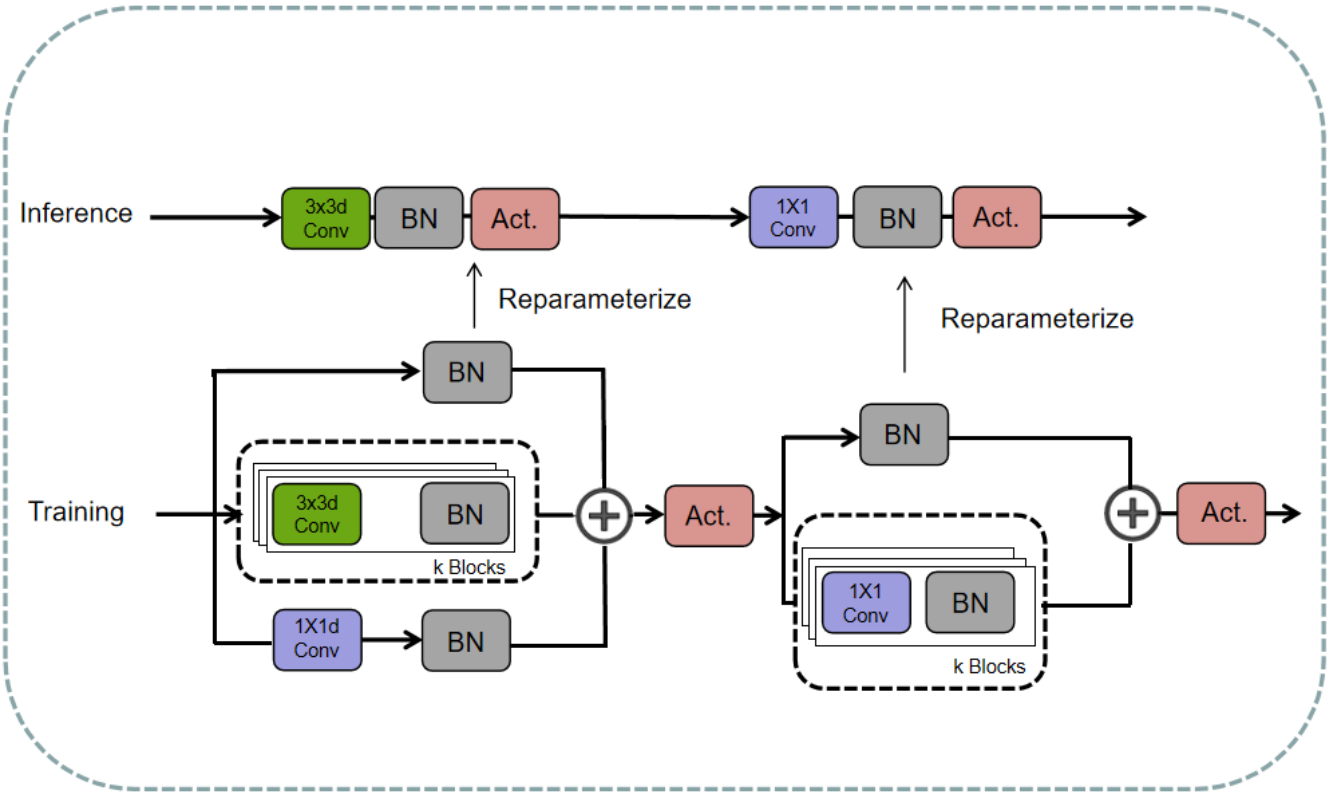

Figure 4. Structure of MobileOne-block.

Table 1. Structure and parameters of the backbone for CURI-YOLOv7.

Stage	Block-Type	Stride	Kernel Size	Input Channels	Output Channels
1	Con des	1		3	16
2	MobileOne-block	2	1	16	32
3	MobileOne-block	2	1	32	64
4	MobileOne-block	2	1	64	128
5	MobileOne-block	2	1	128	256
6	MobileOne-block	2	1	256	512

2.2.2. Spatial Pyramid Pooling and ELAN Improvements

The spatial pyramid pooling used in YOLOv7 is the SPPCSPC structure, which shows excellent performance, but the number of parameters and GFLOPs computed are substantially higher. Given that this study focuses exclusively on recognizing citrus trees as the target, it is worth noting that the structure and morphology of citrus trees are relatively simple. Consequently, it is possible to opt for a spatial pyramid pooling that may result in a slight decrease in detection accuracy compared to SPPCSPC. However, the advantage lies in achieving a notable reduction in both the number of parameters and GFLOPs. Jocher et al. adopted an improved spatial pyramid pooling fast (SPPF) [26] structure to replace the original SPP. The SPPF achieves the same computation result as the original parallel MaxPool layers of three different sizes by serializing multiple MaxPool layers of the same

size, greatly reducing the computation time [27]. The main difference between the two is that the speed of inference varies greatly. The structures of SPPCSPC and SPPF are shown in Figure 5.

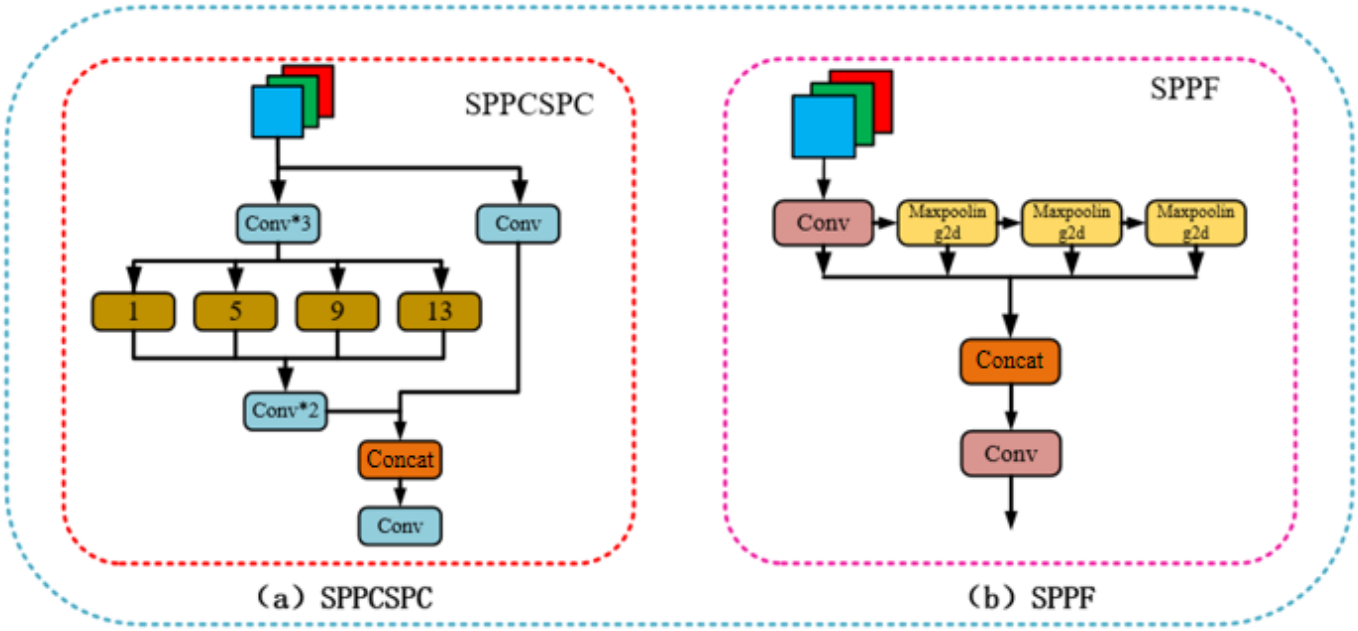

Figure 5. Comparison between the structures of SPPCSPC and SPPF: (**a**) shows the SPPCSPC structure, and (**b**) shows the SPPF structure.

ELAN (extended efficient layer aggregation networks), designed by Wang et al. [28], were first used in the YOLOv7 target detector. Considering the requirements in terms of inference speed in embedded devices, this study designs a lightweight ELAN structure: L-ELAN (lightweight-extended efficient layer aggregation networks). By modifying the paths of ELAN, convolutional layers that are not useful for our target detector are deleted. However, the design concept of YOLOv7 and the fundamental design concept of the ELAN structure remain unchanged. By performing tests and identifying convolutional layers within the ELAN structure that are not useful for this research dataset, these identified convolutional layers were deleted, and the L-ELAN structure was created. Specifically, the focus was on identifying convolutional layers that have little impact on the mean average precision (MAP) after their removal. Figure 6 provides a visual comparison between ELAN in YOLOv7tiny and L-ELAN.

2.2.3. Construction of the Input and Output Layers of the Neck

In both YOLOv7 and YOLOv7tiny, the output feature layer sizes are (80, 80), (40, 40), and (20, 20), respectively. The corresponding detection target types are small targets, medium targets, and large targets [29]. Since convolutional kernels of different sizes can obtain information on different sizes of imagery, when extracting features for small targets, the effect of retaining more local feature information on small targets can be achieved by selecting the appropriate perceptual field size or considering multi-scale perceptual fields [30].

In the dataset constructed for our study, the citrus trees in the images are usually similar and fixed in size because the height of the aerial photograph is set to 50 m. YOLOv7 has a wide feature receptive field, but in our study, it was not necessary to use all of the output feature layers in order to obtain a wide receptive field. To reduce the number of parameters and GFLOPs and improve the inference speed on the embedded device, the proposed CURI-YOLOv7 target detector deletes the smaller target detection layer with output feature layer size (80, 80), deletes the feature layer with input size (80, 80) from the

neck network, and redesigns the neck network to match the number of input and output channels on the neck of YOLOv7tiny.

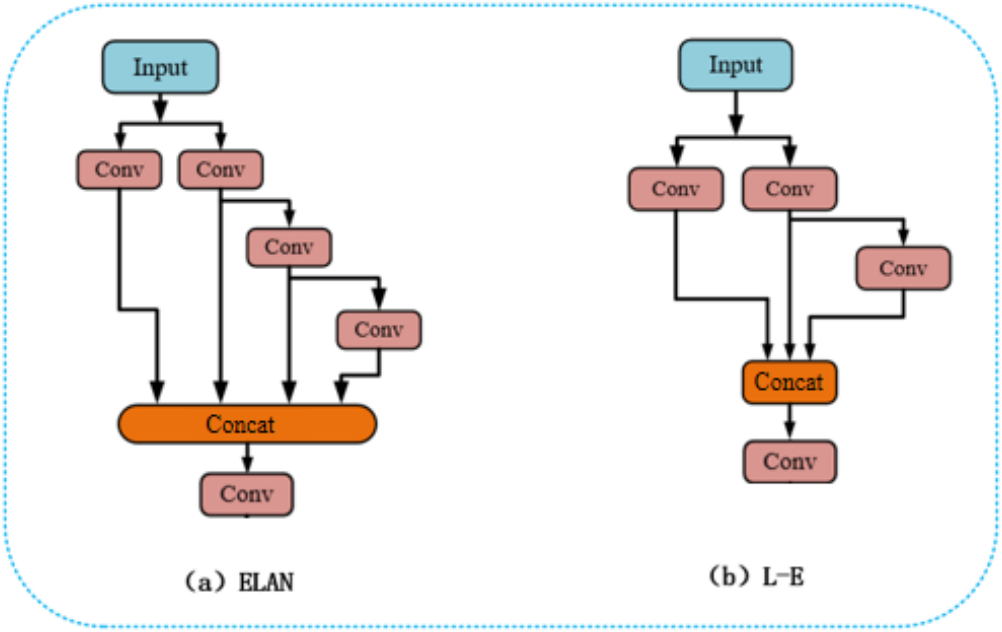

Figure 6. Comparison between ELAN in YOLOv7tiny and L-E.

2.2.4. Fusion of GSConv and Depthwise Separable Convolution into the Neck

CURI-YOLOv7 adopts GSConv [31] and depthwise separable convolution [32] instead of normal convolution in order to reduce the parameters and inference speed, and its structure diagram is shown in Figure 7. Through extensive experiments, we found the best alternative solutions for GSConv and depthwise separable convolution within the design framework of CURI-YOLOv7.

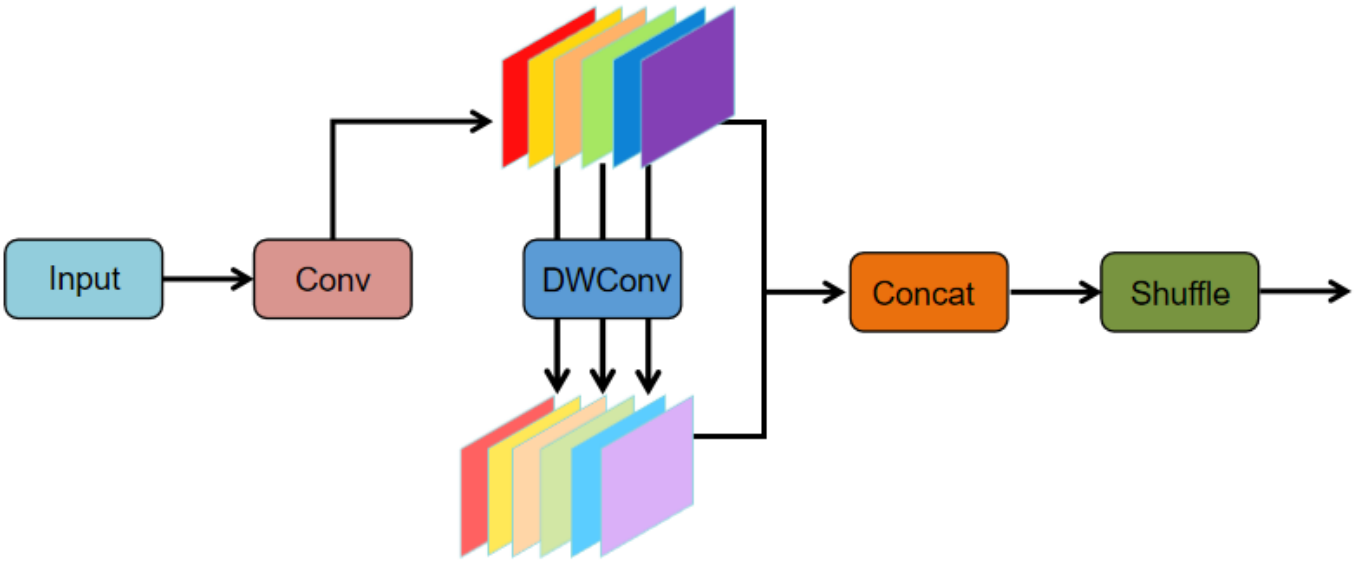

Figure 7. The structure diagram of GSConv.

GSConv is a variant of a convolutional neural network. GSConv retains as many of these connections as possible while keeping the time complexity small, which reduces information loss and enables faster operation [33].

Depthwise separable convolution (DSC) [32] is a convolutional operation whose structure is depicted in Figure 8. The calculation process is described by Equation (1). G stands for the output feature; K stands for the convolution kernel; F stands for the input feature; i,j is the feature pixel position; k,l is the output feature resolution; and m is the number of channels [34]. DSC has gained widespread adoption in recent years for model lightweighting studies. In comparison to standard convolution, it achieves the same feature extraction effect. The key advantage of this convolution is its effective reduction of model parameters.

$$G_{k,l,m} = \sum_{i,j} K_{i,j,m} \cdot F_{K+i-1,l+j-1,m} \quad (1)$$

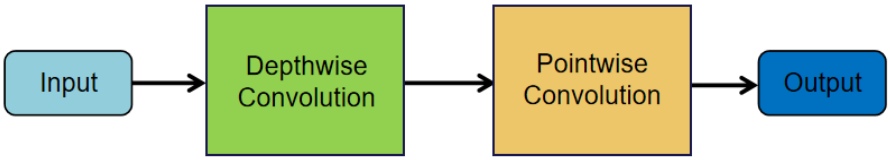

Figure 8. The structure diagram of depthwise separable convolution.

2.3. Embedded Device

The embedded device Jetson Xavier Nx (NVIDIA's GPU edge-computing device to be released in 2020 [35]) with high performance [36] was chosen for our experiment. The Jetson Xavier Nx was equipped with the Jetson Xavier Nx Developer Kit with Ubuntu 18.04, and the Python 3.6 and PyTorch environments were configured for this study. The details of the embedded devices are shown in Table 2.

Table 2. Technical specifications of the embedded devices.

CPU	GPU	Size	DLA	Vision Accelerator
6-core NVIDIA Carmel Arm v8.2 64-bit CPU	384-core NVIDIA Volta™ architecture GPU with 48 Tensor Cores	69.6 mm × 45 mm	2 × NVDLA	2 × PVA

2.4. Evaluation Indicators and Training Environment Setting

Deep learning has various evaluation metrics. In order to quantitatively analyze the performance of target detection algorithms, researchers have formulated many evaluation indicators, such as precision, recall, F1 score, frames per second (FPS), etc., [37]. Precision refers to the ratio of samples correctly classified by the classifier to the total number of samples. It measures the proportion of predicted positive samples that are actually positive, and it is calculated as shown in Equation (2). Recall represents the ratio of positive samples correctly classified by the classifier to the total number of true positive samples. It indicates the ability to correctly identify all positive cases, and it is calculated as shown in Equation (3). F1 score is a metric that represents the weighted average of accuracy and recall, reflecting the overall performance of a classifier. A higher F1 score indicates better classifier performance. The F1 score can be calculated by using Equation (4), as shown in the paper. AP, on the other hand, stands for average precision and is another evaluation metric used in object detection tasks. The calculation of AP is outlined in Equation (5), as presented in the paper.

$$Precision = \frac{TP}{TP + FP} \quad (2)$$

$$Recall = \frac{TP}{TP + FN} \quad (3)$$

$$F1 = \frac{2 \times Precision \times Recall}{Precision + Recall} \tag{4}$$

$$AP = \int_0^1 Precision(Recall)d(Recall) \tag{5}$$

The training experimental environment is configured as shown in Table 3. In order to ensure the reliability of the ablation study and the analysis of comparative models, the input size of the target detectors in this study was uniformly set at 640 × 640. Due to changes in the model structure, unfreeze training was employed without utilizing pre-trained weights. The epoch and batch size were set to 610 and 16, respectively. The study utilized SGD as the optimizer, with a Score_Threshold value set to 0.5.

Table 3. Experimental configuration.

CPU	GPU	CUDA	Pycharm	Pytorch	Numpy	Torchvision
i9-10900KF	RTX-3090	11.0	2020.1 × 64	1.7.1	1.21.5	0.8.2

3. Results

3.1. Ablation Study

In order to verify the design rationality of CURI-YOLOv7, an ablation study was designed in this study, as shown in Table 4.

Table 4. Effect of different modules on CURI-YOLOv7.

Backbone	SPPF&L-E	Neck	GFLOPs	Paras (M)	Weights (MB)	FPS (on Computer)
			13.181	6.014	23.1	83.07
√			6.669	3.726	14.3	95.12
√	√		5.877	3.181	12.2	104.29
√	√	√	1.976	1.018	3.98	128.83

The backbone in the table refers to the MobileOne-block-based backbone constructed by CURI-YOLOv7 and discussed in Section 2.2.1. The abbreviations SPPF and L-E represent the two improvements discussed in Section 2.2.2. "Neck" in Table 4 represents the design of the neck network and the fusion of GSConv and depthwise separable convolution into the neck, as discussed in Sections 2.2.3 and 2.2.4. Since both are improvements pertaining to the neck, they are discussed together in the ablation study.

The experimental data reveal that the parameters and FPS of the YOLOv7tiny model are 6.014 M and 83.07, respectively, which are characterized by a large number of parameters and low computing speed. By gradually incorporating the improvement modules discussed earlier, Table 3 demonstrates that CURI-YOLOv7, with all improvements added or replaced, exhibits significant enhancements. Specifically, compared to YOLOv7tiny, CURI-YOLOv7 showcases an 85.01% reduction in GFLOPs, an 83.07% reduction in the number of parameters, an 82.77% reduction in model weight size, and a 55.09% increase in FPS on a computer in the experimental environment.

3.2. The Comparation of CURI-YOLOv7 on Embedded Device

In this study, we selected Faster-Rcnn [38], SSD [39], YOLOv5s, YOLOv7tiny, and YOLOv8n for conducting comparative experiments alongside the CURI-YOLOv7 proposed in this paper. As YOLOv8n necessitates pre-trained weights to ensure the accurate computation of average accuracy (mAP); it was trained using pre-trained weights. The training process included a freezing training phase with a freeze epoch of 50 and an unfreeze epoch of 610 for optimal results.

The operational flow chart testing on the embedded device is presented in Figure 9. The process begins with training five comparison models and CURI-YOLOv7 separately on the computer using the processed dataset. After training, the weights obtained from the computer training process are saved. The results of training the six networks on the computer are summarized in Table 5. After the completion of training, the weights file is imported into the embedded device Jetson Xavier Nx, which is deployed with the PyCharm and PyTorch environment. All images within the test set were employed, and the detection of an individual image was conducted 100 times consecutively for each FPS test on the embedded device. This meticulous approach was adopted to accurately ascertain the detection speed of the images.

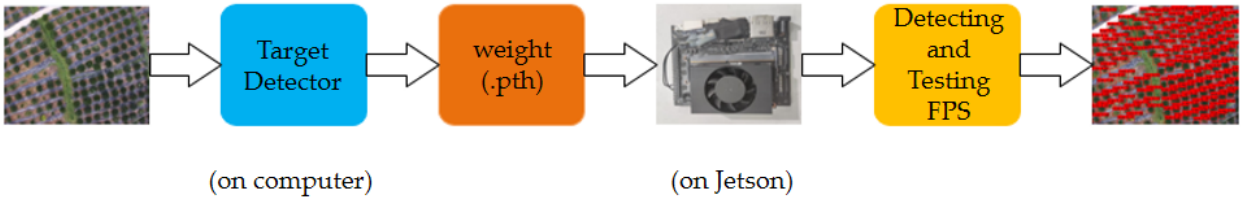

Figure 9. Flow chart for embedded device testing.

Table 5. Results of six models on a computer.

Models	GFLOPs	Paras (M)	Weights (MB)	F1	Recall (%)	Precision (%)	mAP@0.5 (%)
Faster-Rcnn	948.122	28.275	108	0.82	82.37	81.38	82.33
SSD	273.174	23.612	90.6	0.90	97.03	83.19	93.86
YOLOv5s	16.477	7.064	27.1	0.92	94.51	89.62	96.93
YOLOv7tiny	13.181	6.014	23.1	0.92	93.40	90.83	96.97
YOLOv8n	8.194	3.011	11.6	0.92	93.26	91.53	97.46
CURI-YOLOv7	1.976	1.018	3.98	0.86	83.70	89.02	90.34

The average FPS values obtained from above tests are shown in Figure 10. The results indicate that the two classical detectors, Faster R-CNN and SSD, exhibit generally slower average detection speeds. Faster R-CNN achieves an average detection speed of only 0.77, while SSD achieves 1.99 FPS. These speeds fall far below the average speed required for this study. With an average detection speed of 27.01 FPS on embedded devices, CURI-YOLOv7 delivers excellent performance and an 88.61% improvement over the original YOLOv7tiny.

3.3. The Comparison of CURI-YOLOv7 on Computer

Due to the poor performance of Faster R-CNN and SSD on embedded devices, as observed in Section 3.2, as well as their suboptimal mAP@0.5 results on the computer, it was determined that they were not suitable for comparison in this study. Additionally, their high GFLOPs and parameter counts do not meet the real-time image processing requirements of embedded devices. This is compounded by inadequate FPS. So, this section solely focuses on the performance comparison between the three YOLO series target detectors and the CURI-YOLOv7.

Figure 11 shows the PR curves of the four models. The horizontal coordinate is recall and the vertical coordinate is precision. The PR curves are generated by calculating a series of precision and recall points at different thresholds. The PR curve coverage areas for YOLOv8n, YOLOv5s, YOLOv7tiny, and CURI-YOLOv7 are 0.97, 0.96, 0.96, and 0.90, respectively. CURI-YOLOv7 does not cover as much area as the other three models, but also has a coverage area of 0.90. This suggests that while the average accuracy of CURI-YOLOv7 may be slightly lower than that of the comparison models, it is still substantial enough for the purposes of this study.

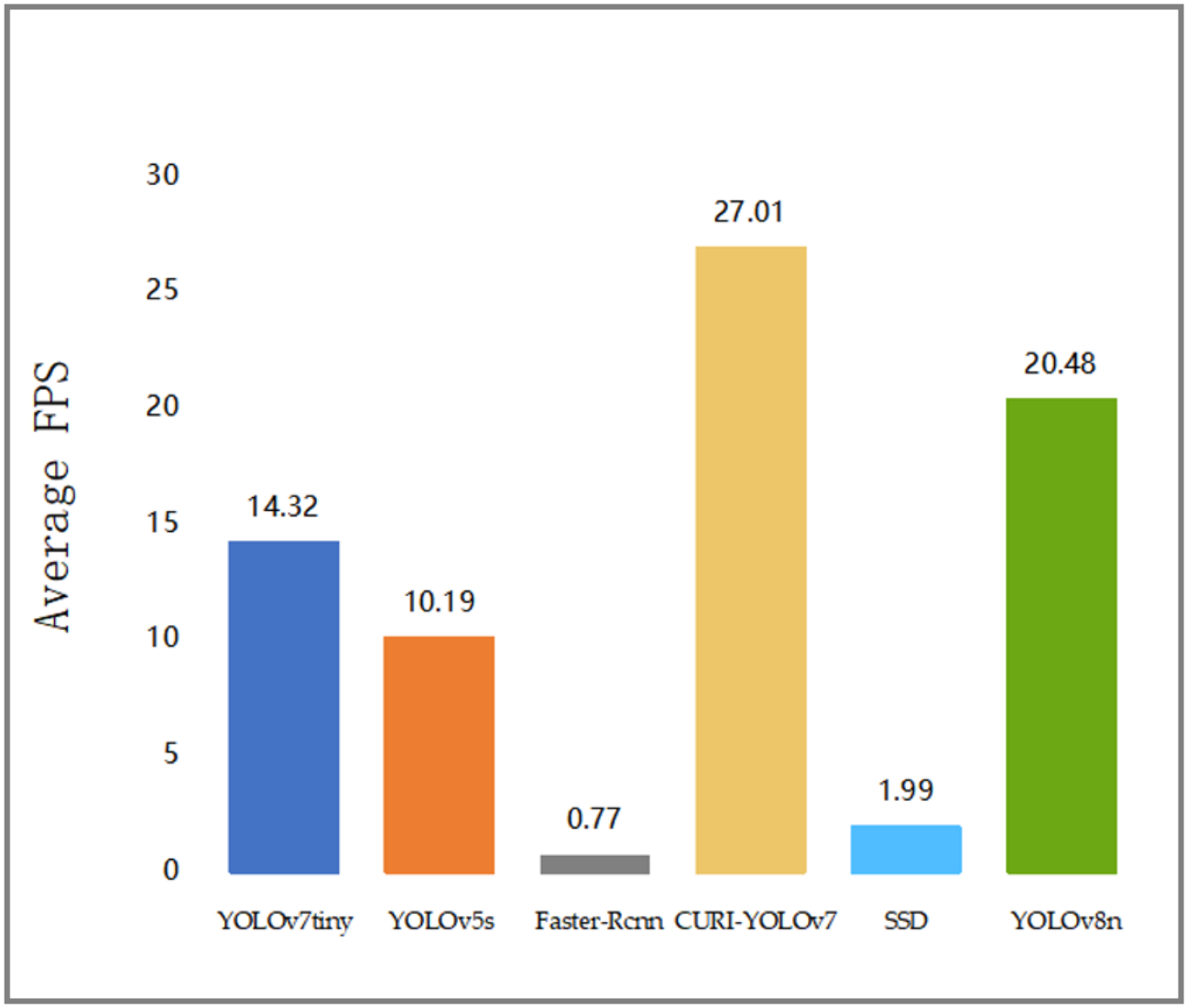

Figure 10. FPS test results for embedded devices.

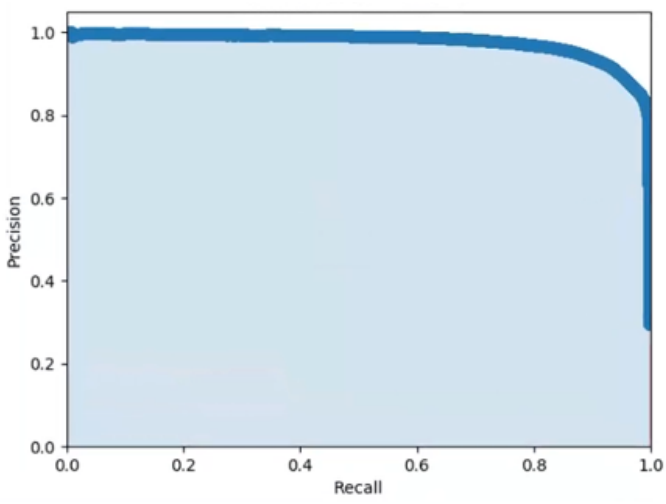

(**a**) YOLOv8n

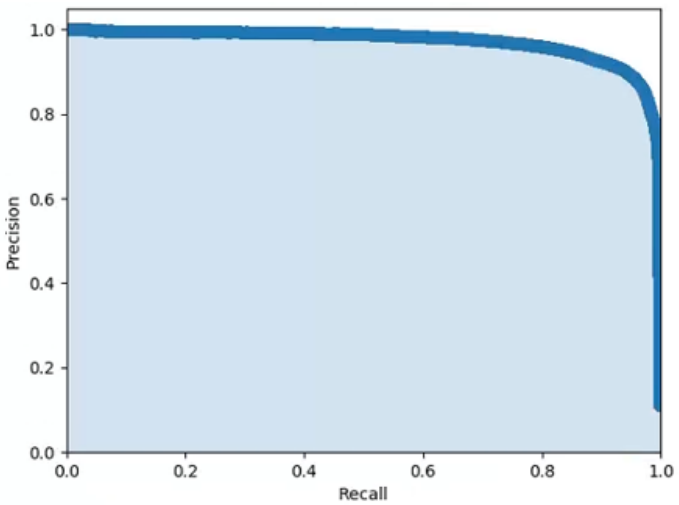

(**b**) YOLOv5s

Figure 11. *Cont.*

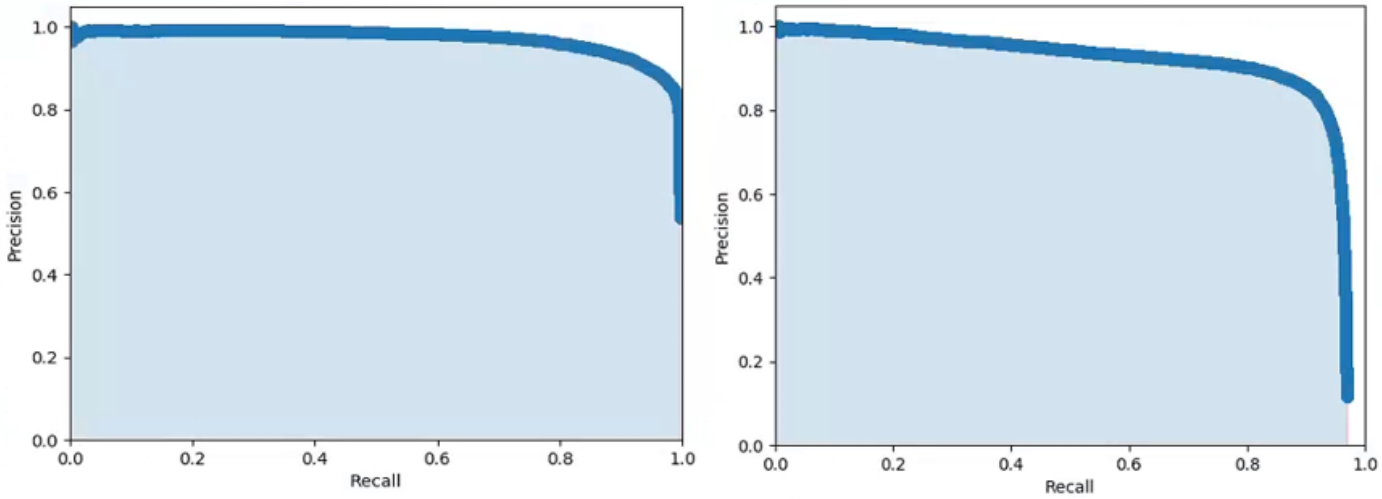

(**c**) YOLOv7tiny (**d**) CURI-YOLOv7

Figure 11. Precision–recall (PR) curves for the four models.

Figure 12 illustrates the loss function curves of the four models. An examination of the loss function indicates that all four models converge within a localized region after approximately 400 iterations. This observation underscores that the design of CURI-YOLOv7 is comparably rational and viable, akin to other target detectors within the YOLO series. Moreover, it is notable that the loss function of CURI-YOLOv7 is the most minimized among the four models during the training process, converging within the range of 0 to 0.5.

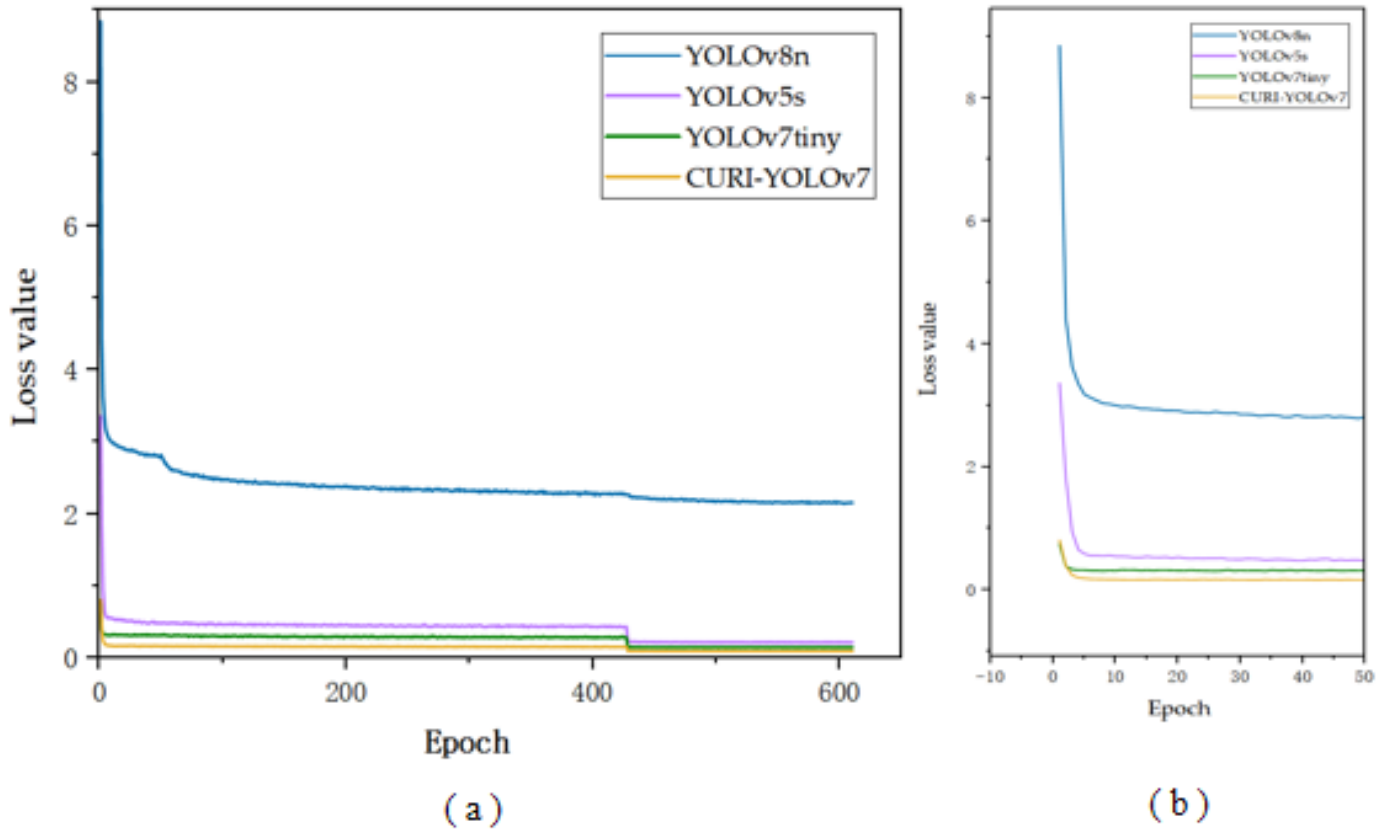

Figure 12. Loss curves: (**a**) complete loss functions for the four models; (**b**) local zooms at 0 to 50 epochs.

In order to ensure algorithm robustness and adapt deep learning algorithm models to different environments [40], in this study, attention heat maps are employed to substantiate the robustness of CURI-YOLOv7. Figure 13 illustrates the attentional heat map outputs for the four models using three different test datasets. Coordinates and feature heat maps in essence output information on the location of key points [41] for the purpose of data visualization. In this study, the attentional heat map is generated by extracting the confidence of the predicted maximum value from the output prediction features and multiplying the two values to produce a visual representation. The output of YOLOv8n shows the best results among three scenarios, while CURI-YOLOv7 exhibits inferior results compared to YOLOv8n. However, CURI-YOLOv7 is still able to accurately focus attention on the correct position of the fruit tree.

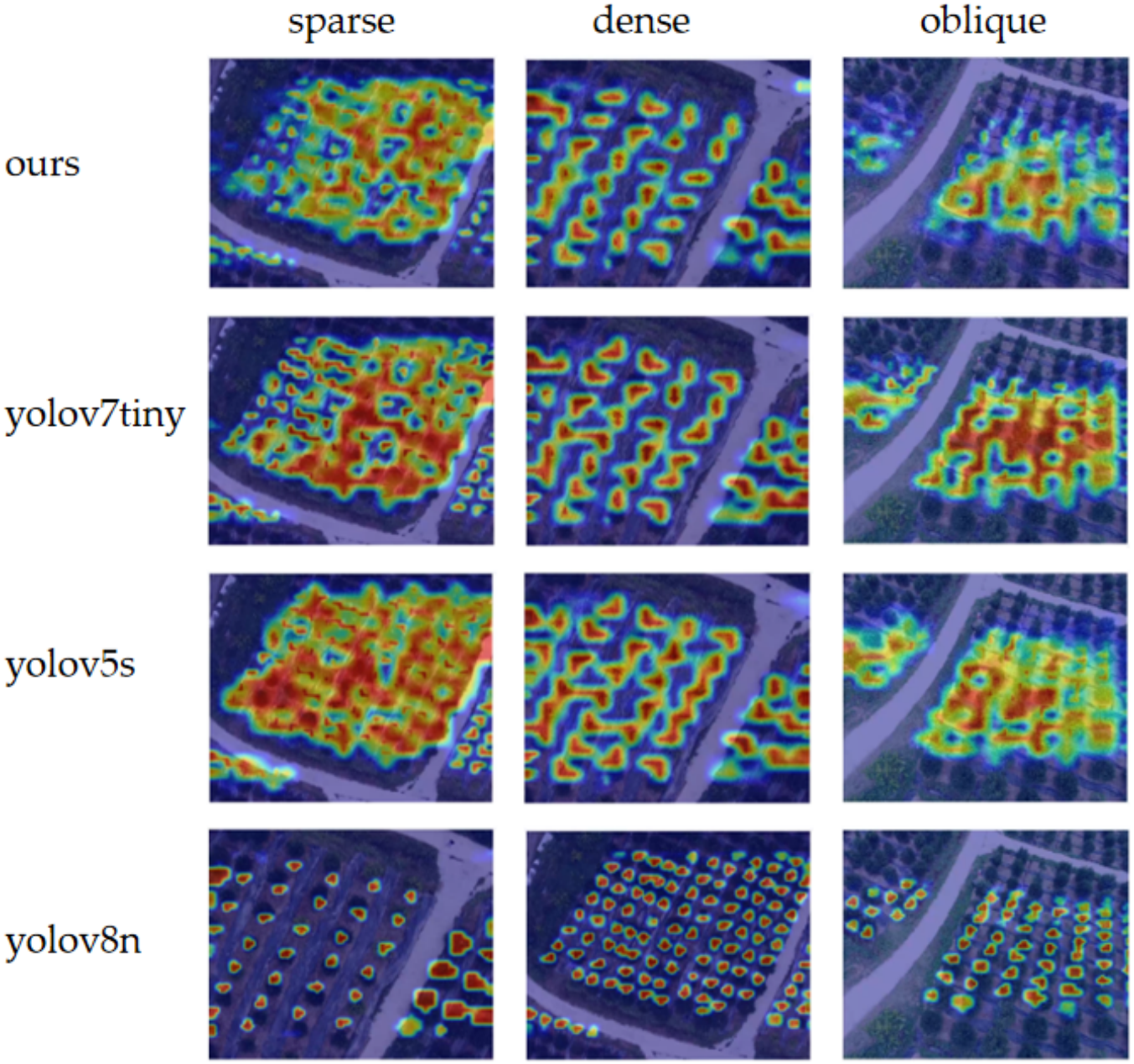

Figure 13. Heat map of attention for four target detectors in three environments.

4. Discussion

In this paper, a lightweight target detector named CURI-YOLOv7 is proposed for deployment on embedded devices. The algorithm is systematically compared and analyzed against five other models, including Faster-Rcnn, SSD, YOLOv5s, YOLOv7tiny, and YOLOv8n. This comparison serves to demonstrate the rationality and effectiveness of the design of CURI-YOLOv7. The experimental results affirm the advantages of CURI-YOLOv7. It achieves significant reductions in both GFLOPs and parameter quantities, resulting in a noteworthy improvement in frames per second (FPS). As a result, it is adept at carrying out real-time target detection when executed on embedded devices. This achievement effectively caters to the need for recognizing individual trees in UAV aerial images of citrus orchards while adhering to the limitations of embedded devices. Importantly, this solution effectively addresses the long-standing challenges related to unwieldy model sizes and slow image processing speeds. The domain of accurate orchard management has long been a focal point of research interest. The real-time remote sensing target monitoring facilitated by the integration of CURI-YOLOv7 into embedded devices emerges as a significant advancement. This innovation has the potential to extract relevant information from citrus tree imagery in real time, thereby underscoring the practical significance of the study.

This study does exhibit certain limitations. The dataset generated focuses exclusively upon UAV remote sensing of citrus trees, and consequently, the proposed model's applicability may not universally extend to other orchard remote sensing scenarios. Evaluating the outcomes, CURI-YOLOv7 attains a citrus tree target detection mean average precision (MAP) exceeding 90%. While marginally trailing behind other target detection algorithms within the YOLO series, this performance variation is noted.

In the realm of future endeavors, the inference speed of CURI-YOLOv7 will be subject to further reduction through techniques such as knowledge distillation and model pruning. These efforts are poised to establish a robust groundwork for subsequent investigations centered on the realm of automated UAV navigation.

5. Conclusions

This study proposes a lightweight YOLOv7tiny target detector CURI-YOLOv7 for the UAV aerial photography of citrus trees based on embedded devices. A dataset of citrus trees from UAV remote sensing imagery was constructed for training. The backbone is designed based on the MobileOne-block and depthwise separable convolution; the original spatial pyramid pooling is replaced by the SPPF, and the Lightweight-ELAN structure is constructed based on the ELAN structure. The neck is redesigned by removing the smaller target detection layer and fusion depth-separable convolution and GSConv to construct the proposed CURI-YOLOv7. The results show that the GFLOPs = 1.976, parameters = 1.018 M, weights = 3.98 MB, and mAP = 90.34% for CURI-YOLOv7. When executed on a computer, CURI-YOLOv7 displays a substantial enhancement in frames per second (FPS), at 128.83. Notably, on an embedded device, CURI-YOLOv7 excels with an impressive FPS improvement, achieving 27.01. This reinforces its adeptness for real-time processing on embedded devices. The progression of CURI-YOLOv7 establishes a fundamental basis for the subsequent advancement of low-altitude remote sensing technology in citrus orchard management and precision agricultural aviation.

Author Contributions: Conceptualization, Y.Z. and X.F.; methodology, Y.Z. and X.F.; validation, Y.Z. and X.F.; formal analysis, X.F. and J.G.; investigation, Y.Z., X.F. and J.G.; resources, X.F. and H.T.; data curation, X.F., J.G. and H.T.; writing—original draft preparation, Y.Z., X.F. and J.G.; writing—review and editing, Y.Z., L.W., H.T. and K.Y.; visualization, X.F. and L.W.; supervision Y.L.; project administration, Y.Z. and Y.L.; funding acquisition, Y.Z. and Y.L. All authors have read and agreed to the published version of the manuscript.

Funding: This research was funded by the Laboratory of Lingnan Modern Agriculture Project, grant number NT2021009, the Key Field Research and Development Plan of Guangdong Province, China, grant number 2019B020221001, and the 111 Project, grant number D18019.

Data Availability Statement: The data presented in this study are available on request from the corresponding author.

Conflicts of Interest: The authors declare no conflict of interest.

References

1. Zhou, Z.; Ming, R.; Zang, Y.; He, X.; Luo, X.; Lan, Y. Development status and countermeasures of agricultural aviation in China. *Trans. Chin. Soc. Agric. Eng.* **2017**, *33*, 1–13.
2. Wang, L.; Lan, Y.; Zhang, Y.; Zhang, H.; Tahir, M.N.; Ou, S.; Liu, X.; Chen, P. Applications and prospects of agricultural unmanned aerial vehicle obstacle avoidance technology in China. *Sensors* **2019**, *19*, 642. [CrossRef] [PubMed]
3. Zhang, D.; Lan, Y.; Chen, L.; Wang, X.; Liang, D. Current status and future trends of agricultural aerial spraying technology in China. *Trans. Chin. Soc. Agric. Mach.* **2014**, *45*, 53–59.
4. Shi, Z.; Liang, Z.; Yang, Y.; Guo, Y. Status and prospect of agricultural remote sensing. *Trans. Chin. Soc. Agric. Mach.* **2015**, *46*, 247–260.
5. Nie, J.; Yang, B. Monitoring Method of Crop Growth on a Large Scale Basedon Remote Sensing Technology. *Comput. Simul.* **2020**, *37*, 386–389+394.
6. Shan, Y. Present situation development trend and countermeasures of citrus industry in China. *J. Chin. Inst. Food Sci. Technol.* **2008**, *8*, 1–8.
7. Dai, J.; Xue, J.; Zhao, Q.; Wang, Q.; Cheng, B.; Zhang, G.; Jiang, L. Extraction of cotton seedling growth information using UAV visible light remote sensing images. *Trans. Chin. Soc. Agric. Eng.* **2010**, *36*, 63–71.
8. Deng, J.; Ren, G.; Lan, Y.; Huang, H.; Zhang, Y. Low altitude unmanned aerial vehicle remote sensing image processing based on visible band. *J. South China Agric. Univ.* **2016**, *37*, 16–22.
9. Lan, Y.; Deng, X.; Zeng, G. Advances in diagnosis of crop diseases, pests and weeds by UAV remote sensing. *Smart Agric.* **2019**, *1*, 1–19.
10. Chen, Y.; Zhao, C.; Wang, X.; Ma, J.; Tian, Z. Prescription map generation intelligent system of precision agriculture based on knowledge model and WebGIS. *Sci. Agric. Sin.* **2007**, *pp*, 1190–1197.
11. Hao, L.; Shi, L.; Cao, L.; Gong, J.; Zhang, A. Research status and prospect of cotton terminal bud identification and location technology. *J. Chin. Agric. Mech.* **2018**, *39*, 72–78.
12. Tian, H.; Fang, X.; Lan, Y.; Ma, C.; Huang, H.; Lu, X.; Zhao, D.; Liu, H.; Zhang, Y. Extraction of Citrus Trees from UAV Remote Sensing Imagery Using YOLOv5s and Coordinate Transformation. *Remote Sens.* **2022**, *14*, 4208. [CrossRef]
13. Shu, M.; Li, S.; Wei, J.; Che, Y.; Li, B.; Ma, T. Extraction of citrus crown parameters using UAV platform. *Trans. Chin. Soc. Agric. Eng.* **2021**, *37*, 68–76.
14. Sun, Y.; Han, J.; Chen, Z.; Shi, M.; Fu, H.; Yang, M. Monitoring method for UAV image of greenhouse and plastic-mulched Landcover based on deep learning. *Trans. Chin. Soc. Agric. Mach.* **2018**, *49*, 133–140.
15. Wang, B.; Yang, G.; Yang, H.; Gu, J.; Zhao, D.; Xu, S.; Xu, B. UAV images for detecting maize tassel based on YOLO_X and transfer learning. *Trans. Chin. Soc. Agric. Eng.* **2022**, *38*, 53–62.
16. Bao, W.; Xie, W.; Hu, G.; Wang, X.; Su, B. Wheat ear counting method in UAV images based on TPH-YOLO. *Trans. Chin. Soc. Agric. Eng.* **2023**, *39*, 155–161.
17. Zhang, Y.; Lu, X.; Li, W.; Yan, K.; Mo, Z.; Lan, Y.; Wang, L. Detection of Power Poles in Orchards Based on Improved Yolov5s Model. *Agronomy* **2023**, *13*, 1705. [CrossRef]
18. Luo, X.; Wu, Y.; Zhao, L. YOLOD: A Target Detection Method for UAV Aerial Imagery. *Remote Sens.* **2022**, *14*, 3240. [CrossRef]
19. Zhu, Y.; Zhou, J.; Yang, Y.; Liu, L.; Liu, F.; Kong, W. Rapid Target Detection of Fruit Trees Using UAV Imaging and Improved Light YOLOv4 Algorithm. *Remote Sens.* **2022**, *14*, 4324. [CrossRef]
20. Basso, M.; Stocchero, D.; Ventura Bayan Henriques, R.; Vian, A.L.; Bredemeier, C.; Konzen, A.A.; Pignaton de Freitas, E. Proposal for an Embedded System Architecture Using a GNDVI Algorithm to Support UA V-Based Agrochemical Spraying. *Sensors* **2019**, *19*, 5397. [CrossRef]
21. Ki, M.; Cha, J.; Lyu, H. Detect and Avoid System Based on Multi Sensor Fusion for UAV. In Proceedings of the 2018 International Conference on Information and Communication Technology Convergence (ICTC), Jeju Island, Republic of Korea, 17–19 October 2018; pp. 1107–1109.
22. Chen, L.; Li, S.; Bai, Q.; Yang, J.; Jiang, S.; Miao, Y. Review of image classification algorithms based on convolutional neural networks. *Remote Sens.* **2021**, *13*, 4712. [CrossRef]
23. Liu, F.; Liu, Y.K.; Lin, S.; Guo, W.Z.; Xu, F.; Zhang, B. Fast recognition method for tomatoes under complex environments based on improved YOLO. *Trans. CSAM* **2020**, *51*, 229–237.
24. labelImg. Available online: https://github.com/tzutalin/labelImg (accessed on 15 June 2023).
25. Vasu PK, A.; Gabriel, J.; Zhu, J.; Tuzel, O.; Ranjan, A. An improved one millisecond mobile backbone. *arXiv* **2022**, arXiv:2206.04040.
26. yolov5. Available online: https://github.com/ultralytics/yolov5 (accessed on 7 July 2023).
27. Li, J.; Ye, J. Edge-YOLO: Lightweight Infrared Object Detection Method Deployed on Edge Devices. *Appl. Sci.* **2023**, *13*, 4402. [CrossRef]

28. Wang, C.Y.; Bochkovskiy, A.; Liao, H.Y.M. YOLOv7: Trainable bag-of-freebies sets new state-of-the-art for real-time object detectors. *arXiv* **2022**, arXiv:2207.02696.
29. Long, Y.; Yang, Z.; He, M. Recognizing apple targets before thinning using improved YOLOv7. *Trans. Chin. Soc. Agric. Eng.* **2023**, *39*, 191–199.
30. Li, Z.; Yang, F.; Hao, Y. Small target detection algorithm for aerial photography based on residual network optimization. *Foreign Electron. Meas. Technol.* **2022**, *41*, 27–33.
31. Li, H.; Li, J.; Wei, H.; Liu, Z.; Zhan, Z.; Ren, Q. Slim-neck by GSConv: A better design paradigm of detector architectures for autonomous vehicles. *arXiv* **2022**, arXiv:2206.02424.
32. Howard, A.G.; Zhu, M.; Chen, B.; Kalenichenko, D.; Wang, W.; Weyand, T.; Andreetto, M.; Adam, H. Mobilenets: Efficient convolutional neural networks for mobile vision applications. *arXiv* **2017**, arXiv:1704.04861.
33. Zhang, M.; Gao, F.; Yang, W.; Zhang, H. Wildlife Object Detection Method Applying Segmentation Gradient Flow and Fea ture Dimensionality Reduction. *Electronics* **2023**, *12*, 377. [CrossRef]
34. Wu, T.; Zhang, Z.; Liu, Y.; Pei, W.; Chen, H. A lightweight small object detection algorithm based on improved SSD. *Infrared. Laser Eng.* **2018**, *47*, 703005.
35. Kong, W.; Li, W.; Wang, Q.; Cao, P.; Song, Q. Design and implementation of lightweight network based on improved YOLOv4 algorithm. *Comput. Eng.* **2022**, *48*, 181–188.
36. Caba, J.; Díaz, M.; Barba, J.; Guerra, R.; de la Torre, J.A.; López, S. Fpga-based on-board hyperspec tral imaging compression: Benchmarking performance and energy efficiency against gpu implementations. *Remote Sens.* **2020**, *12*, 3741. [CrossRef]
37. Wang, C.; Wang, Q.; Wu, H.; Zhao, C.; Teng, G.; Li, J. Low-Altitude Remote Sensing Opium Poppy Image Detection Basedon Modified YOLOv3. *Remote Sens.* **2021**, *13*, 2130. [CrossRef]
38. Ren, S.; He, K.; Girshick, R.B.; Sun, J. Faster R-CNN: Towards Real-Time Object Detection with Region Proposal Networks. *Ieee Trans. Pattern Anal. Mach. Intell.* **2015**, *39*, 1137–1149. [CrossRef]
39. Liu, W.; Anguelov, D.; Erhan, D.; Szegedy, C.; Reed, S.; Fu, C.-Y.; Berg, A.C. SSD: Single Shot MultiBox Detector. *arXiv* **2015**, arXiv:1512.02325.
40. Zhang, Y.; Xiao, W.; Lu, X.; Liu, A.; Qi, Y.; Liu, H.; Shi, Z.; Lan, Y. Method for detecting rice flowering spikelets using visible light images. *Trans. Chin. Soc. Agric. Eng.* **2021**, *37*, 253–262.
41. Liu, Y.; Li, J.; Zhang, J.; Xu, Z. Research progress of two-dimensional human pose estimation based on deep learning. *Comput. Eng.* **2021**, *47*, 1–16.

Disclaimer/Publisher's Note: The statements, opinions and data contained in all publications are solely those of the individual author(s) and contributor(s) and not of MDPI and/or the editor(s). MDPI and/or the editor(s) disclaim responsibility for any injury to people or property resulting from any ideas, methods, instructions or products referred to in the content.

agronomy

MDPI

Review

Advances and Developments in Monitoring and Inversion of the Biochemical Information of Crop Nutrients Based on Hyperspectral Technology

Yali Zhang [1,2,3], Junqi Xiao [1,2,3], Kangting Yan [2,3,4], Xiaoyang Lu [1,2,3], Wanjian Li [1,2,3], Haoxin Tian [5], Linlin Wang [6], Jizhong Deng [1,2,3] and Yubin Lan [2,3,4,*]

1 College of Engineering, South China Agricultural University, Wushan Road, Guangzhou 510642, China; ylzhang@scau.edu.cn (Y.Z.); 20213142028@stu.scau.edu.cn (J.X.); luxiaoyang123@stu.scau.edu.cn (X.L.); 19981002@stu.scau.edu.cn (W.L.); jz-deng@scau.edu.cn (J.D.)
2 Guangdong Laboratory for Lingnan Modern Agriculture, Guangzhou 510642, China; ktyan@stu.scau.edu.cn
3 National Center for International Collaboration Research on Precision Agricultural Aviation Pesticide Spraying Technology, Guangzhou 510642, China
4 College of Electronic Engineering and College of Artificial Intelligence, South China Agricultural University, Wushan Road, Guangzhou 510642, China
5 College of Automation Engineering, Nanjing University of Aeronautics and Astronautics, Nanjing 211106, China; hxtian@stu.scau.edu.cn
6 School of Artifificial Intelligence, Shenzhen Polytechnic University, Shenzhen 518055, China; wanglinlin@szpt.edu.cn
* Correspondence: ylan@scau.edu.cn

Abstract: Crop nutrient biochemical information (mainly including chlorophyll class and nutrient elements mainly nitrogen, phosphorus and potassium) is an important basis for revealing crop growth and development patterns and their relationship with the environment. Hyperspectral technology has been rapidly developed and applied in crop nutrient biochemical information monitoring research. This paper firstly describes the theoretical basis of hyperspectral technology for monitoring crop nutrients and biochemical information. Then, the research progress of hyperspectral technology in monitoring nutrient and biochemical information of crops in different growth periods or different growth environments is outlined. Meanwhile, the shortcomings of the current technology in these research directions and the future research trends are discussed. Finally, the modeling methods for building crop nutrient biochemical information monitoring models by applying hyperspectral data are systematically outlined. And the effects of different spectral pre-processing methods, spectral effective information extraction methods and modeling algorithms on the accuracy of monitoring models are analyzed. On this basis, the challenges and prospects of hyperspectral technology in monitoring crop nutrient biochemical information are presented, aiming to provide relevant theoretical basis and technical reference for the research related to monitoring and inversion of crop physiological parameters based on hyperspectral technology.

Keywords: hyperspectral technology; crop nutrient; biochemical information; monitoring model; feature extraction

check for updates

Citation: Zhang, Y.; Xiao, J.; Yan, K.; Lu, X.; Li, W.; Tian, H.; Wang, L.; Deng, J.; Lan, Y. Advances and Developments in Monitoring and Inversion of the Biochemical Information of Crop Nutrients Based on Hyperspectral Technology. *Agronomy* **2023**, *13*, 2163. https://doi.org/10.3390/agronomy13082163

Academic Editors: Hao Yang, Changping Huang, Dameng Yin, Xiuliang Jin and Zhenhai Li

Received: 15 July 2023
Revised: 9 August 2023
Accepted: 15 August 2023
Published: 18 August 2023

Copyright: © 2023 by the authors. Licensee MDPI, Basel, Switzerland. This article is an open access article distributed under the terms and conditions of the Creative Commons Attribution (CC BY) license (https://creativecommons.org/licenses/by/4.0/).

1. Introduction

The nutrient biochemical information of a crop mainly includes pigments (chlorophyll, carotenoids, anthocyanins, etc.) and nutrients based on nitrogen, phosphorus and potassium elements [1]. Nitrogen, phosphorus and potassium are the three essential nutrients for plant growth and development, and each performs certain physiological functions in the crop. Among them, the level of nitrogen content is closely related to the photosynthetic efficiency and intensity of plants; phosphorus improves the adaptability of crops to the external environment by regulating the metabolic process in crops; potassium is the most

abundant cation in plant cells, which has the functions of regulating water metabolism, enzyme activator, improving resistance and promoting photosynthesis for plants; chlorophyll and other pigments are the most important elements for the growth of crops [2]. Chlorophylls and other pigments are important indicators of photosynthetic efficiency, growth and nutrient status and pest and disease stress. When crops lack certain nutrients or have abnormal pigment content, it will definitely affect their external morphological structure and internal physiological functions, resulting in incomplete growth and development of crops, thus reducing the quality as well as yield of crops. Therefore, rapid and quantitative monitoring of nutrient and biochemical information of crops can determine the real-time critical fertility period of crops, analyze crop growth information and provide data basis for precise fertilization and pest and disease monitoring of farm crops.

In order to learn the nutritional status of crops and determine the content of pigments or nutrients in crops, traditional methods analyze seedling or leaf samples of crops after destructive treatment using chemical analysis, including Kjeldahl nitrogen [3], vanadium-molybdenum yellow [4] for phosphorus, flame photometry [5] for potassium, ethanol leaching [6] for chlorophyll, etc. Although the accuracy of crop elemental content determination by chemical analysis is high, it is time-consuming, cumbersome and requires destructive treatment of crop samples, which cannot allow rapid and convenient detection of crops grown in large areas [7,8]. Spectral imaging technology is a nondestructive, fast and real-time technique [9], which make it highly applicable for determining biochemical information of crop nutrients and indirectly monitoring crop growth and stress. Among them, hyperspectral technology has continuous waveband and large amount of recorded data compared with other spectral methods, which can better establish the correlation between spectral data and biochemical information of crop nutrients, and thus obtain monitoring models with higher accuracy. In recent years, with the continuous progress of remote sensing and computer technology, hyperspectral technology has been applied in agriculture [10,11], environmental monitoring [12], mineral monitoring [13] and marine remote sensing [14]. In the field of agriculture, hyperspectral-based biochemical information monitoring and inversion models of crop nutrients can quickly and accurately respond to the growth and nutritional status of crops. Therefore, the application of composite technology to analyze hyperspectral profiles of crops and construct biochemical information inversion models of crop nutrients has become a hot research topic.

This paper reviews the research results related to the monitoring of crop nutrient biochemical information based on hyperspectral technology. Firstly, the technical features of hyperspectral technology in this field are introduced, including hyperspectral data with high spectral resolution and number of bands, and the ability to obtain crop spectral reflectance information. Then, the research situation that hyperspectral technology can construct a model for monitoring nutrient biochemical information of crops under different growth conditions is described. The effects of choosing different pre-processing methods, feature band extraction methods, spectral indices and modeling methods on the accuracy of the constructed hyperspectral monitoring models of crop nutrients and biochemical information are analyzed. Finally, this paper aims to provide a theoretical basis and technical reference for future research related to the monitoring and inversion of crop physiological parameters based on hyperspectral technology.

2. Hyperspectral Technology to Construct a Model for Monitoring Biochemical Information of Crop Nutrients

2.1. Reflectance Spectral Properties of Plants

The absorption, reflection and transmission of electromagnetic waves of different wavelengths (or frequencies) vary from substance to substance, and this response property to different wavelengths of the spectrum is called spectral characteristics. In addition to the influence of the morphological structure of the crop itself, the spectral characteristics of the crop leaves are also closely related to the crop's growth environment and its own growth conditions. Soil moisture content, soil nutrients and the degree of pests and diseases

suffered by the crop will affect the growth and development of the crop, making the biochemical composition of the crop different, and the reflectance spectrum of the crop with chlorophyll content, nutrient content, water content and other biochemical components will show different patterns in different bands. Numerous studies have shown that the spectral reflectance characteristics of crops are closely related to their morphological structure, pigment content and nutrient content [15–17], so it is feasible to monitor the nutrient and biochemical information of crops using hyperspectral techniques. Figure 1 shows a schematic diagram of the reflectance spectral properties of plant leaves [18,19].

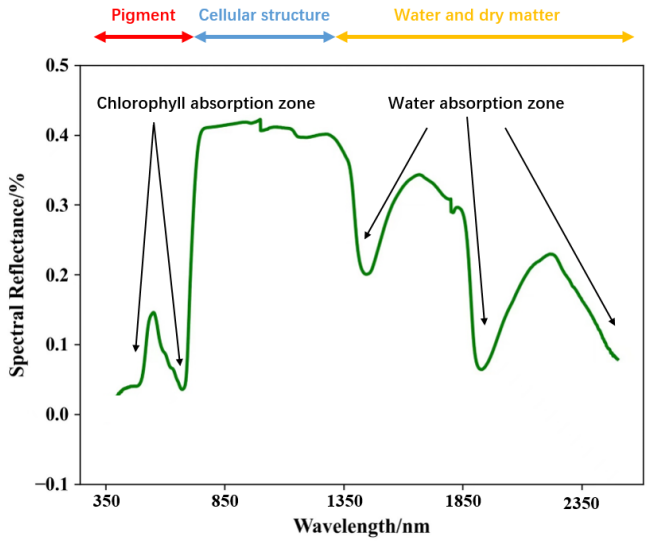

Figure 1. Schematic diagram of reflectance spectral characteristics of plant leaves.

2.2. Hyperspectral Operation Platform of Biochemical Information Monitoring Model of Crop Nutrients

Hyperspectral data can be divided into imaging hyperspectral three-dimensional data and non-imaging hyperspectral two-dimensional data [20]. Meanwhile, the hyperspectral data acquisition equipment styles are diversified, and the common ones are handheld hyperspectral acquisition equipment, airborne imaging hyperspectral cameras, etc. Figure 2 shows the operation schematic of different hyperspectral acquisition equipment.

Compared to multispectral data, hyperspectral data have many more continuous bands and can use more spectral information, allowing for a greater variety of vegetation indices and modelling methods. In addition, the spectral pre-processing method is more robust to the noise interference in the continuous band [21]. The biochemical information monitoring models of crop nutrients based on hyperspectral technology better reflect the correlation between spectral data and biochemical information of crop nutrients, so the monitoring model has better prediction accuracy [22]. Since the physiological characteristics and biochemical components of the crop determine its spectral response, the required experimental studies can be carried out by means of controlled variable methods. By using a UAV with a hyperspectral camera or other spectral data collection device to collect spectral information from the leaves or other tissues of the crop canopy, and then applying relevant machine learning algorithms to construct regression models, it is possible to monitor the nutrient and biochemical information of the crops in different growth states and acquire real-time crop growth conditions.

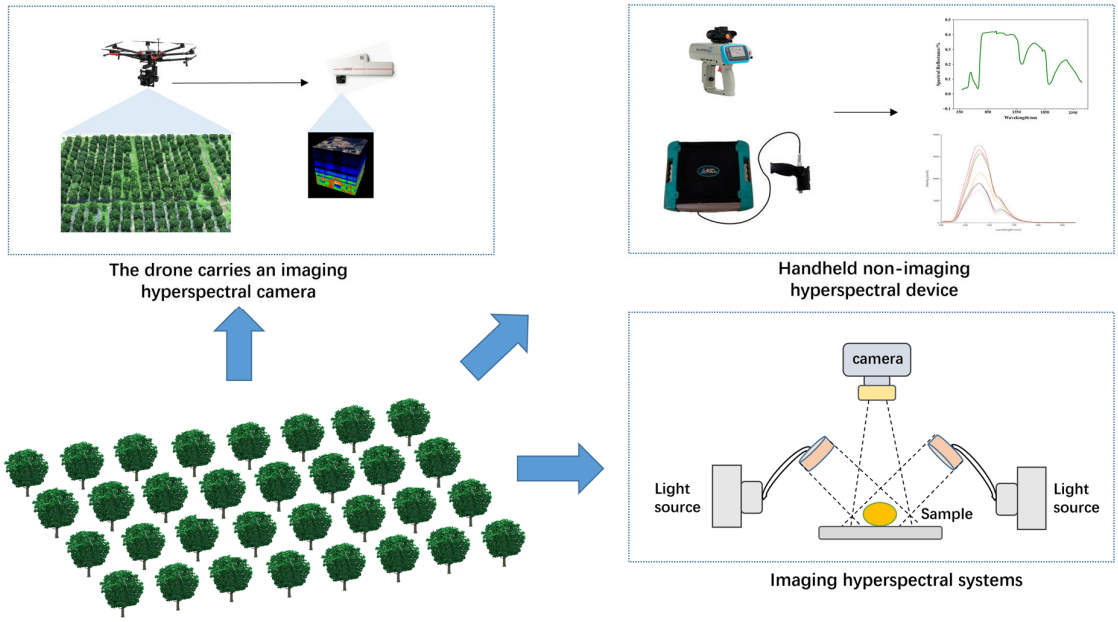

Figure 2. Schematic diagram of the operation of different hyperspectral acquisition platforms.

3. Application of Hyperspectral Technique in the Detection of the Biochemical Information of Crop Nutrients

3.1. Hyperspectral Monitoring of the Biochemical Information of Crop Nutrients at Different Growth Stages of Crops

3.1.1. Single Growth Stage

Crops have different levels of nutrient biochemical information and demand of nutrients at different growth stages. By using hyperspectral technology to collect spectral data of crops at a certain growth stage and then constructing a monitoring model using appropriate data analysis methods, we can quickly and accurately detect nutrient biochemical information of crops during important growth periods, thus obtaining feedback on possible nutrient stresses of crops during growth periods and providing reference for crop nutrient applications. Ryu et al. [23] used airborne hyperspectral remote sensing technology to collect spectral data and nitrogen content of rice during the heading stage for three consecutive years. They established a hyperspectral prediction model for nitrogen content of rice during the heading stage. Zhou et al. [24] used the FieldSpec geopolitical spectrometer produced by ASD to collect leaf spectral data of three different varieties of maize at the six-leaf stage. The correlation between leaf nitrogen content and spectral reflectance of three maize varieties (combinations) was studied by setting different levels of nitrogen supply, and the sensitive wavebands for estimating leaf nitrogen content in six-leaf maize were clarified. An et al. [25] collected the spectral data of leaves of Red Fuji apple trees by using the American ASD FieldSpec 3 spectrometer (Analytical Spectral Devices, Inc., Boulder, CO, USA), and established the hyperspectral estimation model of nitrogen content in leaves of the apple trees at the end of fall growth period. Jiang et al. [26] used PSR-350 portable hyperspectrometer (Yamaha, Shizuoka, Japan) to collect the spectral data of winter wheat canopy during the flowering period. By analyzing the correlation between its spectral reflectance and chlorophyll content, a regression analysis of spectral index and chlorophyll content was constructed by selecting the sensitive waveband of winter wheat during the flowering period. The best inversion model for the chlorophyll content of winter wheat canopy during the flowering period was obtained.

Furthermore, the nutrient level of fruit tree petals during flowering stage reflects the plant's nutritional status and predict the flowering quantity and yield of fruit trees. Potassium content in fruit tree petals can better reflect their nutritional level. Rapid diagnosis and scientific regulation of potassium nutrition in fruit trees is an important

aspect of quality and productive management of fruit trees. Liu et al. [27] characterized the potassium nutrition of citrus flowers using hyperspectral technology. Considering the flower organs of Hovenia orange rootstock 'Caracalla red-fleshed navel orange' as test material, the effective information on extraction method, characteristic spectra, and optimal prediction model was established for the estimation of citrus flower potassium content, laying the foundation for the real-time detection of citrus flower potassium nutrition. Zhu et al. [7] used the canopy hyperspectrum of apple blossom measured using the ASD FieldSpec 3 and laboratory-measured potassium content to correlate the canopy hyperspectral reflectance and its 11 transformed forms with potassium content in the Qixia experimental site. They used the highest correlation coefficient as the independent variable to establish a model for potassium content estimation using a fuzzy identification algorithm.

3.1.2. Multiple Growth Stages

In fact, the nutritional components of crops also change during their growth and development [28]. Considering citrus as an example, Figure 3 shows the correlation between the spectral data of citrus leaves at different stages and their chlorophyll content [29]. High-spectral monitoring models with high nutrient biochemical information content for a single growth period do not have predictive effects on the nutrient status of crops throughout their entire growth cycle. Therefore, it is of great significance to detect the nutrient biochemical information of crops in multiple growth periods and conduct cross-growth period nutrient biochemical information prediction research. To achieve this goal, researchers have used various hyperspectral techniques. Li et al. [30] collected high-spectral data of winter wheat canopies at different growth stages using the American ASD FieldSpec spectrometer, and established a relationship between the high-spectral data and leaf nitrogen content based on the N-PROSAIL model. The results showed that this method can estimate the nutritional status of winter wheat well. Li et al. [31] estimated the leaf nitrogen content of lychee in spring, summer, autumn and winter based on the canopy spectral reflectance, and obtained the best estimation model for leaf nitrogen content in different growth periods through comparative analysis. Huang et al. [32] collected reflection spectra data of citrus during the fruit-picking period and the shoot growth stage, and established a phosphorus content prediction model based on 234 sample data by combining with Partial Least Squares (PLS) and Support Vector Regression (SVR) methods. Yang et al. [33] used the portable spectrometer SVC HR-768 to determine the spectral reflectance and total nitrogen content of pear leaves at the fruit-setting period, fruit expansion period and fruit ripening period, and then constructed a leaf total nitrogen content estimation model for different growth periods of Korla pear. The fitting effect of the estimation model during the fruit-setting period is better, and the prediction accuracy is higher as well. Zhu et al. [34] selected super hybrid early rice as the research object, and used the FieldSpec3 spectrometer produced by the American ASD company to obtain 120 groups of high-spectral data, chlorophyll and leaf nitrogen content of rice leaves at the tillering, booting, full heading, filling and mature period of the rice. They used Partial Least Squares Analysis (PLSR), Random Forest algorithm (RF) and Support Vector Regression (SVR) methods to construct cross-period prediction models for leaf nitrogen content and chlorophyll of early rice leaves.

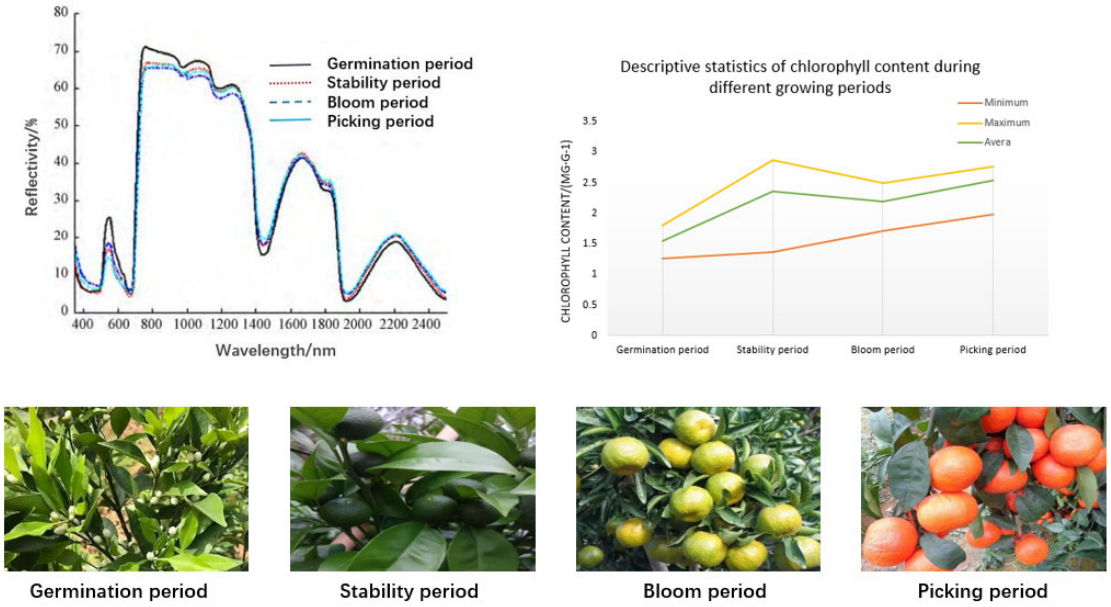

Figure 3. Spectral data and chlorophyll content statistics of citrus leaves in different periods.

Currently, research on monitoring and predicting the biochemical information of crop nutrients using hyperspectral techniques is mainly focused on establishing a correlation between the spectral data of crops and their biochemical information during a single growth stage. However, such models are not very versatile and cannot be applied to the entire growth stage of the crops. Additionally, constructing a model for monitoring biochemical information of crop nutrients requires a large amount of hyperspectral data, which is limited by the long time span and the difficulty in controlling environmental variables. As a result, there are few studies on monitoring models for the biochemical information content of crop nutrients across multiple growth periods or the entire growth period.

3.2. Monitoring the Biochemical Information of Crop Nutrients under Environmental Stress

Crops are often subjected to various environmental stresses, such as drought stress, salt stress, heavy metal stress, low or high temperature stress, etc. Different environmental stresses have different effects on the biochemical information of crop nutrients, thereby altering the spectral reflectance of crops. Yuan et al. [35] found that from the jointing stage to the maturity stage, the chlorophyll content of summer maize leaves decreases with the increasing degree of water stress. Peng et al. [36] discovered that different salt concentrations (0.200 and 400 mmol/L NaCl) significantly reduce the chlorophyll content of alkali bulrush, but increase the values of chlorophyll A and chlorophyll B. Sun et al. [37] found through experiments that different water conditions in wheat fields have a significant impact on the growth and development process of winter wheat, and the significant difference in plant nitrogen content is also an important manifestation. Guan et al. [38,39] found that with the increase in cadmium mass fraction and the extension of stress time, the total chlorophyll mass fraction shows a trend of first increasing and then decreasing.

Therefore, it is crucial for agriculture to identify the type of stress that crops are subjected to quickly and accurately, in order to improve the growth environment of crops in a targeted manner. Hyperspectral remote sensing technology can make full use of the spectral characteristics of objects, monitor the biochemical information of crop nutrients under different environmental stresses and construct a monitoring model for the biochemical information of crop nutrients under environmental stress, providing a reference for monitoring the degree of environmental stress on crops. Ma et al. [40] set up a field water and fertilizer experiment with irrigation and nitrogen gradients, and used the ASD HH2 portable spectrometer to measure the spectral reflectance of cotton canopy during the

cotton growth period, and simultaneously measured the nitrogen content and equivalent water thickness of the cotton canopy. NDSI (570, 500) was selected as the optimal spectral index for modeling, and a high-spectral monitoring model of nitrogen content in cotton canopy was constructed, with a predicted RRMSE of 0.18. Xie et al. [41] studied the effect of water stress on the high-spectral reflectance of winter wheat canopy, and found that important information on chlorophyll density of winter wheat after water stress was present at wavelengths of 427 nm, 434 nm, 749 nm and 814 nm. Feature extraction was carried out on the original spectrum through Correlation Analysis (CA), Partial Least Squares Regression analysis (PLSR) and Successive Projection Algorithm (SPA), and a high-spectral estimation model of chlorophyll density was established. Yao et al. [42] constructed estimation models based on red edge, sensitive bands and spectral indices, and analyzed the correlation between the spectral reflectance of winter wheat under high CO_2 concentration and chlorophyll content. The chlorophyll content of winter wheat under high CO_2 concentration could be better estimated based on sensitive spectral bands and Difference Vegetation Index (DVI).

Currently, the spectral monitoring of environmental stress in crops relies on a binary model, which only determines whether the crop is under stress, without taking into account the degree of stress. To improve the monitoring of environmental stress in crops, a model can be developed to monitor the biochemical information of crop nutrients under stress, which can determine the degree of stress based on the changes in spectral reflectance. Although most research on monitoring environmental stresses in crops focuses on monitoring soil, temperature and other factors that impact crop survival, there is less emphasis on direct monitoring of crop nutrients and biochemical information. In the future, the monitoring of environmental factors and biological parameters can be linked to improve the accuracy of identification and better apply to the actual agricultural production environment. This will provide a more effective monitoring tool for crop production and help improve the efficiency and quality of agricultural production.

3.3. Monitoring the Biochemical Information of Crop Nutrients under Pest and Disease Stress

Due to the differences in pathogen species, pest feeding habits and climatic conditions and the various interaction between different crop pests and their host crops, different physiological responses and changes in biochemical information of nutrients in the host crops occur, which manifest as damaged leaf structure, decreased pigment content and decreased nitrogen content. Xu et al. [43] found that black pine and horsetail pine would be infected after natural infestation by pine wood nematodes, and their chlorophyll content gradually decreased with the deepening of the disease. Jiang et al. [44] showed that the total nitrogen content gradually decreased with increasing stripe rust stress in winter wheat, and showed a highly significant correlation with the first-order differential spectra in the 430–518, 534–608, 660–762 nm and 783–893 nm regions. Tian et al. [45] found that the anthocyanin content of apple leaves increased with increasing severity of mosaic disease, and the spectral reflectance of the diseased area of leaves increased significantly throughout the visible region. There was also a red-edge blue shift phenomenon. Chen et al. [46] found that after cotton was infested with yellow wilt pathogen, the pathogen proliferated or induced a large amount of toxins in the plant, which resulted in blocked water transport within the plant, damaged internal leaf structure and corresponding changes in biochemical components (e.g., chlorophyll, water, etc.). The changes vary with different onset times and degrees of severity. Figure 4 shows the correlation coefficients between leaf spectra and chlorophyll content of bamboo leaves in different insect-infested moso bamboo. In the future, this information can be used to establish more accurate crop pest monitoring models and provide more effective control measures for agricultural production.

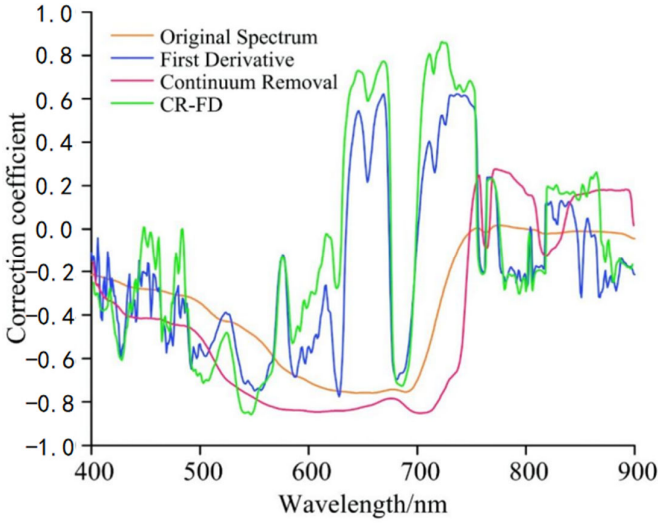

Figure 4. Correlation coefficients between bamboo leaf spectra and chlorophyll content of moso bamboo under different levels of insect damage.

After being attacked by fungi, bacteria or pests, crops undergo a series of changes in their nutrient biochemical information. On one hand, the pathogens or pests attack the plant tissues to acquire nutrients, leading to a decrease in nutrient content in the crops. On the other hand, the affected crops may adjust their nutrient allocation strategy by directing more nutrients to the invaded areas, enhancing their ability to resist pathogens or pests. However, this can result in insufficient nutrient supply to other parts or tissues of the crops, affecting their normal growth and development. When crops are under the stress of disease and pest attacks, their spectral characteristics usually show an increase in visible and shortwave infrared spectral reflectance, while the near-infrared spectral reflectance decreases [47]. This change differs significantly from the typical spectral characteristics of green vegetation. It is important to note that the extent of stress imposed by pests and diseases on crops can vary depending on factors such as crop species, growth stage and environmental conditions. Therefore, the spectral characteristics displayed by these changes may also differ. For instance, when crops are affected by powdery mildew, significant changes occur in their nitrogen and chlorophyll content, which are reflected in the spectral information. During the early growth stage of the crops, there is an increase in hyperspectral reflectance in the visible and infrared regions, while a decrease in reflectance is observed in the visible region during the mature stage. When crops are affected by aphids or moth, significant changes occur in the pigment content in their leaves, which are reflected in the spectral information. This is manifested as an increase in reflectance in the visible region and a decrease in reflectance in the near-infrared region. These changes are more pronounced during the reproductive stage of the crops. Under specific conditions, hyperspectral technology can analyze the changes in the biochemical information of crop nutrients after disease and pest attacks, and even directly locate a specific characteristic band. By constructing a monitoring model for the biochemical information of crop nutrients under disease and pest stress, the relationship equation between hyperspectral data and crop nutrient biochemical information under disease and pest stress can be fitted. This allows for the indirect analysis of the types of diseases and pests affecting crops and the degree of stress they are under. Based on the hyperspectral and chlorophyll content data of jujube leaves under different truncated leaf mite damage levels, Gao et al. [48] analyzed the hyperspectral characteristics of jujube leaves under different truncated leaf mite damage levels and constructed a hyperspectral linear regression estimation model of chlorophyll content of jujube leaves under different truncated leaf mite damage levels based on first-order differential spectroscopy, and the best fit of the estimation model was achieved at truncated leaf mite damage level 0 with R^2 = 0.810. Li et al. [49] applied hyperspectral

imaging to detect the pigment content of citrus red spider-infested leaves and developed a model to predict leaf pigment content based on the best reflectance ratios of 667/522 and 667/647 nm in the characteristic wavebands. He et al. [50] obtained wavelet coefficients at different scales by continuous wavelet transform of wheat canopy spectra infected with stripe rust, and the selected wavelet coefficient features can be used as independent variables for building an inverse model to quantitatively estimate the chlorophyll content of wheat canopy under stripe rust disease stress. Kong et al. [51] constructed a kernel ridge based on the logarithm of the inverse of the original spectrum (log(1/R)), thereby constructing a kernel ridge regression (KRR) model for predicting phosphorus content of soybean leaves inoculated with bushy mycorrhizae.

Research on crop pests and diseases has focused more on the classification and identification of crops using hyperspectral techniques and not on the monitoring of crop nutrient biochemical information under epidemic pest and disease stress. However, prevention and early detection are the keys to crop pest control; therefore, modeling and real-time monitoring of crop nutrient biochemical information under pest and disease stress using hyperspectral techniques provide a new way for early detection of crop pests and diseases. When measuring hyperspectral data and nutrient biochemical information of crops under pest and disease stress, it can be used as a basis for predicting possible pest and disease stress in crops on the one hand, and clarifying the growth characteristics and damage level of crops under pest and disease stress on the other hand. However, there are few relevant research results and the accuracy of the model for analyzing the degree of pest and disease stress is relatively low; therefore, the research on the monitoring model of nutrient and biochemical information of crop pests and diseases still needs to be further developed.

4. Construction of Hyperspectral Biochemical Information Monitoring Model of Crop Nutrients

Hyperspectral remote sensing has strong advantages in building crop nutrient and biochemical information monitoring models because of its many wavebands, high spectral resolution and the ability to quantitatively analyze the fine spectral differences of features, but hyperspectral remote sensing brings great challenges to data processing and analysis due to the large amount of raw data information, many wavebands and high redundancy of information [52]. The choice of modeling raw spectral data, spectral data pre-processing methods, spectral data feature extraction methods, spectral indices and modeling analysis methods are of great significance to the construction of crop nutrient biochemical information monitoring models, which directly affect the model accuracy. Figure 5 is a schematic diagram of the technical framework of the hyperspectral monitoring model for crop nutrients and biochemical information.

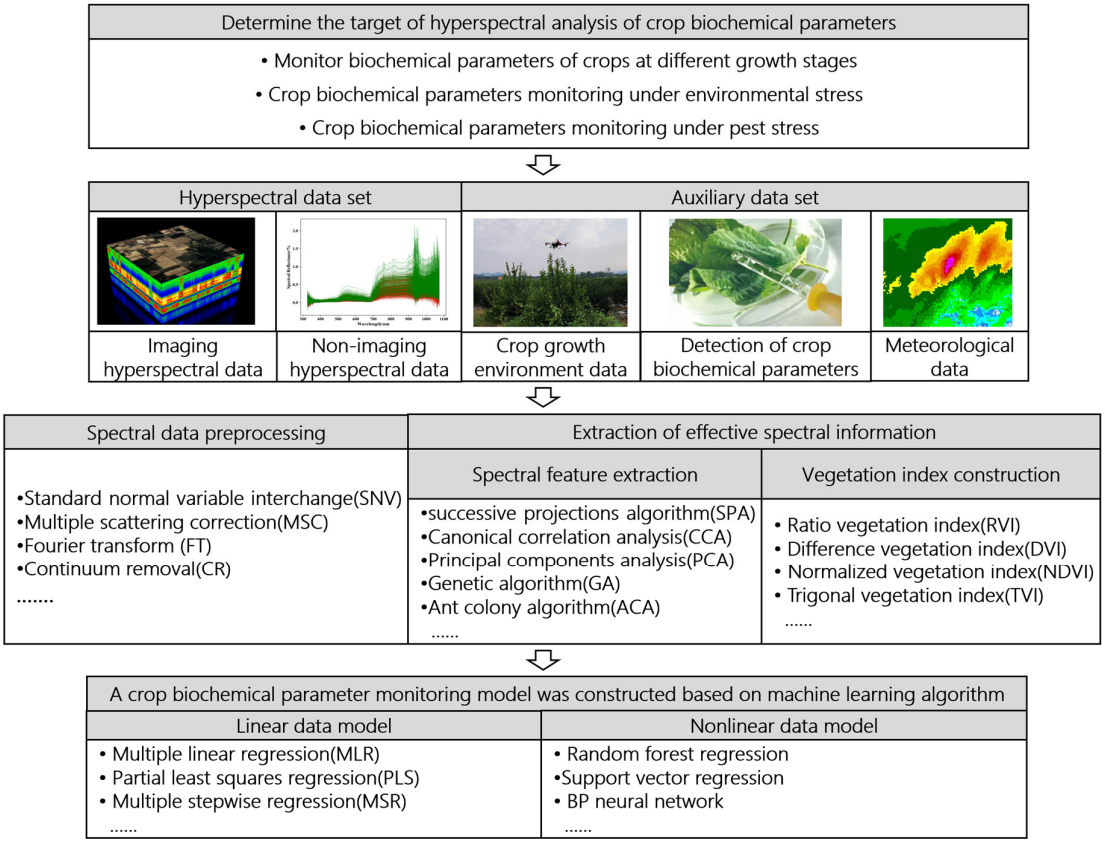

Figure 5. The technical framework of hyperspectral monitoring model for biochemical information of crop nutrients.

4.1. Effect of Different Spectral Data Preprocessing Methods on the Accuracy of the Biochemical Information Hyperspectral Monitoring Model of Crop Nutrients

Common preprocessing methods for spectral data include normalization, Standard Normal Variate (SNV) transformation, Multiple Scatter Correction (MSC), Fourier Transform (FT), Savitzky–Golay (SG), Detrending (DT), Mean Centering, Integer-order Differentiation, Fractional-order Differentiation, baseline correction, Wavelet Transform, etc. Reasonably applying preprocessing methods can effectively eliminate spectral redundancy, noise and other interference factors such as environment, while highlighting the absorption features of the spectrum. Raw spectral data usually need to be preprocessed before being used as input for models, in order to achieve higher prediction accuracy and reduce the workload of parameter adjustment during model tuning. Chen et al. [53] used genetic algorithm combined with Partial Least Squares (PLS) to select leaf chlorophyll features in the chlorophyll spectral region based on the reflectance of rapeseed canopy, with logarithmic and first-order derivative transformations. They found that different spectral preprocessing methods improved the predictive ability of the model. Zhang et al. [54] constructed a hyperspectral monitoring model for nitrogen content in apple leaves, and used wavelet packet analysis to decompose the spectral information, obtaining low-frequency full-spectrum signals and denoised full-spectrum signals. They achieved different levels of denoising effects. Table 1 lists some spectral preprocessing methods used in the construction of crop nutrient and biochemical information monitoring models, as well as their effects on the models.

Table 1. Part of the pretreatment methods to construct crop nutrient biochemical monitoring models and their effects on the models.

Types of Applied Crops	Biochemical Information of Nutrient	Preprocessing Methods	Impact of the Model	Citation
Apple	Chlorophyll and Carotenoids	Fractional Derivative	It provides assistance in extracting sensitive spectral bands by highlighting the number of absorption peaks and reflection peaks.	[55]
Potato	Nitrogen	Reverse Transformation, First Derivative	Reduce background noise in hyperspectral data.	[56]
Potato	Chlorophyll	Standard Normal Variable	It reduces scattering noise and enhances the correlation between spectral data and chlorophyll concentration.	[57]
Winter wheat	Nitrogen	Continuum Removal	It effectively separates and highlights the spectral peak and valley features.	[58]
Winter wheat	Nitrogen	Fractional Derivative	It enhances the correlation between the red edge band and chlorophyll.	[59]
Winter wheat	Chlorophyll	Fractional Derivative, Continuum Removal	It removes spectral information noise and enhances the responsiveness of crop nitrogen and chlorophyll.	[60]
Corn	Chlorophyll and Carotenoids	Unknown Variable Elimination	It reduces the noise in hyperspectral data and eliminates redundant spectral variables.	[61]
Corn	Anthocyanin	Fractional Derivative	It effectively reduces the impact of noise on the target signal, highlights spectral feature information and amplifies the details of the original spectral curve.	[62]
Cotton	Nitrogen	Fractional Derivative	It improves spectral resolution and provides rich absorption features.	[63]

Using preprocessing combined with machine learning to process spectral data can effectively eliminate the environmental effects during data acquisition. However, the results of different preprocessing methods combined with machine learning algorithms cannot be predicted in advance, and repeated experiments are necessary to obtain a combination of algorithms with higher accuracy. Deng et al. [64] selected chlorophyll content in apple leaves as the research object to explore the effects of four different spectral preprocessing methods, i.e., wavelet packet denoising reflectance spectra, reflectance first-order difference spectra, wavelet packet denoising followed by first-order difference spectra and first-order difference followed by wavelet packet denoising spectra, on apple leaf spectral characteristics and chlorophyll content modeling. Results showed that the chlorophyll content prediction model of apple leaves with preprocessing method of first difference followed by wavelet packet denoising algorithm had higher peak signal-to-noise ratio and lower mean square error and maximum error. Rei et al. [65] studied chlorophyll content of mustard leaves and compared the accuracy of chlorophyll monitoring model constructed by five preprocessing methods of first-order derivative reflectance, continuum removal, trend elimination, multiple scattering correction and standard normal transform combined with different machine learning algorithms. With the combination of trend elimination

pre-processing and extreme learning machine, the machine learning algorithm was found to be the most effective method in estimating chlorophyll content. Li et al. [66] determined the phosphorus content and canopy spectral reflectance of oilseed rape leaves at different fertility stages, and applied log(1/R), continuum removal (CR) and first-order differential spectral transforms (FDT) to the original spectra, respectively. Results showed that the FDT-PLS model based on sensitive bands was significantly better than other spectral transformations. Based on the hyperspectrum and measured chlorophyll content of winter wheat canopy, Li et al. [67] applied the original spectrum, Fractional-order Differential spectrum, wavelet energy coefficients obtained from the original spectrum by continuous wavelet transform and measured chlorophyll content for Correlation Analysis, and selected the Fractional-order Differential spectrum and wavelet energy coefficients with better correlation. Stepwise regression analysis, support vector machine, artificial neural network and other methods were then used to construct a model for estimating chlorophyll content of winter wheat. The optimal algorithmic combination model of chlorophyll content of winter wheat based on hyperspectrum for different growth periods was finally obtained.

Spectra without preprocessing can lead to errors in quantitative analysis and incorrect component predictions, making spectral preprocessing a potentially beneficial tool for improving the estimation accuracy of nutrient biochemical information monitoring models [68]. Spectral data preprocessing plays a crucial role in building nutrient biochemical information models, setting the foundation for later stages such as obtaining spectral characteristic bands and selecting modeling methods. Therefore, more attention should be given to spectral data preprocessing in experimental design. Currently, model construction based on hyperspectral data usually involves using separate preprocessing methods and comparing their effects on model accuracy. Fewer studies are based on models constructed by applying multiple preprocessing methods simultaneously. First, the combined effects of different preprocessing methods on the original spectral data are unclear, as there may be interactions between preprocessing methods that lead to different prediction results compared to using the methods individually. Second, a clear and interpretable model is essential for understanding and explaining results. When multiple preprocessing methods are applied simultaneously, the model may become more complex and harder to interpret. Furthermore, over-optimizing preprocessing methods can lead to overfitting, where the model performs well on training data but poorly on new data. Despite these challenges, the combined application of multiple preprocessing methods still has the potential to enhance model prediction performance. Future research can explore this approach, aiming to obtain preprocessing methods that effectively improve model prediction capabilities while minimizing negative impacts.

4.2. Effect of Different Feature Extraction Methods on the Precision of the Biochemical Information of Crop Nutrient Monitoring Model Based on Hyperspectral Techniques

Application of hyperspectral techniques for quantitative analysis of biochemical information of crop nutrients has a large number of samples, numerous bands and high correlation of adjacent bands, which also results in a high redundancy of information in the whole spectral data and adverse effect on the accuracy of monitoring models. Therefore, there is a need to find suitable methods to reduce the analysis indexes while being able to extract sensitive bands from the original bands that contain most of the information needed to predict nutrient biochemical information for the purpose of comprehensive analysis of the original spectral data, which is also an important working basis for further research on monitoring models of crop biochemical parameters. There are two main types of methods to extract effective information from hyperspectral data, one is to obtain the characteristic bands and their combinations by mathematical and statistical analysis or applying intelligent preference algorithms, and the other is to obtain effective information distinguished from the original spectral data by constructing spectral indices.

4.2.1. Selection of Appropriate Spectral Feature Band Extraction Method Can Effectively Improve the Accuracy of the Model

The feature band selection method based on mathematical statistics is commonly used in processing hyperspectral data. It helps to select feature bands that are highly correlated with the target variable or have significant differences, thus improving the predictive performance and interpretability of the model. Common feature band selection methods based on mathematical statistics include Successive Projection Algorithm (SPA), Correlation Coefficient method (CC), Competitive Adaptive Reweighted Sampling (CARS), Gaussian Process Regression (GPR), etc. Liu et al. [69] obtained the hyperspectral data and chlorophyll content of soybean leaves at flowering and podding stage. The selected wavelengths were extracted by continuous projection method, Competitive Adaptive Reweighted Sampling method and Correlation Coefficient method. The PLS modeling of the selected preprocessing method and the characteristic wavelength variables were compared and analyzed. Results showed that the inversion of the selected variables were significantly improved compared with those of the full-wavelength variables. Wang et al. [70] obtained hyperspectral reflectance data and corresponding leaf nitrogen content data at two scales, leaf and canopy, for rice at different fertility stages. Then, Correlation Analysis of single-band raw spectra and first-order derivative spectra and Gaussian Process Regression (GPR) were applied to screen nitrogen sensitive bands at leaf and canopy scales during the whole fertility period of rice. Results show that the sensitive bands screened by GPR conform to the patterns of nitrogen content and spectral changes in rice. Yang et al. [71] compared the accuracy of Monte Carlo-uninformative variable elimination, Random Frog hopping, Competitive Adaptive Reweighting Sampling and Moving Window Partial Least Squares Method of band selection, and proposed a sensitive band selection method combining Competitive Adaptive Reweighting Sampling and Correlation Coefficient method. A nonlinear regression model was established with the screened 30 bands of data. The experimental results show that both the prediction accuracy and modeling accuracy are significantly improved compared with BP neural network model and Support Vector Regression model. Although feature band selection methods based on mathematical statistics can improve the predictive performance of models to some extent, they still have limitations in practical applications. Many feature extraction methods based on mathematical statistics assume a linear relationship between features and the target variable. However, when the relationship between features and the target variable is nonlinear, these methods may fail to capture this relationship effectively. Additionally, feature extraction methods based on mathematical statistics are highly dependent on data preprocessing, which means that the combination of these methods with different preprocessing algorithms can have a significant impact on the model.

Feature band selection methods based on intelligent optimization algorithms have certain advantages, which help improve the effectiveness of feature extraction when dealing with complex datasets. Common feature band selection methods based on intelligent optimization algorithms include Principal Component Analysis (PCA), Genetic Algorithm (GA), Ant Colony Algorithm (ACA), etc. Intelligent optimization algorithms typically possess strong global search capability, adaptability and generalization ability, enabling them to search for optimal solutions throughout the entire search space. They also dynamically adjust search strategies based on problem characteristics, thus enhancing the efficiency of the model. Guo et al. [72] used PCA analysis to compress and extract the main information from the raw spectral data of rubber seedling leaves, and the obtained 20 principal components could explain 99.993% of the information of the original 2151 wavelengths (350–2500 nm). Cao et al. [73] used three dimensionality reduction methods, such as SPA, LASSO and EN, combined with three regression methods, such as MLR, MSR and PLSR, to construct nine maize leaf nitrogen inversion models, and the EN-PLSR model had the best prediction performance for estimating maize leaf nitrogen content under comprehensive comparison. Sun et al. [74] used rice canopy spectral data as the research object, and applied PCA to reduce the dimensionality of the original spectral data. The obtained principal

components were used as input variables to construct high-spectral estimation models for leaf SPAD values using stepwise multiple linear regression analysis and Support Vector Regression. They found that the combination of PCA and support vector machine models could better predict leaf SPAD values compared to models based on Correlation Coefficient methods. In comparison to feature band selection methods based on mathematical statistical analysis, intelligent optimization algorithms have advantages in terms of global search capability, adaptability, parallel computing capability, avoiding overfitting, and handling multi-objective problems. However, such methods also have limitations, such as high computational complexity and slow convergence speed. Table 2 lists some spectral feature extraction methods used in constructing crop nutrient biochemical monitoring models and their effects on the models.

Table 2. The spectral feature extraction method and its influence on the model of crop nutrient biochemical monitoring model were partially constructed.

Types of Applied Crops	Biochemical Information of Nutrient	Feature Extraction Methods	Impact of the Model	Citation
Cotton	Nitrogen	Successive Projection Algorithm	The collinearity between wavelength variables was eliminated, and the sensitive feature bands of leaf nitrogen content were highly correlated with leaf nitrogen content	[75]
Lettuce	Phosphorus	Successive Projection Algorithm, Principal Component Analysis	The dimension of spectral data is reduced, the complexity of the model is reduced and the prediction ability of the model is improved	[76]
Winter wheat	Nitrogen	Discrete Wavelet Transform	On the basis of maintaining the quality of original spectral information and reducing the spatial dimension of canopy spectral data, the feature extraction of hyperspectral canopy spectra is completed	[77]
Winter wheat	Chlorophyll	Continuous Wavelet Transform	The characteristic information of chlorophyll content in winter wheat canopy was captured effectively, which improved the prediction accuracy of the model	[78]
Corn	Chlorophyll	Competitive Adaptive Reweighted Sampling, Successive Projection Algorithm and CARS_SPA	It can effectively extract sensitive hyperspectral features, reduce the number of hyperspectral features and improve the multicollinearity problem	[50]
Rice	Nitrogen	Principal Component Analysis	By lowering the data dimension, the resulting principal component contains almost equal information to the original dataset	[79]
Apple	Anthocyanin	Variable Importance in Projection (VIP)-PLSR-Akaike Information Criterion	The estimation accuracy and conciseness of the model are guaranteed effectively	[80]

The combination of mathematical statistics and intelligent optimization algorithms can improve the accuracy, robustness and efficiency of spectral feature extraction, as well

as expand the feature space to adapt to different types of hyperspectral data. Liu et al. [81] focused on winter wheat at different growth stages. They preprocessed the spectral data using wavelet denoising and multiple scattering correction, applied PCA to reduce the dimensionality of the data, and then used correlation coefficient analysis to select the optimal combinations of principal components for different growth stages. Multivariate regression models were built to estimate chlorophyll content at different growth stages. Results showed better predictive performance and generalization ability for all models. Liu et al. [61] combined CWT with CARS to estimate nitrogen concentration in potatoes. The results show that CARS can retain the coefficients with the least information redundancy, while eliminating the invalid information with large interference in the wavelet coefficients processed by continuous wavelet transform, thus improving the stability and accuracy of the model. Although the combination of mathematical statistics and intelligent optimization algorithms theoretically improves the accuracy and effectiveness of spectral feature extraction, there are limited practical examples of this composite approach. On one hand, the combination of these two types of algorithms requires careful design and adjustment to ensure their collaboration and exploitation of respective advantages, which may increase the difficulty of algorithm design and implementation and restrict the practical application of this method. On the other hand, this composite approach may lead to a significant increase in computational complexity, slower convergence speed and poorer stability of the model. Slow or unstable convergence speed during the search for optimal feature combinations can affect the practical application of the method. Despite these challenges, the combination of mathematical statistics and intelligent optimization algorithms for spectral feature acquisition still holds certain research value. In practical applications, suitable feature selection methods can be chosen based on specific problems and scenarios, and existing optimization techniques and tools can be employed to overcome these challenges.

4.2.2. Appropriate Spectral Index Is Helpful to Improve the Prediction Accuracy of the Model

Spectral index is a powerful spectral parameter that is obtained by applying a specific algorithm to one or more spectral bands [82]. Compared to single-band spectral information, spectral indices have higher sensitivity and can effectively reduce or eliminate noise caused by environmental backgrounds such as soil and water. They are an indispensable tool in spectral data analysis. Spectral indices can be used to construct qualitative or quantitative monitoring models and have been extensively applied in research areas such as monitoring crop growth indicators [83], pest and disease stress [84,85] and growth conditions [86]. Spectral indices can effectively extract useful information from hyperspectral data. Compared to models based on raw spectral data or specific spectral bands, spectral indices amplify the connection between spectral reflectance and crop nutrient and biochemical information, resulting in models constructed based on spectral indices having better predictive performance. Common spectral indices applied to construct crop nutrient biochemical information monitoring models are Ratio Vegetation Index (RVI), Difference Vegetation Index (DVI), Normalized Difference Vegetation Index (NDVI), Triangular Vegetation Index (TVI), Modified Chlorophyll Uptake Rate Index (MCARI), Modified Ratio Vegetation Index (MSR), Modified Chlorophyll Absorption in Reflectance Index/Optimized Soil-adjusted Vegetation Index (MCARI/OSAVI), Soil-adjusted Spectral Index (SASI), Meris Terrestrial Chlorophyll Index (MTCI), etc. Table 1 lists some of the commonly used spectral indices for constructing crop nutrient biochemical information monitoring models. To explore the hyperspectral band combinations that are sensitive to the chlorophyll content of winter wheat canopy, and to compare the estimation effect of different spectral indices on the chlorophyll content of wheat canopy, Luo et al. [87] selected four spectral indices to construct a model for monitoring the chlorophyll content of wheat canopy based on the original spectrum and the first-order derivative spectrum. Pan et al. [88] compared the correlation between six vegetation indices and apple canopy chlorophyll content, and constructed spectral indices for all two-band combinations in the sensitive wavelength region.

Models developed based on these spectral indices achieved a high level of significance. Xu et al. [89] selected strawberry as the test material to measure the chlorophyll content of strawberry leaves and the spectral reflectance of crown height, and studied the correlation between them. Results showed that the correlation between chlorophyll content and the vegetation index DVI, MSAVI, PVI, RDVI, SAVI and TSAVI reached a very significant level. It can be used as characteristic parameter to predict chlorophyll content (Table 3).

Table 3. Common vegetation indexes in the process of building monitoring model for biochemical.

Name of Spectral Index	Composition of Band	Types of Applied Crops	Biochemical Information of Nutrient	Citation
RVI	(R574, R695)	Rice	phosphorus	[90]
DSI	(R648, R738)		nitrogen	[91]
SR	(R537, R553)		nitrogen	[92]
NEW-NDRE	(R550, R790, R720)	Wheat	nitrogen	[93]
NDVI	(R689, R697)		chlorophyll	[94]
SAVI	(R800, R670)	Corn	chlorophyll	[95]
TGI	(R480, R550, R670)		chlorophyll	[96]
RSI	(R1811, R1842)		nitrogen	[97]
TVI	(R731, R713)	Soybean	nitrogen	[98]
MTCI	(R750, R710, R680)	Cotton	chlorophyll	[99]
GNDVI	(R750, R550)		nitrogen	[100]
PRI	(R531, R570)		carotenoids	[101]

The differences in correlation between spectral indices and different crop varieties, growth stages, stress conditions and the types of inferred biochemical information are primarily influenced by the combined effects of variations in plant physiological characteristics, changes in growth stages, impacts of stress conditions and the different types of inferred biochemical information. To enhance the accuracy and reliability of monitoring models, it is crucial to select spectral indices that exhibit a high correlation with the specific target object features and attributes. Diao et al. [102] found that the greenness vegetation index (Green NDVI), soil-adjusted ratio vegetation index (SARVI), ratio vegetation index (RVI) and Difference Vegetation Index (DVI) showed highly significant correlation with the nitrogen fertilizer bias productivity PF-Pn of wheat at tillering and flowering, pulling, tasseling and maturity stages, respectively. Lu et al. [103] experimentally found that the normalized difference spectral index spectral index (NDSI (R1705, R1385)), Ratio Spectral Index (RSI (R1385, R1705)) and Difference Spectral Index (DSI (R1705, R1385)) were well correlated with the Leaf Potassium Content of rice through experiments (R^2 up to 0.68). In their research on the high-spectral inversion model for rice phosphorus content, Ban et al. [104] found that the Leaf Phosphorus Content of rice was highly correlated with three newly constructed spectral indices: NDSI (R498, R606), RSI (R498, R606) and DSI (R498, R586), with correlation coefficients of 0.913, 0.915 and 0.938, respectively.

Spectral indices with higher correlation have better interpretability in specific application scenarios, enabling them to more accurately reflect the spectral variations of the target object and effectively enhance the inference performance of monitoring models. Therefore, in the process of constructing crop nutrient biochemical information monitoring models based on spectral indices, it is necessary to select suitable spectral indices for monitoring and inference based on specific circumstances. Inoue et al. [105] found that spectral indices based on NDSI (R825, R735) or RSI (R825, R735) had high prediction accuracy when modeling and monitoring nitrogen content in rice. Qi et al. [15] found that the optimal spectral indices for determining chlorophyll content in peanut leaves were NDSI (R520, R528), RSI (R748, R561), DSI (R758, R602) and SASI (R753, R624), and all the determined coefficient values for the models based on NDSI, RSI, DSI and SASI were greater than 0.65, while the root mean square error values were all less than 2.04.

To improve the prediction accuracy of inversion models of crop nutrient biochemical information, many scholars have proposed many new spectral indices based on the optimization of published spectral indices to reduce background signals or noise, to resolve overlapping spectral features and to enhance the relationship between spectral data and crop nutrient biochemical information [106]. Liang et al. [107] designed two new spectral indices based on the first-order derivatives of reflectance spectra FD-NDNI and FD-SRNI for estimating the nitrogen content of wheat, and the comparative analysis showed that the accuracy of the models constructed based on FD-NDNI and FD-SRNI was better than that of the commonly used indices such as MNDVI (705) and NDNI. Yu et al. [108] simplified the spectral index NAOC based on integral operations and obtained optimized spectral indices based on dual-band simplification operations. They used the original reflectance spectra R and mathematically transformed spectra LgR, $R^{\frac{1}{2}}$ and 1/R as the basis for calculating spectral indices, and established three rice leaf SPAD inversion models using PLSR, SVM and BP neural networks, respectively. The determination coefficients of these models were all greater than 0.79, and the standardized root mean square error values were less than 5.4%. In order to explore and evaluate the effects of different vegetation indices on winter wheat canopy chlorophyll content (CCC) estimation, Zhang et al. [59] optimized the published and revised indices using a combination of Original Spectra (OS) and first-order differential (FD) processed random bands. They found that Three-band Vegetation Index could resolve the limitation of the number of bands on target information extraction, alleviate the saturation problem of Two-band Vegetation Index and improve the monitoring accuracy of winter wheat chlorophyll content. Overall, the emergence of new spectral indices provides a new approach and methodology for spectral analysis and the study of models for estimating crop nutrient biochemical information. These new indices offer more precise and comprehensive spectral feature information.

4.3. Construction of Biochemical Information Monitoring Model of Crop Nutrient Based on Machine Learning Algorithm

Machine learning algorithms are powerful tools for handling hyperspectral remote sensing data. Predicting crop nutrient biochemical information based on hyperspectral data is a regression problem, and common machine learning algorithms include decision tree algorithms, regression algorithms, ensemble algorithms, clustering algorithms and artificial neural networks. These algorithms have been widely used in constructing monitoring models for crop nutrient biochemical information based on hyperspectral data. Prior to applying machine learning algorithms, preprocessing and extraction of relevant spectral information from hyperspectral data are necessary to ensure the reliability of the models. The preprocessed and spectrally informative hyperspectral data is used as input, while the desired crop nutrient biochemical information is used as output. By fitting a regression model using machine learning algorithms, monitoring of crop nutrient biochemical information can be achieved. These models can generally be classified as linear or nonlinear models. When applying machine learning algorithms for regression modeling of crop nutrient biochemical information, it is important to consider model selection and tuning, handling overfitting and underfitting and model evaluation and interpretation, in order to improve model accuracy.

Linear regression models have lower computational complexity and are better able to reflect causal relationships and relative importance between variables. They also possess strong robustness. Commonly used algorithms for constructing linear data models for crop nutrient biochemical information include Partial Least Squares Regression (PLSR), Multiple Linear Regression (MLR), Stepwise Regression Analysis (SRA) and Multivariate Stepwise Regression (MSR). Li et al. [109] used hyperspectral data of potato leaves under different nitrogen treatment conditions, selected raw spectra and their transformed data in the wavelength range of 430–910 nm and used PLSR to construct a nitrogen content prediction model of potato leaves based on the nitrogen content data of leaves sampled simultaneously in the field. The results showed that the Partial Least Squares regression

modeling method was able to model the nitrogen content of potato leaves under the condition that the independent variables had several multiples. Ye et al. [110] used PLSR and MLR to construct a model to estimate the nitrogen content of apple leaves based on the Raw Hyperspectral Reflectance and first-order derivative reflectance of apple leaves. The MLR model based on raw reflectance was better than the PLS model and the MLR model based on first-order derivative reflectance. Kai Li et al. [111] used MSR to construct a hyperspectral estimation model for chlorophyll content of moso bamboo under insect damage stress. It was found that the MSR could further compress the feature wavelength extracted by the continuous projection algorithm. And the envelope removal and envelope removal first-order derivative MSR models established by combining the continuous projection algorithm with the SPXY sample division method can effectively estimate the chlorophyll content of bamboo leaves. However, linear regression models also have some limitations. For example, when there is multicollinearity among multiple independent variables, the linear regression model may become unstable. Additionally, linear regression models are limited to capturing linear relationships between variables and cannot capture more complex nonlinear relationships or interactions. Although linear regression models may not perform as well as other complex machine learning algorithms in certain situations, they are still a useful and reliable modeling tool for handling linearly related data and problems.

Hyperspectral data are spectral data of continuous wavelengths, and there is a high correlation between adjacent wavelength data. Therefore, the linear model can better solve the problem of multiple covariance that hyperspectral data are usually prone to, thus improve the accuracy and stability of the model. In addition, the relationship between hyperspectral data and crop nutrient biochemical information contains both linear and nonlinear models. Nonlinear models have limited ability to predict linear components in the models. However, a large number of studies have shown that compared with linear models, nonlinear models can further exploit the hidden valid information between spectral data and crop nutrient biochemical information, thus improving the prediction accuracy of the models.

Spectral data typically contains rich information and can capture the reflection or absorption characteristics of crop biochemical components, indicating that there is a direct linear relationship between their concentrations and spectral responses. However, due to the complex nonlinear relationships that may exist between nutrient absorption, transportation, metabolism, crop physiological processes and environmental factors, crop nutrient biochemical information may also exhibit nonlinear characteristics. Nonlinear models have more flexible assumptions about data distribution and can capture interactions between independent variables. Compared to linear models, nonlinear models are better able to explore the relationship between spectral data and crop nutrient biochemical information, providing more accurate and detailed predictions [112]. In a hyperspectral inversion study of chlorophyll content of apple leaves, Liu et al. [113] found that Support Vector Regression had better prediction ability for chlorophyll content of apple leaves compared with polynomial regression. In a hyperspectral-based inversion study of chlorophyll content of winter wheat, Wang et al. [114] found that the prediction accuracy of both nonlinear models constructed by the Gradient Boosted Regression Tree Algorithm and BP neural network were higher than that of the Multiple Linear Prediction model constructed by the ridge regression algorithm. Among them, the Gradient Boosted Regression Tree Algorithm has a greater advantage in predicting chlorophyll content of winter wheat at all fertility stages. Guo et al. [115] selected leaf phosphorus content sensitive bands based on the Correlation Analysis of leaf phosphorus content and spectral variables. This sensitive band was used as the input variable to predict the leaf phosphorus content by combining MLR, PLSR and BP neural network models. The results showed that the model for predicting leaf phosphorus content of rubber seedlings constructed by combining sensitive bands with BP neural network had the highest prediction accuracy. And it was significantly better than other linear models constructed by using various spectral forms as input variables.

In addition to the algorithms mentioned above, common algorithms applied to construct nonlinear data models for crop nutrient biochemical information include Random Forest Regression [58], Gaussian Process Regression [116], K-value proximity [117] and radial basis function neural networks [118]. Although nonlinear regression models have strong predictive capabilities, they also pose challenges and limitations. For example, parameter estimation in nonlinear models can be more difficult and prone to getting stuck in local optima. Additionally, overly complex nonlinear models can introduce overfitting issues. Therefore, when using nonlinear regression models, it is important to carefully choose the model form, address overfitting problems and perform appropriate model evaluation and validation.

Both linear regression models and nonlinear regression models have limitations in real-world applications. The ideal solution is to integrate both types of models, capturing both linear and nonlinear relationships in the data, increasing the flexibility of the model and potentially improving the model's fitting capability and prediction accuracy. It is feasible to integrate linear regression models and nonlinear regression models, and one approach is to use a generalized linear model that combines both linear and nonlinear components. Another approach is to use the predictions of a nonlinear regression model as input for a linear regression model. The specific methods and steps for integrating linear regression models and nonlinear regression models may vary depending on the specific problem and data. When selecting the appropriate approach, it is necessary to consider the practical situation and data characteristics, and perform appropriate model evaluation and validation. Liu et al. [119] collected rice canopy hyperspectral data and chlorophyll content data and developed a hybrid prediction model (GPR-P), which was based on Gaussian Process Regression and PLSR to compensate and predict the chlorophyll content of rice. Moreover, it made full use of the respective advantages of linear and nonlinear models to further improve the prediction accuracy and stability of the model. Integrating linear regression models with nonlinear regression models can improve the model's fitting capability and prediction accuracy. However, it also comes with limitations such as increased complexity, increased data requirements, risk of overfitting, difficulties in parameter selection and reduced interpretability. Currently, most models for crop nutrient biochemical information based on hyperspectral monitoring rely on single data models, and there is limited research on combining two different types of data models. Further development by researchers is needed.

5. Challenges and Prospects of Hyperspectral Technology in Monitoring Biochemical Information of Crop Nutrients

The application of hyperspectral techniques for monitoring crop nutrient biochemical information has an important position in the field of hyperspectral remote sensing agriculture. There are still challenges that require fast and efficient solutions to expand the application of hyperspectral technology for monitoring crop nutrient biochemical information.

1. There are few products for spectral monitoring of crop nutrient biochemical information for agricultural production. The purpose of the research is to obtain the nutrient biochemical information of the target crop, select the combination of characteristic spectral bands or characteristic spectral bands that contribute most to the monitoring model and make a relatively low-cost multispectral device or sensor for application in agricultural production. Although most of the realized models have good predictive capability, they are still less able to be translated into products for application in agricultural production practices. This is mainly because different varieties, different growth conditions, different growth periods and different nutrient biochemical information of the same crop correspond to different spectral sensitive bands, and the models are not very universal. At the same time, different crops have different growth environments, and the shapes and adaptability of the spectral sensors need to be designed to match. Therefore, the application of hyperspectral technology to study

the crop nutrient biochemical information monitoring models into corresponding spectral sensors is very promising commercially.

2. A database of spectral models for monitoring nutrient and biochemical information of different crops has not yet been established. Due to the complexity of crop species and different growing conditions, the equipment for collecting hyperspectral data of crops also varies, and the models established by different researchers for monitoring nutrient and biochemical information are less universally applicable. On the one hand, it is conducive to the exchange of data among researchers studying the same crop species or the same nutrient biochemical information, so as to filter out the spectral fingers with good generality; on the other hand, it can provide research ideas for scholars studying different crop species or different nutrient biochemical information.
3. At present, the hyperspectral monitoring model of crop nutrient and biochemical information is not dynamic and real-time. Most of the spectral data used to construct the monitoring models are static statistics. And the monitoring models constructed by the inversion of single nutrient and biochemical information lack consideration of the linkage between crop nutrient and biochemical information and the interaction mechanism between crop and environment. Therefore, in the subsequent research, the spectral prediction model can be combined with the crop growth mechanism model or remote sensing model to build a more efficient and universal dynamic monitoring model, so as to make accurate judgments on the trends of nutrient and biochemical information and the crop growth in each growth cycle.

6. Conclusions

Building nutrient biochemical information monitoring models based on hyperspectral data can establish the relationship between hyperspectral data, nutrient biochemical information and other plant phenotypes quickly and effectively. This approach is also a research hotspot in the field of precision agriculture. This paper provides an overview and review of academic research on building nutrient biochemical information monitoring models based on hyperspectral data. The main contributions of this paper are as follows: (1) sorting out the main application scenarios of building crop nutrient biochemical information monitoring models based on hyperspectral data in recent years; (2) systematically explaining the advantages, disadvantages and applicability of the methods used in each stage of model construction; and (3) presenting the current challenges and potential future developments. Through this clearer and more comprehensive overview, we aim to provide a reference for future research on building crop nutrient biochemical information monitoring models based on hyperspectral data.

In recent years, numerous researchers in the agricultural field have built hyperspectral remote sensing systems and applied them in monitoring models for crop nutrient biochemical information. Currently, these models have been effectively applied in monitoring nutrient biochemical information of crops at different growth stages or under different growth conditions. However, most of the research focuses on a specific growth period of crops, only providing feedback on the crop's growth status at the time of data collection, without demonstrating future growth prediction. Therefore, future research can focus on monitoring nutrient biochemical information across multiple growth stages of crops, thus enhancing the validation of crop growth prediction and improving the reliability of the models. Additionally, although most studies achieve high model prediction accuracy, there is limited discussion on the applicability of the models in the same crop research. Generality is an important evaluation criterion for models and should also be considered as a significant factor during model construction.

In the various stages of model construction, a large number of traditional machine learning algorithms have been combined. Generally, traditional machine learning techniques exhibit good performance, but the setting of their parameters greatly affects regression accuracy, requiring significant effort in parameter tuning. Currently, researchers have made improvements in classification and recognition algorithms while using different data

mining techniques to identify, classify and quantitatively analyze the spectral features of crop nutrient biochemical information. The achieved research results demonstrate that hyperspectral technology has good predictive capabilities in identifying and monitoring the nutrient biochemical content of crops, revealing the potential of applying hyperspectral technology combined with computer algorithms for analyzing crop phenotypic information. However, as mentioned above, although the monitoring models exhibit excellent predictive abilities after parameter tuning, they are mostly limited to specific application scenarios. Therefore, it is necessary to further increase the dataset of nutrient biochemical information for crops of the same type in different growth environments, enabling the development of models with stronger generalization and dynamic prediction capabilities. Additionally, the development of modeling methods based on multiple algorithm fusion is also crucial, as it may provide an important solution for enhancing model stability, generality and accuracy.

Author Contributions: Conceptualization, Y.L. and Y.Z.; methodology, Y.L., Y.Z. and J.X.; validation, Y.Z. and H.T.; formal analysis, J.X., W.L., Y.L. and X.L.; investigation, Y.L., Y.Z., J.X., X.L., J.D., W.L. and L.W.; re-sources, Y.Z., K.Y. and Y.Z.; data curation, Y.Z. and K.Y.; writing—original draft preparation, Y.L., J.X. and Y.Z.; writing—review and editing, Y.L. and J.X.; visualization, J.X.; supervision Y.L.; project administration, Y.L.; funding acquisition, Y.L. and Y.Z. All authors have read and agreed to the published version of the manuscript.

Funding: This research was funded by the Laboratory of Lingnan Modern Agriculture Project, grant number NT2021009; the Key Field Research and Development Plan of Guangdong Province, China, grant number 2019B020221001; and the 111 Project, grant number D18019.

Data Availability Statement: The data presented in this study are available on request from the corresponding author.

Conflicts of Interest: The authors declare no conflict of interest.

References

1. He, Y.; Peng, J.; Liu, F.; Zhang, C.; Kong, W. Critical Review of Fast Detection of Crop Nutrient and Physiological Information with Spectral and Imaging Technology. *Trans. Chin. Soc. Agric. Eng.* **2015**, *31*, 174–189.
2. Ahmad, Z.; Anjum, S.; Waraich, E.A.; Ayub, M.A.; Ahmad, T.; Tariq, R.M.S.; Ahmad, R.; Iqbal, M.A. Growth, Physiology, and Biochemical Activities of Plant Responses with Foliar Potassium Application under Drought Stress—A Review. *J. Plant Nutr.* **2018**, *41*, 1734–1743. [CrossRef]
3. Yu, F.; Cao, Y.; Xu, T.; Guo, Z.; Wang, D. Precision Fertilization by UAV for Rice at Tillering Stage in Cold Region Based on Hyperspectral Remote Sensing Prescription Map. *Trans. CSAE* **2020**, *36*, 103–110.
4. Tongyu, X.; Zhongyu, J.; Zhonghui, G.; Liu, Y.; Juchi, B.; Shuai, F.; Fenghua, Y. Simultaneous Inversion Method of Nitrogen and Phosphorus Contents in Rice Leaves Using CARS-RUN-ELM Algorithm. *Trans. Chin. Soc. Agric. Eng.* **2022**, *38*, 148–155.
5. Li, X.; Chen, G.; Xu, M.; Ding, H.; Liu, Z.; Yang, C. Study on Hyperspectral Estimation Models for Potassium Content of Rubber Tree Leaves. *Southwest China J. Agric. Sci.* **2020**, *33*, 769–774.
6. Kailun, J.; Jiging, A.; Yuwei, Z.; Junying, L.; Yingli, C. Analysis and Inversion of Rice Chlorophyll Spectral Characteristics Using RNCA-PSO-ELM. *Trans. Chin. Soc. Agric. Eng.* **2022**, *38*, 178–186.
7. Xican, Z.; Gengzing, Z.; Xueyan, S.; Tong, L.; Dingguo, S. Estimation of Kalium Content in Apple Flowers Based on Spectral Analysis Technique. *Infrared* **2010**, *31*, 19–23.
8. Xi-Cun, Z.; Geng-Xing, Z.; Fang, D.; Ling, W.; Tong, L.; Bing, Z. Monitoring Models for Phosphorus Content of Apple Flowers Based on Hyperspectrum. *Yingyong Shengtai Xuebao* **2009**, *20*, 2424–2430.
9. Chen, Y.; Fu, B.; Feng, X. Overview and Outlook of Remote Sensing Inversion of Vegetation Nitrogen Content. *Acta Ecol. Sin.* **2017**, *37*, 6240–6252.
10. Tan, Y.; Sun, J.-Y.; Zhang, B.; Chen, M.; Liu, Y.; Liu, X.-D. Sensitivity of a Ratio Vegetation Index Derived from Hyperspectral Remote Sensing to the Brown Planthopper Stress on Rice Plants. *Sensors* **2019**, *19*, 375. [CrossRef]
11. Lan, Y.; Zhu, Z.; Deng, X.; Lian, B.; Huang, J.; Huang, Z.; Hu, J. Monitoring and Classification of Citrus Huanglongbing Based on UAV Hyperspectral Remote Sensing. *Trans. CSAE* **2019**, *35*, 92–100.
12. Flores, H.; Lorenz, S.; Jackisch, R.; Tusa, L.; Contreras, I.C.; Zimmermann, R.; Gloaguen, R. UAS-Based Hyperspectral Environmental Monitoring of Acid Mine Drainage Affected Waters. *Minerals* **2021**, *11*, 182. [CrossRef]
13. Hou, Y.; Zhu, W.; Wang, E. Hyperspectral Mineral Target Detection Based on Density Peak. *Intell. Autom. Soft Comput.* **2019**, *25*, 805–814. [CrossRef]

14. Ibrahim, A.; Franz, B.; Ahmad, Z.; Healy, R.; Knobelspiesse, K.; Gao, B.-C.; Proctor, C.; Zhai, P.-W. Atmospheric Correction for Hyperspectral Ocean Color Retrieval with Application to the Hyperspectral Imager for the Coastal Ocean (HICO). *Remote Sens. Environ.* **2018**, *204*, 60–75. [CrossRef]
15. Qi, H.; Zhu, B.; Kong, L.; Yang, W.; Zou, J.; Lan, Y.; Zhang, L. Hyperspectral Inversion Model of Chlorophyll Content in Peanut Leaves. *Appl. Sci.* **2020**, *10*, 2259. [CrossRef]
16. Jay, S.; Baret, F.; Dutartre, D.; Malatesta, G.; Héno, S.; Comar, A.; Weiss, M.; Maupas, F. Exploiting the Centimeter Resolution of UAV Multispectral Imagery to Improve Remote-Sensing Estimates of Canopy Structure and Biochemistry in Sugar Beet Crops. *Remote Sens. Environ.* **2019**, *231*, 110898. [CrossRef]
17. Zhao, C.; Li, H.; Li, P.; Yang, G.; Gu, X.; Lan, Y. Effect of Vertical Distribution of Crop Structure and Biochemical Parameters of Winter Wheat on Canopy Reflectance Characteristics and Spectral Indices. *IEEE Trans. Geosci. Remote Sens.* **2016**, *55*, 236–247. [CrossRef]
18. Xu, X.-G.; Zhao, C.-J.; Wang, J.-H.; Huang, W.-J.; Li, C.-J.; Liu, H.-J. Study on Relationship between New Characteristic Parameters of Spectral Curve and Chlorophyll Content for Rice. *Spectrosc. Spectr. Anal.* **2011**, *31*, 188–191.
19. Zhang, N.; Yang, G.; Zhao, C.; Zhang, J.; Yang, X.; Pan, Y.; Huang, W.; Xu, B.; Li, M.; Zhu, X. Progress and Prospects of Hyperspectral Remote Sensing Technology for Crop Diseases and Pests. *Natl. Remote Sens. Bull* **2021**, *25*, 403–422. [CrossRef]
20. Tong, Q.; Xue, Y.; Zhang, L. Progress in Hyperspectral Remote Sensing Science and Technology in China over the Past Three Decades. *IEEE J. Sel. Top. Appl. Earth Obs. Remote Sens.* **2013**, *7*, 70–91. [CrossRef]
21. Diwu, P.; Bian, X.; Wang, Z.; Liu, W. Study on the Selection of Spectral Preprocessing Methods. *Spectrosc. Spectr. Anal.* **2019**, *39*, 2800–2806.
22. Liu, Z.; Wan, W.; Huang, J.; Han, Y.; Wang, J. Progress on Key Parameters Inversion of Crop Growth Based on Unmanned Aerial Vehicle Remote Sensing. *Trans. Chin. Soc. Agric. Eng.* **2018**, *34*, 60–71.
23. Ryu, C.; Suguri, M.; Umeda, M. Multivariate Analysis of Nitrogen Content for Rice at the Heading Stage Using Reflectance of Airborne Hyperspectral Remote Sensing. *Field Crops Res.* **2011**, *122*, 214–224. [CrossRef]
24. Zhou, L.; Feng, H.; Yan, Z.; Liu, K.; Zhou, S. Hyperspectral Diagnosis of Leaf N Concentration of Maize and Variety Difference. *Trans. Chin. Soc. Agric. Eng.* **2010**, *26*, 195–199.
25. Jing, A.; Guoqing, Y.; Xicun, Z. Study of Hyperspectral Detection for Nitrogen Content of Apple Leaves. *Remote Sens. Nat. Resour.* **2016**, *28*, 67–71.
26. Jiang, H.; Li, Y.; Zhao, Y.; Zheng, S.; Li, Y. Study on the inversion of winter wheat canopy chlorophyll content during flowering period based on hyperspectral remote sensing. *J. Jilin Norm. Univ. (Nat. Sci. Ed.)* **2020**, *41*, 133–140.
27. Liu, Y.; He, S.; Yi, S.; Xie, R.; Zheng, Y.; Liu, X.; Deng, L. Characteristics of Potassium Content in Citrus Flowers with Hyperspectral Imagery. *J. Fruit Sci.* **2014**, *31*, 1065–1071.
28. Shen, L.; Gao, M.; Yan, J.; Wang, Q.; Shen, H. Winter Wheat SPAD Value Inversion Based on Multiple Pretreatment Methods. *Remote Sens.* **2022**, *14*, 4660. [CrossRef]
29. Yue, X.; Quan, D.; Hong, T.; Wang, J.; Qu, X.; Gan, H. Non-Destructive Hyperspectral Measurement Model of Chlorophyll Content for Citrus Leaves. *Trans. Chin. Soc. Agric. Eng.* **2015**, *31*, 294–302.
30. Li, Z.; Jin, X.; Yang, G.; Drummond, J.; Yang, H.; Clark, B.; Li, Z.; Zhao, C. Remote Sensing of Leaf and Canopy Nitrogen Status in Winter Wheat (*Triticum Aestivum* L) Based on N-PROSAIL Model. *Remote Sens.* **2018**, *10*, 1463. [CrossRef]
31. Li, D.; Wang, C.; Liu, W.; Peng, Z.; Huang, S.; Huang, J.; Chen, S. Estimation of Litchi (*Litchi Chinensis* Sonn.) Leaf Nitrogen Content at Different Growth Stages Using Canopy Reflectance Spectra. *Eur. J. Agron.* **2016**, *80*, 182–194. [CrossRef]
32. Huang, S.; Hong, T.; Yue, X.; Wu, W.; Cai, K.; Li, Y. Hyperspectral Estimation Model of Total Phosphorus Content for Citrus Leaves. *Nongye Jixie Xuebao Trans. Chin. Soc. Agric. Mach.* **2013**, *44*, 202–207+195.
33. Yang, T.; Wang, X.; Chai, Z.; Ding, K.; Zhao, J.; Ma, X. Study of Spectral Analysis of Nitrogen Content of Kuerle Fragrant Pear Leaves at Different Growth Stages. *Southwest China J. Agric. Sci.* **2016**, *29*, 668–673.
34. Hai-jun, Z.; Hong-yu, F.; Xue-hua, W.; Guo-xian, C.; Ai-long, S.; Wei-chun, X. Preliminary Study on the Intertemporal Predictability of the Physiological Index of Early Rice Based on Hyperspectral. *Spectrosc. Spectr. Anal.* **2022**, *42*, 170–175.
35. Yuan, X.; Zhou, G.; Wang, Q.; He, Q. Hyperspectral Characteristics of Chlorophyll Content in Summer Maize under Different Water Irrigation Conditions and Its Inversion. *Acta Ecol. Sin.* **2021**, *41*, 543–552.
36. Bin, P.; Wei, X.; Rong, S.; Gongneng, F.; Wenyan, S. Growth of Suaeda Salsa Tin Response to Salt Stress in Different Habitats. *Acta Prataculturae Sin.* **2016**, *25*, 81–90.
37. Hui, S.; Meichen, F.; Wude, Y.; Fangzhou, L.; Guangxin, L.; Chao, W. Monitoring Plant Nitrogen Contents of Dry-Land and Irrigation-Land Winter Wheat Using Hyperspectral Dates. *J. Shanxi Agric. Sci.* **2015**, *43*, 273–276.
38. Yanwen, G.; Shuai, L.; Wei, G.; Hong, W. Hyperspectral Estimation for Chlorophyll Contents in the Leaves of *Lpomoea Aquatica* F. Under Cadmium Stress. *J. Southwest Univ. (Nat. Sci. Ed.)* **2015**, *37*, 9–16.
39. Guan, L.; Liu, X. Experimental Research on Remote Sensing Diagnosis Method of Cd Pollution Stress in Rice. *Trans. Chin. Soc. Agric. Eng.* **2009**, *25*, 168–173.
40. Yanchuan, M.; Hao, L.; Zhifang, C.; Kai, Z.; Jinglei, W.; Jingsheng, S. Estimating Nitrogen Content in Cotton Canopy Using Hyperspectral Imaging. *J. Irrig. Drain.* **2020**, *39*, 35–41.
41. Xie, Y.; Feng, M.; Wang, C.; Yang, W.; Sun, H.; Yang, C.; Jing, B.; Qiao, X.; Saleem Kubar, M.; Song, J. Hyperspectral Monitor on Chlorophyll Density in Winter Wheat under Water Stress. *Agron. J.* **2020**, *112*, 3667–3676. [CrossRef]

42. Cai, Y.; Miao, Y.; Wu, H.; Wang, D. Hyperspectral Estimation Models of Winter Wheat Chlorophyll Content under Elevated CO_2. *Front. Plant Sci.* **2021**, *12*, 642917. [CrossRef] [PubMed]
43. Xu, H.; Luo, Y.; Zhang, T.; Shi, Y. Changes of Reflectance Spectra of Pine Needles in Different Stage after Being Infected by Pine Wood Nematode. *Spectrosc. Spectr. Anal.* **2011**, *31*, 1352–1356.
44. Jinbao, J.; Yunhao, C.; Wenjiang, H.; Jing, L. Hyperspectral Estimation Models for LTN Content of Winter Wheat Canopy under Stripe Rust Stress. *J. Agric. Eng. Res.* **2008**, *24*, 34–39.
45. Ming-lu, T.; Song-tao, B.; Qing-rui, C.; Zhuo-ran, Z.; Xu-Mei, W.; Qi, W. Quantified Estimation of Anthocyanin Content in Mosaic Virus Infected Apple Leaves Based on Hyperspectral Imaging. *Spectrosc. Spectr. Anal.* **2017**, *37*, 3187–3192.
46. Li, S.; Zhang, D. The Effects of Disease Stress on Spectra Reflectance and Chlorophyll Fluorescence Characteristics of Cotton Leaves. *Trans. Chin. Soc. Agric. Eng.* **2011**, *27*, 86–93.
47. Feng, W.; Wang, X.; Song, X.; He, L.; Wang, C.; Guo, T. Hyperspectral Estimation of Canopy Chlorophyll Density in Winter Wheat under Stress of Powdery Mildew. *Trans. Chin. Soc. Agric. Eng.* **2013**, *29*, 114–123.
48. Yali, G.; Zhenxi, W.; Ling, L.; Yuxia, S.; Yongqiang, Y. Hyperspectral Estimation Model of Jujube Leaves Chlorophyll Contents under Different Damages of Tetranychus Truncatus Ehara. *Acta Agric. Boreali-Occident. Sin.* **2020**, *30*, 613–621.
49. Li, Z.; Hong, T.; Ni, H.; Li, N.; Wang, J.; Zheng, J.; Lin, H. Pigment Content Measurement for Citrus Red Mite Infected Leaf Using Hyper-Spectral Imaging Technology. *Trans. Chin. Soc. Agric. Eng.* **2014**, *30*, 124–130.
50. He, R.; Li, H.; Qiao, X.; Jiang, J. Using Wavelet Analysis of Hyperspectral Remote-Sensing Data to Estimate Canopy Chlorophyll Content of Winter Wheat under Stripe Rust Stress. *Int. J. Remote Sens.* **2018**, *39*, 4059–4076. [CrossRef]
51. Kong, W.; Huang, W.; Ma, L.; Tang, L.; Li, C.; Bi, Y. *Detecting Leaf Phosphorus Content in Arbuscular Mycorrhizal Fungi-Inoculated Soybean Using Hyperspectral Remote Sensing Data*; SPIE: Bellingham, WA, USA, 2020; Volume 11528, pp. 139–146.
52. Cheng, Z.; Zhang, J.; Meng, P.; Li, Y.; Wang, H.; Li, C. Improvement of Algorithm Used for Extraction Hyperspectral Feature Bands of Vegetation. *Trans. Chin. Soc. Agric. Eng.* **2015**, *31*, 179–185.
53. Chen, X.; Dong, Z.; Liu, J.; Wang, H.; Zhang, Y.; Chen, T.; Du, Y.; Shao, L.; Xie, J. Hyperspectral Characteristics and Quantitative Analysis of Leaf Chlorophyll by Reflectance Spectroscopy Based on a Genetic Algorithm in Combination with Partial Least Squares Regression. *Spectrochim. Acta Part A Mol. Biomol. Spectrosc.* **2020**, *243*, 118786. [CrossRef] [PubMed]
54. Zhang, Y.; Zheng, L.; Li, M.; Deng, X. Predicting Apple Tree Leaf Nitrogen Content Based on Hyperspectral and Wavelet Packet Analysis. *Trans. Chin. Soc. Agric. Eng.* **2013**, *29*, 101–108.
55. Cheng, J.; Yang, G.; Xu, W.; Feng, H.; Han, S.; Liu, M.; Zhao, F.; Zhu, Y.; Zhao, Y.; Wu, B. Improving the Estimation of Apple Leaf Photosynthetic Pigment Content Using Fractional Derivatives and Machine Learning. *Agronomy* **2022**, *12*, 1497. [CrossRef]
56. Guo, F.; Feng, Q.; Yang, S.; Yang, W. Estimation of Potato Canopy Nitrogen Content Based on Hyperspectral Index Optimization. *Agronomy* **2023**, *13*, 1693. [CrossRef]
57. Liu, N.; Xing, Z.; Zhao, R.; Qiao, L.; Li, M.; Liu, G.; Sun, H. Analysis of Chlorophyll Concentration in Potato Crop by Coupling Continuous Wavelet Transform and Spectral Variable Optimization. *Remote Sens.* **2020**, *12*, 2826. [CrossRef]
58. Guo, J.; Zhang, J.; Xiong, S.; Zhang, Z.; Wei, Q.; Zhang, W.; Feng, W.; Ma, X. Hyperspectral Assessment of Leaf Nitrogen Accumulation for Winter Wheat Using Different Regression Modeling. *Precis. Agric.* **2021**, *22*, 1634–1658. [CrossRef]
59. Zhang, X.; Sun, H.; Qiao, X.; Yan, X.; Feng, M.; Xiao, L.; Song, X.; Zhang, M.; Shafiq, F.; Yang, W. Hyperspectral Estimation of Canopy Chlorophyll of Winter Wheat by Using the Optimized Vegetation Indices. *Comput. Electron. Agric.* **2022**, *193*, 106654. [CrossRef]
60. Chen, X.; Li, F.; Shi, B.; Fan, K.; Li, Z.; Chang, Q. Estimation of Winter Wheat Canopy Chlorophyll Content Based on Canopy Spectral Transformation and Machine Learning Method. *Agronomy* **2023**, *13*, 783. [CrossRef]
61. Wang, Z.; Chen, J.; Fan, Y.; Cheng, Y.; Wu, X.; Zhang, J.; Wang, B.; Wang, X.; Yong, T.; Liu, W. Evaluating Photosynthetic Pigment Contents of Maize Using UVE-PLS Based on Continuous Wavelet Transform. *Comput. Electron. Agric.* **2020**, *169*, 105160. [CrossRef]
62. Jiang, S.; Chang, Q.; Wang, X.; Zheng, Z.; Zhang, Y.; Wang, Q. Estimation of Anthocyanins in Whole-Fertility Maize Leaves Based on Ground-Based Hyperspectral Measurements. *Remote Sens.* **2023**, *15*, 2571. [CrossRef]
63. Abulaiti, Y.; Sawut, M.; Maimaitiaili, B.; Chunyue, M. A Possible Fractional Order Derivative and Optimized Spectral Indices for Assessing Total Nitrogen Content in Cotton. *Comput. Electron. Agric.* **2020**, *171*, 105275. [CrossRef]
64. Deng, X.; Li, M.; Zheng, L.; Zhang, Y.; Sun, H. Estimating Chlorophyll Content of Apple Leaves Based on Preprocessing of Reflectance Spectra. *Trans. Chin. Soc. Agric. Eng.* **2014**, *30*, 140–147.
65. Sonobe, R.; Yamashita, H.; Mihara, H.; Morita, A.; Ikka, T. Hyperspectral Reflectance Sensing for Quantifying Leaf Chlorophyll Content in Wasabi Leaves Using Spectral Pre-Processing Techniques and Machine Learning Algorithms. *Int. J. Remote Sens.* **2021**, *42*, 1311–1329. [CrossRef]
66. Li, L.; Wang, S.; Ren, T.; Ma, Y.; Wei, Q.; Gao, W.; Lu, J. Evaluating Models of Leaf Phosphorus Content of Winter Oilseed Rape Based on Hyperspectral Data. *Trans. Chin. Soc. Agric. Eng.* **2016**, *32*, 209–218.
67. Li, C.; Shi, J.; Ma, C.; Cui, Y.; Wang, Y.; Li, Y. Estimation of Chlorophyll Content in Winter Wheat Based on Wavelet Transform and Fractional Differential. *Trans. Chin. Soc. Agric. Mach* **2021**, *52*, 172–182.
68. Qing-liang, J.; Ming, L.; Kung, Y.; Zi-long, L.; Ling-qin, K.; Mei, H.; Li-quan, D.; Yue-jin, Z. Spectral Pre-Processing Based on Convolutional Neural Network. *Spectrosc. Spectr. Anal.* **2022**, *42*, 292–297.

69. Shuang, L.; Hai-ye, Y.; Zhao-jia, P.; Mei-chen, C.; Tong, Y.; Li-juan, K.; Lei, Z.; Jing-min, D.; Yuan-yuan, S. Study on Extracting Characteristic Wavelength of Soybean Physiological Information Based on Hyperspectral Technique. *Spectrosc. Spectr. Anal.* **2020**, *40*, 3542–3548.
70. Jiao-jiao, W.; Xiao-yu, S.; Xin, M.; Gui-jun, Y.; Zhen-hai, L.; He-li, L.; Yang, M. Sensitive Bands Selection and Nitrogen Content Monitoring of Rice Based on Gaussian Regression Analysis. *Spectrosc. Spectr. Anal.* **2021**, *41*, 1722–1729.
71. Yang, B.; Chen, J.; Chen, L.; Cao, W.; Yao, X.; Zhu, Y. Estimation Model of Wheat Canopy Nitrogen Content Based on Sensitive Bands. *Trans. Chin. Soc. Agric. Eng.* **2015**, *31*, 176–182.
72. Pengtao, G.; Yi, S.; Zhengzao, C. Prediction of Rubber Seedling Leaf Phosphorus Contents Based on Hyperspectral Technology and Random Forest Approach. *Chin. J. Trop. Agric.* **2015**, *35*, 56–62.
73. Cao, C.; Wang, T.; Gao, M.; Li, Y.; Li, D.; Zhang, H. Hyperspectral Inversion of Nitrogen Content in Maize Leaves Based on Different Dimensionality Reduction Algorithms. *Comput. Electron. Agric.* **2021**, *190*, 106461. [CrossRef]
74. Xiao-xiang, S.; Fang-dong, W.; Xiao-min, Z. The Estimation Models of Rice Leaf Nitrogen Concentration Based on Canopy Spectrum and BP Neural Network. *Chin. J. Agric. Resour. Reg. Plan.* **2019**, *40*, 35–44.
75. Chen, X.; Lv, X.; Ma, L.; Chen, A.; Zhang, Q.; Zhang, Z. Optimization and Validation of Hyperspectral Estimation Capability of Cotton Leaf Nitrogen Based on SPA and RF. *Remote Sens.* **2022**, *14*, 5201. [CrossRef]
76. Hongyan, G.; Hanping, M.; Xiaodong, Z. Quantitative Determination of Phosphorus in Lettuce Leaf Using Spectroscopy. *Trans. Chin. Soc. Agric. Mach.* **2014**, *45*, 276–280.
77. Li, F.; Wang, L.; Liu, J.; Wang, Y.; Chang, Q. Evaluation of Leaf N Concentration in Winter Wheat Based on Discrete Wavelet Transform Analysis. *Remote Sens.* **2019**, *11*, 1331. [CrossRef]
78. Sudu, B.; Rong, G.; Guga, S.; Li, K.; Zhi, F.; Guo, Y.; Zhang, J.; Bao, Y. Retrieving SPAD Values of Summer Maize Using UAV Hyperspectral Data Based on Multiple Machine Learning Algorithm. *Remote Sens.* **2022**, *14*, 5407. [CrossRef]
79. Sun, J.; Yang, J.; Shi, S.; Chen, B.; Du, L.; Gong, W.; Song, S. Estimating Rice Leaf Nitrogen Concentration: Influence of Regression Algorithms Based on Passive and Active Leaf Reflectance. *Remote Sens.* **2017**, *9*, 951. [CrossRef]
80. Zhang, Z.; Jiang, D.; Chang, Q.; Zheng, Z.; Fu, X.; Li, K.; Mo, H. Estimation of Anthocyanins in Leaves of Trees with Apple Mosaic Disease Based on Hyperspectral Data. *Remote Sens.* **2023**, *15*, 1732. [CrossRef]
81. Liu, H.; Li, M.; Zhang, J.; Sun, H.; Long, Y.; Wu, L.; Zhang, Q. PCA Based Model on Chlorophyll Content Diagnosis of Winter Wheat. *IFAC-Pap.* **2018**, *51*, 643–647. [CrossRef]
82. Jiang, H.; Yang, H.; Chen, X.; Wang, S.; Li, X.K.; Liu, K.; Cen, Y. Research on Accuracy and Stability of Inversing Vegetation Chlorophyll Content by Spectral Index Method. *Guang Pu Xue Yu Guang Pu Fen Xi Guang Pu* **2015**, *35*, 975–981. [PubMed]
83. Hasan, U.; Kasim, N.; Chen, C. Estimation of Winter Wheat LAI based on an Optimized Band Combination Vegetation Indices. *Trans. Chin. Soc. Agric. Mach.* **2022**, *50*, 207–218.
84. Prabhakar, M.; Prasad, Y.; Thirupathi, M.; Sreedevi, G.; Dharajothi, B.; Venkateswarlu, B. Use of Ground Based Hyperspectral Remote Sensing for Detection of Stress in Cotton Caused by Leafhopper (Hemiptera: Cicadellidae). *Comput. Electron. Agric.* **2011**, *79*, 189–198. [CrossRef]
85. Li, W.; Huang, W.; Dong, Y.; Chen, H.; Wang, J.; Shan, J. Estimation on Winter Wheat Scab Based on Combination of Temperature, Humidity and Remote Sensing Vegetation Index. *Trans. Chin. Soc. Agric. Eng.* **2017**, *33*, 203–210.
86. Yu, L.; Cai, H.; Yao, F.; Zheng, Z.; Wang, J.; Li, Z. Applicability of Vegetation Indices to Estimate Fractional Vegetation Coverage. *Trans. Chin. Soc. Agric. Mach* **2015**, *46*, 231–239.
87. Luo, D.; Chang, Q.; Qiy, B. Estimation Modelfor Chlorophyll Content in Winter Wheat Canopy Based on Spectral Indices. *J. Triticeae Crops* **2016**, *36*, 1225.
88. Pan, B.; Zhao, G.-X.; Zhu, X.-C.; Liu, H.-T.; Liang, S.; Tian, D.-D. Estimation of Chlorophyll Content in Apple Tree Canopy Based on Hyperspectral Parameters. *Spectrosc. Spectr. Anal.* **2013**, *33*, 2203–2206.
89. Xu, R.H.Y.Z.; Shen, M. Effects of Low Temperature Stress at Seedling Stage on Chlorophyll Content and Canopy Hyperspectral of "Hongyan" Strawberry. *Chin. J. Agrometeorol.* **2022**, *43*, 148–158.
90. Tongyu, X.; Simin, X.; Fenghua, Y.; Zhonghui, G.; Yadi, L. A BAS-ELM Inversion Method of Japonica Rice Canopy Nitrogen Content Based on A Combination of Multiple Vegetation Indices. *J. Shenyang Agric. Univ.* **2021**, *52*, 577–585.
91. Feng, S.; Xu, T.-Y.; Yu, F.-H.; Chen, C.-L.; Yang, X.; Wang, N.-Y. Research of Method for Inverting Nitrogen Content in Canopy Leaves of Japonica Rice in Northeastern China Based on Hyperspectral Remote Sensing of Unmanned Aerial Vehicle. *Spectrosc. Spectr. Anal.* **2019**, *39*, 3281–3287.
92. Tian, Y.-C.; Gu, K.-J.; Chu, X.; Yao, X.; Cao, W.-X.; Zhu, Y. Comparison of Different Hyperspectral Vegetation Indices for Canopy Leaf Nitrogen Concentration Estimation in Rice. *Plant Soil* **2014**, *376*, 193–209. [CrossRef]
93. Song, X.; Xu, D.-Y.; Huang, S.-M.; Huang, C.-C.; Zhang, S.-Q.; Guo, D.-D.; Zhang, K.-K.; Yue, K. Nitrogen Content Inversion of Wheat Canopy Leaf Based on Ground Spectral Reflectance Data. *Ying Yong Sheng Tai Xue Bao J. Appl. Ecol.* **2020**, *31*, 1636–1644.
94. Weiyi, L.; Mingxin, S.; Fengling, Z.; Fengwen, W. Hyperspectral Estimation of Chlorophyll Content in Winter Wheat Leaves under Low Temperature Stress. *Chin. J. Agrometeorol.* **2022**, *43*, 137–147.
95. Shengbo, C.; Yanbing, C.; Fengdi, R.; Yu, Z. Estimation of Maize Chlorophyll Content Based on Spectral Index. *J. Xinyang Norm. Univ. (Nat. Sci. Ed.)* **2021**, *34*, 225–229.
96. Hunt, E.R., Jr.; Doraiswamy, P.C.; McMurtrey, J.E.; Daughtry, C.S.; Perry, E.M.; Akhmedov, B. A Visible Band Index for Remote Sensing Leaf Chlorophyll Content at the Canopy Scale. *Int. J. Appl. Earth Obs. Geoinf.* **2013**, *21*, 103–112. [CrossRef]

97. Zhang, Y.-J.; Wang, L.; Bai, Y.-L.; Yang, L.-P.; Lu, Y.-L.; Zhang, J.-J.; Li, G. Nitrogen Nutrition Diagnostic Based on Hyperspectral Analysis about Different Layers Leaves in Maize. *Spectrosc. Spectr. Anal.* **2019**, *39*, 2829–2835.
98. Shi, H.; Guo, J.; An, J.; Tang, Z.; Wang, X.; Li, W.; Zhao, X.; Jin, L.; Xiang, Y.; Li, Z. Estimation of Chlorophyll Content in Soybean Crop at Different Growth Stages Based on Optimal Spectral Index. *Agronomy* **2023**, *13*, 663. [CrossRef]
99. Ansardin, A.; Mamat, S.; Jinzhao, L. Estimation of Chlorophyll Content of Long-Staple Cotton Based on Canopy Spectrum Characteristics. *Laser Optoelectron. Prog.* **2022**, *59*, 1–11. [CrossRef]
100. Xin-Jie, H.; Gui-Ying, J.; Li, B.; Shu-Juan, L.; Feng, L. Relationships between Leaf Nitrogen Content and Canopy Reflected Spectral in Cotton. *Xinjiang Agric. Sci.* **2008**, *45*, 776.
101. Wang, Q.; Yi, Q.-X.; Bao, A.-M.; Zhao, J. Discussion on Hyperspectral Index for the Estimation of Cotton Canopy Water Content. *Spectrosc. Spectr. Anal.* **2013**, *33*, 507–512.
102. Diao, W.; Li, S.; Wang, K.; Jin, X.; Wang, F.; Chen, B.; Wang, Q.; Wang, K.; Xiao, C. Estimated Nitrogen Nutrition Index Based on the Hyperspectral for Wheat of Drip Irrigation under Mulch. *Spectrosc. Spectr. Anal.* **2012**, *32*, 1362–1366.
103. Lu, J.; Yang, T.; Su, X.; Qi, H.; Yao, X.; Cheng, T.; Zhu, Y.; Cao, W.; Tian, Y. Monitoring Leaf Potassium Content Using Hyperspectral Vegetation Indices in Rice Leaves. *Precis. Agric.* **2020**, *21*, 324–348. [CrossRef]
104. Songtao, B.; Minglu, T.; Ruiqing, C. Estimation of Rice Leaf Phosphorus Content Using UAV-Based Hyperspectral Images. *Trans. Chin. Soc. Agric. Mach.* **2021**, *52*, 163–171.
105. Inoue, Y.; Sakaiya, E.; Zhu, Y.; Takahashi, W. Diagnostic Mapping of Canopy Nitrogen Content in Rice Based on Hyperspectral Measurements. *Remote Sens. Environ.* **2012**, *126*, 210–221. [CrossRef]
106. Sun, H.; Feng, M.; Yang, W.; Bi, R.; Sun, J.; Zhao, C.; Xiao, L.; Wang, C.; Kubar, M.S. Monitoring Leaf Nitrogen Accumulation with Optimized Spectral Index in Winter Wheat Under Different Irrigation Regimes. *Front. Plant Sci.* **2022**, *13*, 913240. [CrossRef] [PubMed]
107. Liang, L.; Di, L.; Huang, T.; Wang, J.; Lin, L.; Wang, L.; Yang, M. Estimation of Leaf Nitrogen Content in Wheat Using New Hyperspectral Indices and a Random Forest Regression Algorithm. *Remote Sens.* **2018**, *10*, 1940. [CrossRef]
108. Yu, Y.; Yu, H.-Y.; Li, X.-K.; Wang, H.-J.; Liu, S.; Zhang, L.; Sui, Y.-Y. Hyperspectral Inversion Model for SPAD of Rice Leaves Based on Optimized Spectral Index. *Spectrosc. Spectr. Anal.* **2022**, *42*, 1092–1097.
109. Feng, L.; Victor, A.; Hong, Z. PLSR Based Airborne Hyperspectral Remote Sensing Retrieval of Leaf Nitrogen Content in Potato Fields. *Chin. J. Agrometeorol.* **2014**, *35*, 338.
110. Ye, X.; Abe, S.; Zhang, S. Estimation and Mapping of Nitrogen Content in Apple Trees at Leaf and Canopy Levels Using Hyperspectral Imaging. *Precis. Agric.* **2020**, *21*, 198–225. [CrossRef]
111. Li, K.; Chen, Y.-Z.; Xu, Z.-H.; Huang, X.-Y.; Hu, X.-Y.; Wang, X.-Q. Hyperspectral Estimation Method of Chlorophyll Content in Moso Bamboo under Pests Stress. *Spectrosc. Spectr. Anal.* **2020**, *40*, 2578.
112. Sun, H.; Zheng, T.; Liu, N.; Cheng, M.; Li, M.; Zhang, Q. Vertical Distribution of Chlorophyll in Potato Plants Based on Hyperspectral Imaging. *Trans. Chin. Soc. Agric. Eng.* **2018**, *34*, 149–156.
113. Jing, L.; Qingrui, C.; Miao, L. Chlorophyll Content Inversion with Hyperspectral Technology for Apple Leaves Based on Support Vector Regression Algorithm. *Trans. Chin. Soc. Agric. Mach.* **2016**, *47*, 260–265.
114. Wang, T.; Gao, M.; Cao, C.; You, J.; Zhang, X.; Shen, L. Winter Wheat Chlorophyll Content Retrieval Based on Machine Learning Using in Situ Hyperspectral Data. *Comput. Electron. Agric.* **2022**, *193*, 106728. [CrossRef]
115. Guo, P.; Su, Y.; Cha, Z.; Lin, Q.; Luo, W.; Lin, Z. Prediction of Leaf Phosphorus Contents for Rubber Seedlings Based on Hyperspectral Sensitive Bands and Back Propagation Artificial Neural Network. *Trans. Chin. Soc. Agric. Eng.* **2016**, *32*, 177–183.
116. An, G.; Xing, M.; He, B.; Liao, C.; Huang, X.; Shang, J.; Kang, H. Using Machine Learning for Estimating Rice Chlorophyll Content from in Situ Hyperspectral Data. *Remote Sens.* **2020**, *12*, 3104. [CrossRef]
117. Singh, H.; Roy, A.; Setia, R.; Pateriya, B. Estimation of Nitrogen Content in Wheat from Proximal Hyperspectral Data Using Machine Learning and Explainable Artificial Intelligence (XAI) Approach. *Model. Earth Syst. Environ.* **2022**, *8*, 2505–2511. [CrossRef]
118. Liu, W.; Chang, Q.-R.; Guo, M.; Xing, D.-X.; Yuan, Y.-S. Diagnosis of Phosphorus Nutrition in Winter Wheat Based on First Derivative Spectra and Radial Basis Function Neural Network. *Spectrosc. Spectr. Anal.* **2011**, *31*, 1092–1096.
119. Liu, T.; Xu, T.-Y.; Yu, F.-H.; Yuan, Q.-Y.; Guo, Z.-H.; Xu, B. Chlorophyll Content Estimation of Northeast Japonica Rice Based on Improved Feature Band Selection and Hybrid Integrated Modeling. *Spectrosc. Spectr. Anal.* **2021**, *41*, 2556–2564.

Disclaimer/Publisher's Note: The statements, opinions and data contained in all publications are solely those of the individual author(s) and contributor(s) and not of MDPI and/or the editor(s). MDPI and/or the editor(s) disclaim responsibility for any injury to people or property resulting from any ideas, methods, instructions or products referred to in the content.

agronomy

MDPI

Article

Detection of Power Poles in Orchards Based on Improved Yolov5s Model

Yali Zhang [1,2], Xiaoyang Lu [1,2], Wanjian Li [1,2], Kangting Yan [2,3], Zhenjie Mo [1,2], Yubin Lan [2,3] and Linlin Wang [4,*]

[1] College of Engineering, South China Agricultural University, Guangzhou 510642, China; ylzhang@scau.edu.cn (Y.Z.); luxiaoyang@stu.scau.edu.cn (X.L.); 19981002@stu.scau.edu.cn (W.L.); mitor@stu.scau.edu.cn (Z.M.)
[2] National Center for International Collaboration Research on Precision Agricultural Aviation Pesticides Spraying Technology, Guangzhou 510642, China; ktyan@stu.scau.edu.cn (K.Y.); ylan@scau.edu.cn (Y.L.)
[3] College of Electronic Engineering, South China Agricultural University, Guangzhou 510642, China
[4] School of Artificial Intelligence, Shenzhen Polytechnic University, Shenzhen 518055, China
* Correspondence: wanglinlin@szpt.edu.cn

Abstract: During the operation of agricultural unmanned aerial vehicles (UAVs) in orchards, the presence of power poles and wires pose a serious threat to flight safety, and can even lead to crashes. Due to the difficulty of directly detecting wires, this research aimed to quickly and accurately detect wire poles, and proposed an improved Yolov5s deep learning object detection algorithm named Yolov5s-Pole. The algorithm enhances the model's generalization ability and robustness by applying Mixup data augmentation technique, replaces the C3 module with the GhostBottleneck module to reduce the model's parameters and computational complexity, and incorporates the Shuffle Attention (SA) module to improve its focus on small targets. The results show that when the improved Yolov5s-Pole model was used for detecting poles in orchards, its accuracy, recall, and mAP@50 were 0.803, 0.831, and 0.838 respectively, which increased by 0.5%, 10%, and 9.2% compared to the original Yolov5s model. Additionally, the weights, parameters, and GFLOPs of the Yolov5s-Pole model were 7.86 MB, 3,974,310, and 9, respectively. Compared to the original Yolov5s model, these represent compression rates of 42.2%, 43.4%, and 43.3%, respectively. The detection time for a single image using this model was 4.2 ms, and good robustness under different lighting conditions (dark, normal, and bright) was demonstrated. The model is suitable for deployment on agricultural UAVs' onboard equipment, and is of great practical significance for ensuring the efficiency and flight safety of agricultural UAVs.

Keywords: deep learning; power pole; Yolov5; object detection

check for updates

Citation: Zhang, Y.; Lu, X.; Li, W.; Yan, K.; Mo, Z.; Lan, Y.; Wang, L. Detection of Power Poles in Orchards Based on Improved Yolov5s Model. *Agronomy* **2023**, *13*, 1705. https://doi.org/10.3390/agronomy13071705

Academic Editor: José Casanova Gascón

Received: 25 May 2023
Revised: 21 June 2023
Accepted: 24 June 2023
Published: 26 June 2023

Copyright: © 2023 by the authors. Licensee MDPI, Basel, Switzerland. This article is an open access article distributed under the terms and conditions of the Creative Commons Attribution (CC BY) license (https://creativecommons.org/licenses/by/4.0/).

1. Introduction

The planting of fruit trees is an important part of China's agricultural production structure, and the application of agricultural UAVs in orchards has been effective [1–3]. However, the operating environment of orchards is complex, and collisions with power lines are the main cause of agricultural UAV crashes [4,5]. Due to the complexity and variability of the orchard environment and the limitations of different sensor applicability ranges, there is a problem that obstacle avoidance sensors cannot effectively detect power line obstacles directly [6]. For only detecting the power lines themselves, the technical difficulty is high, and it is difficult to achieve maturity in the short term. Therefore, we consider an indirect recognition method, which recognizes substitutes for power lines such as the power pole or tower [7], and establish a feature database of relevant obstacle substitutes to propose a detection model that can be lightweight and deployed on agricultural UAVs. It can not only effectively improve the detection success rate of power line obstacles, but also improves the safety and efficiency of agricultural UAV orchard operations [8,9], promoting the mechanization process of orchards, and providing support for orchard plant

protection [10,11], fruit tree pollination [12,13], information collection [14,15], monitoring and warning [16,17], which have practical production significance.

According to the research trends of industry, academia, and research institutions in recent years, it can be found that the current mainstream trend of obstacle avoidance research uses multi-sensor fusion of vision and non-vision [18–20] to identify field obstacles and improve plant protection operations. Qiu et al. [21] installed a machine vision system consisting of an RGB camera and a desktop computer on a paddy transplanter using an improved Yolov3 and deep SORT combined method to detect and track typical moving obstacles in the paddy field, such as people and water buffalo, and calculated the center point position of them. The results showed that the improved Yolov3 model had a processing speed that was 27.3% faster than the original Yolov3 module. In actual rice field tests, the average processing speed was 5–7 FPS, but this processing speed is difficult to meet the needs of detecting and tracking targets in actual UAV operations; furthermore, this machine vision system is too heavy to mount. Chen et al. [22] proposed an improved Yolov3-tiny target detection model, which uses a panoramic camera mounted on the top of the agricultural machinery to obtain 360° image information, and quickly detects field pedestrians and other agricultural machinery. The average accuracy and recall rates were 95.5% and 93.7%, respectively, which were 5.6% and 5.2% higher than the original network model, respectively. The average time for detecting a single panoramic image was 6.3 ms, and the average frame rate for video stream detection was 84.2 FPS. However, the model's memory requirement of 64 MB renders it unsuitable for embedded devices and deployment. Chen et al. [23] proposed an innovative solution based on Yolov3 for the detection and pole counting of UAV patrol video distribution poles. The detection accuracy of this method was higher than 0.9. However, the high shooting angle of this method is not applicable to the working height of agricultural UAVs, and the effect of lighting on identification was not mentioned in the study.

Due to the limited arithmetic power of the embedded devices carried by agricultural UAVs [24,25], lightweight models are commonly selected for target recognition. Liu et al. [26] proposed an improved SSD (Single Shot MultiBox Detector) insulator and spacer detection algorithm that uses a lightweight network, MnasNet, as a feature extraction network to generate feature maps. Then, two multi-scale feature fusion methods were used to fuse multiple feature maps. The detection accuracy was up to 93.8%. The detection time for a single image on NVIDIA Jetson TX2 was 154 ms, and the capture rate on TX2 was 8.27 fps. Yu et al. [27] proposed a new lightweight neural network called TasselLFANet, which was specifically designed for the accurate and efficient detection and computation of maize male ears in high spatio-temporal image sequences. The method enhances the feature learning capability of TasselLFANet by employing a cross-stage fusion strategy that balances the variability of different layers. In addition, TasselLFANet utilizes multiple receptive fields to capture different feature representations, and incorporates an innovative visual channel attention module that allows for more flexible and accurate feature detection and capture. The network achieves impressive evaluation metrics, with F1 and mAP@50 scores of 94.4% and 96.8%, respectively, while only consisting of 6.0 M parameters.

Therefore, this study optimizes the Yolov5s model with the Shuffle Attention module to focus on important feature learning and reduce the interference of non-critical information. At the same time, to meet the real-time detection needs of embedded modules in agricultural UAVs, the model is made lightweight by replacing the C3 module with the GhostBottleneck module. To solve the problem of a small number of datasets, the Mixup data augmentation technique is used to propose a lightweight detection model Yolov5s-Pole based on Yolov5s, which is specifically used to detect orchard power poles, in order to improve the operation safety of agricultural UAVs and promote the mechanization process of orchards.

2. Materials and Methods

2.1. Power Pole Data Collection

There is no publicly available dataset that contains exactly the same content. Therefore, it was necessary to establish a relevant dataset applicable to this study. The dataset we used was collected from the Cuitian Orange Orchard in Sihui City, Guangdong Province. The planting area of Shatang oranges in the orchard in 2021 exceeded 1000 mu, and various common power poles and other pole-shaped obstacles were distributed throughout the orchard. The data were collected twice, from the end of July to early August 2021, by the DJI aerial survey UAV Phantom 4 RTK. In order to obtain more power pole data in a variety of scenes, the flight speed was set to 2 m/s, and the flight altitude was set to 1–5 m above the citrus canopy, with an absolute altitude of 3–8 m.

Due to the possibility of motion blur caused by UAV steering, the lack of specific operational obstacles, or a high similarity between adjacent frames in the exported images, it was necessary to manually filter the image set to form a preliminary dataset. After screening, the self-built dataset had a total of 305 images as original images, and the training set, validation set, and test set were divided into a ratio of 8:1:1. The power poles in the original images were manually labeled with LabelImg annotation tool, and the label for power poles was set as pole. The operating interface is shown in Figure 1, and the computer configuration used is shown in Table 1.

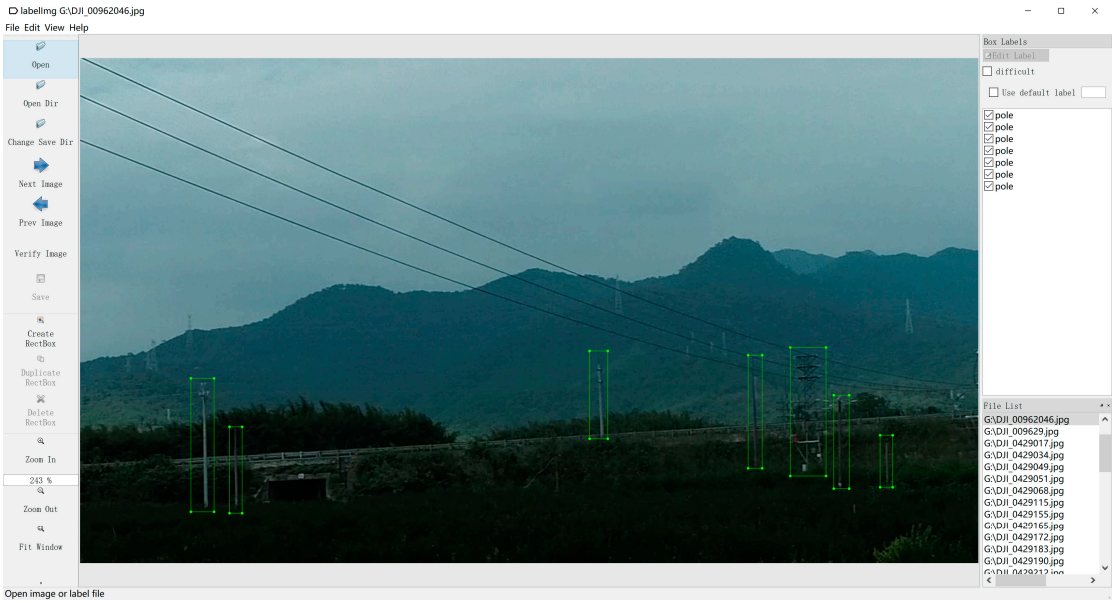

Figure 1. Image annotation of self-built datasets.

Table 1. Server configuration for training the deep learning model.

Components	Parameters
CPU	AMD Ryzen 7 5800X 8-Core Processor (3801 MHz)
Motherboard	MAG B550M MORTAR WIFI (MS-7C94)
Memory	16.00 GB (2133 MHz)
Main Hard Drive	1000 GB (KIOXIA-EXCERIA SSD)
Video Cards	NVIDIA GeForce RTX 3060 (12,288 MB)
Monitors	Redmi Monitor\u0001j 32-bit true color 60 Hz

2.2. Introduction of Yolov5s Model

Yolov5 is an object detection model, and implemented in PyTorch. The model uses a new network structure called CSP (Cross-Stage Partial Network), which effectively reduces computation while retaining the original network characteristics. It also has innovative

features such as adaptive anchor box calculation and adaptive image scaling. Yolov5 has multiple versions, including Yolov5s, Yolov5m, Yolov5l, and Yolov5x. This study used the Yolov5s model, including the input, backbone, neck, and prediction parts. The Yolov5s model uses rich data augmentation techniques during training, such as random size, proportional image clipping, random flip, random rotation, and random adjustments to brightness, contrast, and color balance. The improved Yolov5s-Pole model structure is shown in Figure 2.

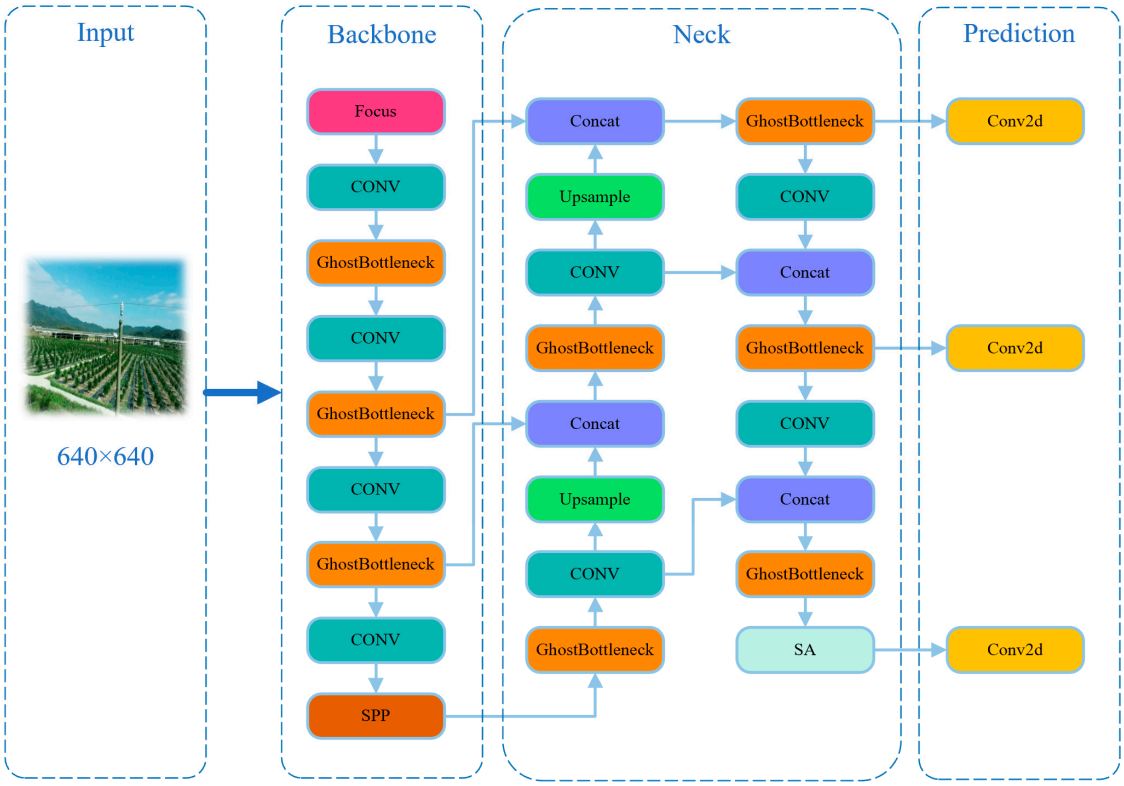

Figure 2. Yolov5s-Pole structure.

2.3. Model Improvement

2.3.1. Mixup Data Enhancement

Mixup is a data augmentation technique that is based on sample interpolation [28]. It is used to increase the diversity of neural network training data, thereby improving the model's generalization ability and robustness. Mixup combines two samples and their label data in proportion to create new sample and label data.

$$\widetilde{x} = \lambda x_i + (1 - \lambda) x_j \quad (1)$$

$$\widetilde{y} = \lambda y_i + (1 - \lambda) y_j \quad (2)$$

In Equations (1) and (2), x_i and x_j are the samples of the two inputs; y_i with y_j are the labels of the two inputs; and $\widetilde{x}$ and $\widetilde{y}$ are the new samples and the new labels of the output, respectively. $\lambda \in [0, 1]$, $\lambda \sim B(\alpha, \beta)$.

It can be seen from Figure 3 that when $\alpha = \beta = 1$, the Beta distribution is equivalent to a uniform distribution with y = 1; when $\alpha = \beta < 1$, the probabilities at both ends of the Beta distribution are higher than those in the middle; when $\alpha = \beta \to 0$, the Beta distribution is equivalent to a binomial distribution with x = 0, 1, indicating no data enhancement; when $\alpha = \beta > 1$, the probabilities at both ends of the Beta distribution are lower than those in the middle, similar to a normal distribution; when $\alpha = \beta \to \infty$, the probabilities of the Beta distribution are always 0.5, equivalent to taking half of each of two samples. Therefore,

using the Beta distribution for data augmentation is very flexible, and various probability distributions within the [0, 1] range can be obtained by adjusting the values of α and β, making it very convenient to use.

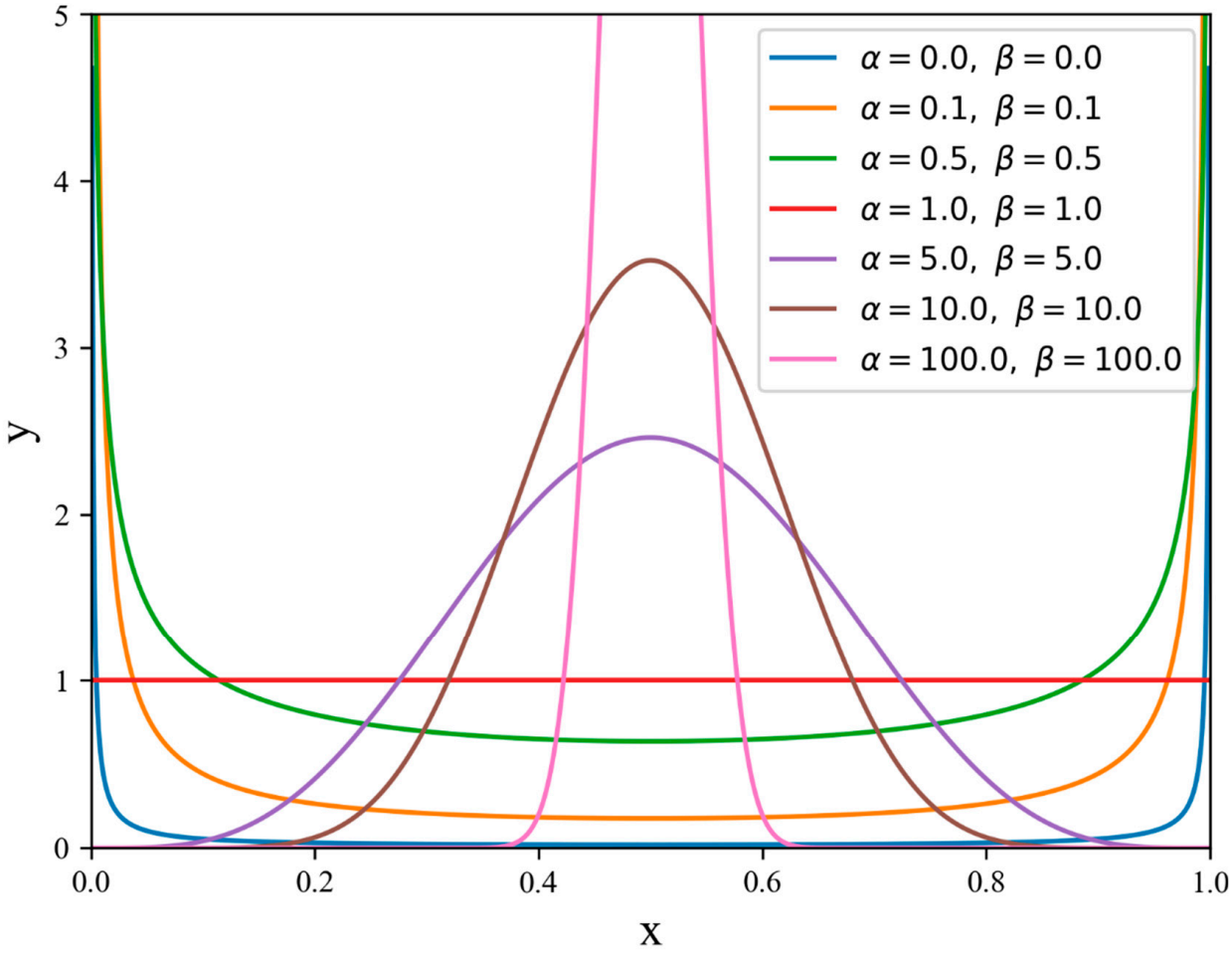

Figure 3. Beta distribution.

2.3.2. Replace the GhostBottleneck Module

GhostBottleneck is a network structure design method for deep neural networks that is aimed at reducing the number of model parameters and computational complexity while improving model performance [29]. The Ghost module divides the original convolution operation into two stages. In the first stage, half of the original convolution is used to generate a small number of feature maps. In the second stage, a 3 × 3 small convolution is used to convolve the feature maps obtained in the first stage, layer by layer, to obtain more feature maps. Finally, these feature maps are combined together. The number of feature maps obtained after the two-stage calculation in the Ghost module is consistent with the number of feature maps obtained by normal convolution operation.

As shown in Figure 4, GhostBottleneck consists of two Ghost modules. The first Ghost module increases the input feature map channel number, and the second Ghost module reduces the output feature map channel number. The two Ghost modules are connected by a diameter structure, and the first Ghost module uses the ReLU activation function, while the subsequent layers use batch normalization. In this way, GhostBottleneck can reduce model parameters and computational complexity while optimizing feature maps and improving model detection efficiency.

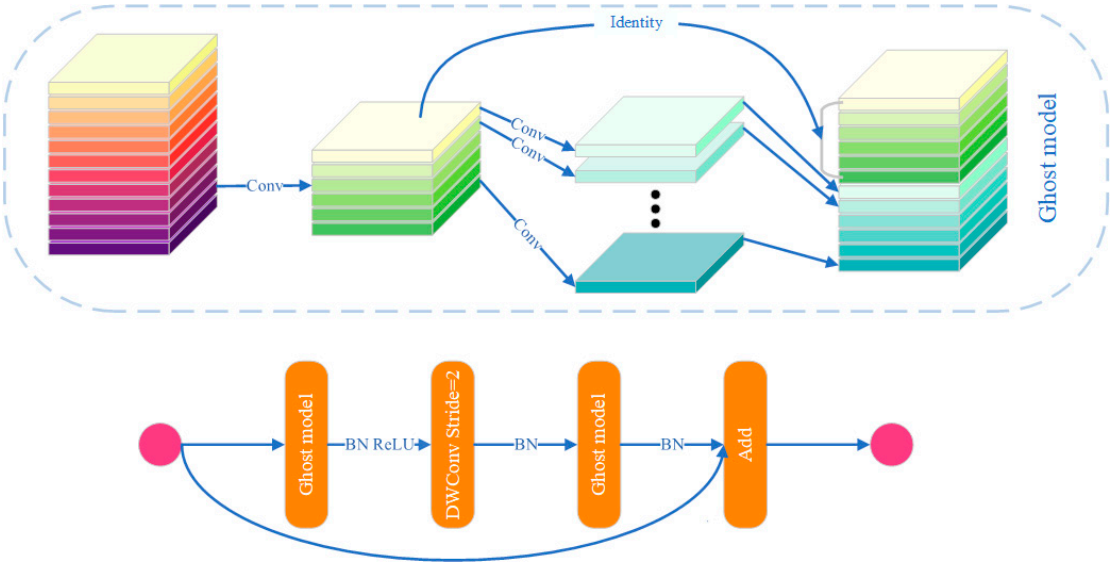

Figure 4. GhostBottleneck structure diagram.

2.3.3. Adding SA Module

The attention mechanism is an important component of deep neural networks; it can accurately focus on input-related information to improve network performance. There are mainly two types of attention mechanisms in the computer vision field, the spatial attention mechanism and the channel attention mechanism, which capture the relationships between pixels and channel dependencies, respectively. Combining these two attention mechanisms may achieve better performance, but this increases computational costs. The SA module can efficiently combine these two attention mechanisms [30].

As shown in Figure 5, the input feature map is grouped and used as an SA unit. Each SA unit is divided into two parts, with one part using channel attention, as shown in the red part of the figure; the specific implementation is similar to the SE attention mechanism, and the other part uses spatial attention, as shown in the green part of the figure; GN means group normalization. The two internal parts of the SA unit are stacked by the channel number to achieve information fusion. Finally, a random mixing operation is performed on all SA units to obtain the final output feature map.

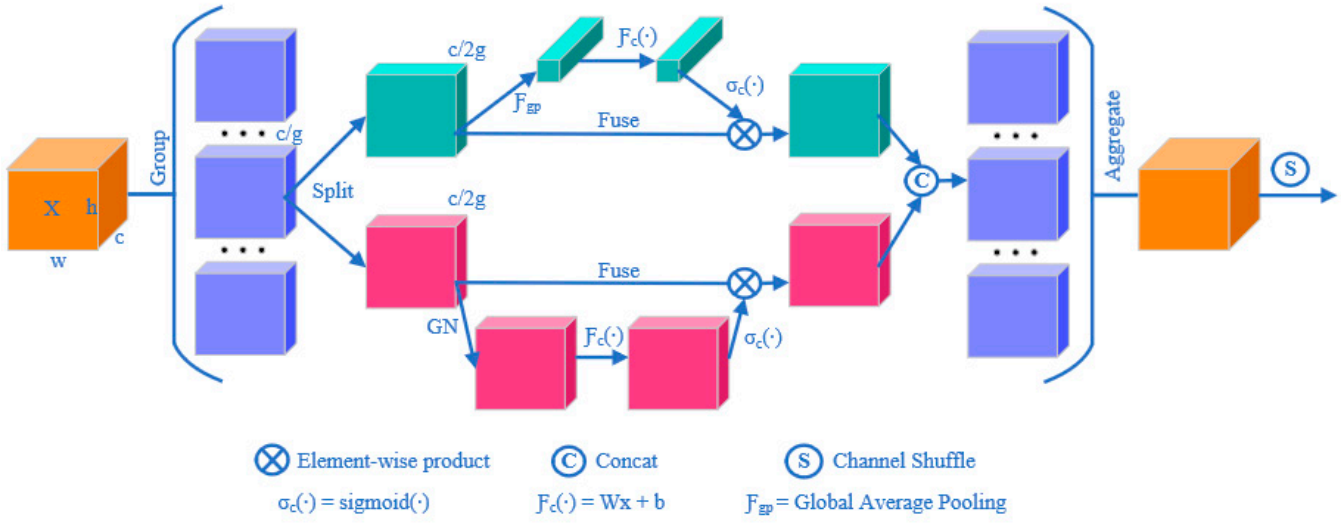

Figure 5. SA module structure.

2.4. Model Evaluation Indicators

Commonly used in target recognition tasks, the evaluation indicators precision, recall, and mAP@50 are derived based on comparisons between the model prediction results and true labels.

1. Precision refers to the proportion of predicted power poles that are truly power poles. For the proportion of correctly predicted samples to the number of samples predicted as power poles, the calculation formula is as follows:

$$\text{Precision} = \frac{\text{TP}}{\text{TP} + \text{FP}}, \tag{3}$$

In Equation (3), TP represents the number of samples that are truly power poles, and FP represents the number of samples that are incorrectly predicted as power poles.

2. Recall refers to the proportion of truly power pole samples that are correctly predicted to be power poles. The calculation formula is as follows:

$$\text{Recall} = \frac{\text{TP}}{\text{TP} + \text{FN}}, \tag{4}$$

In Equation (4), TP represents the number of truly power pole samples, and FN represents the number of samples predicted as background, but are actually power poles.

3. mAP@50 is a composite indicator. mAP@50 is obtained by calculating the area under the precision and recall curves with the following formula. Specifically, mAP@50 is the average value of AP that calculated for all categories when the IoU threshold is 0.5.

$$\text{AP} = \int_0^1 \text{P(R)dR}. \tag{5}$$

In the target recognition task, precision and recall are two important evaluation indicators that can be used to measure the performance of the model in terms of prediction accuracy and coverage. The mAP@50 is a comprehensive evaluation of precision and recall, which can evaluate the performance of the model more comprehensively.

3. Results

The following model training hyperparameters are uniformly used in the following experiments, as shown in Table 2.

Table 2. Experimental hyperparameters.

Hyperparameters	Value
Batch_size	16
Steps	300
Lr0	0.01
Lrf	0.01
Momentum	0.937
Weight_decay	0.0005

3.1. Yolov5s Experiment

In the initial experiments, different input image sizes were chosen for training, 416 × 416, 512 × 512, and 640 × 640, and their effects on the experimental results were compared. The results are shown in Table 3, and it can be seen from the data that the evaluation metrics of the model all improve as the image size increases. Particularly, the best results were achieved with an image size of 640 × 640, although this also resulted in increased recall and inference time. This can be attributed to the fact that a larger image size provides more information, making the model easier to find the target object. Both precision and mAP@50 showed a small improvement when the size was increased from 416 to 512, but

the recall remained the same. This can be explained by the higher resolution offering more information, thereby aiding the model in accurately locating the target object. However, when the size was further increased to 640, the model's recall and mAP@50 also improved, but its precision slightly decreased. This could be due to the fact that the larger image size increases the computational and time costs, making the model less efficient in processing large-size images.

Table 3. Training results at different resolutions.

Image Size	Precision	Recall	mAP@50	Inference Time (ms)
416	0.803	0.7	0.719	2.8
512	0.804	0.7	0.722	4.7
640	0.798	0.731	0.746	6.5

Brightness is one of the important factors affecting image recognition [31], because changes in brightness affect the contrast and color distribution of the image, which affects the recognition ability of the model. To better understand the effect of brightness on image recognition, the OpenCV library was used to convert images to grayscale images and calculate the average brightness value of grayscale images. For the average brightness value, the range of the dataset was 52–198, according to the size of the average brightness value of the image and considering the distribution of the number of datasets after classification. It was divided into three parts, which are dark (52–98), medium (98–112), and bright (112–198). The light in the dark dataset was weak, and the color of the power poles in the image was more similar to the background, which made recognition difficult, and the power poles in individual images needed to be seen by magnifying the image. In the medium dataset, the light was normal, and the poles were better distinguished from the background, which was easier to recognize. For the bright dataset with sufficient light, power poles could be unclear in the sky background, which may lead to incomplete recognition, as shown in Figure 6. Experiments were conducted on the poles under different luminance conditions, and the results are shown in Table 4. It can be seen that the recognition accuracy and the average accuracy of the model improved with an increase in the brightness, and the inference time also increased. In particular, the model had the best recognition effect under bright light conditions, while recall and precision also improved. This may be due to the fact that the contrast and color distribution of the image were more obvious under bright light conditions, helping the model to more easily and accurately recognize objects in the image. On the contrary, in the dark light condition, the model had the worst recognition effect, with low recall and precision. In such conditions, the blurred contrast and color distribution made it challenging for the model to accurately detect objects.



Figure 6. Brightness classification.

Table 4. Test results of different brightnesses.

Brightness Classification	Precision	Recall	mAP@50	Inference Time (ms)
Dark	0.758	0.683	0.696	4.8
Medium	0.797	0.756	0.74	6.7
Bright	0.838	0.88	0.865	6.7

There were some problems in the recognition of power poles using the Yolov5s model, such as false recognition, an inability to recognize occlusion, inaccurate recognition of multiple targets, and incomplete recognition, as shown in Figure 7. All of these problems affected the recognition accuracy and robustness of the model, and subsequent improvement experiments will address and optimize these existing problems.

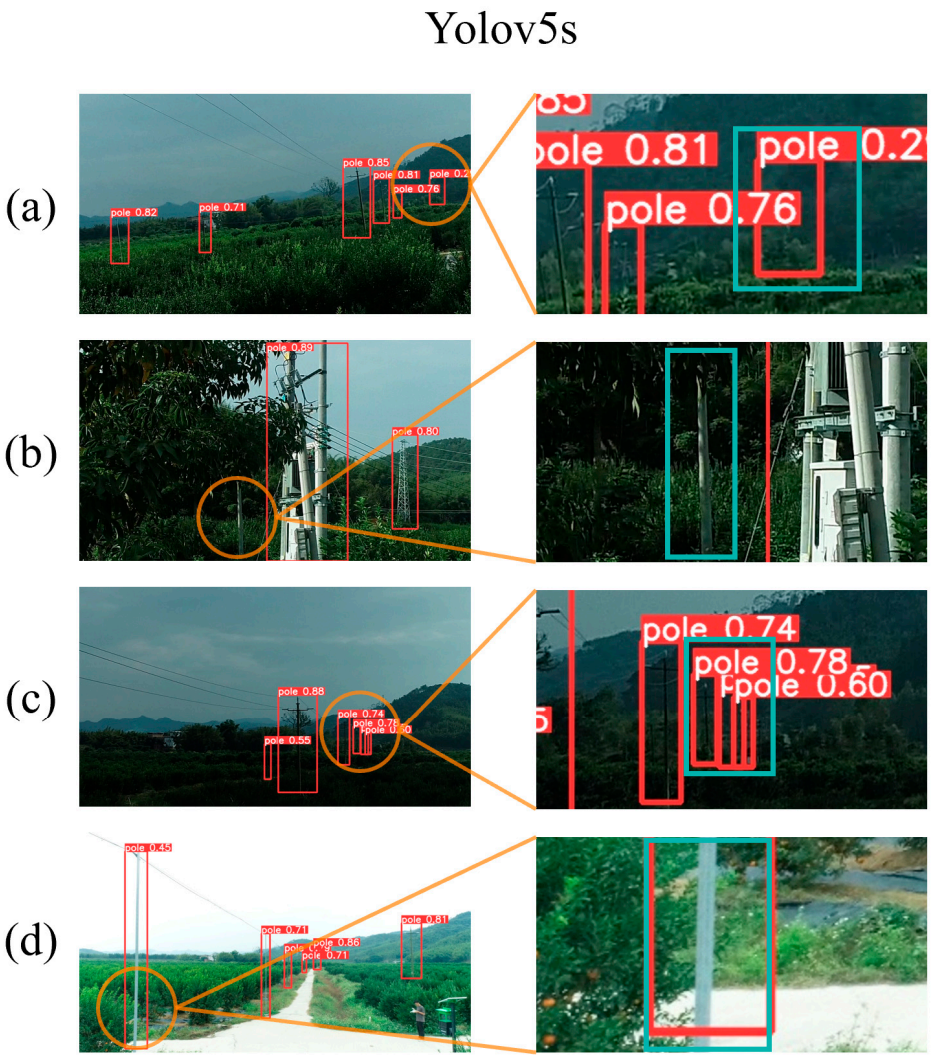

Figure 7. Yolov5s recognition effect. The red box is the recognition result of the Yolov5s model; (**a**) the blue box part is wrong recognition, there is no power pole in this area; (**b**) the blue box area has a power pole that is obscured but not recognized; (**c**) the blue box area has two power poles, but three recognition boxes appear; (**d**) the blue area is the complete area of power poles, and the recognition of power poles is incomplete.

3.2. Experiment with the Improved Yolov5s

3.2.1. Ablation Experiments

In order to verify the optimization effect of each improved module on the Yolov5s model, ablation experiments were conducted on the modules, as shown in Table 5. The constructed pole datasets were trained and tested separately, and the experimental results are shown in Table 6.

After a comparative analysis, it was found that the group with the lowest precision score was group A (0.798), and the highest was group C (0.864). Except for group A, the precision scores of the other groups were all above 0.8. The group with the lowest recall score was group A (0.731), and the highest was group F (0.831). Except for groups E and F, the recall scores of the other groups were below 0.8. The group with the lowest mAP@50

score was group A (0.746) and the highest was group F (0.838), while groups B and E also performed well. Overall, all three evaluation metrics for Group A were below 0.8, which also were the lowest. The best results were found in group F, where all three evaluation metrics were above 0.8, with recall and mAP@50 being the highest values.

Table 5. Ablation experiment setup.

Group	Mixup	GhostBottleneck	SA
A			
B	√		
C		√	
D			√
E	√	√	
F	√	√	√

Table 6. Results of ablation experiments.

Group	Precision	Recall	mAP@50	Weights (MB)	Layers	Parameters (Pieces)	GFLOPs	Inference Time (ms)
A	0.798	0.731	0.746	13.6	214	7,022,326	15.9	6.5
B	0.825	0.796	0.836	13.6	214	7,022,326	15.9	6.4
C	0.864	0.732	0.783	7.86	271	3,974,118	9	4.2
D	0.812	0.785	0.79	13.6	218	7,022,518	15.9	6.6
E	0.823	0.8	0.812	7.86	271	3,974,118	9	4.1
F	0.803	0.831	0.838	7.86	275	3,974,310	9	4.2

All three improved modules improved the evaluation metrics for the model. Mixup increased the recall and mAP@50 metrics by 0.027 and 0.09, respectively, while reducing the inference time by 0.1 ms. GhostBottleneck improved the precision metric of the model by 0.066, increased the number of layers by 57, but reduced the weight by 5.74 MB, and decreased the number of parameters by 3,048,208, reduced GFLOPs by 6.9, and also reduced the inference time by 2.3 ms. SA has improved the recall and mAP@50 metrics of the model combined with Mixup and GhostBottleneck by 0.031 and 0.026, respectively, but increased the inference time by 0.1 ms. Compared to the Yolov5s model, the improved Yolov5s-Pole model improved the precision, recall, and mAP@50 metrics by 0.005, 0.1, and 0.092, respectively. It is worth noting that there is a certain balance between the precision and recall metrics; improving one metric may reduce the other, so the balance of the two metrics should be considered comprehensively. Overall, the improved model showed significant progress in all three metrics.

3.2.2. Different Brightness Comparison

Ablation experiments were carried out to investigate the effect of the improved module with different brightness datasets. Test datasets with different brightness were used in the experiments, and the performance with or without the improvement module was compared; the results are shown in Table 7.

For the three types of datasets, the brighter the dataset was, the higher the three evaluation metrics were, and the higher the upper and lower bounds were. The evaluation metrics of the model were improved by the three improvement modules. The SA module alone did not improve the evaluation metrics as much as the other two modules, but the effect was significant when combined with the other two modules; comparing Group E and Group F on the bright dataset, the improvement in precision, recall, and mAP@50 metrics were 0.056, 0.106, and 0.075, respectively, but the effect on the ark dataset was less effective. This may be due to the fact that the model generated more interest in regions with high brightness, and thus gained more attention. Comparing the different datasets, group F was better than group A in all cases.

Table 7. Ablation experiments for different brightness test sets.

Group	Dark			Medium			Bright		
	Precision	Recall	mAP@50	Precision	Recall	mAP@50	Precision	Recall	mAP@50
A	0.758	0.683	0.696	0.797	0.756	0.74	0.838	0.88	0.865
B	0.756	0.8	0.786	0.821	0.817	0.849	0.944	0.88	0.958
C	0.804	0.684	0.716	0.91	0.733	0.807	0.913	0.839	0.893
D	0.817	0.745	0.736	0.785	0.822	0.799	0.817	0.894	0.917
E	0.827	0.75	0.784	0.816	0.778	0.803	0.905	0.88	0.915
F	0.742	0.783	0.754	0.955	0.778	0.871	0.961	0.986	0.99

3.2.3. Comparison of Yolov5s-Pole and Yolov5s Effects

In response to the problems of false recognition, an inability to recognize occlusion, inaccurate recognition of multiple targets, and incomplete recognition when Yolov5s model recognizes power poles, Yolov5s-Pole solved and optimized the existing problems and obtained better results and higher confidence, as shown in Figure 8.

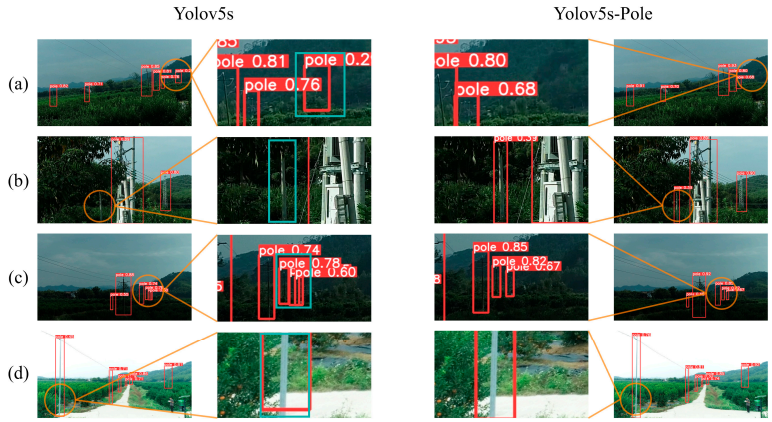

Figure 8. Comparison of Yolov5s and Yolov5s-Pole effects. (**a**) false recognition; (**b**) an inability to recognize occlusion; (**c**) inaccurate recognition of multiple targets; (**d**) incomplete recognition.

4. Discussion

4.1. Comparison of Different Models

For the Yolov5-Pole model proposed in this study with different versions of the Yolov5 and Yolov7-tiny models [32], a comprehensive performance comparison was conducted, and the results are shown in Table 8. Collectively, the different versions of the Yolo model differ in terms of their accuracy, model size, and inference speed.

Table 8. Comprehensive comparison of different models.

Model	Precision	Recall	mAP@50	Weights (MB)	Layers	Parameters (Pieces)	GFLOPs	Inference Time (ms)
Yolov5s	0.798	0.731	0.746	13.6	214	7,022,326	15.9	6.5
Yolov5m	0.768	0.765	0.784	40.1	291	20,871,318	48.2	7.8
Yolov5l	0.796	0.812	0.823	88.4	368	46,138,294	108.2	13
Yolov7-tiny	0.775	0.769	0.783	11.6	255	6,014,038	13.2	3
Yolov5-Pole	0.803	0.831	0.838	7.86	275	3,974,310	9	4.2

Among them, the Yolov5-Pole model performed best in the recall and mAP@50 metrics, while the Yolov5l model performed best in the precision metric. The Yolov5-Pole model had the smallest weight, parameters, and GFLOPs, which were 42.2%, 42.4%, and 43.3% less than the Yolov5s model, respectively. It was the lightest model among all of the models. In terms of layers, the Yolov5-Pole model had 275 layers, which was 61 more than the

smallest Yolov5s model; however, thanks to the smaller number of parameters, the actual running time was faster than the Yolov5s model. The fastest inference time was for the Yolov7-tiny model, but the Yolov5-Pole model did not perform poorly either, being 35.3% faster than the Yolov5s model.

The network structures of the Yolov5m and Yolov5l models are relatively large, but the results did not significantly improve. This may be attributed to the fact that the larger the deep learning network is, the number of parameters and computation time of the model increases, leading to a more complex model and increased time and resource consumption for training and inference. This may lead to problems such as overfitting, gradient disappearance, and gradient explosion, resulting in a decrease in the performance of the model.

Moreover, the Yolov5-Pole model achieved the best results with the smallest network structure. It is possible that for some simple tasks and small datasets, smaller deep learning networks may perform better. Smaller networks are more likely to learn patterns and features in the data, while being less prone to overfitting. In this case, choosing a smaller network can improve the performance and effectiveness of the model. Therefore, when choosing a deep learning network size, it is necessary to select the most suitable network size according to specific application scenarios and datasets, in order to achieve the best performance and effect.

4.2. The Effect of Brightness

When performing a model target recognition task, changes in brightness have a significant impact on the recognition results. Brightness variations affect the appearance of the target in the image, thereby diminishing target recognizability. In low-light conditions, details and edges of the target may be blurred or lost, leading to situations such as missed recognition or false recognition. In the test dataset, these situations mainly occurred in the dark dataset. Therefore, to improve the recognition of the model in low-light conditions, HDR (High Dynamic Range) techniques can be considered to capture images to obtain richer lighting information. In addition, models with robustness, such as those with better robustness to noise and illumination changes, can also be considered for model training to improve the recognition ability of the model. When data acquisition is performed, it should be selected under well-lit conditions as much as possible to improve the quality of the data and, consequently, the accuracy of target recognition [33]. These measures can be combined to improve the recognition performance of the model, and thus better cope with the target recognition tasks under different lighting conditions.

4.3. Adding Identification Classes

In orchard obstacle recognition applications, UAVs can add the recognition of classes such as people and power lines, in addition to recognizing common obstacles such as power poles [34]. These obstacles often appear in UAV operations, so the ability of UAVs to identify the locations of people and power lines can effectively improve the safety and efficiency of operations. For example, when a UAV sprays pesticides, if a person appears in the spraying area, the UAV can automatically stop spraying by recognizing the location of the person, thus avoiding the harm of exposing human beings to toxic pesticides. In addition, UAVs can also help farmers better plan the paths of UAV operations by identifying the locations of power lines. This can avoid collisions between UAVs and power lines and improve operational efficiency and safety. Therefore, for UAV farming operations, it is important to accurately identify and locate these obstacles, which helps to guarantee safer and more efficient agricultural production.

5. Conclusions

The relevant safety distance is determined according to the obstacle category to guarantee the safety of personal and public property. This study used a lightweight deep learning model to enable the rapid deployment of performance-limited embedded devices

on agricultural UAVs. It was able to complete obstacle recognition and detection of specific operations in planting orchards. After improvements, the model's performance was re-evaluated, and the detection results were analyzed. When the improved Yolov5s-Pole model was applied to orchard poles recognition detection, it performed as follows: precision of 80.3%, recall of 83.1%, and mAP@50 of 83.8%. Compared with the previous model, the improvements in these evaluation metrics were by 0.5%, 10%, and 9.2%, respectively. The model weights were compressed from the original version of 13.6 M to 7.86 M, and the model was reduced by 42.2%. The parameters and GFLOPs were compressed by 43.4% and 43.3% to 3,974,310 and 9, respectively. The single-image detection time was 4.2 ms, which indicates that the Yolov5s-Pole model can fully meet the real-time detection needs of orchard obstacles in the working state of the visual module. It was also shown that the Yolov5s-Pole model achieved a significant degree of compression on the basis of basic retention of the original model's performance, which is beneficial to lightweight deployment on the airborne visual module. In future developments, the recognition of more types of obstacles on agricultural UAVs can be added. As the technology continues to advance and the arithmetic power increases, more target recognition models and algorithms can be explored and applied to expand the recognition capability of UAVs.

Author Contributions: Conceptualization, methodology, software, Y.Z. and X.L.; validation, Y.Z., X.L. and Z.M.; formal analysis, X.L. and Z.M.; investigation, X.L., L.W. and W.L.; resources, L.W. and W.L.; data curation, X.L., K.Y. and Z.M.; writing—original draft preparation, X.L. and L.W.; writing—review and editing, L.W., K.Y. and W.L.; visualization, Y.Z. and X.L.; supervision, X.L.; project administration, Y.Z.; funding acquisition, Y.Z. and Y.L. All authors have read and agreed to the published version of the manuscript.

Funding: This research was funded by the Laboratory of Lingnan Modern Agriculture Project, grant number NT2021009, the Key Field Research and Development Plan of Guangdong Province, China, grant number 2019B020221001, and the 111 Project, grant number D18019.

Data Availability Statement: The data presented in this study are available on request from the corresponding author. The data are not publicly available due to the multiple interests involved in the data.

Acknowledgments: Special thanks to Huanzhou Cui for writing assistance.

Conflicts of Interest: The authors declare no conflict of interest.

References

1. Lan, Y.; Chen, S. Current Status and Trends of Plant Protection UAV and Its Spraying Technology in China. *Int. J. Precis. Agric. Aviat.* **2018**, *1*, 1–9. [CrossRef]
2. Yang, S.; Yang, X.; Mo, J. The Application of Unmanned Aircraft Systems to Plant Protection in China. *Precis. Agric.* **2018**, *19*, 278–292. [CrossRef]
3. Huang, Y.; Thomson, S.J.; Hoffmann, W.C.; Lan, Y.; Fritz, B.K. Development and Prospect of Unmanned Aerial Vehicle Technologies for Agricultural Production Management. *Int. J. Agric. Biol. Eng.* **2013**, *6*, 1–10. [CrossRef]
4. Xiongkui, H.; Bonds, J.; Herbst, A.; Langenakens, J. Recent Development of Unmanned Aerial Vehicle for Plant Protection in East Asia. *Int. J. Agric. Biol. Eng.* **2017**, *10*, 18–30. [CrossRef]
5. Uche, U.E.; Audu, S.T. UAV for Agrochemical Application: A Review. *Niger. J. Technol.* **2021**, *40*, 795–809. [CrossRef]
6. Wang, L.; Lan, Y.; Zhang, Y.; Zhang, H.; Tahir, M.N.; Ou, S.; Liu, X.; Chen, P. Applications and Prospects of Agricultural Unmanned Aerial Vehicle Obstacle Avoidance Technology in China. *Sensors* **2019**, *19*, 642. [CrossRef]
7. Qian, S.; Dai, S. Identification of High-Speed Railway Trackside Equipments Based on YOLOv4. In Proceedings of the 2022 China Automation Congress (CAC), Xiamen, China, 25–27 November 2022; pp. 3635–3640.
8. Clothier, R.; Walker, R. Determination and Evaluation of UAV Safety Objectives. In *Proceedings of the 21st International Conference on Unmanned Air Vehicle Systems, Dubrovnik, Croatia, 21–24 June 2022*; Hugo, S., Ed.; University of Bristol: Bristol, UK, 2006; pp. 18.1–18.16; ISBN 978-0-9552644-0-5.
9. Balestrieri, E.; Daponte, P.; De Vito, L.; Picariello, F.; Tudosa, I. Sensors and Measurements for UAV Safety: An Overview. *Sensors* **2021**, *21*, 8253. [CrossRef]
10. Cao, G.; Li, Y.; Nan, F.; Liu, D.; Chen, C.; Zhang, J. Development and Analysis of Plant Protection UAV Flight Control System and Route Planning Research. *Trans. Chin. Soc. Agric. Mach.* **2020**, *51*, 1–16.

11. ShengDe, C.; YuBin, L.; ZhiYan, Z.; JiYu, L.; Fan, O.; XiaoJie, X.; WeiXiang, Y. Test and evaluation for flight quality of aerial spraying of plant protection UAV. *J. South China Agric. Univ.* **2019**, *40*, 89–96.
12. Chen, Y.; Pi, D.; Xu, Y. Neighborhood Global Learning Based Flower Pollination Algorithm and Its Application to Unmanned Aerial Vehicle Path Planning. *Expert Syst. Appl.* **2021**, *170*, 114505. [CrossRef]
13. Broussard, M.A.; Coates, M.; Martinsen, P. Artificial Pollination Technologies: A Review. *Agronomy* **2023**, *13*, 1351. [CrossRef]
14. Wang, X.; Sun, H.; Long, Y.; Zheng, L.; Liu, H.; Li, M. Development of Visualization System for Agricultural UAV Crop Growth Information Collection. *IFAC-PapersOnLine* **2018**, *51*, 631–636. [CrossRef]
15. Tsouros, D.C.; Bibi, S.; Sarigiannidis, P.G. A Review on UAV-Based Applications for Precision Agriculture. *Information* **2019**, *10*, 349. [CrossRef]
16. Xie, C.; Yang, C. A Review on Plant High-Throughput Phenotyping Traits Using UAV-Based Sensors. *Comput. Electron. Agric.* **2020**, *178*, 105731. [CrossRef]
17. Velusamy, P.; Rajendran, S.; Mahendran, R.K.; Naseer, S.; Shafiq, M.; Choi, J.-G. Unmanned Aerial Vehicles (UAVs) in Precision Agriculture. Applications and Challenges. *Energies* **2022**, *15*, 217. [CrossRef]
18. Morgan, B.E.; Chipman, J.W.; Bolger, D.T.; Dietrich, J.T. Spatiotemporal Analysis of Vegetation Cover Change in a Large Ephemeral River: Multi-Sensor Fusion of Unmanned Aerial Vehicle (UAV) and Landsat Imagery. *Remote Sens.* **2021**, *13*, 51. [CrossRef]
19. Fei, S.; Hassan, M.A.; Xiao, Y.; Su, X.; Chen, Z.; Cheng, Q.; Duan, F.; Chen, R.; Ma, Y. UAV-Based Multi-Sensor Data Fusion and Machine Learning Algorithm for Yield Prediction in Wheat. *Precis. Agric.* **2023**, *24*, 187–212. [CrossRef]
20. Mokhtari, A.; Ahmadi, A.; Daccache, A.; Drechsler, K. Actual Evapotranspiration from UAV Images: A Multi-Sensor Data Fusion Approach. *Remote Sens.* **2021**, *13*, 2315. [CrossRef]
21. Qiu, Z.; Zhao, N.; Zhou, L.; Wang, M.; Yang, L.; Fang, H.; He, Y.; Liu, Y. Vision-Based Moving Obstacle Detection and Tracking in Paddy Field Using Improved Yolov3 and Deep SORT. *Sensors* **2020**, *20*, 4082. [CrossRef]
22. Chen, B.; Zhang, M.; Xu, H.; Li, H.; Yin, Y. Farmland Obstacle Detection in Panoramic Image Based on Improved YOLO v3—Tiny. *Trans. Chin. Soc. Agric. Mach.* **2021**, *52*, 58–65.
23. Chen, B.; Miao, X. Distribution Line Pole Detection and Counting Based on YOLO Using UAV Inspection Line Video. *J. Electr. Eng. Technol.* **2020**, *15*, 441–448. [CrossRef]
24. Basso, M.; Stocchero, D.; Ventura Bayan Henriques, R.; Vian, A.L.; Bredemeier, C.; Konzen, A.A.; Pignaton de Freitas, E. Proposal for an Embedded System Architecture Using a GNDVI Algorithm to Support UAV-Based Agrochemical Spraying. *Sensors* **2019**, *19*, 5397. [CrossRef] [PubMed]
25. Ki, M.; Cha, J.; Lyu, H. Detect and Avoid System Based on Multi Sensor Fusion for UAV. In Proceedings of the 2018 International Conference on Information and Communication Technology Convergence (ICTC), Jeju Island, Republic of Korea, 17–19 October 2018; pp. 1107–1109.
26. Liu, X.; Li, Y.; Shuang, F.; Gao, F.; Zhou, X.; Chen, X. ISSD: Improved SSD for Insulator and Spacer Online Detection Based on UAV System. *Sensors* **2020**, *20*, 6961. [CrossRef]
27. Yu, Z.; Ye, J.; Li, C.; Zhou, H.; Li, X. TasselLFANet: A Novel Lightweight Multi-Branch Feature Aggregation Neural Network for High-Throughput Image-Based Maize Tassels Detection and Counting. *Front. Plant Sci.* **2023**, *14*, 1158940. [CrossRef] [PubMed]
28. Zhang, H.; Cisse, M.; Dauphin, Y.N.; Lopez-Paz, D. Mixup: Beyond Empirical Risk Minimization. *arXiv* **2018**, arXiv:1710.09412.
29. Han, K.; Wang, Y.; Tian, Q.; Guo, J.; Xu, C.; Xu, C. GhostNet: More Features from Cheap Operations. In Proceedings of the IEEE/CVF Conference on Computer Vision and Pattern Recognition (CVPR), Seattle, WA, USA, 14–19 June 2020; pp. 1580–1589.
30. Zhang, Q.-L.; Yang, Y.-B. SA-Net: Shuffle Attention for Deep Convolutional Neural Networks. In Proceedings of the ICASSP 2021–2021 IEEE International Conference on Acoustics, Speech and Signal Processing (ICASSP), Toronto, ON, Canada, 6–11 June 2021; pp. 2235–2239.
31. Steffens, C.R.; Messias, L.R.V.; Drews, P.L.J.; da Costa Botelho, S.S. Can Exposure, Noise and Compression Affect Image Recognition? An Assessment of the Impacts on State-of-the-Art ConvNets. In Proceedings of the 2019 Latin American Robotics Symposium (LARS), 2019 Brazilian Symposium on Robotics (SBR) and 2019 Workshop on Robotics in Education (WRE), Joao Pessoa, Brazil, 6–10 October 2019; pp. 61–66.
32. Wang, C.-Y.; Bochkovskiy, A.; Liao, H.-Y.M. YOLOv7: Trainable Bag-of-Freebies Sets New State-of-the-Art for Real-Time Object Detectors. In Proceedings of the IEEE/CVF Conference on Computer Vision and Pattern Recognition (CVPR), New Orleans, LA, USA, 18 June 2022.
33. Kedzierski, M.; Wierzbicki, D. Radiometric Quality Assessment of Images Acquired by UAV's in Various Lighting and Weather Conditions. *Measurement* **2015**, *76*, 156–169. [CrossRef]
34. YuBin, L.; LinLin, W.; YaLi, Z. Application and prospect on obstacle avoidance technology for agricultural UAV. *Trans. Chin. Soc. Agric. Eng.* **2018**, *34*, 104–113.

Disclaimer/Publisher's Note: The statements, opinions and data contained in all publications are solely those of the individual author(s) and contributor(s) and not of MDPI and/or the editor(s). MDPI and/or the editor(s) disclaim responsibility for any injury to people or property resulting from any ideas, methods, instructions or products referred to in the content.

frontiers | Frontiers in Plant Science

TYPE Original Research
PUBLISHED 11 August 2022
DOI 10.3389/fpls.2022.955340

Check for updates

OPEN ACCESS

EDITED BY
Xiuliang Jin,
Institute of Crop Sciences (CAAS), China

REVIEWED BY
Qingfeng Song,
Center for Excellence in Molecular Plant Sciences (CAS), China
Norhashila Hashim,
Putra Malaysia University,
Malaysia

*CORRESPONDENCE
Yubin Lan
ylan@scau.edu.cn

†These authors have contributed equally to this work and share first authorship

SPECIALTY SECTION
This article was submitted to Sustainable and Intelligent Phytoprotection, a section of the journal Frontiers in Plant Science

RECEIVED 28 May 2022
ACCEPTED 08 July 2022
PUBLISHED 11 August 2022

CITATION
Zhang Y, Zhao D, Liu H, Huang X, Deng J, Jia R, He X, Tahir MN and Lan Y (2022) Research hotspots and frontiers in agricultural multispectral technology: Bibliometrics and scientometrics analysis of the Web of Science.
Front. Plant Sci. 13:955340.
doi: 10.3389/fpls.2022.955340

COPYRIGHT
© 2022 Zhang, Zhao, Liu, Huang, Deng, Jia, He, Tahir and Lan. This is an open-access article distributed under the terms of the Creative Commons Attribution License (CC BY). The use, distribution or reproduction in other forums is permitted, provided the original author(s) and the copyright owner(s) are credited and that the original publication in this journal is cited, in accordance with accepted academic practice. No use, distribution or reproduction is permitted which does not comply with these terms.

Research hotspots and frontiers in agricultural multispectral technology: Bibliometrics and scientometrics analysis of the Web of Science

Yali Zhang[1,2†], Dehua Zhao[1,2†], Hanchao Liu[1,2], Xinrong Huang[1,2], Jizhong Deng[1,2], Ruichang Jia[1,2], Xiaoping He[3], Muhammad Naveed Tahir[4] and Yubin Lan[2,5*]

[1]College of Engineering, South China Agricultural University, Guangzhou, China, [2]National Center for International Collaboration Research on Precision Agricultural Aviation Pesticide Spraying Technology, Guangzhou, China, [3]Department of Information Consulting, Library, South China Agricultural University, Guangzhou, China, [4]Department of Agronomy, Pir Mehr Ali Shah-Arid Agriculture University, Rawalpindi, Pakistan, [5]College of Electronic Engineering and College of Artificial Intelligence, South China Agricultural University, Guangzhou, China

Multispectral technology has a wide range of applications in agriculture. By obtaining spectral information during crop production, key information such as growth, pests and diseases, fertilizer and pesticide application can be determined quickly, accurately and efficiently. The scientific analysis based on Web of Science aims to understand the research hotspots and areas of interest in the field of agricultural multispectral technology. The publications related to agricultural multispectral research in agriculture between 2002 and 2021 were selected as the research objects. The softwares of CiteSpace, VOSviewer, and Microsoft Excel were used to provide a comprehensive review of agricultural multispectral research in terms of research areas, institutions, influential journals, and core authors. Results of the analysis show that the number of publications increased each year, with the largest increase in 2019. Remote sensing, imaging technology, environmental science, and ecology are the most popular research directions. The journal *Remote Sensing* is one of the most popular publishers, showing a high publishing potential in multispectral research in agriculture. The institution with the most research literature and citations is the USDA. In terms of the number of papers, Mtanga is the author with the most published articles in recent years. Through keyword co-citation analysis, it is determined that the main research areas of this topic focus on remote sensing, crop classification, plant phenotypes and other research areas. The literature co-citation analysis indicates that the main research directions concentrate in vegetation index, satellite remote sensing applications and machine learning modeling. There is still a lot of room for development of multi-spectrum technology. Further development can be carried out in the areas of multi-device synergy, spectral fusion, airborne equipment improvement, and real-time image processing technology, which will cooperate with each other

to further play the role of multi-spectrum in agriculture and promote the development of agriculture.

KEYWORDS

multispectral, agriculture, CiteSpace, remote sensing, Web of Science, NDVI

Introduction

Precision agriculture is currently in a phase of rapid development, which integrates technologies such as remote sensing, big data, and decision analysis, and aims to achieve efficient use of resources, rational inputs, and co-benefits in environmental and economic terms through variable and controllable scale farm management (Mazzia et al., 2020). Whereas information acquisition is the basis of precision agriculture, farming information is precisely the dynamic tracking of the agricultural environment and the state of plants at various growth periods (Huang et al., 2016), and plant phenotypes are important expressions of information on morphological characteristics that can be observed from plants (Huang et al., 2020). Both are important expressions of information in precision agriculture. Therefore, farming information and plant phenotypes reflect the information status of plants and provide reliable information for decision makers. In this case, how to obtain the required information becomes critical.

The advent of multispectral technology provides an effective and fast way to obtain agricultural information or plant phenotype information. Spectral imaging technology (Garini et al., 2006) emerged in the 1960s and was early applied in remote sensing, military and other fields. With the emergence of semiconductor photodetectors, spectral technology developed rapidly and its applications were extended to agriculture, environmental science, food engineering and other fields. Multispectral imaging technology is a kind of fusion technology of image and spectrum, which can acquire both spatial and spectral information of the object. In recent years, with the development of multispectral technology, its application in the field of agriculture has become more and more extensive. In the field of agriculture multispectral has been deeply applied in several aspects such as grain yield prediction (Zhou et al., 2017), pest and disease detection (Sankaran et al., 2010), nondestructiveness detection (Yu et al., 2018), remote sensing of agricultural drones Berni et al. (2009), weed identification (Pena et al., 2013; Sa et al., 2018), water content detection (Baluja et al., 2012), biomass (Kross et al., 2015), vegetation detection (Candiago et al., 2015), and inorganic matter detection (He et al., 2016). Agricultural multispectral technology is based on multidisciplinary fusion research, which makes use of data fusion techniques with multiple platforms, sensors, and remote sensing to provide data for research in the field of agriculture.

Bibliometrics and scientometrics are quantitative tools commonly used in scientific research. They are applied to analyze the frontiers of a topic or research field from macro- to micro-perspectives, which includes elements such as countries, institutions, authors, keywords, and journals (Raparelli and Bajocco, 2019; Zhang et al., 2019). These tools integrate computer engineering, big data applications, and statistics, and are widely applied in many fields (Chen, 2017) to provide rich assessments and analyses in different areas. The advantages of bibliometrics are reflected in stronger analytical efficiency for keyword analysis, research hotspot frontiers, and reference co-occurrence analysis. Scientometrics is an effective method for discovering research hotspots, and a powerful helper for researchers to understand the evolutionary path of research as well (Xie et al., 2020). It provides a systematic and comprehensive judgment.

The development and application of multispectral technology in agriculture promotes the development of precision agriculture and helps solve problems encountered in today's agricultural development. The bibliometrics and scientometrics analysis was conducted in this paper by reviewing publications related to agricultural multispectral research in agriculture between 2002 and 2021 from the Web of Science (WOS). Multiple softwares, CiteSpace, VOSviewer, and Microsoft Excel were adopted for analyzing and mapping of scientific knowledge to characterize the research hotspots and frontiers of agricultural multispectral technology. Comprehensive analysis was discussed in terms of research areas, institutions, influential journals, core authors, and keywords. Multiple research areas on agricultural multispectral research were identified through keyword co-citation analysis. The main research directions were proposed through literature co-citation analysis as well.

Materials and methods

Literature search strategy

The WOS database was taken as the data source with multispectral as the theme. Agriculture multispectral research mostly focus on crops, soil, moisture, biomass, etc. Therefore, the search formula was determined as: TS = (multispectral)AND TS = (Agricultural UAV or agriculture or crop or tomato or corn or wheat or rice or citrus or cotton or soybean or moisture or soil

or pest or weed or yield or potato or precision agriculture or Sugar cane or Nitrogen or tea or biomass or water fractions or Vegetables or Agricultural Remote Sensing or Chlorophyll or Pesticides). The literature data were searched for the time period from January 2002 to December 2021. Finally, 3,830 publication records were exported with each record containing author, title, source document, abstract, and cited references.

Methodology

Data mining, analysis and visualization were conducted for 3,830 literature related to agricultural multispectral research through CiteSpace 5.8.3, VOSviewer, and Microsoft Excel.

CiteSpace software[1] was developed by Prof. Chaomei Chen, Professor (tenure-track faculty) at School of Information Science and Technology, Drexel University, United States. The software is citation visualization and analysis software gradually developed in the context of scientometrics and data visualization (Chen, 2006; Chen et al., 2010). Thomas' and Kuhn's structure of scientific revolution provides the philosophical basis for CiteSpace. Another design inspiration for this software is a theory called structural holes, which was proposed by Burt at the University of Chicago in his study of social networks and social values (Chen, 2013). The software features dynamic complex network analysis and data visualization, and the visualization of CiteSpace can be divided into two main modes: cluster view and temporal view. The most prominent feature in CiteSpace is the co-citation analysis of the literature as a way to explore the knowledge structure of research. CiteSpace helps summarize clusters research frontiers and reveal the valuable knowledge points in the frontiers of agricultural multispectral research.

VOSviewer,[2] afree JAVA-based software developed by VanEck and Waltman at the Centre for Science and Technology Studies (CWTS), Leiden University, the Netherlands, in 2009 (van Eck and Waltman, 2010), is mainly oriented toward documentary data, relational knowledge units of documents construction. It is adapted to the analysis of one-mode undirected networks and focus on the visualization of scientific knowledge. VOSviewer draws scientific knowledge maps to show the inter-relationships between literatures in agricultural multispectral research. The most valuable advantage of VOSviewer over other bibliometric software is its graphical presentation capabilities, its suitability for large-scale data, and the versatility in adapting to source data in various formats from various databases. VOSviewer also provides text mining capabilities for constructing and visualizing co-occurrence of important terms extracted from scientific literatures about agricultural multispectral research. VOSviewer also provides text mining capabilities for building and visualizing co-occurrence networks of important terms extracted from these literatures.

Keywords are the core summary of a scientific paper. Analysis of the keywords gives a glimpse of the topic of the paper as that keywords given in a paper must have some kind of association. This association can be expressed by the frequency of co-occurrence. It is generally believed that the more frequent a word pair appears in the same literature, the closer the relationship between the two themes. Co-occurrence analysis investigates the common occurrence of lexical pairs of nouns or phrases in a literature set to determine the relationship between themes in the disciplines represented by that literature set. By counting the frequency of occurrences of two theme terms in the same document, a co-word network of these word-pair associations can be formed. The analysis of keywords can explore the research themes and hotspots of the literatures. The statistics of the frequency of keywords can analyze the hotspots of the research field. Two or more papers are cited by one or more papers at the same time, then these papers will constitute a co-citation relationship, and the co-citation relationship of the literature will change with time. A research hotspot is the focus and concentration of a technical field over a period of time, which is manifested by the emergence of a large number of papers and patents on a technical issue. The concept of research hotspot was first introduced by Plath in 1965, and has been developed and extended over the past 60 years to multiple levels. Analyses of research hotspots help clarify the development history, correctly understand the research lineage, and provide reference for future directions of agricultural multispectral technology.

Results

Basic data information

The searched literatures were first processed and removed irrelevant ones, and a total of 3,830 publications and 53,390 references were obtained. The average of 191.5 publications per year from 2002 to 2021 was available in the field of agricultural multispectral research. From the analysis results it is clear that multispectral study is flourishing in agriculture. These literatures involved 12,913 authors and generated a total of 12,899 keywords.

Evolution of publications

The trend of year-on-year growth can be seen in Figure 1, from 54 articles in 2002 to 608 articles in 2021, with an average annual growth rate of 13.5%. The number of publications exceeded 100 for the first time in 2008 and reached 104, then dropped below 100 in the next 2 years. From 2011 the number of publications exceeded 100 again and showed a stable growth trend. From 2002 to 2021, the number of publications increased by 10.25 times. The increasing number of publications year by year indicates that the application of multispectral technology in agriculture is attracting more and more attention.

1 https://sourceforge.net/projects/citespace/
2 https://www.vosviewer.com/

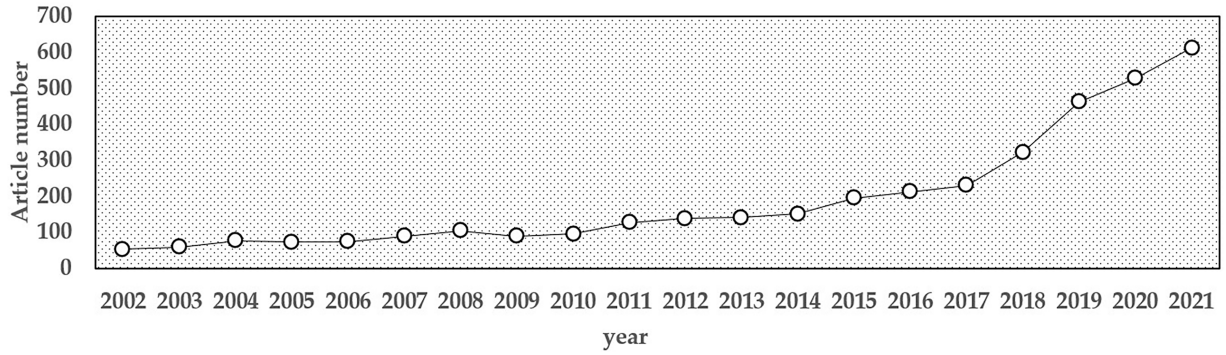

FIGURE 1
Annual distribution of the number of research publications on agricultural multispectral research in 2002–2021.

WOS Research Area

Table 1 lists the main agricultural fields of multispectral study from 2002 to 2021, which are remote sensing, imaging science, environmental science, geology, multi-discipline research, agriculture, electronic engineering, etc. Among them, remote sensing is the field with the largest proportion, followed by a variety of subjects, indicating that multispectral research is concerned by multiple fields and disciplines. From the current perspective, the research of multi-discipline integration will become a hot trend in the future about agricultural multispectral research.

TABLE 1 Main categories of multispectral research literature in agriculture from 2002 to 2021.

Subject categories	Number	Ration%
Remote Sensing	1,691	44.11
Imaging Science Photographic Technology	1,430	37.30
Environmental Sciences	1,124	29.32
Geosciences Multidisciplinary	868	22.64
Engineering Electrical Electronic	372	9.70
Geography Physical	295	7.69
Agriculture Multidisciplinary	265	6.91
Agronomy	239	6.23
Plant Sciences	194	5.06

Analysis of research countries and institutions

Analyzing research institutions help understand the publication and collaboration of major institutions. In total, 3,358 institutions are involved in agricultural multispectral research. Results show that the top five institutions with the highest number of publications are: USDA, Chinese Academy of Sciences, NASA, UNIVERSITY OF CALIFORNIA SYSTEM, and CNRS.A total of 746 articles were published by the above five institutions. The top two institutions have significantly more publications than the others, indicating an imbalance between the research publications of influential institutions. From 2002 to 2021, the USDA is the institution with the highest number of publications, with a total of 247 publications, taking the first place. The institutional co-occurrence mapping in Figure 2 was generated based on the analysis.

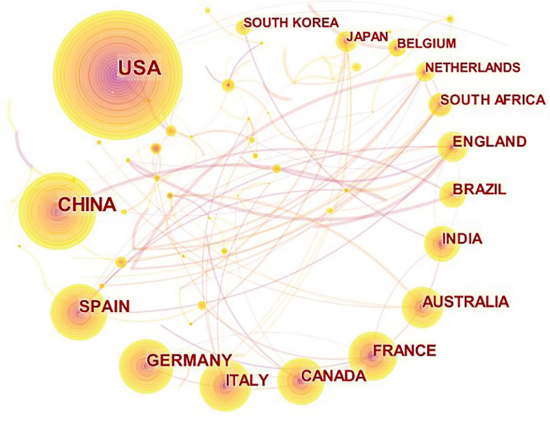

FIGURE 2
Co-current mapping of research institution collaboration on agricultural multispectral research in 2002–2021. The points to circles represent the individual countries, the size of the graph indicates how much literature comes from each country and how influential it is, and the lines represent how close each country is to other countries.

A total of 118 countries are involved in agricultural multispectral research. The density of cooperation among countries is visualized in Figure 3. The research countries analysis shows that the five countries with the highest number of publications are the United States (1,177), China (737), Spain (285), Germany (277), and Italy (231). In addition to the number of publications, centrality is one of the criteria to measure the strength of a country's research in this field. From the data obtained, the top five countries in terms of centrality are: United States, Germany, Italy, Australia, and England. China and Spain, despite being in the top five in terms of number of publications, are not in the top five in terms of centrality ranking.

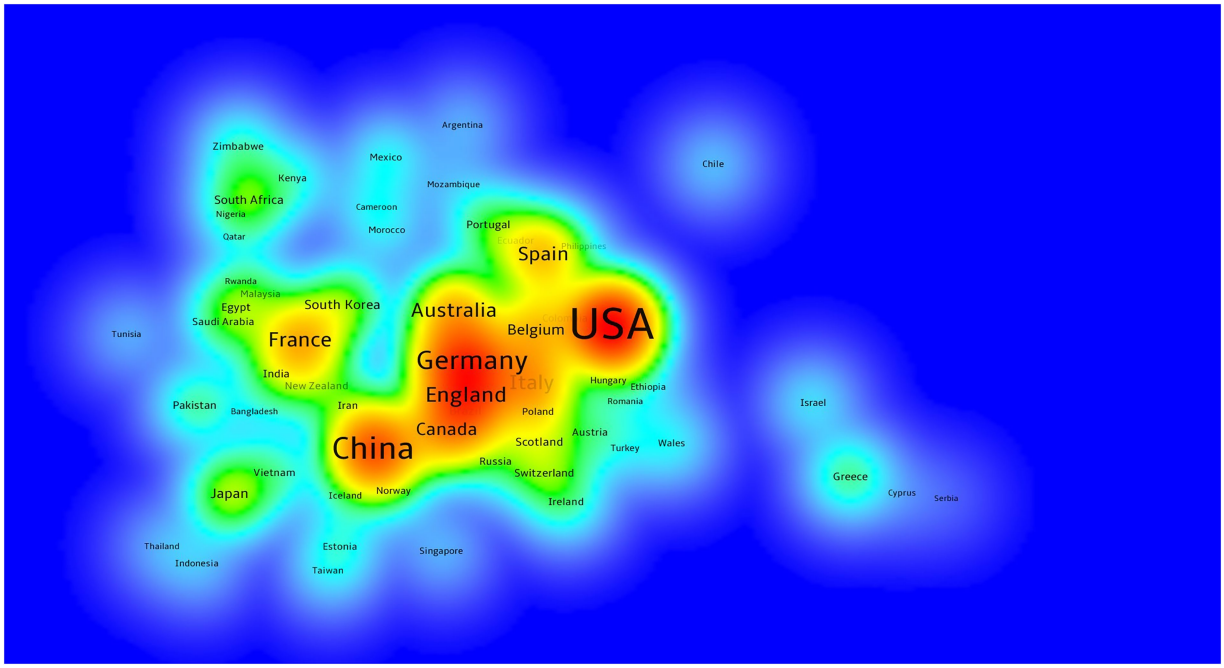

FIGURE 3
Visualization of agricultural multispectral research in terms of the density of cooperation between countries.

Influential journals

Multispectral research in agriculture was published in 702 journals, and the co-occurrence map of journals is shown in Figure 4. The top 20 (2.85%) journals published 2,021 papers, accounting for 52.8% of the total literature. There were 405 journals that published only one paper in agricultural multispectral research, accounting for 57.7% of the total number of journals. There were 200 journals that published 2–5 papers, accounting for 28.5% of the total number of journals. Less than 10 papers were published in 645 journals, representing 91.8% of the total number of journals. The top 3 publishers were Remote sensing (529), International journal of remote sensing (216), and Remote sensing of environment (207). According to this analysis, the agricultural multispectral publications become scattered. Most of the research achievement was published in 12 journals as shown in Table 2. These 12 journals can be considered as the core sources of multispectral research in agriculture, and these journals play an important role as well. Among them, Remote sensing is the most popular journal in the field of agricultural multispectral research with the largest proportion and the fastest growth rate, showing that it has played an important role in promoting multispectral research in agriculture.

Analysis of author groups

The collaborative network of authors enables the analysis of the core authors and collaborations within the field of agricultural multispectral study. The analysis of core authors and their collaborative relationships was performed by VOSviewer to generate a co-occurrence map of authors, as shown in Figure 5. Results show that the top 5 authors with the highest number of published papers are Onisimo Mutanga (52), Timothy Dube (25), Yu Zhang (24), James F. Bell (22), and Jeffrey R. Johnson (22). Zarco-Tejada, P. J. has the most cited papers with an average of 81.9 citations per paper. Authors with more than four publications in the field of study were considered core authors according to its definition, of which there are 675 core authors. The top 10 core authors are shown in Table 3. There are 3,830 papers that involve 12,913 authors, with an average of 0.29 papers per author and 3.37 authors per paper. This also indicates that multispectral research in agriculture is a multi-author collaborative field.

Keyword analysis

A total of 12,899 keywords were detected in 3,830 publications from 2002 to 2021 through software analysis. A total of nine clusters were generated by co-occurrence analysis. The clusters, based on the relationship between the weight of link attributes under different keywords and the strength of total links, are shown in Figure 6. The top 20 keywords in 3,212 publications were ranked by frequency, as shown in Table 4.

Figure 6 shows the keyword network presented by the co-occurrence method on agricultural multispectral research in 2002–2021. The keywords are divided into nine clusters and each cluster is identified by a different color. The thickness and number

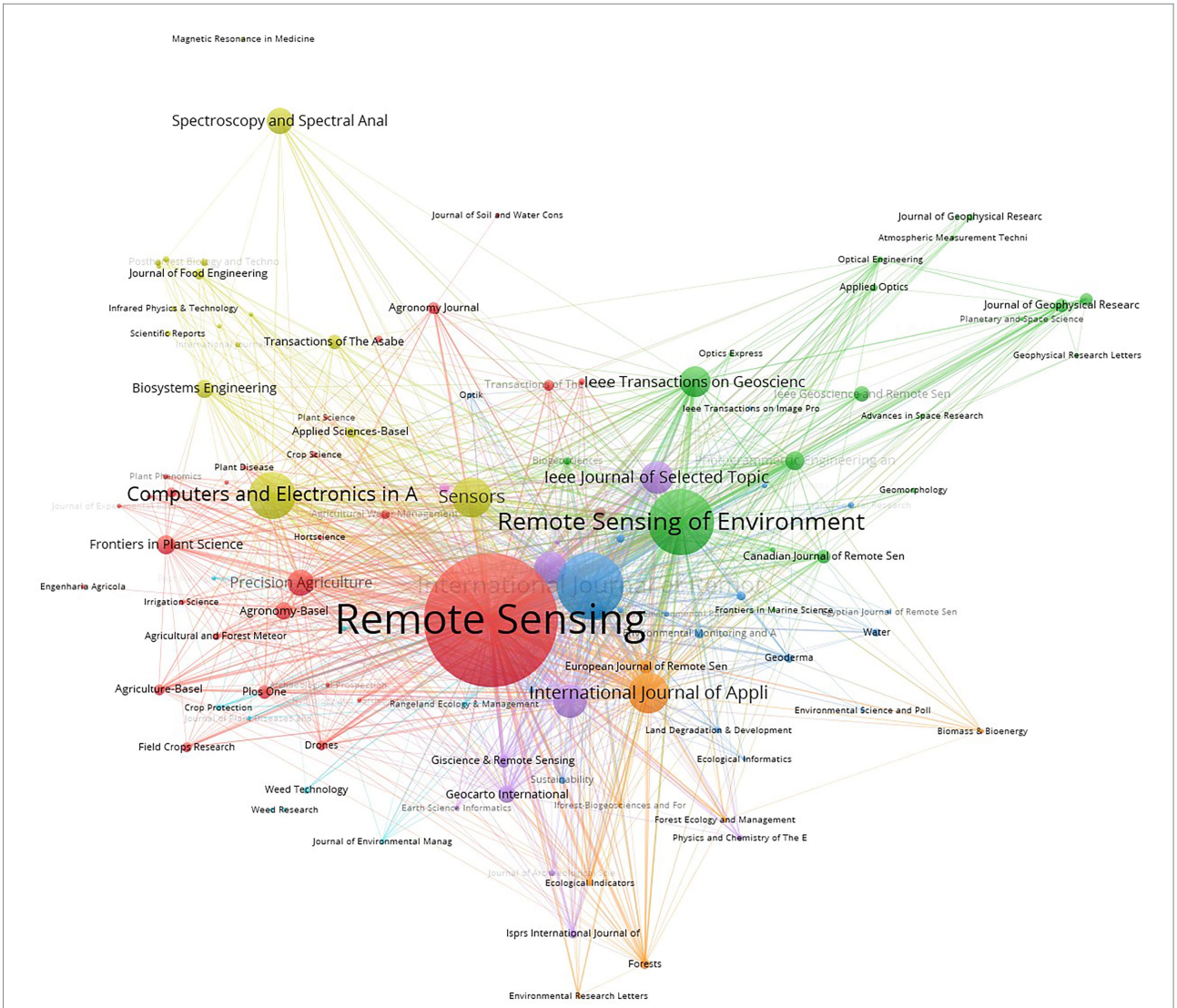

FIGURE 4
Co-occurrence map of influential journals on agricultural multispectral research in 2002–2021.

TABLE 2 Top 12 journals for local citation ranking of agricultural multispectral studies in 2002–2021.

Source	D	Citations	TS	WL
Remote Sensing	532	7,930	1,831	198
International Journal of Remote Sensing	216	4,934	560	123
Remote Sensing of Environment	207	17,268	1,216	172
Computers and Electronics in Agriculture	134	3,982	495	111
International Journal of Applied earth Observation and Geoinformation Sensors	107	2,766	501	106
Sensors	105	1782	400	92
Isprs Journal of Photogrammetry and Remote Sensing	85	3,293	525	89
Ieee Journal of Elected Topics in Applied Earth Observations and Remote Sensing	84	1743	259	54
Journal of Applied Remote Sensing	80	935	213	63
Ieee Transactions on Image Processing	79	4,137	309	75
Precision Agriculture	62	1952	275	29
Spectroscopy and Spectral Analysis	60	174	34	18

D, documents; TS, Total link strength; WL, weight links.

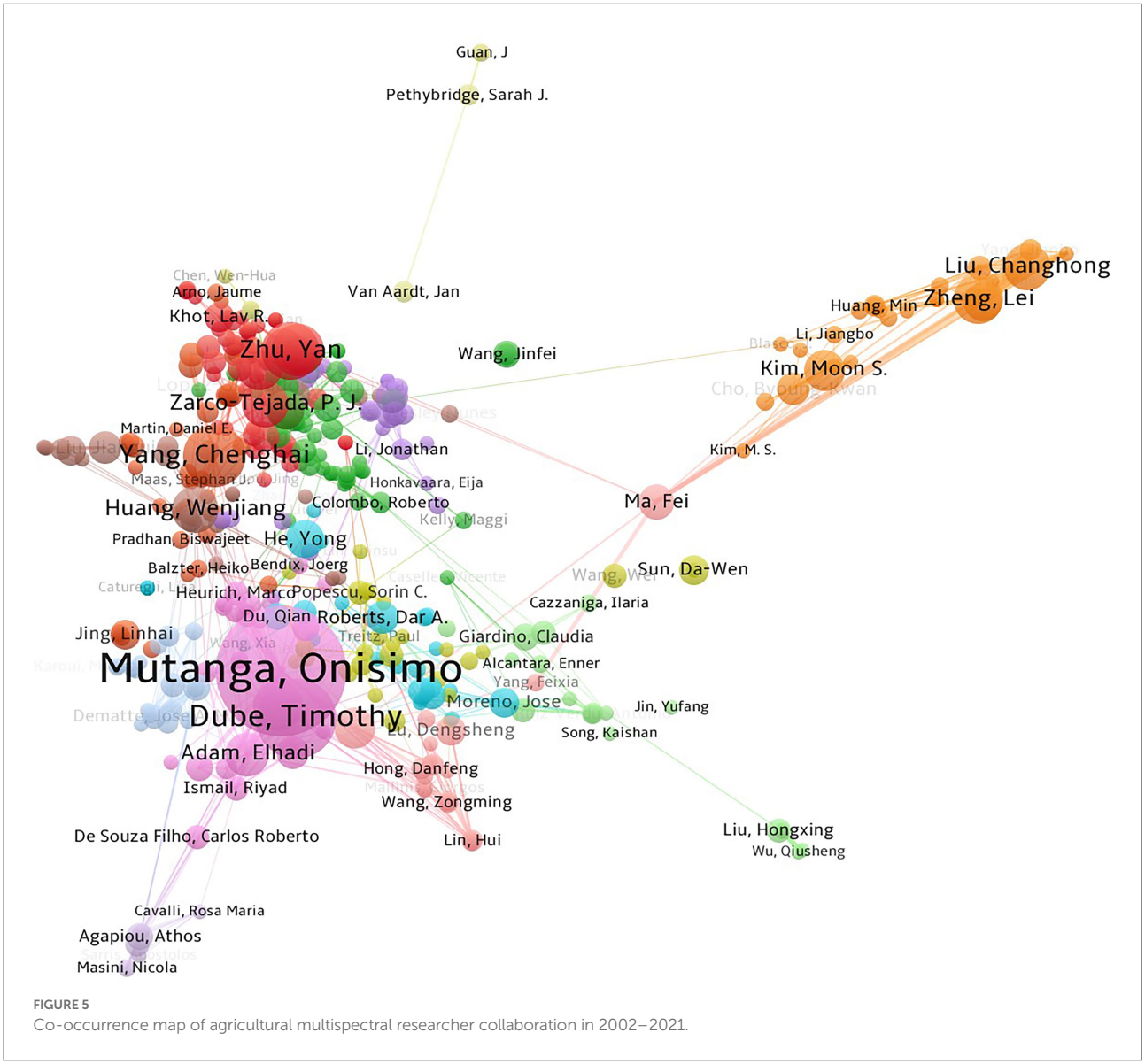

FIGURE 5
Co-occurrence map of agricultural multispectral researcher collaboration in 2002–2021.

TABLE 3 Top 10 authors ranked by total literature on agricultural multispectral research in 2002–2021.

Authors	Dc	Ct	TLS	Institutions	Countries
Onisimo Mutanga	52	1,672	813	University of KwaZulu-Natal	South Africa
Timothy Dube	30	591	427	University of Western Cape	South Africa
Yu Zhang	23	563	320	Chinese Academy of Sciences	China
James F. Bell	22	396	199	Arizona State University	United States
Jeffrey R. Johnson	22	1,228	260	U.S. Geological Survey	United States
Chenghai Yang	22	563	209	USDA-Agricultural Research Service	United States
Moon S. Kim	21	272	68	USDA-Agricultural Research Service	United States
Lopez-granados F	21	891	163	Spanish National Research Council	Spain
Lei Zheng	21	291	568	Hefei University of Technology	United States
Yan Zhu	21	396	199	Nanjing Agricultural University	China

Dc, Documents; Ct, Citations; TLS, Total link strength; JCICTA, Jiangsu Collaborative Innovation Center for the Technology and Application of Internet of Things; UKSARC, USDA-ARS Kika de la Garza Subtropical Agricultural Research Center.

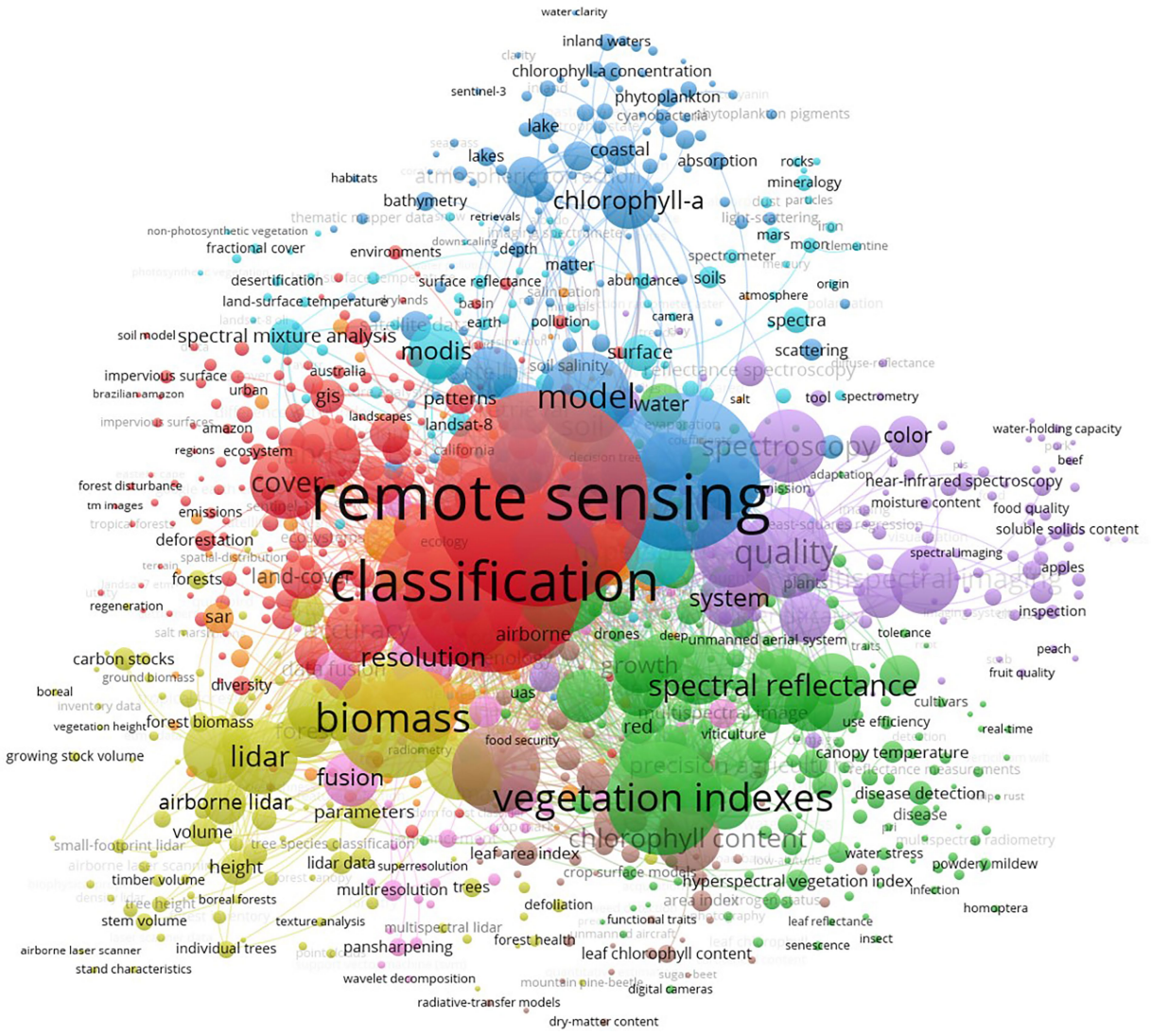

FIGURE 6
Network of keywords based on the co-occurrence method on agricultural multispectral research in 2002–2021.

of connecting lines between different clusters indicate the closeness of the connection between clusters. These nine clusters are cluster 1, red: remote sensing; cluster 2, green: vegetation indexes; cluster 3, cyan: reflectance; cluster 4, yellow: biomass; cluster 5, purple: quality; cluster 6, blue: soil; cluster 7, orange: random forest; cluster 8, brown: leaf-area index; cluster 9, pink: resolution. From the top 20 keywords given on Table 4, cluster 1 remote sensing, cluster 2 vegetation indexes, cluster 3 reflectance, cluster 4 biomass, cluster 5 quality account for the most weight, by clustering with the four keywords that account for the most, we can know the current research hotspots.

By keyword clustering found clustering 1 remote sensing in the field of agricultural multispectral is the most dominant research area, remote sensing technology is generally considered as one of the most important technologies for precision agriculture, and the development of technologies such as imaging of spectral information and multi-directional optical detection has improved the timeliness and operability of remote sensing technology (Tsouros et al., 2019). At present, remote sensing in the field of agriculture mainly focuses on: crop classification, crop coverage, and precise identification. Classification of weeds and crops in the field and accurate management of weeds, crop cover and vegetation coverage in agricultural fields, accurate identification of biomass and trace element content are the current research priorities in remote sensing (Huang et al., 2018; Näsi et al., 2018; Memon et al., 2019; Wijesingha et al., 2021). Remote sensing has made a great contribution to the development of precision agriculture.

Keyword clustering 2 led by vegetation indexes is likewise a current research hotspot in multispectral in agriculture, vegetation indexes have been widely used to qualitatively and quantitatively evaluate the information produced by vegetation,

10.3389/fpls.2022.955340

TABLE 4 Top 20 keywords ranked by frequency on agricultural multispectral research in 2002–2021.

P	Keyword	N	C	L	TS	P	Keyword	N	C	L	TS
1	Remote sensing	532	1	1,267	4,212	11	NDVI	163	2	681	1,493
2	Classification	416	1	1,075	3,475	12	Lidar	160	4	570	1,339
3	Reflectance	374	3	1,062	3,188	13	Spectral reflectance	150	2	621	1,501
4	Vegetation	334	2	991	2,965	14	Uav	149	2	541	1,239
5	Biomass	302	4	791	2,288	15	Soil	145	6	544	1,324
6	Vegetation indexes	251	2	741	2,230	16	Yield	141	2	515	974
7	Leaf-area index	191	8	662	1,511	17	Cover	139	1	542	1,143
8	Imagery	174	5	654	1,446	18	Spectroscopy	137	5	564	1,140
9	Multispectral	171	4	584	1,325	19	Prediction	135	5	538	1,276
10	Model	165	3	605	1,615	20	Precision agriculture	132	5	518	1,137

P, position; N, number of articles; C, Cluster; L, Weight Links; TS, Total link strength.

and vegetation indexes have been applied in a particularly wide range of applications, in which yield prediction, spectral reflection studies, vegetation growth, and vegetation canopy information extraction are hot research directions (Zhou et al., 2017; Marston et al., 2020; Peng et al., 2021; Zhu et al., 2021). Among these research directions, accurate yield prediction of food crops, application research of specific wavelength bands, soil drought and salinity, foliar index, and crop pest monitoring are the focus of research (Farrell et al., 2018; Mazzia et al., 2020; Zhu et al., 2021), and a significant part of these studies use uavs as the main application platform, and the combination of UAVs and multispectral further promotes the development of vegetation indices in agriculture.

keyword clustering 3 reflectance is based on spectral reflectance information to carry out various studies in which the most important thing is to use reflectance information to construct models through which specific problems can be solved. For example, the simple algorithm yield model was used to estimate the foliar index by combining the light energy efficiency and leaf function of the crop (Peng et al., 2021) the SWAP-WOFOST model was used to predict the growth of sugarcane (Hu et al., 2019) and the improved casa model was used to map the crop biomass (Fang et al., 2021). The application of various models helped us to provide a great role in rapid crop monitoring as well as crop yield assessment.

Keywords clustering 4 biomass: Biomass is a common crop parameter based on remote sensing and with the rapid development of remote sensing technology biomass detection techniques have advanced tremendously with the rapid development of precision agriculture from 1980 to 2021. The rapid development of UAV technology, lightweight multispectral, and hyperspectral equipment has provided new tools for biomass detection and during these decades most of the studies on crop parameters were conducted based on spectral information and with the addition of 3D information technology the interplay of the two is a new progress in the detection of crop parameters (Candiago et al., 2015; Näsi et al., 2018; Zhu et al., 2019a; Fei et al., 2021; Jayakumari et al., 2021; Li et al., 2021; Yu et al., 2021).

Keywords clustering 5 quality: Improving the quality of production is one of the goals of agriculture and the development of multispectral technologies in improving the quality of production provides scientific tools to achieve the goal of high-quality agricultural development and the rapid development of UAVs with light and portable sensors capable of capturing multiple spectral images and new image processing methods have promoted high quality agricultural production (Messina et al., 2021). For example, six-band multispectral sensors and accurate orthorectified impact processing methods can improve spatial accuracy and can provide guidance for subsequent research (Mesas-Carrascosa et al., 2017); the use of deep learning methods to segment UAV images a new image alignment method that enables the fusion of information from two different sensors and improves detection accuracy (Kerkech et al., 2020).

Theme term analysis

Co-occurrence analysis of theme term

The theme term was analyzed by CiteSpace. Noun terms were extracted from the titles, author keywords, and system supplementary keywords of the dataset, and the top appearing terms were selected to generate a network time zone map (Figure 7). The time zone map collects the first occurrence of theme terms in the same year and the same time zone, which shows the evolution of the knowledge domain in the time dimension more clearly. Multispectral image, vegetation indices, normalized difference vegetation index (NDVI), the multispectral data, Unmanned aerial vehicle, overall accuracy, square error, spectral bands, random forest, high spatial resolution, hyperspectral data, remote sensing data, spatial distribution, growing season, etc., should be considered as the hot content of multispectral research in the field of agriculture in these years.

Burst Analysis of Theme Term

The theme terms with relatively high salience were analyzed by CiteSpace's burst detection algorithm in order to reflect the research trend and dig out the research hotspots, which are characterized by high frequency of changes within a certain phase in the software. The nodes that show up in red in Figure 7 indicate burst. Since there are relatively more red nodes with prominence from 2002 to 2021, the red nodes with prominence in the 6 years from 2015 to 2021 were selected as shown in Table 5. Satellite data, climate change, forest inventory, standard deviation, growing satellite data, climate change, forest inventory, standard deviation, growing seasons, plant height, sentinel-2 data, unmanned aerial, environmental condition, crop water stress index, point clouds, crop yield, etc., indicate that the recent years of multispectral research in agriculture are based on the above series of themes. The above-mentioned thematic terms have been used as a research method in the field of agriculture. From 2002 to 2010, burst themes included canopy reflectance, spectral mixture analysis, reflectance data, airborne multispectral imagery, aerial photography, and multispectral analysis. Burst themes in 2011–2021 associated with multispectral satellite imagery, remote sensing technique, high resolution, water quality parameter, partial least squares, crop water stress index, and biomass estimation, which indicate that the research and application of vegetation indices and algorithms were the main focus at this phase. Among them, vegetation index is the most researched part of multispectral in the field of agriculture.

Research frontiers

Agricultural multispectral research analysis selects the reference node and generates the cited literature analysis graph by

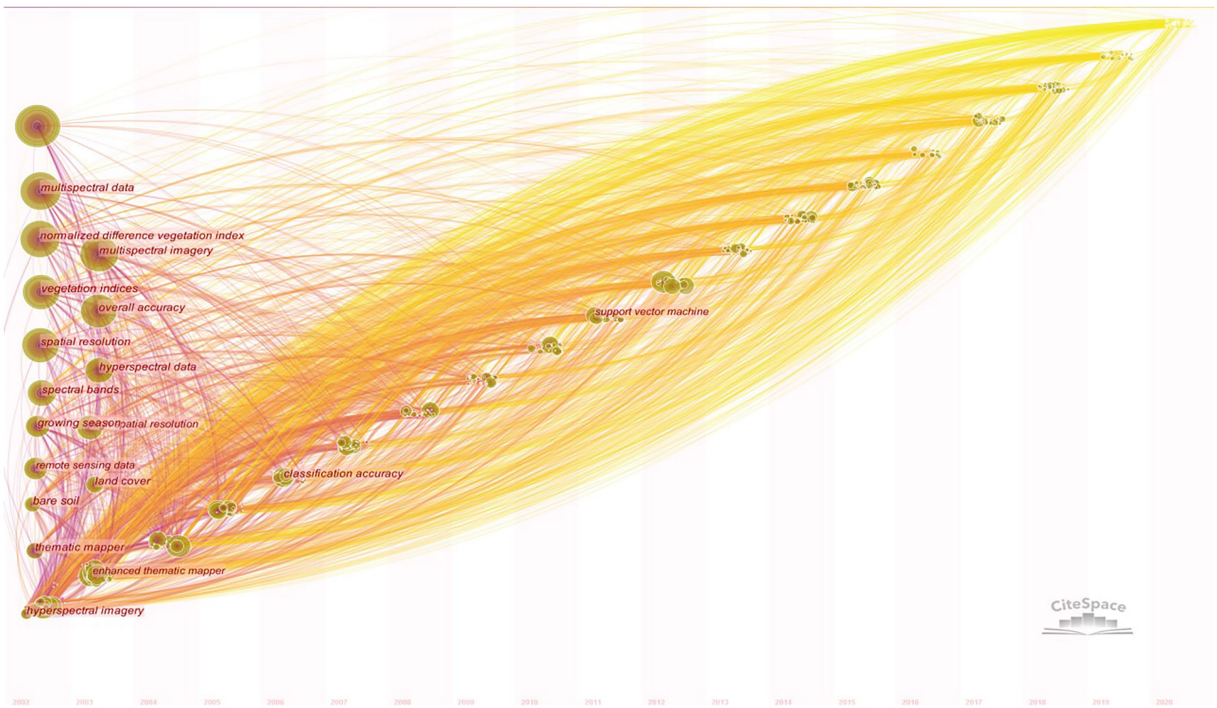

FIGURE 7
Co-occurrence time zone map of theme terms on agricultural multispectral research in 2002–2021. The horizontal axis represents the year, each node represents a topic, and the size of each node represents frequency of occurrence. The lines between each node represent connections to other topics. The circles in the vertical axis represent topics in the multispectral area of agriculture. The size of the circles represents the magnitude of the heat. The years with more topics were arranged in order from the largest to the smallest on the vertical axis.

CiteSpace. Clusters were formed by selecting keywords, and then a total of 17 clusters were generated by LLR algorithm. Each of these clusters represents the activity of its future direction, as shown in Figure 8. The denser and more active the clusters in the graph, the more they represent the current research frontier. The module values of the 17 clusters in Figure 8 are $Q = 0.8208$ and $S = 0.917$. The module values and the average profile values are indicators provided by CiteSpace based on the network structure and the clarity of the clusters, which are used to measure the clustering effect of the map. $Q > 0.3$ indicates that the clustering is significant, and $S > 0.7$ indicates that the clustering is highly convincing. Generally, the clustering above 0.5 can be considered reasonable. Therefore, the present clustering is reasonable and the structure is significant.

The color curves in the figure indicate co-citation links. More connected lines between clusters indicate a strong correlation between clusters. Large nodes indicate that they are worth exploring because they contain important cases that are overcited or mentioned. Nodes that are still active represent cutting-edge directions, scientific themes and novel trends in agricultural multispectral research field. According to the Figure 8, the largest cluster is #0 (vegetation index), located at the top of the image. The duration varies between clusters, with some lasting more than a decade and others having a shorter life span. The four clusters with higher activity and frequency were selected for further analysis.

The largest cluster #0 (UAV) contains 175 reference points between 2012 and 2021. The average reference year is 2016 and the average profile value $S = 0.855$, which was well visualized. This cluster is a corresponding study for vegetation indices in land cover, vegetation classification, crop yield estimation, drought monitoring, and environmental change using UAV remote sensing as the main application platform. UAV is an important vehicle for acquiring a variety of remote sensing data accurately, flexibly and efficiently in the low-altitude field, and UAV remote sensing is now very commonly used in precision agriculture, while UAV-based IoT technology is considered as the future of remote sensing in precision agriculture. Vegetation indices are formed by combining different bands of the spectrum according to the spectral characteristics of vegetation. More than 40 kinds of vegetation indices are available and widely used in the field of agricultural production. The most cited one in this cluster is Bendig et al. (2015), who used vegetation indices and plant height information to estimate summer barley biomass and verified the potential of visible bands to predict biomass. Candiago et al. (2015) demonstrated the great potential of UAVs in the multispectral field by monitoring vegetation indices with UAVs carrying imaging equipment. Zhou et al. (2017) verified that red-edge and infrared bands were more effective in predicting rice yield and foliar index based on a UAV-mounted multispectral photography platform, demonstrating the reliability of the platform for rice yield and growth estimation and identifying the most contraindicated virtual instrument for rice yield. Zaman-Allah et al. (2015) used a multispectral imaging sensor-mounted UAV platform to measure the N content in soil and derive crop performance indices for low N stress in maize fields, showing that the platform is effective in assessing field variability and crop performance. Duan et al. (2017) applied UAV based multispectral camera to detect NDVI indices in wheat field during the growing season through a high-throughput phenotyping platform, showing that NDVI before and after flowering had a strong

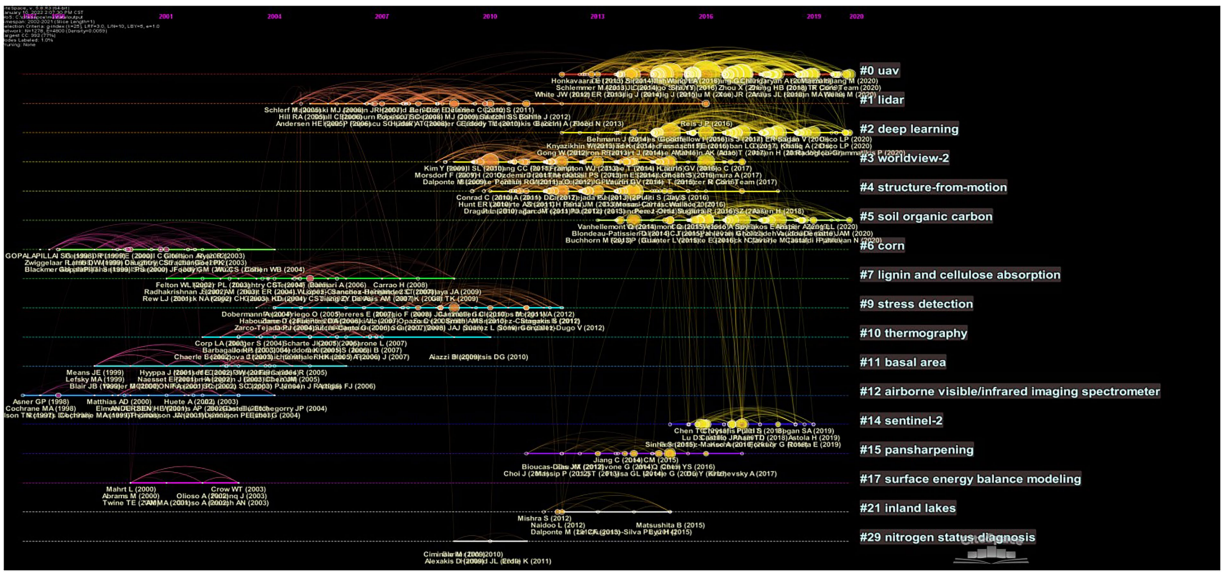

FIGURE 8
Co-citation timeline mapping of publications on agricultural multispectral research in 2002–2021. The horizontal axis represents the year, each node represents a popular cited reference, and the size of each node is proportional to its citation frequency. The line between each node represents the time evolution of the cited literature, and the thickness of the line represents the co-citation intensity.

10.3389/fpls.2022.955340

TABLE 5 Burst theme terms on agricultural multispectral study in 2015–2021.

Term	Strength	Begin	End	2015–2021
Satellite data	3.81	2015	2017	
Climate change	3.44	2015	2017	
Forest inventory	3.15	2015	2018	
Spectral feature	5.07	2016	2018	
Hyperspectral image	4.73	2016	2017	
Standard deviation	3.77	2016	2021	
Growing seasons	3.69	2016	2021	
Soil property	5.91	2017	2018	
Optimal wavelengths	4.6	2017	2021	
Plant height	3.1	2017	2021	
Sentinel-2 data	8.1	2018	2021	
Unmanned aerial system	6.02	2018	2021	
RGB image	5.71	2018	2021	
Field scale	4.82	2018	2021	
Environmental condition	4.02	2018	2021	
Crop water stress index	4.02	2018	2021	
Point clouds	3.62	2018	2021	
Digital surface model	3.19	2018	2021	
Crop yield	3.19	2018	2021	

correlation with yield. From the clustering timeline, the cluster is still highly dynamic until 2021, and UAV remote sensing is still a hot spot for current research.

The average citation time for cluster #2 is 2016. This cluster focuses on the clustering of remote sensing-based algorithms, which summarizes a review of multispectral remote sensing and case studies of algorithm applications. Currently algorithms for remotely sensed vegetation indices is effective and convenient, which have been applied for vegetation cover and growth dynamics research with wide application of UAVs (Xue and Su, 2017). Torres-Sánchez et al. (2015a) newly developed a threshold segmentation OBIA algorithm by UAV images on the Otsu-based method. This algorithm was applied to the Excess Green Index (ExG) and Normalized Vegetation Index (NDVI). Torres-Sánchez et al. (2015b) proposed a method to calculate the 3D geometric features of individual trees and rows with an accuracy of 97% for area quantification with UAVs. Mathews and Jensen (2013) acquired UAV images to collect Leaf Area Index (LAI) of visualized and quantified vineyard canopy through a motion point cloud computer technique. Albetis et al. (2017) proposed a UAV-based images and operational flavescence dorée mapping technique for grape diseases detection. The duration of this clustering is 2012–2021 and, as with the vegetation index, machine learning is also a current hotspot. Machine learning has becomes a hot spot thanks to the development of artificial intelligence, which improves efficiency by combining various algorithms. Integration of machine learning and vegetation indices plays an important role in the field of agricultural multispectral research.

Cluster #3 is well visualized with a mean citation time of 2012 and a mean profile of $S = 0.897$. The clustering is mainly the analysis of ground information using high-altitude images from satellite multispectral remote sensing. Nowadays, more and more UAVs are joining the application of remote sensing mapping, but satellite remote sensing is still the most used method in high-altitude remote sensing. Satellite remote sensing has the characteristics of high point of view, wide field of view, and continuous and fast data collection. It has a broad application prospect in land resources, water resources survey, farming estimation, etc. Dube and Mutanga (2015) applied the medium-resolution multi-spectral Landsat 8 to analyze above-ground biomass in forest plantations. His study concluded that the data provided by satellite could be a more effective data source for analyzing above-ground biomass and spectral vegetation indices, demonstrating the potential and advantages of this Landsat dataset. Immitzer et al. (2016) adopted S2 satellites to map summer and winter crops and different deciduous and tree species to confirm the capability of S2 data for land cover mapping and the high value of red-edge and short-wave infrared bands for vegetation mapping. Clevers and Gitelson (2013) estimated chlorophyll and nitrogen content of crops and grass based on red-edge band remote sensing on Sentinel-2 and-3 satellites, confirming the importance of the red-edge band on satellites for agricultural applications. Ramoelo et al. (2015) used Worldview-2 satellite to monitor leaf nitrogen content and above-ground biomass, demonstrating the importance of high-altitude resolution and the red-edge band in rangeland assessment and detection. Mutanga et al. (2012) obtained red-edge-band images from Worldview-2 satellite and applied random forest regression algorithm to predict biomass in wetland areas. The duration of this clustering was 2009–2017, which indicates that multispectral research in terms of satellites

is no longer a hotspot for research at present. The current direction of research has moved toward multispectral remote sensing research represented by UAVs.

The average citation time for cluster #4 is 2012. The main research in this cluster is summarized for aerial detection. In addition, this cluster is a multispectral research mainly by UAVs. The main research in this cluster is remote sensing mapping of field vegetation by multispectral information, and building higher accuracy classification models, including research on weed identification and yield estimation in crop fields. Yu et al. (2016) adopted UAV platform to obtain multispectral data for soybean breeding, which led to significant improvement in yield estimation models through machine learning. Maimaitijiang et al. (2017) applied UAV multisensor data fusion to extract soybean plant phenotypes and developed a model for extracting plant phenotypes, demonstrating that low-cost multisensors can provide accurate data. Veeranampalayam Sivakumar et al. (2020) conducted experiments on weed identification with low altitude UAV image of soybean field, verifying the accuracy of the Faster RCNN model and fully affirming the importance of the model. Marston et al. (2020) conducted soybean aphid experiments with UAVs and found that NIR reflections are sensitive for aphids detection. The duration of clustering #4 was from 2010 to 2018, and the research on re-clustering provided a basis and reference for the subsequent development of multispectral technology in agriculture in terms of precision management of farmland, as well as crop identification. Along with the rise of vegetation indices as well as machine science, remote sensing mapping classification is gradually approaching this aspect.

In addition, based on the ranking of the burst literature according to the intensity, the top 15 articles were selected from total 162 strongly burst literatures, as shown in Table 6. From the content presented in these 15 literatures, the results are roughly the same as those of the above cluster analysis, with the research frontier trends focusing on the application and expansion of the UAV platform in various aspects, as well as various studies for vegetation indices. Data acquisition mostly relies on multispectral sensors carried by UAVs (Zhang and Kovacs, 2012) and to a lesser extent on satellites (Clevers and Gitelson, 2013), with UAVs gradually occupying the mainstream with their low-cost and flexibility advantages. Moreover, most of the studies are on crop parameters such as biomass (Bendig et al., 2015), species classification (Ke et al., 2010), plant phenotypes (Araus and Cairns, 2014), etc. Machine learning (Mountrakis et al., 2011) also plays a big role in this. The development of new and emerging technologies has played a great role in the development of agriculture.

Discussion

Based on the analysis of the publications searched, it is known that the current research on multispectral in agriculture is mainly focused on vegetation index (Chang et al., 2020; Kim et al., 2020; Mazzia et al., 2020), land cover (Laamrani et al., 2020), vegetation classification (Gibson et al., 2004), crop estimation (Zhou et al., 2017), drought monitoring (Periasamy and Shanmugam, 2016), and environmental change (Brook et al., 2020). Among them, the studies related to vegetation indices involves the most papers. Most of the current monitoring of crops uses remote sensing technology and ground data in conjunction with each other to invert the biological indicators of crops, such as normalized vegetation index and biomass (Li et al., 2020a). Vegetation indices are the key to qualitative and quantitative assessment of vegetation, and vegetation indices have been widely applied for crop monitoring. Research related to vegetation indices is also a hot area of research at present and also a hot area of research in the

TABLE 6 Top 15 highest prominence of cited references.

Begin	End	Strength	Year	References	2002–2021
2011	2015	15.5696	2010	Blaschke, 2010, ISPRS J Photogramm, V65, P2	
2013	2017	13.1026	2012	Zarco-Tejada PJ, 2012, Remote Sens Environ, V117, P322	
2017	2018	12.5081	2013	Clevers JGPW, 2013, Int J Appl Earth Obs, V23, P344	
2015	2018	12.1329	2013	Mulla DJ, 2013, Biosyst Eng, V114, P358	
2014	2017	11.6238	2012	Mutanga O, 2012, Int J Appl Earth Obs, V18, P399	
2012	2014	11.4153	2009	Berni JAJ, 2009, IEEE T Geosci Remote, V47, P722	
2017	2021	10.5978	2014	Bendig J, 2014, Remote Sens, V6, P10395	
2015	2017	9.5025	2012	Zhang CH, 2012, Precis Agric, V13, P693	
2006	2017	9.3241	2012	Berner L T, 2012, Biogeosciences, V9, P3943	
2011	2014	9.2223	2009	Chander G, 2009, Remote Sens Environ, V113, P893	
2018	2021	8.3433	2015	Bendig J, 2015, Int J Appl Earth Obs, V39, P79	
2012	2015	8.1168	2010	KeYH, 2010, Remote Sens Environ, V114, P1141	
2017	2021	7.7503	2014	Torres-Sanchez J, 2014, Comput Electron Agr, V103, P104	
2016	2021	7.1715	2014	Araus JL, 2014, Trends Plant Sci, V19, P52	
2012	2016	7.1502	2011	Mountrakis G, 2011, ISPRS J Photogramm, V66, P247	

future. Vegetation indices can be divided into linear combinations of bands or original band ratio design (RVI; Lee et al., 2020), improvement of original indices by physical and mathematical methods (with universal applicability; Zhu et al., 2019b), and indices born on the basis of remote sensing technology for hyperspectral and thermal infrared remote sensing (with difficulty in data acquisition and difficult to be promoted and developed; Berni et al., 2009). The early studies of vegetation indices were on chlorophyll and nitrogen measurements, and plant data were obtained by tgi indices in conjunction with related factors (Hunt et al., 2013). Many current studies address NDVI indices and are interwoven with various indices such as NDRE and NGRDI (Hassan et al., 2019). The best proof of the application of remote sensing in agricultural monitoring was demonstrated in crop yield estimation (Maimaitijiang et al., 2020). Combined with the 2021 research literature, there is now a shift from large scale and large area detection of satellite data to specific range detection with further improvement in accuracy and precision.

Before the rise of UAVs, land satellites were primary means of acquiring multispectral data. Satellites equipped with multispectral instruments have the capability to detect the full spectral band from visible to thermal infrared. Such satellites are used in land resources (Zanardo et al., 2016), environmental monitoring (Brook et al., 2020), etc. by higher applications. And in recent years the emergence of unmanned aircraft remote sensing detection gradually occupy the mainstream, but from 2002 to the present satellites still mainly undertake the task of data acquisition. The US landlast and sentinel series satellites are typical representatives of multispectral research. Early studies based on satellite data modeled drought environments (Theseira et al., 2002) and constructed drought early warning systems, that is, drought has been the focus of research. There have also been studies on crop leaf area monitoring (Chrysafis et al., 2020) and image classification and identification (Venkatesh and Kumar Raja, 2003; Gibson et al., 2004; Li et al., 2020b) through satellite data. Nowadays, the main research of satellites is for surface biomass (Khan et al., 2020) and monitoring of soil elements over a large area (Sullivan et al., 2004; Periasamy and Shanmugam, 2016; Ramos et al., 2020; Luo et al., 2021). In the future, as satellite technology continues to develop, the application of multispectral aspects will gradually advance, and the ability to monitor large areas as well as the types of objects to be monitored will be greatly improved.

Deep learning and machine algorithms are also extensively covered in the literature of search. The current strong emergence of UAV imaging systems has developed as a means of application in agriculture that can yield benefits. The application of machine learning algorithms (Eskandari et al., 2020; Maimaitijiang et al., 2020; Mazzia et al., 2020; Osco et al., 2020a) has improved the ability of UAV applications and likewise the ability of satellite data for agricultural applications (Datta et al., 2021). Through the study it was shown that 62% studies used regression models and 38% used classification models. With the technology development, machine learning has also gradually derived multiple medium algorithms, including artificial convolutional neural networks (Osco et al., 2020b), support vector machines (Fortin et al., 2014), etc. The early algorithms were simple development of machine vision such as detection of two-dimensional planes (Aleixos et al., 2002), for example, fruit integrity detection (Ariana et al., 2006). The integration of algorithms and equipment has achieved three-dimensional breakthroughs, for example, extraction of tree canopy volume (Li et al., 2020a; Minařík et al., 2020), etc. Currently in the field of remote sensing support vector machines and integrated classifiers are the focus of current development, while deep learning in the field of agricultural multispectral research mainly analyzes images, including image fusion, segmentation, recognition, target detection, obia, supervised training, etc. With the progress of hardware technology, the consequent acquisition of numerous data will also be beneficial to the development of machine learning, and currently big data cloud computing and machine learning are combined together to work on the development of agriculture. Deep learning is being applied to various fields of remote sensing.

In terms of multispectral detection equipment, it lacks of cooperation of ground and UAV and other aerial equipment. In some special terrain areas, the UAVs cannot shoot clearly. In this case, ground equipment will be able to make up for this shortcoming. The cooperation of multiple machinery and equipment in the future may be the focus of development research. Especially in crop modeling, UAVs and scanning instruments can cooperate with each other to combine mathematical models, build internal and external relationships, and generate complete plant images.

At present, it is difficult to achieve the simultaneous existence of multispectral and hyperspectral data on the same machine. The use of multispectral data to simulate hyperspectral data to obtain different data types by image fusion technology will be a valuable research direction in the future. Image fusion techniques can fuse different data types, not only multispectral data. The multispectral data can be extracted from the hyperspectral data or inverse performance data by specific methods such as mathematical equations, but this method is still incomplete and the current research is still focused on traditional linear algorithms. Future research should focus on studying new models or improving the accuracy by further improving machine algorithms.

UAVs play a great role with their unique advantages as the current main application platform of multispectral in agriculture. The most prominent problem with UAVs at present is the endurance problem. In the future, high endurance UAVs should be launched, while stability performance, detection accuracy, and load capacity are also necessary performance enhancements. In addition, economic and efficient multispectral equipment is needed as well. The simplicity of operation can reduce the user's learning costs. At the same time, sensor fusion technology can also improve its application level, eliminate the possible contradictory data between sensors, reduce uncertainty, and improve the speed and correctness of the system.

Real-time image processing technology can eliminate the time gap between data collection and data analysis, and provide the

basis for real-time control of operating equipment. Along with the rapid development of deep learning technology, the research on agricultural information analysis based on artificial intelligence has opened the era of intelligent research on unmanned farms. However, in the actual application operation, the uneven network coverage in the field limits the real-time transmission of images in the cloud, and the current computing performance of embedded chips also limits the real-time processing of images at the edge. Therefore, this technology is still in the early stage of research. In the future, with the popularization of 5G signal, the improvement of embedded chip computing power and the breakthrough of lightweight network model, the feasibility of real-time image processing will be gradually improved, and the foundation for the realization of unmanned and intelligent farms will be laid.

Conclusion

The bibliometrics and scientometric approach were applied to analyze the publications on multispectral research in agriculture from 2002 to 2021. It can be seen that the number of publications in agricultural multispectral research has a rapid growth trend. The growth rate is obviously significant in recent years, maintaining a high growth rate of the literature, which is closely related to the development of precision agriculture. The study shows that the United States, China, and Spain are the countries with the largest research share, with the Chinese Academy of Sciences from China being the institution with the most publications. The most influential journal is Remote Sensing with Mutanga, Dube.timothy, and Chenghai Yang as core authors.

Multispectral technology has undergone nearly 50 years of development from the launch of ground-accessible land satellites in the United States in the 1970s to the present. It is gradually developing from the initial exploration stage to the present mature model with commercialized equipment and system software, and spreading to multiple industries. Based on the analysis, the development of agricultural multispectral technology from 2002 to 2021 is accompanied by advanced sensors and sophisticated algorithms and numerical models in agriculture. Especially along with the development of UAV technology, the application of multispectral technology in agriculture has become more and more extensive, from organic matter monitoring such as crops, to inorganic matter monitoring such as soil, moisture, nitrogen elements. The future development prospect is also more extensive. The advancement of technology has jointly promoted the application of multi-spectrum in agriculture, and also promoted the development of precision agriculture.

Data availability statement

The raw data supporting the conclusions of this article will be made available by the authors, without undue reservation.

Author contributions

YZ and YL: conceptualization, project administration, and funding acquisition. DZ, XHu, and YZ: methodology. DZ: software, data curation, and visualization. DZ and YZ: validation and investigation. DZ and HL: formal analysis. YZ: resources. DZ, HL, and YZ: writing—original draft preparation. JD, RJ, XHe, and MT: writing—review and editing. YL: supervision. All authors contributed to the article and approved the submitted version.

Funding

This research was funded by Key Field Research and Development Plan of Guangdong Province, China, grant number 2019B020221001, Science and Technology Plan Project of Guangdong Province, China, grant number 2018A050506073, Guangdong Modern Agricultural Industry Generic Key Technology Research and Development Innovation Team Project, grant number 2021KJ133, and the 111Project, grant number D18019.

Acknowledgments

The authors would like to thank Chaomei Chen for the computational support of CiteSpace software.

Conflict of interest

The authors declare that the research was conducted in the absence of any commercial or financial relationships that could be construed as a potential conflict of interest.

Publisher's note

All claims expressed in this article are solely those of the authors and do not necessarily represent those of their affiliated organizations, or those of the publisher, the editors and the reviewers. Any product that may be evaluated in this article, or claim that may be made by its manufacturer, is not guaranteed or endorsed by the publisher.

References

Albetis, J., Duthoit, S., Guttler, F., Jacquin, A., Goulard, M., Poilvé, H., et al. (2017). Detection of flavescence dorée grapevine disease using unmanned aerial vehicle (uav) multispectral imagery. *Remote Sens. (Basel)* 9:308. doi: 10.3390/rs9040308

Aleixos, N., Blasco, J., Navarrón, F., and Moltó, E. (2002). Multispectral inspection of citrus in real-time using machine vision and digital signal processors. *Comput. Electron. Agric.* 33, 121–137. doi: 10.1016/S0168-1699(02)00002-9

Araus, J. L., and Cairns, J. E. (2014). Field high-throughput phenotyping: the new crop breeding frontier. *Trends Plant Sci.* 19, 52–61. doi: 10.1016/j.tplants.2013.09.008

Ariana, D., Guyer, D. E., and Shrestha, B. (2006). Integrating multispectral reflectance and fluorescence imaging for defect detection on apples. *Comput. Electron. Agric.* 50, 148–161. doi: 10.1016/j.compag.2005.10.002

Baluja, J., Diago, M. P., Balda, P., Zorer, R., Meggio, F., Morales, F., et al. (2012). Assessment of vineyard water status variability by thermal and multispectral imagery using an unmanned aerial vehicle (uav). *Irrig. Sci.* 30, 511–522. doi: 10.1007/s00271-012-0382-9

Bendig, J., Yu, K., Aasen, H., Bolten, A., Bennertz, S., Broscheit, J., et al. (2015). Combining uav-based plant height from crop surface models, visible, and near infrared vegetation indices for biomass monitoring in barley. *Int. J. Appl. Earth Obs. Geoinf.* 39, 79–87. doi: 10.1016/j.jag.2015.02.012

Berni, J., Zarco-Tejada, P. J., Suarez, L., and Fereres, E. (2009). Thermal and narrowband multispectral remote sensing for vegetation monitoring from an unmanned aerial vehicle. *IEEE Trans. Geosci. Remote Sens.* 47, 722–738. doi: 10.1109/TGRS.2008.2010457

Brook, A., De Micco, V., Battipaglia, G., Erbaggio, A., Ludeno, G., Catapano, I., et al. (2020). A smart multiple spatial and temporal resolution system to support precision agriculture from satellite images: proof of concept on aglianico vineyard. *Remote Sens. Environ.* 240:111679. doi: 10.1016/j.rse.2020.111679

Candiago, S., Remondino, F., De Giglio, M., Dubbini, M., and Gattelli, M. (2015). Evaluating multispectral images and vegetation indices for precision farming applications from uav images. *Remote Sens.* 7, 4026–4047. doi: 10.3390/rs70404026

Chang, A., Yeom, J., Jung, J., and Landivar, J. (2020). Comparison of canopy shape and vegetation indices of citrus trees derived from uav multispectral images for characterization of citrus greening disease. *Remote Sens.* 12:4122. doi: 10.3390/rs12244122

Chen, C. (2006). Citespace ii: detecting and visualizing emerging trends and transient patterns in scientific literature. *J. Am. Soc. Inf. Sci. Technol.* 57, 359–377. doi: 10.1002/asi.20317

Chen, C. (2013). Hindsight, insight, and foresight: a multi-level structural variation approach to the study of a scientific field. *Tech. Anal. Strat. Manag.* 25, 619–640. doi: 10.1080/09537325.2013.801949

Chen, C. (2017). Science mapping: a systematic review of the literature. *J. Data Inform. Sci.* 2, 1–40. doi: 10.1515/jdis-2017-0006

Chen, C., Ibekwe-SanJuan, F., and Hou, J. (2010). The structure and dynamics of co-citation clusters: a multiple-perspective co-citation analysis. *J. Am. Soc. Inf. Sci. Technol.* 61, 1386–1409. doi: 10.1002/asi.21309

Chrysafis, I., Korakis, G., Kyriazopoulos, A. P., and Mallinis, G. (2020). Retrieval of leaf area index using sentinel-2 imagery in a mixed mediterranean forest area. *ISPRS Int. J. Geo Inf.* 9:622. doi: 10.3390/ijgi9110622

Clevers, J. G. P. W., and Gitelson, A. A. (2013). Remote estimation of crop and grass chlorophyll and nitrogen content using red-edge bands on sentinel-2 and-3. *Int. J. Appl. Earth Obs. Geoinf.* 23, 344–351. doi: 10.1016/j.jag.2012.10.008

Datta, S., Das, P., Dutta, D., and Giri, R. K. (2021). Estimation of surface moisture content using sentinel-1 c-band Sar data through machine learning models. *J. Indian Soc. Remote Sens.* 49, 887–896. doi: 10.1007/s12524-020-01261-x

Duan, T., Chapman, S. C., Guo, Y., and Zheng, B. (2017). Dynamic monitoring of ndvi in wheat agronomy and breeding trials using an unmanned aerial vehicle. *Field Crop Res* 210, 71–80. doi: 10.1016/j.fcr.2017.05.025

Dube, T., and Mutanga, O. (2015). Evaluating the utility of the medium-spatial resolution landsat 8 multispectral sensor in quantifying aboveground biomass in umgeni catchment, South Africa. *ISPRS J. Photogramm. Remote Sens.* 101, 36–46. doi: 10.1016/j.isprsjprs.2014.11.001

Eskandari, R., Mahdianpari, M., Mohammadimanesh, F., Salehi, B., Brisco, B., and Homayouni, S. (2020). Meta-analysis of unmanned aerial vehicle (uav) imagery for agro-environmental monitoring using machine learning and statistical models. *Remote Sens.* 12:3511. doi: 10.3390/rs12213511

Fang, P., Yan, N., Wei, P., Zhao, Y., and Zhang, X. (2021). Aboveground biomass mapping of crops supported by improved casa model and sentinel-2 multispectral imagery. *Remote Sens.* 13:2755. doi: 10.3390/rs13142755

Farrell, M., Gili, A., and Noellemeyer, E. (2018). Spectral indices from aerial images and their relationship with properties of a corn crop. *Precis. Agric.* 19, 1127–1137. doi: 10.1007/s11119-018-9570-9

Fei, S., Hassan, M. A., Ma, Y., Shu, M., Cheng, Q., Li, Z., et al. (2021). Entropy weight ensemble framework for yield prediction of winter wheat under different water stress treatments using unmanned aerial vehicle-based multispectral and thermal data. *Front. Plant Sci.* 12:730181. doi: 10.3389/fpls.2021.730181

Fortin, J. G., Anctil, F., and Parent, L. E. (2014). Comparison of multiple-layer perceptrons and least squares support vector machines for remote-sensed characterization of in-field lai patterns - a case study with potato. *Can. J. Remote. Sens.* 40, 75–84. doi: 10.1080/07038992.2014.928182

Garini, Y., Young, I. T., and McNamara, G. (2006). Spectral imaging: principles and applications. *Cytometry A* 69A, 735–747. doi: 10.1002/cyto.a.20311

Gibson, K. D., Dirks, R., Medlin, C. R., and Johnston, L. (2004). Detection of weed species in soybean using multispectral digital images. *Weed Technol.* 18, 742–749. doi: 10.1614/WT-03-170R1

Hassan, M. A., Yang, M., Rasheed, A., Yang, G., Reynolds, M., Xia, X., et al. (2019). A rapid monitoring of ndvi across the wheat growth cycle for grain yield prediction using a multi-spectral uav platform. *Plant Sci.* 282, 95–103. doi: 10.1016/j.plantsci.2018.10.022

He, L., Song, X., Feng, W., Guo, B., Zhang, Y., Wang, Y., et al. (2016). Improved remote sensing of leaf nitrogen concentration in winter wheat using multi-angular hyperspectral data. *Remote Sens. Environ.* 174, 122–133. doi: 10.1016/j.rse.2015.12.007

Hu, S., Shi, L., Huang, K., Zha, Y., Hu, X., Ye, H., et al. (2019). Improvement of sugarcane crop simulation by swap-wofost model via data assimilation. *Field Crop Res* 232, 49–61. doi: 10.1016/j.fcr.2018.12.009

Huang, Y., Reddy, K. N., Fletcher, R. S., and Pennington, D. (2018). Uav low-altitude remote sensing for precision weed management. *Weed Technol.* 32, 2–6. doi: 10.1017/wet.2017.89

Huang, Y., Ren, Z., Li, D., and Liu, X. (2020). Phenotypic techniques and applications in fruit trees: a review. *Plant Methods* 16:107. doi: 10.1186/s13007-020-00649-7

Huang, Y., Thomson, S. J., Brand, H. J., and Reddy, K. N. (2016). Development and evaluation of low-altitude remote sensing systems for crop production management. *Int. J. Agric. Biol. Engineer.* 9:1. doi: 10.3965/j.ijabe.20160904.2010

Hunt, E. R., Doraiswamy, P. C., McMurtrey, J. E., Daughtry, C. S. T., Perry, E. M., and Akhmedov, B. (2013). A visible band index for remote sensing leaf chlorophyll content at the canopy scale. *Int. J. Appl. Earth Obs. Geoinf.* 21, 103–112. doi: 10.1016/j.jag.2012.07.020

Immitzer, M., Vuolo, F., and Atzberger, C. (2016). First experience with sentinel-2 data for crop and tree species classifications in central europe. *Remote Sens.* 8:166. doi: 10.3390/rs8030166

Jayakumari, R., Nidamanuri, R. R., and Ramiya, A. M. (2021). Object-level classification of vegetable crops in 3d lidar point cloud using deep learning convolutional neural networks. *Precis. Agric.* 22, 1617–1633. doi: 10.1007/s11119-021-09803-0

Ke, Y., Quackenbush, L. J., and Im, J. (2010). Synergistic use of quickbird multispectral imagery and lidar data for object-based forest species classification. *Remote Sens. Environ.* 114, 1141–1154. doi: 10.1016/j.rse.2010.01.002

Kerkech, M., Hafiane, A., and Canals, R. (2020). Vine disease detection in uav multispectral images using optimized image registration and deep learning segmentation approach. *Comput. Electron. Agric.* 174:105446. doi: 10.1016/j.compag.2020.105446

Khan, M. R., Khan, I. A., Baig, M. H. A., Liu, Z., and Ashraf, M. I. (2020). Exploring the potential of sentinel-2a satellite data for aboveground biomass estimation in fragmented himalayan subtropical pine forest. *J. Mt. Sci.* 17, 2880–2896. doi: 10.1007/s11629-019-5968-8

Kim, J., Popescu, S. C., Lopez, R. R., Wu, X. B., and Silvy, N. J. (2020). Vegetation mapping of no name key, florida using lidar and multispectral remote sensing. *Int. J. Remote Sens.* 41, 9469–9506. doi: 10.1080/01431161.2020.1800125

Kross, A., McNairn, H., Lapen, D., Sunohara, M., and Champagne, C. (2015). Assessment of rapideye vegetation indices for estimation of leaf area index and biomass in corn and soybean crops. *Int. J. Appl. Earth Obs. Geoinf.* 34, 235–248. doi: 10.1016/j.jag.2014.08.002

Laamrani, A., Joosse, P., McNairn, H., Berg, A., Hagerman, J., Powell, K., et al. (2020). Assessing soil cover levels during the non-growing season using multitemporal satellite imagery and spectral unmixing techniques. *Remote Sens.* 12:1397. doi: 10.3390/rs12091397

Lee, H., Wang, J., and Leblon, B. (2020). Intra-field canopy nitrogen retrieval from unmanned aerial vehicle imagery for wheat and corn fields. *Can. J. Remote. Sens.* 46, 454–472. doi: 10.1080/07038992.2020.1788384

Li, T., Cui, L., Xu, Z., Hu, R., Joshi, P. K., Song, X., et al. (2021). Quantitative analysis of the research trends and areas in grassland remote sensing: a scientometrics analysis of web of science from 1980 to 2020. *Remote Sens.* 13:1279. doi: 10.3390/rs13071279

Li, F., Piasecki, C., Millwood, R. J., Wolfe, B., Mazarei, M., and Stewart, C. N. Jr. (2020a). High-throughput switchgrass phenotyping and biomass modeling by uav. *Front. Plant Sci.* 11:574073. doi: 10.3389/fpls.2020.574073

Li, X., Yang, C., Huang, W., Tang, J., Tian, Y., and Zhang, Q. (2020b). Identification of cotton root rot by multifeature selection from sentinel-2 images using random forest. *Remote Sens. (Basel)* 12:3504. doi: 10.3390/rs12213504

Luo, X. R., Li, S. D., Liu, L., Yang, W. N., Zhang, Y. H., Chen, G., et al. (2021). Quantifying aboveground vegetation water storage combining landsat 8 oli and sentinel-1 imageries. *Geocarto Int.* 37, 2717–2734. doi: 10.1080/10106049.2020.1861662

Maimaitijiang, M., Ghulam, A., Sidike, P., Hartling, S., Maimaitiyiming, M., Peterson, K., et al. (2017). Unmanned aerial system (uas)-based phenotyping of

soybean using multi-sensor data fusion and extreme learning machine. *ISPRS J. Photogramm. Remote Sens.* 134, 43–58. doi: 10.1016/j.isprsjprs.2017.10.011

Maimaitijiang, M., Sagan, V., Sidike, P., Hartling, S., Esposito, F., and Fritschi, F. B. (2020). Soybean yield prediction from uav using multimodal data fusion and deep learning. *Remote Sens. Environ.* 237:111599. doi: 10.1016/j.rse.2019.111599

Marston, Z. P. D., Cira, T. M., Hodgson, E. W., Knight, J. F., Macrae, I. V., and Koch, R. L. (2020). Detection of stress induced by soybean aphid (hemiptera: aphididae) using multispectral imagery from unmanned aerial vehicles. *J. Econ. Entomol.* 113, 779–786. doi: 10.1093/jee/toz306

Mathews, A., and Jensen, J. (2013). Visualizing and quantifying vineyard canopy lai using an unmanned aerial vehicle (uav) collected high density structure from motion point cloud. *Remote Sens.* 5, 2164–2183. doi: 10.3390/rs5052164

Mazzia, V., Comba, L., Khaliq, A., Chiaberge, M., and Gay, P. (2020). Uav and machine learning based refinement of a satellite-driven vegetation index for precision agriculture. *Sensors.* 20:2530. doi: 10.3390/s20092530

Memon, M. S., Jun, Z., Sun, C., Jiang, C., Xu, W., Hu, Q., et al. (2019). Assessment of wheat straw cover and yield performance in a rice-wheat cropping system by using landsat satellite data. *Sustainability* 11:5369. doi: 10.3390/su11195369

Mesas-Carrascosa, F. J., Clavero Rumbao, I., Torres-Sánchez, J., García-Ferrer, A., Peña, J. M., and López Granados, F. (2017). Accurate ortho-mosaicked six-band multispectral uav images as affected by mission planning for precision agriculture proposes. *Int. J. Remote Sens.* 38, 2161–2176. doi: 10.1080/01431161.2016.1249311

Messina, G., Praticò, S., Badagliacca, G., Di Fazio, S., Monti, M., and Modica, G. (2021). Monitoring onion crop "cipolla rossa di tropea Calabria igp" growth and yield response to varying nitrogen fertilizer application rates using uav imagery. *Drones* 5:61. doi: 10.3390/drones5030061

Minařík, R., Langhammer, J., and Lendzioch, T. (2020). Automatic tree crown extraction from uas multispectral imagery for the detection of bark beetle disturbance in mixed forests. *Remote Sens.* 12:4081. doi: 10.3390/rs12244081

Mountrakis, G., Im, J., and Ogole, C. (2011). Support vector machines in remote sensing: a review. *ISPRS J. Photogramm. Remote Sens.* 66, 247–259. doi: 10.1016/j.isprsjprs.2010.11.001

Mutanga, O., Adam, E., and Cho, M. A. (2012). High density biomass estimation for wetland vegetation using worldview-2 imagery and random forest regression algorithm. *Int. J. Appl. Earth Obs. Geoinf.* 18, 399–406. doi: 10.1016/j.jag.2012.03.012

Näsi, R., Viljanen, N., Kaivosoja, J., Alhonoja, K., Hakala, T., Markelin, L., et al. (2018). Estimating biomass and nitrogen amount of barley and grass using uav and aircraft based spectral and photogrammetric 3d features. *Remote Sens.* 10:1082. doi: 10.3390/rs10071082

Osco, L. P., Arruda, M. D. S. D., Marcato Junior, J., Da Silva, N. B., Ramos, A. P. M., Moryia, E. A. S., et al. (2020a). A convolutional neural network approach for counting and geolocating citrus-trees in uav multispectral imagery. *ISPRS J. Photogramm. Remote Sens.* 160, 97–106. doi: 10.1016/j.isprsjprs.2019.12.010

Osco, L. P., Junior, J. M., Ramos, A. P. M., Furuya, D. E. G., Santana, D. C., Teodoro, L. P. R., et al. (2020b). Leaf nitrogen concentration and plant height prediction for maize using uav-based multispectral imagery and machine learning techniques. *Remote Sens.* 12:3237. doi: 10.3390/rs12193237

Pena, J. M., Torres-Sanchez, J., de Castro, A. I., Kelly, M., and Lopez-Granados, F. (2013). Weed mapping in early-season maize fields using object-based analysis of unmanned aerial vehicle (uav) images. *PLoS One* 8:e77151. doi: 10.1371/journal.pone.0077151

Peng, X., Han, W., Ao, J., and Wang, Y. (2021). Assimilation of lai derived from uav multispectral data into the safy model to estimate maize yield. *Remote Sens.* 13:1094. doi: 10.3390/rs13061094

Periasamy, S., and Shanmugam, R. S. (2016). Multispectral and microwave remote sensing models to survey soil moisture and salinity. *Land Degrad. Dev.* 28, 1412–1425. doi: 10.1002/ldr.2661

Ramoelo, A., Cho, M. A., Mathieu, R., Madonsela, S., van de Kerchove, R., Kaszta, Z., et al. (2015). Monitoring grass nutrients and biomass as indicators of rangeland quality and quantity using random forest modelling and worldview-2 data. *Int. J. Appl. Earth Obs. Geoinf.* 43, 43–54. doi: 10.1016/j.jag.2014.12.010

Ramos, T. B., Castanheira, N., Oliveira, A. R., Paz, A. M., Darouich, H., Simionesei, L., et al. (2020). Soil salinity assessment using vegetation indices derived from sentinel-2 multispectral data. Application to lezíria grande, Portugal. *Agric Water Manag* 241:106387. doi: 10.1016/j.agwat.2020.106387

Raparelli, E., and Bajocco, S. (2019). A bibliometric analysis on the use of unmanned aerial vehicles in agricultural and forestry studies. *Int. J. Remote Sens.* 40, 9070–9083. doi: 10.1080/01431161.2019.1569793

Sa, I., Chen, Z., Popovic, M., Khanna, R., Liebisch, F., Nieto, J., et al. (2018). Weednet: dense semantic weed classification using multispectral images and mav for smart farming. *IEEE Robot. Automat. Lett.* 3, 588–595. doi: 10.1109/LRA.2017.2774979

Sankaran, S., Mishra, A., Ehsani, R., and Davis, C. (2010). A review of advanced techniques for detecting plant diseases. *Comput. Electron. Agric.* 72, 1–13. doi: 10.1016/j.compag.2010.02.007

Sullivan, D. G., Shaw, J. N., Mask, P. L., Rickman, D., Luvall, J., and Wersinger, J. M. (2004). Evaluating corn nitrogen variability via remote-sensed data. *Commun. Soil Sci. Plant Anal.* 35, 2465–2483. doi: 10.1081/LCSS-200030339

Theseira, M. A., Thomas, G., and Sannier, C. A. D. (2002). An evaluation of spectral mixture modelling applied to a semi-arid environment. *Int. J. Remote Sens.* 23, 687–700. doi: 10.1080/01431160010019652

Torres-Sánchez, J., López-Granados, F., and Peña, J. M. (2015a). An automatic object-based method for optimal thresholding in uav images: application for vegetation detection in herbaceous crops. *Comput. Electron. Agric.* 114, 43–52. doi: 10.1016/j.compag.2015.03.019

Torres-Sánchez, J., López-Granados, F., Serrano, N., Arquero, O., and Peña, J. M. (2015b). High-throughput 3-d monitoring of agricultural-tree plantations with unmanned aerial vehicle (uav) technology. *PLoS One* 10:e130479. doi: 10.1371/journal.pone.0130479

Tsouros, D. C., Bibi, S., and Sarigiannidis, P. G. (2019). A review on uav-based applications for precision agriculture. *Information* 10:349. doi: 10.3390/info10110349

van Eck, N. J., and Waltman, L. (2010). Software survey: vosviewer, a computer program for bibliometric mapping. *Scientometrics* 84, 523–538. doi: 10.1007/s11192-009-0146-3

Veeranampalayam Sivakumar, A. N., Li, J., Scott, S., Psota, E., Jhala, A. J., Luck, J. D., et al. (2020). Comparison of object detection and patch-based classification deep learning models on mid-to late-season weed detection in uav imagery. *Remote Sens. (Basel)* 12:2136. doi: 10.3390/rs12132136

Venkatesh, Y. V., and Kumar Raja, S. (2003). On the classification of multispectral satellite images using the multilayer perceptron. *Pattern Recogn.* 36, 2161–2175. doi: 10.1016/S0031-3203(03)00013-X

Wijesingha, J., Dayananda, S., Wachendorf, M., and Astor, T. (2021). Comparison of spaceborne and uav-borne remote sensing spectral data for estimating monsoon crop vegetation parameters. *Sensors* 21:2886. doi: 10.3390/s21082886

Xie, H., Zhang, Y., Wu, Z., and Lv, T. (2020). A bibliometric analysis on land degradation: current status, development, and future directions. *Land* 9:28. doi: 10.3390/land9010028

Xue, J., and Su, B. (2017). Significant remote sensing vegetation indices: a review of developments and applications. *J. Sensors* 2017, 1–17. doi: 10.1155/2017/1353691

Yu, N., Li, L., Schmitz, N., Tiaz, L. F., Greenberg, J. A., and Diers, B. W. (2016). Development of methods to improve soybean yield estimation and predict plant maturity with an unmanned aerial vehicle based platform. *Remote Sens. Environ.* 187, 91–101. doi: 10.1016/j.rse.2016.10.005

Yu, J., Wang, J., and Leblon, B. (2021). Evaluation of soil properties, topographic metrics, plant height, and unmanned aerial vehicle multispectral imagery using machine learning methods to estimate canopy nitrogen weight in corn. *Remote Sens.* 13:3105. doi: 10.3390/rs13163105

Yu, D., Xu, T., and Song, K. (2018). Nondestructive testing of external defects on nanguo pear. *Spectrosc. Lett.* 51, 191–197. doi: 10.1080/00387010.2018.1447968

Zaman-Allah, M., Vergara, O., Araus, J. L., Tarekegne, A., Magorokosho, C., Zarco-Tejada, P. J., et al. (2015). Unmanned aerial platform-based multi-spectral imaging for field phenotyping of maize. *Plant Methods* 11:35. doi: 10.1186/s13007-015-0078-2

Zanardo, F. H., Rodrigues, R. A. F., Silva, H. R., Marques, A. P., and Faria, G. A. (2016). Geotechnology application for data acquisition for agricultural and environmental management of the municipality of vitória Brazil-sp. *Engenharia Agrícola* 36, 684–695. doi: 10.1590/1809-4430-Eng.Agric.v36n4p684-695/2016

Zhang, C., and Kovacs, J. M. (2012). The application of small unmanned aerial systems for precision agriculture: a review. *Precis. Agric.* 13, 693–712. doi: 10.1007/s11119-012-9274-5

Zhang, Y., Thenkabail, P. S., and Wang, P. (2019). A bibliometric profile of the remote sensing open access journal published by mdpi between 2009 and 2018. *Remote Sens.* 11:91. doi: 10.3390/rs11010091

Zhou, X., Zheng, H. B., Xu, X. Q., He, J. Y., Ge, X. K., Yao, X., et al. (2017). Predicting grain yield in rice using multi-temporal vegetation indices from uav-based multispectral and digital imagery. *ISPRS J. Photogramm. Remote Sens.* 130, 246–255. doi: 10.1016/j.isprsjprs.2017.05.003

Zhu, W., Rezaei, E. E., Nouri, H., Yang, T., Li, B., Gong, H., et al. (2021). Quick detection of field-scale soil comprehensive attributes via the integration of uav and sentinel-2b remote sensing data. *Remote Sens.* 13:4716. doi: 10.3390/rs13224716

Zhu, W., Sun, Z., Peng, J., Huang, Y., Li, J., Zhang, J., et al. (2019a). Estimating maize above-ground biomass using 3d point clouds of multi-source unmanned aerial vehicle data at multi-spatial scales. *Remote Sens.* 11:2678. doi: 10.3390/rs11222678

Zhu, W., Sun, Z., Huang, Y., Lai, J., Li, J., Zhang, J., et al. (2019b). Improving field-scale wheat lai retrieval based on uav remote-sensing observations and optimized vi-luts. *Remote Sens.* 11:2456. doi: 10.3390/rs11202456

agriculture

MDPI

Article

Detection of Rice Spikelet Flowering for Hybrid Rice Seed Production Using Hyperspectral Technique and Machine Learning

Yali Zhang [1,2], Luchao Bai [1,2], Yuan Qi [3], Huasheng Huang [4], Xiaoyang Lu [1,2], Junqi Xiao [1,2], Yubin Lan [2,5], Muhua Lin [1] and Jizhong Deng [1,2,*]

1 College of Engineering, South China Agricultural University, Guangzhou 510642, China; ylzhang@scau.edu.cn (Y.Z.); blc@stu.scau.edu.cn (L.B.); luxiaoyang@stu.scau.edu.cn (X.L.); 20213142028@stu.scau.edu.cn (J.X.); 20010817@stu.scau.edu.cn (M.L.)
2 National Center for International Collaboration Research on Precision Agricultural Aviation Pesticide Spraying Technology, Guangzhou 510642, China; ylan@scau.edu.cn
3 College of Mechanical Engineering, Nantong Vocational University, Nantong 226007, China; yuanqi@mail.ntvu.edu.cn
4 College of Computer Sciences, Guangdong Polytechnic Normal University, Zhongshan Road, Guangzhou 510642, China; huanghsheng@gpnu.edu.cn
5 College of Electronic Engineering and College of Artificial Intelligence, South China Agricultural University, Guangzhou 510642, China
* Correspondence: jz-deng@scau.edu.cn

Abstract: Effective detection of rice spikelet flowering is crucial to the determination of optimal pollination timing for hybrid rice seed production. Currently, the detection of rice spikelet flowering status relies on manual observation of farmers, which has low efficiency and large errors. This study attempts to acquire rice spikelet flowering information using a hyperspectral technique and machine learning in order to meet the needs of hybrid rice seed pollination rapidly and automatically. Hyperspectral data of rice male parents with flowering and non-flowering in two experimental sites were collected with an ASD FieldSpec® HandHeld™2 spectrometer. Three traditional classifiers, Random Forest (RF), Support Vector Machine (SVM) and Back Propagation (BP) neural network, and Convolutional Neural Network (CNN), were used to build classification models for rice spikelets flowering detection. Three data processing methods, PCA feature extraction, GA feature selection, and the PCA and GA combination algorithm, were used for data dimensionality reduction. By comparing the precision and recall rate of different algorithms and data processing methods, the algorithms applicable to identify rice spikelet flowering were investigated. Results show that by evaluating different feature reduction methods and classifiers, the optimal model for rice spikelets flowering detection is the BP model with PCA feature extraction. The accuracy of the model reaches up to 96–100%. Hyperspectral technology and machine learning algorithm are capable of effective detection of rice spikelet flowering. This study provides technical reference for accurate judgment of rice flowering and helps to determine the optimal operation time for supplementary pollination of hybrid rice.

Keywords: hyperspectral; machine learning; CNN; rice spikelets; RF; SVM; BP neural network; PCA; GA analysis

check for updates

Citation: Zhang, Y.; Bai, L.; Qi, Y.; Huang, H.; Lu, X.; Xiao, J.; Lan, Y.; Lin, M.; Deng, J. Detection of Rice Spikelet Flowering for Hybrid Rice Seed Production Using Hyperspectral Technique and Machine Learning. *Agriculture* **2022**, *12*, 755. https://doi.org/10.3390/agriculture12060755

Academic Editors: Nen-Fu Huang and Ho-Hsien Chen

Received: 12 April 2022
Accepted: 23 May 2022
Published: 25 May 2022

Publisher's Note: MDPI stays neutral with regard to jurisdictional claims in published maps and institutional affiliations.

Copyright: © 2022 by the authors. Licensee MDPI, Basel, Switzerland. This article is an open access article distributed under the terms and conditions of the Creative Commons Attribution (CC BY) license (https://creativecommons.org/licenses/by/4.0/).

1. Introduction

Rice is a non-strict self-pollination crop. Generally, the success rate of rice pollination under natural conditions is only 0.2% to 5%. Supplementary pollination during rice's flowering period is the key to the success of hybrid rice seed production. Rice spikelet flowering requires 28–30 °C and 70–80% relative humidity. Although the flowering period is 10–12 days, its flowering time each day is 1.5–2 h and the pollen life is only 4–5 min; therefore, effective

detection of rice spikelet flowering is crucial for the timely determination of optimal pollination timing for hybrid rice seed production, so as to improve the pollen utilization rate and seed setting rate of the female parent of hybrid rice [1].

Currently, the detection of rice spikelet flowering in hybrid rice seed production mainly relies on manual observation through farmers' naked eyes [2]; however, manual observation is not only time-consuming, laborious, and inaccurate, but also subjective and discontinuous, which makes it easy to miss the best pollination period. In large-scale hybrid rice seed production farms, it is even more important to obtain the rice spikelet's flowering state by machine instead of a farmer [3].

In recent years, experts and scholars have carried out a lot of research on the monitoring of plant flowering, most of which used camera [4–6], multispectral technology [7,8] and hyperspectral technology [9] to obtain flowering information and identify or evaluate the color, shape and appearance characteristics of flowers. Zhao et al. [10] improved Flower Extraction Feature Pyramid Networks (FE-FPN) to extract the local regional features of a tomato bouquet. In addition, the local bouquet images with prioritized order were input into the improved Yolov3 network to realize the accurate identification of tomato flowers with an accuracy of 85.18%. Deng et al. [11] identified and counted the number of citrus flowers based on case segmentation and used a camera to obtain an image of the citrus crown during the flowering period so as to identify and segment the flowers. The experimental results show that the proposed method is superior to the unoptimized MaskR-CNN network in both accuracy improvement and training efficiency. Wang et al. [12] proposed a new algorithm DeepPhenology based on CNN and RGB images to estimate the phenological distribution of apple flowers. The comparison between the algorithm results and the YOLOv5 model further evaluated the performance of the model in this task, and the results showed that the model was superior to the most advanced target detection model. Cai et al. [13] applied three deep neural networks, RetinaNet, YOLOv5 and FtP-RCNN, to extract the spike number of sorghum and found that YOLOv5 indicated the best counting accuracy in estimation of the flowering time of sorghum.

All of these studies use machine learning to identify crop or fruit flowering, but few studies have been reported on flowering rice identification, and only a few studies have applied deep learning techniques to flowering rice status detection. During the process of rice flowering, the content of its biochemical components changes, which makes the spectral reflectance of the rice spikelet change. The spectral data collected by hyperspectral technology are continuous in wavelength and carry a lot of effective information. Hyperspectral data are extremely sensitive to the perception of subtle changes occurring in the target detectors, which is also an advantage of using hyperspectral technology to detect the flowering state of rice spikelets compared with other devices such as visible light cameras or multispectral cameras. This study combines hyperspectral and machine learning techniques to detect the spikelet flowering information of rice for a large-scale hybrid rice seed production farm. Hyperspectral data of flowering and non-flowering rice spikelets were collected for analysis. Three machine learning methods (RF, SVM and BP neural network) and CNN were used to establish the binary classification detection model of the rice flowering state. PCA feature extraction, GA feature selection and PCA and GA combination algorithm were used to reduce the dimensionality of hyperspectral data, and the characteristic bands that could be used for rice spikelet flowering detection were determined. In this study, computer qualitative analysis of rice flowering was used instead of manual qualitative observation to provide technical reference for accurate judgment of rice flowering and help to determine the optimal operation time for supplementary pollination of hybrid rice.

2. Materials and Methods

2.1. Data Acquisition and Preprocessing

2.1.1. Experiment Site

The rice flowering data were obtained in two sites (Figure 1). The first batch of sample data was collected from Hybrid Rice Breeding Base in Dongfang, Hainan Province. The second batch of data was collected from Longping Hi-tech Breeding Base in Shaoyang, Hunan Province. It was sunny and cloudless when collecting data. The temperature was between 28 °C and 31 °C. The above meteorological data were collected from a Kestrel NK5000 series handheld meteorological monitoring instrument (Nielsen-Kellerman, Boothwyn, PA, USA).

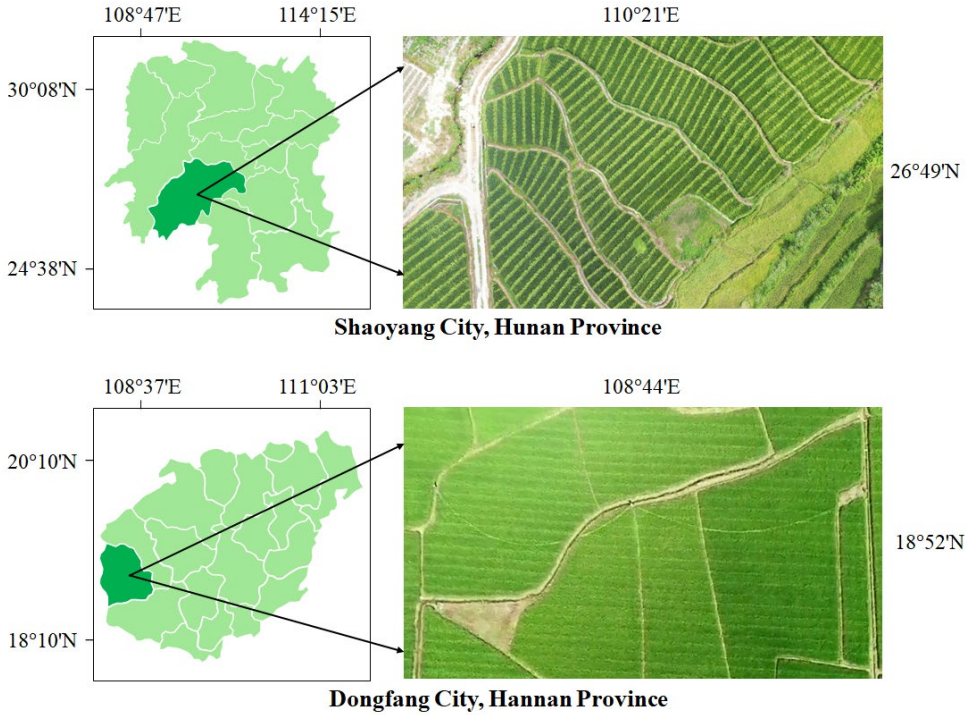

Figure 1. Overview of the experiment site.

The rice in two experimental sites was cultivated by manual transplanting. Experiments were carried out during the jointing and flowering stages of rice. The male parent was planted 24 days earlier than the female parent, and the planting ratio is 2:10 between male and female plants. The male plants will be cut off early after the flowering period, which provides sufficient sunlight and nutrients to the female plants and reduces pests and disease occurrence.

2.1.2. Data Acquisition

Rice flowering information was acquired with an ASD FieldSpec® HandHeld™ 2 spectrometer (Malvern Panalytical Ltd., Malvern, UK), which was equipped with a unique spectral acquisition instrument capable of rapid the nondestructive acquisition of spectra in the wavelength range of 325–107 nm. When measuring the hyperspectral data of the rice spikelet, it is necessary to ensure the normal operation of the handheld spectroscopic radiation spectrum so that it can accurately reflect the spectral reflection information of the rice spikelet. After the instrument startup system is loaded, the standard whiteboard with 100% reflectivity is collected for black-and-white calibration. For each data acquisition, 5 groups of hyperspectral data were collected simultaneously by a handheld spectroradiometer to reduce systematic random errors.

It is necessary to ensure that the data are collected under high light intensity and cloudless weather as far as possible to avoid the influence of external factors such as light intensity on the experimental data. In the case of cloud cover, it is necessary to wait for

the cloud to disperse before continuing to collect, and at the same time, it is necessary to conduct whiteboard calibration again to ensure the accuracy of spectral data collection. In addition, when the instrument is used for collection work for a long time, even if there is no influence of external environmental factors, the whiteboard calibration needs to be carried out every 5 min to reduce the error caused by the heat generated by the instrument that occurs over long periods.

In order to ensure that the measurement is the characterization region of the rice spike, the probe of the handheld spectral radiation spectrum was put directly facing the middle of the rice spike during measurement to ensure that the rice spike is within the coverage range of the radiation spectrometer. At the same time, the instrument and the rice spike to be measured were kept a fixed distance (Figure 2).



Figure 2. Hyperspectral data acquisition of rice spikelets.

In the Hybrid Rice Breeding Base in Dongfang, Hainan Province, 1236 hyperspectral data of rice spikelets were collected, and 1115 effective spectral data were kept for analysis after removing obvious abnormal data, with a wavelength range of 325–1075 nm. In Longping Hi-tech Breeding Base in Shaoyang, Hunan Province, 4036 hyperspectral data of spikelet were collected, and 3000 effective spectral data were obtained after removing obvious abnormal data, with a wavelength range of 325–1075 nm. The experimental data were collected in chronological order. Spectral data of the panicle region were first collected before the flowering of the male parent of hybrid rice and then during flowering time.

Training and test data sets were divided based on a ratio of 4:1, as shown in Table 1. The relationship between spikelet reflectance and wavelength of rice before and after flowering is shown in Figure 3 (Hunan Province) and Figure 4 (Hainan Province). As can be seen from Figures 3a and 4a, there is a large degree of overlap between spectral data of flowering and non-flowering rice, which is difficult to distinguish from artificial observation.

Table 1. Sample size of training and test set of hyperspectral data.

	Training		**Test**	
	Flowering	**Non-Flowering**	**Flowering**	**Non-Flowering**
Hainan sample	400	400	100	100
Hunan sample	400	400	100	100
All samples	800	800	200	200

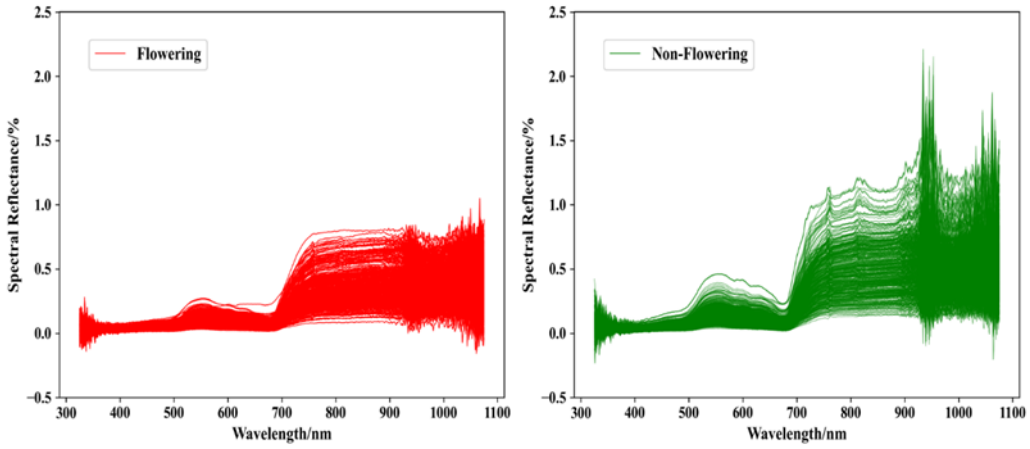

Figure 3. Relationship between reflectance and wavelength of flowering and non-flowering spikelets of rice in Hunan province (**a**) non-flowering spikelets; (**b**) flowering spikelets.

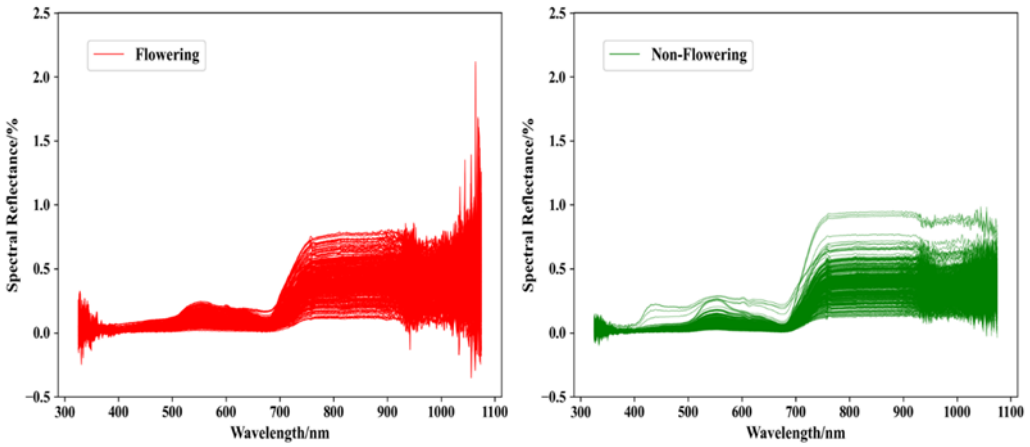

Figure 4. Relationship between reflectance and wavelength of flowering and non-flowering spikelets of Rice in Hainan province (**a**) non-flowering spikelets; (**b**) flowering spikelets.

2.1.3. Data Preprocessing

Considering that weather fluctuation affects data accuracy, multiple pretreatments were carried out for collected hyperspectral data. Hyperspectral data of rice spikelets were preprocessed simply by using ViewSpecPro, the supporting software of the spectrometer.

1. Mean calculation: During data acquisition, the ASD FieldSpec®® HandHeld™ 2 spectrometer was set to repeatedly sample five hyperspectral curves, thus reducing the inherent error of the original spectral data; therefore, in the data preprocessing step, the collected sample data were averaged first.
2. Spectral reflectance calculation: The spectral reflectance of the target can be calculated through Equation (1).

$$R_{goal} = \frac{Rad_{goal}}{Rad_{board}} \times R_{board} \times 100\% \quad (1)$$

where R_{goal} on the left and right sides of the equation, respectively, represents the target spectral reflectance and the target light intensity value; the lower Rad_{board} represents the whiteboard light intensity value of the spectrometer and the other R_{board} represents the whiteboard reflectance.

After simple preprocessing, a total of 3000 hyperspectral data of rice spikelets were obtained, including 1500 non-flowering and 1500 in full bloom. Each set of data has relative independence.

2.2. Classification Model for Detection of Rice Spikelets Flowering

Three traditional machine learning models, Random Forest (RF), Support Vector Machine (SVM), and Back Propagation (BP) neural network, as well as Convolutional Neural Network (CNN), were used to classify rice flowering using full-band spectral data. The generalization ability and deficiency of different classifiers in rice spikelet flowering detection were compared to investigate the suitable algorithm. Hyperparameters were selected using a grid search (for a given hyperparameter, set the start value, end value and interval) to test their performance on the training set and thus find the best parameter. We tested the accuracy of the model with different model hyperparameters. In RF, for the number of subtrees, the accuracy of the model between 10 and 400 was tested with 10 as the interval; for the maximum decision tree depth, the accuracy of the model from 2 to 20 was tested with 1. As in SVM, the penalty parameter C was tested for the accuracy of the SVM between $[2^{-5}, 2^{-4}, \ldots, 2^{9}, 2^{10}]$. As in BP networks, the accuracy of the model with the number of hidden layers between [5, 10, . . . , 180] was tested. The CNN algorithm has a convolutional kernel size of 3×3 and a step size of 2.

2.2.1. RF Algorithm

RF algorithm is widely applied to solve classification and regression type problems in many fields [14–16]. The algorithm adopts the ensemble learning method. By establishing a random forest (i.e., multiple classifiers), also known as a random forest decision tree, each decision tree in the random forest (i.e., each classifier) classifies the input data and then carries out the voting statistics to obtain the overall classification result.

The construction rules of the random forest [17] are as follows: (1) Defining the training sample set N: For each decision tree in the random forest, draw N training samples from the sample set in a releasing manner and arbitrarily, and define it as the training set of the decision tree; (2) assuming that N is the feature dimension of each sample, take a constant value n that is much smaller than N, select any subset of n features from N, and extract the optimal term from the n features obtained whenever the decision tree is split; (3) any decision tree in a random forest needs to grow to the maximum extent allowed by the conditions and has not undergone pruning operations during its growth and division. The algorithm flow chart is shown in Figure 5.

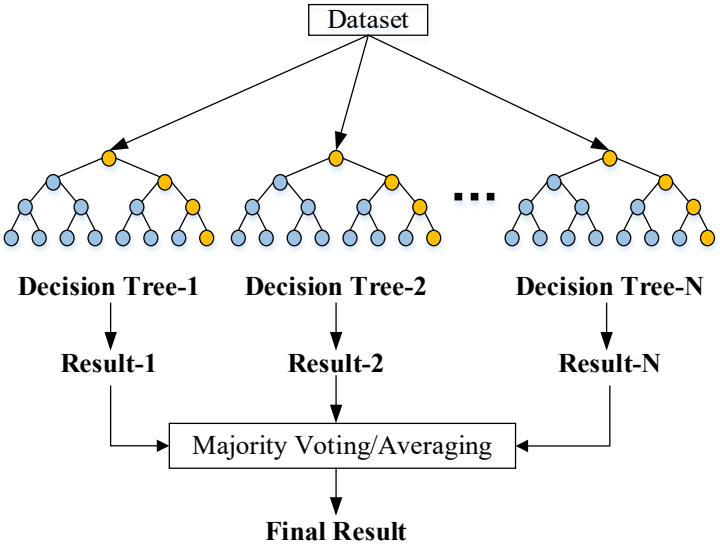

Figure 5. Flow chart of RF algorithm.

RF algorithm uses an integrated algorithm, which is easy to make into a parallelized method because each tree can be generated independently and simultaneously, and the random forest does not easily fall into overfitting; however, when the number of decision trees in the random forest is large, the time and space complexity of model training will be relatively high.

2.2.2. SVM Algorithm

The basic idea of the SVM algorithm is to map data to a high-dimensional feature space through nonlinear mapping and finally build an optimal classification hyperplane in the high-dimensional feature space so as to separate the nonlinear data. It can not only use a relatively simple algorithm to determine key sample feature data but also has good robustness [18].

SVM algorithm has two main principle features. SVM is targeted at linearly separable cases. When dealing with linearly indivisible cases, nonlinear features need to be transformed into linearly separable features. In this case, the low-dimensional input space linearly indivisible samples are converted into high-dimensional feature space by a nonlinear mapping algorithm and then analyzed by a linear algorithm. Based on the theory of minimum structural risk, SVM constructs the optimal classification plane in the feature space to obtain the global optimal solution for the learner. Another point is based on the principle of SVM, where a small number of support vectors determine the final classification decision result.

2.2.3. BP Neural Network

BP neural network [19] is a concept of multi-level feedforward neural network trained according to the backward error propagation algorithm. It is a widely used traditional neural network model. Its training method is an error back propagation algorithm, through which the weight and threshold of the neural network are constantly adjusted and modified to obtain the minimum mean square error value, and finally results in the optimal fitting degree of the data. Its network model topology is composed of three parts: input layer, hide layer and output layer. Figure 6 gives a brief demonstration on the flow chart of BP neural network, where X_1, X_2, X_n represent the input hyperspectral reflectance consisting of 751 channels. BP neural network algorithm consists of two parts: signal forward conduction and error result reverse conduction.

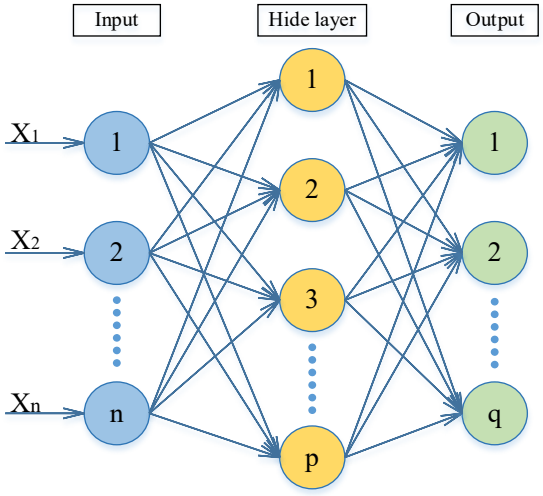

Figure 6. BP neural network flow chart.

The function of the input layer of the BP neural network is to transmit the input information received from the outside to the middle layer, and each neuron in the middle layer transforms the input information. According to the demand for information transformation processing ability to design a single hidden layer structure or more hidden layer structure,

then through the last hidden layer, the processed information is transmitted to the output layer for subsequent processing. Finally, the output layer of the neural network will output the information processing results obtained in the neural network algorithm. At this point, if there is a difference between the actual output value and the expected output value, the error will enter the reverse conduction stage. The weight will be modified and adjusted in all layers of the neural network according to the gradient descent method, and the error will be reverse transmitted through the output layer to the middle layer and then to the input layer. The training process of a neural network that is constantly repeating information forward conduction and error reverse conduction of weights within every level continuously in the process of adjustment. The training process continues until the error of the neural network output achieves an acceptable level or is set in advance of the neural network to build learning.

2.2.4. CNN Algorithm

CNN is one of the representative algorithms of deep learning. It is a type of feed-forward neural network with a deep structure, including convolution computation. The CNN algorithm has been widely used in various fields of classification, retrieval, identification (classification and regression), segmentation, feature extraction, key point positioning (posture recognition) and other scenes [20]. The structure of CNN is usually composed of an input layer, convolutional layer, pooling layer, fully connected layer and output layer. Figure 7 shows the classical structure of the CNN algorithm.

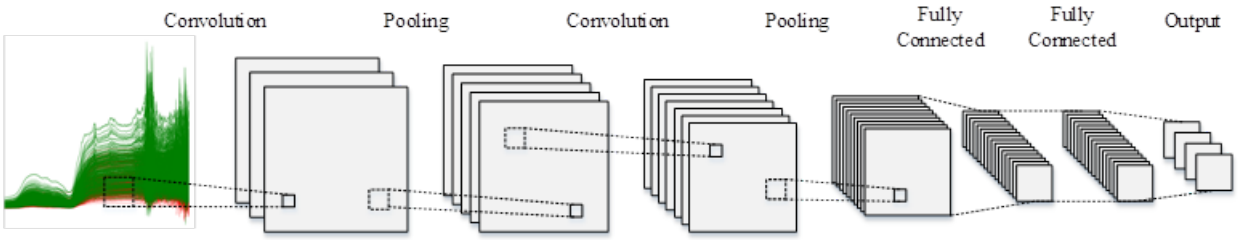

Figure 7. Schematic diagram of CNN algorithm.

The input layer of the CNN inputs the target detection sample into the CNN structure. When the sample data are fed into the input layer, the computer treats the input as a matrix and performs a series of transformations on the matrix before feeding it into the next layer of the structure. The convolutional layer is a unique structure of the CNN algorithm model and a core layer of the whole neural network, which produces most of the computational work. The structure used by the combination of the convolutional layer and the pooling layer can be set repeatedly in the hidden layer. The function of the convolution layer is to deepen the original matrix, and the nodes processed by the convolution layer will obtain a deeper matrix. The pooling layer extracts the main information of the samples based on the principle of local connectivity of the features in order to reduce the amount of data processing. It does not change the depth of the 3D matrix, but the size of the matrix is reduced, thus reducing the parameters in the whole neural network and the number of training dimensions. The fully connected layer is a structure that weighs all the neurons between the two layers, and the last output layer serves as the target result. These two parts are generally configured at the end of the CNN model. CNN uses original samples as input, which can effectively learn corresponding features from a large number of samples and avoid a complex feature extraction process. CNN algorithm can also be used for the classification of 1D data by varying the size of the convolutional kernel.

2.3. Data Dimensionality Reduction Algorithm

Although hyperspectral data receive high classification accuracy under the above four classification models, the original data have a high dimension and a slow operation rate; therefore, dimensionality reduction was performed to improve the running speed

and accuracy of the model. Two commonly used dimensionality reduction methods were selected in this study. Rice flowering detection was then conducted on the basis of feature dimensionality reduction in order to obtain better results.

2.3.1. Principal Component Analysis

Principal Component Analysis (PCA) [21] is the most widely used data dimensionality reduction algorithm. The main idea of the PCA algorithm is to map n-dimensional features to k-dimensional features. These new orthogonal features, also called principal components, are reconstructed from the original n-dimensional features. The job of PCA is to find a set of mutually orthogonal axes in turn from the original space, and the choice of new axes is closely related to the data itself. The first new axis is selected in the direction of the greatest difference in the original data. The second axis is selected in a plane orthogonal to the first axis to maximize the variance. The third axis is selected in a plane orthogonal to the first and second axes to maximize the variance. By analogy, n such axes are obtained. The new axis obtained in this way contains most of the variance of the first k axes, and the variance of the last axis is almost zero. This is equivalent to reducing the dimensionality of the data features by retaining only the dimensional features that contain most of the variance and ignoring the dimensional features that contain almost zero variance.

By calculating the covariance matrix of the data matrix and then obtaining the eigenvalue and eigenvectors of the covariance matrix, the matrix consisting of the eigenvectors corresponding to the k features with the largest eigenvalue (i.e., the largest variance) is then selected. The data matrix is transformed into a new space to achieve dimensionality reduction in data features. At present, there are mainly two methods to obtain the eigenvalue and eigenvector of covariance matrix: the PCA algorithm based on eigenvalue decomposition covariance matrix and the PCA algorithm based on the SVD decomposition covariance matrix.

2.3.2. Genetic Algorithm

A Genetic Algorithm (GA) is a computational model that simulates the biological evolution process of natural selection and genetic mechanism in Darwin's biological evolution theory. It is a method to find out the optimal solution by simulating the natural evolution process. When solving complex combinatorial optimization problems, it usually obtains better optimization results faster than some traditional optimization algorithms. GA has been widely used in combinatorial optimization [22], machine learning [23], signal processing [24], adaptive control [25] and artificial life.

GA starts with a population that represents a set of possible solutions to a problem. A population consists of a certain number of genetically coded individuals. Each individual is actually a chromosomal entity with characteristics. After the initial population is generated, according to the principle of survival of the fittest, it evolves generation by generation to produce better and better approximate solutions. In each generation, individuals are selected according to their fitness in the problem domain, and combined crossover and mutation are performed with the help of natural genetic operators to generate a population representing a new set of solutions. This process will produce a metapopulation similar to natural evolution, which is more adaptable than its predecessors, and the best individuals in the previous generation are decoded and can be used as approximate optimal solutions to the problem.

2.4. Evaluation of Algorithm Accuracy

The prediction results of the model for rice flowering detection were as follows: *TP* (true positive): positive samples were correctly predicted as positive samples, i.e., the data of spikelet flowering were predicted as flowering. *FP* (false positive): a negative sample is incorrectly predicted as a positive sample, i.e., a non-flowering spikelet is predicted as flowering. *TN* (true negative): negative samples were correctly predicted as negative samples, i.e., non-flowering data were predicted as non-flowering. *FN* (false negative):

positive samples were wrongly predicted as negative samples, i.e., the data on flowering of spikelets were predicted as non-flowering.

The evaluation indexes are precision (the proportion of the total number of rice spikelets flowering that can be correctly detected) and recall (the proportion of correctly predicted rice spikelets flowering in total actual flowering), which can be calculated by Equations (2) and (3), respectively.

$$Precision = \frac{TP}{TP + FP} \tag{2}$$

$$Recall = \frac{TP}{TP + FN} \tag{3}$$

3. Results

3.1. Classification Accuracy before Feature Dimensionality Reduction

The 800 sets of 751-dimensional hyperspectral data from Hainan, 800 sets of 751-dimensional data from Hunan and 1600 sets of 751-dimensional mixed data from Hainan and Hunan were input to the traditional classifiers and deep learning model for training. A total of 200 sets of Hainan data, 200 sets of Hunan data, and 400 sets of mixed data were used for validation. The correlation results of each group are shown in Figure 8.

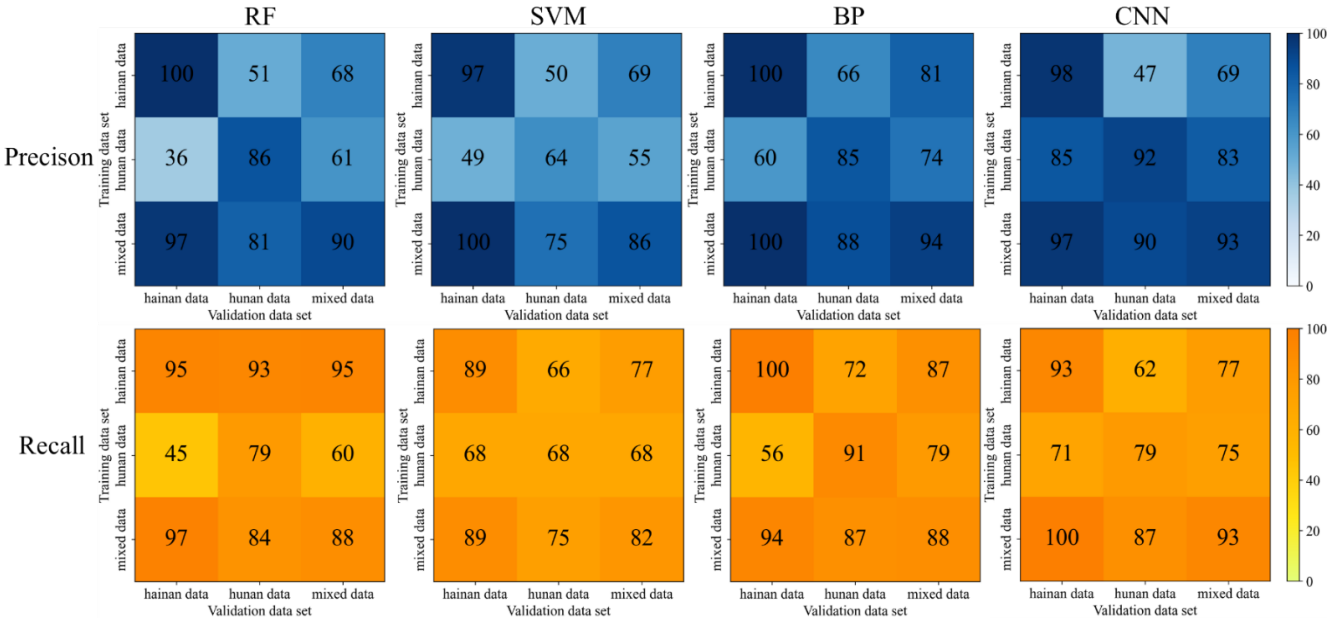

Figure 8. Evaluation results of each algorithm before dimensionality reduction.

As can be seen from Figure 8, the precision and recall rate of validation from the Hainan data set ranges from 36% to 100%. BP neural network model received the highest score, and the accuracy of both evaluations obtained by training with the Hainan data set reached 100%. The RF algorithm obtained the lowest score. Its accuracy of training using the Hunan data was 36–45%. The RF scores for the Hunan validation ranged from 47% to 93%. Among the four models, the highest score was achieved by the CNN algorithm model, which reached 87–90% when trained with mixed data. The lowest scores were also observed in the CNN model, which resulted in 47–62% when trained with Hainan data. The score range of the mixed validation data was 55–95%. The highest score was obtained by the CNN model. When the mixed data were used for training, the evaluation accuracy of the CNN model reached 93%. The lowest was the RF model, which was trained with Hunan data with an accuracy of 60–61%.

The reason that the RF model performed the worst may lie in the fact that it does not provide a continuous output. When performing regression, it cannot make predictions

beyond the range of the training data set. This leads to overfitting when modeling data with some specific noise, or there are many similar decision trees that mask the true results. The CNN model performed the best. The reason may be explained by the fact that convolutional neural networks have a parameter sharing mechanism. This mechanism greatly reduces the number of parameters of the network and trains a better model with fewer parameters, which can effectively avoid overfitting. The sparsity of the network connections allows the data to be given better and more effective weights.

3.2. Classification Accuracy after Feature Dimensionality Reduction

3.2.1. Feature Extraction with PCA algorithm

For each group of 751-dimensional data, the PCA algorithm was used to extract features from the data and the 751-dimensional data were then downscaled to 200 dimensions by optimizing the parameters. After dimensionality reduction, the 800 groups of 200-dimension Hainan data, 800 groups of 200-dimension Hunan data and 1600 groups of 200-dimension mixed data from Hainan and Hunan were input to traditional classifiers and deep learning model for training. Another 200 groups of Hainan data, 200 groups of Hunan data were used and 400 groups of mixed data from Hainan and Hunan were used for validation. The final accuracy result is shown in Figure 9.

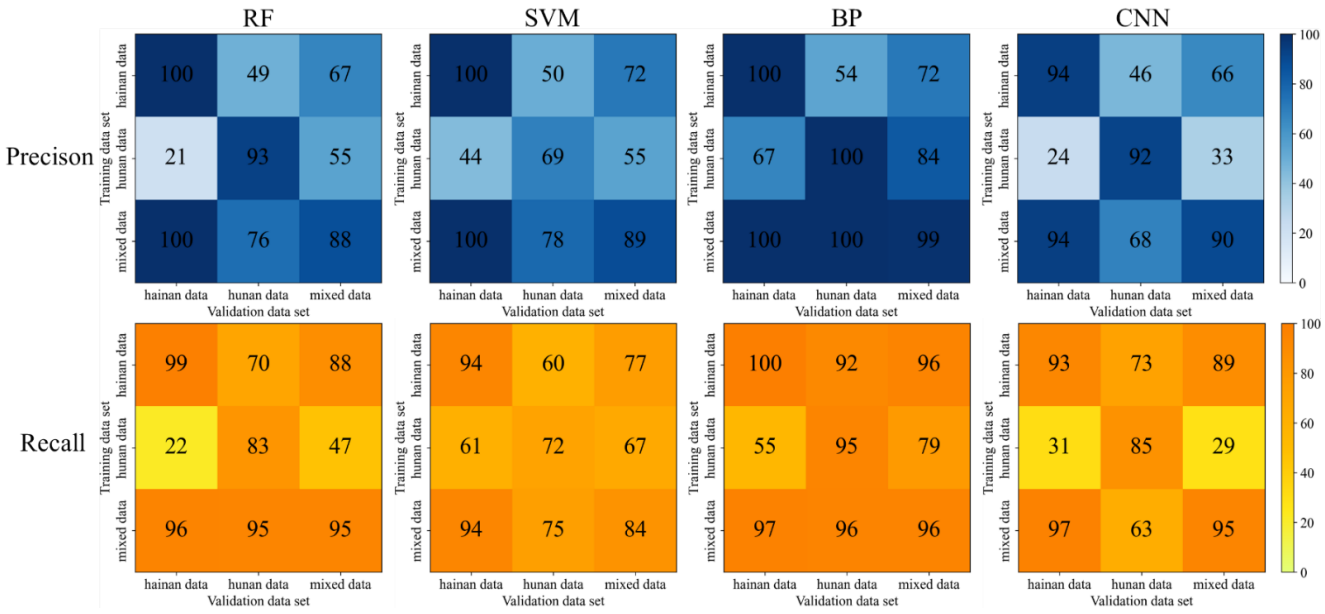

Figure 9. Evaluation results of each algorithm after feature extraction with PCA algorithm.

As can be seen from Figure 9, the correlation range of Hainan validation data was 21–100%, of which the BP model has the highest accuracy. When training with Hainan data, the precision and recall rate are both 100%. The lowest score was observed in the RF model, which was trained with Hunan data, and its accuracy was only 21–22%. The score range for Hunan validation data was 46–100%, in which the BP model received the highest accuracy of 96–100% when trained with the mixed data set. The lowest accuracy was observed in the SVM model, which was only 50–60% when trained with Hainan data. The scores for the mixed validation data ranged from 29–99%, with the highest detection model being the BP model, trained using mixed data, at 96–99%, and the lowest being the CNN model, trained using Hunan data, at 29–33%.

Compared with the original data before dimensionality reduction, the accuracy of the trained models was improved. The best BP algorithm model can handle the data of Hainan up to 100%, which is relatively stable and has good generalization ability. The results of the Hunan validation data have a relatively large improvement, with the highest score of 96–100%. In the four algorithm models with PCA feature extraction, some performance improves and some performance worsens.

3.2.2. Feature Selection with GA

The 751-dimensional original data of Hainan, Hunan and mixed data were used for GA feature selection. After dimensionality reduction, the three sets of data were downscaled to 350, 384 and 362 dimensions by parameter optimization, respectively. Then, 800 sets of 350-dimensional Hainan data were input to the traditional classifier and deep learning model for training. The 200 sets of 350-dimensional Hainan data, 200 sets of 350-dimensional Hunan data and 400 sets of 350-dimensional Hainan–Hunan mixed data were used for validation. The 800 sets of 384-dimensional Hunan data and 1600 sets of 362-dimensional mixed data also performed the same operation. Final accuracy results are shown in Figure 10.

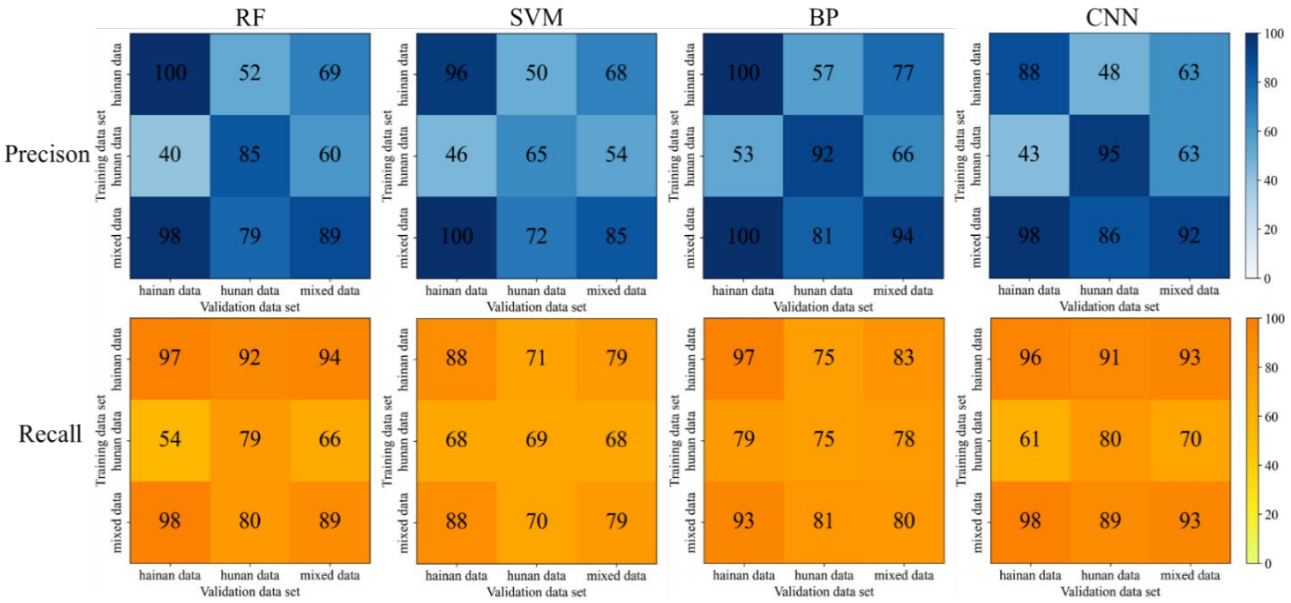

Figure 10. Evaluation results of each algorithm after feature selection with GA algorithm.

By observing the results in Figure 10, the precision and recall rate of Hainan validation data ranged from 40–100%. Among Hunan data, the highest score goes to RF and BP models with 97%–100%. The lowest scores lie in the RF model, which was only 40–54% based on the training results of Hunan data. The scores of the Hunan validation data ranged from 48% to 95%. The optimal model is the CNN model, which was trained with the Hainan–Hunan mixed data, reaching 86% to 89%. The lowest is the SVM model, which received 50–71% based on the training results using Hainan data. The scores of mixed validation data ranged from 54% to 94%, and the highest was the CNN model, which was trained with mixed data from Hainan and Hunan, reaching 92% to 93%. The lowest was the SVM model, which was trained with Hunan data and its accuracy was only 54–68%.

Compared with the original data before dimensionality reduction, the dimensionality reduction data after GA feature selection received about 2% lower accuracy, but the input dimension was reduced by nearly half, which reduced a lot of operations. The less effective model was the SVM model, and the best one was the BP model.

3.2.3. Combination of PCA Feature Extraction and GA Feature Selection

Feature extraction was performed first on the 751-dimensional data from Hainan using the PCA method. Then, the original 751-dimensional data generated new 751-dimensional feature data in order of importance. Finally, GA was performed to reduce the new 751-dimensional data through feature selection to 404-dimensional data. Hunan data and mixed data were similarly reduced to 369 and 388 dimensions by performing the above operations, respectively.

After dimensionality reduction, 800 sets of 404-dimensional Hainan data were input to the traditional classifiers and deep learning model for training. At the same time, 200 sets

of 404-dimensional Hainan data, 200 sets of 404-dimensional Hunan data, and 200 sets of 404-dimensional Hainan-Hunan mixed data were used for validation. The same training and validation operations were performed for the 800 sets of 369-dimensional Hunan data and the 1600 sets of 388-dimensional mixed data. The final results are shown in Figure 11.

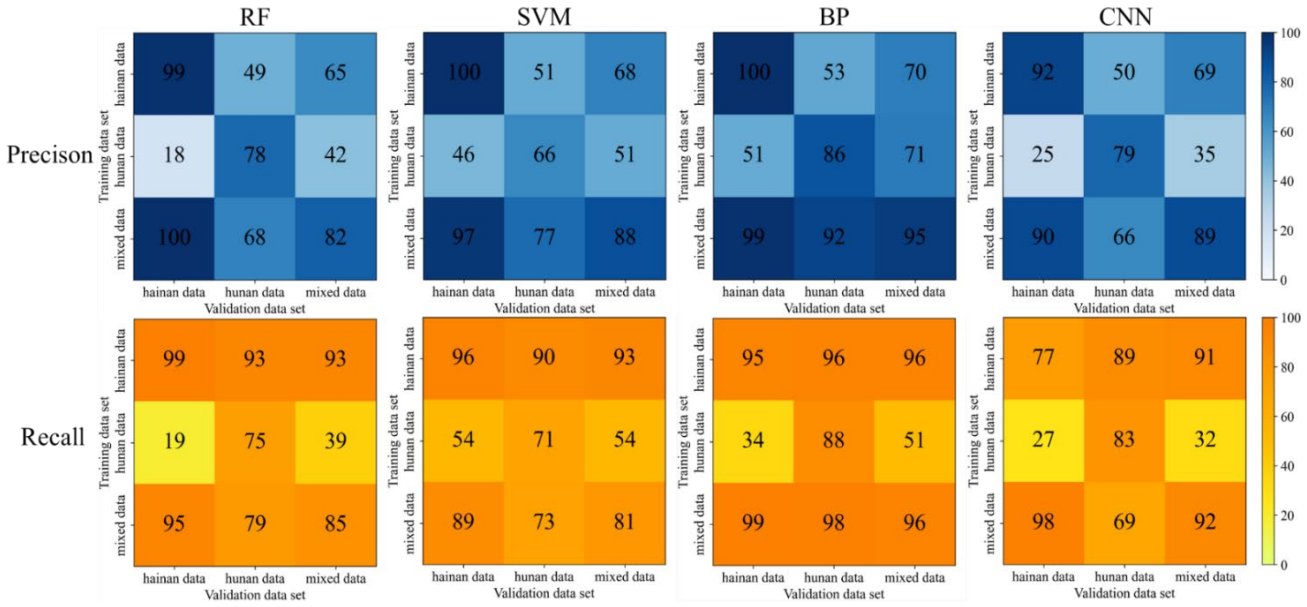

Figure 11. Evaluation results of each algorithm based on feature extraction and feature selection.

The results in Figure 11 show that the precision and recall rate of Hainan validation data ranged from 18–100%, among which the optimal model was the RF model trained by Hainan data and the BP model trained by mixed data. The evaluation results of these two models were 99%. The RF model trained by Hunan data performed the worst with an accuracy of 18–19%. The scores of the Hunan validation data ranged from 49% to 98%. The BP model trained by mixed data reached 92% to 98%, while the CNN model trained by Hainan data only reached 50% to 89%. The score of mixed validation data was 32–96%. The BP model trained by mixed data received an accuracy up to 95–96%. The lowest scores lie in the CNN model trained with Hunan data—the accuracy was only 32–35%.

After PCA feature extraction for the original data and then GA feature selection, the result does not combine the advantages of the two dimensionality reduction methods well. The result is even lower than that of the original data; therefore, the combination of PCA and GA methods for dimensionality reduction is not applicable for hyperspectral data identification of flowering and non-flowering rice spikelets.

4. Discussion

This study innovatively proposed the application of hyperspectral technology to detect the flowering state of rice spikelets and made full use of the advantages of hyperspectral technology to obtain better detection results. Compared with artificially judging the flowering state of rice spikelets, the detection method combining hyperspectral technology and machine learning is faster and more accurate. In the future, the results obtained in this study can be made into hyperspectral sensors, which can realize remote flowering detection, which greatly saves labor costs.

Zhang et al. [26] obtained rice spikelet images from a visible light camera. Series Otsu (SOtsu) was applied in tandem to extract the spikelet anthers through the visible light blue channel. In the meantime, deep learning models, such as FasterRCNN and YOLO-v3, were used to identify the spikelet anthers and the opening spikelet hull. The most suitable method was selected for flowering characteristics detection to compare the precision, recall and the F1 coefficient of different models. Results showed that the precision, recall rate, F1 coefficient and Pearson correlation coefficient of the FasterRCNN model

in spikelet hull detection were 1, 0.97, 0.98 and 0.993, respectively, while those of SOtsu in spikelet anthers detection were 0.92, 0.93, 0.93 and 0.936, respectively. It inferred that the SOtsu and FasterRCNN models were both capable of rice flowering detection, but the opening spikelet hull was more suitable than the spikelet anthers for the rice flowering features detection with the deep learning model; however, compared with the detection method with a visible light camera, the hyperspectral data collected in this study carries more effective information and is easier to process. The hyperspectral data can clearly perceive the changes in spectral reflectance caused by the subtle changes in the flowering process of rice glumes. In addition, the application of machine learning algorithms to build classification models can make full use of the spectral information carried by the hyperspectrum, making the predictive ability of the models more powerful compared to the application of other detection methods.

Due to the overlapping signature and negligible difference between flowering and non-flowering spectra for both Hainan and Hunan locations, we used full-band reflectance data for modeling. In addition, the result of data dimensionality reduction through the GA algorithm shows that it contributes to the detection of rice flowering status in almost the whole waveband range, and the contribution values do not differ significantly.

Among the four data processing methods, PCA feature extraction has the best result in terms of overall effectiveness, followed by the original data modeling, the PCA and GA combination and the GA feature selection. Among the PCA feature extraction processing methods, the BP model achieved the highest evaluation accuracy. The precision and recall rate is between 96% and 100% when trained by Hainan and mixed data, indicating that the BP model has an excellent classification effect and strong generalization ability for rice flowering detection. Although the results derived from the GA feature selection did not improve, the dimensionality of its input was reduced by nearly half while it still maintained the acceptable score, indicating that nearly half of the 751-dimensional data were not very useful for the classification of this study and could be eliminated. From the selected bands, their effective bands were basically evenly distributed, with some concentration in individual places. Most likely, it results from the similarity of the adjacent bands. After GA feature selection, the redundant information was removed to ensure the efficiency of the information; therefore, the feature reduction serves to remove the redundant and interfering features in feature bands, which in turn improves the accuracy of the processing results.

Among the four classification models, the BP algorithm model achieves a comprehensively better result, followed by the CNN model, RF model and SVM model. The results obtained by the BP algorithm model may be due to the (1) nonlinear mapping ability: BP neural network essentially realizes a mapping function from input to output; mathematical theory proves that the three-layer neural network can approach any nonlinear continuous function with arbitrary accuracy, which has strong nonlinear mapping ability. (2) Self-learning and self-adaptive ability: during training, BP neural network automatically extracts "reasonable rules" between input and output data through learning and adaptively memorizes the learning content into the weight of the network with high self-learning and self-adaptation ability. (3) Generalization ability: in the design of the pattern classifier, it cares about whether the network can correctly classify the patterns not seen before or those with noise pollution after training and has the ability to apply the learning results to new knowledge. (4) Fault tolerance: BP neural network will not have a great impact on the global training results after its local or partial neurons are damaged; the system can still work normally when local damage occurs and it has a certain fault tolerance. The reason for the relatively poor results of the CNN algorithm may be that it learns by convolution, which may lose some parts of the data and ignore the correlation between the local and the whole, thus affecting the results. RF model may be overfitted for noisy data. SVM model may not be optimal for the selection of parameters, which can only be chosen empirically and through human selection, with a certain degree of arbitrariness.

From the results of multiple processing, Hainan data have a good classification effect, probably because there is a more obvious difference between the flowering and non-flowering bands in Hainan data; however, the classification effect of Hunan data is poorer, probably because there is more noise in Hunan data or the difference between the flowering and non-flowering bands is not obvious, which makes it more difficult to classify. Comparing the generalization ability of Hainan data alone with that of Hunan data, the classification algorithm has a better generalization ability. The BP algorithm model in PCA feature extraction processing has improved generalization ability for mixed data, and the results of Hunan validation data can have a 1% improvement compared with the training results of Hunan data alone. There is a big difference between Hainan data and Hunan data. When applying the model trained by one site to validate the data from another site, the precision and recall rate is basically around 50%.

In summary, the algorithm adopted in this study is quite effective in detecting the hyperspectral data before and after rice flowering. Considering the operational problems in the data acquisition process and the influence of the objective physical environment on the instrument may cause interference to the acquisition of rice flowering hyperspectral data, there will be some influence on the results of machine identification. In addition, the sample data set adopted in this study is still small, and the algorithm should be further explored to improve the generalization ability of the algorithm for the identification of different varieties of rice flowering in different regions.

5. Conclusions

This study proposed to acquire rice spikelet flowering information using hyperspectral technique and machine learning in order to meet the needs of hybrid rice pollination rapidly and automatically. The hyperspectral data of rice before and after flowering were collected by a spectroradiometer. Based on traditional machine learning algorithms and deep learning algorithms, preliminary classification models were constructed to identify rice flowering status. The traditional classifiers used in this study include the SVM algorithm, RF algorithm and BP network. The deep learning classifier is the CNN algorithm. By comparing the four algorithm models, it can be found that the CNN algorithm model has the best accuracy in the detection of rice flowering. The average accuracy and recall rate of the model is 93% when using the data collected from two locations mixed as data input. Three methods, PCA feature extraction, GA feature selection and the combination of PCA and GA algorithm, were applied to transform hyperspectral data into a new feature space based on the feature dimension reduction method and then carried out the classification of rice flowering in this space combining with machine learning algorithms. It can be found that the PCA algorithm was applied to feature extraction of rice spikelet spectral data, which could make full use of the effective information in the spectral band and improve the accuracy and recall rate of the model. Although the GA algorithm did not improve the accuracy and recall rate of the model, it reduced the dimension of model input information and reduced the complexity of model calculation while maintaining the accuracy of the model. The feature extraction method combined with PCA and GA failed to integrate the advantages of the two algorithms, and its accuracy even decreased when compared with the preliminary classification model based on machine learning algorithms. By comprehensively comparing the combination of different feature dimensionality reduction methods and classification models, the optimal model was constructed by using the data processed by the PCA feature extraction method and then classified by the BP algorithm. The accuracy and recall rate of mixed data is 96–100%. The experimental results show that the hyperspectral technology and machine learning algorithm proposed in this study can effectively obtain the flowering status of rice spikelets, which is expected to provide decision-making information for timely pollination in mechanized seed production of hybrid rice.

Author Contributions: Conceptualization, Y.Z. and J.D.; methodology, L.B. and H.H.; software, X.L. and M.L.; validation, Y.Q. and J.X.; formal analysis, L.B. and Y.Q.; investigation, L.B. and H.H.; resources, Y.Z. and Y.L.; data curation, Y.Q., X.L. and J.X.; writing—original draft preparation, Y.Z. and L.B.; writing—review and editing, Y.Q., X.L. and J.X.; visualization, X.L. and J.X.; supervision, Y.Z. and J.D.; project administration, Y.Z. and J.D.; funding acquisition, Y.L. All authors have read and agreed to the published version of the manuscript.

Funding: This research was funded by Guangdong Modern Agricultural Industry Generic Key Technology Research and Development Innovation Team Project, grant number 2020KJ133, the Key Field Research and Development Plan of Guangdong Province, China, grant number 2019B020221001, and the 111Project, grant number D18019.

Data Availability Statement: The data presented in this study are available on request from the corresponding author.

Conflicts of Interest: The authors declare no conflict of interest.

References

1. Zhang, B.; Rui, W.Y.; Zheng, J.C.; Zhou, B.; Yang, F.; Zhang, W.J. Response characteristics of pollen activity and seed setting rate to high temperature in rice at anrescence stage. *Acta Agron. Sin.* **2007**, *33*, 1177–1181.
2. Liu, J.G.; Zhao, C.J.; Yang, G.J.; Yu, H.Y.; Zhao, X.Q.; Xu, B.; Niu, Q.L. Review of field-based phenotyping by unmanned aerial vehicle remote sensing platform. *Trans. CSAE* **2016**, *32*, 98–106.
3. Earl, R.; Wheeler, P.N.; Blackmore, B.S. Precision farming—The management of variability. *Landwards* **1996**, *51*, 418–423.
4. Borja, M.; Arturo, A.; Maria, P.D.; Javier, T. Image analysis-based modelling for flower number estimation in grapevine. *J. Sci. Food Agric.* **2017**, *97*, 784–792.
5. Javier, T.; Katja, H.; Florian, R.; Patrice, T.; Agnès, D. Automatic Flower Number Evaluation in Grapevine Inflorescences Using RGB Images. *Am. J. Enol. Vitic.* **2020**, *71*, 10–16.
6. Yu, X.; Wang, Z.; Jing, H.T.; Jing, X.L.; Nie, C.W.; Bai, Y.; Wang, Z. Maize tassel segmentation based on deep learning and RGB image. *J. Zhejiang Univ.* **2021**, *47*, 451–463.
7. Wang, L.; Li, Y.J.; Cen, H.Y.; Zhu, J.P.; Yin, W.X.; Wu, W.K.; Zhu, H.Y.; Sun, D.W.; Zhou, W.J.; He, Y. Combining UAV-Based Vegetation Indices and Image Classification to Estimate Flower Number in Oilseed Rape. *Remote Sens.* **2018**, *10*, 1484.
8. Chen, J.Y.; Chen, S.B.; Zhang, Z.Y.; Fu, Q.P.; Bian, J.; Cui, T. Retrieval of photosynthetic parameters of cotton at bud stage by UAV multi-spectral remote sensing. *Trans. Chin. Soc. Agric. Mach.* **2018**, *49*, 230–239.
9. Liu, Y.; Wang, K.J.; Xie, R.J.; Lv, Q.; He, S.L.; Yi, S.L.; Zheng, Y.Q.; Deng, L. Apple blossom estimation based on canopy height spectral information. *Agric. Sci. China* **2016**, *49*, 3608–3617.
10. Zhao, C.J.; Wen, C.W.; Lin, S.; Guo, W.Z.; Long, J.H. Tomato florescence recognition and detection method based on cascaded neural network. *Trans. CSAE* **2020**, *36*, 143–152.
11. Deng, Y.; Wu, H.R.; Zhu, H.J. Recognition and counting of citrus flowers based on instance segmentation. *Trans. CSAE* **2020**, *36*, 200–207.
12. Wang, X.; Tang, J.L.; Whitty, M. DeepPhenology: Estimation of apple flower phenology distributions based on deep learning. *Comput. Electron. Agric.* **2021**, *185*, 106123. [CrossRef]
13. Cai, E.; Baireddy, S.; Yang, C.Y.; Crawford, F.; Delp, E.J. Panicle counting in UAV images for estimating flowering time in sorghum. In Proceedings of the 2021 IEEE International Geoscience and Remote Sensing Symposium IGARSS, Brussels, Belgium, 11–16 July 2021; pp. 6280–6283. [CrossRef]
14. Li, X.; Wang, Z.J.; Wang, L.Y.; Hu, R.L.; Zhu, Q.Y. A multi-dimensional context-aware recommendation approach based on improved random forest algorithm. *IEEE Access* **2018**, *6*, 45071–45085. [CrossRef]
15. Evans, J.; Waterson, B.; Hamilton, A. Forecasting Road traffic conditions using a context-based random forest algorithm. *Transp. Plan. Technol.* **2019**, *42*, 554–572. [CrossRef]
16. De Santana, F.B.; Neto, W.B.; Poppi, R.J. Random forest as one-class classifier and infrared spectroscopy for food adulteration detection. *Food Chem.* **2019**, *293*, 323–332. [CrossRef] [PubMed]
17. Breiman, L. Bagging Predictors. *Mach. Learn.* **1996**, *24*, 123–140. [CrossRef]
18. Vapnik, V.N. *The Nature of Statistical Learning Theory*; Springer: New York, NY, USA, 2000; pp. 25–314.
19. Yuan, B.Q.; Cheng, G.; Zheng, L.G. Basic principle of BP neural networks. *Digit. Commun. World* **2018**, *8*, 28–29.
20. Zhou, J.Y.; Zhao, Y.M. Application of convolution neural network in image classification and object detection. *Comput. Eng. Appl.* **2017**, *53*, 34–41.
21. Herve, A.; Lynne, J.W.; Domininique, V. Multiple factor analysis: Principal component analysis for multitable and multiblock data sets. *Wiley Interdiscip. Rev. Comput. Stat.* **2013**, *5*, 149–179.
22. Liang, C.J.; Chen, W.D.; Cui, J.C. Analysis of coordinated scheduling of twin-armg for automation container terminals. *Comput. Appl. Softw.* **2018**, *9*, 16–21.

23. Wu, Y.M.; Wu, S. Application of structural optimization of artificial neural network based on improved genetic algorithm. *Inf. Technol. Netw. Secur.* **2011**, *3*, 79–81.
24. Li, S.B.; Song, Q.S.; Li, Z.A.; Zhang, X.X.; Zhe, L.X. Review of genetic algorithm in robot path planning. *Sci. Technol. Eng.* **2020**, *20*, 423–431.
25. Fan, W.B.; Zhou, J.; Xu, Z.L. Application of genetic algorithm to assembly line balancing. *Comput. Technol. Dev.* **2010**, *20*, 194–196.
26. Zhang, Y.L.; Xiao, W.W.; Lu, X.Y.; Liu, A.M.; Qi, Y.; Liu, H.C.; Shi, Z.K.; Lan, Y.B. Method for detecting rice flowering spikelets using visible light images. *Trans. CSAE* **2021**, *37*, 253–262.

applied sciences

MDPI

Review

Research Progress and Prospects of Agricultural Aero-Bionic Technology in China

Yali Zhang [1,2,†], Haoxin Tian [1,2,†], Xinrong Huang [1,2], Chenyang Ma [3], Linlin Wang [2,4], Hanchao Liu [1,2] and Yubin Lan [2,4,*]

[1] College of Engineering, South China Agricultural University, Wushan Road, Guangzhou 510642, China; ylzhang@scau.edu.cn (Y.Z.); hxtian@stu.scau.edu.cn (H.T.); xrhuang@stu.scau.edu.cn (X.H.); lhc@stu.scau.edu.cn (H.L.)
[2] National Center for International Collaboration Research on Precision Agricultural Aviation Pesticide Spraying Technology, Wushan Road, Guangzhou 510642, China; wlinlin@stu.scau.edu.cn
[3] College of Aerospace Engineering, Nanjing University of Aeronautics and Astronautics, Nanjing 210016, China; cyma@nuaa.edu.cn
[4] College of Electronic Engineering and College of Artificial Intelligence, South China Agricultural University, Wushan Road, Guangzhou 510642, China
* Correspondence: ylan@scau.edu.cn
† These authors contributed equally to this work and should be considered as co-first authors.

Abstract: Accelerating the development of agricultural aviation technology is the need of China's modern agricultural construction. With the rise of emerging industries such as artificial intelligence, biotechnology, autonomous navigation, and the Internet of Things, agricultural aviation is further developing toward the direction of intelligence to meet the requirements of efficient and sophisticated agricultural aviation operations. Bionics is a multi-discipline and comprehensive border subject. It is produced by the mutual penetration and integration of life science and engineering science. Bionic technology has received more and more attention in recent years, and breakthroughs have been made in the fields of biomedicine and health, military, brain science and brain-like navigation, and advanced manufacturing. This study summarized the research progress of biomimetic technology in the field of agricultural aviation from three aspects of biological perception, biological behavior, and biological intelligence. On this basis, problems of related research and application of agricultural aircraft in real-time obstacle avoidance, path planning, and intelligent navigation were analyzed. Combined with the practice of the rapid development of agricultural aircraft, research and application of bionic technology suitable for agricultural aircraft were then proposed. Finally, prospects of agricultural aero-bionic technology were also discussed from multiple bionic target fusion, three-dimensional spatial information exploration, sensors, and animal brain system mechanism. This review provides a reference for the development of bionic technology in China's agricultural aviation.

Keywords: agricultural aviation; aero-bionic technology; unmanned aerial vehicle; obstacle avoidance; path planning; convolutional neural network; sensors; review

check for updates

Citation: Zhang, Y.; Tian, H.; Huang, X.; Ma, C.; Wang, L.; Liu, H.; Lan, Y. Research Progress and Prospects of Agricultural Aero-Bionic Technology in China. *Appl. Sci.* **2021**, *11*, 10435. https://doi.org/10.3390/app112110435

Academic Editor: Teresa Zielinska

Received: 3 October 2021
Accepted: 4 November 2021
Published: 6 November 2021

Publisher's Note: MDPI stays neutral with regard to jurisdictional claims in published maps and institutional affiliations.

Copyright: © 2021 by the authors. Licensee MDPI, Basel, Switzerland. This article is an open access article distributed under the terms and conditions of the Creative Commons Attribution (CC BY) license (https://creativecommons.org/licenses/by/4.0/).

1. Introduction

Agricultural aviation refers to the aviation industry that serves agricultural production, including agricultural aircraft technology, remote sensing monitoring technology and equipment, aviation operation technology and equipment, etc. [1] It has the characteristics of high efficiency, uniform application, and wide adaptability [2]. Agricultural aviation is widely used in agriculture, forestry, fishery, animal husbandry, and other fields. It is an important development direction in China's construction of efficient and reliable modern agriculture [3]. At present, with the development and application of emerging technologies such as artificial intelligence, autonomous navigation, biotechnology, Internet of Things, big data, smart equipment manufacturing, and 5G in various fields, agricultural

aviation is moving towards intelligence [4,5]. As one of the new technologies that are of great significance to the development of emerging industries in the future [6], bionic technology provides new ideas for the intelligent development of agricultural aviation. Bionic sensing technology can realize the precise operation and real-time obstacle avoidance of agricultural aircraft, which is one of the important directions for the development of intelligent agricultural aviation in the future [7]. Bionic intelligent technology can complete autonomous learning and intelligent decision-making, realize autonomous navigation of agricultural aircraft, and improve operational efficiency [8]. The intelligent bionic algorithm can improve the operational path optimization and multi-aircraft cooperative operation of agricultural aircraft, which is the development trend of mobile robot path planning in the future [9].

Bionics, founded in 1960, is a science that studies biological systems, structures, traits, and working mechanisms. At present, bionic technology has penetrated into almost every field, and scholars from all over the world have carried out related research on bionics and made breakthrough progress. A lightweight and high-strength aircraft [10] was developed by imitating the truss structure of insect wings [11] and the dumbbell-shaped structure of animal bones [12]. Inspired by the sensitivity of cellulose to humidity, the spider egg sac silk was used to develop a humidity sensor with high sensitivity, heat resistance, and repeatability [13]. Through the research of the elephant nose and octopus hand, a flexible robotic arm has been developed, which has the characteristics of strong flexibility and adaptability to complex environments. The combination of bionic technology and agricultural aviation can achieve precise control of aviation aircraft, enabling it to have functions such as intelligent navigation and fine pesticide application, which is of positive significance to the development of precision agricultural aviation.

At present, some Chinese scholars have carried out related research on the intelligent agricultural aviation, but they have not systematically realized that this is aero-bionic, a combination of bionic technology and agricultural aviation. This review sorts out the research history of bionic technology in agricultural aviation in China from the aspects of biological perception, biological behavior, and artificial intelligence, then analyzes the current development of bionic technology in the field of agricultural aviation, and finally discusses the existing problems and future development prospects of agriculture aero-bionic technology in China.

2. Biological Perception and Agricultural Aviation

Agricultural aviation aircraft need to collect information about the surrounding environment in the process of operation, and high-precision and high-reliability sensors are the main means of environmental perception and data acquisition for agricultural aircrafts [14]. Facing the complex and harsh farmland operating environment, how to ensure the efficient and accurate information acquisition of aircraft is an urgent problem for researchers. After hundreds of millions of years of development, the sensing system of organisms can cope with the complex and changeable natural environment, providing ideas for the research of agricultural aviation sensors. At present, relevant Chinese scholars have put forward optimization schemes for how to improve the accuracy and reliability of sensor information acquisition by studying the mechanism of biological system perception. This section introduces the research progress of biological perception in China agricultural aviation through three aspects: echolocation and obstacle avoidance, binocular stereo vision, and compound eyes.

2.1. Echolocation and Obstacle Avoidance

In 1944, Griffin [15] successfully recorded the ultrasound emitted by bats, and named the process of acquiring information about the surrounding environment by bats emitting ultrasound as echolocation. At present, related studies have found that in addition to bats, the rodents of the genus Typhlomys [16], toothed whales [17], and birds [18] all have echolocation capability. Bat echolocation has multiple functions, such as target detection,

information exchange, and environment recognition [19]. Accurate target information can be obtained by adjusting the frequency, intensity, and sound rate of echolocation sound waves. Ultrasonic detection has the characteristics of high resolution, strong directionality, wide application range, and large coverage area in short-range distance measurement [20]. It can detect harsh environments such as dark environment, electromagnetic interference, smoke, etc. [21], but temperature, humidity, gas density, etc., will affect the ultrasonic propagation speed [22], and the sound waves will gradually turn into heat during the propagation process, causing excess attenuation [23], so the accuracy of detecting long-distance targets is poor.

The development of ultrasonic sensor technology is relatively mature, and it is mainly used for ultrasonic detection and obstacle avoidance in agricultural aviation. At present, the research of ultrasonic detection technology is mainly focused on improving the accuracy and robustness of ultrasonic detectors. Zhang [24] proposed a segmented fitting algorithm, which combines the MCU main control chip, ultrasonic radar, collision warning, and other modules to form a collision avoidance warning system, which calculates the control function of each flight distance separately, and finally, summarized the optimal route to realize the safe flight of the aircraft. Zhang [25] proposed an idea to process the data obtained by the ultrasonic sensor and binocular vision through the Federal Kalman filter fusion algorithm to process and fuse the image information taken by the ultrasonic binocular, so as to improve the obstacle avoidance perception accuracy of UAVs (unmanned aerial vehicles). Aiming at the fact that multi-channel ultrasonic sensors occupy a lot of system hardware resources and control system software resources in robot obstacle avoidance, Zheng [26] and others developed the RS485 bus to expand multiple ultrasonic ranging slave stations, which improves the reliability of data communication and high-speed long-distance transmission performance, and saves the hardware and software resources of the robot control system.

Ultrasonic sensors are low in cost, small in size, and simple in structure [27]. They are widely used in obstacle avoidance and detection of plant protection UAVs, and are usually used in fixed altitude flights and the down-looking system of agricultural UAVs [28]. Since ultrasound's accuracy will be affected due to complex environmental obstacles, air temperature, humidity, etc., it cannot be used alone. Therefore, fusing it with multiple sensors is a future research trend [29].

2.2. Binocular Stereo Vision Bionics

Marr [30], from the Massachusetts Institute of Technology, first proposed a visual computing theory, which uses two or more cameras with different angles to acquire image feature points and draw three-dimensional images. The geometric principle of binocular stereo vision is shown in Figure 1.

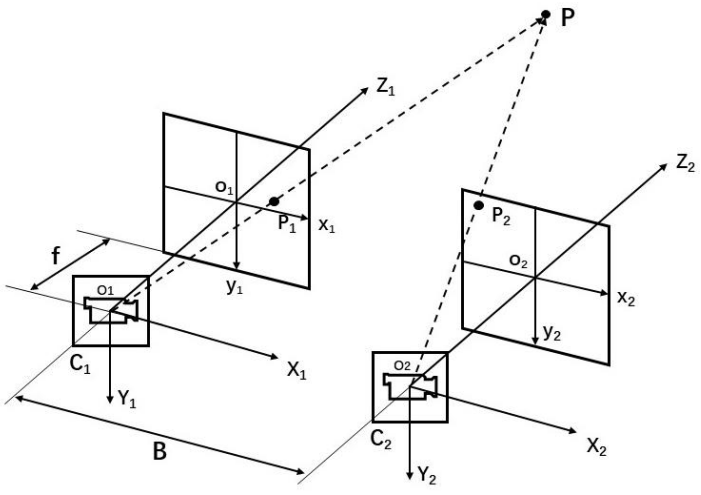

Figure 1. Geometric principle of the binocular stereo vision system.

In Figure 1, C_1 and C_2 are two cameras with optical axes parallel to each other, and P1 and P2 are the imaging points of three-dimensional space point P on two two-dimensional imaging planes, $x_1o_1y_1$ and $x_2o_2y_2$, respectively. The relationship between depth and parallax is as follows:

$$Z = \frac{B \cdot f}{d} \tag{1}$$

where Z is the depth, B is the baseline, d is the difference between p_1 and p_2 in the x-axis direction, and f is the focal length.

Binocular stereo vision technology has the advantages of fast speed measurement at short-range, high accuracy, and no contact [31], but the accuracy is reduced during long-distance detection, and it is difficult to match the object image with low texture [32]. In practical application, camera parameter setting, illumination change, environmental change, equipment performance, etc., will cause differences in image-matching results and affect target detection accuracy [33].

At present, the research on binocular vision systems mainly focuses on the stereo matching algorithm. Liu [34] proposed an improved adaptive weighting algorithm to solve the problems of occlusion and depth discontinuity in binocular matching, which greatly reduced the influence of the depth discontinuity area, optimized the parallax map, and improved the accuracy of generating the parallax map. Wang [35] proposed an autonomous path planning algorithm of plant protection UAV combined with GNSS (Global Navigation Satellite System, Xianyang, China) and binocular vision to solve the problem that plant protection UAV cannot accurately spray in mountain fruit tree planting. First, GNSS navigates the UAV to the operation area, and then the yaw angle of the UAV is adjusted by the binocular vision sensor to complete the precision operation of the UAV. Zhu [36] aimed at improving the efficiency and accuracy of obstacle avoidance during UAV flight, and proposed a method of combining binocular stereo vision and optical flow. The distance of obstacles is obtained through binocular stereo vision, and the instantaneous speed of obstacles to cameras is calculated by the SIFT (scale-invariant feature transform) optical flow method to create the obstacle avoidance strategy. The combined algorithm has significantly improved the calculation speed and obstacle avoidance effect.

In recent years, binocular stereo vision technology has developed rapidly, and the research hotspots mainly focus on the stereo matching algorithm. The future development will also focus on optimizing the calculation speed of the algorithm, researching more comprehensive visual computing theories and matching strategies [37], and fusion of multiple algorithms, etc. Binocular stereo vision is widely used in agricultural aviation, especially plant protection UAVs. For example, the industrial-grade UAV, MATRICE M300 RTK (DJI Innovation Technology Co., Ltd., Shenzhen, China), introduced binocular vision and infrared perception sensors into the six faces of the fuselage at the same time, for the first time. Its sensing system is shown in Figure 2. The system has the characteristics of omni-directional six-way sensing, accurate positioning, fast obstacle avoidance, etc. In addition, Mavic2, Inspire2, and the phantom series of DJI UAVs are equipped with binocular vision systems and infrared sensors in different positions of the fuselage. The plant protection UAV CD-15 (Hanhe Aviation Technology Co., Ltd., Wuxi, China) uses a binocular vision system and a laser detection system to mix and match. The P series plant protection UAVs (the XAG Technology Co., Ltd., Guangzhou, China) is equipped with the Xcope eye vision module, which can perceive objects within 30 m [38], and can effectively avoid obstacles in real time.

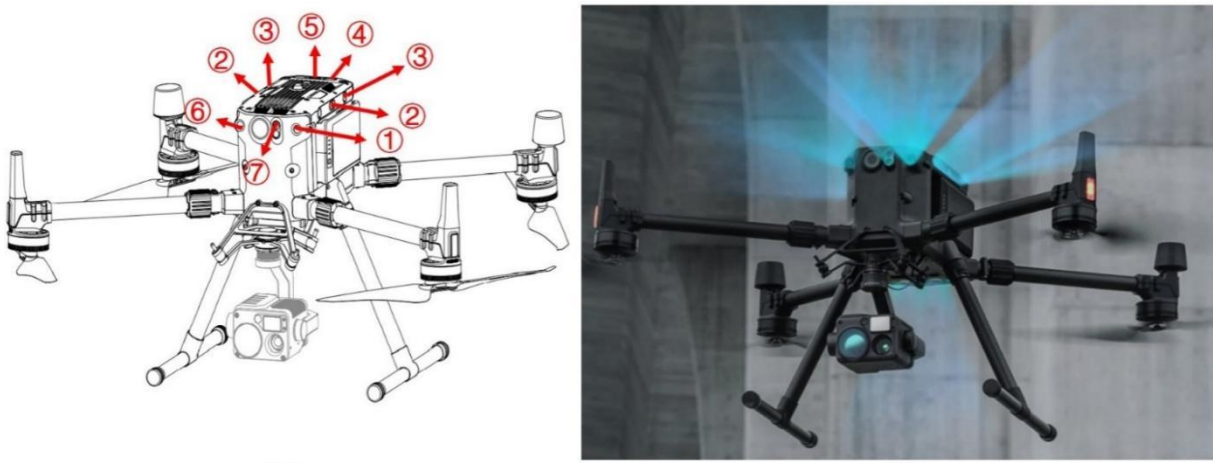

(**a**) (**b**)

Figure 2. MATRICE M300 RTK six-way sensing system: (**a**) function annotation, and (**b**) product in kind [39]. Note: ① front vision system, ② left vision and right vision infrared perception system, ③ left vision and right vision system, ④ top vision system, ⑤ top vision infrared perception system, ⑥ FPV camera, and ⑦ front vision infrared perception system.

2.3. Compound Eye Bionics

In 1826, Miller [40] proposed the Mosaic theory of compound eye. By the middle and late 20th century, as researchers from various countries began to explore the theory and experiment of compound eyes, people's understanding of compound eyes gradually shifted from a biological perspective to an optical perspective. The compound eyes of insects are composed of thousands of sub-eyes, and each sub-eye has an independent optical system, which is finally spliced to obtain a large field-of-view image. A bionic compound eye can obtain the space, position, speed, and other information of the target object by imitating the mechanism of the insect compound eye, so as to achieve the purpose of image acquisition, spatial positioning, and fast obstacle avoidance of the target object. It has the advantages of high sensitivity, fast information acquisition, high time resolution, and large field-of-view [41].

In recent years, the bionic application and research of compound eyes has mainly focused on two aspects: curved array and camera array. However, because the existing curved surface technology is not perfect, the research on curved compound eyes is still in the theoretical stage. Chen [42] used 7 CCD cameras to simulate the compound eyes of flies and designed a bionic compound eye vision system to improve real-time and high-quality image mosaic requirements, which effectively solved the problem of mosaic image misalignment and enhanced the real-time performance of the system. However, this method requires high alignment accuracy of two adjacent sub-images, which is the focus of improvement in the future. Pang [43] imitated the structural characteristics of biological compound eyes and arranged 16 CCD sensors into a curved surface to realize image acquisition without blind spots in the 180 × 75° field-of-view, and to improve the resolution. Aiming at the shortcomings of small drone-borne cameras, such as small field-of-view and narrow imaging range, Yu [44] designed a small size, field angle of up to 106°, micro-miniature bionic compound eye camera. The curved arrangement of the small lens array, optical transformation subsystem, and the data processing unit is composed of three parts. The lens arrangement is shown in Figure 3. In order to increase the overlap rate of the potential fields of adjacent lenses, the lens array in the center A area adopts a regular pentagonal arrangement. The rest of the area is arranged in a hexagonal shape, and the system can collect a target of 0.5 m on the ground at a height of 500 m to achieve a large field-of-view and a high-resolution imaging effect.

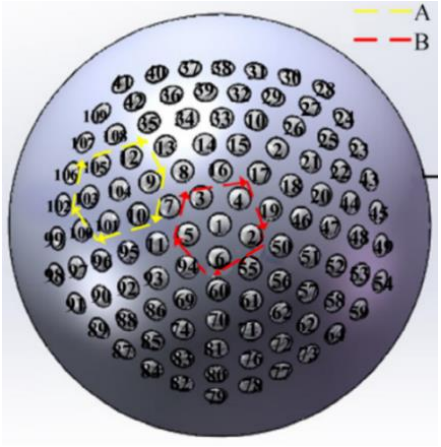

Figure 3. Structure of curved compound eye camera [44]: regular pentagonal arrangement (**A**) and regular hexagonal arrangement (**B**).

The bionic compound eye sensor has the characteristics of high sensitivity, compact structure, large field-of-view, and high resolution. It has broad application prospects in the fields of aviation, detection, robot vision, target recognition, and tracking. Due to the slow progress in optical micro-processing technology, equipment debugging, image acquisition, splicing, etc., in the application of agricultural aviation, the accuracy of the bionic compound eye sensor is easily affected by factors such as harsh environments, and there are still many deficiencies to be improved. The application development in agricultural aviation is still in its infancy. The future development of compound eye bionic technology in agricultural aviation will include fast-precision measurement, real-time obstacle avoidance, a bionic compound eye manufacturing system, and micro-integration.

The list of relevant research on bionic technology mentioned above is compared and analyzed, as shown in Table 1. The characteristics of various bionic technologies, as well as the research hotspots in the field of agricultural aviation, are summarized.

Table 1. Characteristics of bionic technologies and research hotspots in agricultural aviation.

Technology	Application	Advantage	Disadvantage	Maximum Distance	Research Hotspots in Agricultural Aviation
Ultrasonic	Ranging, obstacle avoidance	Low cost	Easy to be interfered by harsh environment, poor accuracy for long-distance detection	<10 m	Short-distance combined obstacle avoidance system
Binocular stereo vision	Ranging, obstacle avoidance, image acquisition	Fast measurement, high resolution at close range	Illumination and harsh environment affect matching accuracy	<100 m	Optimize stereo matching algorithm and fusion algorithm
Compound eyes	Image acquisition, obstacle avoidance	Large field-of-view, high sensitivity, fast measurement, high resolution	Vulnerable to harsh environment, imperfect technological development at present	<100 m	Camera array, curved array

3. Biological Behavior and Agricultural Aviation

During the operation process, the UAV will complete the task according to the artificially planned route. However, in actual operation, due to the influence of external factors such as obstacles, environment, flight conditions, etc., the UAV route will deviate and even cause air accidents, affect the operation efficiency, and increase the operation cost. Path planning of UAV means that UAV optimizes the route during operation, and finds an optimal collision-free path according to specific performance settings, such as optimization time, distance, and energy consumption, so as to improve efficiency and complete operation tasks. In recent years, inspired by the behavior of biological groups, people have proposed a series of intelligent bionic algorithms for optimizing paths and have achieved remarkable results by studying some behavior characteristics of biological groups, such as the ant colony algorithm, fish swarm algorithm, particle swarm algorithm, etc. [45].

3.1. Ant Colony Optimization

Dorigo et al. [46] first discovered and proposed ant colony optimization. Ants have no vision, but they can find the optimal path. This is because ants release a pheromone along the path they walk, and move towards the path with high concentration according to the pheromone concentration on the way to find the optimal path. The process of ants searching for food is shown in Figure 4. The ant colony algorithm is a bionic algorithm proposed through the collective path-finding behavior of ants, and the algorithm mainly includes probability criteria and a pheromone update mechanism. In the algorithm, the ants will judge the probability of going to the next node based on the values of the initial pheromone and heuristic information. After all ants have completed a traversal, the pheromone concentration on the path will be updated. They repeat the above steps until the optimal path is found. The flow chart of the ant colony algorithm is shown in Figure 5. The ant colony algorithm can quickly find the local optimal solution. Compared with other algorithms, it has better time performance [47], search stability, and high accuracy [48]. However, there is random probability and poor pheromone interference in the operation of the algorithm, which will lead to the low quality of the solution [49], and the algorithm has problems such as insufficient initial information, slow convergence speed, and ease of falling into local optimal solutions [50].

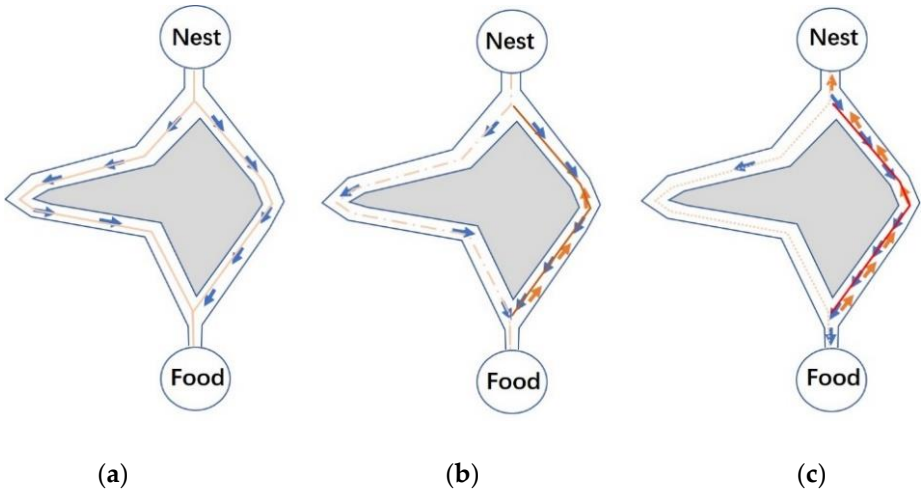

Figure 4. Ant foraging process: (**a**) early path search, (**b**) mid-route search, and (**c**) optimal path.

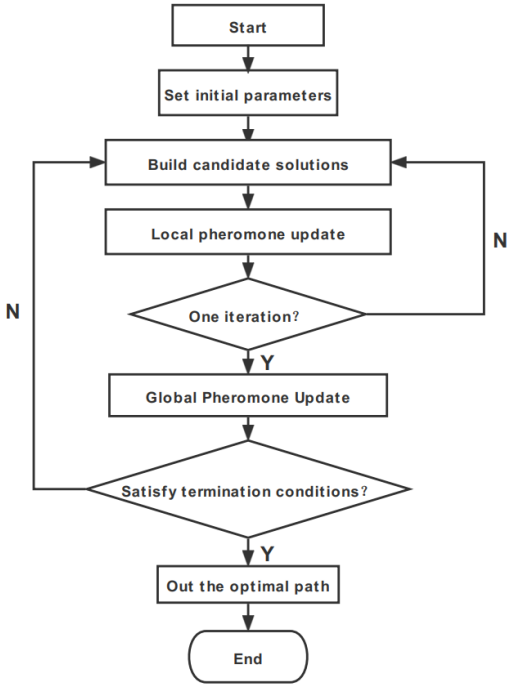

Figure 5. Flow chart of the ant colony algorithm.

Agricultural aviation, especially plant protection UAVs, must face a complex operating environment during the operation. The application of the ant colony algorithm can effectively improve the efficiency of UAVs. Considering the limitations of the ant colony algorithm, it is usually combined with other algorithms to improve the convergence speed of the algorithm and reduce the likelihood of falling into a local optimal solution. Wang [51] proposed an improved ant colony algorithm for the operation area of plant protection UAVs with irregular polygons and internal obstacles, discretized the plane operation path to generate a three-dimensional path, and then reasonably planned the path points in the path. The experimental results show that the optimization path of the algorithm is significantly improved compared with the greedy algorithm and has certain practicability. Wang [52] analyzed the ant colony algorithm through grid environment modeling, and proposed an ant colony opposite search strategy and ant backtracking strategy to improve the search efficiency of the algorithm, while avoiding the algorithm from falling into a U-shaped trap, and redefining the pheromone. The experimental results show that compared with the traditional ant colony algorithm, the improved ant colony algorithm has a faster convergence speed and an optimal path. Feng [53] proposed an intelligent combination algorithm combining the A* algorithm and ant colony algorithm for complex low-altitude environments. The combination algorithm adds the A* algorithm to overcome the problems of slow convergence and falling into a local optimal solution of the ant colony algorithm. The global optimal path is found through the A* algorithm, and then the local optimal path is planned in combination with the ant colony algorithm. The experimental results show that the combined algorithm can not only improve the speed of path optimization, but also avoid obstacles.

The ant colony algorithm was originally proposed to solve the traveling salesman problem. With the development of science and technology, it has been gradually applied to optimization problems in various fields. In the spraying operation of plant protection UAVs, the application of the ant colony algorithm can effectively reduce energy consumption costs, improve efficiency, and help to promote the development of precision agricultural aviation.

3.2. Particle Swarm Optimization

Particle swarm optimization (PSO) is an intelligent algorithm proposed to study the predation behavior of birds [54]. Birds search for food through cooperation among

individuals. Each individual is regarded as a particle, with only position and velocity information. The particles follow the optimal particle to search in space. The particle swarm optimization algorithm first sets up the initial particle swarm and searches for the optimal solution through traversal. In each iteration, the particle will update its position and speed through the individual extreme value, Pbest, and the global extreme value, Gbest, and adjust its fitness value to find the optimal solution [55]. The process is shown in Figure 6.

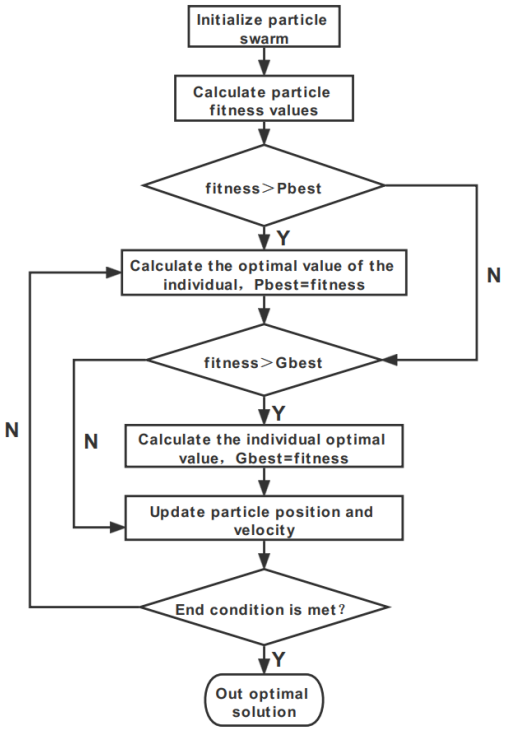

Figure 6. Flow chart of particle swarm optimization.

The particle swarm algorithm has the advantages of being a concise algorithm, easy implementation, good robustness, and fast convergence speed [56], but it is easy to fall into the local optimal solution and has a great impact on the search results [57]. In view of the problems of slow convergence of later calculations and the ease of falling into local optimal solutions when the particle swarm optimization is applied to the multi-aircraft cooperative task assignment of UAVs, Wu [58] proposed a hybrid PSO-BAS (particle swarm optimization-beetle antennae search) algorithm, in which the beetle antennae search algorithm originated from the foraging behavior of beetles. Beetles sense the intensity of food odors in the air through a pair of antennae on the top of their heads, and fly in the direction of the strong odor concentration. The beetle antennae search algorithm regards the food odor as a function. According to the difference of the value of the function in the three-dimensional space, the beetle explores the odor values of two points in the surrounding environment through two whiskers, until the optimal value is found. It combines the advantages of fast local convergence of the beetle antennae search algorithm with the particle swarm optimization algorithm to solve the problem of easily falling into a local optimal solution. The convergence speed of the algorithm is accelerated by adjusting the particle swarm inertia weight. The experimental results prove that the algorithm solves the multi-machine task allocation problem with fast convergence speed and high accuracy. Han [59] aimed at the slow convergence speed of traditional planning in complex environments and the tendency to fall into local optimal solutions. They proposed a repulsive field–particle swarm fusion algorithm to perform raster processing on obstacles in complex environments. The obstacle repulsion potential field constructs a function to

adjust the particle position and velocity to calculate the optimal path. The experimental results verify that the improved fusion algorithm is capable of obtaining the optimal solution of the optimization path with a faster convergence speed. Fang [60] proposed a strategy combining inertia weight adjustment and jumping out of the local optimal solution for the optimization and real-time of UAV trajectory planning. This strategy can reduce the search space and improve the optimization accuracy and stability of the algorithm. The experimental results show that it is possible to generate more trajectories while satisfying online real-time trajectory planning.

As a new intelligent bionic algorithm, particle swarm optimization has been widely used in engineering technology, scientific research, and other fields [61]. Compared with traditional algorithms, particle swarm optimization provides new ideas to solve the path planning problem in the complex environment of agricultural aviation.

3.3. Genetic Algorithm

The genetic algorithm is a global optimization intelligent algorithm, which is inspired by Darwin's evolution theory. Based on the mechanism of natural genetics and natural selection, it uses crossover, mutation, and selection to simulate the process of biological evolution. The core steps in the algorithm mainly include coding, initialization, selection, crossover, and mutation. Firstly, the solution problem is coded and transformed into the solution space of the genetic algorithm. Each code is a feasible solution to form an initial population. Secondly, the individual is evaluated according to the principle of survival of the fittest. Their individual fitness is calculated, and finally, high-quality individuals are selected for cross-mutation to generate a new generation of high-quality solution populations, and the above steps are repeated until the optimal solution is generated [62]. The flow of genetic algorithm operation is shown in Figure 7. The genetic algorithm is a multi-point search algorithm, which can calculate and optimize complex multi-objectives at the same time, avoid falling into local minimum points, and ensure the global optimization ability [63]. The genetic algorithm has fast calculation in the early stage, but large amounts of redundant iterations in the later stage, which is not suitable for real-time trajectory planning [64].

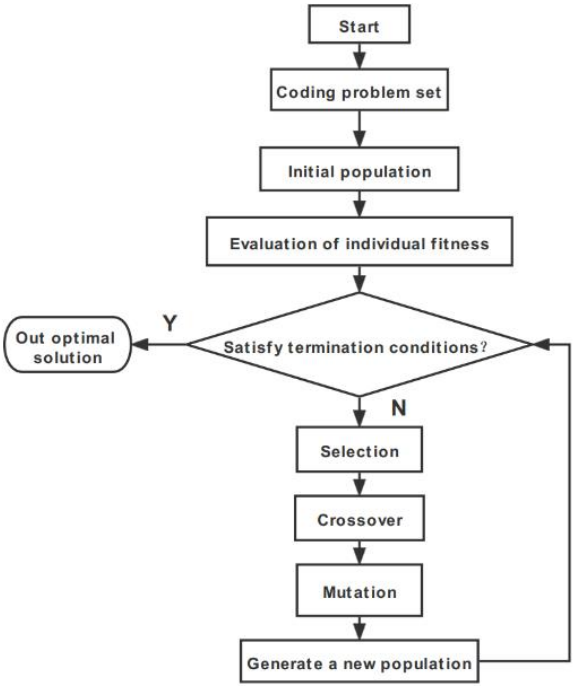

Figure 7. Flow chart of the genetic algorithm.

At present, many scholars have put forward improvement strategies to solve the problems of slow convergence speed and the ease of falling into local optimization in the later stage of the genetic algorithm. Cheng [65] proposed an improved genetic algorithm, the simulated annealing algorithm, which does not easily fall into the local optimal solution. This feature is integrated into the genetic algorithm to better solve the local optimal problem, and the directional mutation is introduced to speed up the search speed of the optimal solution of the genetic algorithm. Huang [66] improved the three operators of selection, crossover, and mutation in the genetic algorithm. Aiming at the premature convergence of the algorithm, a hybrid non-multiple string selection operator was proposed. In order to improve the convergence effect of the algorithm, an asymmetric mapping crossover operator was proposed. Through the heuristic multiple mutation operator, the premature phenomenon of the algorithm is suppressed. The results show that the improved algorithm has good environmental adaptability. Xu [67] proposed a global planning algorithm for plant protection UAVs for multi-regional operations of plant protection UAVs. The algorithm is divided into three parts: single-region route planning, inter-regional operation sequence planning, and inter-regional route scheduling planning. The improved genetics algorithm mainly focuses on the regional operation sequence and inter-regional route planning. The optimal operation area sequence is first solved, and then the optimal inter-area scheduling route is obtained through the improved genetic algorithm. The results show that the algorithm effectively realizes the global planning and improves the operational efficiency of plant protection UAVs.

At present, the research hotspots of the genetic algorithm mainly focus on the improvement of the algorithm. Based on the characteristics of the genetic algorithm being suitable for global search and strong robustness, it can be better applied to agricultural aviation operations in complex environments, and the algorithm is easy to combine with other algorithms [68], which can provide a more suitable fusion algorithm for different plant protection operation requirements.

4. Biological Intelligence and Agricultural Aviation

4.1. Brain-Like Navigation

Brain-like navigation has received extensive attention in recent years and has become one of the research hotspots in the field of artificial intelligence. In 1984, Tolman proposed that animals understand the environment through "cognitive maps" [69], and scholars have begun to explore animal brain navigation. In 1971, O'Keefe found place cells in the hippocampus of rats, then head direction cells, grid cells, border cells, etc., were discovered one after another. The mammalian brain has its own intelligent navigation system, which can form a cognitive map for positioning and navigation of the surrounding environment. This is related to the cells in the brain. The navigational cells mainly include head direction cells, grid cells, place cells, and border cells [70]. Head direction cells are responsible for recognizing the animal's position in the environment, and act as a compass in animal navigation. Grid cells and place cells cooperate to draw a cognitive map. Cells of the brain-like navigation system work together to continuously update the error-correcting cognitive map for precision navigation. The schematic diagram of the mammalian brain navigation system is shown in Figure 8.

Since humans have not yet fully understood the mechanism of the mammalian brain, the current development of brain-like navigation technology is at the stage of theoretical research. Liu [70] analyzed the key technology of the neural dynamics model combined with the neural network and attractor dynamics for navigation. This technology does not require modeling, does not require high sensor accuracy, is suitable for a variety of complex environments, and is robust. It has a strong development prospect. Liu pointed out that how to simulate the brain navigation mechanism from a deeper level, and how to improve the efficiency, accuracy, and real-time capabilities of the brain-like navigation model are the focuses for future research. Han [71] proposed a grid cell construction model based on differential Hebbian learning. This model builds the input correlation between grid

cells and the Mexico model by learning the change value of the positional cell discharge rate. This model provides a reference for the construction of UAVs' brain-like navigation system. Chen [72] used a one-dimensional ring attractor to model the head-facing cells, and used the sinusoidal interference model to obtain the grid-like activity pattern, and finally obtained the optimal movement direction according to all the activity sets, which solved the problem of dynamic adjustment of the network. It is effective and reliable, with superior navigation performance.

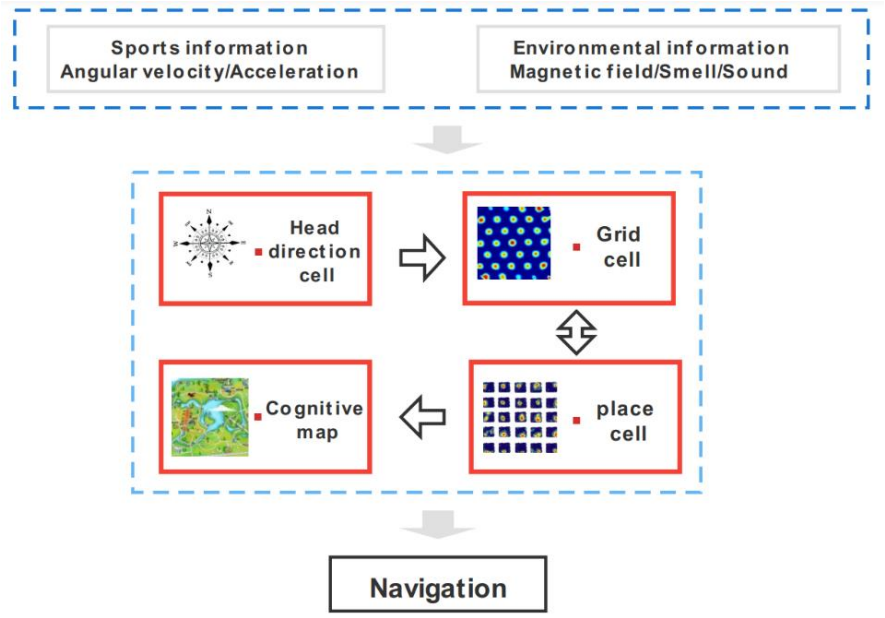

Figure 8. Schematic diagram of the mammalian brain navigation system.

Although brain-like navigation technology is the current hotspot of artificial intelligence, in-depth research on the brain and neurons is still needed. Brain-like navigation can realize unsupervised and autonomous operation of plant protection UAVs, abandon the unreliability of GPS (Global Positioning System) navigation due to signal fluctuations, and can autonomously respond to complex unknown environments such as light, rain, snow, and low visibility, so as to achieve precision agricultural aviation. At present, the research of brain-like navigation is not perfect, and the problems of large environment storage and calculation, and poor stability caused by imperfect algorithms still need to be solved.

4.2. Convolutional Neural Network

An artificial neural network is a kind of simulated bionics of biological neural networks. It is a dynamic network system composed of a large number of nonlinear arrangements of neurons. A convolutional neural network is an artificial neural network that includes convolutional layers, and is usually used to identify two-dimensional images [73], has stronger learning and expression capabilities than traditional machine learning [74], and can simulate the human visual system to classify feature data by extracting target images to achieve target recognition [75]. At present, convolutional neural networks have achieved certain results in the fields of artificial handwriting recognition [76], face detection [77], crop recognition [78], terrain perception [79], and other fields, and they have attracted the attention of many agricultural researchers [80]. Zhang [81] proposed to use the Series Otsu method, Faster Regional Convolutional Neural Network, and YOLO-v3 methods to identify the flowering state of rice, and also use the open and inner glumes. Experimental results show that the combination of the Series Otsu method and the Faster Regional Convolutional Neural Network to identify the flowering state of rice has a high degree of consistency with manual observation, and it can be used instead of the artificial use of a drone for rice flowering detection. In order to improve the accuracy of UAV

image recognition, Zhen [82] proposed the CNN-PNN (convolutional neural network-probabilistic neural network) model, which is a hybrid model combining the convolutional neural network and probabilistic neural network. The convolutional neural network is used to extract sample images. The feature vector is trained by a probabilistic neural network model and the output result. The simulation result shows that the model's recognition rate is as high as 96.3%. Liu [83] proposed a method of a fully convolutional neural network to identify pest areas, using a multi-rotor UAV to acquire pest images from the air, marking the pixels of the pest areas, learning and training, and constructing a model to identify the pest areas. Experiments show that the method has high recognition accuracy, and the pixel accuracy rate is as high as 97.86%. In order to improve the accuracy of pest identification, Yang [84] proposed a deep learning model of the convolutional neural network, which used image saliency analysis and the Grubcut algorithm to locate pests in complex backgrounds, and expressed and classified tea garden pests through the Alexnet convolution neural network architecture, so as to avoid human subjective factors affecting the classification results. Ma [85] built a greenhouse cucumber disease recognition model based on the convolutional neural network through the combination of deep learning and image processing technology. According to the characteristics of mixed colors, the model was compared with traditional colors, and the model was trained through image data collection and calculation. The results show that the accuracy of the model is up to 95.7%.

5. Discussion

This review summarized the application principles of bionics from the three modules of biological perception, biological behavior, and biological intelligence, and analyzed the latest progress of bionic technology in China's agricultural aviation research by enumerating representative literature. From the perspective of the development of bionic technology in human history, the development of bionics has not been smooth sailing since its conception more than 60 years ago. In the development, due to the backwardness of biology, manufacturing technology and equipment, analysis and testing technology and instruments, many bionic research studies cannot be carried out. As can be seen from Figure 9, relevant research on bionics had been carried out before the birth of the word bionics. This development phenomenon of wave-like progress is also one of the main reasons why people do not systematically recognize the combination concept of aero-bionics.

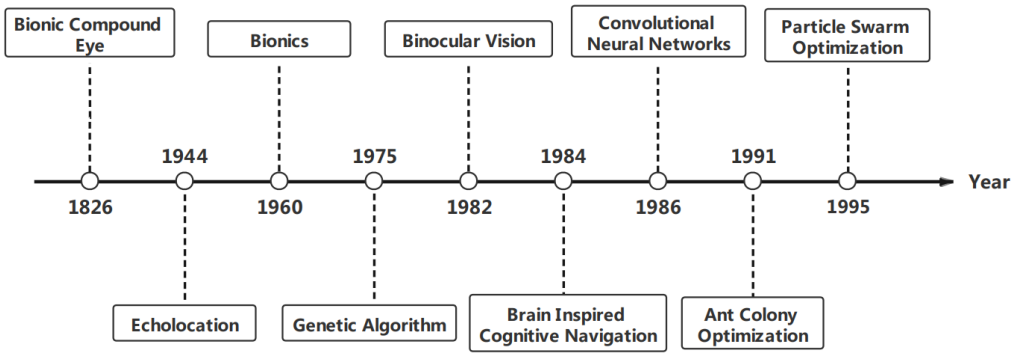

Figure 9. The timeline of research on bionic technology.

In general, bionic technology provides a new direction for the development of agricultural aviation. The proposal and improvement of various intelligent bionic algorithms have enriched agricultural aircraft precision and autonomous operation capabilities. The development of bionic sensors also provides new technical approaches to solve the problems faced by agricultural aircraft in obstacle avoidance and data collection. Bionics is a multi-discipline and comprehensive border subject. It is produced by the mutual penetration and integration of life science and engineering science. Looking to the future, the

research on agriculture aero-bionic technology requires breakthroughs in the following four aspects:

1. Research on multiple bionic targets. In the complex and harsh farmland environment, aviation operations are usually faced with multiple complex problems. While a single bionic target provides an optimized solution to a specific problem, it also has limitations. Only by effectively realizing these goals can the optimal bionic design requirements be better achieved. For example, in the face of complex farmland operating environments in the future, a variety of combinations can be proposed for different sensor characteristics so that agricultural aircraft can cope with complex operating environments and achieve real-time obstacle avoidance requirements, and it can also provide feasibility for the realization of precision spraying and intelligent navigation for agricultural aircraft. A variety of fusion bionic algorithms can propose optimal solutions for farmland environments with different operating requirements, avoiding the problems of slow calculations and ease of falling into local optima in a single algorithm. At the same time, according to the different characteristics of each algorithm, a more optimized bionic fusion algorithm can be designed according to the types of farmland operation and existing problems in the future. Therefore, the fusion of multiple bionic designs will help to efficiently solve the technical problems faced in the field of agricultural aviation.
2. In-depth exploration of three-dimensional spatial information. Three-dimensional spatial information exploration is mainly used in the fields of UAV obstacle avoidance, path planning, and image acquisition. When an aircraft faces complex and changeable operating environments such as terrain and air obstacles, the problem of how to effectively identify obstacles and make correct obstacle avoidance decisions still needs to be resolved. In China, there is relatively little research on the three-dimensional space operation of agricultural aircraft, and the follow-up work should increase the relevant research on the three-dimensional space operation of agricultural aviation.
3. Research on miniaturization, integration, and intelligence of sensor devices. In the face of a harsh operating environment, the operational efficiency of agricultural aircraft is inseparable from the support of communication, navigation, command, and other sensor equipment in the aircraft. At present, in the Chinese agricultural aviation aircraft, sensor equipment can complete the work of information collection and communication of the operating environment. However, the function of the sensor is relatively single, and the product has a large gap with biological perception in terms of power consumption, volume, and anti-interference in a complex environment. Therefore, in the future, it is necessary to improve the equipment manufacturing process, combine with bionic technology, strengthen the development of miniaturized sensor devices, and conduct in-depth research on integrated and intelligent sensor devices.
4. In-depth research on the mechanism of animal brain systems. Poor operating environment, electromagnetic interference, weak signal, and other factors usually affect the operating efficiency of agricultural aircraft, and even make it impossible to operate. Intelligent positioning and navigation technology obtains the surrounding environment information by imitating the mechanism of an animal brain system to construct cognitive maps or deep learning, so as to achieve the purpose of autonomous navigation and image recognition without relying on communication equipment. Agricultural aviation research on animal brain systems mainly focuses on deep learning, intelligent navigation, etc., but the current research is still at the theoretical stage, mainly because human beings have not yet fully understood the brain structure of animals, and the principle of cooperation between various cells and neurons in the brain needs to be further explored. In recent years, the combination of animal brain bionic research and robot learning has gradually become a new development trend, which provides a direction for the future intelligent development of agricultural aviation.

6. Conclusions

With the rapid development of science and technology, people's understanding of bionics is becoming more and more profound. The application of bionic technology in agricultural aviation will show diversified development, and the distribution of its research content is also extremely wide. From macro to micro, part to whole, and function to structure, all the advantages of biological systems can be applied in agricultural aviation. The development of aero-bionics in the field of agricultural aviation is diverse, and the integration of current advanced research results with agricultural aviation technology will enable bionics to make breakthroughs in the field of agricultural aviation. The cross-integration of technology and artificial intelligence, nanotechnology, biological systems, digital technology, remote sensing technology, management technology, and other disciplines is of great significance for promoting the transformation of China's agriculture from traditional agriculture to modern agriculture. The development of agricultural aviation is an indispensable force for the development of agricultural modernization. Therefore, learning the bionic concept and methods of simulating nature will strongly promote the development of precision agricultural aviation in China, and realize the agricultural aviation concept of high efficiency, green, low consumption, and sustainable development.

Author Contributions: Conceptualization, Y.Z. and Y.L.; methodology, H.T., Y.Z. and X.H.; validation, H.T. and L.W.; formal analysis, H.T., X.H. and C.M.; investigation, Y.Z., H.T. and L.W.; resources, H.T. and H.L.; data curation, H.T. and C.M.; writing—original draft preparation, H.T., C.M. and Y.Z.; writing—review and editing, Y.Z., X.H. and C.M.; visualization, H.T. and C.M.; supervision, Y.Z.; project administration, Y.Z. and Y.L.; funding acquisition, Y.L. All authors have read and agreed to the published version of the manuscript.

Funding: This research was funded by the Key Field Research and Development Plan of Guangdong Province, China, grant number 2019B020221001, the Science and Technology Plan Project of Guangdong Province, China, grant number 2018A050506073, and the 111 Project, grant number D18019.

Institutional Review Board Statement: Not applicable.

Informed Consent Statement: Not applicable.

Data Availability Statement: Not applicable.

Conflicts of Interest: The authors declare no conflict of interest.

References

1. Zhou, Z.Y.; Ming, R.; He, X.G.; Luo, X.W.; Lan, Y.B. Development status and countermeasures of agricultural aviation in China. *Trans. Chin. Soc. Agric. Eng.* **2017**, *33*, 1–13.
2. Qi, W.Z.; Wang, F.F.; Meng, Z.; Zhang, D.L.; Wang, H.Y.; Qiao, K.; Ji, X.X. Application status of unmanned aerial vehicle for plant protection in China. *Agrochemicals* **2018**, *57*, 247–254.
3. Luo, X.W.; Liao, J.; Hu, L.; Zang, Y.; Zhou, Z.Y. Improving agricultural mechanization level to promote agricultural sustainable development. *Trans. Chin. Soc. Agric. Eng.* **2016**, *32*, 1–11.
4. Luo, X.W.; Liao, J.; Hu, L.; Zhou, Z.Y.; Zhang, Z.G.; Zang, Y.; Wang, P.; He, J. Research progress of intelligent agricultural machinery and practice of unmanned farm in China. *J. South China Agric. Univ.* **2021**, *43*, 1–15.
5. Zhao, C.J. Current situations and prospects of smart agriculture. *J. South China Agric. Univ.* **2021**, *43*, 1–10.
6. Tao, Y.; Wang, T.M.; Liu, H.; Jiang, S. Insights and suggestions on the current situation and development trend of intelligent robots. *Chin. High Technol. Lett.* **2019**, *29*, 1–10.
7. Lan, Y.B.; Wang, L.L.; Zhang, Y.L. Application and prospect on obstacle avoidance technology for agricultural UAV. *Trans. Chin. Soc. Agric. Eng.* **2018**, *34*, 104–113.
8. Li, D.L.; Li, Z. System Analysis and development prospect of unmanned farming. *Trans. Chin. Soc. Agric. Mach.* **2020**, *51*, 1–12.
9. Lin, S.J.; Dong, C.; Chen, M.Z.; Zhang, F.; Cheng, J.H. Summary of new group intelligent optimization algorithms. *Comput. Eng. Appl.* **2018**, *54*, 1–9.
10. Guo, C.; Lu, Z.Y.; Wu, Y.Q. The application of biomimetic lightweight sandwich panel to the aircraft structure with large cutout and its optimum design. *J. Mech. Eng.* **2017**, *53*, 25–135. [CrossRef]
11. Ma, Y.; Ma, T.B.; Ning, J.G.; Gorb, S. Structure and tensile properties of the forewing costal vein of the honeybee Apis mellifera. *Soft Matter* **2020**, *16*, 4057–4064. [CrossRef] [PubMed]
12. Zhang, Z.H.; Zhang, G.K.; Tong, J.; Lai, Q.H.; Gao, X.H.; Tang, Y.; Stephen, C. Microstructure and tribology characteristics of head and chest exoskeleton of Procambarusclarkii. *Trans. Chin. Soc. Agric. Eng.* **2018**, *34*, 52–58.

13. Guo, Y.Q.; Yu, L.Z.; Mou, J.Z.; Wu, D.H.; Zhou, P.J.; Xu, M.S. Mechanical properties and application analysis of spider silk bionic material. *E-Polym.* **2020**, *20*, 443–457. [CrossRef]
14. Yin, Y. An Overview of smart sensors technology developing. *Microelectronics* **2018**, *48*, 504–507.
15. Li, Y.P.; Yang, J.; Li, X.D.; Tian, J. Texture classification based on echolocation used by bat. *Appl. Acoust.* **2007**, *26*, 335–340.
16. He, K.; Liu, Q.; Xu, D.M.; Qi, F.Y.; Bai, J.; He, S.W.; Chen, P.; Zhou, X.; Cai, W.Z.; Chen, Z.Z.; et al. Echolocation in soft-furred tree mice. *Science* **2021**, *372*, 1305. [CrossRef]
17. Liu, Z.; Bai, Q.; Shi, P. Genetic and lutionary mechanisms of convergent phenotypes in animals. *Sci. Sin. Vitae* **2019**, *49*, 338–344. [CrossRef]
18. Brinkløv, S.; Fenton, M.B.; Ratcliffe, J.M. Echolocation in oilbirds and swiftlets. *Front. Physiol.* **2013**, *4*, 123. [CrossRef]
19. Li, C.R.; Luo, B.; Wang, M.; Feng, J. Research progress on the function of acoustic signals in bats. *Sichuan J. Zool.* **2018**, *37*, 710–720.
20. Li, G.; Meng, X.J.; Wang, X.H.; Wang, C.Q. Research and application status on domestic ultrasonic ranging. *Sci. Surv. Mapp.* **2011**, *36*, 60–62.
21. Ohya, A.; Ohno, T.; Yuta, S. Obstacle detectability of ultrasonic ranging system and sonar map understanding. *Robot. Auton. Syst.* **1996**, *18*, 251–257. [CrossRef]
22. Li, M.S. The principle and practical technology of ultrasonic distance measurement. *China Meas. Test* **1994**, *01*, 12–20.
23. Su, W.; Gong, B.J.; Pan, X. Error analysis of measuring distance with ultrasonic. *J. Transducer Technol.* **2004**, *23*, 8–11.
24. Zhang, Y.Y.; Zhang, Y.J. Design of civil aviation airborne collision avoidance early warning system based on piecewise fitting algorithms. *J. Xi'an Polytech. Univ.* **2019**, *32*, 218–224.
25. Zhang, Y.H. Obstacle Avoidance Control System Design for Quadcopters Based on Machine Vision. Master's Thesis, Nanjing University of Aeronautics and Astronautics, Nanjing, China, 2017.
26. Zheng, K.; Hou, W.G.; Yao, Q.; Hua, Y. Multi-channel Ultrasonic Distance Measuring System of RS485 Bus Based on STM32 Microprocessor. *Instrum. Tech. Sens.* **2018**, *425*, 9–82.
27. Liu, H. Research on Method of Altitude Measuring Based on Ultrasonic Ranging for SUAV. Master's Thesis, Inner Mongolia University of Technology, Inner Mongolia, China, 2015.
28. Wang, M. Localization and obstacle avoidance control of agricultural robot based on DSP and ultrasonic distance measurement. *J. Agric. Mech. Res.* **2017**, *39*, 207–211.
29. He, Y.; Jiang, H.; Fang, H.; Wang, Y.; Liu, Y.F. Research progress of intelligent obstacle detection methods of vehicles and their application on agriculture. *Trans. Chin. Soc. Agric. Eng.* **2018**, *34*, 21–32.
30. Bai, M.; Zhuang, Y.; Wang, W. Progress in binocular stereo matching algorithms. *Control Decis.* **2008**, *23*, 721–729.
31. Sun, J.H.; Zhang, G.J.; Wei, Z.Z.; Zhou, F.Q. Mobile 3D vision measurement system for large-scale free form surface. *Chin. J. Sci. Instrum.* **2006**, *27*, 1688–1691.
32. Shen, T.; Liu, W.B.; Wang, J. Distance measurement system based on binocular stereo vision. *Electron. Meas. Technol.* **2015**, 52–54.
33. Yuan, X.J.; Ran, Q.; Zhao, W.Q.; Feng, J.Q. An iterative local color correction method for binocular stereo vision. *J. Comput. Aided Des. Comput. Graph.* **2019**, *31*, 65–75. [CrossRef]
34. Liu, H. The Research and Application of Stereo-Matching Algorithm Based on Binocular Vision. Master's Thesis, Harbin Institute of Technology, Harbin, China, 2018.
35. Wang, D. Key Technologies of Adaptive Navigation for Plant Protection UAV in Mountain Orchard. Ph.D. Thesis, Northwest A&F University, Xianyang, China, 2019.
36. Zhu, P.; Zhen, Z.Y.; Zhang, H.Q.; Jiang, J. Stereo vision and optical flow based obstacle avoidance algorithm for UAVs. *Electron. Opt. Control.* **2017**, *24*, 31–35.
37. Huang, P.C.; Jiang, J.Y.; Yang, B. Research status and progress of binocular stereo vision. *Opt. Instrum.* **2018**, *40*, 81–86.
38. Wang, H.W. The binocular obstacle avoidance function is coming, giving drones the ability to sense for the first time! *China Rural. Sci. Technol.* **2017**, *1*, 10.
39. DJI, I. Available online: https://dl.djicdn.com/downloads/matrice-300/20210419UM/M300_RTK_User_Manual_CHS_v1.8_20210310_1.pdf (accessed on 3 October 2021).
40. Chen, M.J.; Liu, Y.S.; Li, Z.A.; Zhu, X. New research progress in design and manufacture of artificial optical compound eye. *J. Mech. Eng.* **2011**, *47*, 161–168. [CrossRef]
41. Gao, W.J.; Yang, Y.L.; Xing, Q.; Xu, H.L. Compound eye binocular vision ranging method based on target motion. *J. Appl. Opt.* **2020**, *41*, 571–579.
42. Chen, H.P.; Shen, X.J.; Li, X.F.; Jin, Y.S. Bionic mosaic method of panoramic image based on compound eye of fly. *J. Bionic Eng.* **2011**, *8*, 440–448. [CrossRef]
43. Pang, K.; Song, L.; Fang, F.Z. Large field of view curved compound eye imaging system using optical freeform surface. *J. Optoelectron. Laser* **2018**, *29*, 8–13.
44. Yu, X.D.; Zhang, Y.J.; Wang, Y.Y.; Xu, H.R.; Yu, W.X. Optical design of a compound eye camera with a large-field of view for unmanned aerial vehicles. *Acta Photonica Sin.* **2019**, *48*, 17–24.
45. Yu, Z.Z.; Li, Q.; Fan, Q.G. Survey on application of bioinspired intelligent algorithms in path planning optimization of mobile robots. *Appl. Res. Comput.* **2019**, *36*, 3210–3219.
46. Dorigo, M.; Maniezzo, V.; Colorni, A. Ant system: Optimization by a colony of cooperating agents. *IEEE Trans. Syst. Man Cybern. Part B Cybern. A Publ. IEEE Syst. Man Cybern. Soc.* **1996**, *26*, 29–41. [CrossRef]

47. Wang, H. Comparison of several intelligent algorithms for solving TSP problem in industrial engineering. *Syst. Eng. Procedia* **2012**, *4*, 226–235.
48. Zhang, Y.; Quan, H.; Wen, J.F. Mobile robot path planning based on the wolf ant colony hybrid algorithm. *J. Huazhong Univ. Sci. Technol.* **2020**, *48*, 127–132.
49. Zhu, J.H.; Wang, X.Q.; Zhang, H.T.; Zhao, Y.; Li, Y.F. New ant colony optimization algorithm based on supervisory mechanism. *J. PLA Univ. Sci. Technol.* **2014**, *15*, 165–170.
50. Duan, H.B.; Wang, D.B.; Zhu, J.Q.; Huang, X.H. Development on ant colony algorithm theory and its application. *Control. Decis.* **2004**, *19*, 1321–1326.
51. Wang, Y.; Wang, W.H.; Xu, F.; Wang, J.H.; Chen, H.T. Path planning approach based on improved ant colony optimization for sprayer UAV. *Trans. Chin. Soc. Agric. Mach.* **2020**, *51*, 103–112.
52. Wang, Z.Z. Path planning for mobile robot based on improved ant colony algorithm. *Mach. Des. Manuf.* **2018**, *323*, 242–244. [CrossRef]
53. Feng, G.Q.; Zhao, X.L.; Gao, G.G.; Kou, L. Path planning of UAVs using A* ant colony algorithm. *Flight Dyn.* **2018**, *36*, 49–52.
54. Liang, X.H.; Mu, Y.H.; Wu, B.H.; Jiang, Y. Summary of Planning Algorithms. *Value Eng.* **2020**, *39*, 295–299.
55. Zhang, M.F.; Shao, C.; Gan, Y.; Li, M.J. Hybrid artificial fish swarm optimization algorithm based on mutation operator and simulated annealing. *Acta Electron. Sin.* **2006**, *34*, 1381–1385.
56. Zhang, G.L.; Hu, X.M.; Chai, J.F. Summary of path planning algorithm and its application. *Mod. Mach.* **2011**, *165*, 85–90.
57. Ma, Q.Z.; Lei, X.J. Application of improved particle swarm optimization algorithm in robotic path planning. *Comput. Eng. Appl.* **2011**, *47*, 241–244.
58. Wu, X.E. Coordination Tasks Pre-Allocation and Redistribution Studies in UAVs. Master's Thesis, Nanchang Hang Kong University, Nanchang, China, 2018.
59. Han, M.; Liu, J.M.; Wu, S.M.; Wang, J.T. Path planning algorithm of mobile robot based on particle swarm optimization. *J. Comput. Appl.* **2017**, *37*, 2258–2263.
60. Fang, Q.; Xu, Q. 3D route planning for UAV based on improved PSO algorithm. *J. Northwestern Polytech. Univ.* **2017**, *35*, 66–73.
61. Zhang, C.; Li, Q.; Wang, W.Q.; Chen, P.; Feng, Y.N. Immune particle swarm optimization algorithm based on the adaptive search strategy. *Chin. J. Eng.* **2017**, *39*, 25–132.
62. Huo, F.C.; Chi, J.; Huang, Z.J.; Ren, L.; Sun, Q.J.; Chen, J.L. Review of path planning for mobile robots. *J. Jilin Univ.* **2018**, *36*, 639–647.
63. Xu, X.N.; Lai, R. Present situation and future development of mobile robot path planning technology. *Comput. Simul.* **2006**, 1–4.
64. Hu, Z.H.; Zhao, M.; Yao, M.; Sa, P.F. Research and development trend of path planning for unmanned air vehicle. *Avion. Technol.* **2009**, *40*, 24–29.
65. Cheng, Z.X.; Li, D.S.; Gao, Y. GASA drone path planning to improve mutation strategy. *Comput. Simul.* **2019**, *36*, 31–35.
66. Huang, S.Z.; Tian, J.W.; Qiao, L.; Wang, Q.; Su, Y. Unmanned aerial vehicle path planning based on improved genetic algorithm. *J. Comput. Appl.* **2021**, *41*, 90–397.
67. Xu, B.; Chen, L.P.; Xu, M.; Tan, Y. Path planning algorithm for protection UAVs in multiple operation areas. *Trans. Chin. Soc. Agric. Mach.* **2017**, *48*, 75–81.
68. Xie, K.L.; Yang, H.T.; Xie, H.P. Research sates of intelligent track planning algorithm. *J. Ordnance Equip. Eng.* **2020**, *41*, 8–13.
69. Tolman, E.C. Cognitive maps in rats and men. *Psychol. Rev.* **1948**, *55*, 189–208. [CrossRef] [PubMed]
70. Liu, J.Y.; Yang, C.; Xiong, Z.; Lai, J.Z.; Xiong, J. Attractor neural network-based Brain-inspired navigation technology for UAV. *Navig. Position. Timing* **2019**, *6*, 52–60.
71. Han, K.; Wu, D.W.; Lai, L. Model of generating grid cell based on difference Hebbian learning in brain-inspired navigation. *Syst. Eng. Electron.* **2020**, *42*, 674–679.
72. Chen, Q.Y.; Mo, H.W. A brain-inspired goal-oriented robot navigation System. *Appl. Sci.* **2019**, *9*, 4869. [CrossRef]
73. Liu, D.Y.; Wang, J.L.; Lin, X.Z.; Chen, J.; Yu, H.M. Automatic identification method for sogatella furcifera based on convolutional neural network. *Trans. Chin. Soc. Agric. Mach.* **2018**, *49*, 51–56.
74. Long, M.S.; Ouyang, C.J.; Liu, H.; Fu, Q. Image recognition of Camellia oleifera diseases based on convolutional neural network & transfer learning. *Trans. Chin. Soc. Agric. Eng.* **2018**, *34*, 194–201.
75. Zhang, J.H.; Kong, F.T.; Wu, J.Z.; Zhai, Z.F.; Han, S.Q.; Cao, S.S. Cotton disease identification model based on improved VGG convolution neural network. *J. China Agric. Univ.* **2018**, *23*, 161–171.
76. Zhou, F.Y.; Jin, L.P.; Dong, J. Review of convolutional neural network. *Chin. J. Comput.* **2017**, *40*, 1229–1251.
77. Singh, R.; Om, H. Newborn face recognition using deep convolutional neural network. *Multimed. Tools Appl.* **2017**, *76*, 19005. [CrossRef]
78. Wang, C.; Wu, X.H.; Li, Z.W. Recognition of maize and weed based on multi-scale hierarchical features extracted by convolutional neural network. *Trans. Chin. Soc. Agric. Eng.* **2018**, *34*, 144–151.
79. Luo, S.; Wang, K.; Song, J.G.; Liu, Y.H. A bio-inspired drone design based on neural network. *Res. Explor. Lab.* **2019**, *38*, 62–64.
80. Liang, W.J.; Cao, H.X. Rice pest identification based on convolutional neural network. *Jiangsu Agric. Sci.* **2017**, *45*, 241–243.
81. Zhang, Y.L.; Xiao, W.W.; Lu, X.Y.; Liu, A.M.; Qi, Y.; Liu, H.C.; Shi, Z.K.; Lan, Y.B. Method for detecting rice flowering spikelets using visible light images. *Trans. Chin. Soc. Agric. Eng.* **2021**, *37*, 253–262.

82. Zhen, R.; Yu, J.X.; Zhao, G.H.; Wu, X.L. Simulation research on UAV recognition method based on convolutional neural network. *J. Hebei Univ. Sci. Technol.* **2019**, *40*, 397–403.
83. Liu, W.D.; Tian, H.B.; Xie, J.J.; Zhao, S.T.; Zhang, J.G. Identification methods for forest pest areas of UAV aerial photography based on fully convolutional networks. *Trans. Chin. Soc. Agric. Mach.* **2019**, *50*, 79–185.
84. Yang, G.G.; Bao, Y.D.; Liu, Z.Y. Localization and recognition of pests in tea plantation based on image saliency analysis and convolutional neural network. *Trans. Chin. Soc. Agric. Eng.* **2017**, *33*, 156–162.
85. Ma, J.C.; Du, K.M.; Zheng, F.X.; Zhang, L.X.; Sun, Z.F. Disease recognition system for greenhouse cucumbers based on deep convolutional neural network. *Trans. Chin. Soc. Agric. Eng.* **2018**, *34*, 186–192.

applied sciences

MDPI

Review

Development and Prospect of UAV-Based Aerial Electrostatic Spray Technology in China

Yali Zhang [1,2], Xinrong Huang [1,2], Yubin Lan [2,3], Linlin Wang [2,3], Xiaoyang Lu [1,2], Kangting Yan [1,2], Jizhong Deng [1,2,*] and Wen Zeng [1,2,*]

[1] College of Engineering, South China Agricultural University, Wushan Road, Guangzhou 510642, China; ylzhang@scau.edu.cn (Y.Z.); xrhuang@stu.scau.edu.cn (X.H.); luxiaoyang@stu.scau.edu.cn (X.L.); ktyan@stu.scau.edu.cn (K.Y.)

[2] National Center for International Collaboration Research on Precision Agricultural Aviation Pesticide Spraying Technology, Wushan Road, Guangzhou 510642, China; ylan@scau.edu.cn (Y.L.); wlinlin@stu.scau.edu.cn (L.W.)

[3] College of Electronic Engineering and College of Artificial Intelligence, South China Agricultural University, Wushan Road, Guangzhou 510642, China

* Correspondence: jz-deng@scau.edu.cn (J.D.); zengwen@scau.edu.cn (W.Z.)

Abstract: Aerial electrostatic spray technology for agriculture is the integration of precision agricultural aviation and electrostatic spray technology. It is one of the research topics that have been paid close attention to by scholars in the field of agricultural aviation. This study summarizes the development of airborne electrostatic spray technology for agricultural use in China, including the early research and exploration of Chinese institutions and researchers in the aspects of nozzle structure design optimization and theoretical simulation. The research progress of UAV-based aerial electrostatic spray technology for agricultural use in China was expounded from the aspects of nozzle modification, technical feasibility study, influencing mechanism of various factors, and field efficiency tests. According to the current development of agricultural UAVs and the characteristics of the farmland environment in China, the UAV-based aerial electrostatic spray technology, which carries the airborne electrostatic spray system on the plant protection UAVs, has a wide potential in the future. At present, the application of UAV-based aerial electrostatic spray technology has yet to be further improved due to several factors, such as the optimization of the test technology for charged droplets, the impact of UAV rotor wind field, comparison study on charging modes, and the lack of technical accumulation in the research of aerial electrostatic spray technology. With the continuous improvement of the research system of agricultural aviation electrostatic spray technology, UAV-based electrostatic spray technology will give play to the advantages in increasing the droplets deposition on the target and reducing environmental pollution from the application of pesticides. This study is capable of providing a reference for the development of the UAV-based agricultural electrostatic spray technology and the spray equipment.

Keywords: agricultural aviation; UAV; plant protection; review; electrostatic spray technology; droplet deposition; aerial pesticides application; charge to mess ratio

check for updates

Citation: Zhang, Y.; Huang, X.; Lan, Y.; Wang, L.; Lu, X.; Yan, K.; Deng, J.; Zeng, W. Development and Prospect of UAV-Based Aerial Electrostatic Spray Technology in China. *Appl. Sci.* **2021**, *11*, 4071. https://doi.org/10.3390/app11094071

Academic Editor: Sylvain Bertrand

Received: 12 April 2021
Accepted: 28 April 2021
Published: 29 April 2021

Publisher's Note: MDPI stays neutral with regard to jurisdictional claims in published maps and institutional affiliations.

Copyright: © 2021 by the authors. Licensee MDPI, Basel, Switzerland. This article is an open access article distributed under the terms and conditions of the Creative Commons Attribution (CC BY) license (https://creativecommons.org/licenses/by/4.0/).

1. Introduction

Electrostatic spray technology for agricultural aviation is the application of traditional electrostatic spray technology in an airborne platform. It is one of the research topics that scholars in the field of agricultural aviation always pay attention to. Agricultural aerial electrostatic spray technology is mainly based on induction, corona, and contact charging methods to charge the droplets. Under the action of high voltage static electricity, charged droplets make rapid directional deposition along the electric field line in the air and settle on the target [1,2]. For this reason, aerial electrostatic spray can effectively reduce drift loss during aerial pesticide application, improve droplet deposition, and mitigate

environmental pollution [3,4]. Carlton et al. [5] from the Agricultural Research Service of the United States Department of Agriculture (USDA-ARS) designed an electric rotating electrostatic nozzle in 1966, which was the first scientific research institution in the world to carry out research on aerial electrostatic spray technology for agriculture. Carlton also obtained the invention patent of the aerial electrostatic spray technology in 1999 [6]. The patent was certified by the United States Department of Agriculture as the world's first and only commercially proven airborne electrostatic spray system for agriculture [7]. SES (Spectrum Stack Sprayers, Inc., Houston, TX, USA) has been awarded an exclusive license to manufacture and market this innovative technology. Subsequently, scientific research institutions in the United States, Brazil, Canada, Switzerland, and China have conducted a large number of studies to gradually improve the research and application of electrostatic spray in agricultural aviation [8–10].

The research of electrostatic spray technology for agricultural aviation started relatively late in China but developed rapidly. Especially in recent years, the rapid development of plant protection UAVs in China has attracted scholars to make a lot of attempts on the research and application of UAV-based electrostatic spray technology. This study introduced the early exploration of aerial electrostatic spray technology in China from the aspects of nozzle structure design optimization, theoretical simulation, and field experiment with manned aircraft platforms. Then, the research progress of UAV-based electrostatic spray technology in China was emphatically expounded upon, and the existing problems were discussed as well. It is proposed that future research should be carried out in the measurement technology for charged droplets, the influence of UAV rotor wind field on charged droplets, comparative study of various charging methods, and other aspects, so as to increase the accumulation of research on aerial electrostatic spray technology based on an agricultural UAV platform. This study can provide a reference for the development of the agricultural aviation electrostatic spray technology and the spray equipment.

2. Early Exploration of Aerial Electrostatic Spray Technology in China

In the 1970s, China began to study the new technology of electrostatic spraying for agricultural application [11]. In 1977, Shenyang Spray Factory used hand-held sprayers to carry out field spraying experiments on the seedlings and young trees of cloves and found that the application of electrostatic spraying treatment could increase the amount of pesticides applied per unit area of plants while reducing the labor intensity [12]. After the application of electrostatic spray technology in hand-held and knapsack sprayers, it has also achieved success in the application of ground agricultural machinery equipment in greenhouses, orchards, and other operating scenarios [13,14]. A large number of studies on the effects of electrostatic spray equipment have been carried out on droplet size, droplet deposition distribution in each part of crop canopy, nozzle structure, and working parameters on droplet quality, etc. [15–19].

In 2005, China introduced the electrical parts and nozzles of the aerial electrostatic spray system from the SES company and carried out simulation tests and flight tests [20], marking the beginning of China's research in the field of aerial electrostatic spraying. Two years later, universities and scientific research institutions in China began to comprehensively study the aerial electrostatic spray technology based on manned aircraft platforms in aspects of hardware structure improvement, mechanism of influencing factors, and theoretical simulation.

2.1. Hardware Structure Improvement

Hardware structure improvement research refers to the adjustment or structural modification of system parameters such as electrode material, nozzle size, rotor number, and nozzle position of aerial electrostatic spray systems [21].

In 2007, Ru et al. [22] introduced a structured design on a double-nozzle for an aerial electrostatic sprayer and theoretically analyzed the space field induced by the double-nozzle and the impact on the size and charging droplets from the space field.

Zhou et al. [23] improved the design of an aerial electrostatic single-nozzle from the aspects of an electrostatic electrode, nozzle material, nozzle processing technology, connection mode of high voltage wire and electrode, rotating screw joints, overflow valve body, and so on, in order to meet the requirements for application and large-scale production.

In terms of the electrode of electrostatic nozzles, Ru et al. [24] modified the original cylindrical electrode to a cone-shaped electrode according to the features of aerial electrostatic spraying. The effect of charging voltage on the charge to mass ratio and deposition distribution of the new aerial electrostatic system was tested under simulated flight conditions. It was found that the electrostatic spray was beneficial to increase the average deposition of charged droplets on the lateral, bottom, and back sides of the neutral target significantly. Jin et al. [25] improved the ring electrode of an aerial electrostatic nozzle and conducted an experimental study on the droplet size and the charging effect of droplets after the improvement. Results showed that droplet size was influenced by nozzle diameter, spraying pressure, and charging voltage, of which the spray pressure indicated the strongest effect, and charging voltage showed the weakest effect. The charge to mass ratio increased with the increase in voltage, reaching a maximum of 2.09 mC/kg, and tends to saturation at 8 kV. The charge to mass ratio decreased with the increase in droplet size, but the change was not rapid.

2.2. Research on Mechanism of Influencing Factors

The settling process of charged droplets is restricted by environmental factors, controllable factors, and target parameters during spraying operation, thus affecting the operation quality of the electrostatic spraying system. Among these influencing factors, environmental factors include temperature, humidity, wind speed, soil, etc.; controllable parameters include charging voltage, spraying flow, spraying pressure, flight altitude, flight speed, etc.; target parameters include crop objects, target morphology, leaf inclination, and insect pest types and habits, and so on [21].

Yang et al. [26] studied the influence of different crosswinds wind speed conditions and electrostatic voltage on charging characteristics through indoor simulation of natural wind and constant wind environment, providing a basis for strengthening the anti-drift ability of charged spray droplets in the settling process. Chen et al. [27] analyzed the characteristics of the electrostatic field induced by the ring electrode with the help of Fluent software (Version 6.3). It was found that the higher charging voltage or smaller electrode spacing (when the distance between the induction electrode ring and the nozzle was less than 10 mm) could effectively improve the charge effect and spray quality.

3. Rapid Progress of UAV-Based Electrostatic Spray Technology

3.1. Research Background

In 2014, China's agricultural pesticide application was still dominated by large fixed-wing aircraft, supplemented by rotary-wing UAVs [28]. However, since 2015, with the urbanization process in China, the rural labor force population has become less and less. Meanwhile, with the improvement of living standards, automatic pesticide application tools have gradually been accepted by farmers [29]. Nowadays, plant protection UAVs have maintained a booming trend in the field of agricultural plant protection. China has taken an internationally leading position in terms of technology, quantity, and product types of agricultural plant protection UAVs [30].

Figure 1 shows the increasing number of plant protection UAVs and operating areas covered in China from 2014 to 2020. The number of plant protection UAVs has reached 106,000 units with an operation area covered of 64 million hm^2 in 2020. In this context, Chinese scholars began to put forward the idea of applying aerial electrostatic spray technology to UAVs, while there are few reports on this topic worldwide.

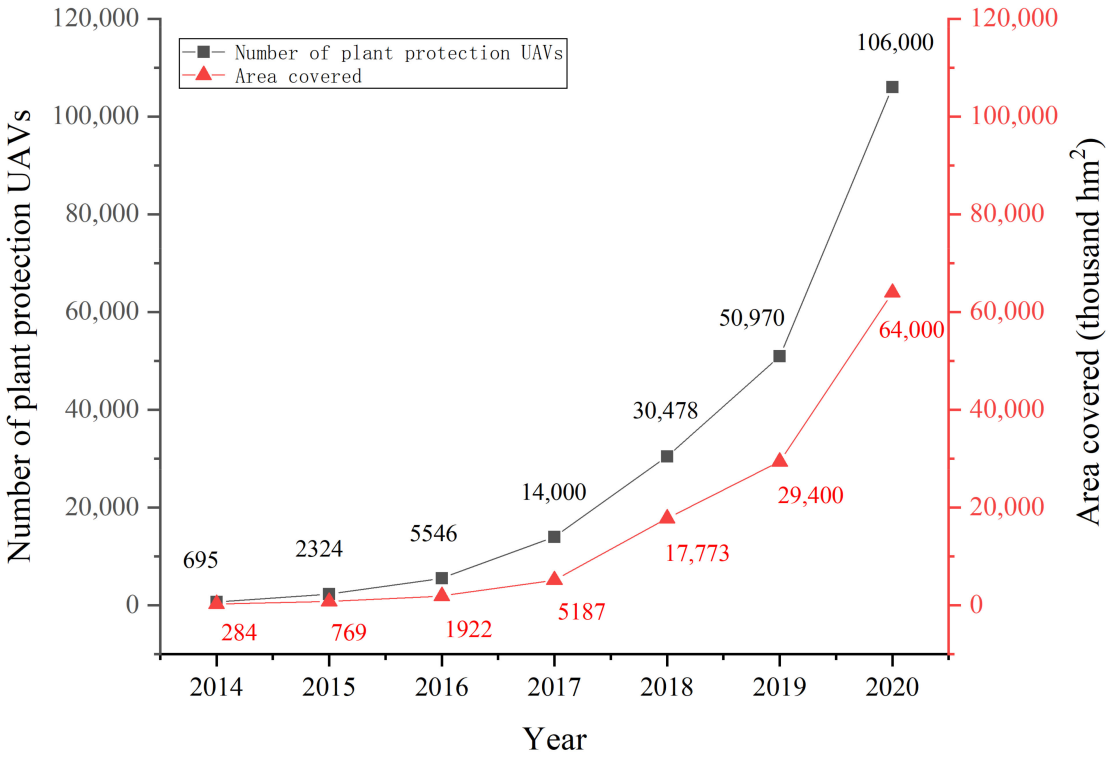

Figure 1. Increasing number of plant protection UAVs and operating area covered in China (2014–2020).

3.2. Beginning of the Research on UAV-Based Electrostatic Spray Technology

In 2015, Ru et al. [31] tried the first combination of electrostatic spray technology and plant protection UAV with an XY8D unmanned helicopter and carried out field tests in a rice field, as shown in Figure 2. A preliminary experiment on spray pressure, flow rate, and charging voltage were conducted to determine the optimal parameters for field tests. Field spraying test results showed that the droplet deposition and coverage rate on the target crop was effectively improved by the UAV-based electrostatic spraying when compared with non-electrostatic spraying. The influence of environmental factors and physical properties of the liquid was not verified in this experiment. However, the first study of carrying the electrostatic spray system on a UAV was of great value. Chinese scholars then began to make continuous innovations and breakthroughs in UAV-based electrostatic spray technology.



Figure 2. Rice field test with an XY8D UAV-based electrostatic spray system [31].

3.3. Continuous Optimization of UAV-Based Electrostatic Spray Technology

Chinese researchers have carried out a series of optimization work from the aspects of nozzle modification, test effect comparison, and mechanism of influencing factors in order to meet the precise operation requirements of UAV-based electrostatic spray system in practical application and to improve the droplet deposition on the target crops.

In terms of nozzles modification, Wang et al. [32] improved the conventional nozzles for multi-rotor plant protection UAVs. An inductive type electrostatic centrifugal nozzle was developed by combining agricultural electrostatic spray technology with a centrifugal atomizing nozzle. Besides, the spraying flow stability test and droplet deposition effect of the system were studied. When the charging voltage of the nozzle reaches 8 kV, the charge to mass ratio reaches the maximum value of 0.59 mC/kg.

In terms of comparison with the test results of non-electrostatic spray, Jin et al. [33] from Nanjing Forestry University designed an electrostatic spray system for the AF-118 helicopter. Through the effective spraying width and droplets deposition characteristics, it is found that the effective spraying width of electrostatic spray was smaller than that of non-electrostatic spray. The total droplet deposition number of electrostatic spray (9–36 drops/cm^2) was higher than that of non-electrostatic spray (6–26 drops/cm^2). Lian [34] used YG-6 six-rotor UAV to carry an electrostatic spray system. Through an indoor performance test, the optimal operating parameter combination of the system was determined (spraying height is 50 cm, charging voltage is 9 kV, spraying pressure was 0.3 MPa). This parameter combination was used to test the electrostatic spray effect of outdoor UAVs. The result showed that the average deposition density of droplets sprayed above the target by electrostatic spray was 16.1 more/cm^2, 13.6% higher than that by non-electrostatic spray. The average sediment density in the middle was 28 more/cm^2, which increased by 32.6%. Cai [35] developed an aerial electrostatic spray system based on an F-50 plant protection UAV. The spray system adopts contact charge, and the experimental research is carried out according to the factors of the rotor wind field, such as wind speed, charge to mass ratio, flight height, and flight speed. Through field spraying experiments, as shown in Figure 3, it was found that the flight height is an important factor affecting the deposition amount and the horizontal deposition uniformity but has little effect on the vertical deposition uniformity. Zhao et al. [36] proposed a method of charging the liquid in two isolated water tanks with positive and negative charges respectively by a high-voltage electrostatic generator based on the contact charge mode to solve the problem of insufficient adsorption rate of droplets on the target back when using an aerial electrostatic spray. Aerial electrostatic spraying test stand and UAV electrostatic spray system were designed, which proved that it was feasible to develop a charge transfer loop in space to improve the adsorption performance of droplets. An electrostatic physical model of aerial electrostatic spray based on charge transfer space loop is shown in Figure 4. Zhang et al. [37] developed a fan-shaped induction electrostatic spray system based on a six-rotor UAV and defined the corresponding operating parameters (spray height 50 cm, spray pressure 0.3 MPa, and charging voltage 9 kV). Compared with non-electrostatic spray, the electrostatic spray had more concentrated droplet deposition and smaller drift. The average droplet deposition density at the top of the electrostatic spray sampling device was 16.1 drops/cm^2 higher than that of non-electrostatic spray, and the deposition density in the middle was 28 drops/cm^2 higher than that of non-electrostatic spray. Therefore, aerial electrostatic spray could significantly improve droplet deposition and prevent drift.



Figure 3. UAV paddy field spraying operations [35].

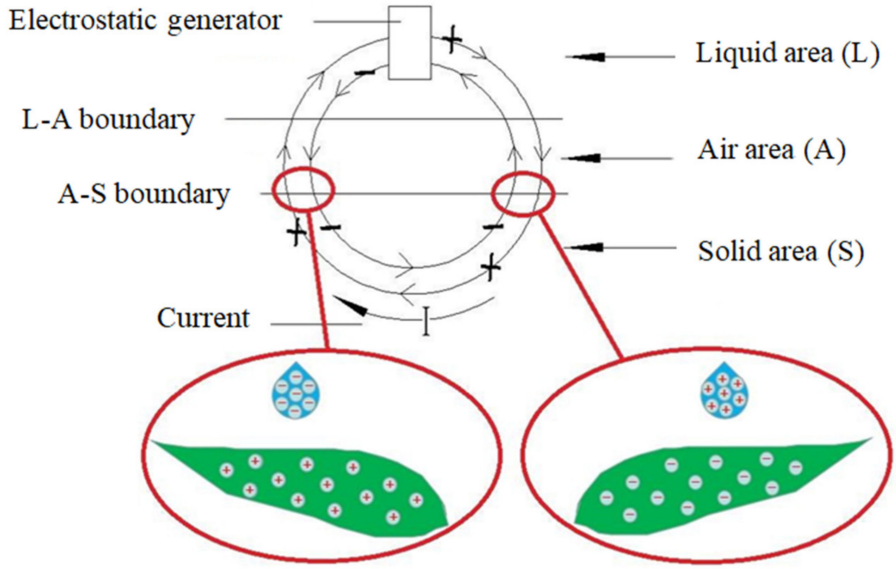

Figure 4. Electrostatics physical model of aerial electrostatic spraying based on charge transfer space loop [36].

In terms of the mechanism of influencing factors, Bu [38] designed an electrostatic spray system based on the FR-200 large-load unmanned helicopter with a maximum load of 80 kg. The charge and spray characteristics of the electrostatic spray system were studied, and the prediction models of the charge to mass ratio and droplet size were established. The characteristics of deposition and drift of electrostatic spray of heavy load unmanned helicopter were analyzed by field experiments. It was concluded that the charge voltage, flight height, and crosswind wind speed were the main factors affecting the drift and deposition of an electrostatic spray of FR-200. The results showed that the charge voltage had the greatest influence, followed by the crosswind wind speed, and the flight height had the least influence. Based on the research results, the mathematical model was established between the center distance of droplet mass and droplet drift rate and the charged voltage, flight height, and crosswind wind speed. Wu et al. [39] introduced response surface analysis (RSM) into the optimization design of spray parameters of Electrostatic spray system of UAVs. A response surface model with injection pressure and nozzle diameter as design variables and droplet charge to mass ratio as optimization objectives was constructed. The performance tests of the new electrostatic spray system under different nozzle diameters, spray pressures, and electrostatic voltages were carried out. It showed that the nozzle met the theoretical requirements of optimal biological particle

size and the requirements of hydraulic spray control for most crop diseases and insect pests. The validity of the model was also proved. In addition, multivariate analysis of variance showed that nozzle diameter, spray pressure, and electrostatic voltage have important effects on performance. The influence of the two factors on the deposition density and uniformity is the spray pressure, the nozzle diameter, and the optimal combination of the factor levels to obtain the best results. Chinese scholars also carried out research on multiple operating parameters and their interaction effects on the performance of aerial electrostatic spray systems. Lu et al. [40] simulated the spray performance of UAV-based electrostatic spray systems at different flight heights by measuring the droplet diameter under different nozzle apertures and system pressures and obtained the optimal flight parameter combination. Zhao et al. [41] studied the spray deposition with three factors: spraying duration, charging voltage, and flight height. The experimental results showed that the back-front ratio of droplets on the back and front of leaf targets could reach 158.8% under indoor conditions, and the droplet size on the back was smaller than that on the front. The number of droplets increased with the accumulation of spraying time without affecting the back-front ratio. Higher charging voltage and lower spraying height for the aerial electrostatic spray system can achieve a better deposition effect and higher back-front ratio. Wang et al. [42] established theoretical equations of droplet group charge based on the water inductive charging theory and then studied the effects of electrode figuration (electrode ring diameter, electrode spacing, spray pressure, and charge voltage) on droplet charging and spray performance through experiments. Under the action of an electrostatic field, the droplet size decreased obviously with the increase in charged voltage. The charge performance improved with the decrease in electrode ring diameter. Lan et al. [43] studied the impact of electrode materials on the deposition characteristics of an aerial electrostatic system with different orifice sizes, system pressures, and charging voltages. The results showed that red copper was the best electrode material. Li et al. [44] simulated five factors, such as temperature, humidity, electrode ring diameter, electrostatic voltage, and nozzle flow, using a BP model based on Neuroshell software and studied the effects on the charge to mass ratio of airborne electrostatic droplets. The final linear regression model indicated that the charging voltage and flow rate were the two main influencing factors on the droplet charge to mass ratio.

3.4. Spray Efficiency Experiments of UAV-Based Electrostatic Spray Technology

Wang et al. [45] designed a bipolar contact oil-powered single rotor aerial electrostatic spray system for plant protection UAVs. The static electricity system was used to spray the static electricity oil agent and the conventional water-based chemical agent. Besides, the spray droplet deposition distribution and the control effect of wheat aphid and rust were tested. The result showed that the deposition per unit area was 0.0486 $\mu g/cm^2$, the standard deviation of deposition amounts was 0.015 $\mu g/cm^2$, and the coefficient of variation was 30.43%. The distribution uniformity of droplet deposition is obviously better than the other two treatments, and the prevention and control of diseases and insect pests in the wheat field showed a good control effect. The aphid control effect was 87.92% on the seventh day after spraying, which was significantly higher than that of the conventional spray treatment (76.43% with the electrostatic oil agent and 66.47% with the conventional water-based agent). Liu [46] designed a high-voltage electrostatic generator with smaller volume and mass based on the optimized structure parameters of the cone-shaped electrode and the determined dosage form of the special electrostatic liquid agent for aviation. It was more suitable for plant protection UAVs, aimed at the current problems such as the poor charging effect of droplets, poor applicability of aerial spraying agents, complex high-voltage electrostatic generator system, and heavy high-voltage electrostatic generator. In addition, a set of electrostatic spray systems that can be applied to six-rotor and single-rotor plant protection UAVs was developed, as shown in Figure 5. The system was mounted on the plant protection UAV and carried out the experiment in the cotton and rice-growing areas of Changji, Xinjing, Shihezi, Xinjing, and Ledong, Hainan. The results of

spraying operation of hybrid breeding rice growth regulator and defoliating cotton agent by plant protection UAV showed that when spraying rice growth regulator by plant protection UAV, the effect of electrostatic spraying could be up to 20% higher than that of non-static spraying, and the effects of spraying different chemicals were different. When sprayed the cotton defoliant, the coverage rate of droplet increased by 140%, the defoliation efficacy increased by 12.22%, and the cotton boll opening rate increased by 18.55%.



(**a**) (**b**)

Figure 5. HY-B-15L single-rotor plant protection unmanned helicopter for cotton defoliant spray (**a**) and TXA616 plant protection UAV for rice growth regulator spray (**b**) [46].

3.5. Summary

To sum up, a large number of field experiments have been conducted in China to test the actual performance of the electrostatic spray system based on UAVs. For the convenience of comparative analysis, Table 1 summarizes the researches on UAV-based electrostatic spray systems. From the perspective of the test scheme, the system pressure, flight height and speed, charging voltage, rotor wind speed, and their effects on each other were studied. Chinese scholars have also completed a lot of work using theoretical simulations of the spray system, the improvement of the electrostatic nozzle, and the optimization of the aerial chemicals. In terms of the mode of charge, most studies adopt the induction mode of charge with the highest safety. The inductive charging voltage is usually between 2 kV and 15 kV, and the electrode making and insulation methods are easy to be realized, which is the most developed method of charging droplets at present [47]. In addition, contact charging has also been tried in China, which has also achieved good results [34–36,41,45]. However, it needs to keep the absolute insulation of the spray system in the charging process, which puts forward high requirements for the design method and safety.

Figure 6 illustrates the key achievements of the aerial electrostatic spray technology and the research groups over a timeline. Since 2015, China's UAV-based aerial electrostatic spray technology has developed rapidly. In general, although the UAV-based electrostatic spray technology is a new technology, it is gradually being improved. Compared with the electrostatic spray system on manned aircraft, plant protection UAVs have more development prospects in China at present. With the operation area covered exceeding 67 million hm^2, the plant protection UAV has developed from an early experimental product into a common agricultural production machine in China [48]. It is of great practical significance to study the fusion and influence mechanism of UAV and aerial electrostatic spray systems, which contributes to the field of agricultural aviation plant protection in the future.

Table 1. Study on UAV-based Electrostatic Spray System.

Test Device	Charged Mode	Test Target	Test Method	Evaluating Indicator	Test Environment	Researchers and Affiliation
XY8D UAV	Induction	Rice	Different flight height	Droplet deposition characteristics	Field test	Ru, et al., Nanjing Forestry University
AF-811 unmanned helicopter	Induction	Copy paper	Comparison of electrostatic spray and non-electrostatic spray	Effective spray amplitude and droplet deposition characteristics	Outdoor	Jin, et al., Nanjing Forestry University
YG20-6 type six-rotor UAV	Induction	Water sensitive paper	Comparison of electrostatic spray and non-electrostatic spray	Measurement of effective spray amplitude, droplet penetration, and droplet deposition	Outdoor	Lian, Heilongjiang Bayi Agricultural University
F-50 plant-based unmanned helicopter	Contact	Sample tape, rice	Comparison of different charge modes (non-electrostatic, induction electrostatic, contact electrostatic)	Droplet deposition measurement and coefficient of variation of deposition amount	Field test	Cai, Jiangsu University
HY-B-15L single rotor plant protection unmanned helicopter, TXA micro six-rotor UAV	Induction	Crossbreeding rice, Cotton picked by machine	Comparison of different water agents, number of rotors, and crops	Droplet deposition characteristics and pharmacodynamics	Field test	Liu, South China Agricultural University
Integrated spray test stand	Induction	Water sensitive paper	Comparison of electrostatic spray and non-electrostatic spray	Density of droplet deposition	Indoor	Zhang et al., Heilongjiang Bayi Agricultural University
3WQF120-12 oil-operated single-rotor plant protection UAV	Contact	wheat	Comparison between electrostatic oil agent and conventional water-based agent, electrostatic spray and conventional spray system	Distribution uniformity of droplet deposition and its control effect on wheat aphid and rust	Field test	Wang et al., China Agriculture University
FR-200 type large-load unmanned helicopter	Induction	Water sensitive paper	Charged voltage, flight speed, flight height, and crosswind wind speed	Droplet deposition characteristics and droplet drift rate	Field test	Bu, Jiangsu University

Table 1. *Cont.*

Test Device	Charged Mode	Test Target	Test Method	Evaluating Indicator	Test Environment	Researchers and Affiliation
response surface methodology (RSM)	Induction	-	Nozzle diameter, nozzle pressure, and electrostatic voltage	Droplet deposition characteristics and charge to mass ratio	Simulation	Wu et al., Guizhou University
Gaoke M45 plant protection UAV	Contact	Mock target	Comparison of electrostatic spray and non-electrostatic spray	Droplet deposition characteristics	Outdoor	Zhao et al., Shandong University of Technology
W730S four-rotor semi-automatic plant protection UAV	Induction	Effusion cylinder	-	Droplet deposition measurement and spray flow stability	Indoor	Wang et al., Hangzhou Dianzi University
An indoor spray bar electrostatic spray system test platform	Induction	Water sensitive paper	Nozzle diameter, nozzle pressure, and spraying height	Droplet deposition characteristics	Indoor	Lu et al., Guizhou University
Aerial electrostatic spraying system suspension test bench	Contact	Art Paper	Spraying height, spray time, and charging voltage	Droplet deposition characteristics and back-front ratio	Indoor	Zhao et al., Shandong University of Technology
Charge aerosol spray test bench	Induction	White plastic board	Charging voltage, spray pressure, electrode ring diameter, and electrode spacing	Spray charge-to-mass ratio and droplet size	Indoor	Wang et al., Jiangsu University
Fixed spray simulator	Induction	Dracaena	Electrode material, charging voltage, spray pressure, and nozzle diameter	Droplet deposition	Indoor	Lan et al., South China Agricultural University
Neuroshell	Induction	-	Temperature, humidity, electrode ring diameter, charging voltage, and nozzle flow	Spray charge-to-mass ratio	Simulation	Li et al., Heilongjiang Bayi Agricultural University

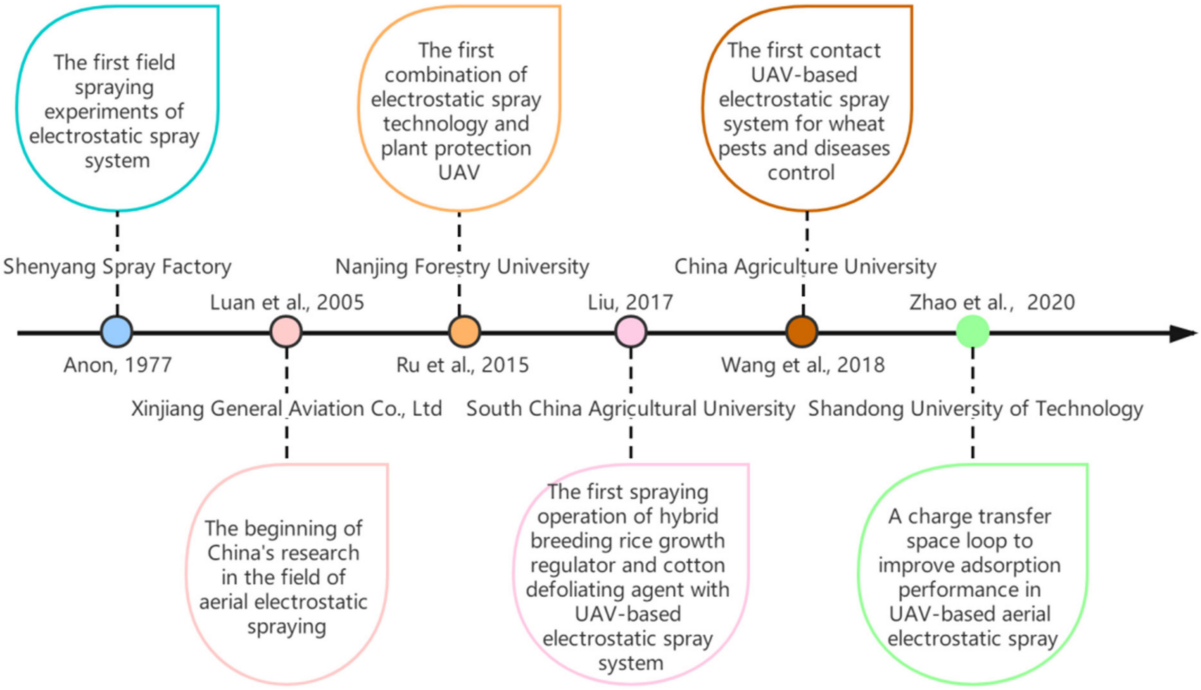

Figure 6. Key milestones and research groups working on aerial electrostatic spray technology.

4. Analysis and Prospects

The exploration of UAV-based electrostatic spray technology expands a new research perspective for the research of agricultural aviation electrostatic spray technology. The continuous improvement of the technology brings new opportunities for the application of aerial electrostatic spray systems on commercial plant protection UAVs in China. However, according to the current research progress, still, the following key technical elements need further exploration.

4.1. Measurement Technology of Charged Droplets

Droplet charge to mass ratio is a term associated with aerial electrostatic spray technology, and the measurement results of charge to mass ratio provide a reference for the evaluation of electrostatic spray system performance. In the absence of interference (e.g., indoors), the droplet charge to mass ratio is positively correlated with the deposition effect [49]. However, when working in an outdoor environment, there is usually a big difference between the droplet charge to mass ratios at the nozzle end and the terminal target, which requires the terminal measuring device to evaluate the charge amount. However, due to the absence of electrical grounding, the device that collects charged droplets often results in an inconsistent result with the actual effect of settling on the target [50]. For the electrostatic spray technology, the electric field intensity varies with the plant form, liquid conductivity, and environmental factors. For example, the electric field near the tip or terminal part of the leaf is the strongest [51]. Law [52] reported that gaseous discharges between sharp leaf tips and incoming charged spray clouds had been shown to limit deposition.

In many studies, aerial electrostatic spray had a better deposition effect compared with conventional electrostatic spray and non-electrostatic spray, but there are not a few reports that the effect of electrostatic spray is not satisfactory [1,49,53]. However, it remains to be further confirmed whether the difference in operation effect is caused by a sharp reduction in the charge to mass ratio of charge droplets, faulty experimental design scheme, or environmental influence. In recent years, more detection methods such as laser particle size analyzer have been continuously applied to the measurement of droplets effect in

China [54,55]. However, there are many problems such as high manufacturing cost, large measurement error, and complex measurement process. Therefore, it is necessary to develop a droplet characteristic detection technology suitable for aerial electrostatic spray systems to monitor the real state of charged droplets.

4.2. Impact of UAV Rotor Wind Field on Charged Droplets

The wind field on a manned fixed-wing aircraft causes charged droplets to settle in the direction of flight towards the area over which the aircraft passes. However, the wind field of a multi-rotor plant protection UAV is chaotic and changeable. It is not a regular wind field in a single direction. Moreover, due to the dual interference of ambient wind and rotor wind field, the charged droplet deposition process is more complicated in the actual operation scenario. Existing studies have basically ignored the working state of bipolar electrostatic spray system under the action of multiple rotor wind fields, the attracting process of positive and negative charged droplets, and the influence of droplets on the humidity of inductive charging electrodes. However, the impact is huge in that the characteristic of charged droplet property undoubtedly loses if the attraction of the charged droplets with positive and negative polarity is affected. In addition, wet electrodes will also make the electrically charged performance worse. Therefore, the influence of UAV rotor wind fields on charged droplets should be paid more attention in future research.

PIV (Particle Image Velocimetry) and other techniques can be used to simulate the droplet settling state under the influence of the rotor wind field, natural environmental wind, multiple gradient crosswinds, and other factors, so as to establish a theoretical system for reducing the influence of the rotor UAV downwash wind field and even utilizing the wind field action.

4.3. Comparative Study of Various Charging Methods

The induction charging mode was determined from the early stage of aerial electrostatic spray technology research in the United States, and it has been adopted in commercial electrostatic spray systems. Induction charging has the advantages of low charging voltage and low application threshold. It is a safe and effective method for charging droplets. Most Chinese scholars have also applied the induction charging method in their research. However, in addition to induction, there are also contact and corona ways to charge droplets. Corona charging voltage is very high, up to 30 kV. It can be used for conductive and non-conductive liquids with low insulation requirements. The contact charging voltage is required to be between corona type and induction type, but the insulation requirements are higher. Although the corona type with high charging voltage and the contact type with high insulation requirements still need a lot of basic research to clarify the charging mechanism and eliminate application risks, the disadvantages of the induction charging mode with poor charging effect cannot be ignored. Previous studies have shown that the contact charging method is able to generate a larger target current when compared with the induction charging method [47]. In recent years, there have been reports on contact charging methods in the research of UAV-based electrostatic spray technology with gratifying test results. In the future, it is necessary to carry out comparative studies of various charging methods in order to evaluate the operation effect of aerial electrostatic spray technology under different charging methods.

4.4. Accumulation of Aerial Electrostatic Spray Technology Research Based on Agricultural UAVs

During the early stage of China's agricultural aviation electrostatic spray technology research, the design and test were carried out on manned fixed-wing aircraft and helicopter platforms. In recent years, plant protection UAVs have provided Chinese growers with a lower barrier to entry and a higher level of applicability. Chinese scholars have carried on beneficial exploration for UAV-based electrostatic spray technology according to different UAV models, field crops, operating parameters, and electrostatic nozzle parameters, but the main research emphasis is still on the contrast test of electrostatic spray and

non-electrostatic spray to verify the operation effect of charged droplets. The research accumulation of airborne electrostatic spray technology based on agricultural UAV platforms is still less. It is not mature at the application level because the morphological characteristics of various crops and the farmland environment need more experimental data support. For example, (1) Relevant studies on the system construction, composition, and weight control of the electrostatic spray system lack continuity; (2) whether the operation with aerial electrostatic spray system is affected by surrounding facilities such as high-voltage lines, or whether it is incompatible with the flight control system of high-precision and fully autonomous plant protection UAV, is still unknown; (3) at present, the practical application of aerial electrostatic spray system in the field is limited to spraying water and water-based pesticides, and there is a lack of in-depth discussion on the research of the special electrostatic liquid pesticides and the electrical conductivity of pesticides for aerial spraying application; (4) working parameters of the spray system, such as charging voltage, system pressure and spraying speed, selection of flight speed and altitude, characteristics of aviation agents, and environmental factors such as temperature, humidity, and wind speed, all affect the settling process of charged droplets. Therefore, it is necessary to observe the droplet characteristics by studying their interaction effects; (5) the development trend of most commercial agricultural UAVs in China is integrating pesticide spraying, seed sowing, and fertilizer spreading together with fully autonomous and high-precision operation. Therefore, it is necessary to consider whether the integration of aerial electrostatic spray system, UAV working systems, and flight control system will cause mutual interference.

5. Conclusions

The development of aerial electrostatic spray technology in China, especially UAV-based aerial electrostatic spray technology, was analyzed in this review from nozzle modification, technical feasibility tests, mechanisms influencing each factor, and field spray efficiency tests. According to the literature retrieved, the research of China's aerial electrostatic spray technology in the past five years has focused on the innovative exploration of UAVs as a platform. Combined with the current development of agricultural plant protection and industrial application practice, UAV-based aerial electrostatic spray technology has wider developmental potential in China. In the future, the development plans should be made around the basic research, field test, commercialization, demonstration, and service guidance. In addition, researchers are recommended to pay attention to the integrated design of UAV and aerial electrostatic spray systems and to formulate the application standard of aerial electrostatic spray technology in China.

Author Contributions: Conceptualization, Y.Z., Y.L., and X.H.; methodology, X.H., Y.Z., and W.Z.; software, X.L. and W.Z.; validation, X.H. and W.Z.; formal analysis, X.H. and L.W.; investigation, Y.Z., X.H., and L.W.; resources, X.H.; data curation, X.H.; writing—original draft preparation, X.H., K.Y., and Y.Z.; writing—review and editing, Y.Z. and K.Y.; visualization, X.L.; supervision, W.Z. and J.D.; project administration, Y.Z., Y.L., and J.D.; funding acquisition, Y.Z. All authors have read and agreed to the published version of the manuscript.

Funding: This research was funded by Key Field Research and Development Plan of Guangdong Province, China, grant number 2019B020221001, Science and Technology Plan Project of Guangdong Province, China, grant number 2018A050506073, Guangdong Modern Agricultural Industry Generic Key Technology Research and Development Innovation Team Project, grant number 2020KJ133, National Key Research and Development Program, grant number 2018YFD0200304, and the 111 Project, grant number D18019.

Institutional Review Board Statement: Not applicable.

Informed Consent Statement: Not applicable.

Data Availability Statement: Not applicable.

Conflicts of Interest: The authors declare no conflict of interest.

References

1. Zhang, Y.L.; Lan, Y.B.; Fritz, B.K.; Xue, X.Y. Development of aerial electrostatic spraying systems in the United States and applications in China. *Trans. Chin. Soc. Agric. Eng.* **2016**, *32*, 1–7, (In Chinese with English abstract). [CrossRef]
2. Martin, D.E.; Latheef, M.A. Efficacy of electrostatically charged glyphosate on ryegrass. *J. Electrost.* **2017**, *90*, 45–53. [CrossRef]
3. Tavares, R.M.; Cunha, J.P.; Alves, T.C.; Bueno, M.R.; Silva, S.M.; Zandonadi, C.H. Electrostatic spraying in the chemical control of Triozoida limbata (Enderlein) (Hemiptera: *Triozidae*) in guava trees (*Psidium guajava* L.). *Pest Manag. Sci.* **2016**, *73*, 1148–1153. [CrossRef] [PubMed]
4. Martin, D.E.; Latheef, M.A.; López, J.D. Electrostatically charged aerial application improved spinosad deposition on early season cotton. *J. Electrost.* **2019**, *97*, 121–125. [CrossRef]
5. Carlton, J.B.; Isler, D.A. Development of a device to charge aerial sprays electrostatically. *Agric. Aviat.* **1966**, *8*, 44–51.
6. Carlton, J.B. Technique to Reduce Chemical Usage and Concomitant Drift from Aerial Sprays. United States Department of. Agriculture Patents No. 5975425, 2 November 1999.
7. Spectrum Electrostatic Sprayers, Inc. Available online: http://spectrumsprayer.com/company.html (accessed on 11 May 2020).
8. Inculet, I.I.; Fischer, J.K. Electrostatic aerial spraying. *IEEE Trans. Ind. Appl.* **1989**, *25*, 558–562. [CrossRef]
9. Da Cunha, J.P.A.R.; Barizon, R.R.M.; Ferracini, V.L. Assalin, Spray drift and caterpillar and stink bug control from aerial applications with electrostatic charge and atomizer on soybean crop. *Eng. Agrícola* **2017**, *37*, 1163–1170. [CrossRef]
10. Martin, D.E.; Latheef, M.A.; Lopez, J.D.; Duke, S.E. Aerial Application Methods for Control of Weed Species in Fallow Farmlands in Texas. *Agronomy* **2020**, *10*, 1764. [CrossRef]
11. Anon. Introduce a new technology of pesticide application-electrostatic spray. *For. Sci. Technol.* **1974**, *1*, 18.
12. Anon. Preliminary test of pesticide electrostatic spray. *For. Sci. Technol.* **1978**, *2*, 16–17.
13. He, X.K.; Yan, K.R.; Chu, J.Y.; Wang, J.; Zeng, A.J.; Liu, Y.J. Design and testing of the automatic target detecting, electrostatic, air assisted, orchard sprayer. *Nongye Gongcheng Xuebao Trans. Chin. Soc. Agric. Eng.* **2003**, *19*, 78–80, (In Chinese with English abstract).
14. Yu, Y.C.; Wang, B.H.; Shi, J.Z.; Li, X.F. Design and experimental study of combined-charging hydraulic electrostatic spraying box. *Trans. Chin. Soc. Agric. Eng.* **2005**, *21*, 85–88, (In Chinese with English abstract).
15. Zhang, J.; Zheng, J.Q. Experiment on the variations of droplet diameter distribution and local flow rate over radial direction for the electrostatic spray process. *Trans. Chin. Soc. Agric. Eng.* **2009**, *25*, 104–109, (In Chinese with English abstract). [CrossRef]
16. Jia, W.D.; Hu, H.C.; Chen, L.; Chen, Z.G.; Wei, X.H. Performance experiment on spray atomization and droplets deposition of wind-curtain electrostatic boom spray. *Trans. Chin. Soc. Agric. Eng.* **2015**, *31*, 53–59, (In Chinese with English abstract). [CrossRef]
17. Zhou, L.F.; Zhang, L.; Xue, X.Y.; Qin, W.C.; Sun, Z.; Zhou, Q.Q.; Chen, C. Design and test of double air channel auxiliary electrostatic sprayer. *Jiangsu Agric. Sci.* **2017**, *45*, 192–196, (In Chinese with English abstract). [CrossRef]
18. Ma, X.; Guo, L.J.; Wen, Z.C.; Wei, Y.H.; Xiao, R.H.; Zeng, H. Atomization characteristics of multi-nozzle electrostatic spray and field experiment. *Trans. Chin. Soc. Agric. Eng.* **2020**, *36*, 73–82, (In Chinese with English abstract). [CrossRef]
19. Dai, Q.F.; Hong, T.S.; Song, S.R.; Li, Z.; Chen, J.Z. Influence of pressure and pore diameter on droplet parameters of hollow cone nozzle in pipeline spray. *Trans. Chin. Soc. Agric. Eng.* **2016**, *32*, 97–103, (In Chinese with English abstract). [CrossRef]
20. Luan, H.; Zhang, Q.; Wang, W.X. Installation and modification of Z03K000B electrostatic spray system and flight tests. *Xin-jiang Reclam. Technol.* **2006**, *5*, 46–47, (In Chinese with English abstract).
21. Zhang, Y.L.; Huang, X.R.; Wang, L.L.; Deng, J.Z.; Zeng, W.; Lan, Y.B.; Muhammad, N.T. Progress in foreign agricultural aviation electrostatic spray technologies and references for China. *Trans. Chin. Soc. Agric. Eng.* **2021**, *37*, 50–59, (In Chinese with English abstract). [CrossRef]
22. Ru, Y.; Zheng, J.Q.; Zhou, H.P.; Shu, C.R. Design and experiment of double nozzle of aerial electrostatic sprayer. *Trans. Chin. Soc. Agric. Mach.* **2007**, *38*, 58–61.
23. Zhou, H.P.; Ru, Y.; Shu, C.R.; Jia, Z.C. Improvement and experiment of aerial electrostatic spray device. *Trans. Chin. Soc. Agric. Eng.* **2012**, *28*, 7–12, (In Chinese with English abstract). [CrossRef]
24. Ru, Y.; Jin, L.; Zhou, H.P.; Shu, C.R. Effect of high-voltage electrostatic field on droplet charging based on cone-shaped electrode. *High Volt. Eng.* **2014**, *40*, 2721–2727, (In Chinese with English abstract). [CrossRef]
25. Jin, L.; Ru, Y.; Sun, M.L.; Jia, Z.C.; Wang, B.X. Performance experiments of aerial electrostatic nozzle with cone shaped electrode. *J. Nanjing For. Univ. (Nat. Sci. Ed.)* **2015**, *39*, 155–160, (In Chinese with English abstract). [CrossRef]
26. Yang, Z.; Niu, M.M.; Li, J.; Xu, X.; Sun, Z.Q.; Xue, K.P. Influence of lateral wind and electrostatic voltage on spray drift of electrostatic sprayer. *Trans. Chin. Soc. Agric. Eng.* **2015**, *31*, 39–45, (In Chinese with English abstract). [CrossRef]
27. Chen, H.L.; Zhao, Y.C. Electrostatic induction field and charging property of droplet in electrostatic spraying process. *High Volt. Eng.* **2010**, *36*, 2519–2524, (In Chinese with English abstract). [CrossRef]
28. Zhang, D.Y.; Lan, Y.B.; Chen, L.P.; Wang, X.; Liang, D. Current status and future trends of agricultural aerial spraying technology in China. *Trans. Chin. Soc. Agric. Mach.* **2014**, *45*, 53–59, (In Chinese with English abstract). [CrossRef]
29. Tian, Z.W.; Xue, X.Y.; Li, L.; Cui, L.F.; Wang, G.; Li, Z.J. Research status and prospects of spraying techology of plant-protection unmanned aerial vehicle. *J. Chin. Agric. Mech.* **2019**, *40*, 37–45, (In Chinese with English abstract). [CrossRef]
30. Li, J.Y.; Lan, Y.B.; Shi, Y.Y. Research progress on airflow characteristics and field pesticide application system of rotary-wing UAV. *Trans. Chin. Soc. Agric. Eng.* **2018**, *34*, 104–118, (In Chinese with English abstract). [CrossRef]

31. Ru, Y.; Jin, L.; Jia, Z.C.; Bao, R.; Qian, X.D. Design and experiment on electrostatic spraying system for unmanned aerial ve-hicle. *Trans. Chin. Soc. Agric. Eng.* **2015**, *32*, 42–47, (In Chinese with English abstract). [CrossRef]
32. Wang, Y.T.; Wu, K.H. Research on an electrostatic spraying system for multi-rotor plant protection UAV. *Jiangsu Agric. Sci.* **2020**, *48*, 225–230, (In Chinese with English abstract). [CrossRef]
33. Jin, L.; Ru, Y. Research on UAV-based aerial electrostatic spraying system. *J. Agric. Mech. Res.* **2016**, *38*, 227–230, (in Chinese with English abstract). [CrossRef]
34. Lian, Q. Experimental Research on Electrostatic Spray System of Multi-Rotor UAV. Master's Thesis, Heilongjiang Bayi Agricultural University, Daqing, China, 2016.
35. Cai, Y.L. Design and Test of Contact Electrostatic Spray System for Low-Altitude UAV. Master's Thesis, Jiangsu University, Zhenjiang, China, 2017.
36. Zhao, D.N.; Lan, Y.B.; Shen, W.G.; Wang, S.Z.; Abhishek, D. Development of a charge transfer space loop to improve ad-sorption performance in aerial electrostatic spray. *Int. J. Agric. Biol. Eng.* **2020**, *13*, 50–55. [CrossRef]
37. Yanliang, Z.; Qi, L.; Wei, Z. Design and test of a six-rotor unmanned aerial vehicle (UAV) electrostatic spraying system for crop protection. *Int. J. Agric. Biol. Eng.* **2017**, *10*, 68–76. [CrossRef]
38. Bu, J.Z. Experimental Study on Deposition and Drift Characteristics of Electrostatic Spray for Large-Load Unmanned Helicopter. Master's Thesis, Jiangsu University, Zhenjiang, China, 2019.
39. Wu, Y.; Lu, J.; Wang, Y. Research on Multiresponse Robustness Optimization for Unmanned Aerial Vehicle Electrostatic Spray System. *Fundam. Mach. Theory Mech.* **2020**, *77*, 719–728. [CrossRef]
40. Lu, J.J.; Chen, J.D.; Wu, Y.D.; Wang, B. Agricultural aviation research aeronautical electrostatic spray system performance. *J. Agric. Mech. Res.* **2019**, *41*, 174–179, (In Chinese with English abstract). [CrossRef]
41. Zhao, D.N.; Lan, Y.B.; Shen, W.G. Building of aerial electrostatic spraying system and exploration on the influencing factors of droplet deposition effect. *J. Agric. Mech. Res.* **2021**, *43*, 204–207, (In Chinese with English abstract). [CrossRef]
42. Wang, J.F.; Gu, W.K.; Wang, X.Y.; Chu, J.J. Experimental study on charging performance and spray characteristics of induction charged spray. *High Volt. Eng.* **2015**, *41*, 504–509, (In Chinese with English abstract). [CrossRef]
43. Lan, Y.B.; Zhang, H.Y.; Wen, S.; Li, S.H. Analysis and experiment on atomization characteristics and spray deposition of electrostatic nozzle. *Trans. Chin. Soc. Agric. Mach.* **2018**, *49*, 130–139, (In Chinese with English abstract). [CrossRef]
44. Li, Y.F.; Hu, J.; Li, Q.D.; Zhao, M.M. Study on influencing factors of airborne electrostatic fog trapping. *Trans. Chin. Soc. Agric. Mach.* **2019**, *41*, 171–176, (In Chinese with English abstract). [CrossRef]
45. Wang, S.L.; He, X.K.; Song, J.L.; Zhong, C.S.; Wang, Z.C.; Qi, P.; Ling, Y. Charging and spraying performance test of bipolar contact electrostatic spraying system for unmanned aerial vehicle. *Trans. Chin. Soc. Agric. Eng.* **2018**, *34*, 82–89, (In Chinese with English abstract). [CrossRef]
46. Liu, W.L. Design and Experiment of Electrostatic Spraying System for Plant Protection Unmanned Aerial Vehicle. Master's Thesis, South China Agricultural University, Guangzhou, China, 2017.
47. Zhao, S.; Castle, G.P.; Adamiak, K. Comparison of conduction and induction charging in liquid spraying. *J. Electrost.* **2005**, *63*, 871–876. [CrossRef]
48. Agropages. China's Crop Protection UAV Development Report 2020. Available online: http://news.agropages.com/News/NewsDetail---38284.htm (accessed on 17 March 2021).
49. Kirk, I.W.; Hoffmann, W.C.; Carlton, J.B. Aerial electrostatic spray system performance. *Trans. ASAE* **2001**, *44*, 1089–1092. [CrossRef]
50. Martin, D.E.; Latheef, M.A. Aerial electrostatic spray deposition and canopy penetration in cotton. *J. Electrost.* **2017**, *90*, 38–44. [CrossRef]
51. Dai, Y.; Law, S. Modeling the transient electric field produced by a charged pollen cloud entering a flower. In Proceedings of the IAS '95. Conference Record of the 1995 IEEE Industry Applications Conference Thirtieth IAS Annual Meeting, Orlando, FL, USA, 8–12 October 1995; Institute of Electrical and Electronics Engineers (IEEE): New York, NY, USA, 2002; Volume 2, pp. 1395–1402.
52. Law, S.E. Electrostatic Pesticide Spraying: Concepts and Practice. *IEEE Trans. Ind. Appl.* **1983**, *2*, 160–168. [CrossRef]
53. Martin, D.E.; Lopez, J.D.; Hoffmann, W.C.; Fritz, B.K.; Lan, Y. Field Evaluation of Spinosad Aerial Applications for Thrips Control on Cotton1. *Southwest. Èntomol.* **2007**, *32*, 221–228. [CrossRef]
54. Zhang, R.R.; Chen, L.P.; Lan, Y.B.; Xu, G.; Kan, J.; Zhang, D.Y. Development of a deposit sensing system for aerial spraying application. *Trans. Chin. Soc. Agric. Mach.* **2014**, *45*, 123–127, (In Chinese with English abstract). [CrossRef]
55. He, Y.; Wu, J.J.; Fang, H.; Zheng, Q.S.; Xiao, S.P.; Cen, H.Y. Research on deposition effect of droplets based on plant protection unmanned aerial vehicle: A review. *J. Zhejiang Univ. (Agric. Life Sci.)* **2018**, *44*, 392–398, (In Chinese with English abstract). [CrossRef]

·农业航空工程·

国外农业航空静电喷雾技术研究进展与借鉴

张亚莉[1,2]，黄鑫荣[1,2]，王林琳[2,3]，邓继忠[1,2]，曾 文[1,2]，兰玉彬[2,3※]，Muhammad Naveed Tahir[4]

（1. 华南农业大学工程学院，广州 510642；2. 国家精准农业航空施药技术国际联合研究中心，广州 510642；3. 华南农业大学电子工程学院，广州 510642；4. Department of Agronomy, PMAS-Arid Agriculture University, Rawalpindi 46300, Pakistan）

摘 要：农业航空静电喷雾技术作为中国发展精准农业航空应用技术的内容之一，对农药的有效利用和减少环境污染有积极意义。农业航空静电喷雾技术在国外发展较早也相对成熟，美国已有应用于有人机的商业化产品，并在美国、巴西等国各类粮食作物、经济作物和杂草防治作业中开展了大规模田间应用。该研究首先从基础研究、田间应用和优化工作等方面梳理了国外农业航空静电喷雾技术的研究进展，分析了农业航空静电喷雾技术在增加雾滴沉积、减少飘移和具备低施药液量等方面的优势。在此基础上结合中国植保无人机快速发展的实际对研究和应用适合中国国情的农业航空静电喷雾技术进行思考，提出了农业航空静电喷雾技术的研究路线，最后从采用接触式等非感应式充电方式、开发农业航空静电喷雾的测量技术，以及思考荷质比作为衡量指标的意义等方面探讨了可进行深入研究的方向。中国农业航空静电喷雾技术研究特别在植保无人机静电喷雾技术方面的研究与应用有很大的发展空间，可参考国外经验，围绕航空静电喷雾技术的基础性研究、田间试验、成果转化、示范推广和服务指导全方面制定发展规划，把单一强调对雾滴带电的实现转向对技术系统的整体研究。

关键词：农业航空；植保；综述；静电喷雾；雾滴沉积；航空施药

doi：10.11975/j.issn.1002-6819.2021.06.007

中图分类号：S252+.3 **文献标志码**：A **文章编号**：1002-6819(2021)-06-0050-10

张亚莉，黄鑫荣，王林琳，等. 国外农业航空静电喷雾技术研究进展与借鉴[J]. 农业工程学报，2021，37(6)：50-59. doi：10.11975/j.issn.1002-6819.2021.06.007 http://www.tcsae.org

Zhang Yali, Huang Xinrong, Wang Linlin, et al. Progress in foreign agricultural aviation electrostatic spray technologies and references for China[J]. Transactions of the Chinese Society of Agricultural Engineering (Transactions of the CSAE), 2021, 37(6): 50-59. (in Chinese with English abstract) doi：10.11975/j.issn.1002-6819.2021.06.007 http://www.tcsae.org

0 引 言

中国农业航空关键技术研究和应用已进入快速发展阶段[1]。在高效作业的同时如何提高药液在作物靶标上的利用率、减少环境污染，一直都是航空植保作业关注的研究课题之一。农业航空静电喷雾技术是传统静电喷雾技术在航空作业平台上的应用，一般通过感应式、接触式、电晕式等充电方式让雾滴带电，使得喷头与作物靶标间形成静电场[2-3]。在高压静电的作用下，带电药液主动吸附于作物靶标的正反面，达到环抱吸附的效果，有助于减少飘移并提高航空植保作业效率[4-5]。农业航空静电喷雾技术在国外发展较早也相对成熟，美国已有应用于有人机的商业化产品。中国对于农业航空静电喷雾技术的研究始于二十一世纪初，以新疆通用航空有限责任公司从美国休斯顿的 SES 公司（Spectrum Electrostatic Sprayers，Inc）引进一套适用于有人机的航空静电喷雾 Z03K000B 系统关键部件和喷嘴，并进行改装试飞试验为标志[6]。南京林业大学等国内科研单位对有人驾驶固定翼飞机、直升机和植保无人机适用的农业航空静电喷雾系统进行了多方面探索[3,5,7-8]。

农业航空静电喷雾技术作为中国发展精准农业航空应用技术的内容之一，对农药的有效利用和减少环境污染有积极意义。由于中国农业航空静电喷雾技术的研究起步相对较晚，研究和应用等方面与国外农业航空静电喷雾技术发展程度较高的国家存在差距。航空静电喷雾系统不是一种单纯地把农药喷洒到植株的工具，由于雾滴带电的属性给农业航空静电喷雾这项技术带来许多动态的复杂问题，甚至其中一些问题的答案目前尚难以确定。本文从农业航空静电喷雾技术的发展驱动力为研究着手点，重点分析国外长期的基础研究与田间应用研究进展，拟为探索适用于中国国情的农业航空静电喷雾技术的研究和应用提供参考。

收稿日期：2020-12-20 修订日期：2021-03-13

基金项目：广东省重点领域研发计划（2019B020221001）；广东省科技计划项目（2018A050506073）；广东省现代农业产业共性关键技术研发创新团队项目（2020KJ133）；国家重点研发计划项目（2018YFD0200304）

作者简介：张亚莉，博士，副教授，主要研究方向为农用传感器技术与应用。Email：ylzhang@scau.edu.cn。

中国农业工程学会高级会员：张亚莉（E041200939S）

※通讯作者：兰玉彬，教授，博士生导师，主要研究方向为精准农业航空应用技术。Email：ylan@scau.edu.cn。

中国农业工程学会高级会员：兰玉彬（E041200725S）

1　农业航空静电喷雾技术基础性研究及商业化

美国农业部农业研究服务署（USDA-ARS）的 Carlton 等[9]最早开展了农业航空静电喷雾技术的研究，并于 1966 年设计出一种电动旋转静电喷头。针对在航空作业中搭载静电喷雾系统出现的飞机残留表面电荷的过度积累，以及航空静电喷雾系统充放电等问题，Carlton 及其合作者通过研究放大电路探测设备，改进优化静电喷头和单双极充电方式，并提出适用于全尺寸飞机的电容与航高函数关系模型等方法解决了上述难题[10-14]。美国田纳西大学的 Kihm 等[15]围绕双极交替充电模式对航空静电喷雾系统的雾化、充电和沉积特性展开研究。美国 CDI（Continuum Dynamics，Inc）公司的 Teske 等[16]研究了航空静电喷雾飘移与雾滴蒸发效应，探索了经喷头释放的雾滴周围局部相对湿度及飞机尾流对雾滴温度的影响。加拿大韦仕敦大学和瑞士汽巴-嘉基公司（Ciba-Geigy AG）的研究人员合作提出两对极性相反的电荷共面云充电技术将飞机的电位保持在合适范围内，为航空应用静电喷雾技术扫除了障碍[17]。

1995 年，Carlton 等[18]在美国德克萨斯 A&M 大学（Texas A&M University）棉田开展了 3 种充电模式（双极、单极、不充电）下航空静电喷雾技术对改善棉花叶片沉积影响的试验研究，测试结果表明带电雾滴的沉积效果明显改善。美国 USDA-ARS 的 Kirk 等[19]以棉花为靶标作物进行航空静电喷雾技术的药效试验发现，采用静电喷雾方式喷洒叶片上的荧光染料平均沉积明显高于非静电喷雾。农业航空静电喷雾技术在提高雾滴沉积效果方面的优势成为其发展的重要驱动力。

Carlton[20]在 1999 年获得了美国航空静电喷雾系统的发明专利。专利中不但介绍了增加雾滴背面沉积和减少飘移的试验现象，还规范了荷质比、电源电压、转速等农业航空静电喷雾系统的设计要求。同年美国 SES 公司购买了专利，并获得美国农业部颁发的独家许可证，以生产和销售这一创新产品。2002 年美国 SES 公司针对固定翼飞机和直升机两种不同机型，开发出商用航空静电喷雾系统[21]。

目前该静电喷雾系统已在巴西大豆锈病、北美棉花、水稻、玉米、马铃薯、甜菜、葡萄等作物病虫害防治，以及非洲甘蔗，澳大利亚谷物等作物植保作业中均有应用[22]。在此过程中，国外学者利用商用农业航空静电喷雾系统开展了大量的农业航空静电喷雾技术田间应用的探索。

2　农业航空静电喷雾技术的田间应用研究

农业航空静电喷雾技术的田间应用研究包括对棉花、大豆、甘蔗等经济作物，小麦、水稻、玉米等粮食作物的喷雾沉积效果、病虫害防治效果等的田间测试，以及对农田杂草的化学防治研究[23]。

2.1　经济作物

2.1.1　棉花

中国和美国是世界上主要的棉花生产国。棉花种植密度大，且棉蚜、蓟马、白粉虱、烟粉虱等棉花主要害虫寄生在棉叶背面，加大了航空植保作业防控棉花虫害的难度。风洞试验结果表明，农业航空静电喷雾技术具有显著增加靶标作物叶片背面雾滴沉积的优势，使这项技术与喜好寄生于叶片背面的棉花各类害虫防治紧密地联系在一起[24-25]。

2007 年，美国 USDA-ARS 的 Martin 等[26]对棉花病虫害防治进行大规模的田间试验，研究常规液压式喷雾、静电喷雾、离心式雾化喷雾 3 种方式对蓟马的防治效果。结果显示，航空静电喷雾系统喷洒药液 2～6 d 蓟马幼虫数和成虫数均显著低于未经处理的对照组，但在喷洒 7 d 后，静电喷雾处理的成虫数量比对照组成虫数量增加了 41%，静电喷雾技术未展现出优势。2009 年，美国 USDA-ARS 的 Latheef 等[27]采用静电喷雾、非静电喷雾和常规喷雾 3 种喷雾技术，以及不同施药液量和杀虫剂，对航空静电喷雾的喷雾沉积特性和棉花烟粉虱的季节性防治效果进行了评估。研究结果显示，在棉花冠层顶部和中部，带电液滴尺寸明显小于常规喷雾；经静电喷雾处理的活卵和活若虫的季节性平均数与常规喷雾处理结果相近；静电喷雾对成虫的半数致死浓度（LC50）与常规喷雾没有显著差异。该研究表明了静电喷雾方式对多种不同化学成分的杀虫剂具有良好的适应性，但仍需进一步研究带电雾滴如何获得高荷质比，以增加杀虫剂在棉叶背面（粉虱栖息位置）的沉积。Martin 等[28]采用航空静电喷头和离心式雾化喷头在棉田喷洒与水混合的日光可见荧光染料（体积浓度为 10%），以研究静电喷雾喷洒出的雾滴在成熟期棉田的沉积试验。结果发现，与不带电的喷雾相比，静电喷雾对棉花冠层顶部叶片正面的雾滴覆盖率增加了 2 倍，在叶片背面的覆盖率比非静电和离心式雾化喷头提高了 3 倍。但无论是离心式雾化喷头还是静电喷头都无法改善雾滴向冠层中部穿透的能力。Martin 等[29]以刺糖多孢菌（Saccharopolyspora Spinosa）产生的多杀菌素为示踪剂，采用双极航空静电喷雾系统以 9.35 L/hm^2 的施药液量对早季棉花进行了喷雾试验。通过静电喷雾系统喷洒的雾滴沉积量增加了 34.5%；同时在通电状态下的双极静电喷雾系统喷洒的带电雾滴谱明显比断电状态下的双极静电喷雾系统喷洒的雾滴谱宽。

2.1.2　大豆

大豆害虫种类多，且易受不同种类昆虫的同时侵袭[30-31]。巴西乌贝兰迪亚联邦大学（Universidade Federal de Uberlândia）的 Cunha 等[32]以大豆为靶标作物，使用航空静电喷雾和离心式雾化喷雾 2 种方式喷洒杀虫剂，研究雾滴飘移和虫害控制，以探索航空静电喷雾技术在提高大豆病虫害防治方面的应用。试验结果证实了带静电的喷洒方式产生的飘移较小，但 2 种施药方式的虫口减退率没有显著差异。这项研究的结果与 Latheef 等[27]的研究结果一致。巴西圣保罗州立大学（Sao Paulo State University）的 Antuniassi 等[33]采用多种航空喷雾方式喷洒杀菌剂防治大豆锈病。其中静电喷雾方式的喷洒试验在相对湿度较高（71%）和较低（64%）2 种条件下进行，

以评估相对湿度对静电喷雾系统性能的影响。试验结果表明在较干燥条件下静电性能发挥更佳，并且靶标作物中下部有更高的沉积量，但不同航空喷雾技术喷洒处理的雾滴沉积量差异不显著。

2.1.3 甘蔗

2005 年，美国 SES 公司在非洲斯威士兰当地最大的甘蔗种植园使用航空静电喷雾系统喷施乙烯利等甘蔗催熟剂[34]。试验结果表明航空静电喷雾系统改善了雾滴沉积和穿透作物树冠的能力。

2.2 粮食作物

2.2.1 小麦

为得到喷洒杀菌剂防治小麦赤霉病的最佳航空作业方式，美国 USDA-ARS 的 Kirk 等[35]和 Fritz 等[36]使用不同施药液量并采用不同航空喷雾技术包括液压喷头、离心喷头和静电喷头等，对小麦穗部的雾滴沉积进行了比较和评估，结果发现航空静电喷雾系统施药液量为 9.4 L/hm^2 和雾滴体积中径 Dv0.5≤150 μm（总体积 50%的雾滴直径不大于 150 μm）的组合在小麦上获得较好的沉积效果。

2.2.2 水稻

巴西圣玛利亚联邦大学（Universidade Federal de Santa Maria）的 Bayer 等[37]为了评价航空静电喷雾等不同航空喷雾技术对水稻产量的影响，采用液压式、离心式航空喷雾和航空静电喷雾 3 种不同的喷雾系统喷洒杀菌剂，并研究雾滴在水稻中下层的穿透能力。结果显示在此次试验研究中，航空静电喷雾技术表现并不突出。2012 年，Bayer 等[38]使用 Ipanema EMB-202 飞机和三氟嘧啶+丙环唑的杀菌剂对水稻进行航空施药，采用液压喷头、离心式喷头和静电喷头 3 种方式搭配不同施药液量，以评估雾滴在水敏纸上的沉积以及对水稻冠层不同部位的穿透效果。试验表明，液压喷头（20 和 30 L/hm^2）以及静电喷雾（10 L/hm^2）的雾滴沉积密度在水稻植株上三分之一处较高，而离心式（15 L/hm^2）在水稻中下部有较高的雾滴沉积密度。对少量的植物提取物经过色谱分析发现，杀菌剂残留量较高的喷施方案是施药液量为 10 L/hm^2 的静电喷雾方式，表明带电雾滴在增加水稻植株表面的沉积量方面有较好的表现，这有助于提高农药利用率和减少环境污染。

2.2.3 玉米

玉米叶螨，即红蜘蛛是美国玉米的主要害虫，Martin 等[39]为了研究防治美国堪萨斯州玉米红蜘蛛的最佳航空施药方式，在成熟玉米田中进行了航空静电喷头和常规扇形压力喷头 CP11-TT 的对比试验。试验采用了 Air Tractor 302 飞机进行喷洒，除了常规的水敏纸测量雾滴沉积以外，还结合遥感技术获取了红蜘蛛的不同危害级别等农情信息。试验结果表明两种喷施方法对红蜘蛛的抑制作用没有显著差异，但静电处理后平均归一化植被指数值（NDVI，Normalized Difference Vegetation Index）比常规处理的略高，表明静电喷雾处理的的玉米叶比常规喷雾处理的叶片健康（植被覆盖度较高）。

2.3 化学除草

除了用于农作物的病虫害防治外，国外学者也致力于探索航空静电喷雾技术在除草方面的应用效果。

为了降低除草剂中草甘膦成分的用量，2006 年巴西佩洛塔斯联邦大学（Federal UniVersity of Pelotas）的 Eugênio 等[40]利用一架伊帕内马 202A 型农用飞机分别用常规喷雾和静电喷雾 2 种方式对除草效果进行对照试验。试验结果表明，静电喷雾系统在处理后 13 d 对杂草的控制效果较好。带电雾滴由于静电作用更好地吸附在杂草上，相同除草效果下静电处理试验组可将施药液量从 30 L/hm^2 减少到 10 L/hm^2，有利于提高除草剂利用率和减轻环境污染。2017 年，Martin 等[41]采用一款适用于直升机施药的 TX-VK3 低流量喷头对静电喷雾条件下草甘膦药液对黑麦草健康状况的影响开展研究，试验结果表明喷洒出的带电草甘膦雾滴体积中位数直径由 106.5 μm 增加到 112.8 μm。与不带电的草甘膦药液处理后 27 d 除草率达 41%相比，经带电草甘膦药液喷洒处理后，15 d 后即达到相同除草效果。2020 年，Martin 等[42]对商用固定翼农用飞机控制休耕农田中单子叶和双子叶杂草的效果进行评估。该研究采用离心、液压和静电 3 种喷头，试验分在 2 年同一季节进行。结果显示，在第一年中，采用静电喷头喷洒对杂草生长具有显著的抑制效果。第二年则是离心喷头效果较为突出。另外，试验结果指出在不降低药效的前提下，航空静电技术的施药液量是常规喷雾技术的三分之一。巴西乌贝兰迪亚联邦大学的 Campos[43]对常规喷雾 150 L/hm^2 施药液量和静电喷雾两种施药液量（50 L/hm^2 和 90 L/hm^2）与是否加入助剂条件下的草甘膦除草防控作用进行了试验研究。该研究测量了不同施药液量、施药技术与是否加入助剂多种变量下的药液理化性质、荷质比、雾滴谱以及杂草上药液沉积和飘移损失等各种参数变化。试验结果表明航空静电喷雾技术减小了药液飘移损失，降低了施药液量，显著提高了农药利用率。

在采用农业航空静电喷雾技术开展的各类田间作物试验中，对于在棉花上的蓟马、白粉虱、烟粉虱等害虫和早季、成熟期等不同时期棉花上已形成较为完整的连续性试验结果评价。农业航空静电喷雾技术对杂草的化学防治方面的研究也取得较为丰富的研究数据。而且，美国亚利桑那州棉花上的烟粉虱控制试验、巴西米纳斯吉拉斯州对大豆喷洒杀虫剂研究，以及 Martin 对休耕农田的除草试验等的研究结果均突出了航空静电喷雾系统具有低施药液量的优势[27,32,42]。同时 Cunha 等[32]和 Campos[43]也在各自试验中证实了航空静电喷雾技术能够减少雾滴飘移的现象。因此，除了能够增加雾滴沉积外，减少雾滴飘移和具有低施药液量的优势也成为农业航空静电喷雾技术发展的有效驱动力。

3 农业航空静电喷雾技术的优化工作

虽然相较于常规的航空喷雾技术，农业航空静电喷雾在增加背面沉积、低施药液量和减少飘移方面有许多优势，然而田间应用效果却并未完全体现出这些优势。

在某些场景下例如棉花白粉虱虫卵和、蓟马成虫等应用研究中，采用航空静电喷雾的防治效果低于常规喷雾。另外在评估静电喷头嘴和常规喷头嘴的雾滴沉积效果时，Martin 等[28]和 Bayer 等[38]发现，由于雾滴直径小和带电雾滴的主动吸附效果受到限制等的原因，使用水敏纸的评价方式影响了试验精度。为了使农业航空静电喷雾技术在田间作业以及病虫害防治方面发挥应有的效果，国外学者对飞行高度、飞行速度、充电电压、荷质比、施药液量等因素及不同因素间的交互作用影响进行了细致的深入研究[44-45]。

美国 USDA-ARS 申请的航空静电喷雾系统专利以感应方式雾化液滴以增加沉积，但没有描述飞行速度或喷孔尺寸的变化对带电雾滴谱的影响。Martin 和 Carlton 进行风洞试验研究飞行速度和静电喷头的喷孔尺寸等因素对固定翼飞机静电喷雾系统施药效果的影响[46]。结果发现，随着飞行速度的增加试验所选取的所有尺寸的喷孔都产生了更小的雾滴。当保持飞行速度一定时，喷孔越大带电雾滴谱越宽。这项工作目前的结果尚难以解释和应用，但为未来获得合适的喷雾参数组合的研究提供了参考。除此以外，Martin 和 Carlton 在同样的测试环境中对旋翼条件下的飞行速度和喷孔尺寸对带电雾滴的影响进行了研究[47]。在高速风洞中，试验人员将飞行速度从 97 km/h 提高到 177 km/h 时，所有尺寸的喷孔都会产生更小的雾滴，飞行速度的增加和喷孔尺寸的减小也增加了带电雾滴的荷质比，这意味着在田间作业时可增加靶标作物上的沉积量。该研究结果与固定翼飞机条件下航空静电喷雾获得的雾滴谱数据一致。

2013 年，巴西维索萨联邦大学（Universidade Federal de Viçosa）的 Sasaki 等[48]在研究评估静电喷雾的影响因素时，重点关注喷头与靶标作物之间的距离，并从相对于目标距离 0～5 m 的纵向和横向两个方向上观察不同距离条件下的荷质比和雾滴沉积。结果表明荷质比与挂载的静电喷雾系统和靶标作物之间的距离成反比，而且当目标与喷洒雾滴流成纵向时，能够产生更好的雾滴沉积，同时得出能够显著增加雾滴沉积量的最小荷质比为 0.6 mC/kg。

上述研究从雾滴沉积效果评价方式、飞行平台作业参数以及静电喷雾系统施药参数等多方面对航空静电喷雾的效果进行探索，为航空静电喷雾技术应用参数的优化提供了进一步的数据支持。

4　国内农业航空静电喷雾技术的应用及发展前景

4.1　实用性与成本

在植保机械的市场中，成本和实用性是用户较为看重的两大因素。美国明尼苏达州的农场主 Newberg 对 SES 公司生产的航空静电喷雾系统初期投入大约 3.8 万美元[49]。由于施药液量的大幅减少（10 L/hm^2），作业面积可达到每天 1011 hm^2 以上，搭载航空静电喷雾系统的飞机施药作业每小时能产生高达 2 000 美元的毛收入，证明了适用的应用场景下在前期高固定成本的投资能使种植者获得相对可观的经济效益。国外的田间试验研究表明[27,32,42-43]，农业航空静电喷雾技术并不仅仅是专用于防治寄生于叶片背面虫害的代名词，它具有的低施药液量、吸附效果好等特点带来的一系列省水省药、省力高效、环保节能、高附着率等潜在优势，对国内航空植保作业农药减施有进一步的促进作用。

4.2　借鉴与改进

近年来中国植保无人机发展迅速。相比农用有人驾驶飞机，植保无人机建造成本和使用门槛低、安全性高、起降条件和维修保障要求都比较低，已成为农药减量、农业提质增效的重要技术手段。据全国农业技术推广服务中心初步统计数据显示，截至 2020 年 11 月中旬，全国专业化防治组织中植保无人机保有量约 8 万架，作业面积近 5300 万 hm^2，加上种植大户通过农机购置补贴购买的植保无人机，预计 2020 年全国农业无人机的保有量将超过 10 万架，作业总面积将突破 6 700 万 hm^2[50]。这意味着未来静电喷雾系统以植保无人机为主要搭载平台在我国农业航空领域具有较大的发展空间。国外农业航空静电喷雾主要以有人驾驶固定翼飞机和直升机为作业平台，而植保无人机静电喷雾技术的研究较少，因此国内开展相关研究也面临着很多挑战[51-52]。

通过对国外农业航空静电喷雾技术的基础研究和田间应用研究进展进行分析，可为国内发展基于植保无人机的航空静电喷雾技术的研究和应用方向提供借鉴。目前国内主流的植保无人机以大疆 T30 植保无人机、极飞 P40、P80、V40 2021 款农业无人机为代表，其主要技术参数对比如表 1 所示[53-56]。

表 1　主流植保无人机型号的技术参数对比

Table 1　Main technical parameters of mainstream plant protection UAVs

技术参数 Technical parameters	大疆 T30 DJI T30	极飞 P40 2021 XAG P40 2021	极飞 P80 2021 XAG P80 2021	极飞 V40 2021 XAG V40 2021
最大支持容量 Max payload /L	30 (药箱) 35 (料箱)	20 (药箱) 25 (料箱)	35 (药箱) 60 (料箱)	16 (药箱) 25 (料箱)
有效喷幅 Spray width/m	9	6	10	10
喷洒速率 Spray rate(hm^2·h^{-1})	16	14.67	20	16
整机质量 Total mass /kg	26.4	20.0	32.0	20.0
最大起飞质量 Max takeoff mass/kg	66.5	48.0	88.0	48.0
最大推重比 Max thrust-mass ratio	1.7	1.8	1.8	1.8
防护等级 Ingress protection rating(IP)	IP67	IP67	IP67	IP67

植保无人机的有效载荷是用户比较关注的参数，由于需要加装静电发生器等配件，静电发生器的重量及大小将成为无人机静电喷雾系统发展的首要影响因素。其次，在国外农业航空静电喷雾技术试验研究中展现出的低施药液量的特点，有利于减少植保无人机作业中频繁加药的问题，增加持续作业时间。此外，植保无人机除精准喷洒，还有集智能播种、撒肥、全自主高精度作业为一体的发展趋势，因此还需要考虑静电喷雾系统与无

人机喷洒、播撒、飞控等系统的集成，以及对于整机结构设计等带来的潜在影响[57-59]。

在田间应用方面，国外许多研究证实了航空静电喷雾系统的作业效果好于常规喷雾系统，但也有相反的研究报道，航空静电喷雾技术的研究和应用仍需确定最适合的应用条件。国外航空静电喷雾的前期理论和硬件设计经过了数十年的技术沉淀，为开展农业航空静电喷雾技术的深入研究工作奠定了基础。中国航空静电喷雾技术研究始于 2005 年，而关于无人机静电喷雾技术的研究始于 2015 年，起步较晚但发展迅速[5-6]。在硬件设计方面，无人机静电喷雾系统挂载方式及其衡量标准有待开发验证。目前国内对有人驾驶飞机已有标准规定了航空静电喷雾器的设备组成、主要技术指标及注意事项等[60]。但对于植保无人机缺少对静电喷雾系统整机协调的详细说明和操作规范，且各研究人员选用的机型、旋翼数量、技术参数各不相同，这种状况不利于已有研究各结果间的相互比较[45,61-62]。中国现阶段不应再重复验证航空静电喷雾系统沉积效果和控制单一变量施药工作，而应重视基础性研究和延续性试验。巴西与中国在农业航空静电喷雾技术发展周期相近，但近年来发展迅猛，在开展试验连续性、研究贡献和试验方案设计等方面均值得参考学习。

综上所述，通过对植保无人机主要技术参数、田间试验、硬件设计等分析表明，中国植保无人机静电喷雾技术研究正处于蓬勃发展阶段，具有广阔的发展前景，但其载重、静电系统与播撒和飞控系统的整机协调性、基础性研究欠缺等问题需要进一步解决。

4.3 农业航空静电喷雾技术的研究路线

在国外农业航空静电喷雾系统的田间应用研究中，尽管不同作物生长特性和形态各不相同，航空作业机型、作业参数也存在差异，但是围绕农业航空静电喷雾技术开展的一系列田间应用研究和室内验证优化工作方案，仍有一定程度的共同特征。图 1 梳理了农业航空静电喷雾技术的研究路线。

如图 1 所示，首先需确定充电方式和搭载平台，包括静电喷头数量及位置、绝缘性、静电喷雾系统构成等。为了寻求系统的最优结构和参数，模拟仿真可作为一种验证手段。在系统的设计阶段可直接在仿真模型上修改各部件和子系统的配置情况，在系统的试验应用阶段也可通过建立一组模拟仿真进行带电雾滴沉降的轨迹，并结合不同的靶标参数获取足够训练数据，以达到促进精准沉降和减少飘移损失的目的[63-64]。在雾滴沉降过程中受环境因素、系统参数、可控参数多种因素的制约。因此对于进行航空静电喷雾的相关试验，应进行包括室内和室外试验双线途径。通过软硬件采样可控参数、环境因素和系统参数，监测在长距离的沉降过程。通过所得试验现象考虑如何在多种因素影响条件下进行参数调整，以取得最佳喷雾效果。例如观察雾滴在环境风和旋翼风场共同影响下的液滴状态下带电雾滴沉降的异性电荷排斥过程等[65-67]。最后，根据特定的应用场景，研究人员需要对应不同的靶标作物确定作业参数。药剂充分发挥药效不仅与沉降过程的可控参数、系统参数和环境因素有密切关系，还与作物对象、靶标形态等靶标参数有关。除了雾滴沉积、虫口减退率和病害防治效果等常规衡量指标外，相类似于 Martin 等[39]研究平均 NDVI 值等指标伴随着时间推移的靶标特性变化同样具有重要意义。同时研究应注重多参数及其交互作用影响，单一变量研究难以提供借鉴意义[68-69]。

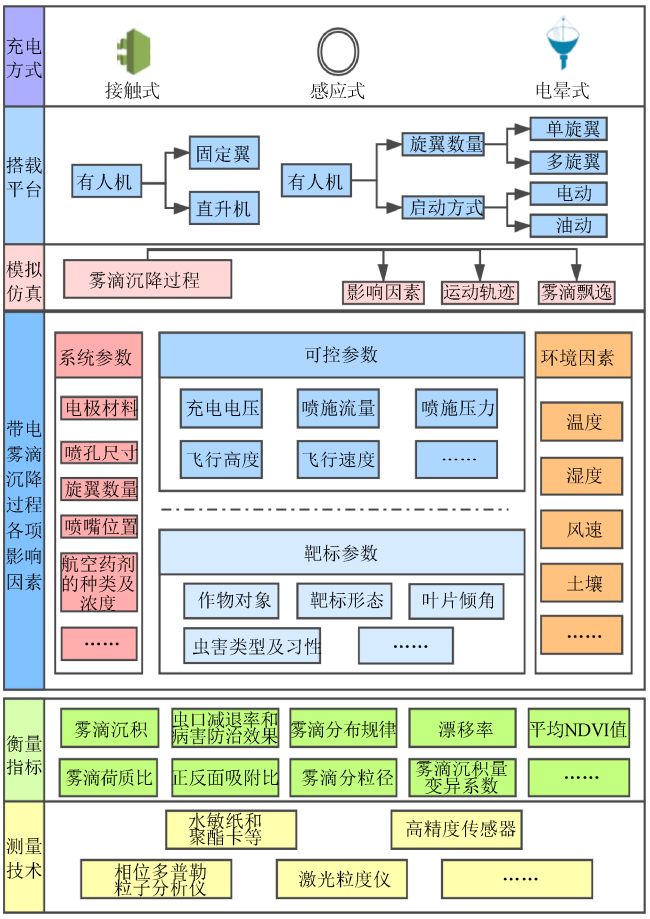

注：NDVI 表示归一化植被指数.
Note: NDVI means normalized difference vegetation index.

图 1 农业航空静电喷雾技术研究路线
Fig.1 Research roadmap of agricultural aviation electrostatic spray technology

5 讨 论

国外农业航空静电喷雾技术发展已有五十多年，已形成理论体系，从主要的粮食作物小麦、水稻、玉米到棉花、大豆等重要经济作物的病虫害，以及杂草防治已有试验研究数据支撑，但在更多的田间场景下和未得到解释的试验研究结果仍待补充。本节聚焦于技术本身，讨论国内外学者仍可对农业航空静电喷雾技术领域进行深入研究的几个方面。

5.1 充电方式多样化

由于感应式充电方式安全、电压较低、电极制作和绝缘方法都较易实现[70-71]，目前国内航空静电喷雾研究沿用了国外采用的感应式充电方式。然而不同于地面静电喷雾系统，航空作业由于难以满足接地条件，造成感

应式静电喷雾的田间施药效果不尽如人意[28]。充电方式其本质是使雾滴带电的途径，除感应式以外，还有电晕式和接触式的充电方式[72]。电晕式充电电压较高，达到30 kV 以上，可用于导电和非导电的液体，且有较低的绝缘要求。但目前暂无足够的研究报道支撑电晕式充电的施药效果。接触式充电电压的要求介于电晕式和感应式之间，但对绝缘性要求较高。这意味着充电电压较高的电晕式和绝缘性要求较高的接触式充电方式需要基础性研究来阐明充电机理和杜绝应用风险。从长远发展的角度来看，电晕式具备很强的带电效应，而接触式充电方式被证实相比于感应式充电，可产生较大目标电流[73]。国内一些科研单位在植保无人机静电喷雾系统的研究中也选用了接触式充电方式，获得了较好效果[3,74-75]。相比之下感应式充电方式的带电效果要弱于其余两种充电方式。电晕式和接触式这 2 种充电方式经过不断完善，有望应用于农业航空静电喷雾技术研究。但是现阶段由于各充电方式在电荷来源和电场分布上都不同，随着喷头到靶标作物的距离增加，空间电荷效应增加，目标电流减小，对于航空作业雾滴长距离沉降有极大的制约。同时在应用推广方面所强调的适用性、成本和安全性方面仍有许多不确定性。因此，需要对接触式以及电晕式 2 种使雾滴带电的方法进行更深入的研究，围绕沉积效果、绝缘性、航空药剂导电率等关键参数与感应式充电方式进行大量的基础性对比试验，以评估不同充电方式在航空静电喷雾作业的应用效果。

5.2　开发适用于农业航空静电喷雾系统的测量技术

沉积效果的测试作为目前表征农业植保作业质量的主要方式，需要保证获取雾滴设备、数据处理及数据比较的合理性和有效性[76-77]。静电喷头通过不同充电方式使喷洒出的雾滴带电，在静电作用下落于植物靶标，其雾滴特性测量面临许多问题。雾滴荷质比作为伴随着静电喷雾技术的名词，其测量结果有助于静电喷头的性能评估。在室内无环境因素干扰的情况下，雾滴荷质比与沉积效果呈正相关的关系[25]。但在室外环境作业时，喷洒端的雾滴和靶标作物上的雾滴二者的荷质比通常会相差较大，这就需要通过有效的测量装置来实时监测喷雾作业过程中带电雾滴的电荷量，以确认静电喷雾系统的正常工作。但是收集带电雾滴的装置可能会由于没有接地的影响导致结果与沉降于靶标的实际效果不符[28]。

对于静电喷雾技术研究来说，电场强度会随着植物的形态、药液电导率、环境因素变化而变化，例如叶片在尖端或末端部分附近的电场是最强的[78]。Law 等[79]的研究也指出了尖锐的叶尖和在落于叶片的带电雾滴云形成气体放电会起到限制沉积的作用。目前对于雾滴沉积分布的检测主要是通过水敏纸等测试卡方式，而沉积量的检测通过示踪剂洗脱的方式，但直径小于 50 μm 的雾滴缺乏足够的水分和重量，在水敏纸上难以产生可测量的标记。另外，航空静电喷雾作业的田间作业效果不佳是带电雾滴荷质比急剧减少的原因，还是环境因素造成的，都需要一种可以实时监测带电雾滴特性的检测装置。Martin 等[28]和 Bayer 等[38]的研究显示，使用水敏纸检测方法受到了严格的限制，添加荧光染料到药剂里的方式虽然能够对带电雾滴的测量有所改善，但也对环境因素要求较高。

近年来在中国，更多的检测手段不断地应用于雾滴效果测量[80-81]，如激光粒度仪、红外热像仪、基于变介电常数电容器原理的雾滴沉积传感器及检测系统、基于驻波率原理的叉指型雾滴采集系统等。不过都存在着制造成本高，测量误差过大、测量过程复杂等各种问题。开发适用于航空静电喷雾系统的雾滴特性检测技术，更好地表征雾滴沉积效果，有利于推动静电喷雾系统的发展。不仅如此，在常规喷雾系统和静电喷雾系统的对比试验也需要针对性开发高精度的测量仪器作为相应的统一检测方法，这样在有效喷幅、雾滴沉积特性、雾滴粒径测量等方面更具有说服力。

5.3　重新思考荷质比测量的必要性

荷质比是指雾滴所带电荷量与雾滴本身质量的比值，是静电喷雾技术独有的衡量指标。该表述意味着荷质比的大小关乎静电喷雾技术的优良与否，荷质比越大越好，而且国外学者均对此有大量研究阐述[19,29]。然而静电喷雾技术的优势体现在能以环抱的方式向靶标作物上吸附，这代表着与靶标端效果检测相关。虽然雾滴具有较高的荷质比是得到良好正反面沉积效果的基础，但在外界因素作用下存在较高的雾滴荷质比却不一定能达到较好的正反面沉积的情况。大田试验条件常有风速、温湿度、土壤等环境因素影响，所得效果与室内荷质比测量装置得到试验结果难以相同，各科研单位对荷质比测量方式、造价、材质等条件也会使相同试验参数所得结果出现偏差。

对于航空应用来说，为解决机身充放电问题双极喷雾系统几乎成为航空静电设备的标配，飞机喷洒出两种极性的雾滴长距离的空中降落过程产生衰减和蒸发，同时旋翼风场对两种极性雾滴的搅浑作用使得雾滴荷质比与最后的环抱效果关系难以确定。雾滴荷质比只能表征该雾滴所带电荷量与质量之比，而与产生低施药液量以及增加沉积尤其是背面沉积的联系有待商榷。鉴于以上情况，研究人员在未来农业航空静电喷雾系统研究中需要重新思考荷质比测量的意义。

6　结束语

国外农业航空静电喷雾技术研究经历了基础性研究、商业化、田间应用、优化工作等阶段，并表现出学科研究范围不断扩大、田间研究作物趋向多样化等趋势。作为航空喷洒设备的选择之一，航空静电喷雾系统作业除了能够显著增加叶片背部沉积，在低施药液量、减少雾滴飘移等方面的优势同样值得关注。

国内农业航空静电喷雾技术研究特别在植保无人机静电喷雾技术方面的研究与应用有很大的发展空间。近五年以植保无人机为搭载平台的农业航空静电喷雾技术研究，结合当前中国农业航空植保领域现状和产业应用推广实际发展迅速。中国可参考国外经验，围绕航空静

电喷雾技术的基础性研究、试验、成果转化、示范推广和服务指导全方面来制定发展规划，把单一强调对雾滴带电的实现转向对农业航空静电喷雾技术系统的整体研究。

[参 考 文 献]

[1] 周志艳，明锐，臧禹，等. 中国农业航空发展现状及对策建议[J]. 农业工程学报，2017，33(20)：1-13.
Zhou Zhiyan, Ming Rui, Zang Yu, et al. Development status and countermeasures of agricultural aviation in China[J]. Transactions of the Chinese Society of Agricultural Engineering (Transactions of the CSAE), 2017, 33(20): 1-13. (in Chinese with English abstract)

[2] 张亚莉，兰玉彬，Fritz B K，等. 美国航空静电喷雾系统的发展历史与中国应用现状[J]. 农业工程学报，2016，32(10)：1-7.
Zhang Yali, Lan Yubin, Fritz B K, et al. Development of aerial electrostatic spraying systems in the United States and applications in China[J]. Transactions of the Chinese Society of Agricultural Engineering (Transactions of the CSAE), 2016, 32(10): 1-7. (in Chinese with English abstract)

[3] 王士林，何雄奎，宋坚利，等. 双极性接触式航空机载静电喷雾系统荷电与喷雾效果试验[J]. 农业工程学报，2018，34(7)：82-89.
Wang Shilin, He Xiongkui, Song Jianli, et al. Charging and spraying performance test of bipolar contact electrostatic spraying system for unmanned aerial vehicle[J]. Transactions of the Chinese Society of Agricultural Engineering (Transactions of the CSAE), 2018, 34(7): 82-89. (in Chinese with English abstract)

[4] Tavares R M, Cunha J P A R, Alves T C, et al. Electrostatic spraying in the chemical control of Triozoida limbata (Enderlein) (Hemiptera: Triozidae) in guava trees (Psidium guajava L.)[J]. Pest Management Science, 2017, 73(6): 1148-1153.

[5] 茹煜，金兰，贾志成，等. 无人机静电喷雾系统设计及试验[J]. 农业工程学报，2015，31(8)：42-47.
Ru Yu, Jin Lan, Jia Zhicheng, et al. Design and experiment on electrostatic spraying system for unmanned aerial vehicle[J]. Transactions of the Chinese Society of Agricultural Engineering (Transactions of the CSAE), 2015, 31(8): 42-47. (in Chinese with English abstract)

[6] 栾华，张青，王稳祥. Z03K000B 静电频谱喷洒系统加改装与飞行试验[J]. 新疆农垦科技，2006，(5)：46-47.
Luan Hua, Zhang Qing, Wang Wenxiang. Installation and modification of Z03K000B electrostatic spray system and flight tests[J]. Xinjiang Reclamation Technology, 2006, (5): 46-47. (in Chinese with English abstract)

[7] 茹煜，周宏平，贾志成，等. 航空静电喷雾系统的设计及应用[J]. 南京林业大学学报：自然科学版，2011，35(1)：91-94.
Ru Yu, Zhou Hongping, Jia Zhicheng, et al. Design and application of electrostatic spraying system[J]. Journal of Nanjing Forestry University Natural Science Edition, 2011, 35(1): 91-94. (in Chinese with English abstract)

[8] 舒朝然，潘宏阳，周宏平，等. 航空静电喷雾与非静电喷雾沉积效果的比较[J]. 林业科学，2012，48(4)：75-80.
Shu Chaoran, Pan Hongyang, Zhou Hongping, et al. Deposition effects of electrostatic and non-electrostatic aerial spray[J]. Scientia Silvae Sinicae, 2012, 48(4): 75-80. (in Chinese with English abstract)

[9] Carlton J B, Isler D A. Development of a device to charge aerial sprays electrostatically[J]. Agricultural Aviation, 1966, 8(2): 44-51.

[10] Carlton J B. Techniques in electrostatic charging of sprays from aircraft[C]//Texas Agricultural Aviation Annual Conference and Short Course on Pest Control, 1968, Texas A&M University-College Station, Texas, The United States.

[11] Carlton J B. Electrical capacitance determination and some implications for an electrostatic spray-charging aircraft[J]. Transactions of the ASABE, 1975, 18(4): 641-644.

[12] Carlton J B, Bouse L F. Distribution of the electric-field for an electrostatic spray charging aircraft[J]. Transactions of the ASABE, 1977, 20(2): 248-252.

[13] Carlton J B, Bouse L F. Spray deposit sampling technique to evaluate electrostatic aerial spray-charging[J]. Transactions of the ASABE, 1978, 21(1): 1-5.

[14] Carlton J B, Bouse L F. Electrostatic spinner-nozzle for charging aerial sprays[J]. Transactions of the ASABE, 1980, 23(6): 1369-1373.

[15] Kihm K D, Kim B H. Atomization, charge, and deposition charactersitics of bipolarly charged aircraft sprays[J]. Atomization and Sprays, 1992, 2(4): 463-481.

[16] Teske M E, Kaufman A E, Thistle H W, et al. Droplet evaporation corrections for aerial spray drift modeling I: Theoretical considerations[J]. Atomization and Sprays, 2003, 13(2-3): 243-250.

[17] Inculet I I, Fischer J K. Electrostatic aerial spraying[J]. IEEE Transactions on Industry Applications, 1989, 25(3): 558-562.

[18] Carlton J B, Bouse L F, Kirk I W, et al. Electrostatic charging of aerial spray over cotton[J]. Transactions of the ASABE, 1995, 38(6): 1641-1645.

[19] Kirk I W, Hoffmann W C, Carlton J B. Aerial Electrostatic Spray System Performance[J]. Transactions of the ASABE, 2001, 44(5): 1089-1092.

[20] Carlton J B. Technique to reduce chemical usage and concomitant drift from aerial sprays: 5975425[P]. 1999-11-2.

[21] Spectrum Electrostatic Sprayers, Inc. Aerial Sprayer Systems[EB/OL]. (2012-12-31)[2020-05-01]. http:// spectrumsprayer. com/aerial. html.

[22] Spectrum Electrostatic Sprayers, Inc. Actual Field Trials of Electrostatic Application[EB/OL]. (2011-04-12)[2020-05-01]. http: //www. spectrumsprayer. com/pdf/ES_ProgressReport_ 2. pdf.

[23] Patel M K, Praveen B, Sahoo H K, et al. An advance air-induced air-assisted electrostatic nozzle with enhanced performance[J]. Computers & Electronics in Agriculture, 2017, 135(5): 280-288.

[24] Law S E, Lane M D. Electrostatic deposition of pesticide spray onto foliar targets of varying morphology[J]. Transactions of the ASABE, 1980, 24(6): 1441-1445.

[25] Matthews G A. Electrostatic spraying of pesticides: A review[J]. Transactions of the ASABE, 1989, 8(1): 3-15.

[26] Martin D E, Lopez J D, et al. Field evaluation of Spinosad

aerial applications for thrips control on cotton[J]. Southwestern Entomologist, 2007, 32(4): 221-228.

[27] Latheef M A, Carlton J B, Kirk I W, et al. Aerial electrostatic-charged sprays for deposition and efficacy against sweet potato whitefly (Bemisia tabaci) on cotton[J]. Pest Management Science, 2009, 65(7): 744-752.

[28] Martin D E, Latheef M A. Aerial electrostatic spray deposition and canopy penetraion in cotton[J]. Journal of Electrostatics, 2017, 90: 38-44.

[29] Martin D E, Latheef M A, López J D. Electrostatically charged aerial application improved spinosad deposition on early season cotton[J]. Journal of Electrostatics, 2019, 97: 121-125.

[30] Cunha J P A R D, Juliatti F C, Reis E F. Tecnologia de aplicação de fungicida no controle da ferrugem asiática da soja: resultados de oito anos de estudos em Minas Gerais e Goiás[J]. Bioscience Journal, 2014, 30(4): 950-957.

[31] Cunha J P A R D, Marques R S, Alves G S. Deposição da calda na cultura da soja em função de diferentes pressões de trabalho e pontas de pulverização[J]. Revista Ceres, 2016, 63(6): 761-768.

[32] Cunha J P A R D, Barizon R R M, Ferracini V L, et al. Spray drift and caterpilar and stink bug control from aerial applications with electrostatic charge and atomizer on soybean crop[J]. Engenharia Agricola, 2017, 37(6): 1163-1170.

[33] Antuniassi U R, Velini E D, Oliveira R B D, et al. Systems of aerial spraying for soybean rust control[J]. Engenharia Agricola, 2011, 31(4): 695-703.

[34] Spectrum Electrostatic Sprayers, Inc. ES Spray System Boost Sugar Cane Sucrose[EB/OL]. (2006-06-30)[2020-05-01]. http:// spectrumsprayer. com/news_2. html.

[35] Kirk I W, Fritz B K, Hoffmann W C. Aerial Methods for Increasing Spray Deposits on Wheat Heads[C]//American Society of Agricultural Engineers. ASAE Annual International Meeting, 2004, Ottawa, Canada.

[36] Fritz B K, Hoffmann W C, Martin D E, et al. Aerial application methods for increasing spray deposition on wheat heads[J]. Applied Engineering in Agriculture, 2007, 23(6): 709-715.

[37] Bayer T, Costa I F D, Lenz G, et al. Equipamentos de pulverização aérea e taxas de aplicação de fungicida na cultura do arroz irrigado[J]. Revista Brasileira de Engenharia Agrícola e Ambiental, 2011, 15(2): 192-198.

[38] Bayer T, Arrué A, Costa I F D, et al. Aplicação aérea de fungicidas na cultura do arroz irrigado com diferentes bicos de pulverização[J]. Ciência Rural, 2012, 42(12): 2185-2191.

[39] Martin D E, Latheef M A. Aerial application methods control spider mites on corn in Kansas, USA[J]. Experimental and Applied Acarology, 2019, 77(4): 571-582.

[40] Eugênio P S, Alci Enimar L. Avaliação do sistema de pulverização eletrostática aérea na redução do volume de calda e dosagem do herbicida glifosate[J]. Current Agricultural Science and Technology, 2007, 12(3): 319-323.

[41] Martin D E, Latheef M A. Efficacy of electrostatically charged glyphosate on ryegrass[J]. Journal of Electrostatics, 2017, 90: 45-53.

[42] Martin D E, Latheef M A, J D. Lopez, Jr, et al. Aerial Application Methods for Control of Weed Species in Fallow Farmlands in Texas[J]. Agronomy, 2020, 10(11): 1764.

[43] Campos S F B. Tecnologia de aplicação eletrostática no controle químico de plantas daninhas avaliado visualmente e por imagem aérea[D]. Uberlândia: Universidade Federal de Uberlândia, 2019.

[44] Gan-Mor S, Ronen B, Ohaliav K. The effect of air velocity and proximity on the charging of sprays from conventional hydraulic nozzles[J]. Biosystems Engineering, 2014, 121(5): 200-208.

[45] Ahmed A, Soban T, Ohyama R. Experimental studies on influence of different conductivities on water mist charging with electrostatic induction[C]//2014 IEEE Conference on Electrical Insulation and Dielectric Phenomena (CEIDP). Institute of Electrical and Electronics Engineers, 2014: 558-561.

[46] Martin D E, Carlton J B. Airspeed and orifice size affect spray droplet spectrum from an aerial electrostatic nozzle for fixed-wing applications[J]. Applied Engineering in Agriculture, 2012, 29(1): 5-10.

[47] Martin D E, Carlton J B. Airspeed and orifice size affect spray droplet spectrum from an aerial electrostatic nozzle for rotary-wing applications[J]. Atomization and Sprays, 2012, 22(12): 997-1010.

[48] Sasaki R S, Teixeira M M, Fernandes H C, et al. Parameters of electrostatic spraying and its influence on the application efficiency[J]. Revista Ceres, 2013, 60(4): 474-479.

[49] Spectrum Electrostatic Sprayers, Inc. Aerial applicators now hitting the ‘bull’s eye’[EB/OL]. (2009-06-12)[2020-05-01]. http: //spectrumsprayer. com/news_1. html.

[50] 新华网. 无人机植保作业将突破 10 亿亩次 精准农业航空助力农业现代化[EB/OL]. 2020-12-01[2021-01-14]. http:// www. gd. xinhuanet. com/zt20/ftym/2020nydh/1203/lyb/index. htm.

[51] 兰玉彬. 精准农业航空技术现状及未来展望[J]. 农业工程技术，2017，37(30)：27-30.

[52] 田志伟，薛新宇，李林，等. 植保无人机施药技术研究现状与展望[J]. 中国农机化学报，2019，40(1)：37-45.
Tian Zhiwei, Xue Xinyu, Li Lin, et al. Research status and prospects of spraying technology of plant protection unmanned aerial vehicle[J]. Journal of Chinese Agricultural Mechanization, 2019, 40(1): 37-45. (in Chinese with English abstract)

[53] 极飞科技. 极飞 P40 2021 款农业无人机[EB/OL]. (2020-12-15)[2020-12-16]. https: //www. xa. com/p40-2021s.

[54] 极飞科技. 极飞 P80 2021 款农业无人机[EB/OL]. (2020-12-15)[2020-12-16]. https: //www. xa. com/p80-2021.

[55] 极飞科技. 极飞 V40 2021 款农业无人机[EB/OL]. (2020-12-15)[2020-12-16]. https: //www. xa. com/v40-2021.

[56] 大疆创新. 大疆农业应用—T30 植保无人飞机[EB/OL]. (2020-11-09)[2020-12-16]. https: //www. dji. com/cn/t30/specs.

[57] Faiçal B S, Costa F G, Pessin G, et al. The use of unmanned aerial vehicles and wireless sensor networks for spraying pesticides[J]. Journal of Systems Architecture, 2014, 60(4): 393-404.

[58] Costa F G, Ueyama J, Braun T, et al. The use of unmanned aerial vehicles and wireless sensor network in agricultural applications[C]//2012 IEEE International Geoscience and Remote Sensing Symposium. Institute of Electrical and Electronics Engineers, 2012: 5045-5048.

[59] Heimfarth T, Araujo J P D. Using unmanned aerial vehicle to connect disjoint segments of wireless sensor network[C]//2014 IEEE 28th International Conference on Advanced Information Networking and Applications. Institute of Electrical and Electronics Engineers, 2014: 907-914.

[60] 全国林业有害生物防治标准化技术委员会. LY/T 2685-2016，航空静电喷雾设备应用技术规范[S]. 北京：中国标准出版社，2016.

[61] Wang Z T, Zhang Y H, Guo T Y, et al. Experimental study on size and velocity of charged droplets[J]. Procedia Engineering, 2015, 126(3): 522-526.

[62] Gan-Mor S, Ronen B, Ohaliav K. The effect of air velocity and proximity on the charging of sprays from conventional hydraulic nozzles[J]. Biosystems Engineering, 2014, 121(5): 200-208.

[63] Colbert S A, Cairncross R A. A computer simulation for predicting electrostatic spray coating patterns[J]. Powder Technol, 2005, 151(1): 77-86.

[64] Mark N H, Malay M, Robert C S. Predicting particle trajectories on an electrodynamic screen-theory and experiment[J]. Journal of Electrostatics, 2013, 71(3): 185-188.

[65] 李继宇，兰玉彬，施叶茵. 旋翼无人机气流特征及大田施药作业研究进展[J]. 农业工程学报，2018，34(12)：104-118.
Li JiYu, Lan Yubin, Shi Yeyin, et al. Research progress on airflow characteristics and field pesticide application system of rotary-wing UAV[J]. Transactions of the Chinese Society of Agricultural Engineering (Transactions of the CSAE), 2018, 34(12): 104-118. (in Chinese with English abstract)

[66] Chen S D, Lan Y B, Li J Y, et al. Effect of wind field below unmanned helicopter on droplet deposition distribution of aerial spraying[J]. International Journal of Agricultural & Biological Engineering, 2017, 10(3): 67-77.

[67] Li J Y, Lan Y B, Wang J W, et al. Distribution law of rice pollen in the wind field of small UAV[J]. International Journal of Agricultural & Biological Engineering, 2017, 10(4): 32-40.

[68] 陈盛德，兰玉彬，周志艳，等. 植保无人机航空喷施飞行质量的试验与评价[J]. 华南农业大学学报，2019，40(3)：89-96.
Chen Shengde, Lan Yubin, Zhou Zhiyan, et al. Test and evaluation for flight quality of aerial spraying of plant protection UAV[J]. Journal of South China Agricultural University, 2019, 40(3): 89-96. (in Chinese with English abstract)

[69] Patel M K, Shamrma T, Nayak M K, et al. Computational modeling and experimental evaluation of the effects of electrode geometry and deposition target on electrostatic spraying processes[J]. International Journal of Computer Applications, 2015, 124(2): 10-15.

[70] Manoj K P, Ghanahyam C, Pawan K. Characterization of electrode material for electrostatic spray charging: Theoretical and engineering practices[J]. Journal of Electrostatics, 2013, 71(1): 55-60.

[71] Patel M K, Kundu M, Sahoo H K, et al. Enhanced performance of an air-assisted electrostatic nozzle: Role of electrode material and its dimensional considerations in spraycharging[J]. Engineering in Agriculture, Environment and Food, 2016, 9(4): 332-338.

[72] 周良富，张玲，薛新宇，等. 农药静电喷雾技术研究进展及应用现状分析[J]. 农业工程学报，2018，34(18)：1-11.
Zhou Liangfu, Zhang Ling, Xue Xinyu, et al. Research progress and application status of electrostatic pesticide spray technology[J]. Transactions of the Chinese Society of Agricultural Engineering (Transactions of the CSAE), 2018, 34(18): 1-11. (in Chinese with English abstract)

[73] Zhao S, Castle G S P, Adamiak K. Comparison of conduction and induction charging in liquid spraying[J]. Journal of Electrostatics, 2005, 63(6): 871-886.

[74] 蔡彦伦. 低空无人机接触式静电喷雾系统设计与试验[D]. 镇江：江苏大学，2017.
Cai Yanlun. Design and Test of Contact Electrostatic Spray System for Low-Altitude UAV[D]. Zhenjiang: Jiangsu University, 2017. (in Chinese with English abstract)

[75] Zhao D N, Lan Y B, Shen W G, et al. Development of a charge transfer space loop to improve adsorption performance in aerial electrostatic spray[J]. International Journal of Agricultural and Biological Engineering, 2020, 13(5): 50-55.

[76] 兰玉彬，彭瑾，金济. 农药喷雾粒径的研究现状与发展[J]. 华南农业大学学报，2016，37(6)：1-9.
Lan Yubin, Peng Jin, Jin Ji, et al. Research status and development of pesticide spraying droplet size[J]. Journal of South China Agricultural University, 2016, 37(6): 1-9. (in Chinese with English abstract)

[77] Zhu H P, Salyani M, Fox R D. A portable scanning system for evaluation of spray deposition distribution[J]. Computers and Electronics in Agriculture, 2011, 76(3): 38-43.

[78] Dai Y, Law S E. Modeling the transient electric field produced by a charged pollen cloud entering a flower[C]//IEEE Industry Applications Conference Thirtieth IAS Annual Meeting. Institute of Electrical and Electronics Engineers, 1995: 1395-1402.

[79] Law S E. Electrostatic pesticide spraying: Concepts and practice[J]. IEEE Transactions on Industry Applications, 1983, 19(2): 160-168.

[80] 张瑞瑞，陈立平，兰玉彬，等. 航空施药中雾滴沉积传感器系统设计与实验[J]. 农业机械学报，2014，45(8)：123-127.
Zhang Ruirui, Chen Liping, Lan Yubin, et al. Development of a deposit sensing system for aerial spraying application[J]. Transactions of the Chinese Society for Agricultural Machinery, 2014, 45(8): 123-127. (in Chinese with English abstract)

[81] 何勇，吴剑坚，方慧，等. 植保无人机雾滴沉积效果研究综述[J]. 浙江大学学报：农业与生命科学版，2018，44(4)：392-398，515.
He Yong, Wu Jianjian, Fang Hui, et al. Research on

deposition effect of droplets based on plant protection unmanned aerial vehicle: A review[J]. Journal of Zhejiang University: Agriculture and Life Sciences, 2018, 44(4): 392-398, 515. (in Chinese with English abstract)

Progress in foreign agricultural aviation electrostatic spray technologies and references for China

Zhang Yali[1,2], Huang Xinrong[1,2], Wang Linlin[2,3], Deng Jizhong[1,2], Zeng Wen[1,2], Lan Yubin[2,3※], Muhammad Naveed Tahir[4]

(1. *College of Engineering*, *South China Agricultural University*, *Guangzhou* 510642, *China*; 2. *National Center for International Collaboration Research on Precision Agricultural Aviation Pesticides Spraying Technology*, *Guangzhou* 510642, *China*; 3. *College of Electronic Engineering*, *South China Agricultural University*, *Guangzhou* 510642, *China*; 4. *Department of Agronomy*, *PMAS-Arid Agriculture University*, *Rawalpindi* 46300, *Pakistan*)

Abstract: Chemical pesticide residues have posed a great impact on crops and the ecological environment in recent years, as the prevention and control of crop diseases and pests have widely been used in agricultural production. Consequently, an aerial pesticide application technology has become an effective way for plant protection in modern agriculture. The powerful technology is characterized to reduce the numbers and residues of pesticides for the better effectiveness of pesticide application. Alternatively, a high-voltage electrostatic device is often used to charge the spray droplets in an electrostatic spray system. Specifically, the chemical liquid is atomized into droplets near the nozzle to obtain a charge of the same polarity as the nozzle. An electrostatic field is then formed between the nozzle and the crop target under the action of high-voltage static electricity. As such, the droplets of opposite polarity are quickly adsorbed on the front and back of crop targets during the spraying process. Aerial electrostatic spraying is a deep integration of electrostatic spray system and aviation pesticide spraying in precision agriculture. The droplets can quickly be deposited along the power line in the process of aircraft spraying, thereby greatly reducing the drift loss for highly efficient deposition of droplets. Furthermore, the electrostatic spray technology has achieved excellent control effects on crops, fruit trees, and greenhouse vegetables in field tests. The top countries of aerial electrostatic spray technology in the world are the United States and Brazil, in terms of technology usage, and innovation. Particularly, the electrostatic spray technology in the United States has been fully commercialized for the aviation spraying equipment. In addition, an efficient aircraft is highly required for large-scale planting and plant protection in vast arable land and mostly plains in some developing countries. The manned fixed-wing aircraft is mainly used in electrostatic spray systems at present. This review outlined the international development of aerial electrostatic spraying technology to further clarify two main lines of reports at home and aboard, ranging from basic theoretical research to commercialization process. An application level of technology was set to analyze in China. The research on aviation electrostatic spray technology in China has presented a promising increase trend, due mainly to small environmental and topographical impacts in field tests. Moreover, the unmanned aerial vehicle (UAV) has become the most suitable aircraft equipped with an electrostatic spray system after long-term research. However, large research gaps still remained in manned vehicles and lately commercial plant protection UAV, compared with the state-of-the-art electrostatic spray technologies overseas. There were also numerously repeated and invalid studies overlapped in the main parameters in China. Anyway, it is still necessary to delve into the specific interaction mechanism between the process of spraying droplets and the operating parameters. The industrialized development of aviation electrostatic spray system was also reviewed at the end, together with the development prospects. Some suggestions were listed as: (1) The performance of each charge needed to be elucidated in the aerial electrostatic spray system. (2) The measurement technology of charged droplet deposition was highly demanding to accurately evaluate the actual properties of electrostatic spray. (3) Measurement of charge-to-mass ratio was necessary to rethinking using the cutting-edged quantum theories. An ever-increasing demand is coming soon using aviation electrostatic spray system for crop protection.

Keywords: agricultural aviation; plant protection; review; electrostatic spray; droplet deposition; aerial pesticides application

基于可见光图像的水稻颖花开花状态检测方法

张亚莉[1,2]，肖文蔚[1,2]，卢小阳[1,2]，刘爱民[3]，祁 媛[1,2]，刘含超[1,2]，施泽坤[4]，兰玉彬[2,5,6※]

（1. 华南农业大学工程学院，广州 510642； 2. 国家精准农业航空施药技术国际联合研究中心，广州 510642；
3. 袁隆平农业高科技股份有限公司，长沙 410125； 4. 海南大学植物保护学院，海口 570228；
5. 华南农业大学电子工程学院，广州 510642；6. 华南农业大学人工智能学院，广州 510642）

摘 要：通过识别水稻开花张开颖花内外颖与吐出颖花花药的特征，进而准确判断颖花开花时间，是及时进行杂交水稻制种授粉的前提。该研究通过可见光相机获取水稻颖花图像，基于可见光蓝色通道串联大津法（Series Otsu，SOtsu）提取颖花花药，同时使用深度学习算法基于区域的快速卷积神经网络（Faster Regional Convolutional Neural Network，FasterRCNN）及 YOLO-v3 识别颖花花药与张开颖花内外颖，通过对比不同算法识别精确率、召回率、F_1 系数以及皮尔逊相关性系数，研究适用于识别颖花开花状态的特征与方法。结果显示，FasterRCNN 算法检测张开颖花内外颖精确率达 1，召回率达 0.97，F_1 系数为 0.98，皮尔逊相关系数为 0.993，串联大津法检测吐出花药精确率达 0.92，召回率达 0.93，F_1 系数为 0.93，皮尔逊相关系数为 0.936。这表明串联大津法与 FasterRCNN 算法适用于水稻颖花开花状态检测，且张开颖花内外颖比吐出花药更适合作为水稻开花状态特征应用于深度学习算法检测。串联大津法可代替 FasterRCNN 算法在模型构建完成前进行检测，保证水稻颖花开花状态检测连续性。

关键词：图像识别；对象识别；水稻；颖花；颖花内外颖；花药；串联大津法；深度学习
doi：10.11975/j.issn.1002-6819.2021.09.029
中图分类号：S252$^+$.3 **文献标志码**：A **文章编号**：1002-6819(2021)-09-0253-10

张亚莉，肖文蔚，卢小阳，等. 基于可见光图像的水稻颖花开花状态检测方法[J]. 农业工程学报，2021，37(9)：253-262.
doi：10.11975/j.issn.1002-6819.2021.09.029 http://www.tcsae.org
Zhang Yali, Xiao Wenwei, Lu Xiaoyang, et al. Method for detecting rice flowering spikelets using visible light images[J]. Transactions of the Chinese Society of Agricultural Engineering (Transactions of the CSAE), 2021, 37(9): 253-262. (in Chinese with English abstract) doi：10.11975/j.issn.1002-6819.2021.09.029 http://www.tcsae.org

0 引 言

杂交水稻制种是水稻异交结实，需父系花粉传播到母系柱头上受精结实，其异交结实率高低，取决于父本花粉散落到母本柱头上的有无与数量。杂交水稻制种授粉时期需父本与母本同期抽穗开花，父系水稻开花时间为每日 10:00－12:00，开花时需人工辅助授粉。水稻颖花开花需要一定的温光条件，一般在亚热带或热带环境下，开花温度为 24～35 ℃，相对湿度为 70%～90%。水稻开花期约 10 d，每天开花 1.5～2 h，花粉寿命为 4～5 min，为保证制种母系的结实率，人工辅助授粉需在花期内完成[1]。因授粉时间短，每天需准确把握授粉时机，要在父系开花高峰期时授粉。

目前，水稻父系颖花开花信息等表型数据的获取主要依靠人工观察[2]，适用于人工辅助授粉，但对于大规模全程机械化制种，采用无人机辅助授粉时，人工观察难以有效准确地获取全部农田水稻开花状态，也难以实现智能授粉作业。通过采集田间水稻颖花可见光图像自动检测开花状态信息[3]，为实现无人农场提供数据支持与决策参考，是降低劳动成本、提高制种率、实现科学制种的重要举措，对实现杂交水稻制种授粉智能化决策与农场无人化作业有积极意义。

国内外学者对视觉识别小麦和水稻等作物穗部和颖花进行了有益尝试。多数学者通过对图像颜色空间的变换处理[4]与阈值设置[5]，分离目标与背景，广泛应用于水果分离计数[6]、小麦穗部计数[7]、田间农作物分类[8-10]等类别间有颜色差异的图像。Fernandez-Gallego 等[11-12]通过对田间小麦可见光图像进行滤波与极大值分割处理，从小麦俯视图中分离出麦穗，识别成功率达 0.9。Guo 等[13]采用尺寸不变特征变换（Scale Invariant Feature Transform，SIFT）算法提取水稻颖花可见光图像特征点和描述算子，再用支持向量机训练模型，准确度为 0.8。对于 SIFT 算法，同一幅图像初始质心选择不同，往往会出现不一样的特征，需要提取特征人员具备足够经验。Sadeghi-Tehran 等[14]采用车载与手持可见光相机采集图像，应用超像素分割算法结合深度学习识别田间小麦麦穗，相对均方误差达 0.11。Alkhudaydi 等[15]采用 4 个作物数量表型工作站固定于试验田中进行高频成像，采集

收稿日期：2021-03-15 修订日期：2021-04-23
基金项目：广东省重点领域研发计划（2019B020221001）；广东省科技计划项目（2018A050506073）；广东省现代农业产业共性关键技术研发创新团队项目（2020KJ133）；国家重点研发计划（2017YFD0701202）
作者简介：张亚莉，博士，副教授，研究方向为农用传感器技术与应用。Email：ylzhang@scau.edu.cn
※通信作者：兰玉彬，博士，教授，博士生导师，研究方向为精准农业航空应用技术。Email：ylan@scau.edu.cn
中国农业工程学会会员：兰玉彬（E041200725S）；张亚莉（E041200939S）

近三年不同生长时期小麦可见光图像侧视图，对每张图像小麦穗部进行标注，再输入全卷积神经网络（Full Convolutional Neural Networks，FCN）训练，模型交并比最高可达 0.53。Hasan 等[16]采用地面小车搭载可见光相机获取小麦穗部图像，经过区域卷积神经网络（Regional Convolutional Neural Networks，RCNN）算法识别计算小麦穗数，准确率达 0.933。Xiong 等[17]通过模拟自然光，采用深度学习与超像素分割方法识别水稻穗部，准确度达 0.767。

上述研究均对作物表型检测进行了一定探索，但目前尚无将张开颖花内外颖作为特征进行颖花开花状态检测的研究报道，也未发现将深度学习技术运用于水稻颖花开花状态检测的研究报道。本文研究基于前人研究结果提出基于视觉图像处理技术串联使用大津法，简称串联大律法（Series Otsu，SOtsu），提取吐出颖花花药，同时使用深度学习[18]算法，基于区域的快速卷积神经网络（Faster Regional Convolutional Neural Network，FasterRCNN）和 YOLO-v3，对水稻开花张开颖花内外颖与吐出颖花花药两种特征进行检测，并探讨了上述三种算法对水稻开花不同特征的识别效果，为自动化检测水稻开花状态提供参考。

1 材料与方法

1.1 图像获取

1.1.1 试验环境

该研究试验地点位于海南省东方市感城镇制种基地（18°52′48″N，108°42′36″E），属热带海洋性季风气候，光照强，无明显季节区别。试验时间为 2020 年 10 月 9 日-2020 年 10 月 23 日。由于颖花一般在中午温度达到 25～33 ℃时开花，故试验时间为北京时间 10:00－14:00。试验地环境相对湿度为 82%左右，东北风 4～5 级，平均海拔高度 6 m，试验水稻制种组合为华煜 4127S/华恢 4156。

1.1.2 数据采集

试验采用可见光相机 Canon EOS 80D（日本佳能株式会社，东京，日本）获取图像，CMOS 传感器，相机快门速度为 1/8000～30 s，图像大小为 2.42×10^8 像素，图像存储格式为.RAW。相机在自动曝光与自动聚焦模式下使相机镜头平行于颖花，于北京时间 10:00－14:00 颖花开花时拍摄两组距离不同图像各 2 000 张，第一组距离颖花 15 cm，第二组距离颖花 45 cm。当环境到达开花条件时，水稻颖花基部浆片吸水膨胀，相互挤压且压迫外颖，把内外颖扣接槽脱开，外颖顶向一边，使得颖花开放，同时吐出花药[19]。原始颖花数据图像如图 1。



a. 15 cm 成像距离 b. 45 cm 成像距离
a. 15 cm imaging distance b. 45cm imaging distance

图 1 原始颖花图像

Fig.1 Raw images of spikelets

1.2 试验方法

1.2.1 基于 SOtsu 检测方法

SOtsu 基于图像灰度信息进行前景与背景的分离。相较于深度学习算法需要人工添加标签与训练模型等繁杂的预处理工作，SOtsu 基于可见光图像各通道间灰度值差异进行目标提取[8,20-21]是一种简单高效的方法。分割结果精确到每个像元点。

该研究使用可见光单反相机采集图像数据，且该型号相机具有自动聚焦功能，在前景选定后，背景自动虚化，可顺利地分离出整株稻穗与背景。串联大津法基于图像灰度值进行分割，而颖花内外颖与绿色水稻叶片颜色相近，因此该研究未使用串联大津法对颖花内外颖进行识别试验。

颖花花药提取步骤见图 2，先将可见光图像进行红/绿/蓝通道分离，生成对应的通道灰度图像，基于蓝色通道灰度图像扫描整幅图像灰度值，将灰度值分为 0～255 共 256 个灰度阶梯，并统计整幅图像中对应灰度阶梯的像素点个数，生成灰度直方图。在此基础上运用最大类间方差法（大津法）分离稻穗与背景，背景灰度置 0。在已提取的颖花花药与颖花内外颖像素点范围内独立使用最大类间方差分析，找出颖花花药与颖花内外颖灰度范围内最大类间方差所对应的灰度值，作为进一步分类操作的阈值，保留花药原有灰度值，颖花内外颖灰度值置 0。最终结合原始图像输出提取效果，并输出以八连通法计算的连通区个数。

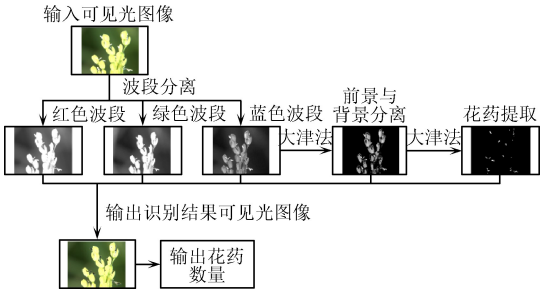

图 2 串联大津法检测颖花花药流程

Fig.2 Process of spikelet anthers detection by SOtsu

类间方差计算公式[5]如式（1）所示：

$$\sigma_B^2 = \rho_1(\mu_1 - \mu_T)^2 + \rho_2(\mu_2 - \mu_T)^2 \quad (1)$$

式中 σ_B 为类间方差值；μ_T 为整幅图像的平均灰度值；μ_1 和 μ_2 分别为类 1 和类 2 的平均灰度值；ρ_1 和 ρ_2 分别为类 1 和类 2 发生的概率。

1.2.2 基于 FasterRCNN 检测方法

目前深度学习算法众多，但 FasterRCNN 依然是深度学习领域的主流。Ren 等[22]开发了 FasterRCNN 算法，该算法将特征抽取、区域选择、边界框回归、分类器分类整合在一个网络中，如图 3 所示。检测方法是通过区域卷积神经网络产生大量可能包含待检测物体的潜在边界框，再用分类器判断每个边界框里是否包含物体，以及物体所属类别的置信度，通过后处理改善边界框，消除重复检测目标。

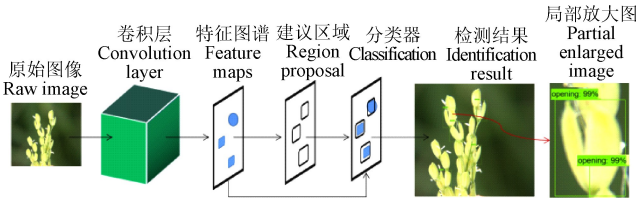

图 3　基于区域的快速卷积神经网络检测系统

Fig.3　FasterRCNN detection system

1.2.3　基于 YOLO-v3 检测方法

YOLO[23]由于其极高的处理速度被广泛[24-27]应用于深度学习目标识别领域。如图 4 所示，YOLO 将输入图像分成 $S\times S$ 个区域，将物体检测任务当作回归问题来处理，使用一个神经网络，直接从一整张图像来预测出边界框坐标、边界框包含物体的置信度和类别概率。YOLO 在训练和测试时都能看到整张图像信息，因此 YOLO 在检测物体时能很好地利用上下文信息。

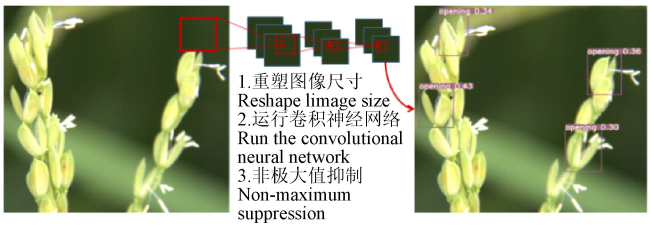

图 4　YOLO 检测系统

Fig.4　YOLO detection system

Redmon 等[28]整理了 PASCAL VOC2007 及 VOC2012 数据集下 FasterRCNN，SSD[29]，YOLO 三种算法的平均均匀精度（mean Average Precision，mAP）以及帧速（Frames Per Second，FPS）。FasterRCNN 的 mAP 达到 76.4%[30]，但是处理频率最慢，为 5 帧/s。YOLO[23]的处理速度较快，为 45 帧/s，但是 mAP 最低，只有 63.4%，而 YOLO-v3 的精度和处理速度均高于先前版本[23,28,31]。

针对颖花开花检测，算法应具有更强的实时性，及时检测水稻开花信息，同时须有较高识别精度，减少误判率。YOLO-v3 版本与系列新版本 YOLO-v4[32]、YOLO-v5 相较，参考资料与开源代码分享较多，且 YOLO 系列主打处理速度，YOLO-v4 较 YOLO-v3 速度上有所提升，但精度提升不明显，故该研究采用 YOLO-v3 进行试验。

1.2.4　深度学习检测技术路线

试验基于 PASCAL VOC2012[33]格式的数据集运用 FasterRCNN 和 YOLO-v3 两种算法进行模型训练，结合精确率与处理时间，综合分析两种算法在水稻颖花开花检测中的应用效果。

训练图像分为两组，第一组图像基于开放颖花内外颖特征，第二组图像基于吐出花药特征，各 2 000 张。采用 NVIDIA GeForce RTX 3090 显卡进行训练。训练模型输入图像均采用分辨率为 6 024×4 022 像素的原始图像。采用基于 PyTorch 框架的 FasterRCNN[34]和 YOLO-v3[35]作为目标检测算法，参与训练图像包括距离相机镜头 15 和 45 cm 的水稻颖花开颖图像。主要技术路线如图 5 所示。

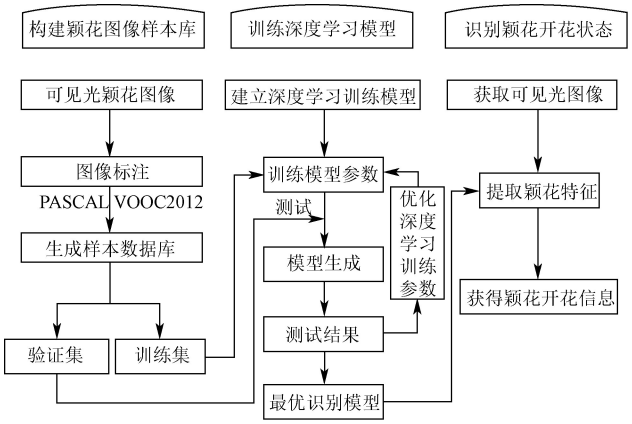

图 5　深度学习识别颖花开花状态技术路线

Fig.5　Deep learning technique route of flowering spikelet detection

1.2.5　图像标注方法

在模型训练前用 LabelImg 软件对可见光颖花图像人工添加标签数据，每张已标注图像会生成后缀为.xml 的文本文件，用于深度学习算法有监督学习。

将标注完成图片按照 8:1:1 的比例分为训练集、验证集与测试集，采用 PASCAL VOC2012 数据集作为样本数据库格式，训练集用于训练模型参数，验证集测试训练好的模型参数，并根据测试结果优化模型参数，最终选出最优识别模型。测试集用于测试训练模型识别颖花开花状态的泛化能力。

训练完成的模型用于识别颖花开花状态，在水稻农田中每获取一张图像都可导入训练好的模型进行识别，识别结果通过矩形框框出并显示识别结果置信度及方框数量。

置信度（Confidence）公式如式（2）所示，置信度取值范围为 0～100%，越接近 0 说明检测到的目标对象（Object）置信度越低，相反，越接近 100%说明检测到的目标置信度越高。置信度与检测目标的交并比（Intersaction over Union, IoU）有关，目标检测中，可通过边界框同时定位目标，通过算法定位的目标边界框与实际目标边界框的交集和并集之比为交并比。交并比可用来评价目标检测算法的定位是否精准，该研究采用 IoU≥0.3 作为阈值进行检测。

$$\text{Confidence}=\Pr(\text{Object})\cdot \text{IoU}_{\text{pred}}^{\text{truth}}\times 100\% \qquad (2)$$

式中 Pr(Object)为边界框中包含监测目标的概率；$\text{IoU}_{\text{pred}}^{\text{truth}}$ 为算法预测的边界框与实际的边界框之间的交并比。

水稻开颖伴随着张开颖花内外颖与吐出颖花花药两个明显特征。颖花内外颖张开形状与闭合形状差别较大，形状与水稻叶片等其他背景差异明显，但颖花内外颖颜色与水稻叶片颜色近乎一致。花药颜色呈淡黄色，颜色与形状明显区别于张开的颖花内外颖、叶片等非花药类别，但是同一幅图像中，花药所占图像的比例小于颖花内外颖，因此该模块通过人工标注花药与张开颖花内外颖，并计算同一深度学习算法中两种标注方法的精确率（Precision）、召回率（Recall）以及 F_1 系数，来研究深

度学习算法下更适合水稻颖花开花的识别特征，标记方法如图 6。

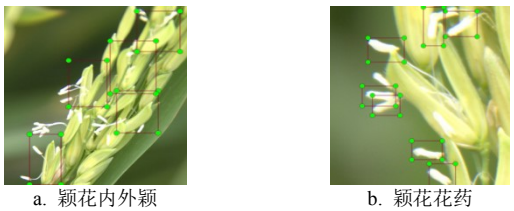

a. 颖花内外颖
a. Spikelet hull

b. 颖花花药
b. Spikelet anthers

注：图中方框用于定位颖花内外颖与颖花花药的位置
Note: Bounding box in the figure is used to locate the position of spikelet hull and spikelet anthers.

图 6 颖花标注方式
Fig.6 Labeling method of spikelet

1.2.6 评估指标

该研究将精确率（Precision），召回率（Recall），F_1 系数，皮尔逊系数 r 以及回归函数作为评估指标。

Precision 表示算法检测到的目标中正确的样本比例。Recall 表示所有实际目标中被算法检测到的比例。F_1 系数为精确率和召回率的加权调和平均，F_1 系数值越高，说明试验效果越好。皮尔逊系数 r 用于分析两个变量 X 和 Y 之间的线性相关性，取值区间为[−1, 1]，1 表示完全正相关，0 表示无关，−1 表示完全负相关。该研究中 r 用于分析人工观察颖花开花数量与算法识别之间的相关性。

从试验结果中有规律地抽取一定数量图像，对每张图像建立相应的混淆矩阵。假设检测目标为正样本，背景为负样本，一个二分类问题可以产生四种结果，真阳性（TP）即正确分类检测目标；假阳性（FP）即错误归类背景为检测目标；假阴性（FN）即将检测目标错误归类为背景；真阴性（TN）即正确归类背景。该研究讨论二进制分类问题，无需正确分类背景，此处 TN 始终为 0[16]。验证指标为精确率，召回率和 F_1 系数，计算公式如式（3）-（5）所示：

$$\text{Precision} = \frac{\text{TP}}{\text{TP} + \text{FP}} \tag{3}$$

$$\text{Recall} = \frac{\text{TP}}{\text{TP} + \text{FN}} \tag{4}$$

$$F_1 = \frac{2 \times \text{Precision} \cdot \text{Recall}}{\text{Precision} + \text{Recall}} \tag{5}$$

2 结果与分析

2.1 串联大津法检测结果

使用 MATLAB 将图 7a 颖花可见光图像分为红（R）/绿（G）/蓝（B）三个波段的灰度图像（图 7b～7d），使用 ENVI 5.3，在每幅图片上均匀选取颖花花药与颖花内外颖各约 28 000 个像素点，绘制灰度直方图（图 8）。

基于三个通道的灰度直方图统计颖花花药与颖花内外颖的三种可见光波段像元灰度值的均值与标准差，如表 1 所示。利用均值作为颖花花药与颖花内外颖像元值差异的评价标准，利用标准差作为颖花花药与颖花内外颖各波段中像元波动范围的评价指标，通过 1 倍标准差与均值相结合判断颖花花药与颖花内外颖各波段像元是否有明显交叉重叠现象，绘制图 9。

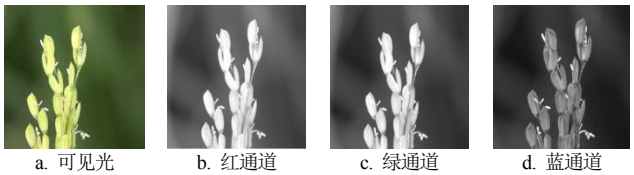

a. 可见光
a. Visible

b. 红通道
b. R-channel

c. 绿通道
c. G-channel

d. 蓝通道
d. B-channel

图 7 水稻颖花红/绿/蓝通道灰度图像
Fig.7 Grayscale images of spikelet in R/G/B channels

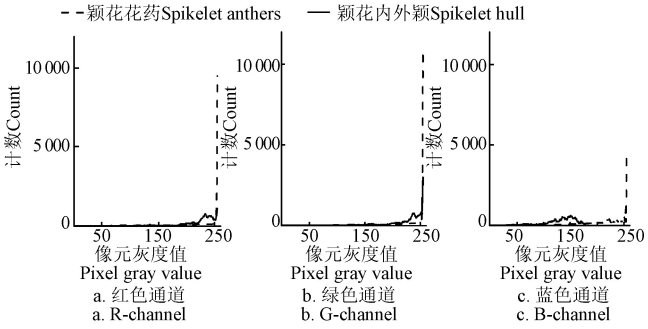

图 8 颖花花药与颖花内外颖在红/绿/蓝通道的灰度直方图
Fig.8 Grayscale histogram of spikelet anthers and spikelet hulls in R/G/B channels

表 1 颖花花药与颖花内外颖在红/绿/蓝通道中的像元统计值
Table 1 Pixels statistic values of spikelet anthers and spikelet hull in R/G/B channel

特征 Feature	红色通道 Red channel		绿色通道 Green channel		蓝色通道 Blue channel	
	均值 Mean	标准差 Standard deviation	均值 Mean	标准差 Standard deviation	均值 Mean	标准差 Standard deviation
颖花花药 Spikelet anthers	213.00	56.86	223.14	46.15	210.23	43.49
颖花内外颖 Spikelet hull	221.31	32.38	229.38	27.34	129.78	30.63

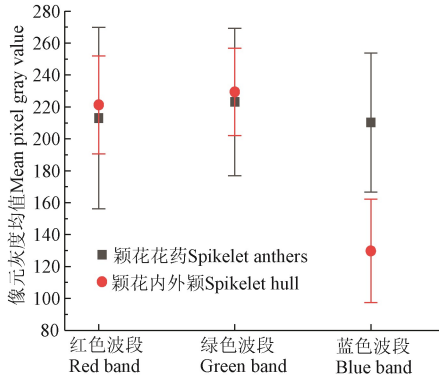

图 9 颖花花药与颖花内外颖红/绿/蓝波段灰度均值与 1 倍标准差范围
Fig.9 Mean gray value and one fold standard deviation ranges of spikelet anthers and spikelet hull in R/G/B channels

通过表 1 和图 9 可知，颖花在红、绿、蓝三个波段中的像元均值都高于 200，颖花内外颖像元均值在红、绿、蓝三个通道中呈上升状态，在蓝波段中颖花内外颖的像元均值与花药差别明显，且在 1 倍标准差范围内无交叉重叠，其他两个波段中，颖花花药与颖花内外颖像元值

相接近。这表明，基于可见光图像蓝色通道进行花药提取是可行的，基于可见光图像蓝波段灰度图像串联大津法进行花药与颖花内外颖分离可得到比其他波段更好的分离效果。

串联大津法提取花药结果示例如图 10 所示，图中黑色像素点为已识别的花药。

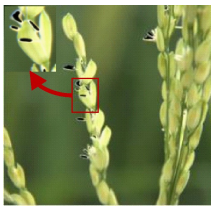

注：黑色像素点为已识别花药。
Note: Black pixels are identified spikelet anthers.

图 10　串联大津法提取颖花花药结果
Fig.10　Extraction results of spikelet anthers by SOtsu

2.2　FasterRCNN 与 YOLO-v3 检测结果

YOLO-v3 与 FasterRCNN 算法的识别结果如图 11 所示，识别结果通过方框表示，并在方框上方显示结果置信度。图 11a 与图 11c 分别是 YOLO-v3 识别颖花内外颖与花药的结果，图 11b 与图 11d 分别是 FasterRCNN 识别颖花内外颖与花药的结果。FasterRCNN 置信度高达 98%，比 YOLO-v3 测试结果置信度高一倍以上。

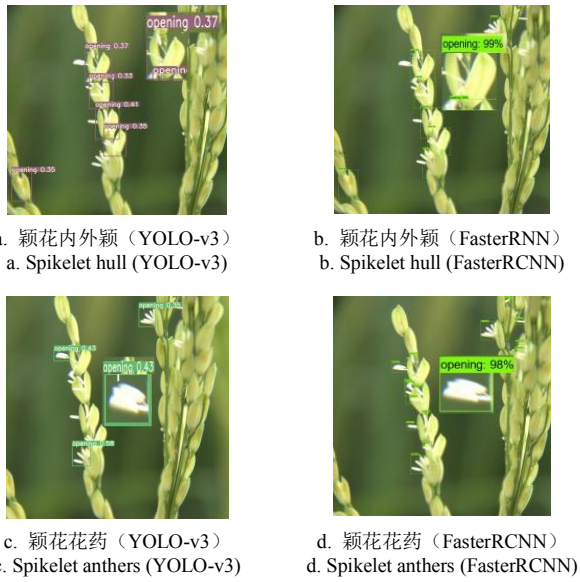

a. 颖花内外颖（YOLO-v3）
a. Spikelet hull (YOLO-v3)

b. 颖花内外颖（FasterRNN）
b. Spikelet hull (FasterRCNN)

c. 颖花花药（YOLO-v3）
c. Spikelet anthers (YOLO-v3)

d. 颖花花药（FasterRCNN）
d. Spikelet anthers (FasterRCNN)

注：识别结果通过方框表示，并在方框上方显示结果置信度。
Note: Detection results are represented by boxes, and the confidence coefficients of results are displayed above boxes.

图 11　两种算法颖花花药与张开颖花内外颖检测结果
Fig.11　Detection results of opening spikelet hull and spikelet anthers by two algorithms

FasterRCNN 与 YOLO-v3 算法识别颖花内外颖与花药的损失函数如图 12 所示。FasterRCNN 算法识别两个特征对象均在第 30 次迭代时趋于最小值，YOLO-v3 算法在第 300 次迭代时曲线斜率近似于 0，损失函数值趋于最小值。

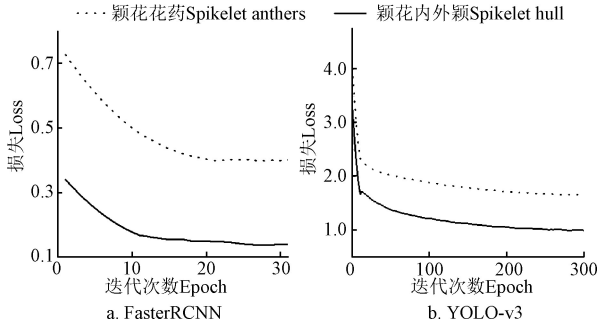

图 12　两种算法的损失函数 20 点 SG 平滑
Fig.12　20 pts SG smooth loss function of two algorithms

图 13 是 FasterRCNN 算法与 YOLO-v3 算法分别进行 30 次与 300 次迭代训练的类别平均均匀精度；颖花内外颖识别平均均匀精度，FasterRCNN 算法为 0.897，YOLO-v3 算法为 0.847。颖花花药识别平均均匀精度，FasterRCNN 为 0.788，YOLO-v3 算法为 0.773。

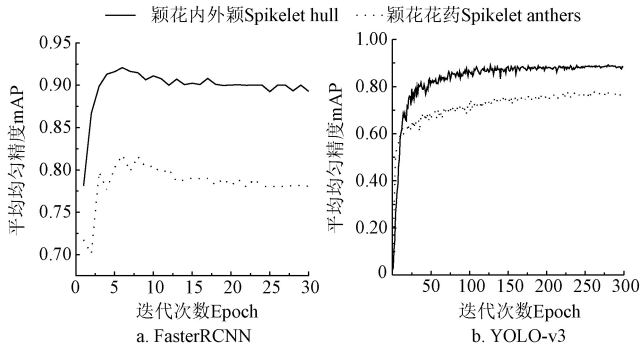

图 13　两种算法识别颖花花药与内外颖平均均匀精度
Fig.13　Mean Average Precision of two algorithms of the spikelet anthers and spikelet hull detection

2.3　三种算法检测结果对比分析

2.3.1　检测精度分析

试验从 227 张可见光测试图片中每 10 张抽取 1 张，共抽取 20 张可见光图像，统计 20 张图像中 YOLO-v3 与 FasterRCNN 及 SOtsu 识别开放颖花内外颖与花药的效果。

三种算法平均检测时间与识别精确率统计结果分别如表 2、表 3 所示。针对花药识别，FasterRCNN 精确率为 0.99，召回率与精度差异较大，只有 0.93，F_1 系数为 0.95，平均处理时间为 169.4 ms。SOtsu 精度为 0.92，召回率与 F_1 系数均为 0.93，平均处理时间为 560 ms。这说明 FasterRCNN 算法更适用于及时检测水稻颖花花药吐出状态，其精度与 F_1 系数均高于 SOtsu，但 SOtsu 更能平衡精度与召回率。明显地，FasterRCNN 算法检测效果优于 SOtsu。

针对开放的颖花内外颖识别，FasterRCNN 对开放颖花内外颖识别结果精度为 1，召回率为 0.97，F_1 系数为 0.98，均优于花药识别。虽然 YOLO-v3 平均检测时间 7.3 ms，比 FasterRCNN（169.4 ms）快约 23 倍，但 YOLO-v3

试验效果不理想，识别开放颖花内外颖和吐出花药效果均逊色于 SOtsu 和 FasterRCNN，且测试结果与模型训练结果差异大，在与 FasterRCNN 使用同一训练集情况下出现了过拟合现象。

试验结果表明，开放颖花内外颖比吐出颖花花药更适用于表征水稻颖花开花状态，FasterRCNN 算法适合用于水稻颖花开花状态检测。

表 2 三种算法的平均检测时间

Table 2 Average detection time of three algorithms

指标 Index	SOtsu	FasterRCNN	YOLO-v3
时间均值 Mean time/ms	560.00	169.40	7.30
标准差 Standard deviation/ms	6.00	1.83	0.70

注：SOtsu 表示串联大律法，FasterRCNN 表示基于区域的快速卷积神经网络，下同。

Note: SOtsu represents Series Otsu; FasterRCNN represents Faster Regional Convolutional Neural Network, the same as below.

表 3 三种算法对张开颖花内外颖与花药检测结果统计

Table 3 Statistical results of the opening spikelet hull and spikelet anthers detection by three algorithms

图像序号 Image number	张开颖花内外颖 Opening spikelet hull						颖花花药 Spikelet anthers								
	精确率 Precision		召回率 Recall		F_1 系数 F_1-measure		精确率 Precision			召回率 Recall			F_1 系数 F_1-measure		
	FasterRCNN	YOLO-v3	FasterRCNN	YOLO-v3	FasterRCNN	YOLO-v3	SOtsu	FasterRCNN	YOLO-v3	SOtsu	FasterRCNN	YOLO-v3	SOtsu	FasterRCNN	YOLO-v3
1	1	0	1	0	1	0	0.89	0.89	0	0.85	0.73	0.67	0.87	0.80	0
2	1	1	1	0.25	1	0.40	1	1	1	0.91	0.71	0.50	0.96	0.83	0.67
3	1	1	1	0.17	1	0.29	0.73	0.91	1	0.80	1	0.44	0.76	0.95	0.61
4	1	1	1	0.33	1	0.50	0.89	1	0	0.94	1	0	0.91	1	0
5	1	0	1	0	1	0	0.94	1	0	1	0.89	0.57	0.97	0.94	0
6	1	1	1	0.13	1	0.22	1	1	1	0.96	0.95	0.64	0.98	0.98	0.78
7	1	1	0.88	0.63	0.93	0.77	0.92	1	1	0.94	1	0.63	0.93	1	0.77
8	1	1	1	0.50	1	0.67	0.79	1	1	0.83	1	1	0.81	1	1
9	1	1	1	0.50	1	0.67	0.96	1	1	1	1	0.71	0.98	1	0.83
10	1	0	1	0	1	0	0.97	1	0	1	1	0.82	0.98	1	0
11	1	1	1	0.60	1	0.75	0.96	1	1	0.95	1	1	0.95	1	1
12	1	0	1	0	1	0	0.93	1	0	0.96	0.33	0	0.94	0.50	0
13	1	0	0.80	0	0.89	0	0.84	1	0	0.78	1	0.60	0.81	1	0
14	1	1	1	0.11	1	0.20	0.83	1	1	0.96	1	0.89	0.89	1	0.94
15	1	0	1	0	1	0	1	1	0	0.94	1	1	0.97	1	0
16	1	1	1	0.25	1	0.40	0.97	1	1	0.88	1	0.67	0.92	1	0.80
17	1	1	1	0.25	1	0.40	0.94	1	1	1.03	1	1	0.98	1	1
18	1	0	1	0	1	0	0.97	1	0	1.03	1	0.54	1	1	0
19	1	0	1	0	1	0	0.93	1	0	0.96	1	0.78	0.94	1	0
20	1	0	0.75	0	0.86	0	0.95	1	0	0.92	1	0.75	0.94	1	0
平均值 Average	1	0.50	0.97	0.19	0.98	0.26	0.92	0.99	0.50	0.93	0.93	0.66	0.93	0.95	0.42

注：串联大津法基于图像灰度值进行分割，因颖花内外颖与绿色水稻叶片颜色相近，未用串联大津法对颖花内外颖进行检测实验。

Note: SOtsu is based on the image gray values for segmentation, because the color of the spikelet hull is similar to that of green rice leaves, SOtsu was not used to detect the spikelet hull in this study.

2.3.2 图像识别与人工识别相关性分析

用 Origin 软件对 227 张可见光图像分别针对三种算法及两种开花特征进行手动计数与自动计数相关性回归统计，统计结果如图 14 所示。FasterRCNN 算法识别开放颖花内外颖存在大量重叠样本，与人工识别具有高度一致性，r 高达 0.993，数据拟合曲线斜率为 0.992，截距为 0.01。相比之下，FasterRCNN 算法识别花药 r 为 0.973，拟合曲线斜率为 0.957，截距为 0.329，与人工识别具有较高一致性，但拟合效果比识别开放颖花内外颖差，有低估花药数量的迹象。

同样，SOtsu 自动计数也低估了花药数量，r 为 0.936，拟合曲线斜率为 0.875，截距为 2.795。

YOLO-v3 相比其他两种算法，在花药与开放颖花内外颖识别上均无优势，与人工识别几乎没有相关性，该算法不适用于检测水稻颖花开花状态。

2.4 算法鲁棒性

为保证算法鲁棒性，使深度学习算法模型适用于不同环境，不同光线强度以及不同大小目标的识别，该研究训练集融合了不同光线强度与不同成像距离的图像。由于颖花一般于北京时间 10:00－12:00，温度为 24～35 ℃，相对湿度为 70%～90%时开花。

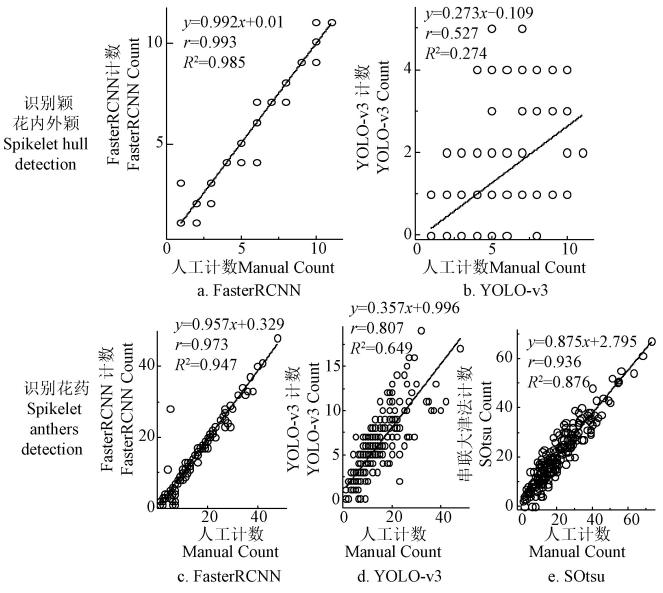

注（Note）：P<0.01。

图 14 图像识别结果与人工识别结果的相关性分析

Fig.14 Correlation analysis of image and manual recognition results

颖花开花时一般天气情况较好，但有云朵遮盖时，采集的水稻颖花图像光照强度比无云朵遮盖时弱，阳光直射情况下，由于水稻颖花间交叠遮挡，同一株水稻会出现光照不均匀情况。故将图像在不同外界光条件下，定性分成三类，分别是低光照强度、高光照强度与光线不均匀。低光照强度、高光照强度与光线不均匀情况下三种算法对花药的识别效果，如图 15 和表 4 所示，在低光照强度条件下，SOtsu 识别效果优于其他两个算法，精度为 0.96，略低于 FasterRCNN，但召回率与 F_1 系数均高于其他两个算法。

在高光照强度下，SOtsu 识别效果与低光照强度下的识别效果接近，略逊色于 FasterRCNN 算法，这说明 SOtsu 不受光照强度变化的制约，可以随着光照强度的改变自动调节阈值大小，也更倾向于在光照强度较低情况下分割前景与背景。

光线不均匀情况下，SOtsu 识别花药的精度、召回率、F_1 系数都低于 0.8，识别效果明显不如 FasterRCNN 算法。光线不均匀会导致同一幅图像中的花药或颖花内外颖呈现不同的灰度值，而 SOtsu 只能计算出规定区域中的单个阈值，所以光线不均匀的情况下，过度曝光的地方会被错误地识别为花药，而暗区域的花药则被归类为背景。



注：对于 SOtsu，黑色像素点为已识别花药。FasterRCNN 和 YOLO-v3 识别结果通过方框表示，并在方框上方显示结果置信度，下同。
Note: For SOtsu, black pixels are identified spikelet anthers. The detection results of FasterRCNN and YOLO-v3 are represented by boxes, and the confidence coefficients of results are displayed above boxes, the same as below.

图 15　低光照强度、高光照强度与光线不均匀条件下三种算法对花药的识别效果

Fig.15　Detection effects of spikelet anthers by three algorithms under the conditions of low light intensities , high light intensities and uneven light

表 4　不同环境下三种算法识别花药结果

Table 4　Results of the three algorithms of spikelet anthers detection in different environments

评估指标 Evaluation indicators	低光照强度 Low light intensity			高光照强度 High light intensity			光线不均匀 Uneven light		
	SOtsu	FasterRCNN	YOLO-v3	SOtsu	FasterRCNN	YOLO-v3	SOtsu	FasterRCNN	YOLO-v3
精确率 Precision	0.96	1	1	1	1	1	0.76	1	1
召回率 Recall	1	0.88	0.59	0.90	1	0.21	0.68	0.90	0.30
F_1 系数 F_1-measure	0.98	0.94	0.74	0.95	1	0.35	0.72	0.95	0.46

SOtsu 识别花药在光线均匀情况下取得了良好的分割效果，该方法或可结合语义分割用于花药的自动添加标签中，基于像素点进行分割，作为语义分割模型的数据集标注图。

如图 16 所示，当图像中的背景是天空或者其他同样呈现白色的物体时，SOtsu 会因背景干扰而无法正确识别花药。FasterRCNN 在白色背景以及光线不均匀下仍能准确识别花药，不受光照强度及不均匀光线的干扰，表现出了极强的鲁棒性。

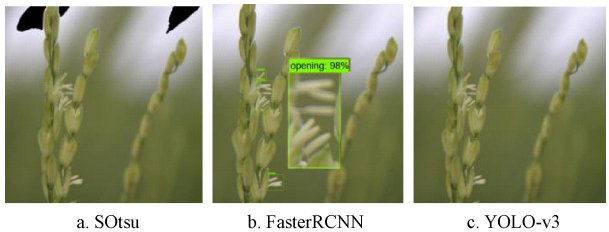

图 16　白色背景下三种算法对花药的识别效果

Fig.16　Detection effects of spikelet anthers under white background by three algorithms

图 17 为低光照强度、高光照强度与光线不均匀情况下 YOLO-v3 与 FasterRCNN 对颖花内外颖的量化识别结果，统计结果见表 5。

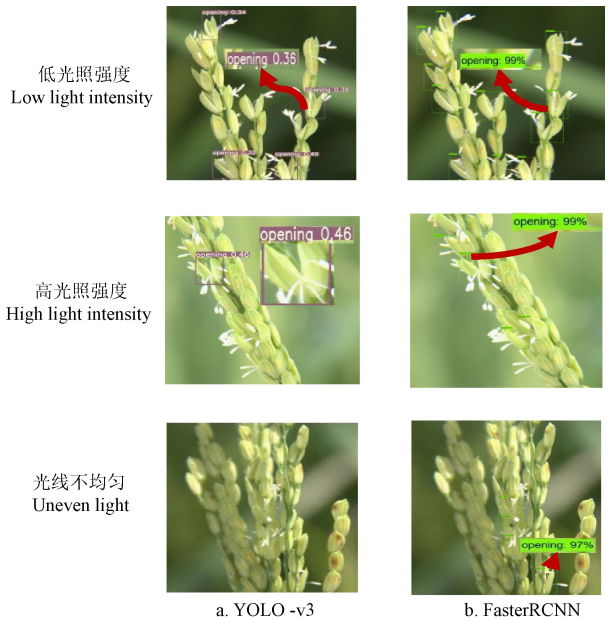

图 17　低光照强度、高光照强度与光线不均匀条件下两种算法颖花内外颖的检测结果

Fig.17　Detection results of spikelet hull by two algorithms under the conditions of low light, high light intensity and uneven light

表 5 不同环境下两种算法识别颖花内外颖结果

Table 5 Results of the two algorithms of spikelet hull detection in different environments

评估指标 Evaluation indicators	低光照强度 Low light intensity		高光照强度 High light intensity		光线不均匀 Uneven light	
	FasterRCNN	YOLO-v3	FasterRCNN	YOLO-v3	FasterRCNN	YOLO-v3
精确率 Precision	1	1	1	1	1	0
召回率 Recall	1	0.36	1	0.25	1	0
F_1 系数 F_1-measure	1	0.53	1	0.40	1	0

如表 5 所示，FasterRCNN 算法在不同强度的光照条件以及光照不均匀情况下在低光照强度条件下对颖花内外颖的识别精度、召回率、F_1 系数均为 1，识别效果均优于 YOLO-v3 算法。明显地，FasterRCNN 算法对颖花内外颖的识别上鲁棒性较强。

2.5 已凋谢（裂药散粉）花药识别效果

当天张开的颖花，会马上吐出花药，吐出的花药在 3～5 min 裂开散出花粉，散出花粉后，花药当天凋谢，凋谢的花药仍挂在稻穗上。识别颖花开花是为了给后续水稻制种授粉决策提供参考信息，凋谢花药不具备花粉，无识别意义。在对花药识别过程中，需避免错误地识别已凋谢花药。由 2.3.2 节可知 YOLO-v3 与 SOtsu 和 FasterRCNN 相比，不适用于水稻颖花开花状态的检测，故只用 SOtsu 和 FasterRCNN 做了对已调谢颖花花药的检测试验。

如图 18 所示，凋谢花药呈淡黄色，与新开放花药在颜色上有明显区别，形状上几乎无差别，但明显区别于开放颖花内外颖的形状与颜色。图 18 中稻穗上黑色部分为已识别到的当天开放的花药，SOtsu 提取花药恰好能完美避开已凋谢花药，而 FasterRCNN 算法识别花药会出现将已凋谢花药错误识别的现象。相比之下，FasterRCNN 算法识别开放颖花内外颖则无此类干扰。故 FasterRCNN 算法在水稻颖花开花状态检测中，可识别开放颖花内外颖进一步判断颖花的开花状态。

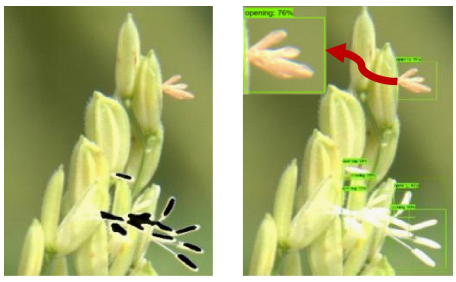

a. SOtsu b. FasterRCNN

图 18 两种算法对已凋谢颖花花药检测效果

Fig.18 Detection effects of two algorithms on withered spikelet anthers

综上所述，FasterRCNN 算法不受光线影响，算法鲁棒性强，但该算法在识别已凋谢花药上还需进一步优化。FasterRCNN 识别前期需要采集一定数量图像样本，人工添加标签，训练识别模型。串联大津法无需做前期工作准备，可直接进行花药识别。故串联大津法适合前期样本数据库无足够样本情况下，代替 FasterRCNN 算法进行水稻颖花开花状态的检测，直到 FasterRCNN 检测模型前期准备工作完成投入检测。

3 结 论

该研究探讨了检测水稻开花张开颖花内外颖和吐出颖花花药两种特征在 SOtsu、FasterRCNN 与 YOLO-v3 三种算法上的实现效果。首次将开放颖花内外颖作为特征运用于水稻颖花开花状态检测，取得了较好识别效果，具有与人工识别较高的一致性。

该研究中，串联大津法与 FasterRCNN 算法适用于检测水稻颖花开花状态，且张开颖花内外颖作为颖花开花特征应用于深度学习检测中效果比花药好。串联大津法识别花药精确率、召回率与 F_1 系数均达到 0.92 以上，与人工识别间的相关性达 0.936，在光线均匀情况下取得了良好分割效果，且能避开对已凋谢花药的识别。FasterRCNN 识别花药精确率为 0.99，召回率为 0.93，F_1 系数为 0.95，与人工识别的相关性达 0.973；FasterRCNN 识别张开的颖花内外颖精确率为 1，召回率为 0.97，F_1 系数为 0.98，与人工识别的皮尔逊相关系数高达 0.993，说明 FasterRCNN 检测颖花开花状态具有与人工观察高度的一致性，可以代替人工观察，检测水稻颖花开花状态，且不同环境条件下鲁棒性强。YOLO-v3 算法对颖花内外颖与花药的识别效果与 SOtsu 和 FasterRCNN 相比较差。

与深度学习算法需要做大量前期工作相较，串联大津法无需进行模型训练准备，可在深度学习算法做前期准备工作时代替进行水稻颖花开花状态检测。

该研究面向杂交水稻制种授粉、农场无人化作业的需求，基于可见光图像对水稻颖花开花状态检测进行了有益尝试。在研究过程中对影像识别结果的因素进行了减少与控制。该研究使用可见光相机进行数据采集，有助于基于串联大津法进行图像分割，虽然分割结果进行了形态学开运算处理，但对于交叠、重合的颖花花药识别具有一定局限性。

后续研究可基于该研究所提出的检测流程进一步研究在无人为干预下，自动获取田间颖花图像，自动添加标签，自动训练模型以及自动切换检测算法，实现水稻颖花开花状态检测全程智能化，并对高通量检测方法进行更深入地探索。

[参 考 文 献]

[1] 张彬，芮雯奕，郑建初，等. 水稻开花期花粉活力和结实率对高温的响应特征[J]. 作物学报，2007，33(7)：1177-1181.
Zhang Bin, Rui Wenyi, Zheng Jianchu, et al. Response characteristics of pollen activity and seed setting rate to high

temperature in rice at anrescence stage[J]. Acta Agronomica Sinica, 2007, 33(7): 1177-1181. (in Chinese with English abstract)

[2] 刘建刚，赵春江，杨贵军，等. 无人机遥感解析田间作物表型信息研究进展[J]. 农业工程学报，2016，32(24)：98-106.
Liu Jiangang, Zhao Chunjiang, Yang Guijun, et al. Review of field-based phenotyping by unmanned aerial vehicle remote sensing platform[J]. Transactions of the Chinese Society of Agricultural Engineering (Transactions of the CSAE), 2016, 32(24): 98-106. (in Chinese with English abstract)

[3] Earl R, Wheeler P N, Blackmore B S, et al. Precision farming the management of variability[J]. Landwards, 1996, 51: 418-423.

[4] Bendig J, Yu K, Aasen H, et al. Combining UAV-based plant height from crop surface models, visible, and near infrared vegetation indices for biomass monitoring in barley[J]. International Journal of Applied Earth Observation and Geoinformation, 2015, 39: 79-87.

[5] Otsu N. A threshold selection method from gray-level histograms[J]. IEEE Transactions on Systems, Man, and Cybernetics, 1979, 9(1): 62-66.

[6] Payne A B, Walsh K B, Subedi P P, et al. Estimation of mango crop yield using image analysis-segmentation method[J]. Computers and Electronics in Agriculture, 2013, 91: 57-64.

[7] Cointault F, Guerin D, Guillemin J P, et al. In field *Triticum aestivum* ear counting using colour texture image analysis[J]. New Zealand Journal of Crop and Horticultural Science, 2008, 36(2): 117-130.

[8] Zhang D, Mansaray L R, Jin H, et al. A universal estimation model of fractional vegetation cover for different crops based on time series digital photographs[J]. Computers and Electronics in Agriculture, 2018, 151: 93-103.

[9] Zhu Y, Cao Z, Lu H, et al. In field automatic observation of wheat heading stage using computer vision[J]. Biosystems Engineering, 2016, 143: 28-41.

[10] Arroyo J, Guijarro M, Pajares G. An instance-based learning approach for thresholding in crop images under different outdoor conditions[J]. Computers and Electronics in Agriculture, 2016, 127: 669-679.

[11] Fernandez-Gallego J A, Kefauver S C, Gutiérrez N A, et al. Wheat ear counting in-field conditions: High throughput and low-cost approach using RGB images[J]. Plant Methods, 2018, 14(1): 1-12.

[12] Fernandez-Gallego J A, Buchaillot M L, Gracia-Romero A, et al. Cereal crop ear counting in field conditions using zenithal RGB images[J]. Journal of Visualized Experiments, 2019 , 144: e58695.

[13] Guo W, Fukatsu T, Ninomiya S. Automated characterization of flowering dynamics in rice using field-acquired time-series RGB images[J]. Plant Methods, 2015, 11(1): 1-15.

[14] Sadeghi-Tehran P, Virlet N, Ampe E M, et al. DeepCount: in-field automatic quantification of wheat spikes using simple linear iterative clustering and deep convolutional neural networks[J]. Frontiers in Plant Science, 2019, 10: 1176.

[15] Alkhudaydi T, Reynolds D, Griffiths S, et al. An exploration of deep-learning based phenotypic analysis to detect spike regions in field conditions for UK bread wheat[J]. Plant Phenomics, 2019, 2019: 7368761.

[16] Hasan M M, Chopin J P, Laga H, et al. Detection and analysis of wheat spikes using convolutional neural networks[J]. Plant Methods, 2018, 14(1): 1-13.

[17] Xiong X, Duan L, Liu L, et al. Panicle-SEG: A robust image segmentation method for rice panicles in the field based on deep learning and superpixel optimization[J]. Plant Methods, 2017, 13(1): 1-15.

[18] Hinton G E, Osindero S, Teh Y W. A fast learning algorithm for deep belief nets[J]. Neural Computation, 2006, 18(7): 1527-1554.

[19] 王忠，顾蕴洁，高煜珠. 水稻开颖机理的探讨：Ⅲ. 浆片的结构及其在开颖过程中内含物的变化[J]. 作物学报，1991，17(2)：96-101.
Wang Zhong, Gu Yunjie, Gao Yuzhu. Mechanism of rice glume opening: Ⅲ. Lodicule structure and the change of the inclusions in the process of glume opening[J]. Acta Agronomica Sinica, 1991, 17(2): 96-101. (in Chinese with English abstract)

[20] Guijarro M, Pajares G, Riomoros I, et al. Automatic segmentation of relevant textures in agricultural images[J]. Computers and Electronics in Agriculture, 2011, 75(1): 75-83.

[21] Meyer G E, Neto J C. Verification of color vegetation indices for automated crop imaging applications[J]. Computers and Electronics in Agriculture, 2008, 63(2): 282-293.

[22] Ren S, He K, Girshick R, et al. Faster R-CNN: Towards real-time object detection with region proposal networks[J]. IEEE Transactions on Pattern Analysis and Machine Intelligence, 2017, 39: 1137-1149.

[23] Redmon J, Divvala S, Girshick R, et al. You only look once: Unified, real-time object detection[C]//Proceedings of the IEEE Conference on Computer Vision and Pattern Recognition, 2016: 779-788.

[24] 周晓彦，王珂，李凌燕. 基于深度学习的目标检测算法综述[J]. 电子测量技术，2017，40(11)：89-93.
Zhou Xiaoyan, Wang Ke, Li Lingyan. A review of target detection algoriths based on deep learning[J]. Electronic Measurement Technology, 2017, 40(11): 89-93. (in Chinese with English abstract)

[25] 赵德安，吴任迪，刘晓洋，等. 基于 YOLO 深度卷积神经网络的复杂背景下机器人采摘苹果定位[J]. 农业工程学报，2019，35(3)：164-173.
Zhao De'an, Wu Rendi, Liu Xiaoyang, et al. Robotic apple picking localization in complex background based on YOLO deep convolutional neural network[J]. Transactions of the Chinese Society of Agricultural Engineering (Transactions of the CSAE), 2019, 35(3): 164-173. (in Chinese with English abstract)

[26] 薛月菊，黄宁，涂淑琴，等. 未成熟芒果的改进 YOLOv2 识别方法[J]. 农业工程学报，2018，34(7)：173-179.
Xue Yueju, Huang Ning, Tu Shuqin, et al. An improved YOLOv2 identification method for immature mango[J]. Transactions of the Chinese Society of Agricultural Engineering (Transactions of the CSAE), 2018, 34(7): 173-179. (in Chinese with English abstract)

[27] 郑志强，刘妍妍，潘长城，等. 改进 YOLO V3 遥感图像飞机识别应用[J]. 电光与控制，2019，26(4)：28-32.
Zheng Zhiqiang, Liu Yanyan, Pan Changcheng, et al. Application of Improved YOLO V3 in aircraft recognition of remote sensing images[J]. Electronics Optics & Control, 2019, 26(4): 28-32. (in Chinese with English abstract)
[28] Redmon J, Farhadi A. Yolov3: An incremental improvement[DB/OL]. 2018, arXiv, 2018. [2013-04-08]. http://wwww.arXiv.org/abs/1804.02767.
[29] Liu W, Anguelov D, Erhan D, et al. SSD: Single shot multibox detector[C]//European Conference on Computer Vision. Springer, 2016: 21-37.
[30] He K, Zhang X, Ren S, et al. Deep residual learning for image recognition[C]//Proceedings of the IEEE Conference on Computer Vision and Pattern Recognition, 2016: 770-778.
[31] Redmon J, Farhadi A. YOLO9000: Better, faster, stronger[C]// Proceedings of the IEEE Conference on Computer Vision and Pattern Recognition, 2017: 7263-7271.
[32] Bochkovskiy A, Wang C Y, Liao H Y M. YOLOv4: Optimal speed and accuracy of object detection[DB/OL]. arXiv, 2020. [2020-04-23]. http://www.arXiv.org/abs/2004.10934.
[33] Everingham M, Van Gool L, Williams C K I, et al. The pascal visual object classes (voc) challenge[J]. International Journal of Computer Vision, 2010, 88(2): 303-338.
[34] GitHub.FasterRCNN.[EB/OL]. (2016-6-18) [2021-05-16]. https://github.com/bubbliiiing/faster-rcnn-pytorch.
[35] GitHub.Yolo3-pytorch.[EB/OL]. (2019-1-18) [2021-05-16]. https://github.com/bubbliiiing/yolo3-pytorch.

Method for detecting rice flowering spikelets using visible light images

Zhang Yali[1,2], Xiao Wenwei[1,2], Lu Xiaoyang[1,2], Liu Aimin[3], Qi Yuan[1,2], Liu Hanchao[1,2], Shi Zekun[4], Lan Yubin[2,5,6※]

(1. *College of Engineering, South China Agricultural University*, *Guangzhou* 510642, *China*; 2. *National Center for International Collaboration Research on Precision Agricultural Aviation Pesticides Spraying Technology*, *Guangzhou* 510642, *China*; 3. *Yuan Longping Agricultural High-tech Co., Ltd., Changsha* 410125, *China*; 4. *College of Plant Protection*, *Hainan University*, *Haikou* 570228, *China*; 5. *College of Electronic Engineering*, *South China Agricultural University*, *Guangzhou* 510642, *China*; 6. *College of Artificial Intelligence, South China Agricultural University, Guangzhou* 510642, *China*)

Abstract: Rice flowering spikelets bloom generally at 10:00-12:00, especially when the temperature is 24-35 ℃ and the relative humidity is 70%-90%. Therefore, the flowering time is necessary to be accurately determined for the timely pollination in the production of hybrid rice seed. In this study, the images were captured by a visible light camera at two flowering characteristics, including the opening of spikelet hull, and the emesis of spikelet anthers. Series Otsu (SOtsu) was applied in tandem to extract the spikelet anthers through the visible light blue channel. An attempt was made to detect the flowering status of rice glumes using visible images, in order to meet the needs of hybrid rice seed pollination. A Canon single-lens reflex (SLR) camera was adopted for data acquisition, which was a benefit to segment the image using the tandem SOtsu. Deep learning models, such as FasterRCNN and YOLO-v3, were used to identify the spikelet anthers and the opening spikelet hull. The most suitable method was selected for flowering characteristics detection to compare the precision, recall, and the F1 coefficient of different models. Two datasets of visible light images were set for spikelets (15 cm and 45 cm imaging distance), each of which used two characteristics. A labeling software was applied to label the category and position of images. As such, a sample database was established for the training of detection models with deep learning. The performance of three models, including SOtsu, FasterRCNN, and YOLO-v3, were evaluated, where the detection was verified from multiple angles. The experiment was also conducted for the model robustness as well. The maximum inter-class variance was utilized in the SOtsu to separate the foreground (rice) from the background using the grayscale image of B-channel, where the grayscale of the background was set to be zero. An analysis was then made for the maximum inter-class variance that applied independently in the pixel range of extracted region, and then the spikelet anthers were further separated from the spikelets hull. The original gray values of spikelet anthers were retained, while the gray values of spikelet hull were set to be zero. Finally, the extraction was evaluated to combine with original images and the number of connected areas that were calculated by the eight-connected output as well. The results showed that the precision, recall rate, F1 coefficient and Pearson correlation coefficient of FasterRCNN model in spikelet hull detection were 1, 0.97, 0.98, and 0.993, respectively, while those of SOtsu in spikelet anthers detection were 0.92, 0.93, 0.93, and 0.936, respectively. It inferred that the SOtsu and FasterRCNN models were both capable of rice flowering detection, but the opening spikelet hull was more suitable than the spikelet anthers for the rice flowering features detection with deep learning model. The model robustness indicated that the highest stability was achieved in the FasterRCNN model to identify the spikelet flowering status with high precision under low, high and uneven light conditions. In addition, the spikelet anthers that opened on the same day split and pollened in 3-5 min, and withered on the same day. There was no recognition significance in the withered spikelet anthers without pollen. It was also necessary to verify the classification ability of detection for the withered anthers, in order to avoid the wrong identification of withered anthers. The SOtsu performed well in the image segmentation using the gray value for the withered spikelets anthers. The SOtsu was also better than FasterRCNN in the identification of withered spikelets. Correspondingly, the SOtsu was expected to replace the FasterRCNN model for the flowering spikelet before the completion of model construction, in order to ensure the detection continuity of rice flowering spikelet. The influencing factors of recognition were reduced to control the process of detection. Since the segmentation was processed for morphological opening operations, there was also some limitation in the recognition of overlapping anthers. A further study can be followed by a more in-depth exploration of high-throughput detection.

Keywords: image recognition; object recognition; rice; spikelet; spikelet hull; spikelet anther; series Otsu; deep learning

张亚莉, 高启超, 邓继忠, 等. M45 型多旋翼植保无人机减量施药对稻飞虱防治效果的影响 [J]. 华南农业大学学报, 2021, 42(6): 36-42.
ZHANG Yali, GAO Qichao, DENG Jizhong, et al. Effects of reduced pesticide application on rice planthopper control by M45 multi-rotor plant protection UAV[J]. Journal of South China Agricultural University, 2021, 42(6): 36-42.

M45 型多旋翼植保无人机减量施药对稻飞虱防治效果的影响

张亚莉[1,2], 高启超[1,2], 邓继忠[1,2], 陈鹏超[2,3], 黄晓宇[2,3], 林芳源[4], 曾　文[1,2], 贾瑞昌[1,2]
(1 华南农业大学 工程学院, 广东 广州 510642; 2 国家精准农业航空施药技术国际联合研究中心, 广东 广州 510642; 3 华南农业大学 电子工程学院/人工智能学院, 广东 广州 510642; 4 广东省江门市新会区农业农村局, 广东 江门 529100)

摘要:【目的】研究多旋翼植保无人机减量施药对雾滴沉积效果以及稻飞虱防治效果的影响, 促进水稻减量施药技术发展。【方法】采用 M45 多旋翼植保无人机开展水稻施药田间试验, 选取 15.0 和 22.5 L/hm^2 的施药液量, 以及人工施药推荐剂量 100%、90%、80% 的 3 种减量农药剂量, 研究不同施药液量和减量农药剂量对雾滴沉积效果以及稻飞虱防治效果的影响。【结果】水稻冠层上部的雾滴沉积量明显优于冠层下部, 2 种施药液量以及 3 种减量农药剂量对雾滴沉积量的影响不显著; 施药 1 周后稻飞虱数量显著减少。在相同施药液量条件下, 减量农药剂量的变化对稻飞虱防治效果影响不明显。80% 的农药剂量能满足稻飞虱防治要求。【结论】无人机水稻施药作业中可选择 80% 的农药剂量进行减量施药。本研究可为水稻减量施药、减少水稻植保作业成本提供有益参考。

关键词: 植保无人机; 减量施药; 雾滴沉积; 稻飞虱; 防治效果
中图分类号: S252　　**文献标志码:** A　　**文章编号:** 1001-411X(2021)06-0036-07

Effects of reduced pesticide application on rice planthopper control by M45 multi-rotor plant protection UAV

ZHANG Yali[1,2], GAO Qichao[1,2], DENG Jizhong[1,2], CHEN Pengchao[2,3], HUANG Xiaoyu[2,3], LIN Fangyuan[4], ZENG Wen[1,2], JIA Ruichang[1,2]
(1 College of Engineering, South China Agricultural University, Guangzhou 510642, China; 2 National Center for International Joint Research on Precision Agriculture Aviation Pesticides Spraying Technology, Guangzhou 510642, China; 3 College of Electronic Engineering/College of Artificial intelligence, South China Agricultural University, Guangzhou 510642, China; 4 Agricultural and Rural Bureau of Xinhui District, Jiangmen City, Guangdong Province, Jiangmen 529100, China)

Abstract: 【Objective】In order to explore the effect of reduced pesticide application on the control effect of rice planthopper by multi-rotor plant protection UAV and promote the development of reduced pesticide application technique for rice.【Method】Field experiment was carried out using an M45 multi-rotor plant protection UAV for rice pesticides application. We used two spray volumes of 15.0 and 22.5 L/hm^2, and three

收稿日期:2021–01–27　　**网络首发时间:**2021–09–26 08:49:01
网络首发地址:https://kns.cnki.net/kcms/detail/44.1110.S.20210924.1621.002.html
作者简介:张亚莉 (1975—), 女, 副教授, 博士, E-mail: ylzhang@scau.edu.cn; 通信作者: 曾　文 (1975—), 男, 讲师, 博士, E-mail: zengwen@scau.edu.cn; 贾瑞昌 (1975—), 男, 讲师, 博士, E-mail: rcjia@scau.edu.cn
基金项目:广东省重点领域研发计划 (2019B020221001); 广东省科技计划 (2018A050506073); 广东省现代农业产业共性关键技术研发创新团队项目 (2020KJ133); 国家重点研发计划 (2018YFD0200304)

pesticide dosages of 100%, 90%, and 80% of the conventional artificial control dosage. The effect of different spray volume and reduced dosage on the droplet deposition and the control of rice planthopper were analyzed. 【Result】The droplet deposition in the upper part of the rice canopy was significantly higher than that in the lower part of the canopy. The differences of two spray volumes and three dosages on the droplet deposition were not significant. At the same time, the number of rice planthopper decreased significantly after one week of treatment. Under the condition of the same spray volume, the effect of reduced dosage on the control effect of rice planthopper was not significant. Rice spray dosage of 80% of manual application met the requirement of rice planthopper control.【Conclusion】The spray dosage of 80% can be considered as feasible dosage in the UAV application for rice. The results provide useful reference for promoting the reductions of pesticide application for rice and the operating cost of rice plant protection.

Key words: plant protection UAV; reduced pesticide application; droplet deposition; rice planthopper; control effect

作为我国主要的粮食作物，2019 年国内水稻种植面积达到了 0.3 亿 hm^2[1]，广东省水稻种植面积已达 179 万 hm^2[2]。水稻是病虫害种类最多和危害程度最高的农作物之一，广东省水稻种植区水稻纹枯病、稻纵卷叶螟、稻飞虱均达中等偏重程度[3-4]。近年来，由于效率高、作业不受地形限制、节水节药等优势，植保无人机施药技术在水稻病虫草害的防治上发展迅速[5-9]。

植保无人机应用于水稻施药已开展大量研究。薛新宇等[10] 对 N-3 型无人直升机喷施药剂防治稻飞虱和稻纵卷叶螟的效果进行了研究。Qin 等[11] 研究了无人机的喷雾高度和速度等作业参数对水稻冠层上雾滴沉积和对稻飞虱的防治效果的影响。陈盛德等[12] 通过不同的飞行高度、飞行速度研究了不同喷雾作业参数对水稻冠层的雾滴沉积分布的影响。漆海霞等[13] 采用 5 款植保无人机进行稻田雾滴沉积分布试验研究。张海艳等[14] 测试并对比了电动单旋翼和电动多旋翼植保无人机在水稻田间的喷施作业效果。Chen 等[15] 在水稻抽穗扬花期和分蘖期比较了不同喷嘴对稻飞虱防治和雾滴沉积效果的影响。然而现有研究多从机型、喷头、飞行参数等方面对雾滴沉积分布规律进行分析，植保无人机不同施药液量和不同施药剂量对水稻病虫害防治效果的影响研究较少。

为了促进减量施药技术在水稻生产中的研究和应用，本研究以 M45 多旋翼植保无人机为施药载体开展了水稻航空喷雾试验，探索不同施药液量和农药剂量在水稻不同冠层的雾滴沉积规律，以及不同农药剂量对稻飞虱的防治效果，以期为植保无人机农药减施增效提供数据参考。

1　材料与方法

1.1　试验机型与试验地点

喷雾试验机型采用 M45 多旋翼植保无人机 (深圳高科新农技术有限公司，深圳)，机身为三角形设计，并搭配压力式喷头，其空机质量达到 27 kg，载荷质量为 20 kg，飞行速度为 0~6 m/s，喷洒宽度为 6~8 m，飞行高度为 2~5 m，整机喷雾量为 1.8~2.6 L/min。无人机作业如图 1 所示。



图 1　M45 多旋翼植保无人机
Fig. 1　M45 multi rotor plant protection UAV

试验地点位于广东省江门市新会区三江镇 (22°27′36″N，113°08′24″E)，具体位置如图 2 所示。试验田晚稻采用撒播方式播种，施药试验时间为晚稻分蘖末期，晚稻平均高度为 0.7~0.9 m。

1.2　气象数据

地面最大风速为 2.6 m/s，平均气温 20 ℃，平均湿度为 53.6%，大气压强为 101.5 kPa，满足《植保无人飞机防治水稻病虫害施药指南》的作业要求[16]。

1.3　试验试剂与材料

铜版纸 (长 8 cm，宽 3 cm)、诱惑红 (ALLURA

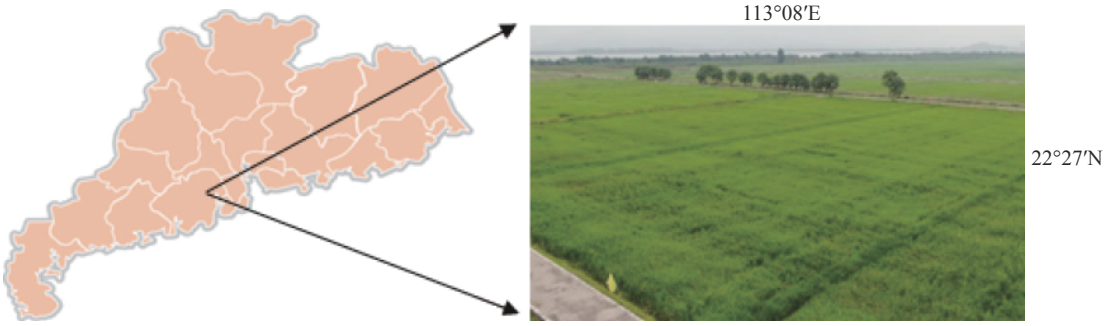

图 2 试验田位置

Fig. 2 Location of test field

RED) 试剂、金龟子绿僵菌 *Metarhizium anisopliae* 油悬浮剂 (有效成分总含量是 8×10^9 mL^{-1}[17])、万向夹、塑料杆、米尺、橡胶手套、自封袋、信封、Kestrel NK-3500 气象风速仪、HP Scanjet 200 扫描仪以及雾滴图像分析处理软件。

1.4 试验设计与数据处理

试验采用了 2 种施药液量：15.0 和 22.5 L/hm^2，以及人工施药金龟子绿僵菌推荐剂量的 100%、90%、80% 3 种减量农药剂量，对不同施药液量和减量农药剂量对雾滴沉积效果以及稻飞虱防治效果的影响进行分析，试验设计如表 1 所示。

表 1 试验田施药测试处理区

Table 1 Treatments for pesticide application test in experimental field

处理区 Processing area	施药液量/(L·hm^{-2}) Spray volume	农药剂量/% Pesticide dosage
1	15.0	100
2		90
3		80
4	22.5	100
5		90
6		80

根据试验需求，将试验田划分为 6 个处理区，每隔 20 m 插一面旗子，作为每个小区的边界点，共放置 14 面旗子，每个小区面积约 0.2 hm^2。在试验田附近放置 Kestrel NK-3500 气象风速仪，用来监测地面实时气象信息。

喷洒药剂使用金龟子绿僵菌油悬浮剂进行现场配置，采取喷洒 1 次调配 1 次的原则，严格遵守标准配药步骤，同时为了在铜版纸上显示的雾滴更明显，在试验药剂里添加诱惑红试剂。

为了研究雾滴沉积与稻飞虱防治效果的关系，按照水稻冠层的垂直方向选取上部和下部布置铜版纸，将铜版纸夹在万向夹上，调整铜版纸水平放置，再将万向夹固定在塑料管上插入稻田里，本次试验塑料管的放置位置按照图 3 所示，每个处理区里设置 2 条雾滴采集带，每条雾滴采集带共设有 11 个采样点 (以−5, …, −1, 0, 1, …, 5 标记)，每个采样点间隔 1 m。作业时，保持无人机的飞行高度在水稻冠层以上 1.5 m，飞行速度为 5 m/s。

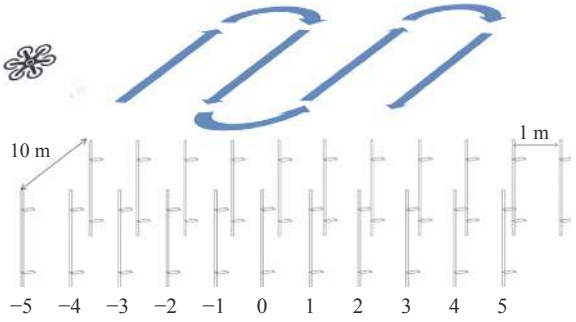

图 3 试验采样点的布置方式以及航线设计

Fig. 3 Layout of test sampling points and route design

本研究进行了 3 次稻飞虱防治效果的田间调查，第 1 次调查为施药前 1 天，第 2 次调查为施药后第 1 天，第 3 次调查为施药后第 7 天。按照《稻飞虱测报调查规范》[18]，在每个处理区内随机选择 30 株水稻，然后采用目测法，观察每株水稻上的稻飞虱数量并记录。根据各处理区施药前后稻飞虱的数量，利用公式[19] 计算虫口减退率和防效。

$$\text{虫口减退率}=\frac{(\text{施药前活虫数}-\text{施药后活虫数})}{\text{施药前活虫数}}\times100\%, \tag{1}$$

$$\text{校正防效}=\frac{(\text{施药区虫口减退率}-\text{对照区虫口减退率})}{(100-\text{对照区虫口减退率})}\times100\%。 \tag{2}$$

当无人机在一个处理区内施药结束后，将铜版纸收好放入自封袋中，然后放入事先编号的信封中，带回实验室处理。使用 HP Scanjet 200 扫描仪，设置图像是灰度、分辨率是 600，将铜版纸扫描下来，然后再通过 DepositScan 图像扫描软件对已扫

描图片进行分析，得到每个采样点的粒径分布、覆盖率、雾滴沉积等信息，同时计算出雾滴分布均匀性，用变异系数 (Coeffecient of variation, CV) 表示，变异系数越小，说明雾滴穿透性越好。数据统计处理在 SPSS23.0 中完成。

2　结果与分析

2.1　不同施药液量的雾滴沉积效果

表 2 为施药液量为 15 L/hm^2 的各采样点的雾滴沉积效果。通过分析雾滴沉积量，可以发现水稻植株上层的雾滴沉积要比水稻植株下层的好，由采样点从左到右，雾滴沉积量呈先增大后减小的趋势，中间的 0 号采样点的水稻植株上层雾滴沉积量最高，为 0.74 μL/cm^2，水稻植株下层最高的是 2 号采样点，为 0.30 μL/cm^2，但差异不显著；雾滴分布均匀性同样呈现先变差后变好的趋势，4 号采样点水稻植株下层的雾滴分布均匀性最佳，为 13.33%；0 号采样点水稻植株下层的雾滴分布均匀性最差，高达 97.02%。

表 2　施药液量为 15.0 L/hm^2 时各采样点的雾滴沉积效果

Table 2　Droplet deposition effect at each sampling point with 15.0 L/hm^2 of spraying solution

采样点 Sampling point	雾滴沉积量[1)]/(μL·cm^{-2}) Droplet deposition		雾滴分布均匀性/% Uniformity of droplet distribution	
	植株上层 Upper level	植株下层 Lower level	植株上层 Upper level	植株下层 Lower level
−5	0.31±0.20a	0.06±0.04ab	30.82	65.66
−4	0.13±0.10a	0.04±0.03a	57.54	69.18
−3	0.17±0.15a	0.12±0.13ab	87.82	78.22
−2	0.49±0.28a	0.07±0.09ab	43.41	36.14
−1	0.46±0.73a	0.19±0.16ab	87.87	73.05
0	0.74±0.54a	0.19±0.18ab	74.67	97.02
1	0.50±0.45a	0.12±0.12ab	75.22	43.33
2	0.35±0.20a	0.30±0.39b	94.39	46.38
3	0.70±1.23a	0.10±0.07ab	44.76	46.84
4	0.15±0.10a	0.14±0.17ab	83.47	13.33
5	0.26±0.24a	0.03±0.03a	60.06	40.02

1) 数据为平均值±标准差；同列数据不同小写字母表示差异显著(P<0.05，Duncan's法)

1) The data are means ± standard deviations; Different lowercase letters in the same column indicate significant differences (P<0.05, Duncan's method)

表 3 为施药液量为 22.5 L/hm^2 的各采样点的雾滴沉积效果。由采样点从左到右，水稻植株上层雾滴沉积量呈一直减小的趋势，其中，−5 号采样点的雾滴沉积量最高，为 0.53 μL/cm^2，水稻植株下层的

表 3　施药液量为 22.5 L/hm^2 时各采样点的雾滴沉积效果

Table 3　Droplet deposition effect at each sampling point with 22.5 L/hm^2 of spraying solution

采样点 Sampling point	雾滴沉积量[1)]/(μL·cm^{-2}) Droplet deposition		雾滴分布均匀性/% Uniformity of droplet distribution	
	植株上层 Upper level	植株下层 Lower level	植株上层 Upper level	植株下层 Lower level
−5	0.53±0.21a	0.17±0.18ab	54.02	75.62
−4	0.34±0.45a	0.05±0.03ab	51.69	69.67
−3	0.43±0.46a	0.06±0.04ab	57.72	86.29
−2	0.30±0.25a	0.09±0.04a	48.14	76.90
−1	0.24±0.32a	0.06±0.04a	81.31	83.63
0	0.34±0.32a	0.08±0.09a	75.92	83.24
1	0.34±0.52a	0.26±0.25b	58.08	86.42
2	0.29±0.25a	0.11±0.10ab	80.20	90.95
3	0.22±0.22a	0.14±0.09ab	94.30	68.42
4	0.34±0.34a	0.23±0.20ab	86.62	95.23
5	0.12±0.08a	0.08±0.05a	89.43	78.26

1) 数据为平均值±标准差；同列数据不同小写字母表示差异显著(P<0.05，Duncan's法)

1) The data are means ± standard deviations; Different lowercase letters in the same column indicate significant differences (P<0.05, Duncan's method)

雾滴沉积量是先增大后减小的趋势，其中，最高的是 1 号采样点，为 0.26 μL/cm^2；水稻植株上层雾滴分布均匀性呈现持续变差的趋势，其中，−2 号采样点的雾滴分布均匀性最佳，为 48.14%，所以该农药剂量的小区内，普遍雾滴分布均匀性较差。

2.2 不同施药液量不同农药剂量的雾滴沉积效果

以雾滴沉积量为基础参数对各施药液量的雾滴沉积效果进行分析评价，结果 (表 4、表 5) 显示，2 个不同施药液量的小区，除了 90% 的农药剂量，其他 2 个农药剂量 22.5 L/hm^2 的小区雾滴沉积量都优于 15.0 L/hm^2 的小区，出现这一现象的原因可能是，在试验时，水稻上方的垂直风场过小，在自然风的影响下，导致雾滴漂移，没有被铜版纸接收到。同时也说明增加施药液量，有助于雾滴沉积，而且水稻植株上层的雾滴均匀性好于水稻植株下层。

表 4 施药液量为 15.0 L/hm^2 时不同农药剂量雾滴沉积量效果试验结果

Table 4 The effect of different pesticide dosages on droplet deposition with 15.0 L/hm^2 of spraying solution

农药剂量/% Pesticide dosage	雾滴沉积量[1]/(μL·cm^{-2}) Droplet deposition		雾滴分布均匀性/% Uniformity of droplet distribution	
	植株上层 Upper level	植株下层 Lower level	植株上层 Upper level	植株下层 Lower level
100	0.377±0.425a	0.122±0.299a	54.02	75.62
90	0.396±0.420a	0.131±0.131a	51.69	69.67
80	0.300±0.345a	0.107±0.112a	57.72	86.29

1) 数据为平均值±标准差；同列数据不同小写字母表示差异显著(P<0.05，Duncan's法)

1) The data are means ± standard deviations; Different lowercase letters in the same column indicate significant differences (P<0.05, Duncan's method)

表 5 施药液量为 22.5 L/hm^2 时不同农药剂量雾滴沉积量效果试验结果

Table 5 The effect of different pesticide dosages on droplet deposition with 22.5 L/hm^2 of spraying solution

农药剂量/% Pesticide dosage	雾滴沉积量[1]/(μL·cm^{-2}) Droplet deposition		雾滴分布均匀性/% Uniformity of droplet distribution	
	植株上层 Upper level	植株下层 Lower level	植株上层 Upper level	植株下层 Lower level
100	0.552±0.547b	0.188±0.181b	54.02	75.62
90	0.188±0.129a	0.097±0.918a	51.69	69.67
80	0.384±0.369ab	0.104±0.070a	57.72	86.29

1) 数据为平均值±标准差；同列数据不同小写字母表示差异显著(P<0.05，Duncan's法)

1) The data are means ± standard deviations; Different lowercase letters in the same column indicate significant differences (P<0.05, Duncan's method)

2.3 稻飞虱防治效果分析

通过对施药前后共计 3 次的稻飞虱数量进行田间调查并分析防治效果，施药后第 1 次调查和第 2 次调查的不同农药剂量以及施药液量对虫口减退率和校正防效如表 6、表 7 所示。

施药后第 1 次调查结果显示，在 22.5 L/hm^2 施药液量、100% 农药剂量下，虫口减退率最高为 38%，其他情况下都集中在 15%~20%，22.5 L/hm^2 施药液量、100% 农药剂量下，校正防效最好 (30%)；施药后第 2 次调查结果显示，在 22.5 L/hm^2 施药液量、100% 农药剂量下，虫口减退率最高为 45%，22.5 L/hm^2 施药液量、100% 农药剂量下，校正防效最好 (53%)。

当施药液量是 15 L/hm^2 时，农药剂量是 100%、90%、80% 的第 2 次调查的虫口减退率分别比第 1 次提高了 8、9 和 10 个百分点，校正防效分别提高了 30、31 和 31 个百分点；当施药液量是 22.5 L/hm^2 时，农药剂量是 100%、90%、80% 的第 2 次调查的虫口减退率分别比第 1 次提高了 7、17 和 13 个百分点，校正防效分别提高了 23、38 和 15 个百分点，明显发现施药后 1 周的防治效果比施药后 1 d 的防治效果好。

在施药液量是 15 L/hm^2 的情况下，农药剂量是 100% 与 80% 的第 2 次虫口退减率相差 3%，在施药液量是 22.5 L/hm^2 时，农药剂量 100% 与 80% 的第 2 次虫口退减率相差 2%，说明农药剂量对稻飞虱的防治效果影响不大。在农药剂量相同的情况下，施药液量多的比施药液量少的防治效果好，跟雾滴沉积量呈正相关关系。

表 6　施药液量为 15.0 L/hm² 时不同农药剂量对稻飞虱的防治效果

Table 6　Different pesticide dosages on the control effect of rice planthopper with 15.0 L/hm² of spraying solution

农药剂量/% Pesticide dosage	施药后第1次调查 The first investigation after application		施药后第2次调查 The second investigation after application	
	虫口减退率/% Decline rate of insect population	校正防效/% Corrected control effect	虫口减退率/% Decline rate of insect population	校正防效/% Corrected control effect
100	16	5	24	35
90	19	8	28	39
80	17	6	27	37

表 7　施药液量为 22.5 L/hm² 时不同农药剂量对稻飞虱的防治效果

Table 7　Different pesticide dosages on the control effect of rice planthopper with 22.5 L/hm² of spraying solution

农药剂量/% Pesticide dosage	施药后第1次调查 The first investigation after application		施药后第2次调查 The second investigation after application	
	虫口减退率/% Decline rate of insect population	校正防效/% Corrected control effect	虫口减退率/% Decline rate of insect population	校正防效/% Corrected control effect
100	38	30	45	53
90	13	2	30	40
80	20	37	43	52

3　结论

以高科新农 M45 多旋翼植保无人机为施药作业平台，在江门新会的水稻试验田进行航空雾滴沉积试验，重点研究了不同施药液量和不同农药剂量在水稻试验田对雾滴沉积量和稻飞虱的防治效果的影响，得出以下结论：

1) 农药剂量相同时，施药液量越大，雾滴沉积效果越好，但是每个小区的雾滴分布不均匀；在施药液量相同时，农药剂量越高，雾滴沉积的效果越好；每个小区明显水稻植株上层的雾滴沉积效果要好于下层。水稻冠层上部的雾滴沉积效果优于下层，主要是由于无人机施药位置高、雾滴小，难以穿透分蘖后期长势茂盛的水稻。

2) 试验结果发现，本研究中的 2 种施药液量、3 种农药剂量以及施药液量和农药剂量的交互作用对雾滴沉积量均没有显著影响。本次试验中设置的参数不能明显地体现其对雾滴沉积量的影响，下次可以把施药参数的间隔增大一些，增加更多组重复试验，减小误差，获得更准确的数据。

3) 100% 农药剂量与 80% 农药剂量对稻飞虱的防治效果没有显著差异，所以可以适当降低金龟子绿僵菌的农药剂量，达到农药减施目的。施药 7 d 后田间调查的稻飞虱防治效果优于施药后第 1 天，经过分析认为，金龟子绿僵菌属于广谱性杀虫真菌，可以让稻飞虱受到致命感染，慢性中毒而死，而施药后 7 d 的调查周期相对较短，导致校正防效不高。在今后的研究工作中可适当延长调查周期，同时其他杀虫剂的减施效果有待进一步研究和分析。

综上所述，本研究使用多旋翼植保无人机减量施药用于防治水稻稻飞虱，防治效果较好，提高了农药利用率，降低了病虫害防治成本，同时对减轻环境污染有利。本研究为促进水稻减量施药研究提供了试验数据参考。由于水稻植株的中下层是稻飞虱集中危害部位，为改善植保无人机减量施药在水稻稻飞虱防治作业上的广泛应用，可从以下 2 个方面进行深入研究：进一步优选多旋翼植保无人机的作业参数，增加施药过程中药液雾滴的穿透性；探索航空静电喷雾等施药技术，增加水稻中下层的雾滴沉积量，提高稻飞虱防治效果。

参考文献：

[1] 中商产业研究院. 2019 年中国粮食种植面积和产量数据分析及 2020 年预测[EB/OL]. (2019-12-06)[2020-12-31]. https://www.askci.com/news/chanye/20191206/1642301155340_2.shtml.

[2] 广东省农业农村厅. 2019 年广东省粮食产销形势分析 [EB/OL]. (2020-02-13)[2020-12-31]. http://dara.gd.gov.cn/cxxsfx/content/post_2894942.html.

[3] 叶延琼, 章家恩, 李逸勉, 等. 1992-2010 年广东省水稻主要病虫害发生动态及防控措施[J]. 湖北农业科学, 2013, 52(15): 3544-3549.

[4] 陈波, 范兵, 陈科海, 等. 基于水稻主要病虫害的发生趋势论种质资源在水稻抗性育种中的应用[J]. 现代农业科技, 2012(3): 234-236.
[5] WANG L, LAN Y, ZHANG Y, et al. Applications and prospects of agricultural unmanned aerial vehicle obstacle avoidance technology in China[J]. Sensors, 2019, 19: 642.
[6] ADITYA S N, PROF S C K. Adoption and utilization of-drones for advanced precision farming: A review[J]. International Journal on Recent and Innovation Trends in Computing and Communication, 2016, 4(5): 563-565.
[7] 李飞, 韩冲冲, 李保同. 阿维菌素无人机喷施的沉积特征及防效研究[J]. 江西农业大学学报, 2019, 41(5): 914-923.
[8] 缪建锟, 齐枫, 杨皓, 等. 植保无人机喷施 30% 肟菌·戊唑醇悬浮剂防治稻瘟病、稻曲病效果评价[J]. 农药, 2020, 59(9): 680-683.
[9] 姚伟祥, 兰玉彬, 郭爽, 等. 赣南山地柑桔园有人驾驶直升机喷雾作业雾滴沉积效果[J]. 中国南方果树, 2020, 49(2): 13-18.
[10] 薛新宇, 秦维彩, 孙竹, 等. N-3 型无人直升机施药方式对稻飞虱和稻纵卷叶螟防治效果的影响[J]. 植物保护学报, 2013, 40(3): 273-278.
[11] QIN W C, QIU B J, XUE X Y, et al. Droplet deposition and control effect of insecticides sprayed with an unmanned aerial vehicle against plant hoppers[J]. Crop Protection, 2016, 85: 79-88. doi: 10.1016/j.cropro.2016.03.018.
[12] 陈盛德, 兰玉彬, 李继宇, 等. 小型无人直升机喷雾参数对杂交水稻冠层雾滴沉积分布的影响[J]. 农业工程学报, 2016, 32(9): 40-46.
[13] 漆海霞, 陈鹏超, 兰玉彬, 等. 不同电动植保无人机稻田雾滴沉积分布试验研究[J]. 农机化研究, 2019, 41(9): 147-151.
[14] 张海艳, 兰玉彬, 文晟, 等. 植保无人机水稻田间农药喷施的作业效果[J]. 华南农业大学学报, 2019, 40(1): 116-124.
[15] CHEN P C, LAN Y B, HUANG X Y, et al. Droplet deposition and control of planthoppers of different nozzles in two-stage rice with a quadrotor unmanned aerial vehicle[J]. Agronomy, 2020, 10(2). doi: 10.3390/agronomy10020303.
[16] 中国农药工业协会. 植保无人飞机防治水稻病虫害施药指南: T/CCPIA020—2019[S]. 北京: 中国农药工业协会, 2019.
[17] 彭国雄, 张淑玲, 夏玉先. 金龟子绿僵菌 CQMa421 农药及应用情况[J]. 中国生物防治学报, 2020, 36(6): 850-857.
[18] 农业部全国农业技术推广服务中心. 稻飞虱测报调查规范: GB/T15794.4—2009[S]. 北京: 中国标准出版社, 2009.
[19] 农业农村部农药检定所. 农药田间药效试验准则: GB/T17980.4—2000[S]. 北京: 中国标准出版社, 2000.

【责任编辑 霍 欢】

欢迎订阅 2022 年《华南农业大学学报》

《华南农业大学学报》是华南农业大学主办的综合性农业科学学术刊物。本刊主要报道农业各学科的科研学术论文、综述等，涵盖动物科学、兽医学、农学、园艺学、土壤肥料、植物保护、生物学、林业科学、农业工程和食品科学等学科。本刊附英文目次和英文摘要。读者对象主要是农业院校师生、农业科研人员和有关部门的专业技术人员。

本刊为《中文核心期刊要目总览》综合性农业科学核心期刊，《中国科学引文数据库 (CSCD)》、《中国科技论文统计源（中国科技核心期刊）》及《中国学术期刊综合评价数据库》等来源期刊，并排列在中国科学引文数据库被引频次最高的中国科技期刊 500 名以内；为《CNKI》《万方数据库》《中国生物学文摘》《化学文摘》《EBSCO》《Scopus》《CABI》《剑桥科学文摘》《动物学记录》《食品科技文摘》《文摘杂志》《日本科学技术振兴机构数据库》等国内外 40 多家数据库（文摘）收录。

双月刊，逢单月上旬出版，A4 幅面。定价 15.00 元/册，全年 90.00 元。自办发行，参加全国非邮发报刊联合征订发行，非邮发代号：6573。国内外公开发行，欢迎订阅！

订阅款邮汇至：300381 天津市卫津南路李七庄邮局 9801 信箱，全国非邮发报刊联合征订服务部。

《华南农业大学学报》编辑部

张亚莉, 莫振杰, 田昊鑫, 等. 基于改进 APF-FMT*的农业机器人路径规划算法 [J]. 华南农业大学学报, 2024, 45(3): 408-415.
ZHANG Yali, MO Zhenjie, TIAN Haoxin, et al. Path planning algorithm of agricultural robot based on improved APF-FMT*[J]. Journal of South China Agricultural University, 2024, 45(3): 408-415.

基于改进 APF-FMT*的农业机器人路径规划算法

张亚莉[1,2]，莫振杰[1]，田昊鑫[1]，兰玉彬[2]，王林琳[3]
(1 华南农业大学 工程学院, 广东 广州 510642； 2 国家精准农业航空施药技术国际联合研究中心, 广东 广州 510642； 3 深圳职业技术大学 人工智能学院, 广东 深圳 518055)

摘要:【目的】解决农业机器人在复杂农业环境下全局路径规划耗时过长、路径最优解求解困难的问题。【方法】提出一种基于改进人工势场法的快速行进树算法 (APF-FMT*)。首先，在引力势场中引入相对距离，根据与目标点的距离改变引力大小，克服了人工势场法距离目标点过远时引力过大的问题；然后，将 FMT*算法与改进人工势场法相结合，采用三阶 B 样条曲线对路径进行平滑处理；最后，建立 3 个农业工作地图进行仿真试验。【结果】仿真结果表明，与 FMT*、RRT*和 Informed-RRT* 3 种算法对比，在地图 Map1 和 Map2 中，APF-FMT*都能快速找到良好的解，且随样本数量增加获得的路径解得到改善，搜索时间比其他 3 种算法减少 45% 以上；在有狭小通道的 Map3 中，APF-FMT*、FMT*搜索时间比 RRT*和 Informed-RRT*减少 75% 以上，并且获得更好的解。【结论】本研究提出的 APF-FMT*算法不仅克服了 FMT*算法冗余探索问题，还有效地解决了人工势场法目标点不可达的问题，提高了农业机器人路径规划效率和作业安全性。

关键词: 路径规划；农业机器人；人工势场法；FMT*算法
中图分类号: TP242.6 **文献标志码:** A **文章编号:** 1001-411X(2024)03-0408-08

Path planning algorithm of agricultural robot based on improved APF-FMT*

ZHANG Yali[1,2], MO Zhenjie[1], TIAN Haoxin[1], LAN Yubin[2], WANG Linlin[3]
(1 College of Engineering, South China Agricultural University, Guangzhou 510642, China; 2 National Center for International Collaboration Research on Precision Agricultural Aviation Pesticide Spraying Technology, Guangzhou 510642, China; 3 School of Artificial Intelligence, Shenzhen Polytechnic University, Shenzhen 518055, China)

Abstract: 【Objective】The study is aimed to address the issue of lengthy global path planning of agricultural robot in complex agricultural environment and the path solution is not optimal.【Method】A fast marching tree algorithm based on an improved artificial potential field method (APF-FMT*) was proposed. Firstly, relative distance was introduced in the gravitational potential field, adjusting the strength of attraction based on the distance from the target point. This overcomed the issue of excessive attraction force in the artificial potential field method when the distance to the target point was too far. The FMT* algorithm was combined with the improved artificial potential field method, and a third order B-spline curve was used to smooth the path. Finally, three agricultural working maps were created for simulation experiments.【Result】APF-FMT* was compared

收稿日期:2023–05–25 **网络首发时间:**2024–03–11 20:38:51
首发网址:https://link.cnki.net/urlid/44.1110.s.20240308.1308.004
作者简介:张亚莉，副教授，博士，主要从事农业航空传感器技术与农产品产地环境监测研究，E-mail: ylzhang@scau.edu.cn；通信作者：王林琳，讲师，博士，主要从事农业航空视觉传感器技术与果园作业障碍物识别研究，E-mail: wanglinlin@szpt.edu.cn
基金项目:岭南现代农业实验室项目 (NT2021009)；高等学校学科创新引智计划 (D18019)；广东省重点领域研发计划 (2019B020221001)；广东省科技计划 (2018A050506073)

with FMT*, RRT*, and Informed-RRT* algorithms. The simulation results demonstrated that in maps Map1 and Map2, APF-FMT* consistently found good solutions quickly, and the path solutions were improved with an increasing number of samples. The search time reduced by over 45% compared with the other three algorithms. In Map3 with narrow channels, the search times of APF-FMT* and FMT* reduced by more than 75% compared with RRT* and Informed RRT*, and better solutions were obtained.【Conclusion】The proposed APF-FMT* algorithm based on the improved artificial potential field method not only overcomes the issue of redundant exploration in the FMT* algorithm, but also effectively solves the problem of unreachable target points in the artificial potential field method. This algorithm improves the efficiency and safety of path planning for agricultural robots.

Key words: Path planning; Agricultural robot; Artificial potential field method; FMT* algorithm

农业机器人是指能够进行自主路径规划和完成特定农业任务的智能化机器人，被广泛应用于采摘、运输、检测等方面[1]。路径规划作为农业机器人自主导航必不可少的一部分，受到研究人员的广泛关注，其目标是找到一个从初始状态到目标状态始终满足特定性能指标的无碰撞的连续解[2-4]。路径成本和解的质量是设计路径规划算法时需要考虑的重要因素。

在各种路径规划算法中，基于采样点的运动规划算法由于适用于大型环境和具有较好的搜索速度和避障碍能力而广受欢迎。快速探索随机树 (Rapidly-exploring random trees, RRT)[5] 和概率路线图 (Probabilistic road map, PRM)[6] 是 2 种常见的采样点运动规划算法。尽管它们在解决路径规划问题上具有代表性，但是试验证明它们不能保证获得最优解，即无法提供最优路径[7]。研究人员在 RRT 和 PRM 的基础上提出了 RRT*和 PRM*算法保证渐进最优性，但它们收敛速度缓慢，都需要大量样本才能找到最优解[7]。此外，Informed RRT*和探索利用树 (Exploration and exploitation trees, EET) 通过构建通道避免探索整个空间从而提高计算效率[8-9]。虽然这些方法能提高计算效率，但并不适用于所有环境，例如复杂农业环境。其中，快速行进树 (Fast marching trees, FMT*)[10] 方法借鉴 Fast marching 方法获得最优路径，兼具 RRT*和 PRM*的优点，更加快速高效。然而在探索空间效率方面，FMT*存在冗余探索的问题，为进一步提高 FMT*探索效率，Starek 等[11] 设计了双向 FMT*方法 (Bidirectional FMT*, BFMT*) 从初始和目标同时搜索样本，以提高计算效率。Xu 等[12] 在 FMT*应用了 Informed-RRT*思想，构建椭球区域 IAFMT* (Informed anytime fast marching trees) 约束探索空间，避免对整个空间探索；Wu 等[13] 采用 (Generalized voronoi graph, GVG) 建立等距路线图，找到初始解并构建安全隧道 (Secure tunnel FMT*, ST-FMT*)，避免整个空间探索。但是，不恰当的预处理和劣质的路径解均会造成 IAFMT*和 ST-FMT*算法区域划分不合理和探索低下的现象，在极端状态下甚至不能收敛于最优解。Ichter 等[14] 利用 GPU 的并行计算能力来处理 FMT*的扩展过程，但此方法对硬件性能要求高。上述方法大多从预处理和局部采样方面进行改进，启发式函数利用特定的环境信息引导规划算法进行探索。Gao 等[15] 利用 A*算法指导算法探索，在 Bidirectional FMT*的基础上形成双向启发式算法 (Heuristic bidirectional FMT*, HBFMT*)，提高计算效率。但是传统的启发函数只利用了部分环境信息，通过改进启发函数来提升算法的探索性能成为人们的关注点。

由于 FMT* 对规划空间的过度探索，有必要对 FMT*进行探索引导，解决冗余探索问题。受自适应人工势场快速探索随机树 (Adaptive artificial potential field RRT*, AAPF-RRT*) 算法[16] 的启发，本文提出了基于改进人工势场的快速行进树方法 (Artificial potential field FMT*, APF-FMT*)。人工势场法是由 Khatib[17] 提出的一种虚拟力场的方法，该方法简单有效，但存在以下问题：当目标点不可达和当移动机器人距离目标点较远时，引力会变得过大，容易陷入局部最优。本文为解决引力过大的问题，引入了相对距离，根据不同距离，自适应调节引力大小，并融合 FMT*算法，解决人工势场法目标不可达的问题。总体来说，本文对于给定的农业环境信息，通过改进人工势场法对环境建立势场，通过样本势场梯度的变化来引导样本向目标方向探索，减少对规划空间的过度探索，有助于保证在具有良好路径质量的同时提高计算效率。最后通过仿真对比，验证所提出的 APF-FMT*算法的有效性。

1 算法构建与分析

FMT*参考 Fast marching 算法对整个空间的所有样本进行动态递归扩展，具有良好的性能，但存在以下问题：1) 当样本数量较少时，由图 1a 可以看出，FMT*难以获得高质量的解；2)FMT*在返回解之前几乎都是探索整个空间，造成资源的大量浪费，无法在嵌入式平台使用；3) 如图 1b 所示，需要大量的样本才能确保获得高质量的解。因此，通过启发函数引导算法向有利规划的方向探索，将极大提升规划效率。

为解决上述问题，本文提出了一种基于改进人工势场法的快速行进树 (APF-FMT*) 方法。

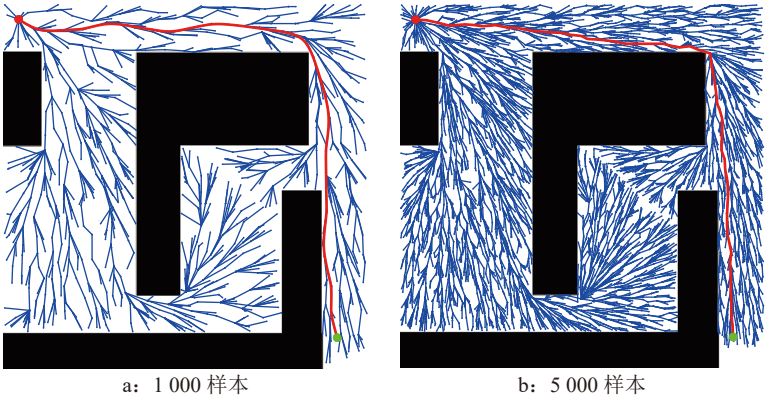

a：1 000 样本
a: 1 000 samples

b：5 000 样本
b: 5 000 samples

红色圆心表示起始点，绿色圆心表示目标点，红色曲线为最终路径

The red circle represents the starting point, the green circle represents the goal point, and the red curve represents the final path

图 1 FMT*规划结果

Fig. 1 FMT* planning result

1.1 改进人工势场法

传统的人工势场法的引力势场函数为：

$$u_{\mathrm{att}}(q)=\frac{1}{2}\varepsilon\rho^2(q,q_{\mathrm{goal}}), \tag{1}$$

式中：$u_{\mathrm{att}}(q)$为引力势场函数；ε为引力增益系数，且$\varepsilon>0$；q 为当前移动机器人的位置；q_{goal}为目标点的位置；$\rho(q,q_{\mathrm{goal}})$为当前移动机器人到目标点的欧氏距离。由式 (1) 可知，当移动机器人与目标点距离过远时，即$\rho(q,q_{\mathrm{goal}})$过大时，$u_{\mathrm{att}}(q)$过大，导致所受的引力过大，容易陷入局部最优。为解决引力过大的问题，本文引入相对距离将引力场划分为恒力场和变力场，改进的引力场函数如下所示：

$$U_{\mathrm{att}}(q)=\begin{cases}\dfrac{1}{2}\varepsilon\rho^2(q,q_{\mathrm{goal}}), & \rho(q,q_{\mathrm{goal}})<d_1,\\ \dfrac{1}{2}[\varepsilon d_1^2+\alpha\rho^2(q,q_{d_1})], & d_1\leqslant\rho(q,q_{\mathrm{goal}})<d_2,\\ \dfrac{1}{2}(\varepsilon d_1^2+\alpha d_2^2), & \rho(q,q_{\mathrm{goal}})\geqslant d_2,\end{cases} \tag{2}$$

式中：$U_{\mathrm{att}}(q)$为改进的引力场函数；d_1和d_2为常量，当 $\rho(q,q_{\mathrm{goal}})<d_1$ 时，$U_{\mathrm{att}}(q)$ 与$u_{\mathrm{att}}(q)$ 相同；当$d_1\leqslant\rho(q,q_{\mathrm{goal}})<d_2$时，引入 α 作为第 2 个引力增益系数，其中$\alpha<\varepsilon$；当$\rho(q,q_{\mathrm{goal}})\geqslant d_2$时，$U_{\mathrm{att}}(q)$为定值。通过设定$d_1$和$d_2$，实现引力场随着$\rho(q,q_{\mathrm{goal}})$的变化进行切换。从图 2 可以观察到，在传统引力场中，当起始点和目标点的距离过远时，引力过大，机器人难以

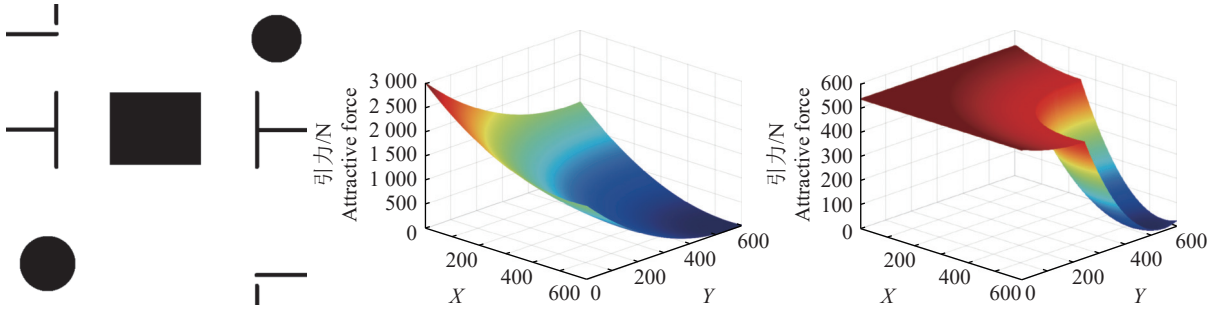

a：农业环境仿真地图 (俯视图)
a: Agricultural environment simulation map (Top view)

b：传统引力场
b: Traditional attractive field

c：改进引力场
c: Improved attractive field

图 2 人工势场法引力场

Fig. 2 Attractive field of artificial potential field method

脱离引力场的束缚并陷入局部最优，而改进后的引力场能够根据距离调节引力，从而避免这一问题的产生，机器人能够更有效地规划出路径。

改进的人工势场法的斥力场函数为：

$$U_{\mathrm{rep}}(q)=\begin{cases}\dfrac{1}{2}\eta\left[\dfrac{1}{\rho(q)}-\dfrac{1}{\rho_0}\right]^2, & \rho(q)<\rho_0,\\ 0, & \rho(q)\geqslant\rho_0,\end{cases}\tag{3}$$

式中：$U_{\mathrm{rep}}(q)$为斥力场函数；η为斥力系数；$\rho(q)$为移动机器人距离障碍物的距离；ρ_0为常量，代表障碍物影响的范围。由图 3 斥力场可知，当移动机器人与障碍物距离过近，即$\rho(q)$变小时，$U_{\mathrm{rep}}(q)$斥力变大，机器人有远离障碍物趋势。

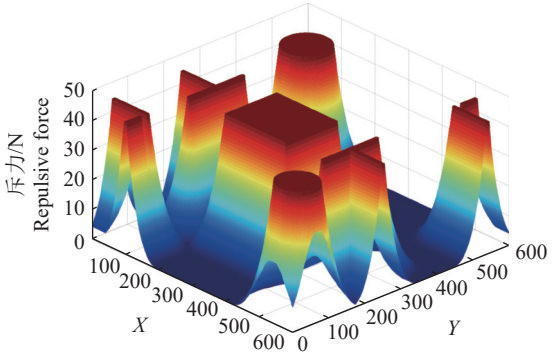

图 3　人工势场法斥力场

Fig. 3　Repulsive field of artificial potential field method

1.2　APF-FMT*算法

本文基于 FMT*算法的局限性，提出了改进的 APF-FMT*算法。APF-FMT*整体算法流程如图 4 所示。首先，在给定的环境地图上建立整体人工势场，并随机生成采样点集 V，将初始点X_{init}添加进已遍历点集V_{open}中，其他点添加进未遍历点集$V_{\mathrm{unvisited}}$中，初始化生成树X_{tree}，然后从V_{open}中选择成本 $F(X)$最小的点作为节点 Z，如图 5a 所示；接下来找出以节点 Z 为中心、半径为r_n的圆内所有在$V_{\mathrm{unvisited}}$集合内的邻近点集 X，如图 5b 所示；循环遍历邻近点集 X 每一个邻近点 x，并重新计算在V_{open}集合内连接成本最小的父节点，并进行碰撞检查，如图 5c 所示；当所有邻近点 x 都被探索，将节点 Z 加入到确认节点集V_{close}中，邻近点集 X 添加进V_{open}中，如图 5d 所示；循环以上步骤，直至V_{open}为空或节点 Z 为目标点。

其中，

$$r_n=\gamma\left(\frac{\lg n}{n}\right)^{\frac{1}{d}},\tag{4}$$

式中，γ为超参数，n 为样本点总数，d 为维度，本文研究的是平面空间，因此取值为 2；

$$F(X)=C(X)+G(X),\tag{5}$$

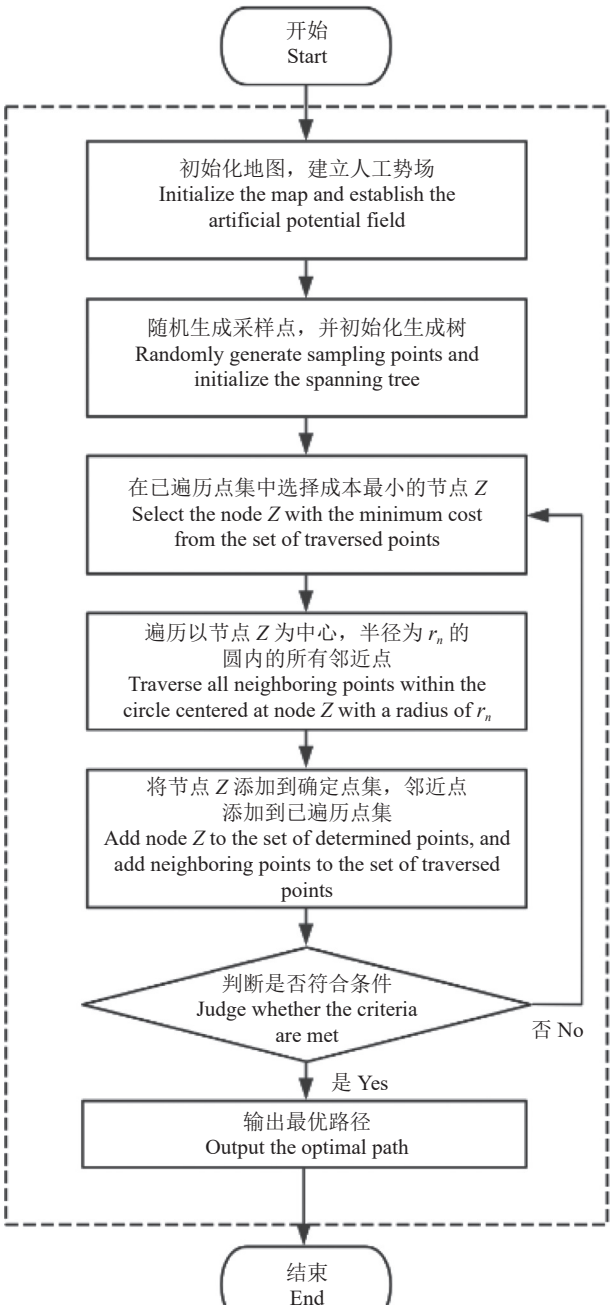

图 4　APF-FMT* 流程图

Fig. 4　APF-FMT* flow chart

式中，$F(X)$ 代表当前点 X 总体成本，$C(X)$ 代表由初始点到当前点 X 的欧氏距离，$G(X)$ 为启发函数，代表当前点 X 在改进人工势场法中的成本。

1.3　路径平滑处理

基于采样点的路径规划算法，得到连续线段的路径，曲率突变严重，影响移动机器人的平顺性和安全性，不符合移动机器人实际路径规划作业，采用三阶 B 样条曲线对得到的路径进行平滑处理，如图 6 所示。

三阶 B 样条曲线具备三阶连续性，表达式为：

$$P(\boldsymbol{u})=\sum_{i=0}^{n}P_iN_{i,k}(\boldsymbol{u}),\tag{6}$$

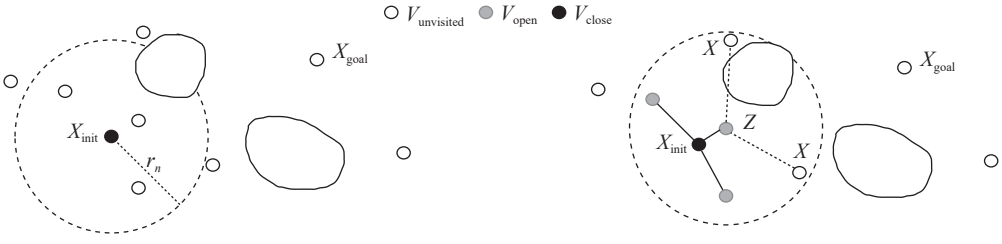

a：V_{open} 中成本最小点为节点 Z
a: The minimum cost points in V_{open} is chosen as the node Z

b：与节点 Z 距离为 r_n 邻近点 X
b: Neighboring point X with a distance of r_n from node Z

c：邻近点 X 重新选择父节点
c: The neighboring point X reselects its parent node

d：连接父节点 Z 与邻近点 X
d: Connect parent node Z with neighboring point X

X_{init}为初始点；X_{goal}为目标点；V_{open}为已遍历点集；$V_{unvisited}$为未遍历点集；V_{close}为确认点集；r_n为搜索半径

X_{init} is the initial point; X_{goal} is the goal point; V_{open} is the traversed point set; $V_{unvisited}$ is the untraversed point set; V_{close} is the confirmed point set; r_n is the search radius

图 5 APF-FMT*节点扩展过程

Fig. 5 APF-FMT* node expansion process

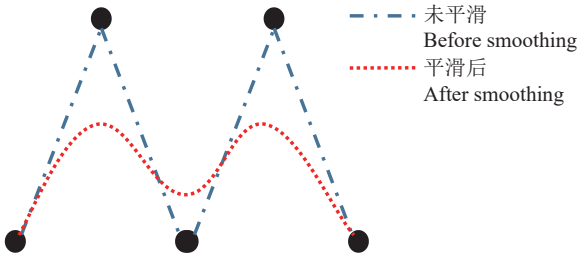

图 6 三阶 B 样条曲线

Fig. 6 Third order B-spline curve

式中，P_i为控制点，具体为 APF-FMT*的路径节点，$\boldsymbol{u}$为节点向量，$\boldsymbol{u}\in[0,1]$，$N_{i,k}(\boldsymbol{u})$是 k 次 B 样条曲线基函数，$P(\boldsymbol{u})$为最终平滑后的路径。

2 理论分析

本节为 APF-FMT*算法提供相应的理论依据。

2.1 定理 1 概率完备性[18]

当路径规划问题存在解时，样本数$n\to\infty$，APF-FMT*算法找到解的概率趋向于 1，即：

$$\lim_{n\to\infty}P\left(\exists x=x_{goal}|\sigma:[0,1]\to X_{free}\right)=1, \tag{7}$$

$$\sigma(0)=x_{init},\sigma(1)=x_{goal}, \tag{8}$$

式中，定义$\sigma:[0,1]\to X_{free}$为无碰撞的路径，如果$\sigma(0)=x_{init}$，$\sigma(1)=x_{goal}$，则为规划问题的可行解。

基于以下 2 种情况证明定理 1：1)APF-FMT*每次从V_{open}取出代价最小的节点进行迭代；2)APF-FMT*在V_{open}为空时中止并返回空路径。因此只要证明所有样本都被加进V_{open}，而且没有重复加入。

对于每个迭代过程，只有$V_{unvisited}$集合中的点才能被加入到V_{open}，并在被加入之后从$V_{unvisited}$中删除，由于样本点只有在初始化阶段加入$V_{unvisited}$中，因此，其只能被加进一次V_{open}。

2.2 定理 2 渐进最优

设 $(X_{free},X_{init},X_{goal})$是$d$维空间中的路径规划问题。令$c_n$表示 APF-FMT*算法在样本数为 n、半径为 r_n下生成路径长度，c^*为最佳路径σ^*的长度，r_n需要满足以下算式：

$$r_n=(1+\eta)2\left(\frac{1}{d}\right)^{1/d}\left[\frac{\mu(x_{free})}{\xi_d}\right]^{1/d}\left(\frac{\lg n}{n}\right)^{1/d}=\gamma\left(\frac{\lg n}{n}\right)^{1/d}, \tag{9}$$

$$\gamma=(1+\eta)2\left(\frac{1}{d}\right)^{1/d}\left[\frac{\mu(x_{free})}{\xi_d}\right]^{1/d}, \tag{10}$$

式中：$\eta>0$，$\mu(x_{free})$表示无障碍空间的勒贝格测度(二维空间为面积，三维空间为体积)，ξ_d为d维空间中单位球的体积。

当样本点趋于无穷大时，APF-FMT*算法获得的路径长度 c_n 趋于最佳路径长度 c^* 的概率为 1，即：

$$\lim_{n\to\infty}P\left(c_n=c^*\right)=1。 \tag{11}$$

用以下方法证明定理 2：首先，APF-FMT*算法基于 FMT*算法建立，FMT*算法已被证明在以r_n为搜索半径时具有渐进最优性，由于启发函数的存在，APF-FMT*算法的总代价$F(n)$始终比实际代价要小，即实际路径长度c_n存在下界：

$$\{F(n)\leqslant c_n\}。 \tag{12}$$

当 APF-FMT*算法加入一个新节点 x_{new} 到路径时，APF-FMT*算法的代价$F(x_{new})$必然不大于实际路径长度c_{new}。当样本点趋于无穷大时，V_{open}存在从初始节点x_{init}到目标节点x_{goal}最优路径的 1 个节点v，即初始节点x_{init}到节点v的实际路径长c_v等于到达节点 v 的最佳路径长度c_v^*。

由于v是最优路径上的节点，APF-FMT*算法的启发函数$G(v)$满足$G(v) \leqslant G^*(v)$，得到$F(v) \leqslant F^*(v) \leqslant c_v^*$，因此 v 必定能被 APF-FMT*找到。

2.3　定理 3 算法复杂度

在考虑样本数为 n，$(x_{free}, x_{init}, x_{goal})$的路径规划问题时，路径规划算法复杂度会影响总体执行效率。APF-FMT*算法计算一个路径可行解花费$O(n\log n)$时间，同时占用$O(n\log n)$空间。

用以下方法证明定理 3：APF-FMT*算法初始化人工势场的时间复杂度不大于$O(n)$。由于 APF-FMT*算法是基于 FMT*算法结构建立的，需要$O(n\log n)$时间计算 n 个样本的解和$O(n\log n)$时间来进行$O(n)$次碰撞检验，占用$O(n)$空间。APF-FMT*算法改进了 FMT*算法的代价函数，增加人工势场法启发函数，占用$O(n)$空间，调用启发函数的次数是$O(n\log n)$，总时间复杂度为$O(n\log n)$，根据大O原则，APF-FMT*的时间复杂度为$O(n\log n)$，空间复杂度为$O(n\log n)$。

3　仿真与试验验证

本文设置仿真区域大小为 600 m × 600 m，并使用二值图代表农业机器人工作环境，建立了 3 个具有代表性的农业环境地图进行测试。Map1 为鱼塘环境，环境条件类似文献 [19]；Map2 为果园环境；Map3 为有狭小果树行间的果园环境。通过将 APF-FMT*算法和现阶段基于采样点的路径规划算法在上述地图中进行模拟仿真，比较 APF-FMT*、FMT*、RRT*和 Informed-RRT*这 4 种算法的优劣。为了确保仿真试验的有效性，所有仿真算法都在 MATLAB R2020b 编写和试验，采用的计算机配置为：Windows 10 操作系统，AMD R5600X 六核处理器，运行内存 16 G。

仿真参数设置如下：地图分辨率为 600 × 600，起始点坐标为 (25，25)，目标点坐标为 (550，550)。对于 APF-FMT*算法和 FMT*算法，使用最近邻搜索寻找邻近点；对于 RRT*算法和 Informed-RRT*算法，设定步长为 20；并在节点选择过程中采用 Lazy collision-checking 减少碰撞检查次数。每个算法基于 10 组试验结果的平均值得出最终结果。图 7 为各算法在不同地图上的路径规划效果。

仿真试验结果如图 8 所示，在地图 Map1 和 Map2 中，4 种路径规划算法获得的长度相差不大，

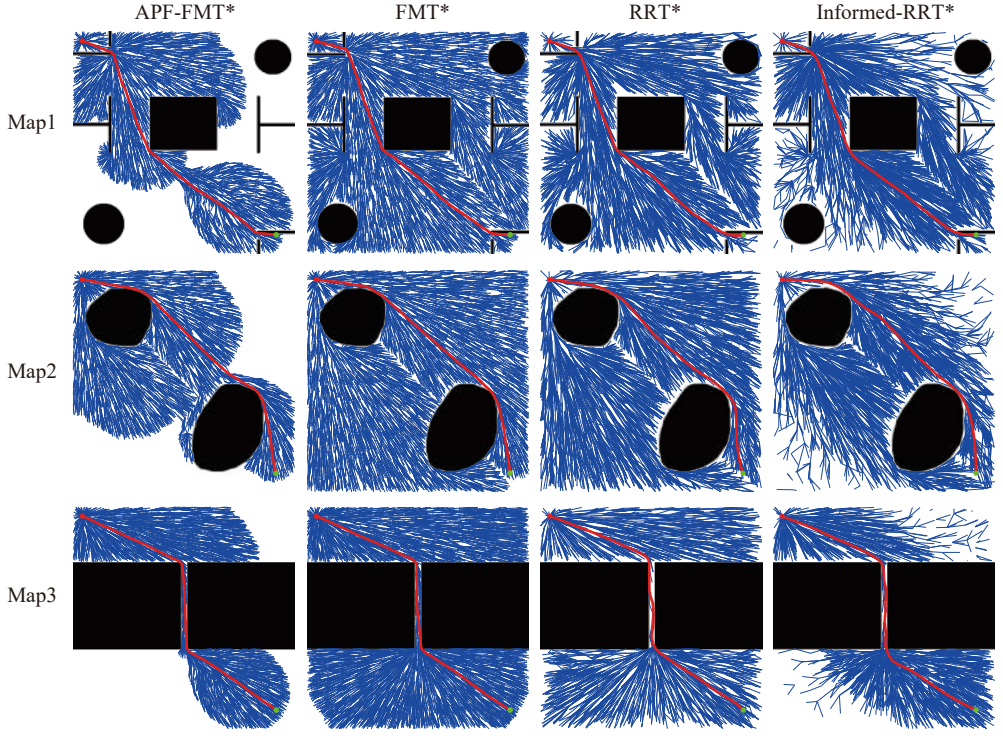

红色圆心表示起始点，绿色圆心表示目标点，红色曲线为最终路径

The red circle represents the starting point, the green circle represents the goal point, and the red curve represents the final path

图 7　4 种算法应用于不同地图的比较

Fig. 7　Comparison of four algorithms applied on different maps

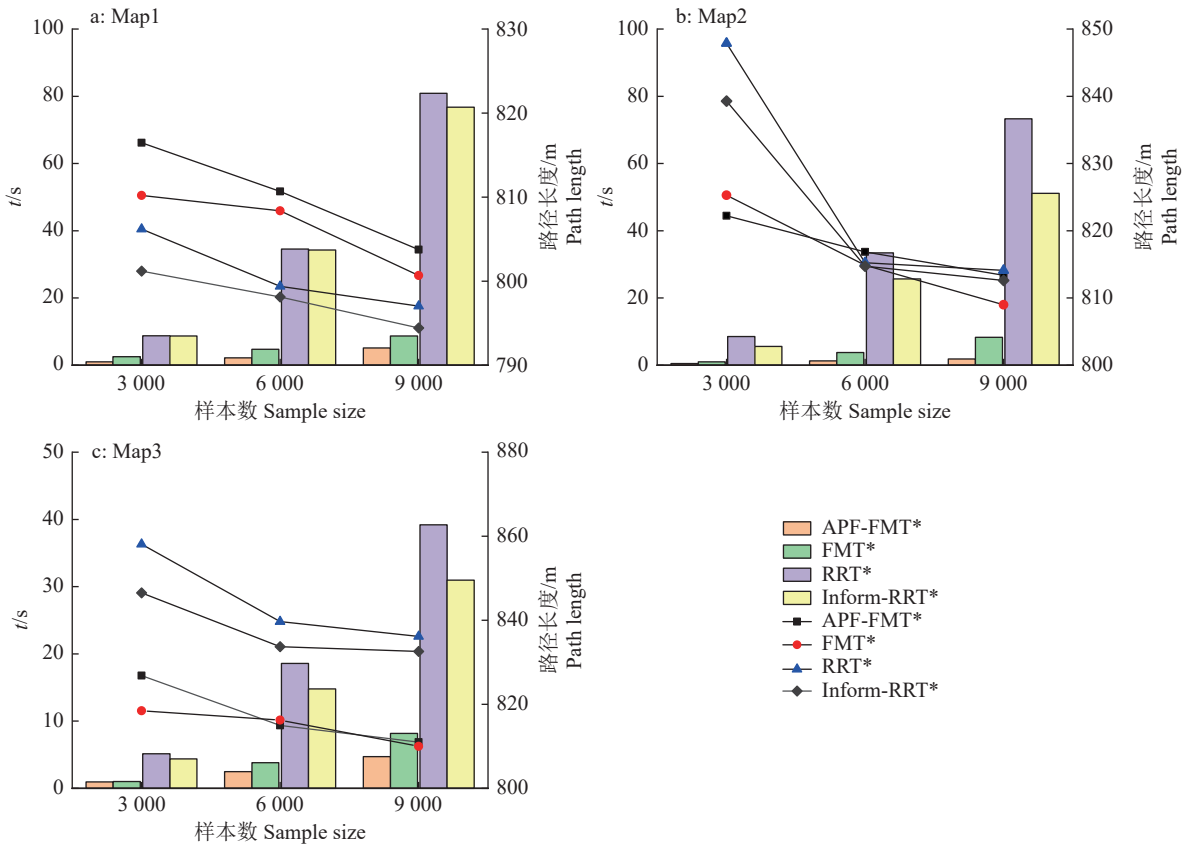

柱状图表示样本数和时间关系，折线图表示样本数和路径长度关系

The relationship between sample size and time is represented by a bar chart, while the relationship between sample size and path length is represented by a line chart

图 8　不同地图上 4 种算法样本数与时间和路径的关系

Fig. 8　Relationship between sample size and time, path of four algorithms on different maps

表明 APF-FMT*以超越其他算法的搜索速度获得质量良好的解，并且随着样本数量增加而得到改善。观察 Map3 可知，RRT*和 Informed-RRT*在通过狭小区域时都无法快速正确地找到解，需要迭代更多次数，获得解的质量低于 FMT*和 APF-FMT*算法的。通过数据比较，APF-FMT*在不同样本数情况下搜索速度优于其他算法，同时可获得良好质量的解。

从柱状图还可以看出，APF-FMT*和 FMT*的搜索时间与搜索时间增长幅度远低于 RRT*和 Informed-RRT*，表明 APF-FMT*因为引导函数执行更少的碰撞检测使得获得解的速度优于其他算法。从折线图可以综合得出，APF-FMT*、FMT*、RRT*和 Informed-RRT*都随着样本数的增加，获得的路径解得到改善，收敛趋势相对一致；在 Map1 和 Map3 中，由于 FMT*搜索整个空间，当样本数较小时，其收敛趋势较其他算法相比变化缓慢；RRT*和 Informed-RRT*难以迭代狭小通道里的路径解，导致获得路径解的质量比其他 2 种算法差；APF-FMT*则能够找到渐进最优解。

4　结论

本文为农业机器人在复杂农业环境进行路径规划并针对 FMT*在广度搜索过程中计算量大、冗余探索问题，提出一种基于改进人工势场法的快速行进树算法 APF-FMT*。该算法通过人工势场法改变 FMT*生成枝干的方式，利用目标点和障碍物信息来选择生长方向，明显降低计算复杂度，并将提出的路径规划算法与其他同类的 3 种算法进行 MATLAB 仿真对比，所提出算法获得较好的解，证明所改进算法在保证路径有良好质量的同时，提高了规划速度、降低了计算复杂度。

由于本文主要研究的是静态运动规划，而实际农业机器人工作环境是动态的，因此在进一步的工作中需要考虑到运动规划的实时性和农田环境的多变性，将 APF-FMT*应用于高维空间。

参考文献：

[1] 孙叶丰. 农业机器人发展现状及展望[J]. 现代农业研究, 2022, 29(3): 92-94.

[2] 艾尔肯·亥木都拉, 穆占海, 郑威强. 采用多策略改进黑

猩猩算法的农业机器人路径规划[J]. 西安交通大学学报, 2023, 57(8): 161-171.
[3] 陆宇豪, 刘义亭, 郁汉琪, 等. 基于改进 BIT 算法的农业机器人路径优化研究[J]. 仪器仪表用户, 2022, 29(11): 1-6.
[4] 石志刚, 梅松, 邵毅帆, 等. 基于人工势场法的移动机器人路径规划研究现状与展望[J]. 中国农机化学报, 2021, 42(12): 182-188.
[5] KAZEMI M, GUPTA K K, MEHRANDEZH M, et al. Randomized kinodynamic planning for robust visual servoing[J]. IEEE Transactions on Robotics: A publication of the IEEE Robotics and Automation Society, 2013, 29(5): 1197-1211.
[6] KAVRAKI L E, SVESTKA P, LATOMBE J C, et al. Probabilistic roadmaps for path planning in high-dimensional configuration spaces[J]. IEEE Transactions on Robotics and Automation, 1996, 12(4): 566-580.
[7] KARAMAN S, FRAZZOLI E. Sampling-based algorithms for optimal motion planning with deterministic μ-calculus specifications[C]//2012 American Control Conference (ACC). Montreal, QC, Canada: IEEE, 2012: 735-742.
[8] RICKERT M, SIEVERLING A, BROCK O. Balancing exploration and exploitation in sampling-based motion planning[J]. IEEE Transactions on Robotics, 2014, 30(6): 1305-1317.
[9] GAMMELL J D, SRINIVASA S S, BARFOOT T D. Informed RRT*: Optimal sampling-based path planning focused via direct sampling of an admissible ellipsoidal heuristic[C]//2014 IEEE/RSJ International Conference on Intelligent Robots and Systems(IROS). Chicago, IL, USA: IEEE, 2014: 2997-3004.
[10] JANSON L, SCHMERLING E, CLARK A, et al. Fast marching tree: A fast marching sampling-based method for optimal motion planning in many dimensions[J]. The International Journal of Robotics Research, 2015, 34(7): 883-921.
[11] STAREK J A, GOMEZ J V, SCHMERLING E, et al. An asymptotically-optimal sampling-based algorithm for bi-directional motion planning[C]//2015 IEEE/RSJ International Conference on Intelligent Robots and Systems(IROS). Hamburg, Germany: IEEE, 2015: 2072-2078.
[12] XU J, SONG K, ZHANG D, et al. Informed anytime fast marching tree for asymptotically-optimal motion planning[J]. IEEE Transactions on Industrial Electronics, 2021, 68(6): 5068-5077.
[13] WU Z, CHEN Y, LIANG J, et al. ST-FMT*: A fast optimal global motion planning for mobile robot[J]. IEEE Transactions on Industrial Electronics, 2022, 69(4): 3854-3864.
[14] ICHTER B, SCHMERLING E, PAVONE M. Group marching tree: Sampling-based approximately optimal motion planning on GPUs[C]//2017 First IEEE International Conference on Robotic Computing(IRC). Taichung, TaiWan: IEEE, 2017: 219-226.
[15] GAO W, TANG Q, YAO J, et al. Heuristic bidirectional fast marching tree for optimal motion planning[C]//2018 3rd Asia-Pacific Conference on Intelligent Robot Systems. Singapore: IEEE, 2018: 71-77.
[16] 臧强, 张国林, 靳雨桐, 等. 一种基于动态步长的 AAPF-RRT*移动机器人路径规划新算法[J]. 中国科技论文, 2021, 16(11): 1227-1233.
[17] KHATIB O. Real-time obstacle avoidance for manipulators and mobile robots[C]//1985 IEEE International Conference on Robotics and Automation. St. Louis, MO, USA: IEEE, 1985: 500-505.
[18] GAMMELL J D, BARFOOT T D, SRINIVASA S S. Batch informed trees (BIT*): Informed asymptotically optimal anytime search[J]. The International Journal of Robotics Research, 2020, 39(5): 543-567.
[19] 杨琛, 陈继洋, 胡庆松, 等. 基于多目标 PSO-ACO 融合算法的无人艇路径规划[J]. 华南农业大学学报, 2023, 44(1): 65-73.

【责任编辑　庄　延】

Postharvest Biology and Technology 227 (2025) 113620

Contents lists available at ScienceDirect

Postharvest Biology and Technology

journal homepage: www.elsevier.com/locate/postharvbio

Non-destructive prediction of soluble solids content and firmness and maturity determination of guava fruit using color and fluorescence imaging

Shaozhen Lin [a,b,1], Kangting Yan [a,c,1], Zhilei Sun [a,b], Zhijie Zhang [a,b], Yubin Lan [a,d], Linlin Wang [e,*], Yali Zhang [a,b,**]

[a] National Center for International Collaboration Research on Precision Agricultural Aviation Pesticides Spraying Technology, Guangzhou 510642, China
[b] College of Engineering, South China Agricultural University, Guangzhou 510642, China
[c] Department of Mechatronic Engineering, Guangdong Polytechnic Normal University, Guangzhou 510665, China
[d] College of Electronic Engineering (College of Artificial Intelligence), South China Agricultural University, Guangzhou 510642, China
[e] School of Artificial Intelligence, Shenzhen Polytechnic University, Shenzhen 518055, China

ARTICLE INFO

Keywords:
Psidium guajava
Excitation-emission matrix
Multi-light source imaging
Ripeness
Quality inspection

ABSTRACT

Guava is a widely grown tropical fruit. Accurate detection of its maturity and quality is important for optimizing harvesting timing and ensuring post-harvest quality. In this study, a non-destructive method based on the combination of color images and fluorescence images was proposed to accurately predict and classify the soluble solids content (SSC), firmness, and maturity of guava fruit. The study measured the excitation-emission matrix of guava fruit using a fluorescence spectrophotometer, analyzed its fluorescence properties, and designed an imaging system that combined ultraviolet light and visible light sources to capture color images and fluorescence images at different maturity stages. After image preprocessing and feature extraction, the partial least squares regression (PLSR) model was used to predict SSC and firmness. The experimental results show that fluorescent image features exhibit higher sensitivity and accuracy in SSC prediction than color image features. After fusing the two image features, the model can achieve the best prediction performance, with the test set R^2 reaching 0.80 and 0.90, and RPD being 2.23 and 3.21, respectively. For maturity classification, the combined feature classification based on the Support Vector Machine (SVM) model had an accuracy of 91 %, and was able to effectively differentiate between immature, green-mature, and yellow-mature stages of guava. This study demonstrates the potential of a multi-light source fluorescence imaging system for nondestructive assessment of guava quality, providing a rapid and cost-effective solution for maturity assessment and quality inspection.

1. Introduction

Guava (*Psidium guajava* L.) is a tropical and subtropical fruit native to the Americas. It is widely grown and consumed worldwide for its excellent nutritional value and unique flavor (Kamle and Baek, 2017). As a "super fruit", guava is rich in vitamin C, dietary fiber and antioxidants. Among them, flavonoids are the main source of its antioxidant properties. These compounds have multiple biological activities such as antioxidant, anti-inflammatory and antibacterial activities, which can effectively protect the human body from free radical damage, thus playing an important role in preventing chronic and degenerative diseases (Angulo-López et al., 2021; M. Kadam et al., 2012; Takeda et al., 2023). With the continuous growth of global demand for healthy food, the economic value of guava in the tropical fruit market has become increasingly prominent, and it has become an important category in international trade.

The maturity of guava fruit plays a crucial role in their post-harvest quality and market value. Studies have shown that significant metabolic changes occur as the fruit transitions from the green mature stage (100 % green fruit) to the yellow mature stage (50 % yellow and 50 % green), and therefore harvesting at the yellow mature stage is usually recommended to ensure safer handling and transportation, thus

* Correspondence to: Shenzhen Polytechnic University, 4089 Shahe West Road, Nanshan District, Shenzhen, Guangdong, China.
** Correspondence to: South China Agricultural University, 483 Wushan Road, Tianhe District, Guangzhou, Guangdong, China.
E-mail addresses: lsz@stu.scau.edu.cn (S. Lin), ktyan@stu.scau.edu.cn (K. Yan), sunzl@stu.scau.edu.cn (Z. Sun), zhijiezhang@stu.scau.edu.cn (Z. Zhang), ylan@scau.edu.cn (Y. Lan), wanglinlin@szpu.edu.cn (L. Wang), ylzhang@scau.edu.cn (Y. Zhang).
[1] These authors contributed equally to this work.

https://doi.org/10.1016/j.postharvbio.2025.113620
Received 29 March 2025; Accepted 24 April 2025
Available online 28 April 2025
0925-5214/© 2025 Elsevier B.V. All rights are reserved, including those for text and data mining, AI training, and similar technologies.

effectively reducing postharvest losses (Dolkar et al., 2017). However, guava reaches peak respiration within days after harvest, leading to rapid deterioration of fruit quality and increasing the difficulty of storage (Deepthi, 2017). For this reason, accurate determination of guava maturity is particularly important, not only to guide the selection of optimal harvest timing and reduce postharvest losses, but also to ensure the stability of fruit quality. In addition, through maturity assessment, the industry can achieve efficient classification of fruit. Mature fruit are given priority to the local market, while less mature fruit are used for long-distance transportation, thereby optimizing the supply chain and improving overall economic benefits.

The maturity of guava directly affects its flavor, texture and nutritional value. However, different varieties of guava exhibit diverse characteristics during maturation. Some varieties do not change color significantly when ripe, or maintain a high firmness even when they reach maturity, which increases the complexity of traditional maturity assessment methods (Low et al., 2024). At present, traditional fruit maturity judgment mainly relies on manual experience observation and destructive testing. These methods have the disadvantages of strong subjectivity, low efficiency and non-repeatability, and are difficult to meet the needs of large-scale production. Therefore, it is particularly important to develop non-destructive testing technologies that adapt to these diverse characteristics. In recent years, the application of non-destructive testing technology in fruit quality assessment has gradually become a research hotspot. The scientific evaluation of guava maturity through non-destructive testing technology can not only improve the efficiency of picking and grading, but also significantly reduce economic losses (Li et al., 2018).

Among the nondestructive testing methods based on spectroscopy, near-infrared (NIR) spectroscopy and hyperspectral imaging (HSI) technologies have been applied to the quality assessment of guava fruit maturity and the detection of soluble solids content (SSC) (Ahmad et al., 2018; Klinbumrung and Teerachaichayut, 2018; Ni et al., 2024). However, these technologies have certain limitations. Although NIR spectroscopy technology is widely used, due to the strong versatility of the instrument and the lack of optimized design for specific fruit, its modeling process is complex and the results are easily affected by changes in environmental conditions and sample characteristics. HSI technology is limited in its wide application in actual production due to its expensive equipment, high technical requirements, complex data processing and slow detection speed (Sun et al., 2023).

In contrast, fluorescence imaging technology has unique advantages in fruit maturity and quality assessment due to its high sensitivity, non-destructiveness, rapidity and ability to simultaneously obtain spatial and spectral information (Momin et al., 2023). Fluorescence imaging technology is based on the absorption and emission characteristics of substances to light of specific wavelengths. It can reflect the chemical composition and maturity state of fruit through the response of fluorescent molecules such as polyphenols, flavonoids, and chlorophyll in fruit to light. This technology has been successfully applied to the maturity detection of fruit such as apples (Noh and Lu, 2007), tomatoes (Fatchurrahman et al., 2020), grapes (Mehretie et al., 2024), kiwis (Nie et al., 2020) and mangoes (Al Riza et al., 2023). Guava fruit is also rich in a variety of bioactive substances, including a large number of phenolic compounds, flavonoids and chlorophyll, and theoretically has fluorescence properties (Gutiérrez et al., 2008). Therefore, it is feasible to detect the maturity and other physical and chemical properties of guava by fluorescence imaging technology. There has been a study on non-destructive detection of guava maturity by fluorescence spectroscopy (Pertiw et al., 2023), but the study was limited to one-dimensional spectral data analysis, which lacked the description of the spatial distribution of fluorescence signals on the fruit surface, and the study performed weakly in firmness prediction. Therefore, guava maturity detection based on fluorescence imaging technology still needs further exploration to make full use of multidimensional information to improve prediction accuracy.

This study aims to explore a non-destructive detection method based on color and fluorescence imaging to predict the SSC, firmness and maturity of guava fruit. First, the excitation-emission matrix (EEM) of the guava fruit epidermis was measured using a fluorescence spectrophotometer to determine the fluorescence characteristics and characteristic excitation-emission wavelength range of the fruit epidermis. Based on the measured fluorescence characteristics, an imaging system was designed and built to collect color and fluorescence images of guava fruit. Subsequently, color features and texture features were extracted from the collected images, and the SSC and firmness of guava fruit were predicted by constructing a partial least squares regression (PLSR) model. At the same time, the support vector machine (SVM) was used to classify the maturity of the fruit into immature, green-mature and yellow-mature stages. The method proposed in this study significantly improved the accuracy and efficiency of guava maturity detection by fusing multi-light source image features, providing a new approach for the automation and intelligence of fruit quality assessment.

2. Materials and methods

2.1. Materials

This study used *Psidium guajava* 'Pearl', a guava variety widely grown in China. Two harvests were carried out on October 19, 2024 and November 23, 2024. Guava fruit harvested each time included three different maturity stages: immature, green-mature and yellow-mature. Fruit that was 80–90 % ripe and had green skin were green-mature fruit, and fruit that had yellow-green skin were yellow-mature fruit (Wang et al., 2023). Guava fruit were obtained from a commercial guava orchard in Aotou Town, Conghua District, Guangzhou City, Guangdong Province, China (23°69′N, 113°38′E). All guava fruit were harvested manually at room temperature and transported to the laboratory on the day of harvesting for storage at 25 °C. A total of 90 guava fruit were selected for this study, 30 at each maturity stage. Once the fruit arrives at the laboratory, it is imaged, measured by EEM, tested for firmness, and analyzed for SSC. All measurements and image acquisition are performed on the same day as sample collection to ensure data consistency and minimize the impact of post-harvest factors.

2.2. Color and fluorescence image acquisition

In this study, a machine vision imaging system was built to collect color images and fluorescence images of guava, as shown in Fig. 1. The system includes three light sources, an industrial camera, and a computer for data acquisition and processing. The light sources are a 365 nm

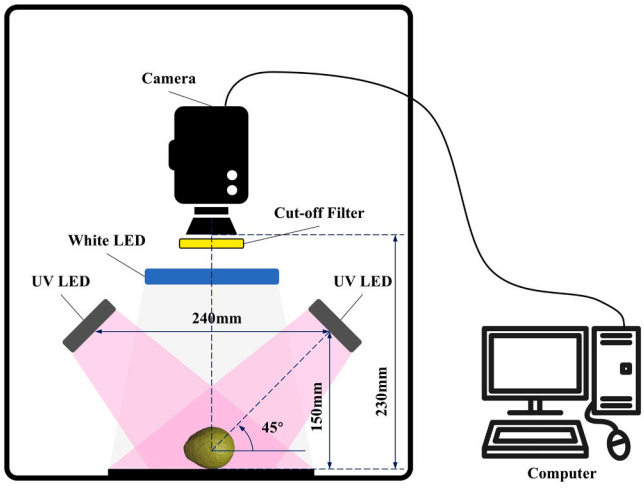

Fig. 1. Color and fluorescence image acquisition system.

ring Ultraviolet (UV) light source (P-RL-100–90-UV365, 6.5 W, Beijing Hi-Laser Technology Co., Ltd., China), a 415 nm ring UV light source (JH-RS9090-UV415, 7.5 W, Dongguan Jutu Optoelectronics Technology Co., Ltd., China), and a white LED ring light source (JH-RS10090-W, 11 W, Dongguan Jutu Optoelectronics Technology Co., Ltd., China). Among them, the color image is taken by the white LED light source, and the fluorescence image is collected by three different light sources and filter combinations, including a 365 nm excitation light source with a 450 ± 20 nm cut-off filter, a 365 nm excitation light source with a 525 ± 20 nm cut-off filter, and a 415 nm excitation light source with a 525 ± 20 nm cut-off filter (the filter is provided by Beijing Blue Heart Times Technology Co., Ltd.). The industrial camera is a USB3.0 color industrial camera (ME2P 900–43U3M, Beijing Daheng Image Vision Technology Branch, China), equipped with a CMOS image sensor, an image resolution of 4200 × 2160 pixels, and an M0828-MPW3 lens. Image acquisition is completed by the GalaxyView SDK software supporting the camera. To ensure the reproducibility of the images, the camera was corrected for white balance by a standard white board before the experiment.

In the experiment, two side images (side image and the other side after rotating 180°) were taken for each guava fruit. During each side shooting process, a color image under a white LED light source was first collected, followed by three fluorescence images, one for each light source combination. A total of 90 fruit images were collected, with 8 images taken for each fruit, resulting in 720 images.

2.3. Fluorescence EEM measurement

The fluorescence EEM of guava peel was measured at room temperature by a fluorescence spectrophotometer (Jasco FP-8300, JASCO Inc., Japan). The experiment was measured by the front-face fluorescence method (Al Riza et al., 2018). The measurement method is shown in Fig. 2. The samples were slices of peel cut from the equatorial region of the guava, with a thickness of about 2 mm and a diameter of about 20 mm, to ensure the representativeness and consistency of the measurements. The excitation wavelength and emission wavelength scanning range of the fluorescence photometer were set to 200–700 nm and 210–750 nm, respectively, with 5 nm interval of measurements. Scan speed was 5000 nm/min and response time was 50 ms. To prevent fluorescence intensity saturation, the sensitivity of the photomultiplier tube (PMT) was set to low. During the measurement, spectral correction was performed to suppress instrument distortion in excitation (Mehretie et al., 2018). At the same time, to reduce the influence of instrument fluctuations, the measured EEM data was normalized to Raman Unit (RU). The normalization process uses pure water with an excitation wavelength of 350 nm as a reference, and converts the data from arbitrary units (AU) to RU by calculating the integral value of its fluorescence emission intensity in the range of 371–428 nm (water Raman peak intensity) (Lawaetz and Stedmon, 2009). In addition, the Rayleigh scattering signal in the EEM data was removed to reduce its interference with the fluorescence signal. All EEM measurements were completed on the day of sample collection to minimize possible changes in fluorescence properties due to sample storage.

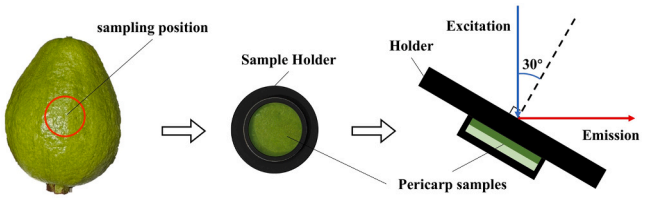

Fig. 2. Sampling position and front-face fluorescence measurement.

2.4. Firmness and SSC measurement

The firmness of guava fruit was measured using a digital fruit firmness tester (GY-4, Yueqing Handpi Instruments Co., Ltd, China) equipped with a probe with a diameter of 8 mm. During the measurement, the probe was inserted vertically into the equatorial region of the fruit to a depth of 10 mm, and the maximum value was recorded. In order to obtain higher measurement accuracy, three locations in the equatorial region of each guava fruit were selected for firmness measurement, and the average value was calculated and expressed in Newton (N).

The SSC of the fruit was measured using a portable digital refractometer (PAL-1, Atago Co., Ltd., Japan). Before the measurement, the refractometer was calibrated with pure water to ensure accuracy. When measuring the samples, each guava was peeled, seeded, cut into pieces, mixed, and the juice sample was obtained by squeezing. Subsequently, 0.2 mL of juice was taken with a pipette and dropped onto the sample plate of the refractometer for measurement. The measurements were repeated three times for each sample and averaged, and the results were expressed in %.

2.5. Image processing and statistical analysis

The collected color images and fluorescence images were preprocessed using Python programming language. First, the background was removed from the original image, and the fruit area was extracted as the region of interest (ROI). For the extracted ROI image, the average value of each channel (R, G, B) in the RGB color space was calculated, and the color ratio parameters, including Rratio (R/ (R + G + B)), Gratio (G/ (R + G + B)) and Bratio (B/ (R + G + B)), were calculated based on the values of these three channels. Meanwhile, in order to more comprehensively describe the color features, the image was converted to HSV and L*a*b* color spaces, and the average value of each channel (H, S, V, L*, a*, b*) was extracted. In addition, the Gray Level Co-occurrence Matrix (GLCM) method was used to describe the texture features of the image (Haralick et al., 1973). Color images and fluorescence images were first converted to grayscale images, and then the GLCM in the horizontal direction (0 degrees) and 1 pixel distance was calculated to extract texture features including contrast, correlation, energy, homogeneity, dissimilarity, and Angular Second Moment (ASM). The calculation of texture features was implemented using the Scikit-Image library (Walt, S. et al., 2014). Ultimately, a total of 18 color and texture features were extracted for each image.

All extracted feature data were subjected to maximum-minimum normalization before subsequent analysis and divided into calibration and prediction sets in the ratio of 7:3. To assess the applicability and reliability of color and fluorescence images in predicting firmness and SSC at the maturity stage of guava, the features of color and fluorescence images were modeled using PLSR. Model performance was assessed by root mean square error (RMSE), coefficient of determination (R^2), and the ratio of prediction to deviation (RPD). In general, a good model must have a high R^2 and a low RMSE. In addition, the RPD value is used to assess the predictive ability of the model. When the RPD is between 1.5 and 2.0, it indicates that the model can distinguish between high and low values but has weak predictive ability; when the RPD is between 2.0 and 2.5, it indicates that the model is suitable for approximate quantitative prediction; when the RPD is between 2.5 and 3.0 and even greater than 3.0, the model exhibits good to excellent predictive performance and can be accurately applied to predictive analysis of target parameters (Cortés et al., 2016).

SVM is one of the best general-purpose classifiers in traditional machine learning, and its main advantages are its simplicity, low computational cost, and the fact that it can be trained with only a small number of samples (Shammi et al., 2023), which is applicable to the dataset of the present study. Therefore, in this study, SVM was utilized to classify and analyze the maturity stages of guava, and the classification performance was evaluated by the metrics of Classification Accuracy,

Precision, Recall, F1-score and receiver operating characteristic (ROC) curve. All models were trained and tested using Leave-One-Out (LOO) Cross-validation (Wong, 2015) to reduce the risk of overfitting. The above relevant evaluation parameters are defined by Eqs. (1)-(7).

$$R^2 = 1 - \frac{\sum_{i=1}^{N}(\hat{y}_i - y_i)^2}{\sum_{i=1}^{N}(\hat{y}_i - \bar{y}_i)^2} \quad (1)$$

$$RMSE = \sqrt{\frac{\sum_{i=1}^{N}(\hat{y}_i - y_i)^2}{N}} \quad (2)$$

$$RPD = \frac{SD(y)}{RMSEP} \quad (3)$$

$$Accuracy = \frac{TP + TN}{TP + TN + FP + FN} \quad (4)$$

$$Precision = \frac{TP}{TP + FP} \quad (5)$$

$$Recall = \frac{TP}{TP + FN} \quad (6)$$

$$F1 = \frac{2 \times Precision \times Recall}{Precision + Recall} \quad (7)$$

where $\hat{y}_i$ is the predicted value of the ith observation, y_i is the measured value of the ith observation, N is the number of observations, SD is the standard deviation of the measured values, TP refers to true positives, TN refers to true negatives, FP refers to false positives, and FN refers to false negatives.

3. Results and discussion

3.1. Firmness and SSC

The SSC and firmness values of 90 guava fruit at three stages of maturity, namely immature, green-mature and yellow-mature, were measured and the corresponding results are shown in Fig. 3. As can be seen in Fig. 3 (A), the SSC of guava fruit increased gradually with the increase in maturity, indicating a gradual increase in the accumulation of soluble sugars during the maturation process of guava. Soluble sugars are highly correlated with fruit sweetness (Qiu et al., 2020), thus SSC is a reliable indicator of changes in guava fruit sweetness. Fig. 3 (B) demonstrated the firmness of guava fruit at different maturity stages, which decreased significantly with increasing maturity, and this change was mainly related to the degradation of pectin and changes in cell wall structure (Braga et al., 2017). Meanwhile, statistical analysis showed that there were significant differences ($p < 0.05$) in SSC and firmness of guava fruit at different stages of maturity. Therefore, the changes in SSC and firmness of guava fruit can be used as an effective indicator for assessing fruit maturity and quality.

3.2. EEM

The EEM characteristics of the epidermis of guava fruit at different maturity levels are shown in Fig. 4. The vertical axis is the excitation wavelength, the horizontal axis is the emission wavelength, and the color is the fluorescence intensity. The analysis shows that the three-dimensional fluorescence images of guava samples at different maturity stages present similar fluorescence regions and show differences in fluorescence intensity at different maturity stages. Among them, region A (excitation wavelength range of 300–380 nm, emission wavelength range of 390–470 nm) and region B (excitation wavelength range of 290–370 nm, emission wavelength range of 500–540 nm) showed stronger fluorescence intensity, which was mainly related to the flavonoids and phenolics (quercetin, gallic acid, and catechin, etc.) in guava (Bylappa et al., 2024; Pertiw et al., 2023). As the fruit enters the yellow-mature stage, the fluorescence intensity of these substances gradually weakens. The fluorescence signal of region C (excitation wavelength range of 390–450 nm and emission wavelength range of 500–540 nm) is mainly derived from vitamin C (Araújo et al., 2015; Bylappa et al., 2024), and its fluorescence intensity changes significantly with increasing maturity. The fluorescence signal in region D (excitation wavelength range of 350–680 nm and emission wavelength range of 660–750 nm) is associated with chlorophyll pigments (García-Plazaola et al., 2015). Although the fluorescence signal of chlorophyll usually shows a trend with maturation, this region did not play a key role in the design of the imaging system, as it did not show significant changes at the intensity range settings of this study and there was some edge noise interference. Region E exhibits edge noise, which is usually stray light from surface scattered light, and these signals do not have a practical impact on the data results in fluorescence signal analysis.

This study finally selected regions A, B, and C as characteristic regions. The changes in fluorescence signals in these regions are closely related to the chemical composition and maturity of guava. Based on these characteristic regions, appropriate excitation light sources and emission filters were selected to ensure that the imaging system can effectively capture the fluorescence signals of the guava fruit skin. This provides reliable technical support for subsequent maturity prediction and quality assessment.

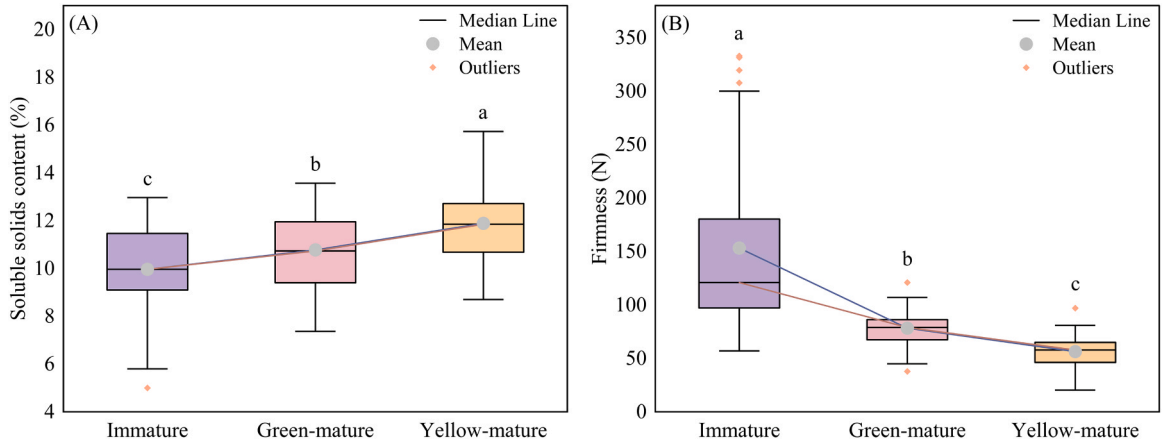

Fig. 3. Changes in (A) soluble solids content and (B) firmness of guava fruit at different maturity stages. Different letters above the groups represent significant differences, and shared letters represent no significant differences.

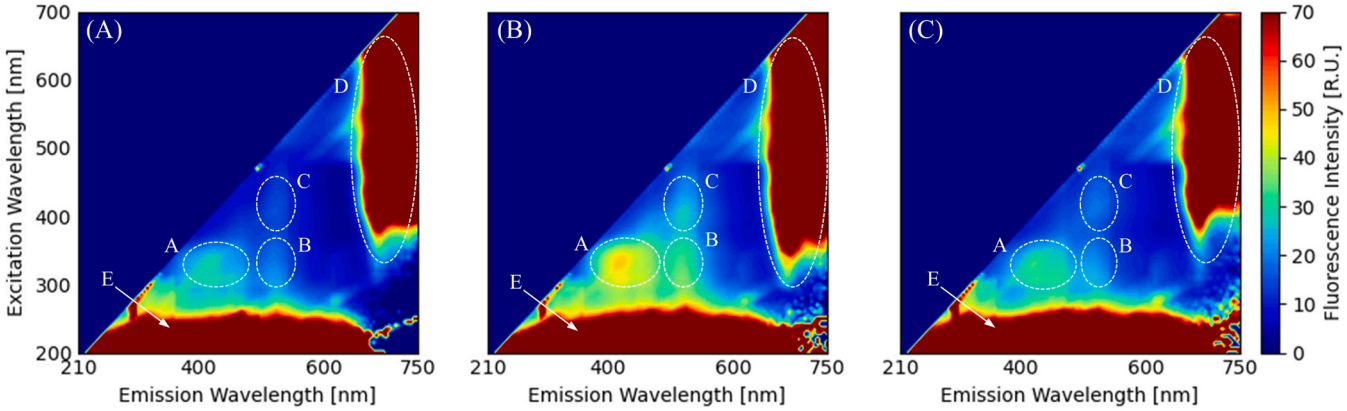

Fig. 4. EEM of epidermis of (A) immature, (B) green-mature and (C) yellow-mature guava fruit.

3.3. Color and fluorescent images

Fig. 5 shows the color and fluorescence images of guava fruit at three maturity stages. In color images, the guava in the immature stage is obviously green. As the fruit matures, the green color gradually weakens, and the fruit skin turns yellow-green in the yellow-mature stage. This change is closely related to the decrease in chlorophyll content and the increase in carotenoids and other components during the maturity of guava fruit (Sharma et al., 2017). In fluorescence images, images excited by different light sources show the fluorescence characteristics of the guava skin at different stages of maturity. The fluorescence signal is weak in the immature stage, indicating that the content of fluorescent substances in the fruit skin is low at this time. Entering the green-mature stage, the fluorescence images under the combination of three light sources show strong fluorescence signals. This indicates that at this stage, the content of fluorescent substances in the guava skin is high, which may be related to the accumulation of flavonoids and phenolic substances. As the fruit further matures and enters the yellow-mature stage, the fluorescence signal gradually weakens. This may be related to the decrease in the content of phenolic compounds and flavonoids in the skin (Bylappa and Nag, 2023), reflecting the changes in these components during the maturation process of guava. Especially in the green-mature and yellow-mature stages, the difference between fluorescence images is more obvious than that of color images. Fluorescence imaging can more effectively capture the signals of changes in chemical composition during the maturation process of guava, allowing the maturation process of the fruit to be more accurately monitored at these stages through fluorescence imaging technology. This shows that fluorescence imaging can not only effectively distinguish guava at different stages of maturation, but also complement the shortcomings of color images in assessing fruit maturity.

3.4. Prediction and classification models using image features

3.4.1. Prediction model

The PLSR model was used to predict the SSC and firmness of guava fruit, aiming to evaluate the prediction performance of different image features. Table 1 and Table 2 show the model prediction results based on different image features (including color images alone, fluorescence images alone, and color and fluorescence images combined) on the calibration set and prediction set.

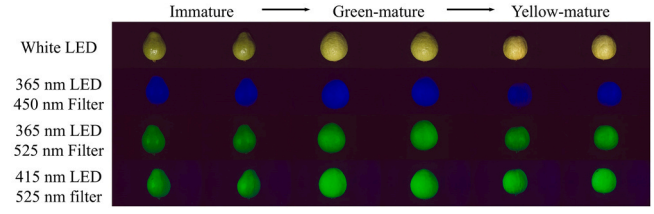

Fig. 5. Color and fluorescence images of guava fruit at immature, green-mature, and yellow-mature stages.

For the prediction of SSC, the model using only color images showed limited predictive ability, with relatively weak performance on both the calibration and prediction sets. In contrast, using fluorescence images improved performance, but the predictive ability was still mediocre. Combining all fluorescence image features significantly enhanced the performance of the model, with stronger predictive ability compared to fluorescence images alone. The combination of color and fluorescence image features performed best, as shown in Fig. 6 (A), with an R^2 of 0.80, RMSE of 0.93, and RPD of 2.23 on the prediction set, indicating that combining these features can significantly improve prediction accuracy.

In terms of fruit firmness prediction, the impact of different image features on model performance is obvious. When using color images, the model shows good prediction accuracy and effectively reflects the changes in firmness. However, for fluorescence images obtained using a single excitation light source and filter combination, the model performs relatively poorly, with prediction results lower than those of color images. When multiple fluorescence image features are combined, the performance of the model is significantly improved, showing stronger prediction ability. The model works best when combining color and fluorescence image features, as shown in Fig. 6 (B), with an R^2 value of 0.90, RMSE of 24.27, and RPD of 3.21 on the prediction set, which greatly improves the prediction accuracy of fruit firmness.

Combined with Fig. 3, it can be seen that the range of SSC changes in guava fruit at different maturity stages is relatively small, while the range of firmness changes is large, which is also reflected in the performance of the prediction model. For SSC prediction, the model was not as effective as the model using fluorescent image features as inputs when using color image features alone for prediction. This is because as the fruit ripens, the starch in the fruit hydrolyzes into soluble sugars, leading to an increase in SSC (Dolkar et al., 2017). This change is presented less on the fruit skin and hence difficult to capture in color images, whereas fluorescence images can be sensitive to reflect this change through the fluorescence properties of the chemical components in the guava epidermis. For firmness prediction, the performance when all fluorescence image features are used is similar to that of the model using color image features. In some cases, the effect of color images is even better than that of using fluorescence images alone. This phenomenon suggests that color images have a better advantage in detecting indicators that change more obviously, such as firmness. During maturity, the decrease in firmness of guava is accompanied by the loss of water (Spiller et al., 2018), which leads to water loss and shrinkage of the pericarp, and may cause the pericarp to wrinkle or become rough. Moreover, changes in firmness and color usually show a high degree of synchrony as they

Table 1
PLSR model prediction results of guava fruit SSC.

Image features	No. of features	No. of Latent Variables	Calibration set		Prediction set		
			R_C^2	$RMSE_C$ (%)	R_P^2	$RMSE_P$ (%)	RPD
Color images	18	4	0.39	1.42	0.39	1.38	1.28
Fluorescence images (Ex. 365 nm/Em. 450 nm)	18	10	0.42	1.37	0.41	1.39	1.31
Fluorescence images (Ex. 365 nm/Em. 525 nm)	18	10	0.64	1.08	0.63	1.11	1.64
Fluorescence image (Ex. 415 nm/Em. 525 nm)	18	11	0.62	1.06	0.62	1.23	1.63
All fluorescence images	54	24	0.79	0.77	0.78	0.98	2.11
Color and Fluorescence images	72	33	0.84	0.67	0.80	0.93	2.23

Table 2
PLSR model prediction results of guava fruit firmness.

Image features	No. of features	No. of Latent Variables	Calibration set		Prediction set		
			R_C^2	$RMSE_C$ (N)	R_P^2	$RMSE_P$ (N)	RPD
Color images	18	7	0.87	20.25	0.82	32.90	2.36
Fluorescence images (Ex. 365 nm/Em. 450 nm)	18	8	0.68	35.30	0.68	38.79	1.76
Fluorescence images (Ex. 365 nm/Em. 525 nm)	18	9	0.78	30.81	0.79	27.18	2.20
Fluorescence image (Ex. 415 nm/Em. 525 nm)	18	4	0.80	29.35	0.81	26.46	2.28
All fluorescence images	54	9	0.88	20.05	0.86	28.62	2.72
Color and Fluorescence images	72	12	0.90	17.76	0.90	24.27	3.21

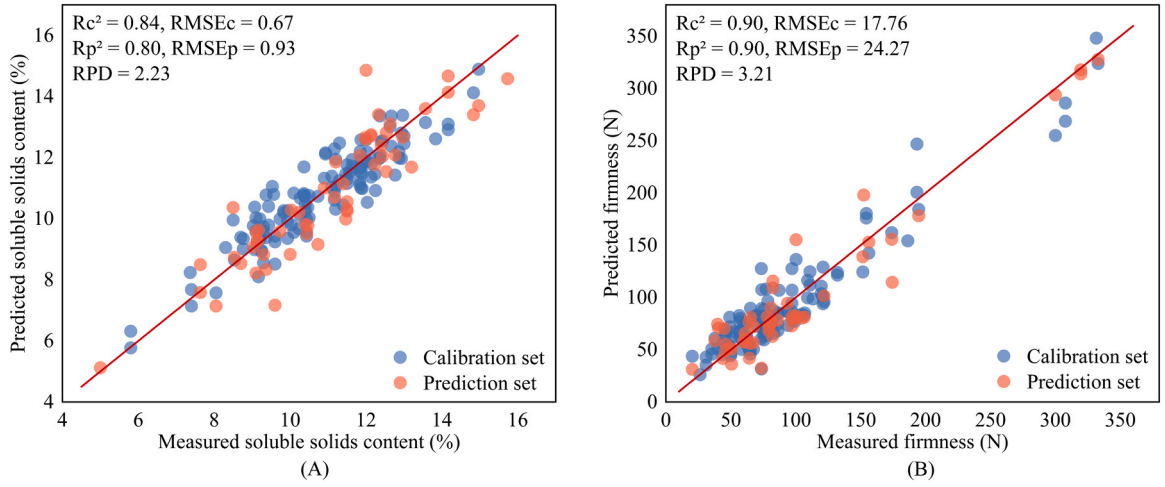

Fig. 6. Comparison of measured and predicted values of the PLSR model combining color and fluorescence images in predicting (A) soluble solids content and (B) firmness of guava fruit.

approach maturity, with a significant decrease in fruit firmness as the rind color shifts (Deepthi, 2017). This physiological phenomenon enables color images to effectively capture the process of firmness change. Combining external visible features and internal physiological changes can provide more comprehensive and accurate information for the maturity assessment of guava fruit. The combination of color images and fluorescent images can complement each other and improve the prediction effect to a certain extent. Therefore, the combination of fluorescent images and color images provides stronger technical support for non-destructive quality assessment of guava.

3.4.2. Classification model

In order to evaluate the classification performance of guava fruit at different maturity stages, the SVM model was used and calibrated and predicted based on different image features. Table 3 shows the classification performance evaluation results of the SVM classification model on the cross validation, calibration set, and prediction set.

Color images can effectively distinguish different maturity stages of guava and show strong classification performance. When all fluorescence image features are used, the classification performance is improved to a certain extent. Because fluorescence images have a strong ability to capture the changes in the chemical composition inside the

Table 3
Evaluation of SVM classification performance of guava fruit at different maturity stages.

Image features	LOO Cross-validation	Calibration set	Prediction set			
	Accuracy	Accuracy	Accuracy	Precision	Recall	F1-score
Color images	0.83	0.88	0.83	0.85	0.83	0.84
All fluorescence images	0.82	0.87	0.87	0.87	0.87	0.87
Color and Fluorescence images	0.91	0.99	0.91	0.92	0.91	0.91

fruit, they can further improve the accuracy of classification. The accuracy of the SVM model combining color image and fluorescence image features reached 0.99, 0.91 and 0.91 on the calibration set, cross validation and prediction set, respectively. The accuracy of the prediction set was 0.92, the recall was 0.91, and the F1-score was 0.91, with the best classification effect. The confusion matrix of the prediction set is shown in Fig. 7. Combining these two image features provided more comprehensive information, enabling the model to perform well in classifying the maturity stage of guava fruit. Fig. 8 shows the ROC curves of the SVM model combining color images and fluorescence images in the immature, green-mature and yellow-mature stages. The figure shows the ROC curves of the three stages and their corresponding area under curve (AUC) values. It can be seen from the figure that the model has very high accuracy in distinguishing immature fruit from other maturity stages. The model performed well in identifying green-mature and yellow-mature fruit, with slightly lower classification performance compared to the immature stage. This may be because the colors of the fruit become closer after maturity, resulting in less visual difference between the two. In addition, the gradual changes in the moisture content and internal composition of the fruit may also lead to smaller changes in the fluorescence signal between the green-mature and yellow-mature fruit, thus affecting the accuracy of the classification. But overall, the SVM model combining color images and fluorescence images showed high performance and still maintained a good classification effect.

When using NIR spectroscopy to predict the SSC of guava fruit, the R^2 of the PLSR prediction model using savitzky-golay second-order derivative filtering to process NIR spectral data was 0.76 (Pratiwi et al., 2023). Another study used standard normal variate transformation to preprocess NIR data, and the correlation coefficient (r) for predicting pulp firmness was 0.88 and the RPD was 2.2 (Ana et al., 2021). Compared with NIR spectroscopy, the optimal model in this study showed stronger predictive ability. In addition, the prediction accuracy of NIR technology depends to a certain extent on the quality and preprocessing method of spectral data, and is easily affected by ambient light, which also limits its widespread use in practical applications. SSC

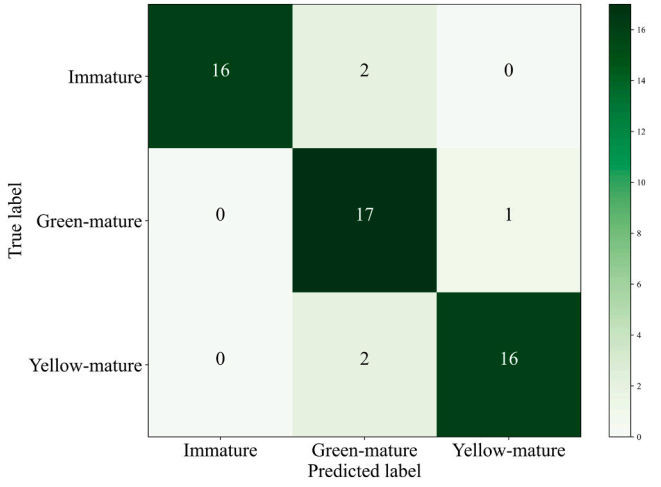

Fig. 7. Confusion matrix of the SVM classification model combining color images and fluorescence images in the prediction set.

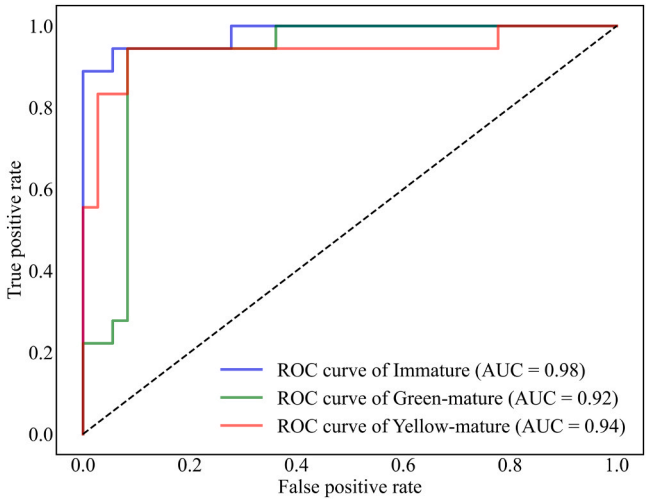

Fig. 8. ROC curve of the SVM classification model combining color images and fluorescence images at different maturity stages of guava fruit.

were predicted using HSI technology (Ni et al., 2024), and the R^2 of the prediction set was 0.92. Although HSI technology can achieve high-precision predictions, its high equipment and operating costs still limit its application in daily production. Compared with the above technologies, the fluorescence imaging technology used in this study shows significant advantages. Fluorescence imaging can be achieved using conventional UV–visible light sources and traditional camera equipment. It is not only low-cost, but also has greater flexibility and feasibility in practical applications. In addition, compared with the study that only used fluorescence spectral data to predict the SSC (RPD = 2.13) and firmness (RPD = 1.82) of guava fruit (Pertiw et al., 2023), this study significantly improved the prediction ability by fusing multi-light source image features, which fully demonstrated the superiority of fluorescence imaging technology in fruit quality assessment.

It is worth mentioning that this study did not use deep learning methods to explore the prediction ability, but its classification accuracy is still comparable to that of studies using deep learning (Azzahra et al., 2025; Low et al., 2024). This shows that the method proposed in this study can still achieve efficient fruit maturity classification in a resource-constrained environment, and has higher practicality and promotion potential. In summary, this study not only achieved a balance between cost-effectiveness and prediction accuracy through fluorescence imaging technology, but also provided a more promising solution for non-destructive testing of fruit quality.

4. Conclusions

In this study, a non-destructive detection method based on color and fluorescence images was proposed for SSC, firmness prediction and maturity classification of guava fruit. Through EEM analysis, the fluorescence characteristic areas of flavonoid compounds and other substances in the guava epidermis were successfully determined, which provided an important basis for the design of the imaging system. The color and fluorescence images of guava were obtained by using the

constructed multi-light source imaging system, and the PLSR and SVM models were combined to achieve accurate evaluation of fruit quality and maturity. The study found that the model using color image features alone did not perform as well as the fluorescence image feature model in SSC prediction. After fusing color and fluorescence image features, the comprehensive prediction performance of the model reached the optimum. The R^2 of PLSR model in SSC and firmness prediction for the prediction set were 0.80 and 0.90, and the RPD was 2.23 and 3.21, respectively. The accuracy, precision, recall, and F1-score of the SVM model in maturity classification were 0.91, 0.92, 0.91, and 0.91, demonstrating excellent prediction and classification capabilities.

Future research will further expand the applicability of this method to different guava varieties and explore its potential in early disease detection. It will also provide theoretical support for the development of convenient fruit quality testing equipment to promote the application of non-destructive testing technology in the guava fruit industry.

CRediT authorship contribution statement

Lin Shaozhen: Conceptualization, Data curation, Formal analysis, Investigation, Methodology, Project administration, Software, Supervision, Validation, Visualization, Writing – original draft, Writing – review & editing. **Yan Kangting:** Investigation, Methodology, Software, Validation, Writing – review & editing. **Zhang Zhijie:** Investigation. **Sun Zhilei:** Software. **Wang Linlin:** Investigation, Writing – review & editing. **Lan Yubin:** Funding acquisition, Project administration. **Zhang Yali:** Conceptualization, Funding acquisition, Project administration, Resources, Supervision, Writing – review & editing.

Declaration of Competing Interest

The authors declare that they have no known competing financial interests or personal relationships that could have appeared to influence the work reported in this paper.

Acknowledgement

The authors express their gratitude to the 111 Project (D18019) and the Laboratory of Lingnan Modern Agriculture Project (NT2021009) for the financial support.

Data availability

Data will be made available on request.

References

Ahmad, U., Purwanto, Y.A., Cahyo, L.D., 2018. Study on measuring the ripeness level of the 'Crystal' guava fruit using NIR (near infrared) spectroscopy. Acta Hortic. (1210), 43–50. https://doi.org/10.17660/ActaHortic.2018.1210.6.

Al Riza, D.F., Kondo, N., Catalano, P., Giametta, F., 2018. A preliminary study on the potential of front face fluorescence spectroscopy for Italian mono-cultivar extra virgin olive oil discrimination. J. Agric. Eng. 50 (1), 5–11. https://doi.org/10.4081/jae.2018.877.

Al Riza, D.F., Rulin, C., Tun, N.T.T., Yi, P.P.L., Thwe, A.A., Myint, K.T., Kondo, N., 2023. Mango (*Mangifera indica* cv. Sein Ta Lone) ripeness level prediction using color and textural features of combined reflectance-fluorescence images. J. Agric. Food Res. 11, 100477. https://doi.org/10.1016/j.jafr.2022.100477.

Ana, A.P., Purwanto, Y.A., Widodo, S., 2021. Prediksi indeks panen jambu "kristal" secara non destruktif menggunakan portable near infrared spectrometer. J. Keteknikan Pertan. 9 (3), 103–110. https://doi.org/10.19028/jtep.09.3.103-110.

Angulo-López, J.E., Flores-Gallegos, A.C., Torres-León, C., Ramírez-Guzmán, K.N., Martínez, G.A., Aguilar, C.N., 2021. Guava (*Psidium guajava* L.) fruit and valorization of industrialization by-products. Processes 9 (6), 1075. https://doi.org/10.3390/pr9061075.

Araújo, H.M., Rodrigues, F.F.G., Costa, W.D., Nonato, C.D.F.A., Rodrigues, F.F.G., Boligon, A.A., Athayde, M.L., Costa, J.G.M., 2015. Chemical profile and antioxidant capacity verification of *Psidium guajava* (Myrtaceae) fruits at different stages of maturation. EXCLI J. 14, 1020–1030. https://doi.org/10.17179/EXCLI2015-522.

Azzahra, S.N., Kamsyakawuni, A., Riski, A., 2025. Determining the ripeness level of Crystal guava fruit using backpropagation neural network. Lontar Komput. J. Ilm. Teknol. Inf. 15 (03), 186. https://doi.org/10.24843/LKJITI.2024.v15.i03.p04.

Braga, M.A., Marques, T.R., Simão, A.A., Botelho, L.N.S., Oliveira, L.S.D., Abreu, C.M.P. D., 2017. Mechanism of firmness loss in guava cv. Pedro Sato during ripening at room temperature. Food Sci. Technol. 38, 26–32. https://doi.org/10.1590/1678-457X.35416.

Bylappa, Y., Balasubramanian, B., Park, S., Joseph, K.S., Mathew Chacko, A., Narasimha Sudheer, W., Pappuswamy, M., Meyyazhagan, A., Liu, W.-C., Nag, A., Mostashari, P., Mousavi Khaneghah, A., 2024. Three decades of advances in extraction and analytical techniques for guava (*Psidium guajava* L.): a review. Results Chem. 10, 101708. https://doi.org/10.1016/j.rechem.2024.101708.

Bylappa, Y., Nag, A., 2023. Evaluation of phenolic and antioxidant profiles of pink Guava peel (*Psidium guajava* L. cv Arka kiran) during fruit ripening and its *in silico* Anti SARS-CoV-2 property. J. Appl. Nat. Sci. 15 (4), 1557–1562. https://doi.org/10.31018/jans.v15i4.5089.

Cortés, V., Ortiz, C., Aleixos, N., Blasco, J., Cubero, S., Talens, P., 2016. A new internal quality index for mango and its prediction by external visible and near-infrared reflection spectroscopy. Postharvest Biol. Technol. 118, 148–158. https://doi.org/10.1016/j.postharvbio.2016.04.011.

Deepthi, V.P., 2017. Physiological and biochemical changes during fruit growth, maturity and ripening of guava: A review. J. Postharvest Technol. 5, 1–6. ⟨https://journals.acspublisher.com/index.php/jpht/article/view/15678⟩.

Dolkar, D., Bakshi, P., Gupta, M., Wali, V.K., Kumar, R., Hazarika, T.K., Kher, D., 2017. Biochemical changes in guava (*Psidium guajava*) fruits during different stages of ripening. Indian J. Agric. Sci. 87 (2). https://doi.org/10.56093/ijas.v87i2.67659.

Fatchurrahman, D., Amodio, M.L., De Chiara, M.L.V., Chaudhry, M.M.A., Colelli, G., 2020. Early discrimination of mature-and immature-green tomatoes (*Solanum lycopersicum* L.) using fluorescence imaging method. Postharvest Biol. Technol. 169, 111287. https://doi.org/10.1016/j.postharvbio.2020.111287.

García-Plazaola, J.I., Fernández-Marín, B., Duke, S.O., Hernández, A., López-Arbeloa, F., Becerril, J.M., 2015. Autofluorescence: biological functions and technical applications. Plant Sci. 236, 136–145. https://doi.org/10.1016/j.plantsci.2015.03.010.

Gutiérrez, R.M.P., Mitchell, S., Solis, R.V., 2008. *Psidium guajava*: a review of its traditional uses, phytochemistry and pharmacology. J. Ethnopharmacol. 117 (1), 1–27. https://doi.org/10.1016/j.jep.2008.01.025.

Haralick, R.M., Shanmugam, K., Dinstein, I., 1973. Textural features for image classification. IEEE Trans. Syst. Man Cybern. 3 (6), 610–621. https://doi.org/10.1109/TSMC.1973.4309314.

Kamle, M., Baek, K.-H., 2017. Somatic embryogenesis in guava (*Psidium guajava* L.): current status and future perspectives. 3 Biotech 7 (3), 203. https://doi.org/10.1007/s13205-017-0844-0.

Klinbumrung, N., Teerachaichayut, S., 2018. Quantification of acidity and total soluble solids in guavas by near infrared hyperspectral imaging. AIP Conf. Proc. 2030 (1), 020209. https://doi.org/10.1063/1.5066850.

Lawaetz, A.J., Stedmon, C.A., 2009. Fluorescence intensity calibration using the Raman scatter peak of water. Appl. Spectrosc. 63 (8), 936–940. https://doi.org/10.1366/000370209788964548.

Li, B., Lecourt, J., Bishop, G., 2018. Advances in non-destructive early assessment of fruit ripeness towards defining optimal time of harvest and yield prediction—a review. Plants 7 (1), 3. https://doi.org/10.3390/plants7010003.

Low, E.S., Ong, P., Sim, J.Q., Sia, C.K., Ismon, M., 2024. Integrating deep learning with non-destructive thermal imaging for precision guava ripeness determination. J. Sci. Food Agric. 104 (13), 7843–7853. https://doi.org/10.1002/jsfa.13614.

M. Kadam, D., Kaushik, P., Kumar, R., 2012. Evaluation of guava products quality. Int. J. Food Sci. Nutr. Eng. 2 (1), 7–11. https://doi.org/10.5923/j.food.20120201.02.

Mehretie, S., Al Riza, D.F., Yoshito, S., Kondo, N., 2018. Classification of raw Ethiopian honeys using front face fluorescence spectra with multivariate analysis. Food Control 84, 83–88. https://doi.org/10.1016/j.foodcont.2017.07.024.

Mehretie, S., Inoue, S., Hayashi, T., Nakashima, H., Panintorn, P., Ninomiya, K., Kondo, N., 2024. Ultra sensor based on color and UV-excited fluorescence images for predicting quality attributes of Shine-Muscat grape bunches at different maturity stages. Food Chem. 461, 140894. https://doi.org/10.1016/j.foodchem.2024.140894.

Momin, A., Kondo, N., Al Riza, D.F., Ogawa, Y., Obenland, D., 2023. A methodological review of fluorescence imaging for quality assessment of agricultural products. Agriculture 13 (7), 1433. https://doi.org/10.3390/agriculture13071433.

Ni, C.-Y., Meng, Q.-H., Wu, Z.-F., Qiu, Z.-Q., Chang, H.-J., Huag, S., Chu, J.-H., Fang, J.-C., Li, Y., 2024. Rapid determination of soluble solids content in Psidium guava fruit based on hyperspectral imaging technology (in Chinese). J. Food Saf. Qual. 15 (11), 116–124. https://doi.org/10.19812/j.cnki.jfsq11-5956/ts.20240315014.

Nie, S., Al Riza, D.F., Ogawa, Y., Suzuki, T., Kuramoto, M., Miyata, N., Kondo, N., 2020. Potential of a double lighting imaging system for characterization of "Hayward" kiwifruit harvest indices. Postharvest Biol. Technol. 162, 111113. https://doi.org/10.1016/j.postharvbio.2019.111113.

Noh, H.K., Lu, R., 2007. Hyperspectral laser-induced fluorescence imaging for assessing apple fruit quality. Postharvest Biol. Technol. 43 (2), 193–201. https://doi.org/10.1016/j.postharvbio.2006.09.006.

Pertiw, S., Hutomo, A.S.F., Widodo, S., 2023. Non-destructive estimation of maturity level of 'Crystal' guava fruit by means of fluorescence spectroscopy. INMATEH Agric. Eng. 115–123. https://doi.org/10.35633/inmateh-71-09.

Pratiwi, E.Z.D., Pahlawan, M.F.R., Rahmi, D.N., Amanah, H.Z., Masithoh, R.E., 2023. Non-destructive evaluation of soluble solid content in fruits with various skin thicknesses using visible–shortwave near-infrared spectroscopy. Open Agric. 8 (1). https://doi.org/10.1515/opag-2022-0183.

Qiu, S.-L., Lin, B.-M., Zhang, S.-P., Zhang, S., Hong, J.-M., Zheng, K.-B., 2020. Quality characteristics and evaluation of guava fruit at different maturity stages (in Chinese).

J. Food Saf. Qual. 11 (24), 9230–9238. https://doi.org/10.19812/j.cnki.jfsq11-5956/ts.2020.24.029.

Shammi, S., Sohel, F., Diepeveen, D., Zander, S., Jones, M.G.K., 2023. A survey of image-based computational learning techniques for frost detection in plants. Inf. Process. Agric. 10 (2), 164–191. https://doi.org/10.1016/j.inpa.2022.02.003.

Sharma, A., Sharma, R.K., Siddiqui, S., Hazarika, T.K., 2017. Physiological changes and hydrolyzing enzyme activities during ripening of guava (*Psidium guajava*) fruits on-tree and in-storage. Indian J. Agric. Sci. 87 (12). https://doi.org/10.56093/ijas.v87i12.76519.

Spiller, S.H., Marques, T.R., Simão, A.A., Braga, M.A., Botelho, L.N.S., Machado, G.H.A., Fráguas, R.M., Santos, C.D.D., 2018. Modifications in the methods to extract pectin from cv. "Pedro Sato" guavas during ripening. Braz. J. Food Technol. 21, e2017032. https://doi.org/10.1590/1981-6723.03217.

Sun, M., Ju, H., Jiang, H., Yuan, W., Zhou, H., 2023. Research progress of nondestructive detection technology in fruit maturity (in Chinese). Food Ferment. Ind. 49 (17), 354–362. https://doi.org/10.13995/j.cnki.11-1802/ts.033166.

Takeda, L.N., Laurindo, L.F., Guiguer, E.L., Bishayee, A., Araújo, A.C., Ubeda, L.C.C., Goulart, R., de, A., Barbalho, S.M., 2023. *Psidium guajava* L.: a systematic review of the multifaceted health benefits and economic importance. Food Rev. Int. 39 (7), 4333–4363. ⟨https://www.tandfonline.com/doi/abs/10.1080/87559129.2021.2023819⟩.

Walt, S, van der, Schönberger, J.L., Nunez-Iglesias, J., Boulogne, F., Warner, J.D., Yager, N., Gouillart, E., Yu, T., 2014. Scikit-image: image processing in Python. PeerJ 2, e453. https://doi.org/10.7717/peerj.453.

Wang, H., Zhong, D., Lin, Z., Ou, Q., Qiu, G., 2023. Differences in volatile components between the mature green and mature yellow fruits of 3 kinds of red flesh guava (*Psidium guajava* L.) analyzed by GC-IMS (in Chinese). Sci. Technol. Food Ind. 44 (24), 301–310. https://doi.org/10.13386/j.issn1002-0306.2023020212.

Wong, T.T., 2015. Performance evaluation of classification algorithms by k-fold and leave-one-out cross validation. Pattern Recognit. 48 (9), 2839–2846. https://doi.org/10.1016/j.patcog.2015.03.009.

Computers and Electronics in Agriculture 237 (2025) 110549

Contents lists available at ScienceDirect

Computers and Electronics in Agriculture

journal homepage: www.elsevier.com/locate/compag

Multiple light sources excited fluorescence image-based non-destructive method for citrus Huanglongbing disease detection

Kangting Yan [a,c], Xipeng Fang [c,e], Weiguang Yang [b,c], Xidan Xu [c,e], Shaozhen Lin [c,e], Yali Zhang [c,e,*], Yubin Lan [b,c,d,*]

[a] Department of Mechatronic Engineering, Guangdong Polytechnic Normal University, Guangzhou 510665, China
[b] College of Electronic Engineering (College of Artificial Intelligence), South China Agricultural University, Guangzhou 510642, China
[c] National Center for International Collaboration Research on Precision Agricultural Aviation Pesticides Spraying Technology, Guangzhou 510642, China
[d] Guangdong Laboratory for Lingnan Modern Agriculture, Guangzhou 510642, China
[e] College of Engineering, South China Agricultural University, Guangzhou 510642, China

ARTICLE INFO

Keywords:
Citrus Huanglongbing
EEM
Non-destructive detection
Fluorescence imaging
Machine learning

ABSTRACT

Citrus Huanglongbing (HLB) poses a significant threat to citrus orchards. Timely HLB screening of citrus trees is essential for citrus orchard management. This study developed a multi-excitation fluorescence imaging system based on the correlation between HLB stress and flavonoid fluorescence characteristics. The feasibility of using fluorescent images to classify healthy, macular (nutrient-deficient, not relate to HLB) and HLB-infected citrus fruits was explored. Initially, three-dimensional fluorescence spectra of citrus peels at maturity were scanned and the obtained Excitation-Emission Matrices (EEMs) were analyzed to screen four fluorescence characteristic regions (FCR1-FCR4) that were sensitive to HLB-infected citrus. Subsequently, four fluorescence imaging conditions (G1: EX = 365 ± 20 nm, EM = 525 ± 20 nm, G2: EX = 415 ± 20 nm, EM = 525 ± 20 nm, B1: EX = 308 ± 20 nm, EM = 450 ± 20 nm, and B2: EX = 365 ± 20 nm, EM = 450 ± 20 nm) were designed based on characteristic fluorescence bands. The imaging system primarily utilizes standard CMOS cameras and optical filters for image acquisition, offering significant advantages in terms of operational simplicity and cost-effectiveness. An HLB classification model was constructed using the Random Forest (RF) algorithm based on color feature parameters of fluorescence images, with a classification accuracy of up to 87.5 %. When the top 10 image feature parameters with the highest contribution rate were selected to construct the classification model considering the equipment cost, the accuracy is 83.33 %. This study demonstrated that fluorescence imaging utilizing flavonoid fluorescence characteristics enables non-destructive and rapid detection of citrus HLB. This approach provides valuable data and technical support for decision-making on spring orchard cleanup and control of HLB.

1. Introduction

Huanglongbing (HLB) is one of the most devasting diseases in citrus production, exhibiting characteristics of strong outbreaks, rapid progression, and significant harm (Bové, 2006; Da Graça et al., 2016). It is widely distributed in major citrus producing areas in China, affecting citrus yield and quality and shortening the economic life of citrus trees (Zheng et al., 2018; Zhou, 2020). Currently, there are no resistant varieties or specific effective treatments for HLB. The primary strategies for control involve the timely detection of infected plants, removal and cleaning of diseased trees, and enhancement of orchard water and fertilizer management (Deng et al., 2012). Consequently, the immediate identification of HLB trees is of paramount importance. In addition, the presence of HLB bacteria is most pronounced on trees in winter, which also represents the most favorable period for detection (Yu et al., 2017). Therefore, for citrus orchard management, conducting a health survey of citrus trees in winter maturity period is beneficial for the subsequent management decisions of the orchard and is a critical step in ensuring the yield of the orchard for the following year.

Currently, screening of HLB-infected trees in citrus orchards is mainly based on manual visual observation or periodic Polymerase Chain Reaction (PCR) identification of suspected diseased trees by professional testing units. Visual observation by humans is subjective, and particularly prone to misdiagnosis due to the similarity between

* Corresponding authors at: South China Agricultural University, 483 Wushan Road, Tianhe District, Guangzhou, Guangdong, China.
E-mail addresses: ktyan@stu.scau.edu.cn (K. Yan), ylzhang@scau.edu.cn (Y. Zhang), ylan@scau.edu.cn (Y. Lan).

https://doi.org/10.1016/j.compag.2025.110549
Received 24 January 2025; Received in revised form 26 April 2025; Accepted 12 May 2025
Available online 21 May 2025
0168-1699/© 2025 Elsevier B.V. All rights are reserved, including those for text and data mining, AI training, and similar technologies.

macular (deficiency yellowing, not relate to HLB) and those of HLB. PCR is a molecular detection technique that amplifies the DNA of HLB bacteria for disease detection (Park et al., 2018; Bao et al., 2020). Common methods include duplex PCR and real-time quantitative PCR, which offer excellent sensitivity and accuracy in detecting HLB bacteria. However, the detection process is invasive, requiring specific primers as amplification templates, and is time-consuming and costly.

In recent years, machine learning has emerged as one of the most transformative technologies of the 21st century (Horvitz and Mulligan, 2015). It has been widely applied in agriculture (Liakos et al., 2018; Benos et al., 2021; Lu et al., 2024) because of its ability to improve data processing (Mahesh, 2019) and to understand data-intensive processes in the agricultural operational environment.

To further improve the detection efficiency of HLB-infected citrus trees, spectral and spectral imaging techniques are applied for the rapid detection of citrus HLB. Common spectral techniques for citrus HLB detection include visible light, hyperspectral, and near infrared (Arredondo Valdés et al., 2016; Xiao et al. 2023). Hyperspectral imaging can obtain high-precision spectral data over a broad range of wavelengths, allowing for more nuanced spectral information detection of HLB samples (Khan et al., 2018; Lu et al., 2020). Some researchers (Liu et al., 2018; Moriya et al., 2019; Lan et al., 2019) utilized hyperspectral technology for monitoring HLB-infected citrus trees and obtained good classification results. Near-infrared spectroscopy involves obtaining absorption spectra in the near-infrared region through the diffuse reflection method based on the overtone or rotational vibrations of hydrogen-containing groups in organic compounds (Anderson and Walsh, 2022). Lan et al. (2020) and Sindhuja Sankaran et al. (2011) explored the effectiveness of using near-infrared multispectral imaging for detecting HLB-infected citrus trees. Currently, most of the citrus HLB detection studies based on the above spectral technologies mainly use the differences in spectral and spectral image features to analyze, which involves a complex spectral data processing process and less exploration of HLB-induced physiological changes in citrus.

Fluorescence imaging primarily utilizes the photoluminescence effect of fluorescent substances (Guilbault, 2020), allowing for a more intuitive reflection of phenotypic parameters of crops by exciting the fluorescence properties of these substances (Muharfiza et al., 2017; Abamba Omwange et al., 2022; Huang et al., 2022). Currently, research on using chlorophyll fluorescence for the detection of HLB in citrus primarily focuses on the detection of citrus leaves (Wetterich et al., 2016; Weng et al., 2020). The stress of HLB affects the content of substances such as starch and sucrose in citrus leaves, and the changes in photochemical reactions can be used to reflect the health status of citrus leaves (Meng et al., 2019; He et al., 2022; Chen et al., 2022). However, experiments using chlorophyll photochemical reactions require 20 min of dark adaptation of citrus leaves to obtain accurate chlorophyll fluorescence signals, which limits the detection efficiency to some extent. There is currently little research on fluorescence imaging of HLB-infected citrus fruits. Relevant studies indicate that citrus peels are rich in flavonoid compounds (Wang et al., 2019; Liu et al., 2022), and their molecular structures possess the characteristics of fluorescent compounds (Guilbault, 2020; Ranulfi et al., 2016). The abundant flavonoid compounds in citrus peels undergo corresponding changes under HLB stress (Massenti et al., 2016; Hijaz et al., 2020; Zhang et al., 2022), making the application of fluorescence imaging technology for HLB detection feasible. This study aims to monitor citrus HLB using the fluorescence characteristics of citrus peels.

The objective of this study is to develop a multi-source excitation fluorescence imaging system capable of non-destructively detecting citrus fruits of varying health statuses (HLB, macular, and healthy). By analyzing the Excitation Emission Matrix (EEM) of citrus peels at different health stages during maturity, we aim to select excitation and emission wavelengths that significantly correlate with the healthiness of citrus. Based on these characteristic wavelengths, we will construct a fluorescence imaging system and image citrus of different health statuses. We will extract feature parameters of citrus fluorescence images in different color spaces, train classification models, and obtain a model capable of classifying citrus fruits by their health status. This study focuses on *Citrus reticulata 'Shiyue Ju'* as the research subject, conducting fluorescence imaging of citrus fruits during the winter harvest phase. The goal is providing more specific and detailed diagnosis of HLB-infected citrus and providing data support for spring orchard cleaning.

The overall data collection and data processing process of this paper is shown in Fig. 1.

2. Materials and methods

2.1. Sample preparation

The samples utilized in this study were obtained from the Shatangju Agricultural Industrial Park, Huangtian Town, Sihui City, Guangdong Province, China (112.52°E, 23.43°N). The citrus leaves and fruit samples collected for this experiment were obtained from *Citrus reticulata 'Shiyue Ju'* trees that had been transplanted to the orchard four years prior and had already begun bearing fruit. Additionally, all HLB-infected citrus trees marked in this study exhibited visible disease symptoms (mottling and yellowing) on less than one-third of their total branches. These HLB-infected trees were classified as mildly to moderately diseased (Mei et al., 2014; Yan et al., 2024).

The samples were derived from four distinct planting areas within the orchard, as depicted in Fig. 2 (a). Due to the similarity in characteristics between HLB-infected trees and those suffering from nutrient deficiency-induced macular, in November 2022, qPCR testing was conducted on citrus trees in the four areas. The qPCR results were used to verify and adjust the classification of the health status of these citrus trees (healthy, macular, HLB). A total of 16 citrus trees were marked for this study (8 trees carrying the HLB pathogen, 4 trees with nutrient deficiency-induced macular, and 4 healthy trees). These trees were subjected to long-term monitoring from November 2022 to December 2023 to ensure accurate assessment of their health status. Citrus fruits were carried out in January 2023 and December 2023, with the time series of sampling and the number of citrus fruits shown in Fig. 2(b). It should be noted that the number of citrus fruits picked from each tree was not fixed due to variations in tree health status affecting their fruit-bearing capacity. Additionally, although citrus fruit size exhibits some differences under HLB stress or nutrient deficiency stress, this study mainly investigated the effect of fluorescent substances within the citrus peels on the characterization of citrus HLB, therefore fruit size variations did not affect the final results of this study.

The citrus fruits collected on January 10, 2023, were primarily utilized for the detection of three-dimensional fluorescence spectra of the peel, comprising a total of 64 fruits. The citrus fruits harvested in December 2023 were mainly employed for fluorescence imaging. On December 13, 2023, a total of 99 citrus fruits were collected, and on December 21, 2023, a total of 156 citrus fruits were gathered. In this experiment, all citrus fruits harvested in the field were preserved in sealed bags labeled with specific citrus tree identifiers and transported to the laboratory on the same day. Subsequently, they were stored in a 5 °C environment to await further experimental procedures.

2.2. EEM measurement

Three-dimensional fluorescence spectroscopy can visually describe the relationship between the fluorescence intensity of the substance with the change of emission wavelength and excitation wavelength, which makes it possible to more intuitively observe the fluorescence characteristics (such as fluorescent characteristic peaks and fluorescent characteristic regions) of the substance. This can also simplify the experimental data screening process. In addition, the three-dimensional fluorescence spectroscopy has fingerprints, which can qualitatively and

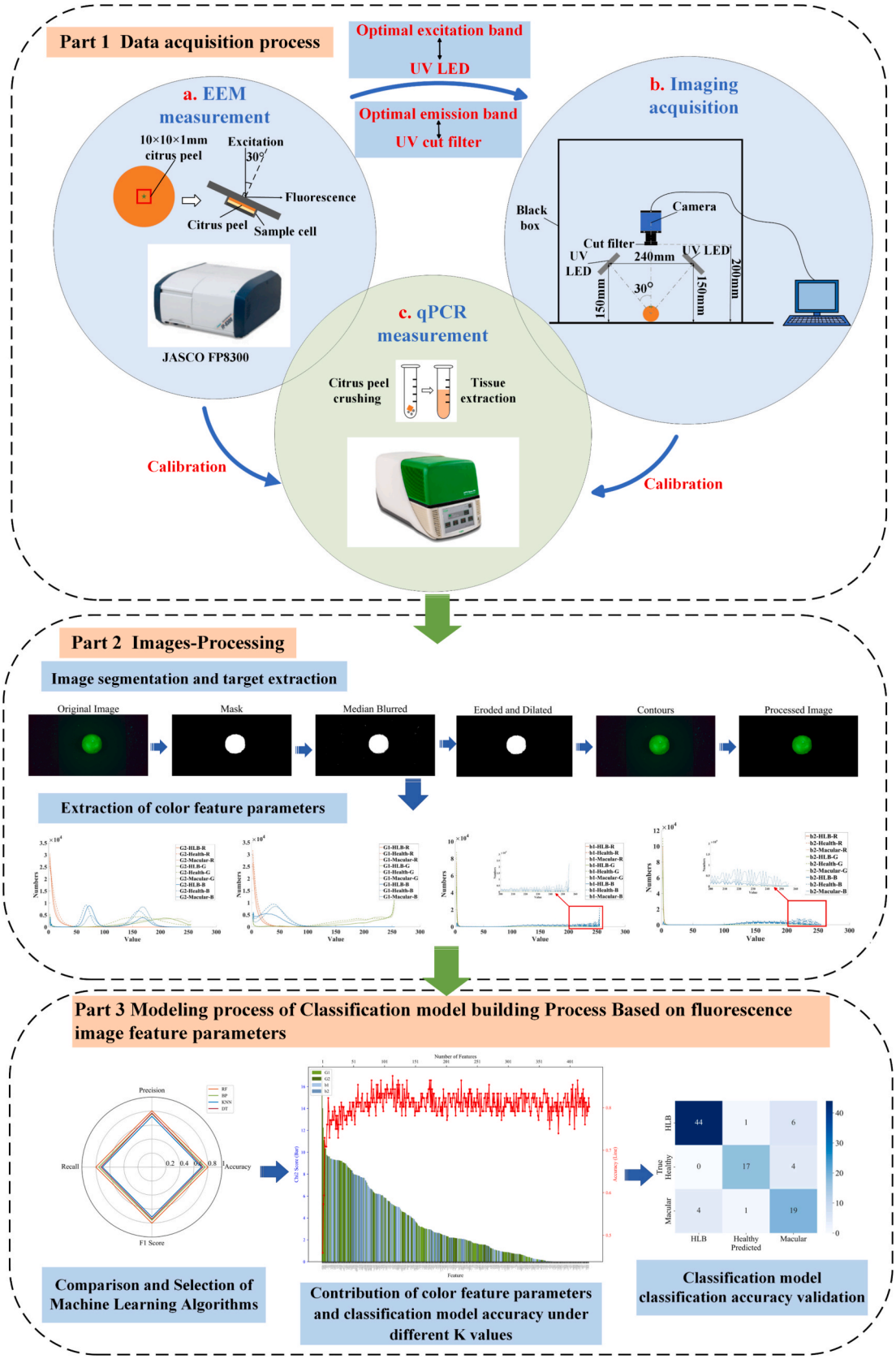

Fig. 1. Data acquisition and data processing technical route.



(a)

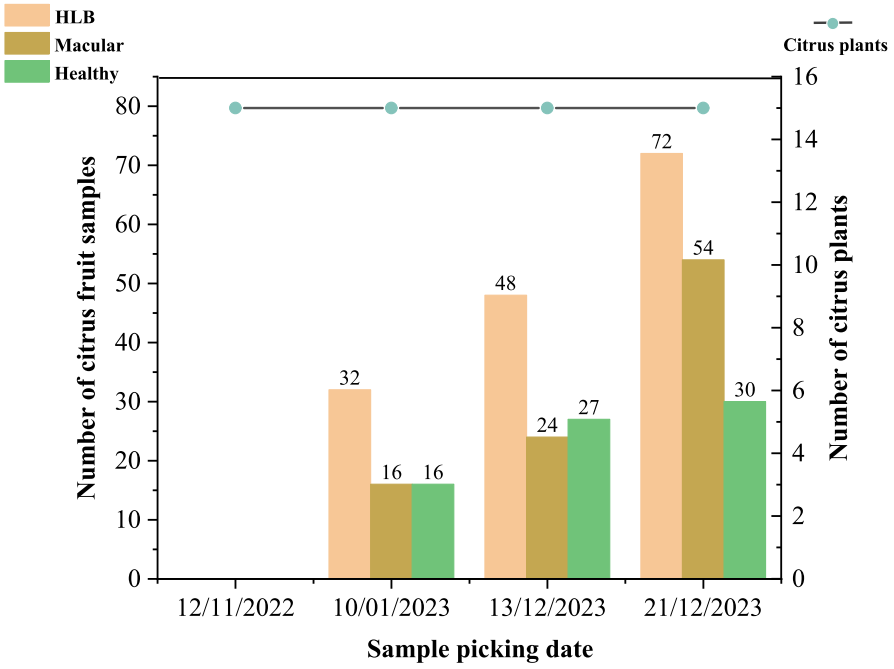

(b)

Fig. 2. Orchard planting area and some marked citrus trees (a) and time series of citrus fruits collection (b).

quantitatively analyze specific substances in multi-component mixtures, and is therefore widely used in the detection of agricultural products (Omwange et al., 2020; Huang et al., 2022). In this study, a fluorescence spectrophotometer (JASCO FP-8300, Jasco Inc., Japan) was used to scan the citrus peel for three-dimensional fluorescence spectra, thereby obtaining the EEM. Initially, the parameters of the fluorescence spectrophotometer were configured as follows: the photomultiplier tube (PMT) was set to Low Sensitivity, with an excitation wavelength range of 200–600 nm and an emission wavelength range of 210–700 nm. The interval and bandwidth for both excitation and emission measurements were set at 5 nm, respectively. Prior to the formal detection of citrus peels, 3 mL of pure water was added to a quartz cuvette with dimensions of 10 mm × 10 mm × 42 mm. A water Raman calibration was performed to convert the subsequent output sample EEM data from arbitrary units to Raman units.

The procedure for three-dimensional fluorescence spectroscopy of citrus peels was as follows: first, the surface of the peel was rinsed with pure water to remove dust and impurities from the surface. The peel was dried with cotton wool. Then, a square peel sample with an area of 10 × 10 mm and a thickness of 1 mm was cut at the top of the fruit using a razor blade, and the sample was transferred to a quartz stone cell (Sapre powder sample cell, MODEL FP-1061, Jasco Inc., Japan). Finally, the quartz stone cell containing the citrus peel was held in the solid sample holder for spectroscopic examination. The schematic diagram of citrus peel sampling and EEM detection is shown in Fig. 3.

2.3. Imaging system construction and fluorescence image acquisition

The imaging system is shown in Fig. 4, which is mainly composed of an image acquisition system, an illuminating system, and a computer. Among them, the image acquisition system contains the imaging camera, lens and filter. The imaging camera (ME2P-900-43U3M, CMOS, China Daheng Co., Ltd., Beijing, China) was vertically mounted above the imaging base plate; The imaging lens (M0828-MPW3, China Daheng Co., Ltd., Beijing, China) was also perpendicular to the imaging base plate, with the front end of the lens 200 mm from the imaging base plate. The lens parameters were set to Focus = 0.15 m and Iris = F2.8. The filter was mounted to the camera lens by means of a threaded structure. The illuminating system consists of three excitation light sources (415 nm ring excitation light JH-RS9090-UV, Dongguan Jutu Optoelectronics Technology Co., Ltd, China; 365 nm ring excitation light P-RL-100–90-UV365, Beijing HaiRam Optoelectronics Co. Ltd, China; 308 nm matrix excitation light GS35WU308-001P20DF-41, Zhongshan Guangsheng Semiconductor Technology Co., Ltd.). The ring light source was symmetrically installed on both sides of the imaging camera, the distance between the left and right light sources is 240 mm, the angle of the light source is 30°, and the vertical distance between the center of the light source and the imaging base plate is 150 mm. The matrix light source was placed above the right side of the sample at an angle of 30°, with the center of the light source at the same vertical height of 150 mm from the imaging base plate. In addition, an acrylic sheet black box was used to provide a dark imaging environment, and the host computer was used to adjust imaging parameters and store imaging data. The imaging system has an image resolution of 4200 (H) × 2160 (V) pixels and an imaging depth of 2 mm. The physical drawing of the imaging system is shown in Fig. 4 (b).

In this study, two kinds of filters were selected (450 ± 20 nm cut-off filter AZURE-BP450 ± 20 nm, 525 ± 20 nm cut-off filter AZURE-BP 525 ± 20 nm, Beijing Blueheart Times Technology Co., Ltd., China). To ensure the accuracy of the filters, a high-precision geophysical spectrometer (FieldSpec® 4, Malvern Panalytical, UK) was used to calibrate the filters for filter light source cut-offs, and the results of the tests were all within the error range, as shown in Fig. 4 (c).

A total of 240 citrus fruits (15 fruits were screened out of the original 255 citrus samples that were damaged due to impacts during transportation), harvested in December 2023, were subjected to fluorescence imaging using four imaging conditions. And prior to fluorescence imaging, citrus fruit samples were simply washed with clean water and air-dried. These imaging conditions were designated as G1: EX = 365 ± 20 nm, EM = 525 ± 20 nm (365 nm ring excitation light and 525 ± 20 nm cut-off filter); G2: EX = 415 ± 20 nm, EM = 525 ± 20 nm; B1: EX = 308 ± 20 nm, EM = 450 ± 20 nm and B2: EX = 365 ± 20 nm, EM = 450 ± 20 nm. The camera exposure time was set to 0.85 s for fluorescence imaging. Each fruit was imaged first at its apex and then rotated 180° to image its base. For each light source combination, 480 fluorescence images were acquired, categorized into HLB (236 images), macular (144 images), and healthy (100 images). Consequently, a total of 1920 fluorescence images were obtained across the four light source combinations. Additionally, to facilitate comparative analysis of image quality under fluorescence imaging conditions versus white light conditions, a set of normal color images was captured for each fruit, resulting in 480 color images in total.

2.4. qPCR measurement

Real-time quantitative PCR (qPCR) is a molecular diagnostic technique capable of precisely identifying the presence of citrus HLB pathogens. In this study, qPCR was primarily employed to quantify the pathogen load within the peel of citrus fruits, thereby facilitating the calibration and categorization of the experimental citrus samples.

The test instrument was a Real-time quantitative PCR instrument (CFX Opus 96, Bio-Rad) and the main materials used were: 0.5 % NaOH, Premix Ex *Taq* (Probe qPCR), HLBas/HLBr (Sangon Biotech (Shanghai) Co. Ltd.). The specific steps for qPCR were as follows: (1) for each citrus

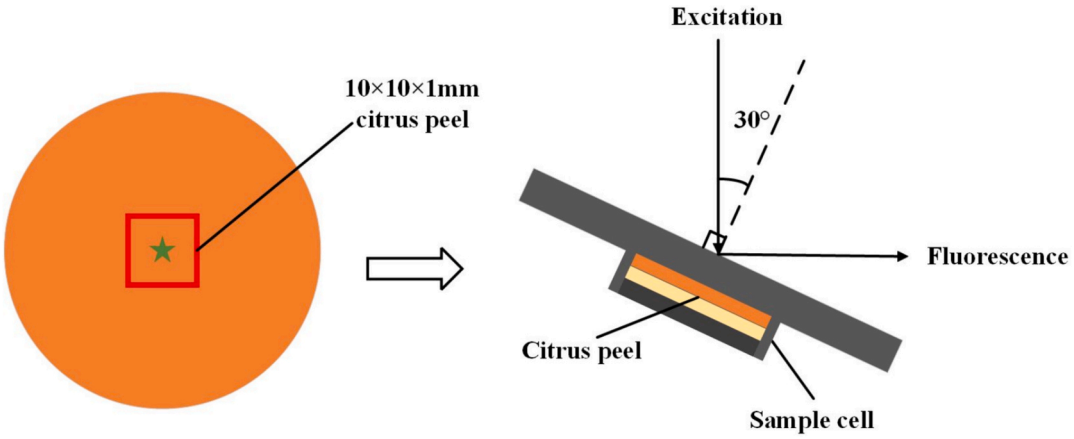

Fig. 3. Schematic diagram of citrus peel sampling and EEM testing.

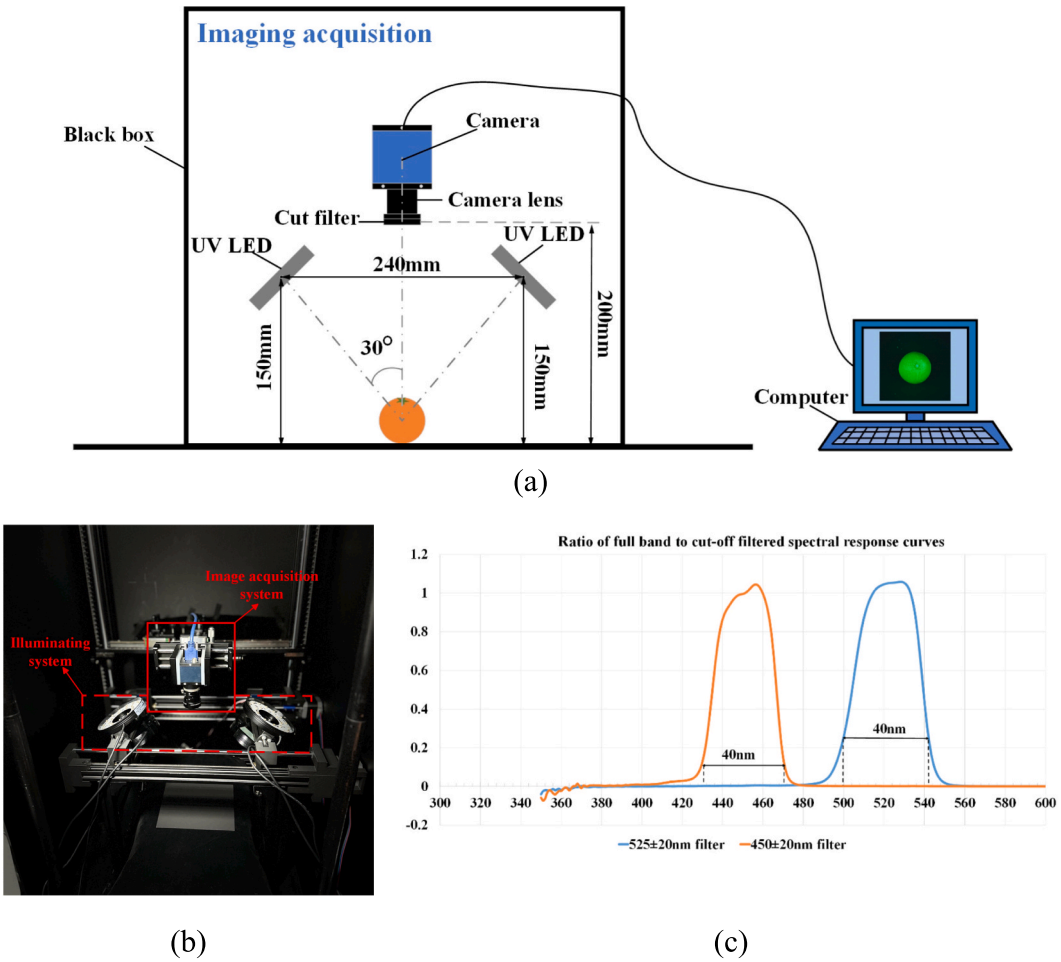

Fig. 4. Schematic diagram of the relative positions of the components of the fluorescence imaging system (a), Physical drawing of the fluorescence imaging system (b), Spectral response curves of two cut filters (c).

fruit tested, a 5 × 5 mm area of citrus peel was taken from the pith and loaded into a 5 mL centrifuge tube with steel beads, and then centrifuged and crushed in a uniform manner; (2) citrus peel genomic DNA was extracted with the addition of 0.5 % NaOH solution; (3) Pipette 10 μL of supernatant from the extraction solution in Step (2) and dilute it in a 5 mL centrifuge tube with 240 μL Te Buffer solution as DNA template; (4) Prepare PCR reaction system: Premix Ex Taq (Probe qPCR) 12 μL, HLBas/HLBr amplification primers 0.5 μL each, HLBp probe 1.0 μL, DNA template 1 μL, add ddH_2O to make up to 25 μL. (5) Perform the qPCR reaction procedure.

2.5. *Fluorescence image processing and classification modeling*

2.5.1. *Segmentation of fruit fluorescence images*

In the acquisition of fluorescence images, background impurities such as dust and fibers may fluoresce under ultraviolet excitation,

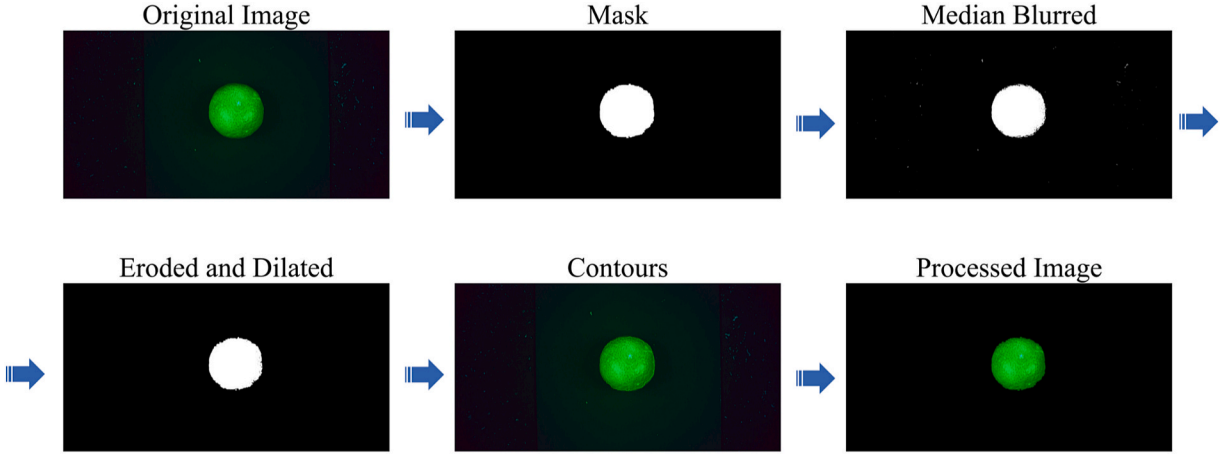

Fig. 5. Fluorescence image pre-processing process.

potentially influencing the data processing outcomes. To uphold the precision and dependability of classification models established on fluorescence image characteristics, this study conducts preprocessing and image segmentation on the obtained fluorescence images to isolate the fruit images. The process was mainly carried out based on Python 3.7 and the OpenCV computer vision library (4.5.3). The procedure is depicted in Fig. 5.

First, the image is read and an exhaustive method is used to determine the segmentation threshold, and then an initial mask is generated based on this threshold segmentation. Subsequently, the noise of the image is eliminated using median filtering and erosion and expansion methods. Next, the contours of fruits in the image are detected and preserved by thresholding to eliminate smaller noise regions. Finally, the final mask is generated by drawing the filtered contours and operated with the original image by bitwise and to obtain the image with background noise elimination.

2.5.2. Image color feature screening

(1) Extraction of color feature parameters

In this study, color feature parameters were extracted using RGB (red, green, blue), HSV (hue, saturation, value), Lab (L: brightness, a: positive for red, negative for green; b: positive for yellow, negative for blue), YCbCr (Y for brightness, U, V for color difference) for color feature parameter extraction. For each color space, the histogram is analyzed to compute the mean, median, maximum values, and their ratios. Additionally, parameters such as the grayscale value and the grayscale co-occurrence matrix of each image are incorporated into the analysis. Under four different lighting conditions (G1, G2, B1, B2), each color space yields 108 sets of features. The relevant computational formulas are detailed in Exhibit A. Feature parameter extraction was conducted using Matlab 2016a on the dataset.

(2) Max-Min Normalization

In data preprocessing, data standardization is important for the effective use of data information and model stability. In this paper, Max-Min Normalization is used for data normalization. Its specific implementation process is shown in formula (1).

$$x_{norm} = \frac{x - x_{\min}}{x_{\max} - x_{\min}} \tag{1}$$

Where x is the original data, x_{norm} is the normalized data, and x_{min} and x_{max} are the minimum and maximu0m values of the features respectively. Through this transformation, the influence of different feature scale differences can be eliminated, and the distribution characteristics of the original data are retained, which is conducive to the subsequent machine learning algorithms for the analysis and extraction of data feature information.

(3) chi-square test

In the process of feature engineering for machine learning, selecting the most representative features can significantly enhance the performance of the model. In this study, the chi-square test was used for the correlation analysis between color feature parameters and health status of citrus samples. In this case, the chi-square test is required to calculate the chi-square statistic between the standardized color feature data and the health status classification of citrus samples. The calculation formula of chi-square statistics is shown in formula (2).

$$\chi^2 = \sum \frac{(O_i - E_i)^2}{E_i} \tag{2}$$

In the formula, O_i represents the observed frequency, and E_i denotes the expected frequency. The steps of chi-square test for color feature parameters in this study are mainly as follows: (1) conduct chi-square independence test for each color feature parameter and citrus health status to obtain the chi-square statistic; (2) use the chi-square statistic to measure the degree of correlation between each color feature parameter and the health status of citrus samples. The larger chi-square statistics indicate the higher degree of correlation between the color feature parameter and the health state of citrus samples.

2.5.3. Classification modeling approach

This study utilizes a total of 1920 fluorescent images obtained under four imaging conditions, G1, G2, B1, and B2, as the sample set. To achieve a more effective classification model for citrus HLB, four commonly used machine learning methods for classification, as reported by Yusuf et al. (2021), were chosen based on the type of the dataset used in this study. These methods include K-Nearest Neighbors (KNN) (Shichao et al., 2017; Zhang et al., 2017a,b; Xiang et al., 2018), Decision Tree (DT) (SONG and LU, 2015; Desai and Chaudhary, 2016; Sutharaan, 2016), Random Forest (RF) (Prajwala, 2015; Cáceres et al., 2017; Wang et al., 2018), and Back Propagation (BP) (Chauvin, 1995; Cilimkovic, 2010). The study was conducted in a Python 3.7 programming environment, utilizing the scikit-learn (0.21.3) and NumPy (1.16.5) libraries to develop classification models for citrus HLB detection. And the fluorescence image data under each imaging condition, 80 % was randomly selected as the training sample set and the remaining 20 % as the test sample set.

2.5.4. Classifier parameter selection

During the training process of machine learning models, the selection of hyperparameters is crucial for the model's performance. This paper employs the Grid Search Cross-Validation method to optimize the hyperparameters of the RF Classifier. The relevant model parameters are shown in Table 1.

2.5.5. Evaluation index

To quantitatively analyze the performance of models, researchers have proposed a variety of evaluation indicator for machine learning classifiers. This study employs four evaluation indicators: *Precision*, *Accuracy*, *Recall*, and the *F*1 score to assess model performance. The formulas are as follows (3)–(6). In the formulas, *TP* represents True Positives, *TN* represents True Negatives, *FP* represents False Positives, and *FN* represents False Negatives.

$$Accuracy = \frac{TP + TN}{TP + TN + FP + FN} \tag{3}$$

$$Precision = \frac{TP}{TP + FP} \tag{4}$$

$$Recall = \frac{TP}{TP + FN} \tag{5}$$

$$F1 = 2 \times \frac{Precision \times Recall}{Precision + Recall} \tag{6}$$

Table 1
Important parameters of the model.

Type of Parameters	Value
Number of estimators	150 ~ 250
Maximum depth	(none, 10, 20)
Minimum samples per split	(1, 2, 3)
Minimum samples per leaf	(1, 2, 3)

3. Results and discussion

3.1. qPCR results

In this study, the qPCR was used to detect the presence of HLB bacteria in citrus peels. The results of qPCR assay were based on the Cycle threshold value (Ct) as an index parameter, and the Ct value is the number of cycles required for the amplification product to reach the detectable level. Samples with Ct $>$ 35 were defined as undetected (negative) for HLB bacteria, while those with Ct $\leq$ 35 were defined as detected (positive). In the experiment, qPCR was performed on 64 citrus fruits from January 2023 and 240 citrus fruits from December 2023.

Among the 64 citrus fruits collected in January 2023, 32 were positive and 32 were negative. For the samples harvested on December 13, 2023, 45 were positive and 48 were negative. For the samples harvested on December 21, 2023, 69 were positive and 78 were negative. Some of the qPCR results are shown in Fig. 6, where the control group consists of HLB positive control samples, ensuring the validity of the qPCR results. These qPCR results are used to calibrate and classify the fluorescence imaging dataset, ensuring the accuracy and reliability of the classification model.

3.2. EEM of citrus peels in different health states

All 64 citrus samples collected in January 2023 were subjected to three-dimensional fluorescence spectroscopy scanning. The typical three-dimensional fluorescence spectra of HLB, macular, and healthy citrus peels are shown in Fig. 7. The color bar on the right of the image represents fluorescence intensity values in Raman units. It can be observed that the three-dimensional fluorescence spectra of citrus peels in different health conditions all exhibit two distinct fluorescence characteristic regions: Fluorescence Characteristic Region A (EX = 300–380 nm, EM = 420–480 nm) and Fluorescence Characteristic Region B (EX = 300–420 nm, EM = 500–580 nm). These regions include four fluorescence characteristic peaks: Fluorescence Peak 1: EX/EM = 365/525 nm, Fluorescence Peak 2: EX/EM = 415/525 nm, Fluorescence Peak 3: EX/EM = 308/450 nm, and Fluorescence Peak 4:EX/ EM = 365/450 nm. Analysis of the three-dimensional fluorescence spectra reveals that within the A and B fluorescence regions, the fluorescence intensity values of the peels generally follow the pattern: HLB peels $<$ macular peels $<$ healthy peels.

Centered on the four fluorescence peaks, spectral data matrices within a range of 20 $\times$ 20 nm were extracted (e.g., based on Fluorescence Peak 1, Fluorescence Characteristic Region (FCR) 1 was defined as EX = 345–385 nm, EM = 505–545 nm) and the mean values were calculated. The data for the 64 citrus fruit samples are shown in Fig. 8. It can be observed that the mean fluorescence intensity values in the FCR1-FCR4 fluorescence characteristic regions for citrus peels of different health conditions exhibit varying degrees of difference. The main trend of variation is that the fluorescence intensity of HLB peels is lower than that of macular peels, which in turn is lower than that of healthy peels.

To further explore the correlation between the health status of citrus and the fluorescence intensity in each fluorescence characteristic region, Analysis of Variance (ANOVA) was conducted on the average fluorescence intensity values of 64 citrus fruits across the various fluorescence characteristic regions, which included three health status treatments (HLB, Macular, Healthy) with unequal replication numbers. The results of the ANOVA, as shown in Table 2, indicate that the p values for FCR1-FCR4 fluorescence characteristic regions are all less than 0.01. This suggests that there is at least one group of data in the fluorescence intensity values of citrus peels with different health statuses that significantly differs from another group in these four fluorescence characteristic regions.

Performing multiple comparison tests on the mean values, the results are presented in Table 3. The p values are all less than 0.01, indicating that there is a significant difference between the two mean values corresponding to that data. Analysis reveals that within the FCR1-FCR4, the fluorescence intensity values of HLB peels significantly differ from those of both macular and healthy peels.

In summary, based on the results of the ANOVA and multiple comparison analysis, it can be concluded that the different health statuses of citrus fruits can be reflected through the FCR1-FCR4 as a window of observation.

According to the literature, the content of flavonoid compounds in the peel of citrus fruits changes when the citrus trees are subjected to the stress of HLB (Hijaz et al., 2020). In addition, the molecular structure of flavonoid compounds exhibits the characteristics of fluorescent substance molecular structures (Guilbault, 2020). Comparative analysis of three-dimensional fluorescence spectra between flavonoid standards and citrus peels in our laboratory (Yan et al., 2024) demonstrated significant spectral overlap between FCR1-FCR4 and characteristic flavonoid regions. This experimental evidence confirms FCR1-FCR4 as specific fluorescence reflection of citrus flavonoids. Thus, these results also demonstrate the feasibility of utilizing flavonoid fluorescence characteristics to classify citrus fruits with different health statuses.

Currently, based on the close relationship between biotic and abiotic stresses and the content of flavonoid compounds in citrus peels, Muharfiza et al. (2017) applied the fluorescence characteristics of flavonoids to detect the quality of citrus, using the characteristic wavelength bands EX = 370 nm, EM = 540 nm. Anielle C. Ranulfi et al.

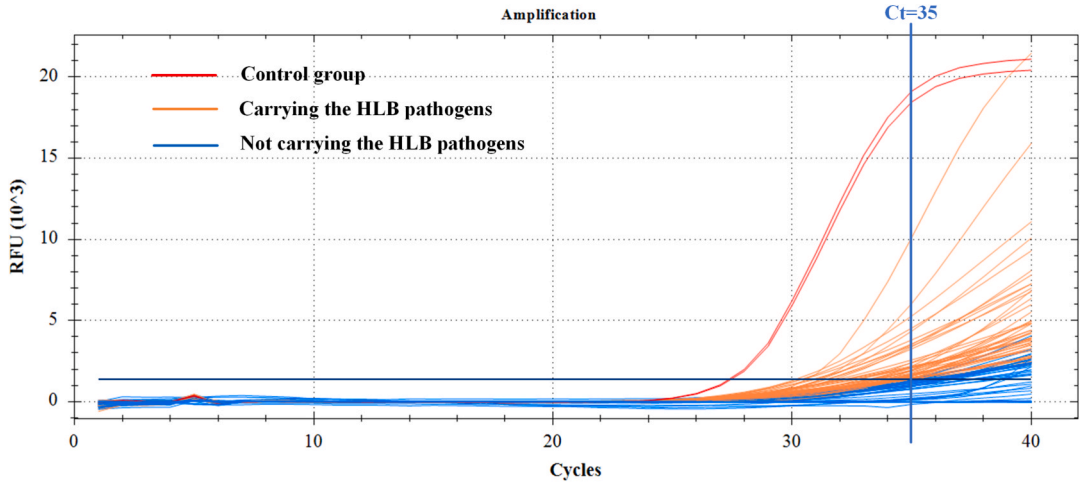

Fig. 6. qPCR results of some citrus peels.

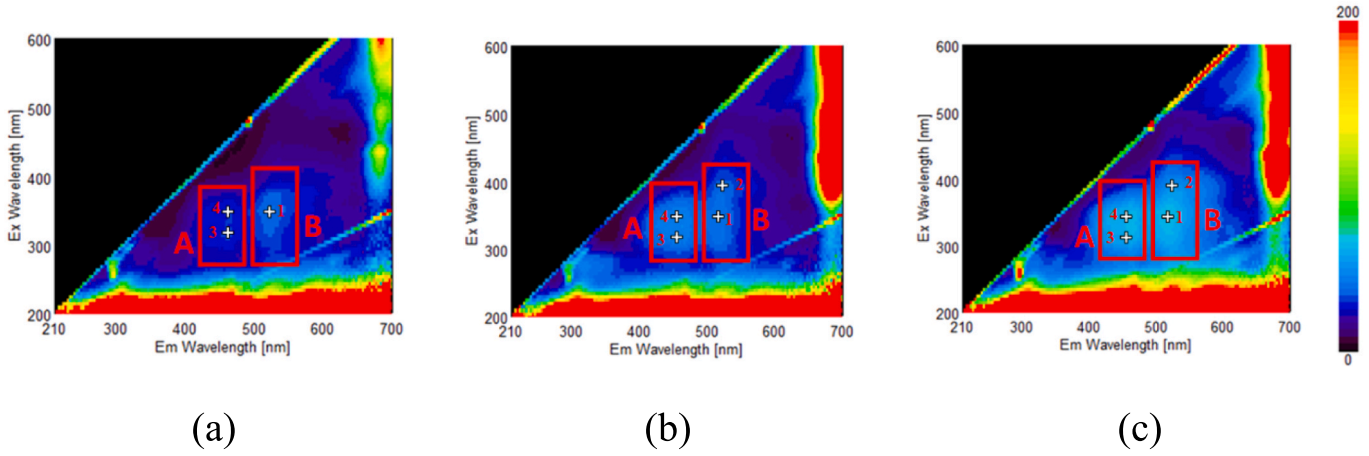

Fig. 7. Three-dimensional fluorescence spectra of typical citrus peels (a) HLB, (b) Macular, (c) healthy. Notes: 1: EX = 365 nm, EM = 525 nm, 2: EX = 415 nm, EM = 525 nm, 3: EX = 308 nm, EM = 450 nm, 4: EX = 365 nm, EM = 450 nm.

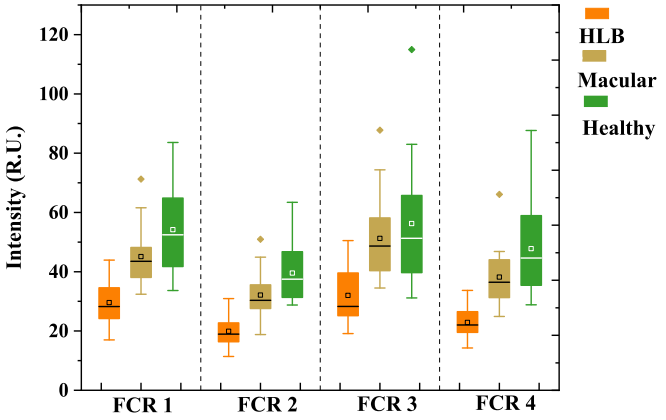

Fig. 8. The mean values of fluorescence intensity in different fluorescence characteristic regions of citrus peels. Notes: Fluorescence Characteristic Region (FCR).

Table 2
Analysis of Variance (ANOVA).

Fluorescence Characteristic Region	HLB (n = 32)	Macular (n = 16)	Healthy (n = 16)	*F*	*p*
	M ± *SD*	*M* ± *SD*	*M* ± *SD*		
FCR1	29.5910 ± 7.47705	45.0917 ± 10.43001	54.1677 ± 15.17341	31.687	0.000**
FCR2	19.8881 ± 4.99102	32.1236 ± 7.97143	39.5550 ± 10.19902	41.891	0.000**
FCR3	31.9907 ± 8.95920	51.2396 ± 14.84976	56.2599 ± 21.38925	18.738	0.000**
FCR4	22.8648 ± 5.15509	38.1895 ± 10.12488	47.8009 ± 15.92443	35.731	0.000**

(2016) used the fluorescence characteristics of flavonoids in citrus leaves to detect citrus HLB, applying flavonoid wavelength bands EX = 325 nm, EM = 425 nm. The results of this study in section 3.2 (Fig. 7) regarding the three-dimensional fluorescence spectrum scans of citrus peels in different health states correspond to the conclusions of other researchers on the fluorescence characteristics of flavonoid compounds. The selected fluorescence characteristic regions, FCR1 and FCR3, show similarities with their research results.

Through EEM data analysis, it was found that citrus peels in different health states exhibited differences in their fluorescence intensity values (Fig. 8.), and further variance analysis confirmed the significant

Table 3
Tamhane's T2 Multiple Comparison results.

Fluorescence Characteristic Region	Health Status (I)	Health Status (J)	Mean difference (I-J)	Std. Error	*p*
FCR1	HLB	Macular	−15.500746	2.923378	0.000**
		Healthy	−24.576684	4.017039	0.000**
FCR2	HLB	Macular	−12.235434	2.179432	0.000**
		Healthy	−19.666854	2.698092	0.000**
FCR3	HLB	Macular	−19.248908	4.036154	0.000**
		Healthy	−24.269222	5.576923	0.000**
FCR4	HLB	Macular	−15.324758	2.690267	0.000**
		Healthy	−24.936147	4.084076	0.000**

relationship between HLB and the fluorescence intensity values of citrus peels. The determination of FCR1-FCR4 provides effective parameter information for the construction of a fluorescence imaging system. Effectively selecting characteristic wavelength bands is beneficial for ensuring the effectiveness of fluorescence imaging.

3.3. Fruit fluorescence images under different imaging condition

Utilizing the fluorescence peaks (Peak 1–4) and fluorescence characteristic regions (FCR1-FCR4) obtained in 3.2, select the appropriate excitation light sources and filters. There are four imaging conditions in total, namely G1 (EX = 365 ± 20 nm, EM = 525 ± 20 nm), G2 (EX = 415 ± 20 nm, EM = 525 ± 20 nm), B1 (EX = 308 ± 20 nm, EM = 450 ± 20 nm), and B2 (EX = 365 ± 20 nm, EM = 450 ± 20 nm). Under each imaging condition, 480 fluorescence images of citrus fruits were acquired. Some images of citrus fruits are shown in Fig. 9. Comparative analysis revealed that citrus fruits in different health conditions exhibited differences in the fluorescence images, primarily reflected in the color of the images.

To better compare the differences between normal color images obtained under white light conditions and fluorescent images obtained under specific excitation light sources, the images obtained under different imaging conditions were uniformly represented by their histograms in RGB channels, as shown in Fig. 10. The horizontal axis of the histogram is 0–255 for a total of 256 pixel intensity values; the vertical axis represents the number of pixels in the image for each intensity value, with higher values indicating that pixels of the corresponding intensity value appear more often in the image. The histograms of the three channels R, G, and B were calculated separately, and different color channels were represented by different colored lines.

Fig. 10 (a) shows the histograms of normal color images of citrus

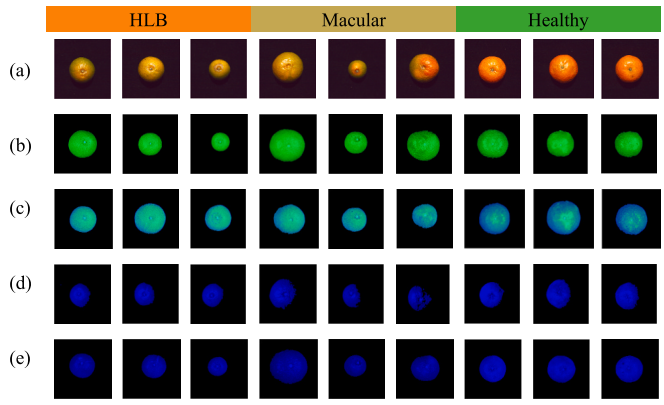

Fig. 9. Normal color images and fluorescence images of citrus fruits: (a) White light, (b) G1, (c) G2, (d) B1, (e) B2.

fruits in R, G, and B color channels obtained under white light environment. Analysis reveals that the frequency distributions of R, G, and B color channels in normal color images with different health statuses are not significantly different, making it difficult to screen for HLB-infected citrus. Fig. 10 (b) and (c) display the performance of green fluorescent images obtained under G1 and G2 imaging conditions in the R, G, and B channels, respectively. It can be observed that images of citrus fruits with different health statuses exhibit more pronounced differences. Notably, for the fluorescent image under G1, the frequency distribution of healthy citrus fruit images is highest in the B color channel within the range of 15–50, while the frequency distribution of HLB citrus fruit images is lowest. Similarly, the same trend is observed in the R color channel within the range of 0–50 and the G color channel within the range of 100–200. Fig. 10 (d) and (e) show the performance of blue fluorescent images captured under B1 and B2 imaging conditions in the R, G, and B channels. Analysis indicates that the frequency distributions under B1 and B2 light conditions in the G channel within the range of 0–10 and the B channel within the range of 200–250 exhibit a trend of healthy higher than macular higher than HLB. This trend aligns with the trend of fluorescence intensity values of citrus peels with different health statuses under FCR1-FCR4 (Fig. 8), further demonstrating that the fluorescence characteristics of flavonoids are also manifested in fluorescent images.

Based on the comprehensive analysis above, it can be concluded that fluorescent images provide a superior reflection of different health statuses in citrus fruits compared to normal color images. Moreover, the frequency distribution trends in specific channels of the fluorescence images align with the trends of fluorescence intensity values of citrus peels in different health states in FCR1-FCR4 (Fig. 8), further demonstrating that the fluorescence imaging system of this study can effectively capture the flavonoid fluorescence characteristics of citrus.

3.4. Image processing and modeling of classification models

3.4.1. Classifier selection

This study employed KNN, DT, RF, and BP to classify 432 image feature parameters and compared the four evaluation indicators of the classification results. The results of *Precision*, *Accuracy*, *Recall*, and *F*1 Score for the four classification models are shown in Fig. 11. For the dataset of this study, the classification model using RF as the classification decision maker is more effective than the other three, with a classification accuracy and recall of 80.20 %. Therefore, this study selects RF for modeling the fluorescence image classification model.

3.4.2. Color feature screening and model performance

To further enhance the performance of the classification model based on the RF algorithm, an optimization of the 432 image feature parameters was conducted. The chi-square statistic of 432 color feature parameters of citrus fluorescence images with different health states were calculated using the chi-square test. According to the chi-square statistics corresponding to each color feature parameter, the correlation degree of each color feature parameter with different citrus health status was obtained respectively. Then, there are 432 rankings ($N = 432$) for the color feature parameters of citrus fruit images. At the same time, the classification accuracy curves of the models modeled with different numbers (K) of color feature parameters selected in the order of the degree of correlation were plotted (Fig. 12). For example, when $K = 2$ is taken, it corresponds to the model classification accuracy of modeling the classification model by taking the first and second color feature parameters in the order of the degree of correlation.

As shown in Fig. 12, the left axis of the image represents the contribution rate of each feature parameter to the classification model, while the right axis shows the classification accuracy of the model at different K values. The change in model accuracy with varying K values is depicted by the red line at the top of the image. Analysis indicates that when $K = 114$, the accuracy of the model reaches its peak, at 87.5 %. And the model has a precision of 87.85 %, a recall of 87.50 % and an $F1$ score of 87.59 %. When $K = 10$, the corresponding model accuracy is the highest within the range of $K = 1$–57, at 83.33 %. And the model has a precision of 84.65 %, a recall of 83.33 % and an $F1$ score of 83.74 %. The $F1$ scores of the model were found to be higher than 83.0 % for both $K = 10$ and $K = 114$, which demonstrated that the model achieved a good balance between specificity and sensitivity. In addition, the confusion matrix of their classification results on the test set are show in Fig. 13.

To further discuss the significance of the application of the two classification models when $K = 10$ and $K = 114$. Elbow method was used in this study for the discussion. The analysis shows that the best classification model performance is indeed obtained at $K = 114$. But the model accuracy curve also shows that after $K = 10$, the classification accuracy of the model fluctuates stably without significant improvement as K increases. This plateau suggests diminishing returns in model performance with additional features. In addition, when $K = 10$, it involves only three imaging conditions, G1, G2 and B1. And among the 10 selected image feature parameters, 9 of them were derived from images captured by a lens equipped with a 525 ± 20 nm filter. This can also make a difference in the cost of imaging equipment. To obtain a model that is more suitable for application and ensures a high level of accuracy, the elbow method was used to determine $K = 10$ based on the histogram of the contribution rate from the chi-square test and the line graph of the change in the accuracy rate as a function of K.

When chose $K = 10$, the selected 10 image feature parameters are shown in Fig. 14 (a)-(j), arranged in descending order of contribution rate. The distribution trends of fluorescence images in the sample set are not entirely consistent across different image feature parameters. However, fluorescence images in different health states exhibit varying degrees of differences in the values of these 10 image feature parameters. For instance, among the top three contributing image feature parameters, in the G2_Median_A parameter, the median distribution of datasets is macular > HLB > healthy. Healthy samples are more concentratedly distributed between 0–10, which allows for effective differentiation from HLB-infected and macular samples. In the G2_Q1_Saturation parameter, the median distribution of datasets is healthy > HLB > macular. Here, macular samples are more concentrated, primarily distributed within the range of 0–2. In the G1_Median_L parameter, the median distribution of datasets is HLB > macular > healthy. The performance of citrus fruits in different health states across various image feature parameters provides richer data information for model construction, collectively assisting in the classification decision-making of the model.

Additionally, this study also compared and analyzed the classification model accuracy using different combinations of color space and light source conditions, as shown in Fig. 15. It is evident that when no filtering is applied ($K = 432$), the model's classification accuracy is

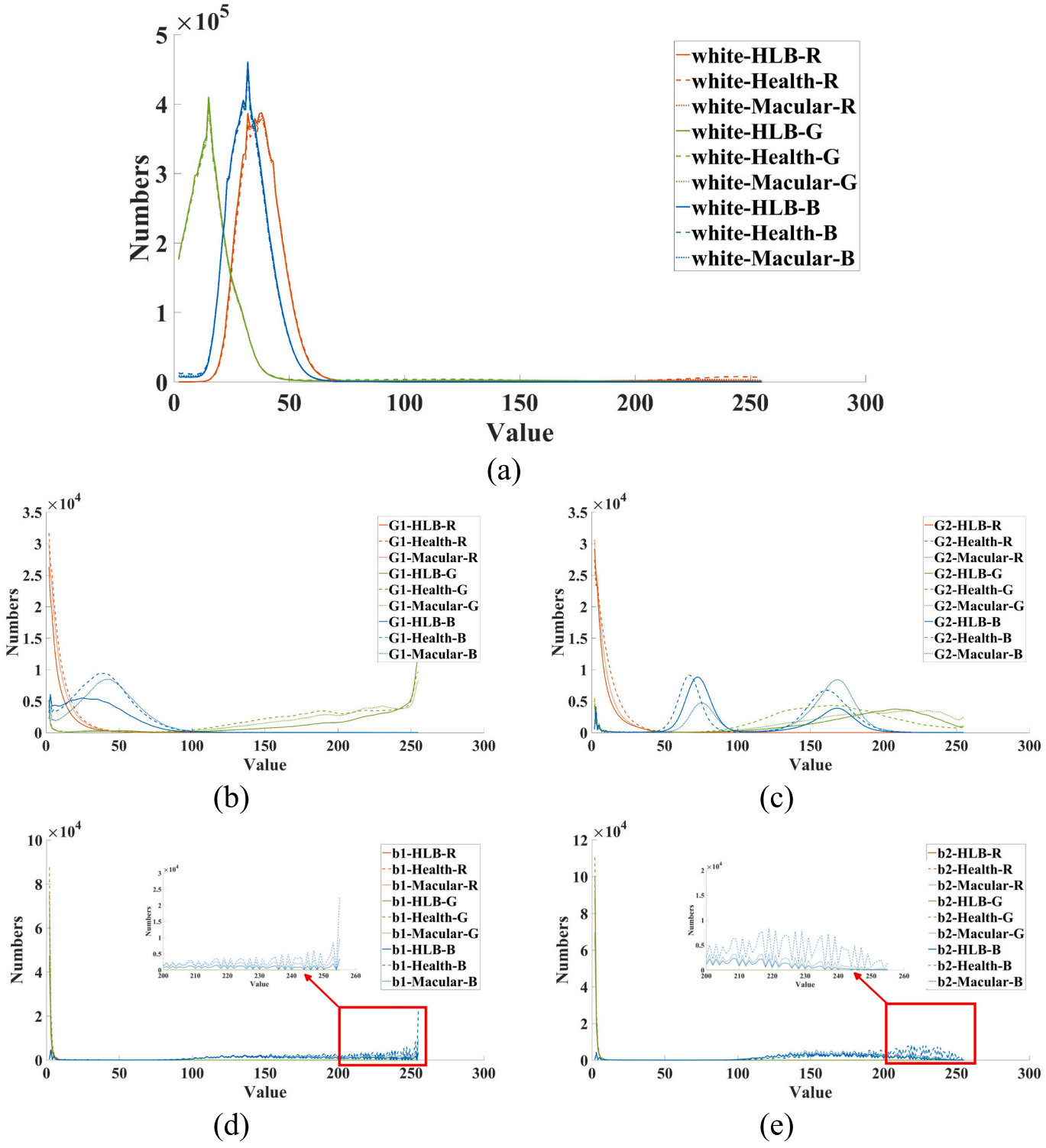

Fig. 10. Frequency distribution of fruit images in RGB channels under different light conditions: (a) White light, (b) G1, (c) G2, (d) B1, (e) B2.

80.20 %, which is lower than the accuracy of 83.33 % achieved after feature selection. Furthermore, analysis revealed that most of the classification models with relatively high accuracy employed RGB or HSV color space feature parameters (indicated by the red circles in Fig. 15) for modeling. This analysis is also reflected in Fig. 16, where it is observed that before the point of the highest model classification accuracy ($K \leq 114$), there is a higher proportion of color feature parameters from the RGB and HSV color spaces. Notably, when $K = 10$, the extracted image feature parameters in RGB and HSV color spaces were only three parameters (G2_Q1_Saturation, G1_Q1_Value, G1_Q1_GREEN), which may account for the observed degradation in model accuracy compared to the model of $K = 114$. Future studies should explore more combined features from green and blue fluorescence images in RGB and HSV color spaces. This exploration should focus on mixing features across different color spaces to improve citrus HLB classification models.

Furthermore, comparative analysis of the classification accuracy when utilizing fluorescence image feature parameters acquired under

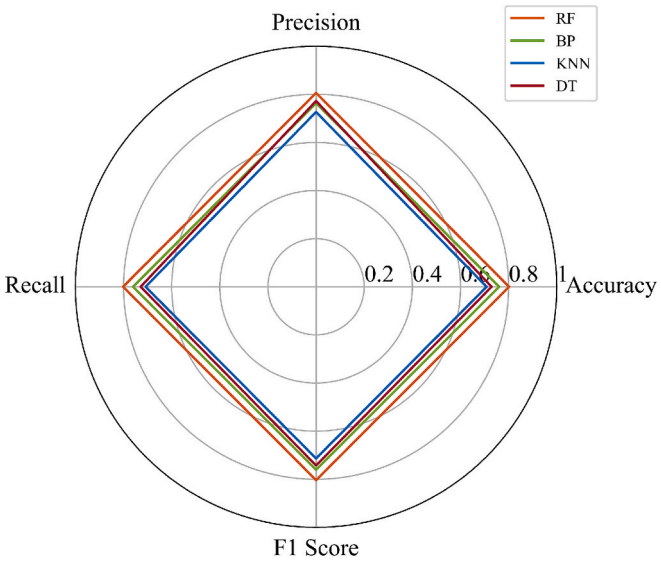

Fig. 11. Comparison of the effectiveness of different classification models.

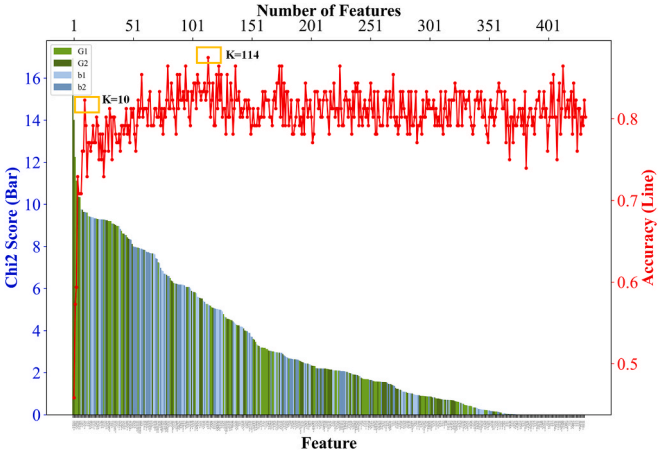

Fig. 12. Contribution of color feature parameters under different light conditions and classification model accuracy under different *K* values.

different imaging conditions (G1, G2, B1, B2) as model inputs demonstrated superior classification performance under G1 and G2 conditions compared to B1 and B2 conditions. This finding can be used to guide the rational adjustment of light sources and filters in the imaging system in subsequent applications, ensuring classification accuracy while controlling the cost of imaging equipment, thereby better adapting to production and practical use.

Fluorescence images can serve as a method to detect the health status of citrus fruits because fluorescence is a phenomenon of photoluminescence. Different excitation wavelengths or varying concentrations of fluorescent substances can exhibit distinct fluorescence characteristics. Therefore, the unique fluorescence properties of fluorescent substances can be utilized for qualitative or quantitative analysis of materials. In this study, due to the fluorescence properties of flavonoids, changes in the content of flavonoid substances in citrus peels of different health states will exhibit different fluorescence characteristics under specific excitation wavelengths. This allows for the capture of changes in the content of fluorescent substances within citrus peels that are not visible in normal color images. Compared to qPCR molecular detection, this method significantly reduces detection time and enables non-destructive testing for citrus HLB. Additionally, the fluorescence images in this study were acquired using a standard CMOS camera, which offers a significant advantage in terms of cost for detection equipment and consumables compared to hyperspectral imaging technology and qPCR molecular detection techniques. Furthermore, the imaging system developed in this study can be integrated into indoor fruit grading and inspection systems, thereby enhancing detection efficiency.

The citrus classification model in this study has an accuracy of up to 87.5 %. Although the accuracy remains slightly lower than certain established detection methods based on hyperspectral techniques (Lan et al., 2019) and chlorophyll fluorescence spectroscopy (Chen et al., 2022), which achieve accuracies ranging from 88 % to 95 %, but it demonstrates significant advantages in terms of equipment cost and operational simplicity.

However, the current study using fluorescence imaging technology has only achieved classification of citrus fruits with different health statuses. Further physicochemical studies are needed to verify the relationship between the content of fluorescent substances and the values of the color parameters of fluorescence images. In addition, the fluorescence imaging systems require imaging in an environment free of interference from other light sources, so a black box is required to provide a stable imaging environment. There are limitations for testing outdoors.

4. Conclusions

This study explored the potential of fluorescence characteristics in citrus peels as a response signal to citrus HLB. Citrus fruits were

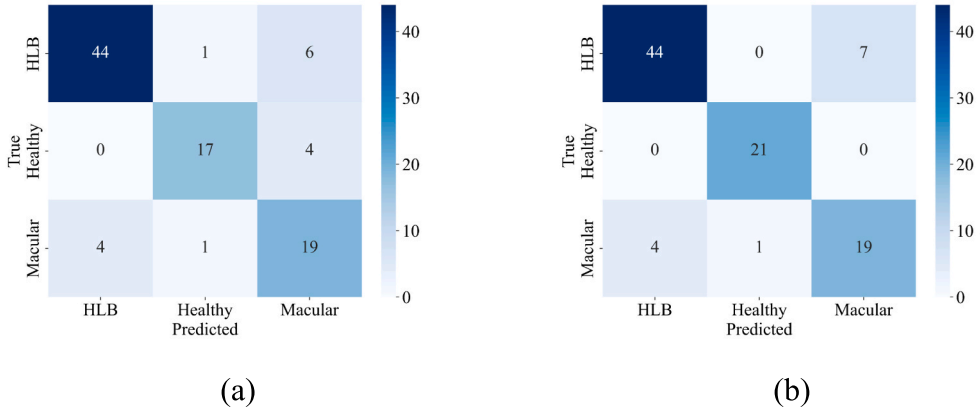

Fig. 13. Confusion matrix for classification model on test set (a)K = 10 (b)K = 114.

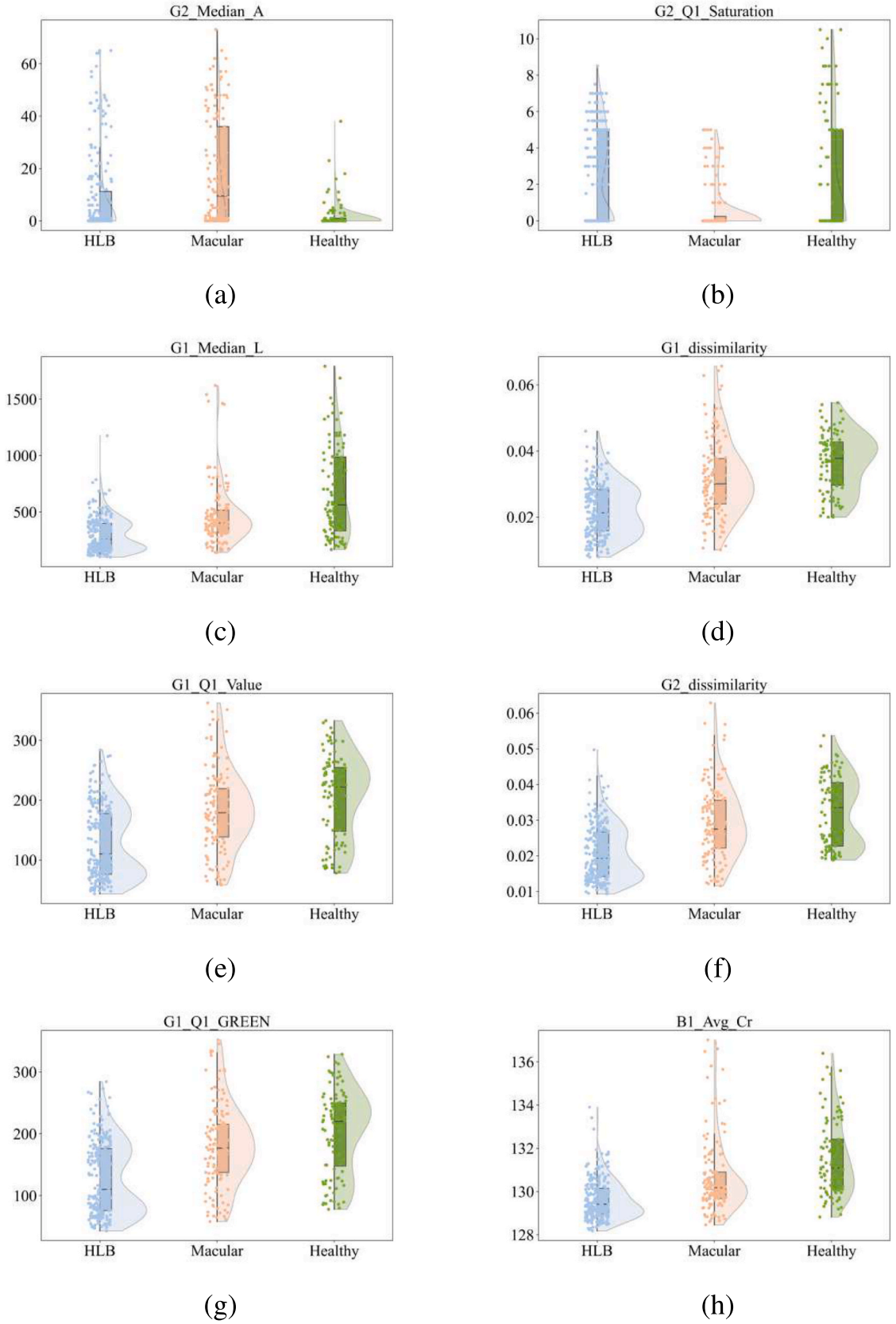

Fig. 14. Performance of fluorescence image data under the top 10 color features. (a) G2_Median_A, (b) G2_Q1_Saturation, (c) G1_Median_L, (d) G1_dissimilarity, (e) G1_Q1_Value, (f) G2_dissimilarity, (g) G1_Q1_GREEN, (h) B1_Avg_Cr, (i) G2_Max_Cr, (j) G2_Q3_A.

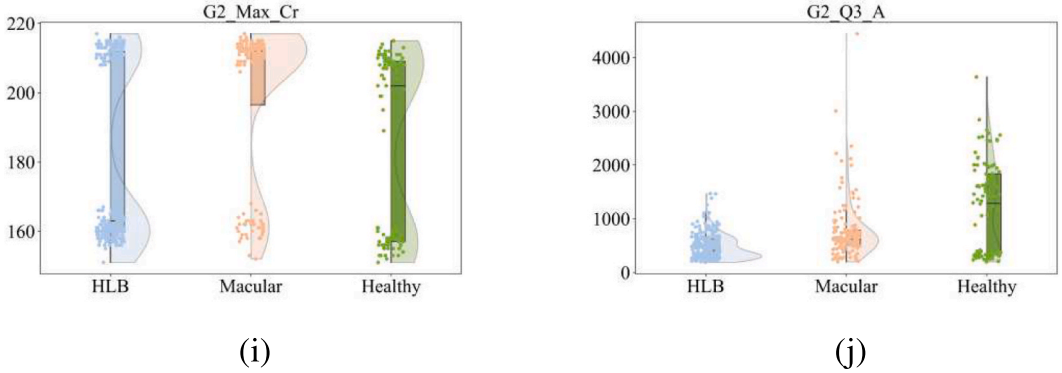

Fig. 14. (*continued*).

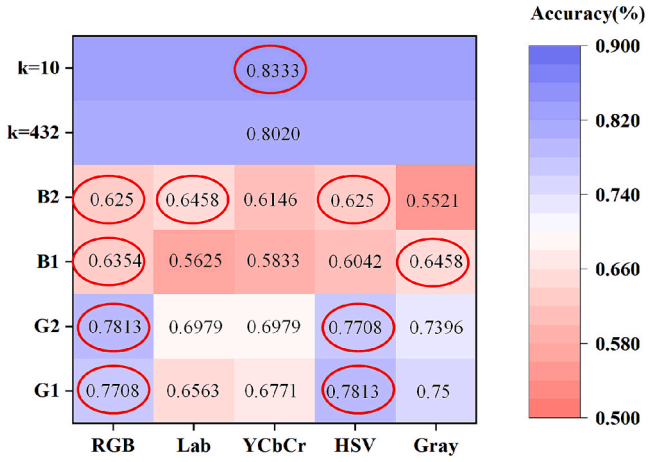

Fig. 15. Accuracy of classification models in different color spaces and under different light source conditions.

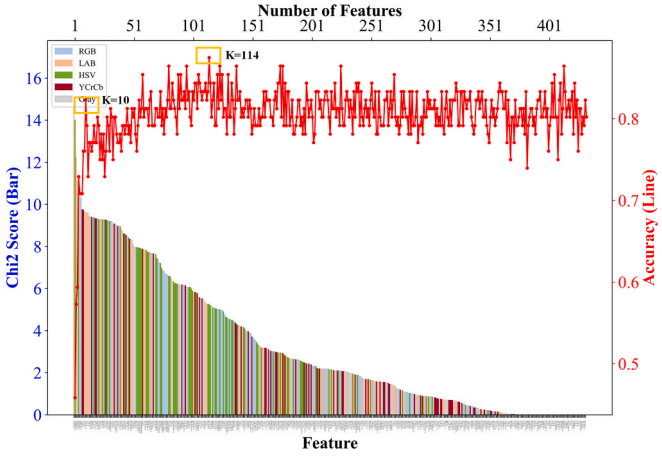

Fig. 16. Contribution of color feature parameters in different color spaces and accuracy of classification models with different K values.

harvested on January 2023, and the differences in fluorescence responses among HLB-infected, macular, and healthy citrus peels were analyzed using three-dimensional fluorescence spectroscopy. After identifying regions with differential fluorescence changes, a variance analysis was conducted between fluorescence intensity values in different regions and health status. Four sensitive fluorescence characteristic regions (FCR1-FCR4) for citrus HLB were identified. Based on this, four fluorescence imaging light source conditions (G1, G2, B1, B2) were determined. Fluorescence imaging was performed on 240 citrus fruits harvested in December 2023. Comparison of images in RGB color channels revealed that fluorescence images could visualize the health status of fruits more effectively than normal color images. A classification model was constructed using image color feature parameters selected by chi-square tests. And the classification model trained with RF algorithm has an accuracy of up to 87.5 % on the test set. The fluorescence imaging-based method for detecting citrus HLB enables non-destructive and rapid detection of citrus fruits. It can provide valuable data support for HLB screening in citrus orchards post-harvest in winter and orchard management decisions in spring.

In the future, we will further expand the application of fluorescence imaging technology to detect HLB-infected fruits of various citrus varieties, enhancing the universality of the HLB classification model. Additionally, we will identify the specific fluorescent substances responsible for the changes in fluorescence characteristics as well as correlate their concentrations with fluorescence intensity values. Furthermore, we will improve the integration and intelligence level of the fluorescence imaging-based HLB detection system, making it suitable for field detection in orchard and providing more timely data feedback for orchard management.

CRediT authorship contribution statement

Kangting Yan: Writing – review & editing, Writing – original draft, Validation, Supervision, Software, Methodology, Investigation, Data curation, Conceptualization. **Xipeng Fang:** Validation, Software, Investigation. **Weiguang Yang:** Software, Investigation, Data curation. **Xidan Xu:** Investigation. **Shaozhen Lin:** Investigation. **Yali Zhang:** Supervision, Resources, Funding acquisition, Conceptualization. **Yubin Lan:** Resources, Project administration, Conceptualization.

Funding

This work was supported by The “111 Center” (D18019), Key Technologies R&D Program of Guangdong Province (Research and application of early diagnosis, monitoring and early warning technology of citrus Huanglongbing) (2024B03J1317), Laboratory of Lingnan Modern Agriculture Project (NT2021009).

Declaration of competing interest

The authors declare that they have no known competing financial interests or personal relationships that could have appeared to influence the work reported in this paper.

Appendix

Exhibit A: Color space feature parameter extraction formula.

Type of Channels	Type of parameters	Formula
RGB *(The calculation formulas of color feature parameters of HSV, LAB and YCbCr are the same as that of RGB)	*Avg _ Red*	$Avg\_Red = \frac{\sum_{i=1}^{N} Red_i}{N}$
	Avg _ Blue	$Avg\_A = \frac{\sum_{i=1}^{N} Blue_i}{N}$
	Avg _ Green	$Avg\_Green = \frac{\sum_{i=1}^{N} Green_i}{N}$
	Max _ Red	$Max\_Red = max\ \ (Red_1, Red_2 \ldots Red_N)$
	Max _ Blue	$Max\_Blue = max\ \ (Blue_1, Blue_2 \ldots Blue_N)$
	Max _ Green	$Max\_Green = max\ \ (Green_1, Green_2 \ldots Green_N)$
	Max _ Hist _ Red	$Max\_Hist\_Red = max\ \ (Hist(Red))$
	Max _ Hist _ Blue	$Max\_Hist\_Blue = max\ \ (Hist(Blue))$
	Max _ Hist _ Green	$Max\_Hist\_Green = max\ \ (Hist(Green))$
	Red _ Avg _ ratio	$Red\_Avg\_ratio = \frac{Avg\_Red}{Avg\_Red + Avg\_Blue + Avg\_Green}$
	Blue_Avg ratio	$Blue\_Avg\_ratio = \frac{Avg\_Blue}{Avg\_Red + Avg\_Blue + Avg\_Green}$
	Green_Avg ratio	$Green\_Avg\_ratio = \frac{Avg\_Green}{Avg\_Red + Avg\_Blue + Avg\_Green}$
	Var_Red	$Var\_Red = \frac{\sum_{i=1}^{M} \{hist(Red)[i] - mean[hist(Red)]\}}{M}$
	Var_Green	$Var\_Green = \frac{\sum_{i=1}^{M} \{hist(Green)[i] - mean[hist(Green)]\}}{M}$
	Var_Blue	$Var\_Blue = \frac{\sum_{i=1}^{M} \{hist(Blue)[i] - mean[hist(Blue)]\}}{M}$
	Median_Red	$Median\_Red = median[hist(red)]$
	Median_ Green	$Median\_Green = median[hist(Green)]$
	Median_ Blue	$Median\_Blue = median[hist(Blue)]$
	Q1_Red	$Q1\_Red = percentile[hist(red, 25)]$
	Q1_ Green	$Q1\_Green = percentile[hist(green, 25)]$
	Q1_ Blue	$Q1\_Blue = percentile[hist(blue, 25)]$
	Q3_Red	$Q3\_Red = percentile[hist(red, 75)]$
	Q3_Green	$Q3\_Green = percentile[hist(green, 75)]$
	Q3_Blue	$Q3\_Blue = percentile[hist(blue, 75)]$
Grayscale Processing	*Avg _ Gray*	$Avg\_Gray = \frac{\sum_{i=1}^{N} Gray_i}{N}$
	Max _ Gray	$Max\_Gray = max\ \ (Gray_1, Gray_2 \ldots Gray_N)$
	Max _ Hist _ Gray	$Max\_Hist\_Gray = max\ \ (Hist(Gray))$
	Var _Gray	$Var\_Gray = \frac{\sum_{i=1}^{M} \{hist(Gray)[i] - mean[hist(Gray)]\}}{M}$
	Median _ Gray	$Median\_Gray = median[hist(Gray)]$
	Q1_Gray	$Q1\_Gray = percentile[hist(Gray, 25)]$
	Q3_Gray	$Q3\_Gray = percentile[hist(Gray, 75)]$
Gray-Level Co-occurrence Matrix	*Contrast*	$Contrast = \sum_{i,j} (i-j)^2 \times GLCM(i,j)$
	Dissimilarity	$Dissimilarity = \sum_{i,j} \lvert i-j \rvert \times GLCM(i,j)$
	Homogeneity	$Homogeneity = \sum_{i,j} \frac{GLCM(i,j)}{1+(i-j)^2}$
	Correlation	$Correlation = \frac{\sum_{i,j} [i \bullet j \bullet GLCM(i,j)] - \mu_x \mu_y}{\sigma_x \sigma_y}$
	ASM	$ASM = \sum_{i,j} GLCM(i,j)^2$

Data availability

Data will be made available on request.

References

Omwange, K.A., Saito, Y., Al Riza, D.F., Zichen, H., Kuramoto, M., Shiraga, K., Ogawa, Y., Kondo, N., Suzuki, T., 2022. Japanese dace (Tribolodon hakonensis) fish freshness estimation using front-face fluorescence spectroscopy coupled with chemometric analysis. Spectrochim. Acta A Mol. Biomol. Spectrosc. 276, 121209.

Anderson, N.T., Walsh, K.B., 2022. Review: the evolution of chemometrics coupled with near infrared spectroscopy for fruit quality evaluation. J. Near Infrared Spectrosc. 30 (1), 3–17.

Arredondo Valdés, R., Delgado Ortiz, J.C., Beltrán Beache, M., Anguiano Cabello, J., Cerna Chávez, E., Rodríguez Pagaza, Y., Ochoa Fuentes, Y.M., 2016. A review of techniques for detecting Huanglongbing (greening) in citrus. Can. J. Microbiol. 62 (10), 803–811.

Bao, M., Zheng, Z., Sun, X., Chen, J., Deng, X., 2020. Enhancing PCR capacity to detect 'candidatus liberibacter Asiaticus' utilizing whole genome sequence information. Plant Dis. 104 (2), 527–532.

Benos, L., Tagarakis, A.C., Dolias, G., Berruto, R., Kateris, D., Bochtis, D., 2021. Machine learning in agriculture: a comprehensive updated review. Sensors 21 (11), 3758.

Bové, J.M., 2006. Huanglongbing: a destructive, newly-emerging, century-old disease of citrus. J. Plant Pathol. 88 (1), 7–37.

Cáceres, L.P., Bischl, B., Stützle, T., 2017. Evaluating random forest models for irace., Proceedings of the Genetic and Evolutionary Computation Conference Companion. Association for Computing Machinery, Berlin, Germany, pp. 1146-1153.
Chauvin, Y., 1995. Backpropagation Theory, Architectures, and Applications. Lawrence Erlbaum Associates, Publishers, Hove, UK.
Chen, S., Shen, Y., Xie, P., Lu, X., He, Y., Cen, H., 2022. In-situ diagnosis of citrus Huanglongbing using sun-induced chlorophyll fluorescence. Trans. Chinese Soc. Agric. Eng.. 38 (9), 324–332.
Cilimkovic, M., 2010. Neural Networks and Back Propagation Algorithm.
Da Graça, J.V., Douhan, G.W., Halbert, S.E., Keremane, M.L., Lee, R.F., Vidalakis, G., Zhao, H., 2016. Huanglongbing: an overview of a complex pathosystem ravaging the world's citrus. J. Integr. Plant Biol. 58 (4), 373–387.
Deng, X., Gao, Y., Chen, J., Pu, X., Kong, W., Li, H., 2012. Current situation of "Candidatus Liberibacter asiaticus" in Guangdong, China, where citrus huanglongbing was first described. J. Integr. Agric. 11 (3), 424–429.
Desai, A., Chaudhary, S., 2016. Distributed Decision Tree., Proceedings of the 9th Annual ACM India Conference. Association for Computing Machinery, Gandhinagar, India, pp. 43–50.
Guilbault, G.G., 2020. Practical fluorescence. CRC Press.
He, C., Li, X., Liu, Y., Yang, B., Wu, Z., Tan, S., Ye, D., Weng, H., 2022. Combining multicolor fluorescence imaging with multispectral reflectance imaging for rapid citrus Huanglongbing detection based on lightweight convolutional neural network using a handheld device. Comput. Electron. Agric. 194, 106808.
Hijaz, F., Al-Rimawi, F., Manthey, J.A., Killiny, N., 2020. Phenolics, flavonoids and antioxidant capacities in Citrus species with different degree of tolerance to Huanglongbing. Plant Signal. Behav. 15 (5), 1752447.
Horvitz, E., Mulligan, D., 2015. Data, privacy, and the greater good. Science 349 (6245), 253–255.
Huang, Z., Omwange, K.A., Tsay, L.W.J., Saito, Y., Maai, E., Yamazaki, A., Nakano, R., Nakazaki, T., Kuramoto, M., Suzuki, T., Ogawa, Y., Kondo, N., 2022. UV excited fluorescence image-based non-destructive method for early detection of strawberry (Fragaria × ananassa) spoilage. Food Chem. 368, 130776.
Khan, M.J., Khan, H.S., Yousaf, A., Khurshid, K., Abbas, A., 2018. Modern trends in hyperspectral image analysis: a review. IEEE Access 6, 14118–14129.
Lan, Y.B., Zhu, Z.H., Deng, X.L., Lian, B.Z., Huang, J.Y., Huang, Z.X., Hu, J., 2019. Monitoring and classification of citrus Huanglongbing based on UAV hyperspectral remote sensing. Trans. Chinese Soc. Agric. Eng. 35 (03), 92–100.
Lan, Y., Huang, Z., Deng, X., Zhu, Z., Huang, H., Zheng, Z., Lian, B., Zeng, G., Tong, Z., 2020. Comparison of machine learning methods for citrus greening detection on UAV multispectral images. Comput. Electron. Agric. 171, 105234.
Liakos, K., Busato, P., Moshou, D., Pearson, S., Bochtis, D., 2018. Machine learning in agriculture: a review. Sensors 18 (8), 2674.
Liu, Y., Xiao, H., Sun, X., Zhu, D., Han, R., Ye, L., Wang, J., Ma, K., 2018. Spectral feature selection and discriminant model building for citrus leaf Huanglongbing. Trans. Chinese Soc. Agric. Eng.. 34 (3), 180–187.
Liu, Y., Zang, W., Liang, X., Wang, Y., Li, X., Sun, C., 2022. Identification of flavonoids from the Flavedo of 23 citrus cultivars fruit and their antioxidant activity. J. Chinese Inst. Food Sci. Tech. 22 (12), 234–246.
Lu, B., Dao, P., Liu, J., He, Y., Shang, J., 2020. Recent advances of hyperspectral imaging technology and applications in agriculture. Remote Sens. 12 (16), 2659.
Lu, J., Wu, Z., Lan, Y., Deng, X., Huang, J., 2024. Study on the prediction model of litchi downy blight damage based on IoT and hyperspectral data fusion. IEEE Internet Things J.
Mahesh, B., 2019. Machine Learning Algorithms -a Review.
Massenti, R., Lo Bianco, R., Sandhu, A.K., Gu, L., Sims, C., 2016. Huanglongbing modifies quality components and flavonoid content of 'Valencia' oranges. J. Sci. Food Agric. 96 (1), 73–78.
Mei, H., Deng, X., Hong, T., Luo, X., Deng, X., 2014. Early detection and grading of citrus huanglongbing using hyperspectral imaging technique. Trans. Chinese Soc. Agri. Eng.. 9, 140–147 in Chinese.
Meng, Y., Weng, H., Cen, H., Li, H., He, Y., 2019. Carbohydrate metabolism and near-infrared spectral characteristics in asymptomatic Huanglongbing infected leaves. Acta Agric. Zhejiangensis. 31 (3), 428–435.
Moriya, É.A.S., Imai, N.N., Tommaselli, A.M.G., Berveglieri, A., Honkavaara, E., Soares, M.A., Marino, M., 2019. Detecting citrus huanglongbing in brazilian orchards using hyperspectral aerial images. The International Archives of the Photogrammetry, Remote Sensing and Spatial Information Sciences XLII-2/W13, 1881-1886.
Muharfiza, Al Riza, D., Saito, Y., Itakura, K., Kohno, Y., Suzuki, T., Kuramoto, M., Kondo, N., 2017. Monitoring of Fluorescence Characteristics of Satsuma Mandarin (Citrus unshiu Marc.) During the Maturation Period. Horticulturae 3(4), 51.
Omwange, K.A., Al Riza, D.F., Sen, N., Shiigi, T., Kuramoto, M., Ogawa, Y., Kondo, N., Suzuki, T., 2020. Fish freshness monitoring using uv-fluorescence imaging on japanese dace (tribolodon hakonensis) fisheye. J. Food Eng. 287, 110111.
Park, J., Louzada, E.S., Braswell, W.E., Stansly, P.A., Da Graça, J.V., McCollum, G., Rascoe, J.E., Kunta, M., 2018. A new diagnostic real-time PCR method for huanglongbing detection in citrus root tissue. J. Gen. Plant Pathol. 84 (5), 359–367.
Prajwala, T.R., 2015. A comparative study on decision tree and random forest using R tool. Ijarcce.
Ranulfi, A.C., Cardinali, M.C.B., Kubota, T.M.K., Freitas-Astúa, J., Ferreira, E.J., Bellete, B.S., Da Silva, M.F.G.F., Villas Boas, P.R., Magalhães, A.B., Milori, D.M.B.P., 2016. Laser-induced fluorescence spectroscopy applied to early diagnosis of citrus Huanglongbing. Biosyst. Eng. 144, 133–144.
Sankaran, S., Mishra, A., Maja, J.M., Ehsani, R., 2011. Visible-near infrared spectroscopy for detection of Huanglongbing in citrus orchards. Comput. Electron. Agric. 77 (2), 127–134.
Song, Y., Lu, Y., 2015. Decision tree methods: applications for classification and prediction. Shanghai Arch. Psychiatry 27 (2), 130–135.
Suthaharan, S., 2016. Decision Tree Learning., Machine Learning Models and Algorithms for Big Data Classification: Thinking with Examples for Effective Learning. Springer US, Boston, MA, pp. 237-269.
Wang, S., Aggarwal, C., Liu, H., 2018. Random-forest-inspired neural networks. ACM Trans. Intell. Syst. Technol. 9 (6), 61–69.
Wang, F., Chen, L., Chen, H., Chen, S., Liu, Y., 2019. Analysis of flavonoid metabolites in citrus peels (Citrus reticulata "Dahongpao") using UPLC-ESI-MS/MS. Molecules 24 (15), 2680.
Weng, H., He, C., Xu, J., Liu, L., Qing, J., Wang, L., Ye, D., 2020. Rapid detection of citrus Huanglongbing based on chlorophyll fluorescence imaging technology. Trans. Chinese Soc. Agric. Eng.. 36 (12), 196–203.
Wetterich, C.B., Felipe, D.O.N.R., Belasque, J., Marcassa, L.G., 2016. Detection of citrus canker and Huanglongbing using fluorescence imaging spectroscopy and support vector machine technique. Appl. Opt. 55 (2), 400–407.
Xiang, Y., Cao, Z., Yao, S., He, J., 2018. In: CW-KNN: an Efficient KNN-Based Model for Imbalanced Dataset Classification. Association for Computing Machinery, Qingdao, China, pp. 7–11.
Xiao H., Liu Y., Liu Y., Xiao, H., Sun, L., Hao, Y., 2023. Diagnosis of Citrus Greening Based on the Fusion of Visible and Near-Infrared Spectra. Appl. Sci. 2023,13(18): 10082.
Yan, K., Lu, X., Xiao, J., Song, X., Xu, X., Guo, J., Yang, W., Zhang, Y., Lan, Y., 2024. Three-dimensional fluorescence spectral characteristic of flavonoids for citrus Huanglongbing disease early detection. Microchem. J. 2024, 112263.
Yu, J., Huang, Z., Zhang, M., Lu, L., Chen, G., Tao, J., Yang, X., Zhong, L., 2017. Annual dynamic change of Asian citrus psyllid in carry Las-bacteria. J. Zhejiang Univ.. 2017, 43(1):89-94.
Yusuf, F., Olayiwola, T., Afagwu, C., 2021. Application of artificial intelligence-based predictive methods in ionic liquid studies: a review. Fluid Phase Equilib. 531.
Zhang, S., Li, X., Zong, M., Zhu, X., Wang, R., 2017a. Efficient KNN classification with different numbers of nearest neighbors. IEEE Trans. Neural Network Learn Syst.
Zhang, S., Li, X., Zong, M., Zhu, X., Cheng, D., 2017b. Learning k for KNN Classification. ACM Trans. Intell. Syst. Technol. 8 (3).
Zhang, J., Zhang, J., Kaliaperumal, K., Zhong, B., 2022. Variations of the chemical composition of Citrus sinensis Osbeck cv. Newhall fruit in relation to the symptom severity of Huanglongbing. J. Food Compos. Anal. 105, 104269.
Zheng, Z., Chen, J., Deng, X., 2018. Historical perspectives, management, and current research of citrus HLB in guangdong Province of China, where the disease has been endemic for over a hundred years. Phytopathology® 108 (11), 1224–1236.
Zhou, C., 2020. The status of citrus Huanglongbing in China. Trop. Plant Pathol. 45 (3), 279–284.

Industrial Crops & Products 163 (2021) 113324

Contents lists available at ScienceDirect

Industrial Crops & Products

journal homepage: www.elsevier.com/locate/indcrop

Droplet distributions in cotton harvest aid applications vary with the interactions among the unmanned aerial vehicle spraying parameters

Pengchao Chen [a,b], Fan Ouyang [a,b], Guobin Wang [c], Haixia Qi [b,d], Weicheng Xu [a,b], Weiguang Yang [a,b], Yali Zhang [b,d,*], Yubin Lan [a,b,*]

[a] South China Agricultural University, College of Electronic Engineering and Artificial Intelligence, Guangzhou, 510642, China
[b] National Center for International Collaboration Research on Precision Agricultural Aviation Pesticides Spraying Technology, Guangzhou, 510642, China
[c] Shandong Provincial Engineering Technology Research Center for Agricultural Aviation Intelligent Equipment, College of Agricultural Engineering and Food Science, Shandong University of Technology, Zibo, 255022, China
[d] South China Agricultural University, College of Engineering, Guangzhou, 510642, China

ARTICLE INFO

Keywords:
Operational parameters
Droplet distribution
Unmanned aerial vehicle (UAV)
Cotton defoliation

ABSTRACT

A common problem of unmanned aerial vehicles (UAVs) spraying is that fewer droplets could reach the lower layer, and the depositions among the spray width show a significant difference. However, ensuring the penetration and uniformity of the spray is particularly important in the cotton harvest aid applications. As a new spraying method, poor droplet penetration and uniformity of droplet distribution may lead to inconsistent defoliation among canopy rows and poor defoliation in the lower part of the cotton canopy. The operational parameters of UAVs have remarkable effects on the droplet distribution, which will improve the defoliation rate of cotton. Therefore, full factorial tests were conducted in two experimental locations in the Xinjiang cotton-producing region in 2018 and 2019. The selected operational parameters in 2018 included the spray volume (three levels: 8.7, 12, and 15 L/ha), droplet size Dv50 (three levels: 100, 150, and 200 μm), and flight height (three levels: 1, 2, and 3 m). Meanwhile, the operational parameters in 2019 included the spray volume (three levels: 18, 22.5, and 30 L/ha) and droplet size Dv50 (three levels: 100, 150, and 200 μm). The main effects and interaction effects among the operational parameters were analyzed and discussed. The spray penetration and uniformity of droplet distribution were compared separately. The results show that flight height, spray volume, and droplet size have significant effects on spray penetration. Lowering the flight height of the drone, increasing the spray volume and Dv50 of droplets can improve the distribution of droplets at the bottom of the cotton canopy. As for droplet distribution uniformity, with the increase of the application volume and decrease of the flight height, the uniformity of the droplet distribution becomes worse. The influence of flight parameters on the uniformity of droplet distribution is very limited.

1. Introduction

As a natural fiber crop, cotton is an essential industrial crop globally (Cao, 2015). In China, Xinjiang Province is the largest cotton production region. The cotton planting area in Xinjiang was approximately 2.54 million hectares in 2019, accounting for 76.1 % of the country (Zhou et al., 2020). Chemical harvest aid application has been an essential step before the harvest (Cathey, 1980). During chemical harvest aid application, chemicals, such as Thidiazuron, Ethephon, and other herbicides, are sprayed on the crops to accelerate the removal of the cotton leaves and stimulate boll opening and maturation, achieving more efficient mechanical harvesting at a certain time. The application efficiency of harvest aid chemicals will affect the mechanical harvesting progress of cotton, as well as the yield and quality of the fiber. However, the application of harvest aid chemicals is always limited by environmental conditions (Siebert et al., 2006), such as rapidly dropping temperatures, rain, and snow or hail. The weather in Xinjiang changes sharply during the cotton harvest period (from the middle of September to October). Therefore, the spraying of defoliants in Xinjiang needs to be completed quickly in a suitable weather window.

* Corresponding authors at: National Center for International Collaboration Research on Precision Agricultural Aviation Pesticides Spraying Technology, South China Agricultural University, Guangzhou, 510642, China.
E-mail addresses: ylzhang@scau.edu.cn (Y. Zhang), ylan@scau.edu.cn (Y. Lan).

https://doi.org/10.1016/j.indcrop.2021.113324
Received 22 June 2020; Received in revised form 2 January 2021; Accepted 4 February 2021
Available online 28 February 2021
0926-6690/© 2021 Published by Elsevier B.V.

Agricultural drones have the characteristics of high efficiency and reliable maneuverability, and could quickly respond to sudden pests and diseases and large-scale spraying needs (Lan and Chen, 2018). Moreover, the drones will not touch the crops, which could avoid the economic losses caused by mechanically crushing cotton. With the development and improvement of the real-time kinematic (RTK) high-precision positioning technology and terrain-following technology, agricultural drones have been widely used as spraying tools in China in recent years, especially for low crops, such as wheat, rice, and cotton (Chen et al., 2020). According to statistics from the Chinese agricultural department, China had more than 50,000 agricultural drones at the end of 2019 (Wang, 2020). More than 33.3 million hectares of farmland were sprayed that year, and over 3000 drones provided cotton defoliation spraying technical services in Xinjiang in September (Wang, 2020). However, because of the market demand, the application of unmanned aerial vehicles (UAV) has occurred earlier than the study of aerial application technology. There are still many unclear technical issues regarding cotton defoliant spraying by UAV, such as the flight height, flight speed, spray volume, droplet size, spraying frequency, environmental conditions, drift, etc. There is no exact technical standard that operators can refer to. The previous studies had reported that the canopy penetration and droplet distribution uniformity of UAV spraying are poor (Qin et al., 2016; Wang et al., 2019a, 2019b). A common problem of UAV spraying is that fewer droplets could reach the lower layer, and the depositions among the different spray widths show a significant difference.

For the cotton defoliation process, the poor cotton defoliation is closely related to the incomplete research of pesticide application technology (McMullan and Thomas, 2003). The performance of poor defoliation is inconsistent defoliation among canopy rows and poor defoliation in the lower part of the cotton canopy. The reason for these is the uneven distribution of droplets, such as inconsistent droplet deposition distribution within the spray width, and large differences in droplet deposition between the upper and lower layers of the canopy. Chemicals, such as Thidiazuron, are contact herbicides, which need leaves covered with more droplets (Fang et al., 2018). Moreover, cotton is planted at a high density in Xinjiang, with the leaves from two adjacent rows severely overlapping (Meng et al., 2019a). It is an urgent problem to improve the spray penetration and distribution uniformity in the application of chemicals to cotton by UAV. Meng et al. (Meng et al., 2019b) explored whether there is a negative impact of UAV application of harvest aids on the fiber quality and lint cotton yield components. The results showed that it is feasible to use plant protection UAV for cotton harvest-aid applications. However, only the UAV's spray volume was analyzed in this research. In addition, few studies focus on the effects of the relationships between the operation parameters and droplet distribution on the cotton harvest aid application.

The flight height, droplet size, and spray volume all affect the droplet deposition distribution of the UAV. Some researchers (Qin et al., 2016; Wang et al., 2017) reported that increasing the flight height can improve the spray coverage on the upper layer, but this research is generally based on lower crops, such as rice and wheat. Some studies (Wang et al., 2020a; Zhang et al., 2020) indicated that increasing the flight height has no significant effect on the canopy coverage of crops, such as sugarcane and areca trees. The droplet size affects the droplet deposition distribution. Some researchers (Chen et al., 2020; Qin et al., 2016) believe that fine droplets can reach the bottom of the canopy, while others believe (Wang et al., 2019a) that coarser droplets cannot easily evaporate and can reach the bottom. There are different results based on specific application methods, planting areas, and crops. It has been proved that increasing the nozzle flow rate can improve the coverage of wheat and pear trees (Meng et al., 2020; Wang et al., 2019a). The droplet movement is also affected by the crop canopy (Campos et al., 2019; Ferguson et al., 2016; Zhu et al., 2008). The existing studies investigated the relationships between these operational parameters and droplet deposition. However, most of the studies only discussed a single factor while ignoring the combination of factors. Moreover, an analysis of the optimized experimental parameters in a single crop needs to be conducted and discussed.

The purpose of this study is to explore the operational parameters of UAVs to improve the droplet distribution on the cotton canopy, which meet the cotton harvest aid requirements (Tian et al., 2017). The field experiments were conducted in two experimental locations in the Xinjiang cotton-producing region in 2018 and 2019. The operational parameters in 2018 included the spray volume (three levels: 8.7, 12, and 15 L/ha), droplet size Dv50 (three levels: 100, 150, and 200 μm), and flight height (three levels: 1, 2, and 3 m). Meanwhile, the operational parameters in 2019 included the spray volume (three levels: 18, 22.5, and 30 L/ha) and droplet size Dv50 (three levels: 100, 150, and 200 μm). The XAG P series plant protection UAV was chosen as the spraying platform, and water-sensitive papers were used to measure the droplet parameters. The main effects and interaction effects among the flight height, spray volume, and droplet size were analyzed and discussed. The indicators of the droplet distribution of UAV applications, such as the spray penetration and uniformity of the droplet distribution, were compared.

This paper is structured as follows: Section 2 describes the details of the field plots, the spraying platform and the spraying systems, the experimental design, characterization of spray deposition, weather conditions, and statistical analysis. Section 3 presents the interaction effects of the spray penetration, droplet distribution uniformity, and further discussion. The droplet deposition, droplet density, and coverage were discussed in each part. Finally, a summary of the main conclusions is presented in Section 4.

2. Materials and methods

2.1. Field plots

Two field experiments were conducted in 2018 and 2019 in the Xinjiang Uygur Autonomous Region, China (Fig. 1). The first trial was conducted on 8 September to 11 September 2018 in Shihezi city (85°58′48″ E, 44°23′21″ N). The cotton plants (Hexin 47) were sown on 28 April 2018, and average canopy height was 0.73 m. The planting density was 192,000/ha. The second trial was conducted on 8 September 2019 in Changji city (87°18′22″ E, 44°7′21″ N). The cotton plants (Xinluzao 57) were sown on 23 April 2019, and the planting density was 180,000/ha. The average canopy height was 0.7 m. Both experimental fields had been planted with cotton for many years and the large row space and small row space are 0.66 m and 0.1 m, respectively.

2.2. Spraying platform and spraying systems

The UAV platform was the XAG P series plant protection UAV (XAG Co., Ltd, Guangzhou, China). This drone (Fig. 2) has the terrain following and real-time kinematic high-precision positioning function, which could adjust the flight height automatically according to the crop canopies and improve the position accuracy to the centimeter-level. A rotary atomization spraying system was used in this drone. The spectrum and flow rate of the atomized droplets can be easily adjusted by controlling the rotational speed of the spray disc and pump to meet different droplet size and spraying volume requirements. The spraying system comprised four centrifugal nozzles, four peristaltic pumps, a control plate, and tanks. The technical parameters of the UAV are presented in Table 1.

In the previous research, the indoor measurements of the droplet size spectrum of the centrifugal nozzle were completed (Wang et al., 2020b). The test was carried out in National Center for International Collaboration Research on Precision Agricultural Aviation Pesticide Spraying Technology (NPAAC) in South China Agricultural University, Guangzhou, China. The DP-02 laser diffraction instrument (OMC instrument co. LTD, Zhuhai, China) was used to measure the droplet size. The laser

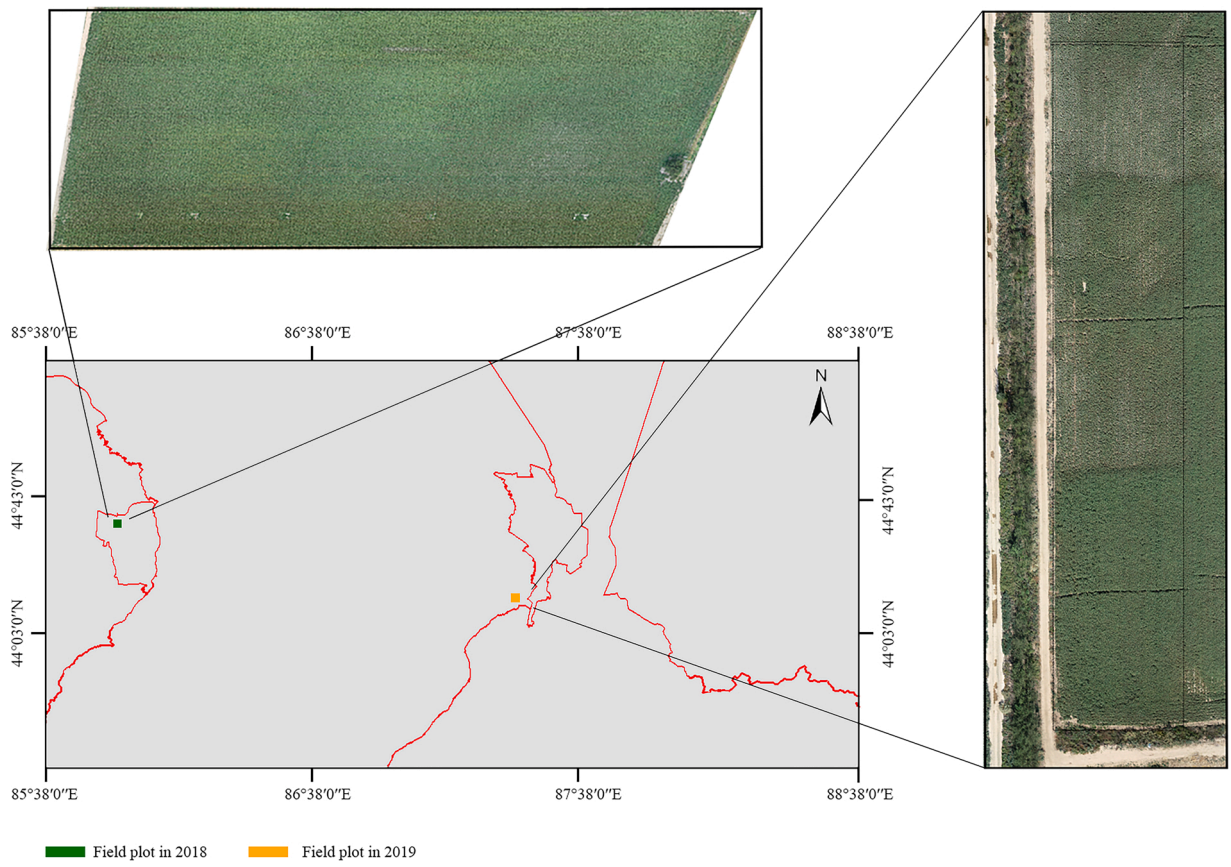

Fig. 1. Experimental location in 2018 and 2019.



Fig. 2. XAG P series plant protection UAV.

Table 1
XAG P series plant protection UAV technical parameters.

Classification	Parameters
Size(m)	1.945*1.945*0.44
Max working efficiency (ha/h)	5.3
Terrain following accuracy (m)	≤0.1
Positioning mode	GNSS RTK
Operation method	Mobile control
Spraying system	Rotary atomization
Number of nozzles	4
Load capacity (L)	15
Spraying width (m)	3.5
Night work	Yes

particle size analyzer consists of a collimated laser generator, a signal acquisition device and a data processing system. The distance between the transmitter and receiver is 2.0 m. And the nozzle placed at about 20 cm distance from vertical plane of the transmitter. In this experiment, the relationship was established between rotation speed and Dv50. The required droplet size can be obtained by controlling the rotational speeds of the centrifugal nozzle.

2.3. Experimental design

Full factorial tests were conducted in 2018 and 2019. The selected factors of the 2018 experiment included the spray volume (8.7, 12, and 15 L/ha), droplet size Dv50 (100,150, and 200 μm), and flight height (1, 2, and 3 m). The 27 treatments (Table 2) were applied to the same test area. As shown in Table 3, there are 9 treatments in the 2019 test. The selected factors of the 2019 experiment included the spray volume (18, 22.5, and 30 L/ha), droplet size Dv50 (100, 150, and 200 μm). The Dv50 at 100, 150, and 200 μm were set by controlling the rotational speeds of the centrifugal nozzle at 13,400, 8100, 5700 rpm, respectively.

In the cotton planting area, a test area away from the boundary is selected to ensure that the drone velocity remained constant in the test area. Four sampling points with 1 m intervals are deployed in the test area. The sample sites are repeated three times along the spray direction (Fig. 3). Two artificial samplers are used in each sampling point, where one artificial sampler is attached in the upper layer (70 cm above the ground), and the other is placed in the bottom layer (30 cm above the ground).

2.4. Characterization of the spray deposition

2.4.1. Spray penetration

Water-sensitive paper (WSP, 25*75 mm) was used as an artificial

Table 2
Experimental parameters in 2018.

Treatment	Droplet size Dv50 (μm)	Flight height(m)	Spray volume (L/ha)
1	100	1	15
2	150	1	15
3	200	1	15
4	100	2	15
5	150	2	15
6	200	2	15
7	100	3	15
8	150	3	15
9	200	3	15
10	100	1	12
11	150	1	12
12	200	1	12
13	100	2	12
14	150	2	12
15	200	2	12
16	100	3	12
17	150	3	12
18	200	3	12
19	100	1	8.7
20	150	1	8.7
21	200	1	8.7
22	100	2	8.7
23	150	2	8.7
24	200	2	8.7
25	100	3	8.7
26	150	3	8.7
27	200	3	8.7

Table 3
Experimental parameters in 2019.

Treatment	Factors Droplet size Dv50 (μm)	Spraying volume (L/ha)
1	100	18
2	100	22.5
3	100	30
4	150	22.5
5	150	30
6	150	18
7	200	30
8	200	18
9	200	22.5

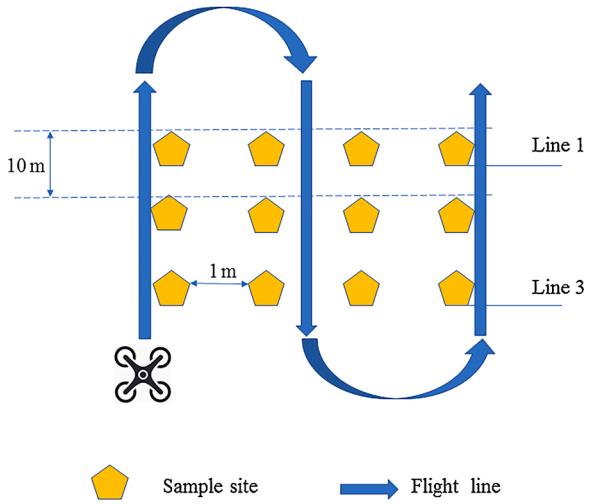

Fig. 3. Experimental layout of each sample site in relation to the UAV sprayer.

sampler. The WSPs were carefully collected using clean tweezers and sealed in Ziploc bags after the UAV spraying. According to the sample site location, the WSPs were scanned in grayscale at 600 DPI to produce a digital image. The images were analyzed using DepositScan™ software (U.S. Department of Agriculture, Agricultural Research Service, Wooster, OH) to calculate the data of droplet deposition.

Cotton is a high-density planting crop, and reasonable high-density planting is the primary measure to increase cotton yield (Feng et al., 2017). However, as the canopy density increases, the spray penetration becomes poor. In the cotton harvest aid application, the defoliation rate in the bottom layer is closely related to the droplet deposition in the lower layer (Meng et al., 2019a). Additionally, the droplet deposition, droplet density and coverage at the bottom of the cotton canopy is used as indicator to describe the spray penetration.

2.4.2. Droplet distribution uniformity

The uniformity of the droplet distribution affects the distribution of pesticide droplets in the horizontal spatial position. In this study, the uniformity of droplet distribution will evaluate the difference in droplet deposition among cotton rows. The distribution uniformity of the droplet deposition, droplet density, and coverage are discussed separately. The Coefficient of Variation (CV) was calculated to study the droplet distribution uniformity. The smaller the CV is, the better the uniformity of the droplet deposition is. The following equation is used to calculate the CV:

$$CV = \frac{SD}{X} \times 100\% \; SD = \sqrt{\frac{\sum_{i=1}^{n} (x_i - X)^2}{n-1}} \quad (1)$$

where SD is the standard deviation; X means the average data of droplet; x_i is the data of droplet per square centimeter of WSP; n is the total number of WSP pieces in each UAV treatment.

2.5. Weather conditions

The environmental parameters were collected by the Kestrel weather station (Model NK-5500, Nielsen-Kellerman Co., Boothwyn, PA, 209 USA) with a collection frequency of 2 s and include the temperature, humidity, wind direction, wind speed, etc. The results in Table 4 show that the temperature and humidity conditions remained relatively stable during the test. The natural wind was the transverse wind perpendicular to the route.

2.6. Statistical analysis

In this research, Statistical Product and Service Solutions (SPSS v. 25.0, SPSS Inc., Chicago, IL, USA) was used for the statistical analysis. The data were compared across all factor combinations and for each experiment separately using multi-way ANOVA. The simple effect was analyzed when the interaction effect was significant. Duncan's multiple range test was used for multiple comparisons.

3. Results and discussion

3.1. Spray penetration

In this section, the effects of the flight height, spray volume, and droplet size on the spray penetration are analyzed. The droplet deposition, coverage and droplet density of the sampling points at the bottom of the cotton canopy were separately counted. Multivariate analysis of variance was performed on the spray penetration data from 2018 and

Table 4
Temperature, humidity and wind speed during the test.

Year	Mean Temperature ℃	Mean Humidity %	Mean Wind Speed m/s
2018	29.0 ± 2.1	19.1 ± 2.0	1.5 ± 0.8
2019	25.2 ± 0.8	36.8 ± 2.6	2.3 ± 0.3

2019. The results of each test in 2018 and 2019 are shown in Figs. 4 and 5 . The droplet distribution results within the treatments and interaction effects of the various factors are shown in Tables 5 and 6 .

3.1.1. Droplet deposition

According to Table 5, droplet size and spray volume have a significant impact on the droplet deposition in the 2018 test. The droplet deposition in the lower part of the canopy gradually increases with the increase of the Dv50. When the Dv50 is 200 μm, the average droplet deposition of each treatment is 0.02 μl/cm^2, compared to 0.01 μl/cm^2 at 100 μm. The maximum droplet deposition is achieved at the T8 (Fig. 4) while the spray volume is 15 L/ha. In addition, flight height and droplet size have an interactive effect on deposition (Table 6, $P = 0.015$). As shown in Fig. 6, when the flight height is 1 m, there is no difference in the deposition among the treatments of droplet size. When the flight height is 2 m or 3 m, the average deposition of the 200 μm treatment is the higher. In the 2019 test, the droplet size has an significant effect on the droplet deposition. As shown in Fig. 5, when the Dv50 is 200 μm (T7, T8,T9 in 2019 test), the result of the deposition is much higher than 100 μm (T1,T2,T3 in 2019 test) and 150 μm (T4,T5,T6 in 2019 test).

From the two-year test data, it can be seen that the droplet size Dv50 affects the penetration of the droplets, and coarse droplets can obtain a better deposition at the bottom of the canopy. Although there was no significant difference among the spray volume treatments in the 2019 test (Table 5), the deposition was much higher than the 2018 test results (compared between Figs. 4 and 5). And as the spray volume increases, the average deposition of each treatment increases.

3.1.2. Coverage

According to Table 6, the droplet size has an interactive effect with the flight height ($P = 0.027$, 2018) and the spray volume ($P = 0.05$, 2019). When the flight height is 3 m, the maximum droplet coverage is 0.49 % when the Dv50 is 150 μm. There is no significant difference in the droplet coverage when the flight heights are 1 m and 2 m (Fig. 7). When the application volume is 18 L/ha and the Dv50 is 150 μm or 200 μm, the coverage is higher than 100 μm. When the application volume is 22.5 L/ha and 30 L/ha, the maximum coverage of the bottom was obtained at the droplet size of 200 μm (Fig. 8). The results show that coarse droplets (compared with 100 μm) could pass through the cotton canopy to the bottom and obtain better droplet coverage, this conclusion is more significant with the increase of the application volume.

In the 2018 test, spray volume also has a significant impact on the coverage (Table 5). When the spray volume is 15 L/ha, the maximum average coverage of 0.395 % was obtained. According to Fig. 4, the coverage results of the 2018 trial range from 0.15 % (T13, 12 L) to 0.65 % (T8, 15 L), while the results in 2019 (Fig. 5) range from 0.5 % (T1, 18 L) to 4.03 % (T7, 30 L). The coverage results in 2019 are much higher than the results in 2018.

3.1.3. Droplet density

According to Table 5, flight height, spray volume, and droplet size have a significant impact on the droplet density. When the flight height is 1 m, the average droplet deposit of each treatment is 7.94 /cm^2, compared with 5.16 /cm^2 at 2 m and 5.07 /cm^2 at 1 m. The droplet density varies with the droplet size. The average droplet deposit is 8.84 /cm^2 when Dv50 is 100 μm, while 3.51 /cm^2 in 200 μm and 5.83 /cm^2 in 150 μm. It is no different between 8.7 L/ha and 12 L/ha. When the spray volume is 15 L/ha, the average droplet density is 7.76 /cm^2. In the 2019 test, the deposition density increases as the droplet Dv50 decreases.

The results in Section 3.1 have shown that the flight height, spray volume, and droplet size have significant effects on spray penetration. Lowering the flight height of the drone, increasing the spray volume and Dv50 can improve the distribution of droplets at the bottom of the cotton canopy. The impact of Dv50 on spray penetration varies with the level of spray volume and flight height. At lower flight heights or larger spray volumes, the droplet size Dv50 will have a more significant impact on spray penetration. In this study, the flight height refers to the drone's distance relative to the upper surface of the crop canopy. Reducing the flight height will shorten the distance that the droplets move in the air. Thereby reducing the effects of environmental factors, such as natural wind, temperature, humidity, etc., on the drift and evaporation (Bueno et al., 2017). Thus, more droplets are deposited on the crop surface. The impact of the droplet size on the penetrability varies from study to study. Chen studied (Chen et al., 2020) the droplet deposition with different nozzle treatments on rice canopy and the control of the rice planthopper. The test results show that the nozzles with fine droplet sizes can obtain better coverage and control of the rice planthopper. After drone spraying, Qin (Qin et al., 2016) counts the droplet size distribution at the bottom of the rice canopy. The results show that the droplets with fine size account for the most significant proportion, so it is considered that the droplets with fine sizes have better penetration. The experimental crops of these two studies are rice, and the application area is located in southern China, which is an area with high humidity. For example, the average humidity in Chen's research is 80 %. The experimental area of this study is Xinjiang, northwest China, which is a typical temperate continental climate, with an average humidity from 19.1 %–36.8 %. The environmental parameters differ significantly from the above studies, and droplets with fine sizes are more likely to evaporate in this environment, so this study believes that the droplet size should be increased in the cotton harvest aid application.

Increasing the spray volume can significantly improve the coverage and penetration. The conclusion is consistent with Wang's research

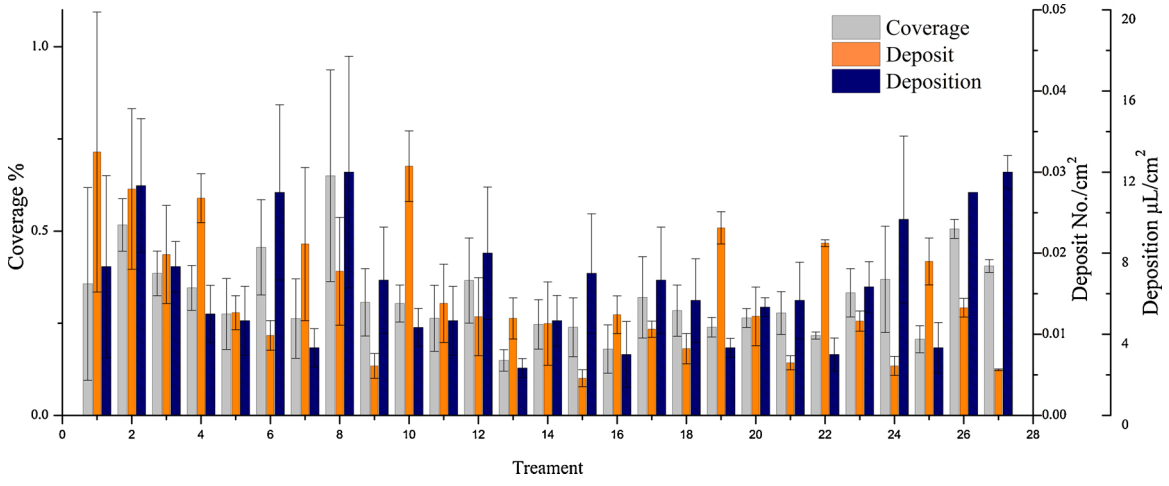

Fig. 4. The spray penetration results of droplet distribution in the 2018 test.

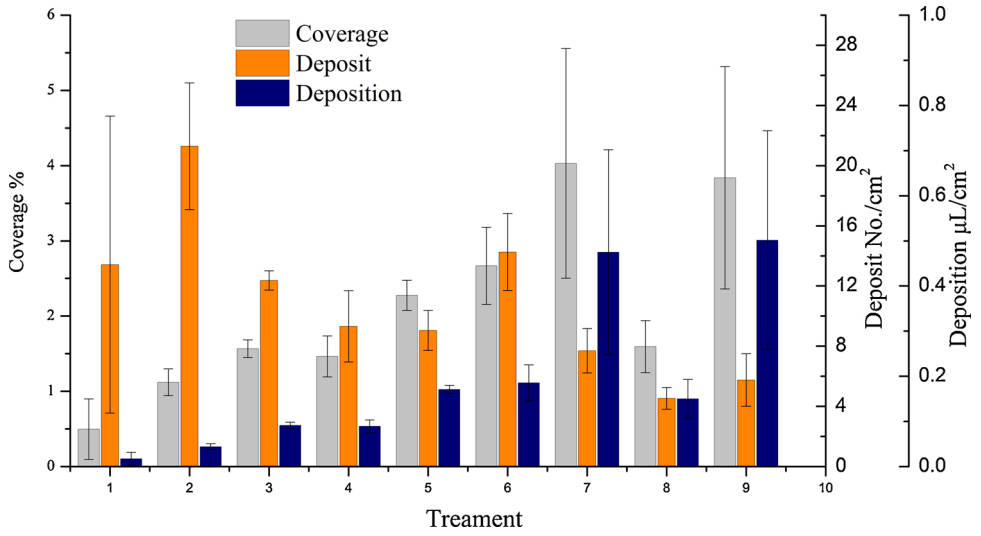

Fig. 5. The spray penetration results of droplet distribution in the 2019 test.

Table 5
The result of droplet distribution at the bottom of cotton.

Factors	Droplet deposition (μl/cm^2)			Coverage (%)			Droplet density (No./cm^2)		
	Level 1	Level2	Level 3	Level 1	Level2	Level 3	Level 1	Level 2	Level 3
2018									
Spray volume	0.017 ± 0.009ab	0.013 ± 0.007b	0.019 ± 0.011a	0.313 ± 0.113b	0.261 ± 0.104b	0.395 ± 0.197a	5.273 ± 2.660b	5.148 ± 3.122b	7.757 ± 4.712a
Flight height	0.016 ± 0.008a	0.015 ± 0.009a	0.018 ± 0.011a	0.330 ± 0.138a	0.292 ± 0.125a	0.347 ± 0.188a	7.944 ± 4.711a	5.161 ± 2.869b	5.073 ± 2.750b
Droplet size	0.010 ± 0.001b	0.019 ± 0.010a	0.020 ± 0.010a	0.251 ± 0.125b	0.375 ± 0.185a	0.343 ± 0.116a	8.837 ± 3.968a	5.831 ± 2.875b	3.510 ± 2.168c
2019									
Spray volume	0.118 ± 0.085a	0.212 ± 0.264a	0.246 ± 0.224a	1.586 ± 1.043b	2.140 ± 1.581ab	2.623 ± 1.449a	10.739 ± 7.801a	12.119 ± 7.721a	9.704 ± 2.444a
Droplet size	0.051 ± 0.034b	0.149 ± 0.052b	0.376 ± 0.266a	1.061 ± 0.542c	2.135 ± 0.652b	3.153 ± 1.764a	15.694 ± 7.820a	10.875 ± 3.419b	5.993 ± 2.018c

[a]Level 1, 2, 3 respectively indicate the test level of each factor, increasing from left to right.
[b]The differences between the three levels of the same factor were compared. Numbers with different letters are significantly different, Duncan's test, $p < 0.05$.

(Wang et al., 2019a). Wang studied the effects of different application volumes on the control of wheat diseases and insect pests by UAV spraying and concluded that increasing the application volume can ensure the impact of droplet deposition and the control of pests and diseases. In recent years, drones have been widely used as spraying tools in China and East Asia. However, due to the take-off weight limitation, the amount of liquid carried by drones is small. The application volume for wheat, rice, and other crops is 12 L/ha -18 L/ha (Meng et al., 2018; Qin et al., 2018; Wang et al., 2019b; Xiao et al., 2019). Because the Chinese government's principle for controlling pests and diseases is prevention, measures are taken at the early pest and disease stages; thus, ultra-low-volume spraying has a good effect on the control of pests and diseases in low crops, such as wheat and rice. However, in this study, cotton is a densely planted crop, and the cotton leaves need to be completely cleared. It is necessary to increase the sprayed volume to ensure the final cotton defoliation effect. This conclusion has been verified in the previous research (Han et al., 2019; Meng et al., 2019b; Xiao et al., 2019).

3.2. Droplet distribution uniformity

In this section, the effects of the flight height, spray volume, and droplet size on the droplet distribution uniformity are compared. The distribution uniformity of droplet deposition, coverage and droplet density were separately analyzed. Multivariate analysis of variance was performed on the droplet distribution uniformity from 2018 and 2019. The results of each test in 2018 and 2019 are shown in Figs. 9 and 10 . The droplet distribution uniformity results within the treatments and interaction effects of the various factors are shown in Tables 7 and 8 .

3.2.1. Droplet deposition

In the 2018 experiment, flight height and spray volume have significant effects on the uniformity of the droplet deposition. As shown in Fig. 9, the uniformity of droplet distribution ranges from 33.5 % (T23) to 89.0 % (T10). The average uniformity of the deposition is better when the height is 2 m, compared with 1 m (Table 7). It can be seen from Table 7 that the average droplet distribution uniformity is 51.1 % at 8.7 L/ha, 64.1 % at 12 L/ha, and 67.9 % at 15 L/ha, respectively. The lower of spray volume, the less difference in droplet distribution between sampling points. There is no significant difference in the distribution uniformity between different droplet size treatments. In the 2019 experiment, there is no significant difference in droplet size and deposition between sampling points. According to Fig. 10, the uniformity of droplet distribution ranges from 40.1 % (T6) to 95.5 % (T3).

3.2.2. Coverage

In the 2018 experiment (Fig. 9), the uniformity of droplet distribution ranges from 32.1 % (T23) to 79.4 % (T10). The spray volume has an interactive effect with the flight height ($P < 0.001$, Table 8). It can be observed from Fig. 11 that when the flight height is 1 m, the uniformity

Table 6
Interaction results of multiple factors on droplet distribution at the bottom layer.

Factors	Df (Factor, error)	Spray Penetration					
		Droplet deposition		Coverage		Droplet density	
		F-value	*P-value*	*F-value*	*P-value*	*F-value*	*P-value*
2018							
Flight height *Spray volume	4,54	2.130	0.090	1.171	0.334	2.135	0.089
Flight height * Droplet size	4,54	3.396	0.015*	2.971	0.027*	0.791	0.536
Spray volume * Droplet size	4,54	0.981	0.426	0.670	0.615	0.500	0.736
Flight height *Spray volume * Droplet size	8,54	1.125	0.362	1.083	0.389	0.956	0.480
2019							
Spray volume * Droplet size	4,18	2.299	0.099	2.918	0.050*	2.030	0.133

[c]Significant at the P <0.05 level, ** significant at the P <0.01 level, *** significant at the P <0.001 level.
[d](2, 54), where 2 corresponds to the factor degree of freedom and 54 refers to the error degree of freedom.

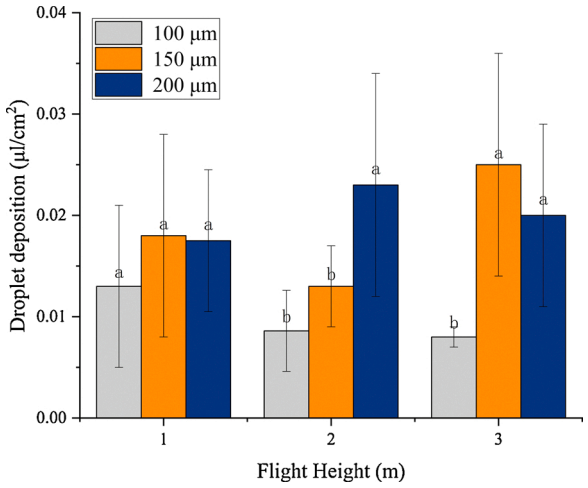

Fig. 6. Droplet deposition results of droplet size at different flight heights.

of the droplet distribution with the different spray volumes are significantly different. The average uniformity of the droplet distribution is 46.8 % (8.7 L/ha, Fig. 11), which is better than at the other levels. When the flight heights are 2 m and 3 m, no significant difference in the uniformity of the droplet distribution with different spray volume levels is found.

Additionally, different droplet size treatments also have differences in the distribution of coverage between sampling points (Table 7). When the Dv50 is 150 μm, the average coverage uniformity of each treatment is better than other treatments, which is 51.4 %. In the 2019 experiment,

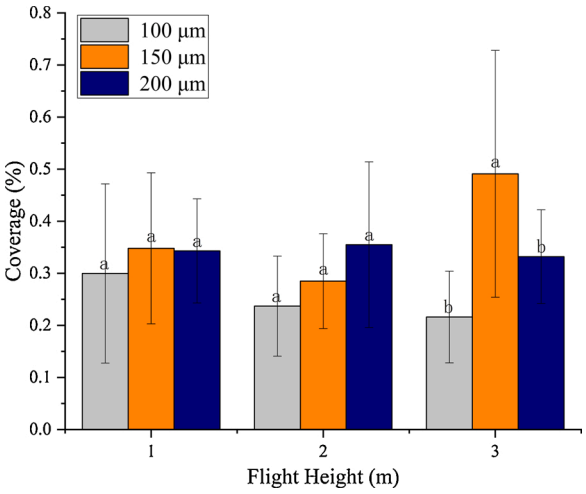

Fig. 7. Coverage results of droplet size at different flight heights.

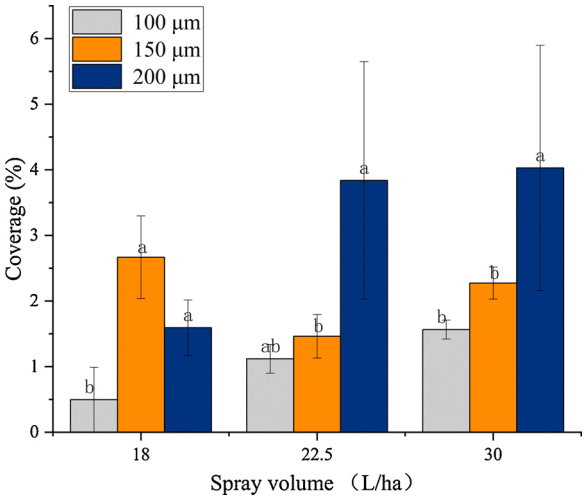

Fig. 8. Coverage results of droplet size at different spray volumes.

there is no significant effect between the spray volume and droplet size on the coverage distribution uniformity (Table 7). As shown in Fig. 10, the uniformity of droplet distribution ranges from 38.1 % (T6) to 81.7 % (T3).

The results show that the increasing flight height helps to improve the uniformity of the droplet distribution. Moreover, when the spray volume is lower than 12 L/ha, the flight height has no significant effect on the uniformity of the distribution of droplets. While the spray volume is15 L/ha, increasing the flight height can improve the uniformity of the droplet distribution in the cotton canopy. The droplet size has little effect on the uniformity of the droplet distribution, only for the droplet coverage, the treatment coverage of 150 μm has better uniformity.

3.2.3. Droplet density

As shown in Fig. 9, the uniformity of droplet distribution ranges from 28.0 % (T24) to 77.2 % (T10) in the 2018 experiment. As shown in Table 7, the spray volume (2018) has a significant impact on the droplet density distribution uniformity. When the spray volume is 8.7 L/ha, the average uniformity of droplet density is 41.4 %, which is better than other treatments. There is no significant difference in the uniformity of the droplet density among the treatments of flight height, droplet size, and spray volume (2019). According to Fig. 10, the uniformity of droplet distribution ranges from 38.9 % (T6) to 76.8 % (T10) in the 2018 experiment.

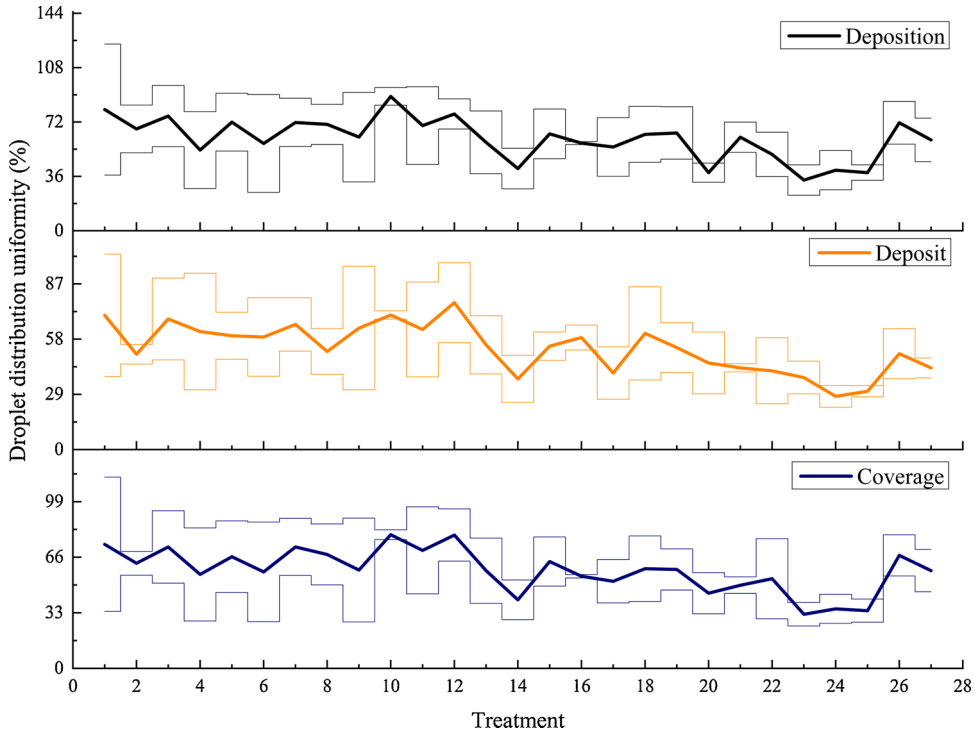

Fig. 9. The uniformity of droplet distribution results of droplet distribution in the 2018 test.

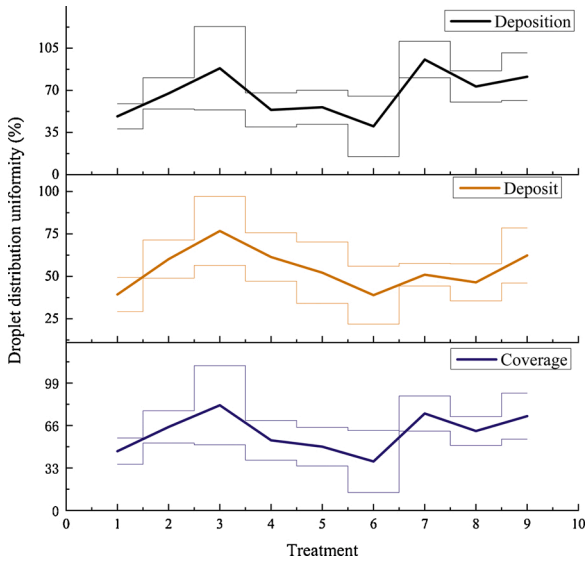

Fig. 10. The uniformity of droplet distribution results of droplet distribution in the 2019 test.

The results in Section 3.2 have shown that the range of droplet distribution uniformity is from 28 % to 89 %. The distribution uniformity of droplet deposition, coverage, and droplet density varies greatly in each treatment. Properly increasing the flight height can reduce the CV value. When the spray volume is lower, the difference in deposition at each sampling point of the canopy becomes smaller. With the increase of the application volume, the uniformity of the droplet distribution becomes worse.

In this study, the uniformity of droplet distribution did not significantly improve with the application parameters. On the contrary, the uniformity deteriorated with the increase of the application volume and the decrease of the flight height. Obviously, increasing the spray volume and reducing the flight height means the improvement of the droplet distribution in Section 3.1. But the location of the test point is fixed, and the original position of high deposition will be higher, which will further aggravate the results between the sampling positions difference.

3.3. *Further discussion of the results*

The phenomenon of poor uniformity and penetration not only occurs in the process of cotton defoliation but is also a common problem encountered by UAV spraying . In this study, the main effects and interaction effects among the operational parameters were analyzed and discussed. As shown in the above results, the penetration of droplets in

Table 7
The result of uniformity of droplet distribution.

Factors	Droplet deposition (μl/cm^2)			Coverage (%)			Droplet density (No./cm^2)		
	Level 1	Level2	Level 3	Level 1	Level2	Level 3	Level 1	Level 2	Level 3
2018									
Spray volume	51.1 ± 18.3a	64.1 ± 21.2b	67.9 ± 27.4b	48.3 ± 17.3a	56.0 ± 16.4a	70.8 ± 27.1b	41.4 ± 13.6a	57.5 ± 20.6b	61.2 ± 23.6b
Flight height	69.4 ± 25.0b	52.4 ± 23.2a	61.3 ± 19.6ab	65.1 ± 26.6b	61.8 ± 20.1b	48.1 ± 17.3a	60.2 ± 22.2a	48.3 ± 20.3a	51.7 ± 20.3a
Droplet size	62.7 ± 25.7a	57.7 ± 22.5a	62.6 ± 22.7a	65.5 ± 23.1b	51.4 ± 23.3a	58.1 ± 20.0ab	56.5 ± 22.4a	48.4 ± 16.9a	55.3 ± 23.8a
2019									
Spray volume	48.1 ± 20.6a	62.9 ± 16.7ab	74.3 ± 31.1b	43.8 ± 16.7a	59.3 ± 14.7a	61.7 ± 27.2a	38.4 ± 12.8a	56.2 ± 12.9a	49.5 ± 25.0a
Droplet size	61.2 ± 32.5a	50.0 ± 11.6a	74.2 ± 23.1a	56.7 ± 29.5a	46.5 ± 10.5a	61.6 ± 18.2a	49.5 ± 24.4a	47.5 ± 17.1a	47.1 ± 15.6a

Table 8
Interaction results of multiple factors on the uniformity of droplet distribution.

Factors	Df (Factor, error)	Spray Penetration					
		Coverage		Droplet deposition		Droplet density	
		F-value	*P-value*	*F-value*	*P-value*	*F-value*	*P-value*
2018							
Flight height *Spray volume	4,54	8.424	<0.001***	0.510	0.728	0.524	0.718
Flight height * Droplet size	4,54	1.489	0.218	0.903	0.469	0.195	0.940
Spray volume * Droplet size	4,54	2.154	0.087	0.400	0.808	0.872	0.487
Flight height *Spray volume * Droplet size	8,54	1.686	0.123	0.619	0.758	0.292	0.966
2019							
Spray volume * Droplet size	4,18	0.729	0.583	0.458	0.766	0.1820	0.169

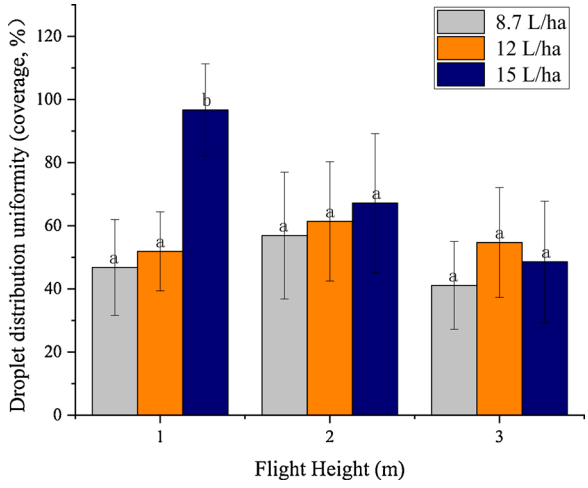

Fig. 11. Droplet distribution uniformity of coverage results of spray volume at different flight heights.

the cotton canopy is indeed improved by changing some operating parameters, especially in lowering the flight height of the drone, increasing the spray volume and the value of Dv50. But the impact on the uniformity of droplet distribution is very limited. Compared with ground spraying equipment and manned aerial spraying equipment, the most notable feature of UAV spraying is its rotor wind field and limited chemical load (Lan and Chen, 2018). Some studies believe that the rotor wind field of the drone can transmit droplets to the bottom of the crop canopy (Chen et al., 2017; Lan and Chen, 2018; Yang et al., 2019), but there is no detailed theoretical analysis. In practical applications, it is found that the droplets sprayed by drones show large differences between the upper and lower layers of the canopy, whether it is low crops or fruit trees (Chen et al., 2020; Wang et al., 2020b). It is an urgent problem to improve droplet penetration. In this study, the difference between the upper and lower layers was not directly compared, but analyzed how to increase the droplet deposition, deposition density and coverage at the bottom. Only by increasing the distribution of the droplets at the bottom to meet the spraying requirements, and which may achieve a consistent control effect the upper and lower layers have a consistent pest control effect. In this paper, lowering the flight height of the drone, increasing the spray volume and Dv50 can improve the distribution of droplets at the bottom . However, it is may not easy to achieve in actual practice. Lowering the flight height means reducing the spray width; and increasing the spray volume means reducing the single spray area, which will reduce the actual operating efficiency of the drone. Due to the lack of mandatory technical specifications or laws, operators are more inclined to improve efficiency rather than droplet deposition effects (Lan and Chen, 2018). In the future development of drones, researchers may improve the safety of drone applications by studying application techniques, and policymakers should pass laws to ensure the accuracy of the application.

Obviously, changing the operating parameters did not affect the uniformity of droplet distribution in this study. According to previous research, the droplet distribution uniformity of the drone was originally lower than that of the other spray machines (Qin et al., 2014, 2016; Tang et al., 2018). The droplet distribution uniformity may be influenced by the wind field of rotors and the nozzle arrangement position (Chen et al., 2017; Yang et al., 2019). That is, the structural parameters of the drone lead to an uneven distribution of droplets. Without considering the rotor wind field, the original nozzle layout may has good uniformity of distribution (Zhou et al., 2017). But in fact, the wind field of the rotor has a greater impact. The appropriate position of the nozzles under rotors may be considered in subsequent research. In addition, the uniformity of droplet distribution is a relative value, which indicates the difference between cotton sampling points, not the actual deposition value of the sampling points. Although increasing the spray volume, the droplet deposition on the horizontal plane varies greatly, but the results of Section 3.1 show that the absolute value of the droplet deposition will increase. Increasing the minimum value of droplet deposition in the cotton canopy may cause waste of pesticides, but it has positive significance in ensuring the consistency of cotton defoliation.

4. Conclusions

This study focuses on the canopy penetration and droplet distribution uniformity of UAV spraying, which meets the requirements of cotton harvest aid application. The XAG P series plant protection drone with centrifugal nozzles was used as the spraying equipment. Full factorial tests of flight height, droplet size, and spray volume were carried out in Xinjiang for two years of field trials. The uniformity of the droplet distribution and spray penetration were analyzed. The droplet deposition, droplet density, and coverage were discussed separately. The results show that flight height, spray volume, and droplet size have significant effects on spray penetration. Lowering the flight height of the drone, increasing the spray volume and Dv50 can improve the distribution of droplets at the bottom of the cotton canopy. The impact of Dv50 on spray penetration varies with the level of spray volume and flight height. At lower flight heights or larger spray volumes, the droplet size Dv50 will have a more significant impact on spray penetration. As for droplet distribution uniformity, with the increase of the application volume and decrease of the flight height, the uniformity of the droplet distribution becomes worse. The influence of flight parameters on the uniformity of droplet distribution is very limited.

CRediT authorship contribution statement

Pengchao Chen: Conceptualization, Validation, Formal analysis, Investigation, Writing - original draft. **Fan Ouyang:** Investigation, Resources, Writing - review & editing. **Guobin Wang:** Conceptualization, Investigation, Formal analysis. **Haixia Qi:** Investigation, Formal analysis. **Weicheng Xu:** Investigation, Visualization. **Weiguang Yang:** Investigation. **Yali Zhang:** Methodology, Data curation, Formal

analysis, Writing - review & editing. **Yubin Lan:** Conceptualization, Investigation, Resources, Writing - review & editing, Supervision, Project administration, Funding acquisition.

Declaration of Competing Interest

The authors report no declarations of interest.

Acknowledgments

We deeply thank XAG Co., Ltd. and Hebei Mingshun Agricultural Technology Co., Ltd. for the agricultural UAV and corresponding materials. This research was supported by the China Agriculture Research System (CARS-15-22), the 111 Project (D18019), the leading talents of the the leading talents of the Guangdong province program (2016LJ06G689) and the Science and Technology Planning Project of Guangzhou (201807010039).

References

Bueno, M.R., Cunha, J.P.A.R.D., De Santana, D.G., 2017. Assessment of spray drift from pesticide applications in soybean crops. Biosyst. Eng. 154, 35–45. https://doi.org/10.1016/j.biosystemseng.2016.10.017.

Campos, J., Llop, J., Gallart, M., 2019. Development of canopy vigour maps using UAV for site-specific management during vineyard spraying process. Precis. Agric. https://doi.org/10.1007/s11119-019-09643-z.

Cao, X., 2015. Whole genome sequencing of cotton—a new chapter in cotton genomics. Sci. China Life Sci. 58, 515–516. https://doi.org/10.1007/s11427-015-4862-z.

Cathey, G.W., 1980. Harvest-aid chemicals and practices for cotton. Outlook Agric. 10, 191–197. https://doi.org/10.1177/003072708001000406.

Chen, S.D., Lan, Y.B., Li, J.Y., Zhou, Z.Y., Mao, Y.D., 2017. Effect of wind field below unmanned helicopter on droplet deposition distribution of aerial spraying. Int. J. Agric. Biol. Eng. 10, 67–77. https://doi.org/10.3965/j.ijabe.20171003.3078.

Chen, P., Lan, Y., Huang, X., Qi, H., Wang, G., Wang, J., Wang, L., Xiao, H., 2020. Droplet deposition and control of planthoppers of different nozzles in two-stage rice with a quadrotor unmanned aerial vehicle. Agronomy 10, 303. https://doi.org/10.3390/agronomy10020303.

Fang, X., Zhao, J., Zhou, Y., Wang, G., Han, X., Wei, F., Deng, J., Lan, Y., 2018. Effects of dosage and spraying volume on cotton defoliants efficacy: a case study based on application of unmanned aerial vehicles. Agronomy 8, 85. https://doi.org/10.3390/agronomy8060085.

Feng, L., Dai, J., Tian, L., Zhang, H., Li, W., Dong, H., 2017. Review of the technology for high-yielding and efficient cotton cultivation in the northwest inland cotton-growing region of China. Field Crops Res. 208, 18–26. https://doi.org/10.1016/j.fcr.2017.03.008.

Ferguson, J.C., Chechetto, R.G., Hewitt, A.J., Chauhan, B.S., Adkins, S.W., Kruger, G.R., O'Donnell, C.C., 2016. Assessing the deposition and canopy penetration of nozzles with different spray qualities in an oat (Avena sativa L.) canopy. Crop Prot. 81, 14–19. https://doi.org/10.1016/j.cropro.2015.11.013.

Han, X., Yu, J., Lan, Y., Kong, F., Yi, L., 2019. Determination of application parameters for cotton defoliants in the Yellow River Basin. Int. J. Precis. Agric. Aviat. 2 https://doi.org/10.33440/j.ijpaa.20190201.0016.

Lan, Y., Chen, S., 2018. Current status and trends of plant protection UAV and its spraying technology in China. Int. J. Precis. Agric. Aviat. 1 https://doi.org/10.33440/j.ijpaa.20180101.0002.

McMullan, P.M., Thomas, J.M., 2003. Cotton Insecticide and Defoliant Efficacy As Influenced by Spray Application Parameters. ASTM International, pp. 184–197. https://doi.org/10.1520/STP11206S.

Meng, Y., Lan, Y., Mei, G., Guo, Y., Song, J., Wang, Z., 2018. Effect of aerial spray adjuvant applying on the efficiency of small unmanned aerial vehicle for wheat aphids control. Int. J. Agric. Biol. Eng. 11, 46–53. https://doi.org/10.25165/ijabe.v11i5.4298.

Meng, Y., Han, Y., Liang, Z., Su, J., Lan, Y., 2019a. Harvest-aid application strategy in different cotton planting densities by unmanned aerial vehicle. Int. J. Precis. Agric. Aviat. 2 https://doi.org/10.33440/j.ijpaa.20190201.0027.

Meng, Y., Song, J., Lan, Y., Mei, G., Liang, Z., Han, Y., 2019b. Harvest aids efficacy applied by unmanned aerial vehicles on cotton crop. Ind. Crops Prod. 140, 111645 https://doi.org/10.1016/j.indcrop.2019.111645.

Meng, Y., Su, J., Song, J., Chen, W.-H., Lan, Y., 2020. Experimental evaluation of UAV spraying for peach trees of different shapes: effects of operational parameters on droplet distribution. Comput. Electron. Agric. 170, 105282 https://doi.org/10.1016/j.compag.2020.105282.

Qin, W., Xue, X., Zhou, L., Zhang, S., Sun, Z., Kong, W., Wang, B., 2014. Effects of spraying parameters of unmanned aerial vehicle on droplets deposition distribution of maize canopies. Trans. Chin. Soc. Agric. Eng. 30, 50–56. https://doi.org/10.3969/j.issn.1002-6819.2014.05.007.

Qin, W.-C., Qiu, B.-J., Xue, X.-Y., Chen, C., Xu, Z.-F., Zhou, Q.-Q., 2016. Droplet deposition and control effect of insecticides sprayed with an unmanned aerial vehicle against plant hoppers. Crop Prot. 85, 79–88. https://doi.org/10.1016/j.cropro.2016.03.018.

Qin, W., Xue, X., Zhang, S., Wei, G., Wang, B., 2018. Droplet deposition and efficiency of fungicides sprayed with small UAV against wheat powdery mildew. Int. J. Agric. Biol. Eng. 11, 27–32. https://doi.org/10.25165/j.ijabe.20181102.3157.

Siebert, J.D., Stewart, A.M., Miller, D.K., Craig, C.C., 2006. Effect of carrier volume and nozzle type on cotton harvest-aid efficacy. J. Cotton Sci.

Tang, Y., Hou, C.J., Luo, S.M., Lin, J.T., Yang, Z., Huang, W.F., 2018. Effects of operation height and tree shape on droplet deposition in citrus trees using an unmanned aerial vehicle. Comput. Electron. Agr. 148, 1–7. https://doi.org/10.1016/j.compag.2018.02.026.

Tian, J., Zhang, X., Yang, Y., Yang, C., Xu, S., Zuo, W., Zhang, W., Dong, H., Jiu, X., Yu, Y., 2017. How to reduce cotton fiber damage in the Xinjiang China. Ind. Crops Prod. 109, 803–811. https://doi.org/10.1016/j.indcrop.2017.09.036.

Wang, T., 2020. National plant protection drones have exceeded 50,000. Farmers Dly 8. http://szb.farmer.com.cn/2020/20200103/20200103_008/20200103_008_1.htm (2020/6/26).

Wang, C., Song, J., He, X., Wang, Z., Wang, S., Meng, Y., 2017. Effect of flight parameters on distribution characteristics of pesticide spraying droplets deposition of plant-protection unmanned aerial vehicle. Trans. Chin. Soc. Agric. Eng. 33, 109–116. https://doi.org/10.11975/j.issn.1002-6819.2017.23.014.

Wang, G., Lan, Y., Qi, H., Chen, P., Hewitt, A., Han, Y., 2019a. Field evaluation of an unmanned aerial vehicle (UAV) sprayer: effect of spray volume on deposition and the control of pests and disease in wheat. Pest Manag. Sci. 75, 1546–1555. https://doi.org/10.1002/ps.5321.

Wang, G., Lan, Y., Yuan, H., Qi, H., Chen, P., Ouyang, F., Han, Y., 2019b. Comparison of spray deposition, control efficacy on wheat aphids and working efficiency in the wheat field of the unmanned aerial vehicle with boom sprayer and two conventional knapsack sprayers. Appl. Sci. 9 https://doi.org/10.3390/app9020218.

Wang, Juan, Lan, Yubin, Wen, Sheng, Hewitt, Andrew John, Chen, Pengchao, 2020a. Meteorological and flight altitude effects on deposition, penetration, and drift in pineapple aerial spraying. Asia Pac. J. Chem. Eng. https://doi.org/10.1002/apj.2382.

Wang, G., Han, Y., Li, X., Andaloro, J., Chen, P., Hoffmann, W.C., Han, X., Chen, S., Lan, Y., 2020b. Field evaluation of spray drift and environmental impact using an agricultural unmanned aerial vehicle (UAV) sprayer. Sci. Total Environ. 737, 139793 https://doi.org/10.1016/j.scitotenv.2020.139793.

Xiao, Q., Du, R., Zhou, T., Han, X., Wang, G., Fu, W., 2019. Effects of alkyl ethyl sulfonate dosage on cotton defoliation efficacy sprayed by UAV. Int. J. Precis. Agric. Aviat. 2 https://doi.org/10.33440/j.ijpaa.20190202.33.

Yang, S., Zheng, Y., Liu, X., 2019. Research status and trends of downwash airflow of spray UAVs in agriculture. Int. J. Precis. Agric. Aviat. 2, 1–8. https://doi.org/10.33440/j.ijpaa.20190201.0023.

Zhang, X., Song, Xiu-Peng, Liang, Yong-Jian, Qin, Zhen-Qiang, Zhang, Bao-Qing, Wei, Jin-Ju, Li, Yang-Rui, Wu, Jian-Ming, 2020. Effects of spray parameters of drone on the droplet deposition in sugarcane canopy. Sugar Tech 1–6. https://doi.org/10.1007/s12355-019-00792-z.

Zhou, Q., Xue, X., Yang, F., Qin, W., 2017. Trajectory and deposition distribution features of centrifugal atomization nozzle droplet. J. Jiangsu Univ. https://doi.org/10.3969/j.issn.1671-7775.2017.01.004.

Zhou, T., Xiao, Q., Du, R., Han, X., zhang, G., Wang, G., 2020. Research advances on cotton harvest aids in China. Cotton Sci. 170–184. https://doi.org/10.11963/1002-7807.ztthxq.20200303.

Zhu, H., Derksen, R.C., Ozkan, H.E., Reding, M.E., Krause, C.R., 2008. Development of a canopy opener to improve spray deposition and coverage inside soybean canopies: part 2: opener design with field experiments. Trans. Asabe 51, 1913–1922. https://doi.org/10.13031/2013.25390.

Crop Protection 188 (2025) 107008



Contents lists available at ScienceDirect

Crop Protection

journal homepage: www.elsevier.com/locate/cropro

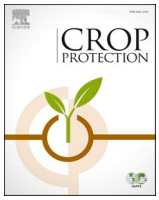

Citrus huanglongbing detection: A hyperspectral data-driven model integrating feature band selection with machine learning algorithms

Kangting Yan [a,b,1], Xiaobing Song [d,1], Jing Yang [a,c], Junqi Xiao [a,c], Xidan Xu [a,c], Jun Guo [a,c], Hongyun Zhu [c], Yubin Lan [a,b,*], Yali Zhang [a,c,**]

[a] National Center for International Collaboration Research on Precision Agricultural Aviation Pesticides Spraying Technology, Guangzhou, 510642, China
[b] College of Electronic Engineering (College of Artificial Intelligence), South China Agricultural University, Guangzhou, 510642, China
[c] College of Engineering, South China Agricultural University, Guangzhou, 510642, China
[d] Institute of Plant Protection, Guangdong Academy of Agricultural Sciences, Guangdong Provincial Key Laboratory of High Technology for Plant Protection, Guangzhou, 510640, China

ARTICLE INFO

Keywords:
Hyperspectral technology
Citrus Huanglongbing
Machine learning
Feature band extraction
Rapid detection

ABSTRACT

This study explored rapid detection techniques for citrus Huanglongbing (HLB), a disease that severely impacts global citrus production. The method based on hyperspectral technology combined with machine learning algorithms provides new ideas for rapid HLB identification. Algorithm selection is crucial for processing efficiency and hyperspectral data interpretation. Hyperspectral data from healthy, mild HLB-infected, and macular (not related to HLB) citrus leaves were captured using a hyperspectrometer, with qPCR validation. Three preprocessing methods were selected to preprocess the spectral data. Competitive Adaptive Reweighted Sampling (CARS) and Successive Projections Algorithm (SPA) were used to extract feature bands from the hyperspectral data, and the range of the number of filtered feature bands as a percentage of the full band was 22.87%–28.31% and 3.27%–4.17%, respectively. Five distinct algorithms were then employed to construct classification models. Upon evaluation, the SPA-STD-SVM algorithm combination proved most effective, boasting a 97.46% accuracy and a 98.55% recall rate. The results demonstrate that suitable machine learning algorithms can effectively classify the hyperspectral data of citrus leaves in three different states: healthy, mild HLB-infected, and macular. This provides an effective approach for using hyperspectral data to differentiate citrus Huanglongbing.

1. Introduction

Citrus HLB is caused by *Candidatus Liberibacter* spp. That parasitizes the phloem of citrus plants. It is capable of infecting a wide range of closely related genera in the Citrus subfamily of the *Subfam. AURANTIOIDAE Engl.*, including *Citrus* L. and *Poncirus Raf.* (Sagaram et al., 2009; Achor et al., 2010). Citrus HLB is a serious infectious disease in citrus fruit crops, which is mainly transmitted by Asian citrus psyllid with high transmission efficiency (Bové, 2006; Gasparoto et al., 2018). After being infected with the pathogen for a period of time, the nutrition and metabolism of citrus would be affected. The leaves become yellowed and curled, the canopy gradually withers, the tree weakens, and eventually leads to the death of citrus trees (Bové, 2014; Achor et al., 2020). Currently, there is no significant prevention and treatment methods for citrus HLB. Farmers frequently employ agronomic practices such as irrigation and nutrient management. For late-stage infected citrus trees, they can only be eradicated completely including the roots after harvest, to prevent the spread of the disease (Boina and Bloomquist, 2015; Lee et al., 2015; Zhang et al., 2020). Consequently, timely detection of citrus HLB-infected trees is very important for disease control in citrus orchards, and is of great significance for the development of the citrus industry.

Traditional farmers discern citrus HLB through ocular assessment, however, this visual approach lacks the precision to diagnose accurately

* Corresponding author. National Center for International Collaboration Research on Precision Agricultural Aviation Pesticides Spraying Technology, Guangzhou, 510642, China.
** Corresponding author. National Center for International Collaboration Research on Precision Agricultural Aviation Pesticides Spraying Technology, Guangzhou, 510642, China.
E-mail addresses: ylan@scau.edu.cn (Y. Lan), ylzhang@scau.edu.cn (Y. Zhang).
[1] These authors contributed equally to this work.

https://doi.org/10.1016/j.cropro.2024.107008
Received 28 December 2023; Received in revised form 24 June 2024; Accepted 29 October 2024
Available online 30 October 2024
0261-2194/© 2024 Elsevier Ltd. All rights are reserved, including those for text and data mining, AI training, and similar technologies.

during the incipient phases of HLB infection or under conditions of mild manifestation. At the same time, nutrient deficiencies can readily be misinterpreted as disease symptoms. The employment of molecular diagnostic techniques for the detection of citrus HLB pathogens can accurately diagnose citrus HLB, and has high sensitivity and specificity (Arredondo Valdés et al., 2016; Park et al., 2018; Hong et al., 2019). However, the cost of this technology is relatively high, and it requires professional laboratory equipment and operation skills, so it is not suitable for widespread application in the field.

In recent years, the combination of machine learning and hyperspectral detection has engendered substantial advancements in the application of rapid detection technology for crop pests and diseases. Hyperspectral technology can be used for the study of pests and disease infections detection in crops (Shi et al., 2017; Xiao et al., 2022; Zhao et al., 2022). The quantitative changes and even qualitative changes of plant leaves and fruit internal materials would be caused, under biological or non-biological stress (Hernández et al., 2009; Lee et al., 2015b). Employing hyperspectral equipment to obtain the spectral data of crop leaves, fruits, and other parts, and the analytical processing of such data yields an extensive array of crop characteristic parameters (Thomas et al., 2018; Liu et al., 2018; Deng et al., 2019). The application of machine learning algorithms is conducive to screening and simplifying disease-sensitive feature parameters, providing a data basis for the automatic identification and prediction of crop pests and diseases. In recent years, spectral technology combined with machine learning detection methods have also been applied to the rapid detection of citrus HLB. Weng et al. (2018) used hyperspectral imaging technology to obtain high-spectral images of citrus leaves in different seasons and different degrees of infection, and combined carbohydrate metabolism analysis to establish a least squares-support vector machine discrimination model, attaining an aggregate discernment precision of 92.6%; Deng et al. (2019) discussed a feature band extraction method based on entropy distance and sequential backward selection, and proposed a nondestructive detection method for citrus HLB in the field based on hyperspectral reflectivity, with an accuracy of 96% in the identification of healthy leaves and symptomatic leaves of HLB; Sun et al. (2017) adopted second-order derivative combined with smooth spectral preprocessing method for reflectance spectrum treatment, and established a partial least squares discrimination model for nutritional deficiency and HLB leaves. The leave-one-out cross-validation method was used to determine the optimal principal component factor number as 17, and the modeling correlation coefficient was 0.96. The application of machine learning algorithms for hyperspectral data processing can effectively extract feature data and reduce the amount of computation during rapid detection. Therefore, continuous exploration is needed for the application of machine learning algorithms in hyperspectral data processing to obtain more efficient, accurate, and stable methods.

In light of the significant risk posed by citrus HLB, early detection and rapid implementation of appropriate measures are essential to mitigate agricultural yield diminution. This study employed hyperspectral technology combined with machine learning algorithms, primarily investigating the disparate impacts of utilizing traditional machine learning classification models or advanced deep learning neural networks for the analysis of citrus HLB sample data, subsequent to varying data preprocessing techniques and feature band selection methodologies. Among them, the effects of CARS algorithm and SPA algorithm as hyperspectral feature band extraction methods on the performance of classification models were mainly compared and analyzed. The preferred combination of algorithms can provide data reference for the study of rapid detection methods for citrus HLB based on hyperspectral technology.

2. Materials and methods

2.1. Overview of experimental base

The experimental site was located in a citrus orchard in Huangtian Town, Sihui City, Zhaoqing City, Guangdong Province, China, as delineated in Fig. 1. The climatic conditions of the area were subtropical monsoon with an average annual temperature of 21 °C and an annual precipitation of 1800 mm.

2.2. Hyperspectral equipment and data acquisition

The hyperspectral data of citrus leaves was acquired using the ASD FieldSpec® HandHeld™ 2 spectrometer (Malvern Panalytical Ltd., UK), which is equipped with a unique spectral acquisition instrument capable of rapidly and non-destructively acquiring spectra in the wavelength range of 325–1075 nm. After the instrument start-up system loading, the spectrometer was calibrated with a standard white plate collecting 100% reflectance. In order to minimize systematic random errors, the instrument was set to acquire 10 sets of hyperspectral data per acquisition during data collection.

The citrus trees selected for this study were of similar age and grew under the same environmental conditions. Data collection of citrus leaves was conducted from 10:00 to 14:00 in November 2022 under sunny weather conditions with sporadic cloud cover and no wind. In addition, the citrus HLB trees used for data collection in this study were trees with less than 1/3 of the total plant in terms of symptomatic branch tips. Based on the HLB disease severity classification criteria studied by Mei et al. (2014), the diseased plants in this study classified as mild to moderate, which suitable for early detection of HLB, and are collectively referred to as “mild HLB-infected” in this paper. The process of hyperspectral data acquisition from citrus leaves is shown in Fig. 2. The samples collected in this study originated from three types of citrus trees: healthy, mild HLB-infected, and macular (leaves that do not carry HLB pathogens but are mottled and yellowed due to nutrient deficiencies or other pests and diseases). The picked citrus trees are from different planting zones within the orchard. During data collection, experimenters wore dark colored clothes to avoid interference from light. Meanwhile, the acquisition angle of the equipment was kept perpendicular to the leaves, and the center of the leaves was selected for data acquisition to reduce the data bias, as shown in Fig. 2.

2.3. Hyperspectral data calibration

Compared with conventional PCR, Real-time Quantitative polymerase chain reaction (qPCR) has more advantages in timeliness, sensitivity and repeatability. It can provide an accurate and reliable quarantine method for the identification of pathogen of citrus HLB.

To ensure the reliability of the sample data in this study, the branches and leaves after the hyperspectral data had been collected were stored in sealed bags (with some gaps for respiration) for preservation and labeling. Afterwards, they were then transported to the laboratory and stored at 5 °C, waiting for qPCR analysis. In the process of qPCR detection, the sample is prepared on the basis of the stem. 6 to 8 leaves were selected from the same branch, and one leaf disc was randomly punched from each leaf using a 1 cm diameter punch. The leaf disc samples obtained from the same branch were then placed in the same centrifuge tube for further extraction and dilution. The qPCR results are shown in Fig. 3. Samples with $Ct < 34$ were defined as positive for HLB. Samples with $Ct \geq 34$, or in which $RFU = 0$, were defined as negative for HLB (Li et al., 2006; Huang et al., 2023).

After qPCR validation, the 20 citrus trees sampled in this study consisted of 4 healthy citrus trees, 8 mildly HLB-infected citrus trees, and 8 macular (not related to HLB) citrus trees. A total of 1380 sets of hyperspectral data were collected in this experiment. The hyperspectral data were classified and calibrated based on the qPCR detection results.

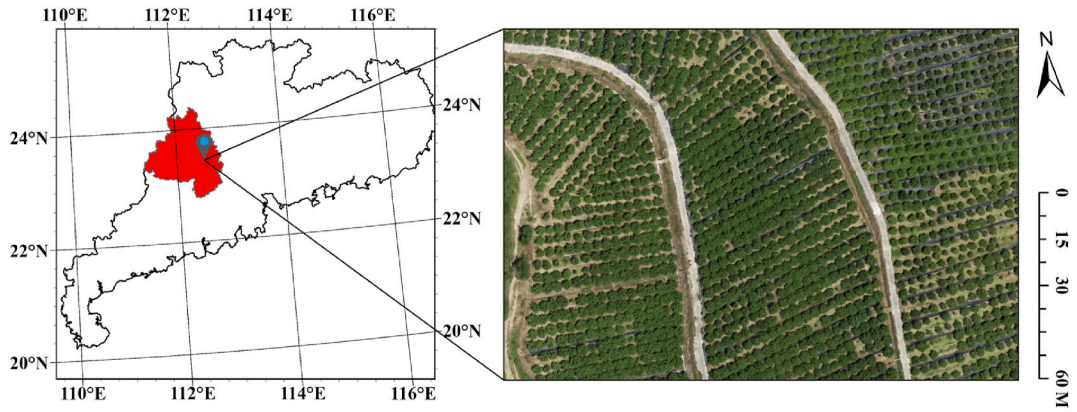

Fig. 1. Geographic location of sampling site.

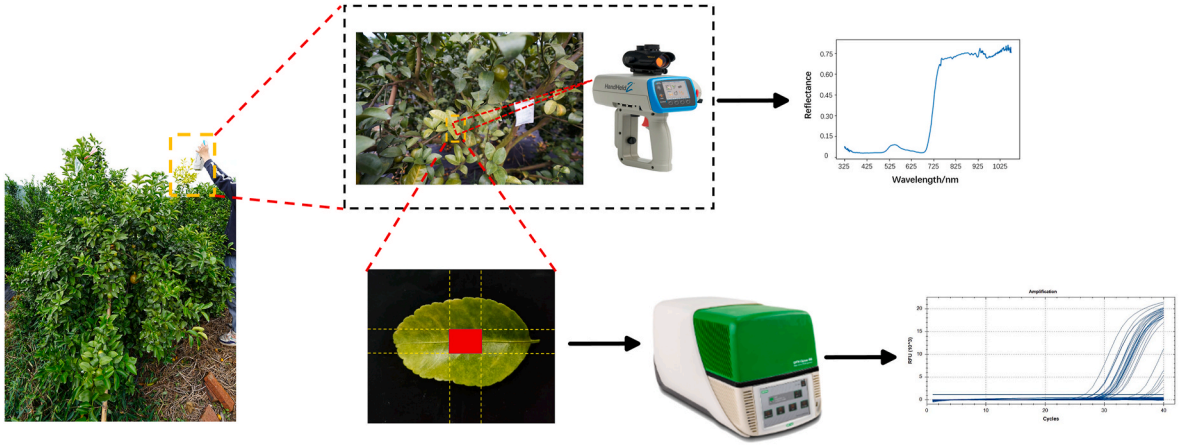

Fig. 2. Flow of citrus leaves hyperspectral data acquisition.

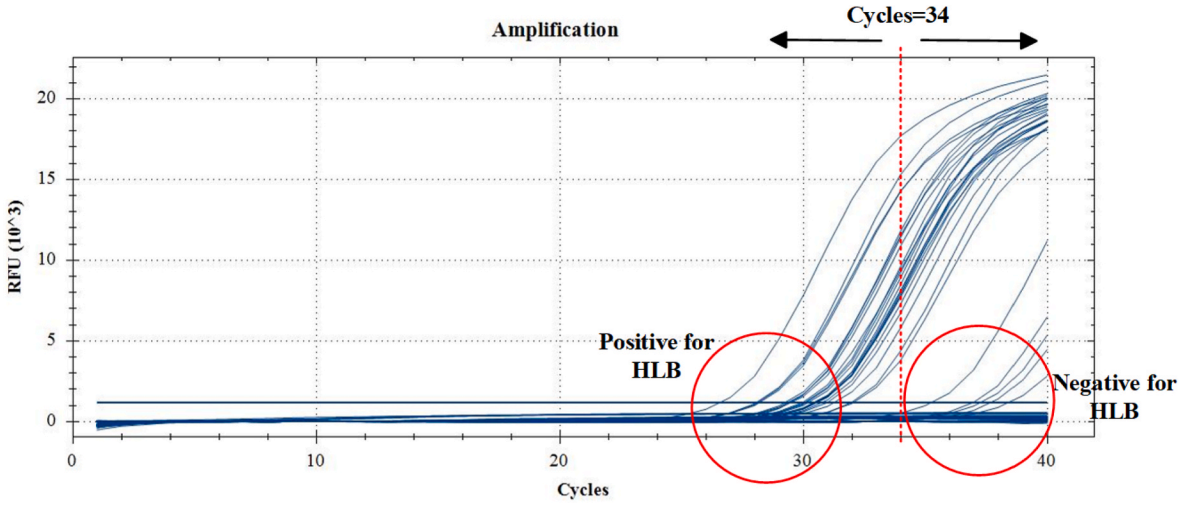

Fig. 3. qPCR results of citrus leaves.

Among them, there were 130 sets of healthy citrus leaf samples, 730 sets of citrus leaf samples with mild HLB-infected, and 520 sets of citrus leaf samples with macular (not related to HLB). Some samples of citrus tree leaves were characterized as shown in Fig. 4.

2.4. Data processing and analysis

2.4.1. Data preprocessing methods

Hyperspectral data from citrus leaves collected outdoors contain a lot of noise and other external interference due to instrumental interference and environmental elements. Consequently, the spectral data must be pre-processed in order to remove irrelevant information. This

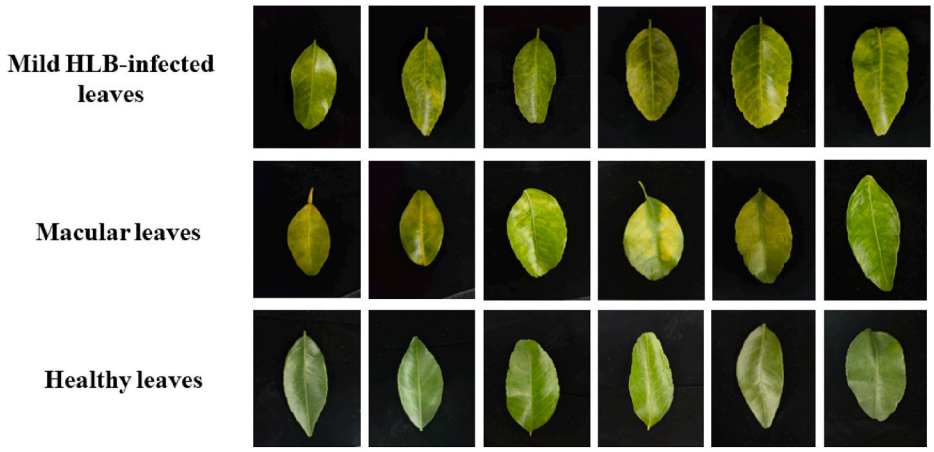

Fig. 4. Some of the tested citrus leaves.

study utilized three spectral preprocessing methods to process the original spectral data, including Standardization (STD), Standard Normal Variate (SNV) and Multiple Scatter Correction (MSC) (Femenias et al., 2021; Derick Malavi and Van Haute, 2023).

(1) Standard Deviation (STD)

STD is a statistical measure that quantifies the amount of variation or dispersion in a dataset. In hyperspectral data, standardizing the data can eliminate differences in intensity between bands, thereby better highlighting target information.

(2) Standard Normal Variate (SNV)

SNV is primarily used to correct for scattering effects in spectral data. Scattering can cause different intensities at the same wavelength for different samples, but this variation is often not due to actual target differences. Preprocessing with SNV can eliminate intensity changes caused by scattering, making the intensities of different samples more consistent at the same wavelength.

(3) Multiple Scatter Correction (MSC)

In hyperspectral data, internal scattering within samples can lead to nonlinear variations in spectral intensity across different bands, which may obscure or confuse actual chemical or physical information. MSC processing can provide a spectrum that is closer to the true spectrum of the sample, helping to improve the accuracy and stability of classification.

2.4.2. Feature band extraction methods

Hyperspectral data contains a large amount of information, which also contains a lot of redundant information, and if all the bands are used directly for analysis, it will lead to excessive dimensionality, which is very difficult to deal with, as well as increasing the amount of computation and storage. Feature selection is a crucial step in hyperspectral data analysis. Subsequent to the extraction of feature bands, there is a marked enhancement in the model's computational efficacy and overall performance. Moreover, feature selection extracts the most representative subset of features from hyperspectral data, identifying and excluding irrelevant features. This methodology forges a clearer connection between data attributes and the target variable, which facilitates a deeper comprehension of the model's decision-making apparatus and principal determinants. Furthermore, it augments the interpretability of the model.

This study, the Competitive Adaptive Reweighted Sampling (CARS) algorithm and Successive Projections Algorithm (SPA) were employed for the extraction of feature bands within hyperspectral data. CARS is a feature variable selection method that combines Monte Carlo sampling with Partial Least Squares (PLS) regression coefficients (Li et al., 2009; Jiang et al., 2015). The algorithm achieves feature band extraction by iteratively performing adaptive weighted sampling, targeting points with larger absolute weight values of the regression coefficients in the PLS model. Subsequently, it generates new subsets and iteratively calculates within the PLS model. Ultimately, it selects the wavelengths from the subset with the minimum Root Mean Square Error of Cross Validation (*RMSECV*) as the feature bands.

SPA is a forward feature variable selection method that reduces the dimensionality of hyperspectral data through sequential projections, thereby selecting the most representative feature bands (Galvão et al., 2008; Canova et al., 2023). The basic idea of this algorithm is to project wavelengths onto other wavelengths and select the maximum wavelength as a candidate wavelength by comparing the size of the projection vector. Then, based on a correction model, the final feature bands are selected. Using the Sequential Projection Algorithm for feature band extraction can filter out redundant and ineffective information, reduce collinearity between variables, and improve modeling efficiency.

2.4.3. Modeling methodology

Traditional machine learning algorithms are esteemed for their robust interpretability, extensive applicability, and modest computational resource demands, which collectively contribute to their adept performance in the multi-class classification of one-dimensional arrays. In this experiment, five machine learning algorithms were selected: Support Vector Machine (SVM), Bootstrap aggregating (Bagging), Extreme Gradient Boosting (XGBoost), Logistic Regression (LR), and Adaptive Boosting (Adaboost) for classification and identification of citrus leaves in three different states of health (Du et al., 2016; Li et al., 2023). During the training process of the model, the datasets was randomly divided into a training set and a testing set in the ratio of 6:4, while ensuring that the proportion of each category in the training and testing sets was the same. Therefore, the overall algorithm framework of this study is shown in Fig. 5.

2.4.4. Evaluation indicators

The evaluation of the model is based on accuracy and recall, with the accuracy formula shown in (1) and the recall formula shown in (2). In the formulas, *TP* represents true positive, *TN* represents true negative, *FP* represents false positive, and *FN* represents false negative.

$$Accuracy = (TP + TN)/(TP + TN + FP + FN) \quad (1)$$

$$Recall = TP/(TP + FN) \quad (2)$$

Accuracy is used for the ratio of predicted instances to the total

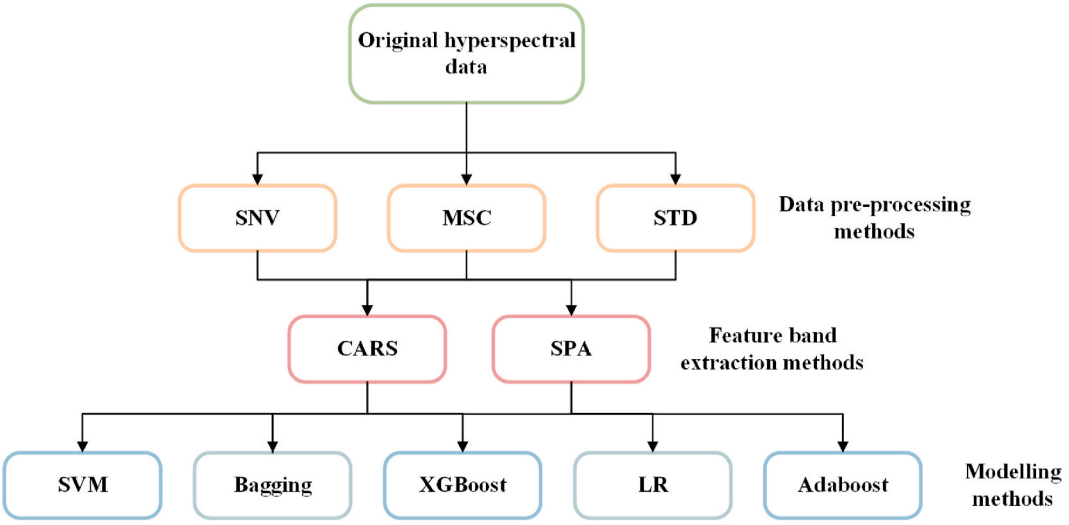

Fig. 5. Hyperspectral data processing framework.

number of samples. The purpose of the accuracy rate is to measure the classification ability of the classifier. The recall rate, also known as the true positive rate, is the proportion of true positive samples that are correctly predicted as positive. In practice, the recall rate can be used to assess whether the classifier is able to detect all positive samples, especially if there are few positive samples. By considering these two important evaluation indicators we can better assess the classification ability of the model.

Root Mean Square Error (*RMSE*) and Root Mean Square Error of Cross Validation (*RMSECV*) are commonly used measures of the difference between the predicted values of a model and the actual observed values. Their formulas are shown in (3), (4). Where y_i is the actual observed value, z_i is the predicted value of the model, and n is the number of samples.

$$RMSE = \sqrt{\sum_{I=1}^{\frac{1}{n}} (Yi - zi)^2} \tag{3}$$

$$RMSECV = \sqrt{\frac{\sum_{i=1}^{n} (y_i - z_i)^2}{n-1}} \tag{4}$$

3. Results

3.1. Analysis of hyperspectral data of citrus leaves in different health states

The reflectance spectra of citrus leaves in three distinct health conditions were illustrated in Fig. 6. By combining the raw spectral reflectance with the first-order derivative spectral reflectance, the trend of the spectral reflectance of the samples can be better observed. Examination of the raw spectra revealed prominent absorption of photosynthetic pigments in the visible range, reaching its peak at 520–570 nm (green band) and reaching a minimum at 650–700 nm. This was followed by a gradual rise in reflectance as the wavelength increased, culminating in the 700–760 nm range (red band), and maintaining high values in the 760–1000 nm range (near-infrared band). The hyperspectral characteristics of citrus leaves collected in this study are similar to those of previous studies. From the first-order derivative spectral reflectance, it can be found that the reflectance of mild HLB-infected and macular leaves exhibited a marginal increase compared to that of healthy leaves within the visible wavelength band (450–625 nm). The spectral reflectance of mild HLB-infected leaves and macular leaves showed different degrees of "red-edge blueshift" in the wavelength range of 675m-780nm, and the "red-edge blueshift" was more obvious in the spectral reflectance of mild HLB-infected leaves. This phenomenon suggests that the spectral reflectance of citrus leaves varied in response to changes in physical and chemical substances caused by biotic and abiotic stresses

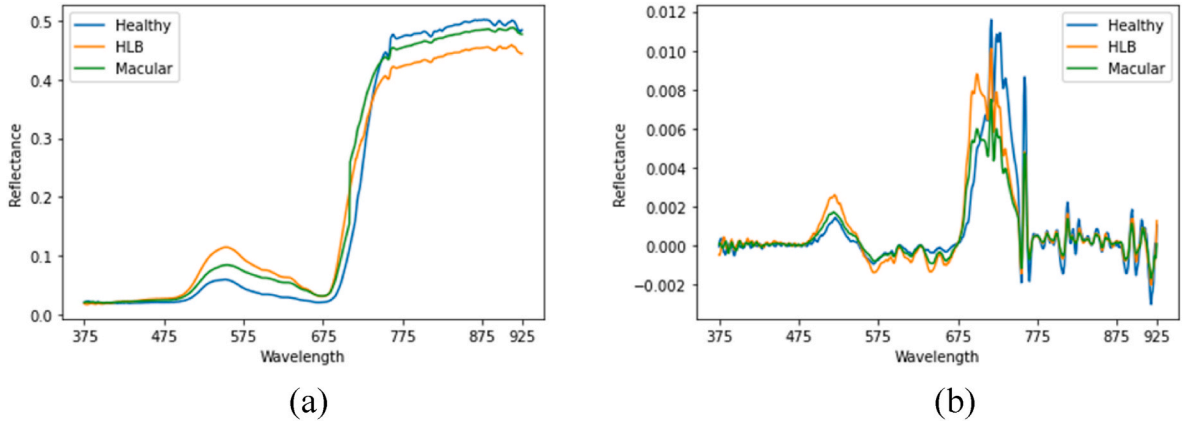

Fig. 6. Original spectrum (a) and first-order derivative (b) spectral reflectance.

(Zhang et al., 2023). This property can be utilized to classify citrus leaves of different health status. Within the near-infrared short-wave range (750–925 nm), the spectral reflectance of mild HLB-infected leaves and macular leaves exhibited lower values in contrast to healthy leaves. The spectral reflectance of mild HLB-infected leaves and macular leaves exhibited remarkable similarity across all regions, rendering it challenging to differentiate between mild HLB-infected leaves and macular leaves suspected of HLB based on hyperspectral data.

3.2. Classification results based on preprocessed spectral reflectance

Due to the equipment operating in the open orchard during data collection, significant noise interference was observed at both ends of the collected spectral data, resulting in a low signal-to-noise ratio. Consequently, the band data at both ends (325–375 nm and 925–1075 nm) were excluded from the experiment prior to data preprocessing, focusing on the spectral data within the range of 375~925 nm for subsequent analysis.

The spectral data underwent preprocessing using three distinct algorithms: SNV, MSC, and STD. Utilizing the preprocessed spectral data, a variety of classification algorithms (LR/SVM/Adaboost/Bagging/XGBoost) were employed to construct the models. Additionally, to facilitate a more comprehensive comparison and analysis of the experimental results obtained through different algorithms, the original spectral data without preprocessing was modeled using the same classification algorithms. The resulting classification accuracy and recall of the models are presented in Fig. 7.

Fig. 7 (a) illustrated that both the original spectral data and the spectral data preprocessed using various methods achieved high precision rates when subjected to the classification model's discrimination, with the majority exceeding 85%. Specifically, utilizing preprocessed spectral data as model inputs resulted in increased accuracy for the classification models compared to using the original spectral data as inputs (Fig. 7 (a)); however, there was a corresponding decrease in recall rates (Fig. 7 (b)). Within the set of classification results, the MSC-XGBoost algorithm combination model achieved the highest recognition accuracy, reaching an impressive 96.56%; however, the corresponding model recall was only 62.5%. Conversely, when using the raw data in combination with the XGBoost algorithm model, the highest recall of 55.25% was achieved, alongside a model accuracy of 90.21%. Further optimization of the classification model based on hyperspectral data is necessary to enhance the classification results.

3.3. Feature band selection and classification results based on dimensionality reduction algorithm

Full-spectrum is effective for detecting citrus HLB; however, the presence of redundant information and collinear variables resulting from the extensive volume of data significantly hampers the accuracy of model discrimination.

3.3.1. Feature band screening and classification results based on CARS algorithm

The CARS algorithm employs a process of repeated random selection of feature subsets, evaluating their classification performance, updating feature weights, and subsequently reselecting features to attain the most optimal feature subset. The primary objective of the CARS algorithm is to identify the feature subset that demonstrates the highest prediction performance (maximum accuracy) while attaining the minimum *RMSE* value. When employing the CARS algorithm for feature band selection, it is common practice to limit the number of feature bands to approximately 20% of the total number of features. Fig. 8 depicted the correlation between the iteration count of the CARS algorithm and the quantity of selected feature bands.

Illustrated in Fig. 9, the *RMSECV* demonstrated an initial decrease followed by an increase as the number of samples rises. This means that when the *RMSECV* value decreased, the bands unrelated to citrus HLB have been removed during the screening process; when the *RMSECV* value increased, the bands related to HLB have been excluded during the screening process. Fig. 9 (a) showed the result of the original hyperspectral data after being screened by the CARS algorithm. The lowest *RMSECV* value was obtained when the number of iterations was 6, and the number of bands obtained at this time was 126. In Fig. 9 (b), the result of the hyperspectral data preprocessed by the MSC algorithm and subsequently screened by the CARS algorithm was displayed. The lowest *RMSECV* value was achieved with 4 iterations, resulting in 146 bands. Fig. 9 (c) exhibited the result of the hyperspectral data that underwent preprocessing with the STD algorithm and subsequent screening by the CARS algorithm. The lowest *RMSECV* value is attained at 5 iterations, yielding 139 bands. The result of the hyperspectral data, which was subjected to preprocessing using the SNV algorithm and then screened by the CARS algorithm, is presented in Fig. 9 (d). The lowest *RMSECV* value was achieved with 4 iterations, resulting in 156 bands.

Table 1 delineated the number of feature bands discerned subsequent to screening the spectral data using the CARS algorithm and their relative proportion to the aggregate band count.

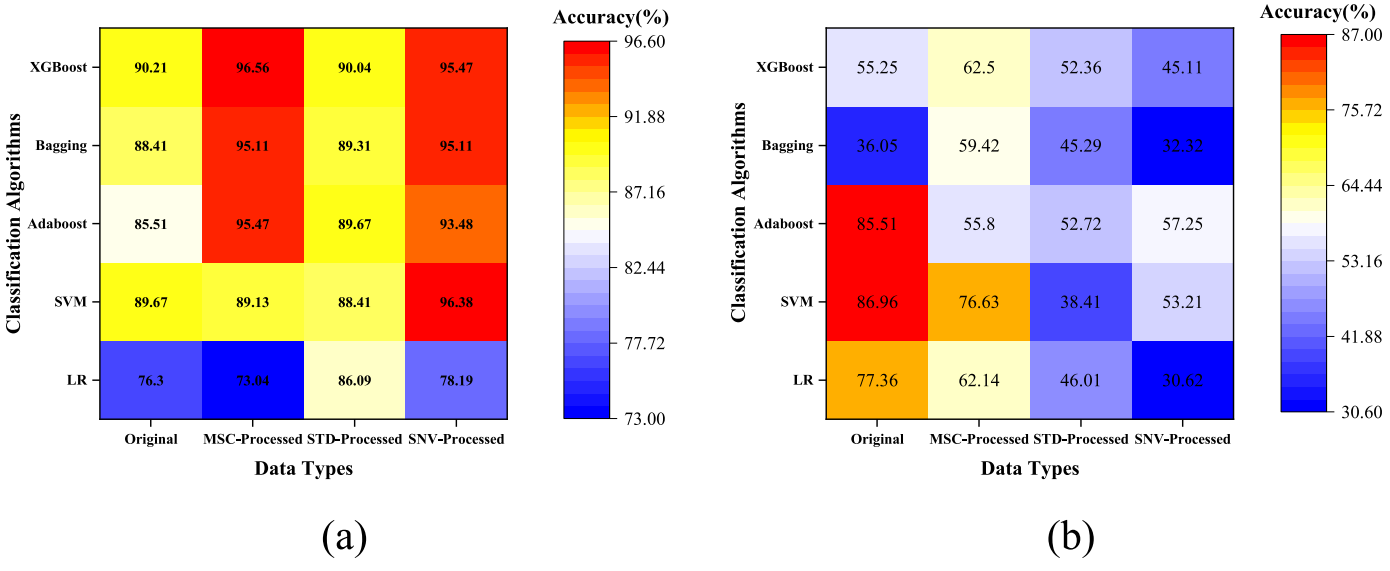

Fig. 7. Accuracy (a) and Recall (b) of the classification model for full-band spectral data.

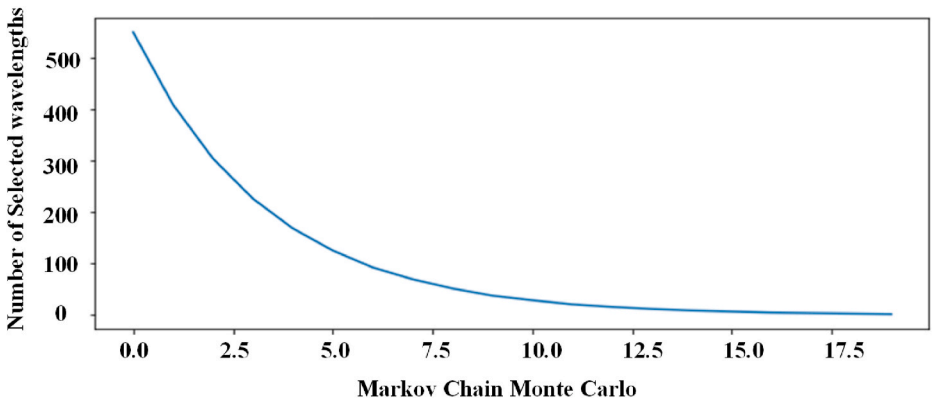

Fig. 8. The relationship between the iteration count of the CARS algorithm and the quantity of selected feature bands.

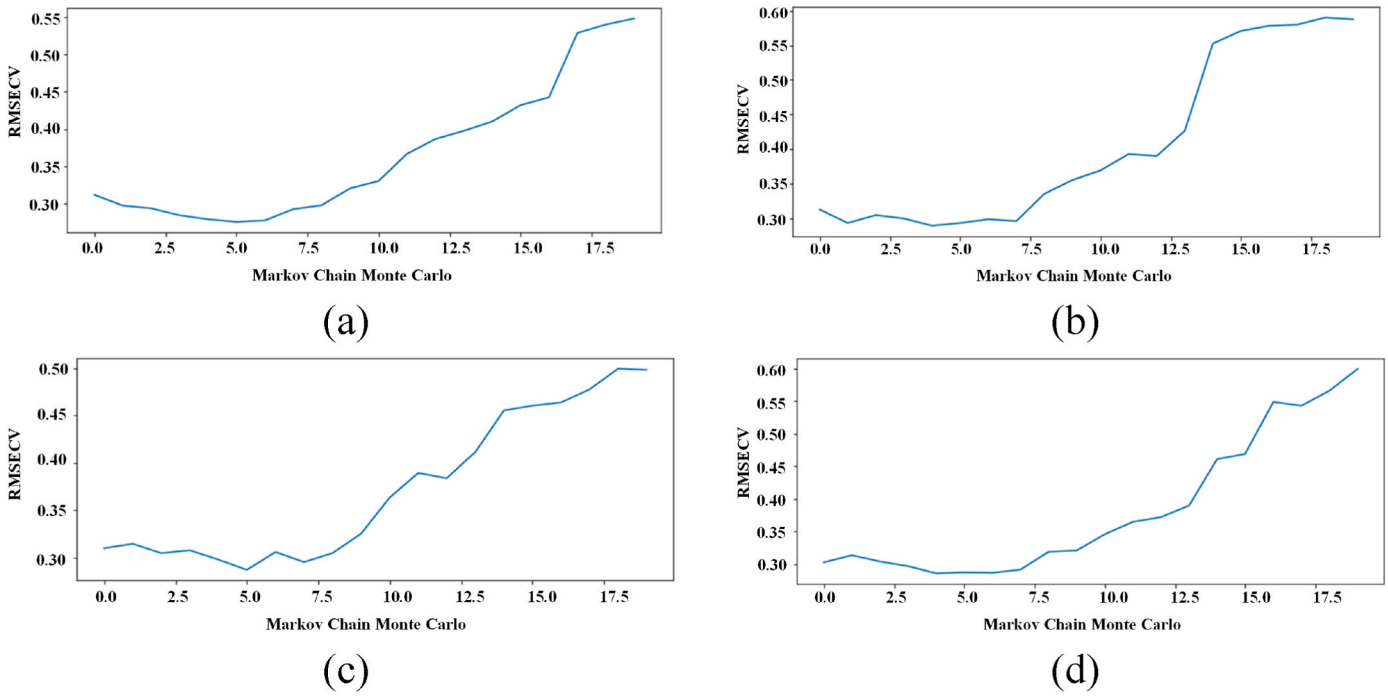

Fig. 9. The screening results of the CARS algorithm on spectral data subjected to different preprocessing: (a) Original hyperspectral data, (b) Data preprocessed by MSC algorithm, (c) Data preprocessed by STD algorithm, and (d) Data preprocessed by SNV algorithm.

Table 1
Number of feature bands and their proportion to the aggregate band count based on the CARS algorithm.

Preprocessing method	Number of bands screened	Proportion to the aggregate band count (%)
ORI	126	22.87
MSC	146	26.50
STD	139	25.23
SNV	156	28.31

The screened bands were used as feature bands for the classification of citrus leaves with different health states using different classification algorithms. The evaluation metrics for the models are depicted in Fig. 10.

Evaluating the classification outcomes for the reflectance of citrus leaves in three health states based on the feature bands selected by the CARS algorithm shows that the classification performance varies compared to the original spectral data without feature selection. The accuracy and recall of the models exhibit different degrees of improvement or decline compared to the models without feature band selection. When the LR and SVM algorithms were applied to the original and preprocessed spectral data (after CARS feature band selection), the classification performance was significantly improved, accompanied by a noticeable increase in both accuracy and recall. Concerning the STD and SNV preprocessed spectral data, subsequent to CARS feature band selection and integration into Adaboost, Bagging, and XGBboost algorithms, the recall was greatly improved, but the accuracy showed some decline. In the case of the original and MSC preprocessed spectral data after CARS feature band selection and subsequent integration into Adaboost, Bagging, and XGBboost algorithms, the recall was significantly improved, while the changes in accuracy were not remarkable.

Among all the models employing feature bands delineated by the CARS algorithm as inputs, the combination of CARS-MSC-LR algorithm s achieved the highest accuracy, with a model accuracy of 96.62%. The combination of CARS-SNV-SVM algorithm achieves the highest recall rate, with a model recall rate of 96.99%.

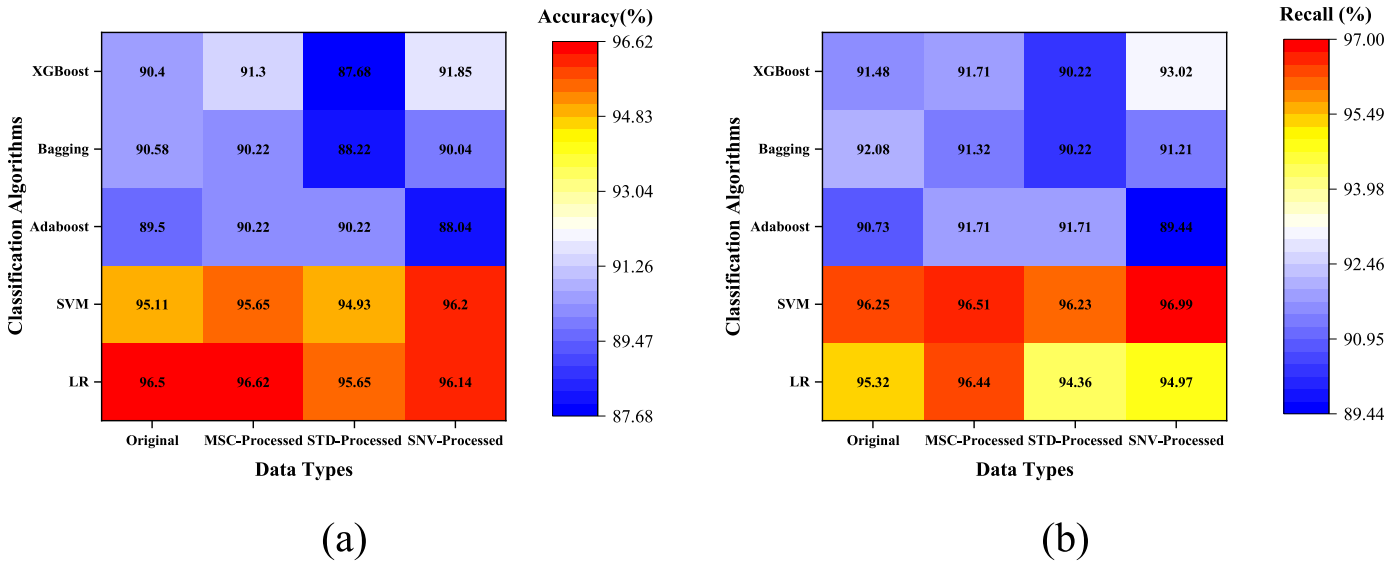

Fig. 10. Models based on CARS algorithm feature band screening: (a) Accuracy and (b) Recall.

3.3.2. *Feature band screening and classification results based on SPA algorithm*

Fig. 11 depicted the results of feature band selection based on the SPA algorithm for the original spectral data and spectral data pre-processed with different methods.

From the results, it can be observed that as the number of bands increases, the *RMSE* values initially decrease and then stabilize. The red inflection point, as shown in Fig. 11, is the recommended number of clusters. That is, after passing this inflection point, the *RMSE* value tends to be stable, and the increase in the number of bands after the inflection

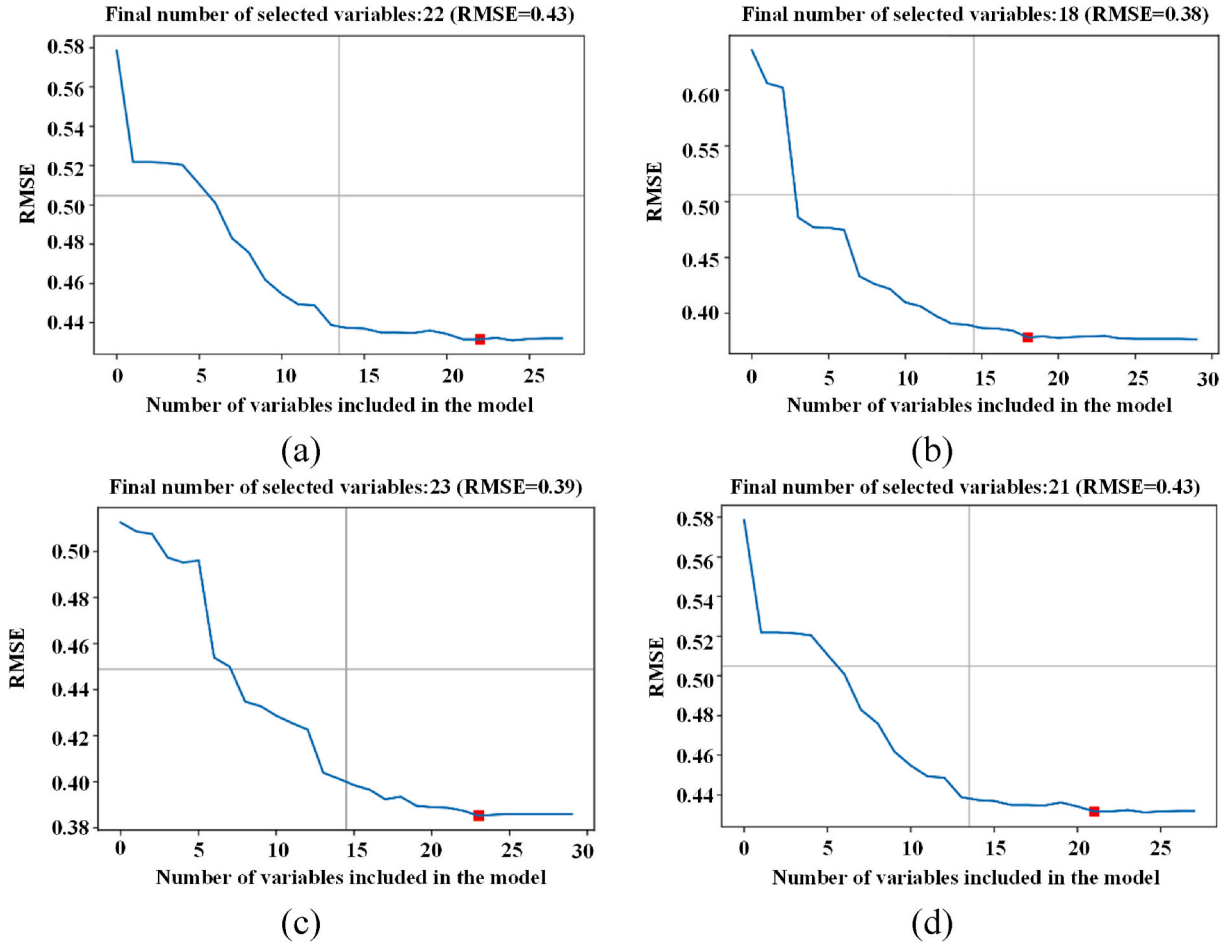

Fig. 11. The screening results of the SPA algorithm on spectral data subjected to different pre-processing: (a) Original hyperspectral data, (b) Data preprocessed by SNV algorithm, (c) Data preprocessed by MSC algorithm, and (d) Data preprocessed by STD algorithm.

point will not have a great impact on the *RMSE* value. The combination of bands screened at this inflection point for classification model construction can better classify citrus Huanglong under the limited feature band. Notably, for the spectral data preprocessed with the SNV algorithm, the SPA algorithm yields a minimum *RMSE* value of 0.3783 when the number of selected bands is 18, as shown in Fig. 11 (b), accounting for only 3.27% of the total bands. Similarly, for the spectral data preprocessed with the MSC algorithm, the SPA algorithm achieved a minimum *RMSE* value of 0.3852 with 23 selected bands, as depicted in Fig. 11 (c), representing only 4.17% of the total bands. Finally, for the spectral data preprocessed with the STD algorithm, the SPA algorithm results in a minimum *RMSE* value of 0.4316 with 21 selected bands, as illustrated in Fig. 11 (d), constituting only 3.81% of the total bands.

Table 2 shows the feature bands selected based on the SPA algorithm for the original spectral data and the spectral data preprocessed with different methods and their proportions in the full band.

The screened bands were used as feature bands to classify citrus leaves of different health states using different classification algorithms. The evaluation indexes of the model are shown in Fig. 12.

The analysis of the classification results for the reflectance of citrus leaves across divergent health states based on spectral bands delineated by the SPA shows that, compared to the classification results utilizing the original spectral data without feature selection (Fig. 7), the model's performance was enhanced when employing the SPA-delineated spectral bands as input variables for the classification algorithms. The models generally exhibit higher accuracy and varying degrees of enhancement in recall. Among all the classification models, the SVM algorithm is distinguished, with the SPA-STD-SVM combination yielding the best classification performance. This model achieves an Accuracy of 97.46% and a Recall of 98.55%, both indices surpassing those of all other algorithmic combinations.

4. Discussion

4.1. Impact of preprocessing as well as feature screening on the performance of classification models

According to Fig. 7, it can be seen that subsequent to preprocessing of the original spectral data by the STD, MSC, and SNV algorithms, the classification accuracy of the classification model for the citrus leaves of three health states generally increased, but the recall of the model generally decreased significantly. This is because amid data preprocessing, certain manipulations are typically enacted to expurgate noise, address absent data points, or normalize the dataset, and these operations might culminate in the forfeiture or contortion of specific information, which precipitates a decrement in the model's performance in some aspects. In machine learning, recall is often closely related to the accuracy and robustness of a model. When accuracy increases and recall decreases, it means that the model is more careful in making positive category determinations and avoiding excessive misclassifications. This may be due to the fact that the preprocessing method excises features from the data that have less importance or are more likely to lead to misclassification, rendering the model more precise in its discriminatory capacity. However, since preprocessing methods might engender data imbalance or informational attrition, this may make it more difficult for the model to capture some true positive category samples, leading to a decrease in recall.

Table 2
Feature bands selected based on the SPA algorithm and their proportions in the full band.

Preprocessing methods	*RMSE*	Feature bands	Proportion in the full band
ORI	0.43	'375' '376' '378' '379' '381' '386' '392''396' '397' '399' '402' '404' '407' '409' '413' '492' '530' '676' '692' '714' '757' '914'	3.99%
SNV	0.38	'511' '644' '678' '691' '737' '758' '761' '767' '806' '814' '868' '890' '893' '904' '907' '909' '915' '920'	3.27%
MSC	0.39	'537' '651' '678' '692' '758' '761' '774' '809''814' '830' '889' '895' '898' '901' '904' '906''907' '909' '915' '917' '920' '923' '925' '927'	4.17%
STD	0.43	'375' '376' '378' '379' '386' '392' '396' '397''399' '402' '404' '407' '409' '413' '492' '530''676' '692' '714' '757' '914'	3.81%

According to Figs. 10 and 12, it is found that after feature screening, the prediction accuracy and recall of the model are enhanced. And the classification algorithm yields superior predictive outcomes for the spectral data refined through the features selected by the SPA and CARS algorithms than for the spectral data unrefined by such feature selection. This is because, when filtered for features, the dataset may be more accurate and compact, characterized by diminished noise and minimized redundancy, and the model selects an optimally discriminative and pertinent feature subset. In turn, the model exhibits enhanced capacity to delineate the features of the samples within the positive category, which improves the recognition ability of the model, consequently enhancing both the model's accuracy and recall.

4.2. Selection of feature screening algorithm

Hyperspectral reflectance data have strong continuity of information capacity bands, but they also have problems such as data redundancy and overfitting. Consequently, the screening of feature bands becomes paramount in the detection of citrus HLB utilizing hyperspectral data. Amongst a multitude of feature band screening methodologies, SPA and CARS were selected, with the selection principally informed by the following considerations:

1. Complementary feature selection strategies. SPA selects features mainly based on their significance, which is evaluated by calculating the information gain or relevance. Conversely, CARS integrates the continuity and prominence of data into its calculus, executing feature selection via iterative processes and updates to weighted values. Among the two different strategies, SPA is adept at swiftly isolating features of elevated import from the dataset, whereas CARS affords a more holistic consideration of the continuity and pertinence of features;
2. Complementary feature representation. Both SPA and CARS algorithms use feature representation techniques to reduce feature dimensions. SPA predominantly utilizes local feature descriptors, such as SIFT and HOG, to project attributes into the feature space. Conversely, the CARS algorithm harnesses both continuity and saliency information for feature representation and models them with multi-scale regional features. Such different feature representation methods can extract different information and features from hyperspectral data;
3. Complementary in Robustness. Both SPA and CARS exhibit inherent robustness and capable of conducting feature selection amidst intricate scenes and variable environments. SPA can quickly screen important features with low computational complexity, while CARS algorithm can better adapt to complex scenes. The combination of CARS and SPA can improve the effect of feature screening to a certain extent. However, both filters may introduce redundant features, increase computational complexity, lead to inconsistent feature selection, and reduce the interpretability of the data. Thus, a merger of the two methodologies is not contemplated in this study.

As illustrated in Figs. 7, 10 and 12, it can be found that before the feature screening process, the accuracy and recall of each classification

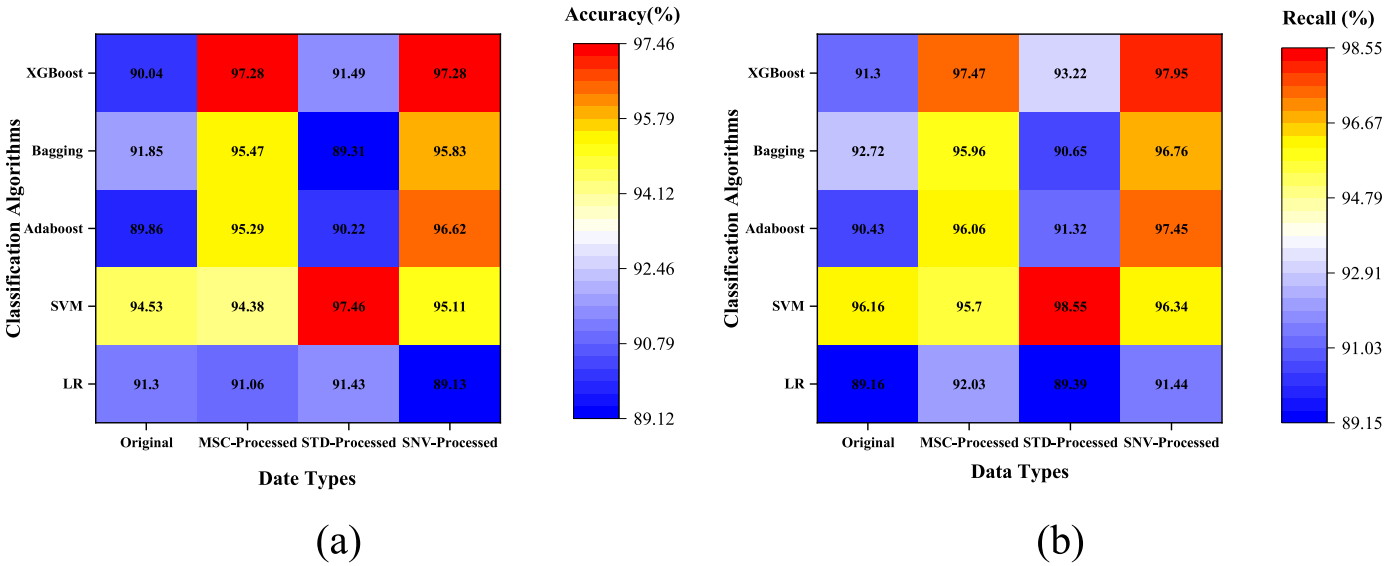

Fig. 12. Models based on SPA algorithm feature band screening (a) Accuracy and (b) Recall.

model have a large difference, and the stability of the model is poor. Following the application of feature selection via SPA and CARS, a discernible enhancement in the accuracy and recall was noted for the majority of models. At the same time, the difference between the accuracy and recall of the models is smaller, and the models have higher predictive ability and stability. In summary, SPA and CARS employ distinct strategies and techniques for feature selection, and they can complement each other in extracting and selecting important features in hyperspectral data of citrus leaves of three health states, thereby more effectively meeting classification requirements and augmenting the predictive performance of the classification models.

4.3. Comparison of the impact of two types of feature screening algorithms on model performance

Upon examining the impact of SPA and CARS algorithms on the classification of citrus leaves in three distinct states of health, it becomes evident that these algorithms, when applied to feature-specific data screening, not only enhance the classification effectiveness but also confer added stability to the models. Specifically, the application of SPA to hyperspectral data significantly boosts the accuracy and recall rates in most classification models, effectively elevating their performance. Conversely, while CARS does improve the accuracy and recall in a subset of models, it concurrently induces a notable decline in accuracy within others.

In the synthesis presented by Fig. 10, the deployment of CARS to sift through spectral data refined by STD and SNV, in tandem with the utilization of ensemble methods like Adaboost, Bagging, and XGBoost for the classification of citrus leaves across three health conditions, resulted in an amplification of model recall yet a diminution in accuracy. This dichotomy may stem from a potential loss of critical spectral information, an escalation in model intricacy, or a skew in data distribution post-CARS algorithm feature selection. Additionally, the variation in performance could be attributed to the ensemble algorithms themselves, where methods such as XGBoost, Bagging, and Adaboost might exhibit suboptimal compatibility with the CARS algorithm's feature selection outcomes. Despite these factors, the precision and recall rates post-screening by the CARS algorithm generally remain lofty, indicating a commendable level of model stability.

In the synthesis presented by Fig. 10, the deployment of CARS to sift through spectral data refined by STD and SNV, in tandem with the utilization of ensemble methods like Adaboost, Bagging, and XGBoost for the classification of citrus leaves across three health conditions, resulted in an amplification of model recall yet a diminution in accuracy. This result may stem from a potential loss of critical spectral information, an escalation in model intricacy, or a skew in data distribution post-CARS algorithm feature selection; Additionally, the variation in performance could be attributed to the ensemble algorithms themselves, where methods such as XGBoost, Bagging, and Adaboost might exhibit suboptimal compatibility with the CARS algorithm's feature selection outcomes. Despite these factors, the accuracy and recall post-screening by CARS generally remain lofty, indicating a commendable level of model stability.

The feature distribution of the original hyperspectral dataset, the data preprocessing methods and the feature selection process of SPA may jointly affect the results obtained by feature screening using SPA. Scrutiny of Table 2 reveals that the spectral bands pinpointed by SPA aggregate primarily around the wavelengths of 375~425 nm, 650~750 nm, and 890~925 nm. These bands align substantially with the spectral curve variances of citrus leaves corresponding to three distinct states of health. There are some similarities and differences in the hyperspectral data of citrus leaves with three different health states, and the distribution of the characteristics may cross or overlap after pretreatment. SPA extracts the main features by gradually selecting the features that have the greatest contribution to the target variables and by projecting the original data. This method can make the selected features closely related to the target variables and can reflect the important information in the spectral data. Therefore, the characteristic bands selected in the screening process can be basically consistent with the parts of the observed spectral curve with slight differences. Thus, the results obtained after feature screening by SPA have a better fit with each classification model, which in turn improves the prediction ability of the model.

5. Conclusion

In this study, hyperspectral data were acquired through field experiments in citrus orchards. Three preprocessing methods (SNV, MSC, STD), two feature band screening methods (SPA, CARS), and five machine learning classifier algorithms (SMV, LR, Adaboost, Bagging, XGBoost) were combined to classify and identify the healthy, macular, and mild HLB-infected citrus leaves. This study reveals that preprocessed hyperspectral data derived from three varieties of citrus leaves exhibit promising predictive accuracy across several classifiers, once refined through the SPA and CARS algorithms. Among them, the data screened by SPA had a better fitness with each classification model,

and the model obtained using the combination of the SPA-STD-SVM algorithm had an accuracy of 97.46% and a recall of 98.55%, which was the best performance among all models. It stands out as a particularly recommendable model for the early detection of citrus HLB, utilizing hyperspectral data. Nonetheless, the robustness of these findings necessitates further empirical trials encompassing a larger dataset. Future research should also delve into the model's versatility with hyperspectral data extracted from citrus leaves at various stages of growth, aiming to refine the efficacy of HLB detection.

CRediT authorship contribution statement

Kangting Yan: Writing – review & editing, Writing – original draft, Validation, Supervision, Software, Investigation, Data curation, Conceptualization. **Xiaobing Song:** Writing – review & editing, Resources, Project administration, Investigation, Data curation, Conceptualization. **Jing Yang:** Validation, Software, Investigation, Data curation. **Junqi Xiao:** Writing – review & editing, Investigation, Conceptualization. **Xidan Xu:** Investigation. **Jun Guo:** Investigation. **Hongyun Zhu:** Validation. **Yubin Lan:** Resources, Project administration. **Yali Zhang:** Writing – review & editing, Supervision, Resources, Funding acquisition, Conceptualization.

Funding

This work was supported by Key Technologies R&D Program of Guangdong Province (Research and application of early diagnosis, monitoring and early warning technology of citrus Huanglongbing) (2024B03J1317), the 111 Project (D18019), Key-Area Research and Development Program of Guangdong Province (2019B020214003).

Declaration of competing interest

The authors declare that they have no known competing financial interests or personal relationships that could have appeared to influence the work reported in this paper.

Acknowledgments

We thank the Provincial Modern Agricultural Industrial Park of Citrus reticulata 'Shiyue Ju' in Sihui, Zhaoqing, for providing us with the sampling site and sample resources.

Data availability

Data will be made available on request.

References

Achor, D.S., Etxeberria, E., Wang, N., Folimonova, S.Y., Chung, K.R., Albrigo, L.G., 2010. Sequence of anatomical symptom observations in citrus affected with huanglongbing disease. Plant Pathol. J. 9 (2), 56–64.

Achor, D., Welker, S., Ben-Mahmoud, S., Wang, C., Folimonova, S.Y., Dutt, M., Gowda, S., Levy, A., 2020. Dynamics of candidatus liberibacter asiaticus movement and sieve-pore plugging in citrus sink cells. Plant Physiol. 182 (2), 882–891.

Arredondo Valdés, R., Delgado Ortiz, J.C., Beltrán Beache, M., Anguiano Cabello, J., Cerna Chávez, E., Rodríguez Pagaza, Y., Ochoa Fuentes, Y.M., 2016. A review of techniques for detecting huanglongbing (greening) in citrus. Can. J. Microbiol. 62 (10), 803–811.

Boina, D.R., Bloomquist, J.R., 2015. Chemical control of the asian citrus psyllid and of huanglongbing disease in citrus. Pest Manag. Sci. 71 (6), 808–823.

Bové, J.M., 2006. Huanglongbing: a destructive, newly-emerging, century-old disease of citrus. J. Plant Pathol. 88 (1), 7–37.

Bové, J.M., 2014. Huanglongbing or yellow shoot, a disease of gondwanan origin: will it destroy citrus worldwide? Phytoparasitica 42 (5), 579–583.

Canova, L.D.S., Vallese, F.D., Pistonesi, M.F., de Araújo Gomes, A., 2023. An improved successive projections algorithm version to variable selection in multiple linear regression. Anal. Chim. Acta 1274, 341560.

Deng, X., Huang, Z., Zheng, Z., Lan, Y., Dai, F., 2019. Field detection and classification of citrus huanglongbing based on hyperspectral reflectance. Comput. Electron. Agric. 167, 105006.

Derick Malavi, A.N.P.A., Van Haute, S., 2023. Detection of saffron adulteration with crocus sativus style using nir-hyperspectral imaging and chemometrics. Food Control 157, 110189.

Du, L., Gong, W., Shi, S., Yang, J., Sun, J., Zhu, B., Song, S., 2016. Estimation of rice leaf nitrogen contents based on hyperspectral lidar. Int. J. Appl. Earth Obs. Geoinf. 44, 136–143.

Femenias, A., Bainotti, M.B., Gatius, F., Ramos, A.J., Marín, S., 2021. Standardization of near infrared hyperspectral imaging for wheat single kernel sorting according to deoxynivalenol level. Food Res. Int. 139, 109925.

Galvão, R.K.H., Araújo, M.C.U., Fragoso, W.D., Silva, E.C., José, G.E., Soares, S.F.C., Paiva, H.M., 2008. A variable elimination method to improve the parsimony of mlr models using the successive projections algorithm. Chemometr. Intell. Lab. Syst. 92 (1), 83–91.

Gasparoto, M.C.G., Hau, B., Bassanezi, R.B., Rodrigues, J.C., Amorim, L., 2018. Spatiotemporal dynamics of citrus huanglongbing spread: a case study. Plant Pathol. 67 (7), 1621–1628.

Hernández, I., Alegre, L., Van Breusegem, F., Munné-Bosch, S., 2009. How relevant are flavonoids as antioxidants in plants? Trends Plant Sci. 14 (3), 125–132.

Hong, Y., Luo, Y., Yi, J., He, L., Dai, L., Yi, T., 2019. Screening nested-pcr primer for 'candidatus liberibacter asiaticus' associated with citrus huanglongbing and application in hunan, China. PLoS One 14 (2), e212020.

Huang, F., Cui, Y., Song, X., Peng, A., Ling, J., Chen, X., 2023. The influences of citrus huanglongbing on phyllosphere microbiome. J. Plant Protect. 50 (5), 1150–1160 (in Chinese).

Jiang, H., Zhang, H., Chen, Q., Mei, C., Liu, G., 2015. Identification of solid state fermentation degree with ft-nir spectroscopy: comparison of wavelength variable selection methods of cars and scars. Spectrochim. Acta Mol. Biomol. Spectrosc. 149, 1–7.

Lee, J.A., Halbert, S.E., Dawson, W.O., Robertson, C.J., Keesling, J.E., Singer, B.H., 2015. Asymptomatic spread of huanglongbing and implications for disease control. Proc. Natl. Acad. Sci. USA 112 (24), 7605–7610.

Li, W., Hartung, J.S., Levy, L., 2006. Quantitative real-time pcr for detection and identification of candidatus liberibacter species associated with citrus huanglongbing. J. Microbiol. Methods 66 (1), 104–115.

Li, H., Liang, Y., Xu, Q., Cao, D., 2009. Key wavelengths screening using competitive adaptive reweighted sampling method for multivariate calibration. Anal. Chim. Acta 648 (1), 77–84.

Li, H., Cui, L., Dou, Z., Wang, J., Zhai, X., Li, J., Zhao, X., Lei, Y., Wang, J., Li, W., 2023. Hyperspectral analysis and regression modeling of spad measurements in leaves of three mangrove species. Forests 14 (8), 1566.

Liu, Y., Xiao, H., Sun, X., Zhu, D., Han, R., Ye, L., Wang, J., Ma, K., 2018. Spectral feature selection and discriminant model building for citrus leaf Huanglongbing. Trans. Chin. Soc. Agric. Eng. 34 (3), 180–187 (in Chinese).

Mei, H., Deng, X., Hong, T., Luo, X., Deng, X., 2014. Early detection and grading of citrus huanglongbing using hyperspectral imaging technique. Trans. Chin. Soc. Agric. Eng. (9), 140–147 (in Chinese).

Park, J., Louzada, E.S., Braswell, W.E., Stansly, P.A., Da Graça, J.V., McCollum, G., Rascoe, J.E., Kunta, M., 2018. A new diagnostic real-time pcr method for huanglongbing detection in citrus root tissue. J. Gen. Plant Pathol. 84 (5), 359–367.

Sagaram, U.S., DeAngelis, K.M., Trivedi, P., Andersen, G.L., Lu, S., Wang, N., 2009. Bacterial diversity analysis of huanglongbing pathogen-infected citrus, using phylochip arrays and 16s rrna gene clone library sequencing. Appl. Environ. Microbiol. 75 (6), 1566–1574.

Shi, Y., Huang, W., Luo, J., Huang, L., Zhou, X., 2017. Detection and discrimination of pests and diseases in winter wheat based on spectral indices and kernel discriminant analysis. Comput. Electron. Agric. 141, 171–180.

Sun, X., Liu, Y., Xiao, H., Zhang, Z., Li, Z., Lv, Q., 2017. Rapid diagnosis of sound yellow and citrus greening leaves with hyperspectral imaging. Spectrosc. Spectr. Anal. 37 (2), 551–556 (in Chinese).

Thomas, S., Kuska, M.T., Bohnenkamp, D., Brugger, A., Alisaac, E., Wahabzada, M., Behmann, J., Mahlein, A., 2018. Benefits of hyperspectral imaging for plant disease detection and plant protection: a technical perspective. J. Plant Dis. Prot. 125 (1), 5–20.

Weng, H., Lv, J., Cen, H., He, M., Zeng, Y., Hua, S., Li, H., Meng, Y., Fang, H., He, Y., 2018. Hyperspectral reflectance imaging combined with carbohydrate metabolism analysis for diagnosis of citrus huanglongbing in different seasons and cultivars. Sensor. Actuator. B Chem. 275, 50–60.

Xiao, Z., Yin, K., Geng, L., Wu, J., Zhang, F., Liu, Y., 2022. Pest identification via hyperspectral image and deep learning. Signal, Image and Video Processing 16 (4), 873–880.

Zhang, F., Qiu, Z., Zhong, B., Feng, T., Huang, A., 2020. Modeling citrus huanglongbing transmission within an orchard and its optimal control. Mathematicl Biosciences and Engineering 17 (3), 2048–2069.

Zhang, Y., Xiao, J., Yan, K., Lu, X., Li, W., Tian, H., Wang, L., Deng, J., Lan, Y., 2023. Advances and developments in monitoring and inversion of the biochemical information of crop nutrients based on hyperspectral technology. Agronomy-Basel 13 (8), 2163.

Zhao, X., Zhang, J., Huang, Y., Tian, Y., Yuan, L., 2022. Detection and discrimination of disease and insect stress of tea plants using hyperspectral imaging combined with wavelet analysis. Comput. Electron. Agric. 193, 106717.

agronomy

MDPI

Article

Design of Chili Field Navigation System Based on Multi-Sensor and Optimized TEB Algorithm

Weikang Han [1,2], Qihang Gu [1], Huaning Gu [1], Rui Xia [1], Yuan Gao [1], Zhenbao Zhou [1], Kangya Luo [1], Xipeng Fang [1,3] and Yali Zhang [1,3,4,*]

[1] College of Engineering, South China Agricultural University, Guangzhou 510642, China; hanweikang@stu.scau.edu.cn (W.H.); 775845468@stu.scau.edu.cn (Q.G.); ghn_scau@163.com (H.G.); xiarui2004@stu.scau.edu.cn (R.X.); 202021110109@stu.scau.edu.cn (Y.G.); viktoradam@stu.scau.edu.cn (Z.Z.); 612116@stu.scau.edu.cn (K.L.); xpfang@stu.scau.edu.cn (X.F.)
[2] Guangdong Provincial Key Laboratory of Agricultural Artificial Intelligence (GDKL-AAI), Guangzhou 510642, China
[3] Guangdong Laboratory for Lingnan Modern Agriculture, Guangzhou 510642, China
[4] National Center for International Collaboration Research on Precision Agricultural Aviation Pesticides Technology, Guangzhou 510642, China
* Correspondence: ylzhang@scau.edu.cn

Abstract: To address issues such as the confusion of environmental feature points and significant pose information errors in chili fields, an autonomous navigation system based on multi-sensor data fusion and an optimized TEB (Timed Elastic Band) algorithm is proposed. The system's positioning component integrates pose data from the GNSS and the IMU inertial navigation system, and corrects positioning errors caused by the clutter of LiDAR environmental feature points. To solve the problem of local optimization and excessive collision handling in the TEB algorithm during the path planning phase, the weight parameters are optimized based on environmental characteristics, thereby reducing errors in optimal path determination. Furthermore, considering the topographic inclination between rows (5–15°), 10 sets of comparison tests were conducted. The results show that the navigation system reduced the average path length by 0.58 m, shortened the average time consumption by 2.55 s, and decreased the average target position offset by 4.3 cm. In conclusion, the multi-sensor data fusion and optimized TEB algorithm demonstrate significant potential for realizing autonomous navigation in the narrow and complex environment of chili fields.

Keywords: multi-sensor; data fusion; positioning; path planning; optimized TEB algorithm

check for updates

Citation: Han, W.; Gu, Q.; Gu, H.; Xia, R.; Gao, Y.; Zhou, Z.; Luo, K.; Fang, X.; Zhang, Y. Design of Chili Field Navigation System Based on Multi-Sensor and Optimized TEB Algorithm. *Agronomy* **2024**, *14*, 2872. https://doi.org/10.3390/agronomy14122872

Academic Editor: Jayme Garcia Arnal Barbedo

Received: 22 October 2024
Revised: 17 November 2024
Accepted: 29 November 2024
Published: 2 December 2024

Copyright: © 2024 by the authors. Licensee MDPI, Basel, Switzerland. This article is an open access article distributed under the terms and conditions of the Creative Commons Attribution (CC BY) license (https://creativecommons.org/licenses/by/4.0/).

1. Introduction

Chili peppers are widely cultivated economic crops and are one of the important industries related to agricultural development [1]. The global area of chili pepper cultivation and its production have been steadily increasing [2–4]. Over 20% of the population consumes spicy food, and since 2019, the total chili pepper production in China has exceeded 64 million tons [5]. Chili peppers play a crucial role in the global agricultural economy [6–9]. In chili pepper cultivation, harvesting is a key factor influencing production efficiency. Currently, in China, chili pepper harvesting is mainly performed manually, which requires significant human and material resources. This not only results in high costs but also low efficiency, limiting the development of the chili pepper industry in China [10]. In modern agriculture, the application of navigation systems is becoming increasingly widespread [11,12]. With the help of advanced navigation systems, precise positioning and automated operations can be achieved, thereby improving harvesting efficiency and reducing labor costs [13–15]. Automated harvesting typically requires fruit recognition, precise navigation to the target location, and then the use of robotic arms for harvesting. Currently, there is no mature autonomous navigation system specifically

designed for chili pepper fields. Therefore, it is of great practical significance to explore the importance of automated navigation systems in chili pepper harvesting, and it has great application potential.

With the rapid development of automation and intelligence in modern agriculture [16,17], traditional autonomous navigation systems that rely on a single sensor can no longer meet the high-precision positioning requirements in the complex environment of chili pepper fields [18]. However, multi-sensor data fusion technology can better meet these demands [19]. For example, Zhong et al. designed an intelligent agricultural machinery integrated navigation system based on the global navigation satellite system (GNSS) and the inertial navigation system (INS) [20]. The system uses Kalman filtering to perform real-time correction of INS errors, thereby calculating the precise position, speed, and orientation information of the agricultural machinery. Dai et al. proposed a combined INS/GNSS navigation method based on a recurrent neural network (RNN) [21], utilizing the computational principles of the INS and the memory function of an RNN to obtain continuous, reliable, and high-precision navigation solutions. The combined navigation system developed by Abdelaziz et al. integrates measurement data from the inertial measurement unit (IMU), LiDAR, and monocular camera [22]. It uses an extended Kalman filter to provide accurate positioning during GNSS signal interruptions and utilizes LiDAR depth measurements to correct scale ambiguity caused by monocular visual odometry. Yu et al. proposed an automatic navigation method for farmland based on a D-S-CNN, which integrates data from satellite navigation, inertial navigation, and visual navigation sensors, offering improved robustness and practicality [23]. Multi-sensor data fusion technology has been applied in various fields and environments with good performance. In the complex environment of chili pepper fields, path planning algorithms play a crucial role in achieving precise navigation. In path planning algorithms, the TEB algorithm has attracted considerable attention due to its superior path planning performance in dynamic environments. However, the traditional TEB algorithm faces issues of insufficient path optimization and poor obstacle avoidance performance when dealing with complex field environments [24]. An increasing number of scholars are improving the existing TEB algorithm to meet the demands of path planning in complex environments [25–28]. For example, Chen et al. combined the improved Bi-RRT algorithm and the TEB algorithm to complete multi-target autonomous path planning [29], demonstrating good effectiveness and feasibility in multi-target path planning. Yin et al. proposed a mobile robot path planning method based on the improved RRT and TEB algorithms [30], enabling the robot to generate smooth global paths while ensuring that local trajectories comply with the kinematic constraints of the mobile robot. Dai et al. incorporated a constraint on speed based on the distance to obstacles in their algorithm [31], performing expansion on detected irregular obstacles and applying a region classification strategy, which improved the rationality of the path planning. However, existing methods still face several challenges in the complex environment of chili pepper fields, such as data redundancy, poor environmental adaptability, and issues with positioning accuracy in narrow and slippery conditions.

Zhong et al. and Dai et al. employed an integrated GPS/INS approach, which has some limitations in terms of environmental adaptability, data redundancy, accuracy, and dynamic response [20,21]. The solutions proposed by Abdelaziz et al. and Yu et al. are susceptible to environmental lighting conditions, which may hinder all-day operation [22,23]. The chili pepper harvester designed by Yang et al. cannot achieve full autonomous navigation [32] and still requires manual operation. Therefore, designing a navigation system suitable for chili pepper fields is of significant importance. Building upon previous works, this study proposes a multi-sensor fusion approach that integrates LiDAR, the IMU, and the GNSS, employing an extended Kalman filter (EKF) for data fusion to achieve high-precision localization in the complex environment of chili pepper fields. Furthermore, we have optimized the traditional TEB algorithm to address challenges in path planning, specifically obstacle avoidance and path optimization, thereby enhancing the practical performance of the autonomous navigation system in chili pepper fields.

The main contributions of the chili pepper field navigation system design based on multi-sensor integration and the optimized TEB algorithm presented in this study are as follows:

1. Using LiDAR scanning to generate an accurate map of the chili pepper field.
2. Implementing an EKF to achieve data fusion of LiDAR, the IMU, and the GNSS, enabling real-time acquisition of environmental and self-localization data, thereby achieving precise localization with multi-sensor collaboration.
3. Optimizing the TEB algorithm and integrating the A algorithm with the TEB algorithm for reasonable path planning in narrow fields and enabling autonomous obstacle avoidance and navigation through narrow, unattended fields to complete automatic cruising in chili pepper fields.
4. Validating the accuracy and feasibility of the multi-sensor fusion and optimizing the TEB algorithm through experimental trials.

2. Materials and Methods

2.1. Measurement of Chili Fields

In this study, the experiment was conducted from 22 to 25 August 2024 in Fogang County, Qingyuan City (23°76′ N, 113°32′ E) in a chili field of the mulching method shown in Figure 1.

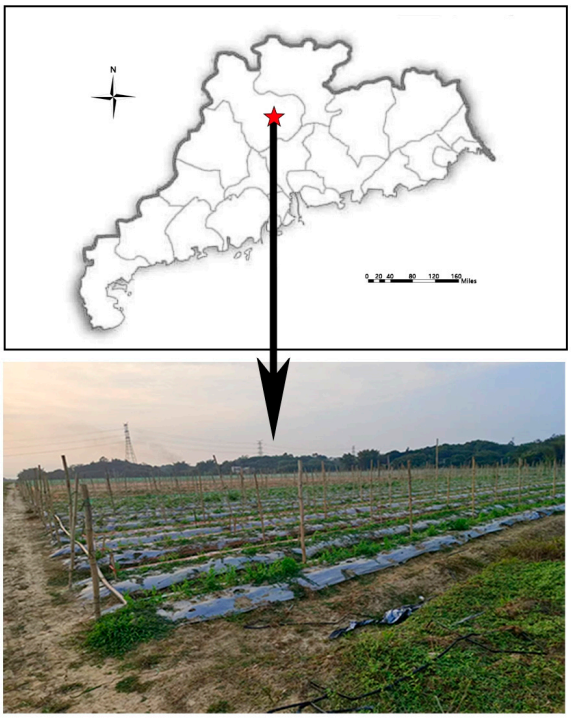

Figure 1. Location of the experimental area in Guangdong.

The locations marked with stars indicate the approximate positions of our experimental sites. Through the management of farmers, the deviation of each row size in this chili field was small. The environment of the chili field is shown in Figure 2. The ridge height is 0.3 m, with a relatively narrow distance between the ridges. The distance between two rows of ridges is 0.75 m, and the width of a single ridge is 0.5 m.



(**a**) (**b**)

Figure 2. (**a**) Ridge height in the experimental chili field; (**b**) The distance between the ridges and the width of the ridges in the experimental chili field.

According to the "Technical Regulations for Land Use Investigation", chili fields are divided into flat land (≤2°, 2°~6°), gentle slope (6~15°, 15~25°), and steep land (>25°) according to the ground slope [33]. The ground slope between each ridge in the experimental chili field is 5°~15°, which belongs to the gentle slope. Through the maintenance and management of the field ridges and the ground between the ridges by chili growers, combined with agronomic practices, the above data will not exhibit significant deviation, effectively ensuring the accuracy and stability of the navigation system.

2.2. Multi-Sensor Data Fusion Positioning

2.2.1. Positioning Overall Scheme

Due to the relatively uneven terrain of chili fields, positioning drift is easily induced. To address this issue, this study proposes a positioning method based on multi-sensor fusion. In order to overcome the limitations of individual sensors and leverage the complementary advantages of different sensor data, the solution integrates LiDAR, the inertial measurement unit (IMU), and the global navigation satellite system (GNSS) for accurate positioning. Specifically, the RPLIDAR S2 LiDAR, WHEELTEC N200 IMU, and WHEELTEC DETA100 GNSS were selected. A series of data fusion processes were performed using the extended Kalman filter (EKF) algorithm running within the ROS unmanned system framework. The detailed node diagram is shown in Figure 3 below:

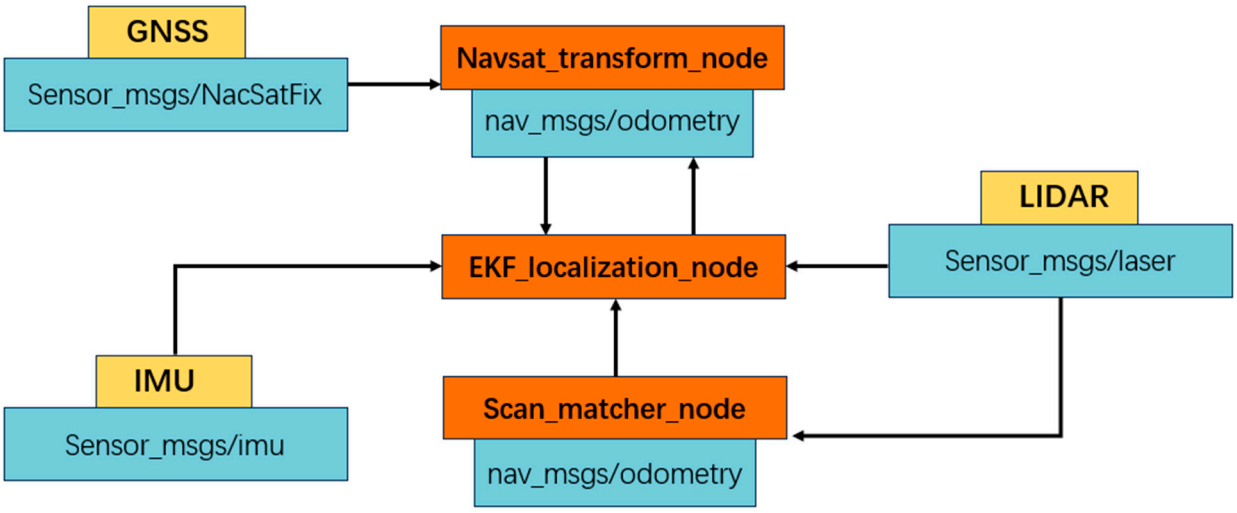

Figure 3. Data fusion node diagram.

In the process of multi-sensor fusion, LiDAR primarily captures the structural characteristics of the external environment and accurately aligns it with the real map. The IMU provides orientation data along with continuous information about the robot's speed and inclination angle, while the GNSS mainly assists in providing macro-level positional information. The data from these three sensors are fused using the extended Kalman filter (EKF) in combination with the adaptive Monte Carlo localization (AMCL) algorithm. This integration effectively leverages the high precision of LiDAR, the global positioning capabilities of the GNSS, and the short-term stability of the IMU. As a result, more accurate and reliable positioning results can be obtained. Accurate pose estimation and updates can not only improve the accuracy of positioning, but also maintain the continuity and accuracy of positioning through IMU and LiDAR information when GPS signals are weak or lost [34].

2.2.2. Data Fusion Analysis

Inaccurate positioning is a primary challenge that hinders reaching the target points in chili field navigation. To address this issue, this approach employs the extended Kalman filter (EKF) to perform data fusion of multiple sensors, including LiDAR, the GNSS global positioning system, and the IMU inertial navigation unit. This fusion enables the real-time determination of the vehicle's precise position and orientation.

The extended Kalman filter (EKF) is an improved version of the Kalman filter (KF), which linearizes the nonlinear function through a Taylor series expansion, retaining only the first-order terms and neglecting higher-order terms. The Kalman filter algorithm is then applied to approximate both the system state and variance estimates. In the fusion of IMU and GNSS data, the IMU motion model and the GNSS measurement model typically exhibit nonlinearity. This is shown in Table 1 below.

Table 1. Comparison of various filters.

	Classical Kalman Filter	**Extended Kalman Filter**	**Untraced Kalman Filter**
Advantage	Optimal estimation can be achieved under a linear model.	Positioning accuracy is high under a weakly nonlinear model	It can effectively address filter divergence issues in nonlinear systems resulting from heightened model nonlinearity or arbitrary noise distributions.
Disadvantage	Not applicable to systems with nonlinear dynamics and non-Gaussian noise.	Not suitable for strong nonlinear systems; Taylor series truncation errors reduce accuracy, and the calculation of the Jacobian matrix is complex.	When the posterior probability density follows a non-Gaussian model, significant errors may occur.

The extended Kalman filter is a nonlinear expansion model of the standard Kalman filter. The nonlinear system model can be expressed as follows:

$$x(k+1) = f(X(k)) + \omega(k) \tag{1}$$

$$Z(k) = h(X(k)) + v(k) \tag{2}$$

Process noise:

$$\omega(k) \sim N(0, Q(k)) \tag{3}$$

Observed noise:

$$v(k) \sim N(0, R(k)) \tag{4}$$

Equations (1)–(4) represent the state-space model of the system by introducing nonlinear state transition and observation models, where the state variables are presented in vector form. Due to the nonlinear nature of these models, the standard Kalman filter cannot

be applied directly. Therefore, the EKF uses Taylor series expansion to linearize the nonlinear model and applies a Jacobian matrix to approximate these nonlinear relationships, thus treating it locally as a linear model.

In the prediction step, the EKF predicts the next state variable and its corresponding covariance using a nonlinear state transition model, as shown in Equations (5)–(7):

$$X(k+1|k) = f(X(k)) \tag{5}$$

$$(k+1|k) = h(X(k+1|k)) \tag{6}$$

$$P(k+1|k) = F(k+1)P(k)F(k+1)' + Q(k+1) \tag{7}$$

In the above formula,

$H(k+1) = \frac{\partial f}{\partial X} = \begin{bmatrix} \frac{\partial h_1}{\partial x_1} & \cdots & \frac{\partial h_1}{\partial x_n} \\ \vdots & \ddots & \vdots \\ \frac{\partial h_n}{\partial x_1} & \cdots & \frac{\partial h_n}{\partial x_n} \end{bmatrix}$ is a linearized observation matrix, and

$F(k+1) = \frac{\partial f}{\partial X} = \begin{bmatrix} \frac{\partial f_1}{\partial x_1} & \cdots & \frac{\partial f_1}{\partial x_n} \\ \vdots & \ddots & \vdots \\ \frac{\partial f_n}{\partial x_1} & \cdots & \frac{\partial f_n}{\partial x_n} \end{bmatrix}$ is the Jacobian matrix of the state transition model.

In the update step, Equations (8)–(10) calculate the Kalman gain by linearizing the observation model, using the Kalman gain to update the state estimates and their covariances:

$$K(k+1) = P(k+1|k)H^T(k+1)\Big[H(k+1)P(k+1|k)H^T(k+1) + R(k+1)\Big]^{-1} \tag{8}$$

$$X(k+1) = X(k+1|k) + K(k+1)[Z(k+1) - Z(k+1|k)] \tag{9}$$

$$P(k+1) = [I - K(k+1)H(k+1)]P(k+1|k) \tag{10}$$

Through these predictions and updating steps, the EKF can effectively provide approximate optimal estimates of states in nonlinear dynamic systems. The specific flow chart is as follows (Figure 4).

In this study, during multi-sensor fusion, each sensor operates independently and provides its own solution, which is then fused in a loosely coupled method to deliver comprehensive navigation information. Each sensor module functions independently, facilitating expansion and maintenance. This approach allows for the correction of errors introduced by sensor noise and environmental factors in the complex field environment. Additionally, system model uncertainty is addressed by adjusting the process noise covariance, enabling smooth state estimation, adjusting the filter response speed, optimizing the fusion effects of different sensors, and enhancing the filter's stability and robustness. As a result, the fused data better meets the positioning requirements of chili field environments.

At the algorithm level, optimization measures are implemented in this study to address an issue where the fusion node cannot determine the position of the robot on the map. In the absence of a GNSS signal, incorrect information may be released. The master node is designed to subscribe to the filter odometry topic, published by the EKF node, to obtain the initial position. By creating data loops through mutual subscriptions, accuracy is improved and errors are minimized.

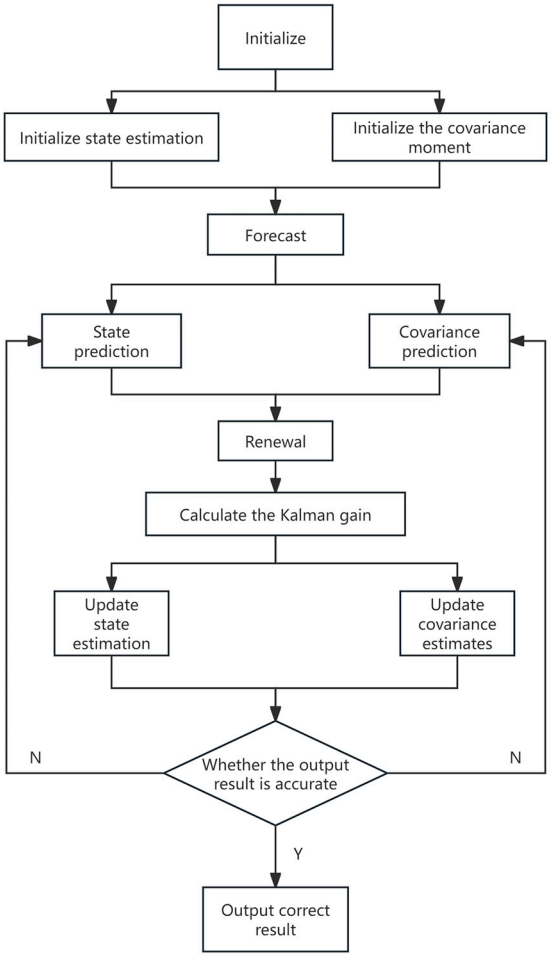

Figure 4. Data fusion process diagram.

2.3. Optimize TEB Algorithm Construction and Analysis

The TEB (Timed Elastic Band) local path planning algorithm is an optimized path planning approach for autonomous robot navigation [35,36]. It achieves local optimization of the path by transforming the global path into an elastic band model, incorporating control points along the dynamic path.

The algorithm introduces some constraints such as fixed pose, obstacle, and kinematics. By applying mutual constraints on acceleration (a), velocity (v), arrival time (ΔT), and distance from obstacles (s), the navigation system's carrier avoids obstacles and reaches the target point at an optimal speed while satisfying kinematic requirements, thereby achieving efficient local path planning, as shown in Figure 5.

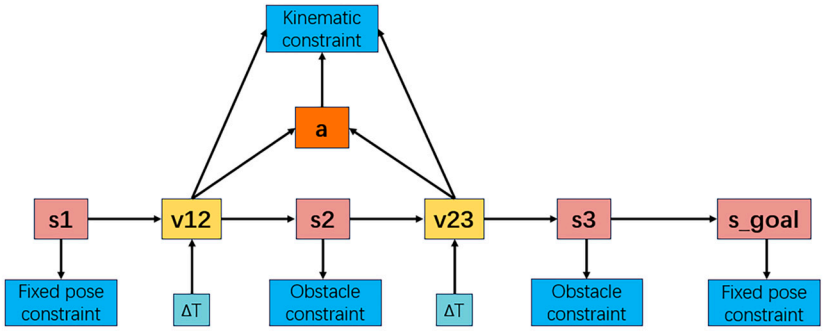

Figure 5. Algorithm constraint.

The standalone use of the TEB algorithm for path optimization primarily employs nonlinear optimization techniques to generate and adjust paths, iteratively optimizing each feasible path across the entire space to find the optimal solution. However, this approach presents the following challenges: (1) The obstacle avoidance capability is limited, often leading to extreme collisions; (2) The high environmental complexity in chili fields reduces the accuracy of optimal path solutions. To address these issues, this study proposes cost function optimization for path smoothness to prevent abrupt motion changes, reduce the likelihood of extreme collisions, and enhance the safety of execution paths. Additionally, an uncertainty strategy optimization is applied to enable more flexible path adjustments, improving obstacle avoidance when encountering dynamic obstacles, sudden barriers, or other environmental changes. This study also integrates the A algorithm with the TEB algorithm, ensuring that the path aligns with the global objective while allowing real-time local path adjustments based on the global path during the planning process, thereby achieving a more rational and optimal path solution.

2.3.1. Cost Function Optimization for Path Smoothness

In the TEB algorithm, path smoothness is typically evaluated based on curvature. The original curvature cost function is derived by calculating the rate of directional change at each point along the path:

$$J_{curvature} = \sum_{i=1}^{N-1} \left\| \frac{d\theta_i}{ds} \right\|^2 \tag{11}$$

In the above formula,

θ_i is the direction angle of the i point on the path; s is the arc length on the path, representing the length of the path; and $\frac{d\theta_i}{ds}$ represents the rate of change of the direction angle with the arc length, that is, the curvature of the path.

For the narrow chili fields, the constraints of acceleration and angle change are introduced, and the dynamic weight parameters are designed:

$$J_{curvature'} = \sum_{i=1}^{N-1} \left(\alpha \left\| \frac{d\theta_i}{ds} \right\|^2 + \beta \left\| \frac{d^2\theta_i}{ds^2} \right\|^2 \right) \tag{12}$$

In the above formula,

α and β are dynamically adjustable weight coefficients, and $\frac{d^2\theta_i}{ds^2}$ represents the acceleration of the change in angle.

When navigating along ridges, the path is narrow and uneven, and the obstacle density is high. Therefore, the weight of α is increased to avoid sharp turns in the path as much as possible, so as to reduce the risk of collision. Conversely, when operating on relatively flat ground outside the chili field, where obstacle density is low, the weight of β is adjusted to ensure the smoothness of the path and improve speed. By generating random target points, the trajectory data is obtained by running the improved planning algorithm in the virtual simulation environment. The trajectory diagram is plotted using the planar coordinates as the horizontal and vertical axes, as shown in Figure 6.

Obstacle-density detection is carried out using the method of grid division:

$$Density = \frac{Number\ of\ Obstacles\ in\ Cell}{Cell\ Area} \tag{13}$$

In the above formula,

Number of Obstacles in Cell indicates the number of obstacles detected in the current grid. Cell Area indicates the area of the grid.

The grid size is set to 0.1 m^2, with a detection range of 100 × 100 grids. Due to the high density of obstacles between fields and ridges, the density threshold is set to 5. If the density exceeds the threshold, the weight of α is increased; if it is below the threshold,

the weight of β is increased. The detection range moves dynamically with the navigation system carrier to enable real-time obstacle density detection.

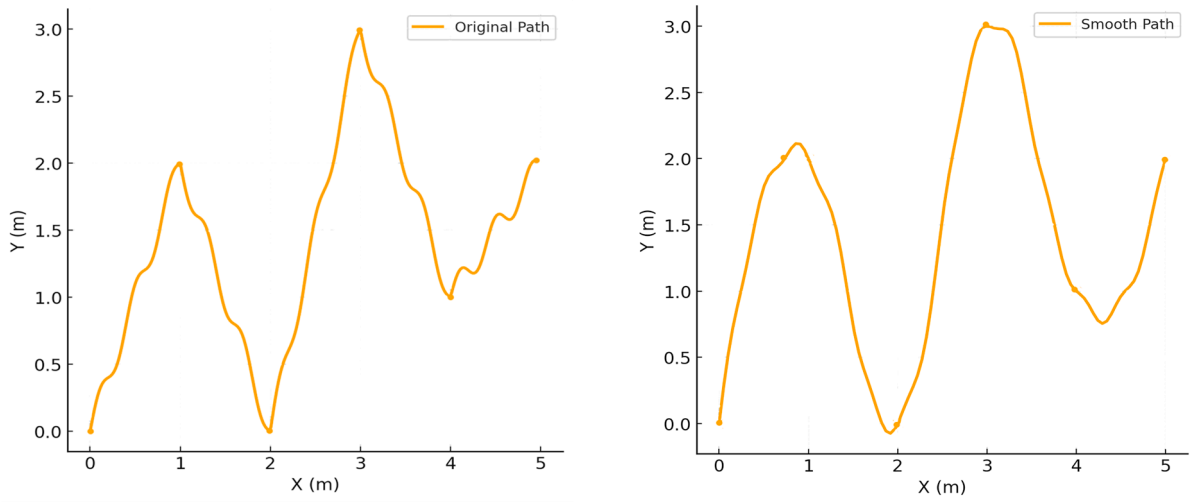

(**a**) (**b**)

Figure 6. (**a**) Original path; (**b**) Smooth path.

2.3.2. Uncertainty Strategy Optimization

Chili fields contain numerous obstacles, such as people, animals, and other entities. By applying a conceptual collision method, a probabilistic obstacle avoidance strategy can assess the collision risk of different paths, and select the path with the lowest collision probability. $P_{collision}$ represents the collision probability.

$$P_{collision} = \int_{Obstacle\ Region} P_{robot}(x) P_{obstacle}(x) dx \tag{14}$$

In the above formula,

$P_{robot}(x) = \frac{1}{\sqrt{2\pi\sigma^2}} exp\left(-\frac{(x-\mu)^2}{2\sigma^2}\right)$ is the probability distribution of the robot at position x, and $P_{obstacle}(x) = \frac{1}{\sqrt{2\pi{\sigma_0}^2}} exp\left(-\frac{(x-\mu_0)^2}{2{\sigma_0}^2}\right)$ is the probability distribution of obstacles at position x.

By utilizing sensors such as LiDAR to acquire environmental information and representing obstacles and robots as probability distributions, collision risks can be more accurately assessed in dynamic and complex environments, allowing for the selection of safer paths. The optimization effect diagram is shown in Figure 7. As illustrated in Figure 7, compared to the original algorithm, the optimized algorithm demonstrates improved avoidance in areas with a high probability of obstacles.

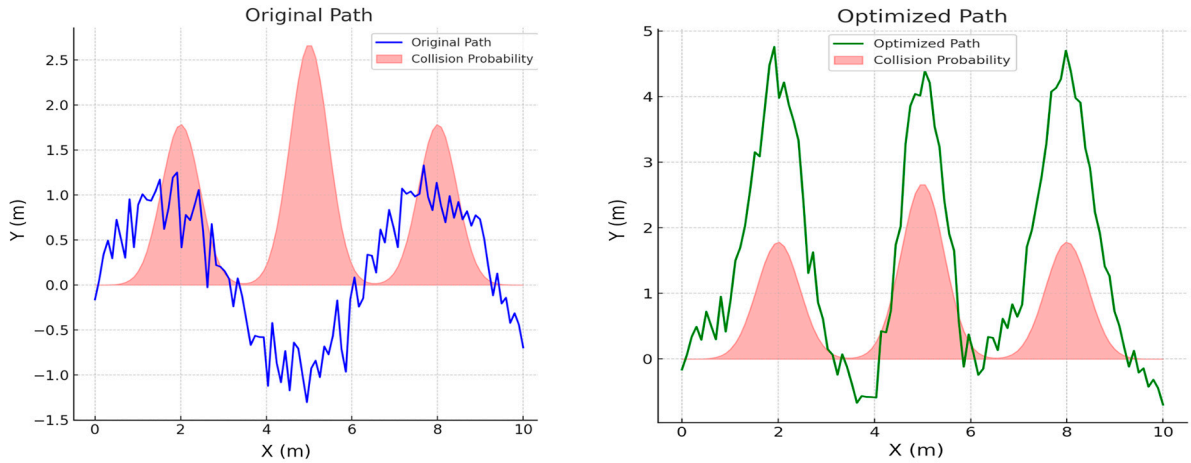

(**a**) (**b**)

Figure 7. (**a**) Original path; (**b**) Optimized path. Horizontal and vertical axes represent the simulated coordinate positions. The red area indicates the probability of collision between the planned path and the obstacle, and the higher the peak value, the greater the probability of collision.

2.3.3. Fusion Solution for Optimal Path

The fusion method of the A* algorithm and the TEB algorithm is employed to update the optimal initialization path for the TEB algorithm [37]. The formula and calculation process for initializing the path mainly involve two key functions: the heuristic function $h(n)$ and the path cost function $g(n)$. Together, these two functions are used to compute the comprehensive evaluation function $f(n)$ of node n:

$$f(n) = g(n) + h(n) \tag{15}$$

In the above formula,

$g(n)$ represents the actual path cost from the start node to the current node n, and

$h(n)$ is a heuristic function that estimates the cost from node n to the target node. Setting this function requires: (1) not overestimating the cost from the node to the target node; (2) that for each node n and its successor node n', the following condition must be satisfied:

$$h(n) \leq c(n, n') + h(n') \tag{16}$$

where $c(n, n')$ is the actual cost from n to n'.

The actual fusion flow chart is shown in Figure 8.

2.4. Experimental Design

In this section, we calibrate and validate the designed navigation system. Experimental tests are conducted to assess the positioning deviation of the positioning module within the navigation system, and to evaluate the effectiveness of the optimal path planning method.

The primary test vehicle in this study is the Pepperland Navigation Robot, shown in Figure 9. The navigation system was deployed on a Republic of Gamers laptop (G634, ASUS, Maricopa County, AZ, USA) equipped with an RTX 4080 discrete graphics card. The robot is equipped with an RPLIDAR S2 LiDAR (Pudong New District, Shanghai, China) featuring a scanning frequency of 10 Hz, a sampling frequency of 32k, and a scanning radius of up to 30 m. Additionally, it includes a WHEELTEC N200 nine-axis IMU inertial navigation module and a WHEELTEC DETA100 GNSS module. To ensure stable operation on steep terrains, the robot is also equipped with a custom-built tracked undercarriage.

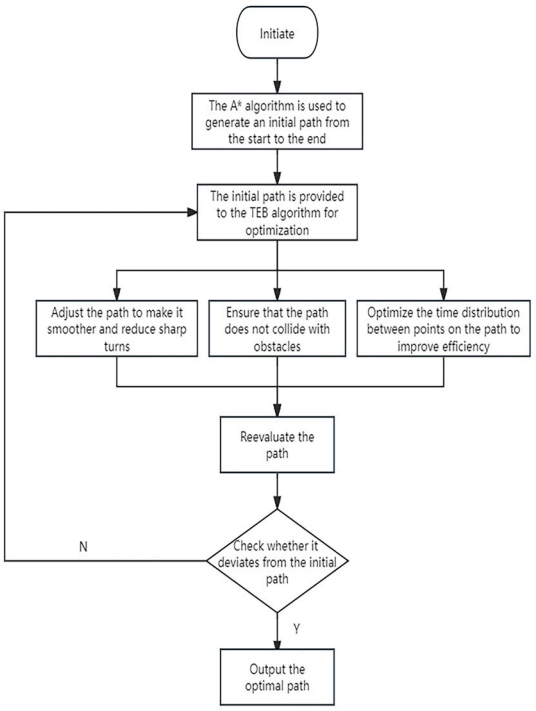

Figure 8. Algorithm fusion process.

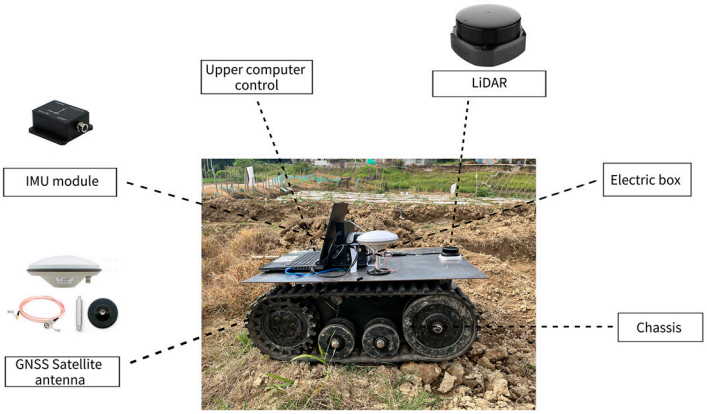

Figure 9. Crawl-based chili field autonomous navigation vehicle.

All programs in the navigation system are implemented within the ROS framework, and the overall navigation process is illustrated in Figure 10.

Experimental Design of Chili Fields Navigation

In a chili field environment with a consistent slope, four different schemes were tested for positioning and navigation effectiveness: Scheme 1: Standard TEB algorithm + LiDAR; Scheme 2: Standard TEB algorithm + LiDAR +IMU+GNSS; Scheme 3: Optimize TEB algorithm + LiDAR; Scheme 4: Optimize TEB algorithm + LiDAR +IMU+GNSS in a chili field environment with the same slope.

The test area was established between the ridges of a typical chili field, as shown in Figure 11.

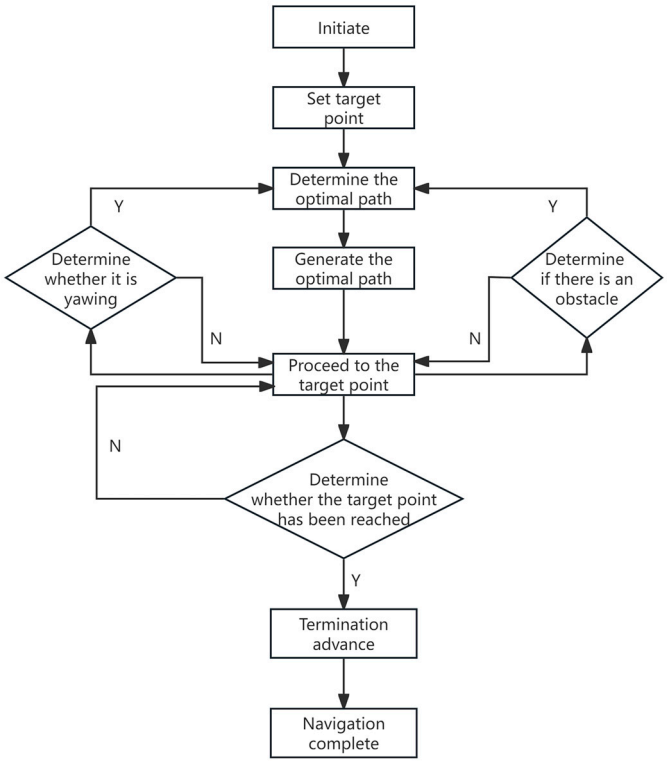

Figure 10. Overall navigation system process.



Figure 11. Chili field scene for experiment.

In this experiment, the same starting point and target point were set, with a maximum speed of 0.5 m/s and a total distance of 10 m for each group. Each group was tested 10 times, with the number of collisions, the path length, the time consumption, and the target position offset recorded and calculated. The entire experimental procedure is shown in Figure 12:

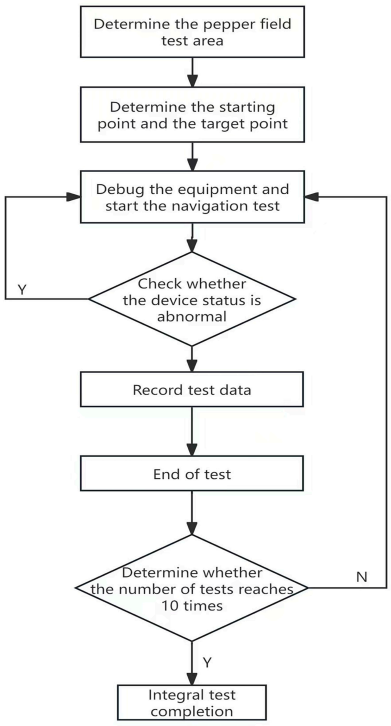

Figure 12. Chili field navigation experiment process diagram.

The number of collisions is defined as the count of noticeable contacts between the robot and obstacles, such as ridges, throughout the entire navigation process. Path length is defined as the length of the navigation planned path between the start and the target points. Time consumption is defined as the average time taken by the robot to reach the target point from the starting point. The target position offset is defined as the distance between the robot's actual position and the target point.

3. Results

The experiment was conducted in the test chili field under sunny conditions. A total of 10 groups of data for each scheme were collected, and the average value of the test results after collation and analysis is shown in Table 2.

Table 2. The total number of collisions and the average value of each dataset.

	LiDAR	IMU + GNSS	Standard TEB Algorithm	Optimized TEB Algorithm	The Number of Collisions/Time	Average Planned Path Length/m	Average Time Consumption/s	Average Target Position Offset/cm
Scheme 1	√		√		8	11.37	30.27	8.35
Scheme 2	√	√	√		4	11.27	30.66	4.44
Scheme 3	√			√	6	10.93	28.13	8.16
Scheme 4	√	√		√	1	10.79	27.72	4.04

The symbol '√' in the table indicates the method used in the corresponding approach.

The test results are presented in Table 2. It is observed that Scheme 1 has a relatively high collision frequency, reaching 8 instances. Multiple collisions occur during testing, with most collision points located at path inflection points. The average path length is 11.37 m, the average time consumption is 30.27 s, and the average target position offset is 8.35 cm. With the integration of the IMU inertial navigation system and the GNSS system, the number of collisions in Scheme 2 is reduced to 4 and the average target position offset decreases to 4.44 cm. Using the improved TEB algorithm, the collision frequency in Scheme 3 and Scheme 4 is further reduced to 6 and 1, respectively, showing a decreasing trend in collision frequency. Notably, Scheme 4 significantly reduces the probability of collisions

with chili ridges. The average path length is reduced to 10.93 m and 10.79 m, the average time is shortened to 28.13 s and 27.72 s, and the average target position offset improves to 8.16 cm and 4.04 cm, respectively.

Comparing the data, the navigation system based on multi-sensor data fusion and the optimized TEB algorithm reduces the average planned path length by 0.58 m, shortens the average time from the starting point to the target by 2.55 s, and decreases the average target position offset by 4.3 cm. As shown in Figure 13, Scheme 4 exhibits less data variation compared to the previous three schemes, indicating an improvement in overall navigation stability.

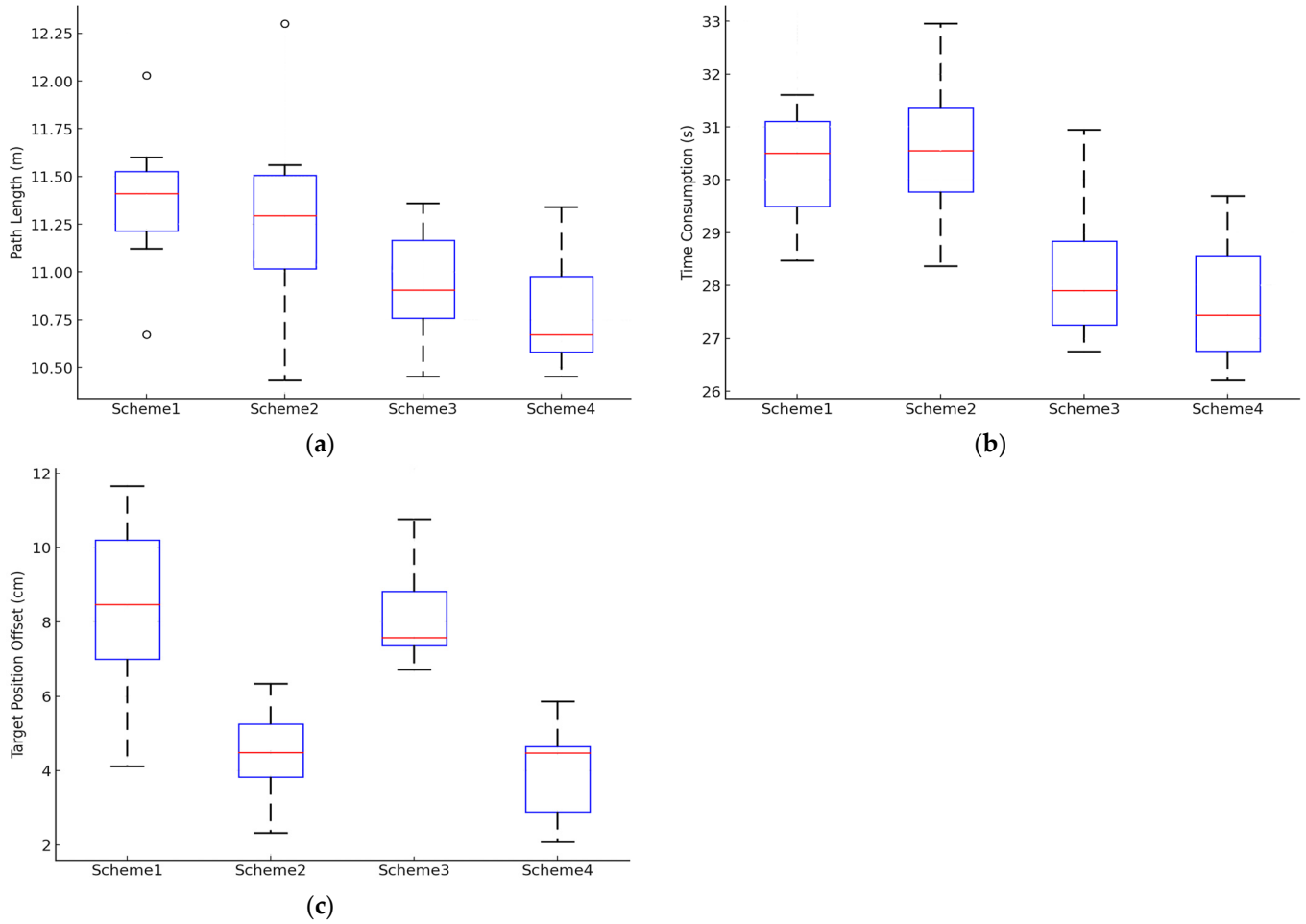

Figure 13. (**a**) The value of path length in 10 experiments. (**b**) The value of time consumption in 10 experiments. (**c**) The value of the target position offset in 10 experiments.

In this study, SPSS v16.0 was used to perform independent sample t-tests on the experimental data. When examining the effect of multi-sensor data fusion, the p-values for time consumption and planned path length were 0.985 and 0.372, respectively, both greater than 0.05. This indicates that the choice between using LiDAR alone or LiDAR + IMU + GNSS has no significant impact on time consumption or planned path length. However, the p-value for target position offset was 4.3×10^{-9}, less than 0.05, indicating a highly significant effect of multi-sensor data fusion on target position offset. Specifically, the use of LiDAR + IMU + GNSS significantly reduces target position offset compared to using LiDAR alone. When assessing the effect of the TEB algorithm, the p-value for target position offset was 0.720, greater than 0.05, suggesting that there is no significant difference in target position offset between the standard TEB algorithm and the optimized TEB algorithm. In contrast, the p-values for time consumption and planned path

length were 4.4×10^{-4} and 1.2×10^{-7}, respectively, both less than 0.05. This indicates that the choice between the standard TEB algorithm and the optimized TEB algorithm has a highly significant effect on time consumption and planned path length, with the optimized TEB algorithm performing better in both aspects.

4. Discussion

In this study, a navigation system for chili fields based on multi-sensor data fusion and an optimized TEB algorithm is proposed. The system utilizes the EKF to integrate data from LiDAR, the IMU, and the GNSS, and combines it with the optimized TEB algorithm using an A* algorithm. This is used to achieve accurate autonomous navigation in chili fields. The combined INS/GNSS navigation method based on a recurrent neural network (RNN) proposed by Dai et al. [21] may be limited by the training dataset in complex environments. When environmental conditions change, the model needs to be retrained. Zhong et al. used an integrated GPS/INS approach [20], which does not easily cope with the problem of slippage in chili fields. The scheme proposed by Abdelaziz et al. and Yu et al. is susceptible to ambient light [22,23]. The multi-sensor and optimized TEB algorithm-based navigation system proposed in this study can adapt to environmental changes in real time and can function effectively in varying slopes and slippery conditions typical of chili fields. Moreover, the system is minimally affected by lighting and is capable of operating continuously throughout the day, thereby enhancing operational efficiency in chili field applications. Dai et al.'s study of local path planning algorithms for optimizing the TEB algorithm [32] was able to reduce the amount of smoothing of the speed control due to speed jumps, but it was still not effective enough to achieve safer path planning in narrow chili fields in order to reduce the number of collisions. Zhang et al. applied the artificial potential field method and dynamic window approach, respectively [38]. However, these methods are designed for path planning in relatively stable environments, and they have difficulty meeting the application requirements in the complex environment of chili pepper fields. The modified TEB algorithm proposed in this study, by introducing the constraints of acceleration and corner change and designing the dynamic weight parameters to make the modified TEB algorithm suitable for path planning in the narrow chili field environment, reduces the risk of collision, and is able to achieve more accurate autonomous navigation in the chili field to satisfy the needs of autonomous chili picking.

This study does have some limitations. The multi-sensor and optimized TEB algorithm-based chili field navigation system focuses on autonomous navigation in chili fields that are generally narrow in southern China, and its navigation methods may not be universally applicable to field navigation environments for all crops. In practical applications, the high computational volume of multi-sensor fusion and optimization algorithms can lead to insufficient arithmetic power of the master control system. Additionally, due to the narrow and complex environment, extreme collisions are still difficult to avoid completely. Future research should focus on enhancing the system's applicability across a wider range of environments, addressing computational power limitations, and further reducing collision occurrences to improve versatility and effectiveness.

5. Conclusions

In this study, a multi-sensor- and optimized TEB algorithm-based navigation system for autonomous localization and navigation in chili fields is proposed. The system utilizes an extended Kalman filter to fuse data from LiDAR, the IMU, and the GNSS, optimizing the TEB algorithm for improved navigation performance. Experimental data collected in a real chili field environment demonstrate the effectiveness of the multi-sensor and optimized TEB algorithm-based navigation system. The results indicate that the system reduces the average value of the planned path length by 0.58 m, decreases the average time from the starting point to the target by 2.55 s, and reduces the average target position offset by 4.3 cm. Notably, the system significantly reduced collision frequency, with only one collision over ten experiments. The design of a multi-sensor- and optimized TEB algorithm-based

navigation system for chili fields facilitates the subsequent development of chili picking fields and smart agriculture.

Author Contributions: Conceptualization, W.H., H.G. and Q.G.; methodology, W.H., H.G. and Q.G.; validation, W.H., R.X. and Q.G.; formal analysis, W.H., R.X. and Q.G.; investigation, W.H., Z.Z., R.X. and Y.G.; resources, W.H. and Y.G.; data curation, W.H., Q.G., Z.Z., H.G., X.F. and Y.G.; writing—original draft preparation, W.H., K.L. and Q.G.; writing—review and editing, Y.Z., X.F. and H.G.; visualization, W.H., K.L. and Q.G.; supervision, Y.Z.; project administration, Y.Z. and Y.G.; funding acquisition, Y.Z. and Y.G. All authors have read and agreed to the published version of the manuscript.

Funding: This research was funded by the Laboratory of Lingnan Modern Agriculture, grant number NT2021009, and the 111 Center, grant number D18019.

Data Availability Statement: Data is contained within the article.

Conflicts of Interest: The authors declare no conflicts of interest.

References

1. Zou, X.; Ma, Y.; Dai, X.; Li, X.; Yang, S. Spread and Industry Development of Pepper in China. *J. Hortic.* **2020**, *47*, 1715–1726. [CrossRef]
2. Lin, Q.; Xin, Z.; Kong, L.; Wang, X.; Yang, X.; He, W. Development status of China's chili pepper industry and breeding countermeasures. *J. China Agric. Univ.* **2023**, *28*, 82–95.
3. Zhang, Z.; Zeng, L.; Zhang, W.; Ren, H.; Liu, L.; Zhang, Z.; Zou, X.; Qin, D.; Ou, L. Process Adaptability Appraisal of Fermented Chopped Chili Pepper Made from Fresh Chili Peppers of Different Varieties. *Agronomy* **2024**, *14*, 1833. [CrossRef]
4. Lillywhite, J.; Tso, S. Consumers within the Spicy Pepper Supply Chain. *Agronomy* **2021**, *11*, 2040. [CrossRef]
5. Zou, Z.; Zou, X. Geographical and Ecological Differences in Pepper Cultivation and Consumption in China. *Front. Nutr.* **2021**, *8*, 718517. [CrossRef]
6. Qiao, L.; Zhao, B.; Zong, Y.; Kou, C.; Dong, Y. Development status, trend and countermeasures of chili industry in China. *Chin. Veg.* **2023**, *11*, 9–15.
7. Wang, L.; Ma, Y.; Zhang, B. Market demand and breeding trend of chili pepper varieties in China. *Chin. Veg.* **2019**, *8*, 1–4. [CrossRef]
8. Wang, D.; Huo, X.; Zong, Y.; Jia, H. The Current Status and Suggestions for High-Quality Development of the "Jize Chili" Industry. *North. Horticult.* **2024**, *20*, 131–136.
9. Deng, C.; Zhong, Q.; Shao, D.; Ren, Y.; Li, Q.; Wen, J.; Li, J. Potential Suitable Habitats of Chili Pepper in China under Climate Change. *Plants* **2024**, *13*, 1027. [CrossRef]
10. Wang, L.; Zhang, B.; Zhang, Z.; Cao, Y.; Yu, H.; Feng, X. Research progress, industrial status and outlook of chili pepper breeding in China during the 13th Five-Year Plan. *Chin. Veg.* **2021**, *2*, 21–29. [CrossRef]
11. Fu, J.; Ji, C.; Liu, H.; Wang, W.; Zhang, G.; Gao, Y.; Zhou, Y.; Abdeen, M. Research Progress and Prospect of Mechanized Harvesting Technology in the First Season of Ratoon Rice. *Agriculture* **2022**, *12*, 620. [CrossRef]
12. Zhang, M.; Ji, Y.; Li, S.; Cao, R.; Xu, H.; Zhang, Z. Progress of agricultural machinery navigation technology. *J. Agric. Mach.* **2020**, *51*, 1–18.
13. Xie, B.; Jin, Y.; Faheem, M.; Gao, W.; Liu, J.; Jiang, H.; Cai, L.; Li, Y. Research progress of autonomous navigation technology for multi-agricultural scenes. *Comput. Electron. Agric.* **2023**, *211*, 107963. [CrossRef]
14. Botta, A.; Cavallone, P.; Baglieri, L.; Colucci, G.; Tagliavini, L.; Quaglia, G. A Review of Robots, Perception, and Tasks in Precision Agriculture. *Appl. Mech.* **2022**, *3*, 830–854. [CrossRef]
15. Tan, C.; Li, Y.; Wang, D.; Mao, W.; Yang, F. Research progress of automatic navigation technology of agricultural machinery. *Agric. Mech. Res.* **2020**, *42*, 7–14+32. [CrossRef]
16. Cui, B.; Zhang, J.; Wei, X.; Cui, X.; Sun, Z.; Zhao, Y.; Liu, Y. Improved Information Fusion for Agricultural Machinery Navigation Based on Context-Constrained Kalman Filter and Dual-Antenna RTK. *Actuators* **2024**, *13*, 160. [CrossRef]
17. Chen, T.; Xu, L.; Ahn, H.; Lu, E.; Liu, Y.; Xu, R. Evaluation of headland turning types of adjacent parallel paths for combine harvesters. *Biosyst. Eng.* **2023**, *233*, 93–113. [CrossRef]
18. Wang, W.; Xing, C.; Feng, W. Development status and trend of autonomous navigation technology. *J. Aviat.* **2021**, *42*, 18–36.
19. Gao, Q.; Lu, K.; Ji, Y.; Liu, J.; Xu, L.; Wei, G. A review of multi-sensor fusion SLAM research. *Mod. Radar* **2024**, *46*, 29–39.
20. Zhong, Y.; Xue, M.; Yuan, H. Design of combined GNSS/INS navigation system for intelligent agricultural machines. *J. Agric. Eng.* **2021**, *37*, 40–46.
21. Dai, H.; Bian, H.; Wang, R.; Ma, H. An INS/GNSS integrated navigation in GNSS denied environment using recurrent neural network. *Def. Technol.* **2020**, *16*, 334–340. [CrossRef]
22. Abdelaziz, N.; El-Rabbany, A. Deep Learning-Aided Inertial/Visual/LiDAR Integration for GNSS-Challenging Environments. *Sensors* **2023**, *23*, 6019. [CrossRef] [PubMed]

23. Yu, J.; Lu, W.; Zeng, M.; Zhao, S. Multi-sensor fusion low-cost automatic navigation method for agricultural machines. *China Test* **2021**, *47*, 106–113+119.
24. Yu, J.; Chen, Y.; Feng, C.; Su, Y.; Guo, J. A review on local path planning for intelligent construction robots. *Comput. Eng. Appl.* **2024**, *60*, 16–29.
25. Zheng, K.; Han, B.; Wang, X. Ackerman robot motion planning system based on improved TEB algorithm. *Sci. Technol. Eng.* **2020**, *20*, 3997–4003.
26. Chen, Y.; Shen, J.; Li, S. Research on dynamic obstacle avoidance strategy for multiple robots with improved TEB algorithm. *Electro-Opt. Control.* **2022**, *29*, 107–112.
27. Chen, J.; Guo, C.; Liu, Y. A mobile robot path optimization method based on temporal elastic band. *Sci. Technol. Eng.* **2021**, *21*, 11212–11219.
28. Wu, T.; Xie, Z.; Chen, K. Improved D*lite and time-elastic band method for mobile robot path planning. *J. Sens. Technol.* **2022**, *35*, 486–494.
29. Chen, H.; Dou, P.; Cheng, C.; Wang, Z. Multi-objective point path planning in wind turbine waters based on Bi-RRT and TEB algorithms. *Mar. Eng.* **2024**, *53*, 130–136.
30. Yin, X.; Dong, W.; Wang, X.; Yu, Y.; Yao, D. Route planning of mobile robot based on improved RRT star and TEB algorithm. *Sci. Rep.* **2024**, *14*, 8942. [CrossRef]
31. Dai, W.; Zhang, L.; Wu, J.; Ma, X. Research on local path planning algorithm with improved TEB algorithm. *Comput. Eng. Appl.* **2022**, *58*, 283–288.
32. Yang, J.; Qin, X.; Lei, J.; Lu, L.; Zhang, J.; Wang, Z. Design and Experiment of a Crawler-Type Harvester for Red Cluster Peppers in Hilly and Mountainous Regions. *Agriculture* **2024**, *14*, 1742. [CrossRef]
33. Wang, K.; Zhang, J.; Xu, Z.; Xu, Y. Interpretation of Land Use Planning Technical Regulations Based on Integration and Oriented to Transformation—"Urban Land Use Classification and Planning Land Use Standards (GB50137-2011)". *Urban Plan.* **2012**, *36*, 42–48+92.
34. Deng, P.; Luo, J. Robot Multi-sensor Fusion positioning Method in Complex Environment. *Chin. J. Electron. Meas. Instrum.* **2023**, *37*, 48–57.
35. Zhang, S.; Zhang, Q.; Wang, G.; Wu, L.; Cai, Z.; Li, Y.; Lin, Z. A Combined Navigation Path Planning Method Based on Improved A* and Optimized TEB. *Laser Mag.* **2024**, *45*, 39–46.
36. Luan, T.; Wang, H.; You, B.; Sun, M. A Pose-Assisted Point TEB Navigation Method for Autonomous Vehicles in Narrow Spaces. *J. Instrum. Sci. Technol.* **2023**, *44*, 121–128.
37. Lv, Z.; Ni, L.; Peng, H.; Zhou, K.; Zhao, D.; Qu, G.; Yuan, W.; Gao, Y.; Zhang, Q. Research on Global Off-Road Path Planning Based on Improved A* Algorithm. *ISPRS Int. J. Geo-Inf.* **2024**, *13*, 362. [CrossRef]
38. Zhang, Y.; Song, J.; Zhang, Q. Local Path Planning of Outdoor Cleaning Robot Based on an Improved DWA. *Robot* **2020**, *42*, 617–625. [CrossRef]

Disclaimer/Publisher's Note: The statements, opinions and data contained in all publications are solely those of the individual author(s) and contributor(s) and not of MDPI and/or the editor(s). MDPI and/or the editor(s) disclaim responsibility for any injury to people or property resulting from any ideas, methods, instructions or products referred to in the content.

Journal of Food Composition and Analysis 130 (2024) 106157

Contents lists available at ScienceDirect

Journal of Food Composition and Analysis

journal homepage: www.elsevier.com/locate/jfca

Fluorescence spectroscopy detection of carbendazim residue in cucumber juice based on BC

Xidan Xu [a,b,1], Kangting Yan [a,c,1], Junqi Xiao [a,b], Jun Guo [a,b], Xiaoyang Lu [a,b], Linlin Wang [d], Yubin Lan [a,c], Yali Zhang [a,b,*]

[a] National Center for International Collaboration Research in Precision Agricultural Aviation Pesticides Spraying Technology, Guangzhou 510642, China
[b] College of Engineering, South China Agricultural University, Guangzhou 510642, China
[c] College of Electronic Engineering (College of Artificial Intelligence), South China Agricultural University, Guangzhou 510642, China
[d] School of Artificial Intelligence, Shenzhen Polytechnic University, Shenzhen 518055, China

ARTICLE INFO

Keywords:
Fluorescence spectrum
BC
Carbendazim
Cucumber juice
Pesticide residues
Food safety
Rapid detection

ABSTRACT

Excessive residues of the carbendazim pesticide in food will cause food safety issues. Particularly, cucumber is one of the common vegetables with carbendazim residues. This study, using fluorescence spectroscopy technology, explored the residues of carbendazim in cucumbers. First, a fluorescence spectrophotometer was used to scan and obtain the three-dimensional fluorescence spectra of carbendazim standard and four carbendazim formulations. Analyzing and comparing their respective fluorescence characteristics, fluorescence peak 1: *Ex/Em*=245/300–320 nm and fluorescence peak 2: *Ex/Em*=280/300–320 nm have been identified as the fluorescence characteristic peaks of carbendazim, and the optimal excitation wavelengths *Ex*=245 nm and *Ex*=280 nm with carbendazim specificity was screened. Subsequently, two-dimensional fluorescence spectroscopy was performed on the carbendazim and cucumber-carbendazim mixed solutions using the optimal excitation wavelength. In order to obtain more effective two-dimensional spectral data, the original fluorescence spectrum of the cucumber-carbendazim mixed solution was subjected to Blank Correction (BC), significantly reducing the impact of cucumber's own fluorescent characteristics on the carbendazim fluorescent peak in the mixed solution. Polynomial models and linear prediction models were developed based on the concentration of carbendazim and the fluorescence peak intensity values obtained after BC. The detection limit value of carbendazim residues in the cucumber-carbendazim mixed system included the maximum pesticide residue limit specified by national food safety regulations. This research provides valuable data and technical support for efficient detection of pesticide residues in cucumbers.

1. Introduction

Carbendazim, also known as Benzimidazole No. 44, is a highly effective and low-toxic broad-spectrum fungicide. It affects the cell division of pathogenic fungi by interfering with the formation of the mitotic spindle, thereby killing the fungi. Carbendazim is widely used in agricultural production and has significant preventive and control effects on fungal diseases in crops. It is commonly used to prevent and control powdery mildew in cucumber, watermelon, and other melon crops; anthracnose in soybeans, peanuts, and other legume crops; and sclerotinia in eggplant and cucumber, as well as various plant diseases in seedlings, such as damping-off and sudden wilt. However, excessive use of carbendazim can pose hazards to human health, and in some countries, carbendazim has been listed as prohibited (Xu et al., 2018). In China, many regions have begun to monitor and assess the risk of pesticide residues in vegetables, fruits, and other crops. Among them, the detection rate and residual concentration of carbendazim in many fruits, vegetables, traditional Chinese medicines, and tea are relatively high (Fan et al., 2023; Kuang et al., 2022; Liu et al., 2023; Wu et al., 2021; Xiao et al., 2019; Xing et al., 2022; Zhang et al., 2021a).

In Asia, cucumber is the fourth largest vegetable after tomatoes, cabbage, and onions (Mallick, 2022). Cucumber has the function of controlling sugar, soothing the skin, and maintaining blood pressure, as well as having a very delicious taste, so it is often eaten as a common

* Corresponding author at: College of Engineering, South China Agricultural University, Guangzhou 510642, China.
E-mail addresses: xxxjy@stu.scau.edu.cn (X. Xu), ylzhang@scau.edu.cn (Y. Zhang).
[1] These authors contributed equally to this work.

https://doi.org/10.1016/j.jfca.2024.106157
Received 23 November 2023; Received in revised form 2 March 2024; Accepted 7 March 2024
Available online 8 March 2024
0889-1575/© 2024 Elsevier Inc. All rights reserved.

ingredient in juices, salads, and cold dishes. However, because these eating methods are mostly raw, the adverse effects of pesticide residues in cucumber on human health are more remarkable. Therefore, it is of great economic importance to monitor pesticide residues in cucumber, especially to explore efficient and rapid detection methods. At present, the main pesticide detection methods for agricultural products are chromatography, including high-performance liquid chromatography (Islam et al., 2009; Jin et al., 2016; Sivaperumal et al., 2015), gas chromatography (Dömötörová & Matisová, 2008; Huang et al., 2007), liquid chromatography-tandem mass spectrometry (Calatayud-Vernich et al., 2017), and gas chromatography-mass spectrometry method (Caldeirão et al., 2023). However, the instruments and reagents used in these methods are relatively expensive, and there are problems such as high operating difficulty, complex sample pretreatment, and cumbersome data processing, which are not suitable for actual agricultural production (Ji et al., 2014; Yan et al., 2018). Fluorescence spectroscopy detection has the characteristics of easy operation and simple pretreatment in early stage (Yan et al., 2022; Yan et al., 2018), and also has the characteristics of fingerprints, which enables qualitative and quantitative analysis of specific substances in mixtures (Zhang et al., 2021b). Moreover, fluorescence has the feature of high sensitivity, as the emission intensity of fluorescent substances in samples measured by fluorescence spectroscopy is much higher than the sensitivity of the absorbance method. In addition, most pesticides contain fluorescent groups, and fluorescence spectroscopy analysis techniques exhibit unique excellence in the detection of pesticide residues in agricultural production (Zhang et al., 2021a). In recent years, there have been great advances in pesticide detection using fluorescence detection technology. Maira D. Carabajal et al. used the method of UV-fluorescence-liquid chromatography for quantitative analysis of multiple agricultural chemicals residues in vegetable, thereby enhancing the sensitivity of fluorescence analysis (Carabajal et al., 2016). Previous research on theoretical aspects of pesticide detection using fluorescence spectroscopy has been relatively perfect. M.J. Rodríguez-Cuesta et al. employed three-dimensional fluorescence combined with parallel factor analysis (PARAFAC) to determine pesticides such as carbendazim, pirazole, and thiabendazole and performed linear calibration, achieving quality factors such as precision, sensitivity, and limit of detection (Rodríguez et al., 2003). In terms of pesticide residue detection applications for food, Vahideh et al. determined the residual amount of carbendazim at different concentrations in cucumber using a UV spectrophotometer, and then analyzed the data using the MCR-ALS method and compared the results with high-performance liquid chromatography (HPLC). The results indicated that the spectrophotometric method exhibited good analytical capabilities (Vahideh et al., 2009); Yinshan Yu et al. measured the fluorescence spectra of apple juice and the mixture solution of Paclobutrazol using traditional fluorescence spectroscopy and its derived spectra, and performed regression analysis (Yu et al., 2020); Ge Xuefeng et al. detected the fluorescence spectra of procymidone solution and honey solution and their mixed solutions based on the basic principles of fluorescence spectroscopy, observed the red shift phenomenon of the fluorescence peak in the mixed solution, and the established prediction model had an accuracy of 96.8% and above (Ge et al., 2017); Wang Na et al. established a fluorescence quenching induced fluorescence quenching of Cys-His-GQD and pesticide aptamer DNA ligation prepared based on functional graphene quantum dots, and realized the fluorescence quantitative detection and analysis of carbendazim, acetamiprid and chlorpyrifos in cucumbers, with detection limits of 0.47, 0.04, and 0.80 nmol•L^{-1}, respectively (Wang et al., 2021).

Cucumber is one of the most common vegetables with carbendazim residues (Xu et al., 2018), and there are currently few studies on the detection of carbendazim residues in cucumber, especially using fluorescence spectroscopy (Jiang et al., 2021; Khoshnam et al., 2022; Leili et al., 2016; Mansour et al., 2009). This study conducted fluorescence analysis on the standard of carbendazim, four formulations of carbendazim produced by different manufacturers, and the cucumber-carbendazim mixed solution system. The main aspects included: (1) analyzing the fluorescence characteristics of the standard and formulations of carbendazim based on three-dimensional fluorescence spectroscopy and excitation-emission matrix (EEM) data, and obtaining the optimal excitation wavelength of carbendazim pesticides; (2) scanning the two-dimensional fluorescence spectrum of the carbendazim formulation solution, cucumber juice, and cucumber-carbendazim mixed solution with the optimal excitation wavelength, using Blank Correction (BC) for data processing of the mixed solution system's spectral data, and achieving the quantitative analysis of carbendazim in the cucumber-carbendazim mixed solution system. This study can provide a reference for the rapid detection of pesticide residues on crop surfaces.

2. Materials and methods

2.1. Instrumentation and materials

Instrumentation: The FP8300 Fluorescence Spectrophotometer (JASCO, Japan) was adopted to record the fluorescence spectrum.

Materials: Fresh cucumbers were bought from the supermarket. The standard of carbendazim (purity $\geq$ 98.1%, CAS: 10605–21–7) is provided by Hubei Kangbaotai Fine Chemical Co., Ltd., and four formulations of carbendazim are as follows: 30% carbendazim suspension (North China Pharmaceutical Group Aino Co., Ltd.), 50% carbendazim suspension (Jiangsu Longdeng Chemical Co., Ltd.), 50% carbendazim moistureable powder 1 (Weihai Hanfu Biochemical Pharmaceutical Co., Ltd.) and 50% carbendazim moistureable powder 2 (Jiangsu Sanshan Pesticide Co., Ltd.).

2.2. Solution preparation and material handling

Cucumber solution: Fresh cucumbers were washed with pure water, chopped, juiced and filtered. The residue was filtered out using a 100-mesh gauze, and then a certain amount of pure water was added for dilution to obtain a cucumber solution with a concentration of 0.134 g•mL^{-1}.

Carbendazim standard solution: The carbendazim standard was dissolved in organic solvent DMSO to prepare the mother solution for the standard solution, and then the mother solution was diluted to prepare 19 concentration gradients.

Carbendazim preparation solution: The carbendazim suspension (or moistureable powder) was diluted with water to prepare mother solution with a concentration of 1 mg•mL^{-1}, and then the mother solution was diluted to prepare 25 concentration gradients of carbendazim preparation solution.

Cucumber-carbendazim mixed solution: The mother liquor of the carbendazim formulation was diluted, and different amounts of carbendazim solution were added to cucumber juice to prepare cucumber-carbendazim mixed solutions with different concentrations.

2.3. Fluorescence spectral scanning and processing

After the sample preparation was completed, it was placed in a low temperature (5℃) and dark environment for approximately 1 hour. The three-dimensional fluorescence spectrum were scanned for the original solution of carbendazim, the formulated solution, and the mixture solution of carbendazim and cucumber. The samples were taken using a pipette to suck 3 mL of the test sample and placed in a 10×10×42 mm quartz dish. The FP8300 fluorescence spectrophotometer was set up with the following parameters: the excitation and emission wavelength intervals were both 5 nm, the scanning range for the excitation wavelength (*Ex*) was 200–450 nm, the emission wavelength (*Em*) was 210–500 nm, the scanning speed was 5000 nm/min, the response time was 20 ms, and then the three-dimensional fluorescence spectrum of the test solution in the quartz dish was scanned.

The parameters for two-dimensional fluorescence spectral scanning were set as follows: the emission wavelength interval was 5 nm, the scanning range of the emission wavelength (*Em*) when *Ex* = 245 nm was 260–500 nm, the scanning range of the emission wavelength (*Em*) when *Ex* = 280 nm was 290–500 nm, the scanning speed was 5000 nm/min, the response time was 50 ms, and the average value of three repeated scans was taken for each sample.

BC pretreatment is a spectral correction of processing method, which can eliminate the complex fluorescence background of the target fluorescent substance, thus better capturing the fluorescence characteristics of the target fluorescent substance. It is an effective method for dealing with issues such as overlapping fluorescence peaks or the inability to directly distinguish different fluorescence peak positions in spectra. For the mixed solution in this study, the original spectrum collected in the experiment contained the spectra of the target sample carbendazim and other samples such as cucumber juice. The spectrum of the cucumber juice was recorded as the blank data, and the original spectrum of the mixed solution was white-corrected, which can minimized the influence of the cucumber juice spectrum and obtained the spectrum of the target sample carbendazim.

3. Results and discussion

3.1. Fluorescence spectral characteristics of carbendazim standard and formulation

From the three-dimensional fluorescence spectrum and EEM data of the carbendazim standard solution, it can be seen that the carbendazim standard has two distinct fluorescence characteristic peaks at *Ex*=245 nm and *Ex*=280 nm, and *Em*=300–320 nm, as shown in Fig. 2. It is preliminarily inferred that these are the characteristic fluorescence peaks of carbendazim. When the concentration of the carbendazim solution is low, the emission wavelength (*Em*) of the fluorescence characteristic peak is 305 nm. With the increase of the concentration, the peak position of the characteristic peak exhibited a redshift phenomenon, and the emission wavelength of the two fluorescence characteristic peaks gradually shifted to 320 nm.

In order to further explore and verify the fluorescence characteristic peaks of carbendazim, nine different concentrations of solutions prepared from four carbendazim formulations were scanned using three-dimensional fluorescence spectroscopy. Some of the three-dimensional fluorescence spectra of carbendazim formulations at various concentrations are shown in Table 2. All of four carbendazim formulations have fluorescence characteristic peaks at *Ex*=245/280 nm and *Em*=300–320 nm, and this measurement result and spectrum of the standard product mutually verified the fluorescence characteristic peak of carbendazim. Two carbendazim powder solutions have fluorescent peak 4 at other excitation and emission wavelengths, and the fluorescent peak 4 of the powder 2 obviously has the effect of extrusion and strong overlap on the fluorescent peak 1 at high concentrations, which is presumably caused by the fluorescent components of the auxiliary agents in the carbendazim moistureable powder. The two carbendazim suspension solutions have an additional fluorescent peak 3: *Ex/Em*=300/315 nm at high concentrations. In summary, the existence of fluorescent peak 1: *Ex*=245 nm, *Em*=300–320 nm and fluorescent peak 2: *Ex*=280 nm, *Em*=300–320 nm are universal in various products of carbendazim, which are confirmed to be the fluorescence characteristic peaks of carbendazim, which is consistent with the research of Wu Wentao et al. (Wu et al., 2017). The excitation wavelength of *Ex*=245/280 nm was selected as the optimal wavelength for carbendazim.

3.2. The change rule of fluorescence intensity in formulations

In order to further verify the characteristic wavelength of carbendazim formulations and explore the relationship between the concentration of carbendazim formulations and fluorescence intensity, the emission spectra at *Em*=260–500/290–500 nm were obtained through two-dimensional fluorescence spectroscopy scanning, using *Ex*=245/280 nm as the excitation wavelength. As can be seen from Fig. 4(c) and (d), when the excitation wavelength is 245 nm and 280 nm, the characteristic peaks of carbendazim formulations are located at 305–320 nm. The fluorescence intensity of carbendazim formulations increases proportionally with the increase of carbendazim solution concentration, with the occurrence of redshift phenomenon.

Using Origin 2019b, the fluorescence spectral data, ranging from

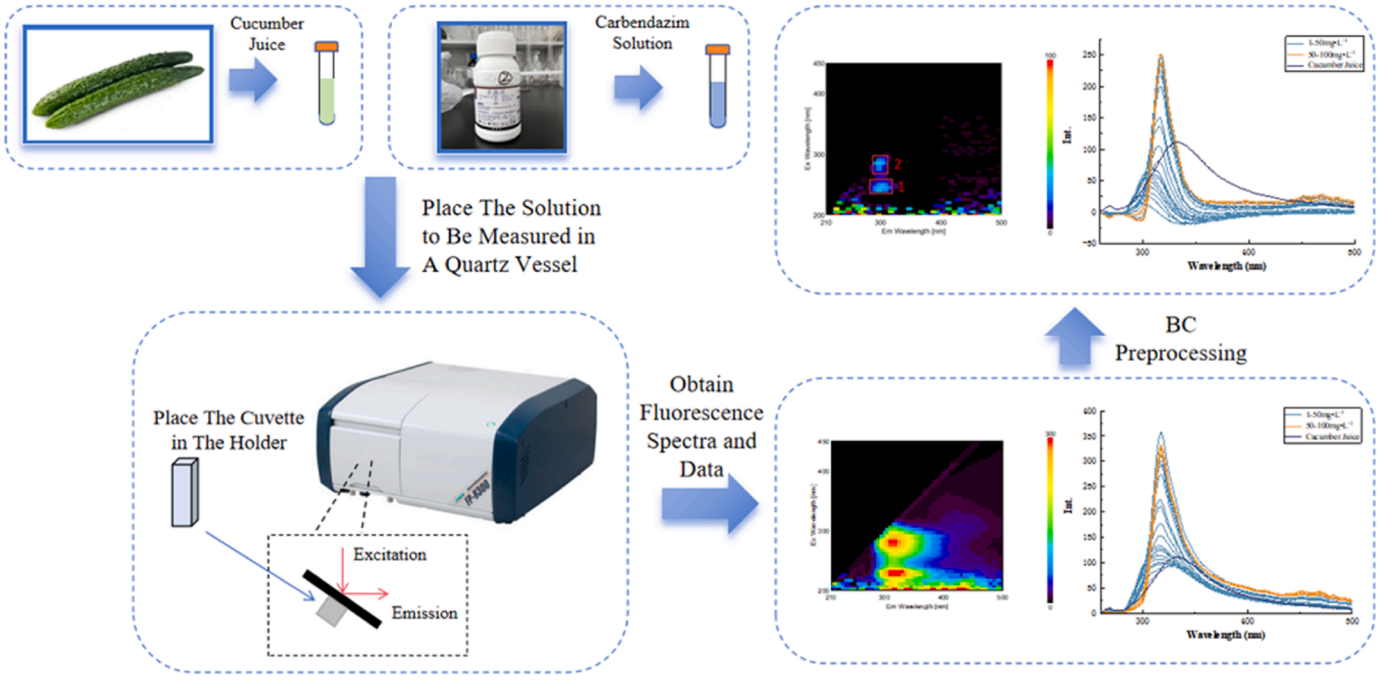

Fig. 1. Sample Detection and Analysis Process Flowchart.

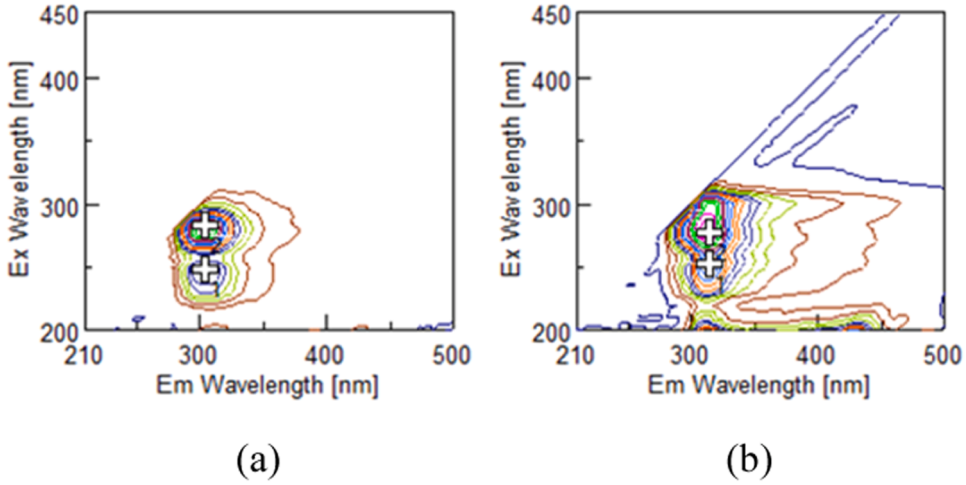

Fig. 2. Three-dimensional fluorescence spectrum of carbendazim standard solution (a for the low-concentration standard solution, b for the high-concentration standard solution).

Table 1
Concentration Gradient of Carbendazim Preparation Solutions and Cucumber-Carbendazim Mixed Solutions.

	Gradient of The Active Ingredient Concentration of Carbendazim /(mg•L^{-1})
Carbendazim Preparation Solutions	0.01、0.05、0.1、0.2、0.3、0.4、0.5、0.75、1、3、5、6、8、10、12、18、20 (Training Set) 0.15、0.25、1.5、2.5、3.5、4.5、7.5 (Testing Set)
Cucumber-Carbendazim Mixed Solutions	1、2、4、5、7、8、10、20、25、35、40、50 (Training Set) 3、6、9、15、30、45 (Testing Set)

0.01 to 20 mg•L^{-1}, of 8 groups of carbendazim preparation solutions with 25 concentration gradients were fitted. The training set and testing set were set at a ratio of 2:1, and outliers were removed. The fitting results are shown in Fig. 3. According to the Beer-Lambert law and the theoretical calculation formula of solution fluorescence intensity-solution concentration, when *abc* is extremely small, the theoretical calculation formula of solution fluorescence intensity-solution concentration is:

$$I_f = Y_f I_0 abc$$

In which, I_f is the fluorescence intensity of the solution, Y_f is the quantum yield of fluorescence of the substance, I_0 is the intensity of the incident light, a is the absorption coefficient, b is the thickness of the absorption layer, and c is the concentration of the solution; when $abc \geq 0.05$, the intensity of the carbendazim fluorescence peak no longer shows a linear relationship with the concentration of carbendazim in the solution. Therefore, considering quadratic or cubic terms in the power series for the analysis of the relationship is necessary (Xu & Wang, 2006).

The fitting results showed that the correlation coefficient r for each model was all greater than 0.99, indicating that the prediction model effect was ideal. This implies that using 245 nm and 280 nm as the optimal excitation wavelengths for the carbendazim solution explains 99% of the specificity of the fluorescence intensity of the carbendazim solution. Furthermore, the good correlation confirmed the fluorescence

Table 2
Three-Dimensional Fluorescence Spectra of Carbendazim Preparation Solutions.

	30% Carbendazim Suspension	50% Carbendazim Suspension	50% Carbendazim Moistureable Powder 1	50% Carbendazim Moistureable Powder 2
Low Concentration	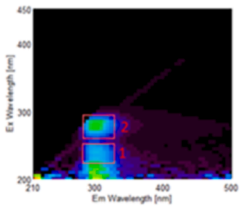	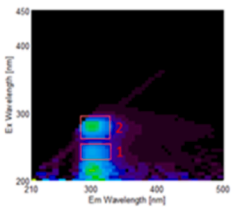	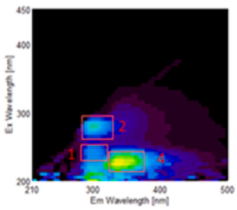	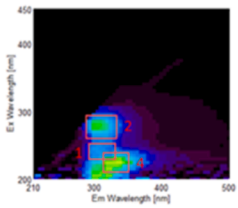
High Concentration	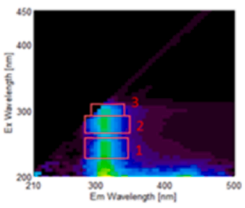	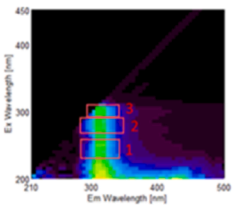	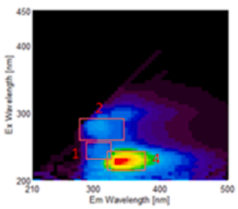	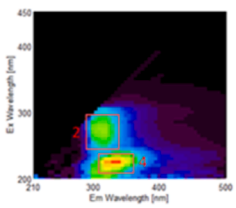

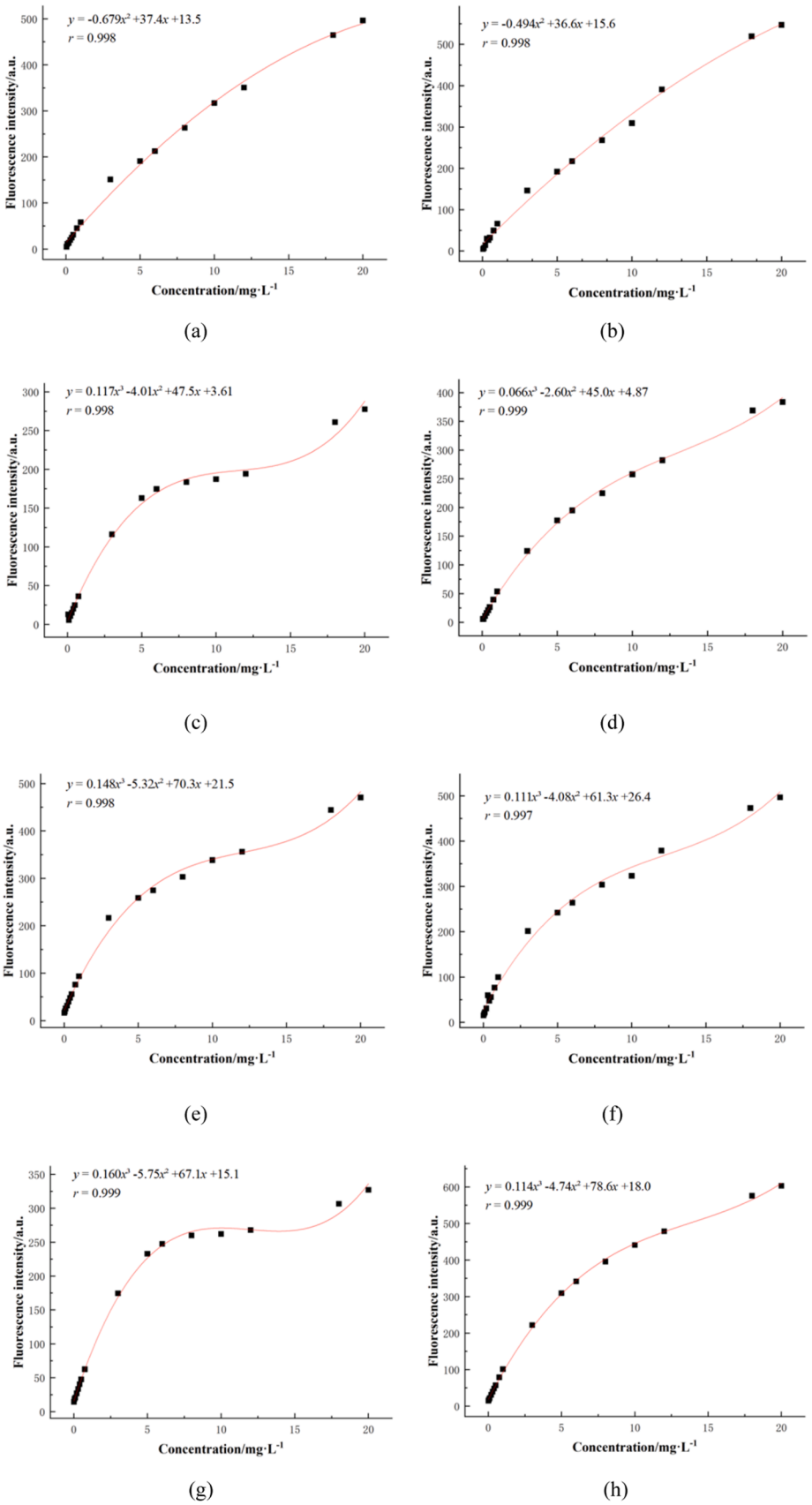

Fig. 3. Prediction Model of Carbendazim Formulations Concentration in Solution (a for the 30% carbendazim suspension with *Ex*=245 nm; b for the 50% carbendazim suspension with *Ex*=245 nm; c for the 50% carbendazim moistureable powder 1 with *Ex*=245 nm; d for the 50% carbendazim moistureable powder 2 with *Ex*=245 nm; e for the 30% carbendazim suspension with *Ex*=280 nm; f for the 50% carbendazim suspension with *Ex*=280 nm; g for the 50% carbendazim moistureable powder 1 with *Ex*=280 nm; h for the 50% carbendazim moistureable powder 2 with *Ex*=280 nm).

regions 1 and 2 as the characteristic peaks of carbendazim fluorescence once again. Therefore, using the intensity of the fluorescence peaks at this optimal excitation wavelength for quantitative analysis is feasible.

The measured values of the test set were fitted into a linear relationship with the predicted values obtained from the established model to assess the accuracy of the prediction model depicted in Fig. 3. Table 3 presents the results of various tests, and it can be seen that the values of r^2 are extremely close to 1 and the *RMSE* values are relatively small, indicating that the predicted values of the predictive model fitted to the training set are very close to the actual values, demonstrating a good prediction accuracy. Comparing the r^2 and *RMSE* values in the two columns of Table 3, it can be observed that the prediction models established at the excitation wavelength of 245 nm for different formulations have slightly samller accuracy errors and better results compared to those established at the excitation wavelength of 280 nm. This indicates that the predictive model established with *Ex*=245 nm can be better applied to the quantitative analysis of carbendazim.

3.3. Cucumber sample testing

Cucumber skin is green due to the presence of chlorophyll, and it is rich in organic compounds such as vitamins, amino acids, quercetin, and astragalus (Feng et al., 2023). When the cucumber skin is exposed to external light, the components containing fluorescent groups in the skin are excited and produce fluorescence (Sun et al., 2016), which may affect the detection of the fluorescein characteristic peak of carbendazim in cucumbers. Therefore, in the experiment, the fluorescence spectrum of the cucumber skin and the cucumber juice was first detected and analyzed to verify the feasibility of the carbendazim fluorescence peak in it. In the middle and both ends of the cucumber sample washed with pure water and dried, thick for the 1 mm and skin for the 1 cm × 1 cm was cut for three-dimensional fluorescence spectrum and two-dimensional fluorescence spectrum scanning with the same excitation wavelength and scanning range as the carbendazim solution. Fig. 4 shows the three-dimensional fluorescence spectrum of cucumber skin (Fig. 4-a) and cucumber juice (Fig. 4-b), and the two-dimensional fluorescence spectrum of *Ex* = 245/280 nm. Compared with Fig. 2 and Table 2, it can be seen that the fluorescence peak range of cucumber in the three-dimensional fluorescence spectrum is very close to that of carbendazim, making it difficult to distinguish between the two. However, in the two-dimensional fluorescence spectrum, the fluorescence spectrum of cucumber is completely different from that of carbendazim. It can be seen that the peak of cucumber juice is at 330 nm, which is a significantly different position from the fluorescence peak of carbendazim formulation solution, allowing for a clear distinction between carbendazim and cucumber.

Table 3
Validation of The Accuracy of The Prediction Model for Carbendazim Formulations Concentration in Solution.

	Ex=245 nm			Ex=280 nm		
	r^2	RMSE	average recovery rate	r^2	RMSE	average recovery rate
30% carbendazim suspension	0.995	0.461	108%	0.994	0.551	109%
50% carbendazim suspension	0.998	0.278	113%	0.994	0.543	100%
50% carbendazim moistureable powder 1	0.998	0.335	103%	0.991	0.650	102%
50% carbendazim moistureable powder 2	0.999	0.159	98%	0.999	0.201	100%

3.4. Trend of fluorescence change in the mixed solution

The ability of a substance to produce fluorescence is mainly determined by its molecular structure, but environmental factors can also affect the observation of fluorescence spectra (Sun et al., 2021). Therefore, selecting one suitable formulation of carbendazim from the four available options and adding it to the cucumber juice to explore the detection of carbendazim in the mixed system. From the three-dimensional fluorescence spectrum of the four carbendazim formulations in Table 2, it can be seen that compared to the two 50% carbendazim moistureable powder formulations, the fluorescence spectrum of the 30% carbendazim suspension and the 50% carbendazim suspension are simpler, without obvious interference from the fluorescence peak of the auxiliaries. The 30% carbendazim suspension is a 42% pentazole·carbendazim compound suspension agent (30% carbendazim and 12% pentazole), with complex ingredients. Therefore, the 50% carbendazim suspension, which has a simple spectrum and single ingredient , was chosen for the detection of the cucumber-carbendazim mixed solution. Add different amounts of a 10 mg•mL^{-1} mother solution of carbendazim to the extracted cucumber juice, and prepare 23 cucumber-carbendazim mixed solutions with a concentration range of 1–100 mg•L^{-1} of carbendazim. The mixed solution to be tested was placed in a cuvette, and the three-dimensional fluorescence spectrum of the mixed solution and the two-dimensional fluorescence spectrum at the optimal excitation wavelengths of carbendazim at 245 nm and 280 nm were measured, respectively.

There are compounds with fluorescent groups in cucumber that exhibit a strong fluorescent peak in three-dimensional fluorescence spectra. The fluorescent peak of cucumber juice in the three-dimensional fluorescence spectrum is relatively close to the carbendazim peak position, and there may be phenomena such as coverage and strong overlap between fluorescence spectra (Zhang et al., 2016). As can be seen from the three-dimensional fluorescence spectrum in Fig. 5, when the concentration of carbendazim is low (Fig. 5(b)), the fluorescence spectrum of the mixed solution is not much different from the spectral intensity, peak position and shape of cucumber juice, indicating that only the fluorescence peak of cucumber juice can be observed, while the fluorescence peak of carbendazim is completely covered and cannot be displayed. When the concentration of carbendazim increased to 10 mg•L^{-1}, the fluorescence intensity of carbendazim increased to the point that it could not be ignored and masked, and the shape of the fluorescence peak of the mixed solution changed significantly, which was different from the fluorescence peak of cucumber juice, and the peak of the mixed solution moved slightly to the fluorescence peak of carbendazim, but the fluorescence peak of carbendazim still could not be clearly and directly observed.

Fig. 6 shows the measurement results of the two-dimensional fluorescence spectrum of the mixed solution. When the concentration of carbendazim was very low (1–2 mg•L^{-1}), the peak position of the mixed solution was extremely close to the peak position of the cucumber juice (330 nm), with only a slight difference in fluorescence intensity, making them almost indistinguishable. However, as the concentration of carbendazim increased (3–50 mg•L^{-1}), the peak position of the mixed solution occurred the blueshift phenomenon, gradually moving to and stabilizing at 316–318 nm (the position of the carbendazim formulation solution), and the fluorescence intensity also increased with the increase of carbendazim concentration. Different from the variation of carbendazim solution (Fig. 4), the occurrence of a blueshift in the fluorescence peak of the mixed solution may be due to the fluorescence peak of carbendazim being masked at low concentrations, with the fluorescence characteristic peaks of carbendazim and cucumber juice being extremely closed in peak position. Regarding fluorescence intensity, at low concentrations, the fluorescence peak of carbendazim is significantly lower compared to the fluorescence peak of cucumber juice,

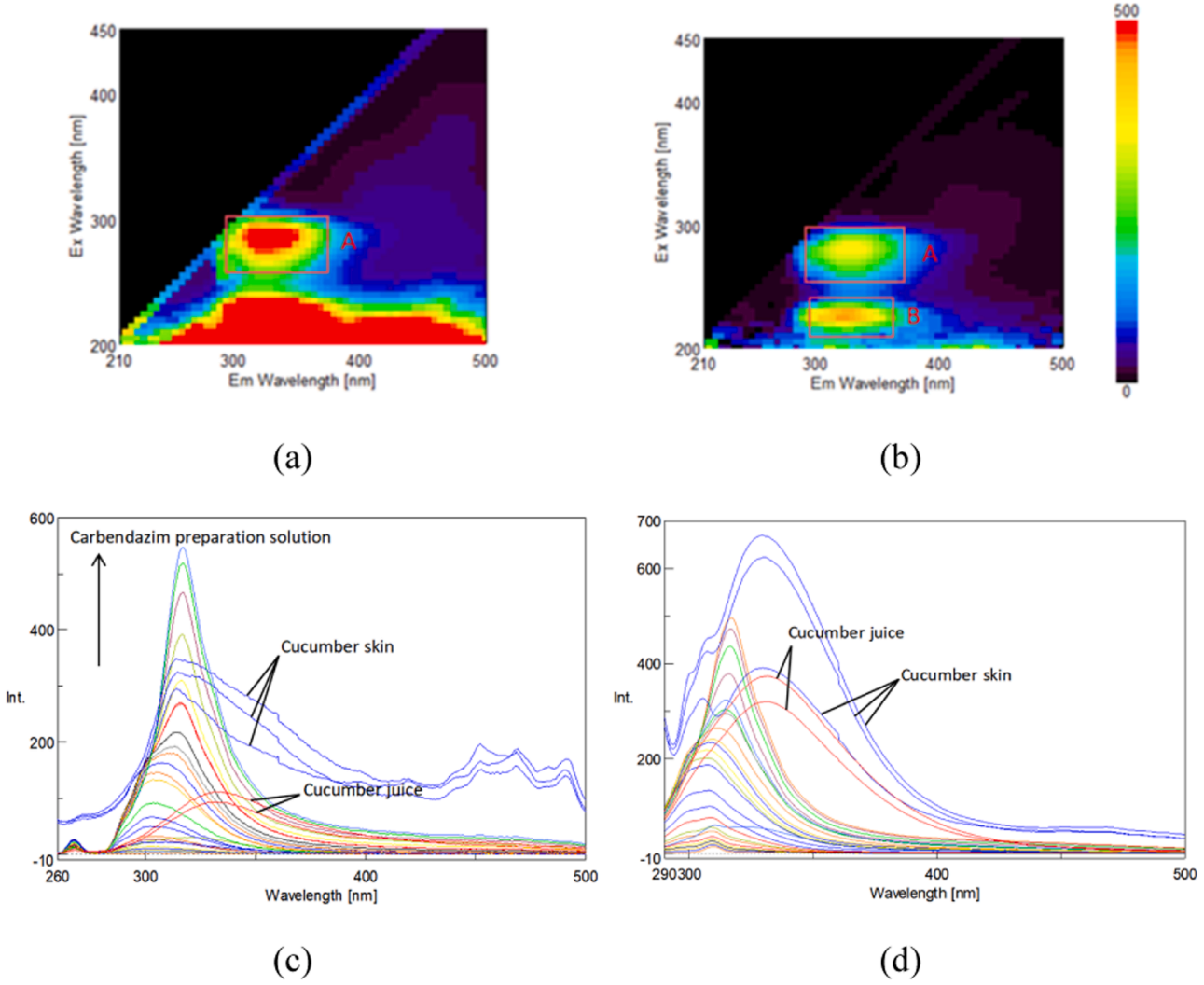

Fig. 4. Fluorescence Spectrum of Cucumber Skin and Cucumber Juice (a for the three-dimensional fluorescence spectrum of cucumber skin; b for the three-dimensional fluorescence spectrum of cucumber juice; c for the two-dimensional fluorescence spectrum of *Ex* = 245 nm; d for the two-dimensional fluorescence spectrum of *Ex* = 280 nm).

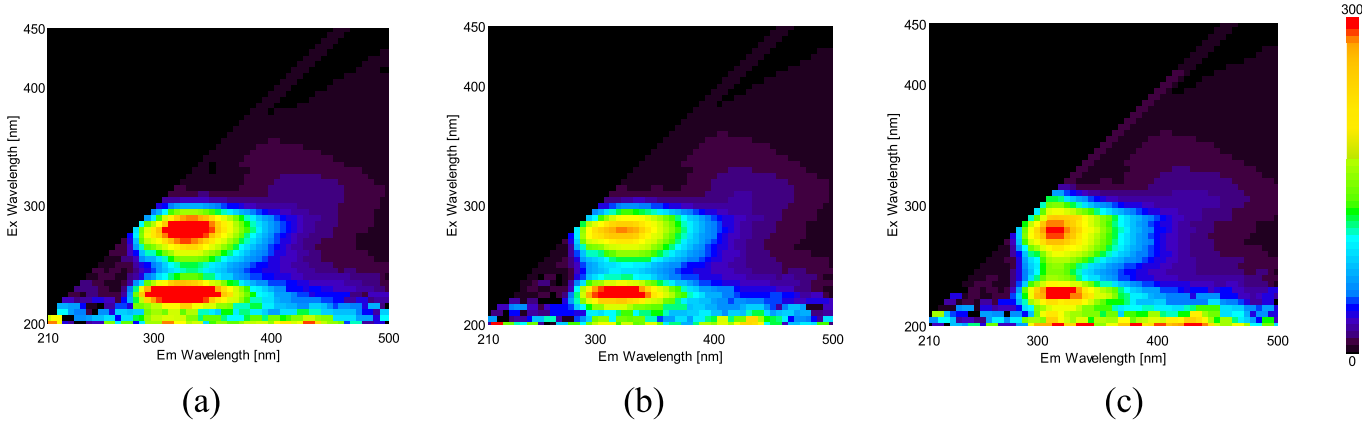

Fig. 5. Three-dimensional fluorescence spectra of cucumber juice and mixed solutions (a for the cucumber juice; b for the mixed solution with a concentration of 2 mg•L^{-1} carbendazim; c for the mixed solution with a concentration of 10 mg•L^{-1} carbendazim).

resulting in the complete covering of the fluorescence peak at this time. As the concentration of carbendazim increases, the fluorescence peak of carbendazim begins to be exposed, no longer being completely overshadowed by the other fluorescence peaks. This causes the peak position of the mixed solution's fluorescence to gradually shift towards the carbendazim fluorescence peak position (305–320 nm), rather than

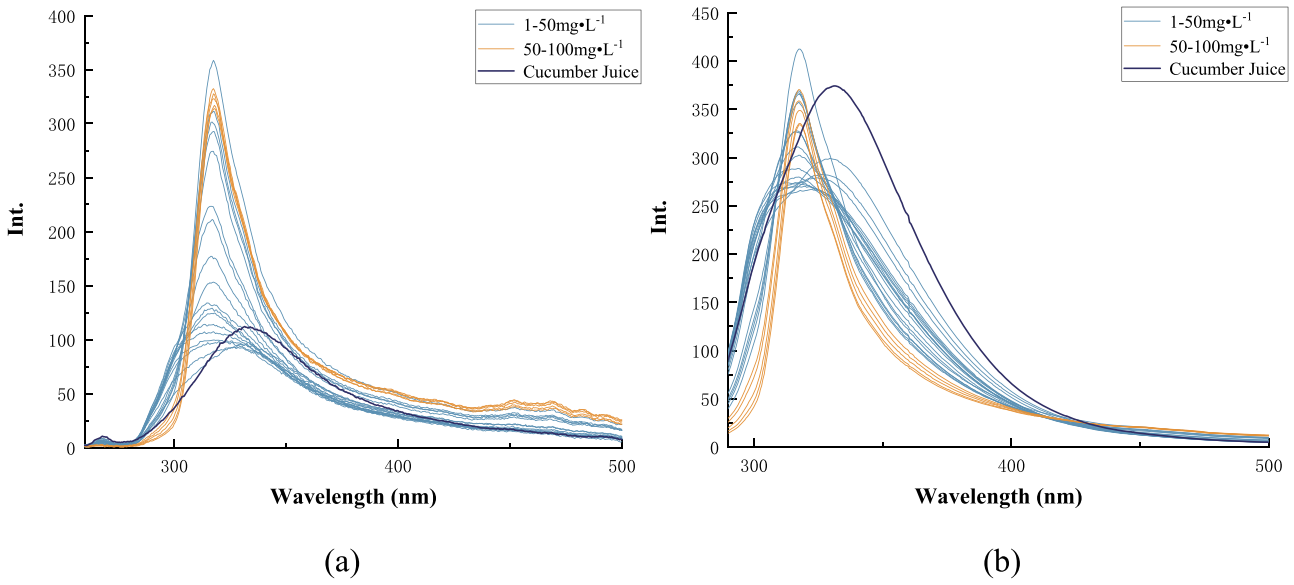

Fig. 6. Two-Dimensional Fluorescence Spectra of Cucumber Juice and Cucumber-Carbendazim Mixed Solutions (a for the *Ex* = 245 nm; b for the *Ex* = 280 nm).

just an increase in the intensity at a single peak position. After the carbendazim concentration increased to 50 mg•L^{-1}, the fluorescence intensity no longer increased steadily, but gradually showed a decreasing trend with the increase of concentration. Xu mentioned in Fluorescence Analysis that the fluorescence spectrum of a highly concentrated solution produces the inner filter effect (Xu & Wang, 2006). The fluorescent substances in the mixed solution will produce fluorescence signals when excited by external light sources. But when the concentration of carbendazim in the solution is too high, the absorption of the incident light by the other substances in the solution increases, and the energy of the electronic transition of the fluorescent substances of carbendazim decreases, so that the fluorescence intensity of the solution decreases.

According to the "National Food Safety Standard Maximum Residue Limits for Pesticides in Food" (GB2763–2021), the maximum residue limit of carbendazim in cucumber is 2 mg•kg^{-1}. Therefore, conventional two-dimensional and three-dimensional fluorescence spectrum techniques cannot effectively detect the active ingredient of carbendazim in the mixed solution within the standard range of pesticide residues, and the fluorescence spectrum of the mixed solution is required to be further processed.

3.5. BC Pre-treatment

This paper used Blank Correction (BC) in Spectra Manager to process the spectral data in the spectrum measurement of the mixed solution, eliminating the overlapping influence of cucumber juice as a fluorescent background on the pesticide residue detection results, and then explored the fluorescence characteristics of low-concentration carbendazim in the mixed solution, to achieve the detection of maximum residue limits of carbendazim that comply with national food safety standards. Repeat the scanning and measurement of the fluorescence spectrum data of cucumber juice three times, take the average value and record and save it as blank data, and then use the blank data for correction when measuring cucumber-carbendazim mixed solutions with different carbendazim concentrations. Fig. 7 shows the three-dimensional fluorescence spectrum after BC pretreatment. Fig. 7(a) and (b) are mixed solutions with carbendazim concentrations of 1 mg•L^{-1} and 2 mg•L^{-1}, respectively. In the spectrum of Fig. 7(a), there are relatively weak fluorescence peaks at *Ex*=240 nm, *Em*=300 nm and *Ex*=280 nm, *Em*=310 nm. The positions of the fluorescence peaks are the same as those of the three-dimensional fluorescence characteristic peaks of carbendazim. Similarly, there are obvious fluorescence peaks at the same positions in Fig. 7(b), and the intensity of the fluorescence peaks

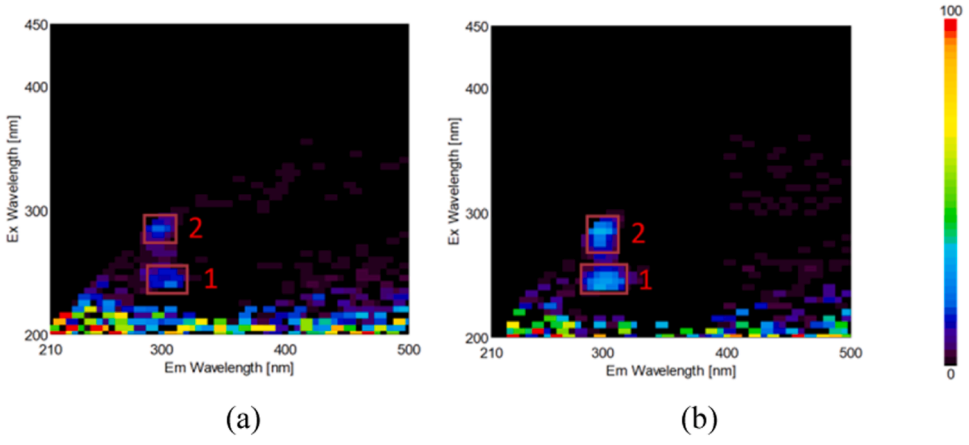

Fig. 7. Three-Dimensional Fluorescence Spectra after BC Preprocessing (a for the mixed solution with a carbendazim concentration of 1 mg•L^{-1}; b for the mixed solution with a carbendazim concentration of 2 mg•L^{-1}).

are enhanced compared with those in (a). It was confirmed that the two fluorescence peaks observed after BC treatment were the fluorescence characteristic peaks of carbendazim. The spectra after processing in Fig. 7 also verify that the reason why the fluorescence characteristic peaks of carbendazim in the mixed solution cannot be directly detected is indeed covered by the fluorescence peaks of cucumber juice, rather than the disappearance of fluorescence peaks due to changes in the molecular structure and other issues. At the same time, it proves that BC pretreatment can effectively solve the interference problem of cucumber juice fluorescence peaks on carbendazim fluorescence peaks in the mixed solution.

The cucumber juice was repeatedly scanned three times at the optimal excitation wavelengths of carbendazim, which are 245 nm and 280 nm. The average value was recorded as the blank data, and this data was used to correct the two-dimensional fluorescence spectra of the mixed solutions. Fig. 8 shows the two-dimensional fluorescence spectrum after BC preprocessing. Compared to the original two-dimensional fluorescence spectrum of the mixed solutions in Fig. 5, the BC-preprocessed spectrum effectively eliminated the fluorescence variability generated by the overlap of the fluorescence peaks of the cucumber juice, and were able to distinguish clearly between the cucumber juice and mixed solutions with different concentration gradients, and the unique fluorescence peak of carbendazim was fully displayed in the BC-preprocessed fluorescence spectrum, which confirmed the feasibility of adopting the fluorescence spectrum for the detection of pesticide residues. This result verified the feasibility of detecting pesticide residues by fluorescence spectroscopy and laid a good foundation for the subsequent quantitative analysis.

Fig. 8(a) shows the fluorescence peak position and the stability of intensity growth at 245 nm, and the *Ex*=245 nm data processed by BC (1–50 mg•L^{-1}) were fitted with the quadratic term function and linear function using Origin 2019b, and the training set and test set were divided into a 2:1 ratio. The fitting results showed that the concentration of carbendazim and the fluorescence intensity of the two models showed a good correlation (R>0.99), and the fluorescence peak of cucumber juice in the sample no longer seriously interfered with the analysis of carbendazim, which confirmed the applicability of the fluorescence peak of the two-dimensional spectrum after treatment at the excitation wavelength for the quantitative detection and analysis of carbendazim. The accuracy of the mixed solution's prediction model was examed by using the testing set. The quadratic function prediction model test showed an equation determination coefficient R^2=0.994, root mean square error *RMSE*=1.86 mg•L^{-1}, and the recall rate was 93~112%; The linear function prediction model was R^2=0.987, *RMSE*=1.74 mg•L^{-1}, and the recall rate was 66~118%. The validation results indicate that the predictive model established by the quadratic function is significantly superior to the one established by the linear function.

The good prediction accuracy of the prediction model indicates that the two-dimensional fluorescence spectra, after BC treatment, not only eliminated the interference of the fluorescence peak of cucumber juice but also the fluorescence signals of carbendazim were clearly highlighted, which can be used to detect carbendazim directly. If in the fluorescence spectrum without BC preprocessing, the interference of the fluorescence signal of cucumber juice will reduce the accurate identification of carbendazim concentration. Furthermore, the intensity of the fluorescence peak after treatment is fully suitable for quantitative analysis of carbendazim. The calibration range used to establish the prediction model was 1–50 mg•L^{-1}, as the inner filter effect of the solution fluorescence exists at high carbendazim concentrations (50–100 mg•L^{-1}). However, considering the concentration range that complies with actual food safety standards, it is considered that the impact of the inner filter effect can be neglected in practical applications. This does not imply that the applicability of the fluorescence spectroscopy detection method after BC pretreatment is limited to this range, whether it is three-dimensional spectrum or two-dimensional spectrum. Since the BC pretreatment is primarily used to address spectral overlap interference and is suitable for substances with fluorescence effects, significant detection limitations have not been observed temporarily. In future research, the detection range can be expanded according to the detection needs.

The fluorescence spectra after BC processing significantly improved the selectivity and sensitivity of the analysis by eliminating the interference of the complex fluorescent background, and the fluorescence characteristics of the pesticides can be better utilized the purpose of detection. Furthermore, when using fluorescence spectroscopy technology for detection, the detection range is set to the specific position of the target carbendazim fluorescence peak, and only the region of the carbendazim fluorescence peak is scanned, which reduces the acquisition of redundant spectral information and helps to reduce the time of spectral processing and analysis. Traditional analysis usually requires the recording of the whole spectral band, the amount of data, low analytical efficiency, while BC preprocessing combined with the detection range optimisation can ensure the quality of the analysis at the same

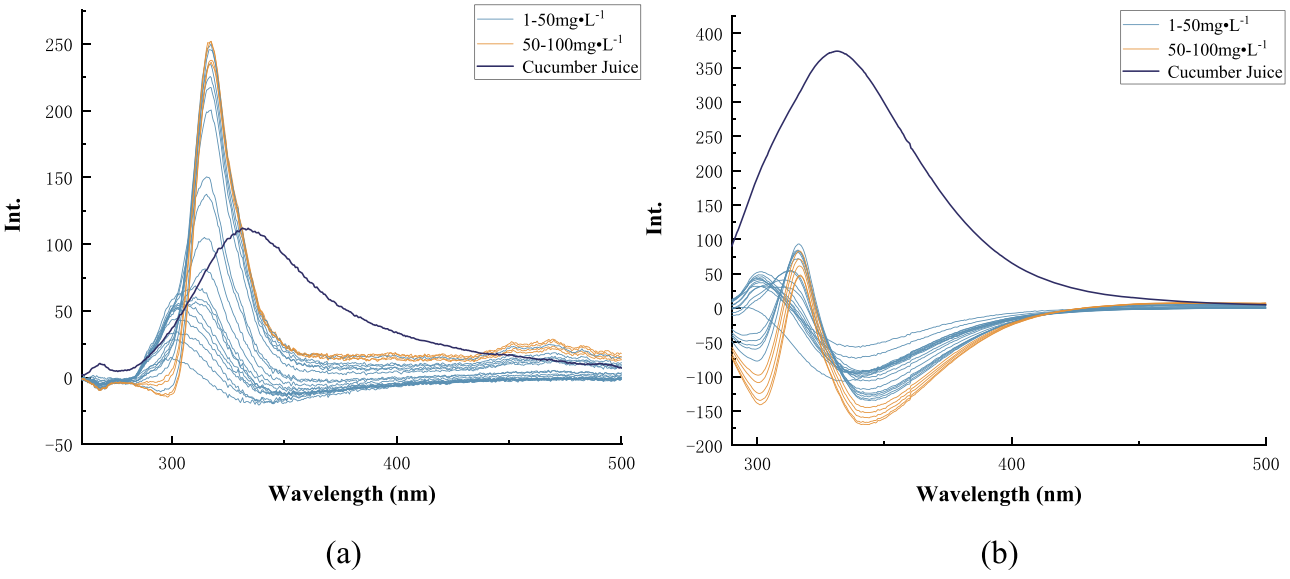

Fig. 8. Two-Dimensional Fluorescence Spectrum of Cucumber-Carbendazim Mixed Solution after BC Preprocessing (a for the *Ex* = 245 nm; b for the *Ex* = 280 nm).

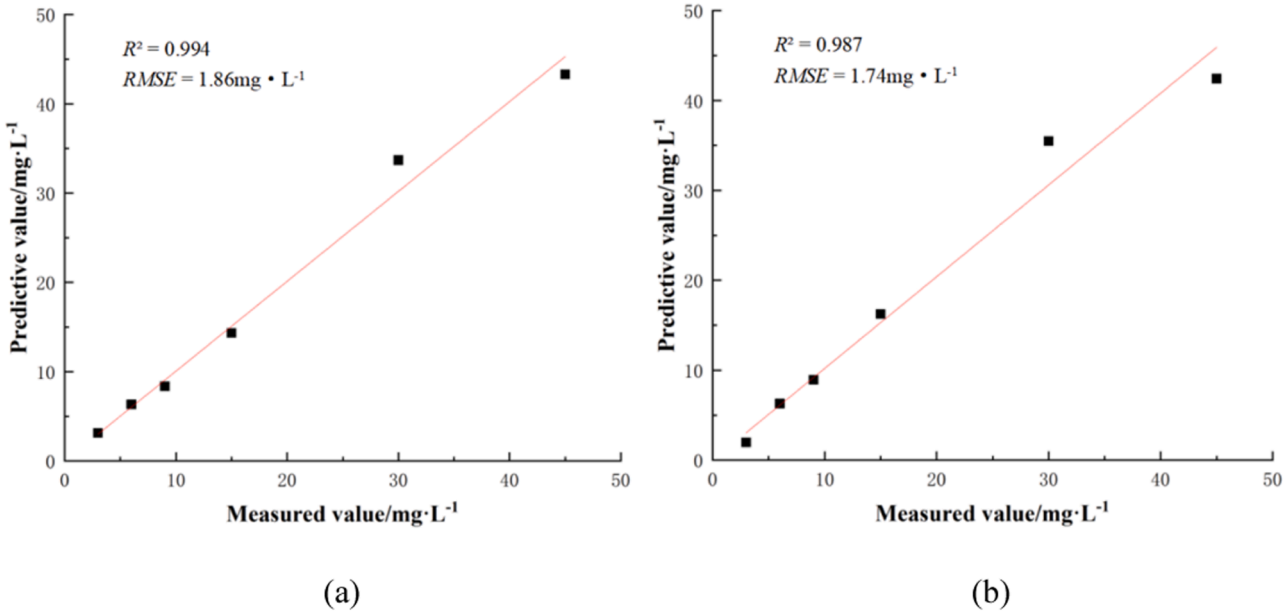

Fig. 9. Fitting of Predicted Values and Actual Measurements (a for the quadratic function model, b for the linear function model).

time, better improve the efficiency of sample detection which is very important for the rapid detection of a large number of samples. Compared with other complicated methods such as chromatography, fluorescence spectroscopy combined with BC processing method gives fully play to the advantages of fluorescence spectroscopy in the rapid quantitative detection of pesticide residues in cucumber juice by removing interfering signals and optimising detection parameters. This provides a highly effective detection method for pesticide residue in food raw materials or finished products.

4. Conclusion

In the text, the fluorescence spectrophotometer was used to measure and analyze the spectral characteristics of carbendazim and the residues of carbendazim in cucumber juice, which proved the feasibility of using fluorescence spectroscopy technology to directly detect pesticide carbendazim residues in cucumber juice.

Through a series of measurement results, it was determined that fluorescence peak 1: *Ex/Em*=245/300–320 nm and fluorescence peak 2: *Ex/Em*=280/300–320 nm are the fluorescence characteristic peaks of carbendazim, *Ex*=245 nm and *Ex*=280 nm are the optimal excitation wavelength of carbendazim; the characteristic fluorescence peak of cucumber is *Ex/Em*=285/330 nm. At the same time, it was confirmed that the reason why carbendazim cannot be directly detected in cucumber juice when the concentration is very low is that the fluorescence peak of carbendazim is covered by the fluorescence peak of cucumber juice.

In order to solve the problem of interference of fluorescence peaks in cucumber juice, the spectra of carbendazim-cucumber juice mixed solution were BC treated in this study. The results showed that no matter it is three-dimensional spectrum or two-dimensional spectrum, the fluorescence spectrum after processing can clearly display the fluorescence peak position of carbendazim when the carbendazim concentration is low (1 mg•L^{-1}); and in the two-dimensional spectrum, the intensity of the fluorescence peak also has the ability to quantitatively analyze the concentration of the solution. It indicates that the processed fluorescence spectrum has considerable potential in the rapid detection of pesticide residues.

Funding

This work was financially supported by Laboratory of Lingnan Modern Agriculture Project (NT2021009).

CRediT authorship contribution statement

Linlin Wang: Validation. **Yubin Lan:** Project administration, Funding acquisition. **Yali Zhang:** Writing – review & editing, Supervision, Resources, Funding acquisition, Conceptualization. **Kangting Yan:** Writing – review & editing, Validation, Software, Methodology, Conceptualization. **Junqi Xiao:** Writing – review & editing, Investigation, Data curation. **Jun Guo:** Writing – review & editing, Validation, Resources. **Xiaoyang Lu:** Investigation. **Xidan Xu:** Writing – review & editing, Writing – original draft, Validation, Supervision, Software, Methodology, Investigation, Data curation, Conceptualization.

Declaration of Competing Interest

The authors declare that they have no known competing financial interests or personal relationships that could have appeared to influence the work reported in this paper.

Data Availability

Data will be made available on request.

References

Calatayud-Vernich, P., Calatayud, F., Simó, E., Picó, Y., 2017. Occurrence of pesticide residues in Spanish beeswax. Sci. Total Environ. 605-606, 745–754.
Caldeirão, L., Godoy, H.T., Fernandes, J., Cunha, S.C., 2023. Pesticide residues in herbs and their transfer for infusions. J. Sep. Sci. 46, e2300069.
Carabajal, M.D., Arancibia, J.A., Escandar, G.M., 2016. A green-analytical chemistry method for agrochemical-residue analysis in vegetables. Microchem. J. 128, 34–41.
Dömötörová, M., Matisová, E., 2008. Fast gas chromatography for pesticide residues analysis. J. Chromatogr. A 1207, 1–16.
Fan, J., An, J., Ren, R., Liu, S., He, H., Zhao, G., 2023. Occurrence and exposure risk assessment of pesticide residues in green tea samples cultivated in Hangzhou area, China. Food Addit. Contam.: Part B 16, 8–13.
Feng, Z., Sun, L., Dong, M., Fan, S., Shi, K., Qu, Y., Zhu, L., Shi, J., Wang, W., Liu, Y., Song, L., Weng, Y., Liu, X., Ren, H., 2023. Novel players in organogenesis and flavonoid biosynthesis in cucumber glandular trichomes. Plant Physiol. 192, 2723–2736.
Ge, X., Wu, Y., Zhao, Z., 2017. Deteramination of procymidone residues content in honey by fluorescence spectroscopy. Chin. J. Lumin. 38, 973–977 (in Chinese).

Huang, Z., Li, Y., Chen, B., Yao, S., 2007. Simultaneous determination of 102 pesticide residues in Chinese teas by gas chromatography–mass spectrometry. J. Chromatogr. B 853, 154–162.
Islam, S., Afrin, N., Hossain, M.S., Nahar, N., Mosihuzzam, M., Mamun, M.I.R., 2009. Analysis of some pesticide residues in cauliflower by high performance liquid chromatography. Am. J. Environ. Sci. 5, 325–329.
Ji, R., Chen, M., Zhao, Z., Zhu, X., Wang, L., Liu, Q., 2014. Study on Experiment of absorption spectroscopy detection of pesticide residues of carbendazim in orange juice. Spectrosc. Spectr. Anal. 721–724.
Jiang, M., Gao, H., Liu, X., Wang, Y., Lan, J., Li, Y., Lv, S., Zhu, K., Gong, P., 2021. Detection of pesticide residues in vegetables sold in Changchun City, China. J. Food Prot. 84, 481–489.
Jin, T., Li, F., Cheng, J., Wu, S., Zhou, H., Cheng, M., 2016. Polymer monolithic column containing embedded graphene oxide sheets for sensitive determination of carbamate insecticides by HPLC. Microchim. Acta 183, 543–551.
Khoshnam, F., Ziaee, M., Daei, M., Mahdavi, V., Mousavi, K.A., 2022. Investigation and probabilistic health risk assessment of pesticide residues in cucumber, tomato, and okra fruits from Khuzestan, Iran. Environ. Sci. Pollut. Res. 29, 25953–25964.
Kuang, L., Xu, G., Tong, Y., Li, H., Zhang, J., Shen, Y., Cheng, Y., 2022. Risk assessment of pesticide residues in Chinese litchis. J. Food Prot. 85, 98–103.
Leili, M., Pirmoghani, A., Samadi, M.T., Shokoohi, R., Roshanaei, G., Poormohammadi, A., 2016. Determination of pesticides residues in cucumbers grown in greenhouse and the effect of some procedures on their residues. Iran. J. Public Health 45, 1481–1490.
Liu, Y., Bei, K., Zheng, W., Yu, G., Sun, C., 2023. Pesticide residues risk assessment and quality evaluation of four characteristic fruits in Zhejiang Province, China. Front. Environ. Sci. 11.
Mallick, P.K., 2022. Evaluating potential importance of cucumber (Cucumis sativus L. -Cucurbitaceae): a brief review. Int. J. Appl. Sci. Biotechnol. 10, 12–15.
Mansour, S.A., Belal, M.H., Abou-Arab, A.A.K., Gad, M.F., 2009. Monitoring of pesticides and heavy metals in cucumber fruits produced from different farming systems. Chemosphere 75, 601–609.
Rodríguez-Cuesta, M.J., Boqué, R., Rius, F.X., Picón Zamora, D., Martínez Galera, M., Garrido Frenich, A., 2003. Determination of carbendazim, fuberidazole and thiabendazole by three-dimensional excitation–emission matrix fluorescence and parallel factor analysis. Anal. Chim. Acta 491, 47–56.
Sivaperumal, P., Anand, P., Riddhi, L., 2015. Rapid determination of pesticide residues in fruits and vegetables, using ultra-high-performance liquid chromatography/time-of-flight mass spectrometry. Food Chem. 168, 356–365.
Sun, J., Tang, B., Zhou, X., Yao, K., Hu, S., Zhang, L., 2021. Design and test of a portable detection instrument for pesticide residues on crop leaves. Trans. Chin. Soc. Agric. Eng. 37, 61–67.
Sun, J., Zhou, X., Mao, H., Wu, X., Yang, N., Zhang, X., 2016. Detection of pesticide residues in lettuce based on fluorescence spectra. Trans. Chin. Soc. Agric. Eng. 32, 302–307.
Wang, N., Li, Z., Li, N., 2021. Fluorescence detection of carbendazim, acetamiprid and chlorpyrifos in cucumbers. J. Food Saf. Qual. 12, 7191–7199.
Wu, P., Wang, P., Gu, M., Xue, J., Wu, X., 2021. Human health risk assessment of pesticide residues in honeysuckle samples from different planting bases in China. Sci. Total Environ. 759, 142747.
Wu, W., Chen, Y., Xiao, X., Yang, R., Zhao, N., 2017. Study on three-dimensional fluorescence spectral characteristics of heterocyclic pesticides in different environmental conditions. Spectrosc. Spectr. Anal. 37, 788–793.
Vahideh, V.M., Bakhsh, M.R.T., Valiyan, A., 2009. Spectrophotometric measurement of carbendazim pesticide residue in cucumber and compare with HPLC. Appl. Entomol. Phytopathol. 77, 59–76.
Xiao, J., Xu, X., Wang, F., Ma, J., Liao, M., Shi, Y., Fang, Q., Cao, H., 2019. Analysis of exposure to pesticide residues from Traditional Chinese Medicine. J. Hazard. Mater. 365, 857–867.
Xing, L., Wang, Y., Luo, R., Li, X., Zou, L., 2022. Determination of 31 pesticide residues in wolfberry by LC-MS/MS and dietary risk assessment of wolfberry consumption. Food Sci. Technol. 42.
Xu, J., Wang, Z., 2006. Fluorescence analysis method. Science Press, Beijing, China.
Xu, X., Chen, J., Li, B., Tang, L., 2018. Carbendazim residues in vegetables in China between 2014 and 2016 and a chronic carbendazim exposure risk assessment. Food Control 91, 20–25.
Yan, K., Han, Y., Wang, L., Ding, F., Lan, Y., Zhang, Y., 2022. Research on the fluorescence spectra characteristics of abamectin technical and preparation solution. Spectrosc. Spectr. Anal. 42, 3476–3481.
Yan, X., Li, H., Su, X., 2018. Review of optical sensors for pesticides. Trac Trends Anal. Chem. 103, 1–20.
Yu, Y., Qu, Y., Zhang, M., Guo, X., Zhang, H., 2020. Fluorescence detection of paclobutrazol pesticide residues in apple juice. Optik 224, 165542.
Zhang, J., Zhao, Z., Zhang, W., 2016. Intelligent identification of two pyrethriod pesticide in tea by flurescence spectroscopy. Chin. J. Lumin. 37, 1023–1030.
Zhang, Y., Si, W., Chen, L., Shen, G., Bai, B., Zhou, C., 2021a. Determination and dietary risk assessment of 284 pesticide residues in local fruit cultivars in Shanghai, China. Sci. Rep. 11, 9681.
Zhang, Y., Yan, K., Wang, L., Chen, P., Han, Y., Lan, Y., 2021b. Research progress on pesticide residue detection based on fluorescence spectroscopy. Spectrosc. Spectr. Anal. 41, 2364–2371.

agronomy

MDPI

Article

Deep-Learning-Based Rice Disease and Insect Pest Detection on a Mobile Phone

Jizhong Deng [1,2,3,†], Chang Yang [1,3,†], Kanghua Huang [3,4], Luocheng Lei [1,3], Jiahang Ye [1,3], Wen Zeng [1,3], Jianling Zhang [1,3], Yubin Lan [2,3,4] and Yali Zhang [1,2,3,*]

[1] College of Engineering, South China Agricultural University, Guangzhou 510642, China; jz-deng@scau.edu.cn (J.D.); changyang@stu.scau.edu.cn (C.Y.); llc@stu.scau.edu.cn (L.L.); yjh@stu.scau.edu.cn (J.Y.); zengwen@scau.edu.cn (W.Z.); jlingzhang@scau.edu.cn (J.Z.)
[2] Guangdong Laboratory for Lingnan Modern Agriculture, Guangzhou 510642, China; ylan@scau.edu.cn
[3] National Center for International Collaboration Research on Precision Agricultural Aviation Pesticides Spraying Technology, Guangzhou 510642, China; kh_huang@stu.scau.edu.cn
[4] College of Electronic Engineering, South China Agricultural University, Guangzhou 510642, China
* Correspondence: ylzhang@scau.edu.cn
† These authors contributed equally to this work.

Abstract: The realization that mobile phones can detect rice diseases and insect pests not only solves the problems of low efficiency and poor accuracy from manually detection and reporting, but it also helps farmers detect and control them in the field in a timely fashion, thereby ensuring the quality of rice grains. This study examined two Improved detection models for the detection of six high-frequency diseases and insect pests. These models were the Improved You Only Look Once (YOLO)v5s and YOLOv7-tiny based on their lightweight object detection networks. The Improved YOLOv5s was introduced with the Ghost module to reduce computation and optimize the model structure, and the Improved YOLOv7-tiny was introduced with the Convolutional Block Attention Module (CBAM) and SIoU to improve model learning ability and accuracy. First, we evaluated and analyzed the detection accuracy and operational efficiency of the models. Then we deployed two proposed methods to a mobile phone. We also designed an application to further verify their practicality for detecting rice diseases and insect pests. The results showed that Improved YOLOv5s achieved the highest F1-Score of 0.931, 0.961 in mean average precision (mAP) (0.5), and 0.648 in mAP (0.5:0.9). It also reduced network parameters, model size, and the floating point operations per second (FLOPs) by 47.5, 45.7, and 48.7%, respectively. Furthermore, it increased the model inference speed by 38.6% compared with the original YOLOv5s model. Improved YOLOv7-tiny outperformed the original YOLOv7-tiny in detection accuracy, which was second only to Improved YOLOv5s. The probability heat maps of the detection results showed that Improved YOLOv5s performed better in detecting large target areas of rice diseases and insect pests, while Improved YOLOv7-tiny was more accurate in small target areas. On the mobile phone platform, the precision and recall of Improved YOLOv5s under FP16 accuracy were 0.925 and 0.939, and the inference speed was 374 ms/frame, which was superior to Improved YOLOv7-tiny. Both of the proposed improved models realized accurate identification of rice diseases and insect pests. Moreover, the constructed mobile phone application based on the improved detection models provided a reference for realizing fast and efficient field diagnoses.

Keywords: rice diseases and insect pests; mobile phone application; deep learning; object detection

check for updates

Citation: Deng, J.; Yang, C.; Huang, K.; Lei, L.; Ye, J.; Zeng, W.; Zhang, J.; Lan, Y.; Zhang, Y. Deep-Learning-Based Rice Disease and Insect Pest Detection on a Mobile Phone. *Agronomy* **2023**, *13*, 2139. https://doi.org/10.3390/agronomy13082139

Academic Editors: Spyros Fountas, Georgios Leontidis and Borja Espejo-García

Received: 30 June 2023
Revised: 3 August 2023
Accepted: 14 August 2023
Published: 15 August 2023

Copyright: © 2023 by the authors. Licensee MDPI, Basel, Switzerland. This article is an open access article distributed under the terms and conditions of the Creative Commons Attribution (CC BY) license (https://creativecommons.org/licenses/by/4.0/).

1. Introduction

Effective detection and monitoring of rice diseases and insect pests is crucial for ensuring a high and stable rice yield [1]. The traditional manual identification method cannot meet the increasing demand for field disease and pest detection due to its low

efficiency and inconsistent diagnostic results. Therefore, it is important to find an objective and efficient automatic detection method for high-quality rice production.

In the last two decades, many scholars have performed research on image-based automatic identification of diseases and insect pests in crops. Traditional machine-learning methods can classify crop diseases and pests through manually designed feature extraction and classification [2–4]. However, due to the difficulty with manually designed features and the poor generalizability of the specific models, many achievements have not been put into actual production [5–7]. With advances of artificial intelligence, the deep-learning method, which has powerful feature learning and extraction capabilities, has been widely used in complex agricultural scenarios [8–10], particularly in disease and insect pest identification in crops such as tomatoes [11], apples [12], cassava [13] and rice. In research on rice diseases and insect pests, Rahman et al. (2020) [14] suggested a real-time classification approach to classify 9 types of rice disease and pest images (e.g., false smut, brown plant hopper, and background leaf blight) conducted by a deep convolutional neural network (CNN). Joshi et al. (2022) [15] proposed a mobile phone application named RiceBioS to identify biotic stress in rice crops (rice blast and bacterial leaf blight). Deng et al. (2021) [16] developed a smartphone rice disease identification application that combined deep-learning classification methods. Using the deep CNN model deployed on an online server, it classified 6 types of rice diseases and insect pests such as rice leaf blast, false smut, and neck blast. The above research categorized crop diseases and insect pests by using deep-learning image classification, but this by itself cannot accurately and effectively detect areas of crop diseases and pests in images. Although the online deployment of deep-learning models and mobile–client interaction can to some extent alleviate the problem of high consumption of computing resources because of the complicated structure deep-learning models, it increases the response time of model inference and identification, which is not conducive to offline detection and identification of rice diseases and insect pests.

Deep-learning object detection is an end-to-end method that accurately identifies categories of diseases and insect pests and extracts occurrence information from images. The current dominant object detection algorithms are mainly two types: two-stage and one-stage. The Faster R-CNN introduced by Ren et al. (2015) [17] is a representative two-stage algorithm. However, it has not been able to achieve rapid identification due to its two-stage detection method of feature extraction and region-proposal generation by a convolutional network. Redmon et al. (2016) [18] introduced the one-stage object detection algorithm You Only Look Once (YOLO), which achieves end-to-end output detection of objects through a single CNN feature extraction network. Unlike Faster R-CNN, this algorithm combines traditional object detection with target location and classification, thereby greatly increasing the model reasoning speed, which makes it useful for detection tasks in complex farmland environments.

The purpose of this study is to achieve offline detection of rice diseases and insect pests based on mobile phone devices. By combining deep-learning object detection with a mobile phone terminal, we proposed two improved detection and identification models. First, the Improved YOLOv5s model was constructed by introducing Ghost modules as the basic extraction feature to replace the standard convolution modules of the YOLOv5s model. The Improved YOLOv7-tiny model was constructed by introducing the Convolutional Block Attention Module (CBAM) into the YOLOv7-tiny model. In addition, SIoU was applied to replace the original model loss function. Then we compared and analyzed the detection accuracy and operational efficiency of the models. Finally, the improved models were transplanted to an Android mobile phone platform, and a rice disease and pest identification application was built to realize offline mobile phone detection of diseases and insect pests.

2. Materials and Methods

2.1. Image Acquisition and Enhancement

2.1.1. Image Acquisition

Due to the diversity of rice diseases and insect pests as well as the high randomness of disease occurrence, there are currently few open-source rice disease databases, so it is difficult to gather a large amount of data on diseases and insect pests. This study carried out research on six diseases and insect pests as shown in Figure 1: Cnaphalocrocis medinalis, rice smut, rice blast, streak disease, sheath blight, and chilo suppressalis. First, we used a mobile phone to obtain visible light images of the diseases and pests in multiple experimental areas. Then we expanded the image dataset through data enhancement methods. Finally, we trained the disease and pest detection models by using the above-enhanced dataset. This research was carried out for the experiments of rice disease and insect pest data photography and collection in three experimental bases in Guangdong, China in 2020 and 2021: Zengcheng District in Guangzhou, Guangdong, China (113.643906 N, 23.242985 E), Gaoyao District in Zhaoqing, Guangdong, China (112.184548 N, 23.134322 E) and Xinhui District in Jiangmen, Guangdong, China (112.828022 N, 22.441844 E). The data collection situation is shown in Table 1.

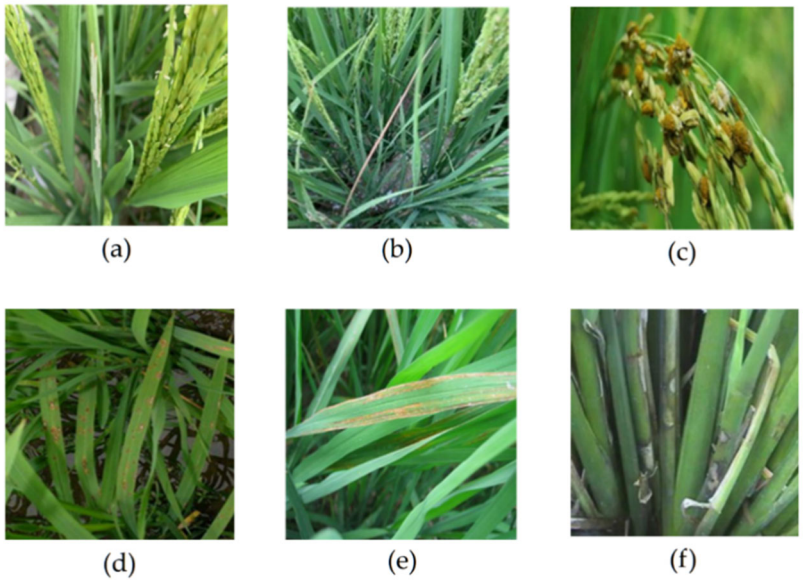

Figure 1. Sample images of rice diseases and insect pests. (**a**) Cnaphalocrocis medinalis; (**b**) Chilo suppressalis; (**c**) Rice smut; (**d**) Rice blast; (**e**) Streak disease; (**f**) Sheath blight.

Table 1. Rice disease and insect pest images dataset.

Disease Name	Acquisition Time	Data Source	Photograph	Data Enhancement	Total
Cnaphalocrocis medinalis	October 2020	Zengcheng District Experimental Base and Gaoyao District Test Base	487	63	550
Chilo suppressalis	October 2020	Zengcheng District Experimental Base	276	274	550
Rice smut	April 2021	Zengcheng District Experimental Base	209	341	550
Rice blast	March 2021	Zengcheng District Experimental Base and Xinhui District Experiment Base	236	314	550
Streak disease	March 2021	Zengcheng District Experimental Base	184	366	550
Sheath blight	March 2021	Zengcheng District Experimental Base	162	388	550

2.1.2. Image Enhancement

Different image enhancement methods were applied to expand the rice diseases and insect pests image dataset to reduce the impact of quantitative differences between the different dataset categories: image scaling, rotation, vertical and horizontal flipping, translation, and HSV adjustment. The data enhancement effect is shown in Figure 2. From Table 1, the total number of expanded image datasets was increased to 3300, and the image samples were divided into training and test sets. In the training set, there were 3000 images, and the number of images of each rice disease and insect pest category was 500. In the test set, there were 300 images, and the number of images of each rice disease and pest category was 50. The test set consisted of original images of rice diseases and insect pests without data enhancement. In this study, the constructed image dataset was labeled by the object detection labeling method. The distribution of labeling boxes of each category in the training and test sets is shown in Figure 3.

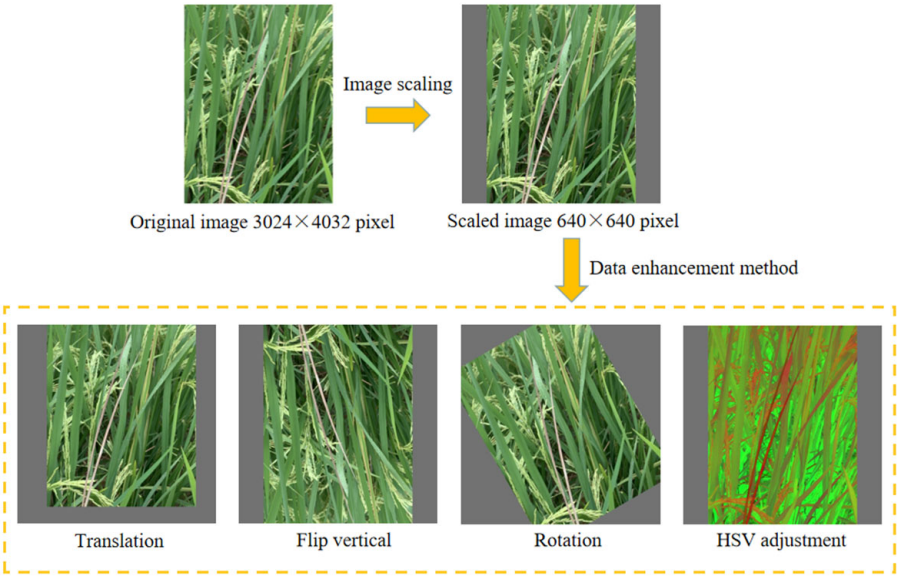

Figure 2. Image enhancement process.

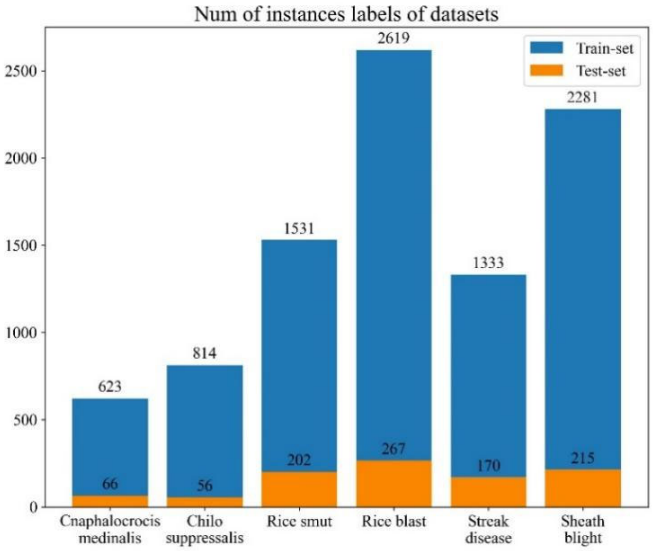

Figure 3. The distribution of labeling boxes of each category in the training set and test set.

2.2. Construction of Rice Disease and Pest Detection Model

2.2.1. Construction of Improved YOLOv5s Rice Diseases and Pests Detection Model

YOLOv5 is an object detection algorithm based on a one-state anchor detection method released by Uitralytics LLC [19]. YOLOv5s is a lightweight model structure of YOLOv5. Its network structure includes three parts: the backbone network, neck, and head structures. Among them, the backbone network includes the CBS, C3, and SPPF modules, the main function of which is to extract image features through down-sampling operations. The neck structure adopts a structure that combines FPN [20] and PAN [21], mainly achieving the fusion of shallow graphic features in the backbone layer and deep semantic features in the detection layer, which enables the model to obtain richer feature information. The head structure outputs the detection results of the target objects in different scales through three detection layers: category probability, probability score, and position information of the target boundary box.

Compared to traditional object detection networks, YOLOv5 has advantages such as higher accuracy and faster inference speed. However, because they use many standard convolutions in the model structure, these modules are not conducive to operation on mobile phones or embedded devices with limited memory and computing resources. Although lightweight models such as the MobileNet [22–24] and ShuffleNet series [25,26] can achieve good performance with very few floating point operations per second (FLOPs), the correlation and redundancy between their feature maps have not been well used. The Ghost module proposed by Han, K. et al. [27] is a model compression method that can generate more feature maps with fewer parameters to ensure redundancy of feature information, reduce network parameters and calculation and ensure network accuracy, thereby improving calculation speed and reducing the latency of the model. The feature extraction process of the Ghost module shown in Figure 4b is as follows: first, it reduces input feature map channels through a convolutional operation to obtain the intrinsic feature map. Then the Ghost feature maps are obtained by using the cheap operations of linear transformation with different convolution kernel sizes (usually 4×4 or 5×5) to process each channel of the intrinsic feature map. Finally, the intrinsic feature map and all the Ghost feature maps are spliced and output by the concatenating operation.

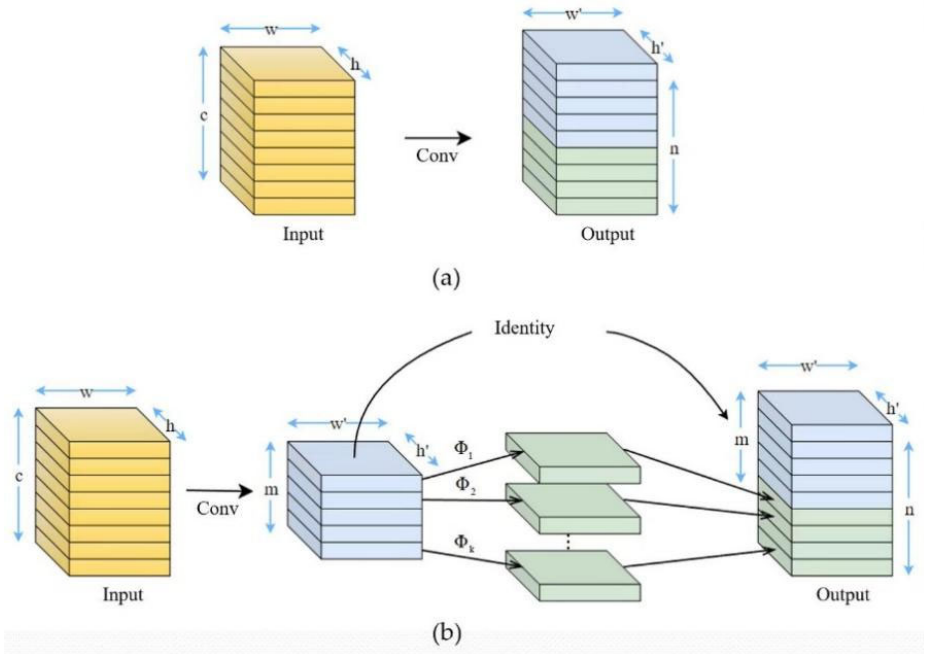

Figure 4. Feature extraction process of Ghost module and standard convolution module. (**a**) The feature extraction process of standard convolution module; (**b**) the feature extraction process of Ghost module.

Assume that the shapes of the input and output maps are $h \times w \times c$ and $h' \times w' \times n$. The convolutional filter size (represented by Conv in Figure 4) is $k \times k$., In the linear transformation process for the Ghost module, it is assumed that the intrinsic feature map channel quantity is m; Φ_k represents the operations of linear transformation; and the transformation quantity is s. Since the Ghost transformation process includes an identity transformation, the effective transformation quantity is $s - 1$. Therefore, the mathematical expression of the parameter calculation-amount ratio between the Ghost module and the standard convolution module is as follows. Generally, s is much smaller than the quantity of input feature map channels c:

$$\frac{\frac{n}{s} \cdot h' \cdot w' \cdot c \cdot k \cdot k + (s-1) \cdot \frac{n}{s} \cdot h' \cdot w' \cdot k \cdot k}{n \cdot h' \cdot w' \cdot c \cdot k \cdot k} = \frac{s + c - 1}{s \cdot c} \approx \frac{1}{s} \quad (1)$$

From Formula (1), the parameter calculation amount of the Ghost module is about $1/s$ of that of the standard convolution. In this study, referring to the parameter settings of GhostNet, the hyperparameter s of the Ghost module was set to 2. Therefore, compared to standard convolution, the Ghost module reduced the parameter calculation amount by about half, and it can be seen that replacing the standard convolution with the Ghost module led to a significant reduction in model computational complexity.

To build a rice disease and insect pest detection model suitable for mobile platform deployment, YOLOv5s was improved by combining the Ghost module and Ghost Bottle neck structure proposed by Han, K. et al. [27]. The Ghost Bottleneck was similar to the basic residual block in ResNet [28], which is mainly composed of two Ghost modules stacked to achieve the expansion and compression of the feature map channels. In this study, the Ghost module was used to replace the convolution module in the backbone and head structure of the original model, and the Ghost bottleneck structure was used to improve the C3 module of the model. The structures of the original YOLOv5s model and the Improved YOLOv5s model are shown in Figure 5a,b.

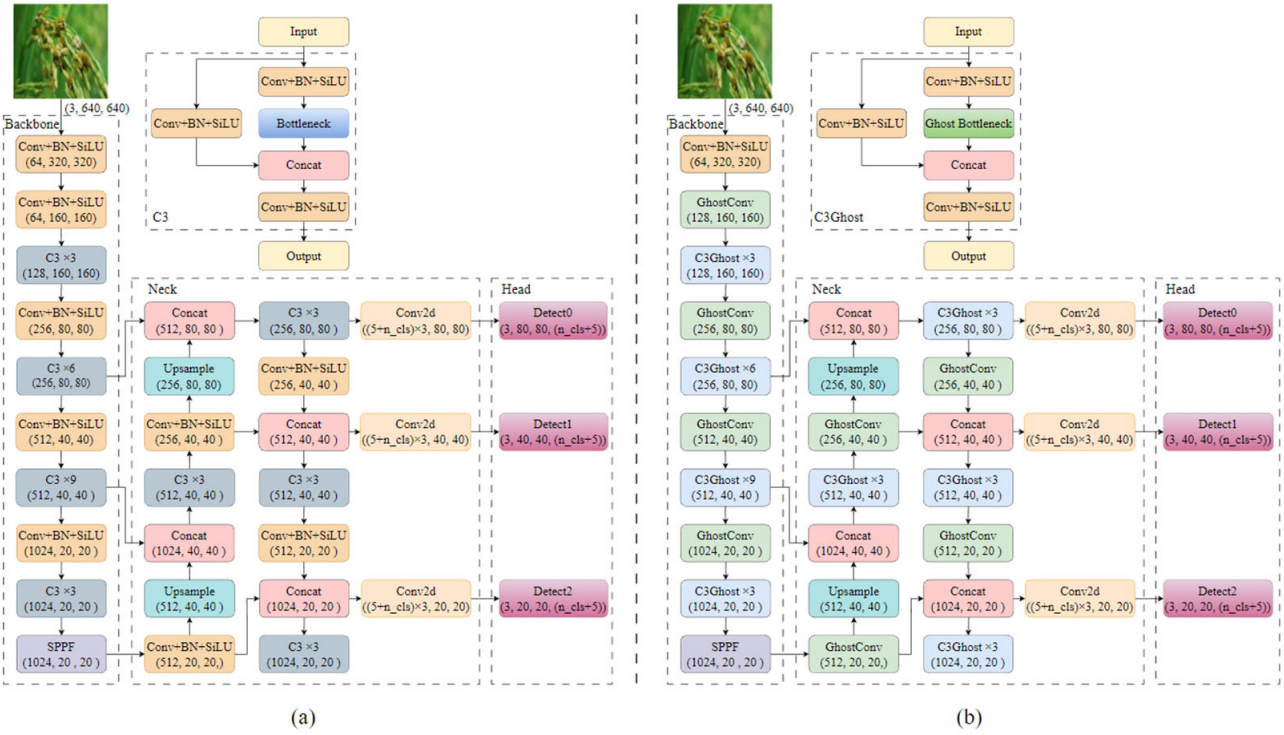

Figure 5. The structure of the YOLOv5s model and the Improved YOLOv5s model. (**a**) The structure of the YOLOv5s model; (**b**) the structure of the Improved YOLOv5s model.

2.2.2. Construction of Improved YOLOv7-Tiny Rice Diseases and Pests Detection Model

The main contribution of YOLOv7 proposed by Wang, C.Y. et al. [29] lies in the introduction of structural reparameterization and dynamic label allocation strategies for model optimization, as well as the introduction of expansion and composite scaling methods, which not only improves the efficiency of model parameters and calculation, but also significantly reduces model parameters, thereby improving inference speed and model detection accuracy. YOLOv7-tiny is also a lightweight model structure of YOLOv7. Its network structure includes two main sections: backbone and head structures. The functions of each section are the same as those of YOLOv5s. The difference is that the neck and head structures are merged into the head structure.

To make the constructed rice disease and insect pest identification model suitable for mobile phone platform deployment, we used YOLOv7's lightweight model YOLOv7-tiny for experimental analysis. To improve the model accuracy, YOLOv7-tiny was combined with the CBAM [30] (as shown in Figure 6). It uses a combination of the Channel Attention Module (CAM) and the Spatial Attention Module (SAM). The feature map is first input into the CAM to complete channel attention recalibration of the original feature through processing of Global Average Pooling (GAP), Global Max Pooling (GMP) and Shared Multilayer Perceptron (MLP) layers. Therefore, the mathematical expression of the channel attention module is as follow:

$$CAM(F) = \sigma(W_1(W_0(GAP(F))) + W_1(W_0(GMP(F)))) \quad (2)$$

where F denotes the input feature map with the shape of $H \times W \times C$; σ denotes the sigmoid function; and W_0 and W_1 denote the weights of the MLP layers. The output of the *CAM* module is a 1D channel attention map of the shape $1 \times 1 \times C$.

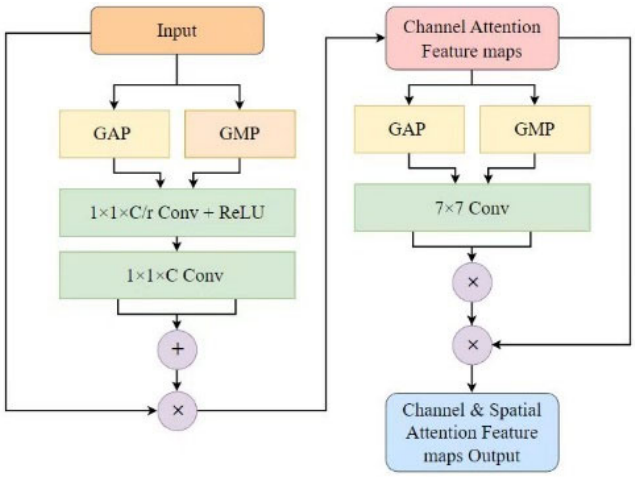

Figure 6. The CBAM module.

The channel attention feature map was then input into the *SAM* module and processed by the *GAP*, *GMP* and a convolution layer. This module can be expressed by the following mathematical expression:

$$SAM(F) = \sigma\left(f^{7\times7}(GAP(F); GMP(F))\right) \quad (3)$$

where $f^{7\times7}$ denotes a convolution layer with a 7×7 filter size, and the output of the *SAM* module is a 2D attention map of the shape of $H \times W \times 1$. Therefore, the *CBAM* module can be expressed as follows:

$$CBAM(F) = SAM(CAM(F) \otimes F) \otimes (CAM(F) \otimes F) \quad (4)$$

where $\otimes$ denotes the element-wise multiplication operation.

After processing the CBAM module, the new feature maps get the attention weight in the channel and space dimensions, which greatly improves the relationship between each feature in the channel and space, so that it is more conducive to extracting the effective features of the target from the model. In this study, the last three convolutional layers of the head structure of YOLOv7-tiny were improved, of which the first two layers retained the RepConv structure [31] of YOLOv7, and the last layer was replaced by the CBAM module. The structures of the original YOLOv7-tiny and the Improved YOLOv7-tiny models are shown in Figure 7a,b.

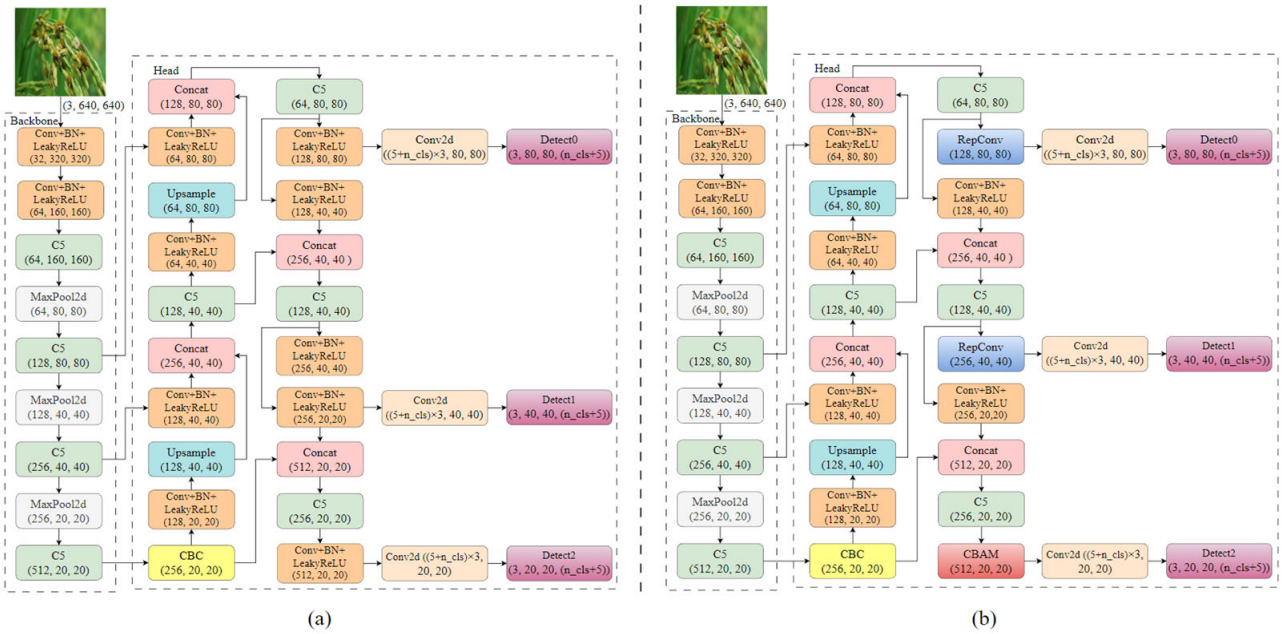

Figure 7. The structure of the YOLOv7-tiny and the Improved YOLOv7-tiny models. (**a**) The structure of the YOLOv7-tiny model; (**b**) the structure of the Improved YOLOv7-tiny model.

In addition, we introduced SIoU [32] to improve the regression loss function of the original model. Based on the characteristics of the traditional regression box loss, SIoU introduces the angle cost to assist the distance calculation between the ground true box and the predicted box of the target to improve convergence speed and feature learning ability of model training. Specifically, the SIoU loss function includes four parts: angle, distance, shape, and IoU costs.

The angle cost describes the convergence process of the minimum angle of the ground true box and the predicted one, which can be expressed as Formula (5).

$$\wedge = 1 - 2 \times sin^2\left(\arcsin(x) - \frac{\pi}{4}\right),\ x = \frac{c_h}{\sigma} = sin(\alpha) \tag{5}$$

where $\wedge$ represents the angle cost; c_h denotes the difference of the two boxes center points in height; σ denotes the distance of the two boxes; and α denotes the radian of the angle of the line connecting the two boxes center points and the Cartesian coordinate x-axis. When α equals 0 or $\pi/2$, the angle loss obtains the minimum value of 0; when α equals $\pi/4$, the angle loss obtains the maximum value of 1.

The distance cost describes the convergence process of the minimum distance between the ground true and the predicted boxes, and the distance loss can be expressed mathematically by Formula (6).

$$\Delta = \sum_{t=x,y}\left(1 - e^{-(2-\wedge)\rho_t}\right) \tag{6}$$

where

$$\rho_x = (\frac{b_{c_x}^{gt} - b_{c_x}^{p}}{bb_w})^2,\ \rho_y = (\frac{b_{c_y}^{gt} - b_{c_y}^{p}}{bb_h})^2 \tag{7}$$

where $(b_{c_x}^{gt},\ b_{c_y}^{gt})$ and $(b_{c_x}^{p},\ b_{c_y}^{p})$ denote the center coordinate points of the two boxes, respectively; and bb_w and bb_h denote the width and height of the bounding box of the two boxes, respectively. When combined with Formula (5), it can be seen that the distance cost correlates positively with the angle cost.

The shape cost describes the overall shape convergence of the minimum difference in border height and width between the ground true box and the predicted box. And the shape cost can be expressed by Formula (8).

$$\Omega = \sum_{t=w,h} \left(1 - e^{-w_t}\right)^{\theta} \tag{8}$$

where

$$\mathrm{w_w} = \frac{\left|\mathrm{w^p} - \mathrm{w^{gt}}\right|}{\max\left(\mathrm{w^p}, \mathrm{w^{gt}}\right)},\ \mathrm{w_h} = \frac{\left|\mathrm{h^p} - \mathrm{h^{gt}}\right|}{\max\left(\mathrm{h^p}, \mathrm{h^{gt}}\right)} \tag{9}$$

where $\left(\mathrm{w^{gt}},\ \mathrm{h^{gt}}\right)$ and $\left(\mathrm{w^p}, \mathrm{h^p}\right)$ denote the width and height of the ground true and predicted boxes, respectively; θ is an adjustable variable to adjust the contribution of shape cost to the overall loss.

Therefore, the expression of the SIoU Loss function can be expressed by Formula (10), where IoU denotes the overlap ratio of the two boxes; Δ denotes the distance cost; and Ω denotes the shape cost.

$$Loss_{box} = 1 - IoU + \frac{\Delta + \Omega}{2} \tag{10}$$

2.3. The Comparison Methods Used in This Study

The classic two-stage object detection network Faster-RCNN was improved based on the R-CNN [33] and Fast-RCNN [34] networks. The process by which the algorithm achieved object detection comprised mainly two stages. In the first stage, the model used the layer stacking method of the VGGNet [35] network to perform feature extraction on the input image. In the second stage, it generated a series of region proposals on the last convolution output feature maps through the region proposal network (RPN); then the generated region proposals were mapped to the feature maps extracted by the convolutional layer through the region-of-interest pooling layer (Roi pooling); finally, the output proposed feature map was used for classification and position regression prediction by using a softmax classifier and the bounding box regression algorithm.

The Single Shot MultiBox Detector (SSD) is a one-stage object-detection algorithm proposed by Liu, W. et al. (2016) [36]. The model is mainly composed of three parts: the VGG-Base backbone, the Extra layers, and the Pred-layers. First, the features of the input image were extracted through the VGG-Base backbone. Then the extracted effective feature information was sent to the extra-layers with different down-sampling operations to obtain a plurality of feature maps with different scales to form a pyramidal feature map set. The extracted multi-scale feature information was then sent to the Pred-layers part of the SSD model for classification prediction and bounding box regression. Finally, the Non-Maximum Suppression (NMS) algorithm was used to filter the prediction result with the best score for the detection and location of the target object. In this study, we compared the Faster-RCNN and SSD models with the improved object detection networks and analyzed the detection effects of different types of object detection models on the rice diseases and insect pests datasets.

2.4. Development Platform for Rice Diseases and Insect Pests Identification Application

Mobile phones have great advantages as image acquisition terminals and devices for loading intelligent identification algorithms to detect rice diseases and insect pests quickly in the field. To verify the practicability of the improved detection models, we developed a mobile phone application to detect of diseases and pests, as shown in Figure 8. The specific development process and experimental platform of the system are as follows.

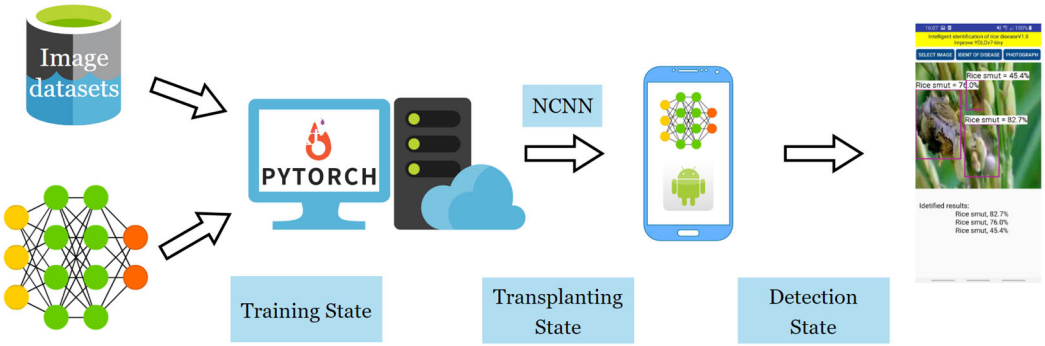

Figure 8. The specific development process of the rice diseases and insect pests identification application.

The experiment was first conducted on a 64-bit server computer with an Ubuntu 16.04.6 system. The configuration is shown in Table 2. The server was configured with two P100 graphics cards with 16G memory, and the system was installed with version 10.2 of Cuda and 7.6.5 Cudnn deep-learning environments. The deep-learning open-source library Pytorch was applied to train and test the object detection models. The NCNN framework was used to optimize the parameters and structure of the trained models, which enabled the models to be deployed and run on a mobile phone. NCNN is a high-performance neural network forward-computing framework suitable for mobile phone deployment, which enables the deep-learning model to achieve efficient reasoning on a mobile phone platform.

Table 2. Experimental platform.

Platform	System	Configuration	Framework/Architecture
Server platform for model training	Ubuntu 16.04.6	P100 16G × 2	Cuda 10.2, Cudnn 7.6.5, Pytorch
Application development platform	Android 9.0	Memory 4G	Android

In this study, the improved object detection models were transplanted to an Android mobile phone platform, and a rice disease and insect pest identification application was developed to verify the practicability of the models. The configuration of the platform is shown in Table 2. The mobile phone was installed with the Android 9.0 version system, and the running memory was 4 GB, which met the running and reasoning of the deep-learning model. The application included two parts: the front-end interaction interface and back-end program. The front-end interaction interface was composed mainly of the tools provided by the Android UI interface to design, including Button, ImgView, TextView. The back-end development processing achieved image-selection and photograph identification by calling the object detection model, which realized the real-time image collection and identification processing of the disease and insect pest image data in the field.

2.5. Evaluation Indicators

In this article, we evaluated constructed models from two aspects: object detection accuracy and model operational efficiency. The accuracy of the models was evaluated mainly using Precision, Recall, F1-score, mAP (0.5), and mAP (0.5:0.9), where mAP (0.5) was the AP value at an IoU threshold of 0.5, which was obtained by integrating the PR curve. mAP (0.5:0.9) was the average of the mAP values at different IoU thresholds. Then the evaluation indicators were as shown in Formulas (11–14), where TP (True Positive) represents the number of originally positive samples that were correctly predicted to be positive samples; FP (False Positive) represents the number of originally negative samples that were incorrectly predicted to be positive samples; FN (False Negative) represents the number of positive samples that were incorrectly predicted to be negative samples.

$$Precision = \frac{TP}{TP + FP} \tag{11}$$

$$Recall = \frac{TP}{TP + FN} \tag{12}$$

$$F1\ score = 2 \times \frac{Precision \times Recall}{Precision + Recall} \tag{13}$$

$$AP = \int_0^1 P(r)dr \tag{14}$$

The operational efficiency of the model was evaluated mainly by the parameter quantity, model size, FLOPs, and inference speed.

3. Results

3.1. Analysis of Experimental Results of Different Models

3.1.1. Analysis of Training Processes of Different Model

The models mentioned in Sections 2.2 and 2.3—Faster-RCNN, VGG16-SSD, YOLOv5s, and YOLOv7-tiny—were used for comparison with the Improved YOLOv5s model and the Improved YOLOv7-tiny models. For model training, we used the rice diseases and insect pests image dataset on the server computer. To achieve better training results, the SGD gradient descent algorithm with momentum was applied to update the gradient during model training, and the hyperparameter momentum was set to 0.937. The purpose of adding momentum gradient optimization was to suppress the oscillation generated by the gradient descent and accelerate the convergence of the model. The LambdaLR learning-rate adjustment strategy was adopted, and the initial learning rate and the weight decay were 0.01 and 0.0005, respectively. Regarding model evaluation, the NMS method was used to optimize the output of the model detection results, in which the NMS-confidence and IOU thresholds of the prediction results were set to 0.25 and 0.6, respectively.

For the training results of different models on the rice diseases and insect pests dataset, the training batch size was set to 32, and the model was trained for a total of 300 epochs. We set it to validate the models every 10 epochs in the training process to record the loss value and mAP (0.5) result on the validation set and save the model training files. From Figure 9a,b, the loss values of each model decreased continuously during training, and they tended to be stable after 300 iterations, indicating that the constructed rice diseases and pests detection models fit the data distribution of the training set samples well. The loss values of Improved YOLOv5s and Improved YOLOv7-tiny were slightly lower than those of the original models, and had better convergence effects. It can be seen from the mAP (0.5) results change curve of the validation set (Figure 9c) that the curves of the improved models were higher than those of the original models, which indicated better detection accuracy.

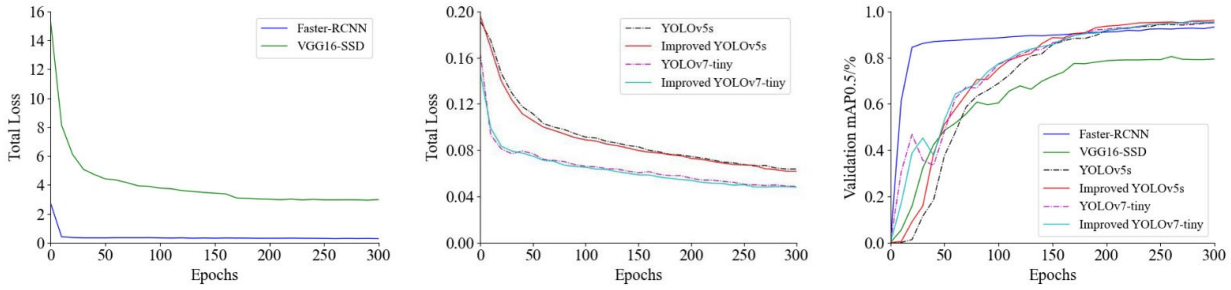

Figure 9. Change curves of loss value and mAP (0.5) of different models. (**a**) Loss value curve of Faster-RCNN and VGG16-SSD; (**b**) loss value curve of the improve models; (**c**) mAP (0.5) curve of different models.

3.1.2. Comparison of Detection Accuracy of Different Models

In this study, we used the test set of the image dataset constructed in Section 2.1 to test the detection accuracy of each model. From Table 3, it can be seen that the Improved YOLOv5s outperformed the original model YOLOv5s in all evaluation indicators. Its precision and recall value improved by 3.2 and 0.3%, respectively, while its F1-Score, mAP (0.5), and mAP (0.5:0.9) improved by 1.7, 0.9, and 3.7%, respectively, and it achieved the highest scores among the six experimental methods with values of 0.931, 0.961, and 0.648. Although the Improved YOLOv7-tiny had a 1.2% decrease in recall compared to the original model, it had improved precision, F1-Score, mAP (0.5), and mAP (0.5:0.9) by 3.5, 1.1, 0.3 and 1.1%, respectively. In addition, the Improved YOLOv7-tiny was second only to Improved YOLOv5s in F1-Score, mAP (0.5), and mAP (0.5:0.9), which are three comprehensive indicators for evaluating the overall identification performance of the model. Therefore, from the above analysis, the detection accuracy of the Improved YOLOv5s and Improved YOLOv7-tiny in this study was better than that of their original models.

Table 3. Comparison of detection accuracy indicators of different models.

Network	Precision	Rcall	F1-Score	mAP	
				IOU = 0.5	IOU = 0.5:0.95
Faster-RCNN	0.888	0.944	0.915	0.933	0.584
VGG16-SSD	0.806	0.939	0.872	0.820	0.476
YOLOv5s	0.908	0.923	0.915	0.952	0.625
YOLOv7-tiny	0.895	0.924	0.909	0.951	0.620
Improved YOLOv5s	0.937	0.926	0.931	0.961	0.648
Improved YOLOv7-tiny	0.926	0.913	0.919	0.954	0.627

3.2. Analysis of Experimental Results of Improved Models

3.2.1. Comparison of Operational Efficiency before and after Model Improvement

In this section, we evaluate the operational efficiency of the improved models using parameter quantity, model size, the FLOPs, and model inference speed. From Table 4 below, it can be seen that in the comparative analysis before and after model improvement the parameters, model size, and FLOPs of the Improved YOLOv5s decreased by 47.5, 45.7, and 48.7%, respectively, whereas the inference speed increased by 38.6% compared to the original model. Therefore, the application of the Ghost module significantly improved the structure of YOLOv5s, thereby greatly improving its operational efficiency. Compared to the original model, Improved YOLOv7-tiny had increased parameter quantity, model size, and the FLOPs by 0.5, 1.7, and 3.1%, respectively, whereas the inference speed decreased by 4.9%. Although the application of the CBAM module improved the accuracy of the model, it increased its complexity to some extent. In a comparative analysis of the performance of

the two improved models, the parameter quantity, model size, and FLOPs of Improved YOLOv5s were all lower by 61, 62.9, and 60%, respectively. And the inference speed of Improved YOLOv5s was 18.6% faster. Therefore, it outperformed Improved YOLOv7-tiny in operational efficiency.

Table 4. Comparison of operation performance indicators of different models.

Network	Parameters/M	Model Size/MB	FLOPs/GFLOPs	Inference Speed/ms (b32)
YOLOv5s	7.03	13.8	15.8	11.4
YOLOv7-tiny	6.02	11.7	13.1	8.2
Improved YOLOv5s	3.69	7.49	8.1	7
Improved YOLOv7-tiny	6.05	11.9	13.5	8.6

3.2.2. Comparison of Different Type Rice Diseases and Insect Pests Detection Accuracy before and after Model Improvement

We also evaluated the detection accuracy of the improved models constructed in this study on different categories of rice diseases and insect pests images using average precision (AP) and PR curves. From the data in Table 5 below, it can be seen that the AP of Improved YOLOv5s on Chilo suppressalis, Rice smut, Streak disease, and Sheath light was 1.9, 0.6, 0.5, and 3.6% greater, respectively, than for the original model. The AP of Improved YOLOv7-tiny in Chilo suppressalis, Rice blast, and Sheath light increased by 0.9, 0.1, and 2.5%, respectively, compared to YOLOv7-tiny. For the comparison and analysis of the detection accuracy of the two improved models, the mAP (0.5) of Improved YOLOv5s reached 0.961, which was 0.7% higher than the mAP (0.5) value of 0.954 for Improved YOLOv7-tiny. The overall detection accuracy of Improved YOLOv5s for rice diseases and insect pests was better than that of Improved YOLOv7-tiny. Moreover, the PR curve shown in Figure 10 was used to evaluate model detection accuracy. The enclosed area of the curve was equal to the mAP (0.5). When the curve area was close to 1, the model detection accuracy was the highest.

3.2.3. Comparison of Detection Results of Different Type Rice Diseases and Insect Pests Images before and after Model Improvement

For validation of the detection effect of the improved object detection models, we randomly selected one image from each type of rice disease and insect pest in the test set to demonstrate the detection effect of each model. In Figure 11, the input and label images of different types of rice diseases and insect pests are shown in the first and second columns, while the detection results of these images and the corresponding predicted probability heat maps of Improved YOLOv5s and Improved YOLOv7 tiny are shown in the third to sixth columns. The figure shows that, for the detection results of the rice smut sample, Improved YOLOv5s had better detection accuracy for each target in the image compared to Improved YOLOv7-tiny, while Improved YOLOv7-tiny had a missed detection. For the detection results of the sheath light and Chilo suppressalis samples, the detection accuracy and identification effect of Improved YOLOv7-tiny were better, while the detection results of Improved YOLOv5s for these two types of diseases and insect pests revealed false and missing detection. For the other three types of disease and insect pest, the two improved models displayed little difference in detection accuracy and both effectively detected the target areas of diseases and pests in the image. In addition, the model identification effects were also analyzed through probability heat maps, in which the color change from red to blue indicated that the probability contribution of the region to the prediction results was gradually decreasing. From the heat map results, Improved YOLOv5s performed better in detecting larger target areas in images, as shown in the large red areas in the heat map results of streak disease and sheath blight samples; Improved YOLOv7 tiny was more accurate in detecting smaller target areas in images, such as the small red areas in the heat map results of rice smut and rice blast.

Table 5. Comparison of different type rice diseases and insect pests detection accuracy before and after model improvement.

Models	Average Precision						mAP (IOU = 0.5)
	Cnaphalocrocis Medinalis	Chilo Suppressalis	Rice Smut	Rice Blast	Streak Disease	Sheath Blight	
YOLOv5s	0.995	0.953	0.970	0.981	0.977	0.836	0.952
YOLOv7-tiny	0.996	0.971	0.959	0.958	0.969	0.852	0.951
Improved YOLOv5s	0.995	0.971	0.976	0.977	0.982	0.866	0.961
Improved YOLOv7-tiny	0.994	0.980	0.956	0.959	0.964	0.873	0.954

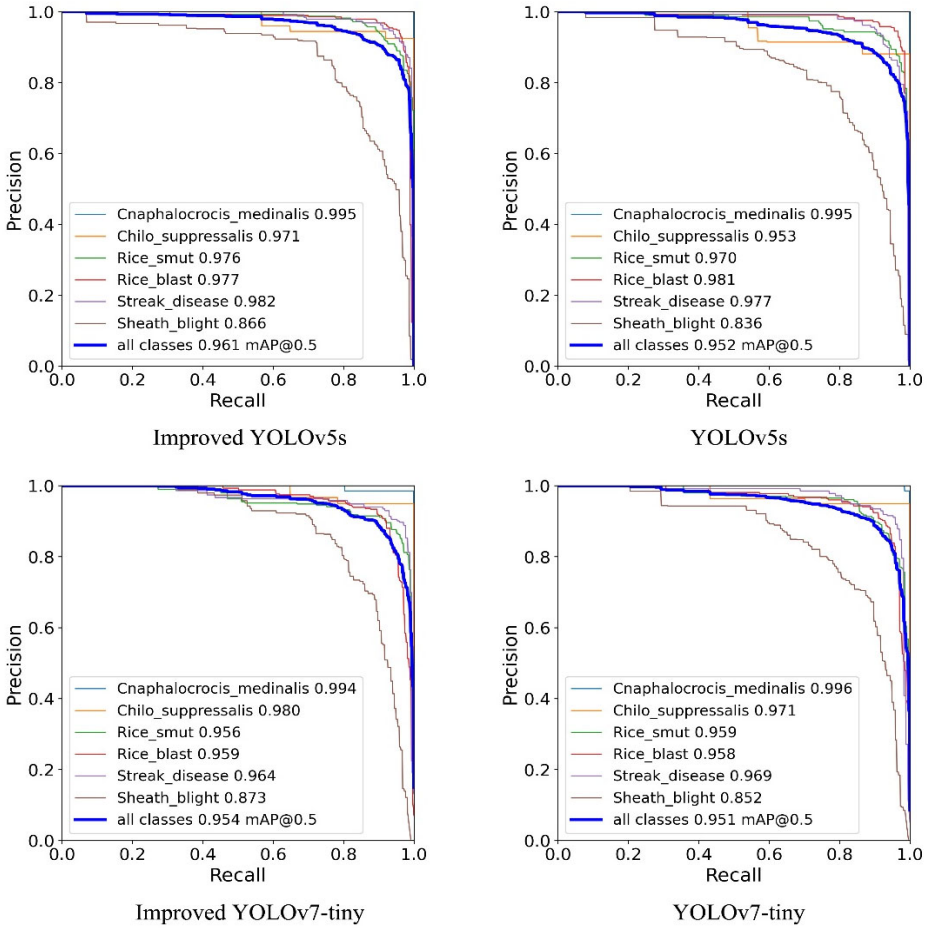

Figure 10. The PR curves before and after model improvement.

3.3. Analysis of Experimental Results of Rice Diseases and Insect Pests Detection Application on Mobile Phone

3.3.1. Identification Results of Rice Diseases and Insect Pests Detection Mobile Phone Application

For further validation of the practicality of the improved models proposed in this study, we transplanted Improved YOLOv5s and Improved YOLOv7-tiny to the mobile phone Android platform to build a rice disease and insect pest identification application. It was designed with image-selection and photo identification functions on which the two models were tested and analyzed using the above test set. In identification accuracy, from Table 6, when the model accuracy was FP16 on the mobile phone, the precision and recall of Improved YOLOv5s reached 0.925 and 0.939, respectively, which were 1.1 and 2.3% higher, respectively, than those of Improved YOLOv7-tiny. The inference speed of Improved YOLOv5s on the Android mobile phone platform was 374 ms/frame, which

was 6.7% faster. In identification results, as shown in Figure 12, both models achieved accurate detection of rice diseases and insect pests in images. And Improved YOLOv5s outperformed Improved YOLOv7-tiny in the detection of rice smut, streak disease, and streak blight, which are three diseases and insect pests sample images that have larger target sizes (as shown in Figure 12a), while Improved YOLOv7-tiny had better detection for rice blast, Cnaphalocrocis medinalis, and Chilo suppressalis, which are three sample images with smaller target sizes (as shown in Figure 12b).

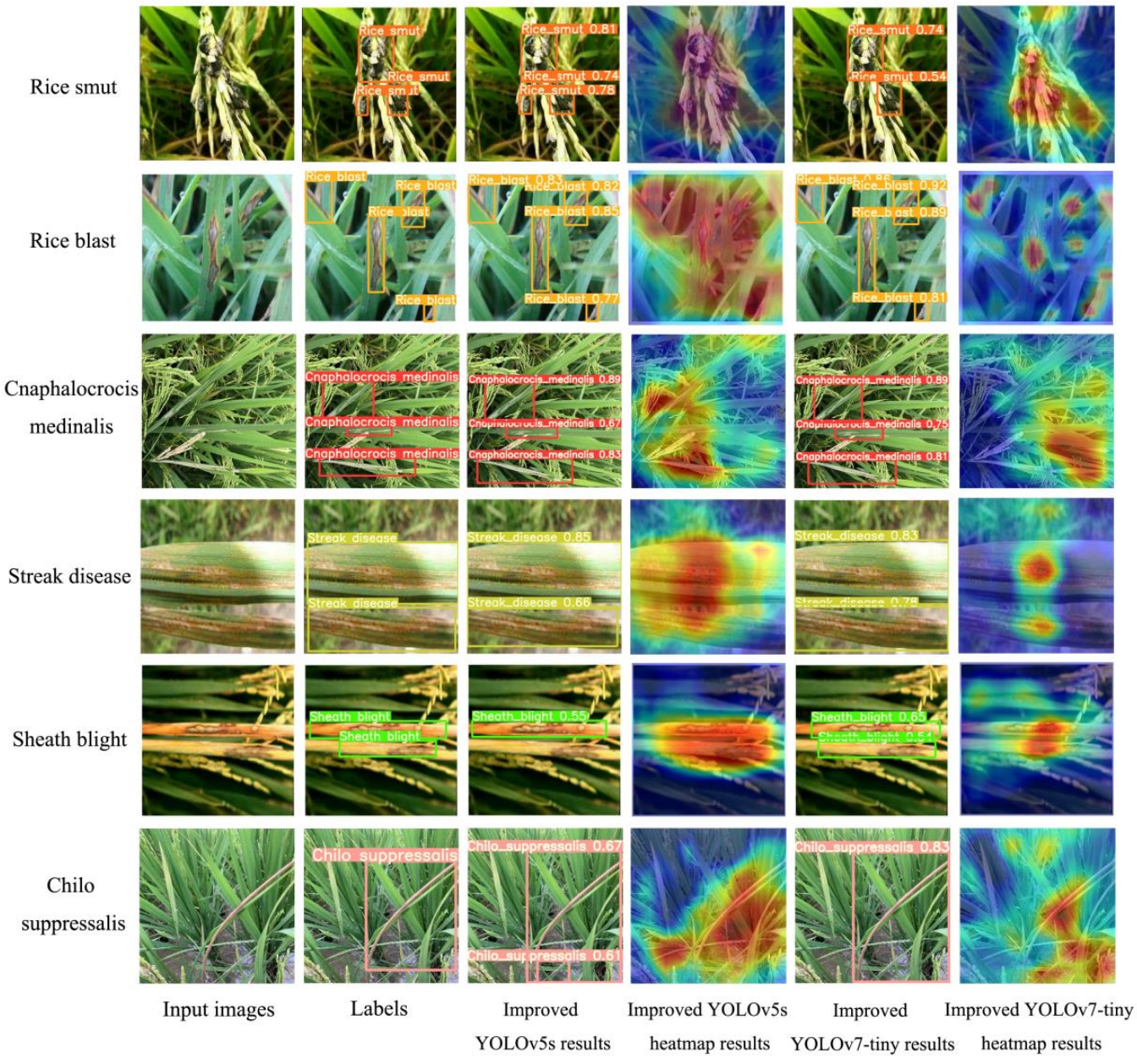

Figure 11. Detection Results of Different Type Rice Diseases and Insect Pests.

Table 6. Identification accuracy of two improved models on the mobile phone platform.

Network	Precision	Recall	Inference Speed/ms
Improved YOLOv5s	0.925	0.939	374
Improved YOLOv7-tiny	0.915	0.918	401



Figure 12. Identification results of rice diseases and insect pests detection mobile phone applications. (**a**) Identification results of Improved YOLOv5s; (**b**) identification results of Improved YOLOv7-tiny.

3.3.2. Runtime Performance of Rice Diseases and Insect Pests Detection Application on a Mobile Phone

To verify the applicability and compatibility of the improved models with mobile phone hardware, we evaluated the runtime performance of the application based on the improved detection models using indicators such as the model size after conversion with NCNN, the CPU usage, and the RAM usage. From Table 7, the results of model size, CPU usage, and RAM usage for Improved YOLOv5s on the phone were 14.3 MB, 49%, and 262.9 MB, respectively, which were 38, 5.8 and 17.4% less than for Improved YOLOv7-tiny. The performance of Improved YOLOv5s was better, but both models can be used for inference on the Android mobile phone platform because the model size, CPU usage, and RAM usage are within a reasonable range of computing resource allocation. Therefore, both proposed models can be applied to most Android mobile phone hardware platforms with similar or better configurations and performance than the platform in this study.

Table 7. Runtime results on the mobile phone platform of two improved models.

Network	Model Size/MB	CPU Usage/%	RAM Usage/MB
Improved YOLOv5s	14.3	49	262.9
Improved YOLOv7-tiny	23.1	52	318.2

4. Discussion

Previous studies have shown that CNN models can be applied to the image classification of rice diseases and insect pests and have achieved good results [37–39]. However, the classification method cannot accurately detect the specific occurrence areas of diseases and pests in the image. In addition to identifying the correct information category when

diagnosing rice diseases and insect pests on actual farmland, detecting the occurrence areas of diseases and insect pests is also important. In this regard, the object detection method based on deep-learning used in our research proved to be a feasible method for achieving accurate classification and location detection of diseases and pests.

In this study, based on the object detection models YOLOv5 and YOLOv7, two lightweight rice disease and insect pest detection models, Improved YOLOv5s and Improved YOLOv7-tiny, were constructed to identify the categories and detect the occurrence locations of rice diseases and insect pests in images. From an analysis of the experimental results of different models, the two improved models outperformed their original models in F1-Score, mAP (0.5) and mAP (0.5:0.9), and Improved YOLOv5s achieved the highest score in these indicators compared to the other methods, which showed that the two improved methods had effectively improved detection accuracy. Regarding operational efficiency, Improved YOLOv5s had significantly improved parameter quantity, model size, FLOPs, and inference speed compared to the original model, indicating that the application of the Ghost module not only improved detection accuracy but also optimized model structure and enhanced the operational inference efficiency.

In addition, Improved YOLOv5s was better than Improved YOLOv7-tiny in various evaluation indicators of detection accuracy. Regarding identification of rice diseases and insect pests, Improved YOLOv5s had a higher AP value compared to Improved YOLOv7-tiny. In addition, the AP value of sheath blight was lower than that of the other five rice diseases and insect pests in the detection results of different models. There were two reasons. First, the original image data of this category of rice disease and insect pest were less than those of the other five categories, and the original features for model learning were relatively less, so it was difficult for the model to cover the complete feature values for this image category in fitting training, thereby causing an increase in model recognition error [40]. Second, although certain data enhancement methods reduced the impact of imbalanced distribution of data in various categories on model performance, the image features of the enhanced image data were similar to those of the real image data, so repeated learning of the same features resulted in overfitting. Therefore, when applied to new data, the accuracy and robustness of the model in that category were not as good as those in categories with rich data features [41]. Furthermore, through probability heat map analysis, Improved YOLOv5s performed better in detecting larger rice disease and insect pest target areas in images, while Improved YOLOv7-tiny performed more accurately in detecting smaller target areas in images. On the mobile phone with the Android platform, the applications combined with the improved models achieved accurate identification of rice diseases and insect pests, and the application based on Improved YOLOv5s performed better in detection accuracy, inference efficiency, and runtime performance. However, both models are compatible with most Android mobile phones with similar or better configurations and performance than the hardware platform in this study.

To sum up, both the proposed improved models can be applied to the task of rice disease and insect pest detection and achieved good identification results. The constructed mobile phone application for rice disease and insect pest detection provided a fast and convenient intelligent mobile terminal offline identification method that is worth promoting.

As for the prospect of the work, the improved models proposed in this study are the general and extensible methods for effectively identifying rice diseases and insect pests, which is not limited to the detection and identification of the six common rice diseases and insect pests mentioned above. If more identification of rice diseases and insect pests need to be conducted in subsequent research, it is only necessary to increase the categories and quantities of their image data and retrain the construction models. For disease and pest identification on the mobile phone platform, considering that detection results are affected by shooting angle, distance, and ambient light of the phone, we can adapt the model to different scenarios and improve generalization performance by expanding the image dataset and using a variety of different image augmentation strategies to improve the detection and identification accuracy.

5. Conclusions

1. We proposed two rice disease and insect pest detection models suitable for mobile phone terminals based on deep-learning detection and realized offline detection by intelligent mobile phone terminals, thus providing an efficient and reliable intelligent detection method for farmers and plant protection personnel. By introducing the Ghost module, Improved YOLOv5s significantly improved detection accuracy and operation efficiency compared to YOLOv5s. It had the highest F1-Score and the highest scores for mAP (0.5) and mAP (0.5:0.9) with values of 0.931, 0.961 and 0.648, respectively. Moreover, the parameter quantity, model size, and FLOPs of Improved YOLOv5s were reduced by 47.5, 45.7, and 48.7%, respectively, while the inference speed improved by 38.6% and model detection accuracy and operation efficiency also significantly improved. By introducing the CBAM attention module and SIoU loss, Improved YOLOv7-tiny outperformed YOLOv7-tiny in detection accuracy, and the model accuracy of F1-Score, mAP (0.5), and mAP (0.5:0.9) were second only to those of Improved YOLOv5s.
2. For the detection of different categories of rice diseases and insect pests, the AP value of Improved YOLOv5s was higher than that of Improved YOLOv7-tiny for the identification of all rice diseases and insect pests. The probability heat maps showed that Improved YOLOv5s had better detection in areas of rice disease and insect pests where there were larger image target sizes, and Improved YOLOv7-tiny had better detection accuracy where there were smaller image target sizes.
3. The two improved models were transplanted to an Android mobile phone. Under FP16, the precision and recall of Improved YOLOv5s was 0.925, and 0.939, and the inference speed was 374 ms/frame. Model accuracy, operational efficiency, and runtime performance were better than for Improved YOLOv7-tiny. The mobile phone application constructed by the improved models is compatible with most Android mobile phone hardware platforms for achieving accurate detection of rice diseases and insect pests.

The improved object detection models proposed in this study can realize the accurate detection of rice diseases and insect pests, and the mobile phone application for rice disease and insect pest identification can provide strong support for the rapid diagnosis and intelligent identification of rice diseases and insect pests in the field.

Author Contributions: Conceptualization, J.D. and C.Y.; methodology, C.Y.; software, C.Y.; validation, C.Y., W.Z. and L.L.; formal analysis, C.Y.; investigation, J.Z.; resources, C.Y.; data curation, K.H.; writing—original draft preparation, C.Y.; writing—review and editing, C.Y.; visualization, C.Y.; supervision, Y.Z.; project administration, C.Y. and J.Y.; funding acquisition, Y.L. All authors have read and agreed to the published version of the manuscript.

Funding: This research was funded by the Guangdong Provincial Innovation Team for General Key Technologies in Modern Agricultural Industry, grant number 2022KJ133, the Laboratory of Lingnan Modern Agriculture Project, grant number NT2021009, and the 111 Project grant number D18019.

Institutional Review Board Statement: Not applicable.

Informed Consent Statement: Not applicable.

Data Availability Statement: The data presented in this study are available on request from the corresponding author. The data are not publicly available due to the privacy policy of the organization.

Acknowledgments: Many thanks to South China Agricultural University plant protection experts Maoxin Zhang and Guohui Zhou for helping us to carry out an investigation in the field of the study site and for giving professional guidance in rice diseases and insect pests image data annotation.

Conflicts of Interest: The authors declare no conflict of interest.

References

1. Liu, T.; Zhong, X.C.; Sun, C.M.; Guo, W.S.; Chen, Y.Y.; Sun, J. Recognition of Rice Leaf Diseases Based on Computer Vision. *Sci. Agric. Sin.* **2014**, *47*, 664–674. (In Chinese)
2. Wen, C.; Guyer, D.; Li, W. Local feature-based identification and classification for orchard insects. *Biosyst. Eng.* **2009**, *104*, 299–307. [CrossRef]
3. Wen, C.; Guyer, D. Image-based orchard insect automated identification and classification method. *Comput. Electron. Agric.* **2012**, *89*, 110–115. [CrossRef]
4. Liu, T.; Chen, W.; Wu, W.; Sun, C.; Guo, W.; Zhu, X. Detection of aphids in wheat fields using a computer vision technique. *Biosyst. Eng.* **2016**, *141*, 82–93. [CrossRef]
5. Xie, C.; Zhang, J.; Li, R.; Li, J.; Hong, P.; Xia, J.; Chen, P. Automatic classification for field crop insects via multiple-task sparse representation and multiple-kernel learning. *Comput. Electron. Agric.* **2015**, *119*, 123–132. [CrossRef]
6. Espinoza, K.; Valera, D.L.; Torres, J.A.; Lopez, A.; Molina-Aiz, F.D. Combination of image processing and artificial neural networks as a novel approach for the identification of Bemisia tabaci and Frankliniella occidentalis on sticky traps in greenhouse agriculture. *Comput. Electron. Agric.* **2016**, *127*, 495–505. [CrossRef]
7. Wang, Z.; Chu, G.K.; Zhang, H.J.; Liu, S.; Huang, X.; Gao, F.; Zhang, C.; Wang, J. Identification of diseased empty rice panicles based on Haar-like feature of UAV optical image. *Trans. Chin. Soc. Agric. Eng.* **2018**, *34*, 73–82. (In Chinese)
8. Wang, D.F.; Wang, J. Crop disease classification with transfer learning and residual networks. *Trans. Chin. Soc. Agric. Eng.* **2021**, *37*, 199–207. (In Chinese)
9. Li, X.Z.; Ma, B.X.; Yu, G.W.; Chen, J.; Li, Y.; Li, C. Surface defect detection of Hami melon using deep learning and image processing. *Trans. Chin. Soc. Agric. Eng.* **2021**, *37*, 223–232. (In Chinese)
10. Hou, J.L.; Fang, L.F.; Wu, Y.Q.; Li, Y.; Xi, R. Rapid recognition and orientation determination of ginger sprouts based on deep learning. *Trans. Chin. Soc. Agric. Eng.* **2021**, *37*, 213–222. (In Chinese)
11. Agarwal, M.; Singh, A.; Arjaria, S.; Sinha, A.; Gupta, S. ToLeD: Tomato leaf disease detection using convolution neural network. *Proc. Comput. Sci.* **2020**, *167*, 293–301. [CrossRef]
12. Zhong, Y.; Zhao, M. Research on deep learning in apple leaf disease recognition. *Comput. Electron. Agric.* **2020**, *168*, 105146. [CrossRef]
13. Ramcharan, A.; Baranowski, K.; McCloskey, P.; Ahmed, B.; Legg, J.; Hughes, D.P. Deep Learning for Image-Based Cassava Disease Detection. *Front. Plant Sci.* **2017**, *8*, 1852. [CrossRef]
14. Rahman, C.R.; Arko, P.S.; Ali, M.E.; Khan, M.A.I.; Apon, S.H.; Nowrin, F.; Wasif, A. Identification and recognition of rice diseases and pests using convolutional neural networks. *Biosyst. Eng.* **2020**, *194*, 112–120. [CrossRef]
15. Joshi, P.; Das, D.; Udutalapally, V.; Pradhan, M.K.; Misra, S. RiceBioS: Identification of Biotic Stress in Rice Crops Using Edge-as-a-Service. *IEEE Sens. J.* **2022**, *22*, 4616–4624. [CrossRef]
16. Deng, R.L.; Tao, M.; Xing, H.; Yang, X.L.; Liu, C.; Liao, K.; Qi, L. Automatic diagnosis of rice diseases using deep learning. *Plant Sci.* **2021**, *12*, 701038. [CrossRef]
17. Ren, S.; He, K.; Girshick, R.; Sun, J. Faster r-cnn: Towards real-time object detection with region proposal networks. *Adv. Neural Inf. Process. Syst.* **2015**, 91–99. Available online: https://arxiv.org/abs/1506.01497 (accessed on 1 February 2023). [CrossRef]
18. Redmon, J.; Divvala, S.; Girshick, R.; Farhadi, A. You only look once: Unified, real-time object detection. In Proceedings of the 2016 IEEE Conference on Computer Vision and Pattern Recognition (CVPR), Las Vegas, NV, USA, 27–30 June 2016; pp. 779–788. Available online: https://arxiv.org/abs/1506.02640 (accessed on 1 February 2023).
19. YOLOv5. Available online: https://github.com/ultralytics/yolov5 (accessed on 1 February 2023).
20. Lin, T.Y.; Dollar, P.; Girshick, R.; He, K.M.; Hariharan, B.; Belongie, S. Feature Pyramid Networks for Object Detection. In Proceedings of the 2017 IEEE Conference on Computer Vision and Pattern Recognition (CVPR), Honolulu, HI, USA, 21–26 July 2017. Available online: https://arxiv.org/abs/1612.03144v2 (accessed on 1 February 2023).
21. Liu, S.; Qi, L.; Qin, H.F.; Shi, J.P.; Jia, J.Y. Path Aggregation Network for Instance Segmentation. In Proceedings of the 2018 IEEE/CVF Conference on Computer Vision and Pattern Recognition, Salt Lake City, UT, USA, 18–23 June 2018. Available online: https://arxiv.org/abs/1803.01534v4 (accessed on 1 February 2023).
22. Howard, A.G.; Zhu, M.; Chen, B.; Kalenichenko, D.; Wang, W.; Weyand, T.; Andreetto, M.; Adam, H. MobileNets: Efficient convolutional neural networks for mobile vision applications. *IEEE Access.* **2017**, *6*, 1–14.
23. Sandler, M.; Howard, A.; Zhu, M.; Zhmoginov, A.; Chen, L.-C. MobileNet V2: Inverted residuals and linear bottlenecks. In Proceedings of the 2018 IEEE/CVF Conference on Computer Vision and Pattern Recognition, Salt Lake City, UT, USA, 18–23 June 2018; pp. 4510–4520. Available online: https://arxiv.org/1801.04381 (accessed on 1 February 2023).
24. Howard, A.; Sandler, M.; Chu, G.; Chen, L.-C.; Chen, B.; Tan, M.; Wang, W.; Zhu, Y.; Pang, R.; Vasudevan, V.; et al. Searching for MobileNetV3. In Proceedings of the 2019 IEEE/CVF Conference on Computer Vision and Pattern Recognition (CVPR), Long Beach, CA, USA, 15–20 June 2019. Available online: https://arxiv.org/abs/1905.02244 (accessed on 1 February 2023).
25. Zhang, X.; Zhou, X.; Lin, M.; Sun, J. ShuffleNet: An Extremely Efficient Convolutional Neural Network for Mobile Devices. In Proceedings of the IEEE Conference on Computer Vision and Pattern Recognition (CVPR), Salt Lake City, UT, USA, 18–22 June 2018.

26. Ma, N.N.; Zhang, X.; Zheng, H.T.; Sun, J. ShuffleNet V2: Practical Guidelines for Efficient CNN Architecture Design. In Proceedings of the 2018 IEEE/CVF Conference on Computer Vision and Pattern Recognition, Salt Lake City, UT, USA, 18–23 June 2018. Available online: https://arxiv.org/abs/1807.11164 (accessed on 1 February 2023).
27. Han, K.; Wang, Y.; Tian, Q.; Guo, J.; Xu, C. GhostNet: More Features from Cheap Operations. In Proceedings of the 2020 IEEE/CVF Conference on Computer Vision and Pattern Recognition (CVPR), Seattle, WA, USA, 13–19 June 2019. Available online: https://arxiv.org/abs/1911.11907 (accessed on 1 February 2023).
28. He, K.; Zhang, X.; Ren, S.; Sun, J. Deep residual learning for image recognition. In Proceedings of the IEEE Conference on Computer Vision and Pattern Recognition, Las Vegas, NV, USA, 27–30 June 2016; pp. 770–778.
29. Wang, C.Y.; Bochkovskiy, A.; Liao, H. YOLOv7: Trainable bag-of-freebies sets new state-of-the-art for real-time object detectors. In Proceedings of the 2022 IEEE/CVF Conference on Computer Vision and Pattern Recognition (CVPR), New Orleans, LA, USA, 18–24 June 2022. Available online: https://arxiv.org/abs/2207.02696 (accessed on 1 February 2023).
30. Woo, S.; Park, J.; Lee, J.-Y.; Kweon, I.S. *CBAM: Convolutional Block Attention Module*; Springer: Cham, Switzerland, 2018; pp. 3–19.
31. Ding, X.H.; Zhang, X.Y.; Ma, N.N.; Han, J.; Ding, G.; Sun, J. RepVGG: Making VGG-style ConvNets Great Again. In Proceedings of the 2022 IEEE/CVF Conference on Computer Vision and Pattern Recognition (CVPR), New Orleans, LA, USA, 18–24 June 2022. Available online: https://arxiv.org/2101.03697 (accessed on 1 February 2023).
32. Gevorgyan, Z. SIoU Loss: More Powerful Learning for Bounding Box Regression. In Proceedings of the 2022 IEEE/CVF Conference on Computer Vision and Pattern Recognition (CVPR), New Orleans, LA, USA, 18–24 June 2022. Available online: https://arxiv.org/abs/2205.12740 (accessed on 1 February 2023).
33. Girshick, R.; Donahue, J.; Darrell, T.; Malik, J. Rich Feature Hierarchies for Accurate Object Detection and Semantic Segmentation. In Proceedings of the 2014 IEEE Conference on Computer Vision and Pattern Recognition, Columbus, OH, USA, 23–28 June 2014; pp. 580–587.
34. Girshick, R. Fast R-CNN. In Proceedings of the 2015 IEEE Conference on Computer Vision and Pattern Recognition (CVPR), Boston, MA, USA, 7–12 June 2015; pp. 1440–1448.
35. Simonyan, K.; Zisserman, A. Very Deep Convolutional Networks for Large-Scale Image Recognition. *Comput. Sci.* **2014**. Available online: https://arxiv.org/abs/1409.1556 (accessed on 1 February 2023).
36. Liu, W.; Anguelov, D.; Erhan, D.; Szegedy, C.; Reed, S.; Fu, C.-Y.; Berg, A.C. SSD: Single shot multibox detector. *arXiv* **2016**, arXiv:1512.02325.
37. Jiang, F.; Lu, Y.; Chen, Y.; Cai, D.; Li, G.F. Image recognition of four rice leaf diseases based on deep learning and support vector machine. *Comput. Electron. Agric.* **2020**, *179*, 105824. [CrossRef]
38. Lu, Y.; Yi, S.J.; Zeng, N.Y.; Liu, Y.R.; Zhang, Y. Identification of rice diseases using deep convolutional neural networks. *Neurocomputing* **2017**, *267*, 378–384. [CrossRef]
39. Wang, Y.B.; Wang, H.F.; Peng, Z.H. Rice diseases detection and classification using attention based neural network and bayesian optimization. *Expert Syst. Appl.* **2021**, *178*, 114770. [CrossRef]
40. Johnson, J.M.; Khoshgoftaar, T.M. Survey on deep learning with class imbalance. *J. Big Data* **2019**, *6*, 27. [CrossRef]
41. Shorten, C.; Khoshgoftaar, T.M. A survey on Image Data Augmentation for Deep Learning. *J. Big Data* **2019**, *6*, 60. [CrossRef]

Disclaimer/Publisher's Note: The statements, opinions and data contained in all publications are solely those of the individual author(s) and contributor(s) and not of MDPI and/or the editor(s). MDPI and/or the editor(s) disclaim responsibility for any injury to people or property resulting from any ideas, methods, instructions or products referred to in the content.

remote sensing

MDPI

Article

Inversion of Leaf Area Index in Citrus Trees Based on Multi-Modal Data Fusion from UAV Platform

Xiaoyang Lu [1,2,3], Wanjian Li [1,2,3], Junqi Xiao [1,2,3], Hongyun Zhu [1], Dacheng Yang [1,2,3], Jing Yang [1,2,3], Xidan Xu [1,2,3], Yubin Lan [2,3,4] and Yali Zhang [1,2,3,*]

1 College of Engineering, South China Agricultural University, Wushan Road, Guangzhou 510642, China; luxiaoyang@stu.scau.edu.cn (X.L.); 19981002@stu.scau.edu.cn (W.L.); 20213142028@stu.scau.edu.cn (J.X.); hongyun@scau.edu.cn (H.Z.); 20223142009@stu.scau.edu.cn (D.Y.); 2022yj@stu.scau.edu.cn (J.Y.); xxxjy@stu.scau.edu.cn (X.X.)
2 Guangdong Laboratory for Lingnan Modern Agriculture, Guangzhou 510642, China; ylan@scau.edu.cn
3 National Center for International Collaboration Research on Precision Agricultural Aviation Pesticide Spraying Technology, Guangzhou 510642, China
4 College of Electronic Engineering and College of Artificial Intelligence, South China Agricultural University, Wushan Road, Guangzhou 510642, China
* Correspondence: ylzhang@scau.edu.cn

Abstract: The leaf area index (LAI) is an important growth indicator used to assess the health status and growth of citrus trees. Although LAI estimation based on unmanned aerial vehicle (UAV) platforms has been widely used for field crops, mainly focusing on food crops, less research has been reported on the application to fruit trees, especially citrus trees. In addition, most studies have used single-modal data for modeling, but some studies have shown that multi-modal data can be effective in improving experimental results. This study utilizes data collected from a UAV platform, including RGB images and point cloud data, to construct single-modal regression models named VoVNet (using RGB data) and PCNet (using point cloud data), as well as a multi-modal regression model called VPNet (using both RGB data and point cloud data). The LAI of citrus trees was estimated using deep neural networks, and the results of two experimental hyperparameters (loss function and learning rate) were compared under different parameters. The results of the study showed that VoVNet had Mean Squared Error (MSE), Mean Absolute Error (MAE), and R-Squared (R^2) of 0.129, 0.028, and 0.647, respectively. In comparison, PCNet decreased by 0.051 and 0.014 to 0.078 and 0.014 for MAE and MSE, respectively, while R^2 increased by 0.168 to 0.815. VPNet decreased by 0% and 42.9% relative to PCNet in terms of MAE and MSE to 0.078 and 0.008, respectively, while R^2 increased by 5.6% to 0.861. In addition, the use of loss function L1 gave better results than L2, while a lower learning rate gave better results. It is concluded that the fusion of RGB data and point cloud data collected by the UAV platform for LAI estimation is capable of monitoring citrus trees' growth process, which can help farmers to track the growth condition of citrus trees and improve the efficiency and quality of orchard management.

Keywords: leaf area index; UAV; data fusion; citrus trees; deep neural network

check for updates

Citation: Lu, X.; Li, W.; Xiao, J.; Zhu, H.; Yang, D.; Yang, J.; Xu, X.; Lan, Y.; Zhang, Y. Inversion of Leaf Area Index in Citrus Trees Based on Multi-Modal Data Fusion from UAV Platform. *Remote Sens.* **2023**, *15*, 3523. https://doi.org/10.3390/rs15143523

Academic Editors: Abdul Rashid Mohamed Sharif, Redmond R. Shamshiri, Sanaz Shafian and Siva Kumar Balasundram

Received: 2 June 2023
Revised: 5 July 2023
Accepted: 10 July 2023
Published: 12 July 2023

Copyright: © 2023 by the authors. Licensee MDPI, Basel, Switzerland. This article is an open access article distributed under the terms and conditions of the Creative Commons Attribution (CC BY) license (https://creativecommons.org/licenses/by/4.0/).

1. Introduction

Citrus trees are an important cash crop belonging to the genus Citrus (Rutaceae). It has a wide area of cultivation worldwide and is an economic pillar in many developing countries [1]. The healthy growth and development of citrus trees is an important guarantee of yield [2]. In order to ensure the high yield and quality of citrus trees, their growth needs to be monitored in a timely manner.

In the field of agriculture, UAVs equipped with various intelligent sensors and devices [3] can be utilized for multiple tasks, including pesticide spraying [4], harvesting [5], field planning [6], and crop growth monitoring [7–9]. Among them, the monitoring of

crop growth is an important function of UAVs [10]. By using various sensors and cameras to acquire crop growth data, and subsequently processing and analyzing the data [11], information such as plant height [12], yield prediction [13], leaf area index [14], and carotenoid content [15] can be obtained. Particularly, the leaf area index is crucial for monitoring crop growth [16] as it enables the accurate diagnosis and management of crop growth conditions.

The leaf area index (LAI) is the sum of plant leaf area per unit of land area and is an important indicator of plant growth and ecosystems [17]. LAI is very important in ecological biophysics. By monitoring and analyzing LAI, it is possible to assess the growth rate, health status, and growth potential of crops and to take timely management measures, such as applying fertilizers, irrigation, and pest control, to maximize crop yield and quality [18]. Generally, the measurement of LAI is divided into direct and indirect methods [19]. The direct method is traditional and destructive, and although it gives the most accurate results, it is difficult to apply it to large-scale farmland measurements [20]. Indirect methods mainly use optical methods and inclined point sampling methods to obtain LAI [20]. The current widely used optical instruments are classified as radiation-based and image-based measurements. Representative instruments of the former are LAI-2000 (Licor Inc., Lincoln, NE, USA), TRAC (Wave Engineering Co., Nepean, ON, Canada), Sunscan (Delta-T Inc., Cambridge, UK), etc. The advantage of radiation measurement instruments is that they are fast and easy to measure, but they are susceptible to weather and often need to work on sunny days and correct for aggregation effects [21]. Typical instruments for image-based measurements are CI-110 (CID Inc., Washington, DC, USA), Image Analysis System (Delta-T Inc., Cambridge, UK), WinScanopy (Regent Inc., Thunder Bay, ON, Canada), etc. Among them, CI-110 is suitable for a low plant canopy and has high measurement accuracy, which is popular for LAI measurements in agricultural fields [22–24].

For estimating the LAI of citrus trees, optical instruments are currently the common measurement tools, but they require labor-intensive and costly efforts to measure the LAI of each citrus tree. In contrast, the use of remote sensing to estimate the LAI of citrus trees can save significant time and labor costs, where multiple data sources are often utilized for estimation. For instance, vegetation feature parameters such as the leaf area and leaf distribution density can be extracted from RGB images to calculate the LAI [25,26]. Additionally, point cloud data can be utilized to estimate the leaf area index by measuring the height and density of the plant canopy [27]. Hyperspectral data, on the other hand, can infer the leaf area index by continuously acquiring spectral reflectance information of vegetation within a narrow wavelength range [28]. Furthermore, vegetation indices can be employed to estimate the leaf area index by analyzing the spectral reflectance of vegetation [29].

In terms of data type selection, the use of remotely sensed images taken by UAVs for estimation can reduce the time to obtain LAI and reduce the effects of topographic difficulties [30]. Hasan et al. [31] used parameters from UAV RGB images to estimate the LAI of winter wheat. Based on gray correlation analysis, five vegetation indices, such as Visible Atmospheric Resistance Index (VARI), were selected to develop models for estimating the LAI of winter wheat. The results showed that partial least squares regression (PLSR) models based on VARI, RGBVI, B, and GLA had the best prediction accuracy among all regression models (R^2 = 0.776, root mean square error (RMSE) = 0.468, and residual prediction deviation (RPD) = 1.838). Yamaguchi et al. [32] compared the LAI estimation model developed via deep learning (DL) using RGB images with three other practical methods: a plant canopy analyzer (PCA), regression models based on color indices (CIs) obtained from an RGB camera, and vegetation indices (VIs) obtained from a multispectral camera. The results showed that the estimation accuracy of the DL model built with RGB images (R^2 = 0.963, RMSE = 0.334) was higher than that of the PCA (R^2 = 0.934, RMSE = 0.555) and CIs-based regression models (R^2 = 0.802–0.947, RMSE = 0.401–1.13), and was comparable to that of the VIs-based regression models (R^2 = 0.917–0.976, RMSE = 0.332–0.644).

Point cloud data can provide very high measurement accuracy, which can avoid human error and measurement errors and improve the reliability and accuracy of data compared to traditional measurement methods [27,33,34]. Yang et al. [35] proposed a 3-D point cloud method using UAV to automatically calculate crop-effective LAI (LAIe). The method accurately estimated LAIe by projecting 3-D point cloud data of winter wheat onto the hemisphere and calculating the gap fraction using both single-angle inversion and multi-angle inversion methods. The results showed that the calculated LAIe had a good linear correlation with the LAIe measured via digital hemispheric photography in the field, and the stereographic projection multi-angle inversion method had the highest accuracy, with an R^2 of 0.63. Song et al. [36] used 3-D point cloud data based on UAVs to automatically calculate LAIe. The method used high-resolution RGB images to generate point cloud data and the 3-D spatial distribution of vegetation and bare ground points and calculate the gap fraction and LAIe from a UAV-based 3-D point cloud dataset. The results showed a strong correlation between the derived LAIe and ground-based digital hemispherical photography (R^2 = 0.76).

Although the estimation of LAI has been widely studied, it has been applied to fruit trees in large fields with relatively little and less than optimal results, and relatively little research has been conducted on citrus trees. Mazzini et al. [37] found that the leaf length, leaf width, and leaf length times leaf width were all strongly correlated with the leaf area and that a linear equation using leaf length times leaf width as a variable was the most accurate and reliable model. Dutra et al. [38] developed separate empirical equations for LAI for single and compound-leafed citrus trees. Raj et al. [39] used RGB images taken by UAV to estimate the LAI of a citrus canopy, and the R^2 of the estimated value with the LAI value measured by the ground instrument was 0.73.

In some studies, better estimation results can be obtained by fusing multi-modal data than using single-modal data. Maimaitijiang et al. [40] estimated soybean yields (R^2 = 0.72, RMSE = 0.159) using RGB and multispectral and thermal sensors within the framework of a deep neural network. Zhang et al. [41] used UAV spectral parameters with texture feature data to estimate the LAI of kiwifruit orchard via the stepwise regression method and random forest approach (R^2 = 0.947, RMSE = 0.048, nRMSE = 7.99%). Wu et al. [42] used UAV images and spectral, structural, and thermal characteristics of a wheat canopy to estimate the LAI of wheat using the random forest approach and support vector machine regression (R^2 = 0.679, RMSE = 1.231).

LAI estimation using deep neural networks is the main method for connecting different data sources, and the main advantage is its ability to learn complex, nonlinear mapping relationships. Compared to traditional linear models, deep neural networks have stronger capabilities in capturing the nonlinear mapping patterns between LAI and input data. By learning from large-scale training data, deep neural networks can accurately estimate LAI values. The multi-modal data fusion used in this study is a combination of RGB data and point cloud data, thus increasing the richness of the data. RGB data provide color and texture information, while point cloud data provide information on position, size, and orientation in 3-D space. This fusion enhances data robustness, reduces reliance on a single data source, and improves model stability and adaptability.

In this study, RGB data and point cloud data acquired by a UAV platform were used to construct regression models for single-modal data and multi-modal data to estimate the LAI of citrus trees using deep neural networks, and a comparative analysis was conducted to verify whether multi-modal data are more beneficial for estimating the LAI of citrus trees.

2. Materials and Methods

2.1. Study Area Overview

The study site is located in a citrus orchard plantation in Huangtian Town, Sihui City, Zhaoqing City, Guangdong Province, China (23°36′N, 112°68′E), as shown in Figure 1. The climatic conditions were subtropical monsoonal, with an average annual temperature

of 21 °C and an annual precipitation of 1800 mm. The 110 citrus trees selected for this study were of similar age and growing in good environmental conditions in March of 2023. These citrus trees were at the stage of spring shoot growth. The management of this stage involves two aspects: promoting shoot growth and preventing pests and diseases, as well as managing the flowering of mature and young trees. Effective management at this stage is crucial for subsequent flowering and fruiting.

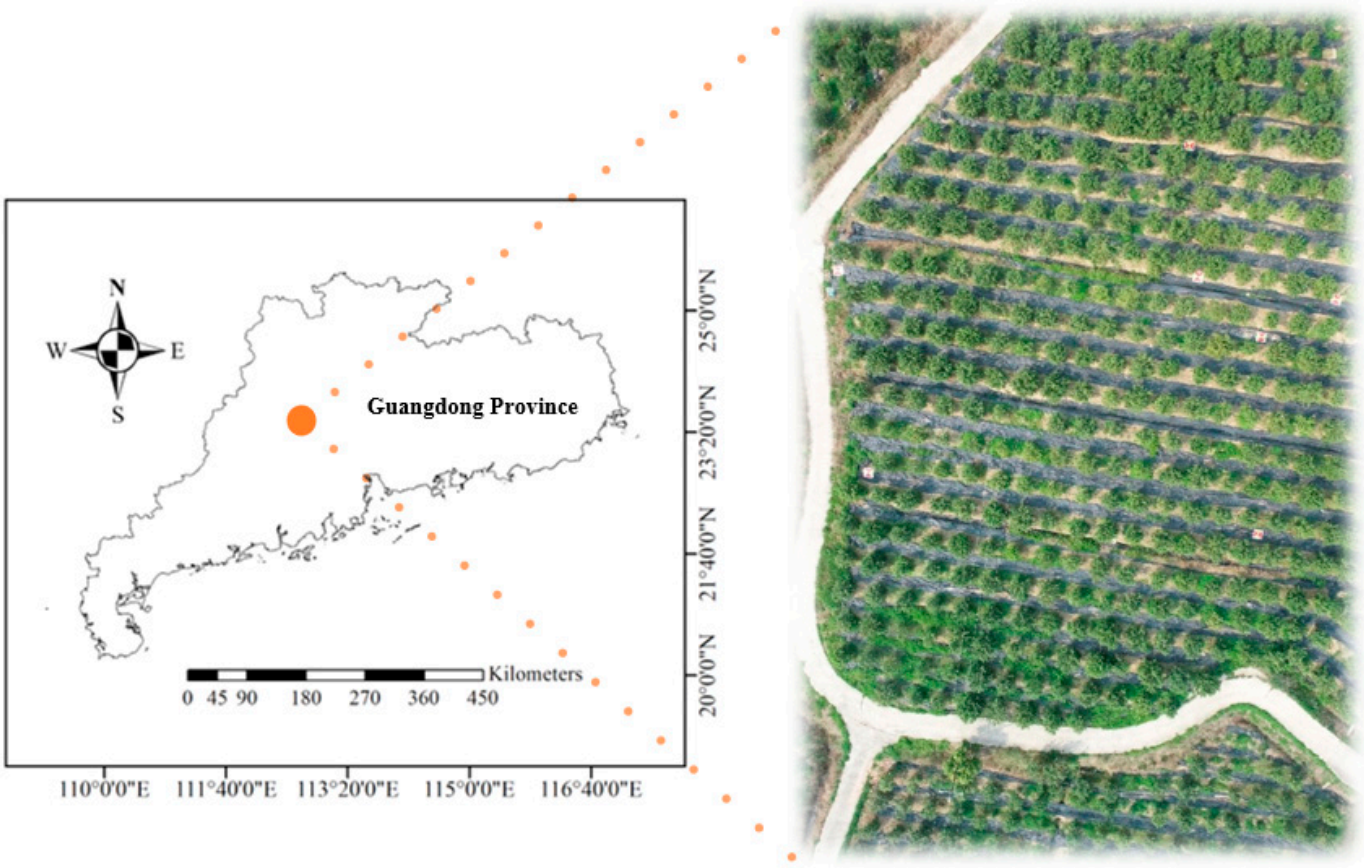

Figure 1. Study site.

2.2. Data Acquisition

2.2.1. Measuring LAI of Citrus Trees

Two image-acquisition measurements were taken using Plant Canopy Imager CI-110 (CID Inc., Washington, DC, USA) on 110 citrus trees at approximately 20 cm from the ground and 20 cm from the trunk, and the average was taken as the LAI value of the citrus tree [22,43]. CI-110 is a non-destructive and efficient tool for measuring plant canopy characteristics with a self-leveling hemispherical lens, a built-in touchscreen display, a GPS and compass, and 24 PAR sensors. LAI was calculated using the CI-110 Plant Canopy Analysis software. During image acquisition, the brightness and contrast were adjusted so that all plant parts in the image appeared green to obtain an accurate processing section. The captured images were imported into this software for further processing by adjusting parameters such as brightness, contrast, and gamma to derive a more accurate LAI. The data collection was conducted on the mornings of 2–3 March 2023. The weather was overcast, which provided favorable lighting conditions for image acquisition and minimized the impact of intense sunlight [44].

2.2.2. UAV RGB Image Acquisition

The DJI Phantom 4 RTK (SZ DJI Technology Co., Shenzhen, China) was used for aerial oblique images to obtain high-quality RGB images for 3-D reconstruction and point cloud data generation of the citrus orchard. The UAV has a 1-inch, 20-megapixel CMOS sensor with a centimeter-level navigation and positioning system and a high-performance imaging system to accurately locate and photograph the area, thus ensuring image quality. The flight time was chosen at midday, with clear and stable weather and good lighting conditions. In this study, a GS RTK APP platform supporting route planning was used for setup to automate flight and route planning. This made the whole process more efficient, accurate, and safe. The specific flight parameters are shown in Table 1. A total of 1072 images were captured, each with a size of 5472 × 3648 pixels. During the process, the UAV automatically recorded the latitude, longitude, and altitude at that time for subsequent 3-D reconstruction. The acquisition process is shown in Figure 2, which coincides with the LAI data collection time.

Table 1. Flight parameter settings.

Parameter	Value/Method
Flight altitude	50 m
Flight speed	3 m/s
Shooting mode	Timed shooting
Pitch gimbal	−90, −60, −45
Side overlap rate	80%
Forward overlap rate	80%

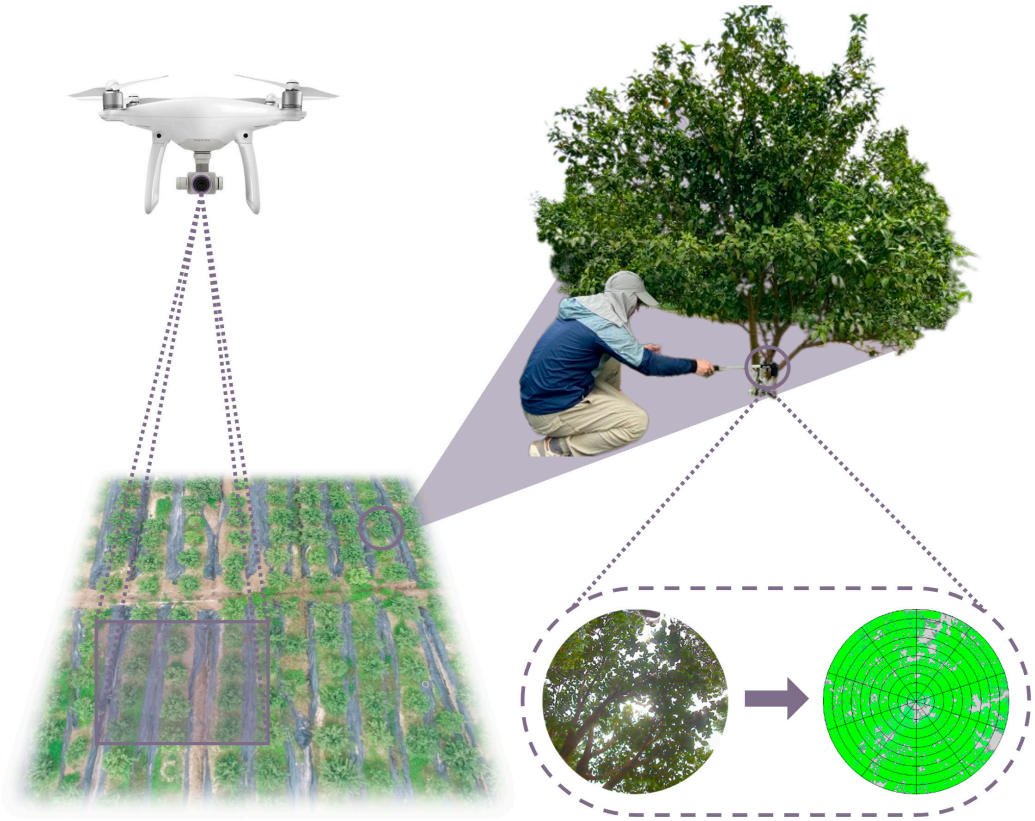

Figure 2. Data-acquisition process.

2.3. Data Pre-Processing

2.3.1. Acquisition of RGB Images of Citrus Trees

The You Only Look Once-v5s (YOLO-v5s) model [45] was used to accurately extract a single citrus tree from the UAV RGB image for target recognition. The model adopts a lightweight structure design and optimization, which can improve the detection speed while ensuring accuracy and achieving the requirement of real-time detection. The YOLO-v5s model has the advantages of high accuracy, high efficiency, and wide scalability and is an excellent target-detection algorithm with a weight size of 13.7 MB. The structural diagram is shown in Figure 3. A total of 635 images of citrus trees were used as the model training dataset, and the images were labeled with the labelImg software to label the location and category of citrus trees, with a total of 76,665 labeled boxes. The accuracy, recall, and map_0.5 of the model were 0.98, 0.98, and 0.99, respectively, which had good recognition accuracy. The recognized target citrus trees would be cropped and saved as RGB images with 3 channels of red, green, and blue, as shown in Figure 4.

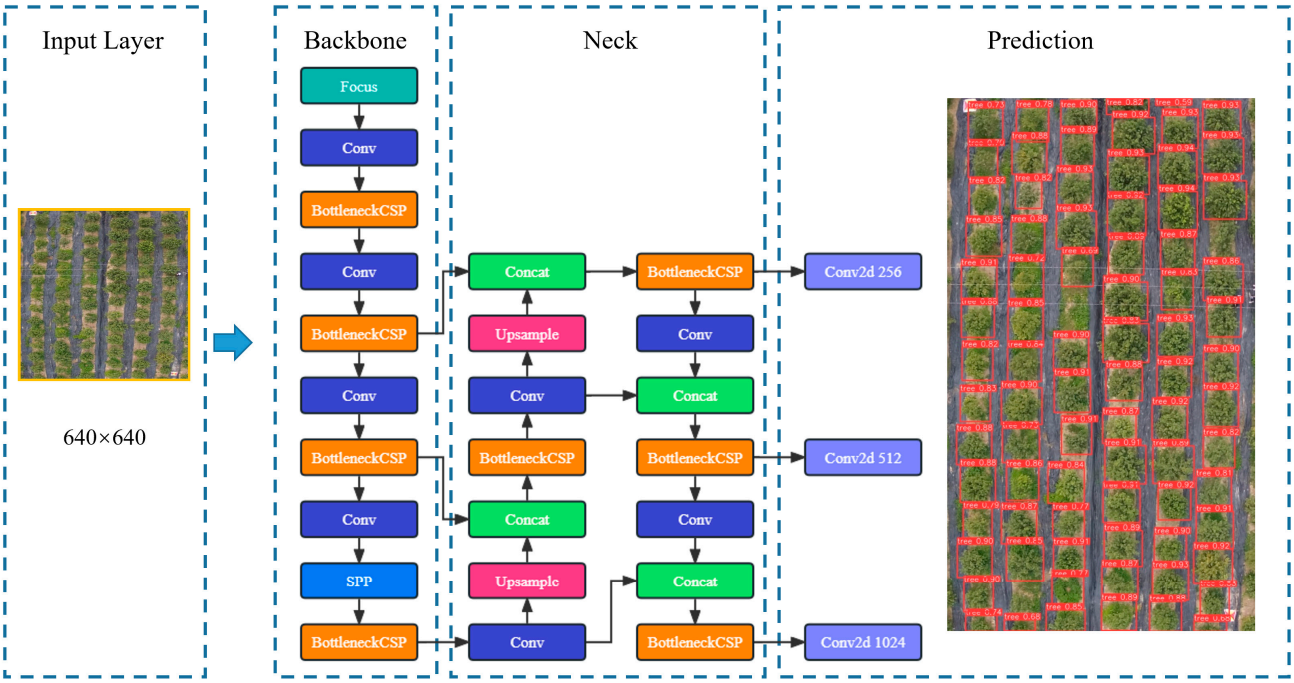

Figure 3. YOLO-v5s structure.

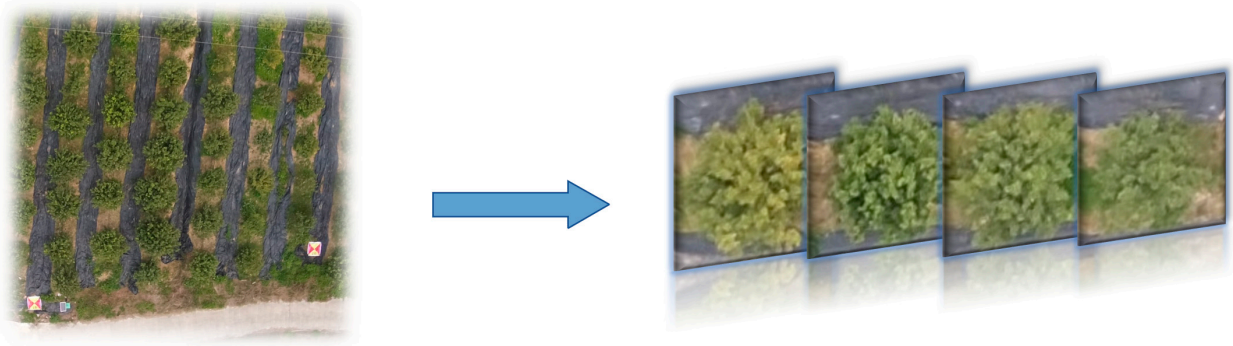

Figure 4. Acquisition of RGB images of citrus trees.

2.3.2. Acquisition of Point Cloud Data of Citrus Tree

The first step was to reconstruct the 3-D model of the oblique images acquired by the UAV using Pix4Dmapper software (Pix4D Co., Prilly, Switzerland). Pix4Dmapper can

convert UAV or other aerial image data into high-precision maps, models, and point cloud data and supports the input and output of multiple data formats. Import the oblique images into Pix4Dmapper, determine the datum as World Geodetic System 1984, the coordinate system as WGS 84, the camera model as FC6310R_8.8_5472×3648 (RGB), and select the "3D Models" processing option template. The 3-D reconstruction model of the citrus orchard was finally obtained after processing by the program. The point cloud data of the citrus orchard were imported into CloudCompare software, which provides powerful point cloud processing and analysis functions, including point cloud alignment, filtering, segmentation, reconstruction, analysis, and visualization operations. In the software, the citrus orchard was first cropped to remove point clouds outside the study area, which can be more convenient for manipulating the 3-D model. Next, the citrus trees were cropped to remove the ground point clouds to obtain the point cloud data of independent citrus trees. The specific process is shown in Figure 5. The citrus tree point cloud data were saved in txt file format, and each piece of point cloud data contained 6 parameter values, which were *X*-axis, *Y*-axis, *Z*-axis, red channel, green channel, and blue channel, as shown in Table 2.

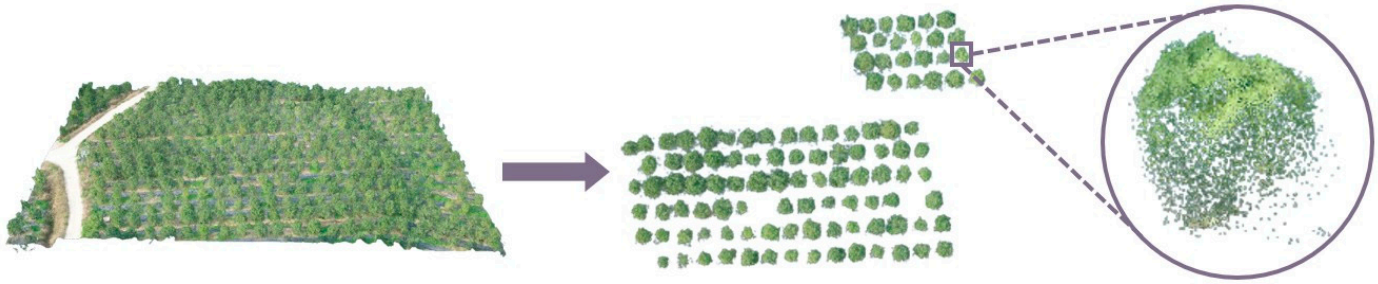

Figure 5. The process of acquiring point cloud of citrus trees.

Table 2. Point cloud data display.

Point Cloud	*X*-Axis	*Y*-Axis	*Z*-Axis	Red	Green	Blue
1	655,215.95899963	2,592,974.80603027	6.21799994	113	138	92
2	655,215.96000671	2,592,974.75402832	6.15500021	146	178	123
3	655,215.96400452	2,592,974.74298096	6.14599991	149	178	123

2.3.3. RGB Data Model

When processing RGB image data, models need to effectively capture features of different scales because RGB images contain rich color and texture information. Additionally, models need to have fast training and inference capabilities and operate efficiently in situations with limited computing resources. Therefore, VoVNet [46] is a good choice. The VoVNet is a convolutional neural network based on One-Shot Aggregation (OSA) modules, which is mainly available in three different configurations, vovnet-27-slim, vovnet-39, and vovnet-57. vovnet-27-slim was chosen for this study. The VoVNet is a Stage 1 consisting of three 3 × 3 convolutional layers, followed by a max pooling layer and four OSA modules connected to form Stages 2–5, and finally, an adaptive average pooling layer and a fully connected layer to form Stage 6. The OSA module is a modified DenseNet [47]; it only aggregates all the previous layers at once at the end, which can reduce the memory access cost and improve the GPU computational efficiency, and it can capture the multiscale receptive domain and effectively present a diverse representation of features, which is good for handling multiscale objects. Its network diagram is shown in Figure 6.

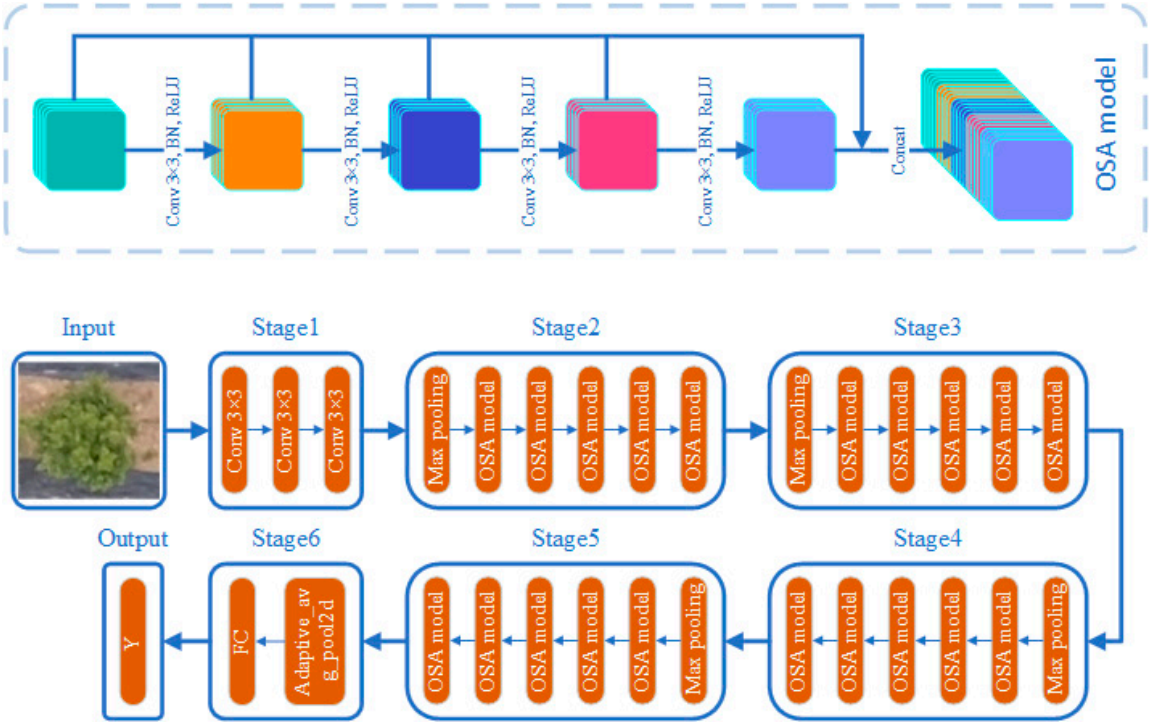

Figure 6. VoVNet structure.

2.3.4. Point Cloud Data Model

Point cloud data contain rich geometric and spatial information. To capture both local and global features of the point cloud, the model needs to incorporate one-dimensional convolutional layers for convolution operations on the data. However, due to the large quantity of point cloud data, not reducing or aggregating the data will result in a significant computational load and waste of computational resources. Therefore, PCNet was used as a model for point cloud data processing, as shown in Figure 7. The PCNet contains multiple convolutional layers, pooling layers, fully connected layers, and activation functions. Specifically, the first layer of the model is a 1-dimensional convolutional layer with 1 input channels, 10 output channels, a convolutional kernel size of 3, and a step size of 2, followed by a SELU activation function. The subsequent layers are similarly structured, where the number of input channels in each layer is the number of output channels in the previous layer. The last three layers of the model are fully connected layers, with 2048- and 1024-dimensional inputs and 1024- and 512-dimensional outputs for the first two layers, and each layer is followed by a ReLU activation function. The final fully connected layer has 512 and 1-dimensional inputs and outputs, respectively. It also includes an adaptive average pooling layer and a maximum pooling layer for extracting important information from the input features.

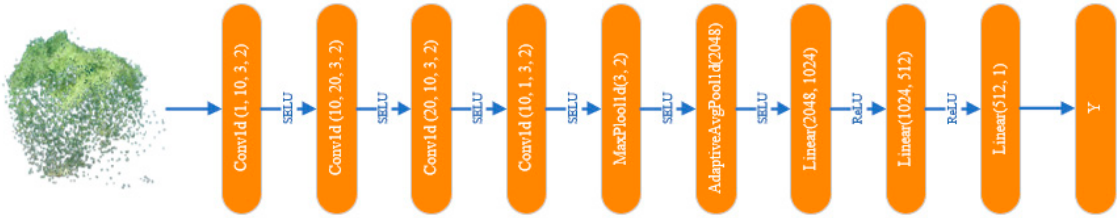

Figure 7. PCNet structure.

2.3.5. Multi-Modal Data Model

The network combining VoVNet and PCNet is VPNet, as shown in Figure 8. VoVNet removes the fully connected layer of Stage 6 from the original and keeps the adaptive level pooling layer, which is used for the adaptive connection between the convolutional layer and the fully connected layer to project high-dimensional features into the low-dimensional space. Stage 6 of VoVNet is connected to the penultimate fully connected layer of PCNet. The connection is followed by five fully connected layers, each of which has a ReLU activation function that enhances the nonlinear capability of the model. The input of the first fully connected layer is a vector of length 1024. The number of neurons in the fully connected layers is 2048, 1024, 512, and 10, and the last layer is 1 neuron for the output of the final prediction. The network is able to make full use of the features of different data, thus improving the prediction accuracy of the model.

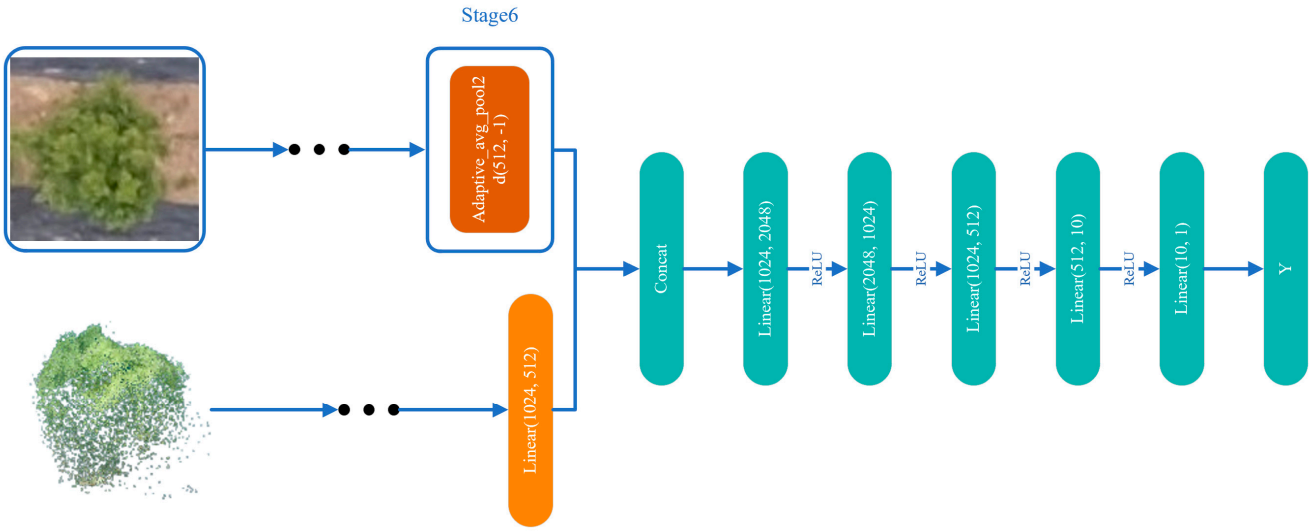

Figure 8. VPNet structure.

2.4. Model Evaluation

In this study, three evaluation metrics, mean squared error (MSE), mean absolute error (MAE), and R-Squared (R^2), were chosen to measure the predictive ability of the model.

MSE measures the predictive power of the model by calculating the squared difference between the predicted and true values. Its calculation formula is as follows:

$$\mathrm{MSE} = \frac{\sum_{i=1}^{n}\left(y_i - \hat{y}_i\right)^2}{n} \quad (1)$$

MAE measures the predictive power of a model by calculating the absolute difference between the predicted and true values. It is calculated by the following formula:

$$\mathrm{MAE} = \frac{\sum_{i=1}^{n}\left|y_i - \hat{y}_i\right|}{n} \quad (2)$$

R^2 calculates the proportion of variance between the predicted and true values to measure the predictive power of the model. It is calculated by the following formula:

$$R^2 = 1 - \frac{\sum_{i=1}^{n}\left(y_i - \hat{y}_i\right)^2}{\sum_{i=1}^{n}\left(y_i - \bar{y}_i\right)^2} \quad (3)$$

where n denotes the number of samples and y_i denotes the true value, $\hat{y}_i$ denotes the predicted value, and $\bar{y}_i$ denotes the average of the true values. Smaller MSE and MAE indicate better predictive ability of the model. Compared with MSE, MAE is more concerned with the absolute difference between the predicted and true values and has less influence on the outliers. R^2 has a range from 0 to 1, and the closer the value is to 1, the better the model's prediction ability is.

3. Results

Different training hyperparameters can lead to different training results. Therefore, researchers typically refer to the experimental parameters used by others and combine them with their own experience to select appropriate model hyperparameters. In the preliminary experiments, different values and methods of hyperparameters were tried, and it was found that the loss function and learning rate were two hyperparameters that had a significant impact on the results. For the comparison experiments of these two hyperparameters, the full-scale experiment method was used, and the hyperparameters of the model were set as shown in Table 3, with six sets of experiments. There were 110 groups of data in the dataset, and the ratio of the number of training, validation, and test set was 7:2:1.

Table 3. Hyperparameter settings.

Parameter	Value/Method
Epochs	500
Batch Size	16
Optimizer	Adam
Loss Function	L1
	L2
Learning Rate	0.001
	0.0001
	0.00001

3.1. Single-Modal Data for LAI Estimation of Citrus Trees

3.1.1. RGB Data for LAI Estimation of Citrus Trees

The training process of VoVNet using RGB data as training data is shown in Figure 9, and the results of the validation and test sets are shown in Table 4. Experimental parameter L1 + LR0.001 had larger data fluctuations during the training process than the other experimental parameters but had the best performance, possibly due to the larger learning rate setting, which caused the training data to constantly change during the search for the optimal solution, resulting in a strong fitting ability. The convergence speed of each experimental parameter group was relatively fast and had already converged before epoch 100. Experimental parameter L2 + LR0.00001 had the smallest data fluctuations during the training process and remained in a stable state, possibly due to the smaller learning rate setting, which found the local optimal solution and maintained a stable state.

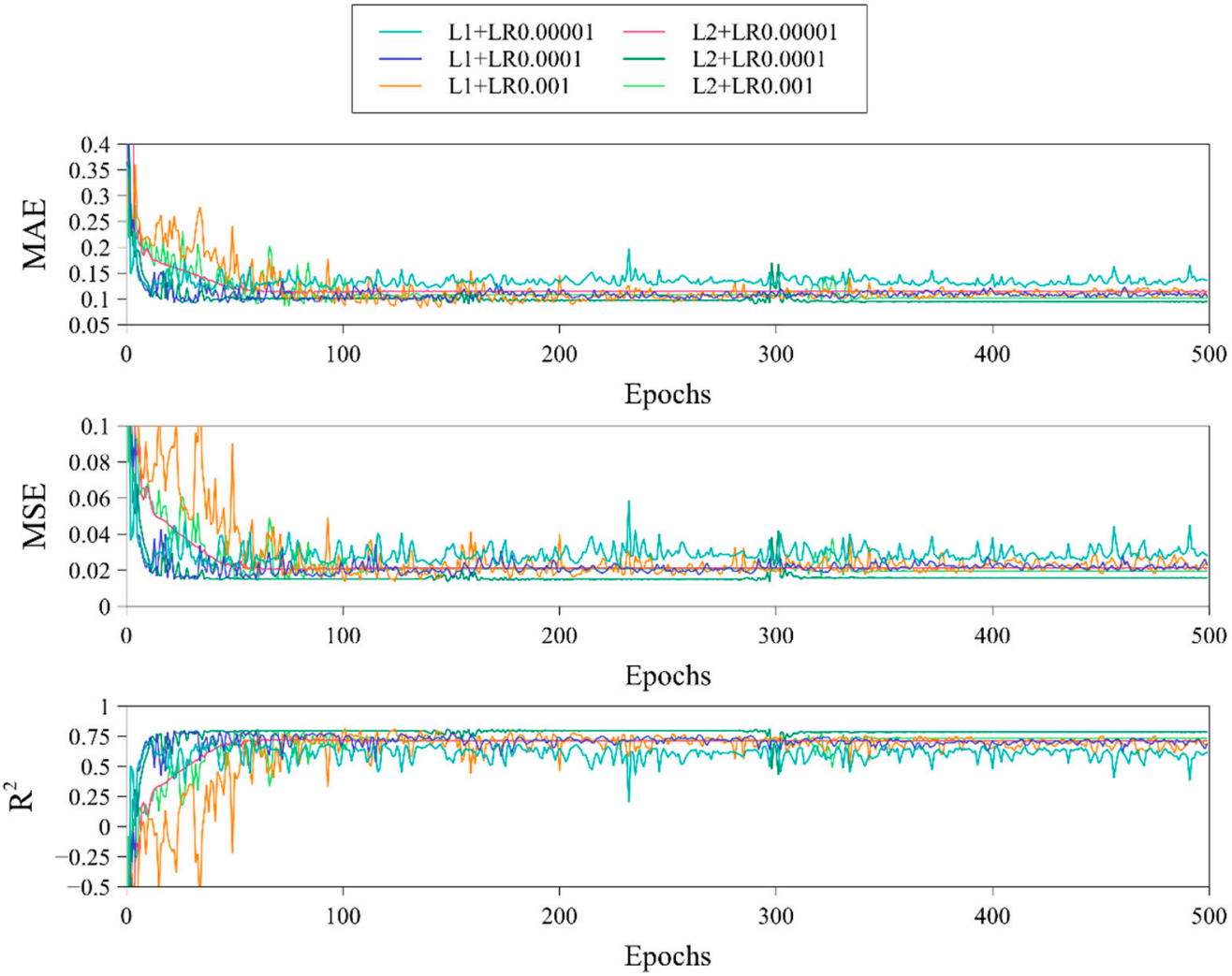

Figure 9. Training process of VoVNet with RGB images as training data.

Table 4. Training results of VoVNet with RGB images as training data.

Experimental Parameters	Validation			Test		
	MAE	MSE	R^2	MAE	MSE	R^2
L1 + LR0.001	0.087	0.013	0.814	0.149	0.037	0.535
L1 + LR0.0001	0.092	0.015	0.795	0.15	0.034	0.575
L1 + LR0.00001	0.11	0.019	0.731	0.129	0.028	0.647
L2 + LR0.001	0.09	0.014	0.802	0.174	0.047	0.407
L2 + LR0.0001	0.092	0.013	0.813	0.149	0.035	0.561
L2 + LR0.00001	0.112	0.02	0.727	0.159	0.04	0.494

The experimental results indicated that there was a significant difference between the evaluation metrics of the validation set and the test set. The MAE and MSE metrics of the validation set were between 0.087–0.112 and 0.013–0.02, respectively, and the R^2 metrics were between 0.727–0.814. However, the MAE and MSE metrics of the test set were between 0.129–0.174 and 0.028–0.047, respectively, and the R^2 metrics were between 0.407–0.647. Among them, the experimental parameters L1 + LR0.001 and L1 + LR0.00001 performed the best in the validation set and the test set, respectively. It was worth noting that the evaluation indicators on the test set were relatively lower than those on the validation set. This was because the test set was used to evaluate the generalization ability of the model,

and the model may have overfit the training data during the training process, resulting in poor performance on the test set.

3.1.2. Point Cloud Data for LAI Estimation of Citrus Trees

The training process of PCNet using point cloud data as training data is shown in Figure 10, and the results of the validation and test sets are shown in Table 5. In the figure, it can be seen that the smaller the learning rate was, the slower the training convergence speed. Experimental parameter L1 + LR0.001 began to converge at about 50 epochs, while experimental parameter L1 + LR0.00001 began to converge at about 200 epochs. Experimental parameter L2 + LR0.001 showed significant data fluctuations during training, which may have been due to the large learning rate setting, hovering near the optimal value and accidentally causing gradient explosion.

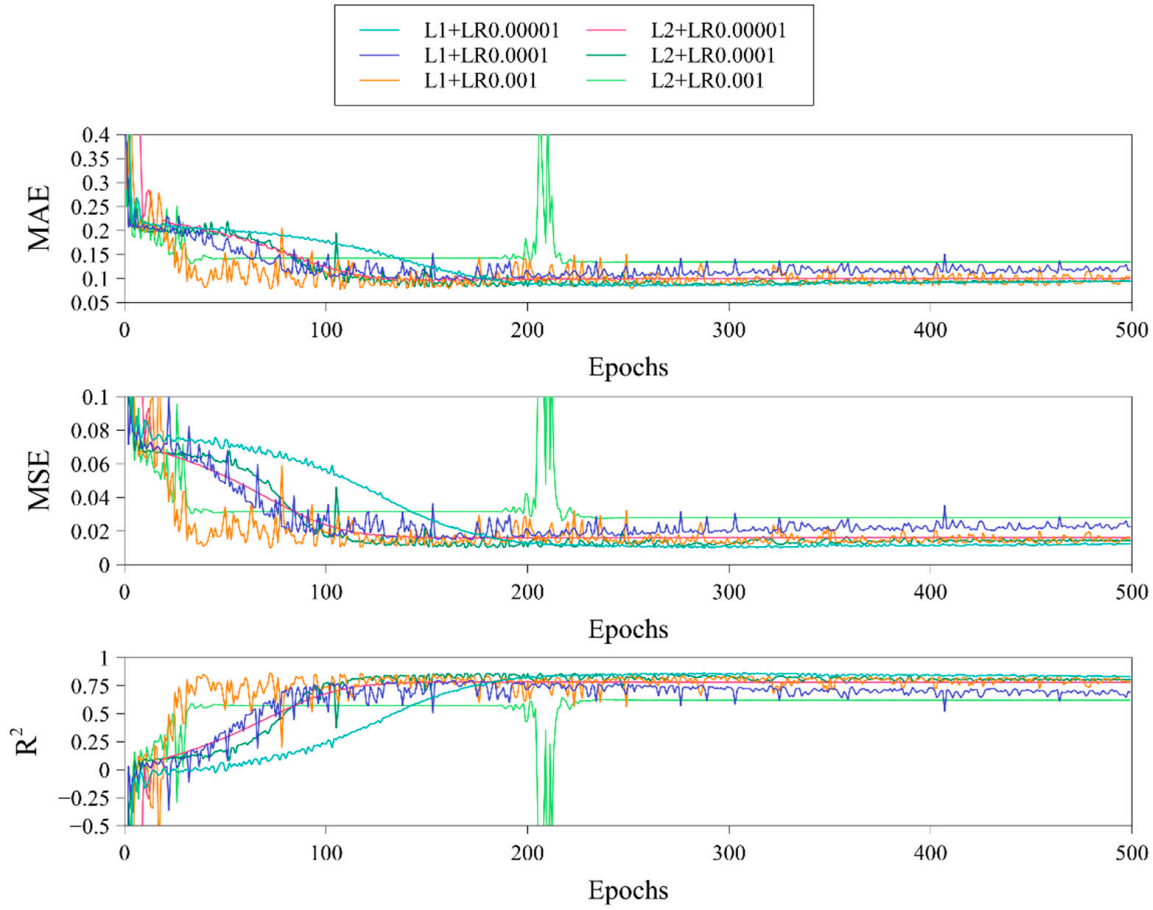

Figure 10. PCNet training process with point cloud data as training data.

Table 5. PCNet training results with point cloud data as training data.

Experimental Parameters	Validation			Test		
	MAE	MSE	R^2	MAE	MSE	R^2
L1 + LR0.001	0.079	0.01	0.864	0.123	0.021	0.74
L1 + LR0.0001	0.096	0.014	0.797	0.11	0.017	0.783
L1 + LR0.00001	0.085	0.01	0.863	0.078	0.014	0.815
L2 + LR0.001	0.133	0.026	0.644	0.194	0.058	0.279
L2 + LR0.0001	0.082	0.01	0.86	0.096	0.016	0.796
L2 + LR0.00001	0.093	0.015	0.791	0.126	0.026	0.671

In summary, the performance of experimental parameter L1 + LR0.00001 was the best. From the experimental data, the evaluation metrics of the test set were relatively lower than those of the validation set, indicating the possibility of overfitting, with the most obvious being experimental parameter L2 + LR0.001, which had MAE, MSE, and R^2 differences of −0.061, −0.032, and 0.365 between the validation and test sets, respectively. Compared with the results of point cloud data and RGB data, the test set of RGB data had more severe overfitting. In the test set, the MAE and MSE values of point cloud data were 0.051 and 0.014 lower than those of RGB data, respectively, and the R^2 value was 0.168 higher than that of RGB data. Overall, the results of point cloud data were better than those of RGB data, which may have been due to the fact that point cloud data are three-dimensional, while RGB data are two-dimensional, providing more information and resulting in better results.

3.2. Multi-Modal Data for LAI Estimation of Citrus Trees

The training process of VPNet using RGB and point cloud data as training data is shown in Figure 11, and the results of the validation and test sets are presented in Table 6. The training models of all experimental parameters converged quickly, with most of them having already converged by epoch 50. The amplitude of data fluctuations was generally small, with the most stable being the experimental parameter L2 + LR0.00001, which converged to a straight line after convergence, while the most volatile was the experimental parameter L1 + LR0.001, although it was the most effective. The training data of each experimental parameter were relatively close, and the results were better.

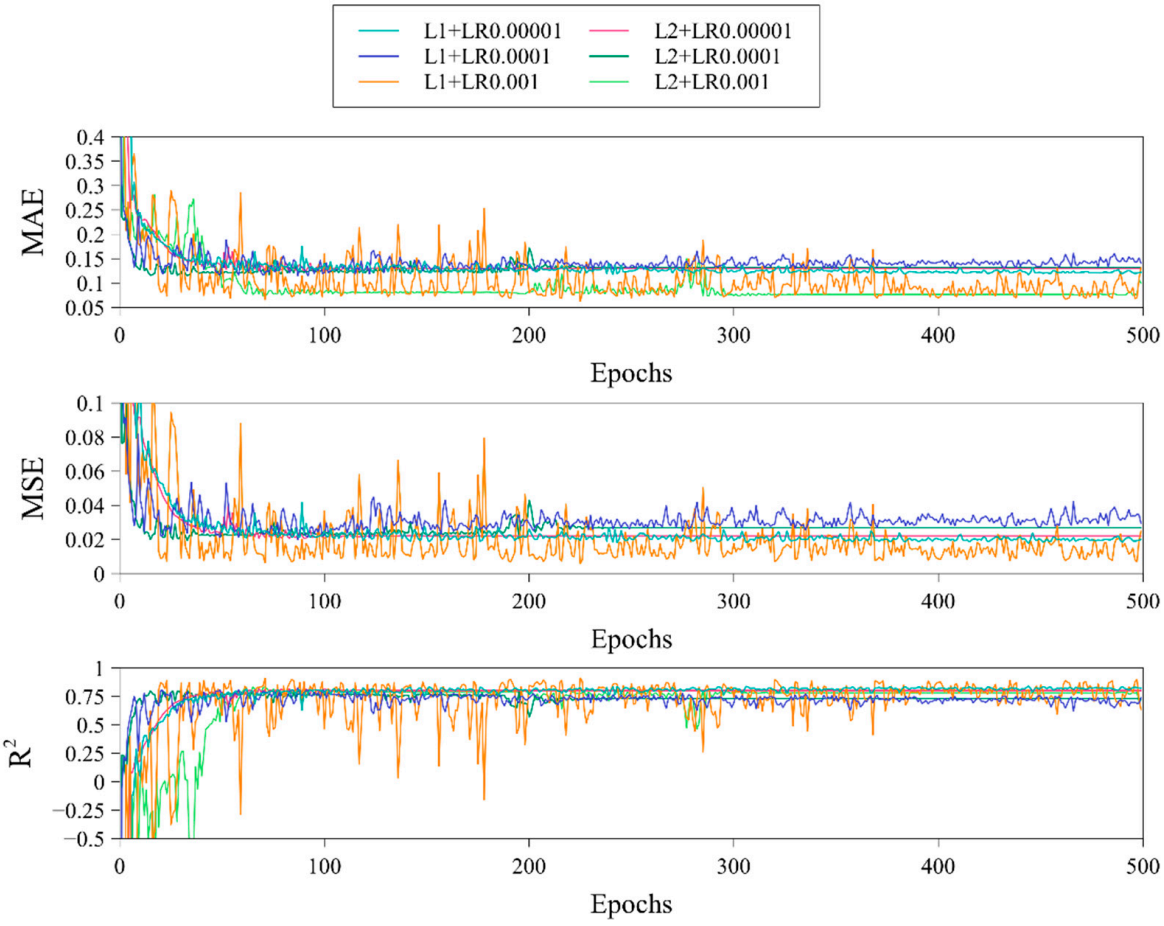

Figure 11. Training process of VPNet with multi-modal data as training data.

Table 6. Training results of VPNet with multi-modal data as training data.

Experimental Parameters	Validation			Test		
	MAE	MSE	R^2	MAE	MSE	R^2
L1 + LR0.001	0.062	0.005	0.914	0.078	0.008	0.861
L1 + LR0.0001	0.114	0.019	0.825	0.08	0.009	0.829
L1 + LR0.00001	0.117	0.017	0.841	0.066	0.010	0.805
L2 + LR0.001	0.076	0.009	0.834	0.079	0.009	0.849
L2 + LR0.0001	0.115	0.019	0.804	0.101	0.017	0.813
L2 + LR0.00001	0.124	0.02	0.816	0.081	0.012	0.765

The MAE values in the test set data were generally below 0.1, the majority of the MSE values were below 0.01, and the majority of the R^2 values were above 0.8. The evaluation metrics were better than those of RGB and point cloud data, which may have been due to the fusion of data supplementing some information and achieving optimal training results. The performance of the experimental parameter L1 + LR0.001 was the best, possibly because the larger learning rate parameter setting made it easier for the model to avoid the limitations of locally optimal solutions and find better results, but the problem it brought was that the volatility of the training data was higher, and the stability was poorer.

The multi-modal data were tested under the experimental parameter L1 + LR0.001, and the results are shown in Figure 12. By observing the graphs, it is clear that the fit of the multi-modal data is good.

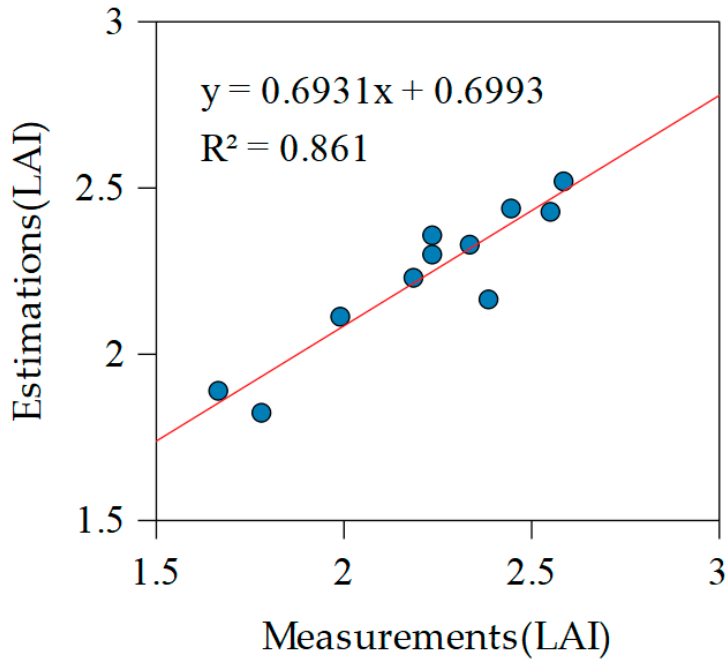

Figure 12. Comparison of LAI from ground measurements with LAI estimated by the inverse model.

3.3. Exploding and Vanishing Gradients of Multi-Modal Data Problem

In the experiments, it was found that the point cloud data have special properties, which may lead to the exploding gradients problem. The point cloud data consist of a large number of discrete points, each with 3-D coordinates and color information, for a total of six parameters. However, the values of these parameters vary greatly from one another, and this instability may be exacerbated when transformed into a 3-D tensor in a deep-learning model, leading to the emergence of the exploding gradients problem. Specifically, as the number of layers of the neural network increases, each layer of the activation function generates a certain amount of gradients. If these gradient values are large, the gradients accumulate during the backpropagation process, which may eventually cause the gradient

values to become very large, even beyond the representation range of the computer, leading to the exploding gradients problem. This problem usually leads to models that do not converge or produce unstable results. To solve this problem, the data can be normalized to limit the values to the range of 0 to 1 to avoid the problems of neuron saturation and non-uniformity of the underlying metric units, thus avoiding the exploding gradients and speeding up the convergence of the neural network. The principle of normalization processing is shown in Formula (4). Examples of the normalization process are shown in Table 7.

$$f(x) = \frac{x - \min(x)}{\max(x) - \min(x)} \tag{4}$$

In PCNet, the problem of vanishing gradients could occur when using the ReLU activation function after the convolution and pooling layers. This was due to the fact that the weights may have negative values during backpropagation, which would become 0 after ReLU processing, resulting in vanishing gradients. Additionally, if the number of network layers was too high, the signal would decay during propagation, causing the gradient to approach 0 in later layers, making the network unable to continue learning. To address this issue, PCNet used the SELU activation function after the convolution and pooling layers [48]. SELU did not have a dead zone when the weight was less than 0, while it could be scaled up when the weight was greater than 0, effectively avoiding vanishing gradients. Therefore, the use of the SELU activation function could effectively solve the problem of vanishing gradients in PCNet.

The experimental parameter L1 + LR0.001 was used as the basis, the activation function and batch normalization were used as the variable parameters, and the specific parameter settings are shown in Table 8. As shown in Figure 13, different parameter settings can have a great impact on the performance of PCNet. When using the ReLU activation function, the MAE, MSE, and R^2 fluctuated slightly around 0.2, 0.08, and 0, respectively, due to vanishing gradients. When no normalization was used, the MAE fluctuated widely above 0.2, the MSE fluctuated widely above 0.08, and the R^2 fluctuated widely below 0. Therefore, proper activation function and normalization were crucial to the performance of PCNet. The principles of ReLU and SELU are shown in Formulas (5) and (6).

$$\mathrm{ReLU}(x) = \max(0, x) \tag{5}$$

$$\mathrm{SELU}(x) = \lambda \begin{cases} x & x > 0 \\ \alpha e^x - \alpha & x \leq 0 \end{cases} \tag{6}$$

where Formula (6) of α is 1.67326324235437728481704299167 17, and λ is 1.05070098735548 04934193349852946.

Table 7. Example of normalized point cloud data processing.

Method	Point Cloud	*X*-Axis	*Y*-Axis	*Z*-Axis	Red	Green	Blue
Original Data	1	655,215.95899963	2,592,974.80603027	6.21799994	113	138	92
	2	655,215.96000671	2,592,974.75402832	6.15500021	146	178	123
	3	655,215.96400452	2,592,974.74298096	6.14599991	149	178	123
Min-Max Normalization	1	0.010779881646158174	0.8936204728670418	0.049631731939932866	0.2924528301886793	0.3368983957219251	0.2431192660550459
	2	0.00040218885987997055	0.8812293692026287	0.018224273530279778	0.48584905660377353	0.588235294117647	0.408256880733945
	3	0.0019987597479484975	0.8763324494939297	0.014734433142619796	0.5	0.588235294117647	0.408256880733945

Table 8. Combinations of different parameter settings for PCNet.

Group	Activation Function	Batch Normalization
Group A	ReLU	YES
Group B	SELU	YES
Group C	SELU	NO

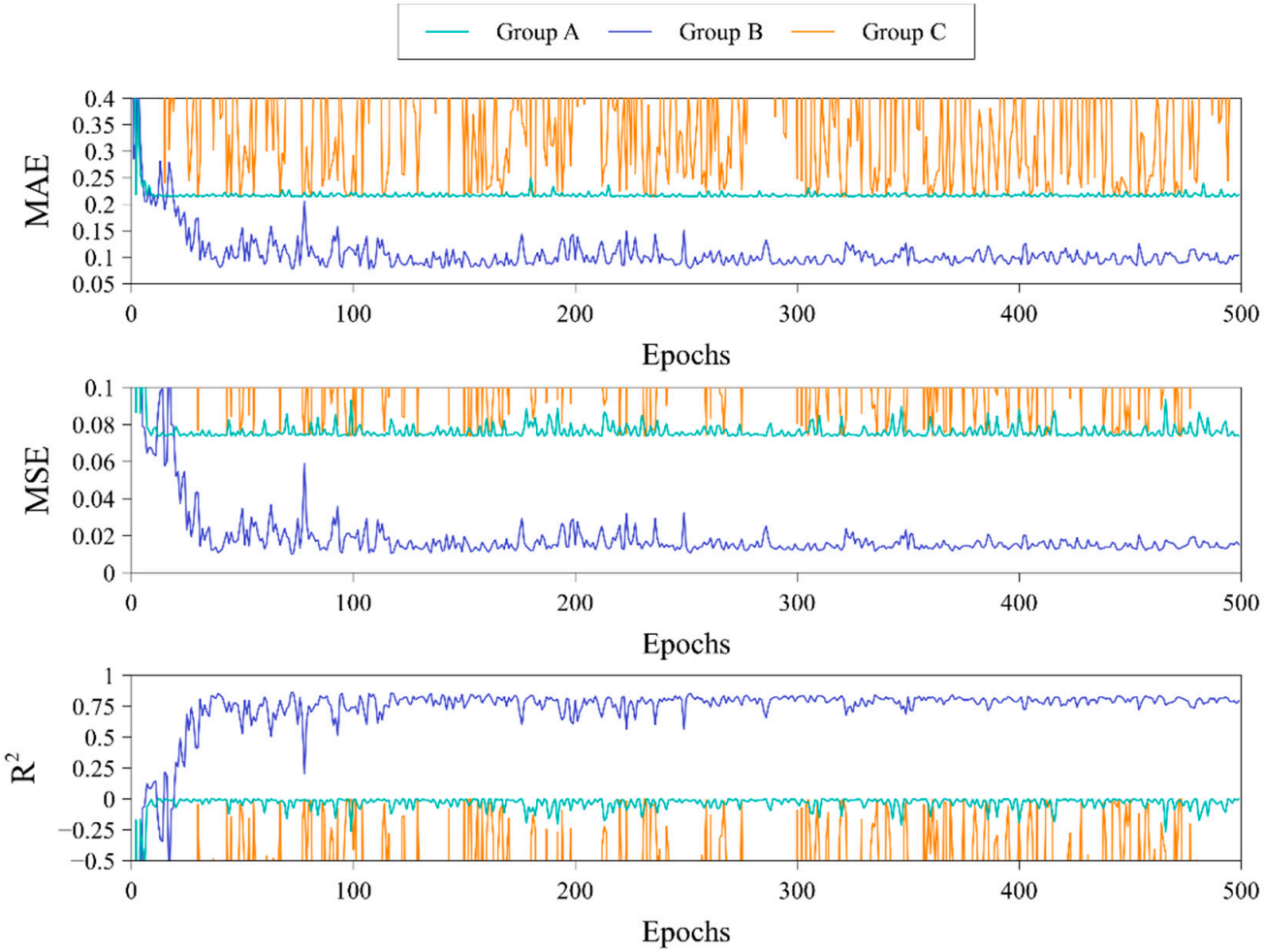

Figure 13. Training process of PCNet with different parameter settings.

4. Discussion

4.1. Feasibility of Estimating LAI from RGB Data and Point Cloud Data

UAV RGB data can provide a wealth of information about vegetation, including vegetation color, texture, and morphology. Among the acquired images of citrus trees, new leaves appear in some images, which are characterized by a more lime green color, and older leaves appear darker in comparison. In addition, the new leaves are also relatively smaller in size, and these characteristics may help to estimate the LAI. Point cloud data are composed of a large number of discrete points, each containing 3-D coordinates and color information of the vegetation. These data can be used to construct a 3-D model of the vegetation, providing additional vegetation information, such as vegetation height, density, and structure, which can be used to further optimize the LAI estimation results. However, there may be some limitations and errors in using these two types of data alone, so fusing them to estimate LAI can improve the precision and accuracy of LAI estimation. The fused use of drone RGB data and point cloud data can make full use of the data and improve data utilization, thus better supporting agricultural production. Deep-learning

networks have been very successful in areas such as image recognition and regression prediction [49], and their application in LAI estimation also has great potential. Deep-learning networks can learn features and relationships automatically without the need for manual feature extraction [50], thus improving the precision and accuracy of LAI estimation. By designing a suitable deep-learning network, the generalization ability and robustness of the model can be improved, making the results of LAI estimation more reliable and accurate.

4.2. Setting of Loss Function and Learning Rate Hyperparameters

In the training process of the three models, using L1 regularization and a larger learning rate (LR0.001) leads to optimal training results with the smallest MAE and MSE values and the highest R^2 value. In contrast, using L2 regularization and a smaller learning rate (LR0.00001) results in poorer training, with larger MAE and MSE and lower R^2. Overall, L1 regularization is more effective than L2 regularization, which indicates that L1 regularization can effectively control the complexity of the model and avoid overfitting. This may be due to the sparsity of L1 regularization, which can select some features with weight values of 0, thus reducing the complexity of the model, as well as having stronger penalties to better suppress the growth of weights. In addition, using a larger learning rate can also obtain better results. This may be due to the fact that a larger learning rate can better capture the information in the data when the data distribution is sparse or noisy, thus improving the model's effectiveness and enabling a better convergence rate. However, it is important to note that a larger learning rate may lead to model instability, so the choice needs to be made on a case-by-case basis.

4.3. The Role of Multi-Modal Data in Estimation Result Improvement

Different data sources can provide different information; for example, RGB data can provide color and texture information, while point cloud data can provide shape and depth information. Using multi-modal data can combine this information to provide more comprehensive data, which in turn can improve the accuracy and precision of prediction results. In fact, prediction results using multi-modal data are more accurate than single data sources [41,51–53]. According to the experimental data, the results of using multi-modal data for estimation showed that compared to the estimation results of RGB data and point cloud data, the MAE was reduced by 0.024 and 0.016, the MSE was reduced by 0.008 and 0.005, and the R^2 was improved by 0.105 and 0.055, respectively. Our method was compared with the method of Raj [39], which used RGB images taken by UAV to estimate the LAI of the citrus canopy, and the results showed that the R^2 of our method was 0.131 higher than Raj's method. These indicate that increasing the data types can improve the generalization ability and robustness of the model, making the estimation results more reliable. Another important advantage of using multi-modal data is that they can reduce the dependence of the model on a single data source, thus improving the robustness of the model. This means that the model can still operate normally even if there is an anomaly in a particular data type, thus making the model more robust to anomalous data. Therefore, adding more data sources can improve the expressiveness of the model, thus allowing the model to better adapt to complex real-world scenarios and improve the precision and accuracy of the prediction results. In practical applications, multi-modal data should be used as much as possible so as to improve the performance and reliability of the model.

4.4. Estimation Model Optimization for Multi-Modal Data

RGB data and point cloud data were used for the LAI estimation of citrus trees. The acquisition of point cloud data takes a long time for extraction, so in future studies, we can try to use faster LiDAR data or other fast-acquired data sources (thermal infrared images, hyperspectral images, etc.) instead to improve data acquisition efficiency and accuracy. This will provide new ideas and possibilities for the LAI estimation of citrus trees. In future

research, more datasets with more time periods can be added. The current dataset was collected at a single time, and adding more data from different time periods can provide the model with a stronger generalization ability and improve the prediction ability of the model in different seasons and growth stages. Also, increasing the number of datasets can enhance the robustness of the model and reduce the risk of overfitting. Data fusion is the key to achieving LAI estimation of citrus trees in this study. The methods and techniques of data fusion need to be continuously optimized and improved. For example, attempts can be made to extract fewer features to reduce the amount of data and improve the accuracy and reliability of the data. Meanwhile, more efficient data-fusion algorithms can be explored to improve the accuracy and stability of estimation models. In addition, in the data-fusion network, a more lightweight estimation model can be attempted to achieve a function that can be loaded on the UAV platform for online real-time LAI estimation. This will provide more efficient and accurate decision support for agricultural production and improve the efficiency and quality of agricultural production. Therefore, future research can explore a variety of different lightweight models to achieve the need for real-time estimation of LAI.

5. Conclusions

RGB data and point cloud data collected by a UAV platform were used to estimate the LAI of citrus trees using deep neural networks, and three models, VoVNet, PCNet, and VPNet, were constructed for the LAI estimation of RGB data, point cloud data, and multi-modal data, respectively. The experimental results demonstrate that the use of multi-modal data yielded the best results in estimating the LAI of citrus trees, and it showed the highest performance in terms of evaluation metrics. Additionally, the use of point cloud data also yielded good results. Specifically, both types of data achieved an R^2 value above 0.8. This confirms that multi-modal data have a better predictive effect on LAI estimation for citrus trees compared to single-modal data, and they effectively improve the accuracy of prediction. Furthermore, the choice of the loss function and learning rate settings significantly impacted the results. In general, the use of the L1 loss function achieved better results than L2, and training with a smaller learning rate resulted in better performance. In conclusion, the proposed method of estimating the LAI of citrus trees via the fusion of RGB data and point cloud data collected by the UAV platform provides a new non-destructive means for agricultural production, which can help farmers better grasp the growth condition of citrus trees and improve the efficiency and quality of agricultural production. In the future, we will further explore the application of the UAV platform in agricultural production and make a greater contribution to the modernization and sustainable development of agriculture.

Author Contributions: Conceptualization, Y.Z. and X.L.; methodology, Y.Z., X.L. and W.L.; validation, X.L. and H.Z.; formal analysis, X.L., W.L., H.Z. and D.Y.; investigation, Y.Z., D.Y., J.Y., X.X., X.L. and J.X.; resources, X.L., W.L. and Y.Z.; data curation, X.L. and H.Z.; writing—original draft preparation, X.L., J.X. and Y.Z.; writing—review and editing, Y.Z. and Y.L.; visualization, J.X.; supervision Y.L.; project administration, Y.Z.; funding acquisition, Y.Z. and Y.L. All authors have read and agreed to the published version of the manuscript.

Funding: This research was funded by the Laboratory of Lingnan Modern Agriculture Project, grant number NT2021009; the Key Field Research and Development Plan of Guangdong Province, China, grant number 2019B020221001; and the 111 Project, grant number D18019.

Data Availability Statement: The data presented in this study are available on request from the corresponding author.

Conflicts of Interest: The authors declare no conflict of interest.

References

1. Rehman, A.; Deyuan, Z.; Hussain, I.; Iqbal, M.S.; Yang, Y.; Jingdong, L. Prediction of Major Agricultural Fruits Production in Pakistan by Using an Econometric Analysis and Machine Learning Technique. *Int. J. Fruit Sci.* **2018**, *18*, 445–461. [CrossRef]
2. Nawaz, R.; Abbasi, N.A.; Ahmad Hafiz, I.; Khalid, A.; Ahmad, T.; Aftab, M. Impact of Climate Change on Kinnow Fruit Industry of Pakistan. *Agrotechnology* **2019**, *8*, 2. [CrossRef]
3. Abdullahi, H.S.; Mahieddine, F.; Sheriff, R.E. Technology Impact on Agricultural Productivity: A Review of Precision Agriculture Using Unmanned Aerial Vehicles. In *Proceedings of the Wireless and Satellite Systems*; Pillai, P., Hu, Y.F., Otung, I., Giambene, G., Eds.; Springer: Cham, Switzerland, 2015; pp. 388–400.
4. Mogili, U.R.; Deepak, B.B.V.L. Review on Application of Drone Systems in Precision Agriculture. *Procedia Comput. Sci.* **2018**, *133*, 502–509. [CrossRef]
5. Lieret, M.; Lukas, J.; Nikol, M.; Franke, J. A Lightweight, Low-Cost and Self-Diagnosing Mechatronic Jaw Gripper for the Aerial Picking with Unmanned Aerial Vehicles. *Procedia Manuf.* **2020**, *51*, 424–430. [CrossRef]
6. Yang, G.; Liu, J.; Zhao, C.; Li, Z.; Huang, Y.; Yu, H.; Xu, B.; Yang, X.; Zhu, D.; Zhang, X.; et al. Unmanned Aerial Vehicle Remote Sensing for Field-Based Crop Phenotyping: Current Status and Perspectives. *Front. Plant Sci.* **2017**, *8*, 1111. [CrossRef]
7. Boursianis, A.D.; Papadopoulou, M.S.; Diamantoulakis, P.; Liopa-Tsakalidi, A.; Barouchas, P.; Salahas, G.; Karagiannidis, G.; Wan, S.; Goudos, S.K. Internet of Things (IoT) and Agricultural Unmanned Aerial Vehicles (UAVs) in Smart Farming: A Comprehensive Review. *Internet Things* **2022**, *18*, 100187. [CrossRef]
8. Zhang, C.; Kovacs, J.M. The Application of Small Unmanned Aerial Systems for Precision Agriculture: A Review. *Precis. Agric.* **2012**, *13*, 693–712. [CrossRef]
9. Nijland, W.; de Jong, R.; de Jong, S.M.; Wulder, M.A.; Bater, C.W.; Coops, N.C. Monitoring Plant Condition and Phenology Using Infrared Sensitive. *Agric. For. Meteorol.* **2014**, *184*, 98–106. [CrossRef]
10. Zhang, H.; Wang, L.; Tian, T.; Yin, J. A Review of Unmanned Aerial Vehicle Low-Altitude Remote Sensing (UAV-LARS) Use in Agricultural Monitoring. *Remote Sens.* **2021**, *13*, 1221. [CrossRef]
11. Pádua, L.; Vanko, J.; Hruška, J.; Adão, T.; Sousa, J.J.; Peres, E.; Morais, R. UAS, Sensors, and Data Processing in Agroforestry: A Review towards Practical Applications. *Int. J. Remote Sens.* **2017**, *38*, 2349–2391. [CrossRef]
12. Anthony, D.; Elbaum, S.; Lorenz, A.; Detweiler, C. On Crop Height Estimation with UAVs. In Proceedings of the 2014 IEEE/RSJ International Conference on Intelligent Robots and Systems, Chicago, IL, USA, 14–18 September 2014; pp. 4805–4812.
13. García-Martínez, H.; Flores-Magdaleno, H.; Ascencio-Hernández, R.; Khalil-Gardezi, A.; Tijerina-Chávez, L.; Mancilla-Villa, O.R.; Vázquez-Peña, M.A. Corn Grain Yield Estimation from Vegetation Indices, Canopy Cover, Plant Density, and a Neural Network Using Multispectral and RGB Images. *Agriculture* **2020**, *10*, 277. [CrossRef]
14. Lin, G.; GuiJun, Y.; BaoShan, W.; HaiYang, Y.; Bo, X.; HaiKuan, F. Soybean leaf area index retrieval with UAV (Unmanned Aerial Vehicle) remote sensing imagery. *Zhongguo Shengtai Nongye Xuebao/Chin. J. Eco-Agric.* **2015**, *23*, 868–876.
15. Zarco-Tejada, P.J.; Guillén-Climent, M.L.; Hernández-Clemente, R.; Catalina, A.; González, M.R.; Martín, P. Estimating Leaf Carotenoid Content in Vineyards Using High Resolution Hyperspectral Imagery Acquired from an Unmanned Aerial Vehicle (UAV). *Agric. For. Meteorol.* **2013**, *171*, 281–294. [CrossRef]
16. Yin, G.; Li, A.; Jin, H.; Zhao, W.; Bian, J.; Qu, Y.; Zeng, Y.; Xu, B. Derivation of Temporally Continuous LAI Reference Maps through Combining the LAINet Observation System with CACAO. *Agric. For. Meteorol.* **2017**, *233*, 209–221. [CrossRef]
17. Watson, D.J. Comparative Physiological Studies on the Growth of Field Crops: I. Variation in Net Assimilation Rate and Leaf Area between Species and Varieties, and within and between Years. *Ann. Bot.* **1947**, *11*, 41–76. [CrossRef]
18. Patil, P.; Biradar, P.U.; Bhagawathi, A.S.; Hejjegar, I. A Review on Leaf Area Index of Horticulture Crops and Its Importance. *Int. J. Curr. Microbiol. App. Sci* **2018**, *7*, 505–513. [CrossRef]
19. Bréda, N.J.J. Ground-based Measurements of Leaf Area Index: A Review of Methods, Instruments and Current Controversies. *J. Exp. Bot.* **2003**, *54*, 2403–2417. [CrossRef] [PubMed]
20. Yan, G.; Hu, R.; Luo, J.; Weiss, M.; Jiang, H.; Mu, X.; Xie, D.; Zhang, W. Review of Indirect Optical Measurements of Leaf Area Index: Recent Advances. Challenges, and Perspectives. *Agric. For. Meteorol.* **2019**, *265*, 390–411. [CrossRef]
21. Leblanc, S.G.; Chen, J.M.; Kwong, M. Tracing radiation and architecture of canopies. In *TRAC Manual, Ver. 2.1.3*; Natural Resources Canada; Canada Centre for Remote Sensing: Ottawa, ON, Canada, 2002; p. 25.
22. Knerl, A.; Anthony, B.; Serra, S.; Musacchi, S. Optimization of Leaf Area Estimation in a High-Density Apple Orchard Using Hemispherical Photography. *HortScience* **2018**, *53*, 799–804. [CrossRef]
23. Chen, L.; Wu, G.; Chen, G.; Zhang, F.; He, L.; Shi, W.; Ma, Q.; Sun, Y. Correlative Analyses of LAI, NDVI, SPAD and Biomass of Winter Wheat in the Suburb of Xi'an. In Proceedings of the 2011 19th International Conference on Geoinformatics, Shanghai, China, 24–26 June 2011; pp. 1–5.
24. Brandão, Z.N.; Zonta, J.H. Hemispherical Photography to Estimate Biophysical Variables of Cotton. *Rev. Bras. Eng. Agríc. Ambient.* **2016**, *20*, 789–794. [CrossRef]
25. Mu, Y.; Fujii, Y.; Takata, D.; Zheng, B.; Noshita, K.; Honda, K.; Ninomiya, S.; Guo, W. Characterization of Peach Tree Crown by Using High-Resolution Images from an Unmanned Aerial Vehicle. *Hortic. Res.* **2018**, *5*, 74. [CrossRef]

26. Raj, R.; Walker, J.P.; Pingale, R.; Nandan, R.; Naik, B.; Jagarlapudi, A. Leaf Area Index Estimation Using Top-of-Canopy Airborne RGB Images. *Int. J. Appl. Earth Obs. Geoinf.* **2021**, *96*, 102282. [CrossRef]
27. Comba, L.; Biglia, A.; Ricauda Aimonino, D.; Tortia, C.; Mania, E.; Guidoni, S.; Gay, P. Leaf Area Index Evaluation in Vineyards Using 3D Point Clouds from UAV Imagery. *Precis. Agric.* **2020**, *21*, 881–896. [CrossRef]
28. Wang, L.; Chang, Q.; Li, F.; Yan, L.; Huang, Y.; Wang, Q.; Luo, L. Effects of Growth Stage Development on Paddy Rice Leaf Area Index Prediction Models. *Remote Sens.* **2019**, *11*, 361. [CrossRef]
29. Zarate-Valdez, J.L.; Whiting, M.L.; Lampinen, B.D.; Metcalf, S.; Ustin, S.L.; Brown, P.H. Prediction of Leaf Area Index in Almonds by Vegetation Computers and Electronics. *Agriculture* **2012**, *85*, 24–32. [CrossRef]
30. Diago, M.-P.; Correa, C.; Millán, B.; Barreiro, P.; Valero, C.; Tardaguila, J. Grapevine Yield and Leaf Area Estimation Using Supervised Classification Methodology on RGB Images Taken under Field Conditions. *Sensors* **2012**, *12*, 16988–17006. [CrossRef]
31. Hasan, U.; Sawut, M.; Chen, S. Estimating the Leaf Area Index of Winter Wheat Based on Unmanned Aerial Vehicle RGB-Image Parameters. *Sustainability* **2019**, *11*, 6829. [CrossRef]
32. Yamaguchi, T.; Tanaka, Y.; Imachi, Y.; Yamashita, M.; Katsura, K. Feasibility of Combining Deep Learning and RGB Images Obtained by Unmanned Aerial Vehicle for Leaf Area Index Estimation in Rice. *Remote Sens.* **2021**, *13*, 84. [CrossRef]
33. Li, S.; Dai, L.; Wang, H.; Wang, Y.; He, Z.; Lin, S. Estimating Leaf Area Density of Individual Trees Using the Point Cloud Segmentation of Terrestrial LiDAR Data and a Voxel-Based Model. *Remote Sens.* **2017**, *9*, 1202. [CrossRef]
34. Li, M.; Shamshiri, R.R.; Schirrmann, M.; Weltzien, C.; Shafian, S.; Laursen, M.S. UAV Oblique Imagery with an Adaptive Micro-Terrain Model for Estimation of Leaf Area Index and Height of Maize Canopy from 3D Point Clouds. *Remote Sens.* **2022**, *14*, 585. [CrossRef]
35. Yang, J.; Xing, M.; Tan, Q.; Shang, J.; Song, Y.; Ni, X.; Wang, J.; Xu, M. Estimating Effective Leaf Area Index of Winter Wheat Based on UAV Point Cloud Data. *Drones* **2023**, *7*, 299. [CrossRef]
36. Song, Y.; Wang, J.; Shang, J. Estimating Effective Leaf Area Index of Winter Wheat Using Simulated Observation on Unmanned Aerial Vehicle-Based Point Cloud Data. *IEEE J. Sel. Top. Appl. Earth Obs. Remote Sens.* **2020**, *13*, 2874–2887. [CrossRef]
37. Mazzini, R.B.; Ribeiro, R.V.; Pio, R.M. A Simple and Non-Destructive Model for Individual Leaf Area Estimation in Citrus. *Fruits* **2010**, *65*, 269–275. [CrossRef]
38. Dutra, A.D.; Filho, M.A.C.; Pissinato, A.G.V.; Gesteira, A.d.S.; Filho, W.d.S.S.; Fancelli, M. Mathematical Models to Estimate Leaf Area of Citrus Genotypes. *AJAR* **2017**, *12*, 125–132. [CrossRef]
39. Raj, R.; Suradhaniwar, S.; Nandan, R.; Jagarlapudi, A.; Walker, J. Drone-Based Sensing for Leaf Area Index Estimation of Citrus Canopy. In *Proceedings of UASG 2019*; Jain, K., Khoshelham, K., Zhu, X., Tiwari, A., Eds.; Springer International Publishing: Cham, Switzerland, 2020; pp. 79–89.
40. Maimaitijiang, M.; Sagan, V.; Sidike, P.; Hartling, S.; Esposito, F.; Fritschi, F.B. Soybean Yield Prediction from UAV Using Multimodal Data Fusion and Deep Learning. *Remote Sens. Environ.* **2020**, *237*, 111599. [CrossRef]
41. Zhang, Y.; Ta, N.; Guo, S.; Chen, Q.; Zhao, L.; Li, F.; Chang, Q. Combining Spectral and Textural Information from UAV RGB Images for Leaf Area Index Monitoring in Kiwifruit Orchard. *Remote Sens.* **2022**, *14*, 1063. [CrossRef]
42. Wu, S.; Deng, L.; Guo, L.; Wu, Y. Wheat Leaf Area Index Prediction Using Data Fusion Based on High-Resolution Unmanned Aerial Vehicle Imagery. *Plant Methods* **2022**, *18*, 68. [CrossRef]
43. Anthony, B.; Serra, S.; Musacchi, S. Optimization of Light Interception, Leaf Area and Yield in "WA38": Comparisons among Training Systems, Rootstocks and Pruning Techniques. *Agronomy* **2020**, *10*, 689. [CrossRef]
44. Chianucci, F.; Cutini, A. Digital Hemispherical Photography for Estimating Forest Canopy Properties: Current Controversies and Opportunities. *iForest-Biogeosci. For.* **2012**, *5*, 290. [CrossRef]
45. Jocher, G.; Chaurasia, A.; Qiu, J. YOLO by Ultralytics. 2023. Available online: https://github.com/ultralytics/ultralytics (accessed on 10 April 2023).
46. Lee, Y.; Hwang, J.; Lee, S.; Bae, Y.; Park, J. An Energy and GPU-Computation Efficient Backbone Network for Real-Time Object Detection. In Proceedings of the 2019 IEEE/CVF Conference on Computer Vision and Pattern Recognition Workshops (CVPRW), Long Beach, CA, USA, 16–17 June 2019.
47. Huang, G.; Liu, Z.; van der Maaten, L.; Weinberger, K.Q. Densely Connected Convolutional Networks. In Proceedings of the IEEE Conference on Computer Vision and Pattern Recognition, Honolulu, HI, USA, 21–26 July 2017; pp. 4700–4708.
48. Klambauer, G.; Unterthiner, T.; Mayr, A.; Hochreiter, S. Self-Normalizing Neural Networks. In Proceedings of the Advances in Neural Information Processing Systems, Long Beach, CA, USA, 4–9 December 2017; Curran Associates, Inc.: New York, NY, USA, 2017; Volume 30.
49. Liu, W.; Wang, Z.; Liu, X.; Zeng, N.; Liu, Y.; Alsaadi, F.E. A Survey of Deep Neural Network Architectures and Their Applications. *Neurocomputing* **2017**, *234*, 11–26. [CrossRef]
50. Pouyanfar, S.; Sadiq, S.; Yan, Y.; Tian, H.; Tao, Y.; Reyes, M.P.; Shyu, M.-L.; Chen, S.-C.; Iyengar, S.S. A Survey on Deep Learning: Algorithms. Techniques, and Applications. *ACM Comput. Surv.* **2018**, *51*, 1–36. [CrossRef]
51. Mohd Ali, M.; Hashim, N.; Abd Aziz, S.; Lasekan, O. Utilisation of Deep Learning with Multi-modal Data Fusion for Determination of Pineapple Quality Using Thermal Imaging. *Agronomy* **2023**, *13*, 401. [CrossRef]

52. Patil, R.R.; Kumar, S. Rice-Fusion: A Multi-modality Data Fusion Framework for Rice Disease Diagnosis. *IEEE Access* **2022**, *10*, 5207–5222. [CrossRef]
53. Zhang, Y.; Han, W.; Zhang, H.; Niu, X.; Shao, G. Evaluating Soil Moisture Content under Maize Coverage Using UAV Multi-modal Data by Machine Learning Algorithms. *J. Hydrol.* **2023**, *617*, 129086. [CrossRef]

Disclaimer/Publisher's Note: The statements, opinions and data contained in all publications are solely those of the individual author(s) and contributor(s) and not of MDPI and/or the editor(s). MDPI and/or the editor(s) disclaim responsibility for any injury to people or property resulting from any ideas, methods, instructions or products referred to in the content.

frontiers | Frontiers in Plant Science

TYPE Original Research
PUBLISHED 02 February 2023
DOI 10.3389/fpls.2023.1101828

Check for updates

OPEN ACCESS

EDITED BY
Lei Shu,
Nanjing Agricultural University, China

REVIEWED BY
Jiandong Hu,
Henan Agricultural University, China
Aqil Tariq,
Wuhan University, China
Mohd Rizal Arshad,
Universiti Sains Malaysia Engineering Campus, Malaysia

*CORRESPONDENCE
Yubin Lan
ylan@scau.edu.cn
Yali Zhang
ylzhang@scau.edu.cn

SPECIALTY SECTION
This article was submitted to Sustainable and Intelligent Phytoprotection, a section of the journal Frontiers in Plant Science

RECEIVED 18 November 2022
ACCEPTED 20 January 2023
PUBLISHED 02 February 2023

CITATION
Tian H, Mo Z, Ma C, Xiao J, Jia R, Lan Y and Zhang Y (2023) Design and validation of a multi-objective waypoint planning algorithm for UAV spraying in orchards based on improved ant colony algorithm. *Front. Plant Sci.* 14:1101828. doi: 10.3389/fpls.2023.1101828

COPYRIGHT
© 2023 Tian, Mo, Ma, Xiao, Jia, Lan and Zhang. This is an open-access article distributed under the terms of the Creative Commons Attribution License (CC BY). The use, distribution or reproduction in other forums is permitted, provided the original author(s) and the copyright owner(s) are credited and that the original publication in this journal is cited, in accordance with accepted academic practice. No use, distribution or reproduction is permitted which does not comply with these terms.

Design and validation of a multi-objective waypoint planning algorithm for UAV spraying in orchards based on improved ant colony algorithm

Haoxin Tian[1,2,3], Zhenjie Mo[1,2,3], Chenyang Ma[4], Junqi Xiao[1,2,3], Ruichang Jia[1,2,3], Yubin Lan[2,3,5]* and Yali Zhang[1,2,3]*

[1]College of Engineering, South China Agricultural University, Guangzhou, China, [2]Guangdong Laboratory for Lingnan Modern Agriculture, Guangzhou, China, [3]National Center for International Collaboration Research on Precision Agricultural Aviation Pesticide Spraying Technology, Guangzhou, China, [4]College of Aerospace Engineering, Nanjing University of Aeronautics and Astronautics, Nanjing, China, [5]College of Electronic Engineering, College of Artificial Intelligence, South China Agricultural University, Guangzhou, China

Introduction: Current aerial plant protection with Unmanned Aerial Vehicles (UAV) usually applies full coverage route planning, which is challenging for plant protection operations in the orchards in South China. Because the fruit planting has the characteristics of dispersal and irregularity, full-coverage route spraying causes re-application as well as missed application, resulting in environmental pollution. Therefore, it is of great significance to plan an efficient, low-consumption and accurate plant protection route considering the flight characteristics of UAVs and orchard planting characteristics.

Methods: This study proposes a plant protection route planning algorithm to solve the waypoint planning problem of UAV multi-objective tasks in orchard scenes. By improving the heuristic function in Ant Colony Optimization (ACO), the algorithm combines corner cost and distance cost for multi-objective node optimization. At the same time, a sorting optimization mechanism was introduced to speed up the iteration speed of the algorithm and avoid the influence of inferior paths on the optimal results. Finally, Multi-source Ant Colony Optimization (MS-ACO) was proposed after cleaning the nodes of the solution path.

Results: The simulation results of the three test fields show that compared with ACO, the path length optimization rate of MS-ACO are 3.89%, 4.6% and 2.86%, respectively, the optimization rate of total path angles are 21.94%, 45.06% and 55.94%, respectively, and the optimization rate of node numbers are 61.05%, 74.84% and 75.47%, respectively. MS-ACO can effectively reduce the corner cost and the number of nodes. The results of field experiments show that for each test field, MS-ACO has a significant optimization effect compared with ACO, with an optimization rate of energy consumption per meter of more than 30%, the optimization rate of flight time are 46.67%, 56% and 59.01%, respectively, and the optimization rate of corner angle are 50.76%, 61.78% and 71.1%, respectively.

Discussion: The feasibility and effectiveness of the algorithm were further verified. The algorithm proposed in this study can optimize the spraying path according to

the position of each fruit tree and the flight characteristics of UAV, effectively reduce the energy consumption of UAV flight, improve the operating efficiency, and provide technical reference for the waypoint planning of plant protection UAV in the orchard scene.

KEYWORDS

UAV, waypoint planning, multi-objective, ant colony optimization, orchard plant protection

1 Introduction

As of 2021, China's total fruit output was 299.702 million tons, of which citrus output is 55.9561 million tons, ranking first in China 's fruit output (Stasistics, 2022). In the process of citrus production, pests and diseases are the main factors affecting the yield and safety of citrus (Du et al., 2011; Bassanezi et al., 2020), and efficient pest control methods are an indispensable and important link to ensure the yield and quality of citrus fruits (Yi, 2007; Zhang et al., 2014; Garcia et al., 2022). In recent years, with the development of precision agriculture, UAVs for plant protection have attracted widespread attention (Lan et al., 2019; Ru et al., 2020). The UAVs can take off and land vertically, with simple operation, high maneuverability and no terrain restrictions (Zhou et al., 2013; Yang et al., 2018), providing a new direction for the development of aerial plant protection technology.

In the research of UAV for plant protection, route planning is one of the key technologies to be solved urgently (Lan et al., 2017; Zhou et al., 2017). Local optimization for operating areas and routes is also a research hotspot for mobile robots (Zhao et al., 2017; Zhang et al., 2018). Liu et al. (2020) developed a short-range, accurate coverage route planning algorithm for aerial spraying with full coverage. In this method, the optimal route is obtained by analyzing the spraying voyage outside the spraying operation area and combining with the full-coverage route planning in order to avoid the problems of repeated and missed application in aerial pesticide application. Han et al. (2021) proposed an infield path planner that can automatically generate pattern-based X-turn path diagrams to provide efficient operation routes for polygonal rice fields. Xu et al. (2020) proposed a UAV route design algorithm for farmland with obstacles. The algorithm uses the characteristic information of the waypoints and combines the hybrid particle swarm algorithm to sort the waypoints, and designs a full-coverage route plan that can effectively avoid obstacles. These studies have carried out local optimization of the route according to the geometry of different farmlands, effectively improving the route coverage and ensuring the operation efficiency. However, this type of research is mainly aimed at densely planted rice field crops, and the operation method is mainly full-coverage reciprocating pesticide application. In the citrus orchard environment, fruit trees are different from field and facility horticultural crops, and have the characteristics of larger plant size, large planting spacing, and non-row planting (Wu et al., 2021). The application of UAVs for full-coverage route spraying may cause repeated and missed applications, and increase operating costs. At present, there are few studies on the precision route planning of UAV in orchard environment. Therefore, it is very important to carry out research on route planning for precision pesticide application in citrus fruit trees.

Route planning is a combinatorial optimization problem. Based on the known environment and operation information, a reasonable movement route was planned according to multiple constraints (Zhang et al., 2020; Zhou and He, 2021). In the route planning research of the orchard environment, we should not only consider the influence of the operating area, but also integrate the flight characteristics of the UAV to plan an operation route suitable for UAV plant protection in orchard. Although rotary-wing UAVs are better able to perform aerial transitions regardless of the terrain, there are still problems that cannot be ignored (Zhu et al., 2022). For example, the turning and starting and stopping of UAV during flight will cause a large energy loss (Fan et al., 2019). Alternatively, the load and battery of the UAV will also affect the battery life (Abeywickrama et al., 2018; Lin et al., 2020). Researchers proposed different solutions to the limitations of rotary-wing UAVs. Li et al. (2019) reduced the flight energy consumption of UAVs during non-working periods and improved operational efficiency by integrating constraints such as the spraying amount of each sortie and the returning point. Peng et al. (2019) used the autonomous constant-speed flight of UAVs and the minimum turning radius constraints to design a route planning method for UAVs in irregular farmland to achieve full-area coverage. Constraints such as distance, energy consumption, and operating time are the optimal route methods often used by researchers, because these constraints directly affect the operating efficiency and cost of UAVs.

At present, commonly used route planning algorithms include artificial potential field method (Zhang et al., 2017), ant colony algorithm (Patle et al., 2019), A* algorithm (Liu et al., 2019), genetic algorithm (Zhao et al., 2021) etc. The artificial potential field method and the A* algorithm have the advantages of simple and small amount of calculation (Huo et al., 2018), and can be better combined with other algorithms to solve various optimization problems. However, the artificial potential field method is mainly used for local trajectory search, usually as an auxiliary algorithm for global path search (Sun et al., 2017; Lin et al., 2019). The A* algorithm can quickly solve the shortest path between the starting point and the ending point, but it is not suitable for independently solving the path optimization problem that traverses all nodes (Erke et al., 2020; Tang et al., 2021a). Genetic algorithm and ant colony algorithm are both bionic algorithms (Tang et al., 2021b). Among them, genetic algorithm has good global optimization ability, but its operation

speed is slow and its search efficiency is low. The path search in the face of a large number of nodes is easy to fall into the local optimal solution, and the effect of solving the optimal path problem of traversing nodes is poor. ACO is a probabilistic algorithm that finds the optimal path through steps such as heuristic search, pheromone feedback, and distributed computing (Cao et al., 2021). This algorithm has good problem optimization ability, and is easy to combine with other algorithms, and is widely used to solve optimization problems such as traveling salesman and secondary allocation of resources (Ebadinezhad, 2020; Zhang et al., 2021b). For example, Liu et al. (2022) realized the plant protection route planning for many tea fields in hilly areas by combining genetic algorithm and ant colony algorithm. Cao et al. (2021) added the influence of agricultural machinery operation execution ability to the pheromone update mechanism of the ant colony algorithm, and realized the collaborative management of agricultural machinery. Therefore, this paper solves the route planning problem of plant protection drones in orchards by improving the ant colony algorithm.

In this study, aiming at the problems that UAV full coverage reciprocating routes cannot accurately cover every fruit tree, repeated application, missed application and high energy consumption, precision planning of UAV plant protection routes based on multi-objective tasks was carried out. By improving the ant colony algorithm and integrating the three constraints of distance factor, rotation angle factor and the number of task nodes, MS-ACO was proposed to improve the efficiency of UAV operation and reduce flight energy consumption. First, the corner factor is introduced into the heuristic function of ACO. At the same time, a ranking optimization mechanism is added to the pheromone update. Finally, node cleaning is performed on the optimized path to obtain the optimal path. The algorithm can effectively optimize the path corner and the number of nodes under the condition of ensuring the path length, and improve the efficiency of plant protection. The results provide a theoretical basis for the research on aerial precision plant protection technology in orchards.

2 Materials and methods

This study mainly includes four parts: environment modeling, algorithm improvement, simulation experiment, and field experiment. The first part is the overview of the test area and the establishment of the environmental model; the second part is the improvement of the algorithm, including heuristic information fusion, pheromone update strategy based on sorting and optimization of optimal path nodes; comparing the paths optimized by MS-ACO and ACO with the number of nodes to verify the feasibility of the improved algorithm; finally, we use the built UAV platform to conduct field experiments, and verify the real validity of the algorithm through the optimization of flight time, range, turning angle and energy consumption per meter degree.

2.1 Experimental area overview

The experimental site is located in a citrus orchard in Sihui City, Guangdong Province, China (23°36′N, 112°68′E), as described in Figure 1A, B. The site is a near-plain terrain with an average slope of less than 5°, subtropical monsoon climate, and an average annual rainfall of about 1900 mm (Niu et al., 2021), which is suitable for citrus growth. The citrus trees in this orchard are mostly irregular terrain, divided by an irregular grid of 30×30m. The height of the fruit trees is between 2m and 5m, the average diameter of the crown is 3m, and the spacing between trees and rows is about 3m. We divided the experimental area into 14 plots according to the actual road distribution in the orchard, and selected the numbered 1, 4 and 6 for simulation experiments and field experiments, as shown in Figure 1C.

2.2 Environment modeling

In order to ensure that the path optimized by the improved algorithm has practical application value, the coordinate system of our

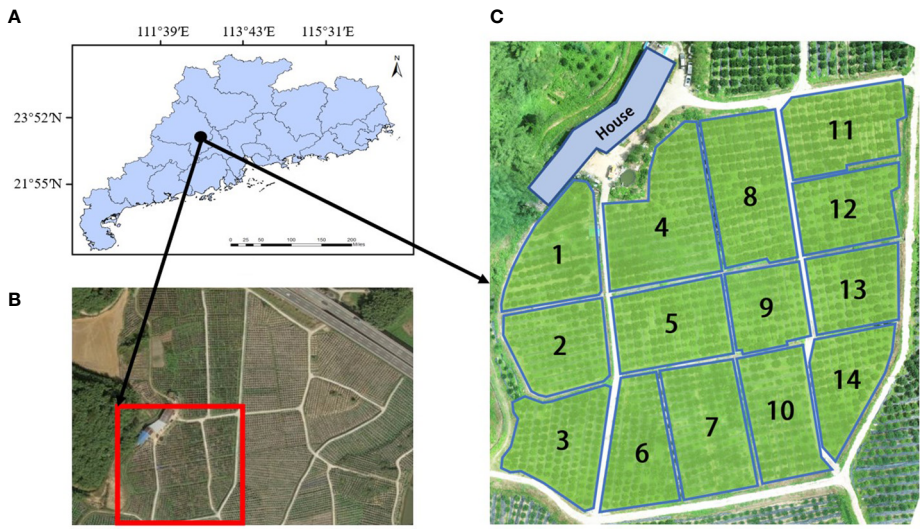

FIGURE 1
Experimental site and site division. **(A)** Geographic location of the experimental site, **(B)** Satellite map of the experimental area, **(C)** Division of the experimental area.

simulation environment was constructed by using the real geographic coordinate system of the orchard, and the simulation environment was constructed by extracting the geographic coordinate information of citrus trees. Since the experimental site of this study is a near-plain terrain with little difference in the height of the fruit trees, the effect of the difference between orchard elevation and tree height is not taken into account, and the coordinate system constructed is a two-dimensional plane coordinate system. At present, there are many methods for coordinate point extraction, such as manual marking, feature point extraction, and image fusion based on geographic information systems (Helmholz et al., 2014; Yu et al., 2020). The method based on manual extraction of coordinate points of fruit trees is cumbersome and not suitable for batch extraction of coordinates of citrus trees. The development of remote sensing images in recent years has make it possible to identify targets or large-scale target research in inaccessible environments (Hu et al., 2021; Ghaderizadeh et al., 2022; Jalayer et al., 2022; Zamani et al., 2022). For example, using satellite remote sensing images to detect the impact of climate change on planting patterns (Tariq et al., 2022a), drawing and detecting the distribution map of farmland and crop types (Tariq et al., 2022b), and large-scale extraction of farmland (Sharifi et al., 2022). Although this approach works very well with high spatial resolution. However, this method is suitable for obtaining large-scale farmland data, and is not suitable for extracting geographic coordinate information of a single fruit tree. Tian et al. (2022) proposed a method for extracting citrus tree coordinates based on YOLOv5s. First, an orchard orthophoto map is drawn using a remote sensing dataset. Secondly, the citrus tree image containing geographic information is identified by the YOLOv5s model and the pixel coordinates of the center of the citrus tree in the image are extracted. Finally, the geographic coordinates of citrus trees are extracted through spatial coordinate system transformation and Gauss Kruger inverse algorithm. This method can automatically identify and extract the geographic coordinates of citrus trees, and the accuracy of the extracted geographic coordinates can reach ±0.15m. It has the characteristics of high recognition and extraction accuracy, and simple and quick extraction steps. Therefore, this method was applied to extract the coordinate information of citrus trees. According to the planting situation of citrus trees and the number of plots, the coordinates of citrus trees were extracted from the three experimental fields numbered 1, 4, and 6 in Figure 1C, and the extracted coordinate information is shown in Figure 2. The coordinate points in the figure are the coordinates of each citrus tree, which is a set of world coordinates containing real geographic information, providing data support for subsequent simulation experiments and field experiments.

2.3 Ant colony optimization improvement

The path planned by the traditional ant colony algorithm has the advantage of the shortest path. However, for the complex orchard environment and the maneuvering characteristics of the UAV, the path optimized by the traditional ant colony algorithm has a large cumulative turning angle and a large number of redundant waypoints. This path is very unfriendly to the flight of the UAV, which will seriously affect the flight time of the UAV, increase the flight energy consumption, and reduce the operation efficiency of the UAV. In order to solve such problems, this study improved the traditional ant colony algorithm, including improving heuristic information, improving pheromone update mechanism and node optimization strategy.

2.3.1 Ant colony optimization

The ACO was originally proposed to solve the traveling salesman problem, which is similar to the research content in this study, both of which are to solve the static task assignment problem. Taking the model as an example, there are n citrus trees in the UAV operation plot, that is, n tasks. Each ant needs to search from the first task, and select the next task according to the pheromone concentration on the path until all tasks are completed. The model records the path cost traversed by each ant after each iteration, and outputs the shortest path after all iterations are completed.

In this model, m is the number of ants, $d_{ij}(i, j = 1, 2,\cdots,n$ represents the distance between task i and task j, and $\tau_{ij}(t)$ represents the pheromone concentration between task i and task j at time t. At the initial moment, the pheromone concentration on each path is the same, that is, $\tau_{ij} = 0 = C$ (C is a constant), and P_{ij}^{k} represents the probability of the Kth ant transferring from task i to task j, and the equation is as follows:

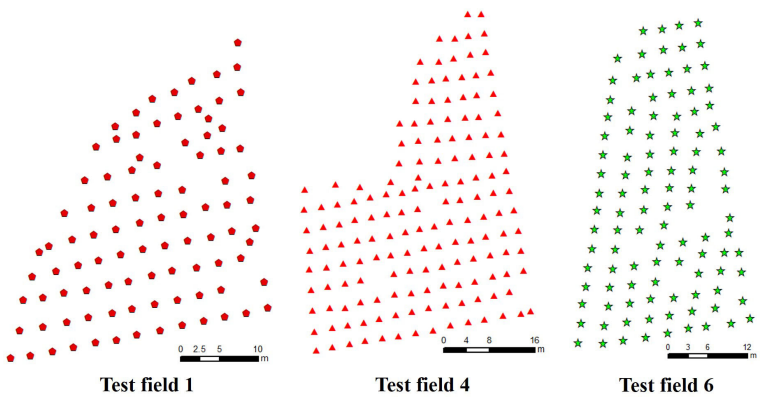

FIGURE 2
Extraction of citrus tree coordinates.

$$P_{ij}^{k} = \begin{cases} \dfrac{\tau_{ij}^{\alpha}(t)\eta_{ij}^{\beta}(t)}{\sum_{s\in allowed_k}\tau_{is}^{\alpha}(t)\eta_{is}^{\beta}(t)} & (j \in allowed_k) \\ 0 & otherwise \end{cases} \quad (1)$$

where $\eta_{ij}(t) = \frac{1}{d_{ij}}$; $allowed_k$ represents the set of tasks that ant k is allowed to access.

After each iteration, the pheromone concentrations on all paths will be updated again, and the pheromone update equation are as follows:

$$\tau_{ij}(t+1) = \rho\tau_{ij}(t) + \Delta\tau_{ij}(t, t+1) \quad (2)$$

$$\Delta\tau_{ij}(t, t+1) = \sum_{k=1}^{m}\Delta\tau_{ij}^{k}(t, t+1) \quad (3)$$

$$\Delta\tau_{ij}^{k}(t) \begin{cases} \frac{Q}{L_k} & Path\ (i,j)\ traversed\ by\ ant\ k \\ 0 & otherwise \end{cases} \quad (4)$$

where $\Delta\tau_{ij}^{k}$represents the pheromone concentration of the Kth ant between task i and task j in this iteration; $\Delta\tau_{ij}(t, t+1)$ represents the sum of the pheromone concentrations of all ants between task i and task j in this iteration; Q is the pheromone intensity; ρ is the pheromone volatile factor; L_k is the total length of the path searched by ant k in this iteration.

2.3.2 Heuristic information improvement

During the plant protection operation of the UAV, if the task nodes i, j and k are not in a straight line, there is a UAV steering phenomenon, that is, the UAV flies from node i to node j, and then flies to node k after turning. The angle between the extension line of line segment ij and line segment jk is called the steering angle of the UAV, denoted as θ_j, as shown in Figure 3.

In the waypoint planning, the influence of the turning angle on the flight energy consumption of the UAV cannot be ignored (Fan et al., 2019). Therefore, the route planning considering the corner factor is particularly important for the plant protection operation of the UAV. The heuristic function in the traditional ACO algorithm only considers the influence of the distance between different nodes on the probability selection of the next node. In this study, the node corner factor is added to the heuristic information of the traditional ACO algorithm, so that the ants can choose a path with the smallest turning angle while ensuring the optimal path. The calculation equation of the corner evaluation function is as follows.

$$R_{ijk} = c\star\theta_j \quad (5)$$

where, R_{ijk} is the turning angle factor;c is the turning angle weight coefficient; θ_j is the turning angle.

The improved ACO can ensure that the ants take into account the dual factors of path length and turning angle when selecting nodes. The improved heuristic function equation is as follows.

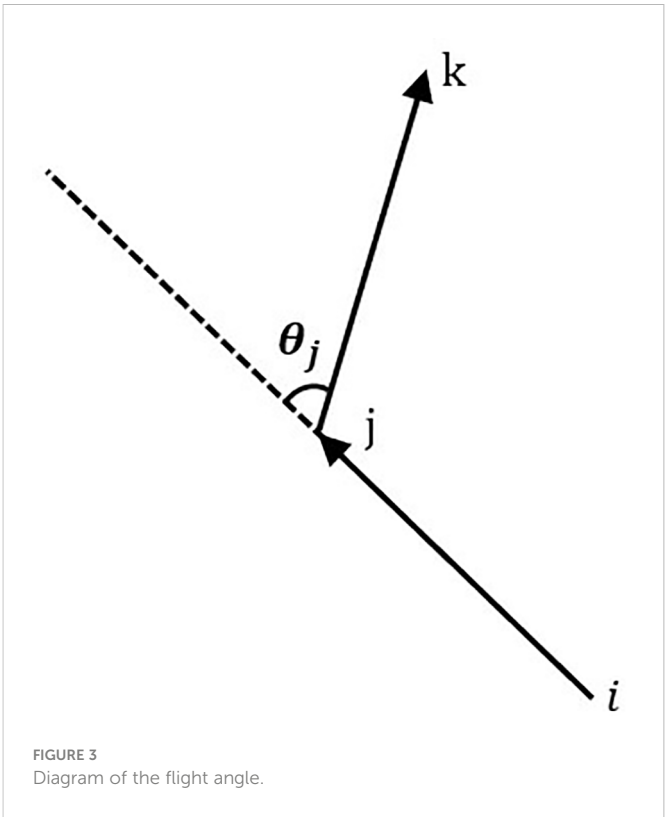

FIGURE 3
Diagram of the flight angle.

$$\eta_{ij}^{\star}(t) = \frac{1}{d_{ij} + R_{ijk}} \quad (6)$$

2.3.3 Pheromone update improvement

Ant colony algorithm is a parallel positive feedback computing mechanism, that is, each ant performs tasks independently according to the same mechanism. In ant colonies, some ants may find poor paths due to probabilistic problems, resulting in slow algorithm convergence, falling into local optimal solutions, and large fluctuations in results. Therefore, in order to improve the convergence speed and reduce the impact of inferior paths on the algorithm, a sorting optimization mechanism was added to the algorithm to update pheromone, that is, to enhance the pheromone concentration in the high-quality paths, thereby reducing the impact of inferior paths on the algorithm results.

Specifically, the sorting optimization mechanism will sort the paths traveled by all ants according to the path length ($L_1 \le L_2 \le \cdots \le L_m$) after each iteration. The higher the ranking, the better the searched path. The pheromone weighting is carried out according to the ant's ranking μ, and the pheromone on the high-quality path is enhanced, so that the ants are more inclined to choose the high-quality path with more pheromone in the next iteration. At the same time, according to the mechanism of elite ants, set the ant ranking w, only the first w−1 ants are allowed to release pheromone, the improved pheromone update equation are as follows.

$$\tau_{ij}(t+1) = \rho\tau_{ij}(t) + \Delta\tau_{ij}^{\star}(t, t+1) \quad (7)$$

$$\Delta\tau_{ij}^{\star}(t, t+1) = \sum_{k=1}^{w-1}(w-k)\Delta\tau_{ij}^{k}\ \ (t, t+1) \quad (8)$$

$$\Delta(t)\begin{cases}\frac{Q}{L_k} & Path\ (i,j)\ traversed\ by\ ant\ k \\ 0 & otherwise\end{cases} \tag{9}$$

2.3.4 Node cleaning

The planting methods of fruit trees are mostly arranged in a nearly straight line, that is, the arrangement of the fruit tree hearts in each row is close to a straight line. When UAV carry out plant protection operations, such arrangement of fruit trees can be regarded as a linear arrangement, and precise operations can be carried out by adjusting the spray width and spray direction of plant protection drone spray nozzles. However, in the path planning of such fruit trees, ACO has a large number of redundant nodes and unnecessary turning nodes that approximate straight line segments. Therefore, this study cleans the redundant nodes in the ACO algorithm by setting the error threshold.

The step of node cleaning is set after planning the optimal path. According to the node coordinate information, the algorithm can obtain the rotation angle θ_j of all nodes except the starting node and the end node. According to the node coordinate information, the algorithm can obtain the rotation angle θ_j of all nodes except the starting node and the end node, and carry out the redundant node cleaning work through the set heading angle error threshold φ. For example, when cleaning and judging node j, the steering angle θ_j of node j can be obtained from the angle between node j and the line connecting two adjacent nodes. When $\theta_j \leq \varphi$, it is considered that θ_j is an invalid steering angle and is deleted; otherwise, node is preserved. The cleaning node logic is shown in Figure 4.

2.3.5 Algorithm implementation process

The path search process of MS-ACO is shown in Figure 5, and the pseudo code is shown in **Algorithm 1**. The algorithm mainly includes three important functions of task node search, pheromone update and node optimization, as follows:

(1). Task node search. Ants search for task nodes based on the improved heuristic function, and select task nodes through the dual factors of path length and corner factor.

(2). Pheromone update. After each iteration, the paths searched by all ants are sorted. Strengthen the pheromone concentration on the top-ranked paths, thereby improving the algorithm optimization ability.

(3). Node optimization. According to the optimization formula, node optimization is performed on the searched optimal path.

```
Algorithm : MS-ACO.
Output: R_best
Input: coordinate of nodes
initialize parameters
while iter ≤ iter_max do
put all ants to the starting point of the task
for each ant k do
for each node i do compute η_ij(t) according to the formula (5) and (6)
choose next node with probability according to the formula (1) and (6)
end for
add node i to tabu_k
end for
computer the length of the shortest path
update the pheromone value according to the formula (7)
end while
for j=1 to length(tabu) do
if θ_j ≤ α then
delete node_j
else
add node j to R_best
end if
end for
```

ALGORITHM 1. PSEUDO CODE OF MS-ACO

2.4 Simulation experiment

Simulation experiments were carried out in the MATLAB R2019b simulation environment, and 20 simulation experiments were carried out on the three experimental fields using ACO and MS-ACO. The

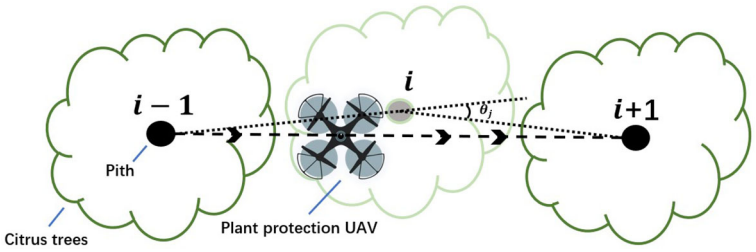

FIGURE 4
Redundant node clearing logic.

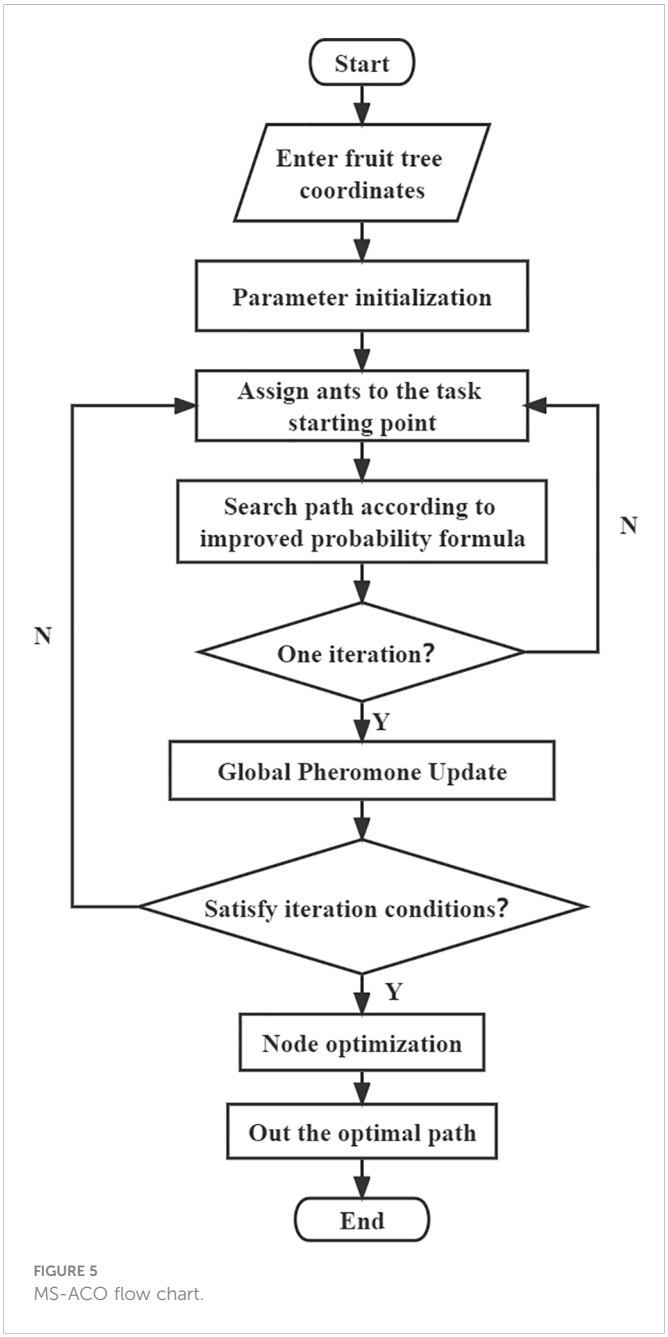

FIGURE 5
MS-ACO flow chart.

simulation results of each test field are solved by averaging several experiments. The simulation results are compared in terms of path length, total angle, total node, and simulation path result graph to verify the feasibility and effectiveness of MS-ACO algorithm. There is no detailed theoretical method for the value of the parameters related to the ant colony algorithm, so this study repeated experiments to find the best values based on experience. The parameters of the ant colony algorithm mainly include the number of ants m, the rank of ants w, and the pheromone volatilization factor ρ, Pheromone importance factor α, Heuristic function importance factor β, Angle weight coefficient c, heading angle error threshold φ. The parameter values are shown in the Table 1.

2.5 Field experiment

In order to further verify the real validity of the simulation experiment, we used the built UAV to conduct field experiments. The experiment time is September 17, 2022, the wind direction is north wind, the wind speed is 0.1m/s, the flying height of the drone is 7m, and the flight speed at the waypoint is 3m/s. The field experiments were analyzed from two aspects of flight trajectory and flight data. In the flight trajectory analysis, we used ArcMap software to project the GPS information recorded during the operation of the UAV to the orthophoto image of the orchard to analyze the trajectory of the UAV when it performed the route mission. ArcMap developed by Environment System Research Institute, has the functions of spatial analysis, map making, etc. It can match and transform the spatial coordinate system and is widely used in surveying and mapping (Wu et al., 2006). Digital orthophoto map is a kind of map containing geographic information, which has the characteristics of high precision, rich information and strong intuition (Fang, 2007). The flight data obtains the current, voltage and GPS information of the UAV during operation through the UAV flight log, and calculates the voyage time, range, turning angle and energy consumption per meter of the UAV during operation. The range and rotation angle are solved by basic geometric formulas. The calculation formula of the UAV's flight energy consumption is as follows:

$$P = UI \tag{10}$$

$$W = \sum_{k=1}^{n} P_k \Delta t \tag{11}$$

where P is the instantaneous power of the drone, w. U is the working voltage of the drone, V. I is the sampling current of the drone, A. Δt is the sampling time, s. P_k is the power value collected at the kth moment, w. W is the flight energy consumption, J.

A quadrotor small UAV was applied as a verification platform for waypoint path planning. The built small quadrotor UAV (left in Figure 6) includes: YH-2216 motor, HOBBYWING XRotor-20A -V1 -Asia Edition electronic governor, HEX MAUCH power module, 1047 carbon fiber propeller, F450 frame, HEX Cube Black flight control, Here+ positioning module. In the field test, in order to ensure the accuracy of UAV waypoint flight positioning and power detection, we use RTK base station for real-time dynamic differential positioning, and the positioning accuracy can reach 0.025m. The current and voltage module is the MAUCH002+015 power module, which uses the ACS758-200 version of the Hall current sensor, which can measure 200A of current with a measurement accuracy of ±3% (Zhang et al., 2021a). The four-rotor UAV cooperates with ground equipment to form a UAV flight platform. The built UAV flight platform is shown in Figure 6 (right).

TABLE 1 Related parameter values of improved ant colony algorithm.

Parameter	m	w	ρ	α	β	c	φ
Value	200~300	50	0.2	1	5	75~100	10

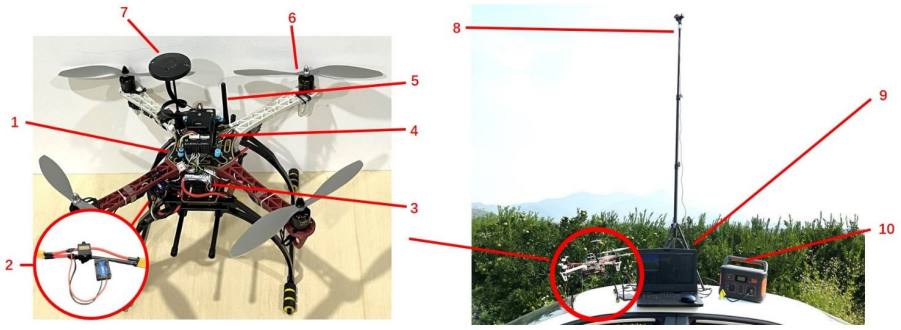

FIGURE 6
The real UAV (left) and UAV platform equipment (right). 1. Control signal receiver;2. MAUCH002+015 power module; 3. Power supply; 4. HEX Cube Black; 5. Data transmission module; 6. Brushless motor; 7. GPS module; 8. RTK base station; 9. Ground station; 10. Power bank.

3 Result

3.1 Analysis of simulation results

According to the analysis of the statistical results in Table 2, it can be seen that MS-ACO has improved in both the optimal path and the total turning angle, among which the optimization effect of the total turning angle is the most obvious. Compared with ACO, the optimization effect of MS-ACO in the three experimental fields increased by 21.94%, 45.06% and 55.94% respectively. The main reason is that ACO searches the path through the path cost, which will cause the ants to fall into the local optimal solution in the densely planted area of citrus trees when searching for the path, increasing the total value of the path angle. In the path length optimization, MS-ACO is improved by 3.89%, 4.6% and 2.86% respectively compared with ACO, and the improvement effect is weak, which also shows that ACO has great advantages in path length optimization, and the improvement space is small. In terms of node optimization, the node optimization effect of the three experimental fields is obvious, all reaching more than 60%. It can be seen from the data in Table 3 that the optimized total nodes and the total rotation angle show a positive correlation phenomenon, but there is no accurate correlation. The main reason is that each experimental field is not planted regularly, and the arrangement of fruit trees will have different degrees of influence on the optimization results. In general, ACO has certain advantages in path length optimization, but this algorithm is not suitable for the path planning of plant protection UAV in orchards. Although MS-ACO has a weak optimization ability in terms of path length, it has a strong ability to optimize the total turning angle of the path. Therefore, the overall optimization performance of MS-ACO is stronger than that of ACO, which is suitable for plant protection UAV orchard waypoint planning.

Figure 7 shows the optimal paths of MS-ACO and ACO in the three experimental fields. The first column in the figure is the optimal path for the MS-ACO to solve the three experimental fields, and the second column is the optimal path for the ACO to solve the three experimental fields. It can be seen from the pictures of the three experimental fields that the arrangement of citrus trees in each experimental field is roughly divided into regular areas and irregular areas. For example, the upper part of field 1 and field 4 are irregularly planted, the lower part is linearly arranged, the left side of field 6 is linearly arranged, and the right side is irregularly planted. The route optimized by MS-ACO roughly retains the advantages of full coverage reciprocating route planning in the regular planting area of citrus trees. However, unlike the full coverage reciprocating route method, MS-ACO can make accurate planning based on the coordinate information of fruit trees, and ensure that the route accurately covers the center of each fruit tree within the range of the tree center deviation threshold; in irregular areas, MS-ACO can more clearly highlight the advantages of its path optimization. Under the condition of ensuring the optimal route, the route is adjusted according to the position of each fruit tree. This also means that the UAV needs to make too many turns to accurately cover each fruit tree, which is inevitable. It can also be clearly seen in the ACO that the algorithm also roughly follows the planning characteristics of full coverage reciprocating routes. However, due to the intensive planting of citrus trees, ACO tends to fall into a local optimal solution, thus increasing the corner cost. At the same time, the increase of nodes also means an increase in the number of plant protection drones. The UAV will experience deceleration and acceleration when passing through each task node. Frequent acceleration and deceleration will greatly increase the

TABLE 2 Simulation results of traditional ant colony algorithm and improved ant colony algorithm.

Experimental field	MS-ACO			ACO			Optimization effect		
	Average path length	Average total turning angle	Total node	Average path length	Average total turning angle	Total node	Path length	Total corner	Total node
1	283.03	2686.69	37	294.47	3441.80	95	3.89%	21.94%	61.05%
4	493.12	3243.98	40	516.90	5904.77	159	4.60%	45.06%	74.84%
6	321.68	1986.32	26	331.14	4508.30	106	2.86%	55.94%	75.47%

TABLE 3 Statistical results of flight energy consumption.

Experimental field	MS-ACO				ACO				Optimization effect			
	Flight time/s	Voyage/m	Corner/°	Energy consumption per meter/kJ	Flight time/s	Voyage/m	Corner/°	Energy consumption per meter/kJ	Flight time	Voyage	Corner	Energy consumption per meter
Field 1	70.5	276.82	3403.81	0.128	131.7	282.26	6913.18	0.183	46.47%	1.93%	50.76%	30.05%
Field 4	95.7	485.38	4110.48	0.117	217.5	485.93	10753.95	0.176	56.00%	0.11%	61.78%	33.52%
Field 6	59.8	318.71	2445.59	0.119	145.9	311.33	8461.19	0.184	59.01%	-2.37%	71.10%	35.33%

energy consumption of the UAV and reduce the cruising time of the UAV. To sum up, although ACO has the advantage of the shortest path, the algorithm is not suitable for orchard waypoint planning due to too many task nodes and total turning angles. MS-ACO can not only better balance the cost of paths and corners, but also effectively reduce the number of task nodes, which has a strong advantage in orchard waypoint planning.

3.2 Experimental verification and discussion in the field environment

3.2.1 Flight path analysis

Figure 8 shows the GPS trajectory map of the UAV, which is composed of an orthophoto image and the UAV flight trajectory. In Figure 8, the first row is the flight trajectory of MS-ACO, and the second row is the flight trajectory of ACO. The blue, red and yellow colors represent the GPS trajectories of the three experimental fields respectively. Through the flight trajectory, we can better analyze the state of the UAV during operation. Here we mainly focus on the degree of coincidence between the trajectory and the fruit tree and the degree of fluctuation of the trajectory, which will directly affect the precision operation and flight energy consumption of the UAV. It can be seen from Figure 8 that no matter the route optimized by MS-ACO or ACO, the flight trajectory and fruit trees have a high degree of overlap, indicating that the UAV can accurately execute the route task.For the degree of trajectory fluctuation, the route based on ACO optimization fluctuates greatly, which is not conducive to UAV plant protection operations. The route optimized based on MS-ACO is smoother and more in line with the flight characteristics of UAVs. The main factors affecting trajectory fluctuations are the mission nodes and turning angles in the route. When the UAV passes through each node, it will go through the process of acceleration and deceleration. Frequent acceleration and deceleration will lead to large fluctuations when the UAV is flying, thereby increasing unnecessary energy consumption, which is not conducive to UAV plant protection operations.

3.2.2 Flight data verification

The statistical results of the flight data of the UAV are shown in Table 3. It can be seen that in the field experiment, the flight energy consumption of the path optimized by the MS-ACO is smaller than that of the ACO optimized path. For the three experimental fields, the voyage time optimization rates of MS-ACO are 46.47%, 56%, and 59.01%, respectively, and the energy consumption per meter optimization rates are 30.05%, 33.52%, and 35.33% respectively. Both optimization effects were significant and both improved significantly. The optimization effect of the voyage is less obvious, and even a negative value appears. The main reason is that the optimization effects of the two algorithms on the path are similar, and due to the influence of environmental factors (such as wind speed and GPS signal) in the field experiment, the flight stability of the UAV is poor, resulting in fluctuations in the data results. The optimization effect of the total turning angle of the path can reach more than 50%, but there are some differences. Because the planting of fruit trees is

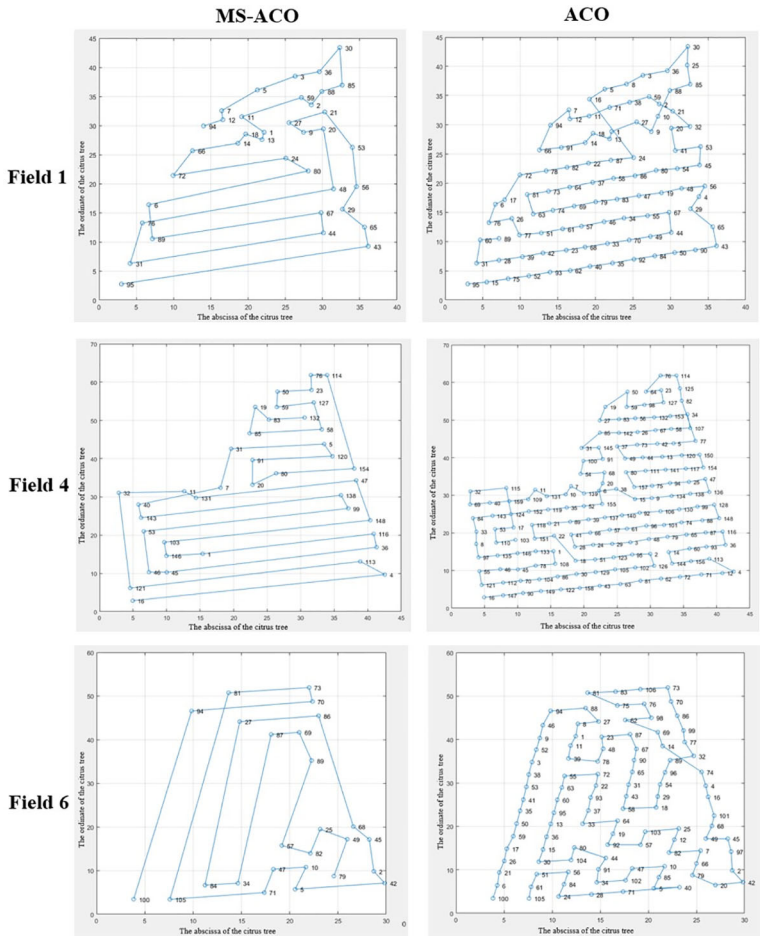

FIGURE 7
Comparison of the best paths for MS-ACO and ACO solutions.

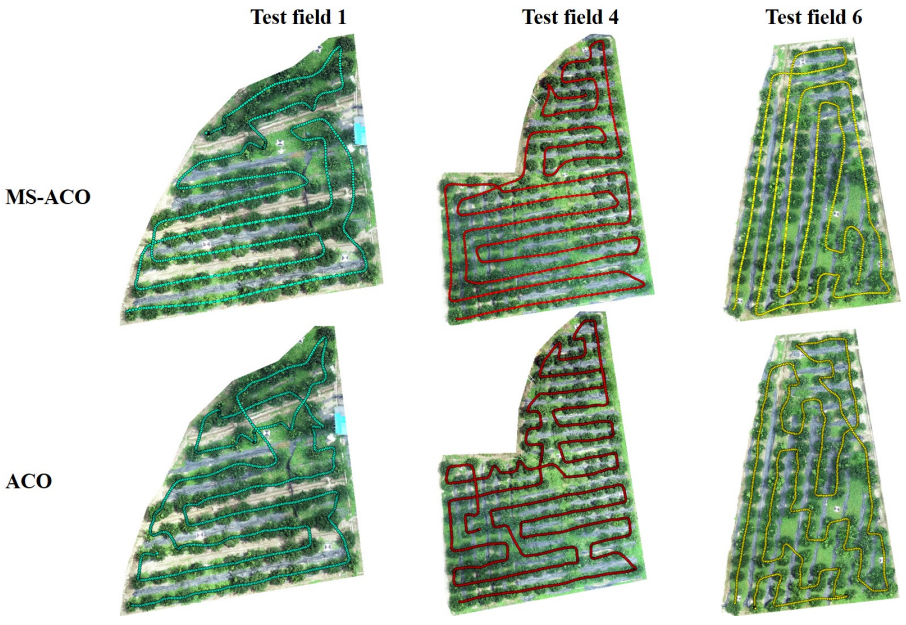

FIGURE 8
GPS flight trajectory of MS-ACO algorithm and ACO algorithm to solve the path.

random, the optimization effect of the total turning angle will change with the distribution of fruit trees. The field experiment results show that compared with ACO, MS-ACO can greatly reduce the total turning angle of the UAV flight path, and the energy consumption per meter optimization rate can reach 30%. Although the voyage optimization effect is poor, it shortens the voyage time and reduces the flight energy consumption, which verifies the feasibility and effectiveness of MS-ACO in the waypoint planning in irregular orchards.

3.3 Comparison of simulation and field experiment results

In the above two sections, we analyzed the optimization effects of the two algorithms in simulation experiments and field experiments respectively. In order to further verify the reliability of the improved algorithm, this section carries out visual analysis on the simulation results and experimental results of the algorithm from two parts: Voyage and Turning angle. The comparison of the results of the voyage is shown in Figure 9. The broken line part represents the result of the optimization of the ACO algorithm, and the bar part represents the result of the optimization of the MS-ACO algorithm. It can be seen that, whether it is a simulation experiment or a field experiment, the results of the two algorithms are not much different, indicating that the simulation results are consistent with the experimental results, and the UAV can perform the path flight mission well. For the corner optimization results (Figure 10), we can still see that the simulation experiment of the MS-ACO algorithm is not much different from the field experiment results, showing consistency. However, there is a big difference between the simulation experiment and the field experiment in the corner optimization effect of the ACO algorithm. The main reason is that there are too many path nodes planned by the ACO algorithm, and the UAV has frequent deceleration and acceleration when performing flight tasks, so the trajectory fluctuates greatly, which also causes a surge in the total path angle and increases the flight energy consumption. From this point, it can be shown that the path optimized by the ACO is not suitable for the waypoint planning of plant protection UAVs. In general, the results of MS-ACO both from simulation experiments and field experiments are within the error range, and the optimization results are relatively stable, which proves the reliability and effectiveness of the optimization path.

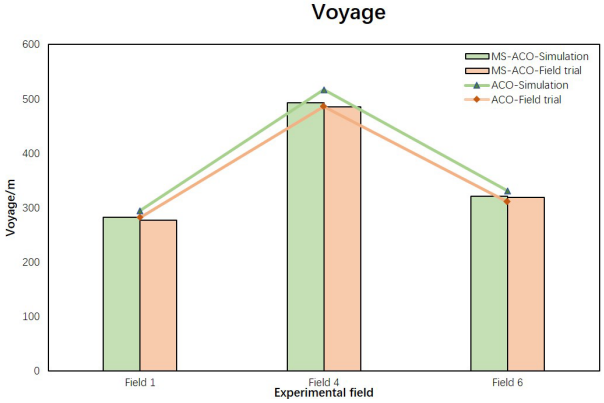

FIGURE 9
Comparison of path results between simulation experiment and field experiment.

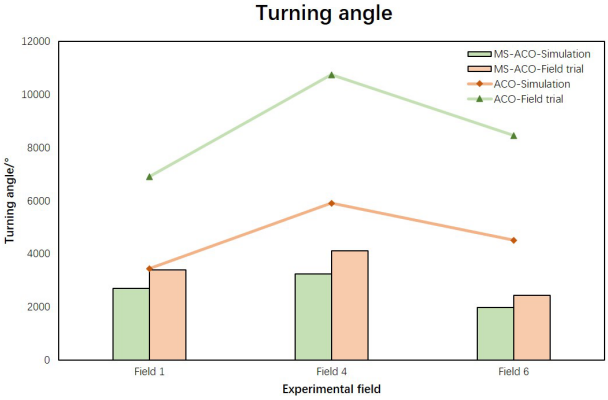

FIGURE 10
Comparison of corner results between simulation experiment and field experiment.

4 Discussion

Agricultural UAVs have received extensive attention in recent years, and related scholars have also carried out a lot of research on aerial plant protection technology, of which route planning is an important development direction for plant protection drones. At present, the flight path planning mainly focuses on the research on the coverage rate and operation efficiency of the farmland regulation degree, and lacks the waypoint planning for the fruit tree farmland. In this study, an exploration of waypoint path planning based on orchard was carried out to solve this problem. By improving the ant colony algorithm, the drone can achieve point-to-point precision flight operation of fruit trees.

At present, there are few researches on path planning for plant protection UAV node traversal. The ACO can quickly solve the shortest path, and it is easy to combine with other algorithms, which has a significant advantage in the waypoint planning of traversing nodes. Therefore, the ACO algorithm was used to carry out a preliminary exploration of the path optimization of the UAV waypoint. Most route planning studies use raster maps for environmental modeling. For example, Cheng et al. (2021) proposed an improved fusion algorithm of wolf swarm and particle swarm in order to solve the problems of premature convergence and local optimization of traditional particle swarm algorithm, which was effectively verified in the grid map constructed. Dai et al. (2019) combined the characteristics of MAX-MIN ant system and A* algorithm, proposed an improved ant colony algorithm to improve the high search ability of mobile robot complex map path, and verified it in grid map. Although the above research has been successful, the constructed grid map limits the freedom of movement of the robot, which has certain limitations in practical applications. In this study, a simulation environment is constructed according to the geographical coordinates of the orchard, and the optimal

path is planned by combining the flight characteristics of the UAV and the position information of each fruit tree. It avoids the influence of grid maps, operation objects and other factors on the final path, and has practical application value.

This research focuses on improving the efficiency of plant protection UAV waypoint flight, including the flight time and energy consumption during UAV operation. In UAV plant protection operations, the primary issue affecting energy consumption is not the range, but the number of corners and waypoints in the path. In this study, the ACO algorithm was improved aiming at this problem. On the premise of ensuring the performance of ACO distance optimization, the corners, redundant nodes and iterations of the algorithm were optimized. The proposed MS-ACO can plan a reasonable spraying path based on the location information of multiple target fruit trees and integrate the three constraints of distance factor, turning angle factor and the number of task nodes. The results of simulation experiments and field experiments show that compared with the ACO algorithm, MS-ACO has been greatly improved in terms of corner optimization and node optimization, which enhances the operating efficiency of UAVs and reduces flight energy consumption. The distance difference between the two algorithms in the simulation experiment and the field experiment is within the error range, showing a high degree of consistency. However, there is a big difference in the total turning angle, and the total turning angle of the path planned by the ACO is multiplied. This further shows that although the path lengths planned by ACO and MS-ACO are not much different, the energy consumption and turning angle are greatly increased, and ACO does not have practical application value. However, the results of MS-ACO in the two sets of experiments are relatively stable, and the optimization of the corner and energy consumption is more consistent with the expected assumptions, and has good energy consumption optimization performance.

A preliminary investigation was conducted in this study on the waypoint planning of the plant protection UAV orchard scene, and the selected orchard is the orchard scene in the near-plain area. In such scenarios, elevation and slope of the orchard, and tree height have less impact on spraying efficiency. The proposed algorithm is capable of 2D optimal trajectory planning for such scenarios. In orchard areas with obvious height differences, elevation and tree height are one of the important factors affecting spraying efficiency. In the vast area of hilly mountainous terrain in China, orchard and tea gardens are commonly planted along the slopes (Wang et al., 2019; Liu et al., 2022). The path planning based on MS-ACO has more application value for such scenarios. Therefore, the waypoint planning for mountain and hilly scenes is one of the important directions of future research (Zheng et al., 2020). In the analysis of algorithm optimization, this study verified the quality of the results by comparing the optimization performance of ACO and MS-ACO algorithms. In future research work, we plan to carry out comparative research on other intelligent optimization algorithms to further improve the optimization performance of the MS-ACO algorithm and make it more generalizable. In addition, ACO has great advantages in solving combinatorial optimization problems. In the future research, it should also be combined with the dynamic changes of the load during the UAV spraying process, the battery life of the UAV, obstacles and other factors.

5 Conclusion

This study conducts research on the problem of UAV waypoint planning, and proposes an improved ant colony algorithm to solve the problem of point-to-point pesticide application in plant protection UAV orchard scenes. The improved algorithm incorporates the corner factor into the original heuristic function, which improves the corner optimization ability of the algorithm. At the same time, a ranking optimization mechanism is added to the pheromone update, which speeds up the convergence speed and avoids the influence of inferior solutions. Finally, the redundant nodes in the path are cleaned to further improve the energy consumption optimization rate of the algorithm. The method proposed in this study can carry out precision plant protection operation route planning according to the geographical location of each fruit tree. In the simulation and field experiment results, we have verified that the algorithm can plan a more low-consumption and efficient UAV plant protection route through performance indicators such as flight time optimization rate and energy consumption optimization rate per meter.

In future research, the influence of different obstacles in the field, take-off point and return point on the optimization rate of route energy consumption will be combined. At the same time, the environment perception of the sensor is used to improve the obstacle avoidance ability of the UAV during the route flight, making the algorithm more generalized and intelligent.

Data availability statement

The original contributions presented in the study are included in the article/supplementary material. Further inquiries can be directed to the corresponding authors.

Author contributions

YZ and YL: conceptualization, project administration, and funding acquisition. YZ, HT, and ZM: methodology. HT: software, data curation, and visualization. HT and YZ: validation and investigation. JX and HT: formal analysis. YZ: resources. CM, and YZ: writing—original draft preparation. YZ, YL, and RJ: writing—review and editing. YL: supervision. All authors contributed to the article and approved the submitted version.

Funding

This study was supported by Laboratory of Lingnan Modern Agriculture Project (NT2021009), The 111 Project (D18019).

Conflict of interest

The authors declare that the research was conducted in the absence of any commercial or financial relationships that could be construed as a potential conflict of interest.

Publisher's note

All claims expressed in this article are solely those of the authors and do not necessarily represent those of their affiliated organizations, or those of the publisher, the editors and the reviewers. Any product that may be evaluated in this article, or claim that may be made by its manufacturer, is not guaranteed or endorsed by the publisher.

References

Abeywickrama, H. V., Jayawickrama, B. A., He, Y., and Dutkiewicz, E. (2018). Comprehensive energy consumption model for unmanned aerial vehicles, based on empirical studies of battery performance. *IEEE Access* 6, 58383–58394. doi: 10.1109/ACCESS.2018.2875040

Bassanezi, R. B., Lopes, S. A., de Miranda, M. P., Wulff, N. A., Volpe, H. X. L., and Ayres, A. J. (2020). Overview of citrus huanglongbing spread and management strategies in Brazil. *Trop. Plant Pathol.* 45 (3), 251–264. doi: 10.1007/s40858-020-00343-y

Cao, R., Li, S., Ji, Y., Zhang, Z., Xu, H., Zhang, M., et al. (2021). Task assignment of multiple agricultural machinery cooperation based on improved ant colony algorithm. *Comput. Electron. Agr.* 182, 105993. doi: 10.1016/j.compag.2021.105993

Cheng, X., Li, J., Zheng, C., Zhang, J., and Zhao, M. (2021). An improved PSO-GWO algorithm with chaos and adaptive inertial weight for robot path planning. *Front. Neurorobot.* 15, 770361. doi: 10.3389/fnbot.2021.770361

Dai, X., Long, S., Zhang, Z., and Gong, D. (2019). Mobile robot path planning based on ant colony algorithm with a* heuristic method. *Front. Neurorobot.* 13. doi: 10.3389/fnbot.2019.00015

Du, D., Lu, L., Zhang, L., Hu, X., Huang, Z., and Chen, G. (2011). Research progress in control technology of diaphorina citr. *Chin. Agric. Sci. Bull.* 27 (25), 178–181.

Ebadinezhad, S. (2020). DEACO: Adopting dynamic evaporation strategy to enhance ACO algorithm for the traveling salesman problem. *Eng. Appl. Artif. Intell.* 92, 103649. doi: 10.1016/j.engappai.2020.103649

Erke, S., Bin, D., Yiming, N., Qi, Z., Liang, X., and Dawei, Z. (2020). An improved a-star based path planning algorithm for autonomous land vehicles. *Int. J. Adv. Robot. Syst.* 17 (5), 1729881420962263. doi: 10.1177/1729881420962263

Fang, J. (2007). Discussion on several technical problems about producting DOM. *Geomatics Spatial Inf. Technol.* 03), 91–93. doi: 10.3969/j.issn.1672-5867.2007.03.026

Fan, Y., Wang, D., Shen, K., and Zhang, H. (2019). Design and experiment of the test system for steering energy consumption of electric multi-rotor unmanned aerial vehicle. *Sci. Technol. Eng.* 19 (10), 126–131. doi: 10.3969/j.issn.1671-1815.2019.10.019

Garcia, A. G., Jamielniak, J. A., Diniz, A. J. F., and Parra, J. R. P. (2022). The importance of integrated pest management to flatten the huanglongbing (HLB) curve and limit its vector, the Asian citrus psyllid. *Entomol. Gen.* 42 (3), 349–359. doi: 10.1127/entomologia/2021/1247

Ghaderizadeh, S., Abbasi-Moghadam, D., Sharifi, A., Tariq, A., and Qin, S. (2022). Multiscale dual-branch residual spectral–spatial network with attention for hyperspectral image classification. *IEEE J. Selected Topics Appl. Earth Observations Remote Sens.* 15, 5455–5467. doi: 10.1109/JSTARS.2022.3188732

Han, X., Kim, H.-J., Jeon, C.-W., Moon, H. C., Kim, J. H., and Seo, I.-H. (2021). Design and field testing of a polygonal paddy infield path planner for unmanned tillage operations. *Comput. Electron. Agr.* 191, 106567. doi: 10.1016/j.compag.2021.106567

Helmholz, P., Rottensteiner, F., and Heipke, C. (2014). Semi-automatic verification of cropland and grassland using very high resolution mono-temporal satellite images. *ISPRS J. Photogramm. Remote Sens.* 97, 204–218. doi: 10.1016/j.isprsjprs.2014.09.008

Huo, F., Chi, J., Huang, Z., Ren, L., Sun, Q., and Chen, J. (2018). Review of path planning for mobile robots. *J. Jilin University(Information Sci. Edition)* 36 (06), 639–647. doi: 10.19292/j.cnki.jdxxp.2018.06.007

Hu, P., Sharifi, A., Tahir, M. N., Tariq, A., Zhang, L., Mumtaz, F., et al. (2021). Evaluation of vegetation indices and phenological metrics using time-series MODIS data for monitoring vegetation change in punjab, Pakistan. *Water* 13 (18), 2550. doi: 10.3390/w13182550

Jalayer, S., Sharifi, A., Abbasi-Moghadam, D., Tariq, A., and Qin, S. (2022). Modeling and predicting land use land cover spatiotemporal changes: A case study in chalus watershed, Iran. *IEEE J. Selected Topics Appl. Earth Observ. Remote Sens.* 15, 5496–5513. doi: 10.1109/JSTARS.2022.3189528

Lan, Y., Chen, S., Deng, J., Zhou, Z., and Ou, Y. (2019). Development situation and problem analysis of plant protection unmanned aerial vehicle in China. *J. South China Agric. Univ.* 40 (05), 217–225. doi: 10.7671/j.issn.1001-411X.201905082

Lan, Y., Chen, S., and Fritz, B. K. (2017). Current status and future trends of precision agricultural aviation technologies. *J. Agric. Biol. Eng.* 10 (3), 1–17. doi: 10.3965/j.ijabe.20171003.3088

Li, J., Luo, H., Zhu, C., Li, Y., and Tang, F. (2019). Research and implementation of combination algorithms about UAV spraying planning based on energy optimization. *Trans. Chin. Soc. Agric. Machinery* 50 (10), 106–115. doi: 10.6041/j.issn.1000-1298.2019.10.012

Lin, J., Lan, Y., Ou, Y., Li, J., and Chen, P. (2020). Construction and experimental verification of power consumption model for multi rotor agricultural UAV. *J. Agric. Mechan. Res.* 42 (05), 143–149. doi: 10.13427/j.cnki.njyi.2020.05.025

Lin, N., Tang, J., Li, X., and Zhao, L. (2019). A novel improved bat algorithm in UAV path planning. *CMC-Comput. Mater. Con.* 61 (1), 323–344. doi: 10.32604/cmc.2019.05674

Liu, C., Mao, Q., Chu, X., and Xie, S. (2019). An improved a-star algorithm considering water current, traffic separation and berthing for vessel path planning. *Appl. Sci. Basel* 9 (6), 1057. doi: 10.3390/app9061057

Liu, Y., Ru, Y., Liu, B., and Chen, X. (2020). Algorithm for planning full coverage route for helicopter aerial spray. *Trans. Chin. Soc. Agric. Eng.* 36 (17), 73–80. doi: 10.11975/j.issn.1002-6819.2020.17.009

Liu, Y., Zhang, P., Ru, Y., Wu, D., Wang, S., Yin, N., et al. (2022). A scheduling route planning algorithm based on the dynamic genetic algorithm with ant colony binary iterative optimization for unmanned aerial vehicle spraying in multiple tea fields. *Front. Plant Sci.* 13. doi: 10.3389/fpls.2022.998962

Niu, W., Li, Q., Li, C., Cheng, J., Ji, D., Jiang, X., et al. (2021). Multi-scale spatial variability and environmental drivers of soil nutrient distributions in the pearl river delta, south China. *Ecol. Environ. Sci.* 30 (04), 743–755. doi: 10.16258/j.cnki.1674-5906.2021.04.010

Patle, B. K., Babu, G. L., Pandey, A., Parhi, D. R. K., and Jagadeesh, A. (2019). A review: On path planning strategies for navigation of mobile robot. *Defence Technol.* 15 (4), 582–606. doi: 10.1016/j.dt.2019.04.011

Peng, X., Lan, Y., Hu, J., Ou, Y., Xiao, K., and Gao, Z. (2019). Turning mode and whole region-coverage path planning and optimization of agricultural small UAV. *J. South China Agric. Univ.* 40 (02), 111–117. doi: 10.7671/j.issn.1001-411X.201805011

Ru, Y., Liu, Y., Qu, R., and Patel, M. K. (2020). Experimental study on spraying performance of biological pesticides in aerial rotary cage nozzle. *Int. J. OF Agric. AND Biol. Eng.* 13 (6), 1–6. doi: 10.25165/j.ijabe.20201306.5511

Sharifi, A., Mahdipour, H., Moradi, E., and Tariq, A. (2022). Agricultural field extraction with deep learning algorithm and satellite imagery. *J. Indian Soc. Remote Sens.* 50 (2), 417–423. doi: 10.1007/s12524-021-01475-7

Stasistics (2022). Available at: http://www.stats.gov.cn/tjsj/ (Accessed July 31, 2022).

Sun, J., Tang, J., and Lao, S. (2017). Collision avoidance for cooperative UAVs with optimized artificial potential field algorithm. *IEEE Access* 5, 18382–18390. doi: 10.1109/ACCESS.2017.2746752

Tang, J., Liu, G., and Pan, Q. (2021b). A review on representative swarm intelligence algorithms for solving optimization problems: Applications and trends. *IEEE/CAA J. Automatica Sin.* 8 (10), 1627–1643. doi: 10.1109/JAS.2021.1004129

Tang, G., Tang, C., Claramunt, C., Hu, X., and Zhou, P. (2021a). Geometric a-star algorithm: An improved a-star algorithm for AGV path planning in a port environment. *IEEE Access* 9, 59196–59210. doi: 10.1109/ACCESS.2021.3070054

Tariq, A., Siddiqui, S., Sharifi, A., and Shah, S. H. I. A. (2022a). Impact of spatio-temporal land surface temperature on cropping pattern and land use and land cover changes using satellite imagery, hafizabad district, punjab, province of Pakistan. *Arabian J. Geosciences* 15 (11), 1045. doi: 10.1007/s12517-022-10238-8

Tariq, A., Yan, J., Gagnon, A. S., Khan, M. R., and Mumtaz, F. (2022b). Mapping of cropland, cropping patterns and crop types by combining optical remote sensing images with decision tree classifier and random forest. *Geo. Spat. Inf. Sci.* 1–19. doi: 10.1080/10095020.2022.2100287

Tian, H., Fang, X., Lan, Y., Ma, C., Huang, H., Lu, X., et al. (2022). Extraction of citrus trees from UAV remote sensing imagery using YOLOv5s and coordinate transformation. *Remote Sens.* 14 (17), 4208. doi: 10.3390/rs14174208

Wang, D., Fan, Y., Xue, J., Yuan, D., Shen, K., and Zhang, H. (2019). Flight path control of UAV in mountain orchards based on fusion of GNSS and machine vision. *Trans. Chin. Soc. Agric. Machinery* 50 (04), 20–28. doi: 10.6041/j.issn.1000-1298.2019.04.002

Wu, W., Li, X., and Zhang, B. (2006). Probe of GIS developing technology based on ArcGIS engine. *Sci. Technol. Eng.* 6 (02), 176–178. doi: 10.3969/j.issn.1671-1815.2006.02.018

Wu, S., Wen, W., Wang, C., Du, J., and Guo, X. (2021). Research progress of digital fruit trees and its technology system. *Trans. Chin. Soc. Agric. Eng.* 37 (09), 350–360. doi: 10.11975/j.issn.1002-6819.2021.09.039

Xu, L., Yang, Z., Huang, Z., and Ding, W. (2020). Route planning method for plant protection unmanned aerial vehicles combined with hy-brid particle swarm optimization. *J. Chin. Comput. Syst.* 41 (09), 1826–1832. doi: 10.3969/j.issn.1000-1220.2020.09.006

Yang, S., Yang, X., and Mo, J. (2018). The application of unmanned aircraft systems to plant protection in China. *Precis. Agric.* 19 (2), 278–292. doi: 10.1007/s11119-017-9516-7

Yi, X. (2007). Discussion on the present situation and development trends of plant protection equipment in China. *J. Agric. Mechanization Res.* 03), 218–220. doi: 10.3969/j.issn.1003-188X.2007.03.071

Yu, Y., Guan, H., Li, D., Jin, S., Chen, T., Wang, C., et al. (2020). 3-d feature matching for point cloud object extraction. *IEEE Geosci. Remote Sens. Lett.* 17 (2), 322–326. doi: 10.1109/LGRS.2019.2918073

Zamani, A., Sharifi, A., Felegari, S., Tariq, A., and Zhao, N. (2022). Agro climatic zoning of saffron culture in miyaneh city by using WLC method and remote sensing data. *Agriculture* 12 (1), 118. doi: 10.3390/agriculture12010118

Zhang, M., Ji, Y., Li, S., Cao, R., Xu, H., and Zhang, Z. (2020). Research progress of agricultural machinery navigation technology. *Trans. Chin. Soc. Agric. Machinery* 51 (04), 1–18. doi: 10.6041/j.issn.1000-1298.2020.04.001

Zhang, D., Lan, Y., Chen, L., Wang, X., and Liang, D. (2014). Current status and future trends of agricultural aerial spraying technology in China. *Trans. Chin. Soc. Agric. Machinery* 45 (10), 53–59. doi: 10.6041/j.issn.1000-1298.2014.10.009

Zhang, H., Lerner, E., Cheng, B., and Zhao, J. (2021a). Compliant bistable grippers enable passive perching for micro aerial vehicles. *IEEE-ASME T Mech* 26 (5), 2316–2326. doi: 10.1109/TMECH.2020.3037303

Zhang, H., Su, Z., Hernandez, D. E., and Su, B. (2018). Energy optimal path planning for mobile Robots based on improved AD* algorithm. *Trans. Chin. Soc. Agric. Machinery* 49 (09), 19–26. doi: 10.6041/j.issn.1000-1298.2018.09.002

Zhang, Y., Tian, H., Huang, X., Ma, C., Wang, L., Liu, H., et al. (2021b). Research progress and prospects of agricultural aero-bionic technology in China. *Appl. Sci. Basel* 11 (21), 10435. doi: 10.3390/app112110435

Zhang, S., Yu, J., Mei, Y., Sun, H., and Du, Y. (2017). Unmanned aerial vehicle trajectory planning by an integrated algorithm in a complex obstacle environment. *Proc. Inst. Mech. Eng. G. J. Aerosp Eng.* 231 (11), 2048–2067. doi: 10.1177/0954410016662058

Zhao, D., Duan, J., Chen, P., and Su, J. (2017). Optimal path planning for 3D map based on a * algorithm. *Comput. Syst. Appl.* 26 (07), 146–152. doi: 10.15888/j.cnki.csa.005859

Zhao, W., Wang, Y., Zhang, Z., and Wang, H. (2021). Multicriteria ship route planning method based on improved particle swarm optimization-genetic algorithm. *J. Mar. Sci. Eng.* 9 (4), 357. doi: 10.3390/jmse9040357

Zheng, Y., Jiang, S., Chen, B., Lyu, H., Wan, C., and Kang, F. (2020). Review on technology and equipment of mechanization in hilly orchard. *Trans. Chin. Soc. Agric. Machinery* 51 (11), 1–20. doi: 10.6041/j.issn.1000-1298.2020.11.001

Zhou, J., and He, Y. (2021). Research progress on navigation path planning of agricultural machinery. *Trans. Chin. Soc. Agric. Machinery* 52 (09), 1–14. doi: 10.6041/j.issn.1000-1298.2021.09.001

Zhou, Z., Ming, R., Zang, Y., He, X., Luo, X., and Lan, Y. (2017). Development status and countermeasures of agricultural aviation in China. *Trans. Chin. Soc. Agric. Eng.* 33 (20), 1–13. doi: 10.11975/j.issn.1002-6819.2017.20.001

Zhou, Z., Zang, Y., Luo, X., Yubin, L., and Xue, X. (2013). Technology innovation development strategy on agricultural aviation industry for plant protection in China. *Trans. Chin. Soc. Agric. Eng.* 29 (24), 1–10. doi: 10.3969/j.issn.1002-6819.2013.24.001

Zhu, L., Xu, Z., Wang, Y., and Cheng, C. (2022). Correlation analysis of energy consumption of agricultural rotorcraft. *CMC-Comput. Mater. Con.* 71 (2), 3179–3192. doi: 10.32604/cmc.2022.023293

remote sensing

MDPI

Article

Extraction of Citrus Trees from UAV Remote Sensing Imagery Using YOLOv5s and Coordinate Transformation

Haoxin Tian [1,2], Xipeng Fang [1,2], Yubin Lan [2,3], Chenyang Ma [4], Huasheng Huang [5], Xiaoyang Lu [1,2], Dehua Zhao [1,2], Hanchao Liu [1,2] and Yali Zhang [1,2,*]

1 College of Engineering, South China Agricultural University, Wushan Road, Guangzhou 510642, China
2 National Center for International Collaboration Research on Precision Agricultural Aviation Pesticide Spraying Technology, Guangzhou 510642, China
3 College of Electronic Engineering and College of Artificial Intelligence, South China Agricultural University, Wushan Road, Guangzhou 510642, China
4 College of Aerospace Engineering, Nanjing University of Aeronautics and Astronautics, Nanjing 210016, China
5 College of Computer Sciences, Guangdong Polytechnic Normal University, Zhongshan Road, Guangzhou 510665, China
* Correspondence: ylzhang@scau.edu.cn

Abstract: Obtaining the geographic coordinates of single fruit trees enables the variable rate application of agricultural production materials according to the growth differences of trees, which is of great significance to the precision management of citrus orchards. The traditional method of detecting and positioning fruit trees manually is time-consuming, labor-intensive, and inefficient. In order to obtain high-precision geographic coordinates of trees in a citrus orchard, this study proposes a method for citrus tree identification and coordinate extraction based on UAV remote sensing imagery and coordinate transformation. A high-precision orthophoto map of a citrus orchard was drawn from UAV remote sensing images. The YOLOv5 model was subsequently used to train the remote sensing dataset to efficiently identify the fruit trees and extract tree pixel coordinates from the orchard orthophoto map. According to the geographic information contained in the orthophoto map, the pixel coordinates were converted to UTM coordinates and the WGS84 coordinates of citrus trees were obtained using Gauss–Krüger inverse calculation. To simplify the coordinate conversion process and to improve the coordinate conversion efficiency, a coordinate conversion app was also developed to automatically implement the batch conversion of pixel coordinates to UTM coordinates and WGS84 coordinates. Results show that the Precision, Recall, and *F*1 Score for Scene 1 (after weeding) reach 0.89, 0.97, and 0.92, respectively; the Precision, Recall, and *F*1 Score for Scene 2 (before weeding) reach 0.91, 0.90 and 0.91, respectively. The accuracy of the orthophoto map generated using UAV remote sensing images is 0.15 m. The accuracy of converting pixel coordinates to UTM coordinates by the coordinate conversion app is reliable, and the accuracy of converting UTM coordinates to WGS84 coordinates is 0.01 m. The proposed method is capable of automatically obtaining the WGS84 coordinates of citrus trees with high precision.

Keywords: UAV; orthophoto map; remote sensing; Hough transform; YOLOv5; Gauss–Krüger; UTM; WGS84; coordinate transformation; deep learning

check for updates

Citation: Tian, H.; Fang, X.; Lan, Y.; Ma, C.; Huang, H.; Lu, X.; Zhao, D.; Liu, H.; Zhang, Y. Extraction of Citrus Trees from UAV Remote Sensing Imagery Using YOLOv5s and Coordinate Transformation. *Remote Sens.* **2022**, *14*, 4208. https://doi.org/10.3390/rs14174208

Academic Editors: Chunbo Huang, Ximing Ren and Jia Sun

Received: 22 July 2022
Accepted: 23 August 2022
Published: 26 August 2022

Publisher's Note: MDPI stays neutral with regard to jurisdictional claims in published maps and institutional affiliations.

Copyright: © 2022 by the authors. Licensee MDPI, Basel, Switzerland. This article is an open access article distributed under the terms and conditions of the Creative Commons Attribution (CC BY) license (https://creativecommons.org/licenses/by/4.0/).

1. Introduction

China is the largest citrus-producing country in the world. As of 2021, the orchard yield of citrus had reached 55.96 million tons [1], ranking first in China's fruit production and playing an important role in the growth of China's agricultural economy [2]. Citrus orchard management in China has been developed from manual management to an intelligent and large-scale production pattern [3]. Accurately identifying citrus trees and extracting the coordinate information of fruit trees helps monitor growth differences among citrus trees and ensure precision orchard management. It is the basis for agricultural robots

to implement precision operations such as route planning [4–6], weeding and pesticide application [7–9], and opening furrows and fertilization [10]. The traditional method of fruit tree identification and localization relies on manual measurement and statistics [11], which is time-consuming, labor-intensive, and inefficient. Computer vision-based recognition mainly includes sensor recognition [12], traditional image recognition algorithms [13], and image recognition algorithms based on deep learning [14]. It is of great significance to the intelligent, informatized, and large-scale management of citrus orchards.

Unmanned aerial vehicle (UAV) remote sensing is a low-cost and high-efficiency image acquisition method [15] that allows researchers to collect and analyze high-resolution images on demand. At present, remote sensing images based on UAVs are widely used in the detection of crop growth [16], soil moisture [17], pests and diseases [18], and other agricultural information. In recent years, the application in fruit tree identification and analysis has received more and more attention [19]. For example, Malek et al. [20] used the scale-invariant feature transform (SIFT) to extract key points from UAV remote sensing images of palm farms. They applied extreme learning machine (ELM) classifiers to analyze the extracted key points and used an active contour method based on level sets (LSs) and local binary patterns (LBPs) to integrate and analyze the key points to obtain palm trees from UAV remote sensing images. Surový et al. [21] proposed a low-cost and high-efficiency detection method for the position and height of a single tree in a forest. They used a low-altitude UAV integrated with RGB sensors to collect remote sensing image data and then create 3D point clouds and an orthophoto map. On this basis, the position and height of a single tree were estimated by identifying the local maxima of the point cloud. However, this method has certain limitations, and its measurement accuracy varies with the regularity of canopy shape and tree volume. Goldbergs et al. [22] adopted a similar approach to obtain structure from motion (SfM) 3D point clouds through UAV systems for the detection of individual trees in Australian tropical savannas. They tested the canopy height models (CHMs) of the SfM image using the max and watershed segmentation tree detection algorithm. The above research mainly uses traditional image processing algorithms to obtain individual plant information through remote sensing images. These approaches have limitations due to the accuracy of image detection such as plant occlusion and irregularity.

Many researchers have combined deep learning with aerial remote sensing images to detect ground targets, achieving excellent results. Luo et al. [23] proposed an improved YOLOv4 algorithm for the problems of small targets in aerial images and the difficult detection of complex backgrounds. By changing the different activation functions in YOLOv4 shallow and deep networks, the improved algorithm is more suitable for target identification in UAV remote sensing images. Wang et al. [24] applied a two-stage idea to identify *Papaver somniferum*. In the first stage, the YOLOv5s algorithm was used to detect and identify all the suspicious *Papaver somniferum* images from the original data. In the second stage, the DenseNet121 network was used to classify the detection results from the first stage and only retain the images containing *Papaver somniferum*. Qi et al. [11] combined the point cloud deep learning algorithm with volume calculation algorithms to achieve the automatic acquisition of citrus tree canopy volume. However, there are few studies on extracting geographic coordinate information of fruit trees. The automatic acquisition of geographical coordinates of citrus trees can give each location information and realize the digital modeling of orchards, which is of great significance to precision orchard management by "one tree one code". Therefore, it is necessary to carry out research on the extraction of the geographic coordinates of citrus trees.

Coordinate extraction and coordinate system transformation is a basic method of spatial measurement data processing [25], which is widely used in geographic surveying and mapping [26], engineering surveying [27], geographic information systems [28], and other fields. The coordinate transformation method uses the coordinate information of the existing common points to match the coordinate system and then completes the transformation of coordinate points under different coordinate systems. In order to realize the conversion

between World Geodetic System 1984(WGS84) and China Geodetic Coordinate System 2000 (CGCS2000) coordinate systems, Peng et al. [29] first converted the WGS84 coordinates to International Terrestrial Reference Frame (ITRF) coordinates through the seven-parameter method, then it was converted to CGCS2000 coordinates by frame conversion. Liu et al. [30] discussed two methods for converting WGS84 coordinates to local coordinates. One is to convert WGS84 coordinates to local national geodetic coordinates, then to Gaussian projection, and finally to local coordinates. The other method is to project based on the reference ellipsoid of WGS84 and convert it to the local national coordinate system through the plane coordinate system. It is pointed out that the latter method has a high level of computational efficiency and operability, allowing applications in navigation, monitoring, and other fields. The above studies mainly work on the coordinate transformation under different coordinate systems, and few studies follow the automatic acquisition of target coordinates, such as the extraction of the coordinates of citrus and other fruit trees in agricultural applications. Pei et al. [31] realized the coordinate positioning of tea leaves based on image information, obtained the binarized image of tea leaves through image post-processing, extracted the minimum circumscribed rectangle according to the outer contour of the tea leaves, and marked the center point of the rectangle, so as to obtain the picking of tea leaves point. However, it is only suitable for obtaining local coordinate points of the target, and cannot be used for extracting the coordinates of fruit trees.

By combining image recognition with coordinate extraction, this study proposes a method of citrus tree coordinate recognition and extraction based on UAV remote sensing images for obtaining the coordinate information of citrus trees efficiently and accurately. The main work is as follows:

1. UAV remote sensing images were collected to generate the orthophoto map of the citrus orchard.
2. The accuracy of the traditional target detection algorithm, based on the Hough transform and the YOLOv5-based deep learning algorithm, were analyzed to determine the higher-precision algorithm as the method to extract the pixel coordinates of the citrus tree.
3. The extracted pixel coordinates were transformed into the Universal Transverse Mercator (UTM) coordinate system according to the geographic information in the orthophoto map, and the transformation accuracy was also verified.
4. The geodetic coordinate transformation of the space rectangular coordinate system was carried out according to the inverse calculation formula of Gauss–Krüger and the transformation accuracy was verified as well.
5. A coordinate conversion app was developed to achieve the batch conversion of pixel coordinates to UTM coordinates and geodetic coordinates, which helps improve coordinate conversion efficiency and simplify work complexity.

2. Materials and Methods

2.1. Overview of the Experimental Site

The experimental site is located in a citrus orchard in Sihui City, Guangdong Province, China (23°36′N, 112°68′E). It lies in a subtropical monsoon climate with an average annual air temperature of 21.2 °C and an average annual rainfall of about 1650 mm [32]. The site receives sufficient sunlight and abundant rainfall and is suitable for citrus growth. The overview of the experimental site is shown in Figure 1.

The citrus orchard possesses a near-plain terrain with an average slope of less than 5° and the orchard is divided by an irregular grid of about 50 × 50 m. The height of the citrus trees is between 1.5 m and 2 m with an average crown diameter of 2 m. Both the tree spacing and row spacing are around 3 m. Water tanks and irrigation pipes are installed between rows, resulting that ground equipment cannot pass between the rows of citrus trees.

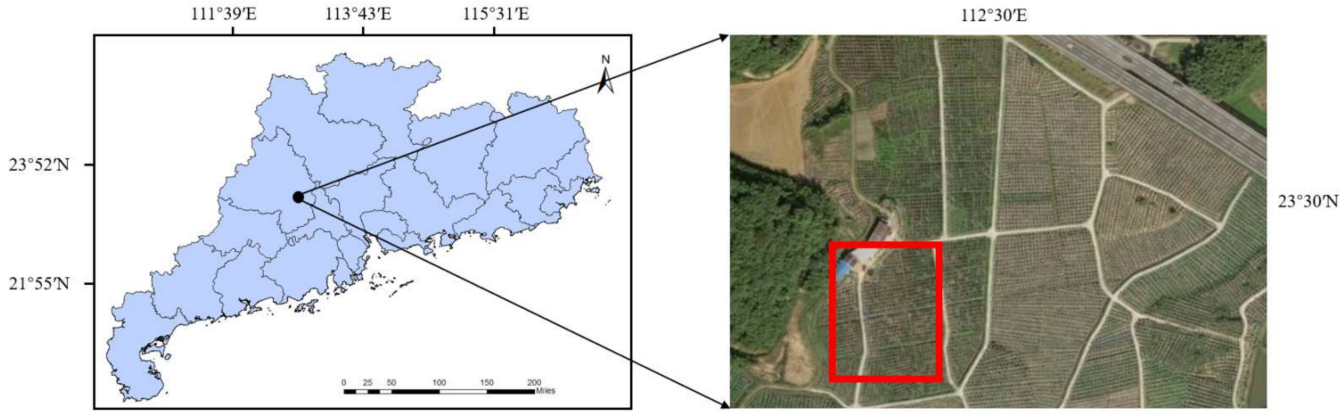

Figure 1. The study area (**right**) circled by the red box is located in Guangdong Province (**left**), China (23°36′N, 112°68′E).

2.2. The Overall Scheme of Fruit Tree Identification and Coordinate Extraction

A method for the automatic identification and coordinate extraction of citrus trees based on an orthophoto map was proposed in this study. The remote sensing images of the citrus orchard were collected with UAVs to generate the orthophoto map of the orchard. The pixel coordinates of the citrus trees were then extracted through the image recognition algorithm and a series of coordinate transformations. Finally, the geographical coordinates of the citrus trees were obtained. The overall flow chart is shown in Figure 2.

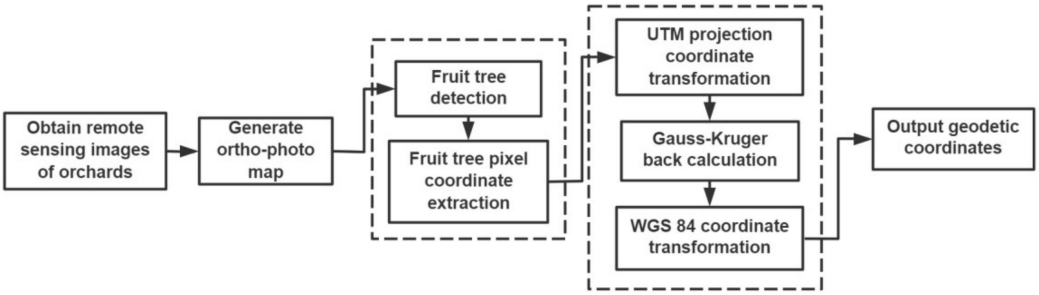

Figure 2. Overall flow chart: image acquisition, orthophoto map production, citrus tree identification, coordinate conversion.

2.3. Remote Sensing Data Collection and Orthophoto Mapping

A DJI Phantom 4 RTK quadrotor UAV was selected to acquire field remote sensing images and its operational parameters are shown in Table 1. UAV remote sensing images of the orchard for Scene 1: after weeding (Figure 3a), and Scene 2: before weeding (Figure 3b) were both collected to facilitate an accurate comparison between the image recognition algorithms. High-altitude acquisition images present large-scale orchard scenes, whereas low-altitude acquisitions receive high-resolution target images. To ensure the effectiveness of image processing, the flight altitude of the UAV was set to 50 m. Meanwhile, the heading overlap rate was set to 80% and the side overlap rate was 80% in order to ensure the quality of the later orthophoto map. On the days of data collection, it was sunny with a side southwest wind, a temperature of 35.2 °C, and relative humidity of 61.7%.

Table 1. UAV operational parameters [33].

Name	Parameter	Value
UAV	Takeoff Weight/g	1391
	Max Flight Time/min	30
	Horizontal Hover Accuracy (RTK)/m	±0.1
	Vertical Hover Accuracy (RTK)/m	±0.1
Sensor	Pixels/$\times 10^4$	2000
	Max Image Size	5472 × 3648 (3:2) 4864 × 3648 (4:3)
	Field Of View FOV/°	84



(**a**) (**b**)

Figure 3. Orchard remote sensing image datasets: (**a**) Scene 1: after weeding, (**b**) Scene 2: before weeding.

A digital orthophoto map is a map containing geographic information obtained by digital processing, which has the characteristics of high precision, rich information, and strong intuition [34]. This study intends to extract the coordinates of citrus trees through an orthophoto map. A D-RTK 2 high-precision GNSS mobile station (Figure 4a) was employed together with the DJI Phantom 4 RTK UAV to obtain high-precision positioning remote sensing images in order to ensure a high level of geographic accuracy required by the orthophoto map of the citrus orchard. Considering the impact of illumination, haze, and photo distortion on the positioning accuracy, six image control points were arranged in the experimental field to further improve the geographic accuracy of the orthophoto map. The layout of the control points and the arrangement are shown in Figure 4.



(**a**) (**b**) (**c**)

Figure 4. Mobile base station and control point layout: (**a**) D-RTK 2 high-precision GNSS mobile station, (**b**) the red box is the test field, and "x" is the six control points selected in the test field, (**c**) control point.

UAV remote sensing data was imported into Pix4D Mapper for initial processing and the preprocessed model was checked and stabbed with control points to automatically generate point clouds, 3D mesh textures, and orthophoto maps. The result of the orthophoto map is shown in Figure 5.



Figure 5. Orchard orthophoto map drawn based on UAV remote sensing image.

2.4. Citrus Tree Identification

After the orthophoto map is generated, it is necessary to identify the citrus trees in the orthophoto map in order to obtain the pixel coordinates of each tree. In order to find an efficient and accurate way to identify citrus trees, both a traditional image processing algorithm based on the Hough transform and a deep learning image processing algorithm based on YOlOv5 were applied for comparative analysis, and the recognition method with higher precision was selected for citrus tree identification and coordinate extraction.

2.4.1. Citrus Tree Detection Method Based on Hough Transform

The geometric features of a citrus canopy are usually circular, therefore, the digital processing of remote sensing images to extract circular features enables citrus tree identification. Circular detection is one of the important research aspects in digital image processing and it has a wide application in automatic detection and pattern recognition [35,36]. Commonly used circular detection methods include the shape analysis method [37], the differential method [38], the Hough transform, and so on [39]. Among them, the Hough transform is the most widely used circular detection method at present, with high reliability and high applicability to noise, deformation, and partial edge discontinuity [40]. The detection of citrus trees based on the Hough transform mainly involves: threshold analysis; binary morphological processing; edge detection; and the Hough transform. The flowchart is shown in Figure 6.

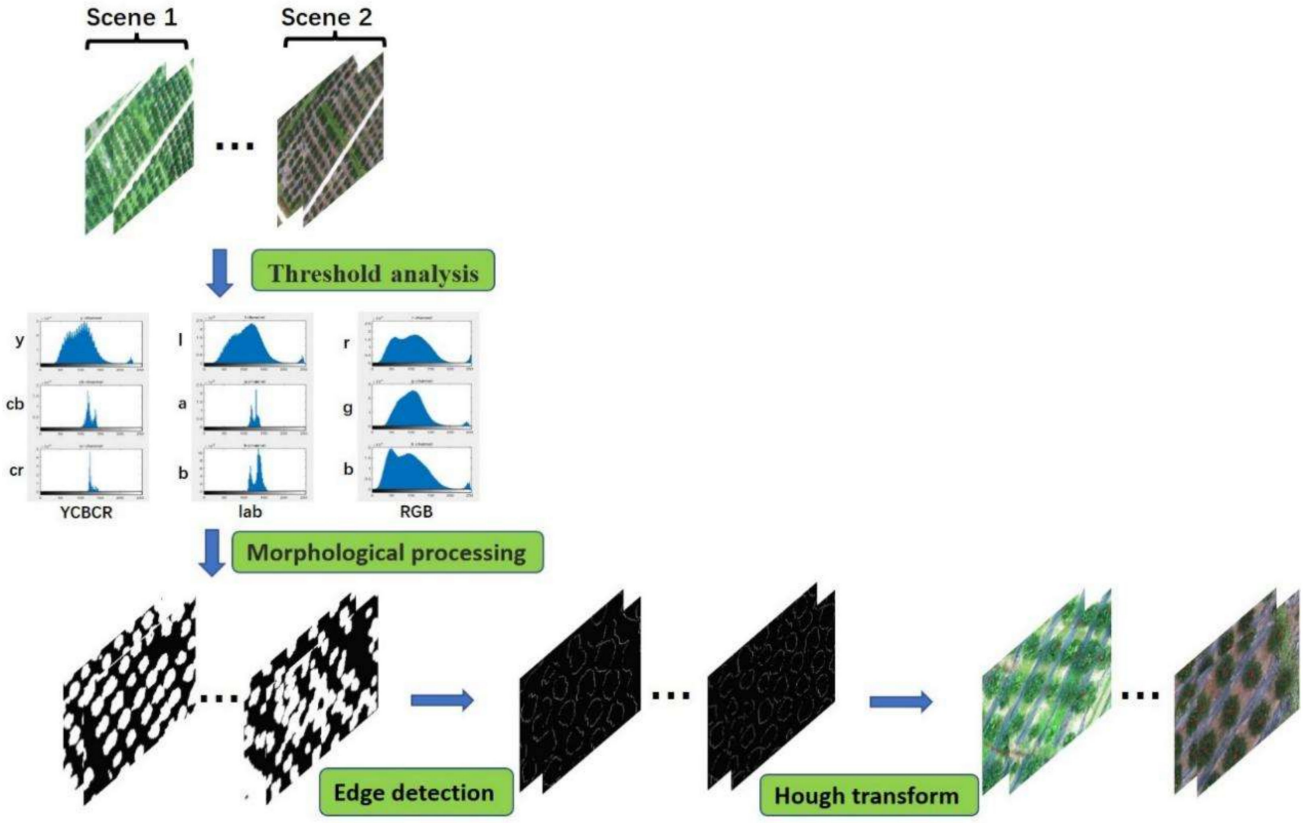

Figure 6. Flow chart of citrus tree detection based on Hough transform.

Image segmentation using the color features of citrus trees is currently a widely used segmentation algorithm [41]. Due to the complex background of orchard images, the selection of color space for image segmentation becomes very important in extracting the citrus tree objects. The color spaces include: RGB (red, green, blue), Lab, YCbCr, HIS (hue, intensity, saturation), HSV (hue, saturation, value) etc. [42,43]. A comparative analysis of three color spaces (RGB, Lab, YCbCr) commonly used in image processing shows that the YCbCr channel has a more pronounced peak, and is suitable for threshold segmentation of citrus trees.

The impacts of temperature, light, wires, etc., result in noise and holes in the segmented binary images. Without effective processing, large errors will occur in the subsequent edge detection and the Hough transform. Therefore, three basic morphologies—erosion, dilation, and hole filling—are employed to deal with the noise and holes in the binary images. Erosion refers to removing unwanted parts by continuously compressing the boundary inward and the specific erosion result depends on the objects and structural elements in the binary images. If the objects in the images are smaller than the structural elements, erosion can ablate the objects in the image, such as noise in the area of citrus trees. If the object is large and possesses structural elements, erosion can compress the object boundary, such as large noise, holes, etc. The effect of dilation is just the opposite of that of erosion, which means that the boundary of the object is enlarged by continuous expansion and the noise in the binary image can be better eliminated by the process of erosion and dilation. However, erosion and dilation only consider the removal of small noise in the target area of citrus trees. For larger holes, it is necessary to apply hole filling.

The above morphological processing achieves the segmentation of the target citrus tree and the background, but it does not extract the target citrus tree yet. The edge of the citrus tree image was extracted and the circular edge was detected through the Hough transform, so as to identify the citrus tree. The Sobel operator was used for edge detection of the citrus tree targets since the Sobel operator has a certain ability to suppress noise [44]. The Sobel operator convolves the x and y directions of each pixel in the image through the

horizontal and vertical templates to obtain the approximate gradient and then the edge image. The horizontal and vertical templates of Sobel are shown in Figure 7.

$$\begin{bmatrix} -1 & 0 & 1 \\ -2 & 0 & 2 \\ -1 & 0 & 1 \end{bmatrix} \quad \begin{bmatrix} -1 & -2 & -1 \\ 0 & 0 & 0 \\ 1 & 2 & 1 \end{bmatrix}$$

(**a**) (**b**)

Figure 7. The horizontal and vertical templates of Sobel: (**a**) vertical templates of Sobel, (**b**) horizontal templates of Sobel.

The Hough transform achieves the fitting of straight lines and curves to image edges by transforming the image coordinates into parameter space and describing the points in parameter space [45]. Hough circular detection is mainly determined by the following five parameters: circle radius (step_r), circle angle (step_angle), minimum circle radius (minr), maximum circle radius (maxr), and threshold parameter (thresh). In this study, the threshold parameter was multiplied by the parameter space (Hough_space) as the threshold of Hough circular detection, and the optimal detection parameters were determined through repeated debugging of the test set. The Hough transform is applicable to all circulars represented by f (x, a) = 0. The parametric equation is as follows:

$$r = x\cos\theta + y\sin\theta \quad (1)$$

where r represents the vertical distance from the line to the origin, θ represents the angle from the x-axis to the vertical line of the line, and the value range is $\pm 90^{\circ}$.

2.4.2. Detection Method Based on YOLOv5 Target Detection Algorithm

The object detection algorithm based on a deep convolutional neural network (DCNN) was applied to process the aerial images of citrus trees. DCNN has shown great advantages in the field of target detection in recent years by extracting targets in complex environments according to their high-dimensional features [46]. The detection of DCNN includes two-stage region-based detection and one-stage regression-based detection. Compared with two-stage detection, one-stage detection has the advantage of fast speed and is suitable for real-time detection, and is widely used in image recognition, video target detection, and other fields [47]. As the most typical one-stage target detection algorithm, the YOLO (You Only Look Once) series is superior to other algorithms in accuracy and speed [48]. The YOLOv5 in the YOLO series has a total of four network models, and users can choose the network model according to their individual needs, which provides a high degree of flexibility. Among them, the YOLOv5s model has the smallest size compared to the other three models, and the inference speed per image can reach 0.007 s [49]. Therefore, the YOLOv5s model was selected for the target detection of citrus trees.

The YOLOv5s target detection algorithm consists of four parts, namely the input terminal, the backbone network, the path aggregation network, and the detection terminal [50]. On the input terminal, a series of preprocessing and data enhancement operations are performed on the image to increase the number of training samples and to improve the generalization ability of the model, such as mosaic data enhancement, adaptive anchor box calculation, and adaptive image scaling [51]. In the backbone network, the YOLOv5 algorithm uses CSPDarknet as the backbone feature extraction network, and finally extracts three effective feature layers and inputs them to the next path aggregation network. In the path aggregation network, the YOLOv5s algorithm uses the combined structure of the feature pyramid network (FPN) and the path aggregation network (PAN) to enhance the model's learning of location information, thereby comprehensively improving the robustness of the model. On the detection terminal, the YOLOv5s outputs three YOLO heads to predict the results. The citrus tree target detection process based on YOLOv5s is shown in Figure 8. Label data needs to be added to the dataset samples before model training. Data labeling tools mainly include Mechanical Turk, LabelImg, LabelMe, and

RectLabel, among which LabelImg is an open-source labeling tool that is widely used by researchers [52]. Therefore, this paper used LabelImg software to manually add label data to the aerially photographed citrus trees of Scene 1 and Scene 2 and generate text files with the suffix xml, which are used for supervised learning of deep learning algorithms.

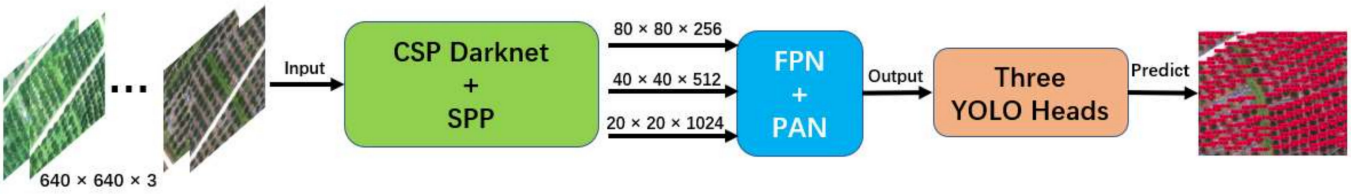

Figure 8. Flowchart of citrus tree target detection based on YOLOv5s.

2.4.3. Training Parameter Setting and Evaluation

The experimental environments of the two algorithms are unified as Intel Core i9-10900KF CPU, NVIDIA GeForce RTX 3090, Pytorch 1.2.0, cuda10.0, torchvision0.4.0, and MATLAB 2019b. The datasets of the two scenes in this experiment are 767 aerial images, respectively. The datasets of each scene are divided into training: validation: test = 8.1:0.9:1. Some initial parameter settings are shown in Table 2.

Table 2. Some initial training parameters of Hough transform and YOLOv5s.

Scene	Hough Transform					YOLOv5s					
	step_r	step_angle	minr	maxr	Thresh	Input Size	Batch Size	Epoch	Weights	Optimizer	Score_Threhold
1	0.5	0.15	30	150	0.58	640 × 640	8	300	s	SGD	0.5
2	0.4	0.1	40	150	0.57	640 × 640	8	300	s	SGD	0.5

In order to quantitatively analyze the performance of target detection algorithms, researchers have formulated many evaluation indicators, such as *Precision*, *Recall*, *F*1 Score, frame per second (FPS), etc. [53]. These indicators reflect the performance of target detection algorithms in different aspects to a certain extent. *Precision* is the probability that all predicted positive samples are actually positive samples. *Recall* is the ability of the classifier to identify positive samples. *F*1 Score is a compromise between *Precision* and *Recall*. Four indicators, *Precision*, *Recall*, *F*1 Score, and FPS were applied to analyze the performance of the two algorithms. The definitions of *Precision*, *Recall*, and *F*1 Score are shown in Equations (2)–(4), respectively.

$$Precision = \frac{TP}{TP + FP} \tag{2}$$

$$Recall = \frac{TP}{TP + FN} \tag{3}$$

$$F_1 = \frac{2 \times Precision \times Recall}{Precision + Recall} \tag{4}$$

where *TP* represents the number of images that are actually citrus tree targets and the model is correctly detected; *FP* represents the number of images that do not belong to the citrus tree target but are incorrectly detected by the model; *FN* represents the number of images that are actually citrus trees but are incorrectly detected by the model.

2.5. Citrus Tree Coordinate Extraction

After the target detection algorithm is determined, it can be used to detect the citrus trees in the orthophoto map to extract the pixel coordinates of the trees. In order to complete the conversion of the geographical coordinates of the citrus tree, it is necessary to first convert the pixel coordinates into the same UTM projection coordinate system in the orthophoto map. Then, the UTM projection coordinates are converted into geographic

coordinates through a Gaussian inverse calculation to complete the coordinate information extraction of the citrus trees.

2.5.1. Conversion of Citrus Tree Pixel Coordinates to UTM Projection Coordinates

The output coordinate system selected for the orthophoto map is the WGS84-UTM (Universal Transverse Mercator) space projection coordinate system [54], so it is necessary to convert the pixel coordinates to UTM projection coordinates. The same point has different coordinate values in different coordinate systems. Performing a coordinate conversion between different coordinate systems usually requires three or more common coordinate points to complete the transformation between two spatial coordinate systems through rotation, translation, and scaling [55]. The pixel coordinates in this study are extracted based on the UTM coordinate system in the orthophoto map, as shown in Figure 9. In the figure, $x_1y_1z_1$ is the coordinate system of the orthophoto map and $x_2y_2z_2$ is the pixel coordinate system. There is no offset in the z-axis direction. Therefore, the conversion from pixel coordinates to UTM projection coordinates only needs to be scaled in equal proportions, and the conversion scaling factor equations are shown in Equations (5) and (6).

$$k_l = \frac{U_r - U_l}{l} \tag{5}$$

$$k_h = \frac{U_r - U_l}{h} \tag{6}$$

where U_r is the UTM coordinate value of the right border of the orthophoto map, U_l is the UTM coordinate value of the left border of the orthophoto map, l is the pixel length of the orthophoto map, h is the pixel width of the orthophoto map, and k_l and k_h are the scale factors of the abscissa and ordinate of the pixel, respectively.

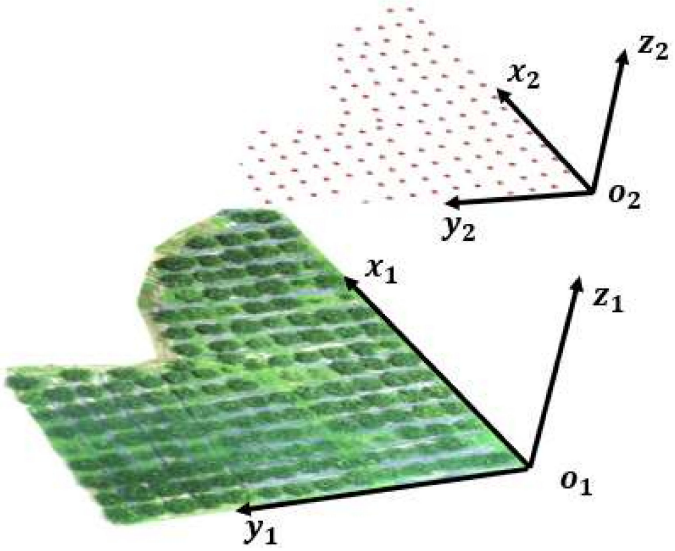

Figure 9. Pixel coordinate system and UTM coordinate system: $x_1y_1z_1$ is the UTM coordinate system; $x_2y_2z_2$ is the pixel coordinate system.

After the scale factor is obtained, the UTM coordinate system conversion can be completed according to Equations (7) and (8):

$$U_x = U_l + k_l \times x \tag{7}$$

$$U_y = U_d + k_h \times y \tag{8}$$

where U_d is the UTM coordinate value of the lower boundary of the orthophoto map, and x and y are the abscissa and ordinate of the fruit tree pixel, respectively.

2.5.2. Conversion from UTM Projection Coordinates of Fruit Trees to WGS84 Coordinates

The WGS84 coordinate system is the coordinate system currently used by the Global Positioning System [56]. It is also a general coordinate system used for positioning and navigation [57]. The extraction of the geographic information of the citrus tree is completed by converting the UTM projection coordinates of the citrus tree into WGS84 geodetic coordinates. The Gauss–Krüger inverse algorithm was used to convert UTM projection coordinates to WGS84 geodetic coordinates. The Gauss–Krüger projection is a crosscut equirectangular elliptical projection drawn up by Johann Karl Friedrich Gauss (Gauss), and later supplemented by Krüger, hence the name, Gauss–Krüger projection. The conversion of UTM (X, Y) projected coordinates to WGS84 (L, B) geodetic coordinates is what we usually call a Gaussian inverse calculation. The calculation equations are shown in Equations (9) and (10):

$$B = B_f - \frac{t_f}{2M_f N_f \cos B_f} y^2 + \frac{t_f}{24 M_f N_f^3}\left(5 + 3t_f^3 + \eta_f^3 - 9\eta_f^2 t_f^2\right) y^4 - \frac{t_f}{720 M_f N_f^5} y\left(61 + 90t_f^2 + 45t_f^4\right) y^6 \quad (9)$$

$$L = L_0 + \frac{y}{N_f \cos B_f} - \frac{y^3}{6N_f^3 \cos B_f}(1 + 2t_f^2 + \eta_f^2) + \frac{y^5}{120 N_f^5 \cos B_f}\left(5 + 28t_f^2 + 24t_f^4 + 6\eta_f^2 + 8\eta_f^2 t_f^2\right) \quad (10)$$

where B_f is the latitude of the bottom point, that is, when $y = 0$, the latitude of the projection point of the ordinate on the ellipsoid is the latitude of the bottom point; M is the radius of curvature of the meridian circle, $M = \frac{c}{\sqrt{(1+e'^2)^3}}$; N is the radius of curvature of the unitary circle, $N_f = \frac{a}{\sqrt{1-e^2 sin_B^2}}$; $\eta^2 = e'^2 cos_B^2$, e, e' are the first and second curvature radii; c is the radius of curvature of the pole; $t = \tan B$; a is the semimajor axis of the ellipsoid, in m; L_0 is the central meridian, in radians (rad). The derivation equation of L_0 is shown in (11):

$$L_0 = (6 \times Zone - 3) - 180 \quad (11)$$

where $Zone$ is the zone number of the local projection zone.

In order to facilitate program compilation, $\frac{1}{M} = \frac{1+\eta^2}{N}$ is brought into the above equations and arranged as Equations (12) and (13):

$$B = B_f - \frac{N_f t_f}{2M_f}\left[\left(\frac{y}{N_f}\right)^2 - \frac{1}{12}\left(5 + 3t_f^2 + \eta_f^2 - 9\eta_f^2 t_f^2\right)\left(\frac{y}{N_f}\right)^4 + \frac{1}{36}\left(61 + 90t_f^2 + 45\eta_f^4\right)\left(\frac{y}{N_f}\right)^6\right]\frac{180}{pi} \quad (12)$$

$$L = L_0 + \frac{1}{\cos B_f}\left[\left(\frac{y}{N_f}\right) - \frac{1}{6}\left(1 + 2t_f^2 + \eta_f^2\right)\left(\frac{y}{N_f}\right)^3 + \frac{1}{120}\left(5 + 28t_f^2 + 24\eta_f^4 + 6\eta_f^2 + 8\eta_f^2 t_f^2\right)\left(\frac{y}{N_f}\right)^5\right]\frac{180}{pi} \quad (13)$$

3. Results

3.1. Comparison and Analysis of Citrus Trees Identification

The target detection of citrus trees based on the Hough transform adopted manual parameter adjustment and manual evaluation index calculation. The parameters were repeatedly adjusted through the training set and verified by the validation set and the optimal parameter values in two scenes (after and before weeding) were then determined. Due to the excessive amount of data, it is impossible to calculate the overall indicators of all test sets. Therefore, a random sampling method was used to select 10 pictures for testing in the two test sets. *TP*, *FP*, and *FN* values were calculated manually, and finally the *Recall*, *F*1 Score, and *Precision* were achieved. The statistical results based on the Hough transform are shown in Table 3. It can be seen that for the citrus tree target detection in Scene 1: after weeding, the average *Precision* of the Hough transform is 0.88, the average *Recall* and *F*1 Score are both 0.87. The differences among the three indicators are small, showing relatively stable detection performance. In Scene 2: before weeding, the average

Precision of the Hough transform is 0.48, which is 0.4 lower than that of Scene 1. The *Recall* and *F*1 Score are 0.35 and 0.38, respectively, which is lower than that of Scene 1 as well. This shows that the Hough transform is more suitable for citrus tree detection in Scene 1 with clearer background and has relatively stable detection performance.

Table 3. Statistics of citrus tree detection results based on Hough transform.

Image Number	Scene 1: After Weeding				Scene 2: Before Weeding			
	Precision	*Recall*	*F*1 Score	FPS	*Precision*	*Recall*	*F*1 Score	FPS
1	0.96	0.94	0.95	0.0241	0.40	0.53	0.46	0.0135
2	0.87	0.86	0.86	0.0243	0.50	0.41	0.45	0.0717
3	0.88	0.84	0.86	0.0251	0.56	0.50	0.53	0.0349
4	0.87	0.87	0.87	0.0257	0.34	0.54	0.42	0.0547
5	0.88	0.90	0.89	0.0258	0.35	0.48	0.41	0.0371
6	0.86	0.87	0.87	0.0258	0.48	0.55	0.51	0.0371
7	0.93	0.80	0.86	0.0242	0.52	0.52	0.52	0.0389
8	0.83	0.93	0.88	0.0216	0.57	0.48	0.52	0.0456
9	0.81	0.80	0.81	0.0238	0.44	0.50	0.47	0.0337
10	0.92	0.82	0.87	0.0205	0.63	0.64	0.63	0.0608
Average	0.88	0.87	0.87	0.0241	0.48	0.52	0.49	0.0428

Figure 10 shows the loss curve of YOLOv5s training. It can be seen from the loss function that the data sets of the two scenes tend to converge after 200 epochs of training, indicating that the training accuracy of the YOLOv5s algorithm will not be too complex due to the environment. However, the loss function of the Scene 1 dataset (Figure 10a) is lower than the loss function of the Scene 2 dataset (Figure 10b) during the training process. The Scene 1 dataset finally converges to 0.25, about 0.4 different from that of Scene 2, which indicates that the training effect of Scene 1 (after weeding) is better than that of Scene 2 (before weeding). The complexity of the image background will still affect the training of the YOLOv5s model.

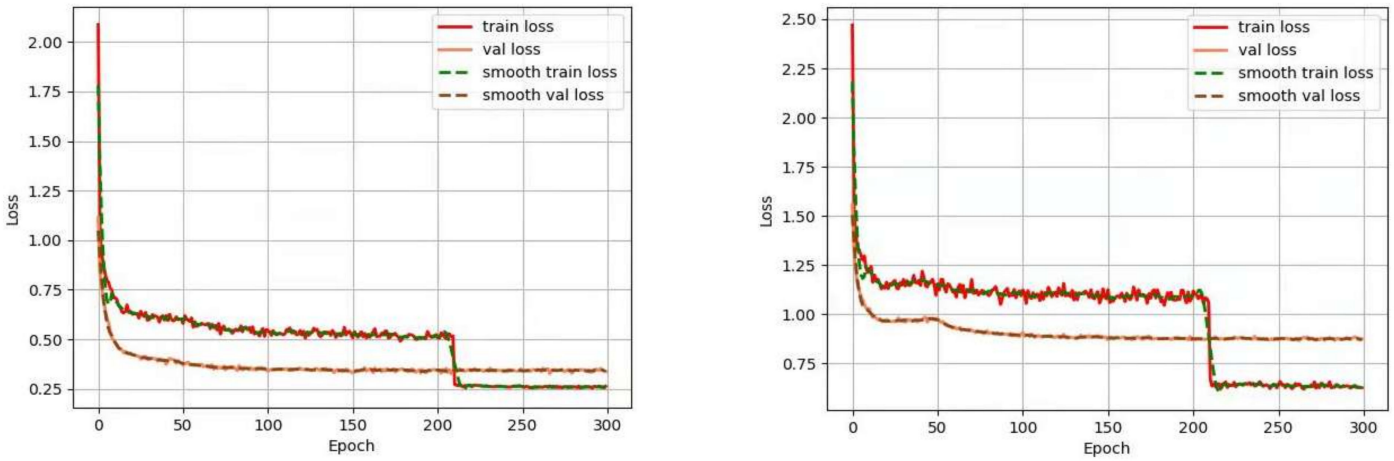

Figure 10. Calculation result of YOLOv5s loss. (**a**) Calculation result of YOLOv5s loss in Scene 1: after weeding; (**b**) calculation result of YOLOv5s loss in Scene 2: before weeding.

The comparison results of the two algorithms in each scene are shown in Table 4. It can be seen that in Scene 1, the *Precision* difference between the two algorithms is 0.01, indicating that the two algorithms can correctly identify the citrus tree target with similar performance. The *Recall* difference between the two algorithms is 0.1, indicating that in terms of recognition rate, YOLOv5s performs better. The *F*1 Score difference between the two algorithms is 0.05, suggesting that the two algorithms have a similar recognition

performance in general. However, in the target recognition of citrus trees in Scene 2 (before weeding), the detection results of the Hough transform show serious errors, whereas the YOLOv5s model still maintains high accuracy. For example, the *F*1 Score of YOLOv5s is 0.45 higher than that of the Hough transform. In addition, in terms of detection speed, the FPS of YOLOv5s achieved about 60 for both scenes, which is superior to that of the Hough transform algorithm. Based on the comparison and analysis, the YOLOv5s model was selected as the target recognition algorithm for citrus trees for its better identification accuracy and higher speed.

Table 4. Comparison results of Hough transform and YOLOv5s algorithm.

Scene	Hough Transform				YOLOv5s			
	***F*1 Score**	***Recall***	***Precision***	**FPS**	***F*1 Score**	***Recall***	***Precision***	**FPS**
1	0.87	0.87	0.88	0.0241	0.92	0.97	0.89	63
2	0.49	0.52	0.48	0.0428	0.91	0.90	0.91	60

3.2. Orthophoto Map Accuracy Verification

The high-precision orthophoto map is the premise to ensure the extraction of geographical coordinates of citrus trees. Six sampling points were randomly arranged in the orchard. A XAG Agricultural Beidou differential positioning terminal (XAG Technology Co., Ltd., Guangzhou, China) with high precision was used to extract the WGS84 coordinates of the sampling points. The result was then compared with the WGS84 coordinates information of the sampling points in the point cloud model to verify the correctness. The horizontal positioning accuracy of the XAG positioning terminal is ±10 mm [58], which meets the accuracy verification requirements. Figure 11a shows the process of extracting WGS84 coordinates of sampling points on site, and Figure 11b indicates the process of extracting coordinates of sampling points in a point cloud model.



(a) **(b)**

Figure 11. Field sampling and point cloud sampling: (**a**) on-site extraction of WGS 84 coordinates of sampling points; (**b**) point cloud model extraction coordinates.

The coordinate information of the sampling points in the point cloud model and the field sampling points were compared and analyzed. The experimental comparison results are shown in Table 5. The measured values in the table are the coordinate information extracted from the orthophoto map and the actual value is the coordinate information extracted by using the XAG agricultural Beidou differential positioning terminal. By

calculating the Euclidean distance between the actual and the measured value, it can be seen that the average accuracy of the Euclidean distance of the orthophoto map is 0.15 m, which is reliable and meets the extraction requirements of the citrus tree coordinates of the subsequent orthophoto map.

Table 5. UTM coordinate comparison of sampling points.

Sampling Point	Coordinate Information/(X, Y)		Horizontal Error/m	Euclidean Distance Error/m
	Actual Value	Measured Value		
5	(655,123.054, 2,593,077.514)	(655,123.093, 2,593,077.607)	(0.041, 0.093)	0.101
4	(655,143.585, 2,593,080.156)	(655,143.669, 2,593,080.21)	(0.084, 0.054)	0.099
3	(655,101.704, 2,593,067.178)	(655,101.896, 2,593,067.318)	(0.192, 0.14)	0.238
6	(655,135.416, 2,592,983.677)	(655,135.616, 2,592,983.785)	(0.2, 0.118)	0.227
12	(655,143.153, 2,592,974.833)	(655,143.272, 2,592,974.714)	(0.119, 0.119)	0.168
1	(655,111.020, 2,593,050.100)	(655,111.049, 2,593,050.112)	(0.029, 0.012)	0.031
Mean Euclidean distance error: 0.15 m, average horizontal distance error: (0.11, 0.089)				

3.3. UTM Coordinate Verification

In the work of spatial coordinate system transformation, the reverse comparison with ArcMap software was applied to verify the accuracy of the coordinates. This method imports the converted UTM coordinate data of the citrus tree into the orthophoto map for comparison to verify whether it is located in the center of the fruit tree. ArcMap is an application program developed by the Environment System Research Institute with functions such as map making, spatial analysis, and spatial data database building. It is widely used in the field of surveying and mapping [59]. The ArcMap software was used to import the orthophoto map, and ArcToolbox was used to add the XY data to the new layer. Then, the added (X, Y) coordinate points were displayed on the layer page of the image map. Since the geometry of the citrus tree canopy is usually a circle with a diameter of 3 m, the precise coordinates of the tree center are not clearly specified. Therefore, the space rectangular coordinate verification was carried out through visual inspection to compare and verify its accuracy.

We selected three test areas for UTM coordinate verification, as shown in Figure 12, where a–c are test field 1, d–f are test field 2, and g–h are test field 3. The UTM projection coordinate points automatically converted from the pixel coordinates of citrus trees collected in three experimental plots were imported into ArcMap, as shown in Figure 12a,d,g. Similarly, the orthophoto map containing geographic coordinate information was imported into ArcMap, as shown in Figure 12b,e,h. The geographic coordinates of the orthophoto map were used as the benchmark to verify the accuracy of the coordinate transformation by comparing the mapping relationship between the two coordinates, as shown in Figure 12c,f,i. It can be seen based on visual inspection that the UTM coordinates of the trees through the conversion are basically located in the center of each citrus tree, and the accuracy is reliable and meets the requirements of subsequent experiments.

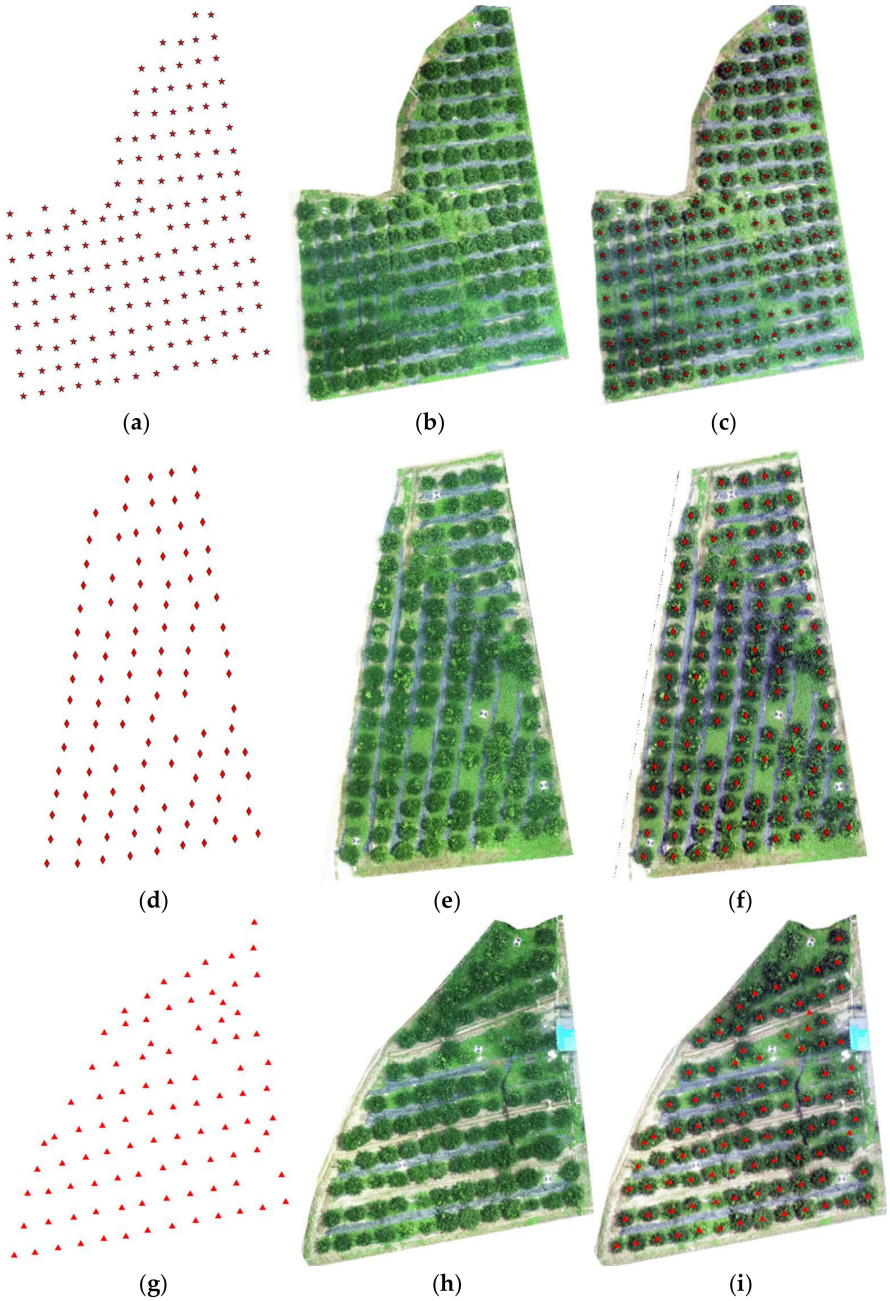

Figure 12. UTM coordinate verification. (**a**–**c**) are experimental plot 1; (**d**–**f**) are experimental plot 2; (**g**–**i**) are experimental plot 3; (**a**,**d**,**g**) are converted UTM projection coordinate points; (**b**,**e**,**h**) are the orthophoto map of the extracted fruit tree pixels; (**c**,**f**,**i**) are the correspondence between the coordinate point and the orthophoto map in the UTM coordinate system.

3.4. Coordinate Conversion App Design and WGS84 Coordinate Verification

According to the coordinate conversion requirements, the process of converting fruit tree pixel coordinates to geodetic coordinates is extremely cumbersome. In order to simplify the coordinate conversion process, a citrus tree coordinate conversion app was developed using MATLAB software, which realizes the batch conversion of pixel coordinates to coordinates and the single-point conversion of UTM coordinates to WGS84 coordinates. The flow chart of the program is shown in Figure 13. This application has a single-point conversion function and batch conversion function. The single-point conversion function can perform coordinate conversion on a single UTM-projected coordinate and convert it to a WGS84 coordinate or XIAN80 coordinate. The batch conversion function can convert the

pixel coordinates of citrus trees extracted from the orthophoto map into UTM projection coordinates and WGS84 coordinates, and then, the two coordinates are saved in Excel format for subsequent data processing and analysis.

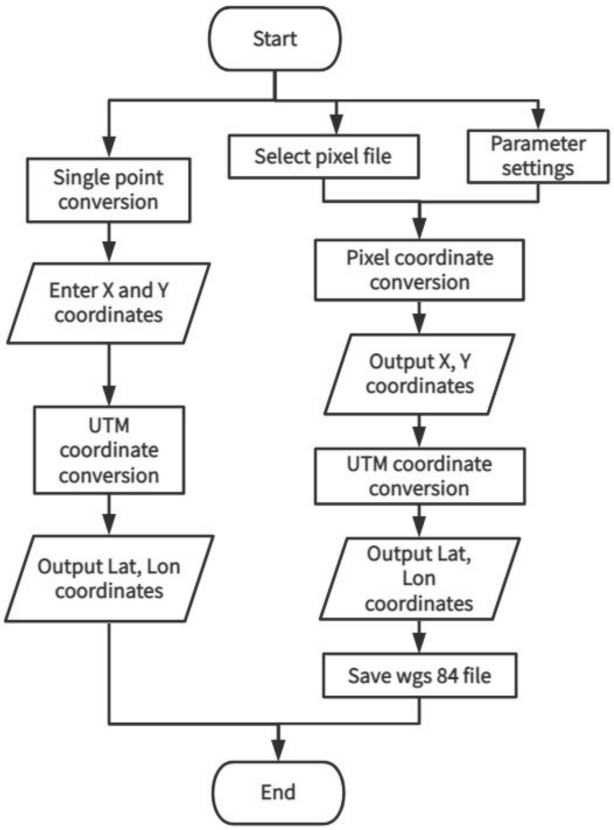

Figure 13. Flowchart of the coordinate conversion application.

In order to verify the conversion accuracy, the coordinate conversion application developed in this study and the commercial software ArcMap were both used to convert the same set of UTM projection coordinates to WGS84 coordinates. Due to the huge amount of data, only six sets of data were randomly selected from each experimental plot for comparison analysis. The results are shown in Table 6.

Table 6. UTM coordinate result comparison.

	Experimental Plot 1						**Experimental Plot 2**						**Experimental Plot 3**					
Longitude error/10^{-6}	0.11	0.10	0.10	0.11	0.10	0.10	0.11	0.11	0.10	0.11	0.11	0.11	0.11	0.10	0.11	0.11	0.11	0.10
Latitude error/10^{-6}	−0.1	−0.2	−0.1	−0.1	−0.2	−0.1	−0.2	−0.1	−0.1	−0.2	−0.1	−0.2	−0.1	−0.2	−0.1	−0.1	−0.2	−0.2

Usually, the geometric shape of the citrus canopy is circular with a diameter of 3 m [11], which has a large footprint, so there is a certain error allowed for the extracted coordinates, and the accuracy of the coordinate error is required to be 0.1 m. The latitude and longitude values of the sampling points in Table 6 were expressed in decimal. According to the distribution characteristics of the earth's latitude and longitude, the latitude difference is 111 km every 1°. The latitude and longitude at this experimental site are 23°36′N and 112°68′E, respectively. The longitude difference is 104,043.976 m every 1° [60], that is, the longitude difference is about 0.1 m every 0.000001°. The decimal latitude and longitude coordinates are accurate to 0.1 m, that is, it can be reserved to six decimal places. Therefore, we only need to focus on the last six digits of the latitude and longitude information in

Table 6 to compare the conversion accuracy. It can be seen from the table that the same set of UTM data is converted by the developed application and ArcMap, and the difference in longitude and latitude is 0.1×10^{-6}. The conversion accuracy of the method proposed in this study can reach centimeter-level precision, which meets the requirements of the geodetic coordinate conversion of citrus trees.

4. Discussion

Precision management of citrus orchards using plant protection UAVs in China requires obtaining the geographic coordinates of a single citrus tree. The citrus tree extraction from UAV remote sensing imagery proposed in this study is capable of automatically obtaining the WGS84 coordinates of citrus trees with high precision by using YOLOv5s and coordinate transformation. The accurate geographic coordinate information of single citrus trees provided the feasibility for precision orchard management by "one tree one code". The variable rate application of agricultural production materials according to the growth differences of trees is possible in future research.

This study applied UAVs to collect remote sensing images of orchards and generate a high-precision orthophoto map. On this basis, traditional image recognition and deep learning algorithms were used to identify citrus trees in an orthophoto map. Pei et al. [31] also used the traditional binary image processing method to extract the coordinates of tea sprouts. However, this method requires manual debugging, resulting in the fact that the degree of automation is low and the recognition rate of tea sprouts in complex scenes is also poor. To better improve the recognition performance of the algorithm, the traditional target detection method based on the Hough transform was compared with the YOLOv5s algorithm based on deep learning. After comparison analysis, the YOLOv5s model based on deep learning showed strong robustness in citrus tree target detection in different scenarios, thereby ensuring its recognition accuracy of citrus trees. In terms of extracting citrus tree coordinates, the automatic conversion of citrus tree coordinates with high precision was achieved through spatial coordinate system transformation and Gauss–Krüger inverse calculation. Compared with the manual extraction of citrus tree coordinates, the automatic coordinates extraction method proposed in this study saves time and labor. In addition, the extraction of citrus trees from UAV remote sensing images is also superior to terrestrial mechanical sensors by providing a low-cost solution.

The accuracy of the orchard orthophoto map depends on the layout of image control points, image quality, overlap rate, flying height, and other factors. A DJI Phantom 4 RTK UAV was selected for remote sensing image acquisition, which can obtain high-quality remote sensing images with a resolution of 5472×3648. At the same time, it is equipped with a D-RTK 2 high-precision GNSS mobile station to ensure the accuracy of an orchard orthophoto map. However, in the process of aerial photography, the impact of factors such as light, wind speed, and distance on the positioning accuracy of the UAV cannot be ignored. Therefore, six control points in the field were arranged to further improve the accuracy of the orthophoto map. In terms of overlap rate, we adopted a higher side overlap rate and heading overlap rate, which allow the inability to complete data collection in one flight. UAV remote sensing images were taken at the time of day when the light is better. In terms of UAV flight height selection, the higher the flight, the lower the image resolution, which will reduce the effectiveness of citrus tree target detection. If the flight is too low, the feature points of the target in the images will be reduced, and the quality of the image orthophoto map will be drawn. The flight height was finally determined to be 50 m.

Visible light remote sensing images were used in this study for citrus tree target detection. The YOLOv5s model shows good robustness for citrus tree target detection in visible light remote sensing images, but the recognition accuracy of traditional algorithms is poor. Traditional image processing methods have high accuracy in extracting citrus trees with regular distribution and without weeds interference. However, its recognition accuracy of citrus trees in complex environments is poor. The main reasons lie in the fact that the thresholds corresponding to weeds and citrus trees are similar. It is difficult to

perform effective threshold segmentation, thereby reducing the recognition accuracy. A similar method is also reflected in the literature [21]. This method judges the location of trees by identifying the local maxima of the point cloud model. However, this method often leads to large errors due to the size of the tree and the shape of the canopy. From this point of view, the YOLOv5s algorithm has certain robustness for citrus tree identification in environments with different degrees of complexity, so using the YOLOv5s model to identify fruit trees is a key step in extracting fruit tree coordinates. In addition to visible light remote sensing images, related research has also used thermal infrared remote sensing images [61], multispectral imagery [62], a digital elevation model (DEM) [63], and other methods to extract target features, achieving high target detection results. These methods are also suitable for the extraction of citrus tree coordinate information in this study. It is expected to solve the recognition accuracy of citrus trees based on the Hough transform in complex background. In future research, we also need to improve the robustness of this method, study different varieties of fruit trees, and realize the coordinate extraction of all varieties of fruit trees.

Identifying crop varieties and obtaining growth information through UAV remote sensing images is an important means for farmers to facilitate the digital management of orchards. However, with a new generation of farmers rapidly increasing their interest in using digital solutions, the cumulative archive of UAV imagery data is a concern. Kayad et al. [64] estimated the data storage disc space requirements in the last two decades from a 22 ha field located in Northern Italy. The results showed that the total accumulated data size from the study field reached 18.6 GB in 2020 mainly due to the use of UAV images. Through the method in this paper, the archived data of UAV images can be effectively reduced. In terms of citrus tree target detection, we use the YOLOv5s model to train remote sensing images. While ensuring recognition accuracy, the remote sensing data set of 7.69 GB is effectively converted into a training weight file of 54.7 MB. In the extraction of citrus tree geographic coordinates, the method used in this paper can convert the 40 MB orthophoto map into a 12.6 KB coordinate file. Reasonable archiving of remote sensing images can effectively reduce the storage space of data and help farmers manage their orchards more accurately. UAV remote sensing images not only provide farmers with rich data but also increase storage costs. In future research, we also need to optimize the utilization and benefits of UAV remote sensing images to provide more efficient orchard management plans.

5. Conclusions

This study proposed a method for citrus tree identification and coordinate extraction based on UAV remote sensing imagery and coordinate transformation. In the first stage, UAV remote sensing images were used to generate an orchard orthophoto map. Control points and RTK mobile base stations were applied to ensure the geographic accuracy of orthophoto maps. In the second stage, after comparing the detection accuracy of the YOLOv5s algorithm and the Hough transform, the YOLOv5s algorithm with a better identification performance of citrus trees was selected to extract the coordinate information of citrus trees. Finally, the spatial coordinate system transformation and Gaussian inverse calculation were conducted to extract the WGS84 coordinates of the citrus tree. The experimental results show that the average Euclidean distance accuracy of the orthophoto map reaches 0.15 m. In object detection, the YOLOv5s model has better detection performance in both scenes (Scene 1 after weeding: *Precision* = 0.89, *Recall* = 0.97, *F*1 Score = 0.92; Scene 2 before weeding: *Precision* = 0.91, *Recall* = 0.90, *F*1 Score = 0.91). The coordinate conversion method proposed in this study can convert WGS84 coordinates with an accuracy of 1 cm. The high-precision WGS84 coordinates of citrus trees can be automatically extracted based on the citrus tree identification and coordinate extraction method. This method is suitable for the extraction and transformation of target coordinates in all orthophoto maps and is featured with high precision, high efficiency, and a high-recognition rate.

Author Contributions: Conceptualization, Y.Z. and H.T.; methodology, Y.Z., H.T. and X.F.; validation, H.T. and Y.L.; formal analysis, H.T., X.F., H.H. and C.M.; investigation, Y.Z., H.H., H.T., C.M., D.Z. and H.L.; resources, H.T., D.Z. and H.L.; data curation, H.T. and C.M.; writing—original draft preparation, H.T., C.M. and Y.Z.; writing—review and editing, Y.Z. and C.M.; visualization, C.M.; supervision X.L.; project administration, Y.Z.; funding acquisition, Y.Z. All authors have read and agreed to the published version of the manuscript.

Funding: This research was funded by Guangdong Science and Technology Plan Project, grant number 2018A050506073, and the 111 Project, grant number D18019.

Data Availability Statement: The data presented in this study are available on request from the corresponding author.

Conflicts of Interest: The authors declare no conflict of interest.

References

1. Annual Report on Fruit Production in China. Available online: https://data.stats.gov.cn/index.htm (accessed on 20 July 2022).
2. Shan, Y. Present situation, development trend and countermeasures of citrus industry in China. *J. Chin. Inst. Food Sci. Technol.* **2008**, *1*, 1–8.
3. Shu, M.Y.; Li, S.L.; Wei, J.X.; Che, Y.P.; Li, B.G.; Ma, T.Y. Extraction of citrus crown parameters using UAV platform. *Trans. Chin. Soc. Agric. Eng.* **2021**, *37*, 68–76.
4. Wang, H.; Noguchi, N. Navigation of a robot tractor using the centimeter level augmentation information via Quasi-Zenith Satellite System. *Eng. Agric. Environ. Food* **2019**, *12*, 414–419. [CrossRef]
5. Zhou, J.; He, Y.Q. Research progress on navigation path planning of agricultural machinery. *Trans. Chin. Soc. Agric. Mach.* **2021**, *52*, 1–14.
6. Guo, C.Y.; Zhang, S.; Zhao, L.; Chen, J. Research on autonomous navigation system of orchard agricultural vehicle based on RTK-BDS. *J. Agric. Mech. Res.* **2020**, *8*, 254–259.
7. Chen, K.; Tian, G.Z.; Gu, B.X.; Liu, Y.F.; Wei, J.S. Design and Simulation of front frame of orchard automatic obstacle avoidance Lawn Mower. *Jiangsu Agric. Sci.* **2020**, *48*, 226–232.
8. Qiu, W.; Sun, H.; Sun, Y.H.; Liao, Y.Y.; Zhou, L.F.; Wen, Z.J. Design and test of circulating air-assisted sprayer for dwarfed orchard. *Trans. Chin. Soc. Agric. Eng.* **2021**, *37*, 18–25.
9. Qiu, W.; Li, X.L.; Li, C.C.; Ding, W.M.; Lv, X.L.; Liu, Y.D. Design and test of a novel crawler-type multi-channel air-assisted orchard sprayer. *Int. J. Agric. Biol. Eng.* **2020**, *13*, 60–67. [CrossRef]
10. Song, C.C.; Zhou, Z.Y.; Wang, G.B.; Wang, X.W.; Zang, Y. Optimization of the groove wheel structural parameters of UAV-based fertilizer apparatus. *Trans. Chin. Soc. Agric. Eng.* **2021**, *37*, 1–10.
11. Qi, Y.; Dong, X.; Chen, P.; Lee, K.-H.; Lan, Y.; Lu, X.; Jia, R.; Deng, J.; Zhang, Y. Canopy Volume Extraction of Citrus reticulate Blanco cv. Shatangju Trees Using UAV Image-Based Point Cloud Deep Learning. *Remote Sens.* **2021**, *13*, 3437. [CrossRef]
12. Zhang, Y.; Tian, H.; Huang, X.; Ma, C.; Wang, L.; Liu, H.; Lan, Y. Research Progress and Prospects of Agricultural Aero-Bionic Technology in China. *Appl. Sci.* **2021**, *11*, 10435. [CrossRef]
13. Li, V.; Selam, A.; Beniamin, A.; Kamal, A. A novel method for detecting morphologically similar crops and weeds based on the combination of contour masks and filtered Local Binary Pattern operators. *Comput. Electron. Agric.* **2020**, *9*, giaa017.
14. Hamuda, E.; Glavin, M.; Jones, E. A survey of image processing techniques for plant extraction and segmentation in the field. *Comput. Electron. Agric.* **2016**, *125*, 184–199. [CrossRef]
15. Hogan, S.D.; Kelly, M.; Stark, B.; Chen, Y. Unmanned aerial systems for agriculture and natural resources. *Calif. Agric.* **2017**, *71*, 5–14. [CrossRef]
16. Zhang, N.; Yang, G.J.; Zhao, C.J.; Zhang, J.C.; Yang, X.D.; Pan, Y.C.; Huang, W.J.; Xu, B.; Li, M.; Zhu, X.C.; et al. Progress and prospects of hyperspectral remote sensing technology for crop diseases and pests. *Natl. Remote Sens. Bull.* **2021**, *25*, 403–422.
17. Shi, Z.; Liang, Z.Z.; Yang, Y.Y.; Guo, Y. Status and Prospect of Agricultural remote Sensing. *Trans. Chin. Soc. Agric. Mach.* **2015**, *46*, 247–260.
18. Zhang, J.C.; Yuan, L.; Wang, J.H.; Luo, J.H.; Du, S.Z.; Huang, W.J. Research progress of crop diseases and pests monitoring based on remote sensing. *Trans. Chin. Soc. Agric. Eng.* **2012**, *28*, 1–11.
19. Liu, S.Y.; Wang, X.Y.; Chen, X.A.; Hou, X.N.; Jiang, T.; Xie, P.F.; Zhang, X.M. Fruit tree row recognition with dynamic layer fusion and texture-gray gradient energy model. *Trans. Chin. Soc. Agric. Eng.* **2022**, *38*, 152–160.
20. Malek, S.; Bazi, Y.; Alajlan, N.; AlHichri, H.; Melgani, F. Efficient Framework for Palm Tree Detection in UAV Images. *IEEE J. Sel. Top. Appl. Earth Obs. Remote Sens.* **2014**, *7*, 4692–4703. [CrossRef]
21. Surový, P.; Almeida Ribeiro, N.; Panagiotidis, D. Estimation of positions and heights from UA V-sensed imagery in tree plantations in agrosilvopastoral systems. *Int. J. Remote Sens.* **2018**, *39*, 4786–4800. [CrossRef]
22. Goldbergs, G.; Maier, S.W.; Levick, S.R.; Edwards, A. Efficiency of Individual Tree Detection Approaches Based on Light-Weight and Low-Cost UAS Imagery in Australian Savannas. *Remote Sens.* **2018**, *10*, 161. [CrossRef]
23. Luo, X.; Wu, Y.; Zhao, L. YOLOD: A Target Detection Method for UAV Aerial Imagery. *Remote Sens.* **2022**, *14*, 3240. [CrossRef]

24. Wang, Q.; Wang, C.; Wu, H.; Zhao, C.; Teng, G.; Yu, Y.; Zhu, H. A Two-Stage Low-Altitude Remote Sensing Papaver Somniferum Image Detection System Based on YOLOv5s+DenseNet121. *Remote Sens.* **2022**, *14*, 1834. [CrossRef]
25. Guo, Y.G.; Li, Z.C.; He, H.; Wang, Z.Y. A simplex search algorithm for the optimal weight of common point of 3D coordinate transformation. *Acta Geod. Cartogr. Sin.* **2020**, *49*, 1004–1013.
26. Li, G.Y.; Li, Z.C. *The Principles and Applications of Industrial Measuring Systems*; Surveying and Mapping Press: Beijing, China, 2011.
27. Zeng, A.M.; Zhang, L.P.; Wu, F.M.; Qin, X.P. Adaptive collocation method to coordinate transformation from XAS80 to CGCS2000. *Geomat. Inf. Sci. Wuhan Univ.* **2012**, *37*, 1434–1437.
28. Li, B.F.; Shen, Y.Z.; Li, W.X. The seamless model for three-dimensional datum transformation. *Sci. China Earth Sci.* **2012**, *42*, 1047–1054. [CrossRef]
29. Peng, X.Q.; Gao, J.X.; Wang, J. Research of the coordinate conversion between WGS84 and CGCS2000. *J. Geod. Geodyn.* **2015**, *35*, 119–221.
30. Liu, F.; Zhou, L.L.; Yi, J.F. Study on the practical method to transform GPS geodetic coordinates to coordinates of localsystem. *J. East China Norm. Univ. Nat. Sci.* **2005**, *2005*, 73–77.
31. Pei, W.; Wang, X.L. The two-dimension coordinates extraction of tea shoots picking based on image information. *Acta Agric. Zhejiangensis* **2016**, *28*, 522–527.
32. Deng, S.S.; Xia, L.H.; Wang, X.X.; Pan, Z.K. Fuzzy comprehensive evaluation for the tourism climate in Zhaoqing city. *Guangdong Agric. Sci.* **2010**, *37*, 242–246.
33. PHANTOM 4 RTK Specs. Available online: https://www.dji.com/id/phantom-4-rtk/info#specs (accessed on 20 July 2022).
34. Fang, J.Q. Discussion on several technical problems about producing DOM. *Geomat. Spat. Inf. Technol.* **2007**, *3*, 91–93.
35. Li, D.; Liu, J.; Yu, D. Indent round detection of Brinell test images based on Snake model and shape similarity. *Chin. J. Sci. Instrum.* **2011**, *32*, 2734–2739.
36. Li, Z.; Liu, M.; Sun, Y. Research on calculation method for the projection of circular target center in photogrammetry. *Chin. J. Sci. Instrum.* **2011**, *32*, 2235–2241.
37. Lin, J.; Shi, Q. Circle Recognition Through a Point Hough Transformation. *Comput. Eng.* **2003**, *29*, 17–18.
38. Daugman, J.G. High Confidence Visual Recognition of Persons by a Test of Statistical Independence. *IEEE Tran. Pattern Mach. Intell.* **1993**, *15*, 1148–1161. [CrossRef]
39. Davies, E.R. A Modified Hough Scheme for General Circle Location. *Pattern Recognit. Lett.* **1987**, *7*, 37–43. [CrossRef]
40. Zhu, G.; Zhang, R. Circle detection using Hough transform. *Comput. Eng. Des.* **2008**, *29*, 1462–1464.
41. Xiong, J.; Zhou, X.; Chen, L.; Cai, H.; Peng, H. Visual position of picking manipulator for disturbed litchi. *Trans. Chin. Soc. Agric. Eng.* **2012**, *28*, 36–41.
42. Xiang, R.; Ying, B.; Jiang, H. Development of Real-time Recognition and Localization Methods for Fruits and Vegetables in Field. *Trans. Chin. Soc. Agric. Mach.* **2013**, *44*, 208–223.
43. Cui, Y.; Su, S.; Wang, X.; Tian, Y.; Li, P.; Zhang, N. Recognition and Feature Extraction of Kiwifruit in Natural Environment Based on Machine Vision. *Trans. Chin. Soc. Agric. Mach.* **2013**, *44*, 247–252.
44. Li, D.; Wu, Q.; Yang, H.S. Design and implementation of edge detection system based on improved Sobel operator. *Inf. Technol. Netw. Secur.* **2022**, *41*, 13–17.
45. Chen, K.; Zhou, X.; Xiong, J.; Peng, H.; Guo, A.; Chen, L. Improved fruit fuzzy clustering image segmentation algorithm based on visual saliency. *Trans. Chin. Soc. Agric. Eng.* **2013**, *29*, 157–165.
46. Zhao, D.A.; Wu, R.D.; Liu, X.Y.; Zhao, Y.Y. Apple positioning based on YOLO deep convolutional neural network for picking robot in complex background. *Trans. Chin. Soc. Agric. Eng.* **2019**, *35*, 164–173.
47. Liu, F.; Liu, Y.K.; Lin, S.; Guo, W.Z.; Xu, F.; Zhang, B. Fast Recognition Method for Tomatoes under Complex Environments Based on Improved YOLO. *Trans. Chin. Soc. Agric. Machiner.* **2020**, *51*, 229–237.
48. Tan, S.L.; Bei, X.B.; Lu, G.L.; Tan, X.H. Real-time detection for mask-wearing of personnel based onYOLOv5 network mode. *Laser J.* **2021**, *42*, 147–150.
49. Cheng, Z.; Jia, J.M.; Jiang, Z.; Wang, X. Research on Stuttering Type Detection Based on YOLOv5. *J. Yunnan Minzu Univ. Nat. Sci. Ed.* **2022**, *1*, 1–11.
50. Cheng, Q.; Li, J.; Du, J. Ship detection method of optical remote sensing image based on YOLOv5. *Syst. Eng. Electron.* **2022**, *1*, 1–9.
51. Hou, Y.; Shi, G.; Zhao, Y.; Wang, F.; Jiang, X.; Zhuang, R.; Mei, Y.; Ma, X. R-YOLO: A YOLO-Based Method for Arbitrary-Oriented Target Detection in High-Resolution Remote Sensing Images. *Sensors* **2022**, *22*, 5716. [CrossRef]
52. Cai, L.; Wang, S.; Liu, J.; Zhu, Y. Survey of data annotation. *J. Softw.* **2020**, *31*, 302–320.
53. Wang, C.; Wang, Q.; Wu, H.; Zhao, C.; Teng, G.; Li, J. Low-Altitude Remote Sensing Opium Poppy Image Detection Based on Modified YOLOv3. *Remote Sens.* **2021**, *13*, 2130. [CrossRef]
54. Sun, L.D. Gauss-Kruger Projection and Universal Transverse Mercator Projection of the Similarities and Differences. *Port Eng. Technol.* **2008**, *5*, 31–51.
55. Guo, Y.; Tang, B.; Zhang, Q.; Zhang, W.; Hei, L. Research on Coordinate Transformation Method of High Accuracy Based on Space Rectangular Coordinates System. *J. Geod. Geodyn.* **2012**, *32*, 125–128.
56. Ning, J.S.; Yao, Y.B.; Zhang, X.H. Review of the development of Global satellite Navigation System. *J. Navig. Position.* **2013**, *1*, 3–8.
57. Cui, H.; Lin, Z.; Sun, J. Research on UAV Remote Sensing System. *Bull. Surv. Mapp.* **2005**, *5*, 11–14.
58. XAG. Product Manual. Available online: https://www.xa.com/service/downloads (accessed on 20 July 2022).

59. Wu, W.; Li, X.S.; Zhang, B. Probe of developing technology based on ArcGIS Engine. *Sci. Technol. Eng.* **2006**, *2*, 176–178.
60. Li, Z.X.; Li, J.X. Quickly Calculate the Distance between Two Points and Measurement Error Based on Latitude and Longitude. *Geomat. Spat. Inf. Technol.* **2013**, *36*, 235–237.
61. Li, L.; Jiang, L.; Zhang, J.; Wang, S.; Chen, F. A Complete YOLO-Based Ship Detection Method for Thermal Infrared Remote Sensing Images under Complex Backgrounds. *Remote Sens.* **2022**, *14*, 1534. [CrossRef]
62. Han, S.; Zhao, Y.; Cheng, J.; Zhao, F.; Yang, H.; Feng, H.; Li, Z.; Ma, X.; Zhao, C.; Yang, G. Monitoring Key Wheat Growth Variables by Integrating Phenology and UAV Multispectral Imagery Data into Random Forest Model. *Remote Sens.* **2022**, *14*, 3723. [CrossRef]
63. Lin, J.; Wang, M.; Ma, M.; Lin, Y. Aboveground Tree Biomass Estimation of Sparse Subalpine Coniferous Forest with UAV Oblique Photography. *Remote Sens.* **2018**, *10*, 1849. [CrossRef]
64. Kayad, A.; Sozzi, M.; Paraforos, D.; Rodrigues, F.; Cohene, Y.; Fountas, S.; Francisco, M.; Pezzuolo, A.; Grigolato, S.; Marinello, F. How many gigabytes per hectare are available in the digital agriculture era? A digitization footprint estimation. *Comput. Electron. Agric.* **2022**, *198*, 107080. [CrossRef]

remote sensing

MDPI

Article

Canopy Volume Extraction of *Citrus reticulate* Blanco cv. Shatangju Trees Using UAV Image-Based Point Cloud Deep Learning

Yuan Qi [1,2], Xuhua Dong [3], Pengchao Chen [2,4], Kyeong-Hwan Lee [3], Yubin Lan [2,4], Xiaoyang Lu [1,2], Ruichang Jia [1,2], Jizhong Deng [1,2] and Yali Zhang [1,2,*]

1 College of Engineering, South China Agricultural University, Guangzhou 510642, China; yuanqi@stu.scau.edu.cn (Y.Q.); luxiaoyang@stu.scau.edu.cn (X.L.); rcjia@scau.edu.cn (R.J.); jz-deng@scau.edu.cn (J.D.)
2 National Center for International Collaboration Research on Precision Agricultural Aviation Pesticide Spraying Technology, Guangzhou 510642, China; pengchao@stu.scau.edu.cn (P.C.); ylan@scau.edu.cn (Y.L.)
3 Department of Rural and Biosystems Engineering, Chonnam National University, Gwangju 500-757, Korea; 177708@jnu.ac.kr (X.D.); khlee@chonnam.ac.kr (K.-H.L.)
4 College of Electronic Engineering and College of Artificial Intelligence, South China Agricultural University, Guangzhou 510642, China
* Correspondence: ylzhang@scau.edu.cn

Abstract: Automatic acquisition of the canopy volume parameters of the *Citrus reticulate* Blanco cv. Shatangju tree is of great significance to precision management of the orchard. This research combined the point cloud deep learning algorithm with the volume calculation algorithm to segment the canopy of the *Citrus reticulate* Blanco cv. Shatangju trees. The 3D (Three-Dimensional) point cloud model of a *Citrus reticulate* Blanco cv. Shatangju orchard was generated using UAV tilt photogrammetry images. The segmentation effects of three deep learning models, PointNet++, MinkowskiNet and FPConv, on Shatangju trees and the ground were compared. The following three volume algorithms: convex hull by slices, voxel-based method and 3D convex hull were applied to calculate the volume of Shatangju trees. Model accuracy was evaluated using the coefficient of determination (R^2) and Root Mean Square Error (RMSE). The results show that the overall accuracy of the MinkowskiNet model (94.57%) is higher than the other two models, which indicates the best segmentation effect. The 3D convex hull algorithm received the highest R^2 (0.8215) and the lowest RMSE (0.3186 m^3) for the canopy volume calculation, which best reflects the real volume of *Citrus reticulate* Blanco cv. Shatangju trees. The proposed method is capable of rapid and automatic acquisition for the canopy volume of *Citrus reticulate* Blanco cv. Shatangju trees.

Keywords: canopy volume; UAV tilt photogrammetry; point cloud; deep learning; *Citrus reticulate* Blanco cv. Shatangju trees

check for updates

Citation: Qi, Y.; Dong, X.; Chen, P.; Lee, K.-H.; Lan, Y.; Lu, X.; Jia, R.; Deng, J.; Zhang, Y. Canopy Volume Extraction of *Citrus reticulate* Blanco cv. Shatangju Trees Using UAV Image-Based Point Cloud Deep Learning. *Remote Sens.* **2021**, *13*, 3437. https://doi.org/10.3390/rs13173437

Academic Editors: Lorenzo Comba, Jordi Llorens and Alessandro Biglia

Received: 22 July 2021
Accepted: 26 August 2021
Published: 30 August 2021

Publisher's Note: MDPI stays neutral with regard to jurisdictional claims in published maps and institutional affiliations.

Copyright: © 2021 by the authors. Licensee MDPI, Basel, Switzerland. This article is an open access article distributed under the terms and conditions of the Creative Commons Attribution (CC BY) license (https://creativecommons.org/licenses/by/4.0/).

1. Introduction

Citrus have a long history of cultivation in China, especially in the southern hilly areas, where there are abundant citrus planting resources and various varieties. Among them, *Citrus reticulate* Blanco cv. Shatangju is one of the famous and superior varieties of citrus. It is well liked by the public and is a common cash crop in south China. Fertile planting land and high-quality orchard management are required to ensure the stable and increased production of *Citrus reticulate* Blanco cv. Shatangju. Among them, the volume and external structure of the canopy of *Citrus reticulate* Blanco cv. Shatangju trees are important indicators to measure the growth and biological characteristics of the fruit trees [1–4]. The fruit growers can judge the nutrient required by the trees and the number of fruits in the fruiting period according to the volume of the canopy. Moreover, the canopy volume is closely related to water evaporation. These factors have a direct impact on the

precision management and economic benefits of the orchard [5,6]. Therefore, the automatic acquisition of the canopy volume of the *Citrus reticulate* Blanco cv. Shatangju tree are of great significance to the precision management of the orchard.

The traditional manual measurement of tree canopy is time-consuming, labor-intensive and inefficient. Ground machinery relies on expensive LiDAR (Light Detection and Ranging) [7], infrared photoelectric sensors [8], ultrasonic sensors [9], etc. for data acquisition and canopy structure evaluation from the side of the trees. In recent years, scholars have carried out wide research on UAV (Unmanned Aerial Vehicle) tilt photogrammetry images acquisition using multi-angle photogrammetry and point cloud modeling of trees. Qin et al. [10] segmented individual trees over large forest areas with airborne LiDAR 3D (Three-dimensional) point cloud and very high-resolution optical imagery and obtained phenotypes characteristics at the individual tree level successfully. Tian et al. [11] compared point cloud data obtained from ground-based laser scanner and UAV images to conduct a feasibility analysis of the canopy height extraction of a planted coniferous forest. Gülci [12] established a canopy height model with UAV remote sensing technology to estimate the number, height and canopy coverage of pine trees. On the basis of UAV tilt photogrammetry images and point cloud reconstruction, Jurado et al. [13] developed an automatic detection method of grapevine trunk using 3D point cloud data with good robustness. Camarretta et al. [14] used UAV-LiDAR for rapid phenotyping of eucalyptus trees to study inter-species differences in productivity and differences in key features of tree structure. Wang et al. [15] combined UAV tilt photogrammetry and machine learning classification algorithms to classify street tree species, in which the BP (Back Propagation) neural network showed the best segmentation effect. UAV tilt photogrammetry images combined with point cloud data processing has become the most popular method of individual tree volume assessment.

In the whole orchard or the forest scenario, it is first necessary to locate and segment each tree to measure the canopy volume of a single tree. The extraction of single tree information mainly includes single tree identification and single tree canopy extraction. With the continuous development of deep learning, the segmentation and extraction of trees is also constantly improving. For the segmentation of 2D (Two-Dimensional) images, scholars have tended to use a convolutional neural network in deep learning [16–18] from traditional segmentation methods based on edge detection, threshold, region and specific theoretical tools. For example, Martins et al. [19] segmented the trees in the urban environment image, Yan et al. [20] identified different tree species and Chadwick et al. [21] extracted the height of the crown of a single coniferous tree. However, 2D images have problems such as insufficient spatial information and occlusion. Therefore, 3D point cloud data containing rich spatial information is gradually dominating. Deep learning point cloud semantic segmentation has become a research hotspot in the fields of autonomous driving, navigation and positioning, smart city and medical image segmentation [22–25]. However, there is relatively less research in the field of tree segmentation, especially in the orchard scenario. In addition, fruit tree parameters include tree height, canopy diameter and canopy volume. Due to the fractal nature of plants, the definition of fruit tree volume is quite subjective [26]. At present, the volume calculation algorithms of trees are mainly geometric calculation methods and voxel-based methods. The geometric calculation method treats the acquired point cloud data as a geometric body, and directly takes the volume of the geometric body as the volume of the canopy. Among them, the most commonly used geometric calculation method is the 3D convex hull algorithm, which has been applied in many studies [27–29]. Fernández-Sarría et al. [30] improved the overall 3D convex hull algorithm by using a height interval of 5 cm for segmentation. By applying the 3D convex hull, the volume of each segmented block was calculated and then the volumes of the small blocks were summed to obtain the canopy volume. The slicing convex hull method can also be adopted to calculate the canopy volume by dividing the plane area of a single canopy slice into small pieces, and then adding the convex hull volume of the slices to obtain the canopy volume [31]. The voxel-based method [32,33] uses conventional

3D grids to represent discrete canopy point clouds. For example, Wu et al. [34] applied the voxel-based method to separate the canopy and trunk of a single tree from the point cloud data, and estimated the tree height, canopy diameter and canopy height. However, the volume calculation algorithms mentioned above are all results of a single tree, ignoring the importance of the segmentation of the entire orchard or forest. Therefore, the point cloud deep learning algorithm combined with the volume calculation algorithm is used to segment the canopy of the *Citrus reticulate* Blanco cv. Shatangju trees. In this way, the advantages of both can be effectively combined to quickly, automatically and accurately obtain the canopy volume of a single Shatangju tree.

A set of methods to extract the canopy volume parameters of an individual *Citrus reticulate* Blanco cv. Shatangju tree using UAV tilt photogrammetry images and point cloud deep learning was proposed in this study, in order to provide a reference for the precision management of an orchard. UAV tilt photogrammetry images of *Citrus reticulate* Blanco cv. Shatangju trees were acquired to generate a 3D point cloud model of the orchard. Point cloud deep learning algorithms were applied to the model for the segmentation of individual trees. The height, canopy width and volume of each tree were calculated and then compared by different volume algorithms.

2. Materials and Methods

2.1. Point Cloud Data Acquisition

2.1.1. Experimental Site

The experimental site of this study is located in an orchard of Sihui City, Guangdong Province, with geographical coordinates of 112.68°E and 23.36°N (Figure 1). This area has a subtropical monsoon climate with an average annual temperature of about 21.9 °C and an average precipitation of about 1716 mm. A total of 160 *Citrus reticulate* Blanco cv. Shatangju trees in 16 rows × 10 columns were selected for this study, of which 128 trees were determined as the training set and 32 trees as the validation set. A total of four trials were conducted with an interval of about 20 days in order to collect canopy data of *Citrus reticulate* Blanco cv. Shatangju trees in different growth periods. Experiments were conducted on sunny days with low wind speed to ensure the accuracy of the images captured using the UAV.

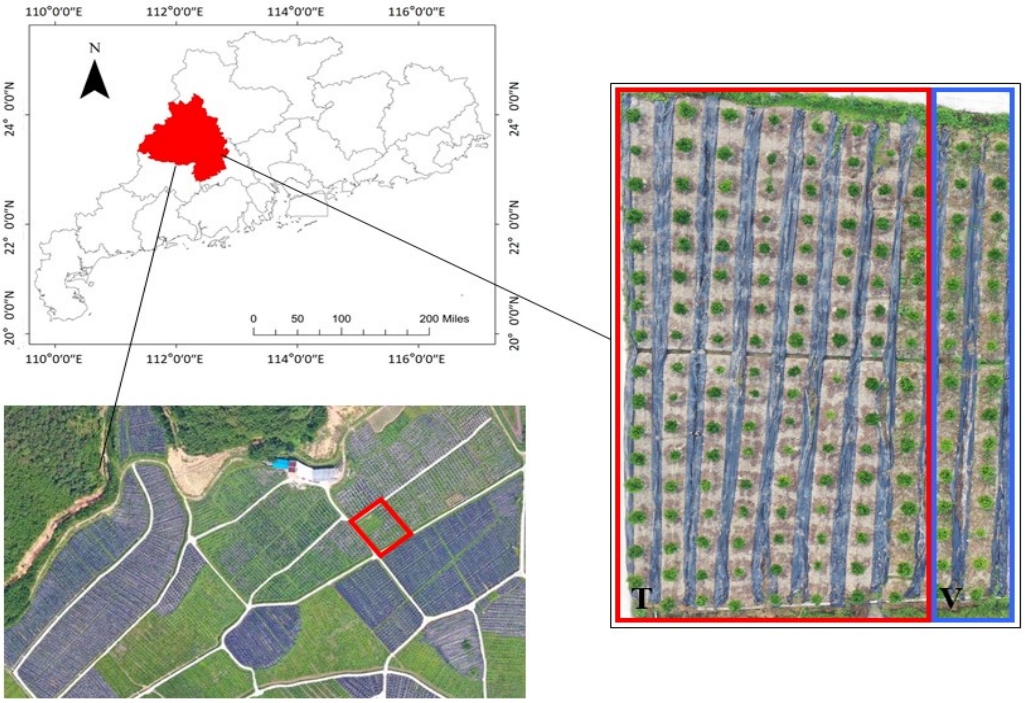

Figure 1. Experimental site.

2.1.2. Acquisition of UAV Tilt Photogrammetry Images

The acquisition platform is DJI Phantom 4 RTK (Real Time Kinematic) UAV (DJI, Shenzhen, China), which is equipped with a 20-megapixel CMOS (Complementary Metal-Oxide-Semiconductor) sensor. The RTK and six-way vision sensors allow the flight of the UAV safer and more stable [35–37]. The Phantom 4 RTK has a maximum take-off weight of 1391 g, and a maximum horizontal flight speed of 14 m/s. Its maximum ascent and descent speed is 5 and 3 m/s, respectively. The pitch angle range of the camera is approximately −90° to +30°. UAV tilt photogrammetry images were acquired with a flight height of 10 m and a cruise speed of 1 m/s. The overlap of flight path is 85% in both the side and heading directions. The image resolution is 5472 pixels × 3648 pixels, and the ground resolution is 0.37 cm. The DJI platform and the UAV tilt photogrammetry image acquisition scene are shown in Figure 2.



(**a**) (**b**)

Figure 2. UAV tilt photogrammetry images acquisition: (**a**) DJI Phantom 4 RTK UAV; (**b**) Image acquisition in orchard.

Ground Control Points (GCPs) were added and RTK base station were set up in this experiment to ensure the accuracy of the subsequent point cloud information. The horizontal accuracy of RTK base station is 1 cm + 1 ppm, and the vertical accuracy is 2 cm + 1 ppm (1 ppm means that the accuracy deteriorates 1 mm with every 1 km increase). The high-precision GPS (Global Positioning System) information of the locating points was obtained using a punter (Figure 3). This method can control the error within 6 cm between point cloud analysis and the true value from manual measurement.

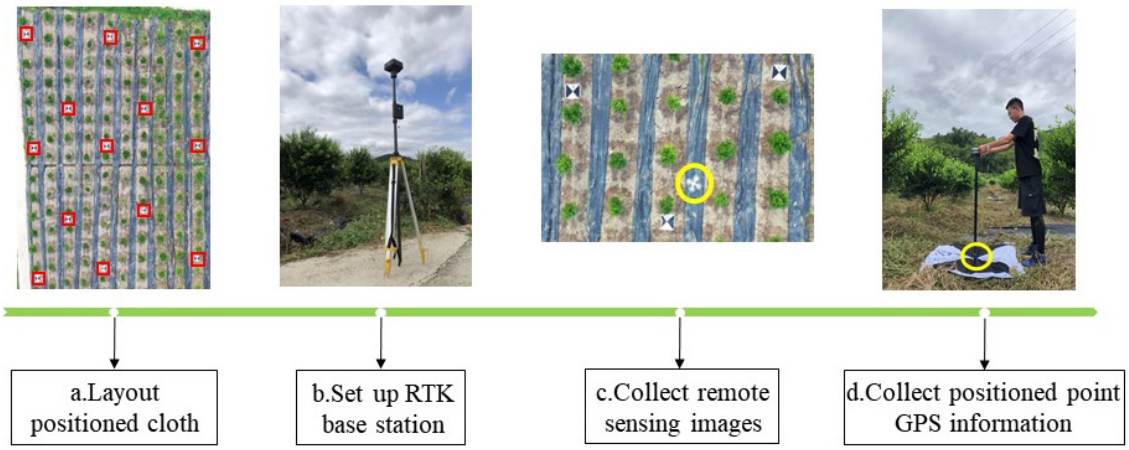

Figure 3. Flow chart of data acquisition.

2.1.3. Reconstruction of 3D Point Cloud

Pix4Dmapper was applied to process the tilt photogrammetry images obtained using the UAV. This software can quickly and automatically convert thousands of images into professional and accurate planar maps or 3D models. Pix4Dmapper obtains point cloud data and carries out post-process through the principle of multi-angle reconstruction of photogrammetry and aerial photographs. It is widely used in the fields of aerial and engineering photogrammetry, computer animation and remote sensing [38].

After importing the image data obtained in this experiment into Pix4Dmapper, the software automatically reads the pose information of the images based on the selected coordinate system. WGS 84 (World Geodetic System-1984)/UTM (Universal Transverse Mercator) Zone 50N projection coordinate system is used by default. The software first monitors the regional integrity and data quality of aerial photogrammetry, then marks control points, and automatically generates point cloud and texture information, and finally generates 3D textured mesh to form a 3D model of the experimental site (Figure 4).

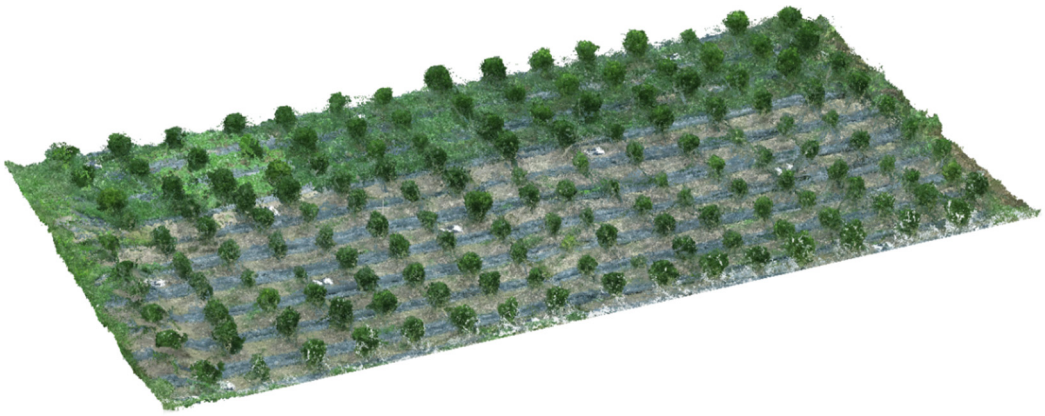

Figure 4. Point cloud results of the experimental site.

In CloudCompare software, the point cloud cropping tool was used to manually separate the trees from the land of the whole experimental site, and remove point cloud noise. The samples for training and validation were determined as well.

2.2. Deep Learning Algorithms for Point Clouds Data

2.2.1. Deep Learning Algorithms

Point cloud semantic segmentation is a technology to divide the point cloud into several specific regions with unique properties, and to identify the point cloud information [39]. Traditional point cloud feature extraction methods are mainly classified into local features [22], regional features [23], global features and multi-scale features [40,41]. Direct classification of point cloud data is ideal to avoid transformation error. Researchers have proposed many point-cloud-based 3D deep learning architectures, among which the PointNet algorithm first proposed by Qi et al. [42] has become the most classical deep learning algorithm for point cloud segmentation due to its fewer model parameters and faster training speed. In this study, a classical point cloud deep learning network and two recent innovative network models were selected to carry out semantic segmentation on the point clouds of fruit trees and non-fruit trees. The algorithms suitable for this scenario were compared as well.

PointNet++ [43] is an extension of the architecture of PointNet with an additional hierarchical structure, which performs hierarchical feature extraction by building a pyramid-like aggregation scheme to combine features at multiple scales. Its network structure is divided into sampling layer, grouping layer and PointNet layer. Figure 5 shows the overall network architecture of PointNet++.

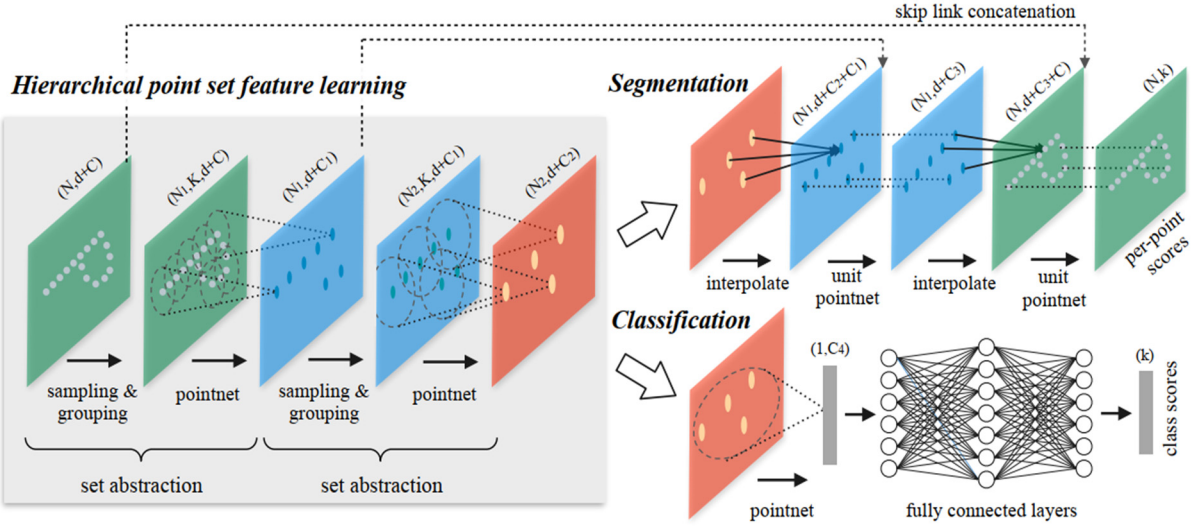

Figure 5. PointNet++ network architecture. Reprinted with permission from ref. [43], 2017, Cornell University.

In the sampling layer, Farthest Point Sampling (FPS) method is selected in the input point cloud samples in order to cover the whole 3D spatial point cloud as much as possible. The principle of FPS method is as follows: firstly, a starting point is selected from the N points of the input point cloud data and denoted as K0; secondly, the Euclidean distance between the remaining N-1 points and the starting point is calculated, and the point with the largest distance is recorded as K1; then the shortest Euclidean distance between N-2 points and K0 and K1 is calculated and summed up, respectively, and the point with the largest distance is recorded as K2, etc. until the specified number of points is reached. In the grouping layer, PointNet++ implements the grouping of point clouds through K neighborhood algorithm and Ball query algorithm. K-neighborhood algorithm finds the nearest neighbors around the center point and creates multiple subsets of the point cloud according to the number of points. Ball query algorithm selects a central point and regards the points in a spherical region within a certain radius of the center point as a local region. The input sample point cloud is divided into overlapping local regions by sampling and layering/grouping operations. PointNet network is then used to convolve and pool the point clouds to obtain higher-order feature representations of these point cloud subsets. In addition, a density-adaptive entry layer is added to the PointNet layer to learn the features of different scale regions when the input sampling density is changed.

The PointNet++ network solves the problem of uneven sampling of point cloud data and considers the distance measurement between points at the same time. It learns local regional features of point clouds through the hierarchical structure, which makes the network structure faster and more stable. However, PointNet++ has the same problem as PointNet network, which is that is extracts the local features of points individually without establishing the connection between points. The learning of point cloud data is not sufficient.

MinkowskiNet is a generalized sparse 3D convolutional algorithm proposed by Choy et al. [44] for efficient processing of high-dimensional data, which solves the problem of low efficiency in the application of dense convolutional neural networks on spatial sparse data with better accuracy than 2D (Two-dimensional) or hybrid deep learning algorithms.

Convolution is a fundamental operation in many fields. This network adopts convolution on sparse tensors, and proposes a generalized convolution on sparse tensors. Originally, the most common representations for extracting feature-intensive data were vectors, matrices and tensors. However, for 3D or even higher dimensional space, such intensive representations are inefficient and the effective information occupies only a small portion of that space, resulting in a waste of resources. Therefore, information can only be stored in non-empty regions of the space, as if it is stored in a sparse matrix. This

representation is the N-dimensional extension of the sparse matrix, which is called the sparse tensor. MinkowskiNet network defines neural networks specific to these input sparse tensor networks, which process and generate sparse tensors. To build a sparse tensor network, all standard neural network layers are constructed in the same way as those defined on dense tensors and implemented in the network model, such as MLP (Muti-Layer Perception), nonlinear, convolution, pooling and other operations.

Generalized sparse convolution treats all discrete convolutions as its subclass, which is crucial for high-dimensional perception. It calculates only the outputs of predefined coordinates and saves them into a compact sparse tensor. MinkowskiNet network convolves universal input and output coordinates and arbitrary kernel shapes. It allows the sparse tensor network to extend to very high spaces and dynamically generate task coordinates, especially for high-dimensional data, which can serve as a memory and computation saver. The operational flow of the MinkowskiNet network is specified in Figure 6.

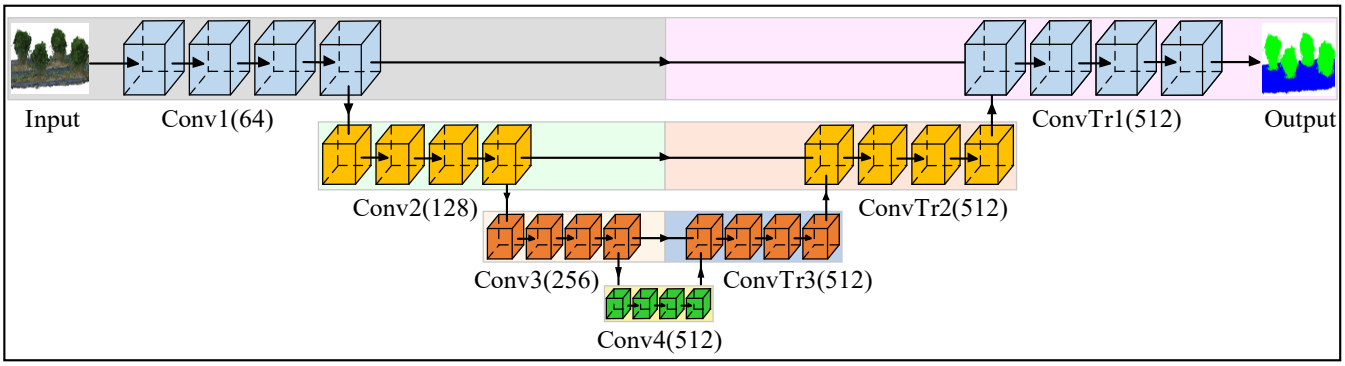

Figure 6. Overall network architecture of MinkowskiNet.

The MinkowskiNet network starts with data processing to generate the sparse tensor, which uses batch indexing to expand the sparse tensor coordinates, converting them into unique coordinates, associative features and optional labels during training semantic segmentation. Then, the output coordinates Cout are generated by inputting the given coordinates Cin. This process requires the addition of kernel mapping on the basis of the convolutional step size, the input coordinates and the step size (minimum distance between coordinates) of the input sparse tensor, as it defines how to map the input to the output through the kernel. Since the pooling process of this method may remove the density information, a variant is proposed that does not divide the number of inputs and is named the total pool, dividing the merged elements by the number of inputs mapped to each output. Finally, a generalized sparse convolution is used to create a high-dimensional network, which makes the network easier and more universal. For the U-shaped variant, multiple cross-sparse convolutions and cross-sparse transposed convolutions are added to the basic residual network, and the layers with the same span size are connected using skip connections. Figure 6 shows the overall network architecture of MinkowskiNet.

FPConv [45] is a 2D convolution algorithm that can directly process the surface geometry of a point cloud without converting it to an intermediate representation (e.g., a 3D grid or graph). FPConv is able to apply regular 2D convolution to effective feature learning by automatically learning weight maps to gently project surrounding points onto a 2D grid for local expansion. This network model cleverly maps the local point cloud into a 2D plane through interpolation, and finally uses 2D convolution to compute the features.

FPConv maps N points within a point neighborhood into a 2D plane of Mw×Mh, with Mw and Mh denoting the width and height of the plane, respectively. Then, PointNet algorithm is applied to calculate the local features of the relative coordinates of the N points, and the local features are mosaicked together with the coordinates of each point. Each position on the plane can be filled with a new feature obtained by feature interpolation of the N points. Interpolation is essentially a weighted sum of the N features. A network

is then built to learn and obtain the weights of the corresponding weighted sum at each position. Since there are N points, each position corresponds to N weight parameters, which are obtained through the MLP network. There are Mw×Mh positions on the mapping plane; therefore, there is a total of N×(Mw×Mh) parameters to learn. After learning these parameters, the features of N points can be used to interpolate Mw×Mh features. Finally, the interpolation result is considered as a 2D picture, and a feature is computed to represent the point features using traditional 2D convolutional network and pooling operation. Figure 7 shows the network architecture of FPConv.

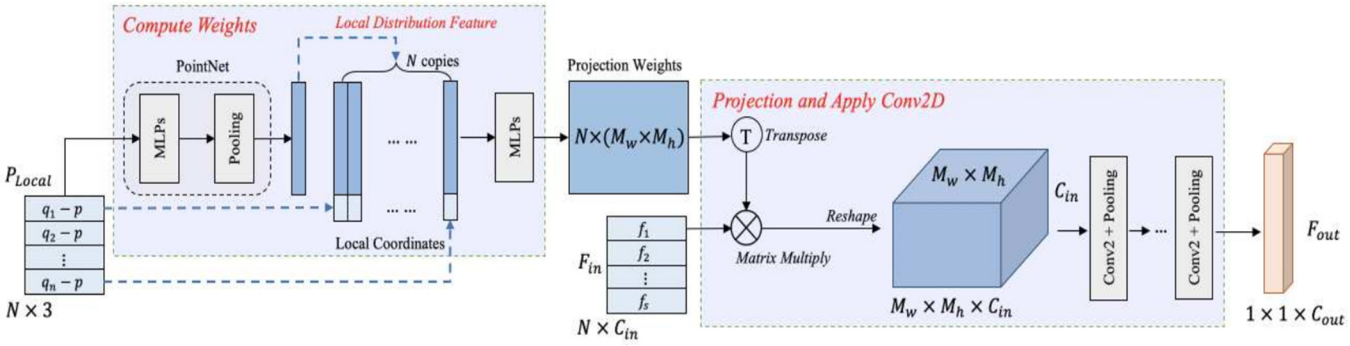

Figure 7. Network architecture diagram of FPConv. Reprinted with permission from ref. [45], 2020, CVPR 2020.

2.2.2. Accuracy Evaluation of Algorithms

In this study, the performance of the semantic segmentation model is evaluated by accuracy and mIoU (mean Intersection over Union). The segmentation accuracy is implemented based on the confusion matrix by dividing the sum of the diagonals of the confusion matrix by the sum of the elements of this matrix. The mIoU calculates the average value of the IoU (Intersection over Union) for each class, while IoU is obtained by measuring the ratio of intersection and union between the actual and model annotations. The two evaluation indexes are calculated as follows:

$$Accuracy = \frac{TP + TN}{TP + TN + FP + FN} \quad (1)$$

$$mIoU = \frac{1}{C}\sum_{i=1}^{C} \frac{p_{ii}}{\sum_{j=1}^{C} p_{ij} + \sum_{j=1}^{C} p_{ji} - p_{ii}} \quad (2)$$

where *TP* denotes correct classification of detection target, *TN* denotes correct classification of background, *FP* denotes wrong classification of background as detection target, *FN* denotes wrong classification of detection target as background, *C* is category and p_{ij} is the number of objects or points that belong to the *i*-th category but are predicted to be in the *j*-th category.

2.3. Tree Phenotype Parameter Extraction and Accuracy Evaluation

2.3.1. Manual Calculation Method

This experiment requires large amount of manual measurement, which is time-consuming and laborious. Thirty-two Citrus reticulate Blanco cv. Shatangju trees were selected for manual measurement. A total of four trials were taken with a field rod and tape measure. Figure 8 shows the measured parameters. Since the Shatangju trees in this study are nearly spherical in shape, the volume of spherical canopy was calculated using the following equation [46,47]:

$$V_M = \frac{\pi D^2}{4}\left[\frac{2(H_t - H_c)}{3} + (H_c - H_s)\right] \quad (3)$$

where V_M is manually measured volume (m^3), D is mean maximum diameter (m), H_t is total canopy height (m), H_c is height from the ground to the maximum diameter of the canopy (m) and Hs is height from the ground to the bottom of the canopy (m).

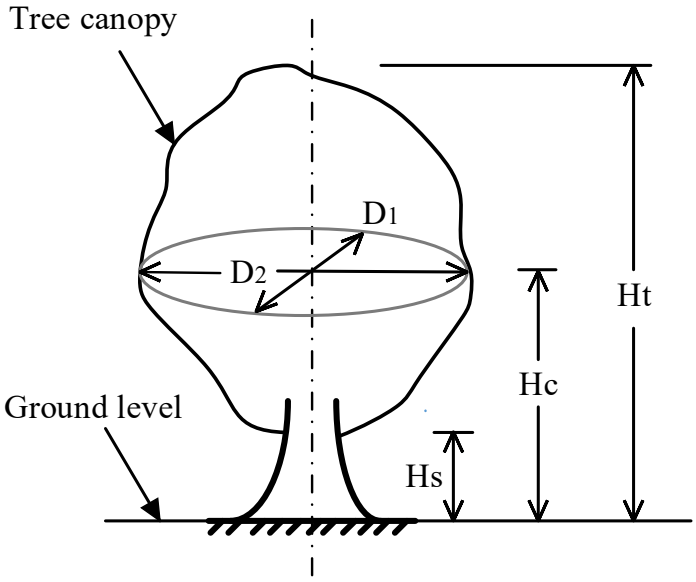

Figure 8. Schematic diagram of *Citrus reticulate* Blanco cv. Shatangju tree measurement parameters.

2.3.2. Phenotypic Parameters Obtained by the Algorithms

Point cloud data of the Citrus reticulate Blanco cv. Shatangju trees is placed in the Cartesian coordinate system, where the value of the highest point in the Z direction is *Zmax*, the value of the lowest point is *Zmin* and the difference between them is the height of tree, *Ht*, in meters (m).

$$Ht = Z_{max} - Z_{min} \tag{4}$$

The canopy width is usually divided into width in east–west direction, D_1, and north–south direction, D_2. Since the coordinate system in the Pix4Dmapper software is WGS 84, the X and Y axes of the point cloud data in the 3D coordinate system correspond to the east–west and north–south directions in the geographic location, respectively. After projecting 3D point cloud data onto a 2D plane, the maximum distance in the two directions is calculated, and then the average value is taken as the average maximum diameter, D.

$$D_1 = X_{max} - X_{min} \tag{5}$$

$$D_2 = Y_{max} - Y_{min} \tag{6}$$

$$D = \frac{D_1 + D_2}{2} \tag{7}$$

The key to the precision spraying with agricultural UAVs in orchards lies in the accurate volume calculation. In this study, the following three algorithms were selected with reference to the relatively well-researched volume algorithms: convex hull by slices, voxel-based method and 3D convex hull.

Convex hull by slices method divides the point cloud into several irregular polyhedrons and an irregular cone at the top layer according to the composition shape of the canopy point cloud. The whole canopy point cloud is stratified in the direction of the Z axis according to a certain interval Δh. The setting of the parameter Δh is related to the density of the point cloud; if Δh is too large, the volume estimation is not accurate; if Δh is too small, the calculation is complicated and inefficient. In actual data processing, it is usually set to 1 to 5 times the average point cloud spacing. The Δh in this study was finally set to 2 cm. The contour points of each layer of slices are extracted, and the vertices of the convex hull are connected in turn to form a closed polygon. Then, the convex hull area, Si, of each point cloud slice is calculated, and the volume of each part is calculated by

using the volume calculation equation of polyhedron and cone. Finally, the overall canopy volume is obtained by summing up the volumes of each part [31,48]. A schematic diagram of convex hull using the slices method is shown in Figure 9.

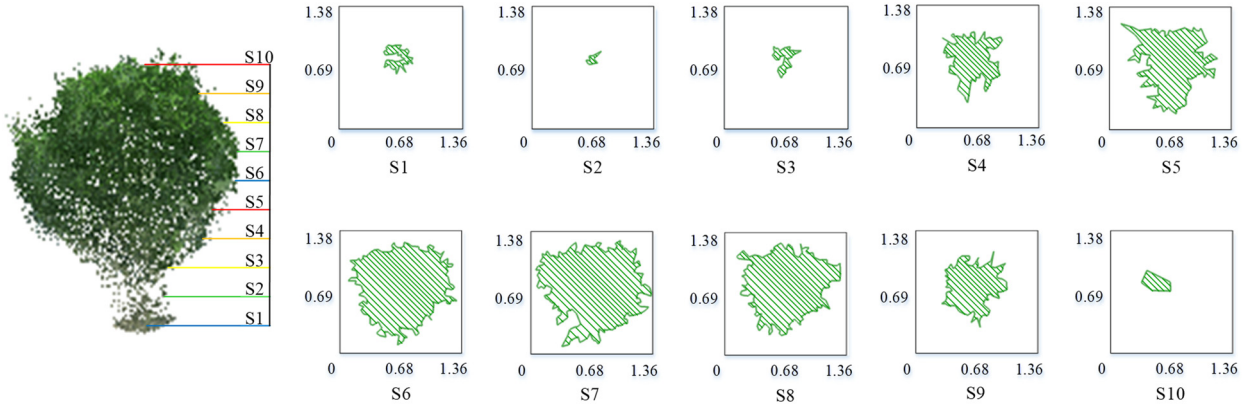

Figure 9. Schematic diagram of convex hull by slices algorithm.

Voxel-based method allows simple and efficient segmentation of a point cloud and represents it as a group of volume elements [32,34]. A voxel is a cuboid building block whose geometry is defined by length, width and height. Voxel-based method can transform discrete points with disordered distribution into voxel filtering with topological relations [33]. Firstly, the maximum and minimum values of the point cloud data in the X, Y and Z directions are calculated to determine a cuboid block that encloses the overall canopy point cloud. Secondly, the three-dimensional space of this block is equally divided to n small cubes (the step size in this study was set to 1 cm in all three directions). Then, the coordinates of the point cloud data are traversed to determine whether each small cube contains point cloud data. If it does, a small cube is created with that grid point as the center; otherwise, no small cubes are built. Finally, all grid points are iterated and the number of cubes containing point cloud is counted. The canopy volume of the Shatangju tree can be calculated given the volume of each cube. The schematic diagram of this method is shown in Figure 10a.

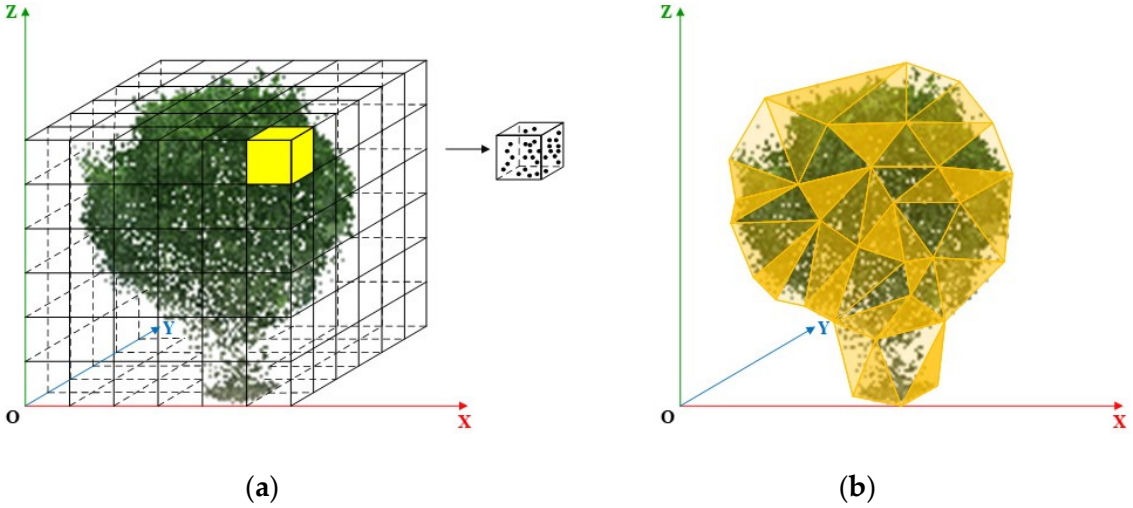

(**a**) (**b**)

Figure 10. Schematic diagram of (**a**) voxel-based method and (**b**) 3D convex hull method.

The 3D convex hull method involves the creation of a minimal convex hull that encloses all point clouds in 3D space for the point cloud data of Shatangju trees, which is defined by the set of external small planes that wrap the entire point cloud [27,48]. The

merge is performed to ensure that the whole shape is convex and does not contain errors caused by non-convex solutions. The volume of the convex hull is then calculated using the small planes as boundaries. Its boundary consists of many Delaunay triangles. The internal gaps of the convex hull are filled to generate the solids (Figure 10b). Generally, convex hulls are mainly calculated using the incremental algorithm, gift-wrapping algorithm, divide-and-conquer method and quick-hull algorithm [28,29]. The quick-hull algorithm was selected in this study. Its algorithm steps are as follows:

1. The point cloud of the Shatangju tree canopy was converted to .txt format data. Six coordinate points in the point cloud (including the maximum and minimum values of the coordinates) were selected to generate an irregular octahedron and form the initial convex hull model. At this moment, there were some points outside the octahedron. These points formed the new convex hull boundary, which were divided into eight separate regions by the octahedron. The point cloud inside the initial convex hull was removed when the polyhedron was built.
2. Among the points in the eight regions that were divided, the vertical distances of these points to the corresponding planes were compared and the point with the largest distance in each region was selected. The points selected in step 1 were merged with the newly selected points to form a new triangle and convex hull. Again, the points inside the new convex packet were deleted.
3. By repeating step 2, the point farthest from each new triangular plane was selected to create a new convex hull. The points inside the convex hull were deleted until there were no points outside the convex hull. Finally, an n-sided convex hull is formed, and the volume of this 3D convex hull model was taken as the volume of the tree canopy.

2.3.3. Evaluation of Model Accuracy

The accuracy of the model in this study is evaluated by the following two indicators: coefficient of determination (R^2) and Root Mean Square Error (RMSE). An R^2 value close to 1 indicates a better fit of the volume calculation. The smaller the RMSE is, the smaller the deviation of the predicted value is from the true value, i.e., the closer the calculated value of the volumetric algorithm is to the true value of the manual measurement, the higher the prediction accuracy of the model is. The calculation equation is as follows.

$$R^2 = 1 - \frac{SSE}{SST} \tag{8}$$

$$\text{RMSE} = \sqrt{\frac{1}{M}\sum_{j=1}^{M}(Y_j - X_j)^2} \tag{9}$$

where SSE is the Sum of Squares for Error, SST is the Sum of Square for total, Y_j is the sample predicted value, X_j is the sample true value and M is the number of samples.

3. Results

3.1. Segementation Accuracy of Deep Learning

Three deep learning models were applied to classify orchard point cloud data as described previously. Table 1 shows the prediction performance of each model based on the validation set of mIoU. The PointNet++ model has the lowest value in all three evaluation indexes, where the segmentation accuracy of trees is only 27.78%. The MinkowskiNet model achieved the highest value in all three evaluation indexes, with a mIoU value as high as 94.57%, and the best segmentation effect. The FPConv model also has a better classification, but the segmentation accuracy of trees is slightly lower. MinkowskiNet has a higher accuracy than PointNet++ for both trees and ground. The latter only uses the spatial information of the point cloud, while the former can learn the spatial information and color information of each point.

Table 1. Mean Intersection over Union (mIoU) (%) of the segmentation results.

Method	mIoU	Segmentation Accuracy	
		Tree	Ground
PointNet++	53.72	27.78	79.67
MinkowskiNet	94.57	90.82	98.32
FPConv	81.92	68.68	95.16

In the training process (Figure 11), the accuracy of the PointNet++ model started to fluctuate as it converged from the 100th epoch, and almost converged after the 200th epoch, but there were still small fluctuations in the later stages. The accuracy of the MinkowskiNet model was as high as 80% in the initial training and converged after the 50th pass. The accuracy of the FPConv model in the initial training was 57% for the initial training and increased rapidly between the 180th and 200th epoch, and basically converged after the 200th time. By comparing the three deep learning models, it can be seen that the MinkowskiNet model requires fewer training epochs, and it is faster and more stable as well.

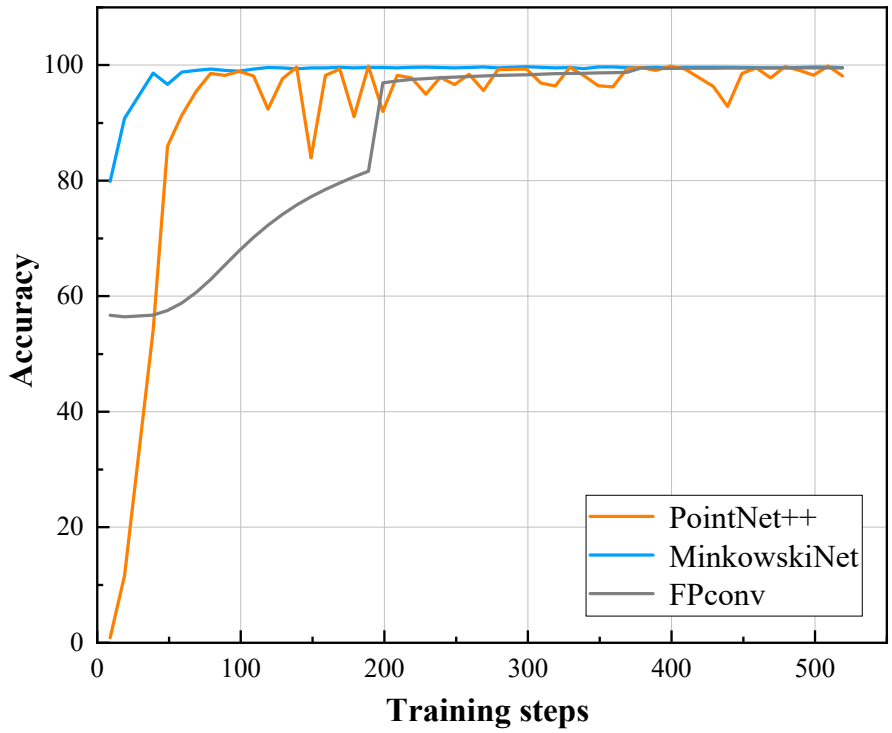

Figure 11. Visualization of the training process.

The qualitative results of the three segmentation models are shown in Figure 12. Each point represents a classified component (tree or ground). The segmentation accuracy of the PointNet++ model is relatively low. There were points of the ground incorrectly segmented as points of the trees, and most of the incorrectly segmented points were concentrated on the left side of the figure. There were missed segmentations of points of each tree; therefore, its segmentation accuracy of trees was low. The segmentation accuracy of both the trees and the ground in the MinkowskiNet model was very high, only some points of individual trees were incorrectly segmented as points of the ground. The ground segmentation accuracy of the FPConv model was relatively high, and each tree had points that were wrongly divided into ground points. Therefore, it can be concluded that the MinkowskiNet model has the best effects for the point segmentation of the trees and the ground.

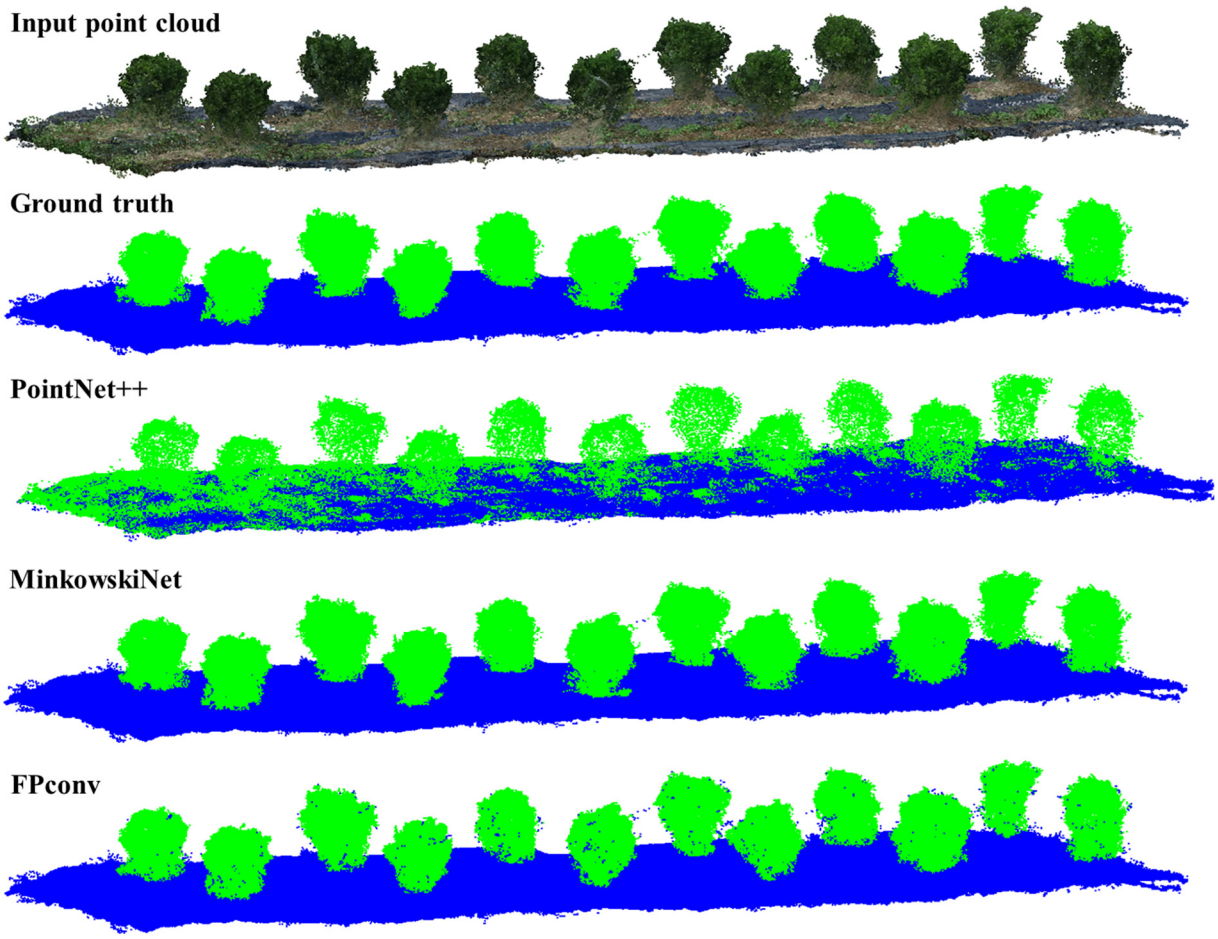

Figure 12. Semantic segmentation results for the orchard dataset.

In conclusion, the MinkowskiNet model achieved the best results among the three deep learning models with the highest segmentation accuracy and the least convergent training times.

3.2. Accuracy of Phenotypic Parameters Acquisition Model

The canopy volumes of 32 sample trees were calculated using the four calculation methods proposed in Section 2.3. The results of the three volume algorithms are shown schematically in Figure 13, which demonstrates the volume morphology of the Shatangju trees. The calculation results of the measurement sample in the first trial are listed in Table 2. The statistics of the total results of the four trials show that the height of the Shatangju trees ranged in 1.06–2.15 m and the tree canopy width ranged in 0.92–1.94 m. In addition, the volumes calculated from the manual measurement, convex hull by slices algorithm, voxel-based method and 3D convex hull algorithm were 0.53–4.28, 0.48–4.64, 0.40–2.94 and 0.46–4.02 m^3, respectively. For the same tree, the volume calculated using the convex hull by slices algorithm was the largest value, followed by the voxel-based method and the 3D convex hull algorithm. The significant differences in the calculated results are closely related to the acquired point clouds of the trees and the characteristics of the different algorithms.

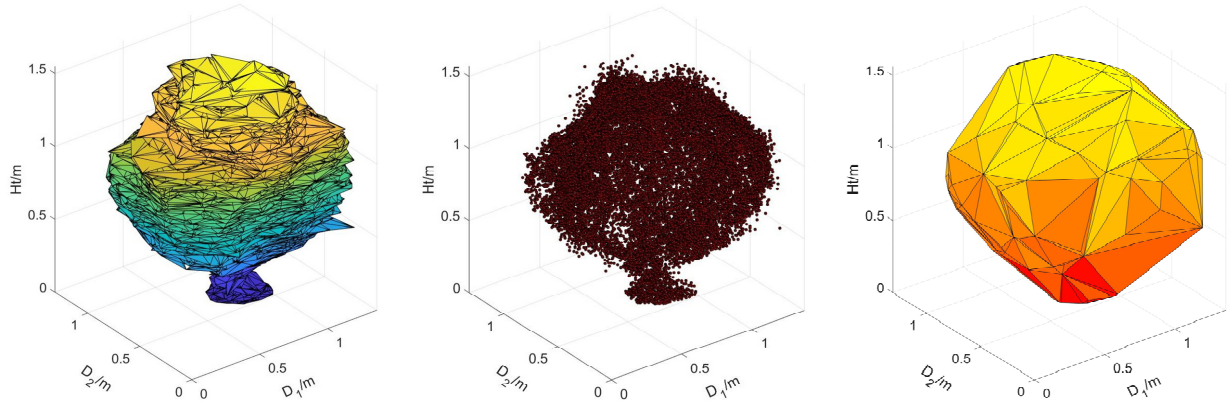

(**a**) (**b**) (**c**)

Figure 13. Schematic diagram of the results of three volume algorithms: (**a**) Convex hull by slices; (**b**) Voxel-based method; (**c**) 3D convex hull.

Table 2. Canopy volumes obtained using the four calculation methods.

Tree Number	Height Ht (m)	Diameter D (m)	Volume (m^3)			
			M1	M2	M3	M4
1	1.83	1.61	2.29	2.46	1.29	2.05
2	1.51	1.09	0.92	0.96	0.75	0.75
3	1.85	1.71	2.63	2.71	1.56	2.21
4	2.05	1.78	3.66	3.52	1.95	2.91
5	1.90	1.60	2.61	2.59	1.66	2.25
6	1.79	1.72	3.28	3.16	1.85	2.55
7	1.83	1.37	2.01	1.71	1.24	1.45
8	1.81	1.61	2.75	2.67	1.77	2.42
9	2.00	1.64	2.60	3.15	2.05	2.46
10	1.95	1.71	3.72	3.46	2.37	3.06
11	1.77	1.66	2.86	2.85	1.98	2.26
12	1.73	1.63	2.11	2.01	1.91	2.09
13	2.05	1.94	4.28	4.64	2.90	3.98
14	2.10	1.77	3.28	4.08	2.53	3.57
15	1.86	1.51	2.33	2.66	1.81	2.28
16	1.95	1.68	3.04	3.80	2.28	3.15
17	2.10	1.72	3.07	3.24	1.75	3.19
18	1.90	1.71	2.63	3.13	1.63	2.78
19	1.95	1.49	2.40	2.70	1.59	2.41
20	2.20	1.73	3.05	3.61	2.20	3.18
21	1.98	1.66	2.68	2.71	1.64	2.38
22	1.87	1.48	2.29	2.35	1.51	1.96
23	1.90	1.60	2.47	2.69	1.60	2.28
24	1.46	1.27	0.88	1.25	1.05	1.18
25	1.53	1.46	1.90	1.74	1.21	1.70
26	1.11	0.92	0.57	0.59	0.40	0.48
27	1.85	1.52	2.24	2.32	1.59	2.17
28	1.39	1.19	0.99	1.11	0.79	1.03
29	1.60	1.44	1.56	2.02	1.24	1.71
30	1.73	1.40	1.75	2.06	1.53	1.91
31	1.79	1.42	1.69	2.02	1.35	1.71
32	1.93	1.46	2.05	2.25	1.66	2.21
Max	2.20	1.94	4.28	4.64	2.90	3.98
Min	1.11	0.92	0.88	0.59	0.40	0.48
Mean	1.78	1.55	2.39	2.57	1.64	2.25
S.D.	0.24	0.21	0.85	0.91	0.52	0.77

Definitions: M1, Manual measurement; M2, Convex hull by slices; M3, Voxel-based method; M4, 3D convex hull; S.D., Standard deviation.

Regression models between each attribute and the manually obtained true values were analyzed to verify whether the point cloud results obtained from trees reliably represent the canopy structure. The manually measured height and diameter mean values were taken as true values. The point cloud heights and canopy widths acquired in CloudCompare software were compared with the true values. From the results shown in Figure 14, it can be seen that the R^2 between the heights acquired based on the point clouds and the manually measured height is 0.9571 with an RMSE of 0.0445 m. The R^2 between the canopy width acquired from the point clouds and the manually measured diameter is 0.9215 with an RMSE of 0.0587 m. It indicates that the Shatangju tree parameters obtained from the point clouds can reliably reflect the real tree height and canopy width. There was a high correlation between the different growth periods. Therefore, in order to automate the calculation of volume parameters, the point cloud data can be directly applied as true values for volume calculation.

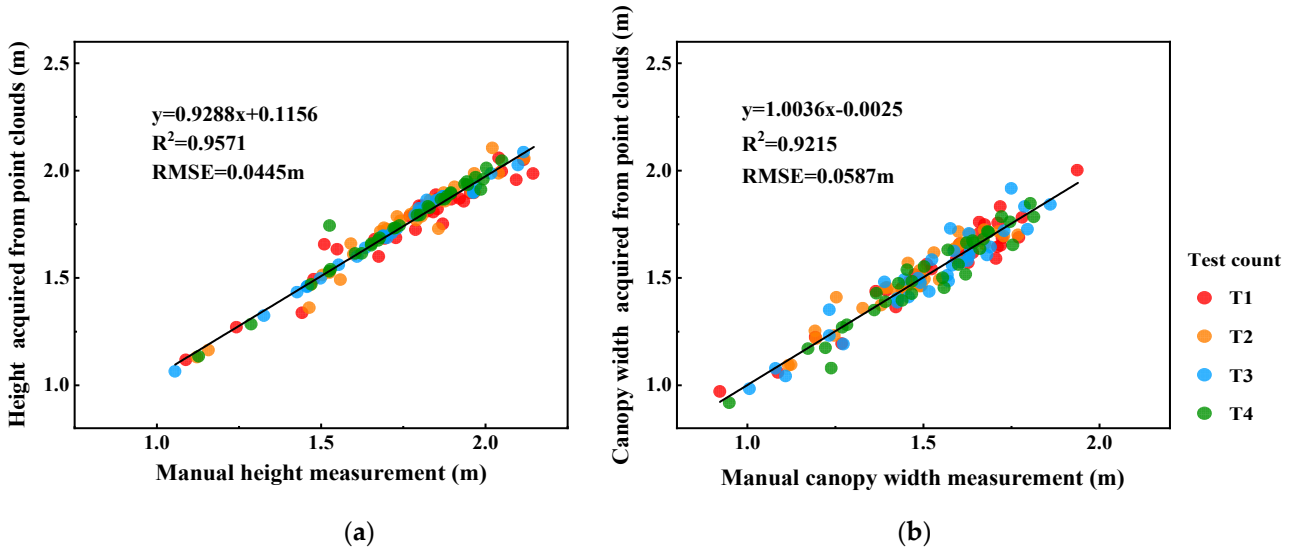

Figure 14. Scatter plot of manual measurements and point cloud data: (**a**) Height acquired from point clouds vs. manual height measurement; (**b**) Canopy width acquired from point clouds vs. manual canopy width measurement.

In order to select the optimal algorithm for Shatangju tree volume calculation, linear regression analysis was also performed between each of the three volume algorithms and the manual measurement. The calculated volume value of the spherical canopy was taken as the true value, and the calculation of different volume algorithms was used as the comparison value. From the results in Figure 15, it can be seen that the volume of the trees as calculated using the convex hull by slice algorithm showed an R^2 of 0.8004 and RMSE of 0.3833 m^3 compared with the manually measured data. It exceeded the voxel-based method with an R^2 and RMSE of 0.5925 and 0.3406 m^3, respectively. However, the 3D convex hull algorithm performed the best with the strongest correlation (0.8215) and the lowest RMSE (0.3186 m^3). That is, the 3D convex hull algorithm achieved the highest correlation that was close to one, followed by the convex hull by slices algorithm. The correlation of the voxel-based method was poor. Based on the analysis of Figure 13c, it can be observed that the 3D convex hull algorithm encloses the whole canopy, and its principle is closest to the formula for calculating the volume of the spherical canopy. However, due to the fact that the triangular planes that enclosed the canopy were not smooth spherical surfaces, the calculated volume of the 3D convex hull algorithm is slightly smaller than the true value of volume. The convex hull by slices algorithm (Figure 13a) took part of the point cloud as the calculation object, and there were still a large number of gaps in the established sliced convex hull and the segmented body, resulting in the fact that the computed volume is larger than the actual canopy volume. The voxel-based algorithm (Figure 13b) built the point cloud into small cubes with a known volume and calculated the tree volume by

counting the number of small cubes. However, since the point cloud itself was built based on the surface of images and missed the internal point cloud information, the computed volume was less than the true value. The correlation was also poor. Therefore, the 3D convex hull algorithm was determined as the algorithm to automatically calculate the volume of Shatangju trees.

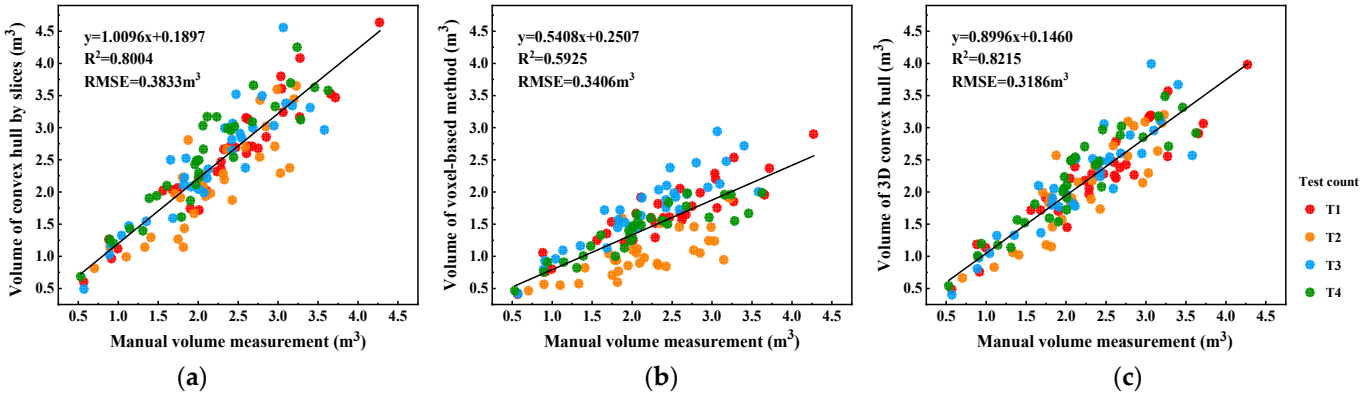

Figure 15. Scatter plot of volume calculated using three volume algorithms vs. manual calculation: (**a**) Convex hull by slices; (**b**) Voxel-based method; (**c**) 3D convex hull.

4. Discussion

The results indicate that it is feasible to use the point cloud deep learning algorithm combined with the volume calculation algorithm to automatically obtain the canopy volume parameters of the *Citrus reticulate* Blanco cv. Shatangju tree. With the development of UAV technology, UAV images have also been widely used [49–56]. Studies [10–13] have shown that UAV tilt photogrammetry can quickly and conveniently obtain images and texture information of forests, pine trees, eucalyptus, etc. UAV tilt photogrammetry is also suitable to obtain the image of the *Citrus reticulate* Blanco cv. Shatangju orchard, in order to further establish the 3D model of the orchard. It saves time and labor compared to manual measurement and provides a low-cost solution compared to ground mechanical sensors. For the acquisition of the canopy volume of a single *Citrus reticulate* Blanco cv. Shatangju tree, the proposed method in this research considers the segmentation optimization of the whole orchard, and uses the cutting-edge point cloud deep learning segmentation algorithm. Moreover, the point cloud data obtained by segmentation is directly input into the volume algorithm to improve the accuracy of the volume calculation of a single tree.

In this study, tilt photogrammetry images of *Citrus reticulate* Blanco cv. Shatangju trees were acquired with a DJI UAV. Experiments should be conducted at noon, when no shadow was in the image affecting the accuracy of the 3D point cloud model. However, data acquisition could not be completed within a short period of time at noon due to the large area of the experimental site. In this case, a time period with better light conditions in the daytime was selected for UAV tilt photogrammetry image acquisition in this study. In addition, *Citrus reticulate* Blanco cv. Shatangju trees were easily obscured by branches and leaves of adjacent trees during UAV tilt photogrammetry [15], resulting in the occlusion of the lower part and bottom of the trees. Therefore, the angle of the camera and the flight path need to be adjusted. Different head angles of −90°, −60°, −45° and −30°, as well as a flight path of 30° east of north, were set in the experiments to ensure that the bottom of the trees could be photographed.

Pix4Dmapper software was applied to build the 3D point cloud model of the experimental site based on UAV tilt photogrammetry images. In order to reduce the computational complexity and noise error in the preprocessing process, three network models, PointNet++, MinkowskiNet and FPConv, were selected for the feature information extraction directly. Although PointNet++ solves the problem of the uneven sampling of point cloud data, it is the same as the PointNet network with insufficient learning of local

features, resulting in misclassification with large error. MinkowskiNet makes use of sparse 3D convolution and takes all the discrete convolutions as its subclasses to enhance the information interaction between points and to better distinguish the high-dimensional data. Therefore, MinkowskiNet was able to produce high-quality segmentation effects for the 3D point cloud data in this study. FPConv also achieved good segmentation results, especially for the orchard ground, because its local features were mosaicked with the coordinate information of each point. However, fewer points of trees were classified as ground, possibly because the 2D surface convolution lost a small part of the 3D information of the point cloud. In this study, only the above three network models were adopted for learning. A variety of network models should be investigated in subsequent studies for comparative analysis to determine the most suitable deep learning network for orchard scenes.

The canopy volume and internal structure of Shatangju trees are important indicators for their growth volume and biological characteristics, which provide scientific reference for precision spraying. After the point cloud deep learning algorithm segments a single tree, the height, canopy width and volume of the Shatangju tree are then automatically calculated using volume algorithms. The height and canopy width of the point cloud showed high correlation with the manual measurement values, and the volume algorithm also presented high correlation, except for the voxel-based method. However, as the manual measurement calculated the hull volume through the outermost branches of the canopy, there were certain gaps and holes in the canopy. As a result, the calculated volume could be larger than the true value of the tree canopy without removing these spaces [48]. For the error caused by manual measurement, LiDAR scan data can be used as the true value instead to explore whether there is a certain linear relationship between the point cloud models established using UAV tilt photogrammetry images [49]. The LiDAR point cloud could be applied to calculate a more accurate volume of Shatangju trees, in order to improve the accuracy of spraying volume in pesticide applications.

The purpose of this study is to automatically obtain the canopy volume of the *Citrus reticulate* Blanco cv. Shatangju trees, in order to provide a reference for the precision management of an orchard. The canopy volume parameters of a single tree were automatically obtained using UAV tilt photogrammetry, deep learning and the volume algorithm. A volume grading map can be achieved to present the growth information of the orchard based on the results in this study. In agricultural practice, producers can transform the growth information map of the orchard into an operational prescription map based on their spraying experience and decision making to achieve precision spraying by plant protection UAVs. Subsequent research is suggested to use this dataset to explore algorithms of generating a prescription map for pesticides application. A transmission protocol is also required to transfer the prescription map to plant protection UAVs in order to guide the practical pesticides spraying applications.

5. Conclusions

This study established a set of automatic acquisition methods for the canopy volume of *Citrus reticulate* Blanco cv. Shatangju trees. The point cloud model established based on UAV tilt photogrammetry images was trained by three deep learning networks, PointNet++, MinkowskiNet and FPConv. The results show that the MinkowskiNet model works best for point segmentation between *Citrus reticulate* Blanco cv. Shatangju trees and the ground. The overall accuracy of the MinkowskiNet model was higher than that of the other two models, with an average mIoU of 94.57%. The segmentation accuracy of the MinkowskiNet model was 90.82 and 98.32% for trees and ground, respectively. The MinkowskiNet model achieved an accuracy as high as 80% for the first training epoch, and it converged after the 50th epoch. It required less training steps, and it was faster and more stable as well.

Both the height and canopy width obtained from the point cloud were highly correlated with the manually measured values and were not affected by the growth period of the *Citrus reticulate* Blanco cv. Shatangju trees. The R^2 and RMSE values for the height and canopy width were 0.9571 and 0.0445 m, and 0.9215 and 0.0587 m, respectively. The

accuracy evaluation of the proposed point cloud model indicates that the model has high estimation accuracy and can be used to obtain the volume values of *Citrus reticulate* Blanco cv. Shatangju trees by volume algorithms.

From the results of linear regression analysis between each of the three volume algorithms and the manual volume measurement, it is clear that the 3D convex hull algorithm achieved the highest R^2 of 0.8215, followed by the convex hull by slices algorithm and the voxel-based method. Therefore, the 3D convex hull algorithm was selected as the optimal algorithm for automatic volume of *Citrus reticulate* Blanco cv. Shatangju trees.

Author Contributions: Conceptualization, Y.Z., K.-H.L. and Y.L.; methodology, Y.Q., X.D. and P.C.; software, Y.Q., X.D. and X.L.; validation, Y.Q., X.D. and X.L.; formal analysis, Y.Q., X.D. and X.L.; investigation, Y.Q. and X.L.; resources, Y.Z., R.J. and J.D.; data curation, Y.Q. and X.L.; writing—original draft preparation, Y.Q.; writing—review and editing, Y.Z., P.C. and X.L.; visualization, Y.Q. and X.D.; supervision, Y.Z., K.-H.L. and J.D.; project administration, Y.Z. and Y.L.; funding acquisition, Y.Z. and Y.L. All authors have read and agreed to the published version of the manuscript.

Funding: This research was funded by Guangdong Science and Technology Plan Project, grant number 2018A050506073, Guangdong Modern Agricultural Industry Generic Key Technology Research and Development Innovation Team Project, grant number 2020KJ133, National Key Research and Development Program, grant number 2018YFD0201506 and the 111 Project, grant number D18019.

Conflicts of Interest: The authors declare no conflict of interest.

References

1. Wang, W.; Hong, T.; Li, J.; Zhang, F.; Lu, Y. Review of the pesticide precision orchard spraying technologies. *Trans. Chin. Soc. Agric. Eng.* **2004**, *20*, 98–101.
2. Zhou, L.; Xue, X.; Zhou, L.; Zhang, L.; Ding, S.; Chang, C.; Zhang, X.; Chen, C. Research situation and progress analysis on orchard variable rate spraying technology. *Trans. Chin. Soc. Agric. Eng.* **2017**, *33*, 80–92.
3. Fox, R.D.; Derksen, R.C.; Zhu, H.; Brazee, R.D.; Svensson, S.A. A History of Air-Blast Sprayer Development and Future Prospects. *Trans. ASABE* **2008**, *51*, 405–410. [CrossRef]
4. Feng, Z.; Luo, X.; Ma, Q.; Hao, X.; Chen, X.; Zhao, L. An estimation of tree canopy biomass based on 3D laser scanning imag-ing system. *J. Beijing For. Univ.* **2007**, *29*, 52–56.
5. Wei, X.; Wang, Y.; Zheng, J.; Wang, M.; Feng, Z. Tree crown volume calculation based on 3-D laser scanning point clouds data. *Trans. Chin. Soc. Agric. Mach.* **2013**, *44*, 235–240.
6. Ding, W.; Zhao, S.; Zhao, S.; Gu, J.; Qiu, W.; Guo, B. Measurement methods of fruit tree canopy volume based on machine vision. *Trans. Chin. Soc. Agric. Mach.* **2016**, *47*, 1–10.
7. Wallace, L.; Lucieer, A.; Watson, C.; Turner, D. Development of a UAV-LiDAR system with application to forest inventory. *Remote Sens.* **2012**, *4*, 1519–1543. [CrossRef]
8. MacFaden, S.W.; O'Neil-Dunne, J.P.; Royar, A.R.; Lu, J.W.; Rundle, A. High-resolution tree canopy mapping for New York City using LIDAR and object-based image analysis. *J. Appl. Remote Sens.* **2012**, *6*, 63567. [CrossRef]
9. Gangadharan, S.; Burks, T.F.; Schueller, J.K. A comparison of approaches for citrus canopy profile generation using ultrasonic and Leddar® sensors. *Comput. Electron. Agric.* **2019**, *156*, 71–83. [CrossRef]
10. Qin, Y.; Ferraz, A.; Mallet, C.; Iovan, C. Individual tree segmentation over large areas using airborne LiDAR point cloud and very high resolution optical imagery. In Proceedings of the 2014 IEEE Geoscience and Remote Sensing Symposium, Quebec City, QC, Canada, 13–18 July 2014; pp. 800–803. [CrossRef]
11. Tian, J.; Dai, T.; Li, H.; Liao, C.; Teng, W.; Hu, Q.; Ma, W.; Xu, Y. A Novel Tree Height Extraction Approach for Individual Trees by Combining TLS and UAV Image-Based Point Cloud Integration. *Forests* **2019**, *10*, 537. [CrossRef]
12. Gülci, S. The determination of some stand parameters using SfM-based spatial 3D point cloud in forestry studies: An analysis of data production in pure coniferous young forest stands. *Environ. Monit. Assess.* **2019**, *191*, 495. [CrossRef]
13. Jurado, J.; Pádua, L.; Feito, F.; Sousa, J. Automatic Grapevine Trunk Detection on UAV-Based Point Cloud. *Remote. Sens.* **2020**, *12*, 3043. [CrossRef]
14. Camarretta, N.; Harrison, P.A.; Lucieer, A.; Potts, B.M.; Davidson, N.; Hunt, M. From drones to phenotype: Using UAV-LiDAR to de-tect species and provenance variation in tree productivity and structure. *Remote Sens.* **2020**, *12*, 3184. [CrossRef]
15. Wang, Y.; Wang, J.; Chang, S.; Sun, L.; An, L.; Chen, Y.; Xu, J. Classification of street tree species using UAV tilt photogramme-try. *Remote Sens.* **2021**, *13*, 216. [CrossRef]
16. Zamboni, P.; Junior, J.; Silva, J.; Miyoshi, G.; Matsubara, E.; Nogueira, K.; Gonçalves, W. Benchmarking Anchor-Based and Anchor-Free State-of-the-Art Deep Learning Methods for Individual Tree Detection in RGB High-Resolution Images. *Remote. Sens.* **2021**, *13*, 2482. [CrossRef]

17. Egli, S.; Höpke, M. CNN-Based Tree Species Classification Using High Resolution RGB Image Data from Automated UAV Observations. *Remote. Sens.* **2020**, *12*, 3892. [CrossRef]
18. Nezami, S.; Khoramshahi, E.; Nevalainen, O.; Pölönen, I.; Honkavaara, E. Tree Species Classification of Drone Hyperspectral and RGB Imagery with Deep Learning Convolutional Neural Networks. *Remote Sens.* **2020**, *12*, 1070. [CrossRef]
19. Martins, J.; Nogueira, K.; Osco, L.; Gomes, F.; Furuya, D.; Gonçalves, W.; Sant'Ana, D.; Ramos, A.; Liesenberg, V.; dos Santos, J.; et al. Semantic Segmentation of Tree-Canopy in Urban Environment with Pixel-Wise Deep Learning. *Remote Sens.* **2021**, *13*, 3054. [CrossRef]
20. Yan, S.; Jing, L.; Wang, H. A New Individual Tree Species Recognition Method Based on a Convolutional Neural Network and High-Spatial Resolution Remote Sensing Imagery. *Remote Sens.* **2021**, *13*, 479. [CrossRef]
21. Chadwick, A.; Goodbody, T.; Coops, N.; Hervieux, A.; Bater, C.; Martens, L.; White, B.; Röeser, D. Automatic Delineation and Height Measurement of Regenerating Conifer Crowns under Leaf-Off Conditions Using UAV Imagery. *Remote Sens.* **2020**, *12*, 4104. [CrossRef]
22. Rusu, R.B.; Blodow, N.; Beetz, M. Fast Point Feature Histograms (FPFH) for 3D registration. In Proceedings of the 2009 IEEE International Conference on Robotics and Automation, Kobe, Japan, 12–17 May 2009; pp. 3212–3217.
23. Joachim, N.; Franz, R.; Uwe, S. Contextual classification of LiDAR data and building object detection in urban areas. *ISPRS J. Photogramm.* **2014**, *87*, 152–165.
24. Shen, Z.; Liang, H.; Lin, L.; Wang, Z.; Huang, W.; Yu, J. Fast Ground Segmentation for 3D LiDAR Point Cloud Based on Jump-Convolution-Process. *Remote Sens.* **2021**, *13*, 3239. [CrossRef]
25. Aboutaleb, A.; El-Wakeel, A.; Elghamrawy, H.; Noureldin, A. LiDAR/RISS/GNSS Dynamic Integration for Land Vehicle Robust Positioning in Challenging GNSS Environments. *Remote Sens.* **2020**, *12*, 2323. [CrossRef]
26. Phattaralerphong, J.; Sinoquet, H. A method for 3D reconstruction of tree crown volume from photographs: Assessment with 3D-digitized plants. *Tree Physiol.* **2005**, *25*, 1229–1242. [CrossRef] [PubMed]
27. Olsoy, P.J.; Glenn, N.F.; Clark, P.E.; Derryberry, D.R. Aboveground total and green biomass of dryland shrub derived from terrestrial laser scanning. *ISPRS J. Photogramm. Remote Sens.* **2014**, *88*, 166–173. [CrossRef]
28. Lauri, K.; Jari, V.; Anni, V.; Aarne, H.; Ilkka, K. Estimation of tree crown volume from airborne lidar data using computational geometry. *Int. J. Remote Sens.* **2013**, *34*, 7236–7248.
29. Lin, W.; Meng, Y.; Qiu, Z.; Zhang, S.; Wu, J. Measurement and calculation of crown projection area and crown volume of individual trees based on 3D laser-scanned point-cloud data. *Int. J. Remote Sens.* **2017**, *38*, 1083–1100. [CrossRef]
30. Fernández-Sarría, A.; Martínez, L.; Velázquez-Martí, B.; Sajdak, M.; Estornell, J.; Recio, J.A. Different methodologies for calculating crown volumes of Platanus hispanica trees using terrestrial laser scanner and a comparison with classical dendro-metric measurements. *Comput. Electron. Agric.* **2013**, *90*, 176–185. [CrossRef]
31. Li, L.; Li, D.; Zhu, H.; Li, Y. A dual growing method for the automatic extraction of individual trees from mobile laser scanning data. *ISPRS J. Photogramm.* **2016**, *120*, 37–52. [CrossRef]
32. Popescu, S.C.; Zhao, K. A voxel-based lidar method for estimating crown base height for deciduous and pine trees. *Remote Sens. Environ.* **2008**, *112*, 767–781. [CrossRef]
33. Wang, Y.; Cheng, L.; Chen, Y.; Wu, Y.; Li, M. Building Point Detection from Vehicle-Borne LiDAR Data Based on Voxel Group and Horizontal Hollow Analysis. *Remote Sens.* **2016**, *8*, 419. [CrossRef]
34. Wu, B.; Yu, B.; Yue, W.; Shu, S.; Tan, W.; Hu, C.; Huang, Y.; Wu, J.; Liu, H. A coxel-based method for automated identification and morphological parameters estimation of individual street trees from mobile laser scanning data. *Remote Sens.* **2013**, *5*, 584–611. [CrossRef]
35. Castro-Arvizu, J.; Medina, D.; Ziebold, R.; Vilà-Valls, J.; Chaumette, E.; Closas, P. Precision-Aided Partial Ambiguity Resolution Scheme for Instantaneous RTK Positioning. *Remote Sens.* **2021**, *13*, 2904. [CrossRef]
36. Nakata, Y.; Hayamizu, M.; Ishiyama, N.; Torita, H. Observation of Diurnal Ground Surface Changes Due to Freeze-Thaw Action by Real-Time Kinematic Unmanned Aerial Vehicle. *Remote Sens.* **2021**, *13*, 2167. [CrossRef]
37. Cheng, Q.; Chen, P.; Sun, R.; Wang, J.; Mao, Y.; Ochieng, W. A New Faulty GNSS Measurement Detection and Exclusion Algorithm for Urban Vehicle Positioning. *Remote Sens.* **2021**, *13*, 2117. [CrossRef]
38. Barbasiewicz, A.; Widerski, T.; Daliga, K. The analysis of the accuracy of spatial models using photogrammetric software: Agisoft Photoscan and Pix4D. *E3S Web Conf.* **2018**, *26*, 00012. [CrossRef]
39. Koguciuk, D.; Chechliński, Ł.; El-Gaaly, T. 3D object recognition with ensemble learning-a study of point cloud-based deep learning models. In *Advances in Visual Computing*; Springer: Cham, Switzerland, 2019; pp. 100–114.
40. Zhang, Z.; Zhang, L.; Tong, X.; Mathiopoulos, P.T.; Guo, B.; Huang, X.; Wang, Z.; Wang, Y. A Multilevel Point-Cluster-Based Discriminative Feature for ALS Point Cloud Classification. *IEEE Trans. Geosci. Remote Sens.* **2016**, *54*, 3309–3321. [CrossRef]
41. Chen, G.; Maggioni, M. Multiscale geometric dictionaries for point-cloud data. In Proceedings of the International Conference on Sampling Theory and Applications, Singapore, 2–6 May 2011; pp. 1–4.
42. Qi, C.R.; Su, H.; Mo, K.; Guibas, L.J. PointNet: Ddeep learning on point sets for 3D classification and segmentation. In Proceedings of the IEEE Conference on Computer Vision and Pattern Recognition, Honolulu, HI, USA, 21–26 July 2017.
43. Qi, C.R.; Yi, L.; Su, H.; Guibas, L.J. PointNet++: Deep hierarchical feature learning on point sets in a metric space. In Proceedings of the 31st Conference on Neural Information Processing Systems (NIPS 2017), Long Beach, CA, USA, 8 December 2017.

44. Choy, C.; Gwak, J.; Savarese, S. 4D Spatio-Temporal ConvNets: Minkowski Convolutional Neural Networks. In Proceedings of the 2019 IEEE/CVF Conference on Computer Vision and Pattern Recognition (CVPR), Beach, CA, USA, 16–20 June 2019; pp. 3070–3079.
45. Lin, Y.; Yan, Z.; Huang, H.; Du, D.; Liu, L.; Cui, S.; Han, X. FPConv: Learning Local Flattening for Point Convolution. In Proceedings of the 2020 IEEE/CVF Conference on Computer Vision and Pattern Recognition (CVPR), Seattle, WA, USA, 13–19 June 2020; pp. 4292–4301.
46. Tumbo, S.D.; Salyani, M.; Whitney, J.D.; Wheaton, T.A.; Miller, W.M. Investigation of laser and ultrasonic ranging sensors for measurements of citrus canopy volume. *Appl. Eng. Agric.* **2002**, *18*, 367. [CrossRef]
47. Zaman, Q.-U.; Schumann, A.W. Performance of an Ultrasonic Tree Volume Measurement System in Commercial Citrus Groves. *Precis. Agric.* **2005**, *6*, 467–480. [CrossRef]
48. Yan, Z.; Liu, R.; Cheng, L.; Zhou, X.; Ruan, X.; Xiao, Y. A concave hull methodology for calculating the crown volume of Indi-vidual Trees Based on Vehicle-Borne LiDAR Data. *Remote Sens.* **2019**, *11*, 623. [CrossRef]
49. Parmehr, E.G.; Amati, M. Individual Tree Canopy Parameters Estimation Using UAV-Based Photogrammetric and LiDAR Point Clouds in an Urban Park. *Remote Sens.* **2021**, *13*, 2062. [CrossRef]
50. Aeberli, A.; Johansen, K.; Robson, A.; Lamb, D.; Phinn, S. Detection of Banana Plants Using Multi-Temporal Multispectral UAV Imagery. *Remote Sens.* **2021**, *13*, 2123. [CrossRef]
51. Weiss, M.; Jacob, F.; Duveiller, G. Remote sensing for agricultural applications: A meta-review. *Remote Sens. Environ.* **2020**, *236*, 111402. [CrossRef]
52. Lim, P.-C.; Rhee, S.; Seo, J.; Kim, J.-I.; Chi, J.; Lee, S.-B.; Kim, T. An Optimal Image–Selection Algorithm for Large-Scale Stereoscopic Mapping of UAV Images. *Remote Sens.* **2021**, *13*, 2118. [CrossRef]
53. Lim, P.C.; Seo, J.; Son, J.; Kim, T. Feasibility study for 1:1000 scale map generation from various UAV images. In Proceedings of the International Symposium on Remote Sensing, Taipei, Taiwan, 17–19 April 2019.
54. Rhee, S.; Hwang, Y.; Kim, S. A study on point cloud generation method from UAV image using incremental bundle adjust-ment and stereo image matching technique. *Korean J. Remote Sens.* **2019**, *34*, 941–951.
55. Zhou, Y.; Rupnik, E.; Meynard, C.; Thom, C.; Pierrot-Deseilligny, M. Simulation and Analysis of Photogrammetric UAV Im-age Blocks—Influence of Camera Calibration Error. *Remote Sens.* **2019**, *12*, 22. [CrossRef]
56. Dai, Y.; Gong, J.; Li, Y.; Feng, Q. Building segmentation and outline extraction from UAV image-derived point clouds by a line growing algorithm. *Int. J. Digit. Earth* **2017**, *10*, 1077–1097. [CrossRef]

agriculture

MDPI

Article

Identification of Male and Female Parents for Hybrid Rice Seed Production Using UAV-Based Multispectral Imagery

Hanchao Liu [1,2], Yuan Qi [3], Wenwei Xiao [4], Haoxin Tian [1,2], Dehua Zhao [1,2], Ke Zhang [1], Junqi Xiao [1,2], Xiaoyang Lu [1,2], Yubin Lan [2,5] and Yali Zhang [1,2,*]

1 College of Engineering, South China Agricultural University, Guangzhou 510642, China; lhc@stu.scau.edu.cn (H.L.); hxtian@stu.scau.edu.cn (H.T.); z@stu.scau.edu.cn (D.Z.); zhangke1998@stu.scau.edu.cn (K.Z.); 20213142028@stu.scau.edu.cn (J.X.); luxiaoyang@stu.scau.edu.cn (X.L.)
2 National Center for International Collaboration Research on Precision Agricultural Aviation Pesticide Spraying Technology, Guangzhou 510642, China; ylan@scau.edu.cn
3 College of Mechanical Engineering, Nantong Vocational University, Nantong 226007, China; yuanqi@stu.scau.edu.cn
4 Mechanical and Electrical Department, Foshan Huacai Vocational and Technical School, Foshan 528000, China; xiaowenwei@stu.scau.edu.cn
5 College of Electronic Engineering and College of Artificial Intelligence, South China Agricultural University, Wushan Road, Guangzhou 510642, China
* Correspondence: ylzhang@scau.edu.cn

Abstract: Identifying and extracting male and female parent of hybrid rice and then accurately judging the spikelet flowering of male parents is the basis of hybrid rice pollination. Currently, male parent flowering information extraction for hybrid rice is basically obtained by manual recognition. In this study, remote sensing images of parental rice fields were obtained with a multispectral camera carried by a UAV (Umanned Aerial Vehicle). Six kinds of visible light vegetation indices and four kinds of multispectral vegetation indices, together with two classification methods, pixel-based supervised classification and sample-based object-oriented classification, were applied to identify the male and female parents of hybrid rice, after which the accuracies of the methods were compared. The results showed that the visible vegetation index had a better effect in pixel-based supervised classification. The kappa coefficient of ExGR (Excess Green minus Excess Red index) classification was 0.9256 and the total accuracy was 0.9552. The extraction accuracy was higher than that of the other vegetation indices and object-oriented classification. In pixel-based supervised classification, the maximum likelihood method achieved the highest identification accuracy and shortest calculation time. Taking the remote sensing images obtained with a UAV as a data source, maximum likelihood supervised classification based on ExGR index can more effectively and quickly identify the field information of male and female parents of hybrid rice so as to provide a reference for determining optimal pollination timing for hybrid rice in large-scale seed production farms.

Keywords: UAV; hybrid rice; pollination; multispectral imagery; vegetation index; supervised classification; object-oriented classification; kappa coefficient; maximum likelihood; extraction accuracy

check for updates

Citation: Liu, H.; Qi, Y.; Xiao, W.; Tian, H.; Zhao, D.; Zhang, K.; Xiao, J.; Lu, X.; Lan, Y.; Zhang, Y. Identification of Male and Female Parents for Hybrid Rice Seed Production Using UAV-Based Multispectral Imagery. *Agriculture* **2022**, *12*, 1005. https://doi.org/10.3390/agriculture12071005

Academic Editor: Koki Homma

Received: 2 June 2022
Accepted: 7 July 2022
Published: 11 July 2022

Publisher's Note: MDPI stays neutral with regard to jurisdictional claims in published maps and institutional affiliations.

Copyright: © 2022 by the authors. Licensee MDPI, Basel, Switzerland. This article is an open access article distributed under the terms and conditions of the Creative Commons Attribution (CC BY) license (https://creativecommons.org/licenses/by/4.0/).

1. Introduction

Hybrid breeding is one of the most important methods for increasing rice yield. The yield of hybrid rice is of great significance in solving the problem of food shortage in the world [1,2]. Hybrid rice has outcrossing characteristics. During the flowering period, the pollen provided by the male parent falls to the female parent with male sterility to complete the pollination. The mature fruit of the female parent is an excellent variety of hybrid rice. Since the male parent has a longer growth time, it is usually sown earlier than the female parent of rice. The sowing time of the female parent is determined according to leaf age difference, time difference and the weather conditions after the male parent sows so that the

male parent and the female parent of a rice plant reach the heading period at the same time to achieve better pollination. The flowering period of a plant's male and female parents is only 1.5~2 h per day, and the active time of pollen is only 4~5 min. The amount of effective pollen provided by male parents will directly affect the seed production yield of hybrid rice. Rapid and accurate identification of male and female parents is key to determining the optimal pollination timing so as to ensure that the pollen of male and female parents meet at the flowering period [3,4]. In addition, when the pollination is finished, the male parent must be cut off in advance in order to provide sufficient nutrients for the female parent, maintain ventilation, reduce pests and diseases, and facilitate mechanical harvesting [5,6]. Therefore, identifying the male and female parents is also an important prerequisite for monitoring the agricultural characteristics of hybrid rice. However, currently, the male parent flowering information extraction of hybrid rice is basically obtained by manual experience, and the timeliness of information is insufficient, making it difficult to grasp the male parent flowering status in time, especially in the vast planting areas of hybrid rice seed production farms [7].

The automatic acquisition and classification of agricultural information based on remote sensing images is receiving increasing attention. Although satellite remote sensing has been a mature technology for acquiring ground object information, it is susceptible to weather conditions and has low temporal and spatial resolution, which usually make it difficult to meet the high precision and time-effective requirements needed for monitoring hybrid rice flowering status [8].

Due to their small sizes, ease of operation, high spatial resolution and high efficiency, UAVs have a wide application prospect in the real-time acquisition of information on farmland conditions [9,10]. Scholars at home and abroad have done a lot of research on extracting vegetation information from remote sensing images. Most scholars establish the relationship between vegetation index and remote sensing imaging to separate the target and background. It is widely used in images with color differences between categories, such as crop monitoring [11] and field crop classification [12,13]. Zhang et al. [14] used visible light remote sensing images collected by a UAV to calculate the vegetation index in research on the aboveground biomass estimation of Zoige grassland and established an exponential regression model of biomass and various vegetation indices to estimate biomass, with the highest simulation accuracy of R^2 = 0.856. Wan et al. [15], based on remote sensing images obtained by a multispectral camera carried by a UAV, explored and predicted the relationship between the numbers of oilseed rape flowers using the random forest algorithm and eight common visible vegetation indices and two multispectral vegetation indices. The RMSE (Root-Mean-Square Error) of their model was 14.13, which has great potential for the monitoring of the numbers of oilseed rape flowers. Enyn et al. [16] used three different deep neural network structures to quickly predict the counting and flowering time of sorghum panicles using RGB images obtained by a UAV. The timely acquisition of flowering time improves sorghum panicle yields. Hardanto et al. [17] compared the land use classification (LUC) from Landsat 8 and UAV using the minimum distance supervised classification method. The results showed that the supervised classification of UAV images was more detailed and more accurate than satellite images. Jing et al. [18] generated a visible vegetation index based on micro UAV image data and compared pixel-based supervised classification with object-oriented classification. The kappa coefficient of the object-oriented classification method reached 0.9, which proved the feasibility of this kind of method for aquatic vegetation information extraction and greatly improved the accuracy of aquatic vegetation information extraction.

The flexibility and timeliness of UAV is helpful in classifying the male and female parents of hybird rice automatically and accurately in large-scale hybrid rice seed production farms and can effectively improve the utilization rate of pollen and increase the yield of hybrid rice. In this study, the male and female parents of hybrid rice plants in visible and multispectral images obtained by UAV are taken as the research objects. Two algorithms, pixel-based supervised classification and sample based object-oriented classification, were

used to extract the male and female parents of hybrid rice from the ten vegetation index calculation result graphs in order to obtain a simple, convenient and effective parent extraction method of hybrid rice. This provides a reference for quickly obtaining the distribution of male and female parents of hybrid rice, ensuring that the pollen of male and female parents meet at flowering, monitoring the field situation in real time, and improving the seed production rate of hybrid rice.

2. Materials and Methods

2.1. Overview of the Experimental Site

The experimental site is located in Hainan Province (18.25° N, 109.51° E). It belongs to a tropical maritime monsoon climate, with no frost and snow all year round, sufficient light and heat resources, and a multi-year average temperature of 24–25 °C. Between 8:00 and 18:00, the annual average sunshine hours are 2777.15 h, and the annual average rainfall is 1000–1900 mm, which is suitable for hybrid rice seed production. The male parent variety of hybrid rice is 534, and the female parent variety is Mengliangyou. An overview of the site is shown in Figure 1.

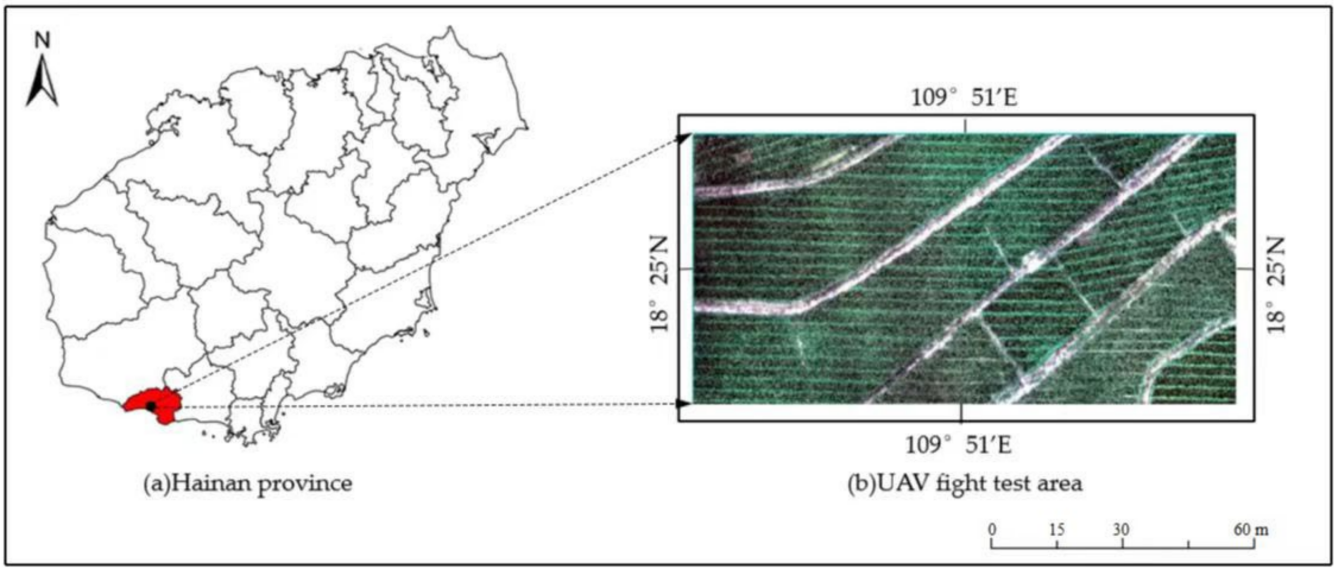

Figure 1. Overview of the experimental site.

2.2. Data Acquisition

This experiment used a DJI P4 Multispectral quad-rotor UAV with a diagonal wheelbase of 350 mm, an unloaded endurance flight time of about 27 min, a signal maximum effective distance of 7 km, a maximum take-off mass of 1487 g, and six 1/2.9-inch CMOS sensors, including a color sensor for visible light imaging and five monochromatic sensors for multispectral imaging in blue, green, red, red edge and near-infrared. The image resolution was 1600 pixels × 1300 pixels. The information parameters for each band are shown in Table 1. The captured images were stored in the internal SD card of the camera. In total, 2875 images of the target area were acquired by aerial photography with a flight altitude of 50 m, a flight speed of 2.6 m/s, a course overlap of 85% and a side overlap of 85%. The image spatial resolution was 2.6 cm/pixel. A total area of 6300 m^2 was covered.

Table 1. Band parameters of the multispectral sensor.

Band Number	Band Name	Central Wavelength (nm)	Band Width (nm)
1	Blue	450	16
2	Green	560	16
3	Red	650	16
4	Near Infra-red	730	16
5	Red Edge	840	26

2.3. Data Processing

2.3.1. Selection of Vegetation Index

In the field of remote sensing, there are hundreds of vegetation indices in use at present [19–21]. Based on the vegetation indices that have been researched more fully and with higher precision, six visible vegetation indices and four multispectral vegetation indices were selected in this study: ExR (Excess Red index) [22], ExG (Excess Green index) [23], ExB (Excess Blue index) [24], ExGR (Excess Green minus excess Red index) [25], G (Green coordinate) [26], CIVE (Color Index of Vegetation Extraction) [27], NDVI (Normalized Difference Vegetation Index) [28], LCI (Leaf Chlorophyll Index) [29], NDRE (Normalized Difference Red Edge Vegetation Index) [30] and GNDVI (Green Normalized Difference Vegetation Index) [31]. The calculation formulas and theoretical ranges of six visible light vegetation indices and four multispectral vegetation indices are shown in Table 2.

Table 2. Vegetation indices based on visible spectrum.

Vegetation index	Equation	Theory Interval
ExR	1.4R-G	[−255, 357]
ExG	2G-R-B	[−255, 510]
ExB	1.4B-G	[−255, 357]
ExGR	3G-2.4R-B	[−612, 765]
G	G	[0, 255]
CIVE	0.441r-0.881g+0.385b+18.78745	[17, 20]
NDVI	(NIR-R)/(NIR+R)	[−1, 1]
LCI	(NIR-RedEdge)/(NIR+R)	[0, 1]
NDRE	(NIR-RedEdge)/(NIR+RedEdge)	[−1, 1]
GNDVI	(NIR-G)/(NIR+G)	[−1, 1]

Note: R: Red channel; G: Green channel; B: Blue channel; NIR: Near-infrared channel; RedEdge: Red edge channel; r: Standardization of red channel; g: Standardization of green channel; b: Standardization of blue channel. r = R/(R + G + B); g = G/(R + G + B); b = B/(R + G + B); r + g + b = 1; the value range of r, g, b is [0, 1].

2.3.2. Data Image Processing

The orthophoto images of the experimental site were obtained by stitching, geometric correction and radiometric correction of the images with Pix4DMapper software. ENVI 5.3 software was used to crop the images to the target area, as shown in Figure 1. According to the formula in Table 1, the Band Math tool was applied to calculate each visible light vegetation index, and the ROI (Region of Interest) tool was combined with visual interpretation to randomly select ten samples each for the female parent, male parent, weed and bare land from the target area of the visible light images. Each category contained thousands of pixel values. The separability of the samples was calculated using the Calculate ROI Separability tool in ROI. When the separability is below 1.0, this means that the sample is not highly separable and needs to be re-selected; when the separability is 1.8–2.0, it means that the sample is well-distinguished. As shown in Figure 2, all kinds of ground objects have excellent separation and can be used as supervised classification objects.

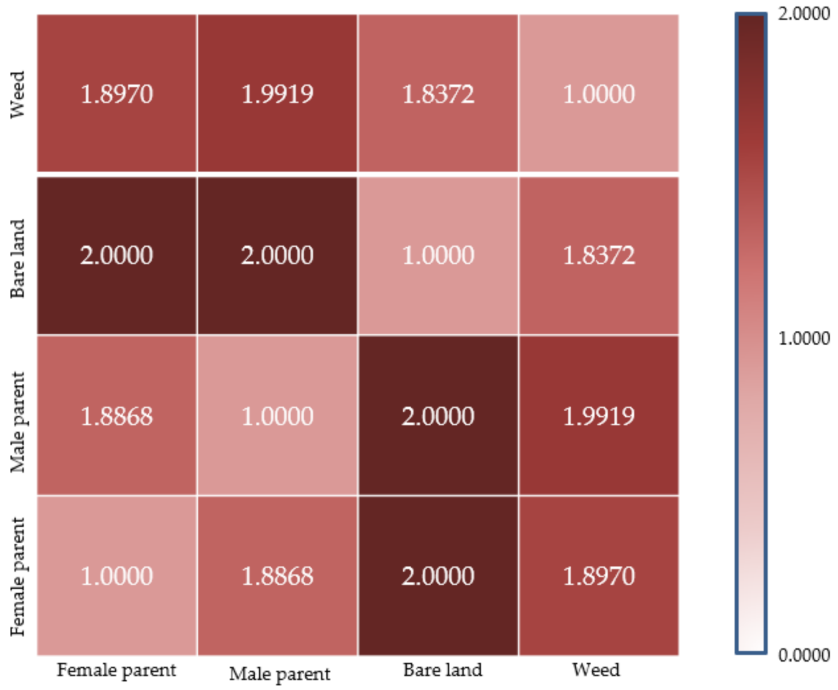

Figure 2. Separability of four types of ground feature samples.

2.4. The Classification and Extraction Method for Male and Female Parents

Two different classification methods were used to extract male and female parents. Pixel-based supervised classification was used to classify the results of six visible vegetation indices and four multispectral vegetation indices using five supervised classification methods based on image elements, namely, the parallelepiped method [32], the minimum distance method [33], the Mahalanobis distance method [34], the maximum likelihood method [35] and the neural network method [36]. For the other method, sample-based object-oriented information was used to supervise and classify visible light images so as to extract hybrid rice male and female parent information. The classification accuracies of the two types of methods were compared as well. Five supervised pixel-based classification methods classified pixels with similar spectral characteristics into corresponding categories according to certain rules. The difference between the object-oriented classification method and the pixel-based classification method is that it is no longer for a single pixel, but the object formed after image segmentation [37,38].

In the pixel-based supervised classification, according to the calculation results for the visible vegetation index in Figure 3, the calculation results for the multispectral vegetation index obtained in Figure 4 and the selected male and female parent training samples, five supervised classification methods—the parallelepiped method, the minimum distance method, the Mahalanobis distance method, the maximum likelihood method and the neural network classification method—were selected for classification using the supervised classification classifier in ENVI software. Among them, the parameter settings of the parallelepiped method and the minimum distance method classified the 10 vegetation indices by setting the appropriate thresholds in Table 3 based on the means and standard deviations. The maximum distance error of the Mahalanobis distance method and the likelihood threshold of the maximum likelihood method were both set to None for supervised classification in this study. The classification parameter setting of the neural network classification method selected the logistic activation function. The weight adjustment speed was set to 0.2, the number of iterations was set to 1000 and other values were set as default as the parameter settings.

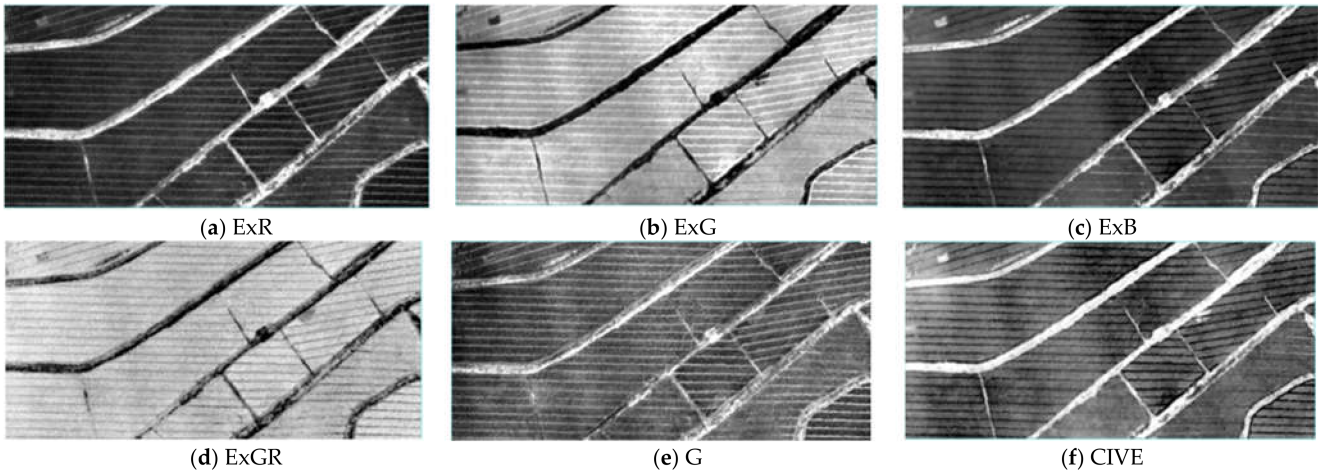

(**a**) ExR (**b**) ExG (**c**) ExB

(**d**) ExGR (**e**) G (**f**) CIVE

Figure 3. Calculation results for six visible light vegetation indices.

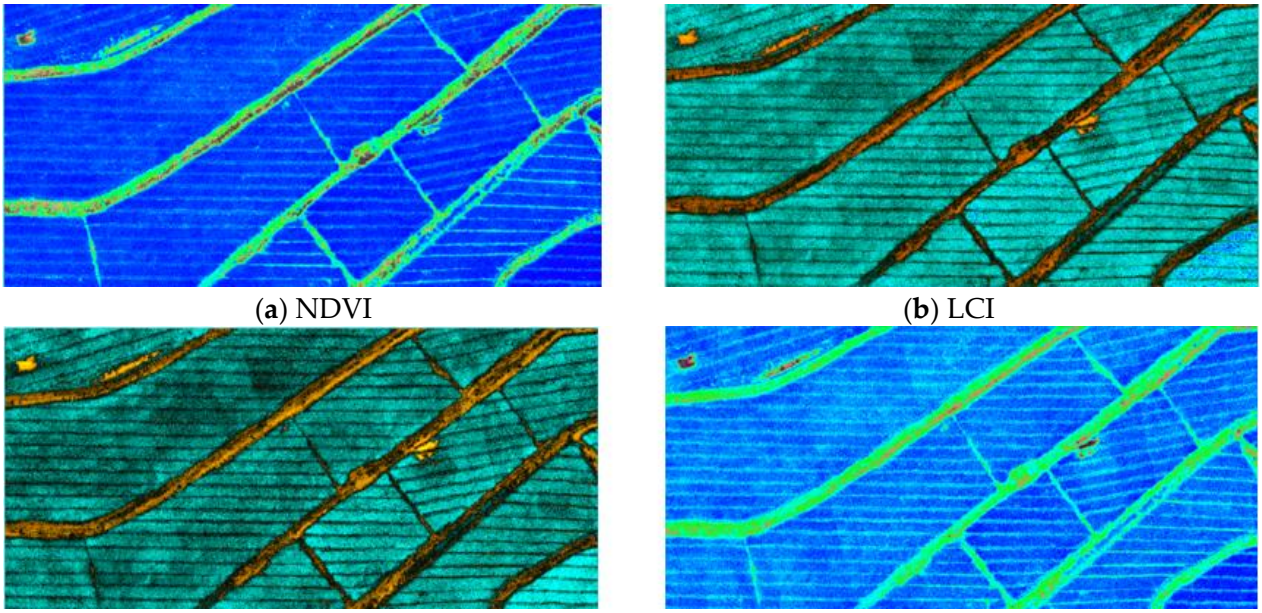

(**a**) NDVI (**b**) LCI

(**c**) NDRE (**d**) GNDVI

Figure 4. Calculation results for four kinds of multispectral vegetation indices.

Table 3. Statistics for six visible light vegetation indices based on region of interest.

Vegetation Index	Female Parent		Male Parent	
	Mean	Standard Deviation	Mean	Standard Deviation
ExR	22.6060	8.2644	37.2445	8.4157
ExG	57.0360	5.9429	81.9466	7.8365
ExB	−24.6368	7.5854	−41.4909	8.9551
ExGR	−154.9807	46.5724	−229.0859	41.8490
G	94.1847	20.5128	132.1748	19.3481
CIVE	−9.0989	3.1446	−24.1322	3.1630
NDVI	51.2282	26.1922	91.4345	36.5648
LCI	152.2266	47.1218	91.8878	45.5290
NDRE	81.8439	36.3162	40.4195	30.5533
GNDVI	189.8396	46.2561	134.6661	40.4023

In the object-oriented supervised classification based on samples, we used the object-oriented supervised classification function in ENVI5.3 software to classify the male parent and female parent of the vegetation index calculation results obtained in Figures 3 and 4. After repeated tests, the edge detection method was selected for image segmentation, and the threshold was set to 15 to segment the ground objects in the image to form a single object. The Full Lambda Schedule algorithm was selected for merging, and the threshold was set to 80 to merge and fuse adjacent objects with similar spectral, texture and geometric features into more complete objects. After the objects were divided, 50 samples from the female parent, 50 samples from the male parent, 20 samples from the weeds and 20 samples from the bare ground were selected as the training set according to the visual interpretation. The images were automatically classified using the SVM (Support Vector Machine) method [39]. The threshold parameter was set to 5, the degree of the kernel polynomial was set to 2, the kernel gamma value was set to 0.03, the bias in the kernel function was set to 1 and the penalty parameter was set to 100.

2.4.1. Parallelepiped Method

The parallelepiped method is a method of forming an n-dimensional parallelepiped data space according to the brightness value of the training sample. If the spectral values of other pixels fall in the area corresponding to any parallelepiped training sample, they are classified into their corresponding categories. The proportion of parallel hexahedrons is determined by the standard deviation threshold [32].

2.4.2. Minimum Distance Method

The minimum distance method uses the training sample data to calculate the mean vector and standard deviation vector of each class and then uses the mean vector as the center position of the class in the feature space to calculate the distance from each pixel to the center of the input hybrid rice image. A pixel is classified according to the distance between the pixel and the center of which kind is the smallest [33].

2.4.3. Mahalanobis Distance Method

The principle of the Mahalanobis distance method is to calculate the Mahalanobis distance from the input image to each sample and finally count the smallest Mahalanobis distance, which is this category [34].

2.4.4. Maximum Likelihood Method

The principle of the maximum likelihood method is to assume that each category of statistics in each band of a hybrid rice image is normally distributed and calculate the likelihood that a given pixel belongs to a training sample. The pixel is finally merged into the category with the maximum likelihood [35].

2.4.5. Neural Network Classification Method

This method involves the abstraction of a human brain neural network from the perspective of information processing. It forms different networks according to different connection modes and establishes related simple models. A neural network is essentially an operational model composed of a large number of nodes connected to each other. Each node can be regarded as a neuron. Each node contains an excitation function and its output is judged according to its input. The nodes of adjacent layers are connected in pairs, and their relationship is called weight, which is equivalent to the memory process of the human brain [36]. In this work, the neural network uses the approximation of some algorithm or function to distinguish male parents from female parents of hybrid rice plants as one of the modes of pixel-based supervised classification to classify the results of six visible vegetation indices and four multispectral vegetation indices.

2.4.6. SVM Method

SVM is a machine learning method based on statistical learning theory. SVM can automatically find those support vectors that have great ability to distinguish classifications so as to construct a classifier that can maximize the interval between classes and which therefore has better generalization and higher classification accuracy [39]. In this study, the SVM method was used for the automatic classification of images in the sample-based object-oriented classification.

2.5. Evaluation Index

After supervised classification of various samples in the target test area, the recognition accuracy of various samples was evaluated. At present, the most commonly used evaluation method is to use the true state of the image combined with field survey data for visual interpretation. Due to the large-scale planting areas and complex planting conditions, this type of evaluation method is limited by manpower and material resources [40,41]. In this study, the confusion matrix was used to test the accuracy of the classification results, and the total accuracy and kappa coefficient were used to evaluate six supervised classification methods. The closer the total accuracy is to 100%, the higher the accuracy. The kappa coefficient represents the consistency between classification results and real categories, and the value range is [−1, 1]. Generally, the kappa coefficient is between 0.81–1.0, indicating that the classification result is almost completely consistent with the real category. The kappa coefficient can be calculated according to the following formula [42–44]:

$$P_0 = \frac{a_{11} + a_{22} + a_{33} + \ldots + a_{nn}}{N} \quad (1)$$

$$P_e = \frac{a_1 b_1 + a_2 b_2 + a_3 b_3 + \ldots + a_n b_n}{N} \quad (2)$$

$$\mathrm{K} = \frac{P_0 - P_e}{1 - P_e} \quad (3)$$

where P_0 is the overall classification accuracy, P_e is the chance consistency, n is the order of the confusion matrix equation and N is the total number of samples, which is the sum of all values in the column (row).

3. Results and Analysis

3.1. Calculation and Analysis of Vegetation Indexes

With the cropped orthographic map in Figure 1, each visible vegetation index was calculated according to the formula in Table 2 using the Band Math tool in ENVI software. The calculation results are shown in Figure 3. Then, using the 2D multispectral reconstruction function of the DJI mapping software, the RGB images and five single-band images acquired by the multispectral camera were calculated to obtain four multispectral vegetation index images. The calculation results are shown in Figure 4.

From the calculated results for each vegetation index, it can be seen that there is a large difference in gray value between vegetation and non-vegetation, and the contrast is obvious. In order to better compare the 10 vegetation indices, this study divided the feature types into female parent, male parent, weed and bare land. On the calculated vegetation index map, 10 regions of interest for each feature were selected for statistics, and the eigenvalues of male parents and female parents were calculated. It can be seen from Table 3 that there was little difference in the standard deviations between the male parents and the female parents, but the average values were quite different. For the visible light vegetation index, the average difference between the male parent and the female parent was about 15 in the three vegetation indices, ExR, ExB and CIVE, and the ExG and G vegetation indices were slightly higher than the first three, while the difference in the mean values for the ExGR vegetation index is particularly obvious, reaching 74.1052. For the four multispectral vegetation indices, the difference in average value was between 40

and 60, and the difference in average values for the LCI vegetation index among the four multispectral vegetation indices was the largest, reaching 60.3388. In general, using the *t*-test function of SPSS software, there was a significant difference ($p < 0.05$) between the information on hybrid rice parents, with excellent results for the identification of male and female parents of hybrid rice plants with visible light and multispectral imaging.

3.2. Results and Analysis of Supervised Classification of Male and Female Parents Based on Pixels

The pixel-based supervised classification was performed according to the above method, and the supervised classification results are shown in Figures 5 and 6.

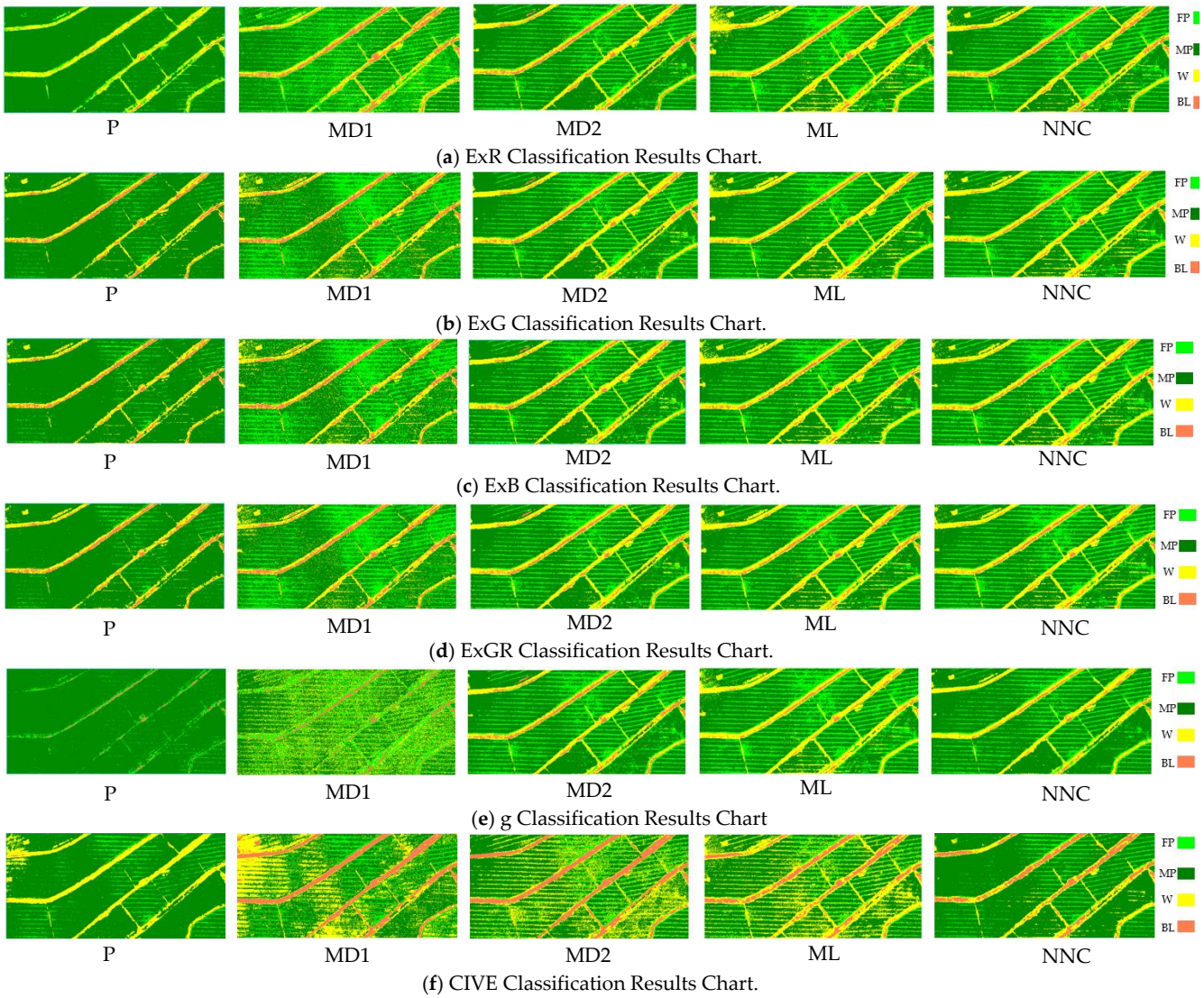

Figure 5. Results of visible light vegetation indices. FP: Female parent; MP: Male parent; W: Weed; BL: Bare land; P: Parallelepiped; MD1: Minimum Distance; MD2: Mahalanobis Distance; ML: Maximum Likelihood; NNC: Neural Network Classification.

Based on the supervised classification results for the vegetation indices obtained in Figures 5 and 6, ten samples of each of the four categories of female parent, male parent, weed and bare land were selected as validation samples based on the visual interpretation on the visible light images. The confusion matrix was calculated for the four types of features to obtain the accuracy statistics for each vegetation index. The kappa coefficient and total classification accuracy results for male and female parents are shown in Table 4. It can be seen from Table 4 that from the classification accuracy of the visible light vegetation index, the kappa coefficient and the total classification accuracy were generally lower than

the other three methods in the parallelepiped method and the minimum distance method. The total classification accuracy of the parallelepiped method was the lowest, and even the kappa coefficient reached 0.2084 in the G vegetation index. Both the maximum likelihood method and the neural network method had better classification accuracy. The kappa coefficient and the total accuracy of classification basically reached more than 0.9, and the total accuracy of the ExGR index in neural network classification was the highest among all vegetation indices, reaching 0.9599. From the classification accuracy of the multispectral vegetation index, the classification accuracy of the four multi spectral vegetation indices was generally low, basically between 0.5–0.8. According to the combination of visible light vegetation index and multispectral vegetation index, the classification accuracy of the four multispectral vegetation indices was generally lower than that of the six visible light vegetation indices in the five classification methods, and, among the five classification methods, the ten vegetation indices achieved better classification accuracy in the maximum likelihood method and the neural network method. Neural network classification was used to generate the confusion matrix. The confusion matrix calculation results for four types of ground objects on the ExGR index with the highest classification accuracy are shown in Table 5. It can be seen from Table 5 that there was still a misclassification phenomenon in the vegetation index with the highest classification accuracy. Among the weeds, 3147 pixels were wrongly classified as the female parent, accounting for 0.1316 of the total weeds.

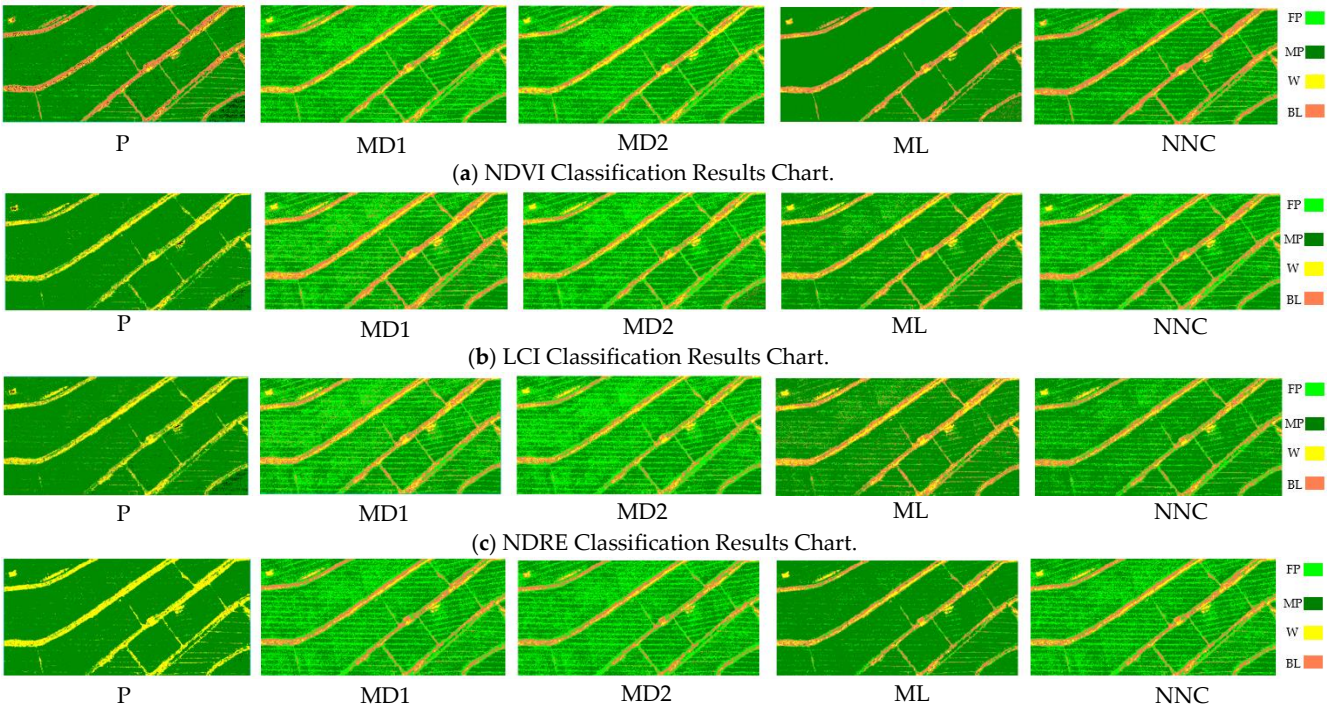

(**a**) NDVI Classification Results Chart.

(**b**) LCI Classification Results Chart.

(**c**) NDRE Classification Results Chart.

(**d**) GNDVI Classification Results Chart.

Figure 6. Supervised classification results of multispectral vegetation indices. FP: Female parent; MP: Male parent; W: Weed; BL: Bare land; P: Parallelepiped; MD1: Minimum Distance; MD2: Mahalanobis Distance; ML: Maximum Likelihood; NNC: Neural Network Classification.

Table 4. Statistics for six visible light vegetation indices based on region of interest.

Vegetation Index	Precision Statistics	P	MD1	MD2	ML	NNC
ExR	Kappa	0.4028	0.6417	0.8567	0.9145	0.9062
	Total accuracy	0.6427	0.7534	0.9065	0.9431	0.9380
ExG	Kappa	0.5977	0.7919	0.8390	0.9117	0.9276
	Total accuracy	0.7782	0.8768	0.9066	0.9476	0.9575
ExB	Kappa	0.6349	0.7063	0.8692	0.9043	0.9123
	Total accuracy	0.8016	0.8140	0.9216	0.9457	0.9466
ExGR	Kappa	0.3595	0.5722	0.8983	0.9256	0.9330
	Total accuracy	0.6837	0.7256	0.9402	0.9552	0.9599
G	Kappa	0.2084	0.4584	0.8368	0.8817	0.8458
	Total accuracy	0.6787	0.6709	0.9145	0.9354	0.9208
CIVE	Kappa	0.4441	0.6396	0.8183	0.9206	0.8962
	Total accuracy	0.6796	0.7683	0.8871	0.9519	0.9389
NDVI	Kappa	0.5607	0.6400	0.6321	0.4956	0.6873
	Total accuracy	0.7742	0.7844	0.7796	0.7490	0.8251
LCI	Kappa	0.3965	0.5742	0.5942	0.6001	0.6224
	Total accuracy	0.7005	0.7357	0.7502	0.7788	0.7752
NDRE	Kappa	0.4081	05448	0.5579	0.5392	0.5917
	Total accuracy	0.7020	0.7135	0.7241	0.7453	0.7731
GNDVI	Kappa	0.3514	0.6179	0.6069	0.5566	0.6411
	Total accuracy	0.6723	0.7664	0.7601	0.7737	0.7844

P: Parallelepiped; MD1: Minimum Distance; MD2: Mahalanobis Distance; ML: Maximum Likelihood; NNC: Neural Network Classification.

Table 5. Confusion matrix calculation based on ExGR index.

Class	Female Parent	Male Parent	Weed	Bare Land	Total
Female parent	93,347	2148	3147	0	98,642
Male parent	2494	29,532	145	0	32,171
Weed	333	377	20,975	65	21,150
Bare land	0	0	253	9754	10,007
Total	96,174	32,057	23,920	9819	161,970

3.3. Object-Oriented Classification Results and Analysis of the Male the Female Parents Based on Samples

In the sample-based object-oriented approach, after merging and fusing neighbouring objects with similar spectral, textural and geometric features into a more complete object, the segmentation effect is shown in Figure 7. Automatic supervised classification is then performed according to the SVM classification method. The supervised classification results are shown in Figures 8 and 9.

Based on the vegetation index classification results obtained in Figures 8 and 9, ten samples for each of the female and male parents were taken as the verification samples according to the visual interpretation. The classification result and the validation set were regarded as the true values. The confusion matrix of the real region of interest was calculated to obtain the accuracy statistics for each vegetation index. The results are shown in Figure 10. As can be seen from Figure 10, in the sample-based object-oriented classification method, the classification accuracy of the visible light vegetation index was still generally higher than that of the multispectral vegetation index, but the difference between the maximum and minimum values of the four multispectral vegetation indices was not as large as that of the six visible light vegetation indices. In the classification accuracy of the visible light vegetation indices, the CIVE received the lowest kappa coefficient with only 0.6256, while the kappa coefficient of the ExGR index, with the highest classification accuracy, reached 0.8698, and the total accuracy reached 0.9442, which is slightly lower than the pixel-based ExGR classification accuracy. In general, the object-oriented classification

method also showed excellent performance regarding the extraction of male and female parents of hybrid rice.

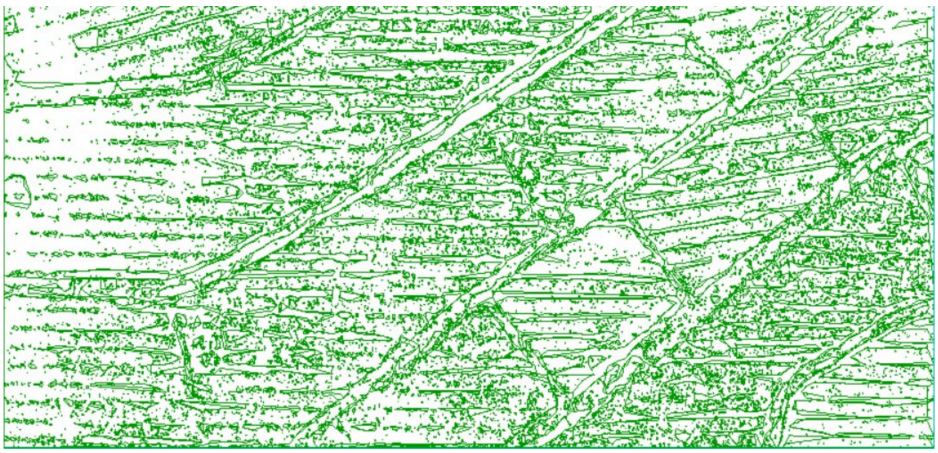

Figure 7. Sample graph of the object-oriented image segmentation.

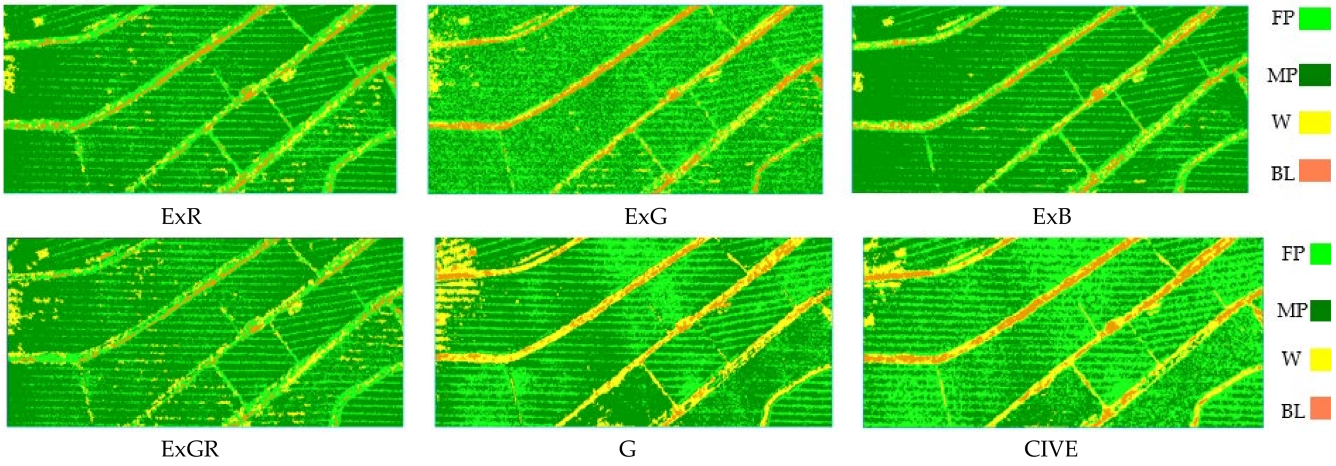

Figure 8. Object-oriented classification results for the visible light vegetation index. FP: Female parent; MP: Male parent; W: Weed; BL: Bare land.

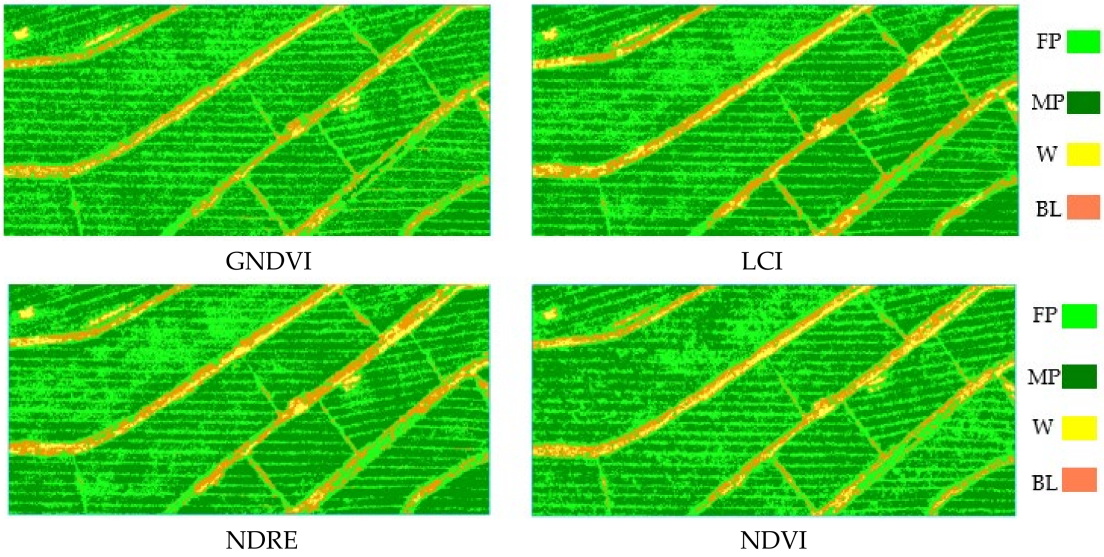

Figure 9. Object-oriented classification results for the multispectral vegetation index. FP: Female parent; MP: Male parent; W: Weed; BL: Bare land.

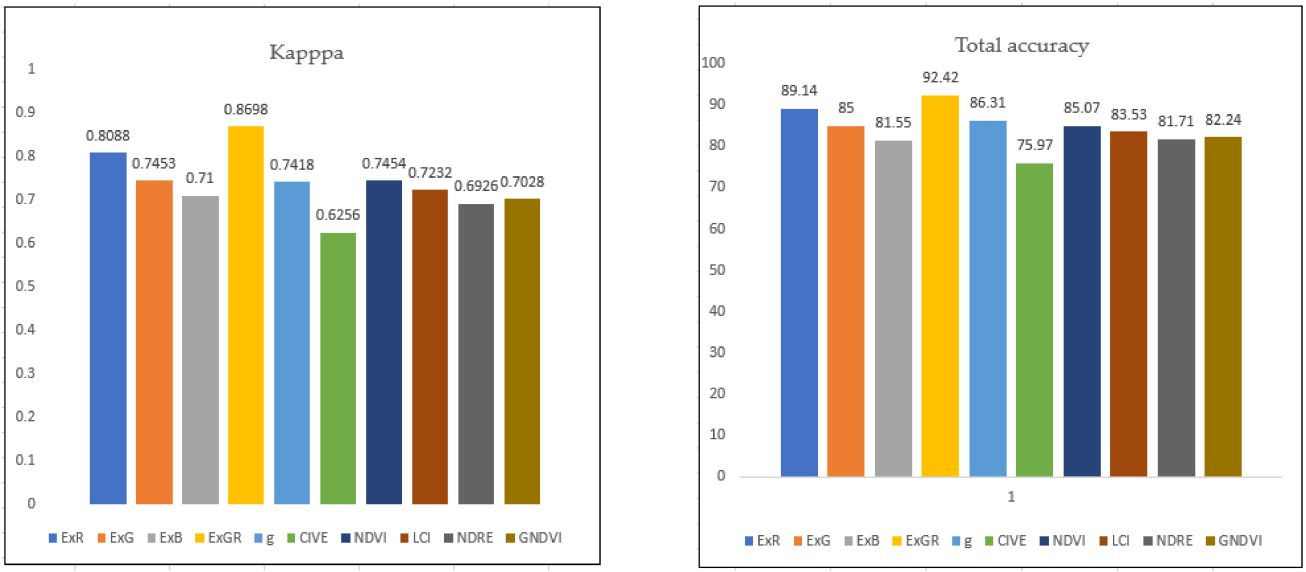

(**a**) (**b**)

Figure 10. Accuracy comparison of the object-oriented classification methods for the ten vegetation indexes: (**a**) Kappa coefficient comparison; (**b**) Total accuracy comparison.

4. Discussion

This study innovatively proposed to identify hybrid rice parents by UAV-based multispectral imagery analysis and realize the rapid and non-destructive identification and extraction of hybrid rice parents. The study solved the problem of time-consuming, labor-intensive and low-efficiency manual identification of rice parents in large-scale hybrid rice seed production farms, improved the timeliness of monitoring, and achieved monitoring with comparable accuracy to and in a shorter time than manual recognition. In the future, the results obtained through this research could be applied to unmanned smart farm management, which promises to realize the remote monitoring of hybrid rice parent identification, with great savings in terms of labor costs. Based on the results of this study, we will be able to further investigate the flowering rate estimation of hybrid rice, master the flowering habit of hybrid rice automatically and conduct a more in-depth exploration of unmanned monitoring.

When considering crop classification based on the images obtained by UAV as the data source, vegetation indices have been widely used to evaluate vegetation coverage qualitatively and quantitatively, and the use of vegetation indices can greatly improve vegetation monitoring. Wan et al. [15] used the random forest algorithm, eight common visible light vegetation indices and two multispectral vegetation indices to predict the flower number of rapeseed. In this study, we selected six commonly used visible light vegetation indices and four multispectral vegetation indices from the existing range of vegetation indices. Multispectral vegetation indices were added in this work for better comparison between the performance of multispectral vegetation indices and visible vegetation indices in the identification of male and female parents of hybrid rice plants using differences in spectral information.

In the selection of samples, the difference between the object-oriented classification method and the pixel-based classification method was that it was no longer for a single pixel but for the objects formed after image segmentation, and the objects formed after segmentation were consistent in spatial resolution. However, the total number of pixels in the sample was roughly the same as that of the supervised classification based on pixels, so there were enough object-oriented samples, and the training sets used by the two methods were the same. The training results showed that the pixel-based supervised classification method was generally more accurate than the sample-based object-oriented method. Therefore, in general, the supervised classification method based on pixels was

superior to the object-oriented method based on samples in this study, and the maximum likelihood method in the supervised classification method based on pixels was found to be more applicable in the extraction of hybrid rice parents than the neural network classification method. In the follow-up study, we suggest research with more training samples to improve the classification accuracy.

In terms of algorithms, this study also proved the feasibility of the supervised classification method in the identification of male and female parents of hybrid rice. We also used sample based object-oriented and five pixel-based supervised classification methods to extract male and female parents of hybrid rice. By comparing various algorithms, we can better select the optimal algorithm for identifying crops than by examining single algorithms. Among the ten vegetation indices studied, the ExGR index had the highest accuracy in the neural network supervised classification method. The kappa coefficient reached 0.9330 and the total accuracy was 0.9599, which was higher than the object-oriented classification method based on samples. Compared with the five supervised classification methods based on pixels, the classification accuracies of the maximum likelihood method and the neural network method were significantly higher than those of the parallel hexahedron method, the minimum distance method and the Mahalanobis distance method. In comparison, the classification accuracy of the maximum likelihood method was slightly lower than that of neural network classification, but in terms of processing time, the classification time of the neural network method was much longer than that of the maximum likelihood method. In practical applications, researchers can choose neural network classification with high accuracy requirements and the maximum likelihood method with fast prediction speed through demand selection algorithms. In this study, because field monitoring needs to reflect male and female parent information quickly and in real time, the maximum likelihood method is more suitable for the identification of male and female parents of hybrid rice plants.

In terms of accuracy comparison, Wang et al. [44] comprehensively evaluated the application range and limitations of the kappa coefficient and proved the feasibility of the kappa coefficient in a classification accuracy evaluation. In this study, the total accuracy was added to the kappa coefficient to jointly evaluate the accuracy of classification of the male and female parents of hybrid rice, which made up for the limitation of the kappa coefficient in the classification accuracy and improved the reliability of the accuracy evaluation.

Jing et al. [18] used pixel-based supervised classification and object-oriented classification to extract aquatic vegetation, in which the kappa coefficient of the object-oriented classification method reached 0.9, which greatly improved the extraction accuracy of aquatic vegetation. Although both pixel-based supervised classification and object-oriented classification methods can represent the differences between different objects based on the spectral information and spatial information of the objects in the supervised classification method, it should be pointed out that in this study the male and female parents of rice plants showed similar spectral information to weeds. The selection of male parent, female parent and weed samples was more difficult than the selection of aquatic plants, which may eventually have led to misclassification across the three categories. In particular, the proportion of weeds wrongly classified as female parents was quite large, resulting in a decrease in the overall classification accuracy of sample-based object-oriented classification.

5. Conclusions

In this study, we propose a method for the identification and extraction of hybrid rice parents based on UAV remote sensing images for the needs of hybrid rice seed production. In the calculation of the separation degree of the male parent and the female parent, a good separation degree close to 1.9 was obtained. Six kinds of visible light vegetation indices and four multispectral vegetation indices, which were excellent regarding the parental information on hybrid rice in previous studies, were selected. In terms of algorithms, pixel-based supervised classification was found to be more suitable for hybrid rice parent identification than the sample-based object-oriented classification pair, and the ExGR

index had the highest accuracy in neural network supervised classification, with a kappa coefficient of 0.9330 and a total accuracy of 0.9599. At present, misclassification still exists in the classification process, and weeds are misclassified as female parents. In general, this study used the spectral information of male and female parents on the vegetation index to provide a useful reference for the utilization of UAV remote sensing images to identify male and female parents of hybrid rice plants. The aim of our overall study is to explore the cultivar-free relations of flowering under spectral responses. In our future work, we will further extend the research to multiple rice cultivars to develop and validate the model's generalization capabilities with respect to unknown rice cultivars.

Author Contributions: Conceptualization, Y.Z.; methodology, H.L.; software, H.L.; validation, Y.Q. and W.X.; formal analysis, H.L.; investigation, H.L., H.T., D.Z., J.X., X.L. and K.Z.; resources, Y.Z.; data curation, H.L.; writing—original draft preparation, H.L.; writing—review and editing, Y.Q. and W.X.; visualization, H.L.; supervision, Y.L.; project administration, Y.Z.; funding acquisition, Y.Z. and Y.L. All authors have read and agreed to the published version of the manuscript.

Funding: This research was funded by the Key Field Research and Development Plan of Guangdong Province, China, grant number 2019B020221001, and the 111Project, grant number D18019.

Institutional Review Board Statement: Not applicable.

Informed Consent Statement: Not applicable.

Data Availability Statement: The data presented in this study are available on request from the corresponding author.

Conflicts of Interest: The authors declare no conflict of interest.

References

1. Yuan, L.P. Developing of hybrid rice to ensure food security. *Rice Sci.* **2014**, *21*, 1–2. [CrossRef]
2. Khush, G.S. What it will take to feed 5.0 billion rice consumers in 2030. *Plant Mol. Biol.* **2005**, *59*, 1–6. [CrossRef]
3. Tang, C.; Wang, H.; Li, M.; Li, Z.; Huang, Z.; Luo, H.; Jian, M.; Zhang, H. Study status and developmental strategies of mechanical pollination for hybrid rice breeding. *Trans. Chin. Soc. Agric. Eng.* **2012**, *28*, 1–7.
4. Wang, H.; Tang, C.; Li, M.; Li, Z.; Huang, Z.; Wu, M.; He, J.; Zhang, H. Effect of airflow speed on pollens distribution for hybrid rice breeding pollination. *Trans. Chin. Soc. Agric. Eng.* **2012**, *28*, 63–69.
5. Li, Z.C. Research and Application of Cutting off the Male Parent after Pollination in Hybrid Rice Seed Production. *Hybrid. Rice.* **2020**, *35*, 41–43.
6. Ma, G.H.; Yuan, L.P. Hybrid rice achievements, development and prospect in China. *J. Integr. Agric.* **2015**, *14*, 197–205. [CrossRef]
7. Zhang, Y.L.; Xiao, W.W.; Lu, X.Y.; Liu, A.M.; Qi, Y.; Liu, H.C.; Shi, Z.K.; Lan, Y.B. Method for detecting rice flowering spikelets using visible light images. *Trans. Chin. Soc. Agric. Eng.* **2021**, *37*, 253–262.
8. Zhang, J.; Yao, F.; Li, B.; Yan, H.; Hou, Y.; Cheng, G.; Boken, V. Progress in monitoring high-temperature damage to rice through satellite and ground-based optical remote sensing. *Sci. China Earth Sci.* **2011**, *54*, 1801–1811. [CrossRef]
9. Chen, P.C.; Chiang, Y.C.; Weng, P.Y. Imaging using unmanned aerial vehicles for agriculture land use cmlassification. *Agriculture* **2020**, *10*, 416. [CrossRef]
10. Ju, C.; Son, H.L. Multiple UAV systems for agricultural applications: Control, Implementation, and Evaluation. *Electronics* **2018**, *7*, 162. [CrossRef]
11. Li, C.; Li, H.; Li, J.; Lei, Y.; Li, C.; Manevski, K.; Shen, Y. Using NDVI percentiles to monitor real-time crop growth. *Comput. Electron. Agric.* **2019**, *162*, 357–363. [CrossRef]
12. da Silva, C.A.; Nanni, M.R.; Teodoro, P.E.; Silva, G.F.C. Vegetation indices for discrimination of soybean areas: A New Approach. *Agron. J.* **2017**, *109*, 1331–1343. [CrossRef]
13. Niazmardi, S.; Homayouni, S.; Safari, A.; McNairn, H.; Shang, J.; Beckett, K. Histogram-based spatio-temporal feature classification of vegetation indices time-series for crop mapping. *Int. J. Appl. Earth Obs. Geoinf.* **2018**, *72*, 34–41. [CrossRef]
14. Zhang, Z.J.; Li, A.N.; Bian, J.H.; Zhao, W.; Nan, X.; Jin, H.A.; Tan, J.B.; Lei, G.B.; Xia, H.M.; Yang, Y.S.; et al. Estimating aboveground biomass of grassland in Zoige by visable vegetation index derived from unmanned aerial vechicle image. *Remote Sens. Technol. Appl.* **2016**, *31*, 51–62.
15. Wan, L.; Li, Y.; Cen, H.; Zhu, J.; Yin, W.; Wu, W.; Zhu, H.; Sun, D.; Zhou, W.; He, Y. Combining UAV-Based vegetation indices and image classification to estimate flower number in oilseed rape. *Remote Sens.* **2018**, *10*, 1484. [CrossRef]
16. Cai, E.; Baireddy, S.; Yang, C.; Delp, E.J.; Crawford, M. Panicle Counting in UAV Images For Estimating Flowering Time in Sorghum. In Proceedings of the 2021 IEEE International Geoscience and Remote Sensing Symposium IGARSS, Brussels, Belgium, 11–16 July 2021; pp. 6280–6283.

17. Hardanto, A.; Mustofa, A. Crop stage classification using supervised algorithm based on UAV and Landsat 8 image. *IOP Conf. Ser. Earth Environ. Sci.* **2021**, *653*, 12102. [CrossRef]
18. Jing, R.; Deng, L.; Zhao, W.J.; Gong, Z.N. Object-oriented aquatic vegetation extracting approach based on visible vegetation indices. *Ying Yong Sheng Tai Xue Bao J. Appl. Ecol.* **2016**, *27*, 1427–1436.
19. Imanishi, J.; Morimoto, Y.; Imanishi, A.; Sugimoto, K.; Isoda, K. The independent detection of drought stress and leaf density using hyperspectral resolution data. *Landsc. Ecol. Eng.* **2007**, *3*, 55–65. [CrossRef]
20. Ji, D.B.; Shi, J.C.; Letu, H.; Wang, T.X.; Zhao, T.J. Atmospheric effect analysis and correction of the microwave vegetation index. *Remote Sens.* **2017**, *9*, 606. [CrossRef]
21. Yoshioka, H.; Miura, T.; Obata, K. Derivation of relationships between spectral vegetation indices from multiple ensors Based on Vegetation Isolines. *Remote Sens.* **2012**, *4*, 583–597. [CrossRef]
22. Meyer, G.E.; Neto, J.C. Verification of color vegetation indices for automated crop imaging applications. *Comput. Electron. Agric.* **2008**, *63*, 282–293. [CrossRef]
23. Upendar, K.; Agrawal, K.N.; Chandel, N.S.; Singh, K. Greenness identification using visible spectral colour indices for site specific weed management. *Plant Physiol. Rep.* **2021**, *26*, 179–187. [CrossRef]
24. Guijarro, M.; Pajares, G.; Riomoros, I.; Herrera, P.J.; Burgos-Artizzu, X.P.; Ribeiro, A. Automatic segmentation of relevant textures in agricultural images. *Comput. Electron. Agric.* **2011**, *75*, 75–83. [CrossRef]
25. Zou, K.; Chen, X.; Zhang, F.; Zhou, H.; Zhang, C. A Field Weed Density Evaluation Method Based on UAV Imaging and Modified U-Net. *Remote Sens.* **2021**, *13*, 310. [CrossRef]
26. Peichl, M.; Sonnentag, O.; Nilsson, M.B. Bringing color into the picture: Using digital repeat photography to investigate phenology controls of the carbon dioxide exchange in a boreal mire. *Ecosystems* **2015**, *18*, 115–131. [CrossRef]
27. Hague, T.; Tillett, N.D.; Wheeler, H. Automated Crop and Weed Monitoring in Widely Spaced Cereals. *Precis. Agric.* **2006**, *7*, 21–32. [CrossRef]
28. Lee, G.; Hwang, J.; Cho, S. A novel index to detect vegetation in urban areas using UAV-Based multispectral images. *Appl. Sci.* **2021**, *11*, 3472. [CrossRef]
29. Lima, J.S.; Altoe, M.S.; Silva, S.A.; Fonseca, A.S.; Medauar, C.C. Spatial variability of the nutritional status and the leaf chlorophyll index of from rubber tree. *An. Acad. Bras. Ciências* **2021**, *93*, e20191336. [CrossRef]
30. Fernández-Manso, A.; Fernández-Manso, O.; Quintano, C. SENTINEL-2A red-edge spectral indices suitability for discriminating burn severity. *Int. J. Appl. Earth Obs. Geoinf.* **2016**, *50*, 170–175. [CrossRef]
31. Song, B.; Park, K. Detection of aquatic plants using multispectral UAV imagery and vegetation index. *Remote Sens.* **2020**, *12*, 387. [CrossRef]
32. Li, L.; Sun, C.; Lin, L.; Li, J.; Jiang, S.; Yin, J. A dual-kernel spectral-spatial classification approach for hyperspectral images based on Mahalanobis distance metric learning. *Inf. Sci.* **2018**, *429*, 260–283. [CrossRef]
33. Gong, X.; Shen, L.; Lu, T. Refining training samples using median absolute deviation for supervised classification of remote sensing images. *J. Indian Soc. Remote Sens.* **2019**, *47*, 647–659. [CrossRef]
34. Ma, L.; Ma, A.; Ju, C.; Li, X. Graph-based semi-supervised learning for spectral-spatial hyperspectral image classification. *Pattern Recognit. Lett.* **2016**, *83*, 133–142. [CrossRef]
35. Egorov, V.A.; Bartalev, S.A.; Kolbudaev, P.A.; Plotnikov, D.E.; Khvostikov, S.A. Land cover map of Russia derived from Proba-V satellite data. *Sovrem. Probl. Distantsionnogo Zondirovaniya Zemli Iz Kosmosa.* **2018**, *15*, 282–286. [CrossRef]
36. Konar, D.; Panigrahi, B.K.; Bhattacharyya, S.; Dey, N.; Jiang, R. Auto-Diagnosis of COVID-19 using lung CT images with Semi-supervised shallow learning network. *IEEE Access* **2021**, *9*, 28716–28728. [CrossRef]
37. Forget, Y.; Linard, C.; Gilbert, M. Supervised classification of built-Up areas in sub-Saharan african cities using landsat imagery and openStreetMap. *Remote Sens.* **2018**, *10*, 1145. [CrossRef]
38. Wu, J.; Bauer, M.E. Evaluating the effects of shadow detection on quickBird image classification and spectroradiometric restoration. *Remote Sens.* **2013**, *5*, 4450–4469. [CrossRef]
39. Negri, R.G.; Dutra, L.V.; Sant'Anna, S.J.S. An innovative support vector machine based method for contextual image classification. *ISPRS J. Photogramm. Remote Sens.* **2014**, *87*, 241–248. [CrossRef]
40. Sari, I.L.; Weston, C.J.; Newnham, G.J.; Volkova, L. Assessing accuracy of land cover change maps derived from automated digital processing and visual interpretation in tropical forests in indonesia. *Remote Sens.* **2021**, *13*, 1446. [CrossRef]
41. Tarko, A.; de Bruin, S.; Fasbender, D.; Devos, W.; Bregt, A.K. Users' assessment of orthoimage photometric quality for visual interpretation of agricultural fields. *Remote Sens.* **2015**, *7*, 4919–4936. [CrossRef]
42. Foody, G.M. Explaining the unsuitability of the kappa coefficient in the assessment and comparison of the accuracy of thematic maps obtained by image classification. *Remote Sens. Environ.* **2020**, *239*, 111630. [CrossRef]
43. Tang, W.; Hu, J.; Zhang, H.; Wu, P.; He, H. Kappa coefficient: A popular measure of rater agreement. *Shanghai Arch. Psychiatry* **2015**, *27*, 62–67. [PubMed]
44. Wang, J. Research on the Application of Kappa Coefficient in Consistency Evaluation. Master's Thesis, Sichuan University, Chengdu, China, 2016.

applied sciences

MDPI

Article

Lightweight Semantic Segmentation Network for Real-Time Weed Mapping Using Unmanned Aerial Vehicles

Jizhong Deng [1,2], Zhaoji Zhong [1,2], Huasheng Huang [3], Yubin Lan [2,4], Yuxing Han [2,4,*] and Yali Zhang [1,2,*]

1 College of Engineering, South China Agricultural University, Wushan Road, Guangzhou 510642, China; jz-deng@scau.edu.cn (J.D.); zhongzhaoji@stu.scau.edu.cn (Z.Z.)
2 National Center for International Collaboration Research on Precision Agricultural Aviation Pesticide Spraying Technology, Wushan Road, Guangzhou 510642, China; ylan@scau.edu.cn
3 College of Computer Sciences, Guangdong Polytechnic Normal University, Zhongshan Road, Guangzhou 510642, China; huanghsheng@126.com
4 College of Electronic Engineering, South China Agricultural University, Wushan Road, Guangzhou 510642, China
* Correspondence: yuxinghan@scau.edu.cn (Y.H.); ylzhang@scau.edu.cn (Y.Z.)

Received: 19 September 2020; Accepted: 12 October 2020; Published: 13 October 2020



Abstract: The timely and efficient generation of weed maps is essential for weed control tasks and precise spraying applications. Based on the general concept of site-specific weed management (SSWM), many researchers have used unmanned aerial vehicle (UAV) remote sensing technology to monitor weed distributions, which can provide decision support information for precision spraying. However, image processing is mainly conducted offline, as the time gap between image collection and spraying significantly limits the applications of SSWM. In this study, we conducted real-time image processing onboard a UAV to reduce the time gap between image collection and herbicide treatment. First, we established a hardware environment for real-time image processing that integrates map visualization, flight control, image collection, and real-time image processing onboard a UAV based on secondary development. Second, we exploited the proposed model design to develop a lightweight network architecture for weed mapping tasks. The proposed network architecture was evaluated and compared with mainstream semantic segmentation models. Results demonstrate that the proposed network outperform contemporary networks in terms of efficiency with competitive accuracy. We also conducted optimization during the inference process. Precision calibration was applied to both the desktop and embedded devices and the precision was reduced from FP32 to FP16. Experimental results demonstrate that this precision calibration further improves inference speed while maintaining reasonable accuracy. Our modified network architecture achieved an accuracy of 80.9% on the testing samples and its inference speed was 4.5 fps on a Jetson TX2 module (Nvidia Corporation, Santa Clara, CA, USA), which demonstrates its potential for practical agricultural monitoring and precise spraying applications.

Keywords: semantic segmentation network; UAV; real time; embedded device; weed mapping; deep learning

1. Introduction

In farmland, timely weed control is crucial for ensuring optimal crop production. To minimize the negative effects of herbicides, site-specific weed management (SSWM) protocols [1] are essential. For SSWM, farmers obtain orthophoto maps of their fields, formulate an application plan, and generate

prescription maps. Methods for obtaining orthophoto maps include satellite imaging and UAV imaging [2]. The resulting remote sensing images are analyzed to map weed distribution information, which can provide decision-making support information for precise spraying applications [3].

Based on their high spatial resolution, UAVs have been found to be appropriate for weed mapping tasks. Ortizet et al. [4] collected UAV images and achieved good performance for weed mapping using a semi-supervised method. Castaldi et al. [5] used UAV multispectral images to classify maize and weeds. However, in previous studies, most image processing has been conducted offline, which results in a significant time gap between image collection and spraying applications. This disadvantage significantly limits the applications of SSWM because agronomy conditions may change during large time gaps. In SSWM applications, the time gaps should be less than one day so that the herbicide treatment can be applied before the agronomy conditions change. One possible solution to address this issue is to utilize real-time image processing onboard UAVs. Based on real-time data collection performed by embedded devices, UAVs can perform corresponding spraying actions immediately, which can solve the problem of time gaps in the current model of SSWM.

Although there has been no related work in the domain of SSWM research, we identified some related studies in industrial domains. One of the barriers in real-time image processing is that the image data is large and difficult to process by embedded devices, and some studies have exploited to reduce the amount of data while maintaining the monitoring objective. Barmpoutis et al. [6] used a 360-degree camera mounted on a UAV for fire detection. The use of 360-degree camera significantly reduces the amount of data, which is meaningful in real-time processing scenarios. In addition to the data catastrophe, the employment of deep learning models utilized by connecting desktops to embedded devices is a major challenge in the industrialization of artificial intelligence. Currently, most studies on employing deep learning models using embedded devices focus on reducing the model size while maintaining reasonable accuracy. Alexander et al. [7] introduced a tiny solid-state drive architecture that requires a storage space of only 2.3 MB to achieve a mean average precision of 61.3% on the VOC 2007 challenge. Sabir et al. [8] proposed a lightweight model for multiple-object detection and tracking that can integrate a deep-learning-based association metric approach with simple online and real-time tracking. Their algorithm was deployed on an NVIDIA Jetson TX module and Intel Neural Compute Stick. The results demonstrated the effectiveness of their algorithms for real-time experiments onboard UAVs. Arpit et al. [9] proposed a modified MobileNetV2 architecture for fire classification. They modified the last fully-connected layer of the MobileNetV2 architecture to fit the fire detection task, and the resulting model exhibited better performance than that of previous models. The proposed model was deployed on a Raspberry Pi 3B device and achieved a speed of 5 fps with an accuracy of 0.92 on the dataset presented in [10].

However, regarding the requirements of SSWM applications, there are some limitations to the methods proposed in the aforementioned studies. (1) Although previous studies have developed various approaches to reduce the number of model parameters, they have largely focused on classification [9] and detection models [7,8,11]. In studies on SSWM, semantic segmentation models [12] have proven to be effective at weed mapping tasks [13,14]; however, their optimization cannot be guaranteed based on the results of the aforementioned studies. One of the greatest obstacles for implementing such deep learning networks for widespread deployment on embedded devices is their high computational and memory requirements. In general, semantic segmentation models are difficult to optimize for small devices because they use 2D information that requires significant computation, making them less suitable for the research described in this paper. (2) The aforementioned studies only considered model design and optimization, while ignoring the optimization of the inference process, which may have the potential to achieve better efficiency. (3) Most previous studies have only conducted model design and validation on computers or embedded devices. However, in the context of SSWM applications, a real-time spraying machine requires modules for map visualization, flight control, image collection, image processing, and spraying. Based on the objectives of this study, it was

necessary to construct a basic hardware environment to support modules for map visualization, route planning, image collection, and image processing.

Therefore, the main goals of this study were to (1) develop a hardware system integrating map visualization, flight control, image collection, and image processing; (2) perform model design to achieve a compact size while maintaining reasonable prediction accuracy; and (3) exploit the optimization of the inference process, which can further improve inference speed. There are two main contributions of this work. First, we propose a lightweight network architecture for weed mapping tasks, which improves inference speed while maintaining reasonable accuracy. Second, we propose combining precision calibration with model design to improve speed, which has not been discussed in other related papers.

2. Hardware Development for a UAV System

The developed system can be divided into three main components: (1) a map visualization module for selecting flight areas and generating flight plans, (2) flight control module for controlling the UAV, and (3) onboard image collection and processing module. These components are illustrated in Figure 1a. To apply this system in an experiment, a user must first select an area of interest on a map. The software on the laptop then automatically generates corresponding routes. Waypoints are then uploaded to the flight control system via wireless serial communication. The flight control system controls the UAV and begins to collect images. During the flight process, newly collected images are processed directly by the image processing module. In this step, a fully convolutional network (FCN) is used to map weed distributions at the pixel level. Finally, a weed cover map is generated in real-time, which can provide decision support information for spraying machines. In this study, we adopted the M100 UAV platform (DJI Co., Ltd., Shenzhen, China). The Jetson TX2 module (Nvidia Corporation, Santa Clara, CA, USA) was selected as a control center to realize flight control, image collection, and! timage processing. The main components of the UAV can be observed in Figure 1b. The M100 UAV platform was chosen for its flight stability against airflow disturbance, and the Jetson TX2 was chosen for its GPU unit which is powerful in the inference of the deep learning models.

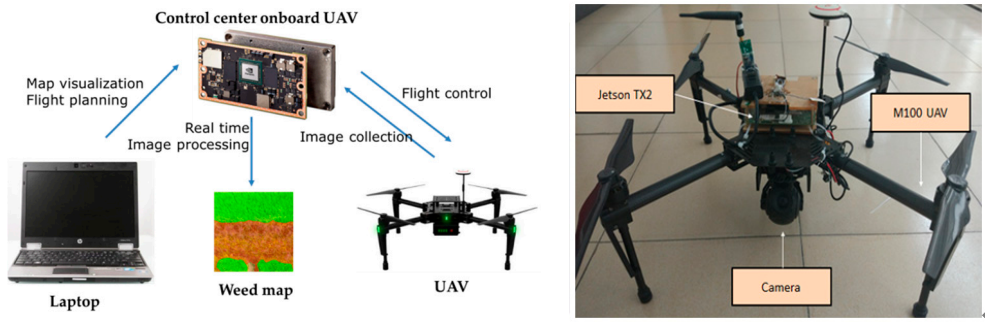

Figure 1. Composition of the developed system. (**a**) Components of the developed system. (**b**) Main components of the UAV system.

2.1. Map Visualization Module

In this study, the map visualization module (see Figure 2a) was developed using the Google Maps API (Google Inc., Mountain View, CA, USA). The ground station software has two main functions: (i) selecting areas of interest on the map and automatically generating routes, and (ii) transferring flight points to the flight control system via serial communication. The main objective of the ground station software is to provide a map for a user to select an area of interest. The selection of an area of interest is a basic requirement for the subsequent route planning procedure, autonomous flight, and image acquisition performed by the UAV. The map used in this software is a mosaic of map tiles downloaded from Google Maps. Map tiles are offline resources on the laptop that do not need to be accessed via

the internet. The map only provides a real-world overview of the area and does not contain specific location information, such as building locations, obstacles, and real-time weather data. Before flight planning begins, the user must define the forward lap and side lap. The overlap rate, flight altitude, and resolution of the camera are then used to generate flight routes. As shown in Figure 2b, during the course of a flight mission, UAVs perform image acquisition along the planned waveform path.

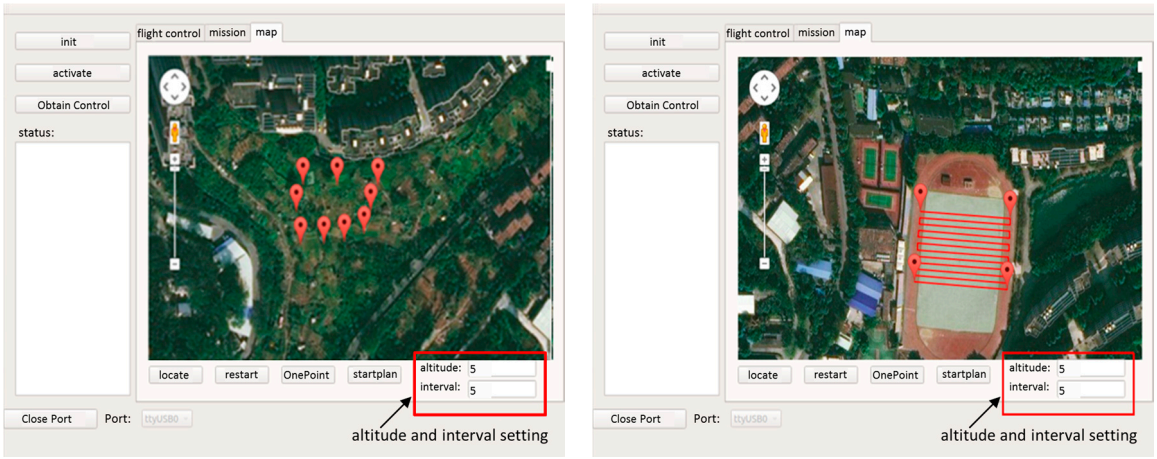

Figure 2. The map module. (**a**) User interface of the map module. (**b**) One example of route planning.

2.2. Flight Control Module

In this study, the flight control system was developed using the open-source Onboard Software Development Kit provided by the producer of the M100 (DJI Co., Ltd., Shenzhen, China). The flight control system realizes secondary control of the UAV platform. Communication between the flight control system and laptop is realized using a wireless serial module. Communication between the flight control system and UAV platform is realized using the controller area network protocol [15].

2.3. Image Collection and Processing

The image processing module in the UAV has two main functions: (i) automatically directing image acquisition according to the planned routes and predefined overlaps and (ii) processing collected images in real time. The camera (see Figure 1b) used in the image acquisition module of the system is a TOP-T10X camera (Tuopu Lianchuang co., ltd., Beijing, China) [16], which is stabilized by an optimized three-axis gimbal. On the M100 UAV, image acquisition is accomplished using the "opencvsdk" library [17]. Figure 3 presents the overall workflow of the system. The software acquires the most recent frame from the camera at a resolution of 1280 × 720 pixels. Images are cropped according to the central 720 × 720 pixel area and then resized to 1000 × 1000 pixels, which was proven to be a suitable image size for weed mapping by the previous work of our team [14]. The camera can acquire images at up to 60 fps. The overall processing speed is determined by the network model and the capabilities of the GPU.

2.4. Task Assignment

During flight, the Jetson TX2 module performs several tasks. It is necessary to assign these tasks to different components onboard the Jetson TX2 module. It is equipped with a 256 core NVIDIA Pascal GPU and six core ARMv8 64-bit CPU complex. According to the designs presented in related papers, the CPU serves as the host and is responsible for task scheduling, while the GPU serves as a device and performs the computing tasks required for image processing. For semantic segmentation models, more than 80% of the operation time of most algorithms is consumed by convolution, deconvolution, and matrix operations. A GPU can handle these high-density and high-volume operations using

highly parallel multi-threading, while the CPU is responsible for the UAV flight control program and communication processing, as shown in Figure 4.

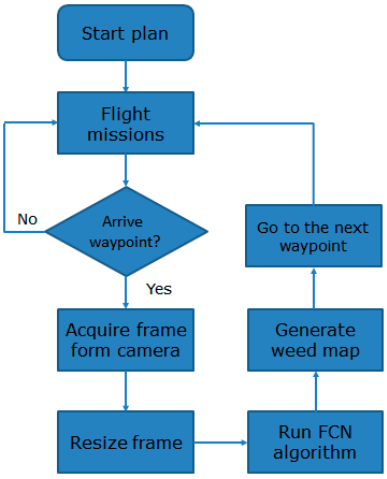

Figure 3. Overall workflow for image collection and processing.

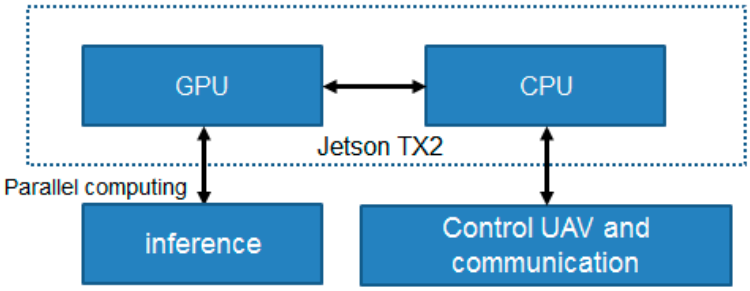

Figure 4. Task assignment on the Jetson TX2 module.

3. Model Design and Optimization

3.1. Model Design

Related studies have demonstrated that a FCN is appropriate for weed mapping tasks. In contrast to a traditional convolutional neural network, an FCN is an end-to-end network structure that can perform dense prediction tasks, allowing it to determine the weed densities at a target site, which can be directly used as references for accurate spraying tasks. For an FCN, input data can be images of arbitrary size and a corresponding output size can be obtained through effective inference. An FCN transforms all fully-connected layers into convolutional layers. In this form, the spatial information of an input image is preserved. By using deconvolutional operations, the feature maps screened from the final convolutional layer are up-sampled and the output image is restored to the same size as the input image. The general architecture of an FCN is presented in Figure 5.

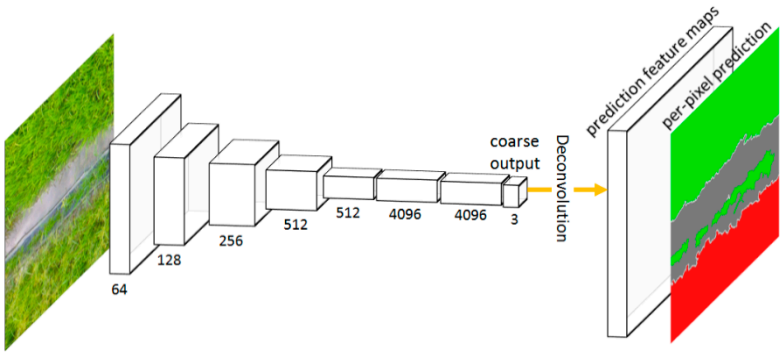

Figure 5. General architecture of an FCN.

Similar to other studies, we adopted a pre-trained network and fine-tuned it using a relevant dataset. Commonly used pre-trained networks include the ResNet [18] and VGGNet [19] models. These models tend to outperform their counterparts in terms of accuracy. However, according to the research presented in [14], these models are relatively time consuming, that is, they are inappropriate for real-time tasks. Therefore, we selected AlexNet as a pre-trained model because it is a relatively lightweight framework. As shown in Figure 6, AlexNet contains five convolutional layers and three fully connected layers. To reduce the number of model parameters, we removed the FC6 and FC7 layers. Additionally, the number of neurons in the final fully connected layer was reduced to three to match the number of classes (each pixel was classified as "rice", "weed", or "other"). Next, the last fully connected layer was transformed into a convolutional layer and a deconvolutional layer was appended to restore the feature map to the original image resolution.

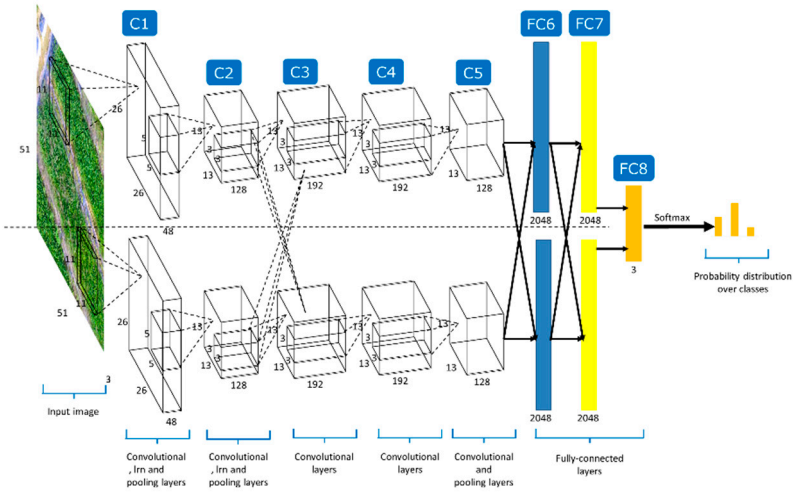

Figure 6. General architecture of AlexNet.

3.2. Optimization of the Inference Process

Most deep learning models train and evaluate neural networks with full 32-bit precision (FP32). However, once a model is fully trained, inference computations can use half-precision FP16 instead because gradient backpropagation is not required for inference. Using a lower precision results in a smaller model size, lower memory utilization and latency, and higher throughput. In this case, we applied FP32 for training and used FP16 for inference. However, it is worth noting that this will have an impact on recognition accuracy.

4. Results

In this section, we proposed a light weight network for weed mapping and compared its performance with the mainstream segmentation models. After that, the proposed network was transferred from the desktop to the embedded devices. Precision calibration was used to optimize the inference process. All models were evaluated in terms of accuracy and efficiency. For the accuracy, the metrics of overall accuracy and mean intersection over union (IoU) were applied. The overall accuracy is computed using the ratio of the pixels accurately classified to all pixels, and the mean intersection over union is calculated using the percent overlap between the target mask and our prediction output. For the efficiency, the frames per second (fps) was used as the metric, which represents how many images can be processed in one second.

4.1. Data Collection

In this study, experimental data were collected from a rice field located in Southern China (113.636888 N, 23.240441 E). Data collection was conducted when the weeds and crops were in their early tillering stages. The flight height was set to 6 m above the ground and the forward lap and side lap for imaging were set to 50% and 60%, respectively. A total of 1092 samples were collected and each sample was a 1000 × 1000 pixel RGB UAV image, where each image corresponds to a 30 cm × 30 cm field area. Each pixel in each image was classified as one of three classes: rice, weed, and other. To perform network training and validation, the images were manually labeled at the pixel level, as shown in Figure 7. In our dataset, 892 samples were used for training and the remaining 200 images were used for network validation.

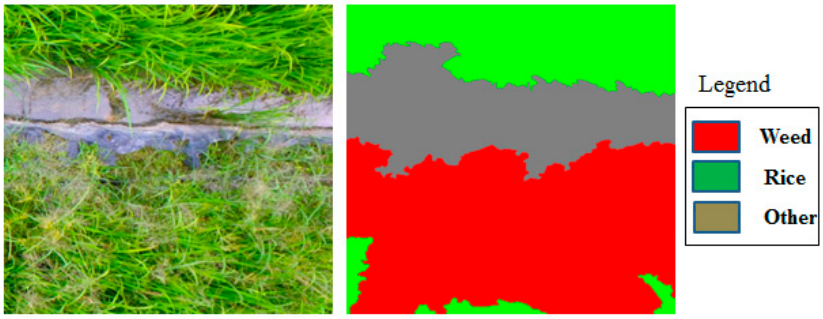

(**a**) (**b**)

Figure 7. Example of image labeling: (**a**) Input images, and (**b**) labels.

4.2. Model Design

As described in Section 3.2., a lightweight classification architecture (AlexNet) was selected as a baseline network. To reduce the number of network parameters, the first two fully-connected layers were removed, the number of neurons of the final fully-connected layer was set to three, and this layer was eventually transformed into a convolutional layer. A deconvolutional layer was appended to restore the feature map to the original image resolution. The training data were augmented using data enhancement (translation, rotation, and tailoring).

During the training process, the Adam optimizer was used for adaptive momentum estimation. The Adam gradient descent method is an adaptive learning rate method with different parameters that yields a fast convergence speed. The entire training process was limited to 30 epochs, where each iteration traversed all training samples. After forward computation, the sigmoid cross-entropy loss function was used as a cost function. The initial learning rate was set to 0.00001. Since the learning rate can be adjusted adaptively according to the rate of gradient descent, the convergence speed of the model was improved, as shown in Figure 8. After 30 epochs, testing on the validation dataset resulted in an overall accuracy of 91.2%. As shown in Table 1, the model operates on a GTX1060 GPU at 0.9 fps,

while implementing the same network on the Jetson TX2 module results in a rate of only 0.11 fps, which is insufficient for real-time processing applications.

Our modified AlexNet-FCN was compared with the classic VGGNet, GoogLeNet, and ResNet. For the VGGNet-FCN, the skip architecture was omitted to increase speed. For the GoogLeNet, ReLU was used as the activation function, and the dropout strategy was used to overcome the problem of overfitting. For the ResNet-FCN, the ResNet-101 model was selected as a baseline architecture because it provides the best balance of accuracy and efficiency [20]. The performances of all models are summarized in Table 1. One can see that the accuracy of AlexNet-FCN is slightly lower than that of VGGNet-FCN and GoogLeNet-FCN. However, it is almost four times faster than the VGGNet-FCN and two times faster than the GoogLeNet-FCN, meaning it can meet the requirements of real-time scenarios. The accuracy of the ResNet-FCN is the highest among the three models based on its deep structure and residual architecture. However, this model is so large that the GTX 1060 GPU could not even perform the forward computation. In this case, we used the GTX 1080 TI GPU for network training and evaluation. However, the GPU resources of the GTX 1060 are greater than those of embedded devices. Therefore, it is impossible to copy the ResNet-FCN from the GTX 1080 TI GPU to the embedded Jetson TX2 module.

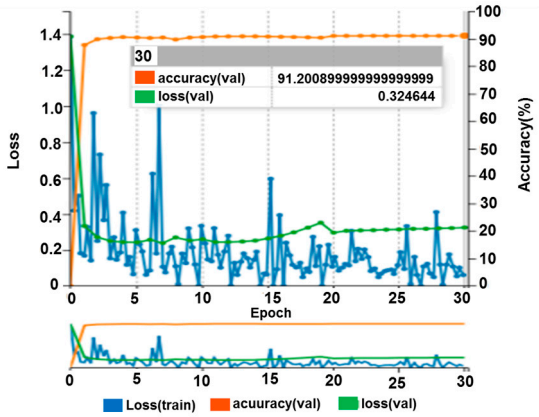

Figure 8. The loss and accuracy curves during training process.

Table 1. Comparisons of the proposed FCN-Alexnet with other mainstream network architectures.

Model	Device	Overall Accuracy (%)	Mean IoU (%)	Frames Per Second
The proposed FCN-Alexnet model	GTX 1060	91.2	70.5	12.5
VGGNet-FCN by Simonyan et al. [19]	GTX 1060	92.3	72.8	3.1
GoogLeNet-FCN by Szegedy et al. [21]	GTX 1060	91.9	71.3	5.9
ResNet-FCN by He et al. [18]	GTX 1080 TI	94.2	77.2	9.3

4.3. Optimization of the Inference Process

To reduce the model size, the data precision requirement of the network was changed from FP32 to FP16. The Jetson TX2 module uses half-precision mode to reduce the size of the model to half of its original size. Table 2 lists the results of precision calibration for the modified AlexNet-FCN. One can see that precision calibration improves inference efficiency by approximately three to four times on both the GTX 1060 (Nvidia Corporation, Santa Clara, CA, USA) and Jetson TX2 module. Although the prediction accuracy decreases slightly, the overall accuracy is acceptable for agricultural applications because it can provide rapid judgments regarding weed density.

Table 2. Inference optimization in the desktop and the embedded devices.

Device	Precision Clibration	Overall Accuracy (%)	Mean IoU (%)	Frames Per Second
GTX 1060	FP32	91.2	70.5	12.5
Jetson TX2	FP32	91.2	70.5	1.2
GTX 1060	FP16	80.9	62.8	35.6
Jetson TX2	FP16	80.9	62.8	4.5

Figure 9 presents the output images corresponding to several testing samples before and after precision calibration. In Figure 9c, one can see that our modified AlexNet-FCN can correctly distinguish the rice and weed areas. Following precision calibration, the prediction accuracy decreases by a small amount. The weed area in the third sample (blue dotted lines) was classified as the "other" category by the model following precision calibration. However, following precision calibration, our model still correctly classifies most areas in the input images, demonstrating its capability to provide decision support information for spraying machines.

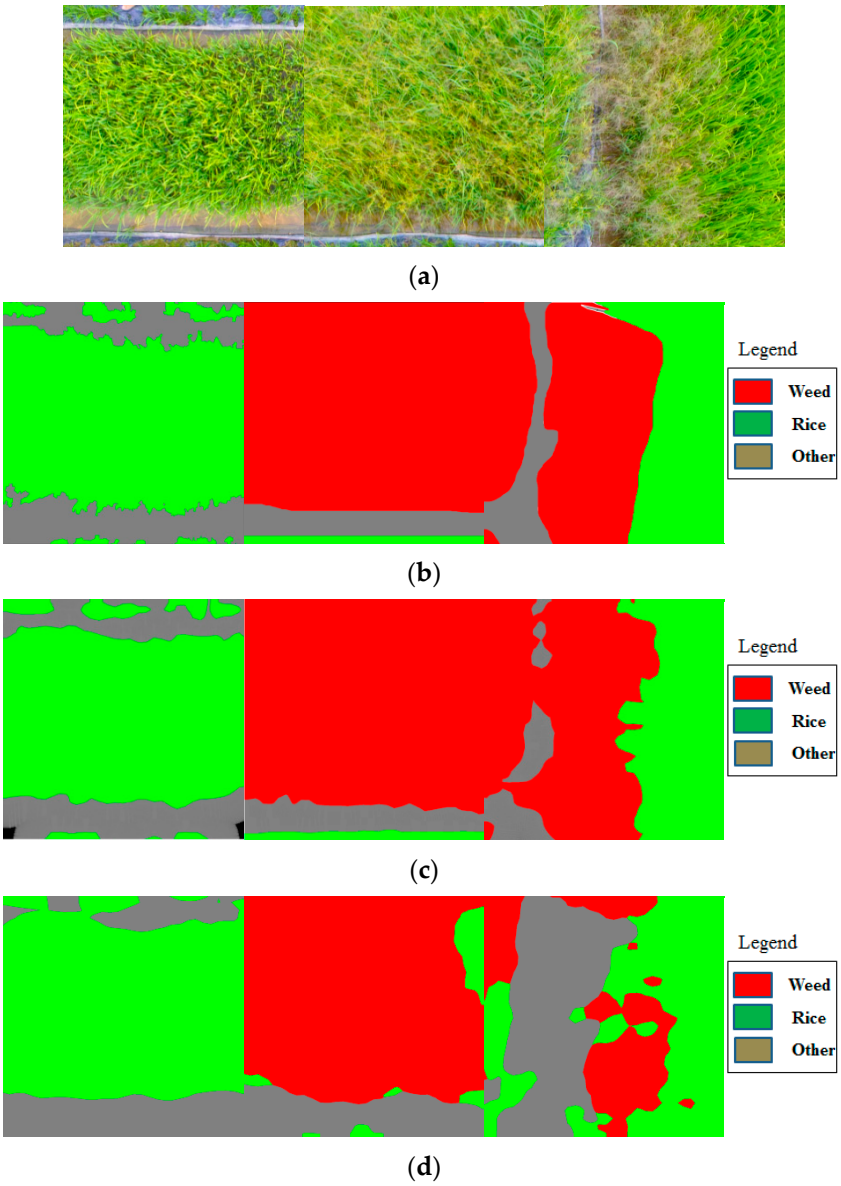

Figure 9. (**a**) UAV imagery, (**b**) corresponding labels, (**c**) results obtained by FCN-AlexNet, and (**d**) results obtained by FCN-AlexNet optimized with precision calibration.

5. Conclusions

UAV remote sensing and precision spraying are two important components of SSWM. However, the time gap between image collection and herbicide treatment significantly limits the application of SSWM technology. This study used real-time image processing onboard a UAV with the goal of eliminating the time gap between image collection and herbicide treatment. First, we established a hardware environment for real-time image processing that integrates map visualization, flight control, image collection, and real-time image processing onboard a UAV based on secondary development. Second, we exploited the proposed model design and presented a lightweight network architecture for weed mapping tasks. The proposed network architecture was evaluated and compared with mainstream semantic segmentation models. Experimental results demonstrated that the proposed network is almost two times faster than the mainstream segmentation models with competitive accuracy. Next, we conducted optimization of the inference process. Precision calibration was applied on both desktop and embedded devices and the precision was reduced from FP32 to FP16. Experimental results demonstrated that precision calibration further improves inference speed while maintaining reasonable prediction accuracy. Our modified network architecture achieved an accuracy of 80.9% on the testing samples and the inference speed of 4.5 fps on the Jetson TX2 module, which demonstrates its potential for practical agricultural monitoring and precise spraying applications.

In the future, we plan to collect additional UAV images for model training and validation. Additionally, we plan to combine our system with variable spraying technology. The classification results of UAV images can provide decision-making information for sprayers, which can help maintain pesticide effects while reducing the use of chemicals.

Author Contributions: Conceptualization: J.D., Y.H., and Y.Z.; funding acquisition: Y.L. and Y.Z.; methodology: Z.Z. and H.H.; project administration: J.D. and Y.Z.; software: Z.Z. and H.H.; writing—original draft: Z.Z.; writing—review and editing: J.D., H.H., and Y.Z. All authors have read and agreed to the published version of the manuscript.

Funding: This research was funded by the Key Area Research and Development Planning Project of Guangdong Province (grant no. 2019B020221001), Guangdong Provincial Innovation Team for General Key Technologies in Modern Agricultural Industry (grant no. 2019KJ133), the Science and Technology Planning Project of Guangdong Province, China (grant no. 2018A050506073), the National Natural Science Foundation of Guangdong Province, China (Grant No. 2018B030306026), the National Key Research and Development Plan, China (grant no. 2016YFD0200700), and the 111 Project, China (D18019).

Conflicts of Interest: The authors declare no conflict of interest.

References

1. López-Granados, F. Weed detection for site-specific weed management: Mapping and real-time approaches. *Weed Res.* **2010**, *51*, 1–11. [CrossRef]
2. Wang, D.; Shao, Q.; Yue, H. Surveying wild animals from satellites, manned aircraft and unmanned aerial systems (UASs): A Review. *Remote Sens.* **2019**, *11*, 1308. [CrossRef]
3. Balafoutis, A.T.; Beck, B.; Fountas, S.; Vangeyte, J.; Van Der Wal, T.; Soto, I.; Gómez-Barbero, M.; Barnes, A.P.; Eory, V. Precision agriculture technologies positively contributing to GHG emissions mitigation, farm productivity and economics. *Sustainability* **2017**, *9*, 1339. [CrossRef]
4. Pérez-Ortiz, M.; Peña, J.; Gutiérrez, P.; Torres-Sánchez, J.; Hervás-Martínez, C.; López-Granados, F. A semi-supervised system for weed mapping in sunflower crops using unmanned aerial vehicles and a crop row detection method. *Appl. Soft Comput.* **2015**, *37*, 533–544. [CrossRef]
5. Castaldi, F.; Pelosi, F.; Pascucci, S.; Casa, R. Assessing the potential of images from unmanned aerial vehicles (UAV) to support herbicide patch spraying in maize. *Precis Agric.* **2016**, *18*, 76–94. [CrossRef]
6. Barmpoutis, P.; Stathaki, T.; Dimitropoulos, K.; Grammalidis, N. Early fire detection based on aerial 360-degree sensors, deep convolution neural networks and exploitation of fire dynamic textures. *Remote Sens.* **2020**, *12*, 3177. [CrossRef]
7. Womg, A.; Shafiee, M.J.; Li, F.; Chwyl, B. Tiny SSD: A Tiny Single-Shot Detection Deep Convolutional Neural Network for Real-Time Embedded Object Detection. In Proceedings of the 2018 15th Conference

on Computer and Robot Vision (CRV), Toronto, ON, Canada, 9–11 May 2018; Institute of Electrical and Electronics Engineers (IEEE): New York, NY, USA, 2018; pp. 95–101.
8. Hossain, S.; Lee, D.-J. Deep learning-based real-time multiple-object detection and tracking from aerial imagery via a flying robot with GPU-based embedded devices. *Sensors* **2019**, *19*, 3371. [CrossRef] [PubMed]
9. Jadon, A.; Varshney, A.; Ansari, M.S. Low-complexity high-performance deep learning model for real-time low-cost embedded fire detection systems. *Procedia Comput. Sci.* **2020**, *171*, 418–426. [CrossRef]
10. Foggia, P.; Saggese, A.; Vento, M. Real-timfire detection for video-surveillance applications using a combination of experts based on color, shape and motion. *IEEE Trans. Circuits Syst. Video Technol.* **2015**, *25*, 1545–1556. [CrossRef]
11. Chen, S.; Lin, W. Embedded System Real-Time Vehicle Detection Based on Improved YOLO Network. In Proceedings of the 2019 IEEE 3rd Advanced Information Management, Communicates, Electronic and Automation Control Conference (IMCEC), Chongqing, China, 11–13 October 2019; Institute of Electrical and Electronics Engineers (IEEE): New York, NY, USA, 2019; pp. 1400–1403.
12. Fu, G.; Liu, C.; Zhou, R.; Sun, T.; Zhang, Q. Classification for high resolution remote sensing imagery using a fully convolutional network. *Remote. Sens.* **2017**, *9*, 498. [CrossRef]
13. Huang, H.; Deng, J.; Lan, Y.; Yang, A.; Deng, X.; Zhang, L. A fully convolutional network for weed mapping of unmanned aerial vehicle (UAV) imagery. *PLoS ONE* **2018**, *13*, e0196302. [CrossRef] [PubMed]
14. Huang, H.; Lan, Y.; Yang, A.; Zhang, Y.; Wen, S.; Deng, J. Deep learning versus object-based image analysis (OBIA) in weed mapping of UAV imagery. *Int. J. Remote. Sens.* **2020**, *41*, 3446–3479. [CrossRef]
15. Kvaser CAN Protocol Tutorial. Available online: https://www.kvaser.com/can-protocol-tutorial/ (accessed on 18 September 2020).
16. TOP Pod. Available online: http://www.topotek.com/typo-en.html (accessed on 18 September 2020).
17. Culjak, I.; Abram, D.; Pribanic, T.; Dzapo, H.; Cifrek, M. A Brief Introduction to OpenCV. In Proceedings of the 35th International Convention MIPRO, Opatija, Croatia, 21–25 May 2012; Institute of Electrical and Electronics Engineers (IEEE): New York, NY, USA, 2012; pp. 2142–2147.
18. He, K.; Zhang, X.; Ren, S.; Sun, J. Deep Residual Learning for Image Recognition. In Proceedings of the 2016 IEEE Conference on Computer Vision and Pattern Recognition (CVPR), Las Vegas, NV, USA, 26 June–1 July 2016; Institute of Electrical and Electronics Engineers (IEEE): New York, NY, USA, 2016; pp. 770–778.
19. Simonyan, K.; Zisserman, A. Very Deep Convolutional Networks for Large-Scale Image Recognition. In Proceedings of the 3rd International Conference on Learning Representations (ICLR), San Diego, CA, USA, 7–9 May 2015; Available online: https://arxiv.org/pdf/1409.1556.pdf (accessed on 13 October 2020).
20. Huang, H.; Lan, Y.; Deng, J.; Yang, A.; Deng, X.; Zhang, L.; Wen, S. A Semantic labeling approach for accurate weed mapping of high resolution UAV imagery. *Sensors* **2018**, *18*, 2113. [CrossRef] [PubMed]
21. Szegedy, C.; Liu, W.; Jia, Y.; Sermanet, P.; Reed, S.; Anguelov, D.; Erhan, D.; Vanhoucke, V.; Rabinovich, A. Going Deeper with Convolutions. In Proceedings of the 2015 IEEE Conference on Computer Vision and Pattern Recognition (CVPR), Boston, MA, USA, 7–12 June 2015; Institute of Electrical and Electronics Engineers (IEEE): New York, NY, USA, 2015; pp. 1–9.



© 2020 by the authors. Licensee MDPI, Basel, Switzerland. This article is an open access article distributed under the terms and conditions of the Creative Commons Attribution (CC BY) license (http://creativecommons.org/licenses/by/4.0/).

sensors

MDPI

Article

WSN-Assisted UAV Trajectory Adjustment for Pesticide Drift Control

Jie Hu [1,2], Tuan Wang [1,2], Jiacheng Yang [1,2], Yubin Lan [1,2], Shilei Lv [1] and Yali Zhang [2,3,*]

1 College of Electronic Engineering, South China Agricultural University, Wushan Road, Guangzhou 510642, China; hjgz79@scau.edu.cn (J.H.); twang@stu.scau.edu.cn (T.W.); yangjc@stu.scau.edu.cn (J.Y.); ylan@scau.edu.cn (Y.L.); lvshilei@scau.edu.cn (S.L.)

2 National Center for International Collaboration Research on Precision Agricultural Aviation Pesticide Spraying Technology, Wushan Road, Guangzhou 510642, China

3 College of Engineering, South China Agricultural University, Wushan Road, Guangzhou 510642, China

* Correspondence: ylzhang@scau.edu.cn

Received: 23 August 2020; Accepted: 20 September 2020; Published: 24 September 2020



Abstract: Unmanned Aerial Vehicles (UAVs) have been widely applied for pesticide spraying as they have high efficiency and operational flexibility. However, the pesticide droplet drift caused by wind may decrease the pesticide spraying efficiency and pollute the environment. A precision spraying system based on an airborne meteorological monitoring platform on manned agricultural aircrafts is not adaptable for. So far, there is no better solution for controlling droplet drift outside the target area caused by wind, especially by wind gusts. In this regard, a UAV trajectory adjustment system based on Wireless Sensor Network (WSN) for pesticide drift control was proposed in this research. By collecting data from ground WSN, the UAV utilizes the wind speed and wind direction as inputs to autonomously adjust its trajectory for keeping droplet deposition in the target spraying area. Two optimized algorithms, namely deep reinforcement learning and particle swarm optimization, were applied to generate the newly modified flight route. At the same time, a simplified pesticide droplet drift model that includes wind speed and wind direction as parameters was developed and adopted to simulate and compute the drift distance of pesticide droplets. Moreover, an LSTM-based wind speed prediction model and a RNN-based wind direction prediction model were established, so as to address the problem of missing the latest wind data caused by communication latency or a lack of connection with the ground nodes. Finally, experiments were carried out to test the communication latency between UAV and ground WSN, and to evaluate the proposed scheme with embedded Raspberry Pi boards in UAV for feasibility verification. Results show that the WSN-assisted UAV trajectory adjustment system is capable of providing a better performance of on-target droplet deposition for real time pesticide spraying with UAV.

Keywords: WSN; UAV; trajectory adjustment; drift control; DQN; PSO

1. Introduction

Crop protection UAVs have achieved rapid development in recent years for their high pesticide spraying efficiency and strong environmental adaptation. Meanwhile, greater demands have also been made for precision pesticide spraying along with the advancement of precision agriculture. Pesticide droplet deposition is a critical indicator for measuring the effect of precision pesticide spraying. The wind speed and wind direction in meteorological conditions have greater influences on the deposition and drift of the pesticide droplets, in comparison to the flying height of the UAV and the droplet size, etc. In particular, the crosswind-induced pesticide drift, which can be defined as the process whereby the pesticide droplet disappears or re-settles after being carried out of the target area by the airflow

perpendicular to its motion, is a principal factor affecting aerial spraying [1]. Since the pesticide droplet drifting outside of the target area could lead to the ineffective spraying dosage of pesticides, it not only affects the control efficiency and reduces the utilization of pesticides, but also seriously impacts the growth of sensitive crops in non-target areas and pollutes the ecological environment [2].

Deposition and drift models of UAV spraying droplets have been established through wind tunnel experiments and field experiments to predict the drift distance and deposition distribution under various meteorological conditions, as well as to evaluate according to weather station data whether a particular time is suitable for pesticide spraying to help select the appropriate operational parameters for UAV spraying [3–6]. However, these models have poor real-time performance. In other words, there is no corresponding improvement measure for the droplet drift problem resulting from crosswind outburst and local climate changes. Hence, it is imperative to spray accurately based on the real-time wind speed and direction of the spraying area in the entire pesticide spraying process. Affected by the downwash generated by the UAV, the airborne meteorological sensor system might present inaccurate data, despite still being capable of monitoring weather variations in the working area in real time. Moreover, the airborne meteorological sensor system, in general, is mounted on the manned aircraft with favorable loading capacity. The crop protection UAV, however, possesses a limited net payload since it is already carrying such facilities as spraying kits and pesticides. Clearly, equipment and methods that can provide real-time and accurate meteorological data for UAV spraying, without giving the UAV additional burden, are needed.

The wireless sensor network has been vigorously developed in the field of precision agriculture such as crop condition monitoring, precision fertilization and irrigation. With the cost decline in various agricultural sensors, crop growth condition monitoring will certainly be popularized in all stages of agricultural production. Environmental data collected in the working area can be sent to the UAV in real time by the wireless sensor network. Then, the UAV can reduce pesticide drift through adaptive route adjustments according to changes in meteorological conditions. Moreover, leaf wetness sensors, which detect the distribution of droplet deposition, can feedback the spraying effect to the UAV and help in ensuring accurate spraying [7].

Rapid development has been witnessed in research concerning the UAV-WSN system in recent years. In UAV-WSN systems, UAVs mainly assist WSN in performing the following four functional categories:

- Collecting sensor node data as a relay or mobile sink. UAVs help in performing time-sensitive tasks [8–11], monitoring emergencies [12], saving energy of WSN [13–17], extending the lifetime of WSN network [14,18], connecting separate nodes and networks [12,19], and enabling data aggregation [17,20]. Measures such as optimizing the flight routes [9,12,14–16,19] and locations [15,19,21] of UAVs, designing clustering mechanisms [17,18,22], media access control mechanisms [10,18,23,24], and sleeping schedules of WSN [14] and the like have been adopted to achieve these targets.
- Assisting in locating the WSN nodes [25–27].
- Performing wireless charging for the WSN nodes [28–30].
- Dispersing the WSN nodes in large areas [31].

On the other hand, the WSN enable UAVs to operate better in different fields. Di Gennaroa et al. [32] proposed the use of micro UAVs equipped with multispectral cameras along with WSN meteorological data to evaluate the correlation between grapes quality and measured values. Based on the data sensed by the wireless sensor network deployed in the crop field, an architecture [33] and a computer-based system approach [34], which adjust the plant protection UAV route to changes in wind intensity and direction, were evaluated. Experimental results showed they can provide a more accurate deposition of pesticides. Droplet deposition was monitored [33] by setting sensors on both sides of the working area in such a way that the UAV route can be adjusted at intervals according to the difference in the concentration of droplet deposition until droplets on both sides are evenly distributed. Trajectory

optimization was used [34] to minimize the difference between the total amount of pesticide used and the total amount of pesticide deposited in the target area. Note that it is difficult to acquire the total amount of pesticide deposited in the target area, since calibrating the waiting time for the pesticide droplet depositing onto the sensor is difficult. Assuming that the waiting time is long enough to obtain the accurate amount of deposition, there is still the issue of delay that needs to be dealt with during the real-time trajectory adjustment. Moreover, it is also challenging to determine how to convert the deposition volume sampled from the sensor node into the amount of pesticide deposited in the entire target area. On top of these, in the above cases, environmental pollution drift models were applied for simulating the deposition of pesticide droplets during verification, when it should have been a droplet drift model that was taken into account for UAV pesticide spraying.

With the view to controlling pesticide drift, this study consults previous research findings to design a system that adjusts the UAV flight route in line with the wind direction and wind speed monitored by the ground wireless sensor network. Contributions made by this study are summarized as follows:

- Pesticide drift was controlled by optimizing the spraying route of the crop protection UAV using deep Q-network (DQN) and particle swarm optimization (PSO).
- A pesticide droplet drift model that includes wind speed and wind direction as parameters was developed and adopted to simulate and compute the drift distance of pesticide droplet.
- Communication latency between the UAV and WSN has been measured and proven that it can meet the real-time requirements of the system.
- A LSTM-based wind speed prediction model and an RNN-based wind direction prediction model were established to deal with the problem of failing to acquire the latest wind speed and direction data due to the delayed communication or temporary disconnection with the ground node.
- An embedded development system was built to run the wind speed and wind direction prediction models as well as the PSO trajectory optimization algorithm based on the Raspberry Pi 4B+. It has also been proven that this approach can satisfy the real-time requirements of the practical application.

The rest of this paper is organized as follows. In Section 2, based on the simplified UAV pesticide drift model, the DQN-based and PSO-based UAV trajectory adjustment schemes were proposed. Meanwhile, a short-term wind speed and direction prediction model was also presented. This is followed by the assessment that DQN-based and PSO-based UAV trajectory adjustment schemes can potentially be applied in pesticide drift control. In Section 3, the simulation of trajectory adjustment algorithms based on DQN and PSO were described and discussed, and the effectiveness of the wind speed and direction prediction model was analyzed as well. Hardware testing and implementation were presented and discussed in Section 4. A final section summarizes the conclusions and proposed directions for future research.

2. System Model

Due to the drifting effect of natural wind, it is possible for pesticide droplets to be blown out of the target area, leading to not only poor droplet deposition within the target area, but also pollution to the surrounding environment. In response to this problem, a UAV trajectory adjustment scheme has been proposed, as shown in Figure 1. The plant protection UAV is equipped with a communication module (e.g., a ZigBee coordinator), which enables data collection from ground WSN arranged on the crop fields. While spraying, the UAV optimizes the spraying route according to the real-time wind speed and wind direction presented by ground sensor nodes. The black dashed line in the figure indicates the scheduled UAV spraying trajectory (normally, it is the central axis of the operation zone). In the case of sudden wind gusts, the UAV adjusts its flight trajectory by turning at a track angle to a certain side, deviating from the central axis (the red dotted line in the figure). When the displacement (the vertical distance between the UAV position and the original route) is adjusted to a proper value, the

UAV returns to the start track angle and flies parallel to the central axis. By this means, the pesticide deposition is more balanced in the target area. During the trajectory adjustment process, pesticide spraying isn't interrupted.

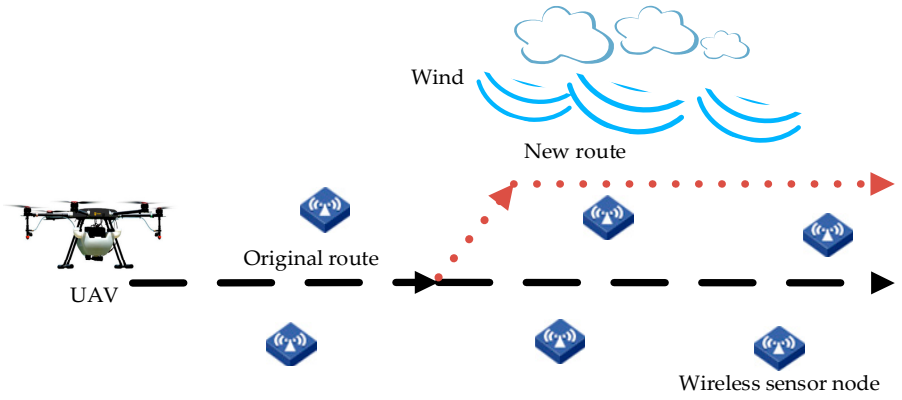

Figure 1. UAV spraying route changed based on ground sensor data.

It is assumed that a crop field is divided into adjacent operation zones by taking the UAV spray swath as the width of each operation zone and the straight-line distance of the UAV flying in a route changing period as the length of the operation zone. In this study, the route changing period is set as 10 s, so as to match the wind change on real time basis. Figure 2 shows the steps to acquire route changing parameters by the UAV while spraying in an operation zone: (i) Collecting the wind speed and wind direction data from the ground sensors at 10 s intervals; (ii) Calculating the route changing parameters for the next operation zone based on the sensor data with the algorithms DQN or PSO; (iii) Exporting the route changing parameters to the steering control unit of the UAV. This process runs sequentially for each operation zone until the end of the spraying process.

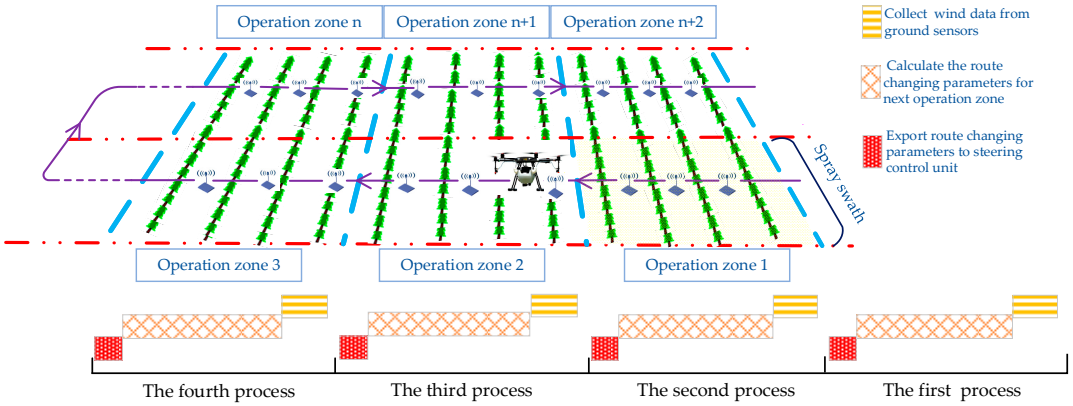

Figure 2. Operation environment and data process of the spraying UAV.

When the spraying starts in an operation zone, the UAV sends a broadcast message to the ground sensor nodes, requesting the wind speed and wind direction. In the case of long operation zone, querying the sensor nodes located in the next operation zone is needed and can be performed by using multi-hop links wireless communication between UAV and ground WSN. As the operation zone is relatively short in this research (the distance that a plant protection UAV can fly in 10 s with a typical speed from 5 m/s to 10 m/s), the wind data from the sensor node in the current operation zone is also suitable for the next operation zone trajectory adjustment. The wind speed and wind direction are sampled every 1 s. At the other times, ground sensor nodes switch into a sleeping state and regularly wake up for messages. The sensor nodes that receive the UAV message transmit the latest wind data to

the UAV in one hop. The UAV then takes the average of the acquired sensor data to obtain the wind information. By this means, communication delay can be decreased compared with the multi-hop transmission. To make sure at least one sensor node can respond to the UAV's requests at any time, the distance between adjacent nodes in an operation zone or among neighboring zones is set as nearly 50 m for a network of the ZigBee protocol, while the node sleep time is set as 30 ms. On receiving the wind data, the DQN algorithm or PSO algorithm are applied to generate the route changing parameters for the next operation zone, which are illustrated in detail in Sections 2.1 and 2.3. When the spraying of the next operation zone starts, the UAV updates its flight trajectory according to the route changing parameters, and in the meantime, another cycle of acquiring the adjustment parameters is executed.

There are two constraint conditions for successfully executing the route changing process. One important condition is that the computational cost (runtime) of acquiring the route changing parameters should be lower than the time required for spraying a single operation zone. The other condition is that the wind data should be received by the UAV in time. In the event of packet loss that prevents the timely wind information from being received by the UAV, two backup settings can be used: (i) In the case of wind data missing in a short time, the wind speed and direction is predicted based on the previously received sensor data, which will be discussed in Section 2.4. (ii) In the case of wind data missing in a longer time, the UAV keeps the spraying trajectory to the default route (it is mostly the central axis of the operation zone).

2.1. The DQN-Based UAV Trajectory Adjustment Scheme

Served by the data from field wireless sensors, the crop protection UAV accepts droplet drift and deposition data as feedback and adjusts its flight route in real time based on the wind speed and wind direction data of the farmland during the spraying process. In this approach, a closed control loop is formed, which requires a mechanism to collect the environmental status information (wind speed and direction). This can also be analogized to accumulating experience through learning and exploration, before gradually adjusting the strategy (i.e., spraying trajectory) through environmental feedback (i.e., droplet deposition).

Reinforcement learning [35] is a learning mechanism that is executed via the interaction between the agent and the dynamic environment. It evaluates in accordance with the feedback of the environment on the actions taken by the agent subject to guide the subsequent actions, so that good actions can be reinforced. This implies that a satisfactory action strategy can be acquired through trials to adapt to the environment. DQN [36] approximates value functions using the deep learning technique compared with the traditional reinforcement learning method. By doing so, it can not only alleviate the curse of dimensionality caused by the excessively large state and action space, but also address the unstable function approximation in RL using experience replay and a destination network.

2.1.1. Working Environment

The UAV employs cattle ploughing reciprocation and is capable of spraying the whole farmland with an effective spraying width. The default spraying trajectory is set along the central axis of each operation zone, with wind speed and direction sensors arranged in each operation zone as needed. If feedback on droplet deposition is needed from the sensor during reinforcement learning, both sides of the central axis in the operation zone will be configured with two rows of wireless sensor nodes and leaf wetness sensors at equal distances. If the droplet deposition feedback is not needed, then the wind speed and direction sensors will be arranged as desired, rather than placed in symmetry.

2.1.2. States

UAV is an intelligent learning agent that can perceive its environment in multidimensional states. Therefore, it is important to select the states which have direct association with trajectory optimization effect for observation. However, if too many states are selected, an excessively large state space will be formed, leading to calculation overload and reducing the convergence speed. If insufficient states are

selected, some of the important environment information will be lost, hindering the UAV from learning the optimal strategy. The following state spaces were constructed on the basis of the acquirable sensor data:

$$S = (U, X_w, \theta_w) \tag{1}$$

where U represents the position of the UAV, X_w the wind speed, and θ_w the wind direction. The wind speed and wind direction are delivered to the UAV via ground sensor nodes, whereas the position statuses are obtained by the GPS and built-in sensors of the UAV.

2.1.3. Action

During the reinforcement learning, the agent selects an action from the set of optional actions according to a certain strategy to be executed upon observing the current states (wind speed, wind direction, and position) of the environment. The determination of the optional action space exerts a crucial influence on the agent's learning process. In this study, the UAV action is to advance a step by selecting a certain steering angle at the current position and to fly in parallel with the central axis of the working area after adjusting to an appropriate position (as shown in Figure 1). In view of the spraying width and steering characteristics of the crop protection UAV, if the steering angle is too large, the UAV will move too far away from the central axis in a step, resulting in the fact that the route adjustment is not precise, and it may even move the UAV outside the operating area. Therefore, a small angle of –15° to +15° is applied to fine-tune the deviation of the UAV. Since at each step the DQN algorithm calculates the Q values for all actions in the action space, overlarge action space will cause too many output units, increasing the calculation time and weakening the recognition ability of the deep neural network. Therefore, discrete steering angles were selected rather than continuous angles [37] to form the action space. The difference between the angles is 5 degrees, which is sufficient for the application of plant protection UAVs. The action space was designed based on 7 steering angles, as shown below:

$$A = \{-15°, -10°, -5°, 0°, 5°, 10°, 15°\} \tag{2}$$

By doing so, it can not only reduce the complexity of the neural network approximator of the action value function, but also improve the timeliness of planning.

2.1.4. Reward

The action feedback of UAV is acquired by means of environmental reward functions in the process of deep reinforcement learning. The reward function has a direction impact on the performance and the convergence speed of the reinforcement learning algorithm since it implicitly defines the learning target. When the UAV sprays down at a farmland distributed with leaf wetness sensors, it will receive droplet deposition data on both sides of the central axis in real time while spraying. When the difference of the droplet deposition concentration on both sides is greater than a certain threshold T, the pesticide droplets in that area will be regarded as having drifted towards a certain side of the work area. Since reinforcement learning is targeted at droplet deposition as uniformly as possible in the targeted work area, the reward can be given in accordance with the difference Δc in droplet deposition concentrations read by the leaf wetness sensors on both sides of the central axis. The specific definition of reward in this paper is shown in Equation (3):

$$r = \exp[-1.3 \times (\Delta c - T)] - 1 \tag{3}$$

where T is the predefined threshold. If $\Delta c < T$, the agent will obtain a positive reward, which will increase with the decrease of Δc. If $\Delta c < T$, the agent will obtain a negative reward, and if $\Delta c = T$, zero reward will be given. This design ensures the continuity of the reward function and accelerates the convergence speed of the algorithm. It is worth noting that, since the deposition amount on the sensor increases with observation time, the difference Δc in droplet deposition concentration on both

sides of the central axis will also be proportional to the monitoring time after the droplets spraying, both of which affects the determination of the threshold T. Hence, the threshold should be practically calibrated through experiments.

For environments not distributed with leaf wetness sensors, the distance d between the center of droplet deposition, which can be computed by the droplet drift model, and the central axis of the work area can be used to indicate the immediate reward, which can be defined as Equation (4):

$$r = \begin{cases} -a, & \text{if } d > I \\ \exp(1.3d), & \text{if } d \le I \end{cases} \tag{4}$$

where d is the vertical distance between the center of droplet deposition and the central axis of the working area, I ($I > 0$) is the set threshold, and a ($a > 0$) is a constant. Algorithm 1 shown below describes the DQN algorithm used for the UAV trajectory adjustment.

Algorithm 1 DQN-based UAV Trajectory Adjustment

Initialize: Initialize an experience replay memory with capacity D
Initialize the online network Q with random weight $\theta = \theta_0$
Initialize the target network Q' with the weight $\theta' = \theta_0$
for episode $l = 1$ to M **do**
Initialize the activity state of UAV
for t = 1 to T **do**
According to current state s_t, with probability ε randomly select an action a_t,
otherwise select $a_t = \text{argmax}_a (s_t , a_t , \theta)$
Receive reward r_t by formula (4) and observe new state s_{t+1}
Store transition $(s_t , a_t , r_t , s_{t+1})$ in the replay memory D
Sample a random minibatch of transitions $(s_i , a_i , r_i , s_{i+1})$ from D
Set $y_i = \begin{cases} r_i, & \text{if } terminal \\ r_i + \gamma \max_{a'} Q\prime(s_{i+1}, a'; \theta\prime), & \text{otherwise} \end{cases}$
Calculate the loss $\left(y_i - Q(s_i, a_i; \theta)\right)^2$
Perform a gradient descent step on the loss function with respect to θ
Train and update Q network weights θ
Every C step set $\theta' \leftarrow \theta_0$
$s_t \leftarrow s_{t+1}$
end for
end for

2.1.5. Neural Network Approximation of DQN Value Function

DQN is a reinforcement learning method that approximates the value function Q using a neural network. The neural network structure constructed in this paper, as shown in Figure 3, is composed of two fully connected layers instead of the convolutional layer in the common deep Q network. Moreover, a rectified linear unit (ReLU) is used as the activation function, and the number of neurons in each layer is 32. Its input is the state $S = (U, X_w, \theta_w)$, and its output is the corresponding Q value.

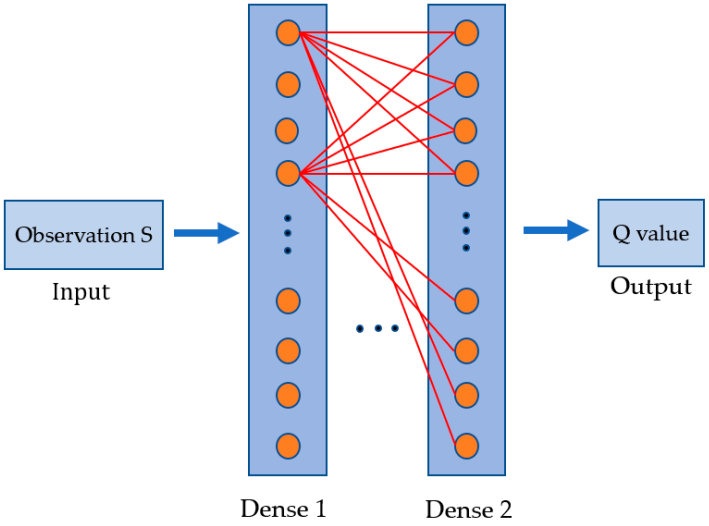

Figure 3. Neural network based value function approximator of Reinforcement learning.

2.2. The Simplified UAV Pesticide Drift Model

The droplet drift model, which focuses on the drift distance of pesticide droplets under the influence of various factors, has important guiding significance for adjusting the pesticide spraying trajectory in this study. Rotor wind field, UAV flight height and speed, wind speed and direction as well as droplet size and nozzle pressure are critical factors affecting droplet drift. Because this study is focused on the method of adjusting the spraying route based on real-time wind speed and direction, a simplified droplet drift model that depends primarily on wind speed and direction was proposed, while the UAV model, flight height and speed, as well as the droplet size and nozzle pressure were set as fixed options.

The regression equation for the drift distance of the droplet deposition center obtained via wind tunnel experiments [5] can be expressed as:

$$Y = 0.167X_w + 0.085X_p + 0.308X_h - 0.667, \quad \left(R^2 = 0.774\right) \tag{5}$$

where X_w (m/s) is the wind speed, X_p (Mpa) is the nozzle pressure, X_h (m) is the spraying height, Y (m) is the drift distance of the droplet deposition center, and R^2 is the coefficient of determination.

It can be seen from Figure 4 that the coordinate system is set with the UAV position as the origin, the positive axis of the x axis as the direction of due east, and the positive axis of the y axis as the direction of due north. In this study, the height was excluded. With regards to various position and distance parameters, only their projections on the xy coordinate plane were taken into account. Assuming that θ_w is the angle formed between the wind direction and the positive axis of x, and θ_f is the angle between the flight direction and the positive axis of x, performing an orthogonal decomposition on X_w will obtain the drift distance component H_x of the droplet deposition center in the vertical to the UAV flight direction, and the drift distance component H_y of the droplet deposition center along the UAV flight direction.

$$H_x = 0.167X_w \sin\left(\theta_w - \theta_f\right) + 0.085X_p + 0.308X_h - 0.667 \tag{6}$$

$$H_y = 0.167X_w \cos\left(\theta_w - \theta_f\right) + 0.085X_p + 0.308X_h - 0.667 \tag{7}$$

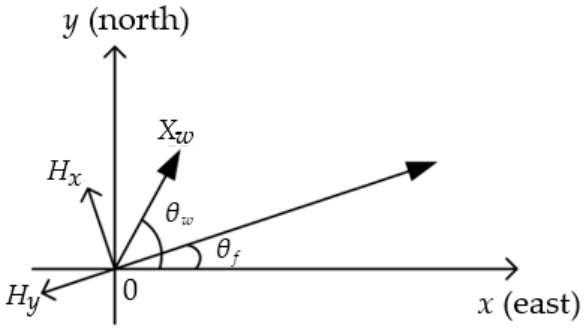

Figure 4. Schematic diagram of flight direction, wind direction, and deposition components.

The above conclusion describes the influence of wind speed on the drift of the droplet deposition center when the UAV is hovering. Since the actual flying operation of the UAV should be considered in this study, the influence of the flight speed of UAV on the droplet drift should be also taken into account. Notice that pesticide droplets drift toward the opposite of UAV flight direction. For a M234-AT model quadrotor fitted with a pressure nozzle made by Lechler GmbH (Metzingen, Germany), the relationship between the drift and the distance behind the UAV, given that the nozzle position is 0.5 m, the distance between nozzles is 0.25 m, the flight height is 1.5 m, and the flight speed 6 m/s, can be expressed as [38]:

$$y = 41.34 - 22.22\log(x), \quad \left(R^2 = 0.991\right) \tag{8}$$

where y represents the percentage of the drift behind the UAV to the total drift, in percentage; x represents the distance to the rear of the fuselage, in meters. Furthermore, Equation (8) can be rewritten as:

$$x = \exp\left(\frac{41.34 - y}{22.22}\right) \tag{9}$$

Using the above equation, $x = 0.677$ is computed upon substituting $y = 50$ into the expression. That is to say, the amount of droplet deposition within the range of 0.677 m behind the fuselage under windless conditions can reach up to 50% of the total deposition amount. Taking Equation (7) into account, the drift distance component of the droplet deposition center directly behind a flying M234-AT quadrotor under windy conditions can be expressed as:

$$H_y = 0.167X_w\cos\left(\theta_w - \theta_f\right) + 0.085X_p + 0.308X_h - 0.667 - 0.677 \tag{10}$$

Substituting nozzle pressure X_p = 1 MPa and spraying height X_h = 1.5 m into Equations (6) and (10), H_x and H_y can be rewritten as:

$$H_x = 0.167X_w\sin\left(\theta_w - \theta_f\right) - 0.12 \tag{11}$$

$$H_y = 0.167X_w\cos\left(\theta_w - \theta_f\right) - 0.797 \tag{12}$$

from the above expression, the drift distance components of the droplet deposition center in the positive x axis direction and the positive y axis direction are:

$$x = H_x\sin\theta_f + H_y\cos\theta_f \tag{13}$$

$$y = H_x\cos\theta_f + H_y\sin\theta_f \tag{14}$$

Then, substituting Equations (11) and (12) into Equations (13) and (14), the simplified pesticide droplet drift model can be obtained:

$$D\left(X_w, \theta_w, \theta_f\right): \begin{pmatrix} x = 0.167X_w \cos\left(\theta_w - 2\theta_f\right) - 0.12\sin\theta_f - 0.797\cos\theta_f \\ y = 0.167X_w \sin\theta_w - 0.12\cos\theta_f - 0.797\sin\theta_f \end{pmatrix} \quad (15)$$

where $D\left(X_w, \theta_w, \theta_f\right)$ represents the relative distance of the droplet deposition center to the UAV under wind speed X_w, wind direction θ_w, and UAV flight direction θ_f.

2.3. UAV Trajectory Adjustment Based on the PSO Algorithm

Particle swarm optimization is a kind of self-adaptive random algorithm based on group hunting strategy featuring fast convergence rate, as well as easiness in programming and implementation since the optimized function is not required to be differentiable, derivable, and continuous. It is hence perfect for solving a high-dimensional UAV trajectory optimization problem that demands high real-time performance but tolerates lower-precision solutions.

As can be seen from Figure 5, a coordinate system is established with the starting point of the central axis in the current work area set as the origin of the coordinates. The due East and due North directions are respectively represented with the x axis and y axis to match with the pesticide drift model. Without a loss of generality, the central axis of the work area is assumed to coincide with the due east direction in Figure 5. The initial position of UAV in the current trajectory adjustment cycle is set as $\boldsymbol{U}_P^0$. $\boldsymbol{U}_P^0 = (0, 0)$ is assumed in Figure 5. If the trajectory is not adjusted, the UAV flies and applies pesticide at the speed of v_f along the central axis of the work area or in a direction parallel with the central axis. Given the central axis is assumed to coincide with the due east direction, thus the angle θ_f formed by the flight direction and the due east direction is 0° in Figure 5. The UAV spraying position at every $t(t \in N)$ can be expressed by:

$$\boldsymbol{U}_P^t = \boldsymbol{U}_P^0 + \boldsymbol{G}(v_f, \theta_f, t) \quad (16)$$

where $\boldsymbol{G}(v_f, \theta_f, t)$ represents the distance of the UAV moving in a XY coordinate plane during time period of t. Note that the distances and positions discussed in this section are those of XY coordinate plane, excluding the height. Moreover, the distance between the droplet deposition center and the UAV is $\boldsymbol{D}(X_w^t, \theta_w^t, \theta_f)$ upon computing with the droplet drift model mentioned in Section 2.2, where X_w is wind speed and θ_w is wind direction. Then, under windy conditions, the position P^t of the droplet deposition center of the sprayed pesticide droplet at time t can be calculated as

$$\boldsymbol{P}^t = \boldsymbol{U}_P^0 + \boldsymbol{G}(v_f, \theta_f, t) + \boldsymbol{D}(X_w^t, \theta_w^t, \theta_f) \quad (17)$$

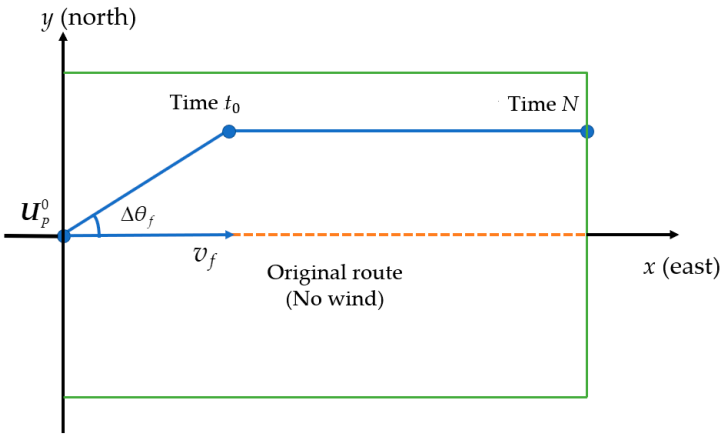

Figure 5. The principle of PSO-based trajectory adjustment.

The UAV sprays pesticide along the central axis of the work area is the optimal strategy under windless conditions. In this scenario, the position of the deposition center point of the sprayed pesticide droplet at time t is

$$\boldsymbol{P}_0^t = \boldsymbol{G}(v_f, \theta_f, t) + \boldsymbol{D}(0, 0, \theta_f) \tag{18}$$

This position is the optimal position for droplet deposition at time t. Under windy conditions the central points of the droplet deposition would drift out of these optimal positions, the flying angle and speed of the UAV should be adjusted in a manner shown in Figure 5. Assuming that the UAV turns to $\Delta\theta_f$ from the original flight direction with increased flight speed Δv_f , and the rotational direction maintained for time period of t_0 , upon resuming a flight direction that is parallel with the central axis and the original flight speed v_f at the end of the turn. When $\Delta\theta_f$ is positive, it indicates that the UAV is deflected northeast, and when it is negative, it indicates that the UAV is deflected southeast.

The target of PSO-base trajectory optimization is to minimize the distance sum between the droplet deposition centers of spraying along the new route and the droplet deposition centers of spraying along the central axis under windless conditions at the sampling moments. In this study, the sampling interval is 1 s, and the range of N seconds is a cycle for route adjustment. The trajectory optimization function is expressed as

$$\begin{aligned} & f(\Delta v_f, \Delta\theta_f, t_0) \\ = & \underset{\Delta v_f, \Delta\theta_f, t_0}{\operatorname{argmin}} \sum_{t=1}^{N} \|P^t - P_0^t\| \\ = & \underset{\Delta v_f, \Delta\theta_f, t_0}{\operatorname{argmin}} \left\{ \begin{array}{l} \sum_{t=1}^{t_0} \|\boldsymbol{u}_P^0 + \boldsymbol{G}(v_f + \Delta v_f, \theta_f + \Delta\theta_f, t) + \boldsymbol{D}(X_w^t, \theta_w^t, \theta_f + \Delta\theta_f) - \boldsymbol{G}(v_f, \theta_f, t) - \boldsymbol{D}(0, 0, \theta_f)\| + \\ \sum_{t=t_0}^{N} \|\boldsymbol{u}_P^0 + \boldsymbol{G}(v_f + \Delta v_f, \theta_f + \Delta\theta_f, t_0) + \boldsymbol{G}(v_f, \theta_f, t - t_0) + \boldsymbol{D}(X_w^t, \theta_w^t, \theta_f) - \boldsymbol{G}(v_f, \theta_f, t) - \boldsymbol{D}(0, 0, \theta_f)\| \end{array} \right\} \end{aligned} \tag{19}$$

The trajectory fine-tuning model can be regarded as a function expression whose independent variables are Δv_f , $\Delta\theta_f$, t_0 and search space dimension $D = 3$.

Algorithm 2 describes the optimization process. First, by initializing the particle swarm, each particle has a random initial position and initial speed. Then, the maximum number of iterations of the algorithm is set. A possible solution should be detected when the maximum number of iterations or the given conditions is met. Fitness values of all particles are obtained through optimizing the function f (Δv_f, $\Delta\theta_f$, t_0). At any instance during the iteration, when the fitness of a particle is the optimal value obtained among the completed iterations, the particle position is saved as the optimal in history. When the fitness of a particle is the optimal value of all particles, the particle position is saved as the optimal in the swarm. An optimal solution or a sub optimal will be obtained by the end of the algorithm iteration.

Algorithm 2 PSO-based UAV Trajectory Adjustment

```
Initialize particles (random velocities and positions for particles)
for iteration = 1 to Max_iterations do
    if expected conditions are met then
        break
    end if
    for each particle i do
        Calculate the fitness value according to the function (19)
        if the fitness value is the best of the particle then
            Store the position of the corresponding particle in the particle
        end if
        if the fitness value is the best of the swarm then
            Store the position of the corresponding particle in the swarm
        end if
    end for
    Update the particles' velocities and positions
end for
Output the best particle
```

2.4. Establishment of a Short-Term Wind Speed and Direction Prediction Model

The DQN and PSO algorithms proposed in this paper perform trajectory optimization in accordance with wind speed and direction data sent by the ground wireless sensor network to the UAV. Nevertheless, isolated nodes and networks might occur due to the large farmland area, causing the UAV to fail to receive the wind speed and direction data. Moreover, large communication latency might be caused by re-transmission because of packet loss, affecting the real-time operation of the trajectory adjustment mechanism. At this point, a method that can be used for quickly predicting the wind speed and direction is required. For this reason, a short-term wind speed and direction prediction model is established to predict the wind speed and direction in the area to be sprayed when the communication latency becomes large.

Based on the collected wind direction and wind speed data, LSTM wind speed prediction and RNN wind direction prediction were selected in this study after comparing the wind speed and direction prediction effects of a fully connected neural network, one-dimensional convolutional neural network, recurrent neural network (RNN), and long and short-term memory network (LSTM).

The wind speed and wind direction prediction model is designed into a three-input and single-output network structure, and its inputs are two-dimensional tensor composed of wind speed and wind direction data, as well as average humidity data and average temperature data.

The wind speed prediction model consists of wind speed and direction feature extraction layer, humidity feature extraction layer, temperature feature extraction layer, feature stitching layer and wind speed vector prediction layer. The feature extraction layer is comprised of an LSTM layer and dropout layer. Specifically, the LSTM layer involving several neurons is used for extracting shallow features of sequence data. Dropout discards neurons, with the probability of p to break the contingency of feature combination, are used to transform shallow features of the sequence data. The feature stitching layer combines and compresses wind speed, wind direction, humidity and temperature features extracted by the feature extraction layer to obtain more abstract features. Finally, the wind speed sequence value over a short term in the future is computed via the wind speed vector prediction layer according to the features output by the feature stitching layer.

The wind direction prediction model consists of the wind speed and direction feature extraction layer, humidity feature extraction layer, temperature feature extraction layer, feature stitching layer, and wind direction vector prediction layer. The feature extraction layer is comprised of the RNN layer and dropout layer. The number of neurons in the RNN layer in the wind direction prediction model is twice the number of neurons in the LSTM layer in the wind speed prediction model. Similarly, compared with the wind speed prediction model, the wind direction prediction model also increases the number of neurons in the feature stitching layer without performing feature compression. The wind direction sequence value over a short term in the future is the output of the wind direction prediction model.

3. Results

In this section, the performances of two proposed trajectory adjustment algorithms are evaluated in simulation using the collected wind speed and direction data and the predicted wind speed and direction data, respectively.

3.1. Simulation of Trajectory Adjustment Algorithm of Crop Protection UAV for Pesticide Drift Control

A STM32F103ZET6 single-chip microcomputer, a RS-FXJT05-V05 anemometer and an SD card were adopted for environmental data monitoring. The meteorological data of certain areas in the university from 20 June 2019 to 20 September 2019 were collected at the data collection cycle of 1 s. Parts of the collected wind speed data are shown in Figure 6. The accuracy of the anemometer is eight orientations.

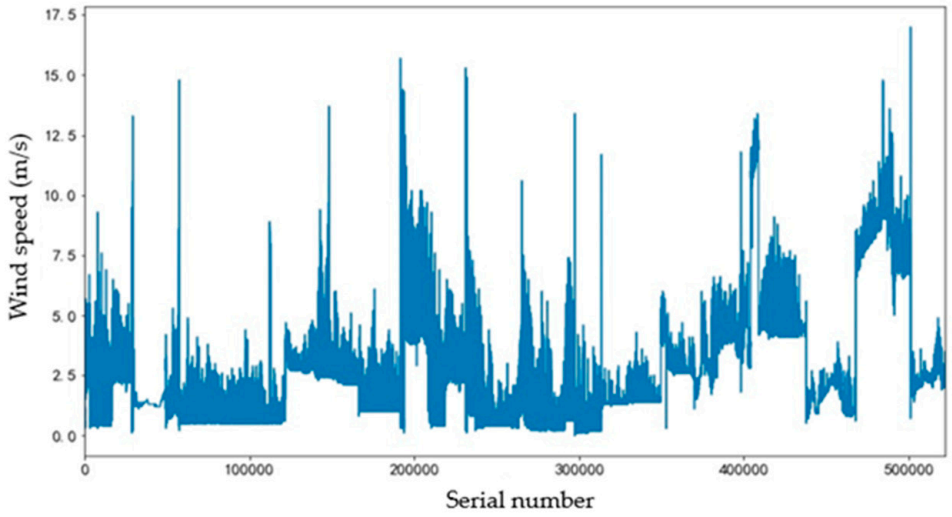

Figure 6. Wind speed data.

10 s are set as the cycle period of trajectory adjustment. In the meantime, each 10 consecutive wind speeds and direction values are included in a set for one cycle period of trajectory adjustment. Table 1 is a set of data selected from the collected data with large changes, which are applied as wind speed and direction data for the following trajectory adjustment simulations.

Table 1. Wind speed and direction data for the algorithms.

Wind Speed (m/s)	Wind Direction (Radian)
0.9	$\pi/2$
2.1	$\pi/2$
3.5	$3\pi/4$
2.1	$3\pi/4$
2.7	$3\pi/4$
2.7	$\pi/2$
4.9	$\pi/2$
7.5	$\pi/4$
6.5	$\pi/4$
5.5	$\pi/4$

3.1.1. Simulation of DQN-Based UAV Trajectory Adjustment Algorithm

Concerning the reward design of the DQN algorithm, the concentration difference of the leaf wetness sensors on both sides of the central axis as mentioned in Section 2.1.4 can be adopted to express the reward function. Nevertheless, the relationship among the time of droplets depositing to the sensor node, the difference Δc in the Equation (3) and the threshold T is not calibrated. Hence, the droplet drift model is adopted to replace the leaf wetness sensors to obtain the feedback of trajectory adjustment in verifying the effectiveness of the algorithm, namely, the reward of deep reinforcement learning is computed with the Equation (4). The initial position of UAV in the simulation is set as (0, 0.2), and the initial flight direction is due east. The UAV reaches the next state at a step size of 6 m. The threshold and the constant in Equation (4) are set as $I = 1$ m and $a = 5$, respectively. DQN training parameters are presented in Table 2. In this study, the DQN network architecture was developed with Python and implemented on TensorFlow. The simulations were carried out under Windows 10 system and the model of the processor is AMD Ryzen 5 2500U (2 GHz).

Table 2. DQN training parameters.

Parameters	Value
Learning rate α	0.001
Discount factor γ	0.95
Exploration rate ε^t	$0.99\varepsilon^{t-1}$
Replay memory size	128,000
Network training times	300

After 300 times of training, the curve of cumulative reward value with the number of training is shown in Figure 7. The convergence speed of the DQN algorithm is the key factor influencing whether the algorithm meets the real-time requirement of the UAV route changing scheme. It can be seen from the figure that the cumulative reward value tends to be stable when the number of iterations reaches about 85, indicating the fast convergence of the proposed DQN algorithm. During training, the more positive reward values are obtained, the more correct the judgment made by the UAV. As shown in Figure 7, the cumulative reward varies between −5 to 15 during the early stage of iteration, which illustrates that the agent (the UAV) is exploring and learning the action strategies, and inappropriate action will cause the cumulative reward value to decrease or even be negative. After multiple explorations, the agent can select the action with high reward values according to the status of the environment as it gradually understands the environment. As can be seen from Figure 7, when the iteration number reaches 85, the reward values obtained by the UAV no longer appear negative, indicating that the UAV can make correct judgment since then. In this study, the higher the cumulative reward value obtained indicates the fact that the closer the distance between the droplet deposition center and the target area during trajectory adjustment, the closer the trajectory approaching the optimal.

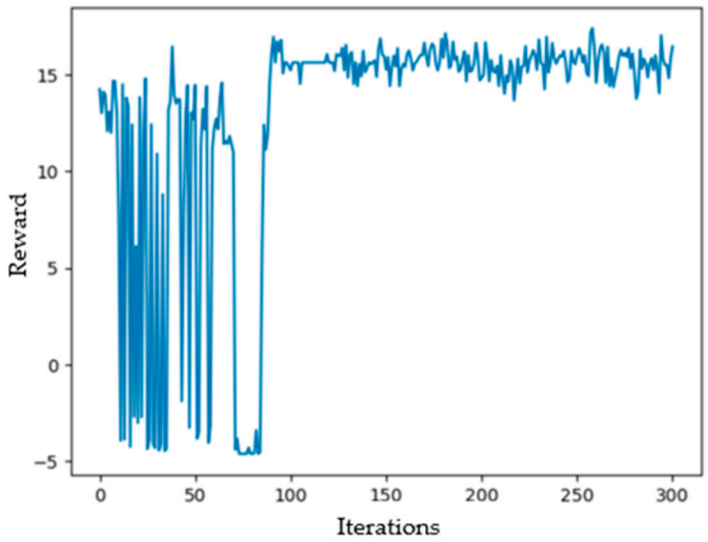

Figure 7. DQN cumulative rewards.

After the algorithm convergence, the adjusted UAV spraying route is shown in Figure 8, of which, $y = 0$ in the figure is the central axis of the work area. The starting point is not necessarily located on the central axis, since the current starting point is the end point of the last trajectory adjustment. As can be seen from the figure, the blue triangles are the optimal spraying positions of UAV at each second, which are calculated with the pesticide drift model under the wind speed and direction data in Table 1. The dotted line in red is the spraying trajectory adjusted by the DQN algorithm. The trajectory shows that the UAV should make four steering adjustments in 10 time steps. Such an adjustment is too frequent to implement in the actual environment. Therefore, the Bezier curve [39] is adopted in this

study to smooth the trajectory connecting the start point and the end point. The n-order Bezier curve is defined as Equation (20):

$$Y(t) = \sum_{k=0}^{n} \left(\frac{n!}{k!(n-k)!} \right) Y_k t^k (1-t)^{n-k}, \quad t \in [0,1] \tag{20}$$

where $Y(t)$ represents the Bezier curve; Y_k represents the kth control point; and t represents the normalized time variable. In this paper, 10-order Bezier curve, i.e., $n = 10$ is adopted. The smoothed UAV route is shown in the green line in Figure 8.

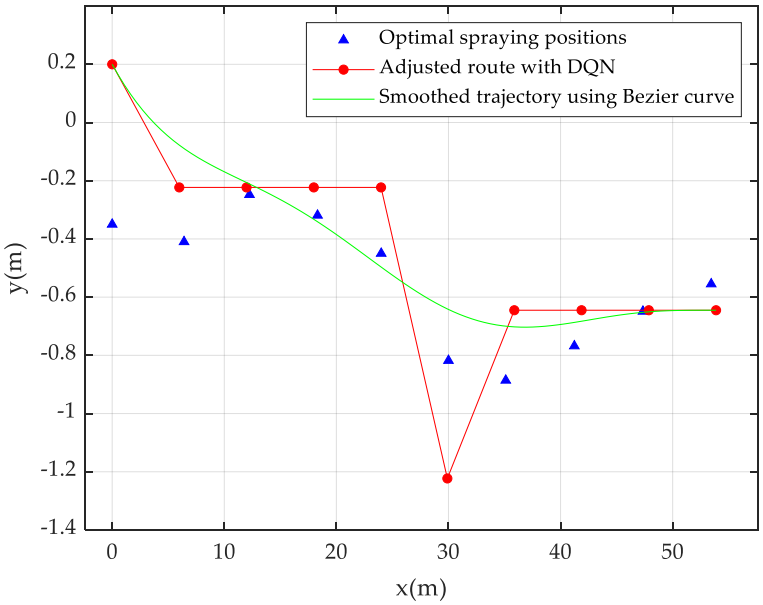

Figure 8. DQN-based UAV pesticide spraying trajectory adjustment.

3.1.2. Simulation of PSO-Based UAV Trajectory Adjustment Algorithm

Wind speed and direction data in the table are also selected for algorithm verification in the simulation of the PSO-based UAV trajectory adjustment algorithm. The trajectory adjustment cycle N is set as 10 s. Fitness values of all particles are computed according to the trajectory optimization function $f(\Delta v_f, \Delta\theta_f, t_0)$ in Section 2.3. Parameter settings of the particle swarm algorithm are shown in Table 3. The value Δv_f is assigned randomly $-1\text{m/s} \sim 1\text{m/s}$; $\Delta\theta_f$ is $-\pi/6 \sim \pi/6$; and t_0 is $1 \sim 5$ s in the initial particle position. Δv_f is assigned randomly $-0.2\text{ m/s} \sim 0.2\text{ m/s}$, $\Delta\theta_f$ is $-\pi/18 \sim \pi/18$, and t_0 is $-1\text{ s} \sim 1\text{ s}$ at the initial particle speed. The inertia factor w is adaptively adjusted according to the current iteration number *iter* and the maximum number of iterations $iter_{max}$, as shown in Equation (21):

$$w = \frac{0.5 \times (iter_{max} - iter)}{iter_{max}} + 0.4 \tag{21}$$

t_0 of all particles should be checked after the particles have been updated in each iteration. If $t_0 < 0$, then it is set as zero. If $t_0 > N$, then it is set as N, so as to prevent ineffective particles. In our simulation experiments, the PSO-based route changing algorithm was developed with Python and NumPy. We executed the simulation of PSO scheme on the Ubuntu 16.04 operation system with 2 GB NVIDIA GeForce GT 750 M graphics and Intel CORE i7-4500U (8 G).

Table 3. PSO parameter settings.

Parameters	Value
Number of particles	20
Max iterations	100
Learning factors c1, c2	1.4961

Assume that the initial position of UAV is (0, 0.2); the flight speed is 6 m/s, and the flight direction is due east. This experiment is converged upon 9 rounds of iterations. Fine-tuned trajectory parameters obtained are $\Delta v_f = 0.0$ m/s, $\Delta\theta_f = -\pi/90$, and $t_0 = 7$ s. Values of Δv_f , $\Delta\theta_f$, t_0 and f (Δv_f , $\Delta\theta_f$, t_0) in the iterative process are shown in Table 4, and the trajectory of pesticide spraying upon iterative convergence is shown in Figure 9. Similarly to Figure 8, the blue triangles represent the optimal spraying positions at each sampling time point under current wind speed and direction without considering the limitations in the UAV steering angle and steering times. The dashed line in red presents the optimal UAV spraying position upon the PSO-based pesticide spraying trajectory adjustment, and the green dots indicate the spraying position of each sampling time point on the trajectory optimized by the PSO algorithm.

Table 4. Changes in Δv_f , $\Delta\theta_f$, t_0 and f (Δv_f , $\Delta\theta_f$, t_0) in the iterative process.

Δv_f (m/s)	$\Delta\theta_f$(Radian)	t_0 (s)	$f(\Delta v_f, \Delta\theta_f, t_0)$
−0.4	$-\pi/18$	2	5.544
−0.2	$-\pi/36$	3	5.326
−0.2	$-\pi/36$	3	5.326
−0.2	$-\pi/30$	2	5.263
−0.2	$-\pi/30$	2	5.263
−0.3	$-\pi/45$	2	5.123
−0.2	$-\pi/60$	4	4.963
−0.1	$-\pi/180$	7	4.937
−0.1	$-\pi/90$	7	4.750
−0.4	$-\pi/18$	2	5.544
−0.2	$-\pi/36$	3	5.326

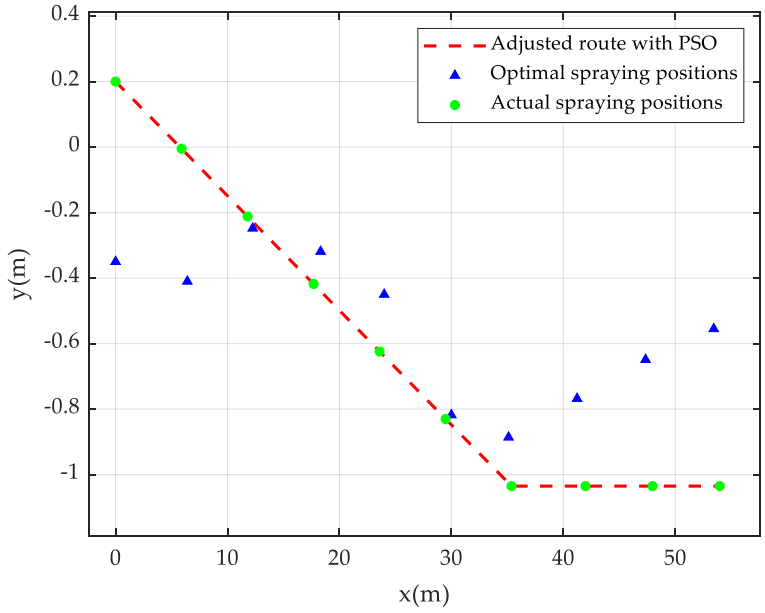

Figure 9. PSO-based UAV pesticide spraying trajectory adjustment.

3.1.3. Comparison of DQN-Based and PSO-Based Trajectory Adjustment Effects

Droplet deposition centers obtained by DQN-based and PSO-based trajectory optimization methods are demonstrated in Figure 10. The straight line in purple represents the central axis of the work area, or the target position of the droplet deposition center. The red dot indicates the central positions of droplet deposition without route adjustment, i.e., the droplet deposition centers when spraying along the central axis. The blue rhombus presents the central positions of droplet deposition upon DQN-based route adjustment, and the green triangle represents the central positions of droplet deposition upon PSO-based route adjustment. It is observed that the deposition centers of pesticide droplets are approaching to the central axis of the work area upon adjusting the trajectory using two optimizing approaches, indicating that both approaches can effectively control pesticide drift under windy conditions. Based on the statistics from the figure, the sum of the vertical distances between the droplet deposition center and the target position (the central axis) upon route adjusting using the DQN algorithm and the PSO algorithm are 1.52 m and 2.558 m, respectively, in a route adjustment cycle. Whereas, when the UAV is spraying along the central axis, the sum of the distances between the position of the droplet deposition center and the target position is 5.453 m. Compared with no route adjustment, the DQN-based route optimizes the drift of the droplet deposition center points by 72.1%, and the PSO-based route optimizes by 53.1%.

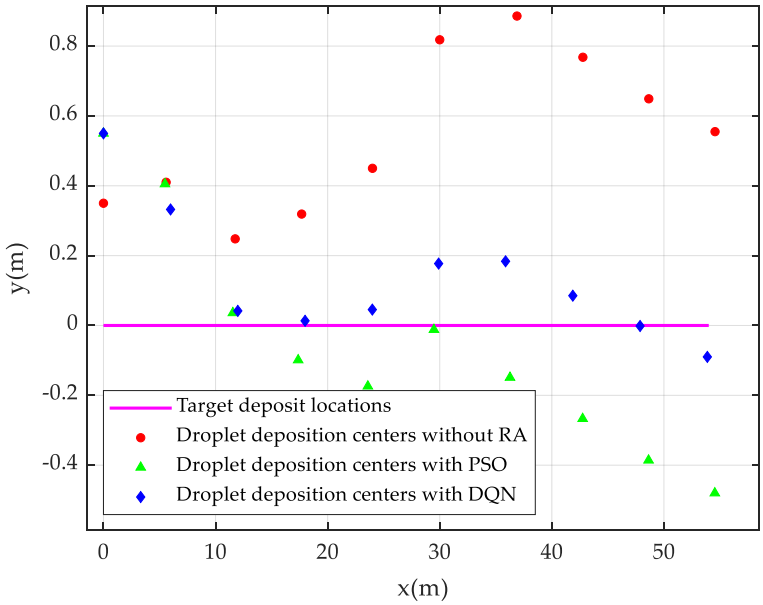

Figure 10. Positions of droplet deposition centers before and after route adjustments.

3.2. Experiment on the Effectiveness of Trajectory Adjustment Based on the Predicted Wind Speed and Direction

This section examines whether trajectory adjustment using the predicted value of wind direction and speed can meet the requirement of accuracy. Among them, the predicted wind speed value is obtained by the LSTM-based model, and the predicted wind direction value is obtained by the RNN-based model. The wind speed and direction prediction model was developed with Python and implemented on TensorFlow. A graphics processing unit (GPU) was applied for neural network training and inference. We executed the simulation on the Ubuntu 16.04 operation system with 2 GB NVIDIA GeForce GT 750 M graphics and Intel CORE i7-4500U (8 G).

Figure 11 shows the mean absolute error (MAE) indicator of the wind speed prediction model. Further, the MAE indicator of the wind direction prediction model is presented in Figure 12.

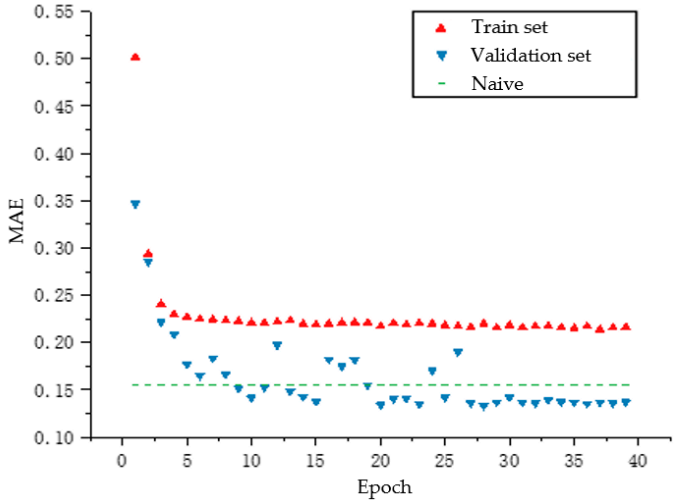

Figure 11. MAE indicator of the LSTM-based wind speed prediction model.

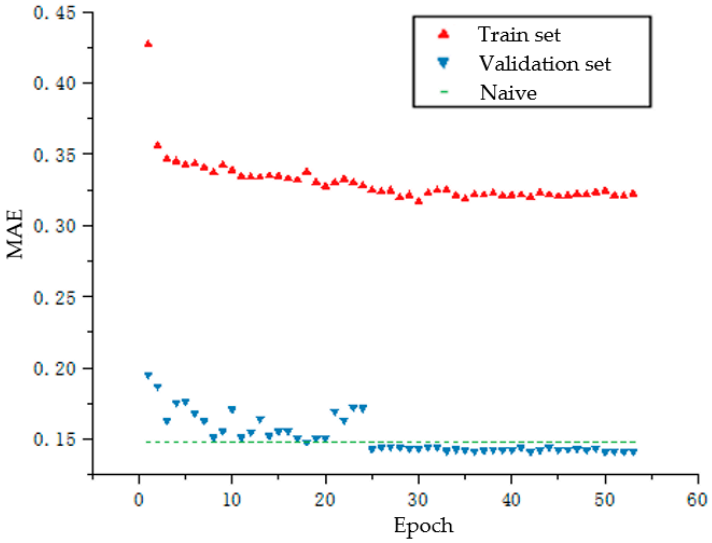

Figure 12. MAE indicator of the RNN-based wind speed prediction model.

Next, the results of DQN-based and PSO-based trajectory optimization are compared with the following four types of wind speed and direction data:

- Route adjustment (RA) is not performed under the real wind speed and direction values, i.e., pesticide spraying along the central axis of the work area.
- Route adjustment is conducted by replacing the wind speed and direction values in the next 10 s with the current wind speed and direction value.
- Route adjustment is conducted with the predicted wind speed and direction values for the next 10 s.
- Route adjustment is performed with the predicted wind speed and direction values when the mean variation of wind speeds in the past 10 s is greater than the threshold. Otherwise, the current wind speed and direction value will take place of the wind speed and direction values in the next 10 s for trajectory adjustment.

The mean variation of wind speeds refers to the average sum of the difference of the wind speed minus the average wind speed per second in the past 10 s. According to changes in collected wind speed and direction data, the threshold W is set as 0.35 m/s, 0.5 m/s, and 1 m/s. The distance sum of the droplet deposition center of pesticide spraying along the new route in the trajectory adjustment cycle

and the droplet deposition center under windless conditions is selected as the measuring indicator in the experiment, denoting as spraying accuracy f.

$$f = \sum_{t=1}^{10} \|\boldsymbol{P}^t - \boldsymbol{P}_0^t\| \tag{22}$$

where P_0^t is the droplet deposition center of pesticide spraying along the central axis at the time of t under windless conditions, and P^t is the droplet deposition center of pesticide spraying along the corrected trajectory at the time of t under windy conditions. When evaluating the f value, 1000 sets of data randomly selected from the collected wind speed and direction data were set as the test data set. Moreover, ten wind speed and direction values are included in a trajectory adjustment cycle.

Different types of wind speed and direction data are applied to PSO-based trajectory optimization, as shown in Figure 13a–f. It can be seen from Figure 13a that the pesticide spraying effect is poor without trajectory adjustment. In Figure 13b, using the currently received wind speed and direction data for trajectory optimization for the next 10 s can significantly improve the spraying accuracy. As can be observed from Figure 13c, the spraying accuracy of new route optimized with the predicted wind speed and direction data is even worse than that without trajectory adjustment. Nonetheless, data distribution is polarized in observation. In Figure 13d–f, the predicted wind speed and direction data are used for trajectory optimization when the average wind speed change in the past 10 s is greater than the set threshold, otherwise, the current wind speed and direction data will be used for the next ten-second trajectory optimization. Evidently, as the threshold value increases, the test group with a larger f value begins to disappear. When the threshold value is 1 m/s, the performance effect is comparable to that in Figure 13b.

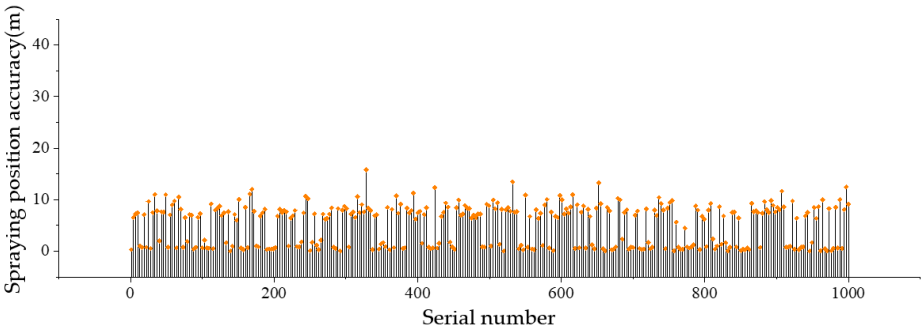

(**a**)

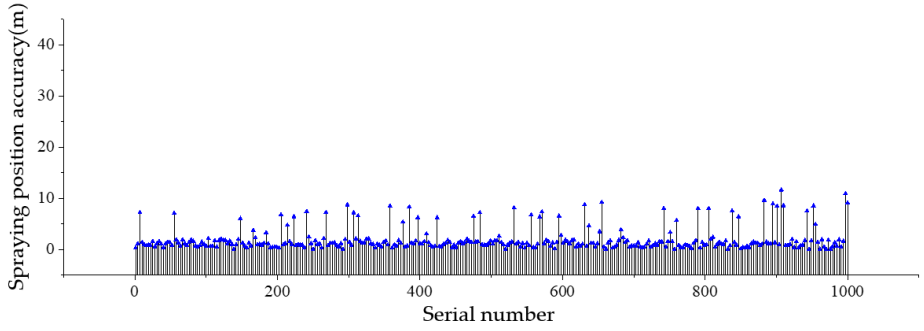

(**b**)

Figure 13. *Cont.*

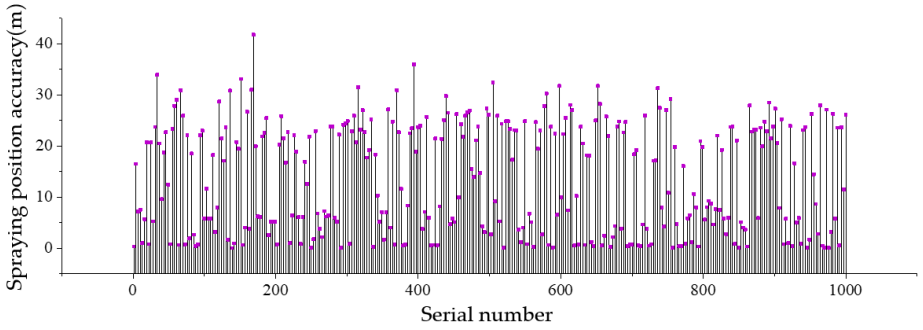

(**c**)

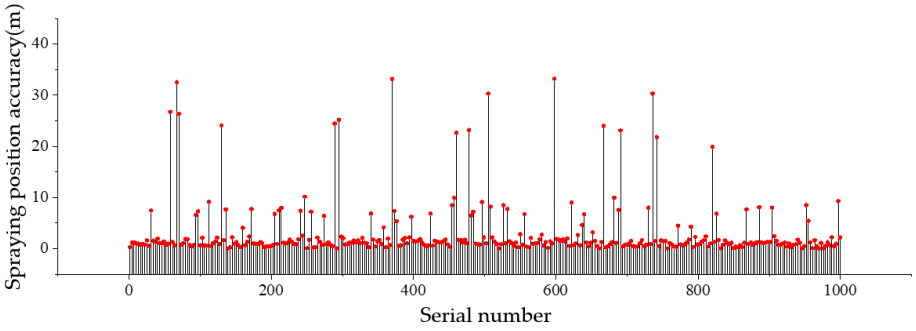

(**d**)

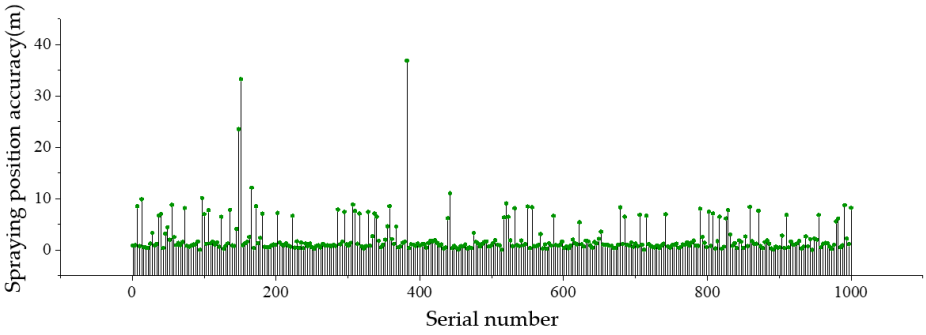

(**e**)

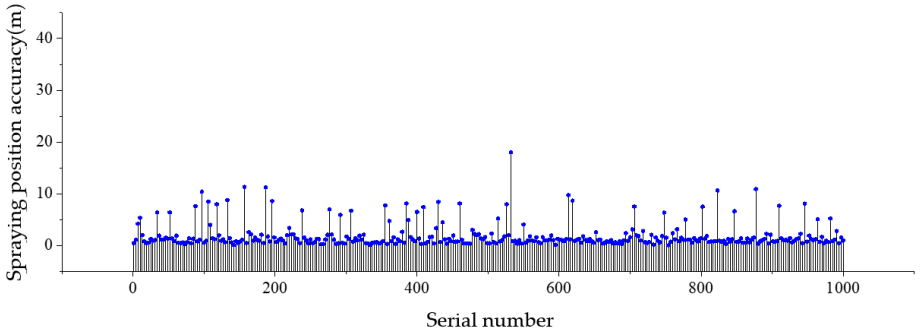

(**f**)

Figure 13. Spraying accuracy of PSO optimization under different wind data. (**a**) no route adjustment; (**b**) route adjustment with current wind data; (**c**) route adjustment with predicted wind data; (**d**) route adjustment with combined wind data ($W = 0.35$ m/s); (**e**) route adjustment with combined wind data ($W = 0.5$ m/s); (**f**) route adjustment with combined wind data ($W = 1$ m/s).

The average spraying accuracy by using different wind speed and direction data in the DQN and PSO trajectory optimization is presented in Table 5. The average spraying accuracy $\overline{f}$ is obtained upon the test of 1000 sets of data. It can be seen that trajectory optimization using the combined wind data of the current and the predicted with the threshold of 1 m/s present a slightly improved effect, in comparison to the trajectory optimization using merely the current wind direction and speed data. It is because predicting the wind data of the next time period based on the recent changes in wind speed and direction can capture some changing trend of wind in the case of great changes happening, which is more effective than merely using the current wind speed and direction to replace the future wind speed and direction.

Table 5. Average spraying accuracy under different wind data.

Settings	Metaheuristic	Average Spraying Accuracy(m)
No RA	None	5.34736
RA with current wind data	DQN	1.62043
RA with predicted wind data	DQN	10.48642
RA with combined wind data (W = 0.34 m/s)	DQN	2.33512
RA with combined wind data (W = 0.5 m/s)	DQN	1.98373
RA with combined wind data (W = 1 m/s)	DQN	1.47751
RA with current wind data	PSO	2.03988
RA with predicted wind data	PSO	13.99703
RA with combined wind data (W = 0.34 m/s)	PSO	2.99026
RA with combined wind data (W = 0.5 m/s)	PSO	2.3516
RA with combined wind data (W = 1 m/s)	PSO	1.96046

4. Hardware Testing and Implementation

In this section, the communication time between UAV and WSN is tested, as well as the feasibility of running the PSO-based trajectory adjustment on the embedded hardware is verified.

4.1. Communication Test between UAV and WSN

CC2630 Zigbee modules were used in this test for networking, one of which was placed on the DJI Drone Phantom IV and configured as a coordinator, as shown in Figure 14a, while the other four modules were applied for simulating ground sensor nodes, and configured as terminals nodes, as shown in Figure 14b.



(**a**) (**b**)

Figure 14. Communication test between UAV and ground WSN nodes. (**a**) UAV with Zigbee Coordinator; (**b**) Ground wireless sensor nodes.

During the experiments, it was found that without obvious obstacles, the received signal became weak and the communication was affected when the plane projection distance between the UAV and

the nearest node on the ground exceeds 80 m. In the following tests, ground nodes are arranged at the four corners of a rectangle with 50 m in length and 30 m in width. When the UAV flies at a speed of 5 m/s with the respective altitude of 5 m and 10 m, it starts from the midair above node A, and flies to node B, node C, and node D in turn, and finally returns to node A without hovering. The UAV sends a data request to the ground nodes during flighty. A retransmission mechanism is adopted in the data transmission of nodes. And the UAV will send a new data request upon receiving data from all nodes. A total of 120 rounds of data collection are carried out in a single flight. Communication latency of nodes A and B and the number of requests sent by the coordinator to the node in each data collection are presented in Figures 15–18. From the comparison between Figures 15 and 16, and the comparison between Figures 17 and 18, it can be seen that the UAV flight height of 5 or 10 m has little effect on the communication delay. Therefore, the impact of the plant protection UAV's flight height on communication is ignored in this study when considering the deployment of wireless sensor nodes on the ground.

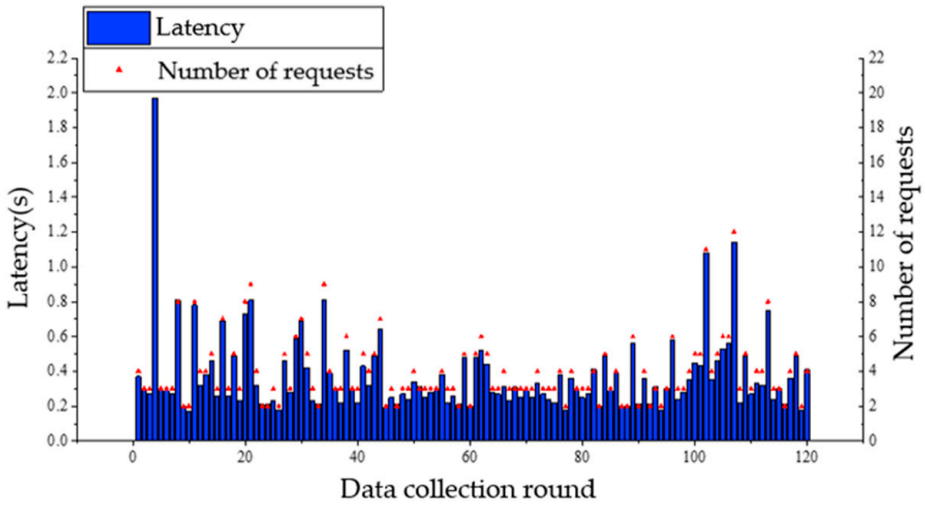

Figure 15. Communication latency of node A and the number of requests from UAV when flight altitude is 5 m.

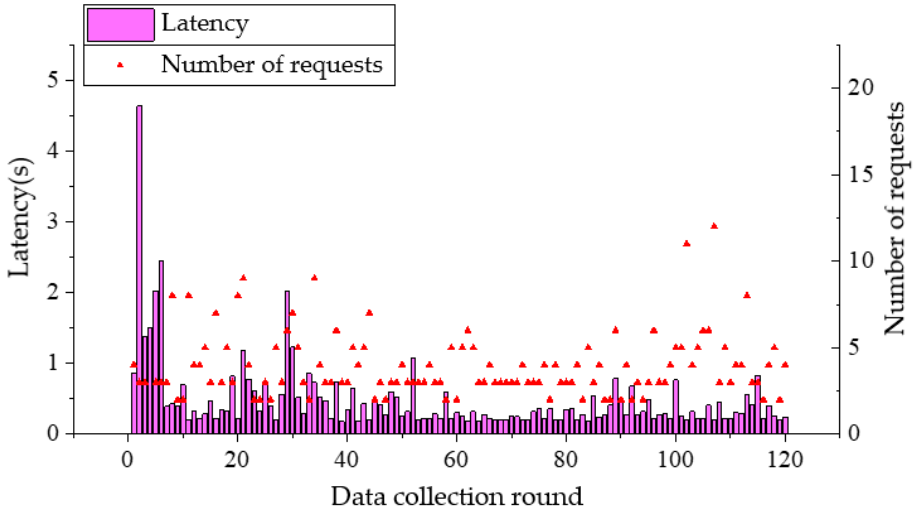

Figure 16. Communication latency of node A and the number of requests from UAV when flight altitude is 10 m.

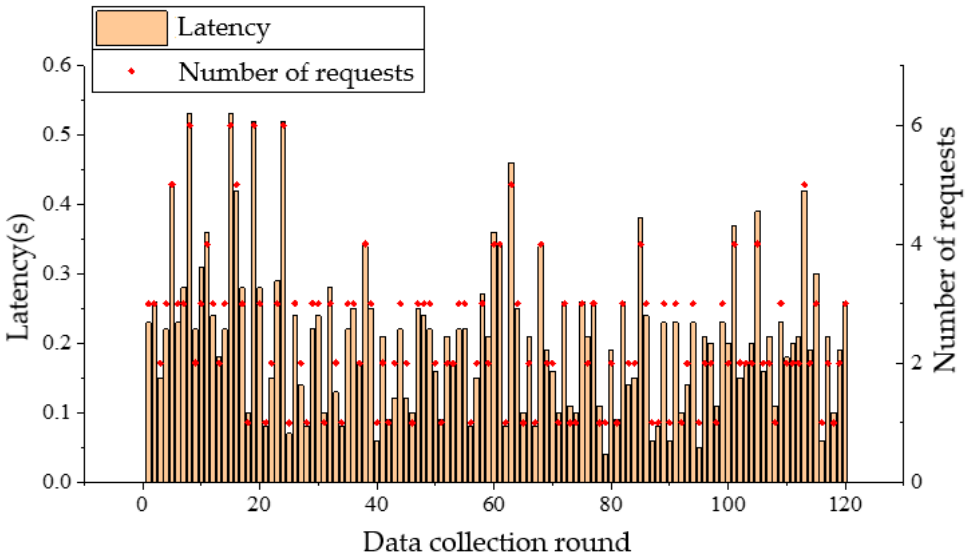

Figure 17. Communication latency of node B and the number of requests from UAV when flight altitude is 5 m.

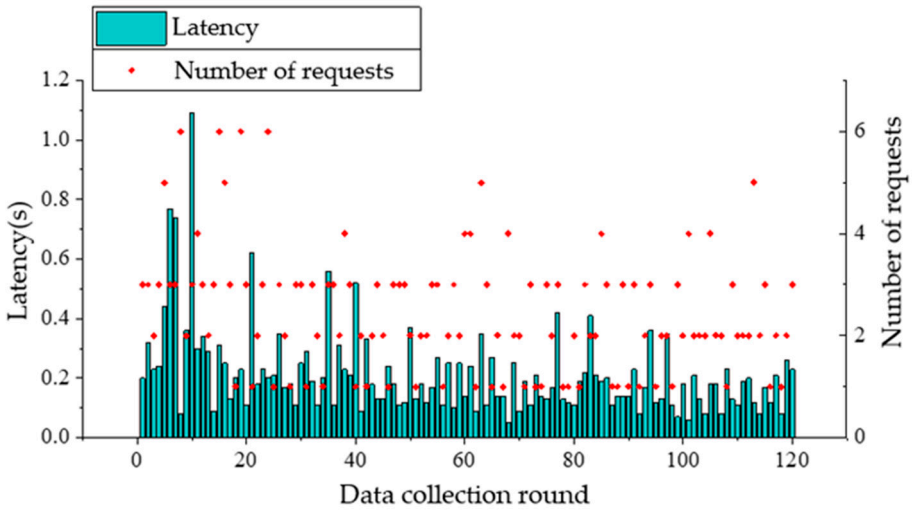

Figure 18. Communication latency of node B and the number of requests from UAV when flight altitude is 10 m.

The average communication latency between the UAV and the average number of requests to each node in each data collection is shown in Figure 19. As can be observed from Figure 19, the communication latency between each node and the UAV is less than 0.5 s for most of the rounds with few rounds greater than 1 s, showing a satisfactory network communication performance. In other words, latency can meet the real-time requirement of the UAV trajectory adjustment. By observing the average transmission latency of each node and the average number of requests received, it can be found that the average latency of node A is less than 0.5 s, and the average latency of other nodes is between 0.15 s and 0.3 s. Hence, speculation that some inference might present in the vicinity of node A can be made. At the same time, the average communication latency difference of each node when the UAV flight altitude is 5 m and 10 m is less than 0.1 s, indicating that the flight altitude has little effect on the communication latency in low-altitude flight.

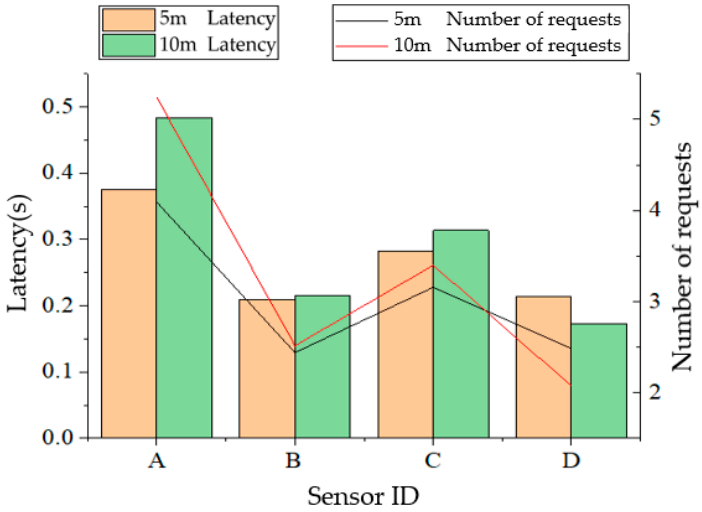

Figure 19. Average transmission latency of each node and average number of requests received.

4.2. Realization of the Scheme on Embedded Hardware

The wind speed and direction prediction model and the PSO-based trajectory adjustment algorithm are operated on the Raspberry Pi 4B+ (as shown in Figure 20), so as to evaluate whether they can meet the real-time requirements of trajectory adjustment of UAV. Because Python and TensorFlow have good portability and version compatibility, the PSO path optimization simulation program, the wind speed and direction prediction model, and the library files used for simulation testing on the embedded hardware device-Raspberry Pi 4B+ remain the same as those on the PC. Due to the limitations of the Raspberry Pi GPU performance and related code library support, the Raspberry Pi uses the CPU processor to infer the wind speed and direction prediction model, which is different from the PC end.

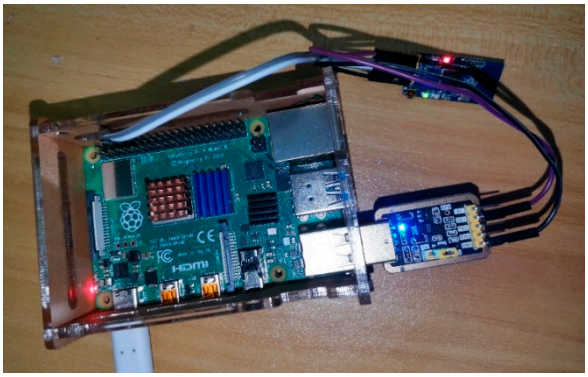

Figure 20. Algorithm evaluation on Raspberry Pi 4B+.

3000 sets of data are randomly selected from the collected wind speed and direction data set. 10 wind speed and direction values in consecutive time are included in each set of data, and the time corresponding to each set of wind speed and direction values is a cycle of trajectory adjustment. The running time of the test is stipulated as follows: It starts by receiving current wind data, then predicting wind speed and direction, and it is not stopped until parameters of PSO-based trajectory adjustment is output. The running time for obtaining parameters of trajectory adjustment of the first 1000 sets of data is shown in Figure 21. The possible reason for the long running time of the first set of data is that the processor needs to load the corresponding library file for the first time. The average running time of 3000 sets of data is 0.229 s. That is to say, the average time consumed by the Raspberry Pi from receiving environmental data to outputting trajectory fine-tuning parameters is 0.229 s. Considering that the communication latency between the UAV and the ground nodes is about 0.5 s, the communication

time and the algorithm running time test show that the WSN-based trajectory adjustment system of UAV in this study can meet the real-time requirements in the actual pesticide spraying operation.

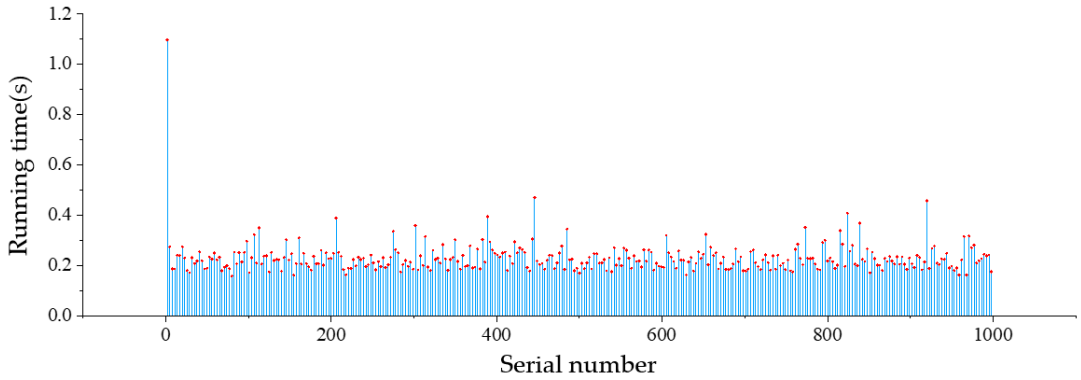

Figure 21. Running time of the wind prediction model and PSO-based algorithm on Raspberry Pi 4B+.

5. Conclusions

A system was designed for adjusting the spraying trajectory of a crop protection UAV based on data obtained from ground wireless sensors with the view to controlling pesticide drift. First of all, a UAV droplet drift model under the influence of wind speed and direction was established. On this basis, the UAV spraying trajectory was optimized using DQN and PSO algorithms, respectively. The simulation results show that both algorithms can decrease the droplet drift dramatically with the reduction in the drift distance of the droplet deposition center by up to 50%.

Moreover, LSTM and RNN were applied for predicting wind speed and wind direction, respectively, so as to address the problem of missing the latest wind speed and direction data caused by communication latency or lack of connection with the ground nodes. The simulation results show that using the predicted wind speed and direction value for trajectory optimization can further enhance the pesticide drift control effect in comparison to using merely the current wind speed and direction value for trajectory optimization, when the average wind speed change is greater than 1 m/s in a short period of time in the past.

At last, the implementation of the UAV route adjustment system was discussed. The communication test between the UAV and the ground WSN proves that the communication latency is, in general, within 0.5 s. Also, the average time consumed for running the wind speed and direction prediction model and the PSO-based trajectory optimization algorithm on the Raspberry Pi 4B+ is 0.229 s, indicating that the UAV trajectory adjustment system can meet the real-time requirement in the pesticide spraying operation.

Researches concerning the following aspects will be carried out. Firstly, since the droplet drift model used in this study is only for one UAV model, the droplet drift and deposition in more mainstream UAV models and nozzles under the influence of wind speed and direction should be studied in the future. Moreover, relevant research on the relationship between the deposit amounts on the leaf wetness sensor and the deposition time would be carried out, in order to provide the operation guiding for UAV trajectory adjustment or support the analysis of deposition indicators upon spraying. In addition, the accuracy of wind direction and wind speed sensors also affect the accuracy of trajectory adjustment. The wind direction sensors used in this study can only acquire wind directions in eight orientations. In order to reduce the error, sensors with higher accuracy are required. Finally, the flight control system of the UAV will be developed, so that the trajectory adjustment method can be verified in the field test.

Author Contributions: Conceptualization, J.H. and Y.L.; Data curation, T.W. and J.Y.; Formal analysis, J.H. and T.W.; Funding acquisition, Y.Z.; Investigation, T.W. and J.Y.; Methodology, J.H. and S.L.; Project administration, Y.Z.; Resources, Y.L. and Y.Z.; Software, T.W. and J.Y.; Supervision, Y.L. and Y.Z.; Validation, T.W. and J.Y.; Visualization,

J.Y.; Writing—original draft, J.H. and T.W.; Writing—review & editing, J.H., T.W. and Y.Z. All authors have read and agreed to the published version of the manuscript.

Funding: This research was funded by the Key Area Research and Development Plan of Guangdong Province, China (2019B020221001), the Science and Technology Project of Guangdong Province, China (2018A050506073), the Guangzhou Science and Technology Project, China (201807010039), National Natural Science Foundation of China (61601189) and the 111 Project, China (D18019).

Conflicts of Interest: The authors declare no conflict of interest.

References

1. Wang, J.; Lan, Y.B.; Wen, S.; Hewitt, A.J.; Yao, W.X.; Chen, P.C. Meteorological and flight altitude effects on deposition, penetration, and drift in pineapple aerial spraying. *Asia Pac. J. Chen. Eng.* **2020**, *15*, e2382. [CrossRef]
2. Baseca, C.C.; Diaz, J.R.; Wen, S.; Lloret, J.; Yao, W.X.; Chen, P.C. Communication Ad Hoc Protocol for Intelligent Video Sensing using AR Drones. In Proceedings of the 2013 IEEE Ninth International Conference on Mobile Ad-hoc and Sensor Networks (MSN 2013), Dalian, China, 11–13 December 2013; pp. 449–453.
3. Teske, M.E.; Wachspress, D.A.; Thistle, H.W. Prediction of Aerial Spray Release from UAVs. *Trans. ASABE* **2018**, *61*, 909–918. [CrossRef]
4. Wang, L.; Chen, D.; Yao, Z.; Ni, X.D.; Wang, S.M. Research on the Prediction Model and its Influencing Factors of Droplet Deposition Area in the Wind Tunnel Environment Based on UAV Spraying. *IFAC Papers OnLine* **2018**, *51*, 274–279.
5. Zhu, H.; Li, H.Z.; Zhang, C.; Li, J.X.; Zhang, H.H. Performance Characterization of the UAV Chemical Application Based on CFD Simulation. *Agronomy* **2019**, *9*, 308. [CrossRef]
6. Meng, Y.H.; Su, J.Y.; Song, J.L.; Chen, W.H.; Lan, Y.B. Experimental evaluation of UAV spraying for peach trees of different shapes: Effects of operational parameters on droplet distribution. *Comput. Electron. Agric.* **2020**, *170*, 105282. [CrossRef]
7. Hornero, G.; Gaitan-Pitre, J.E.; Serrano-Finetti, E.; Casas, O.; Pallasa-Reny, R. A novel low-cost smart leaf wetness sensor. *Comput. Electron. Agric.* **2017**, *143*, 286–292. [CrossRef]
8. Zhan, C.; Zeng, Y. Completion Time Minimization for Multi-UAV-Enabled Data Collection. *IEEE Trans. Wirel. Commun.* **2019**, *18*, 4859–4872. [CrossRef]
9. Qin, Z.; Li, A.J.; Dong, C.; Dai, H.P.; Xu, Z.Q. Completion Time Minimization for Multi-UAV Information Collection via Trajectory Planning. *Sensors* **2019**, *19*, 4032. [CrossRef]
10. Yang, X.; Wang, L.; Xie, J.; Wang, Y.X. Medium Access Control for Unmanned Aerial Vehicle Based Mission Critical Wireless Sensor Networks in 3D Monitoring Networks. *IEEE Access.* **2019**, *7*, 102274–102283. [CrossRef]
11. Cambra, C.; Díaz, J.R.; Lloret, J. Deployment and performance study of an Ad Hoc network protocol for intelligent video sensing in precision agriculture. In Proceedings of the International Conference on Ad-Hoc Networks and Wireless, Benidorm, Spain, 22–27 June 2014; pp. 165–175.
12. Cao, H.R.; Liu, Y.X.; Yue, X.J.; Zhu, W.J. Cloud-Assisted UAV Data Collection for Multiple Emerging Events in Distributed WSNs. *Sensors* **2017**, *17*, 1818. [CrossRef]
13. Fu, S.; Zhao, L.; Su, Z.; Jian, X. UAV Based Relay for Wireless Sensor Networks in 5G Systems. *Sensors* **2018**, *18*, 2413. [CrossRef] [PubMed]
14. Zhan, C.; Zeng, Y.; Zhang, R. Energy-Efficient Data Collection in UAV Enabled Wireless Sensor Network. *IEEE Wirel. Commun. Lett.* **2018**, *7*, 328–331. [CrossRef]
15. Baek, J.; Han, S.I.; Han, Y. Energy-Efficient UAV Routing for Wireless Sensor Networks. *IEEE Trans. Veh. Technol.* **2020**, *69*, 1741–1750. [CrossRef]
16. Zhan, C.; Zeng, Y. Aerial–Ground Cost Tradeoff for Multi-UAV-Enabled Data Collection in Wireless Sensor Networks. *IEEE Trans. Commun.* **2020**, *68*, 1937–1950. [CrossRef]
17. Ebrahimi, D.; Sharafeddine, S.; Ho, P.H.; Assi, C. UAV-Aided Projection-Based Compressive Data Gathering in Wireless Sensor Networks. *IEEE Internet Things J.* **2019**, *6*, 1893–1905. [CrossRef]
18. Tarighi, R.; Farajzadeh, K.; Hematkhah, H. Prolong network lifetime and improve efficiency in WSN-UAV systems using new clustering parameters and CSMA modification. *Int. J. Commun. Syst.* **2020**, *33*, e4324. [CrossRef]

19. You, C.; Zhang, R. 3D Trajectory Optimization in Rician Fading for UAV-Enabled Data Harvesting. *IEEE Trans. Wirel. Commun.* **2019**, *18*, 3192–3207. [CrossRef]
20. Wang, X.D.; Zhou, Q.F.; Cheng, C.T. A UAV-assisted topology-aware data aggregation protocol in WSN. *Phys. Commun.* **2019**, *34*, 48–57. [CrossRef]
21. Gong, J.; Chang, T.H.; Shen, C.; Chen, X. Flight Time Minimization of UAV for Data Collection over Wireless Sensor Networks. *IEEE J. Sel. Areas Commun.* **2018**, *36*, 1942–1954. [CrossRef]
22. Uddin, M.A.; Mansour, A.; Le, J.D.; Ayaz, M.; Aggoune, E.M. UAV-Assisted Dynamic Clustering of Wireless Sensor Networks for Crop Health Monitoring. *Sensors* **2018**, *18*, 555. [CrossRef]
23. Araghizadeh, M.A.; Teymoori, P.; Yazdani, N.; Safari, S. An efficient medium access control protocol for WSN-UAV. *Ad Hoc Netw.* **2016**, *52*, 146–159. [CrossRef]
24. Say, S.; Inata, H.; Liu, J.; Shimamoto, S. Priority-Based Data Gathering Framework in UAV-Assisted Wireless Sensor Networks. *IEEE Sens. J.* **2016**, *16*, 5785–5794. [CrossRef]
25. Annepu, V.; Anbazhagan, R. Implementation of an efficient extreme learning machine for node localization in unmanned aerial vehicle assisted wireless sensor networks. *Int. J. Commun. Syst.* **2019**, *33*, e4173. [CrossRef]
26. Nguyen, C.L.; Raza, U. LEMOn: Wireless Localization for IoT Employing a Location-Unaware Mobile Unit. *IEEE Access.* **2019**, *7*, 40488–40502. [CrossRef]
27. Sayyed, A.; De Araujo, G.M.; Becker, L.B. EGL: Efficient geometry-based localisation in wireless sensor networks. *Int. J. Sens. Netw.* **2017**, *25*, 218–228. [CrossRef]
28. Yi, J.M.; Yoon, I. Efficient Energy Supply Using Mobile Charger for Solar-Powered Wireless Sensor Networks. *Sensors* **2019**, *19*, 2679. [CrossRef]
29. Liu, G.Y.; Jiang, W.J.; Tan, W.Q.; Lan, X.J. Sensor network with unmanned aerial vehicle-enabled wireless power transfer: Optimal clustering and trajectory designing. *Sens. Mater.* **2020**, *32*, 1141–1157. [CrossRef]
30. Wu, P.F.; Xiao, F.; Sha, C.; Huang, H.P.; Sun, L.J. Trajectory Optimization for UAVs' Efficient Charging in Wireless Rechargeable Sensor Networks. *IEEE Trans. Veh. Technol.* **2020**, *69*, 4207–4220. [CrossRef]
31. Ouyang, F.; Cheng, H.; Lan, Y.B.; Zhang, Y.L.; Yin, X.C.; Hu, J.; Peng, X.D.; Wang, G.B.; Chen, S.D. Automatic delivery and recovery system of Wireless Sensor Networks (WSN) nodes based on UAV for agricultural applications. *Comput. Electron. Agric.* **2019**, *162*, 31–43. [CrossRef]
32. Di Gennaro, S.F.; Matesea, A.; Gioli, B.; Toscano, P.; Zaldei, A.; Palliotti, A.; Genesio, L. Multisensor approach to assess vineyard thermal dynamics combining high resolution Unmanned Aerial Vehicle (UAV) remote sensing and wireless sensor network (WSN) proximal sensing. *Sci. Hortic.* **2017**, *221*, 83–87. [CrossRef]
33. Faical, B.S.; Costa, F.G.; Pessin, G.; Ueyama, J.; Freitas, H.; Colombo, A.; Fini, P.H.; Villas, L.; Osorio, F.S.; Vargas, P.A.; et al. The use of unmanned aerial vehicles and wireless sensor networks for spraying pesticides. *J. Syst. Architect.* **2014**, *60*, 393–404. [CrossRef]
34. Faial, B.S.; Freitas, H.; Gomes, P.H.; Mano, L.Y.; Pessin, G.; de Carvalho, A.C.P.L.F.; Krishnamachari, B.; Ueyama, J. An adaptive approach for UAV-based pesticide spraying in dynamic environments. *Comput. Electron. Agric.* **2017**, *138*, 210–223.
35. Yin, S.X.; Zhao, S.; Zhao, Y.F.; Yu, F.R. Intelligent Trajectory Design in UAV-Aided Communications with Reinforcement Learning. *IEEE Trans. Veh. Technol.* **2019**, *68*, 8227–8231. [CrossRef]
36. Arulkumaran, K.; Deisenroth, M.P.; Brundage, M.; Bharath, A.A. Deep Reinforcement Learning: A Brief Survey. *IEEE Signal Process. Mag.* **2017**, *34*, 26–38. [CrossRef]
37. Li, B.H.; Wu, Y.J. Path Planning for UAV Ground Target Tracking via Deep Reinforcement Learning. *IEEE Access* **2020**, *8*, 29064–29074. [CrossRef]
38. Wen, S.; Han, J.; Ning, Z.H.; Lan, Y.B.; Yin, X.C.; Zhang, J.T.; Ge, Y.F. Numerical analysis and validation of spray distributions disturbed by quad-rotor drone wake at different flight speeds. *Comput. Electron. Agric.* **2019**, *166*, 105036. [CrossRef]
39. Simba, K.R.; Uchiyama, N.; Sano, S. Real-time smooth trajectory generation for nonholonomic mobile robots using Bezier curves. *Robot. Comput. Integr. Manuf.* **2016**, *41*, 31–42. [CrossRef]



© 2020 by the authors. Licensee MDPI, Basel, Switzerland. This article is an open access article distributed under the terms and conditions of the Creative Commons Attribution (CC BY) license (http://creativecommons.org/licenses/by/4.0/).

·农业航空工程·

基于深度强化学习的农田节点数据无人机采集方法

胡 洁[1,3]，张亚莉[2,3※]，王 团[1]，望梦成[1]，兰玉彬[1,3]，张植勋[2]

（1. 华南农业大学电子工程学院，广州 510642；2. 华南农业大学工程学院，广州 510642；3. 国家精准农业航空施药技术国际联合研究中心，广州 510642）

摘 要：利用无人机采集农田传感器节点数据，可避免网络节点间多次转发数据造成节点电量耗尽，近网关节点过早死亡及网络生命周期缩短等问题。由于相邻传感器数据可能存在冗余、无人机可同时覆盖多个节点进行采集等特点，该研究针对冗余覆盖下部分节点数据采集和全节点数据采集，对无人机数据采集的路线及方案进行优化，以减轻无人机能耗，缩短任务完成时间。在冗余覆盖下部分节点数据采集场景中，通过竞争双重深度 Q 网络算法（Dueling Double Deep Q Network，DDDQN）优化无人机节点选择及采集顺序，使采集的数据满足覆盖率要求的同时无人机能效最优。仿真结果表明，该算法在满足相同感知覆盖率要求下，较深度 Q 网络（Deep Q Network，DQN）算法的飞行距离缩短了 1.21 km，能耗减少 27.9%。在全节点数据采集场景中，采用两级深度强化学习联合（Double Deep Reinforcement Learning，DDRL）方法对无人机的悬停位置和顺序进行优化，使无人机完成数据采集任务时的总能耗最小。仿真结果表明，单节点数据量在 160 kB 以下时，在不同节点个数及无人机飞行速度下，该方法比经典基于粒子群优化的旅行商问题（Particle Swarm Optimization-Traveling Salesman Problem，PSO-TSP）算法和最小化能量飞行控制（Minimized Energy Flight Control，MEFC）算法的总能耗最少节约 6.3%。田间试验结果表明，相比 PSO-TSP 算法，基于 DDRL 的数据采集方法的无人机总能耗降低 11.5%。研究结构可为无人机大田无线传感器节点数据采集提供参考。

关键词：无人机；数据采集；深度强化学习；节点感知冗余；DQN；DRL

doi：10.11975/j.issn.1002-6819.2022.22.005

中图分类号：S126；S-3 **文献标志码**：A **文章编号**：1002-6819(2022)-22-0041-11

胡洁，张亚莉，王团，等．基于深度强化学习的农田节点数据无人机采集方法[J]．农业工程学报，2022，38(22)：41-51.
doi：10.11975/j.issn.1002-6819.2022.22.005 http://www.tcsae.org

Hu Jie, Zhang Yali, Wang Tuan, et al. UAV collection methods for the farmland nodes data based on deep reinforcement learning[J]. Transactions of the Chinese Society of Agricultural Engineering (Transactions of the CSAE), 2022, 38(22): 41-51. (in Chinese with English abstract) doi：10.11975/j.issn.1002-6819.2022.22.005 http://www.tcsae.org

0 引 言

各种农业传感器在农业生产中起着监测作物生长环境、协助精准灌溉和施肥及病虫害防治等作用[1-2]。在网络基础设施缺乏的部分边远地区，农田无线传感器节点的数据采集存在困难[3-4]。因此，利用各种移动设备采集田间无线传感器节点数据成为一种解决措施[5-6]。相比地面移动设备，无人机具有不受限于地面环境、不破坏地面作物、信号传输所受阻挡小等优势，是采集传感器节点数据的有利途径[7]。目前农业无人机普遍采用牛耕法的方式进行喷药、撒播等作业，然而当采集随机布置的传感器节点数据时，相邻节点间的数据可能存在冗余[8-9]，且无人机在一个悬停点可能覆盖多个节点[10]，因此需要对无人机数据采集的路线及方案进行优化，以减小无人机能耗、缩短任务完成时间。

针对无人机采集传感器节点数据的方法，国内外学者开展了相关研究，大部分优化方案主要集中在降低能耗[11-12]、任务完成时间最短[13]、轨迹距离最小[14-17]等。Luo 等[11]提出了一种智慧农场的数据采集方案，根据传感器节点的接收信号强度（Received Signal Strength Indication，RSSI）确定簇和簇头，采用改进的 Dijkstra 和遗传算法（Genetic algorithm，GA）寻求最佳轨迹。Ben 等[12]提出了一种使用无人机从无线传感器网络节点采集数据的解决方案，可以同时减小通信与无人机飞行能耗。Just 等[14]针对无人机采集大面积节点数据，使用时隙概念结合飞行禁止列表，将无人机路径与每个节点的激活周期进行同步，大大缩短了飞行距离和飞行时间。Zhang 等[15]提出了一种基于分层深度强化学习（Hierarchical Deep Reinforcement Learning，HDRL）算法解决可充电多无人机数据采集场景的路径规划问题，最大限度地缩短无人机的总飞行时间。蒋宝庆等[16]提出了一种基于 Q 学习的无人机辅助采集小规模无线传感器节点数据，减少了无人机的任务完成时间和有效数据量，提高了无人机能效。Yi 等[17]研究了一种基于深度强化学习（Deep Reinforcement Learning，DRL）的无人机辅助物联网采集最优信息年龄（Age of Information，AoI）数据，得到最

收稿日期：2022-07-21 修订日期：2022-10-27
基金项目：高等学校学科创新引智计划项目（D18019）；国家自然科学基金项目（32271997）；广东省重点领域研发计划项目（2019B020221001）；广东省科技计划项目（2018A050506073）
作者简介：胡洁，博士，副教授，研究方向为农业人工智能，农业物联网。Email：hjgz79@scau.edu.cn
※通信作者：张亚莉，博士，副教授，研究方向为农业航空传感器技术与农产品产地环境监测。Email：ylzhang@scau.edu.cn

优的无人机飞行轨迹和传感器节点的传输调度方案。文献[15-18]采用强化学习算法研究无人机数据采集问题，无人机通过与环境进行交互得到反馈，通过自主学习获得最优数据采集策略。上述研究大多针对无人机的飞行距离进行优化，忽略了节点数据量大小和通信范围等因素。

作者在无人机果树喷药的研究中发现，悬停能耗对无人机整体能耗的影响更大，需综合考虑悬停时间和飞行时间。因此，针对能量受限的农业无人机不同数据采集场景，本文基于深度强化学习算法，在考虑传感器节点冗余覆盖的情况下，研究如何对无人机进行调度，有选择地采集部分节点数据及规划采集顺序，使数据采集在满足覆盖率要求的同时达到无人机能效最优，在需要采集全部传感器节点数据的情况下优化无人机的悬停位置和采集顺序，使无人机能耗最小。

1 作业场景及相关模型

1.1 冗余覆盖下部分节点数据采集场景

在布设传感器时，为了对整个作业区域进行全面覆盖，传感器之间往往存在感知范围交叉重叠的情况，这种情况在随机布设传感器的环境中尤其明显。无人机受限于自身能量和续航时间，在采集传感器数据时需要对传感器进行甄选，对飞行路径进行优化，以求在感知覆盖率要求和无人机能耗之间获得最佳平衡。

假定农田随机分布的传感器节点总数为 N，每个节点的感知范围是以节点为中心的圆（本文假设所有节点的感知半径相同），如图 1 所示。在采集数据过程中无人机悬停在节点的正上方，在一个悬停位置只采集一个节点的数据，传感器节点在收到无人机的信标信息后被唤醒并向无人机发送数据，无人机采集完该节点数据后飞向下一个被选择的节点。数据采集过程中，假设无人机可以获知各节点的位置及当前自身能量。无人机以固定高度飞行，为简便表示，后续统一采用平面二维坐标表示无人机的悬停位置。

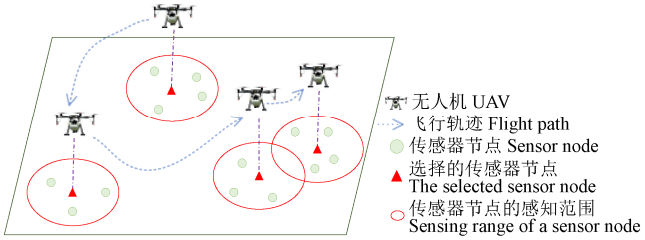

图 1 冗余覆盖下部分节点数据采集场景

Fig.1 Partial node data collection scenario under sensing redundant overlay

1.2 全节点数据采集场景

农业生产中，有些情况下需要采集田间所有传感器节点的数据，若每采集一个节点数据都要悬停，悬停点过多，无人机会有巨大的能量消耗。由于无人机的通信区域是以悬停点在地面投影为中心的圆，在这个范围内的节点都可以与无人机进行数据传输，通过合理选择无人机的悬停点位置和采集顺序，让无人机在每个悬停点时采集其通信范围内的传感器节点数据，达到减少无人机悬停次数及能耗的目标，最终完成所有传感器节点的数据采集。

如图 2 所示，假设田间有 N 个无线传感器节点，每个节点都有准确定位（配备 GPS 或北斗天线），每个传感器都具有相同的通信范围和数据缓冲区大小。无人机在飞行高度固定为 H 的情况下，在某个悬停点可正常通信的是图 2 中圆形区域内的传感器节点，设该区域的半径为 R（通过信道传输模型计算得出），区域中的传感器节点以单跳方式与无人机进行通信。假设无人机匀速飞行，飞行高度固定，通过对悬停位置选择及飞行路径规划，使无人机在采集完所有传感器节点数据时总能耗最小。为简便表示，后续统一用平面二维坐标表示无人机的悬停位置。

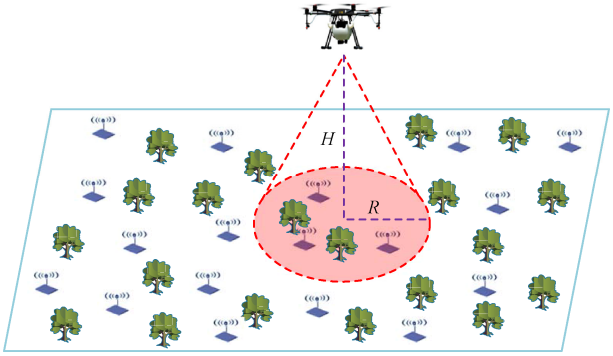

注：H 为无人机飞行高度，m；R 为无人机在某个悬停点可与传感器正常通信的区域半径，m。

Note: H is the flying height of the UAV, m; R is the radius of the area where the UAV can normally communicate with the sensor at a certain hovering point, m.

图 2 全节点数据采集场景

Fig.2 All node data collection scenario

1.3 信道传输模型

无人机悬停采集田间节点数据，其悬停时间与数据传输速率相关，而数据传输速率受信道损耗和衰落的影响。

无人机在采集节点数据时，对于矮秆作物，可将无线传感器节点与无人机间的无线信道假设为视距衰落（Line of Sight，LoS）信道模型；对于高秆作物，为获得较好的信号传输质量，可考虑将无线模块架高。为简化处理，本文以视距衰落模型为例，以 α 表示发送接收点之间每单位距离（1 m）的信道增益，则在悬停位置 p 的无人机与地面节点 i 之间的信道功率增益 w_i 可基于自由空间路径损耗模型[19]表示为

$$w_i = \frac{\alpha}{d_{p,i}^2} = \frac{\alpha}{\left\| U_p - S_i \right\|^2 + H^2} \tag{1}$$

式中 $d_{p,i}$ 为无人机在悬停位置 p 与传感器节点 i 之间的距离，m；U_p 为悬停位置 p 的二维坐标平面位置；S_i 为第 i 个地面传感器节点的二维平面位置；$\left\| U_p - S_i \right\|$ 为 U_p 与 S_i 之间的欧式距离，m。

假设在通信过程中传感器节点的发射功率为 P，根据

香农定理可得位置p的无人机与节点i间的数据传输速率$R_{p,i}$ (bit/s)为

$$R_{p,i}=B\log_2\left(1+\frac{P\cdot w_i}{\sigma^2}\right)=B\log_2\left(1+\frac{\beta}{\left\|U_p-S_i\right\|^2+H^2}\right) \tag{2}$$

式中B为信道带宽，Hz；σ^2为信道高斯白噪声；β为无人机与传感器节点之间单位距离（1 m）时的信噪比，$\beta=\alpha P/\sigma^2$。

从式（2）可以看出，在其他参数不变的情况下，无人机与节点的距离越远，数据传输速率越慢，则无人机悬停时间越长。

1.4　无人机能耗模型

假设SN_i为无人机的第i个悬停位置，$i\in\{0,1,\cdots,M\}$，其中SN_0表示无人机的初始位置，悬停位置数量M小于等于传感器节点的数量N。无人机从上一位置SN_{i-1}以速度v匀速飞行至当前位置SN_i采集数据过程中产生的能耗主要由飞行能耗、悬停能耗、数据传输能耗组成，其中数据传输能耗是由信号发射、接收和通信电路等产生，远小于无人机的飞行与悬停能耗，忽略不计，则无人机在位置SN_{i-1}采集完数据后起飞到完成SN_i位置的数据采集所消耗的能量E^{SN_i} (kJ)为

$$E^{SN_i}=P_f(v)\times\frac{D_{i,i-1}}{v}+P_h\times t^{SN_i} \tag{3}$$

式中$P_f(v)$为无人机在速度v时的飞行功率，W；$D_{i,i-1}$为无人机当前采集位置SN_i与上个采集位置SN_{i-1}的距离，$D_{i,i-1}=\sqrt{\left[x_i-x_{i-1}\right]^2+\left[y_i-y_{i-1}\right]^2}$，m；$P_h$为无人机悬停功率，W；$t^{SN_i}$为在位置$\mathrm{SN}_i$的悬停时间，s。

无人机在某个位置的悬停时间由该位置需采集的传感器节点数据量及数据传输速率决定。假设在SN_i需采集的数据量为Q_i，则在冗余覆盖下部分节点数据采集场景中，无人机在位置SN_i的悬停时间为

$$t^{SN_i}=\frac{Q_i}{R} \tag{4}$$

在全节点数据采集场景中，假定无人机在位置SN_i采集所覆盖的n个传感器节点的数据，总数据量为Q_i，则每个节点的数据量为Q_i/n。考虑到每个传感器节点与无人机之间的距离和信道衰减差异，即数据传输速率不同，设R_k为第k个传感器与无人机的数据传输速率，则无人机在悬停位置SN_i的悬停时间为

$$t^{SN_i}=\sum_{k=1}^{n}\frac{Q_i}{n\times R_k} \tag{5}$$

本文采用 Zeng 等[19]的旋翼无人机功率模型：

$$P_f(v)=P_{bl}\left(1+\frac{3v^2}{U_{tip}^2}\right)+P_{ind}\left(\sqrt{1+\frac{v^4}{4v_0^4}}-\frac{v^2}{2v_0^2}\right)^{\frac{1}{2}}+\frac{1}{2}d_r\rho\delta Sv^3 \tag{6}$$

式中U_{tip}为转子的叶尖速度，m/s；v_0为无人机悬停时平均旋翼诱导速度，m/s；d_r为机身阻力比；ρ为空气密度，kg/m^3；δ为旋翼实度；S为旋翼桨盘面积，m^2。

无人机在悬停状态下的桨叶剖面功率P_{bl}（W）和诱导功率P_{ind}（W）都为常数。无人机悬停时，v=0，则悬停功率为

$$P_h=P_f(0)=P_{bl}+P_{ind} \tag{7}$$

由式（3）～（4）、式（6）～（7）可知，在冗余覆盖下部分节点数据采集场景中，无人机从SN_{i-1}起飞到结束SN_i的数据采集所消耗的能量（kJ）为

$$E^{SN_i}=\left[P_{bl}\left(1+\frac{3v^2}{U_{tip}^2}\right)+P_{ind}\left(\sqrt{1+\frac{v^4}{4v_0^4}}-\frac{v^2}{2v_0^2}\right)^{\frac{1}{2}}+\frac{d_r\rho\mu Sv^3}{2}\right]\times\frac{|D_i|}{v}+\frac{Q_i\left(P_{bl}+P_{ind}\right)}{R} \tag{8}$$

同理，在全节点数据采集场景中，从SN_{i-1}起飞到结束SN_i的数据采集所消耗的能量（kJ）为

$$E^{SN_i}=\left[P_{bl}\left(1+\frac{3v^2}{U_{tip}^2}\right)+P_{ind}\left(\sqrt{1+\frac{v^4}{4v_0^4}}-\frac{v^2}{2v_0^2}\right)^{\frac{1}{2}}+\frac{1}{2}d_r\rho\mu Sv^3\right]\times\frac{|D_i|}{v}+\left(P_{bl}+P_{ind}\right)\times\sum_{k=1}^{n}\frac{Q_i}{n\times R_k} \tag{9}$$

最终，无人机完成M个悬停位置的数据采集任务所需要的总能耗E^{total}（kJ）为

$$E^{total}=\sum_{i=1}^{M}E^{SN_i} \tag{10}$$

2　基于 DRL 的节点数据采集方法

2.1　深度强化学习 DRL

强化学习是一类特定的机器学习方法，可解决关于序列决策的相关问题[20]。深度强化学习（Deep Reinforcement Learning，DRL）将深度学习的感知能力和强化学习的决策能力相结合[21-22]，通过深度学习对环境状态信息进行特征提取，传递给智能体进行决策并执行动作，执行动作后得到由环境反馈的奖惩信号以及环境状态的改变，促进智能体进行下一步的动作。智能体通过与环境迭代交互选取一系列动作以最大化累积奖励，即在有限反馈中实现序列决策的优化[23]。田间节点数据采集本质上是在多种影响因素变化情况下对无人机悬停位置的选择和采集时序的安排；每采集一个节点数据，或会带来相邻节点数据的效用变化，或会带来去往其余节点的距离成本变化，这可以转化为序列决策问题。本文基于 DRL 方法，针对前述 2 个场景设计了竞争双重深度 Q 网络（Dueling Double Deep Q Network，DDDQN）及两级深度强化学习（Double Deep Reinforcement Learning，DDRL）算法。

2.2 冗余覆盖下基于 DDDQN 的部分节点数据采集方法

2.2.1 任务环境

设农田为一个矩形区域，如图 3 所示，无人机按照虚线所示的路线采集节点数据。采集节点 a 数据时，无人机获取的数据覆盖范围增量是以 a 为中心的整个圆范围；采集节点 b 数据时，数据覆盖范围增量是以 b 为中心、去掉阴影区域 1 的剩余圆；采集节点 c 数据时，数据覆盖范围增量是以 c 为中心、去掉阴影区域 2 的剩余圆；而采集节点 d 的数据覆盖率增量只有阴影区域 3 的范围，节点 d 与已采集的节点间数据冗余比例高，无人机根据奖励函数（公式（12））确定当前动作，可能会将节点 d 舍弃。

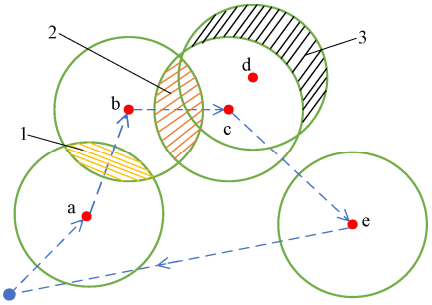

注：a～e 为传感器节点；1 为节点 a 与节点 b 的冗余覆盖部分；2 为节点 b 与节点 c 的冗余覆盖部分；3 为节点 d 带来的数据覆盖率增量。
Note: a-e are the sensor nodes; 1 refers to the redundant overlay between nodes a and b; 2 refers to the redundant overlay between nodes b and c; 3 refers to the incremental data coverage from node d.

图 3 冗余覆盖下部分节点数据采集示意图

Fig.3 Schematic of partial node data collection under sensing redundancy overlay

2.2.2 DDDQN 算法

DDDQN 算法将双重深度 Q 网络（Double DQN）[24]与竞争深度 Q 网络（Dueling DQN）[25]相融合。图 4 为 DDDQN 算法框架[26]。该算法结合了 2 种算法的优势，将 DQN 算法存在的网络 Q 值估计过高的问题与网络的结构同时进行优化。

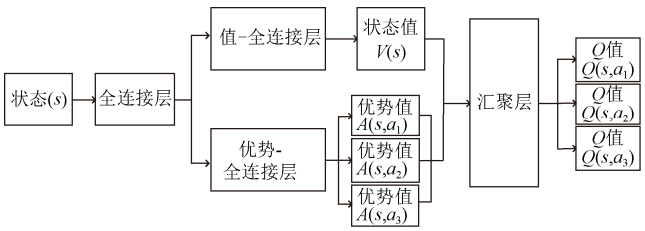

注：s 为无人机当前状态；$V(s)$为在状态 s 下通过神经网络得到的状态值；$A(s,a)$为在状态为 s 下执行动作 a 时通过神经网络得到的优势值；$Q(s,a)$为在状态值 $V(s)$和优势值 $A(s,a)$的总和。
Note: s is the current status of UAV; $V(s)$ is the state value by neural network under state s; $A(s,a)$ is the advantage value of taking action at state s by neural network; $Q(s,a)$ is the sum of the state value $V(s)$ and the advantage value $A(s,a)$.

图 4 DDDQN 算法框架

Fig.4 DDDQN (Dueling Double Deep Q Network) algorithm framework

在冗余覆盖场景中，无人机强化学习模型中的状态-动作-奖励框架如下：

1）状态空间 S：状态空间由 3 个部分组成：$S=\{L(t),C(t),G(t)\}$，其中 $L(t)=\left(x_j^t,y_j^t\right)$ 是无人机 t 时刻悬停位置二维坐标，对应当前正在采集的传感器节点坐标，取值范围是 N 个传感器节点的位置；$C(t)=\dfrac{F_{coverd}(t)}{F_{total}}$ 表示当前已采集数据的感知覆盖率，$F_{coverd}(t)$ 表示 t 时刻已采集节点的感知面积总和，F_{total} 表示所有传感器节点的感知覆盖面积；$G(t)=(g_1^t,g_2^t,\cdots,g_i^t,\cdots,g_N^t)$ 表示 t 时刻农田中所有传感器节点被无人机采集的情况，$g_i^t\in\{0,1\}$，0 表示该节点数据未被采集，1 表示已被采集。

2）动作空间 A：无人机每次动作选择都是在当前未采集的节点中选择下一步的采集对象，用 $a_i(t)$ 表示无人机 t 时刻的动作是从当前位置飞到 i 节点上方采集数据。动作空间 A 可表示为

$$A=\{a_i(t)\,|\,i=1,2,\cdots,N\} \tag{11}$$

3）奖励函数：考虑到无人机续航能力有限，需要尽可能快地从分散的传感器节点采集数据，避免花费大量时间和能耗采集冗余覆盖部分数据。因此，在建立奖励函数时需要兼顾正向和负向奖励，定义如下：

$$r=\lambda r_c-\omega r_e \tag{12}$$

其中，正向奖励 $r_c=r_i-r_{i\text{-}1}$ 表示采取动作后新增的感知覆盖面积，激励无人机选择有效感知区域面积较大的节点，r_i 为采取当前动作后已采集节点的感知覆盖面积总和，$r_{i\text{-}1}$ 表示采取当前动作前已采集节点的感知覆盖面积总和。负向奖励 r_e 根据公式（8）计算，表示无人机从上一个节点位置飞行到所选择的下一个节点位置所需消耗的能量，目的是尽可能减少无人机的飞行距离。λ 和 ω 为调节因子，调节正向奖励与负向奖励的重要程度，若 $\lambda>\omega$，说明无人机在任务过程中更为看重采集节点的感知覆盖面积需求；若 $\lambda=\omega$，说明两者影响相当；若 $\lambda<\omega$，说明优先考虑能耗因素。

2.3 基于 DDRL 的全节点数据采集方法

2.3.1 任务环境

全节点数据采集与部分节点数据采集的区别是：（1）要求采集所有节点的数据；（2）悬停位置不局限在节点的正上方；（3）在一个悬停位置可以采集多个在通信范围内的节点数据。

全节点数据采集示意图如图 5 所示，设农田为矩形区域，为定位无人机的悬停位置，将农田区域离散为 $k\times k$ 个小栅格，每个小栅格中心是无人机可选的悬停点。栅格越小，对悬停位置的优化程度越高，但算法复杂度越高。图中三角形代表某个飞行策略确定的悬停采集点，虚线代表飞行路径。无人机在悬停点 2 采集传感器 b 和 c 的数据，在悬停点 3 采集传感器 d 和 e 的数据。

针对全节点数据采集场景，若直接采用 DQN 算法对系统进行建模，会导致系统状态空间维数爆炸、模型训练困难，无人机甚至难以完成数据采集任务。本文提出一种基于两级深度强化学习（DDRL）的数据采集策略，将该问题分解为 2 个子问题进行研究，以简化模型，避

免出现直接采用 DQN 算法产生的问题。分解后的 2 个子问题为：1）选择无人机最优采集区域，采用深度 Q 网络（Deep Q Network，DQN）算法；2）在得到的最优采集区域内，采用 n 步深度 Q 网络（Option n-step Deep Q Network，OnDQN）算法选择悬停位置以及确定遍历顺序。

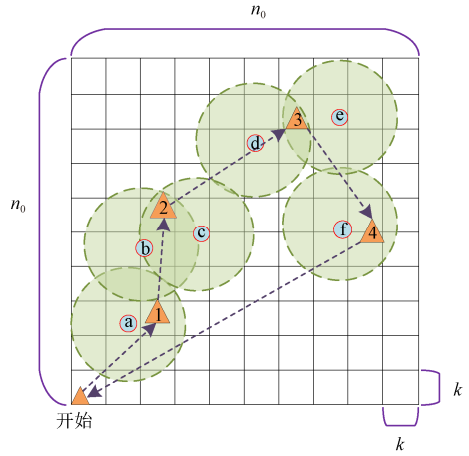

注：n_0 为矩形区域长度；k 为小栅格长度；f 为传感器节点；1～4 为无人机悬停采集点。
Note: n_0 is the length of the rectangular area; k is the small grid length; f is sensor nodes; 1-4 are hovering collection points of UAVs.

图 5　全节点数据采集示意图

Fig.5　Schematic diagram of all node data collection

2.3.2　基于 DQN 的最优采集区域选取

假设每个传感器节点的通信范围都是以节点为中心，半径相同的圆，图 6 以 3 个节点为例，将传感器节点 a、b、c 的通信范围根据其交叠情况划分为 7 个子区域 h_1~h_7，其中区域 h_5 是无人机能与 3 个节点通信的区域，h_2,h_4,h_6 是无人机能与 2 个节点通信的区域，在剩余子区域悬停时无人机只能与 1 个节点通信。假设农田范围有 N 个传感器节点，形成 n_1 个通信子区域 $H=\{h_1,h_2,...,h_{n_1}\}$。全节点数据采集的第一步是从集合 H 中选取最优子集，该子集需要确保无人机可采集所有节点数据并且所消耗的能量最小。本文采用 DQN 算法进行最优子集的选取，状态空间、动作空间、奖励函数表示如下：

1）状态空间：状态空间定义为 $S=\{U(t),G(t),E(t)\}$，其中 $U(t)=(x^t,y^t)$ 表示无人机 t 时刻的坐标，这里将各子区域中所有悬停点组成的多边形重心作为无人机在该区域的悬停位置，进一步的悬停位置优化在第二个子问题中实现。$G(t)=(g_1^t,g_2^t,\cdots g_i^t,\cdots g_N^t)$ 表示在 t 时刻每个传感器数据的采集情况，其中 $g_i^t\in\{0,1\}$，0 表示未被采集，1 表示已被采集。$E(t)$ 表示 t 时刻无人机的剩余能量。

2）动作空间：设置离散的动作空间 $A=\begin{Bmatrix}a_i(t),\ i=1,2,\cdots,N\\ -1\end{Bmatrix}$，$a_i(t)$ 表示 t 时刻无人机向第 i 个子区域以速度 v 直线飞行并在该区域采集通信范围内的传感器数据；−1 表示无人机完成所有数据采集任务返回起点。

3）奖励函数：奖励函数由 3 个部分组成，其中能量效率表示当前动作执行后采集的传感器节点数增量与当前动作执行所消耗的能量之比，如式（13）所示。

$$r_1=\frac{\Delta m(t)}{\Delta e(t)}=\frac{m(t)-m(t-1)}{e(t-1)-e(t)} \tag{13}$$

式中 $\Delta m(t)$ 为采集的传感器节点数增量；$m(t)$ 为 t 时刻已采集的传感器节点的总数量；$m(t-1)$ 为 t−1 时刻已采集的传感器节点总数量；$e(t)$ 为无人机在 t 时刻的剩余能量，kJ；$e(t-1)$ 为无人机在 $t-1$ 时刻的剩余能量，kJ；$\Delta e(t)$ 为无人机消耗的能量，kJ。

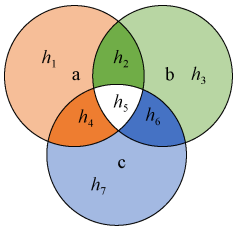

注：h_1～ h_7 是根据传感器节点通信范围交叠情况划分的子区域。
Note: h_1-h_7 is a sub-region divided by overlapping communication ranges of the sensor nodes.

图 6　数据采集子区域的划分示意图

Fig.6　Schematic diagram of data collection subarea division

为避免无人机在强化学习训练过程中出现一直悬停在某个子区域的情况，规定 $\Delta m(t)$ 小于 1 时（即不再飞往下一子区域采集数据）对其进行惩罚，即

$$r_2=\begin{cases}k, & \Delta m(t)<1\\ 0, & \Delta m(t)\geqslant 1\end{cases} \tag{14}$$

式中 k 为负常数。

另外，为避免无人机耗尽电量，在数据采集过程中，若无人机出现电量不足的情况也给出惩罚：

$$r_3=\begin{cases}l, & e(t)<0\\ 0, & e(t)\geqslant 0\end{cases} \tag{15}$$

式中 l 为负常数。

综上得到无人机的奖励函数 r 为

$$r=r_1+r_2+r_3 \tag{16}$$

2.3.3　基于 OnDQN 的最优航迹规划

无人机悬停点距离传感器位置越远，数据传输速率越低，悬停时间就越长。选定无人机的最优采集子区域后，需对子区域的采集顺序和悬停位置进行决策，以平衡无人机的飞行距离与悬停时间，从而最大限度地减少无人机能耗。在该问题中，无人机动作空间包括飞向某一子区域、悬停在子区域某个位置、数据采集 3 个动作，本文采用基于选项（option）的分层强化学习思想来解决该问题[15,27]，将状态空间、动作空间、奖励函数以及 option 建模如下：

1）状态空间：无人机的状态由 3 部分组成，$S=\{S_1(t),S_2(t),S_3(t)\}$，其中 $S_1(t)$ 为 t 时刻无人机的位置，$S_1(t)=(x^t,y^t)$。$S_2(t)$ 为 t 时刻最优子区域数据采集情况组成的向量，$S_2(t)=(g_1^t,g_2^t,\cdots,g_i^t,\cdots g_M^t)$，$g_i^t\in\{0,1\}$ 表示 t 时刻子区域 i 是否被采集（若被采集则为 1，反之为 0）。$S_3(t)$ 为 t 时刻无人机剩余能量。

2）动作空间：无人机的动作空间包含 3 个基本动作 $A=\{a_f(t),a_h(t),a_c(t)\}$，其中 $a_f(t)$ 表示 t 时刻向某一子区域匀速直线飞行，$a_h(t)$ 表示在 t 时刻悬停在某一子区域，$a_c(t)$ 表示 t 时刻采集某一子区域数据。

3）option 空间：option 集合定义为 $O=\{o_1,\cdots,o_i,\cdots,o_M,o_e\}$，其中 o_i 表示无人机采集第 i 个子区域，o_e 表示任务结束。option 空间中任意 $o\in O$ 都是由 3 元组 $\langle I,\pi,\beta\rangle$ 组成，π 表示 option 内部策略，为已知的固定策略，不用进行训练；$\beta\in[0,1]$ 表示该 option 的终止条件，I 表示 option 的初始状态集合。无人机可以在任意状态下选择一个 option。

4）奖励函数：若无人机的采集任务未完成，则奖励为 $r=-1$；反之，则根据无人机的总能耗奖励为 $r=\exp(E^{total}/C)$，其中 C 为正常数。

当奖励函数为稀疏奖励时，可能会导致算法学习效率低，甚至难以收敛[28]。本文采用 n-step 回报代替 1-step 回报来加快算法迭代速度 [29]。定义 n-step 回报函数为

$$G_{t:t+n}=\sum_{k=0}^{n-1}\gamma^k r_{t+k+1}+\gamma^n\max_a\left[Q(s_{t+n},a)\right] \quad (17)$$

式中 $\sum_{k=0}^{n-1}\gamma^k r_{t+k+1}$ 为给定状态 s_t 下的截断 n-step 回报；$Q(s_{t+n},a)$ 为在状态 s_{t+n} 下执行动作 a 时的 Q 值函数

利用该回报函数来更新价值函数 Q：

$$Q(s_t,a_t)\leftarrow Q(s_t,a_t)+\alpha\left[G_{t:t+n}-Q(s_t,a_t)\right] \quad (18)$$

需要说明的是，本文的研究基于一些假设前提：假定无人机匀速飞行，没有考虑从悬停到起飞以及飞行到悬停的速度变化过程的能量消耗变化；假定无人机从一个位置到另一个位置是直线飞行，实际应用中还需考虑无人机的转向问题。

3 仿真分析

为验证节点数据采集算法的有效性，分别在冗余覆盖下部分节点数据采集场景和全节点数据采集场景进行仿真试验，试验在 windows10 系统下进行，处理器为 AMD Ryzen 5 2500U，频率为 2.0 GHz。网络架构使用谷歌的开源 Tensorflow 模块构建，利用 Python 搭建深度强化学习仿真环境。表 1 为旋翼无人机的功率模型参数。

表 1 旋翼无人机参数

Table 1 The parameters of Rotor UAV

参数 Parameters	值 Value
机身阻力比 Fuselage resistance ratio d_r	0.3
空气密度 Air density ρ /(kg·m^{-3})	1.225
旋翼实度 Rotor solidity δ	0.05
旋翼桨盘面积 Rotor disc area S_0/m^2	0.79
转子的叶尖速度 Tip velocity of the rotor U_{tip} /(m·s^{-1})	200
平均旋翼诱导速度 Mean rotor induced velocity v_0 /(m·s^{-1})	7.2

3.1 冗余覆盖下部分节点数据采集场景的仿真分析

仿真假设在 640 m×640 m 的农田随机均匀部署 20 个无线传感器节点，每个节点的感知覆盖半径均为 80 m，无人机飞行速度为 5 m/s，飞行高度为 10 m，每个传感器存储的数据为 160 kB。经平衡运算复杂度和优化结果，将农田离散为 40 m×40 m 的网格，共计 256 个网格单元。以覆盖率和有效覆盖平均能耗评估算法性能，定义如下：

1）覆盖率 V：已采集节点的总感知面积 $\sum_{\forall i}S_{valid}(i)$ 与所有节点的总感知面积 S_{total} 的比值：

$$V=\frac{\sum_{\forall i}S_{valid}(i)}{S_{total}} \quad (19)$$

2）有效覆盖平均能耗：无人机采集每个节点数据的平均能耗与覆盖率的比值。设 m 为采集的节点数量，τ_k 为无人机采集第 k 个节点数据的能耗（包括从上一节点飞行到该节点的飞行能耗及在该节点的悬停能耗），则有效覆盖平均能耗 E_{mean}(kJ)为

$$E_{mean}=\frac{\sum_{\forall k}\tau_k}{V\times m} \quad (20)$$

根据式（12）设置奖励函数，在实际训练过程中发现，负向奖励的取值范围远大于正向奖励，导致正向激励几乎不起作用。为此使用对数函数变换对原始奖励计算结果进行归一化处理：

$$r'=\frac{\lambda\ln(1+r_c)}{\lambda+\omega}-\frac{\omega\ln(1+r_e)}{\lambda+\omega} \quad (21)$$

由于式（12）中的调整因子 λ 和 ω 影响无人机的行动，训练中设置不同调节因子进行比较，表 2 为不同调节因子配置。

图 7a 为本文 DDDQN 算法与 DQN 算法在 20 个回合（episode）的覆盖率计算结果，图 7b 为 DDDQN 与 DQN 在 20 个回合的有效覆盖平均能耗计算结果。可以看出，配置 4 的效果最好，配置 5 次之，配置 6 的效果最差。λ 越大，智能体受正向奖励的影响较大，其覆盖率越大。当 λ 略大于 ω 时，覆盖率和有效覆盖平均能耗达到最佳。若 λ 与 ω 的比值小于 1，有效覆盖平均能耗较大，覆盖率较低，无法满足任务要求。从图 7 可看出，在相同配置下 DDDQN 的覆盖率更大，有效覆盖平均能耗更低，说明 DDDQN 的性能更佳。

图 8 为以最佳配置 4 作为奖励函数调节因子时，DDDQN 算法与 DQN 算法的学习差异。DDDQN 的学习过程比 DQN 更稳定，在学习结束时获得更高的周期奖励。在调节因子配置 4 下 DDDQN 算法每个 episode 可获得 12 的累积奖励，而 DQN 最多只能获得 9 的累积奖励。

表 2 调节因子配置

Table 2 Regulatory factors configuration

N_2	λ	ω
1	1.5	1.5
2	2	1
3	2.5	1
4	2	1.5
5	2.5	1.5
6	1.5	2

注：λ, ω 为奖励函数的调节因子，N_2 为调节因子配置组编号。

Note: λ and ω are the moderators of the reward function, N_2 indicates the No. of the moderator configuration group.

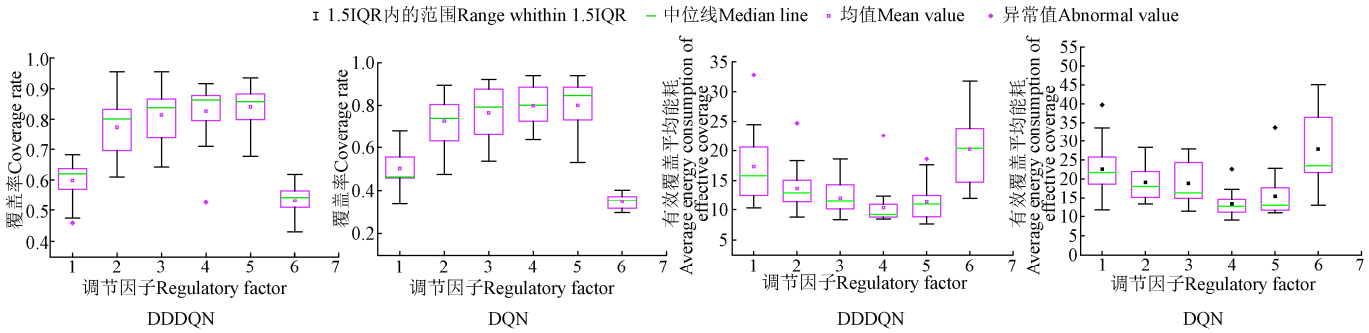

a. 覆盖率　　b. 有效覆盖平均能耗

a. Coverage rate　　b. Average energy consumption of effective coverage

图 7　不同调节因子配置下的覆盖率与有效覆盖平均能耗

Fig.7　Coverage rate and average energy consumption of effective coverage under different regulatory factor configurations

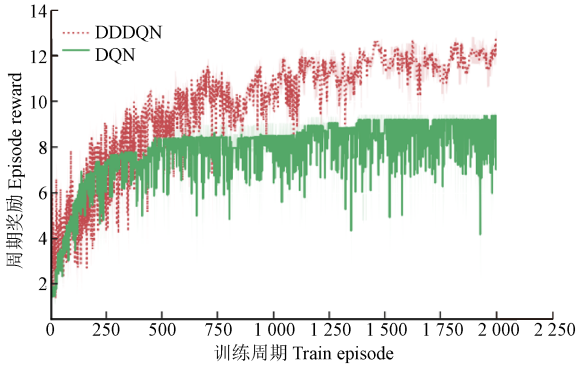

图 8　DDQN 和 DQN 算法的训练奖励值对比

Fig.8　Comparison of training reward value between DDDQN and DQN（Deep Q Network）

图 9 为采集节点覆盖率超过 80%时 DDDQN 和 DQN 算法的无人机数据采集方案。经计算，DDDQN 算法的飞行距离为 3.13 km，相比 DQN 算法的 4.34 km，无人机能耗减少了 27.9%，飞行距离缩短 1.21 km。根据式（19）～（20）计算可得，DDDQN 相比 DQN 的有效覆盖平均能耗降低了 26.3%。

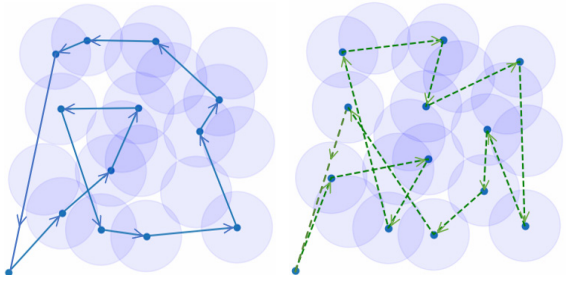

a. DDDQN　　b. DQN

图 9　DDDQN 和 DQN 算法的数据采集方案

Fig.9　Data collection schemes of DDDQN and DQN algorithm

3.2　全节点数据采集场景的仿真与结果分析

在仿真中，假设无线传感器节点随机分布在 600 m×600 m 的矩形区域内，将该矩形区域划分为 15 m×15 m 的网格。设置矩形区域左下角为无人机的飞行起点，飞行高度为 10 m；无人机与传感器节点间单位距离（1 m）的信噪比 β=34 dB；通信带宽 B=10 kHz。

图 10 是不同条件下本文 DDRL 算法与经典 PSO-TSP 算法的结果对比。PSO-TSP 算法是在 Chen[30]等提出的 IGA 方法的基础上提出来的。PSO-TSP 算法要求无人机遍历每个节点，在每个节点正上方悬停采集数据。

图 10a 是无人机的飞行速度对总能耗和总工作时间的影响。在仿真中设置 20 个传感器，每个传感器储存的数据为 160 kB，通信半径为 80 m。对于 2 种算法来说，飞行速度的增加都会减小无人机的总能耗和工作时间。在相同速度下，DDRL 算法比 PSO-TSP 算法的能耗更低，当速度较低时 DDRL 算法优势更明显，无人机飞行速度为 5 m/s 时，相比 PSO-TSP，采用 DDRL 算法的无人机总能耗减少 7.8%，工作时间减少 9.2%。

图 10b 为节点数据负载量对无人机能耗的影响。仿真中传感器节点数设置为 20 个，传感器的通信半径分别设为 60 和 80 m。从图 10b 中可以看出，本文 DDRL 算法在节点数据量较少（少于 160 kB）的情况下比 PSO-TSP 算法的能耗低；通信半径 60 m 时 DDRL 算法的优势较 80 m 更明显。节点数据量变大后，相比 PSO-TSP 算法在节点正上方采集数据（距离近采集时间短），DDRL 算法在每个悬停点采集多个节点数据，由于有些节点的距离远导致采集时间延长，导致悬停时间和能耗加大，总能耗超过 PSO-TSP 算法，通信范围大时更加明显。随着节点数据量增加，无人机飞行能耗占比减少，这是因为无人机悬停能耗增加。同等数据量前提下，DDRL 算法的飞行能耗占比比 PSO-TSP 算法低，节点通信距离 80 m 时的飞行能耗占比比 60 m 时低，即悬停能耗占比高。

图 10c 是飞行速度对无人机悬停采集时间的影响。设置节点的水平通信距离为 80 m，节点数据量为 160 kB。由于 PSO-TSP 算法中无人机悬停在每个传感器正上方采集数据，数据传输距离近，故其悬停采集时间最低且不受飞行速度影响。而在 DDRL 算法中，悬停采集时间随着飞行速度的增加而减少，这是因为 DDRL 算法通过悬停点选择和采集顺序决策来优化总能耗，飞行速度增加，飞行能耗变小，此时悬停能耗成为影响总能耗的主要因素。

图 10d 为水平通信距离 60 m、节点数据量 160 kB 时传感器节点个数对总能耗的影响。将本文 DDRL 算法与 PSO-TSP 及 MEFC(Minimized Energy Flight Control)算法[31]对比可知，MEFC 算法考虑了无人机的飞行速度与转弯角度对能耗的影响，找到最优飞行速度并优化了飞行轨

迹，将悬停点规划在传感器传输范围边缘，使无人机以低能耗完成数据采集。从图 10d 中可以看出，PSO-TSP 的无人机总能耗最大，这是因为无人机需要飞到每个传感器节点正上方采集数据，由于飞行路径增加使其飞行能耗大大增加。MEFC 算法规划的悬停点均在传感器传输范围边缘，且未考虑传输范围重叠的情况，虽然减少了飞行距离和飞行能耗，但增加了悬停点的数据传输时间，即增加了悬停时间和悬停能耗。随着节点数量的增加，3 种算法的总能耗都增加。因此在数据量不大的情况下，本文 DDRL 算法的总能耗较另两种算法更具优势。

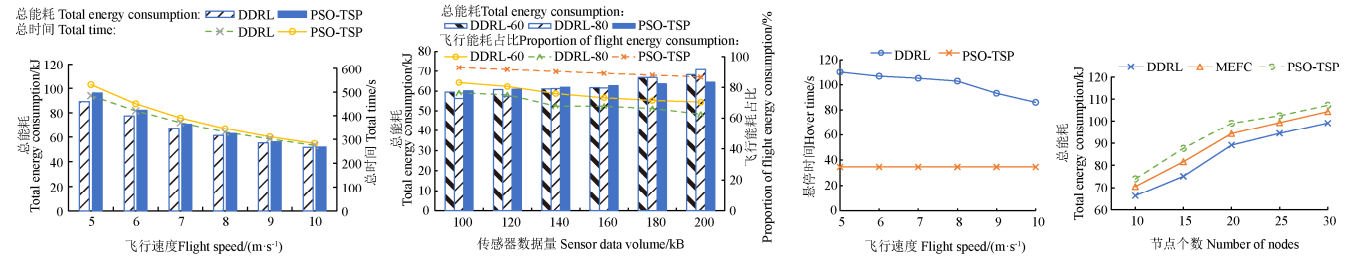

a.飞行速度对总能耗的影响
a. Influence of flight speeds on total energy consumption

b.数据负载量对总能耗和飞行能耗占比的影响
b. Influence of different data volumes on total energy consumption and proportion of flight energy consumption

c.飞行速度对悬停时间的影响
c. Influence of flight speeds on hover time

d.节点个数对总能耗的影响
d. Influence of different number of nodes on total energy consumption

DDRL: Double Deep Reinforcement Learning; PSO-TSP: Particle Swarm Optimization-Traveling Salesman Problem; MEFC: Minimized Energy Flight Control; 60，80: Horizontal communication distance, m.

图 10 不同飞行速度、数据负载量及节点个数下无人机总能耗及悬停时间的仿真结果

Fig.10 Simulation results of total energy consumption and hover collection time of UAV under different flight speeds, sensor data volume and number of nodes

4 全节点数据采集算法的田间试验与结果分析

针对全节点数据采集场景，本研究通过田间试验对所提方法进行评估并验证其可行性。试验在广州华南农业大学增城教研基地开展，采用自制的四旋翼无人机在 210 m×400 m 的平坦农田中进行测试，无人机飞行高度为 5 m。为了验证无人机接收数据的丢包率，同时对田间的通信路径损耗进行估测，以更精确地计算无人机悬停时间，利用 2 个 DRF1609H 型 Zigbee 模块测试无人机接收模块与地面数据发送模块之间的丢包情况和接收信号强度值，其中地面数据发送模块由 Zigbee 通信模块与单片机 STM32 组成，DRF1609H 型 Zigbee 模块的发送功率为 22 dbm。

如图 11 所示，无人机从地面节点正上方开始，每隔 10 m 水平距离，到与节点水平距离 120m 为止，当地面节点接收到无人机的数据请求后，发送 200 个数据包，每个数据包的长度为 0.5 kB，丢包率测试结果如表 3 所示。接收信号强度值取每个位置采集 10 次数据的接收信号强度平均值。

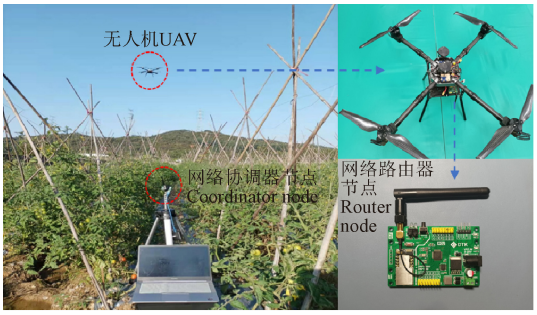

图 11 田间试验

Fig.11 Field test

从表 3 中可以看出，在水平通信距离 80 m 以外，随着测试距离的增加，丢包率增加，80 m 以内范围满足数据传输稳定性要求。

表 3 水平通信距离对丢包率的影响

Table 3 Influence of horizontal communication distance on packet loss rate

水平通信距离 Horizontal communication distance/m	数据包丢失数量 Number of packets lost	丢包率 Packet loss rate/%
10～80	0	0
90	5	2.5
100	8	4
110	8	4
120	12	6

采用 MATLAB 中的曲线拟合方法对路径损耗模型进行评估，确定水平通信距离与接收信号强度值之间的关系。如图 12 所示，经过多次试验发现，指数函数的拟合效果最佳，田间 ZigBee 传输的接收信号强度值 RSSI 与水平通信距离 x 的关系为

$$RSSI = -55.2e^{0.001151x} + 69.05e^{-0.09076x} \quad (R^2 = 0.9815) \quad (22)$$

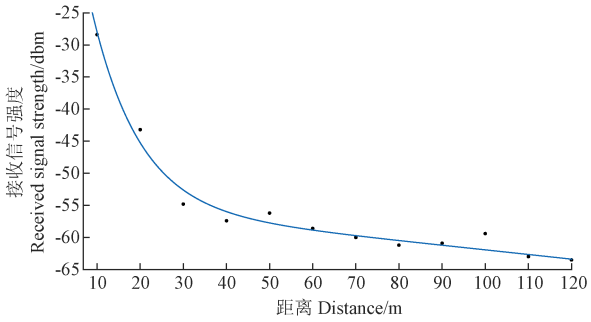

图 12 接收信号强度与水平通信距离的拟合关系

Fig.12 The fitting relationship between received signal strength and horizontal communication distance

为了进一步评估所提算法对无人机能耗优化的效果，在无人机上配备电流计模块获取瞬时电流并计算无

人机能耗。首先测试无人机的飞行功率和悬停功率，测试方案如下：无人机以 5 m/s 速度和 5 m 高度进行匀速直线飞行 100 m，利用每隔 0.1 s 获取的瞬时电流和电压计算无人机的飞行功率。同理，计算单位时间内无人机的悬停能耗。经过实际测试，本试验所采用的四旋翼无人机的平均飞行功率为 746.38 W，平均悬停功率为 771.86 W，无人机电池的最大容量为 22 000 mAh。

最后，在田间随机布置 11 个 Zigbee 模块模拟节点，结合田间路径损耗模型，运行算法得到 DDRL 算法及 PSO-TSP 算法规划的悬停点、悬停时间及采集顺序，然后令无人机按照规划方案进行数据采集试验。设置节点数据量为 160 kB，数据包长度为 0.5 kB，无人机飞行高度 5 m，飞行速度 5 m/s。图 13a 为 PSO-TSP 算法的飞行路径；图 13b 为本文算法 DDRL 优化的悬停点和飞行路径。最终的试验结果表明，DDRL 算法的无人机总能耗为 354.56 kJ，飞行距离为 1 189.23 m，丢包率为 0.28%；PSO-TSP 算法的总能耗为 400.83 kJ，飞行距离为 1 556.21 m，丢包率为 0.15%。相比 PSO-TSP，DDRL 算法的总能耗减少了 11.5%，飞行路径减少了 366.98 m；DDRL 算法的丢包率略高于 PSO-TSP 算法，这是因为 DDRL 算法的规划方案中无人机悬停采集点不在节点正上方，且在一个悬停点采集多个节点数据，而 PSO-TSP 算法的规划方案中无人机悬停在节点正上方采集数据，丢包概率降低。

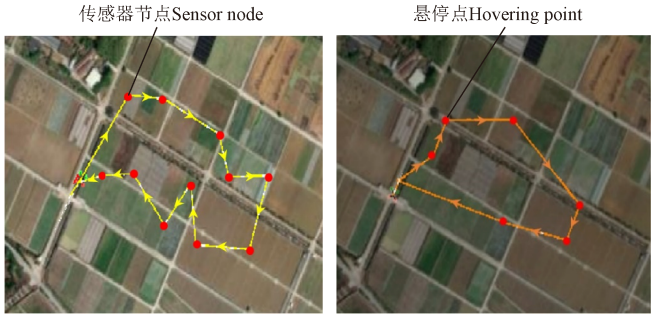

a. PSO-TSP 算法　　b.DDRL 算法
a. PSO-TSP algorithm　　b. DDRL algorithm

图 13　PSO-TSP 和 DDRL 算法无人机悬停点及数据采集顺序示意图

Fig.13　Schematic diagram of UAV hover points and data collection sequences in PSO-TSP and DDRL algorithms

5　结　论

利用无人机采集田间无线传感器节点数据，能克服农田无网络基础设施及节点多跳转发数据耗电快、网络生命周期短的问题。本研究将节点采集的情况分为感知冗余覆盖下部分节点数据采集及全节点数据采集两个场景，基于深度强化学习规划无人机的节点选择、悬停位置及采集顺序，以节省无人机能耗缩短任务完成时间。感知冗余覆盖下部分节点数据采集方案适用于节点间冗余覆盖面积比例比较高，无人机能量无法完成所有节点的数据采集任务，以及对数据的完整性要求不高的应用场景；全节点数据采集方案适用于对数据有完整性要求的应用场景。通过对研究结果的分析，得到以下结论：

1）在考虑感知冗余覆盖下部分节点数据采集场景中，采用竞争双重深度 Q 网络（DDDQN）算法选择采集节点及规划采集顺序，提高了无人机的能效和减少了冗余数据的采集。仿真验证了在相同配置下，DDDQN 算法比 DQN 算法的覆盖率和平均能耗更优，算法性能更加稳定；在相同的覆盖率要求下，DDDQN 算法比 DQN 算法的飞行距离缩短了 1.21 km，能耗减少了 27.9%。

2）在全节点数据采集场景中，提出了两级深度强化学习（DDRL）算法对无人机的悬停位置及采集顺序进行优化，减少了无人机完成任务时的总能耗。本文从传感器不同数据负载量、无人机飞行速度、传感器节点数量对 DDRL 与 PSO-TSP 及 MEFC 算法的总能耗、总时间、飞行能耗占比、悬停采集时间进行仿真对比，结果证明无人机采用 DDRL 算法采集数据的总能耗最低。最后，通过田间试验测试了四旋翼无人机的飞行功率与悬停功率，并对 DDRL 算法及经典 PSO-TSP 算法的采集方案进行了实际田间飞行试验。结果表明，DDRL 算法能同时考虑飞行距离与数据传输时间两个因素，在采集相同的数据情况下较 PSO-TSP 算法能耗降低了 11.5%。

［参　考　文　献］

[1] García L, Parra L, Jimenez J M, et al. DronAway: A proposal on the use of remote sensing drones as mobile gateway for WSN in precision agriculture[J]. Applied Sciences, 2020, 10(19): 6668.

[2] 宋成宝，柳平增，刘兴华，等. 基于 HSIC 的日光温室温度传感器优化配置策略[J]. 农业工程学报，2022, 38(8)：200-207.
Song Chengbao, Liu Pingzeng, Liu Xinghua, et al. Optimal configuration strategy for temperature sensors in solar greenhouse based on HSIC[J]. Transactions of the Chinese Society of Agricultural Engineering (Transactions of the CSAE), 2022, 38(8): 200-207. (in Chinese with English abstract)

[3] Bandur D, Jaksic B, Bandur M, et al. An analysis of energy efficiency in Wireless Sensor Networks (WSNs) applied in smart agriculture[J]. Computers and Electronics in Agriculture, 2019, 156: 500-507.

[4] Polo J, Hornero G, Duijneveld C, et al. Design of a low-cost wireless sensor network with UAV mobile node for agricultural applications[J]. Computers and Electronics in Agriculture, 2015, 119: 19-32.

[5] Zhang B T, Meng L Y. Energy efficiency analysis of wireless sensor networks in precision agriculture economy[J]. Scientific Programming, 2021, 2021: 8346708.

[6] Huang S C, Chang H Y. A farmland multimedia data collection method using mobile sink for wireless sensor networks[J]. Multimedia Tools and Applications, 2017, 76(19): 19463-19478.

[7] Singh P K, Sharma A. An intelligent WSN-UAV-based IoT framework for precision agriculture application[J]. Computers and Electrical Engineering, 2022, 100: 107912.

[8] Yemeni Z, Wang H, Ismael W M, et al. Reliable spatial and

temporal data redundancy reduction approach for WSN[J]. Computer Networks, 2021, 185: 107701.

[9] Kumar S, Chaurasiya V K. A strategy for elimination of data redundancy in internet of things (IoT) based wireless sensor network(WSN)[J]. IEEE Systems Journal, 2018, 13(2): 1650-1657.

[10] Rezende J D V, da Silva R I, Souza M J F. Gathering big data in wireless sensor networks by drone(dagger)[J]. Sensors, 2020, 20(23): 6954.

[11] Luo C W, Chen W P, Li D Y, et al. Optimizing flight trajectory of UAV for efficient data collection in wireless sensor networks[J]. Theoretical Computer Science, 2021, 853: 25-42.

[12] Ben Ghorbel M, Rodríguez-Duarte D, Ghazzai H, et al. Joint position and travel path optimization for energy efficient wireless data gathering using unmanned aerial vehicles[J]. IEEE Transactions on Vehicular Technology, 2019, 68(3): 2165-2175.

[13] Gong J, Chang T H, Shen C, et al. Flight time minimization of UAV for data collection over wireless sensor networks[J]. IEEE Journal on Selected Areas in Communications, 2018, 36(9): 1942-1954.

[14] Just G E, Pellenz M E, Lima L A D, et al. UAV path optimization for precision agriculture wireless sensor networks[J]. Sensors, 2020, 20(21): 6098.

[15] Zhang Y, Mou Z Y, Gao F F, et al. Hierarchical deep reinforcement learning for backscattering data collection with multiple UAVs[J]. IEEE Internet of Things Journal, 2021, 8(5): 3786-3800.

[16] 蒋宝庆，陈宏滨. 基于 Q 学习的无人机辅助 WSN 数据采集轨迹规划[J]. 计算机工程，2021，47(4)：127-134.
Jiang Baoqin, Chen Hongbin. Trajectory planning for unmanned aerial vehicle assisted WSN data collection based on Q-Learning[J]. Computer Engineering, 2021, 47(4): 127-134. (in Chinese with English abstract)

[17] Yi M J, Wang X J, Liu J, et al. Deep reinforcement learning for fresh data collection in UAV-assisted IoT networks[C]//IEEE INFOCOM 2020-IEEE Conference on Computer Communications Workshops (INFOCOM WKSHPS). Toronto, ON, Canada: IEEE, 2020: 716-721.

[18] 付澍，杨祥月，张海君，等. 物联网数据收集中无人机路径智能规划[J]. 通信学报，2021，42(2)：124-133.
Fu Shu, Yang Xiangyue, Zhang Haijun, et al. UAV path intelligent planning in IoT data collection[J]. Journal on Communications, 2021, 42(2): 124-133. (in Chinese with English abstract)

[19] Zeng Y, Xu J, Zhang R. Energy minimization for wireless communication with Rotary-Wing UAV[J]. IEEE Transactions on Wireless Communications, 2019, 18(4): 2329-2345.

[20] Padakandla S. A survey of reinforcement learning algorithms for dynamically varying environments[J]. ACM Computing Surveys, 2021, 54(6): 127.

[21] 陈佳盼，郑敏华. 基于深度强化学习的机器人操作行为研究综述[J]. 机器人，2022，44(2)：236-256.
Chen Jiapan, Zheng Minhua. A survey of robot manipulation behavior research based on deep reinforcement learning[J]. Robet, 2022, 44(2): 236-256. (in Chinese with English abstract)

[22] Fenjiro Y, Benbrahim H. Deep reinforcement learning overview of the state of the art[J]. Journal of Automation, Mobile Robotics and Intelligent Systems, 2018, 12: 20-39.

[23] 张自东，邱才明，张东霞，等. 基于深度强化学习的微电网复合储能协调控制方法[J]. 电网技术，2019，43(6)：1914-1921.
Zhang Zidong, Qiu Caiming, Zhang Dongxia, et al. A coordinated control method for hybrid energy storage system in microgrid based on deep reinforcement learning[J]. Power System Technology, 2019, 43(6): 1914-1921. (in Chinese with English abstract)

[24] Zhang W Y, Gai J Y, Zhang Z G, et al. Double-DQN based path smoothing and tracking control method for robotic vehicle navigation[J]. Computers and Electronics in Agriculture, 2019, 166: 104985.

[25] Wang Z Y, Schaul T, Hessel M, et al. Dueling network architectures for deep reinforcement learning[C]. //In Proceedings of the 33rd International Conference on International Conference on Machine Learning. New York, NY, USA: ICML, 2016: 1995-2003.

[26] Kumar H, Mammen P M, Ramamritham K. Explainable AI: deep reinforcement learning agents for residential demand side cost savings in smart grids[J]. arXiv e-prints, 2019: 1910. 08719.

[27] 赵铭慧，张雪波，郭宪，等. 基于分层强化学习的通用装配序列规划算法[J]. 控制与决策，2022，37(4)：861-870.
Zhao Minghui, Zhang Xuebo, Guo Xian, et al. A general assembly sequence planning algorithm based on hierarchical reinforcement learning[J], Control and Decision, 2022, 37(4): 861-870. (in Chinese with English abstract)

[28] 杨惟轶，白辰甲，蔡超，等. 深度强化学习中稀疏奖励问题研究综述[J]. 计算机科学，2020，47(3)：182-191.
Yang Weiyi, Bai Chenjia, Cai Chao, et al. Survey on sparse reward in deep reinforcement learning[J]. Computer Science. 2020, 47(3): 182-191. (in Chinese with English abstract)

[29] Hernandez-Garcia J F, Sutton R S. Understanding multi-step deep reinforcement learning: A systematic study of the DQN target[J]. arXiv e-prints, 2019:1901. 07510.

[30] Chen J, Ye F, Li Y B. Travelling salesman problem for UAV path planning with two parallel optimization algorithms[C]//2017 Progress in Electromagnetics Research Symposium-Fall(PIERS-FALL). Singapore, 2017: 832-837.

[31] 吴媚. 工业物联网环境下面向能耗优化的无人机飞行规划系统设计与实现[D]. 南京：东南大学，2019.
Wu Mei. Energy Efficient UAV Flight Planning System for the Industrial IoT Environment[D]. Nanjing:Southeast University, 2019. (in Chinese with English abstract)

UAV collection methods for the farmland nodes data based on deep reinforcement learning

Hu Jie[1,3], Zhang Yali[2,3※], Wang Tuan[1], Wang Mengcheng[1], Lan Yubin[1,3], Zhang Zhixun[2]

(1. *College of Electronic Engineering*, *South China Agricultural University*, *Guangzhou* 510642, *China*; 2. *College of Engineering*, *South China Agricultural University*, *Guangzhou* 510642, *China*; 3. *National Center for International Collaboration Research on Precision Agricultural Aviation Pesticide Spraying Technology*, *Guangzhou* 510642, *China*)

Abstract: Unmanned Aerial Vehicle (UAV) has been widely used to collect data from the wireless sensor node in fields. Some problems can be solved in this case, such as no network infrastructure in farmland, fast power consumption of multi-hop data forwarding, premature death of nodes near the gateway, and shortened network life cycle. However, the multiple nodes overlapping can often occur during UAVs collection at the same time, due to the possible redundancy of adjacent sensor data. In this study, a UAV data collection method was proposed to plan the node selection, hovering position, and collecting order using improved deep reinforcement learning. The UAV data collection from the sensor nodes was then divided into two scenarios: data collection from the partial nodes under perceptual redundancy coverage, and data collection from all nodes. The optimization was made to save the UAV energy consumption in less mission completion time. The data collection of partial nodes under perceived redundancy coverage was suitable for the relatively high proportion of redundant coverage area among nodes. The UAV energy also failed to complete the data collection tasks of all nodes, indicating the low requirements of data integrity. By contrast, the all-node data collection fully met the high requirement of data integrity. In the scenario of partial node data collection with perceived redundant coverage, the Dueling Double Deep Q Network (DDDQN) was used to select the collection nodes and then plan the collecting order, indicating the high energy efficiency of the UAV with the less redundant data. Simulation results show that the DDDQN presented greater data coverage and lower effective coverage average energy consumption than the Deep Q Network (DQN) under the same configuration. The training process of DDDQN was more stable than that of DQN, particularly for the higher returns at the end of learning. More importantly, the flight distance and energy consumption of the DDDQN were reduced by 1.21 km, and 27.9%, respectively, compared with the DQN. In the scenario of all-node data collection, a Double Deep Reinforcement Learning (DDRL) was proposed to optimize the hovering position and UAV collection sequence, in order to minimize the total energy consumption of the UAV during data collection. A comparison was made on the DDRL with the classical PSO-TSP and MEFC. A systematic evaluation was made to clarify the impact of the UAV flight speed on the total energy consumption and total working time, the impact of different node data loads on the UAV energy consumption, the impact of different flight speeds on the UAV hover collection time, and the impact of the number of sensor nodes on the total energy consumption. The simulation results show that the total energy consumption of the improved model was at least 6.3% less than that of the classical PSO-based Travel Salesman Problem (PSO-TSP), and the Minimized Energy Flight Control (MEFC) under different node numbers and UAV flight speeds, especially at the data load of a single node less than 160 kB. Finally, the flight and hover powers of the quadrotor UAV were tested to determine the packet loss rate and received signal strength of the UAV in the field experiments. The actual field flight experiments were carried out on the DDRL and the data collection of the classical PSO-TSP. Field experiment results show that the DDRL-based data collection was reduced by 11.5% for the total energy consumption of UAV, compared with the PSO-TSP. The DDDQN and DDRL approaches can be expected to provide the optimal energy consumption for the UAVs' data collection of wireless sensor nodes in the field.

Keywords: UAV; deep reinforcement learning; node data collection; perceptual redundancy; DQN; DRL

·农业航空工程·

用 P20 型植保无人机减量施药防治稻纵卷叶螟

曾 文[1,2]，邓继忠[1,2]，高启超[1,2]，贾瑞昌[1,2]，兰玉彬[2,3]，
张建瓴[1,2]，陈鹏超[2,3]，肖汉祥[4]，张亚莉[1,2※]

（1. 华南农业大学工程学院，广州 510642；2. 国家精准农业航空施药技术国际联合研究中心，广州 510642；
3. 华南农业大学电子工程学院，广州 510642；4. 广东农业科学研究院植物保护研究所，广州 510640）

摘 要：为探讨植保无人机（UAV）减量施药对水稻病虫害的防治效果，该研究采用 P20 型植保无人机进行水稻田间施药作业。分别在水稻分蘖末期、孕穗期开展了两种施药液量（15、22.5 L/hm^2）的水稻冠层雾滴沉积试验，以及两种施药液量下 480、540、600 mL/hm^2 3 种农药剂量（阿维·氯苯酰推荐剂量的 80%、90%、100%）的防治稻纵卷叶螟减量施药田间药效试验，并与背负式电动喷雾器（Knapsack Electric Sprayer，KES）人工施药的常规防治方法进行施药效果对比。雾滴沉积试验结果表明，水稻冠层上部的雾滴分布均匀性优于水稻冠层下部；施药液量 15、22.5 L/hm^2 的冠层上部雾滴沉积有显著差异，且施药液量 22.5 L/hm^2 的冠层上部雾滴沉积显著优于施药液量 15 L/hm^2。药效试验结果表明，农药剂量越大稻纵卷叶螟防治效果越好，采用农药剂量 100%的植保无人机施药防治效果最好，并优于 KES 人工施药；施药液量 15、22.5 L/hm^2 的稻纵卷叶螟防治效果有显著差异，且施药液量 22.5 L/hm^2 较 15 L/hm^2 的防治效果更好；施药液量 15 L/hm^2 且农药剂量 90%、施药液量 22.5 L/hm^2 且农药剂量 80%与 KES 人工施药的防治效果没有显著差异。采用植保无人机施药防治稻纵卷叶螟，施药液量 22.5 L/hm^2 可以获得更好的雾滴沉积和稻纵卷叶螟防治效果；施药液量 22.5 L/hm^2 时，减少 20%的农药剂量也能保证稻纵卷叶螟防治效果。该结果对水稻田间植保无人机减量施药具有实践指导意义。

关键词：无人机；喷雾；减量施药；雾滴沉积；稻纵卷叶螟
doi：10.11975/j.issn.1002-6819.2021.15.007
中图分类号：S252 **文献标志码**：A **文章编号**：1002-6819(2021)-15-0053-07

曾文，邓继忠，高启超，等. 用 P20 型植保无人机减量施药防治稻纵卷叶螟[J]. 农业工程学报，2021，37(15)：53-59.
doi：10.11975/j.issn.1002-6819.2021.15.007 http://www.tcsae.org
Zeng Wen, Deng Jizhong, Gao Qichao, et al. P20 plant protection UAV to control cnaphalocrocis medinalis by reduced pesticide application[J]. Transactions of the Chinese Society of Agricultural Engineering (Transactions of the CSAE), 2021, 37(15): 53-59. (in Chinese with English abstract) doi：10.11975/j.issn.1002-6819.2021.15.007 http://www.tcsae.org

0 引 言

水稻是中国的主要粮食作物之一，也是世界上主要的粮食作物，是全世界超过 30 亿人口的主要食粮[1]。水稻病虫害是制约水稻安全生产的主要因素。水稻病虫害种类繁多，水稻的病害据记载有 61 种，害虫有 78 种，其中稻飞虱、稻纵卷叶螟、二化螟、稻瘟病、纹枯病、稻曲病等经常发生且严重影响产量[2-3]。目前，国内水稻病虫害防治施药作业的主要方式有人工喷施、地面机械喷施和航空喷施三种方式。由于水稻田的特殊作业条件，地面机械在水稻田中作业困难，且易压坏秧苗，其作业成本高、农药利用较低[4-6]。人工喷施劳动强度大，喷药均匀性差，对施药人员会产生严重药害，同时大容量喷雾导致农药有效利用率较低，对生态环境造成严重的危害[7]。航空喷施作业效率高、成本低、施药效果好，克服了地面机械水田作业困难、人工喷施劳动强度大及药害的问题。

近年来，植保无人机航空喷施的迅猛发展和应用引起了人们的广泛关注，并得到了广泛的推广应用[8-11]。各国学者也针对植保无人机航空施药的作业参数、工效、喷雾系统[12-15]，雾滴飘移沉积规律[16-18]，病虫害防治效果[19-20]等开展了大量的研究。陈盛德等[21]比较分析了植保无人机和人工两种水稻施药作业的喷施方式，发现航空喷施优于人工喷施的雾滴沉积效果，且作业效率高、成本低、效益高。薛新宇等[22]开展了飞机不同作业高度和不同喷洒浓度的田间药效试验，结果显示，N-3 型无人直升机对稻飞虱和稻纵卷叶螟的防治效果均优于传统担架式喷雾机。陈盛德等[23]研究了单旋翼无人机不同飞行高度、飞行速度下水稻冠层的雾滴沉积分布，结果显示，飞行高度和飞行速度对雾滴平均沉积量有显著影响，对雾滴沉积均匀性影响不显著。漆海霞等[24]研究了不同旋翼类型和喷头类型对雾滴沉积的影响，发现相比液力式喷头，离心喷头雾滴沉积粒径更小，且可以获得更好的雾滴穿

收稿日期：2021-04-23 修订日期：2021-07-21
基金项目：国家重点研发计划（2018YFD0200304）；广东省重点领域研发计划（2019B020221001）；广东省科技计划项目（2018A050506073）；广东省现代农业产业共性关键技术研发创新团队项目（2020KJ133）；广州市科技计划项目（201807010039）；高等学校学科创新引智计划（D18019）
作者简介：曾文，博士，讲师，研究方向为农业机械装备设计、植保无人机精准施药技术。Email：zengwen@scau.edu.cn
※通信作者：张亚莉，博士，副教授，研究方向为农业航空传感器技术与农产品产地环境监测。Email：ylzhang@scau.edu.cn
中国农业工程学会高级会员：张亚莉（E041200939S）

透效果。李继宇等[25]研究了无人机 4 种喷雾粒径的水稻冠层雾滴沉积效果，发现 4 种粒径的雾滴在水稻冠层的分布均匀性和穿透性都较好，且雾滴粒径越小，沉积量越大，分布均匀性越好。张海艳等[26]测试和对比了电动单旋翼与电动多旋翼植保无人机在水稻田间的作业效果，结果表明，单旋翼植保无人机喷施效果更好，两种类型的植保无人机对水稻病虫害的防治效果均能达到国家防效标准。Qin 等[27]研究了单旋翼无人机飞行高度、飞行速度等参数对水稻冠层和底部的雾滴沉积、稻飞虱防效的影响，发现飞行高度 1.5 m、飞行速度 5 m/s 时冠层底部的雾滴沉积量最大，同时稻飞虱防治效果最好。

目前国内外学者在水稻植保无人机施药技术领域主要研究了不同的旋翼、飞行高度、飞行速度、喷头类型、施药液量下的雾滴沉积分布规律，植保无人机施药与人工施药的作业效率与病虫害防效对比。对于植保无人机不同施药液量下减量施药对水稻病虫害防治效果的研究尚未见相关报导。因此，本文通过 P20 植保无人机两种施药液量下水稻冠层的雾滴沉积分布试验、两种施药液量下的不同农药剂量对稻纵卷叶螟防治效果的田间试验，研究不同施药液量、农药剂量等因素下，植保无人机减量施药对水稻病虫害防治效果的影响，拟为植保无人机农药减施增效提供理论指导和数据支持，促进农药减量使用，提升农药利用率。

1 材料与方法

1.1 试验材料

本次试验的试验田位于中国广东省肇庆市高要区（23°13'56"N，112°19'26"E）。水稻品种为自留种籼稻，采用久保田（2ZGQ-6D1）乘座式高速插秧机进行移栽，其行距为 30 cm，穴距为 18 cm，漏秧率≤2%，移栽密度为 1.82×10^5 穴/hm^2。

药剂为阿维·氯苯酰（Acitretin · Chlorobenzoyl），生产厂家：先正达南通作物保护有限公司，剂型：悬浮剂，有效成分为阿维菌素 17 g/L、氯虫苯甲酰胺 43 g/L，推荐剂量：600～750 mL/hm^2，防治对象：稻纵卷叶螟、二化螟。

1.2 施药设备

本试验使用的植保无人机为广州极飞科技有限公司生产的 P20 型 4 旋翼无人机（如图 1a 所示）。该植保无人机搭载 SUPERX®3 Pro RTK 飞控系统，可实现厘米级精准导航；搭载使用离心雾化喷头的喷洒系统，可通过控制离心雾化喷头的转速调整雾化颗粒的大小。P20 植保无人机作业时可根据需求设置飞行高度、飞行速度、喷幅、雾滴粒径、施药液量等作业参数，喷洒系统根据飞行速度、喷幅、施药液量等参数自动计算泵的流量，以保证施药液量的精确性。对照使用的电动喷雾器为艺锦园公司 3WBD-20 型背负式电动喷雾器（如图 1b 所示），经水敏纸测试，其雾滴体积中径（DV50）为 410 μm。P20 型植保无人机与 3WBD-20 型背负式电动喷雾器的参数如表 1 所示。

依据前人研究基础[21,23,26-27]及作业实践经验，除施药液量外，植保无人机施药的其他作业参数均设置为飞行速度 4 m/s、高度 2 m、喷幅 3.5 m，雾滴粒径 125 μm。背负式电动喷雾器的施药液量按农药兑水建议设置为 450 L/hm^2。



a. 极飞植保无人机 P20
a. XAG P20 plant protection UAV



b. 背负式电动喷雾器
b. Knapsack Electric Sprayer (KES)

图 1 施药设备

Fig.1 Spraying equipment

表 1 P20 植保无人机及背负式电动喷雾器参数

Table 1 Parameters of the P20 plant protection UAV and the KES

参数 Parameters	P20 植保无人机 P20 plant protection UAV	背负式电动喷雾器 KES
旋翼数量 Rotor numbers	4	/
飞行速度 Flight speed/(m·s^{-1})	1~12	/
飞行高度 Flight height/m	1~10	/
喷幅 Spraying width/m	2~5	1
雾滴粒径 Droplet size/μm	90~300	410
泵类型 Pump type	蠕动泵	隔膜泵
喷头类型 Nozzle type	离心雾化喷头	压力雾化喷头
喷头数量 Nozzle numbers	4	1
药箱容积 Tank capacity/L	10	20

1.3 试验设计

为验证无人机施药时不同施药液量和不同农药剂量对水稻病虫害防治效果的影响，根据作业实践经验设置 2 个施药液量，分别为 15、22.5 L/hm^2；设置 3 个农药剂量为 480、540、600 mL/hm^2，分别为阿维·氯苯酰推荐剂量（600 mL/hm^2）的 80%、90%、100%。为与无人机减量施药进行对比，设置 1 个背负式电动喷雾器（Knapsack Electric Sprayer, KES）人工施药的常规防治处理区，以及 1 个不施用农药的空白对照（CK）处理区。根据试验田情况，将试验田划分成如表 2 所示的 8 个处理区，为避免相邻处理区间雾滴漂移的影响，每个处理区距边缘 3 m 内作为缓冲区，缓冲区内不采集雾滴沉积数据，也不调查防效数据。在防效调查时，按处理区长度将每个处理区等量划分成 5 个小区，作为同一处理的多次重复。

表 2 试验田处理区

Table 2 Treatment plots in the experiment field

处理 Treatments	施药方式 Spray method	施药液量 Spray volume/(L·hm^{-2})	农药剂量 Pesticide dosage/%	宽度 Width/m	长度 Length/m	面积 Area/hm^2
T1	UAV	15	80	30	100	0.3
T2	UAV	15	90	30	100	0.3
T3	UAV	15	100	30	100	0.3
T4	UAV	22.5	80	20	100	0.2
T5	UAV	22.5	90	20	100	0.2
T6	UAV	22.5	100	20	100	0.2
T7	KES	450	100	20	100	0.2
T8	CK	0	0	20	30	0.06

1.4　雾滴沉积测试与方法

为研究雾滴沉积与水稻病虫害防治效果的关系，在无人机施药过程中，同时开展水稻雾滴沉积试验。在植保无人机施药作业时，沿幅宽方向和喷雾路径方向的雾滴沉积会随气象条件和操作员水平产生变化[28]。为尽可能消除这种变化的影响，本次研究中在喷雾路径方向设置了两条雾滴沉积的采样带，采样带间隔为 20 m。在幅宽方向布置了 11 个采样位置，幅宽方向采样位置间隔为 1 m（图 2a）。为避免相邻田块施药的交叉影响，所有采样位置布置在田块中心位置。由于植保无人机施药时，相同施药液量下雾滴沉积的差异很小，所以本次研究选取了处理区 T3（农药剂量 100%，施药液量 15 L/hm^2）、处理区 T6（农药剂量 100%，施药液量 22.5 L/hm^2）设置了雾滴沉积数据采集。

雾滴沉积测试中常采用水敏纸收集雾滴，但在水稻田使用时，水敏纸易受到稻田中水的污染，因此试验中改用铜版纸进行雾滴收集。同时采用罗丹明 B 玫瑰红染色剂作为雾滴示踪剂，每升水中添加 10 g 罗丹明 B 染色剂。

每个采样位置处插一根塑料杆，使用双头夹将两片铜版纸水平布置在杆上下两个位置，上层位置的铜版纸位于水稻冠层顶部位置，下层位置的铜版纸位于水稻冠层下部位置（图 2b），分别用来采集水稻冠层上部和下部沉积的雾滴。

在施药结束后，为避免收集铜版纸时水稻叶面上的雾滴掉落到铜版纸上，待水稻叶面和铜版纸上的雾滴干燥后收集铜版纸。铜版纸收集后，为保护罗丹明 B 的示踪效果，将每片铜版纸单独装入拉链密封袋中，在密封袋上标记处理区号、采样点等信息，并尽快送回实验室进行雾滴数据分析。

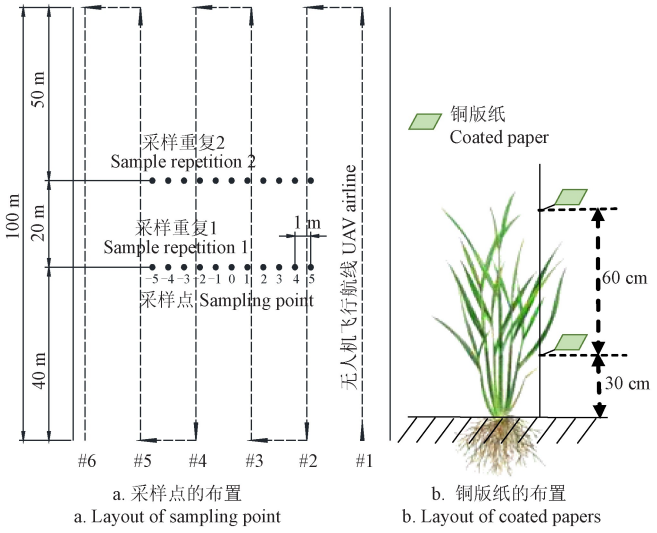

a. 采样点的布置　a. Layout of sampling point　　b. 铜版纸的布置　b. Layout of coated papers

注：#1～#6 为 UAV 飞行航线。
Note: #1-#6 is airlines of UAV.

图 2　雾滴沉积采样点及铜版纸布置示意图

Fig.2　Schematic diagram of droplet deposition sampling point and coated papers layout

铜版纸使用分辨率 600 dpi 的扫描仪进行扫描，然后用图像处理软件 DepositScan (USDA, USA)[29]进行图像识别与分析，获取纸卡选取区域中的所有雾滴，计算雾滴直径、体积，并最终获得雾滴覆盖率、雾滴密度、雾滴沉积量等数据[29-30]。雾滴直径计算公式为

$$d=1.06\,A^{0.455} \tag{1}$$

式中 d 为雾滴直径，μm；A 为图像识别后的雾滴面积，μm^2。雾滴面积用扫描图像雾滴的像素数量进行计算。

雾滴体积计算公式为

$$V=\frac{\pi d^3}{6} \tag{2}$$

式中 V 为雾滴体积，μm^3。

雾滴覆盖率、雾滴密度、雾滴沉积量计算公式分别为

$$C_{\mathrm{cov}}=\frac{A_N}{A_S}\times 100\% \tag{3}$$

$$D_{\mathrm{den}}=\frac{N}{A_S} \tag{4}$$

$$E_{\mathrm{dep}}=\frac{V_N}{A_S} \tag{5}$$

式中 C_{cov} 为雾滴覆盖率，%；D_{den} 为雾滴密度，滴/cm^2；E_{dep} 为雾滴沉积量，μL/cm^2；N 为纸卡选取区域内雾滴的总数量；A_N 为纸卡选取区域内所有雾滴的总面积，cm^2，A_S 为纸卡选取区域面积，cm^2；V_N 为纸卡选取区域内所有雾滴的体积，μL。

1.5　稻纵卷叶螟减量施药测试与防效调查

在本次施药作业时，试验田水稻纹枯病、稻瘟病、稻飞虱、二化螟不明显，以预防为主。稻纵卷叶螟较严重，因此本次试验主要防治稻纵卷叶螟。为保证施药效果，分别于水稻分蘖末期和孕穗期进行了两阶段施药作业。两阶段施药的处理区划分、农药、农药剂量、施药液量均相同。使用气象仪记录两次试验期间气象数据，试验期间田间温度、相对湿度、风速分别为 27.3～34.5 ℃、52.3%～65.4%、0.15～1.52 km/h。

依据农药田间药效试验准则[31]，针对水稻稻纵卷叶螟进行了施药效果调查与记录。共进行了 3 次稻纵卷叶螟的调查，第一次调查为施药前 1 天，第二次调查为第一次施药后 15 天，第三次调查为第二次施药后 7 天。将每个处理区划分为 5 个小区，每个小区采用 5 点平行取样方法，每点取样 5 穴水稻，共 25 穴。记录每个取样点的处理区号、小区号、株数、叶片数（每株水稻按 4 片叶子计算）、卷叶数。利用以下公式计算每个处理区的卷叶率（Leaf Roll Rate，R_{LRR}）和防治效果（Control Efficacy，R_{CE}）指标[31]。

$$R_{\mathrm{LRR}}=\frac{N_R}{N_T}\times 100\% \tag{6}$$

$$R_{\mathrm{CE}}=\frac{R_{\mathrm{CK}}-R_{\mathrm{PT}}}{R_{\mathrm{CK}}}\times 100\% \tag{7}$$

式中 R_{LRR} 为卷叶率，%；R_{CE} 为防治效果指标，%；N_R 为调查卷叶数；N_T 为调查总叶数；R_{CK} 为空白对照区药后卷叶率，%；R_{PT} 为处理区药后卷叶率，%。

1.6　数据分析

试验数据采用 EXCEL2013(Microsoft Inc., USA)软件进行录入、整理，利用 SPSS19.0(SPSS Inc., USA) 统计分

析软件进行 Duncan 法多重比较及显著性分析（α=0.05），分析图采用 EXCEL 2013 软件绘制。

2 结果与分析

2.1 雾滴沉积与分布情况

2.1.1 不同施药液量的雾滴分布均匀性

雾滴在田间的分布均匀性对水稻病虫害的防治有重要影响。为描述雾滴田间分布的均匀性，采用各采样点雾滴密度的变异系数（Coefficient of Variation，CV）作为雾滴分布均匀性的指标。图 3a、3b 分别为水稻分蘖末期、孕穗期两阶段施药后，田间各雾滴采样点水稻冠层上部（Upper Canopy，UC）、冠层下部（Lower Canopy，LC）的雾滴沉积分布。水稻分蘖末期，施药液量 22.5 L/hm^2 时水稻冠层上部、下部的雾滴密度变异系数分别为 35.04%、82.71%；施药液量 15 L/hm^2 时水稻冠层上部、下部的雾滴密度变异系数分别为 49.3%、72.44%。水稻孕穗期，施药液量 22.5 L/hm^2 时水稻冠层上部、下部的雾滴密度变异系数分别 44.55%，143.95%；施药液量 15 L/hm^2 时水稻冠层上部、下部的雾滴密度变异系数分别 55.61%，57.94%。结果表明，冠层上部的雾滴分布均匀性明显优于冠层下部。冠层上部的雾滴分布主要取决于无人机离心雾化喷头的雾滴分布。冠层下部雾滴分布均匀性较差，可能主要有以下原因：水稻每个位置的疏密、长势有区别，导致雾滴穿透量不一致；无人机的下旋风场使水稻产生倒伏，倒伏中心位置冠层底部裸露，因而雾滴沉积量大，倒伏四周水稻堆叠使得雾滴无法穿透，因此雾滴沉积量极少。

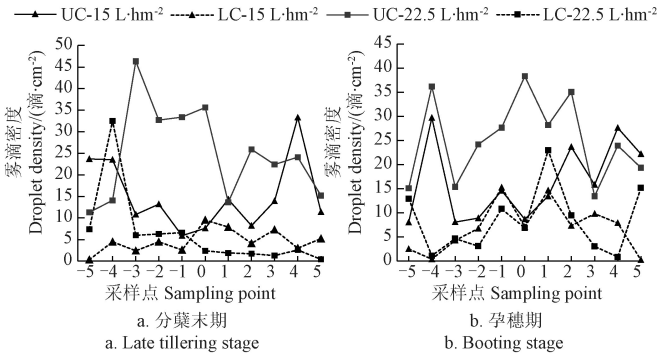

注：UC 为冠层上部，LC 为冠层下部。15, 22.5 为施药液量。
Note: UC is upper-canopy, LC is lower-canopy. 15, 22.5 is spray volume.

图 3 不同施药液量下两生育阶段施药的水稻冠层雾滴沉积分布

Fig.3 Droplets distribution on the rice canopy for two growth stages under different spray volume

2.1.2 不同施药液量对雾滴沉积的影响

水稻分蘖末期、孕穗期两施药阶段，水稻冠层的雾滴沉积如表 3 所示。结果显示，分蘖末期、孕穗期水稻冠层上部的雾滴沉积均远远大于下部，相同施药阶段与施药液量时，水稻冠层上部和下部的雾滴沉积量均有极显著差异（P<0.01）。施药液量 22.5、15 L/hm^2 时，水稻冠层上部雾滴沉积量分别较冠层下部增加了 208.42%、152.81%。可能主要是因为水稻分蘖末期、孕穗期，水稻高度已接近 90 cm，长势茂盛，无人机施药的雾滴穿透性不足。

水稻分蘖末期、孕穗期两施药阶段，施药液量 22.5 与 15 L/hm^2 的水稻冠层上部雾滴沉积量均有显著差异（分别为 P=0.02，P=0.005），施药液量 22.5 L/hm^2 较 15 L/hm^2 的水稻冠层上部雾滴沉积量分别增加了 64.77%，60.53%。施药液量 22.5 与 15 L/hm^2 对水稻冠层下部的雾滴沉积量没有显著差异。

相同施药液量时，分蘖末期、孕穗期两施药阶段的水稻冠层上部雾滴沉积量没有显著差异，冠层下部雾滴沉积量也没有显著差异。

从以上分析可知，无人机施药时水稻冠层上部的雾滴沉积效果较好，且增加施药液量对水稻冠层上部雾滴沉积的增加比较显著，有助于农药的利用。但水稻冠层下部的雾滴沉积远低于冠层上部，可能原因为当水稻比较茂盛时，无人机施药时雾滴难以穿透水稻冠层。因此，采用无人机施药，对于防治稻纵卷叶螟、水稻纹枯病等主要在水稻冠层上部的病虫害，增加施药液量会有更好的防效。

表 3 不同施药液量下水稻上、下冠层的雾滴沉积

Table 3 Droplet deposition of upper-canopy and lower-canopy under different spray volume

冠层 Canopy	施药时期 Spray period	施药液量 Spray volume/(L·hm^{-2})	雾滴覆盖率 Droplet coverage/%	雾滴密度 Droplet density/(滴·cm^{-2})	雾滴沉积量 Droplet deposition/(μL·cm^{-2})
冠层上部 Upper-canopy	分蘖末期 Late tillering	15	4.36±3.94b	16.43±8.1b	0.39±0.37b
		22.5	7.47±4.47a	25.17±8.82a	0.67±0.49a
	孕穗期 Booting stage	15	3.52±2.05b	15.07±8.38b	0.38±0.17b
		22.5	6.28±3.72a	24.96±11.12a	0.61±0.56a
冠层下部 Lower-canopy	分蘖末期 Late tillering	15	1.53±1.44a	6.93±5.02a	0.18±0.12a
		22.5	1.58±1.75a	8.27±6.84a	0.23±0.31a
	孕穗期 Booting stage	15	1.06±0.69a	4.66±2.7a	0.12±0.07a
		22.5	1.25±1.39a	6.28±9.4a	0.17±0.11a

注：表中数据为均值±标准差。数据列的字母表示相同冠层及施药时期下不同施药液量间存在显著差异（P<0.05）。
Note: Data in the table are the average value ± the standard deviation. The letter in the data column express that there are significant differences between different spray volume under the same canopy and spray period (P<0.05).

2.2 不同施药液量的稻纵卷叶螟减量施药防治效果

在水稻分蘖末期、孕穗期两阶段，两种施药液量下的减量施药对稻纵卷叶螟的防治效果如表 4 所示。同一施药阶段、施药液量时，农药剂量对稻纵卷叶螟的防治效果均有显著差异（P<0.05）。农药剂量 100%时，稻纵卷叶螟防治效果最好；农药剂量 80%时，稻纵卷叶螟防治效果最差。与人工电动喷雾器施药（KES）的常规防治效果相比，两阶段施药结果表明：农药剂量 100%时，施药液量 15、22.5 L/hm^2 的稻纵卷叶螟防治效果均优于人工电动喷雾器施药（KES）。施药液量 15 L/hm^2、农药剂量 90%时，两阶段的防治效果与人工电动喷雾器（KES）均没有显著差异，即施药液量 15 L/hm^2、农药减量 10%可达到人工电动喷雾器（KES）的常规防治效果。施药液量 22.5 L/hm^2、农药剂量 80%时，两阶段的防治效果与人工

电动喷雾器（KES）均没有显著差异，即施药液量 22.5 L/hm^2、农药减量 20%可达到人工电动喷雾器（KES）的常规防治效果。

农药剂量相同条件下，在分蘖末期、孕穗期两阶段，施药液量 22.5、15 L/hm^2 时的稻纵卷叶螟防治效果均存在显著差异。分蘖末期施药后，农药剂量 80%、90%、100%时，施药液量 22.5 L/hm^2 的防效较 15 L/hm^2 分别提升了 26.8%、25.11%、14.32%；孕穗期施药后，农药剂量 80%、90%、100%时，施药液量 22.5 L/hm^2 的防效较 15 L/hm^2 分别提升了 11.25%、5.88%、4.37%。由雾滴沉积试验结果分析可知，施药液量 22.5 与 15 L/hm^2 对水稻冠层上部的雾滴沉积有极显著差异，施药液量 22.5 L/hm^2 时水稻冠层上部的雾滴沉积量较 15 L/hm^2 时增加了 60.53%。因此，在相同农药剂量下，由于施药液量 22.5 L/hm^2 较 15 L/hm^2 有更好的雾滴沉积效果，水稻叶片表面雾滴沉积量更大不仅有利于内吸性农药的吸收，也有利于非内吸性农药增大触杀面积，从而有效提高稻纵卷叶螟的防治效果。

表 4　不同施药液量下无人机减量施药的稻纵卷叶螟防效

Table 4　Control efficacy of cnaphalocrocis medinalis for UAV reduced pesticide application under different spray volume

施药方式 Spray method	施药液量 Spray volume/(L·hm^{-2})	农药剂量 Pesticide dosage/%	防治效果指标 Control efficacy/%	
			分蘖末期 Late tillering stage	孕穗期 Booting stage
UAV	15	80	57.83±8.14b	81.63±8.74b
		90	63.64±12.03ab	90.96±2.48ab
		100	74.31±5.5a	93.21±3.49a
	22.5	80	73.33±7.33b	90.82±4.09b
		90	79.62±8.07ab	96.31±2.19a
		100	84.95±5.25a	97.28±1.88a
KES	450	100	62.66±8.41	89.89±2.19

注：表中数据为均值±标准差。数据列的字母表示相同施药方式及施药液量下不同农药剂量间存在显著差异（P<0.05）。

Note: Data in the table are the average value ± the standard deviation. The letter in the data column express that there are significant differences between different pesticide dosage under the same spray method and spray volume (P<0.05).

3　讨　论

雾滴沉积试验结果表明，无人机施药时，水稻冠层上部的雾滴沉积效果要极大的优于冠层下部，施药液量 22.5、15 L/hm^2 时水稻冠层上部的雾滴沉积量较冠层下部分别增加了的 208.42%、152.81%；增大施药液量有利于提升水稻冠层上部的雾滴沉积效果，施药液量 22.5 L/hm^2 时，水稻冠层上部的雾滴沉积量比 15 L/hm^2 时的提升了 60.53%。Wang 等[28]在小麦无人机施药中测试了 3 种施药液量（9.0、16.8、28.1 L/hm^2）下小麦冠层的雾滴沉积，结果显示，施药液量 9.0 L/hm^2 时雾滴沉积量较小，且防治效果较差。Qin 等[27]在水稻无人机施药中测试了两种飞行高度（0.8、1.5 m）、两种飞行速度（3、5 m/s）下水稻冠层的雾滴沉积，雾滴采样数据显示上层的雾滴沉积量显著大于下层。Chen 等[32]在水稻无人机施药中测试了 3 种喷嘴（LU110-01、LU110-015、LU110-02）下水稻冠层的雾滴沉积，雾滴沉积量数据也显示上层显著高于下层。但以上文献没有对上下层雾滴沉积进行量化对比分析，也没有分析上层的雾滴沉积量显著高于下层的原因。水稻冠层上部的雾滴沉积极大的优于下层，主要是由于在无人机施药位置高、雾滴小，难以穿透分蘖后期长势茂盛的水稻。虽然无人机的下压风可以增加部分位置的水稻冠层下部的雾滴沉积，但下压风同时也使得水稻向四周倒伏，同样使得雾滴难以穿透到倒伏处水稻冠层下部，同时导致冠层下部的雾滴分布均匀性变差。施药液量 22.5 L/hm^2 较 15 L/hm^2 水稻冠层上部的平均雾滴沉积量提升了 60.53%，高于施药液量 50%的提升。可能主要原因应为两种施药液量下穿透到水稻冠层下部的雾滴沉积量差异较小，且都较少，大部分沉积在冠层上部。

两种施药液量、3 种农药剂量的水稻稻纵卷叶螟防治试验结果表明，施药液量越大稻纵卷叶螟的防效越好，施药液量 22.5 L/hm^2 较 15 L/hm^2 的防治效果在水稻分蘖末期、孕穗期分别提升了 21.51%、7%；农药剂量越大稻纵卷叶螟的防效越好；处理（施药液量 22.5 L/hm^2、农药剂量 80%）、处理（施药液量 15 L/hm^2、农药剂量 90%）和背负式电动喷雾器（KES）人工施药的稻纵卷叶螟防治效果没有显著差异。薛新宇等[22]在 N-3 型无人直升机施药方式对稻纵卷叶螟防治效果的田间试验中，测试了不同剂量和不同飞行高度下稻纵卷叶螟的防治效果，结果表明四种农药剂量（60%、70%、80%、100%）下剂量 100%的防治效果最好，3 种飞行高度（3、5、7 m）下高度 3 m 时的防治效果最好。张海燕等[26]测试了电动单旋翼与电动多旋翼无人机水稻田间的农药喷施作业效果，试验结果表明电动单旋翼在防治稻纵卷叶螟时效果更好。但没有涉及施药液量、农药剂量组合与水稻稻纵卷叶螟的防治效果关系及农药减量的研究。施药液量越大稻纵卷叶螟的防效越好，主要原因应为施药液量越大时雾滴的沉积越好。施药液量 22.5 L/hm^2、农药剂量 80%时与常规背负式电动喷雾器（KES）人工施药的稻纵卷叶螟防治效果没有显著差异，主要是因为常规背负式电动喷雾器（KES）人工施药高度低、施药液量大、雾滴大，雾滴的穿透性较好，下层的雾滴沉积量相对较大，同时流失到稻田中的雾滴也多，导致水稻冠层上部的农药沉积量相对较少。

4　结　论

本文使用了罗丹明 B 示踪剂及铜版纸测量了无人机施药时不同施药液量下水稻冠层上部和下部的雾滴沉积，测试了无人机施药时两种施药液量、3 种农药剂量组合及背负式电动喷雾器人工施药下水稻稻纵卷叶螟的防治效果。对试验结果的分析得到以下结论：1）无人机施药较人工施药，对稻纵卷叶螟的防治有更好的防效；2）无人机施药时，施药液量 22.5 L/hm^2 较 15 L/hm^2 的水稻冠层上部的雾滴沉积效果更好，农药利用率更高，对主要危害水稻冠层上部的稻纵卷叶螟有更好的防治效果；3）无人机施药时，施药液量 22.5 L/hm^2 较 15 L/hm^2 有更好的农药减量效果，施药液量 22.5 L/hm^2、农药剂量 80%的无人机施药可达到农药剂量 100%时背负式电动喷雾器人工施药的稻纵卷叶螟防治效果。

［参 考 文 献］

[1] 张玲. 水稻重要病虫害综合防治技术与应用研究[D]. 长沙：湖南农业大学，2018.
Zhang Ling. Studies of Integrated Control Technology and Application of Important Pests and Diseases in Rice[D]. Changsha: Hunan Agricultural University, 2018. (in Chinese with English abstract)

[2] 王艳青. 近年来中国水稻病虫害发生及趋势分析[J]. 中国农学通报，2006，22(2)：343-347.
Wang Yanqing. Analysis on the occurrence and development of rice diseases and insects in China[J]. Chinese Agricultural Science Bulletin, 2006, 22(2): 343-347. (in Chinese with English abstract)

[3] 全国农业技术推广服务中心. 2017 年全国水稻主要病虫害发生趋势预报[J]. 种业导刊，2017(3)：11.

[4] 何雄奎. 中国植保机械与施药技术研究进展[J]. 农药学学报，2019，21(5/6)：921-930.
He Xiongkui. Research and development of crop protection machinery and chemical application technology in China[J]. Chinese Journal of Pesticide Science, 2019, 21(5/6): 921-930. (in Chinese with English abstract)

[5] 何雄奎. 改变我国植保机械和施药技术严重落后的现状[J]. 农业工程学报，2004，20(1)：13-15.
He Xiongkui. Improving severe draggling actuality of plant protection machinery and its application techniques[J]. Transactions of the Chinese Society of Agricultural Engineering (Transactions of the CSAE), 2004, 20(1): 13-15. (in Chinese with English abstract)

[6] 弋晓康. 我国植保机械的现状及发展趋势探讨[J]. 农机化研究，2007(3)：218-220.
Yi Xiaokang. Discussion on the present situation and development trends of plant protection equipment in China[J]. Journal of Agricultural Mechanization Research, 2007(3): 218-220. (in Chinese with English abstract)

[7] 华小梅，江希流. 我国农药环境污染与危害的特点及控制对策[J]. 环境科学研究，2000，13(3)：40-43.
Hua Xiaomei, Jiang Xiliu. Characteristics and control countermeasures of pesticide pollution and its damage on environment in China[J]. Research of Environmental Sciences, 2000, 13(3): 40-43. (in Chinese with English abstract)

[8] Lan Y B, Chen S D, Fritz B K. Current status and future trends of precision agricultural aviation technologies[J]. International Journal of Agricultural and Biological Engineering. 2017, 10(3): 1-17.

[9] 袁会珠，薛新宇，闫晓静，等. 植保无人飞机低空低容量喷雾技术应用与展望[J]. 植物保护，2018，44(5)：152-158.
Yuan Huizhu, Xue Xinyu, Yan Xiaojing, et al. Applications and prospects in the unmanned aerial system for low-altitude and low-volume spray in crop protection[J]. Plant Protection, 2018, 44(5): 152-158. (in Chinese with English abstract)

[10] Wang L L, Lan Y B, Zhang Y L, et al. Applications and prospects of agricultural unmanned aerial vehicle obstacle avoidance technology in China[J]. Sensors 2019, 19: 642.

[11] Yang S L, Yang X B, Mo J Y. The application of unmanned aircraft systems to plant protection in China[J]. Precision Agriculture, 2018(19): 278-292.

[12] Kim J, Kim S, Ju C, et al. Unmanned aerial vehicles in agriculture: A review of perspective of platform, control, and applications[J]. Ieee Access, 2019(7): 105100-105115.

[13] Huang Y, Hoffmann W C, Lan Y, et al. Development of a spray system for an unmanned aerial vehicle platform[J]. Applied Engineering in Agriculture, 2009, 25(6): 803-809.

[14] Hassler S C, Baysal-Gurel F. Unmanned aircraft system (UAS) technology and applications in agriculture[J]. Agronomy, 2019, 9: 618.

[15] Fritz B K, Hoffmann W C. Update to the USDA-ARS fixed-wing spray nozzle models[J]. Transactions of the ASABE, 2015, 58(2): 281-295.

[16] Lan Y B, Hoffmann W C, Fritz B K, et al. Spray drift mitigation with spray mix adjuvants[J]. Applied Engineering in Agriculture, 2008, 24(1): 5-10.

[17] Wang C L, He X K, Wang X N, et al. Testing method and distribution characteristics of spatial pesticide spraying deposition quality balance for unmanned aerial vehicle[J]. International Journal of Agricultural and Biological Engineering, 2018, 11(2): 18-26.

[18] Teske M E, Wachspress D A, Thistle H W. Prediction of aerial spray release from UAVs[J]. Transactions of the ASABE, 2018, 61(3): 909-918.

[19] Meng Y H, Song J L, Lan Y B, et al. Harvest aids efficacy applied by unmanned aerial vehicles on cotton crop[J]. Industrial Crops & Products, 2019, 140: 111645.

[20] Zhou Q Q, Xue X Y, Qin W C, et al. Analysis of pesticide use efficiency of a UAV sprayer at different growth stages of rice[J]. International Journal of Precision Agricultural Aviation, 2020, 3(1): 38-42

[21] 陈盛德，兰玉彬，李继宇，等. 航空喷施与人工喷施方式对水稻施药效果比较[J]. 华南农业大学学报，2017，38(4)：103-109.
Chen Shengde, Lan Yubin, Li Jiyu, et al. Comparison of the pesticide effects of aerial and artificial spray applications for rice[J]. Journal of South China Agricultural University, 2017, 38(4): 103-109. (in Chinese with English abstract)

[22] 薛新宇，秦维彩，孙竹，等. N-3 型无人直升机施药方式对稻飞虱和稻纵卷叶螟防治效果的影响[J]. 植物保护学报，2013，40(3)：273-278.
Xue Xinyu, Qin Weicai, Sun Zhu, et al. Effects of N-3 UAV spraying methods on the efficiency of insecticides against plant hoppers and cnaphalocrocis medinalis[J]. Acta Phytophylacica Sinica, 2013, 40(3): 273-278. (in Chinese with English abstract)

[23] 陈盛德，兰玉彬，李继宇，等. 小型无人直升机喷雾参数对杂交水稻冠层雾滴沉积分布的影响[J]. 农业工程学报，2016，32(17)：40-46.
Chen Shengde, Lan Yubin, Li Jiyu, et al. Effect of spray parameters of small unmanned helicopter on distribution regularity of droplet deposition in hybrid rice canopy[J]. Transactions of The Chinese Society of Agricultural Engineering (Transactions of the CSAE), 2016, 32(17): 40-46. (in Chinese with English abstract)

[24] 漆海霞，陈鹏超，兰玉彬，等. 不同电动植保无人机稻田雾滴沉积分布试验研究[J]. 农机化研究，2019(9)：147-151.
Qi Haixia, Chen Pengchao, Lan Yubin, et al. Experimental study on droplet deposit distribution of different electric uavs in rice fields[J]. Journal of Agricultural Mechanization Research, 2019(9): 147-151. (in Chinese with English abstract)

[25] 李继宇，兰玉彬，彭瑾. 无人机喷雾粒径对水稻冠层雾滴沉积效果的影响[J]. 湖南农业大学学报：自然科学版，2018，44(4)：442-446.
Li Jiyu, Lan Yubin, Peng Jin. Effect of droplet size spraying by unmanned aerial vehicle on droplet deposition in rice

canopy[J]. Journal of Hunan Agricultural University: Natural Sciences, 2018, 44(4): 442-446. (in Chinese with English abstract)

[26] 张海艳，兰玉彬，文晟，等. 植保无人机水稻田间农药喷施的作业效果[J]. 华南农业大学学报，2019，40(1)：116-124. Zhang Haiyan, Lan Yubin, Wen Sheng, et al. Operational effects of unmanned helicopters for pesticide spraying in rice field[J]. Journal of South China Agricultural University, 2019, 40(1): 116-124. (in Chinese with English abstract)

[27] Qin W C, Qiu B J, Xue X Y, et al. Droplet deposition and control effect of insecticides sprayed with an unmanned aerial vehicle against plant hoppers[J]. Crop Protection, 2016, 79-88.

[28] Wang G B, Lan Y B, Qi H X, et al. Field evaluation of an unmanned aerial vehicle (UAV) sprayer: Effect of spray volume on deposition and the control of pests and disease in wheat[J]. Pest Management Science, 2019, 75: 1546-1555.

[29] Zhu H P, Salyani M, Fox R D, A portable scanning system for evaluation of spray deposit distribution[J]. Computers and Electronics in Agriculture, 2011, 76: 38-43.

[30] Hoffmann W C, Hewitt A J. Comparison of three imaging systems for water-sensitive papers[J]. Applied Engineering in Agriculture, 2005, 21(6): 961-964.

[31] 中华人民共和国农业部农药检定所. 农药田间药效试验准则（一）杀虫剂防治稻纵卷叶螟：GB/T179802—2000[S]. 北京：中国标准出版社，2000.

[32] Chen P C, Lan Y B, Huang X Y, et al. Droplet deposition and control of planthoppers of different nozzles in two-stage rice with a quadrotor unmanned aerial vehicle[J]. Agronomy, 2020, 10: 303.

P20 plant protection UAV to control cnaphalocrocis medinalis by reduced pesticide application

Zeng Wen[1,2], Deng Jizhong[1,2], Gao Qichao[1,2], Jia Ruichang[1,2], Lan Yubin[2,3], Zhang Jianling[1,2], Chen Pengchao[2,3], Xiao Hanxiang[4], Zhang Yali[1,2※]

(1. *College of Engineering, South China Agricultural University, Guangzhou* 510642, *China*; 2. *National Center for International Collaboration Research on Precision Agricultural Aviation Pesticides, Spraying Technology* (*NPAAC*), *Guangzhou* 510642, *China*; 3. *College of Electronics Engineering, South China Agricultural University, Guangzhou* 510642, *China*; 4. *Plant Protection Institute, Guangdong Agricultural Science Academy*, *Guangzhou* 510640, *China*)

Abstract: Plant protection Unmanned Aerial Vehicles (UAV) have widely been applied for rice diseases and pest control in China. This study aims to promote the reduced application of pesticides in rice, thereby exploring the control efficacy of pests and diseases using plant protection UAV. A field experiment was also conducted using a P20 quad-rotor plant protection UAV with a centrifugal spray system at the late tillering and booting stage of rice. A droplet deposition experiment of rice canopy was performed on two spray volume levels of 15 and 22.5 L/hm^2. Three levels of pesticide dosage were determined to be 480, 540, and 600 mL/hm^2 (80%, 90%, and 100% of recommended dosage) for the cnaphalocrocis medinalis control efficacy with the same two spray volume levels (15, and 22.5 L/hm^2). Meanwhile, a pesticide spraying test was conducted with a knapsack electric sprayer (KES) for comparison as well. The droplet deposition test showed that the droplet was evenly distributed in the upper-canopy, better than that in the lower-canopy. There was an extreme difference in the droplet deposition on the upper- and lower-canopy of rice at the same spray period and spray volume. In particular, the droplet deposition on the upper-canopy was much larger than that on the lower-canopy. There were also significant differences among the droplet deposition on the upper-canopy between 15 and 22.5 L/hm^2. Compared with that of 15 L/hm^2, the spray volume of 22.5 L/hm^2 increased the droplet deposition on the upper-canopy by 64.77%, and 60.53% at the late tillering and booting stage, respectively. Nevertheless, there was no significant difference among the droplet deposition of upper- and lower-canopy between the late tillering and the booting stage. The control efficacy test showed that the pesticide dosage presented a great effect on the control efficacy of cnaphalocrocis medinalis, indicating that the larger pesticide dosage achieved better, where the control efficacy of 100% pesticide dosage was the best. Specifically, the control efficacy of plant protection UAV was better than that of KES at the same pesticide dosage. There was a significant difference in the control efficacy between the spray volume of 15 and 22.5 L/hm^2. The control efficacy at the late tillering and booting stage with 22.5 L/hm^2 increased by 21.51% and 7%, respectively, compared with 15 L/hm^2. No significant difference was found on the control efficacy in the treatment of spray volume 22.5 L/hm^2 and pesticide dosage 80%, spray volume 15 L/hm^2 and pesticide dosage 90%, as well as KES application. The plant protection UAV with a spray volume of 22.5 L/hm^2 achieved better droplet deposition on the upper-canopy, and higher control efficacy. Additionally, a spray volume of 22.5 L/hm^2 and pesticide dosage of 80% achieved the same cnaphalocrocis medinalis control efficacy as that with the KES with the pesticide dosage of 100%. This finding can provide a sound reference to the parameters set for the plant protection UAV spraying pesticides, thereby promoting the reduction of pesticides in rice.

Keywords: UAV; spray; reduced pesticide application; droplet deposition; cnaphalocrocis medinalis

祁媛, 徐伟诚, 王林琳, 等. 基于无人机遥感影像的沙糖橘果树提取方法研究 [J]. 华南农业大学学报, 2020, 41(6): 126-133.
QI Yuan, XU Weicheng, WANG Linlin, et al. Study on the extraction method of sugar tangerine fruit trees based on UAV remote sensing images[J]. Journal of South China Agricultural University, 2020, 41(6): 126-133.

基于无人机遥感影像的沙糖橘果树提取方法研究

祁　媛[1,2]，徐伟诚[2,3]，王林琳[2,3]，贾瑞昌[1,2]，兰玉彬[2,3]，张亚莉[1,2]
(1 华南农业大学 工程学院，广东 广州 510642； 2 国家精准农业航空施药技术国际联合研究中心，广东 广州 510642；
3 华南农业大学 电子工程学院/人工智能学院，广东 广州 510642)

摘要:【目的】通过无人机获取沙糖橘果园的遥感图像，快速提取果树分布位置，为果树的长势监测和产量预估提供参考。【方法】以无人机拍摄的可见光遥感图像为研究对象，计算超红指数、超绿指数、超蓝指数、可见光波段差异植被指数、红绿比指数和蓝绿比指数 6 种可见光植被指数，使用双峰阈值法选取阈值进行果树的提取。在使用光谱指数进行识别的基础上，结合数字表面模型作为识别模型的输入变量，进行对比试验。【结果】相比使用单一光谱指数，结合数字表面模型提高了果树和非果树像元的提取精度，6 次波段融合后的总体精度均大于 97%。超红指数与数字表面模型结合后的总体精度最高，为 98.77%，Kappa 系数为 0.956 7，植被信息提取精度优于其他 5 种可见光植被指数与数字表面模型结合后的提取精度。【结论】数字表面模型结合可见光植被指数的提取方法能够更深层次地挖掘遥感数据蕴含的信息量，为影像中色调相似地物的提取提供参考。

关键词: 无人机遥感；果树提取；可见光植被指数；数字表面模型；面向对象法
中图分类号: TP79　　**文献标志码:** A　　**文章编号:** 1001-411X(2020)06-0126-08

Study on the extraction method of sugar tangerine fruit trees based on UAV remote sensing images

QI Yuan[1,2], XU Weicheng[2,3], WANG Linlin[2,3], JIA Ruichang[1,2], LAN Yubin[2,3], ZHANG Yali[1,2]
(1 College of Engineering, South China Agricultural University, Guangzhou 510642, China; 2 National Center for International Collaboration Research on Precision Agricultural Aviation Pesticides Spraying Technology, Guangzhou 510642, China; 3 College of Electronic Engineering /College of Artificial Intelligence, South China Agricultural University, Guangzhou 510642, China)

Abstract: 【Objective】To obtain remote sensing image of sand sugar tangerine orchard by UAV, rapidly extract the distribution position of fruit trees, and provide references for growth monitoring and yield prediction of fruit trees.【Method】The visible light remote sensing images taken by drones were used as the research object. Six visible light vegetation indexes of excess red index, excess green index, excess blue index, visible band differential vegetation index, red-green ratio index and blue-green ratio index were calculated. We used the double peak threshold method to select the threshold for fruit tree extraction. Based on the spectral index identification, digital surface model was added as input variable of the identification model, and the comparative test was conducted.【Result】Compared with using a single spectral index, the addition of digital surface model improved the extraction accuracies of fruit tree and non fruit tree pixels. The total accuracies of six band fusions

收稿日期:2020–07–22　　**网络首发时间:**2020–10–10 14:07:09
网络首发地址:https://kns.cnki.net/kcms/detail/44.1110.S.20201010.1119.002.html
作者简介:祁　媛 (1995—)，女，硕士研究生，E-mail: yuanqi@stu.scau.edu.cn；通信作者：兰玉彬 (1961—)，男，教授，博士，E-mail: ylan@scau.edu.cn；张亚莉 (1975—)，女，副教授，博士，E-mail：ylzhang@scau.edu.cn
基金项目:广东省重点领域研发计划 (2019B020221001)；广东省科技计划 (2018A050506073)；广州市科技计划 (201807010039)

were all greater than 97%. The total accuracy of excess red index combined with digital surface model was the highest (98.77%) with Kappa coefficient of 0.956 7, and the vegetation extraction accuracies were superior to those of other five combinations of visible light vegetation indexes with digital surface model. 【Conclusion】The combination of digital surface model with visible light vegetation index can excavate more deeply the information contained in the remote sensing data, and provide a reference for the extraction of similar tonal features in the image.

Key words: UAV remote sensing; fruit tree extraction; visible light vegetation index; digital surface model; object-oriented method

沙糖橘是我国岭南地区的重要水果，需要优质的种植地和高质量的栽培管理保证产量和口感。为了确保当地农村的支柱产业有效平稳地发展，需要对沙糖橘的果树长势进行监测。提取果园中的沙糖橘果树对分析植被分布影响因素和评价果树生长环境有重要意义。

无人机作业灵活，作业效率高，影像分辨率高，与传统卫星遥感影像和人工地面采集数字影像方法形成互补趋势，在各领域的遥感监测中发挥重要作用[1-4]。国内外学者基于无人机遥感影像技术和植被指数模型对植被信息的提取进行了大量研究。Xu 等[5] 利用无人机平台收集农田的可见光遥感图像，监测和提取耕地的可见光植被指数获取其面积、形状和地理位置信息；Choi 等[6] 运用固定翼无人机获取多光谱图像，建立沙丘的植被指数模型，对沙丘的部分植被覆盖进行估算；Zhang 等[7] 统计分析得到 9 种可见光植被指数与玉米、棉花、甘蔗和水稻 4 种植被覆盖度之间的关系，发现每种作物对应的最佳植被指数不一定相同，对应的植被覆盖度模型准确度也不相同；高永平等[8] 通过无人机获取荒漠区的可见光图像，建立植被指数与植被覆盖度的关系模型，成功以高精度提取荒漠区中的植被。

上述研究的共同点是通过无人机遥感获取可见光图像，利用一种或几种可见光植被指数提取植被信息。遥感图像不仅包含光谱特征，还具有空间特征和纹理特征。本研究运用无人机影像，结合空间特征中的高度模型与 6 种可见光植被指数模型，对沙糖橘果树的提取精度进行对比分析，以期获得一种简单、方便、有效的沙糖橘植被提取方法，扩大无人机遥感技术在果园中的应用，为我国果园果树的监测提供参考。

1　材料与方法

1.1　无人机影像数据的获取

研究地点位于广东省肇庆市四会市果园(23°36′N，112°68′E)，亚热带季风气候，雨热充足，适合沙糖橘的生长。试验地概况如图 1 所示。

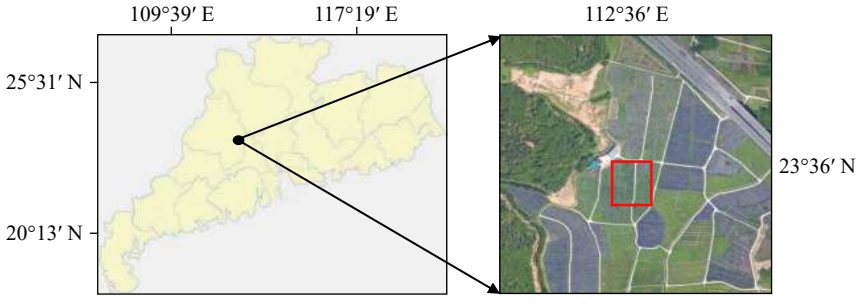

图 1　试验地概况

Fig. 1　The overview of experimental site

试验采集平台为深圳大疆精灵 4 无人机，配备 6.17 mm×4.55 mm 的 2 000 万像素 CMOS 传感器，无需在特定的场地起飞与降落，可在空中长时间悬停，配备的 RTK 和六向视觉传感器使飞行更加安全稳定。试验数据采集于 2020 年 6 月 2 日，如图 2 所示，飞行高度为 100 m，巡航速度为 20 km/h，飞行航线的旁向和航向重叠度均为 80%，单次采集 320 张 RGB 图像，图像分辨率为 5 472 像素×3 648 像素，地面分辨率为 3.66 cm。通过 Pix4DMapper 软件对图像进行拼接，获得试验地的



图 2 试验数据采集

Fig. 2 Experiment data collection

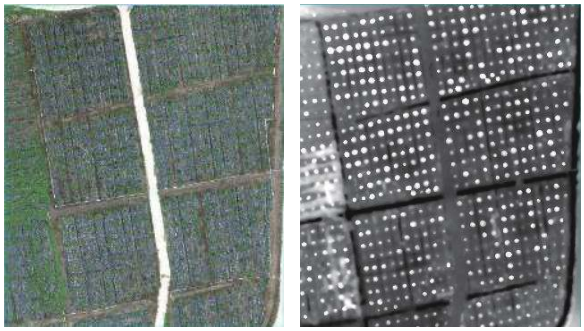

a: 正射图 a: Orthophoto

b: 数字表面模型 b: Digital surface model

图 3 正射图和数字表面模型

Fig. 3 Orthophoto and digital surface model

正射图像和数字表面模型 (Digital surface model)，如图 3 所示。

1.2 果树植被覆盖度的提取方法

1.2.1 *植被指数的选取* 遥感领域中使用大量的植被指数评价植被覆盖度及生长情况，但目前基于可见光波段的植被指数相对较少。本研究参考目前研究相对较多且精度较高的可见光植被指数，选取了 6 种植被指数：超红指数 (Excess red index)[9]、超绿指数 (Excess green index)[10]、超蓝指数 (Excess blue index)[11]、可见光波段差异植被指数 (Visible band differential vegetation index)[5]、红绿比指数 (Red-green ratio index)[12]、蓝绿比指数 (Blue-green ratio index)[13]。这 6 种植被指数的计算公式和理论区间如表 1 所示。

表 1 可见光植被指数

Table 1 Vegetation indexes based on visible spectrum

植被指数 Vegetation index	表达式[1)] Equation	理论区间 Theory interval
超红指数 Excess red index	$1.4R-G$	[−255, 357]
超绿指数 Excess green index	$2G-R-B$	[−255, 510]
超蓝指数 Excess blue index	$1.4B-G$	[−255, 357]
可见光波段差异植被指数 Visible band differential vegetation index	$\frac{2G-R-B}{2G+R+B}$	[−1, 1]
红绿比指数 Red-green ratio index	$\frac{R}{G}$	[−1, 1]
蓝绿比指数 Blue-green ratio index	$\frac{B}{G}$	[−1, 1]

1) *R*: 红光波段, *G*: 绿光波段, *B*: 蓝光波段

1) *R*: Red light wave band, *G*: Green light wave band, *B*: Blue light wave band

1.2.2 *阈值的确定和植被信息的提取* 基于无人机遥感图像的植被提取的关键在于选取合适的阈值区分植被和非植被，本研究选取双峰阈值法提取沙糖橘果树和非果树。双峰阈值法通常是选取 2 种地物，生成具有 2 个明显波峰的直方图。这 2 个波峰分别对应所选对象较多数目的像元，波峰之间的波谷则对应所选对象边缘相对较少数目的像元，一般选择两峰之间的最低点或者交点作为最佳阈值[14-15]，示意图如图 4 所示。果树与非果树的直方图具有明显的双峰性质，因此该方法可以呈现较好的分割效果。

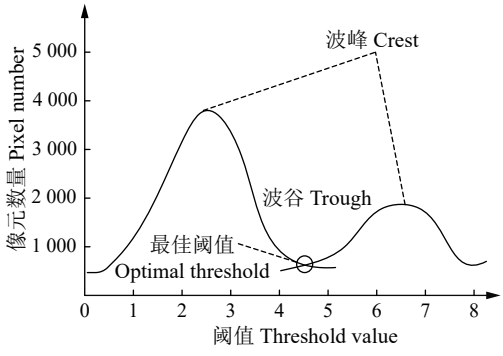

图 4 双峰阈值法示意图

Fig. 4 Schematic diagram of the double peak threshold method

利用遥感信息提取植被的方法中，面向对象的分类技术是将集合临近像元作为对象，识别感兴趣的光谱元素来提高分类结果的精度或者实现矢量输出，此法充分利用多光谱数据的空间、纹理和光谱信息进行分割和分类[16]。本研究通过基于规则的面向对象分类方法，根据其空间特征和光谱特征对对象进行分类，克服像元层次分类中的不足，具有良好的平滑性和较高的分类精度[17]。采用此分类方法从光谱和形状 2 个方面刻画果树和非果树像元，通过 ENVI 软件设定、提前统计完成的阈值规则，对上述 6 种植被指数模型进行果树与非果树的分类，能够有效地提供对象的几何和拓扑信息，更精准地提取出果树。

1.2.3　*数字表面模型中的植被信息提取*　可见光植被指数主要反映植被在可见光下反射与土壤背景之间的差异，在一定条件下可定量说明植被的生长情况。但是仅根据植被的光谱特性对植被进行提取，很难有效地解决同谱异物与同物异谱的问题，从而造成错分漏分且分类精度低。数字表面模型包含了地表果树和非果树等高度的地面高程模型，涵盖了除去地面以外的其他地表信息的高程，可以最真实地表达果园地面的起伏情况，如图 5所示。数字表面模型有益于区分果园中果树和草地这 2 类色调相类似的地物。

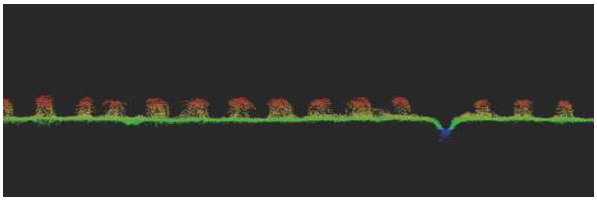

图 5　数字表面模型高程示意图

Fig. 5　Elevation diagram of digital surface model

本文拟将 6 种可见光植被指数计算结果图像与数字表面模型进行融合，加入果树与非果树的高程信息，使用基于规则的面向对象分类方法进行果树的提取，并将得到的分类精度与使用单一可见光植被指数的植被提取精度进行对比。

1.2.4　*植被信息提取结果的评价方法*　目前较为常用的植被提取评价方法是通过人机交互的方式，利用感兴趣区域把试验地块分为植被像元和非植被像元，结合地面调查数据和图像真实状态进行目视解译。此法受人力物力等条件的限制，不适合作为复杂大区域下的植被指数覆盖度提取精度评价。本研究使用混淆矩阵进行准确性评价，该矩阵是评估分类模型精度的一种可视化显示工具，通过目视判读的方法在遥感图像上各选取 60 个果树与非果树区域作为验证样本，样本的采样遵循随机原则，确保选择每个单个样本的概率完全相同。将每个实测像元的位置和分类与图像中相应的位置和分类相比较获得分类精度，并根据以下公式计算 Kappa 系数 (K)。

$$p_0 = \frac{a_{11} + a_{22} + a_{33} + \cdots + a_{nn}}{N}, \tag{1}$$

$$p_e = \frac{a_1 b_1 + a_2 b_2 + a_3 b_3 + \cdots + a_n b_n}{N^2}, \tag{2}$$

$$K = \frac{p_0 - p_e}{1 - p_e}, \tag{3}$$

式中，p_0是总体分类精度，p_e 是机遇一致性，n 是混淆矩阵方程的阶，N 是样本总数，$a_n b_n$ 是列 (行) 中所有值的总和。

2　结果与分析

2.1　可见光植被指数的计算与分析

以无人机采集的遥感影像作为数据源，根据表 1 的公式分别计算各可见光的植被指数，植被和非植被可以清晰地呈现，计算结果如图 6 所示。

为了更好地对比这 6 种可见光植被指数的提取结果，本研究只提取果树，将地物分为果树和非果树，每种地物选取 100 个感兴趣区域进行统计，并统计特征值。由表 2 可知，这 6 种可见光植被指数在植被信息和非植被信息之间差异较大，无重叠交叉部分，对于利用可见光进行植被信息识别具有较好的效果。

2.2　植被信息提取与精度评价

为获取通过这 6 种可见光植被指数进行植被信息提取时的阈值，本研究通过 ENVI 软件统计分析沙糖橘果树与非果树的直方图。本研究试验时天气晴朗，忽略天气因素对图像处理结果的影响。从图 7 可知，6 种可见光植被指数的直方图呈明显的双峰分布，表明相对应的地物区分性较强，适合可见光波段植被信息的提取，并且果树像元与非果树像元的峰值相差较大，在图像中易于选择合适的数值作为分割阈值。

根据确定的阈值，利用基于规则的面向对象分类方法，设定阈值规则，进行植被信息的提取，得到 6 种可见光植被指数对应的植被分类提取结果。以无人机遥感图像作为数据源，根据目视判读在图像上选取 60 个果树和 60 个非果树的验证样本，将分类结果当作真值，分别对这 2 种地物的分类结果计算混淆矩阵，得到各可见光植被指数的提取精度评

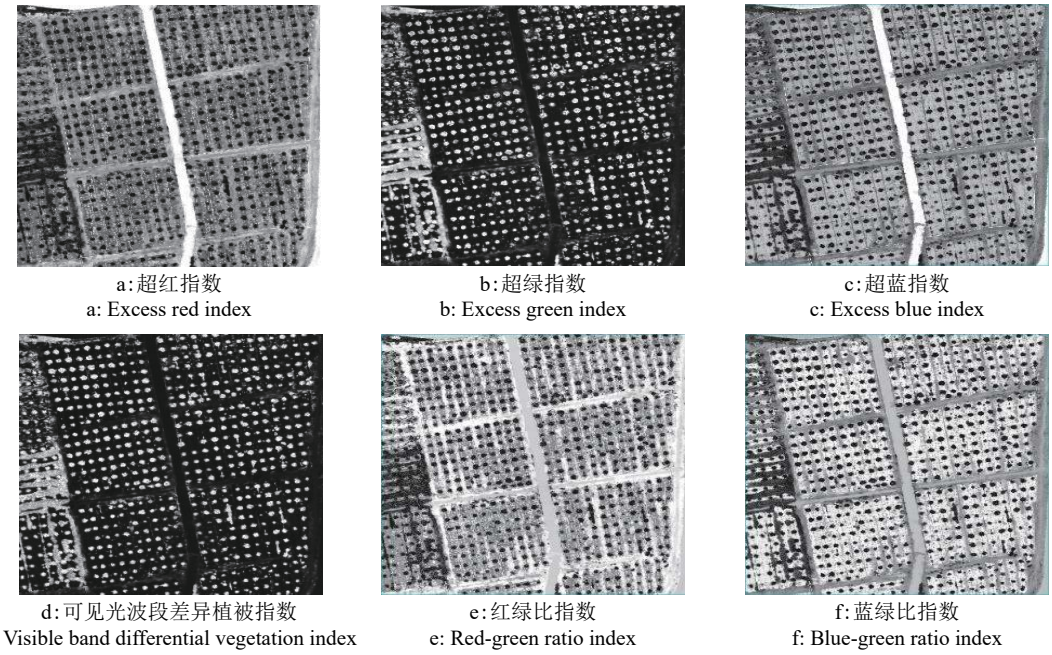

a:超红指数
a: Excess red index

b:超绿指数
b: Excess green index

c:超蓝指数
c: Excess blue index

d:可见光波段差异植被指数
d: Visible band differential vegetation index

e:红绿比指数
e: Red-green ratio index

f:蓝绿比指数
f: Blue-green ratio index

图 6　6 种可见光植被指数计算结果

Fig. 6　Calculation results of six visible light vegetation indexes

表 2　基于感兴趣区域的 6 种可见光植被指数的统计值

Table 2　Statistics of six visible light vegetation indexes based on region of interest

植被指数 Vegetation index	果树 Fruit tree		非果树 Non fruit tree	
	平均值 Mean	标准差 Standard deviation	平均值 Mean	标准差 Standard deviation
超红指数 Excess red index	−27.293 4	11.959 8	46.642 1	30.383 9
超绿指数 Excess green index	115.230 7	25.873 2	9.023 5	18.045 8
超蓝指数 Excess blue index	−39.266 7	15.487 6	44.257 4	28.460 9
可见光波段差异植被指数 Visible band differential vegetation index	0.339 2	0.087 9	0.021 8	0.046 3
红绿比指数 Red-green ratio index	0.532 7	0.097 3	0.960 9	0.119 6
蓝绿比指数 Blue-green ratio index	0.466 5	0.104 1	0.960 5	0.130 6

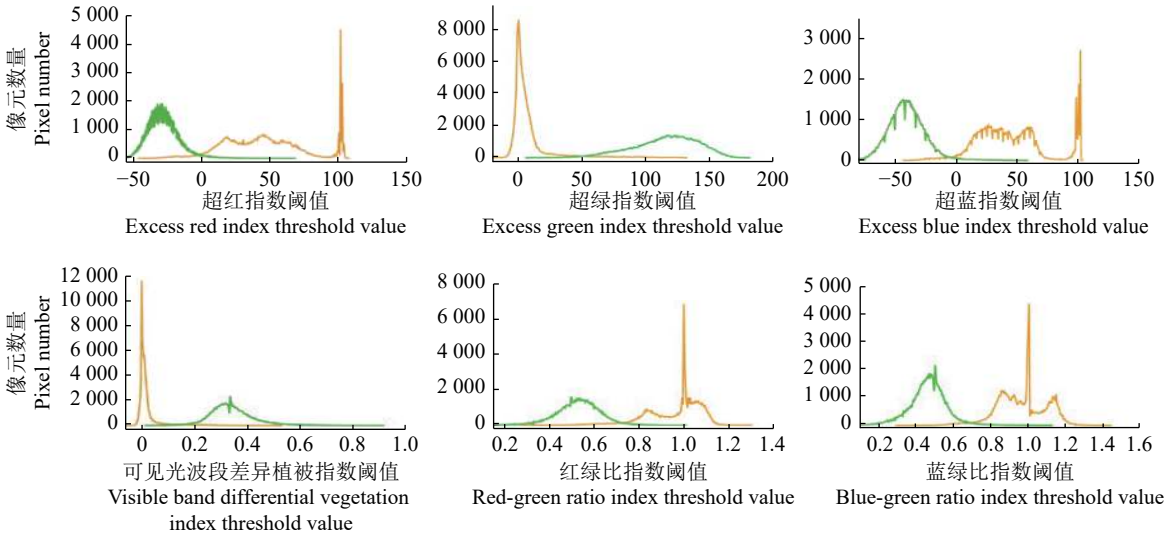

图 7　6 种可见光植被指数统计直方图

Fig. 7　Statistical histograms of six visible light vegetation indexes

价 (表 3)。6 种可见光植被指数对应的植被分类提取结果如图 8 所示。从表 3 和图 8 可以看出，果树的提取精度均在 99% 以上，提取精度较好；非果树的提取精度较低，主要原因是非果树区域的草地部分色调与果树相似，易导致将草地分为果树，造成错分现象。

2.3　结合数字表面模型的提取与精度评价

基于“2.2”的提取结果和提取精度，非果树区域中的草地部分被错分成了果树，导致非果树的提取精度和总精度降低。在数字表面模型中，沙糖橘果树和其他地物的高度具有较大差异，可以清晰地呈现出不同的亮度值。因此，我们将数字表面模型和上述 6 种可见光植被指数进行波段融合，提高草地的提取精度和提取结果的总精度。

同样利用基于规则的面向对象分类方法，对融合后的波段进行植被信息的提取，得到结合数字表面模型的 6 种可见光植被指数对应的植被分类提取结果，如图 9 所示。依然使用 60 个果树和 60 个非果树的验证样本，将分类结果当作真值，分别对这 2 种地物的分类结果计算混淆矩阵，得到融合波

表 3　6 种可见光植被指数的植被提取精度评价

Table 3　Accuracy assessments of vegetation extraction for six visible light vegetation indexes

植被指数 Vegetation index	阈值 Threshold	精度/% Accuracy			Kappa系数(K) Kappa coefficient
		果树 Fruit tree	非果树 Non fruit tree	总体 Total	
超红指数 Excess red index	−1.886	99.78	90.63	95.18	0.903 6
超绿指数 Excess green index	50.000	99.68	87.58	93.60	0.872 0
超蓝指数 Excess blue index	−4.675	99.77	94.62	97.18	0.943 6
可见光波段差异植被指数 Visible band differential vegetation index	0.133	99.98	88.28	94.10	0.882 0
红绿比指数 Red-green ratio index	0.724	99.84	89.25	94.52	0.890 4
蓝绿比指数 Blue-green ratio index	0.682	99.79	91.40	95.57	0.911 4

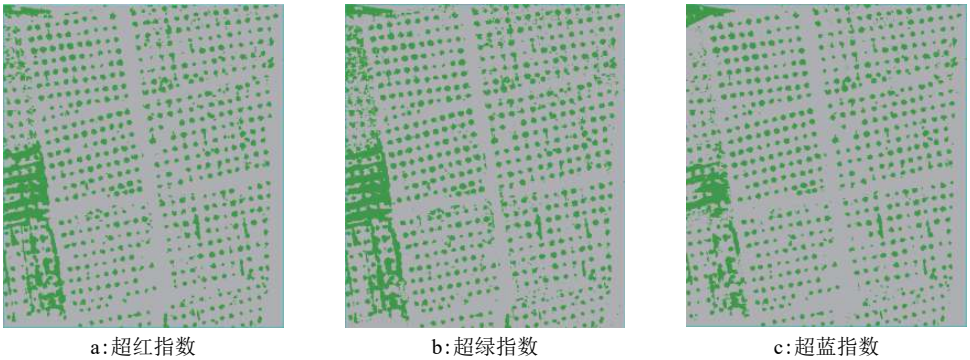

a：超红指数 a: Excess red index　　b：超绿指数 b: Excess green index　　c：超蓝指数 c: Excess blue index

d：可见光波段差异植被指数 d: Visible band differential vegetation index　　e：红绿比指数 e: Red-green ratio index　　f：蓝绿比指数 f: Blue-green ratio index

绿色部分代表果树，灰色部分代表非果树

The green part indicates fruit tree, the gray part indicates non fruit tree

图 8　6 种可见光植被指数的植被信息提取结果

Fig. 8　Vegetation extraction results of six visible light vegetation indexes

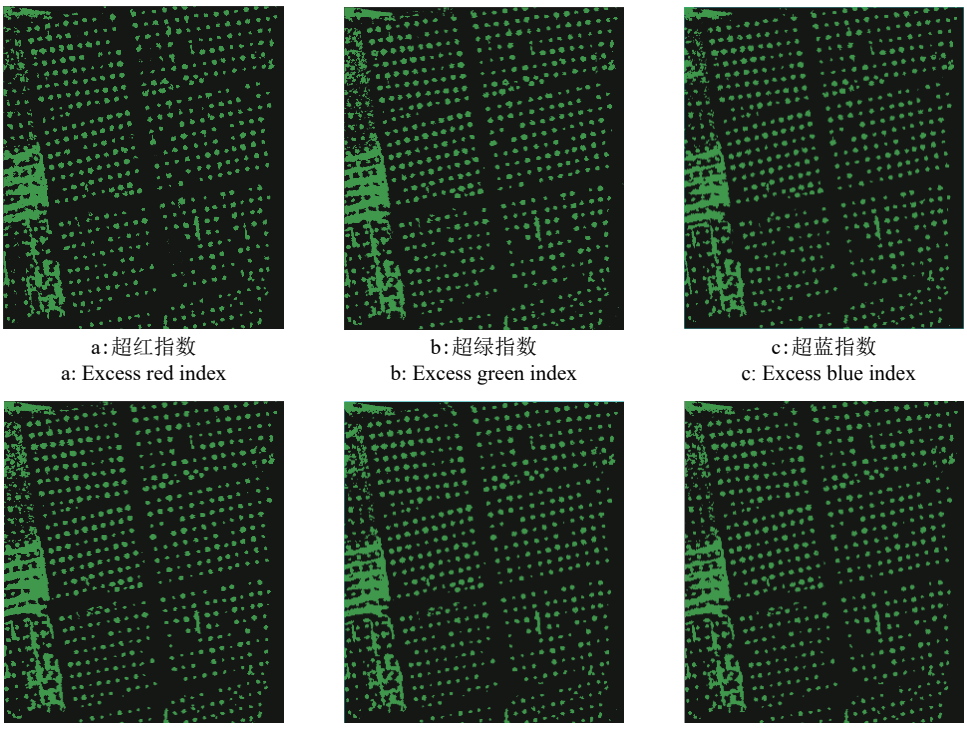

绿色部分代表果树，黑色部分代表非果树

The green part indicates fruit tree, the black part indicates non fruit tree

图 9 结合数字表面模型的 6 种可见光植被指数信息提取结果

Fig. 9 Extraction results of six visible light vegetation indexes combined with digital surface model

段各植被指数的提取精度评价，结果如表 4 所示。6 种结合后的植被指数混淆矩阵中，总体分类精度分别为 98.77%、97.27%、97.44%、97.67%、97.84% 和 97.84%，相较于对应的未结合数字表面模型的植被指数精度均有小幅度提升；非果树的提取精度分别提高了 8.22%、8.77%、0.86%、8.27%、7.97% 和 5.53%；表明数字表面模型与可见光植被指数图像结合适用于提高非果树的提取精度，有效抑制和果树同为绿色的草地信息，不会过多地造成错分现象。

表 4 6 种可见光植被指数融合数字表面模型提取精度评价

Table 4 Accuracy assessments of vegetation extraction for six visible vegetation indexes combined with digital surface model

植被指数 Vegetation index	精度/% Accuracy			Kappa系数(K) Kappa coefficient
	果树 Fruit tree	非果树 Non fruit tree	总体 Total	
超红指数 Excess red index	99.46	98.08	98.77	0.956 7
超绿指数 Excess green index	99.28	95.26	97.27	0.945 4
超蓝指数 Excess blue index	99.45	95.43	97.44	0.948 9
可见光波段差异植被指数 Visible band differential vegetation index	99.76	95.58	97.67	0.953 4
红绿比指数 Red-green ratio index	99.31	96.37	97.84	0.956 8
蓝绿比指数 Blue-green ratio index	99.23	96.45	97.84	0.956 8

3 结论

本研究在现有的可见光植被指数的植被提取基础上，提出了结合数字表面模型中的高程信息进一步提取果树和非果树的方法。在得到可见光植被指数 (超红指数、超绿指数、超蓝指数、可见光波段差异植被指数、红绿比指数、蓝绿比指数) 的计算图后，分析各植被指数的光谱特征和统计直方图，获得提取植被覆盖度合适的阈值，进行果树信息的提取。数字表面模型与可见光植被指数波段融合后的

总体精度均大于 97%，且非果树的提取精度均有所提升。超红指数与数字表面模型结合后的总精度最高，为 98.77%，Kappa 系数为 0.956 7，植被信息提取精度不同程度地优于其他 5 种可见光植被指数与数字表面模型结合后的提取精度。可见光植被指数结合数字表面模型提取植被信息的方法可有效区分与果树色调相类似的地物，提高此类地物的提取精度，减少错分概率。本研究的研究对象为沙糖橘果树和非果树，下一步的研究重点是将此法推广至其他不同作物上，进一步验证其适用性。

参考文献：

[1] 牛亚晓, 张立元, 韩文霆, 等. 基于无人机遥感与植被指数的冬小麦覆盖度提取方法[J]. 农业机械学报, 2018, 49(4): 212-221.

[2] GITELSON A A, KAUFMAN Y J, STARK R, et al. Novel algorithms for remote estimation of vegetation fraction[J]. Remote Sens Environ, 2002, 80(1): 76-87.

[3] YANG H B, ZHAO J, LAN Y B, et al. Fraction vegetation cover extraction of winter wheat based on spectral information and texture features obtained by UAV[J]. Int J Precis Agric Aviat, 2019, 2(2): 54-61.

[4] TAHIR M N, LAN Y B, ZHANG Y L, et al. Real time estimation of leaf area index and groundnut yield using multispectral UAV[J]. Int J Precis Agric Aviat, 2020, 3(1): 1-6.

[5] XU W, LAN Y, LI Y, et al. Classification method of cultivated land based on UAV visible light remote sensing[J]. Int J Agr Biol Eng, 2019, 12(3): 103-109.

[6] CHOI S K, LEE S K, JUNG S H, et al. Estimation of fractional vegetation cover in sand dunes using multispectral images from fixed-wing UAV[J]. Journal of the Korean Society of Survey, Geodesy, Photogrammetry, and Cartography, 2016, 34(4): 431-441.

[7] ZHANG D, MANSARAY L R, JIN H, et al. A universal estimation model of fractional vegetation cover for different crops based on time series digital photographs[J]. Comput Electron Agr, 2018, 151: 93-103.

[8] 高永平, 康茂东, 何明珠, 等. 基于无人机可见光波段对荒漠植被覆盖度提取的研究[J]. 兰州大学学报(自然科学版), 2018, 54(6): 770-775.

[9] MEYER G E, NETO J C. Verification of color vegetation indices for automated crop imaging applications[J]. Comput Electron Agr, 2008, 63(2): 282-293.

[10] WOEBBECKE D M, MEYER G E, VON BARGEN K, et al. Color indices for weed identification under various soil, residue, and lighting conditions[J]. Transactions of the ASAE, 1995, 38(1): 259-269.

[11] GUIJARRO M, PAJARES G, RIOMOROS I, et al. Automatic segmentation of relevant textures in agricultural images[J]. Comput Electron Agr, 2011, 75(1): 75-83.

[12] GAMON J A, SURFUS J S. Assessing leaf pigment content and activity with a reflectometer[J]. New Phytol, 1999, 143(1): 105-117.

[13] SELLARO R, CREPY M, TRUPKIN S A, et al. Cryptochrome as a sensor of the blue/green ratio of natural radiation in Arabidopsis[J]. Plant Physiol, 2010, 154(1): 401-409.

[14] PUREVDORJ T, TATEISHI R, ISHIYAMA T, et al. Relationships between percent vegetation cover and vegetation indices[J]. Int J Remote Sens, 1998, 19(18): 3519-3535.

[15] 赵德升, 毛罕平, 陈树人, 等. 杂草识别中背景分割方法的比较研究[J]. 农机化研究, 2009(11): 76-79.

[16] 邓书斌, 陈秋锦. EVVI 遥感图像处理方法[M]. 北京: 高等教育出版社, 2014: 204.

[17] 王民, 樊潭飞, 贠卫国, 等. PFWG 改进的 CNN 多光谱遥感图像分类[J]. 激光与光电子学进展, 2019, 56(3): 031003.

【责任编辑　李庆玲】

广东省农业技术推广奖

获奖证书

为表彰在农业技术推广工作中做出贡献的单位和个人，特颁发此证书，以资鼓励。

获奖项目：智能植保无人机装备及施药技术的研发与示范推广

奖励等级：一等奖

奖励个人：张亚莉

奖励日期：2024年12月25日

证 书 号：2023-1-N03-R03

广东省农业技术推广奖
评审委员会

大北农科技奖

证 书

为表彰在我国农业科技进步工作中作出突出贡献的大北农科技奖获得者，特颁发此证书，以资鼓励！

奖项类别：创新奖

项目名称：植保无人飞机精准喷施关键技术创新与应用

获 奖 者：张亚莉（第八完成人）

完成单位：华南农业大学
农业农村部南京农业机械化研究所
山东理工大学
安阳全丰航空植保科技有限公司
中国农业科学院植物保护研究所

获奖年份：2021年（第十二届）

2022年3月

证书编号：2021-C-25-D08

证书号第8304121号

专利公告信息

发明专利证书

发明名称：一种用于检测植物表皮荧光特性的图像获取装置

专利权人：华南农业大学

地　　址：510640 广东省广州市天河区五山路483号

发 明 人：张亚莉;孙智磊;颜康婷;林少臻;彭婉航;张智杰;郭俊
许曦丹;杨达成;方熙鹏;杨景;林叶清;杨达诗;卢梓帆

专 利 号：ZL 2024 1 1444730.0　　授权公告号：CN 119198661 B

专利申请日：2024年10月15日　　授权公告日：2025年09月26日

申请日时申请人：华南农业大学

申请日时发明人：张亚莉;孙智磊;颜康婷;林少臻;彭婉航;张智杰;郭俊
许曦丹;杨达成;方熙鹏;杨景;林叶清;杨达诗;卢梓帆

国家知识产权局依照中华人民共和国专利法进行审查，决定授予专利权，并予以公告。

专利权自授权公告之日起生效。专利权有效性及专利权人变更等法律信息以专利登记簿记载为准。

局长
申长雨

国家知识产权局
2025年09月26日

证书号第7351186号

专利公告信息

发明专利证书

发明名称：一种用于DS18B20温度传感器的总线信号隔离电路

专利权人：华南农业大学

地　　址：510642 广东省广州市天河区五山路483号

发 明 人：张亚莉;黄鑫荣;肖文蔚;王林琳;颜康婷;高启超;赵德华
田昊鑫;刘含超;卢小阳;祁媛

专 利 号：ZL 2020 1 1525284.8　　授权公告号：CN 112564674 B

专利申请日：2020年12月22日　　授权公告日：2024年09月06日

申请日时申请人：华南农业大学

申请日时发明人：张亚莉;黄鑫荣;肖文蔚;王林琳;颜康婷;高启超;赵德华
田昊鑫;刘含超;卢小阳;祁媛

国家知识产权局依照中华人民共和国专利法进行审查，决定授予专利权，并予以公告。

专利权自授权公告之日起生效。专利权有效性及专利权人变更等法律信息以专利登记簿记载为准。

局长
申长雨

国家知识产权局
2024年09月06日

证书号第7005526号

发明专利证书

发 明 名 称：一种专用于农田信息检测小车的电路系统

发 明 人：张亚莉;肖文蔚;黄鑫荣;王林琳;白禄超;祁媛;刘峰
刘轶伦;颜康婷;高启超;欧阳帆

专 利 号：ZL 2019 1 1119885.6

专利申请日：2019年11月15日

专 利 权 人：华南农业大学

地 址：510642 广东省广州市天河区五山路483号

授权公告日：2024年05月14日　　授权公告号：CN 110843645 B

国家知识产权局依照中华人民共和国专利法进行审查，决定授予专利权，颁发发明专利证书并在专利登记簿上予以登记。专利权自授权公告之日起生效。专利权期限为二十年，自申请日起算。

专利证书记载专利权登记时的法律状况。专利权的转移、质押、无效、终止、恢复和专利权人的姓名或名称、国籍、地址变更等事项记载在专利登记簿上。

局长
申长雨

国家知识产权局
2024年05月14日

其他事项参见续页

证书号第6996274号

发明专利证书

发明名称：基于手持式分光辐射谱仪的水稻颖花开花状态检测方法

发　明　人：张亚莉;肖骏祺;卢小阳;李万坚;莫振杰;张子超;颜康婷
刘含超;赵德华;田昊鑫;黄鑫荣;高启超;韩沂芳;廖铠丰

专　利　号：ZL 2022 1 0040671.5

专利申请日：2022年01月14日

专利权人：华南农业大学

地　　址：510642 广东省广州市天河区五山路483号

授权公告日：2024年05月14日　　授权公告号：CN 114548220 B

国家知识产权局依照中华人民共和国专利法进行审查，决定授予专利权，颁发发明专利证书并在专利登记簿上予以登记。专利权自授权公告之日起生效。专利权期限为二十年，自申请日起算。

专利证书记载专利权登记时的法律状况。专利权的转移、质押、无效、终止、恢复和专利权人的姓名或名称、国籍、地址变更等事项记载在专利登记簿上。

局长
申长雨

国家知识产权局
2024年05月14日

其他事项参见续页

证书号第6990681号

发明专利证书

发明名称：一种搭载于植保无人机的静电喷雾装置

发　明　人：张亚莉;黄鑫荣;肖文蔚;王林琳;祁媛;颜康婷;高启超;田昊鑫;刘含超;赵德华

专　　利　　号：ZL 2020 1 1020971.4

专利申请日：2020年09月24日

专利权人：华南农业大学

地　　址：510642 广东省广州市天河区五山路483号

授权公告日：2024年05月10日　　授权公告号：CN 112109896 B

国家知识产权局依照中华人民共和国专利法进行审查，决定授予专利权，颁发发明专利证书并在专利登记簿上予以登记。专利权自授权公告之日起生效。专利权期限为二十年，自申请日起算。

专利证书记载专利权登记时的法律状况。专利权的转移、质押、无效、终止、恢复和专利权人的姓名或名称、国籍、地址变更等事项记载在专利登记簿上。

局长
申长雨

国家知识产权局
2024年05月10日

其他事项参见续页

证书号第6903391号

发明专利证书

发明名称：一种基于无人机遥感影像的杂交水稻父母本识别提取方法

发　明　人：张亚莉;刘含超;莫振杰;赵德华;田昊鑫;黄鑫荣;高启超
颜康婷;肖骏祺;卢小阳;李万坚;张子超;王林琳

专　利　号：ZL 2022 1 0022642.6

专利申请日：2022年01月10日

专利权人：华南农业大学

地　　址：510642 广东省广州市天河区五山路483号

授权公告日：2024年04月16日　　授权公告号：CN 115035423 B

国家知识产权局依照中华人民共和国专利法进行审查，决定授予专利权，颁发发明专利证书并在专利登记簿上予以登记。专利权自授权公告之日起生效。专利权期限为二十年，自申请日起算。

专利证书记载专利权登记时的法律状况。专利权的转移、质押、无效、终止、恢复和专利权人的姓名或名称、国籍、地址变更等事项记载在专利登记簿上。

局长
申长雨

国家知识产权局
2024年04月16日

其他事项参见续页

证书号第6409474号

发明专利证书

发明名称：一种植保无人机液位测量装置

发　明　人：张亚莉;刘轶伦;兰玉彬;陈盛德;王林琳;白禄超;祁媛;刘峰;史志斌

专　利　号：ZL 2018 1 1393436.6

专利申请日：2018年11月21日

专利权人：华南农业大学

地　　址：510642 广东省广州市天河区五山路483号

授权公告日：2023年10月20日　　授权公告号：CN 109353515 B

国家知识产权局依照中华人民共和国专利法进行审查，决定授予专利权，颁发发明专利证书并在专利登记簿上予以登记。专利权自授权公告之日起生效。专利权期限为二十年，自申请日起算。

专利证书记载专利权登记时的法律状况。专利权的转移、质押、无效、终止、恢复和专利权人的姓名或名称、国籍、地址变更等事项记载在专利登记簿上。

局长
申长雨

国家知识产权局
2023年10月20日

其他事项参见续页

证书号第4258818号

发明专利证书

发明名称：太阳能农用无人机及农情遥感监测方法

发明人：张亚莉;黄明明;李继宇;赖佳锋;黄耀明;张筱涵

专利号：ZL 2018 1 0382602.6

专利申请日：2018年04月26日

专利权人：华南农业大学

地址：510642 广东省广州市天河区五山路483号

授权公告日：2021年02月19日　　授权公告号：CN 108773490 B

国家知识产权局依照中华人民共和国专利法进行审查，决定授予专利权，颁发发明专利证书并在专利登记簿上予以登记。专利权自授权公告之日起生效。专利权期限为二十年，自申请日起算。

专利证书记载专利权登记时的法律状况。专利权的转移、质押、无效、终止、恢复和专利权人的姓名或名称、国籍、地址变更等事项记载在专利登记簿上。

局长
申长雨

2021年02月19日

其他事项参见续页

证书号第6985877号

发明专利证书

发明名称：一种航空静电喷雾设备中的喷头调节装置

发　明　人：张亚莉;黄鑫荣;颜康婷;王林琳;祁媛;高启超;肖文蔚
刘含超;赵德华;田昊鑫;白禄超

专　利　号：ZL 2020 1 1019738.4

专利申请日：2020年09月24日

专利权人：华南农业大学

地　　址：510642 广东省广州市天河区五山路483号

授权公告日：2024年05月10日　　授权公告号：CN 112138908 B

国家知识产权局依照中华人民共和国专利法进行审查，决定授予专利权，颁发发明专利证书并在专利登记簿上予以登记。专利权自授权公告之日起生效。专利权期限为二十年，自申请日起算。

专利证书记载专利权登记时的法律状况。专利权的转移、质押、无效、终止、恢复和专利权人的姓名或名称、国籍、地址变更等事项记载在专利登记簿上。

局长
申长雨

国家知识产权局
2024年05月10日

其他事项参见续页

证书号第15323870号

实用新型专利证书

实用新型名称：一种存储式采摘机器人

发　明　人：张亚莉;赵德华;黄鑫荣;王林琳;高启超;刘含超;田昊鑫
颜康婷;卢小阳;祁媛;肖文蔚

专　利　号：ZL 2020 2 3057004.3

专利申请日：2020年12月16日

专利权人：华南农业大学

地　　址：510642 广东省广州市天河区五山路483号

授权公告日：2021年12月28日　　授权公告号：CN 215301623 U

国家知识产权局依照中华人民共和国专利法经过初步审查，决定授予专利权，颁发实用新型专利证书并在专利登记簿上予以登记。专利权自授权公告之日起生效。专利权期限为十年，自申请日起算。

专利证书记载专利权登记时的法律状况。专利权的转移、质押、无效、终止、恢复和专利权人的姓名或名称、国籍、地址变更等事项记载在专利登记簿上。

局长
申长雨

2021年12月28日

其他事项参见续页

证书号第14661642号

实用新型专利证书

实用新型名称：一种陆空两用单驱动的多旋翼无人机

发　明　人：张亚莉;田昊鑫;卢小阳;黄鑫荣;马晨阳;王林琳;白禄超
颜康婷;高启超;肖文蔚;祁媛;赵德华;刘含超

专　利　号：ZL 2021 2 0639333.4

专利申请日：2021年03月29日

专利权人：华南农业大学

地　　址：510642 广东省广州市天河区五山路483号

授权公告日：2021年11月09日　　授权公告号：CN 214649016 U

国家知识产权局依照中华人民共和国专利法经过初步审查，决定授予专利权，颁发实用新型专利证书并在专利登记簿上予以登记。专利权自授权公告之日起生效。专利权期限为十年，自申请日起算。

专利证书记载专利权登记时的法律状况。专利权的转移、质押、无效、终止、恢复和专利权人的姓名或名称、国籍、地址变更等事项记载在专利登记簿上。

局长
申长雨

2021年11月09日

其他事项参见续页

证书号第13315768号

实用新型专利证书

实用新型名称：一种航空静电喷雾设备中的挂载安装机构

发　明　人：张亚莉;黄鑫荣;高启超;王林琳;祁媛;肖文蔚;颜康婷
刘含超;田昊鑫;赵德华

专　利　号：ZL 2020 2 2129819.1

专利申请日：2020年09月24日

专利权人：华南农业大学

地　　址：510642 广东省广州市天河区五山路483号

授权公告日：2021年06月01日　　授权公告号：CN 213323701 U

国家知识产权局依照中华人民共和国专利法经过初步审查，决定授予专利权，颁发实用新型专利证书并在专利登记簿上予以登记。专利权自授权公告之日起生效。专利权期限为十年，自申请日起算。

专利证书记载专利权登记时的法律状况。专利权的转移、质押、无效、终止、恢复和专利权人的姓名或名称、国籍、地址变更等事项记载在专利登记簿上。

局长
申长雨

2021年06月01日

其他事项参见续页

证书号第11238942号

实用新型专利证书

实用新型名称：一种可收集式小功率马铃薯收获机

发　明　人：张亚莉;高启超;肖文蔚;王林琳;白禄超;祁媛;刘轶伦
刘峰;颜康婷;黄鑫荣;欧阳帆

专　利　号：ZL 2019 2 1974559.9

专利申请日：2019年11月14日

专利权人：华南农业大学

地　　址：510642 广东省广州市天河区五山路483号

授权公告日：2020年08月14日　　授权公告号：CN 211240841 U

国家知识产权局依照中华人民共和国专利法经过初步审查，决定授予专利权，颁发实用新型专利证书并在专利登记簿上予以登记。专利权自授权公告之日起生效。专利权期限为十年，自申请日起算。

专利证书记载专利权登记时的法律状况。专利权的转移、质押、无效、终止、恢复和专利权人的姓名或名称、国籍、地址变更等事项记载在专利登记簿上。

局长
申长雨

2020年08月14日

其他事项参见续页

证书号第11238369号

实用新型专利证书

实用新型名称：一种便携式光谱仪检测装置

发　明　人：张亚莉;祁媛;史志斌;王林琳;白禄超;刘峰;刘轶伦
肖文蔚;颜康婷;黄鑫荣;高启超;欧阳帆;蔡迎虎;梁佳佳

专　利　号：ZL 2019 2 1973106.4

专利申请日：2019年11月14日

专利权人：华南农业大学

地　　址：510642 广东省广州市天河区五山路483号

授权公告日：2020年08月14日　　授权公告号：CN 211263159 U

国家知识产权局依照中华人民共和国专利法经过初步审查，决定授予专利权，颁发实用新型专利证书并在专利登记簿上予以登记。专利权自授权公告之日起生效。专利权期限为十年，自申请日起算。

专利证书记载专利权登记时的法律状况。专利权的转移、质押、无效、终止、恢复和专利权人的姓名或名称、国籍、地址变更等事项记载在专利登记簿上。

局长
申长雨

2020年08月14日

其他事项参见续页

证书号第11276407号

实用新型专利证书

实用新型名称：一种水体参数检测装置

发　明　人：张亚莉;祁媛;史志斌;王林琳;白禄超;刘峰;刘轶伦
肖文蔚;颜康婷;黄鑫荣;高启超;欧阳帆;蔡迎虎;梁佳佳

专　利　号：ZL 2019 2 1970585.4

专利申请日：2019年11月14日

专利权人：华南农业大学

地　　址：510642 广东省广州市天河区五山路483号

授权公告日：2020年08月18日　　授权公告号：CN 211292864 U

国家知识产权局依照中华人民共和国专利法经过初步审查，决定授予专利权，颁发实用新型专利证书并在专利登记簿上予以登记。专利权自授权公告之日起生效。专利权期限为十年，自申请日起算。

专利证书记载专利权登记时的法律状况。专利权的转移、质押、无效、终止、恢复和专利权人的姓名或名称、国籍、地址变更等事项记载在专利登记簿上。

局长
申长雨

2020年08月18日

其他事项参见续页

证书号第11132750号

实用新型专利证书

实用新型名称：一种可防潮除湿的电气箱

发　明　人：张亚莉;黄鑫荣;高启超;王林琳;白禄超;祁媛;刘峰
刘轶伦;肖文蔚;颜康婷;欧阳帆

专　利　号：ZL 2019 2 1970012.1

专利申请日：2019年11月14日

专利权人：华南农业大学

地　　址：510642 广东省广州市天河区五山路483号

授权公告日：2020年07月31日　　授权公告号：CN 211151263 U

国家知识产权局依照中华人民共和国专利法经过初步审查，决定授予专利权，颁发实用新型专利证书并在专利登记簿上予以登记。专利权自授权公告之日起生效。专利权期限为十年，自申请日起算。

专利证书记载专利权登记时的法律状况。专利权的转移、质押、无效、终止、恢复和专利权人的姓名或名称、国籍、地址变更等事项记载在专利登记簿上。

局长
申长雨

2020年07月31日

其他事项参见续页

证书号第11129657号

实用新型专利证书

实用新型名称：一种水流速度检测装置

发　明　人：张亚莉;刘峰;王林琳;白禄超;祁媛;刘轶伦;黄欣荣
肖文蔚;高启超;颜康婷

专　利　号：ZL 2020 2 0023512.0

专利申请日：2020年01月06日

专利权人：华南农业大学

地　　址：510642 广东省广州市天河区五山路483号

授权公告日：2020年07月31日　　授权公告号：CN 211148692 U

国家知识产权局依照中华人民共和国专利法经过初步审查，决定授予专利权，颁发实用新型专利证书并在专利登记簿上予以登记。专利权自授权公告之日起生效。专利权期限为十年，自申请日起算。

专利证书记载专利权登记时的法律状况。专利权的转移、质押、无效、终止、恢复和专利权人的姓名或名称、国籍、地址变更等事项记载在专利登记簿上。

局长
申长雨

2020年07月31日

其他事项参见续页

证书号第9229514号

实用新型专利证书

实用新型名称：一种植保无人机的药液余量检测装置

发　明　人：张亚莉;祁媛;兰玉彬;王林琳;白禄超;刘轶伦;刘峰
王东东

专　利　号：ZL 2018 2 1930553.7

专利申请日：2018年11月21日

专利权人：华南农业大学

地　　址：510642 广东省广州市天河区五山路483号

授权公告日：2019年08月13日　　授权公告号：CN 209241328 U

国家知识产权局依照中华人民共和国专利法经过初步审查，决定授予专利权，颁发实用新型专利证书并在专利登记簿上予以登记。专利权自授权公告之日起生效。专利权期限为十年，自申请日起算。

专利证书记载专利权登记时的法律状况。专利权的转移、质押、无效、终止、恢复和专利权人的姓名或名称、国籍、地址变更等事项记载在专利登记簿上。

局长
申长雨

国家知识产权局
2019年08月13日

其他事项参见背面

证书号第9068545号

实用新型专利证书

实用新型名称：一种农田水层高度在线监测装置

发　明　人：张亚莉;白禄超;兰玉彬;王林琳;刘轶伦;祁媛;刘峰

专　利　号：ZL 2018 2 1930328.3

专利申请日：2018年11月21日

专利权人：华南农业大学

地　　址：510642 广东省广州市天河区五山路483号

授权公告日：2019年07月09日　　授权公告号：CN 209085715 U

国家知识产权局依照中华人民共和国专利法经过初步审查，决定授予专利权，颁发实用新型专利证书并在专利登记簿上予以登记。专利权自授权公告之日起生效。专利权期限为十年，自申请日起算。

专利证书记载专利权登记时的法律状况。专利权的转移、质押、无效、终止、恢复和专利权人的姓名或名称、国籍、地址变更等事项记载在专利登记簿上。

局长
申长雨

国家知识产权局
2019年07月09日

其他事项参见背面

ICS 65.060.40
CCS B 91

NY

中华人民共和国农业行业标准

NY/T 3893—2021

遥控飞行喷雾机棉花脱叶催熟作业规程

Operating specification of cotton harvest aids applied by remote control aerial sprayer

2021-05-07 发布　　2021-11-01 实施

中华人民共和国农业农村部 发布

前　言

本文件按照GB/T 1.1—2020《标准化工作导则　第1部分：标准化文件的结构和起草规则》的规定起草。

请注意本文件的某些内容可能涉及专利。本文件的发布机构不承担识别专利的责任。

本文件由农业农村部农业机械化管理司提出。

本文件由全国农业机械标准化技术委员会农业机械化分技术委员会(SAC/TC 201/SC 2)归口。

本文件起草单位：华南农业大学、安阳工学院、山东理工大学、河南标普农业科技有限公司、中国农业科学院棉花研究所、安阳全丰生物科技有限公司、中国农业科学院植物保护研究所、拜耳作物科学(中国)有限公司、国家航空植保科技创新联盟。

本文件主要起草人：兰玉彬、蒙艳华、王志国、马艳、胡红岩、张亚莉、刘越、袁会珠、齐枫、梁自静、李好海。

遥控飞行喷雾机棉花脱叶催熟作业规程

1 范围

本文件规定了遥控飞行喷雾机棉花脱叶催熟作业的术语和定义、作业条件、作业前准备、现场作业要求、作业后要求和紧急事故处理。

本文件适用于使用遥控飞行喷雾机开展棉花脱叶催熟作业。

2 规范性引用文件

下列文件中的内容通过文中的规范性引用而构成本文件必不可少的条款。其中，注日期的引用文件，仅该日期对应的版本适用于本文件；不注日期的引用文件，其最新版本(包括所有的修改单)适用于本文件。

NY/T 1464.26—2007 农药田间药效试验准则 第26部分：棉花催枯剂试验

3 术语和定义

下列术语和定义适用于本文件。

3.1

操控员 operator

取得操作资质，在飞行期间适时操控遥控飞行喷雾机且负责其运行的人员。

3.2

喷洒服务商 spraying service provider

提供农药喷洒服务的个人、组织或者企业。

3.3

作业警示牌 operation warning sign

放置于作业棉田四周用于提醒周边群众遥控飞行喷雾机作业期间勿闯入作业区的起警示作用的标牌。

4 作业条件

4.1 植株及棉铃成熟度要求

4.1.1 棉花植株营养生长停止、进入自然衰老期，有效棉铃已经基本处于生理性成熟。棉铃横切后可见种皮，且种皮呈棕褐色、棉籽坚硬。

4.1.2 一般情况下棉铃自然吐絮率宜不小于30%。

4.2 气象条件要求

4.2.1 大雨、霜冻时不应作业。

4.2.2 喷洒前应查看天气预报，选择施药后连续7 d～10 d平均气温应不低于20 ℃，最低气温应不低于12 ℃的气象条件。

4.3 田间调查

4.3.1 调查作业区域棉花品种、株高、种植密度、成熟度及吐絮率。

4.3.2 调查棉田的面积及周围情况，棉田周边20 m之内有菜地、居民饮水源、养蜂场等不应作业。

4.4 确定脱叶剂、催熟剂和作业参数

4.4.1 选择正式登记的脱叶剂、催熟剂和脱叶剂助剂。

AGRICULTURAL STANDARD PUBLISHING RESEARCH CENTER

4.4.2 根据棉铃成熟度确定脱叶剂、催熟剂的使用剂量。

4.4.3 根据棉铃吐絮率、种植密度、高度等选择脱叶剂、催熟剂、遥控飞行喷雾机喷雾参数和喷施次数。若需喷施2遍脱叶剂、催熟剂时，2次喷施时间间隔为7 d。

4.4.4 根据棉花种植密度和高度确定遥控飞行喷雾机的施药液量、飞行高度和飞行速度。遥控飞行喷雾机施药液量宜不低于18 L/hm^2，飞行高度宜距离棉株顶部1.5 m～2.0 m，飞行速度宜为3 m/s～5 m/s。

5 作业前准备

5.1 作业前应选择干净无杂质的清水作为施药用水，不应使用强酸强碱的水。

5.2 作业组人员应准备保护人员安全的防护服、手套、口罩。

5.3 作业组人员应根据作业日期，在作业棉田四周安置含有作业名称、作业时间、服务商名称、联系电话、注意安全的作业警示牌。

5.4 作业组人员应检查遥控飞行喷雾机的电池或燃油，确保遥控飞行喷雾机能满足作业需求。

6 现场作业要求

6.1 脱叶剂、催熟剂应现配现用，配药前应将原包装脱叶剂、催熟剂摇匀。

6.2 根据施药液量和使用剂量配制药液，将称量好的脱叶剂、催熟剂和脱叶剂助剂分别用少量水进行稀释，配药时先加入所需用水量的1/3，按脱叶剂-脱叶剂助剂-催熟剂-飞防助剂的顺序加入配好的母液，用所需水量的1/3清洗盛药器皿及包装，并将清洗液一并倒入配药桶中，最后加足剩余的1/3清水至配置所需药液，将药液搅拌均匀后倒入遥控飞行喷雾机药箱中。

6.3 喷洒前操控员和其他作业组人员穿戴好防护服、口罩、手套。

6.4 喷洒前在作业棉田四周放置作业警示牌，确保田中无人、自然风速不大于5 m/s时，方可进行喷洒作业。当自然风速大于5 m/s时，应停止喷洒作业，遥控飞行喷雾机返回起降点，待风速符合要求后再进行喷洒作业。

6.5 作业区域喷洒完成后，应对作业区域的前后边缘区10 m范围进行扫边处理。

6.6 同一棉田内有2架或2架以上遥控飞行喷雾机作业时，相邻遥控飞行喷雾机之间应保持10 m以上的安全距离。

6.7 作业过程中操控员应站在上风处，背对阳光操控遥控飞行喷雾机，操控员和作业组人员应与遥控飞行喷雾机保持10 m以上安全距离。

7 作业后要求

7.1 作业组人员应按附录A中的规定及时记录作业情况。

7.2 喷洒剩余的药液应稀释后再喷洒到废弃区域。配药时清洗过的脱叶剂、催熟剂包装应及时回收妥善处理，不应将脱叶剂、催熟剂的空包装袋丢弃在作业区域。

7.3 及时清理配药桶及配药器皿，并将清洗液倒入废弃区域。

7.4 及时清洗遥控飞行喷雾机喷头、滤网及药箱，擦拭遥控器、充电器、电池后储存。

7.5 撤回作业警示牌，同时在作业区域设置安全警示牌，标明施药时间、安全间隔期。

7.6 作业组人员应及时更换工作服，清洗手、脸，并用清水漱口。

7.7 第一次作业7 d后调查棉株脱叶率和棉铃吐絮率，根据脱叶率和吐絮率确定第二次喷施脱叶剂、催熟剂的使用剂量，并开展第二次喷施。机收前，田间棉株脱叶率应不低于90%，棉铃吐絮率应不低于95%。棉株脱叶率和棉铃吐絮率的测定和计算按NY/T 1464.26—2007中4.3.3的规定执行。

8 紧急事故处理

8.1 作业过程中，如出现人员药物过敏、中毒现象，应立即停止作业及时就医。

8.2 操控员发现遥控飞行喷雾机发生故障且失控时，应在确认遥控飞行喷雾机周围无人且周边安全的情况下，立即关闭遥控飞行喷雾机，进行迫降。

8.3 当发生人身伤害、伤亡或重大农药泄露事故时，应及时采取应急措施，并向相关部门报告。

附 录 A
（规范性）
遥控飞行喷雾机棉花脱叶催熟作业记录表

遥控飞行喷雾机棉花脱叶催熟作业需记录的信息见表 A.1。

表 A.1 遥控飞行喷雾机棉花脱叶催熟作业记录表

喷洒服务商			联系电话		
作业组人员	操控员： 作业组其他人员：				
作业负责人			联系电话		
作业地点				作业面积	hm^2
作业地农户				联系电话	
作业日期及时间段	第一次作业时间：　　年　　月　　日 时间段：　　时　　分至　　时　　分 第二次作业时间：　　年　　月　　日 时间段：　　时　　分至　　时　　分				
棉花品种			棉花种植密度		株/hm^2
棉花株高			平均棉铃数量		个/株
棉铃成熟度			作业前吐絮率		
脱叶剂、催熟剂名称及使用剂量	脱叶剂： 催熟剂： 脱叶剂助剂： 飞防助剂：				
作业棉田四周作物情况	作物名称： 所处生育期： 距离作业田的距离：				
第一次作业气象因素	温度，℃		湿度，%		
	风向		风速，m/s		
第二次作业气象因素	温度，℃		湿度，%		
	风向		风速，m/s		
遥控飞行喷雾机型号		旋翼数量		旋翼直径	mm
飞行高度（距离作物冠层上部高度）		m		飞行速度	m/s
施药液量（脱叶剂＋催熟剂＋脱叶剂助剂）		L/hm^2	喷头流量	mL/min	
第一次药后 7 d 调查	脱叶率		吐絮率		
第二次药后 7 d 调查	脱叶率		吐絮率		
第二次药后 14 d 调查	脱叶率		吐絮率		
备注					

记录人：　　联系电话：

AGRICULTURAL STANDARD PUBLISHING RESEARCH CENTER

ICS 65.060.40
CCS B 91

NY

中华人民共和国农业行业标准

NY/T 4260—2022
代替 NY/T 1436—2007

植保无人飞机防治小麦病虫害作业规程

Operation code for wheat diseases and pests' control by crop protection UAS

纸质文本为正式版本
参考件

2022-11-11 发布　　2023-03-01 实施

中华人民共和国农业农村部 发布

前　言

本文件按照GB/T 1.1—2020《标准化工作导则　第1部分：标准化文件的结构和起草规则》的规定起草。

请注意本文件的某些内容可能涉及专利。本文件的发布机构不承担识别专利的责任。

本文件由农业农村部农业机械化管理司提出。

本文件由全国农业机械标准化技术委员会农业机械化分技术委员会(SAC/TC 201/SC 2)归口。

本文件起草单位：华南农业大学、安阳全丰航空植保科技股份有限公司、山东理工大学、安阳全丰生物科技有限公司、安阳工学院、国家航空植保科技创新联盟、农业农村部南京农业机械化研究所、中国农业科学院植物保护研究所、河南省植保植检站、安阳市植保植检站、淄博市数字农业农村发展中心、河南省农药检定站、拜耳作物科学(中国)有限公司、深圳市大疆创新科技有限公司、河北威远生物化工有限公司、先正达(中国)投资有限公司、北方天途航空技术发展(北京)有限公司。

本文件主要起草人：兰玉彬、王志国、薛新宇、袁会珠、李好海、刘越、蒙艳华、闫晓静、王国宾、陈盛德、张亚莉、周真、张朋飞、张廷琴、王刚、王朝阳、周玉红、梁自静、张国伟、杨涛、曹琼、赵建芹、王轩、齐枫、杨苡、孟香清。

出版纸质文本为准
参考件
联系电话010-59194426

植保无人飞机防治小麦病虫害作业规程

1 范围

本文件规定了应用植保无人飞机防治小麦病虫害的基本要求和作业流程。

本文件适用于植保无人飞机喷施农药防治小麦病虫害。

2 规范性引用文件

下列文件中的内容通过文中的规范性引用而构成本文件必不可少的条款。其中，注日期的引用文件，仅该日期对应的版本适用于本文件；不注日期的引用文件，其最新版本(包括所有的修改单)适用于本文件。

GB/T 17980.22 农药 田间药效试验准则(一)杀菌剂防治禾谷类白粉病

GB/T 17980.23 农药 田间药效试验准则(一)杀菌剂防治禾谷类锈病(叶锈、条锈、秆锈)

GB/T 17980.78 农药 田间药效试验准则(二)第78部分：杀虫剂防治小麦吸浆虫

GB/T 17980.79 农药 田间药效试验准则(二)第79部分：杀虫剂防治小麦蚜虫

NY/T 1276 农药安全使用规范总则

NY/T 1464.15 农药 田间药效试验准则 第15部分：杀菌剂防治小麦赤霉病

NY/T 3213 植保无人飞机 质量评价技术规范

3 术语和定义

下列术语和定义适用于本文件。

3.1

飞防助剂 adjuvants for UAS application

植保无人飞机施药作业中，添加在喷雾药液中具有抗飘移、促沉降等性能的辅助物质。

4 基本要求

4.1 人员

植保无人飞机运营人、操控员及所有参与施药的作业人员均应符合相关规定。

4.2 植保无人飞机

植保无人飞机应符合NY/T 3213的规定，并已直接或间接加入了政府主管部门批准的远程监管平台。

4.3 药剂

4.3.1 药剂应符合NY/T 1276的有关规定。根据病虫害抗性治理的原则，选择不同作用机理的农药交替轮换使用，合理混配。

4.3.2 在低稀释倍数下的农药稀释液应稳定，适合低容量喷雾或超低容量喷雾，且不会对小麦产生药害。多种药剂混配使用时，应当提前做预混配试验，避免药剂产生反应。

4.3.3 药剂有效成分的选择见附录A。

4.4 飞防助剂

飞防作业时，可选择添加飞防助剂。不同类型飞防助剂产品应按照标签要求使用，并保证对靶标作物安全，且与药液溶液有很好的兼容性，无分层、絮凝、沉淀等问题。

4.5 气象条件

应在无雨、少露、无雾，气温在5℃～35℃，风速＜5 m/s的天气下作业。

5 作业流程

5.1 作业前

5.1.1 勘察作业条件

作业人员在施药作业前，应充分调查作业区域及周边环境信息，综合评估本次施药作业的安全性。若喷洒区域周边 500 m 内且位于下风向存在以下安全隐患，不应作业：

——有其他作物、家畜、桑蚕、蜂类、渔类等农药敏感生物；

——有幼儿园、学校、医院等公共设施或人口稠密区；

——有水源地、河流、水库等。

5.1.2 调查病虫害发生情况

选择有代表性的小麦田地块，查明病虫害的发生种类、程度、面积和区域。综合考虑以下病虫害的混合发生与防治适宜期，确定防治时期，并结合病虫害实际发生情况，选择药剂组合。

小麦主要病虫害防治指标/条件及防治时期见表 1。

表 1 小麦主要病虫害防治指标/条件及防治时期

防治对象	防治指标/条件	防治时期
蚜虫 白粉病 锈病 红蜘蛛	百株蚜虫达 500 头 白粉病田间病叶率 5% 条锈病苗期病叶率 0.5%，叶锈病田间病叶率 5% 红蜘蛛每片叶不少于 10 头	返青拔节期
赤霉病 穗蚜 吸浆虫 白粉病 锈病	小麦扬花期遇高湿天气 百株穗蚜达 500 头 吸浆虫苗期淘土每平方米大于 5 头 白粉病田间病叶率 5% 条锈病苗期病叶率 0.5%，叶锈病田间病叶率 5%	穗期，扬花 10%时第一次施药，结合实际天气，7 天后根据情况进行第二次施药

5.1.3 制定作业方案

5.1.3.1 作业方案包括植保无人飞机作业参数制定、作业人员分工、药剂配制及作业安全事项等。

5.1.3.2 作业参数的制定应当综合考虑地块、天气、病虫害情况、植保无人飞机性能等因素，并结合植保无人飞机厂家的建议参数，选择合适的作业高度、作业速度和喷幅宽度。

5.1.3.2.1 作业参数的确定按公式(1)计算。

$$V=\frac{Q\times 10\ 000}{q\times D\times 60} \quad \cdots\cdots (1)$$

式中：

V ——飞行速度，单位为米每秒(m/s)；

Q ——喷头总流量，单位为升每分钟(L/min)；

q ——每公顷喷液量，单位为升每公顷(L/hm^2)；

D ——喷幅，单位为米(m)。

5.1.3.2.2 防治以下病虫害组合时，一般推荐作业参数符合表 2 的要求。

表 2 小麦田防治混合靶标病虫害时一般推荐作业参数

防治时期	防治对象	作业参数		
		作业高度[a]，m	作业速度，m/s	施药液量[b]，L/亩
返青拔节期	蚜虫、白粉病、锈病、红蜘蛛等	1.5～3.0	3～7	1.0～2.0
穗期	赤霉病、穗蚜、吸浆虫、白粉病、锈病等	1.5～3.0	3～7	1.5～2.0
[a] 植保无人飞机喷洒时距离作物冠层顶端的高度。 [b] 农药、助剂和水的量。				

5.1.4 配制药剂

应按照二次稀释法的要求进行药剂配制，配好的药液应现混现用。用带有搅拌装置的配药箱为植保无人飞机正常作业提供配药服务。步骤如下：

a) 称量药剂后，在混药桶中加入少量水，充分搅拌稀释成一定浓度的“母液”；

b) 配药桶中先注入1/4－1/3的水，分别将“母液”按照“先固体后液体”的顺序进行桶混，具体顺序为：固体肥料→水溶性粉剂→水溶性粒剂→水分散粒剂→水基悬浮剂→水溶性液剂→悬乳剂→可分散油悬浮剂→乳油→表面活性剂、油、助剂、液态肥料；

c) 用少量水清洗盛药器皿和包装至少3次，将清洗液倒入配药桶；

d) 根据施药液量，加水稀释至所需用量，充分搅拌均匀。

5.1.5 **调试机具**

5.1.5.1 确保植保无人飞机整机及辅助设备，包括电池、遥控器等配备齐全，并处于正常可使用状态。

5.1.5.2 校准喷头流量、飞行控制系统、标定点等。

5.1.6 **起降点与航线规划**

5.1.6.1 起降点应处于作业区域上风处，且周围视野开阔，无障碍物遮挡。

5.1.6.2 应综合考虑作业区域、天气条件、小麦病虫害情况等因素，合理规划航线。

5.2 **作业中**

5.2.1 作业人员添加清水开展模拟作业，以确保植保无人飞机适合喷洒作业。

5.2.2 植保无人飞机按照灌药、安检、起飞、喷洒、降落5个步骤开展循环操作作业，直至喷洒完成。具体步骤如下：

a) 将配药桶中配置好的药液通过灌药机自动灌装或通过漏斗手动灌装到植保无人飞机药箱。

b) 开展安全检查，以确保桨叶、机架固定牢固，无裂痕、损坏，确保电池、药箱固定牢固。接通动力电源，完成设备自检。

c) 选择作业模式，为保证作业质量，推荐采用全自主飞行模式。根据作业方案，设置作业参数。确保所有作业人员与机具保持15 m以上或参照生产企业说明书规定的安全距离，操作植保无人飞机起飞。

d) 开启喷洒系统，按照规划的航线执行喷洒，作业完成后，关闭喷洒系统。

e) 确保起降点无障碍物后，将机具返航至起降点，关闭电源。

5.2.3 若发生意外情况，应采取相应的应急处理措施。

5.2.3.1 若遇天气剧烈变化，应当立即停止作业，并将植保无人飞机返回起降点，等天气条件符合要求后再进行作业。

5.2.3.2 若喷洒系统故障时，应立即停止喷洒，并将机具返航至起降点，及时维修。

5.2.3.3 若发生信号干扰、人员闯入时，应酌情选择就地迫降或返航，避免发生事故。

5.2.3.4 若发生失控状况时，要及时提醒周边区域人员，紧急避让，并追踪失控无人机，直至落地。

5.2.3.5 若发生飞机摔机事故时，应检查飞机损坏程度。满足修理条件的，应修复试飞后继续作业；若不能及时修复，应更换备用机继续作业。

5.2.3.6 喷溅到身上的农药应立即清洗，如发生头昏、恶心、呕吐等中毒症状时，应及时采取救治措施，并向医院提供所用农药有效成分、个人防护等相关信息。

5.3 **作业后**

5.3.1 检查携带物品，避免遗漏及丢失。

5.3.2 填写田间喷雾情况及用药档案记录，见附录B。

5.3.3 植保无人飞机、废弃包装、剩余药液、作业人员、运输和存放等应按照有关规定执行。

5.3.4 作业质量可采用纸卡法或水敏纸法检查雾滴密度和雾滴密度分布均匀性进行评估。

5.3.5 应定期对作业区域防治效果进行调查、评估。蚜虫（包括穗蚜）、白粉病、锈病、吸浆虫、赤霉病的防治效果可按GB/T 17980.22、GB/T 17980.23、GB/T 17980.78、GB/T 17980.79、NY/T 1464.15的有关规定执行。

附 录 A
（资料性）
小麦主要病虫害防治常用药剂成分

小麦主要病虫害防治常用药剂成分参见表 A.1。

表 A.1 小麦主要病虫害防治常用药剂成分

防治对象	药剂中文通用名
蚜虫	吡虫啉、吡蚜酮、啶虫脒、呋虫胺、氟啶虫酰胺、高效氯氰菊酯、高效氯氟氰菊酯、联苯菊酯、氯虫菊酯、噻虫嗪、噻虫胺、溴氰菊酯
红蜘蛛	阿维菌素、联苯菊酯、哒螨灵
白粉病	吡唑醚菌酯、丙环唑、粉唑醇、氟环唑、环丙唑醇、己唑醇、甲基硫菌灵、腈菌唑、嘧菌酯、醚菌酯、咪鲜胺、氯啶菌酯、三唑酮、肟菌酯、戊唑醇、烯唑醇、烯肟菌胺
锈病	吡唑醚菌酯、丙环唑、啶氧菌酯、粉唑醇、氟环唑、环丙唑醇、己唑醇、嘧菌酯、噻呋酰胺、戊唑醇、申嗪霉素、烯唑醇
赤霉病	丙硫菌唑、多菌灵、粉唑醇、己唑醇、甲基硫菌灵、嘧菌酯、醚菊酯、咪鲜胺、咪鲜胺锰盐、氰烯菌酯、噻霉酮、肟菌酯、戊唑醇
纹枯病	苯醚甲环唑、丙环唑、氟环唑、木霉菌、己唑醇、井冈霉素、咪鲜胺、三唑醇、肟菌酯、戊唑醇

附 录 B
（资料性）
田间喷雾情况及用药档案记录

田间喷雾情况及用药档案记录参见表 B.1。

表 B.2 田间喷雾情况及用药档案记录

<table>
<tr><td colspan="2">作业地点</td><td colspan="2"></td><td colspan="2">作业时间</td><td colspan="2"></td></tr>
<tr><td colspan="2">作业人员</td><td colspan="2"></td><td colspan="2">飞机类型</td><td colspan="2"></td></tr>
<tr><td colspan="2">小麦生育期</td><td colspan="2"></td><td colspan="2">防治靶标</td><td colspan="2"></td></tr>
<tr><td colspan="8">小麦飞防用药名称及使用剂量</td></tr>
<tr><td rowspan="2">药剂名称</td><td>杀虫剂</td><td>杀菌剂</td><td>调节剂</td><td>助剂</td><td rowspan="2">总药剂量
mL</td><td colspan="2" rowspan="2">亩用水量
mL</td></tr>
<tr><td></td><td></td><td></td><td></td></tr>
<tr><td>药剂剂量</td><td></td><td></td><td></td><td></td><td></td><td colspan="2"></td></tr>
<tr><td colspan="8">施药过程中气象条件</td></tr>
<tr><td colspan="2">风向，°</td><td colspan="2">风速，m/s</td><td colspan="2">温度，℃</td><td colspan="2">相对湿度，%</td></tr>
<tr><td colspan="2"></td><td colspan="2"></td><td colspan="2"></td><td colspan="2"></td></tr>
<tr><td colspan="2">飞机载药量，L</td><td colspan="6"></td></tr>
<tr><td colspan="2">作业面积/亩</td><td colspan="2"></td><td colspan="2">个人防护设备</td><td colspan="2"></td></tr>
</table>

华南农业大学科学研究院

关于调整国家精准农业航空施药技术国际联合研究中心负责人的通知

各学院、部处、各单位:

根据《国家国际科技合作基地管理办法》（国科发外〔2011〕316号）的有关规定，经中心提名，依托单位推荐，决定对国家精准农业航空施药技术国际联合研究中心负责人进行调整，调整后的人员组成如下:

主　任: 兰玉彬　电子工程学院教授

副主任: 张亚莉　工程学院副教授

陈盛德　电子工程学院讲师

龙拥兵　电子工程学院教授

特此通知。

华南农业大学科学研究院

2022年7月23日

获 奖 证 书

CERTIFICATE OF AWARD

华南农业大学 代表队：

在第二十七届中国机器人及人工智能大赛全国总决赛中，表现优异，成绩突出，荣获 机器人应用赛（授粉机器人）

二等奖

团队成员：钟启超、程美娟、张钊珲

指导老师：张亚莉、贾瑞昌

特发此证，以资鼓励。

中国机器人及人工智能大赛组委会

二〇二五年八月

证书编号：CRAIC2025-NF-LJ7O6V

获奖证书

参赛院校：华南农业大学

参赛学生：郑依桐、陈泓儒、罗佳龙

指导老师：张亚莉

荣获"2025年睿抗机器人开发者大赛（RAICOM）全国总决赛"银龄守护适老化服务机器人创新竞赛项目三等奖。

特发此证，以资鼓励！

工业和信息化部人才交流中心

2025年10月31日

证书编号：IITCHJRAIC25026374

荣誉证书

2024 年第 21 届全国大学生信息安全与对抗技术竞赛

（智能安全赛-全国总决赛-植保机器人）

竞赛奖项：　二等奖

获奖成员：　钟启超　陈嘉奋　陈梓锋

获奖单位：　华南农业大学

指导教师：　张亚莉

中国兵工学会　北京理工大学

中国兵工学会信息安全与对抗专业委员会

NO.ISCC-USC-ZNAQ-NF-2024-2-87A　　0832　　2024 年 12 月 19 日

获 奖 证 书

CERTIFICATE OF AWARD

华南农业大学 代表队:

在第二十五届中国机器人及人工智能大赛全国总决赛中，表现优异，成绩突出，荣获 机器人应用赛（智慧农业）

二等奖

团队成员：徐文宇、李扬、陈彦学

指导老师：张亚莉、陈学深

特发此证，以资鼓励。

中国机器人及人工智能大赛组委会

二〇二三年六月

证书编号：CRAIC2023-NF-KM5R40

荣誉证书

CERTIFICATE OF ACHIEVEMENT

证书编号：CAAI-IRFCS-20250391

INTELLIGENT ROBOT FIGHTING AND GAMING COMPETITION（Student Competition）

2025 中国智能机器人格斗及竞技大赛（学生赛）

一等奖

获奖项目：智能机器人创新设计

参赛学校：华南农业大学

参赛队员：吴诗瑶 陈杰 陈嘉乐 林炳钿

队伍名称：西园战队

指导老师：张亚莉

领队：罗东宇

中国人工智能学会

2025 年 12 月 1 日

CADC
China Aeromodelling Design Challenge

中国国际飞行器设计挑战赛

暨科研类全国航空航天模型锦标赛

获奖证书

参赛项目 Competition item	创新竞赛
参赛单位 Team	华南农业大学
运动员姓名 Name	吴志坤 许绍聪 李大志
指导教师（教练） Supervisor	张亚莉 李继宇
项目名称 Event	模拟搜救
获奖名次 Award	二等奖
时间地点 Time & Place	辽宁 阜新 2021.10.09-19

国家体育总局航空无线电模型运动管理中心 1100000116321

中国航空运动协会 AERO SPORTS FEDERATION OF CHINA

荣誉证书

张亚莉老师在广东省“菱朗杯”第十届广东省汽车与农机电子环保大赛中指导学生成绩突出，被评为

优秀指导老师

特发此证，以资鼓励。

广东省电子学会 广东省汽车行业协会 广东省机械行业协会

广东省电子信息行业协会 广东省测量控制技术与装备应用促进会 广东省仪器仪表行业协会

2025 年 12 月 28 日

荣誉证书

张亚莉：

被评为华南农业大学2022-2024年度“十佳本科生班主任”。

特发此证，以资鼓励。

华南农业大学

二〇二五年六月

荣誉证书

张亚莉：

被评为华南农业大学2025年“七一”表彰优秀共产党员。

特发此证，以资鼓励。

中共华南农业大学委员会

2025年6月

验签二维码　证书编码：2025033094

国家航空植保科技创新联盟文件

国家航空植保科技创新联盟 [2023] 13 号

关于“智慧植保（北京）创新科技有限公司”作为“ 国家航空植保科技创新联盟”实体化机构的声明

为促进联盟长久持续发展，加强联盟运行机制，保障航空植保产业“产学研”一体化，积极响应农业农村部科教司及国家农业科技创新联盟的实体化工作要求，在国家航空植保科技创新联盟管理机构2022年4月8日年度会议、2023年4月4日年度会议和2023年6月30日理事会议的推动下，联盟实体“智慧植保（北京）创新科技有限公司”正式成立。此公司全权代表国家航空植保科技创新联盟用于开展联盟联合试验、学术会议、技术培训、技术推广、技术开发等航空植保相关的科学研究与行业服务工作。

特此声明！

联盟实体化机构具体信息如下：

单位名称：智慧植保（北京）创新科技有限公司

税号：91110108MACEY0J75X

单位地址：北京市海淀区东北旺西路58号院东侧C楼一层1074

开户银行：中国农业银行股份有限公司北京硅谷亮城支行

账号：11251401040006005

国家航空植保科技创新联盟

智慧植保（北京）创新科技有限公司

2023年7月25日

航空植保联盟管理机构

一、理事长单位及理事长：安阳全丰航空植保科技股份有限公司 王志国

二、常务副理事长单位及常务副理事长：华南农业大学 兰玉彬

三、副理事长单位及副理事长

农业农村部南京农业机械化研究所	薛新宇	中国农业科学院植物保护研究所	袁会珠
中国农业大学	何雄奎	北大荒通用航空公司	刘国驰
山东瑞达生态技术有限公司	谢春春	广州极飞科技有限公司	彭 斌
广西田园生化股份有限公司	李卫国	江苏克胜集团（蜻蜓农服）	吴成伟
农飞客农业科技有限公司	孔建强	深圳华越无人机技术有限公司	毛越东
深圳大疆创新科技有限公司	聂宏远	先正达（中国）投资有限公司	钟嘉颖

四、秘书长： 闫晓静

五、副秘书长：杨帅 刘越 宋坚利 张亚莉 张宋超 王国宾

国家留学基金管理委员会

留金美〔2024〕36号

关于确定2025年创新型人才国际合作培养项目资助项目的通知

华南农业大学:

经评审，国家留学基金管理委员会（以下简称国家留学基金委）现确定2025年创新型人才国际合作培养项目（以下简称创新项目）资助项目（见附件）。具体事宜通知如下:

一、项目单位承担获批项目执行、人员选派及管理工作的主体责任。

二、获批项目实施与管理、人选基本条件、人员选拔及录取、人员派出与管理等要求以当年度最新《创新型人才国际合作培养项目实施办法》为准。详情请参见国家留学网创新项目综合专栏。

三、本批次获批项目执行期为三年（2025-2027年），主要依托项目单位做好项目实施和管理工作。获批项目选派规模、选派类别、选派专业、留学国别、留学单位原则上不予调整。涉及学费资助的项目，学费资助类别与资助额度以本通知为准，后期不再调整。

四、创新项目依托项目单位获批项目进行人员选派，国家留学基金委不直接受理个人申请。创新项目录取人员均为国家公派出国留学人员，由国家留学基金提供资助，资助内容一般为一次往返国际旅费和资助期限内的奖学金。除本通知规定的学费资助类别外，其余类别人员不资助学费。

五、项目单位根据本通知及本单位制定的项目执行和管理办法，按照“公开、公平、公正”的原则，选拔符合条件的优秀人选。有多个国内参与单位的项目，由项目牵头单位组织参与单位开展人员选拔和管理等工作。项目推荐人员在进行国家留学基金委网申时，受理单位应选择项目牵头单位，并由项目牵头单位统一向国家留学基金委推荐。

六、2025 年人员申请网上报名及申请受理时间：第一批为 3 月 1-10 日；第二批为 9 月 1-10 日。项目单位须统一组织推荐人选在规定时间内登陆国家公派留学信息管理平台（http://sa.csc.edu.cn/student）进行网上报名。

项目单位承担所推荐人选申报资格及材料审核工作。项目单位应分别于 3 月 20 日（第一批）、9 月 20 日（第二批）前对推荐人选的申请材料进行认真审核，通过信息平台受理单位管理端（http://sa.csc.edu.cn/manager）为申请人填写具有针对性的单位推荐意见，并将单位推荐公函（须含单位内部公示链接及截图）、《推荐人员名单》等材料通过信息平台在线提交至国家留学基金委。具体要求请以当年人员申报通知为准。

工作中有任何情况和问题，请与国家留学基金委美大事务部联系。

联 系 人：冯喆芃（项目相关）/姜鹏（人员相关）

联系电话：010-66093974/3558

电子邮件：cxxm@csc.edu.cn

附件：2025年创新型人才国际合作培养项目资助项目列表

国家留学基金管理委员会

2024年12月26日

2025年创新型人才国际合作培养项目资助项目列表

项目单位	项目名称	申报类别	国内参与单位	留学国家	留学单位	选派专业大类	年度规模	留学身份及规模	学费资助内容
华南农业大学	精准农业航空应用技术国际化创新型人才培养项目	首次申报		澳大利亚、英国、法国、日本、韩国	昆士兰大学、哈珀亚当斯大学、法国国家农业食品与环境研究院、京都大学、国立全南大学	农业工程;农业工程	8	联合培养博士研究生4人/年、高级研究学者2人/年、访问学者2人/年	无

创新型人才国际合作培养项目

申 请 书 模 板

（供上传至系统中使用）

项 目 名 称：	精准农业航空应用技术国际化创新型人才培养项目
申 报 情 况：	☐执行满三年 ☑首次申报
申 报 单 位：	华南农业大学
专 项 类 别：	“双一流”建设高校
执 行 年 份：	2025-2027
国内参与单位：	无
项 目 负 责 人：	张亚莉
联 系 电 话：	Email：ylzhang@scau.edu.cn
校内主管部门及联系人：	研究生院 陈华全
联 系 电 话：	020-85280856 Email：pyk@scau.edu.cn
申 报 日 期：	2024 年 10 月 16 日

一、基本情况

是否交叉学科	是
申报项目学科门类	工学、农学
合作国别	澳大利亚、英国、法国、日本、韩国
年度选派总规模	8 人/年
留学身份及选派规模	☐攻读博士学位研究生 _____人/年 ☑联合培养博士研究生 __4__人/年 ☐攻读硕士学位研究生 _____人/年 ☐联合培养硕士研究生 _____人/年 ☑高级研究学者 __2__人/年 ☑访问学者 __2__人/年 ☐博士后 _____人/年 ☐本科插班生 _____人/年

选派专业	
选派专业大类 **（如系统中无该专业请选择相近专业）**	选派专业小类 **（如系统中无该专业请选择相近专业）**
农业工程	农业机械化与装备工程
农业工程	农业电气化与信息化工程

留学单位		
留学国别	留学单位（英文）	留学单位（中文）
澳大利亚	University of Queensland	昆士兰大学
英国	Harper Adams University College	哈珀亚当斯大学
法国	National Research Institute for Agriculture, Food and the Environment	法国国家农业食品与环境研究院
日本	Kyoto University	京都大学
韩国	Chonnam National University	国立全南大学

申请学费资助额度				
留学身份	留学国别	留学单位(英文)	留学单位(中文)	申请资助学费

二、项目简介

培养目标 (通过国际合作，为哪些行业、领域或部门培养何种特定人才)	华南农业大学是国家**双一流建设高校**，农业工程学科为广东省攀峰重点一级学科及广东省高水平建设一级学科，拥有华南农业大学获批的首个国际联合研究中心**“国家精准农业航空施药技术国际联合研究中心”**，和首个高等学校学科创新引智计划（111 计划）项目**“精准农业航空应用技术研究学科创新引智基地”**，国内第一家省级农业航空技术研究中心“广东省农业航空应用工程技术研究中心”，广东省科技厅“国际农业航空施药技术联合实验室”，广东省教育厅“农业航空应用技术国际联合实验室，3 个国家现代农业产业技术体系研究室（柑橘、甘蔗、荔枝龙眼），农业工程国家级实验教学示范中心和 5 个广东省实验教学示范中心。 华南农业大学**农业工程学科**是国内较早开展精准农业以及农业航空应用技术研究的单位，精准农业航空相关研究居国内领先地位并达到国际先进水平，具有扎实的国际科技合作基础。本学科申报精准农业航空应用技术国际化创新型人才培养项目，拟与澳大利亚、英国、法国、日本、韩国等五所**国外合作高校开展联合培养博士研究生、高级研究学者和访问学者的项目**，将有力促进**以精准农业航空为特色**的华南农业大学农业工程学科人才培养。 **联合培养博士研究生**的培养目标是，培养具有国际竞争力的高层次学术创新人才，提升华南农业大学农业工程学科国际化人才培养质量，推动精准农业航空产业和农业工程技术进步。本项目围绕高素质创新型人才培养目标，将拓展学生的全球化视野，培养学生的国际交往能力，提高学生的综合素质，为我国农林类高校、国内大型涉农企业以及精准农业航空产业的发展着力培养一批**“复合型、高层次、国际化”**优秀人才。 对于派出国外研修的**高级研究学者/访问学者**培养目

	标是，提升华南农业大学农业工程一级学科师资队伍国际化水平，加快培养和引进一批具有国际视野、擅长国际交往与合作、具有国际学术影响力的**“高端化、年轻化、国际化”**师资队伍，提高承担重大国际科技合作项目的能力，并要求完成学业归国以后开设双语/全英文教学课程。
培养模式 (创新点)	华南农业大学农业工程学科依托国家精准农业航空施药技术国际联合研究中心和精准农业航空应用技术研究学科创新引智基地（111 基地），开展精准农业航空应用技术国际化创新型人才培养。针对国内主要粮食作物生产中存在的施药技术与器械落后而导致农药有效利用率低、过量施用和对环境污染严重等问题，围绕**“精准农业航空”技术理念**，基于遥感数据分析的精准/变量施药技术内涵，本学科紧密结合国内农业航空产业界发展的需求，立足实践，与国外合作高校联合培养**以产业化需求为导向的精准农业航空应用技术国际化创新型人才**。 本项目与澳大利亚昆士兰大学农药应用和安全中心、英国哈帕亚当斯大学（英国国家精准农业研究中心）、法国国家农业食品与环境研究院(INRAE)、日本京都大学地域环境工学科、韩国国立全南大学农业机器人与自动化研究中心等国外顶尖的农业航空应用技术研究机构，共同开展农业航空遥感、航空精准变量喷雾等相关技术及装备的创新研究，培养具有国际视野的高水平人才。通过项目实施，引进国外先进理念，与国内外农业航空产业界建立紧密的合作关系，大力促进精准农业航空技术在我国实现深度应用与示范推广。

三、项目负责人简介

姓名	张亚莉	姓名拼音	ZHANG YALI
所在单位	华南农业大学		
所在院系所	工程学院		
职称	副教授		
行政职务	农业工程系副主任 国家精准农业航空施药技术国际联合研究中心副主任		
毕业学校	美国堪萨斯州立大学		
最高学位	博士		
学位授予国别	美国		
学位授予地区	堪萨斯州		
授予年份	2009		
授予学校	美国堪萨斯州立大学		
学科专业大类	农业工程		
学科专业小类	农业电气化与信息化工程		
具体研究方向	精准农业航空应用技术		
近五年主要科研成果概述	美国堪萨斯州立大学生物与农业工程系博士毕业。现为华南农业大学工程学院副教授，农业工程系副主任，国家精准农业航空施药技术国际联合研究中心副主任，国家航空植保科技创新联盟副秘书长，《国际精准农业航空学报》执行主编，联合国粮农组织数字农业焦点组应用案例与解决方案工作组术语标准组主席。主持“十四五”国家重点研发计划课题、国家自然科学基金、广东省重点研发计划、广东省国际科技合作项目等 10 余项课题，发表论文 40 余篇，授权专利 20 余件。参与制定农业部行业标准 1 项，获第十二届大北农科技奖 1 项，主要从事农用无人机避障、仿地飞行技术以及基于		